



AGARD-CP-489

AGARD-CP-489

AD-A226 987

AGARD

ADVISORY GROUP FOR AEROSPACE RESEARCH & DEVELOPMENT

7 RUE ANCELLE 92200 NEUILLY SUR SEINE FRANCE

AGARD CONFERENCE PROCEEDINGS No.489

Space Vehicle Flight Mechanics

(La Mécanique du Vol des Véhicules Spatiaux)

Approved for public release;
Distribution Unlimited

DTIC
ELECTE
SEP 25 1990
E D

NORTH ATLANTIC TREATY ORGANIZATION



DISTRIBUTION AND AVAILABILITY
ON BACK COVER

90 09 21 065

NORTH ATLANTIC TREATY ORGANIZATION
ADVISORY GROUP FOR AEROSPACE RESEARCH AND DEVELOPMENT
(ORGANISATION DU TRAITE DE L'ATLANTIQUE NORD)

AGARD Conference Proceedings No.489

Space Vehicle Flight Mechanics

(La Mécanique du Vol des Véhicules Spatiaux)



on For	
DAI	<input checked="" type="checkbox"/>
ED	<input type="checkbox"/>
ed	<input type="checkbox"/>
ication	
Distribution/	
Availability Codes	
Dist and/or	
Dist	Special
A-1	

DISTRIBUTION STATEMENT A
Approved for public release;
Distribution Unlimited

Copies of papers presented at the Flight Mechanics Panel Symposium
held in Luxembourg from 13th to 16th November 1989.

The Mission of AGARD

According to its Charter, the mission of AGARD is to bring together the leading personalities of the NATO nations in the fields of science and technology relating to aerospace for the following purposes:

- Recommending effective ways for the member nations to use their research and development capabilities for the common benefit of the NATO community;
- Providing scientific and technical advice and assistance to the Military Committee in the field of aerospace research and development (with particular regard to its military application);
- Continuously stimulating advances in the aerospace sciences relevant to strengthening the common defence posture;
- Improving the co-operation among member nations in aerospace research and development;
- Exchange of scientific and technical information;
- Providing assistance to member nations for the purpose of increasing their scientific and technical potential;
- Rendering scientific and technical assistance, as requested, to other NATO bodies and to member nations in connection with research and development problems in the aerospace field.

The highest authority within AGARD is the National Delegates Board consisting of officially appointed senior representatives from each member nation. The mission of AGARD is carried out through the Panels which are composed of experts appointed by the National Delegates, the Consultant and Exchange Programme and the Aerospace Applications Studies Programme. The results of AGARD work are reported to the member nations and the NATO Authorities through the AGARD series of publications of which this is one.

Participation in AGARD activities is by invitation only and is normally limited to citizens of the NATO nations.

The content of this publication has been reproduced directly from material supplied by AGARD or the authors.

Published June 1990

Copyright © AGARD 1990
All Rights Reserved

ISBN 92-835-0567-0



Printed by Specialised Printing Services Limited
40 Chigwell Lane, Loughton, Essex IG10 3TZ

Preface

In the last thirty years we have seen a great increase in both manned and unmanned space flights for scientific studies, for communication and navigation, and for military purposes such as surveillance, reconnaissance and as a possible area of deployment for both offensive and defensive weaponry.

The possible uses of flight at near-space conditions (i.e. above about 150,000ft.) are also under consideration and, at these heights, many of the technical problems have a common basis with those of space vehicles during the launch, recovery and transatmospheric phases.

In all these areas, many problems remain only partly resolved and the relevant technologies are developing rapidly. It was considered that resolution of these problems and finding ways of using new technologies would benefit from the combined thought of the technology communities of the NATO nations. A symposium sponsored by the Flight Mechanics Panel of AGARD was seen as a timely forum for discussions on at least the flight mechanics aspects of this important topic.

The symposium included the control and trajectory aspects of launch and recovery, in-orbit dynamics, trans-atmospheric flight and the dynamic aspects of assembly and operation in space and also covered simulation and flight test.

Avant-Propos

Au cours des trente dernières années nous avons assisté à un nombre croissant de vols spatiaux, habités et non habités, effectués soit dans le cadre d'études scientifiques, soit aux fins des télécommunications et de la navigation, soit pour des raisons militaires telles que la surveillance et la reconnaissance ainsi que le déploiement éventuel d'armes offensives et défensives.

Les applications possibles du vol dans des conditions quasi-spatiales (c'est à dire au-dessus de 150,000 pieds) sont également à l'étude, et il s'avère que bon nombre des problèmes techniques rencontrés à ces altitudes sont comparables à ceux des véhicules spatiaux lors des phases de lancement, récupération et de passage transatmosphérique.

Dans tous ces domaines, il existe des problèmes qui ne sont résolus que partiellement, tandis que les technologies en question sont en pleine expansion. De l'avis du Panel, une réflexion commune sur ce sujet, entreprise par la communauté technologique des pays membres de l'OTAN porterait ses fruits pour ce qui concerne la recherche d'applications des nouvelles technologies et la résolution de ces problèmes. Le Panel AGARD de la Mécanique du Vol a donc décidé d'organiser un Symposium, afin de permettre tout au moins la discussion des aspects mécanique du vol sur ce sujet important.

Le Programme du Symposium comprend les aspects de contrôle et de trajectoire des phases de lancement et de récupération, la dynamique en orbite, le vol transatmosphérique, les aspects dynamiques d'assemblage et d'exploitation dans l'espace, ainsi que la simulation et les essais de vol.

Flight Mechanics Panel Officers

Chairman: Mr R.C.A'Harrah
O.C.N.R.
Code OOJDL
800 N Quincy Street BCT/1
Arlington
Virginia 22217-5000
United States

Deputy Chairman: ICA J.-M.Duc
Commission des Communautés Européennes
DG 12-H
Rue de la Loi, 200
B-1049 Brussels
Belgium

TECHNICAL PROGRAMME COMMITTEE

Mr J.Levine
Director
Flight Projects Division
OAST
NASA Headquarters
Mail Code RX
Washington, DC 20546
United States

Mr J.-P.Marec
Directeur pour les
Applications Aéronautiques
ONERA
29, Avenue de la Division Leclerc
92320 Chatillon-sous-Bagneux
France

HOST NATION COORDINATOR

Mr F.Kirch
Ministère de la Force Publique
Plateau de St. Esprit
L-1475 Luxembourg

PANEL EXECUTIVE

Mr M.K.Foster
Flight Mechanics Panel
AGARD/NATO
7 rue Ancelle
92200 Neuilly-sur-Seine
France

ACKNOWLEDGEMENT

The Flight Mechanics Panel wishes to express its thanks to the National Authorities of Luxembourg for the invitation to hold this meeting in Luxembourg, and for the facilities and personnel which made the meeting possible.

Le Panel du Mécanisme du Vol tient à remercier les Autorités Nationales du Luxembourg pour leur invitation à tenir cette réunion au Luxembourg ainsi que des installations et du personnel mis à sa disposition.

Contents

	Page
Preface/Avant-Propos	iii
Panel Officers	iv
	Reference
Keynote Address by J.A.van der Blik	K1
Keynote Address by K.Doetsch	K2
Flight Control Issues of the Next Generation Space Transportation Launch Vehicles by R.W.Powell, J.C.Nafel and C.I.Cruz	3
Ascent and Descent Trajectory Optimization of Ariane V/Hermes by C.Jänsch, K.Schnepfer and K.H.Well	4
Advanced Launch Vehicle Configuration and Performance Trades by P.R.Gord, K.J.Langan and M.E.Stringer	5
Possible Trajectory Profiles to Achieve the Geostationary Orbit without Any Drift Phase by G.Vulpetti	6
Reentry Trajectory Optimization and Control by P.Strohmaier, A.Kiefer, D.Burkhardt and K.Horn	7
Trajectoires de Sauvegarde au Lancement d'Hermes. Consequences sur la Trajectoire d'Ariane 5. par Ph.Delattre et A.Wagner	8
Space Shuttle Descent Flight Verification by Simulation: A Challenge in Implementing Flight Control System Robustness by V.H.Nguyen, J.T.Nishimi, T.H.Payne and E.W.Woosley	9
Une Introduction aux Trajectoires Spatiales par J.-P.Marec	10
Calcul d'Orbites par P.Exertier, P.Sengenes et G.Tavernier	11
Optimisation de la Mise a Poste d'un Couple de Satellites sur des Orbites Geosynchrones, Excentriques et Inclinees par J.Bouchard et C.Aumasson	12
Noncoplanar Orbit Transfer Optimization for an Aeroassisted Sortie Vehicle by H.A.Karasopoulos and R.B.Norris	13
Hermes Rendez-Vous with the Space Station by M.Caldichoury, C.Champetier and E.Desplats	14
Spacecraft Attitude Dynamics: Evolution and Current Challenges by V.J.Modi	15
A Model of the Perturbed Spinning Motion of the San Marco 5th Spacecraft by C.Arduini, G.La Neve, D.Mortari and A.de Micco	16

	Page
The Instrument Pointing System — Precision Attitude Control in Space by R.Hartmann and A.Woelker	17
Flexible Structure Control and Rigid Body Dynamics by V.B.Venkayya	18
Dynamics and Dynamics Experiments in TSS-1 by S.Bergamaschi	19
National Aero-Space Plane — Flight Mechanics by D.E.McIver and F.R.Morrell	20
Optimal Trajectories for Sänger-Type Vehicles by G.Sachs, R.Bayer and J.Drexler	21
Ascent and Descent Optimizations of an Air-Breathing Launch Vehicle by S.G.Furniss and I.M.Walters	22
Paper 23 withdrawn.	
Global Optimization of Air Breathing Launch Vehicle Trajectories by F.Martel	24
The Challenge of Assembling a Space Station in Orbit by V.D.Brand	25
In-Space Construction and Dynamics of Large Space Structures by M.M.Mikulas, Jr.	26
A New Method for a Tethered System Aided Space Station Assembly by S.Ciaro and S.Bergamaschi	27
Deployment of Large Flexible Space Structures by M.Gérardin, A.Cardona and D.Granville	28
The Dynamics of Orbital Maneuvering: Design and Evaluation of a Visual Display Aid for Human Controllers by S.R.Ellis and A.J.Grunwald	29
Effects of Low Bond Number Liquid Motions on Spacecraft Attitude by J.P.B.Vreburg and R.F. van den Dam	30
Flexible Space-Based Robot Modelling and Real-Time Simulation by J.I.M.Prins, P.Dieleman and P.Th.L.M.van Woerkom	31
Flight Mechanics Applications for Tethers in Space: Cooperative Italian-US Programs by F.Bevilacqua, P.Merlina and J.L.Anderson	32
Testing DOD Space Systems: The Challenge by W.A.Wisdom and L.C.Keel	33

KEYNOTE ADDRESSFMP Symposium "Space Vehicle Flight Mechanics"
13-16 November 1989, Luxembourg

Jan A van der Blik,
Director, AGARD,
7 rue Ancelle
92200 Neuilly sur Seine
France

1. INTRODUCTION

It was the intention of the organisers to start this Symposium with two Keynote Addresses: presenting the European and the North American situation. I was to present the European situation and possibly the European point of view. However, even if I were in a position to do that I would, as AGARD Director, rather concentrate on the opportunities for transatlantic cooperation in the area of technology within NATO and AGARD. There are indeed tremendous opportunities for transatlantic cooperation in the 1990s and beyond.

Until recently specific space technology subjects were a relatively small part of AGARD's activities. Nevertheless, long before the meaning of the second A in AGARD was changed from "Aeronautical" to "Aerospace" in 1965, space-related subjects were part of the AGARD Programme. For instance, during the Ninth General Assembly meeting in 1959 a round table discussion was held on "Space Research Techniques and Recent Experimental Data". Also from time to time the Panels organised Symposia on space-related subjects.

There is, of course, no clear border line between aeronautical and space technology and many subjects treated by the FMP over the years have applications to both. However, this is the first FMP Symposium fully dedicated to space subjects. The five selected Session Headings: Launch and Recovery, In-orbit Dynamics, Transatmospheric Flight, Dynamic Aspects of Assembly and Operation in Space, Simulation and Flight Test, obviously cannot, in the limited time available, cover all aspects of current interest.

One of the results of this Symposium may be a clear identification of technical-scientific areas in which the FMP can further contribute to the development of space vehicles and their operation. The interest is high among scientists and engineers

within the Alliance on both sides of the Atlantic. The prospects for transatlantic cooperation in selected areas of space technology are good. As an indication of the current direct involvement of AGARD Panels in space technology, Table I lists the titles of Symposia and Lecture Series dedicated to space during the years 1988-1990. It is about 10 per cent of our activities over these years, but nevertheless it is significant.

Space transportation systems have recently received increased attention. Research and development, being carried out in several countries, may ultimately lead towards fully re-usable one- or two-stage vehicles capable of going to a low-earth orbit and returning to earth. More so than in aeronautics, this calls for a very high degree of integration of disciplines such as: hypersonics, flight mechanics, flight control, avionics, structures, materials, propulsion and propulsion aerodynamics and human engineering.

2. SPACE TRANSPORTATION SYSTEMS

Space flight became a reality after the development of rocket engines and guidance systems. Space flight has been carried out by means of single and multi-stage rocket launchers since 1957. The launchers were not recovered. It is only recently, beginning with the NASA shuttle transportation system that part of the transportation system has become recoverable.

Expendable launchers are now well developed. A further increase in efficiency and reduction of the cost will undoubtedly take place during the coming decades. Thousands of payloads have been launched into space with rockets and an enormous experience exists in the various launching organizations. Nevertheless, the payload that can be launched into, say a 300 km orbit is only a few per cent of the total lift-off mass.

This is illustrated by Figure 1 (from Ref. 1) where the mass fraction delivered to a low-earth

orbit is given as a function of the total take-off mass. Although this fraction increases up to 6 per cent for the NASA Orbiter for a take-off mass of about 2000 tons, and an orbiter mass of 120 tons, the mass fraction related to the actual cargo carried by the orbiter, up to 29 tons, is still only up to 1.5 per cent.

The structure of a rocket launch vehicle is typically of the order of 10 per cent of the lift-off mass and the mass of the fuel close to 90 per cent.

The ultimate, ideal vehicle to transport payloads back and forth to, say a 300 km orbit, is undoubtedly a space plane which can take off and land at several more or less conventional airports. Four of the major advantages of such a transportation system are:

- First, a reduction in launch costs through the re-use of the vehicle; the aim is an order of magnitude improvement compared to conventional launchers. Typically, the launch cost should become of the order of hundreds of dollars per kg payload as compared to thousands of dollars per kg for conventional rockets. Actually real cost figures are difficult to obtain since the research and development are usually not taken into account and there are a variety of factors influencing the pricing policy of the launch organizations.

- Second, less mass left in orbit; during the first decades of space flight the debris left in orbit was not a serious problem, but as the use of space increases, particularly at certain favoured orbits, an international agreement will be required not to leave any debris behind in near-earth or geostationary orbits.

- Third, a reduction of the launching loads on the payload due to severe acceleration and hence a simplification of the construction of the payloads and a reduction of the cost.

- Fourth, a considerable increase in the payload since during part of the flight airbreathing engines could be used, reducing the requirement of carrying all the oxygen required for combustion as with the conventional rocket.

Of the various proposals for re-usable launchers made over the years, there are at present at least four concepts being pursued. Figure 2 (from Ref. 2) shows these as possibly being

available early in the 21st century. The figure also shows the systems that could be operational between now and 2010.

Returning to the present: the only partially re-usable system in operation is the NASA Space Transportation System, the Shuttle. An enormous experience has been gained with the system. NASA is studying extensions of the shuttle system and also a booster series with a payload of up to five per cent of the total mass.

On 15 November 1988 the USSR launched the Buran, a Russian version of the NASA Shuttle, with the Energia booster. The vehicle was unmanned and ground controlled. It made orbital flights and an automatic landing. Although this flight appeared to be successful, the Russian cosmonaut Igor P Volk, who had flown 18 of the 24 atmospheric flights with the Buran, said in May 1989 at the AIAA Annual Meeting that the second unmanned flight was planned in late 1990 and that the first manned flight would probably not take place before 1992. He also said that there are at present seven Buran pilots. The Buran vehicle was on display at the Paris Air Show in June 1989, mounted on top of the six-engine AN-225 transport plane and this combination was demonstrated in flight. Obviously the Russian developments of re-usable launch vehicle follow the developments in the USA, in spite of the fact that the present USSR launches far exceed that of the rest of the world, both numerically and in total mass. It seems that the development of re-usable transportation systems in the USSR trails the developments in the USA by almost a decade.

The Hermes Space Shuttle, to be launched by the Ariane V launcher was conceived by the French space organization, CNES. It is now incorporated in the programme of the European Space Agency, ESA, and at the ESA Ministerial Conference in November 1987 in The Hague US \$ 600 million was committed to the first phase of the design and development programme. Recently major design changes were introduced. The total mass was increased from 15 to 24 tons with a crew of three. Hermes is meant to serve the international space station Columbus and the projected man-tended free flyer (MTFF) but possibly the USSR MIR Space Station also.

Initially up to 12-day missions are foreseen. The mass of Hermes at landing is projected to be 15 tons

with the resource module, the docking module and the propulsion unit to be discarded. Hermes will have a crew escape system. The remotely-controlled manipulator, the Hermes Arm, HERA, originally planned to be part of the vehicle will now become expendable or attached to the Columbus space laboratory.

The mass of Hermes is about one-fifth of that of the NASA shuttle orbiter. The maximum re-entry temperature will be 1830°C , that is 300°C higher than that of the Shuttle. The first manned flight is expected to take place around the year 2000.

The concept of the fully re-usable space plane is credited to Eugen Sanger (1905 - 1964). His idea was that space flight should ultimately be achieved via an aircraft type vehicle rather than via rockets as pioneered by Ziolkowsky, Goddard, Obert and others. In cooperation with Irene Bredt, who he later married, he produced a study in 1942 which basically outlined this concept. The USAF/Boeing X-20 Dyna-Soar project, a delta-winged vehicle, to be launched by a rocket and to return to earth as a glider, was the first step in that direction. Unfortunately this project was cancelled at the end of 1963. The next step was the NASA Space Transportation System. Originally the system was conceived as a two-stage vehicle with a winged re-usable first stage which could land at an airfield. The NASA shuttle finally became the rocket-assisted-take-off vehicle as we know it.

The present concepts of the fully re-usable space planes are indicated in Figure 2.

There is at present a five-year systems definition study being carried out in Germany, for this two-stage fully re-usable space transportation system. The first stage vehicle, called Sanger, will boost a second stage called HORUS, a manned 90 ton vehicle, to an altitude of 35 km at Mach number of seven or, alternatively a second stage called CARGUS, an expendable rocket stage for cargo transport to space. It is envisaged that the first stage will have commonality with a global hypersonic transport plane for typically 250 passengers to be carried over a distance of 10,000 kilometres or more.

The British concept, HOTOL, is a single-stage, horizontal take-off and landing vehicle. It is unmanned in its primary role of satellite launch. Manned capability, when required, is provided by a capsule placed in the payload bay. The engine is a dual

mode cycle combining a heavily pre-cooled cycle for the airbreathing ascent, converting to conventional rocket power for the final ascent to orbit. The project is currently continuing on BAE private funding.

In Japan several space-plane concepts are being studied resembling the HOTOL concept and the American X-30 designs.

There is little doubt that the greatest efforts towards the development of a space plane are being made in the USA. The first single stage-to-orbit flight of the US X-30 is expected to take place in the late 1990s. Technical and funding problems make it almost impossible to predict an operational date.

3. HYPERSONICS

The key to the development of re-entry vehicles and re-usable transportation systems is the development of adequate knowledge of hypersonics. Hypersonics, flight at Mach numbers greater than 5, was developed in the 1950s and 60s. Major projects were:

- Ballistic re-entry vehicles from speeds up to 8 km/sec
- The USAF project Dynasoar, a delta-winged vehicle launched by a rocket, cancelled in 1963
- The NASA projects Mercury and Gemini
- The NASA project Apollo
- The NASA Space Shuttle Transportation System.

Figure 3 gives the flight regimes in an altitude velocity diagram. Note that the energy per unit mass to be absorbed before landing on earth when returning from a lunar flight (10-11 km/sec) is 80 per cent higher than when returning from a low earth orbit (say 300 km). The figure also indicates that projects like HOTOL (and the space plane) are aiming at a higher lift (higher L/D) and greater cross range.

Typical velocity differences of interest are given in Figure 4. Note that $\Delta v_{\text{moon} \rightarrow \text{earth}} = 8.2 + 3.9 + 1.6 = 13.7 \text{ km/sec}$ and $\Delta v_{\text{GEO} \rightarrow \text{earth}} = 8.2 + 4.3 = 12.5 \text{ km/sec}$. The escape velocity is only slightly higher.

Hypersonics is characterised by the fact that the shock angle is very small. There is a "merged shock-boundary layer" near the body, the shock stand-off distance is of the order of one tenth of the nose radius. Gas temperatures in the stagnation region become several thousands degrees Kelvin. The gas will dissociate, several

chemical reactions occur and radiation becomes important in the stagnation region, Figure 5.

Figure 6 indicates the regions where these effects take place.

All the phenomena associated with these flight conditions were studied in great detail in the 1950s and 1960s. Then there was a period of twenty years with greatly reduced activities. The resurgence of interest in hypersonics in the 1980s took place in a period with a greatly reduced number of hypersonic windtunnel facilities operational and a greatly increased capability in computational fluid mechanics. In several AGARD publications (References 3, 4 and 5) this situation was recognized. A new generation of scientists and engineers took over, hopefully just in time to benefit from the experience gained in the 1950s and 60s.

4. PROPULSION

If hypersonics is the key to the development of re-entry and re-usable transportation systems, propulsion is certainly the key to the development of a space plane. The word space plane is used here generically for vehicles capable of flying to a low-earth orbit, with or without take-off assistance and return to earth landing on an airfield.

The X-30/NASP (National Aero-Space Plane) studies being carried out by three contractors in the USA (McDonnell-Douglas, General Dynamics and North American Rockwell) are reported to include various modes of propulsion:

- for $M < 4.5$ subsonic combustion
- for $M > 6$ supersonic combustion

In the range $4.5 < M < 6$ presumably a mixed subsonic/supersonic combustion takes place. All proposals incorporate rocket engines, but of different sizes.

The system proposed for the German Sänger project is different in that it consists of two stages. The first stage is to fly up to $M=7$ at an altitude of 35 km and being propelled by a subsonic/supersonic combustion system, a turbo-ramjet engine, while the second stage is planned to be rocket-propelled. The first stage would basically use the technology that could be applied to a hypersonic, transcontinental or transatlantic transport plane (the "Orient Express").

The British HOTOL concept would use an airbreathing engine with variable inlet geometry, converting to H₂/O₂ rocket propulsion above $M=5$. Eventually the ramjet/scramjet (supersonic combustion ramjet) may be developed to operate at Mach numbers considerably higher than 7; goals of $M=15$ and higher have been reported in the press. This would require enormous frontal capture areas (~100 per cent) and relatively low altitudes in order to capture a sufficient air mass to produce the required thrust at these Mach numbers. It is clear that here is an area for much research and development of imaginative concepts.

5. STRUCTURES AND MATERIALS

During re-entry the amount of energy to be dissipated is typically 30 million Joule per kg mass, well above the heat of vaporization of all materials. For a vehicle of 20 tons re-entering from an altitude of 150 km at a speed of 8000 m/sec this amounts to 6.8×10^{10} Joule. Fortunately only a small portion, of the order of 0.05 to 0.1 per cent is absorbed by the vehicle but nevertheless stagnation temperatures of 1000 to 1800° C will occur over periods of 10 minutes or more. The use of metallic materials is generally limited to about 1000° C. Ceramic materials can stand a much higher temperature but their incorporation as structural elements is very difficult. The NASA Space Shuttle solution of tiles for thermal protection is well known and apparently the Buran uses the same idea for thermal protection. It is likely that some of the ceramic materials and possibly carbon/carbon material with a protective layer will be developed to such a stage that they can be applied in spacecraft structures in the 1990s and beyond.

Finally, a fully re-usable space plane must be able to take off and land at an airfield. Present day civil transport aircraft have landing speeds of about 250 km/hour (155 mph) and typically need a landing field length of 2000 m. For most modern fighter aircraft these figures are much the same.

The NASA Space Shuttle has a nominal landing speed of 335 km/hour and it is reported that a landing speed of 420 km/hour has been demonstrated. It is also reported that the tires could stand a speed of 560 km/hour but they could only be used once. Apparently the US space plane and Sänger aim at landing speeds of 500 km/hr or

more. This would mean a 50 per cent increase compared to the proven NASA Space Shuttle landing speed and the kinetic energy per unit mass at landing would be 2.25 times as much. This is indeed a formidable challenge.

6. CONCLUDING REMARKS

Only some of the technical-scientific areas associated with the development of space transportation vehicles have been mentioned. There are many other subjects such as flight control and human engineering which are of equal importance for the successful realization of space transportation systems.

In the 1970s the European goals were mainly concentrated on the development of a reliable expendable launcher system, the Ariane Series. The European contribution to the NASA Shuttle Programme was limited to the development of Spacelab, a payload of the shuttle. Unfortunately only a few spacelab flights have been carried out so far. With the advent of the Ariane V - Hermes system a much broader technology base is being built up in Europe. This does not yet open up all the relevant technology areas for full cooperation and information exchange within AGARD. However it is quite possible that in the 1990s several of the concepts now being developed in various nations, will merge into a single series of space transportation systems. The main reasons for this would be the necessity to share the development costs and the sheer necessity to pool all the available talent and the facilities available to solve the technical problems. The individual nations (or combined, as in ESA) must however, develop a strong enough technology base for cooperation on an equal footing, at least in selected areas.

The following quotations from a report of the US Defense Department's Science Board (DSB), published in Reference 6, are an indication of the magnitude of the problems involved in developing the National Aerospace Plane. The article states that the DSB was essentially supportive of the NASP Programme. The Task Force Members were "impressed with the progress being made. But we were even more impressed by what has yet to be done to reduce the remaining uncertainties to a reasonably manageable level". Some of the chief anxieties were as follows:

Aerodynamics - The "largest uncertainty" is the location of the transition point between laminar and turbulent air flow. This affects engine performance, structural heating and drag, to the extent that there is an "uncertainty factor" of two or more in estimates of gross take-off weight. Computational fluid dynamics cannot yet resolve all such problems, especially when dealing with three-dimensional flows, because of lack of real-world experimental data for calibration. It is important that CFD should not be discredited on this account. But ground test facilities that might provide valid data for Mach numbers between 10 and 20 do not yet exist.

Propulsion system design - This is also hampered by the same uncertainty about NASP airflow dynamics. The transition point from ramjet to supersonic scramjet operation is likely to be the most critical phase of flight. Very little is known about the mixing and combustion of hydrogen at high supersonic velocities. Once again, physical test facilities are urgently needed. Even so, it is likely that flow anomalies will require partial redesign of the propulsion system during the flight test programme.*

Materials and Structures - With the likelihood that some 15 per cent of the surface area of NASP may be exposed to temperatures above 1425° C, there is obviously a need to choose between entirely new materials, or extensive use of active cooling. Promising new materials have been identified, but in general they are currently available only in laboratory quantities. The DSB Task Force states that industrial quantity production might be 12-15 years away. Until sufficient quantities become available to fabricate large-scale test articles, the many uncertainties associated with structural testing will continue.

* In a paper in Reference 7, J A Vandenkerckhove concludes with respect to the problem of supersonic combustion: "It is certainly not possible, with our current understanding, to claim with certainty that scramjet is the way to go, but it would equally be very rash to ignore it altogether and to decide on the full scale development of either a two-stage or a single-stage-to-orbit vehicle (without supersonic combustion) without having explored in some depth the scramjet alternative." Apparently the US is investigating this alternative extensively.

Controls - There are "large uncertainties" about the stability and control laws applicable to a vehicle such as NASP. Problems such as thermoelastic deformation of key structures tend to be outside conventional design experience. It seemed to the Task Force that it would be impossible to design such a vehicle without some understanding of its likely control system.

These quotations from the report of the Task Force of the DSB may seem overly pessimistic with respect to the space plane, although the DSB appeared to be very positive about the final possibilities, but at least they have the great merit to highlight the enormous challenges for the aerospace research and development community. Undoubtedly this Symposium will have a similar effect. We hope that it will lead to the stimulation of your work and where possible, towards increased cooperation among the nations of the Alliance.

REFERENCES

1. G PARDOE, H G R ROBINSON - The European potential for the creation of independent space transportation systems. Paper given at the 2nd European EGEE Space Congress, Munich, November 1987.
2. H A PFEFFER - ESA's long-term planning for space transportation systems. Paper given at the 2nd European EGEE Space Congress, Munich, November 1987
3. Aerodynamics of Hypersonic Lifting Vehicles, AGARD CP-428, November 1987
4. S M BOGDONOFF - Technical Evaluation Report on the Fluid Dynamics Panel Symposium on Aerodynamics of Hypersonic Lifting Vehicles. AGARD AR-246, April 1988
5. Special Course on Aero-thermodynamics of Hypersonic Vehicles, AGARD Report 761, June 1989
6. D F ROBERTSON - NASP keeps moving. Interavia Space Markets, Volume 4 No 2, May/June 1989, page 87
7. Progress in Space Transportation. Proceedings of the 2nd European Aerospace Conference. Bonn Bad-Godesberg, 22-24 May 1989, European Space Agency, ESA, SP-293

TABLE I

PEP

Design Methods used in Solid Rocket Motors
Lecture Series No 150, April 1988.

EPP

Ionospheric Structure and Variability on a Global Scale and Interactions with the Atmosphere and the Magnetosphere
Symposium, May 1988.

FDP

Aerothermodynamics of Hypersonic Vehicles
Special Course with VKI (BE), June 1988

AVP

The NAVSTAR GPS System
Lecture Series No 161, September 1988.

AMP

Implication of Advanced Technologies for Air and Spacecraft Escape
Symposium, April 1989.

AVP

High Resolution Air- and Space-borne Radar
Symposium, May 1989.

AVP

Tactical Applications of Space Systems
Symposium, October 1989.

FMP

Space Vehicle Flight Mechanics
Symposium, November 1989.

PEP

Hypersonic Combined Cycle Propulsion
Symposium, May 1990.

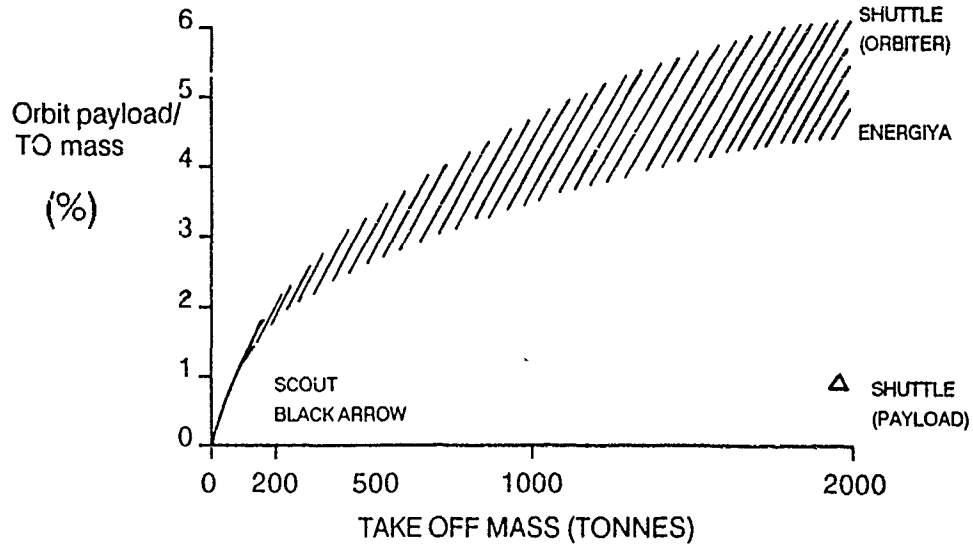


FIG 1 - PAYLOAD FRACTION VERSUS TAKE-OFF MASS FOR LOW-EARTH ORBITS

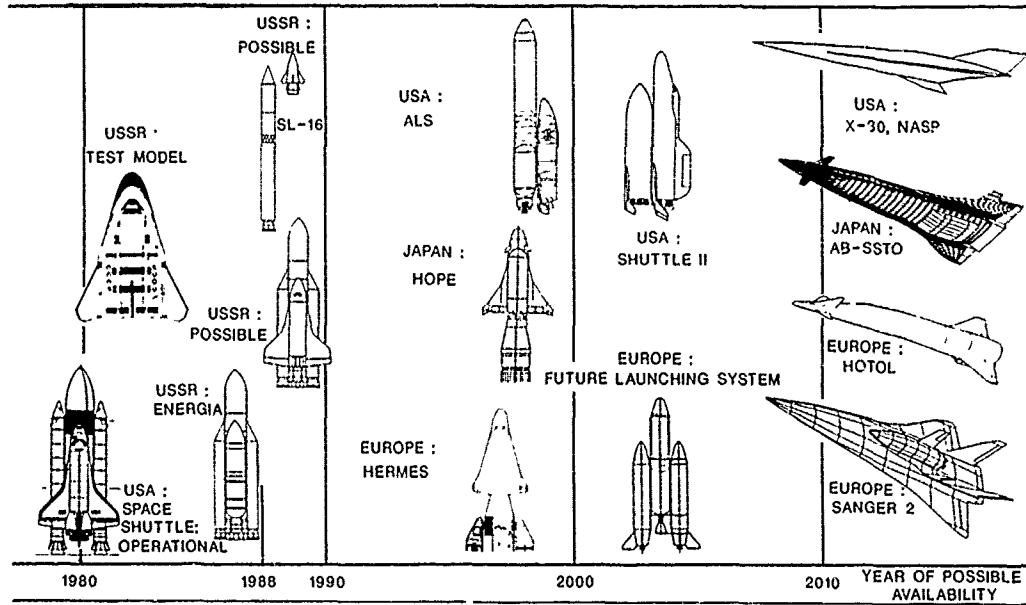


FIG 2 - REALISATIONS AND PLANS IN REUSABILITY TO EASE ACCESS TO SPACE

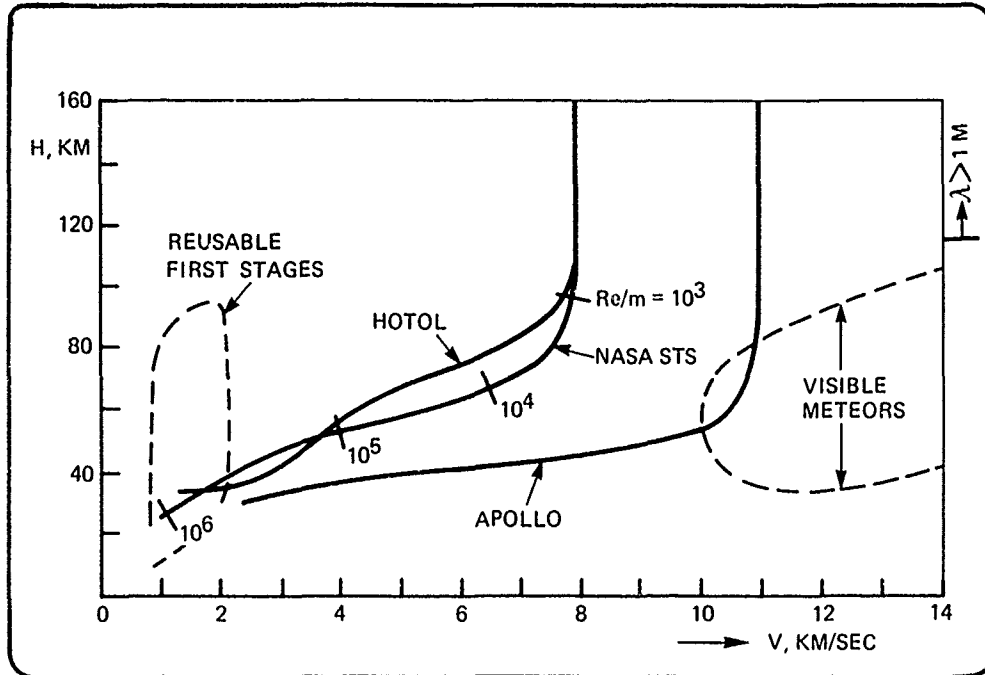


FIG 3 - RE-ENTRY FLIGHT REGIMES

Δ V, KM / SEC		
⊕ →	LEO (200 - 400 KM, 28.5°)	8.2
→	LEO → LLO	3.9
→	LLO →)	1.6
→	LEO → GEO (33,900 KM, EQUAT.)	4.3

FIG 4 - VELOCITY DIFFERENCES (IMPULSE) REQUIRED IN SPACE FLIGHT

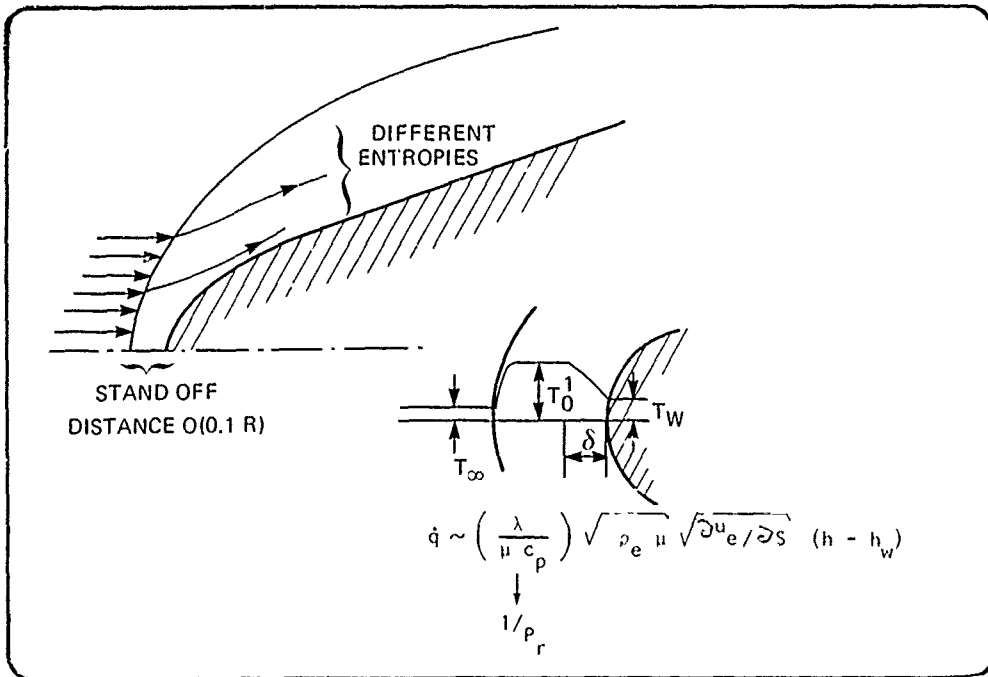


FIG 5 - HYPERSONIC FLOW AROUND LEADING EDGE OR NOSE

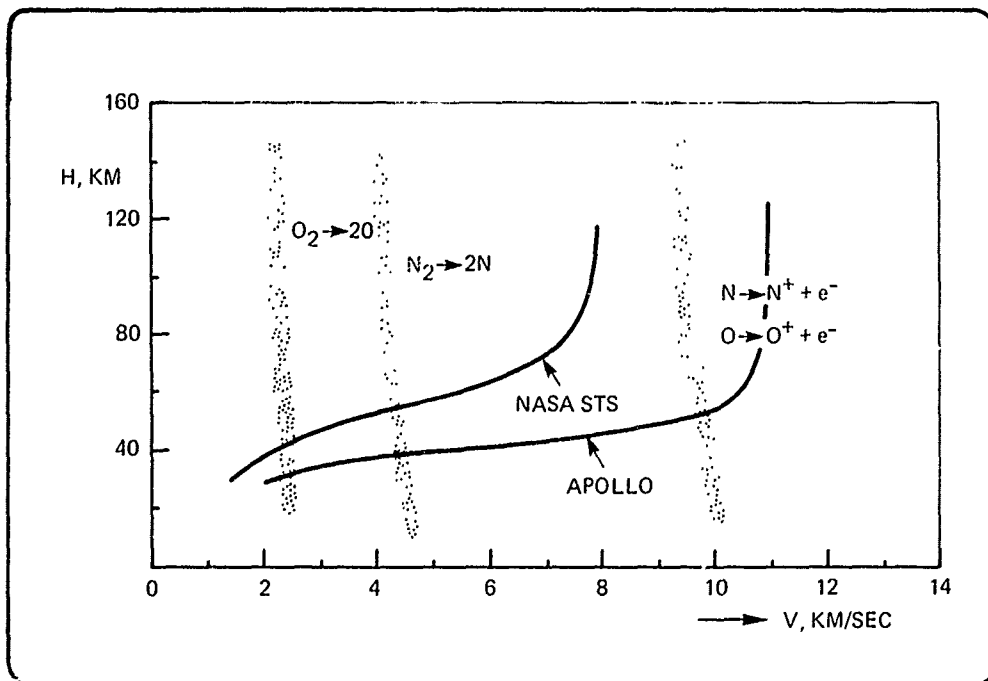


FIG 6 - AIR DISSOCIATION AND IONIZATION AT THE STAGNATION REGION

KEYNOTE ADDRESS
 AGARD Flight Mechanics Panel Symposium
 "Space Vehicle Flight Mechanics"
 November 13-16, 1989, Luxembourg.

K.H. Doetsch
 Director, Canadian Space Station Program
 Canadian Space Agency
 Ottawa, Ontario, K1A 0R6

SPACE DEVELOPMENT - A CONTINUING CHALLENGE

ABSTRACT

Space flight development, just as its atmospheric counterpart, encompasses a broad range of disciplines. In contrast to aircraft development, however, considerable emphasis has been placed to date on the operation of unmanned vehicles. The space environment is inherently hostile to human life, and as such, even for manned space flight, efforts are made to minimise crew size, and to automate or control remotely from Earth, much of the on-orbit vehicular activity.

Unmanned spaceflight has expanded human knowledge significantly and uniquely, through the exploration, often remotely, of Earth, our solar system and the universe, and through the communication channels that have been opened by satellites. Manned space flight has added another dimension with direct and local human intervention in the space environment, thereby adding the sensory and perceptual, intellectual, psychomotor and motor capabilities of humans.

Behind each successful space mission, starting with the small and relatively unsophisticated scientific probes of the 1950's and 1960's and leading to the great observatories such as the Hubble Space Telescope to be launched this decade, or in the manned space field, beginning with the first orbital flight of humans to their landing on the moon or to manning space stations orbiting Earth, there exists an enormous infrastructure of scientists, engineers, managers and politicians who together allow these ventures to come to fruition. This paper addresses the evolution of space flight, the technical and management challenges associated with its success, and the direction that is being mapped out on a global scale for the future exploration and exploitation of space.

INTRODUCTION

It gives me great pleasure to speak at this symposium on the subject of space development. To be able to address such a broad topic within the confines of a single paper is a daunting task, and I look to assistance in this by relying on the paper just presented by Dr. A van der Bliek to complement some of the thoughts which would otherwise deserve to be developed in greater depth in this paper. I would also refer readers to the Reference for a more comprehensive overview of the factors that will have a strong influence on space developments during the next decades.

Earth is one of nine planets circling the sun, which in turn is one of one trillion stars in our galaxy, the Milky Way, which, again in turn, is one of one hundred billion galaxies in the known universe. Space flight from Earth allows humans to remove one barrier to the understanding and benign exploitation of this universe.

Orbital space flight commenced with the pathfinder flight of Sputnik in 1957. Progress thereafter was remarkable, even when measured against a backdrop of the prevailing, technically progressive aeronautics industry. There was the political will in several countries to make space exploration a key element in the development of technocracies, in which the large scale of investment in research and development was seen as the path to future leadership and prosperity. In 1961, homo sapiens lived for 108 minutes in outer space. By the late 1980's, humans were regularly in space: in 1968 individuals set foot for the first time on another celestial body, the Moon, and, later, others lived continuously in the microgravity environment of space for more than a year. Meanwhile, scientific observations from space were causing fundamental reassessments of the hypotheses surrounding our understanding of the solar system, the universe and their origins, and, perhaps for the first time in human history, were allowing the ordinary person to view his own planet and its survival from a global rather than national or local point of view. Communication satellites, one of the first commercially exploitable applications of space, were soon to dominate long distance, global communications.

Apart from the technical and management aspects, perhaps two areas of space flight should be singled out as clearly having their genesis in the aeronautics world. First, a major impetus for the activity arose from strategic military considerations by the dominant pursuers of space activity, the USA and the USSR. Second, the costs and long time horizon for realising commercial returns were such that it was only through the national and political commitments of significant levels of government funding necessary to undertake the research and development and to build the infrastructure,

that space projects could proceed. While the military stimulus to the development of many aspects of space continues, it should be noted that international treaties exist which limit the use of space to peaceful purposes, and that many of the nations which now participate in the development of space, specifically exclude all military applications, whether defensive or not, and pursue instead, only scientific, commercial and exploratory goals.

THE HISTORICAL PERSPECTIVE

Before speculating on the future exploitation of the space environment, it is worth identifying some of the major milestones that have been achieved in the short history of orbital space flight. Many milestone events can be chosen to characterise its rapid development, and from these the following have been selected somewhat arbitrarily:

SELECTED SPACE HIGHLIGHTS

SPUTNIK 1	FIRST SATELLITE	1957
LUNA 2	FIRST SPACECRAFT ON MOON	1959
VENUS 1	VENUS FLYBY	1961
VOSTOK 1	HUMAN ORBITS EARTH	1961
EARLY BIRD	COMMERCIAL TV COMMUNICATIONS	1965
APOLLO 11	HUMANS LAND ON MOON	1969
LANDSAT 1	FIRST EARTH RESOURCES SATELLITE	1972
SKYLAB 2	FIRST SPACE STATION	1973
VENERA 9	FIRST PICTURE FROM SURFACE OF ANOTHER PLANET	1975
STS 1	FIRST SPACE SHUTTLE FLIGHT	1981
VARIOUS	ALL PLANETS EXCEPT PLUTO PROBED	1989
NUMBER OF LAUNCHES 1957 - 1989		3200

From the launch of the 84 kg Sputnik 1, the world's first artificial satellite, progress was rapidly made in placing first animals and then humans into space; in mapping the Moon, and landing humans on it; in flying satellites past our solar system's planets and their moons, and in sending to some of their surfaces, probes which would transmit back data about surface conditions to eagerly waiting scientists; in commercialising space, first through communication satellites in geosynchronous orbit and then through remote sensing satellites located in polar orbits around Earth, with which to provide information about the Earth's surface and its atmosphere; and during this entire process, in developing both in space and on the ground, an infrastructure which allowed the methodical and often rapid movement from the achievement of one goal to the next. Important to this process were both the development of new management techniques which allowed the work of widely distributed centres of activity to be successfully integrated, and the stimulation by space activity of ordinary people to be excited by scientific and technological progress.

DEVELOPING THE SPACE INFRASTRUCTURE

Significant strides have been made in the 32 years since the launch of Sputnik 1 in developing various elements of the space infrastructure. Such an infrastructure starts with the ground support systems necessary to initiate and sustain effective space flight. The ground infrastructure includes test, development and operations facilities, as well as user support facilities. It contributes significantly to the cost of conducting space flight but is essential. The transportation system to, from and in space remains as the most critical element in the infrastructure. Other essential elements are the space based communications and tracking networks which are generally well developed but, with continuing, rapid advances in information systems technologies, will no doubt be refined significantly in future. Shortage of available frequency bands and physical crowding in the geosynchronous orbit used for the majority of communication satellites will become increasingly important during the next decade. Remote sensing networks continue to be developed to provide essential information characterising the physical and chemical properties of Earth and other planets and of their atmospheres. Planetary missions to be launched over the next few years will lead to a renaissance of space science in the 1990's. Also, on the scientific front, great observatories are being developed for deployment in low-earth orbit, which will allow observations of the entire electromagnetic spectrum to study events and objects in the universe. In the area of manned space flight, general purpose facilities such as space stations in low-earth orbit for undertaking a variety of tasks have been developed and will continue to be developed, whereas major on-orbit assembly, servicing, manufacturing and transportation facilities will be built as precursors to the establishment of lunar bases and manned missions to Mars.

From this broad, although not what one would yet describe as a mature or robust base of space activity, consideration is given to some of the major missions that are currently being proposed or developed.

The Planetary Missions

The exploitation of the space environment for planetary observations has led to a remarkable epoch in the history of science. We live in an age of astounding discovery and adventure in which space probes from the USA and the USSR have investigated, at least superficially, between 1962 and 1989, almost the full extent of the planetary part of our solar system.

Four spacecraft are presently travelling out of the solar system, Pioneers 10 and 11, and Voyagers 1 and 2, after having earlier flown unscathed through the asteroid belt and provided fundamental information on the planets Jupiter, Saturn, Uranus and Neptune during fly-by of these planets.

Except for Pluto, each of the planets of the solar system has now been observed from satellites passing in their proximity or landing there. The most recent was the observation of Neptune from Voyager 2 in 1989, surely a mission that will go down in history as one of the most significant scientific achievements of the century. Magellan and Gallileo, launched in 1989 after an eight year launch gap in the USA planetary exploration program, will make detailed studies of Venus and Jupiter respectively. The Mars Observer is scheduled for launch in 1992 to make a global study of the planet, and will be followed by two sophisticated satellites, the Comet Rendezvous Asteroid Flyby, CRAF, scheduled to be launched in 1995 to liaise with and observe Comet Kopff, and Cassini, the fourth mission to Saturn, which will be launched in 1996 to arrive in 2003 to study the rings, atmosphere, magnetosphere and moons of Saturn.

The new planetary probes provide higher resolution, sensitivity and broader coverage than previous satellites. Their missions are planned to terminate in the proximity of their target planets. This leaves only the two Pioneer and the two Voyager satellites to continue to fly and gather data beyond our solar system limits.

In all, NASA alone plans to launch 36 space science missions over the next five years, including, next year, the Hubble Space Telescope, an astrophysics spacelab mission, Astro, the Gamma Ray Observatory, Spacelab Life Sciences -1 and ESA/NASA Ulysses.

The Great Observatories

In addition to the planetary probes which are sent to their target planets to allow observations in their proximity, there is presently planned to be launched into low Earth orbit a series of space observatories which will allow observations, without atmospheric interference, of the entire electromagnetic spectrum. Removing the filtering and distorting influence of the atmosphere will allow unparalleled resolution to be achieved. The following great observatories are currently planned to be launched by the USA, with international participation in the development of some of the instruments:

- o Hubble Space Telescope
- o Gamma Ray Observatory
- o Advanced X-Ray Astrophysics Facility
- o Space Infrared Telescope Facility

The weight, size and power of these observatories are limited by launch capabilities from Earth. Space stations will make possible on-orbit assembly of such facilities, thereby allowing increases in size and the corresponding increases in instrument sensitivity and resolution. Observatories may also be established on the far side of the moon to avoid the radio frequency interference emanating from Earth.

Major technological challenges in bringing these large facilities into operation will be their design for assembly on-orbit into rigid structures, and their precise pointing once assembled. New capabilities will also need to be developed to handle the high information rates expected to be generated by the observatories.

Observing Earth from Space

Among the earliest applications of space flight was the observation of Earth from orbiting satellites outfitted with cameras, radars and other sensors. Observations with instruments sensitive to different parts of the electromagnetic spectrum have allowed the mapping of Earth's surface, both land and sea, and its variations with time, and of Earth's atmospheric variations.

Increasing sensitivity to and concerns about the effect of human habitation on the Earth's environmental robustness are leading many nations to participate in a new program called "Mission to Planet Earth" the intent of which is to provide continual and synchronised updates on various aspects of the environment's characteristics in order to allow its better management.

The data provided through remote sensing techniques has considerable commercial and strategic value and, as a result, demand for it is expected to grow continually. Significant development effort is needed to enhance image analysis, and sensor sensitivity and resolution.

Space Transportation

The key to space exploitation lies with the availability of suitable space transportation systems. These determine the weight and volume of elements that may be placed in various orbits or escape trajectories. Launches are presently either by means of expendable rockets or partially reusable launch vehicles pioneered by the USA in the form of the Space Shuttle. Typically, for expendable launch vehicles, the payload mass which may be placed in geosynchronous orbit ranges from 2000 to 5000 kg, whereas the shuttle is able to place payloads of up to 20,000 kg into low-earth orbit.

On a world wide basis, approximately one hundred launches per year have been carried out for the past several years with about ninety per year by the USSR. In all, there have been about 3200 launches into Earth orbit or beyond. Although launch reliability and lift and volume capacity had been improving in the western world at the time of the Challenger accident in 1986 (which subsequently led to the grounding of the shuttle fleet for over two years at the same time that ESA's Ariane was having development problems), the resulting, even if temporary, grounding of almost all of the western world's launch capability clearly illustrated the fragile nature of its launch capacity. As a result, considerable activity has been stimulated in the USA to develop again commercial, expendable launch vehicles to complement the capability of the shuttles which will be exploited, in future, predominantly in support of those missions requiring intervention by astronauts. As well, independent national orbital launch capabilities have been or are being developed by India, Japan, China and, of course, the USSR.

The major areas of launch capability requiring improvement are the lift capability, launch reliability and launch costs. Evolution is leading to a fleet mix which will include passenger transport vehicles, heavy lift transporters and transfer vehicles for round trip travel beyond low-earth orbit. It will be necessary to reduce launch costs from Earth by an order of magnitude from the current level of about \$10,000 per kilogram before space exploitation can become routine. Significant advances in propulsion system design and increases in reliability will be the focus of attention to achieve this and the emphasis will be on systems in which all stages are recoverable.

Typical of the new propulsion systems under consideration for manned space vehicles which would be horizontally launched from Earth to low-earth orbit, are:

Two-stage engines with an airbreathing, liquid hydrogen engine first stage, and a hydrogen/liquid oxygen rocket second stage (Saenger)

Single-stage, combined-cycle engines using hydrogen/oxygen and an airbreathing capability to orbit (Aerospace plane, HOTOL).

The technologies that will need to be developed to allow these systems and the attendant operating cost savings to be realised include the following:

- Durability of the thermal protection system
- Development of light weight structures and materials
- Advances in information, guidance and control systems
- Supersonic combustion ramjet engine (SCRAMJET)
- High Mach Number operation of SCRAMJET (Mach 15)

It is expected that these new transportation systems will be developed for operational use during the first decade of the next century.

For on-orbit transportation systems, or space transfer vehicles, the possibility of using electrical power rather than chemical power sources exists when used in conjunction with accelerators, either in the form of "ion engines" or of "mass driver engines". When operating far from the sun, in the outer solar system where "ion engines" are most effective, nuclear power systems become essential as their power source.

Communications and Tracking

Communication and tracking capabilities are essential for monitoring and supporting space activity. The facilities which have been developed use complementary space and ground networks to provide for communications, data relay, navigation and tracking. Mature systems are in place, although the limited life of the current generation of satellites in geosynchronous orbit (approximately 7.5 - 10 years for Western satellites and 2.5 years for USSR satellites) requires the regular replacement of satellites with associated costs. Crowding in geosynchronous orbit will have a significant influence on the size and sophistication of these satellites in future, and it is envisaged that on-orbit servicing will eventually be available to extend the service life of the satellites. Evolution will increase the coverage provided and the bandwidth of the data being transmitted. The present TDRSS satellite system developed by NASA to provide for data management for the shuttle and space station requires three satellites in geosynchronous orbit to provide continuous coverage of vehicles such as space station or the shuttle in low Earth orbit.

As operations expand to require frequent communications contact with orbital facilities and transfer vehicles in the inner solar system, a number of new tracking, navigation, communications and data relay satellites will be needed.

A major and growing concern arises from space debris in both low Earth and geosynchronous orbits. Even minute debris of the order of 1mm in size can destroy a satellite because of its kinetic energy. Such debris can result from failed or disintegrated satellites and is an increasing hazard in heavily used orbits.

Space Stations

Both the USA and the USSR moved quickly to develop space stations early in their space programs. The USA gained experience with the Skylab space station in 1973/1974, whereas the USSR has developed a series of stations which have continually provide a capability to support human life in space since 1974 through its Salyut and Mir space stations. The USSR has a significant lead in accumulated experience of long term operations by cosmonauts in space.

Present space stations and those under development, are multi function facilities which provide for many of the following capabilities:

- o Long duration space flight
- o Micro-gravity research and development
 - materials processing
 - life sciences
- o Earth and space observation
- o Space science
- o On-orbit assembly and servicing
- o Transportation Node
- o Technology development base
- o Exploration base

Space Station Freedom, presently being developed by the USA, Canada, ESA and Japan represents the largest international cooperative technology development project ever undertaken. When completed, the space station will be 135m long, weigh 200,000kg, have 75kw of power, one pressurised habitation module and three pressurised scientific laboratories. It will be manned continuously by an eight person crew and will possess significant external assembly and servicing capability. It will fly in a circular orbit with an inclination to the equator of 28.5 degrees, and at an altitude of about 500km. The station is expected to evolve over time and have a thirty year operational life. It will be assembled in orbit over four years starting in 1995 and, in that period will require 29 dedicated shuttle missions to be built and to have provided the necessary logistics support to maintain the station in an operational permanently-manned state. It will cost in the order of \$35,000 million dollars to develop.

Among the many challenges associated with the development of space station, those of its assembly in orbit, the subsequent operation of the entire research and development complex with an eight person crew, and the continual maintenance and updating of its systems for a thirty year operational life, must rank as unique and amongst the most demanding.

Space stations in low Earth orbit will evolve to become assembly and maintenance bases and staging posts for other destinations, such as to geosynchronous orbit, the Moon or Mars. They will be improved to provide a better environment for undertaking scientific and commercial development work through crew size increases and the introduction of enhanced automation and robotics in the pressurised volumes to increase the productivity. Power unquestionably will be increased to allow manufacturing processes in space to be developed, and efforts will be made to maintain the micro-gravity level as close to 10^{-6} g as possible, and to develop closed ecology life support systems and contamination-free control engines using hydrogen and oxygen as fuel. As well, designers and station operators will need to satisfy the demand for rapid responses to scientific experiment development and crew health needs. Much is still to be learned about the design for efficiency of human operations under micro-gravity conditions and considerable design effort will go into the creation of crew- and user friendly designs. To keep operations efficient, reliability and maintainability of station components will be enhanced and the designs will incorporate the hooks and scars necessary to maintain a facility of this nature for an operational life of some thirty years. Every effort will be made to reduce the on-line ground support necessary to operate space stations.

The Role of Humans in Space

Much has been made of the debate as to whether manned space flight should continue with its inherent cost and safety implications, or whether much more effective use of scarce resources could be made by concentrating instead only on unmanned robotic space missions. The answer is of course, that the two are complementary and not mutually exclusive. A characterisation has been made in Table 1 of the advantages and disadvantages of humans in space.

TABLE 1
ROLE OF HUMANS IN SPACE

<u>PROS</u>	<u>CONS</u>
- HAVE EXPLORATION INSTINCTS	- CONTAMINATE AND DISTURB
- HAVE SENSORY/PERCEPTUAL CAPABILITIES	- USE SCARCE RESOURCES
- HAVE PSYCHOMOTOR/MOTOR CAPABILITIES	- ADD SAFETY ENVIRONMENTAL AND HEALTH CONTROL REQUIREMENTS
- HAVE INTELLECTUAL CAPABILITIES	- ARE STRESS SENSITIVE
- cognition	- ADD TO COST
- memory	
- divergent and convergent production	
- evaluation	

It is readily seen that just as in aviation, there are certain human abilities which cannot yet be adequately duplicated by machines. Even if they could be, an intangible factor, however, will remain, and that is that humanity is driven by an irresistible instinct for exploring, and this makes continued human ventures into space virtually inevitable. The variable is the pace at which this occurs, and that is determined more by economic factors than by technological factors. It is clear that the costs of supporting humans in space are significant and, as a result, considerable advances will be made to ensure that those humans who are privileged to work in space are working as effectively as possible through the application of advanced automation and robotics techniques including the application of artificial intelligence methodologies.

MAJOR SPACE INITIATIVES OF THE FUTURE - BEYOND SPACE STATION

The scale of space initiatives is such that by the time they are approved for development, the ideas that spawned them will have had the opportunity to mature for many years. Thus it is that the space station program currently being developed by the USA, Europe, Japan and Canada had its origins in the 1950's. The space station is a component in the methodical development of an infrastructure that has been undertaken by the USA since it entered into the space arena. Although providing a versatile, and in many regards, an autonomous capability, it is not an end in itself. It will also be part of the infrastructure necessary to undertake the next major initiatives of human exploration. Those currently under most active consideration, particularly after President Bush's stimulus to NASA on the 20th anniversary of humans first setting foot on the moon, to assess in detail the components of future USA civilian space activity, are:

- o Mission to Planet Earth
- o Outpost on the Moon
- o Humans to Mars

These complement the already approved initiatives leading to the further exploration of the solar system.

Mission to Planet Earth

Planning is in place for an international thrust during the next two decades to undertake an integrated, long range study of planet Earth through a global satellite-based observing system complemented by Earth-based systems and measurements. When taken together with modern data processing capabilities this should allow simultaneous observations, their correlation and analysis to provide a greater understanding of the physical and biological processes of our planet and of their interactions. The Mission to Planet Earth has found widespread favour among space faring nations.

One of the most significant challenges for this endeavour will be the development of artificial intelligence techniques to allow the effective handling and processing of the reams of data that will be generated. Another will be the incorporation into the platforms of appropriate automation and robotics capabilities as well as the necessary redundancy and self diagnostics to ensure years of trouble free operation. Finally, the precise coordinated pointing and synchronisation of several instruments on the platforms will prove to be a significant technical challenge.

This program requires strong international links to be established to reap maximum benefits.

Outpost on the Moon

A new phase of lunar exploration, building on the legacy of Apollo, will lead to the first human outposts on another world. It will support scientific research and exploration and allow humans to learn to live and work in the hostile environments characteristic of other planets while remaining relatively close to Earth (within a two to three day journey time). Over time, the dependence on support from Earth will be reduced and the unique research environment offered by the moon will establish the capability of humans to undertake the more demanding settlement of other worlds. As well, the favourable location on its far side, where it is shielded from the radio noise of Earth, for undertaking many experiments and observations of scientific significance, should lead to important advances in astronomy and physics.

Long term human presence would best be preceded by robotic lunar polar prospectors to identify the best locations for outposts. Clearly the discovery of water or other volatiles would be very significant.

The technologies required revolve round the availability of a robust transportation system, well developed closed loop life support systems and a space station in low Earth orbit as a staging base for supplies, equipment and propellants.

Humans to Mars

Besides Earth, Mars is the only potentially habitable planet in our solar system. It may once have supported life. Earlier robotic visits to Mars showed many similarities with Earth, but also many important differences, for example, no organic compounds were found in the survey area. Detailed exploration of Mars may shed light on whether the origin of life in the universe is common and possible under a wide range of conditions or whether it is rare, taking place only under a very restricted set of conditions. Because it is so far away, on average 1000 times as far away as Earth's moon, it is most likely that the planet will be visited from Earth for exploration rather than for development reasons. Manned visits will be preceded by robotic exploration to establish detailed images and a mapping of the surface; to investigate potential landing sites for their suitability as manned bases; to gather and analyse surface and sub-surface samples to establish whether the local areas could support human habitation; and to investigate, from the surface, geological features that could shed light on the history of the planet. An enhanced support infrastructure posing considerable technological challenges will need to be put in place to acquire the detailed data necessary before committing to systematic human exploration of the planet. It should be noted that a round trip from Earth to Mars, including a six month stay on Mars, will take about two years to complete.

Manned exploration of Mars will be a massive undertaking requiring international cooperation on an unprecedented scale. President Bush, in 1989, indicated the USA's interest in pursuing this as part of a long term space exploration plan of the USA.

TECHNOLOGICAL CHALLENGES

Many technological challenges remain to be overcome to put in place the previously identified exploration and exploitation programs. A selection of the key ones, many of which have been addressed earlier, is provided for reference in Table 2.

TABLE 2

TECHNOLOGICAL CHALLENGES

- o TRANSPORTATION SYSTEMS - EARTH TO ORBIT
- o SPACE TRANSFER VEHICLES
- o EFFICIENT HUMAN LIFE SUPPORT SYSTEMS
- o EXTENDED HUMAN STAY AWAY FROM EARTH
- o SPACE CONSTRUCTION
- o AUTOMATION AND ROBOTICS
- o SPACE SUITS
- o NUCLEAR POWER
- o ESTABLISHING BIOSPHERES ON OTHER PLANETS

MANAGEMENT AND POLITICAL CHALLENGES

In addition to the significant technical challenges posed by the exploration and exploitation of the space environment, there are several important management and political questions to be addressed.

Are the financial and human resources adequate to undertake methodically the discussed ventures?

On the question of finances, with a well planned and phased program leading to, for example, a human base on Mars in 2025, the financial resources of the nations that have traditionally participated in space projects are adequate, if used cooperatively, providing that science and technology programs of this nature continue to receive approximately the same share of government budgets. On the human resource question, much of the development requires simultaneously, thousands of skilled scientists, technologists and project managers for its timely completion. There exists, at this time, a shortage of the appropriate skill levels, particularly in the technical, middle management positions. Growth in the space program must be carefully phased to ensure that the adequate human resources are developed and available to allow the building of robust, safe systems. Alternatively, these resources must become available from other advanced technology programs requiring similar disciplines and skills.

Will international cooperation be necessary?

As discussed in the following section, all indications are that the cooperation between nations involved in space development will need to be strengthened as proposed programs proceed.

Can effective program coordination and integration be achieved for programs of this magnitude, with their implementation widely separated both geographically and temporally?

In the author's opinion this challenge is the equal of any of the technical challenges facing the program. Experience on a smaller scale has been gained in this area through the space shuttle and in the Ariane developments. More is being gained in the Space Station Freedom program. The latter is the largest international science and technology cooperative development ever undertaken. The lessons learned in its development will need to be carefully applied to future, even more comprehensive, programs. Many of the management challenges involve striking the right balance between accountability, authority and responsibility among the various participants in the development and operation of the facilities. This becomes particularly important in the control of requirements, design specifications and interfaces between elements and components provided by various partners or the suppliers to the partners, such that systems which cannot be tested as an integrated whole on Earth, can be assembled and operated safely for decades in space.

Are the interests of maximising commercial benefits and spin off opportunities for individual participants consistent with the technology transfer that inevitably will occur between participants?

This question will doubtless exercise program partners and participants continually, but is probably overrated in terms of its actual significance. It is now generally accepted that cooperation in these large, technically sophisticated, one-off projects is much more beneficial to all participants than would be out-and-out competition without cooperation.

Does the political will exist to pursue these "megaprojects"?

It is recognised that the world economy is presently such that many of the principal participating countries in space activity are having to balance priorities carefully in establishing national budgets. Notwithstanding this, one consistent thread has been found in surveys of the population of many of these countries, and that is that this type of activity finds widespread favour and is considered to add to the long-term health of society. Such popular encouragement is an important factor in obtaining the continuing political support of these projects.

INTERNATIONAL COOPERATION

Space activity, since its earliest days, has been characterised by international competition and cooperation. The two dominant nations in space activity, the USA and the USSR, have each chosen to develop space systems or instruments with their respective friends and allies. In the manned space flight arena, they also cooperated effectively with each other in the Apollo-Soyuz Test Project. In general, cooperation between these two nations has tended towards coordination of parallel activities rather than towards joint developments.

The cooperative space projects that the USA has undertaken with friends and allies have been impressive. Over 1000 agreements with over 100 countries have been entered. The

most significant to date is that for the development of space station. In this role as a partner, the USA has done much to nurture the space capabilities of other nations, and has in turn benefitted from the particular skills and resources these nations can bring to the table.

Europe too has developed through ESA, an impressive space program which is far stronger than would have been possible without an international cooperative framework.

What then will be the level of international cooperation in space activity in future? The major projects under consideration are of such magnitude that they will require for their completion resources on a global rather than a national scale. That is true not only of the financial demands that these large projects create, but also of the demands for skilled human resources. It is clear that for the future exploration of Mars, for example, much would be gained through the coordination of complementary efforts which would include those of both the USA and of the USSR. This would be entirely appropriate, as establishing new human communities beyond Earth needs to be an international rather than a national effort. Without such cooperation, it is unlikely that projects of this nature would be completed within the working life of an aerospace engineer.

The future then looks exciting. Significant and worthwhile projects that will challenge and harness the skills of many sectors of society have been identified on a quest of human exploration as significant as any ever previously undertaken. The skill will lie in pacing the activity so that it may proceed at a digestible pace.

CONCLUDING COMMENTS

Space developments over the last thirty years or so have been remarkable: the solar system has been probed, humans have left the bonds of Earth and a space infrastructure has been put in place. As one considers the next phases of space exploration, it is perhaps worthwhile returning to the question of why society should have an interest in assigning resources of the required magnitude into space development. At the most fundamental level, it extends the understanding of the universe. As well, it allows humanity to follow a strongly developed instinct to explore, prospect and settle the solar system as a natural extension of having settled Earth. In the process, the creative energy of humans will be harnessed in a noble pursuit that finds a positive response in all levels of society. Finally, even though the initial investment in establishing the infrastructure is large, it is expected that its development will continue to be a major catalyst for beneficial terrestrial spinoff.

In this paper, it has only been possible to touch briefly on the highlights of significant space activity, but even from this survey it may readily be seen that the identified present and future space missions have sufficient scope and depth that they can provide a challenge to humanity and, in particular, to the young scientists and engineers starting out on their careers to pursue a peaceful and systematic exploration of our solar system and of the universe. Moreover, because of the exploratory and fundamental nature of much of space activity, it lends itself well to cooperation between enterprises and nations that would traditionally prefer to compete. Commercial benefits will follow later.

REFERENCE

Pioneering the Space Frontier Report of the National Commission On Space,
Bantam Books, May 1986

FLIGHT CONTROL ISSUES OF THE NEXT GENERATION SPACE TRANSPORTATION LAUNCH VEHICLES

by

Richard W. Powell

J. Christopher Naftel

Christopher I. Cruz

NASA Langley Research Center
Hampton, Virginia 23665-5225 U.S.A.

ABSTRACT

A study has been conducted that investigated some of the issues that affect the flight control and guidance system designs for vertical-takeoff and horizontal-takeoff vehicles. The study used a two-stage all-rocket vehicle to represent the vertical-takeoff system and a generic aerospace plane concept to represent the horizontal-takeoff vehicle. Two flight control issues for the vertical-takeoff rocket were uncovered. The first was the large gimbal angle range required for pitch trim when using parallel mated vehicles. The second was control during staging. Two issues were also identified for the air-breathing vehicle. The first is that the drag losses due to aerodynamic trim are a significant fraction of the total ideal velocity required to achieve orbit. The second issue is that since the vehicle flies at high dynamic pressure for most of the ascent, the guidance system design will be more difficult to ensure accurate insertion than that for the vertical-takeoff rocket system.

INTRODUCTION

The Space Shuttle represents a major technological achievement in the space transportation capabilities of the United States; however, one of the goals of the Space Shuttle, namely low-cost space transportation, has not been met. These higher than anticipated costs can be traced to lower than expected flight rates, labor-intensive ground and flight operations, and recurring hardware costs. The next generation of launch vehicles must reduce the costs of delivering payloads to space, or mission planners will continue to be faced with the prospect of restricted space activities in an era of budget constraints.

Many studies are currently being performed within the space community to determine launch systems that could provide this payload delivery service at a much lower cost than either the current expendables or space shuttles. These studies can be grouped into those vehicles that use near-term technology in their design and those that use more advanced technology. Each of these categories is composed of many vehicles. This paper will analyze one design from each category that would have potential flight control system issues not seen with today's vehicles.

Within the near-term technology vehicles, the one that was chosen for this study is a vertical-takeoff, two-stage, all-rocket vehicle that uses both parallel thrusting (both the orbiter and the booster are thrusting at lift-off) and propellant crossfeed from the booster to the orbiter. When a later technology readiness date is chosen, vehicles that employ air-breathing propulsion may become practical. Because of this, an aerospace plane concept, which represents a horizontal-takeoff, single-stage-to-orbit vehicle that uses air-breathing propulsion, was chosen for this study. Because many performance studies have been done and more are currently underway on both these categories of vehicles, this paper concentrates on issues that affect the design of the flight control and guidance systems.

This paper discusses the optimal ascent flight profile for each of these vehicles, the design of the guidance algorithms, the off-nominal conditions used to evaluate the flight control issues, and the results of simulations with these off-nominal conditions.

NOMENCLATURE

A_c	engine capture area, m^2
c	mean aerodynamic chord, m
C_D	drag coefficient, $(drag/q_\infty S)$, n.d.
$C_{D\delta_e}$	drag increment coefficient due to elevon deflection $(drag\ increment / q_\infty S)$, n.d.
C_L	lift coefficient, $(lift/q_\infty S)$, n.d.
$C_{L\delta_e}$	lift increment coefficient due to elevon deflection $(lift\ increment / q_\infty S)$, n.d.
C_m	pitching-moment coefficient $(pitching\ moment / q_\infty S c)$, n.d.
$C_{m\delta_e}$	pitching-moment increment coefficient due to elevon deflection $(pitching-moment\ increment / q_\infty S c)$, n.d.
C_T	thrust coefficient $(thrust / q_\infty A_c)$, n.d.
C_I	constant in commanded pitch angle polynomial, deg/sec

3-2

C_2	constant in commanded pitch angle polynomial, deg/sec^2
h	altitude, m
K_p	roll rate gain, sec
K_q	pitch rate gain, sec
$K_{\dot{q}}$	pitch acceleration gain, sec^2
K_r	yaw rate gain, sec
K_α	angle-of-attack error gain, n.d.
$K_{\alpha I}$	integral of angle-of-attack error gain, sec^{-1}
K_β	sideslip angle gain, n.d.
K_ϕ	roll error gain, n.d.
I_{sp}	specific impulse, sec
LH ₂	liquid hydrogen
LOX	liquid oxygen
p	roll rate, deg/sec
q	pitch rate, deg/sec
\dot{q}	pitch acceleration, deg/sec^2
q_c	commanded pitch rate, deg/sec
q_∞	dynamic pressure, Pa
r	yaw rate, deg/sec
S	reference area, m^2
\mathcal{S}	Laplace operator, n.d.
ΔA_{apogee}	change in apogee at orbital insertion as compared with optimal trajectory, km
ΔG_{rad}	change in geocentric radius at orbital insertion as compared with optimal trajectory, m
$\Delta A_{\text{perigee}}$	change in perigee at orbital insertion as compared with optimal trajectory, km
$t_{\text{me;init}}$	time predictor-corrector algorithm is invoked, sec
ΔT_{ime}	change in orbital insertion time as compared with optimal trajectory, sec
$\Delta A_{\text{payload}}$	change in delivered payload as compared to optimal trajectory, kg
ΔV_{IDEAL}	ideal velocity increment, m/sec
ΔV_{THRUST}	velocity loss increment due to reduced thrust induced by atmospheric pressure, m/sec
ΔV_{CIRC}	ΔV required to circularize, m/sec
ΔV_{COR}	velocity loss increment due to coriolis effect, m/sec
$\Delta \dot{V}_{\text{AERO}}$	velocity loss increment due to aerodynamics, m/sec
ΔV_{GRAV}	velocity loss increment due to gravity, m/sec
ΔV_{LOSS}	total velocity loss increments, m/sec

ΔV_{TV}	velocity loss increment due to thrust vector not being aligned with velocity vector, m/sec
$\Delta \gamma$	change in flight path angle at orbital insertion as compared with optimal trajectories, deg
α	angle of attack, deg
α_c	commanded angle of attack, deg
α_{nom}	nominal angle of attack, deg
β	sideslip angle, deg
γ	flight path angle, deg
γ_c	commanded flight path angle, deg
δ_a	aileron deflection $((\delta_{e_l} - \delta_{e_r}) / 2)$, deg
δ_{a_c}	commanded aileron deflection, deg
δ_e	elevator deflection $((\delta_{e_l} + \delta_{e_r}) / 2)$, deg
δ_{e_c}	commanded elevator deflection, deg
δ_{e_l}	initial elevator deflection, deg
δ_{e_l}	left elevon deflection (positive trailing edge down), deg
δ_{e_r}	right elevon deflection (positive trailing edge down), deg
δ_{i_p}	engine pitch gimbale angle (positive up), deg
δ_{i_y}	engine yaw gimbale angle (positive left), deg
δ_r	rudder deflection (positive trailing-edge left), deg
δ_{r_c}	commanded rudder deflection, deg
θ_c	commanded pitch angle, deg
θ_{init}	pitch angle when predictor-corrector guidance algorithm is invoked, deg
ϕ	roll angle, deg
ϕ_c	commanded roll angle, deg
σ	standard deviation, n.d.

VERTICAL DESCRIPTION

Vertical-Takeoff Rocket Vehicle

The all-rocket vehicle (Fig. 1) used in this study was taken from the Advanced Manned Launch System vehicle studies currently underway at NASA. Table 1 shows its major characteristics. This vehicle is composed of an unmanned booster and a manned orbiter. The unmanned booster stages at Mach 3 and performs an unpowered glide to the launch site. Mach 3 was chosen for staging for two major reasons. The first is that this is the highest Mach number that would allow an unpowered return to the launch site after staging with adequate performance reserves. The second is that at this low Mach number, no thermal protection system is required. Both the booster and the orbiter engines use liquid hydrogen and liquid oxygen as propellants. The orbiter engines use propellant from the booster until staging, and internal propellant for the remainder of the ascent. For more information on this configuration, refer to reference 1.

Horizontal-Takeoff Air-Breathing Description

The air-breathing vehicle chosen for this study is a generic National Aero-Space Plane (NASP) concept. This vehicle uses all air-breathing propulsion from takeoff to orbit insertion. Figure 2 shows this concept, and table 2 shows its major characteristics. This vehicle is composed of an axisymmetric 5-deg half-angle conical forebody, a cylindrical engine nacelle section, and a cone frustum nozzle. The wing has a leading-edge sweep of 78 deg and is set at 0 deg incidence and dihedral. The wing is a 4-percent thick diamond airfoil. Elevons are located at the trailing edge of the wing with their hinge line perpendicular to the fuselage centerline. The vertical tail is a 4-percent thick diamond airfoil with a leading-edge sweep angle of 70 deg, and includes a rudder with a hinge line at the 75 percent chord position measured from the leading edge. The specific impulse and thrust coefficient characteristics for the propulsion system are shown in figures 3 and 4. These propulsion system characteristics were estimated for individual engine modules in an annulus arrangement at the aft end of the conical forebody.

AERODYNAMICS

The aerodynamic data base for both vehicles was generated using the Aerodynamic Preliminary Analysis System (APAS).²⁻⁴ APAS is an interactive computer code that predicts the aerodynamic characteristics of a vehicle from subsonic to hypersonic speeds using a common geometric definition. APAS incorporates a variety of engineering techniques to estimate the basic longitudinal and lateral-directional characteristics of aerospace vehicles as well as control effectiveness and dynamic derivatives. Slender body, vortex panel, wave drag, and viscous drag methods are used in the subsonic to low supersonic speed regime. At the higher speeds, tangent-cone, tangent-wedge, and reference enthalpy methods are utilized to approximate the pressure and shear stress distributions on the vehicle. The APAS program has been used on many previous vehicles, and through comparisons with wind-tunnel and flight data, has been shown to give results accurate to the fidelity required for this study.

TRAJECTORY SIMULATIONS

All the trajectories presented in this paper, with the exception of the separation trajectories, were generated by either the 3-degree-of-freedom or 6-degree-of-freedom version of the Program to Simulate Optimal Trajectories (POST).⁵ POST is a generalized event-oriented trajectory program that can be used to analyze ascent, on-orbit, and entry trajectories. POST can be used to optimize any calculated variable which may be subjected to a combination of both equality and inequality constraints. The program has been modified to include a predictor-corrector guidance capability. This scheme was implemented by including a 3-degree-of-freedom simulation as an inner loop to the main simulation. This allows the predictor-corrector guidance model to have nominal environmental characteristics (planet, atmosphere, gravity, aerodynamic, propulsion, weights, etc.), while the main simulation can have perturbed characteristics.

The trajectory that was simulated for both vehicles was a due east launch from the NASA Kennedy Space Center into a 185-km circular orbit. The vertical-takeoff rocket first inserted into a 93- by 185-km orbit and circularized at apogee. The horizontal-takeoff vehicle inserted into an orbit with a 185-km apogee and circularized at apogee with rockets. The perigee can not be specified because of the nature of the transfer orbit. This transfer orbit takes the vehicle from the high dynamic pressure trajectory that is required for the use of air-breathing propulsion to apogee. The altitude of the trajectory while using air-breathing propulsion is determined by the atmospheric density and thus could vary greatly.

GUIDANCE ALGORITHMS

Vertical-Takeoff Rocket Vehicle

The guidance philosophy of the two-stage all-rocket vehicle was to fly the trajectory that would maximize payload while not exceeding any vehicle constraints. These constraints were a maximum dynamic pressure of 40.7 kPa, a maximum wing normal force of $\pm 2.15 \times 10^6$ N for the orbiter and $\pm 1.27 \times 10^6$ N for the booster, and an angle of attack at staging between -6 and 2 deg. This angle-of-attack limitation was imposed as a result of an initial staging analysis. This staging analysis is discussed in more detail later. This optimal ascent was determined by using the 3-degree-of-freedom version of POST. This POST simulation included the gimbaling of the engines in pitch by requiring the vehicle to be statically trimmed longitudinally throughout the ascent. Because this vehicle does not use aerodynamic control surfaces during ascent, it was determined that a 3-degree-of-freedom simulation that required the vehicle to be statically trimmed both longitudinally and directionally with the use of engine pitch and yaw gimbaling would be suitable to analyze flight control issues.

The guidance algorithm for this vehicle was divided into two parts. In the first part, the vehicle was commanded to fly a reference trajectory. This was done by calculating an error signal that was a linear combination of the differences between the current and optimal geocentric radii and flight path angles. This error signal was then used to command the pitch attitude of the vehicle. . . . 350 sec into the trajectory ($\cong 100$ sec before orbital insertion), the guidance algorithm switched to a predictor-corrector algorithm, which was designed to ensure an accurate insertion. This algorithm determined the linear and quadratic coefficients of a polynomial that described the commanded pitch attitude ($\theta_c = \theta_{ini} + C_1(\text{time} - \text{time}_{ini}) + C_2(\text{time} - \text{time}_{ini})^2$). This predictor-corrector algorithm was utilized to update the control history at 10-sec intervals until orbital insertion. The predictor-corrector algorithm used 3-degree-of-freedom equations modified to include longitudinal static trim through the use of engine gimbaling. For this study, the predictor-corrector model used the same planet, gravity, propulsive, and aerodynamic models as the actual simulations. The atmospheric model was the 1976 standard (Ref. 6). The predictor-corrector models were unaware of atmospheric dispersions or winds. This was done to simulate the case where no day-of-launch atmospheric conditions and no onboard measurements would be used to provide atmospheric information. If the algorithm provides for accurate insertions using only a standard atmospheric model, operational costs will be

reduced. If atmospheric data are available, either through day-of-launch operations or through the use of onboard systems, this information could be passed to the predictor-corrector algorithm and would decrease the number of required updates.

Horizontal-Takeoff Air-Breathing Vehicle

As with the vertical-takeoff vehicle, the guidance philosophy of the air-breathing vehicle was to fly a trajectory that would maximize inserted payload without violating any vehicle constraints. The most significant constraint was a dynamic pressure limit of 57.5 kPa for velocities less than Mach 1 and a limit of 95.8 kPa for velocities greater than Mach 3. Between Mach 1 and Mach 3, the dynamic pressure constraint was varied linearly between these limits. The optimal trajectory as determined by POST was to reach 95.8 kPa as soon as possible and then to fly this boundary until sufficient velocity was obtained that the vehicle could pull up to a transfer orbit. At this velocity, the vehicle performed a powered pull up until dynamic pressure was reduced to 23.9 kPa. At this point, the engines were shut down and the vehicle coasted to apogee and then circularized with rocket propulsion. This optimal trajectory used the elevons to statically trim the vehicle in pitch.

It was found that if the pull-up maneuver was modeled as a constant angle of attack pull up at a constant throttle setting, it would agree closely with the optimal maneuver. Therefore, this simplified technique was simulated for this flight control issues analysis. Because of the use of aerodynamic control surfaces and the long flight times at high dynamic pressure, it was determined that a 6-degree-of-freedom simulation would be necessary to assess the flight control issues. The guidance algorithm was designed to follow the optimal profile with the predictor-corrector algorithm operating as an outer loop control to determine the pull-up point. This optimal profile was characterized by dynamic pressure (q), flight path angle (γ), and acceleration. A schematic of this guidance is shown in figure 5.

The predictor-corrector algorithm used 3-degree-of-freedom equations of motion that were modified to include longitudinal static trim by elevon deflections. For this study, the predictor-corrector model used the same planet, gravity, and propulsive models as the actual simulations. The aerodynamic model was composed of the untrimmed C_L and C_D coefficients as well as $C_{L\delta_e}$, $C_{D\delta_e}$, and $C_{m\delta_e}$ which describe the elevator effectiveness. These aerodynamic data were derived from the aerodynamic data used in the 6-degree-of-freedom simulation. The basic atmospheric model used in the predictor-corrector algorithm was the 1976 standard. However, this model had to be modified because the vehicle flies a dynamic pressure profile when it enters the predictor-corrector guidance. If the atmospheric model was not modified, the guidance laws for the predictor-corrector algorithm would see an immediate unrealistic dynamic pressure error. To correct this defect, the atmospheric density used by the predictor-corrector algorithm is the 1976 standard atmosphere modified by a constant factor. This factor is the ratio of the actual dynamic pressure to the dynamic pressure predicted by 1976 standard atmosphere. This factor is calculated whenever the predictor-corrector algorithm is invoked.

AIR-BREATHING FLIGHT CONTROL SYSTEM

The requirement for a 6-degree-of-freedom simulation dictated that a control system for the air-breathing vehicle had to be designed. A schematic of the control system is shown in figure 6. The philosophy was to use the elevons for both pitch and roll control. This was accomplished by differentially deflecting the elevons so that they would function for both elevators (δ_e) and ailerons (δ_a). Thus, the elevons were used to control both angle of attack and bank angle. The rudder was used to control sideslip angle. The engines were throttled to maintain the optimal acceleration profile. The engines were not gimbaled for this study.

OPTIMAL TRAJECTORIES

The optimal ascent trajectory for the vertical-takeoff rocket vehicle from launch to orbital insertion is shown in figure 7. The orbiter inserts into a 93- by 185-km orbit, then coasts to apogee where the orbit is circularized. The ideal velocity (ΔV) and velocity losses for this trajectory are shown in table 3. This table also shows the velocity losses associated with using engine gimbal for trim.

This optimal ascent points out two potential flight control system issues. This class of vehicle, namely two-stage employing parallel burn and crossfeed, will have a large lateral center-of-gravity shift during ascent until staging. If the pitch trim is provided solely by engine gimbaling, this will result in a large gimbal angle requirement. For this case, a ± 25 -deg range was required solely for trim. Studies are currently underway to assess the significance of this large gimbal angle requirement. This is discussed in more detail in the following section.

The second issue is the control requirement to ensure a successful staging. The trim requirements alone require that the orbiter engines gimbal over a range of >25 deg at staging. Many other issues, such as interference aerodynamics, will make the staging of any multiple-staged parallel-mounted vehicle a serious control issue.

The optimal ascent trajectory for the horizontal-takeoff air-breathing vehicle is shown in figure 8. The ΔV and velocity losses for this trajectory are shown in table 3. The table also shows the velocity losses associated with using the elevons for trim. The one potential flight control issue uncovered by this simulation is the large value of velocity loss associated with trim. This indicates that the use of active center-of-gravity control or thrust vectoring should decrease the amount of propellant required.

RESULTS AND DISCUSSION

Vertical-Takeoff Rocket Vehicle

Atmospheric Density Variations

The first off-nominal conditions used in the flight control sensitivity analysis were constant bias factors applied to the standard atmospheric density. The optimal trajectory discussed in the previous section was determined with the 1976 standard atmosphere. The off-nominal densities were simulated by applying factors of 0.8 to 1.2 to the standard density. The results of these cases are shown in table 4. The guidance algorithm was able to successfully fly these off-nominal conditions, and no performance issues were uncovered. The total amount of payload variation, when compared with the optimal profile, ranged from -3452 to 782 kg.

To simulate a more realistic variation in atmospheric density, mean density profiles for each month of the year as determined by the Global Reference Atmosphere Model (GRAM) were used. The GRAM (see Ref. 7), was developed to provide realistic atmospheric data including winds. The GRAM provides both mean and perturbation data. The results from the simulations are shown in table 5. The total amount of payload variation, when compared with the optimal profile, ranged from -504 to -208 kg.

Atmospheric Density Variations Including Winds

Simulations were also conducted with these same atmospheric density profiles with winds added. The results of these simulations are shown in table 6. The total amount of payload variation, when compared with the optimal profile, ranged from -504 to -189 kg.

In addition, trajectories were simulated using 10 perturbed profiles for a single date (July 1, 1989). The results of these simulations are shown in table 7. The total amount of payload variation, when compared with the optimal profile, ranged from -472 to -603 kg. In addition, trajectories were simulated with a $\pm 3 \sigma$ variation in the mean density for this same date. These results are given in table 7 and show a payload variation when compared with the optimal of -1056 to -118 kg.

Gimbal Angle Reduction

While studies are underway to assess the impact on vehicle design of large pitch-gimbal angles, control studies are being conducted to assess the relative merits of alternate control techniques. The most promising solution found to date is to provide control both throttling and gimbaling the engines. To illustrate this technique, the optimal trajectory was determined with a maximum allowable gimbal angle of 10 deg. To provide the additional required pitch control, the booster engines were throttled when the engines reached this gimbal limit. After staging, the engines remain within the 10-deg limit. The comparison trajectories are shown in figure 9, and figure 8 illustrates the performance differences. For this study, all the booster engines were throttled equally. In actual practice, engines would be shut down to avoid the deep throttling required for trim. The use of this technique results in a reduction in inserted weight of 1288 kg. Thus, this technique would be worthwhile if the penalty to allow the large gimbal angles exceeds this value.

Separation Analysis

One of the significant design issues for any multi-stage vehicle is to provide a safe separation at staging. This vehicle is different from any that have been flown to date in that both the orbiter and booster are winged. An additional complication is that at staging, the booster (the lower vehicle) is empty, and the orbiter is fully fueled as a result of using propellant crossfed from the booster to fuel the engines of the orbiter until staging. Because of these issues, a preliminary analysis of the staging maneuver was conducted.

The computer program used in this analysis is described in reference 8. This program provides for the 6-degree-of-freedom analysis of multiple bodies. For this study, only the longitudinal modes were analyzed, and no interference effects were added to the aerodynamic data base. The separation sequence that would provide a successful separation was to shut down the booster engines, release the forward attachment strut, allow the booster to rotate until the angle between the two vehicles reached 2 deg, and then release the aft attachment strut. After staging, the booster was commanded to fly an angle of attack of -10 deg. The control system used by the booster during the separation is shown in figure 10. The nominal separation is shown in figure 11 relative to the orbiter. The state conditions at staging are shown in table 9, and the angle-of-attack and elevator histories are shown in figure 12. Separation trajectories were also analyzed at off-nominal staging angles of attack. This analysis showed that a successful separation required that the staging angle of attack must be between -6 and 2 deg.

Conclusions

The predictor-corrector guidance algorithms provided for accurate insertions with errors in geocentric radius at insertion of <1 m for all cases. In all the atmospheric dispersion cases studied, no additional flight control issues other than those discussed previously, namely large engine gimbal angles and the staging maneuver itself, were uncovered. Solutions to both of these concerns have been developed, and a preliminary analysis of each has been completed.

Horizontal-Takeoff Air-Breathing Vehicle

Nominal Trajectory

The predictor-corrector algorithm is used only to determine the velocity at which to begin the pull-up maneuver. The target conditions of the predictor-corrector algorithm were modified such that for the nominal case the 6-degree-of-freedom simulation using the predictor-corrector guidance algorithm would give the same results as the optimal trajectory.

Atmospheric Density Variations

The same strategy that was used to assess the flight control issues for the vertical-takeoff rocket vehicle was used for the horizontal-takeoff vehicle. The first off-nominal conditions were the constant factor biases applied to the standard atmosphere. As with the rocket vehicle, these factors were varied from 0.8 to 1.2. Because the predictor-corrector guidance algorithm calculates a density factor that matches dynamic pressure when the algorithm is first entered, the atmospheric model used by the algorithm was identical to the one used by the simulation. The results of these simulations are given in table 10. The total payload variation, including the ΔV required for circularization, when compared with the optimal profile, ranged from -381 to 177 kg.

The results of the simulations using the density profiles from GRAM are shown in table 11. These density variations also uncovered no flight control issues, and the total payload variation, when compared with the optimal profile, ranged from 38 to 581 kg.

Atmospheric Density Variations Including Winds

The simulations that used the GRAM density and wind profiles are shown in table 12. These density variations also uncovered no flight control issues, and the total payload variation, when compared with the optimal profile, ranged from 22 to 611 kg.

In addition, trajectories were also simulated using the same 10 perturbed profiles used by the all-rocket vehicle for a single date (July 1, 1989). The results of these simulations are shown in table 13. The total amount of payload variation, when compared with the optimal profile, ranged from 452 to 546 kg. In addition, trajectories were simulated with a $\pm 3\sigma$ variation in the mean density for this same date. These results are given in table 13 and show a payload variation when compared with the optimal of 406 to 583 kg.

Conclusions

As with the vertical-takeoff rocket system, the addition of off-nominal atmospheric conditions did not uncover additional significant flight control issues over those uncovered during the determination of the optimal trajectories. However, when one compares the insertion accuracy of the vertical-takeoff system (tables 4-7), with the insertion accuracy of the horizontal take-off vehicle (tables 10-13), one notes that the vertical-takeoff rocket was inserted with accuracies of 1 m, whereas the horizontal take-off airbreathing vehicle had insertion errors as high as 4.8 km. To improve this accuracy will require that the air-breathing vehicle be able to modulate its acceleration after the main engines are shut down (23.9 kPa to insertion). The required change to the guidance algorithm would be minor, but more fuel would be required for ascent.

SUMMARY

A study has been conducted that investigated some of the issues that affect the flight control and guidance system designs for vertical-takeoff and horizontal-takeoff vehicles. The study used a two-stage all-rocket vehicle to represent the vertical-takeoff system and a generic aerospace plane concept to represent the horizontal-takeoff vehicle. To conduct this study, a robust guidance algorithm was designed for both vehicles. These algorithms demonstrated very accurate insertion capability under the conditions simulated for the vertical-takeoff all-rocket vehicle and moderate insertion accuracy for the horizontal-takeoff air-breathing vehicle.

Two flight control issues for the vertical take-off rocket were uncovered. The first was the large gimbal angle range required for pitch trim when using parallel mated vehicles. The second was control during staging.

Two issues were also identified for the air-breathing vehicle. The first was that since the drag losses are a significant fraction of the total ideal velocity required, the drag associated with trimming needs to be reduced. The second issue was that since the vehicle flies at high dynamic pressure for most of the ascent, the guidance system design will be more difficult to insure accurate insertion.

FUTURE WORK

No flight control issue has been identified in this paper that would preclude the selection of either of these two classes of vehicle for the next launch vehicle. However, this paper has been able to address only a few of the issues that will affect the design of the flight control and guidance systems for the next-generation spacecraft. Some major areas that were not discussed, but which are currently being examined at the NASA Langley Research Center, include additional atmospheric anomalies such as gusts and turbulence, control during staging, as well as alternate trim techniques.

REFERENCES

1. Talay, T.A. and Morris, W.D., Advanced Manned Launch Systems, 1989, EAC Paper EAC '89-17, AAF/DGLR/AeS/ESA Second European Aerospace Conference Progress in Space Transportation, Bonn - Bad Godesberg, Federal Republic of Germany.
2. Bonner, E., Clever, W., and Dunn, K., Aerodynamic Preliminary Analysis System II, Part I - Theory, 1989.
3. Sova, G., Divan, P., Aerodynamic Preliminary Analysis System II, Part II - User's Manual, 1989.

4. Cruz, C. and Wilhite A., Prediction of High Speed Aerodynamic Characteristics Using the Aerodynamic Preliminary Analysis System, 1989, AIAA Paper 89-2173.

5. Brauer, G. L., Cornick, D. E., and Stevenson, R., Capabilities and Applications of the Program to Optimize Simulated Trajectories (POST), February 1977, NASA CR-2770.

6. U.S. Standard Atmosphere, 1976. National Oceanic and Atmospheric Administration, National Aeronautics and Space Administration, and United States Air Force, Washington, D.C., October 1976.

7. Justus, C. G., et al., The NASA/MSFC Global Reference Atmospheric Model - Mod 3 (With Spherical Harmonic Wind Model), 1980, NASA CR 3256.

8. Hurley, M. J., A Six-Degree, Multiple-Body Separation Simulation for Hinge and/or Linked Lifting-Entry Vehicle Clusters, December 1969, GDC-ERR-1377, Convair Division of General Dynamics, San Diego, California.

TABLE 1. CHARACTERISTICS OF VERTICAL-TAKEOFF ROCKET VEHICLE

<u>BOOSTER</u>	
Gross mass, kg.....	453,742
Dry mass, kg.....	48,699
Number of engines.....	6
Vacuum engine thrust, N.....	1.557×10^6
Engine vacuum I_{sp} , sec.....	438
Wing reference area, m^2	144
<u>ORBITER</u>	
Gross mass, kg.....	538,361
Dry mass, kg.....	69,387
Payload, kg.....	9,100
Number of engines.....	4
Engine vacuum thrust, N.....	1.557×10^6
Engine vacuum I_{sp} , sec.....	438
Wing reference area, m^2	185

TABLE 2. CHARACTERISTICS OF HORIZONTAL-TAKEOFF AIR-BREATHING VEHICLE

Gross mass, kg.....	136,079
Dry mass, kg.....	58,968
Payload, kg.....	9,100
Circularization engine I_{sp} , sec.....	465
Wing reference area, m^2	335
Span, m.....	18
Mean aerodynamic chord, m.....	24
Engine thrust and I_{sp} characteristics are shown in figures 3 and 4	

TABLE 3. RELATIVE VELOCITY LOSSES OF ROCKET AND AIR-BREATHING VEHICLES

	<u>ROCKET</u>	<u>AIR-BREATHING</u>
ΔV , m/sec	9,334	10,749
ΔV_{LOSS} , m/sec	1,872	3,372
ΔV_{AT} , m/sec	200	0
ΔV_D , m/sec	193	2,725
ΔV_G , m/sec	1,327	636
ΔV_{TV} , m/sec	156	16
ΔV_{CP} , m/sec	-4	-5
ΔV_{CIRC} , m/sec	26	162
Velocity losses due to gimballing, m/sec	0	0
Vector losses due to elevation deflection, m/sec	0	366

TABLE 4. VERTICAL-TAKEOFF ROCKET SIMULATION RESULTS FOR CONSTANT FACTOR ATMOSPHERIC DENSITY VARIATIONS

	<u>FACTOR=0.8</u>	<u>FACTOR=0.9</u>	<u>FACTOR=1.1</u>	<u>FACTOR=1.2</u>
Δ Payload, kg	782	464	-849	-3452
Δ Time, sec	-1.1	-0.7	1.2	5.1
ΔG_{rad} , m	-0.6	-0.15	0.2	-0.03
$\Delta \gamma$, deg	-0.0003	-0.0001	0.0003	-0.0001

TABLE 5. VERTICAL-TAKEOFF ROCKET SIMULATION RESULTS FOR GRAM ATMOSPHERIC DENSITY VARIATIONS
(Monthly Mean Density With No Winds)

	<u>JANUARY</u>	<u>FEBRUARY</u>	<u>MARCH</u>	<u>APRIL</u>	<u>MAY</u>	<u>JUNE</u>
Δ Payload, kg	-254	-208	-225	-277	-339	-416
Δ Time, sec	0.4	0.3	0.3	0.4	0.5	0.6
ΔG_{rad} , m	0.44	0.03	0.24	0.15	0.12	0.06
$\Delta \gamma$, deg	0.0004	0.0002	0.0003	0.0004	0.0003	-0.0001
	<u>JULY</u>	<u>AUGUST</u>	<u>SEPTEMBER</u>	<u>OCTOBER</u>	<u>NOVEMBER</u>	<u>DECEMBER</u>
Δ Payload, kg	-504	-470	-411	-334	-286	-282
Δ Time, sec	0.7	0.7	0.6	0.5	0.4	0.4
ΔG_{rad} , m	-0.09	0.18	0.33	0.4	0.4	0.09
$\Delta \gamma$, deg	-0.0001	0.0002	0.0004	0.0004	0.0004	0.0003

TABLE 6. VERTICAL-TAKEOFF ROCKET SIMULATION RESULTS FOR GRAM ATMOSPHERIC DENSITY VARIATIONS
(Monthly Mean Density With Winds)

	<u>JANUARY</u>	<u>FEBRUARY</u>	<u>MARCH</u>	<u>APRIL</u>	<u>MAY</u>	<u>JUNE</u>
Δ Payload, kg	-212	-189	-250	-329	-364	-411
Δ Time, sec	0.3	0.3	0.4	0.5	0.5	0.6
ΔG_{rad} , m	0.34	0.03	0.24	0.15	0.12	0.06
$\Delta\gamma$, deg	0.0004	0.0001	0.0003	0.0004	0.0003	-0.0002
	<u>JULY</u>	<u>AUGUST</u>	<u>SEPTEMBER</u>	<u>OCTOBER</u>	<u>NOVEMBER</u>	<u>DECEMBER</u>
Δ Payload, kg	-504	-449	-398	-315	-269	-255
Δ Time, sec	0.7	0.7	0.6	0.5	0.4	0.4
ΔG_{rad} , m	-0.09	0.21	0.37	0.40	0.40	0.09
$\Delta\gamma$, deg	-0.0001	0.0003	0.0004	0.0004	0.0004	0.0003

TABLE 7. VERTICAL-TAKEOFF ROCKET SIMULATION RESULTS FOR GRAM ATMOSPHERIC DENSITY VARIATIONS
(Perturbations for July 1, 1989 With Winds)

	<u>PERT #1</u>	<u>PERT #2</u>	<u>PERT #3</u>	<u>PERT #4</u>	<u>PERT #5</u>
Δ Payload, kg	-603	-502	-564	-566	-570
Δ Time, sec	0.9	0.8	0.8	0.8	0.8
ΔG_{rad} , m	-0.24	-0.31	0.15	-0.18	-0.30
$\Delta\gamma$, deg	0.0004	-0.0005	0.0004	-0.0003	-0.0005
	<u>PERT #6</u>	<u>PERT #7</u>	<u>PERT #8</u>	<u>PERT #9</u>	<u>PERT #10</u>
Δ Payload, kg	-562	-562	-528	-526	-472
Δ Time, sec	0.8	0.8	0.8	0.8	0.7
ΔG_{rad} , m	0.06	-0.21	-0.18	0.18	-0.15
$\Delta\gamma$, deg	0.0002	-0.0001	-0.0002	-0.0001	-0.0002
	<u>3σ PERT</u>	<u>-3σ PERT</u>			
Δ Payload, kg	-1056	-118			
Δ Time, sec	1.5	-0.2			
ΔG_{rad} , m	0.49	-0.49			
$\Delta\gamma$, deg	-0.001	0.001			

TABLE 8. COMPARISON OF ROCKET VEHICLE WITH AND WITHOUT ENGINE GIMBAL CONSTRAINTS

	<u>WITHOUT GIMBAL CONSTRAINTS</u>	<u>PITCH GIMBAL ANGLES LIMITED TO ± 10 DEGREES</u>
ΔV , m/sec	9,334	9,381
ΔV_{LOSS} , m/sec	1,872	1,918
ΔV_{THRUST} , m/sec	200	211
ΔV_{AERO} , m/sec	193	194
ΔV_{GRAV} , m/sec	1,327	1,342
ΔV_{TV} , m/sec	156	175
ΔV_{COR} , m/sec	-4	-4
ΔV_{CIRC} , m/sec	26	26
Time to staging, sec	104.8	114.4
Time to insertion, sec	438.3	449.5

TABLE 9. VERTICAL-TAKEOFF ROCKET STAGING CONDITIONS

Altitude, m	24,687
Velocity, m/sec.....	.835
γ , deg.....	37.5
α , deg.....	1.7
Mach.....	2.8

TABLE 10. HORIZONTAL TAKE-OFF AIR-BREATHING SIMULATION RESULTS FOR CONSTANT FACTOR ATMOSPHERIC DENSITY VARIATIONS

	<u>FACTOR=0.8</u>	<u>FACTOR=0.9</u>	<u>FACTOR=1.1</u>	<u>FACTOR=1.2</u>
Δ Payload, kg.	-381	-176	150	177
Δ Time, sec	15.5	7.0	-5.9	-6.9
Δ Apogee, km	-0.6	0.2	0	0
Δ Perigee, km	7.8	3.5	-3.3	-6.9

TABLE 11. HORIZONTAL-TAKEOFF AIR-BREATHING SIMULATION RESULTS FOR GRAM
ATMOSPHERIC DENSITY VARIATIONS
(Monthly Mean Density With No Winds)

	<u>JANUARY</u>	<u>FEBRUARY</u>	<u>MARCH</u>	<u>APRIL</u>	<u>MAY</u>	<u>JUNE</u>
Δ Payload, kg	307	249	270	475	581	557
Δ Time, sec	-8.5	-6.8	-5.2	6.2	-9.7	-9.0
Δ Apogee, km	4.8	3.5	2.0	2.6	4.1	3.0
Δ Perigee, km	-7.4	-6.1	-4.3	-4.3	7.6	-5.7
	<u>JULY</u>	<u>AUGUST</u>	<u>SEPTEMBER</u>	<u>OCTOBER</u>	<u>NOVEMBER</u>	<u>DECEMBER</u>
Δ Payload, kg	485	341	295	239	38	289
Δ Time, sec	-7.5	-7.6	-6.3	-6.0	-7.4	-7.1
Δ Apogee, km	2.0	1.7	0.9	1.5	2.8	3.1
Δ Perigee, km	-4.8	-5.9	-4.8	-4.8	-7.2	-6.1

TABLE 12. HORIZONTAL-TAKEOFF AIR-BREATHING SIMULATION RESULTS FOR GRAM
ATMOSPHERIC DENSITY VARIATIONS
(Monthly Mean Density With Winds)

	<u>JANUARY</u>	<u>FEBRUARY</u>	<u>MARCH</u>	<u>APRIL</u>	<u>MAY</u>	<u>JUNE</u>
Δ Payload, kg	257	198	230	458	596	611
Δ Time, sec	-8.2	-5.7	-4.3	-5.3	-9.5	-10.3
Δ Apogee, km	4.6	3.0	1.5	2.2	4.1	3.7
Δ Perigee, km	-9.3	-8.9	-6.9	-5.6	-7.2	-3.3
	<u>JULY</u>	<u>AUGUST</u>	<u>SEPTEMBER</u>	<u>OCTOBER</u>	<u>NOVEMBER</u>	<u>DECEMBER</u>
Δ Payload, kg	482	369	307	240	22	249
Δ Time, sec	-10.3	-8.9	-6.9	-4.8	-5.2	-5.0
Δ Apogee, km	3.0	2.2	1.1	0.9	1.3	2.2
Δ Perigee, km	-2.4	-3.9	-4.3	-6.5	-10.7	-9.1

TABLE 13. HORIZONTAL-TAKEOFF AIR-BREATHING SIMULATION RESULTS FOR GRAM
ATMOSPHERIC DENSITY VARIATIONS
(Perturbations for July 1, 1989 With Winds)

	<u>PERT#1</u>	<u>PERT#2</u>	<u>PERT#3</u>	<u>PERT#4</u>	<u>PERT#5</u>
Δ Payload, kg	487	504	508	522	507
Δ Time, sec	-9.0	-11.4	-9.0	-11.9	-9.6
Δ Apogee, km	1.1	2.8	1.4	3.0	2.4
Δ Perigee, km	2.2	-3.3	0.4	-5.0	-1.7
	<u>PERT#6</u>	<u>PERT#7</u>	<u>PERT#8</u>	<u>PERT#9</u>	<u>PERT#10</u>
Δ Payload, kg	503	452	474	509	546
Δ Time, sec	-6.8	-12.0	-9.5	-8.9	-11.3
Δ Apogee, km	1.7	3.7	2.8	2.6	1.5
Δ Perigee, km	3.1	-6.1	-1.3	-0.2	0.6
	<u>3σ PERT</u>	<u>-3σ PERT</u>			
Δ Payload, kg	583	406			
Δ Time, sec	-19.1	-0.2			
Δ Apogee, km	4.4	1.3			
Δ Perigee, km	-12.6	9.4			

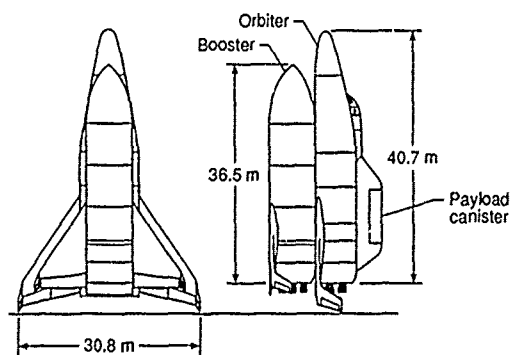


Figure 1. Vertical-takeoff rocket vehicle.

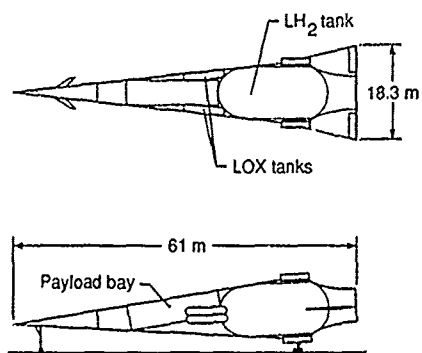


Figure 2. Horizontal-takeoff of air-breathing vehicle.

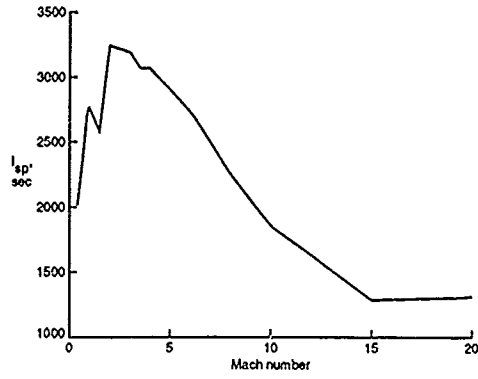


Figure 3. I_{sp} characteristics of air-breathing vehicle.

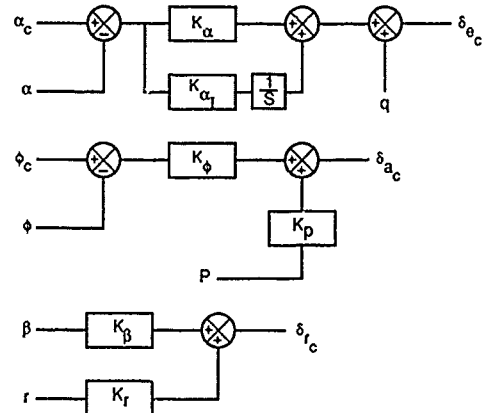


Figure 6. Schematic of control system for air-breathing vehicle.

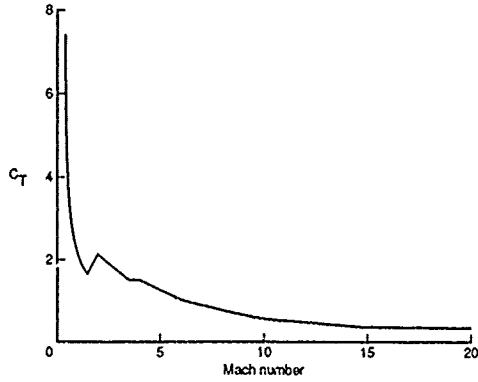
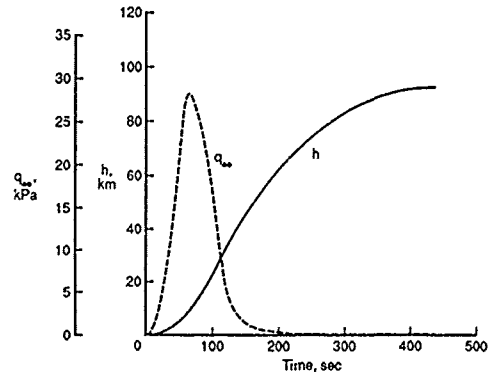


Figure 4. Thrust coefficient characteristics of air-breathing vehicle.



(a) Dynamic pressure and altitude histories.

Figure 7. Optimal ascent trajectory for vertical-takeoff rocket system.

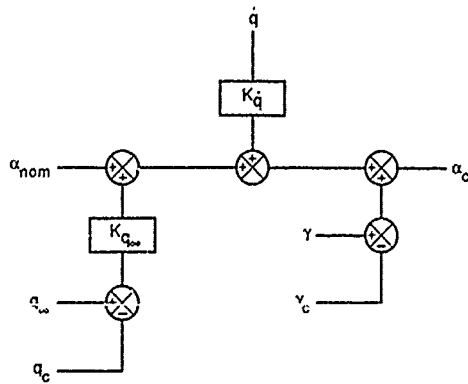
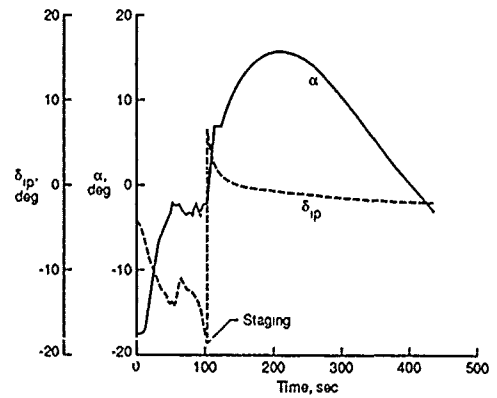


Figure 5. Schematic of guidance algorithm for air-breathing vehicle.



(b) Engine pitch gimbal angle and angle-of-attack histories.

Figure 7. Concluded.

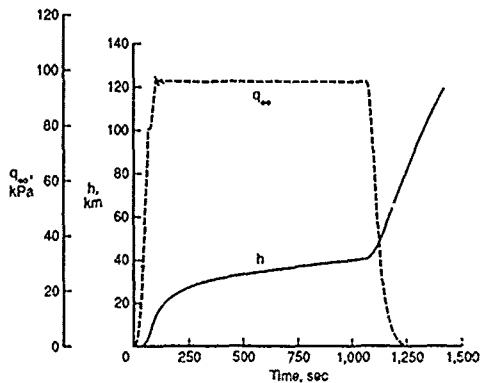
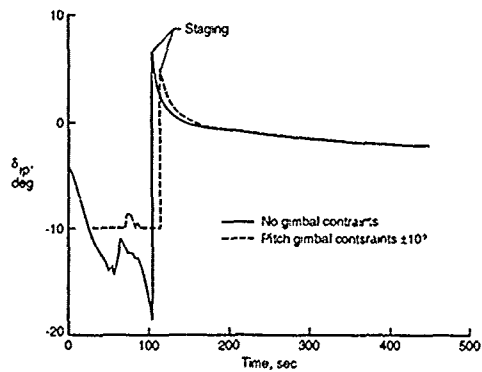
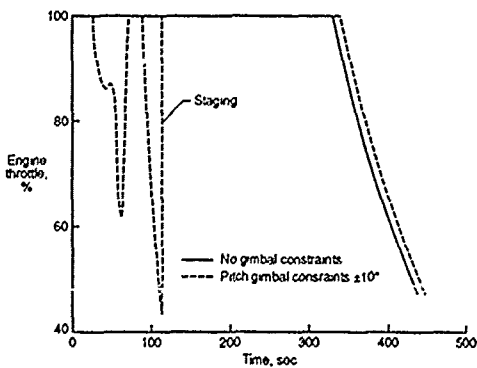


Figure 8. Optimal ascent trajectory for horizontal-takeoff air-breathing vehicle.



(a) Engine pitch gimbals history.

Figure 9. Comparison of control histories for vertical-takeoff rocket vehicle with and without engine pitch gimbals limits.



(b) Engine throttle history.

Figure 9. Concluded.

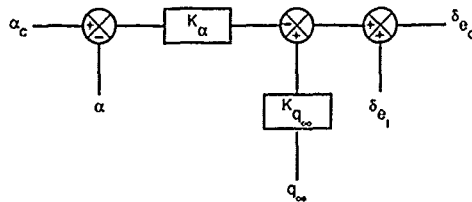


Figure 10. Booster pitch flight control system for separation maneuver.

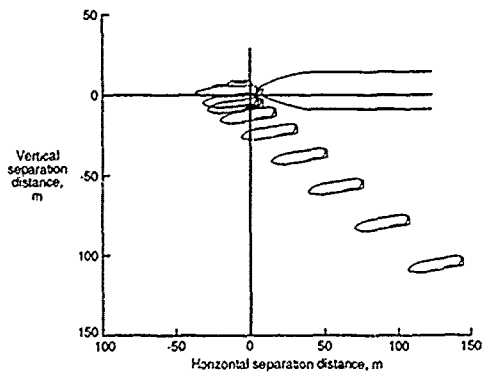
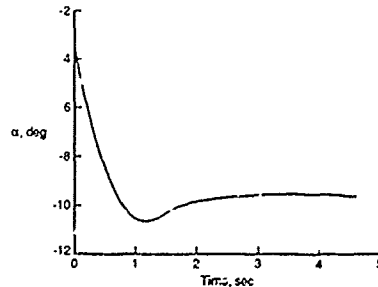
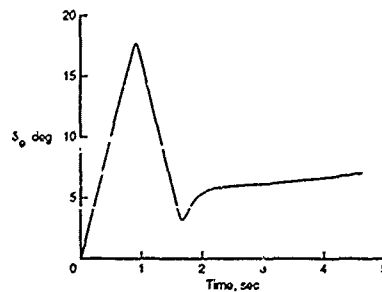


Figure 11. Separation time history of booster and orbiter.



(a) Angle of attack.

Figure 12. Time history of booster angle of attack and elevator deflection during separation maneuver.



(b) Elevator.

Figure 12. Concluded.

ASCENT and DESCENT TRAJECTORY OPTIMIZATION of ARIANE V/HERMES

C.Jänsch, K.Schnepper, K.H.Well

Institute for Flight Systems Dynamics
Deutsche Forschungsanstalt für Luft-und Raumfahrt(DLR)
(German Aerospace Research Establishment)
Oberpfaffenhofen, Federal Republic of Germany

Summary

An overview over the state of the art of trajectory optimization of aerospace vehicles is given with emphasis on applications to ARIANE V ascent trajectories and HERMES reentry trajectories. The paper briefly reflects on some of the numerical methods used in the past and describes in more detail two relatively new methods under development, both of which need efficient sequential quadratic programming for solving the associated nonlinear programming problems. A detailed description of the equations of motion, the boundary conditions and the flight path constraints for the ARIANE V ascent and the HERMES reentry is presented and numerical results are given for an optimal ascent into geostationary transfer orbit, into a sun-synchronous orbit, into a 28.5° transfer orbit for the ARIANE V/HERMES combination, and an optimal reentry from a 28.5° orbit to Istres. The paper concludes with an outlook into trajectory optimization of space vehicles with airbreathing engines.

1. INTRODUCTION

Ascent trajectory optimization of rockets has been one of the driving applications for developing new optimization methods, more efficient algorithms and software for almost 30 years. This is not surprising since only a small fraction of the total lift-off mass of a rocket can be utilized as payload and, therefore, it is most important to select the best ascent profile. For this purpose the motion of the vehicle can be analyzed by looking at the motion of the center of mass and neglecting the rotational dynamics. Mathematically this requires the solution of a set of ordinary differential equations[1] which are controlled by pitch- and yaw-angles from lift-off until burn-out of the last stage. The purpose of optimization is to select the time histories of the control functions in such a way as to maximize the payload in the desired orbit while observing all vehicle- and mission constraints.

Descent trajectory optimization has been of interest ever since reentry vehicles are capable of generating lift forces during the reentry and using these to change their flight paths. Here, too, the analysis can be done by considering mass point motion only, and the control functions are for instance angle of attack and velocity bank angle. There are various performance criteria of interest such as maximizing the crossrange or minimizing the total heat load accumulated along the flight path. Most important are temperature constraints at various critical points of the vehicle, for instance at the stagnation point, at the leading edge of the wings, or at critical points at the lower wing/fuselage surface. Other constraints are on maximum permitted deceleration, on maximum permitted dynamic pressure and on maximum permitted hinge moments of some of the control surfaces.

The above described optimization problems are optimal control problems which can not be solved analytically except in rare cases where one makes simplifying assumptions such as neglecting the effect of the atmosphere and considering impulsive accelerations or neglecting the atmosphere and assuming flat earth and constant gravitational forces for the ascent problem, or assuming zero flight path angle and neglecting gravitational forces during for the descent problem. Solutions obtained with these kind of simplifying assumptions can serve the analyst quite well, they must be checked, however, by comparing them with numerical solutions obtained using a full order dynamic model. To this end various optimization methods are available.

The first class of methods are gradient and conjugate gradient methods which have been applied for these kind of problems successfully in the past, f.i. Ref. [2]–[5]. Parameterizing the control functions over a user specified grid has been a successful approach for solving trajectory optimization problems, too. This technique transforms the optimal control problem into a nonlinear programming problem and was first applied to rocket trajectories in [6], later in [7]–[9]. Improvements in methods for solving nonlinear programs have been utilized in the later papers. The ascent trajectory of the US–Shuttle has been designed using this approach. At the European Space Agency (ESA) there exists software based on this approach. In [10] and [11] the ideas of Davidon Fletcher Powell on Quasi–Newton Methods for nonlinear programming was extended to function space and applied to ascent trajectory optimization. All these methods are considered first order methods since they make use of first order information only. First order algorithms need the system– and the adjoint differential equations, which have to be solved in backward or forward direction once in each iteration. Second order information is built up – where required – during the course of the iteration sequence.

Second order methods for solving trajectory optimization problems have been proposed early in the development, too. The most widely used one is the Multiple Shooting Algorithm (MSA) first presented in [12] with later extensions in [13]. Second order methods – except the MSA – need analytical second partial derivatives of the system equations which are cumbersome to get for complex trajectory problems. The MSA generates the second order information numerically and, therefore, is the only competitive optimization method in its class. Here, the system equations must be integrated forward together with the adjoints in each iteration. The switching structure of the optimal solution must be known in advance. It has been successfully applied to ascent and descent problems in [14] and [15].

A different computational method is due to Bellman's Principle of Dynamic Programming. Here, the constrained optimal control problem is discretized and a multistage decision making problem is obtained which is being solved by a special recursion formula based on Bellman's optimization principle. This method suffers from the so called "curse of dimensionality" because computer time and RAM storage demands increase exponentially with the dimension of the state vector. This has limited its applicability to small problems, say three state variables at most. Indirectly related to the dynamic programming method through the Hamilton–Jacobi partial differential equation is the differential dynamic programming method. In [17] numerical experience with a first and a second order version of the algorithm for aerospace problems is reported. This method needs adjoint differential equations and in its second order version even analytical second partials with respect to the state. DDP methods have seen only limited applications.

The significant advance in solving constrained nonlinear programming problems has been the development of efficient quadratic programming (QP) solvers within the last 10 years and this has renewed the interest in trajectory optimization algorithms based on parameterizing the optimal control problem. In [18]–[21] recursive quadratic programming is applied to space trajectory optimization in connection with an indirect method. QP solvers are used in connection with direct methods in [22]–[23] and in [24]. Here a multiple shooting structure is introduced into the parameterized optimal control problem thus making forward differencing for generating estimates for partial derivatives with respect to the parameters as efficient as using adjoints. In [25] a special integrator is presented which enhances the performance of the algorithms for parameterized control calculations even further. Results for ascent and descent optimization are given in [25]–[29]. Another new approach which utilizes the advance in solving QP's efficiently is presented in [30] using direct collocation for satisfying the differential system. The associated software is known in the United States under the Name OTIS and has found widespread use at many government laboratories, in industry, and at some universities. It has been applied successfully for analyzing the ascent trajectories of new launch vehicles with airbreathing engines.

In this paper two new methods under development at DLR are presented, one based on parameterizing the control functions and multiple shooting for integrating the system equations numerically. This algorithm is presented under the name PROMIS. It has several advanced features such as a separate discretization grid for each component of the control vector, variable control model function selection options, a separate grid for handling state

constraints, efficient integration of the system equations by using the integrator from [25], and it does not need adjoint differential equations. The other method is based on direct collocation for satisfying the system differential equations. It is an extension of the method presented in [30] with additional features such as automatic scaling and variable grid selection. The system equations need not to be integrated explicitly and the method does not need adjoints. This one is presented under the name TROPIC. These methods are being developed with the primary goal of having efficient software for trajectory optimization of aerospace vehicles. Particular emphasis is placed on an advanced user interface which makes it easy to set up a new optimization problem, change the models, perform iteration sequences, analyze intermediate and final results, and switch from one type of method to another one. These methods will be applicable for trajectory optimization of winged launchers with airbreathing engines, for instance HOTOL or SÄNGER II.

2. MATHEMATICAL MODELS for SIMULATION and OPTIMIZATION

2.1 Equations of motion

The point mass equations of motion in a flight path coordinate system over a spherical, rotating earth with no wind in the atmosphere are [1]

$$\begin{aligned}
 \dot{V} &= r\omega_E^2(\cos^2\delta \sin\gamma - \sin\delta \cos\delta \cos\gamma \cos\chi) - g \sin\gamma + (T/m)\cos\sigma \cos\epsilon + X_w/m \\
 \dot{\chi} &= (V/r)\cos\gamma \sin\chi \tan\delta + 2\omega_E(\sin\delta - \cos\delta \cos\chi \tan\gamma) + r\omega_E^2(V\cos\gamma)^{-1}\sin\chi \sin\delta \cos\delta \\
 &\quad - T(mV\cos\gamma)^{-1}\cos\sigma \sin\epsilon - Y_w(mV\cos\gamma)^{-1} \\
 \dot{\gamma} &= (V/r)\cos\gamma + 2\omega_E\sin\chi \cos\delta + (r\omega_E^2/V)(\cos^2\delta \cos\gamma + \sin\delta \cos\delta \sin\gamma \cos\chi) \\
 &\quad - (g/V)\cos\gamma + (mV)^{-1}(T\sin\sigma + Z_w) \\
 \dot{\Lambda} &= (V/r)\cos\gamma \sin\chi (\cos\delta)^{-1} \\
 \dot{\delta} &= (V/r)\cos\gamma \cos\chi \\
 \dot{r} &= V\sin\gamma \\
 \dot{m} &= -\dot{b}
 \end{aligned} \tag{1}$$

Here, V is the vehicle velocity relative to an earth fixed coordinate system, r its radius vector from the center of the earth, χ, γ are azimuth and path inclination which measure the orientation of the flight path coordinate system relative to a local horizontal system. Λ, δ are geographical latitude and longitude of the vehicle. T is the thrust, m the vehicle mass, X_w, Y_w, Z_w are the aerodynamic forces acting on the vehicle. The angles σ and ϵ are the directions of the thrust vector with respect to the flight path coordinate system. They represent the control functions in the differential system. $\omega_E (7.2921 \cdot 10^{-3} \text{ rad/s})$ is the angular velocity of the earth's rotation. σ and ϵ can be replaced by body pitch and yaw angles θ and ψ through the transformation

$$\begin{bmatrix} \cos\sigma \cos\epsilon \\ \cos\sigma \sin\epsilon \\ \sin\epsilon \end{bmatrix} = A \begin{bmatrix} \sin\theta \cos\psi \sin\chi_0 + \sin\psi \cos\chi_0 \\ \sin\theta \cos\psi \cos\chi_0 - \sin\psi \sin\chi_0 \\ \cos\theta \cos\psi \end{bmatrix} \tag{2}$$

where the subscript $_0$ indicates angles at $t=0$ and where $A(\chi_0, \delta_0, \Lambda, \delta, \chi, \gamma)$ is a transformation matrix depending on the angles consisting of five orthogonal transformations from the local horizontal system to the body axis system, for details see f.i. [26]. With this expression σ and ϵ can be replaced in (1) by θ and ψ , these being the new control variables for the differential system. For descent there is no thrust, and all terms containing T are not present. In this case the control functions are angle of attack α and velocity bank angle μ , both controls will be discussed below.

The aerodynamic forces are given in vehicle coordinates and are defined as

$$X_f = qc_x S, Y_f = qc_y S, Z_f = qc_z S$$

with $q = (\rho/2)V^2$ the dynamic pressure and S the reference area. The coefficients c_x, c_y, c_z are functions of angle of attack α , side slip angle β , and Machnumber M . For simplification we assume no wind. In this case $\alpha \equiv \sigma$ and $\beta \equiv \epsilon$ and α and β can be used as controls. Then

$$c_x = c_x(M) = -c_{D0}(M), c_y = -\frac{\partial c_y(M)}{\partial \alpha_f} \alpha_f \sin \varphi, c_z = -\frac{\partial c_z(M)}{\partial \alpha_f} \alpha_f \cos \varphi \quad (3)$$

with c_{D0} as drag coefficient at zero angle of attack, α_f and φ as defined in Fig.1. The relation between α , β , α_f and φ is

$$\alpha = \alpha_f \cos \varphi, \beta = -\alpha_f \sin \varphi.$$

The coefficients for the ARIANE V with and without HERMES are taken from Figs.1 and 2 and are approximated in the numerical examples by cubic splines or by linear functions. The aerodynamic forces in the wind axis system are

$$\begin{aligned} X_w &= \cos \alpha \cos \beta X_f - \sin \beta Y_f - \sin \alpha \cos \beta Z_f \\ Y_w &= \cos \alpha \sin \beta X_f + \cos \beta Y_f - \sin \alpha \sin \beta Z_f \\ Z_w &= \sin \alpha X_f + \cos \alpha Z_f \end{aligned} \quad (4)$$

For descent optimization it is customary to use angle of attack α and velocity bank angle μ . In this case the aerodynamic forces are obtained by

$$\begin{aligned} X_w &= -D = -qSc_D(\alpha, M), M: \text{Machnumber}, \\ Y_w &= L \sin \mu = qSc_L(\alpha, M) \sin \mu, \\ Z_w &= L \cos \mu = qSc_L(\alpha, M) \cos \mu \end{aligned} \quad (5)$$

where the lift- and drag coefficients as functions of Machnumber are given in tabular form and are approximated for the numerical examples by polynomial functions.

Air density $\rho(h)$ and speed of sound $a(h)$ are approximated by differentiable functions using the U.S. Standard Atmosphere between 0 and 80 km (see Ref.[14]). The gravitational acceleration is given by

$$g(r, \delta) = (\mu_e / r^3) (1 + 3/2 J_2 (R_E / r)^2 (1 - 3 \sin^2 \delta)) \quad (6)$$

with R_E (6378.155 km) as equatorial radius of the earth and J_2 (0.0010826) as oblateness parameter, μ_e ($398602 \text{ km}^3/\text{s}^2$) is the gravitational constant of the earth. With these equations of motion trajectories can be computed numerically once initial conditions are specified and control time histories $\theta(t), \psi(t)$ in the case of ascent or $\alpha(t), \mu(t)$ in the case of descent are given.

2.2 Masses and specific impulses for ascent

[31] contains a good description of typical ascent trajectories for ARIANE V into geostationary transfer orbit(GTO), into highly eccentric 24h and 48h orbits, into so-called Molnija orbits, and into escape orbits. To achieve these orbits the ARIANE V vehicle has three stages. The first stage is the H155 together with the two boosters P230. The second stage is defined as the flight with the H155 after jettisoning of the boosters. The third stage is the L5 after burn out of the H155 and stage separation. Thrust of a P230 booster is a function of time as depicted in Fig.3. It is approximated as T_{P230} using linear interpolation. Thrust of the other engines is defined as

$$T_{H155} = I_{spH155} \dot{b}_{H155}, \quad T_{L5} = I_{spL5} \dot{b}_{L5}$$

with I_{sp} as the specific impulse of the respective engines and \dot{b} the mass flow. Table 1 contains the numerical values.

$I_{spH155}(s)$	$I_{spL5}(s)$	$\dot{b}_{H155}(kg/s)$	$\dot{b}_{P230}(kg/s)$	$\dot{b}_{L5}(kg/s)$
430	317	253	1933	6.75

Table 1: Spec. Impulses and fuel consumption for various engines of the ARIANE V vehicle

For optimization it is sometimes useful to define "optimization stages". In each of these optimization stages the solution of the differential system (1) is continuous. Table 2 summarizes the ascent sequence and defines the optimization stages for an ascent into GTO.

2P230+H155	H155	COAST	L5
1	2	3	5
$t_0=t_1$	t_2	t_3	t_4
t_f			
SPLASH DOWN			
4			
t_3 t_5			

Table 2: Stages in the optimization problem

Stage 1 is the first stage of the vehicle and the first stage of the optimization problem. At t_2 the boosters are jettisoned, t_2 is fixed(119.177 s). t_3 marks the burn-out of the H155 and is fixed too(600 s). Stage 2 is for $t_2 \leq t \leq t_3$. Stage 3 is the third optimization stage and is a coasting arc after separation of the H155 from the upper stage. t_4 is to be chosen optimally. Stage 4 is the flight of the empty H155 for $t_3 \leq t \leq t_5$. The empty H155 is supposed to splash down in either the Atlantic or the Pacific Ocean at t_5 . More about the splash-down constraint below. Stage 5 is the ascent of the third rocket stage from ignition of the L5 at t_4 until burn-out at t_f which is to be selected optimally.

2.3 Boundary conditions for ascent

The initial conditions are

$$V(0)=5 \text{ m/s}, \quad \chi(0)=90^\circ, \quad \gamma(0)=90.0^\circ, \quad \Lambda(0)=-52.82^\circ(\text{Kourou}), \quad \delta(0)=5.25^\circ(\text{Kourou}), \\ r(0)=R_E+5 \text{ m}, \quad m(0)=m_1,$$

where m_1 is the initial mass in the first optimization stage. Initial masses for the other four stages are given in Table 3.

m_1 (kg)	m_2 (kg)	m_3 (kg)	m_4 (kg)	m_5 (kg)
7 17348	150558	13085	14188	1 3085

Table 3: Initial stage masses

The upper stage of the vehicle has to reach the desired target orbit. In order to relate the state at t_f to the orbital elements the state in the wind axis system is transformed into an inertial coordinate system. The relations for velocity, path inclination, and azimuth are

$$\begin{aligned} V_I^2 &= V^2(t_f) + r(t_f)\omega_E \cos\delta(t_f) \left[2V(t_f)\cos\gamma(t_f)\sin\chi(t_f) + r(t_f)\omega_E \cos\delta(t_f) \right] \\ \sin\gamma_I &= V(t_f)\sin\gamma(t_f)/V_I \\ \cos\chi_I &= V(t_f)\cos\gamma(t_f)\cos\chi(t_f)/(V_I\cos\gamma_I) \end{aligned} \quad (7)$$

where the subscript I designates variables in the inertial coordinate system. The semi-major axis a is obtained from

$$a = r(t_f)\mu_e / (2\mu_e - r(t_f)V_I^2). \quad (8)$$

Eccentricity e and true anomaly f are related to the state vector by

$$e\sin f(1+e\cos f)^{-1} = \tan\gamma_I \quad (9)$$

$$a(1-e^2)(1+e\cos f)^{-1} = r(t_f) \quad (10)$$

The orbital inclination i is computed from

$$\cos i = \cos\delta(t_f)\sin\chi_I. \quad (11)$$

The argument of perigee ω is obtained from

$$\sin(\omega+f) = \sin\delta(t_f)/\sin i, \quad \cos(\omega+f) = \cos\alpha_k \cos\delta(t_f) \quad (12)$$

where the right ascension with respect to the ascending node α_k is computed from

$$\begin{aligned} \sin\alpha_k &= (\sin\delta(t_f)/\cos\delta(t_f))/|\cos i/\sin i| \\ \cos\alpha_k &= \text{sgn}(\cos\chi_I)(1-\sin^2\alpha_k)^{1/2}. \end{aligned} \quad (13)$$

Altogether, perigee and apogee altitude, inclination, and the argument of the perigee are prescribed at injection. These are four conditions for the six state variables. Table 4 gives the required orbital elements for injection into GTO, into a sun-synchronous orbit (SSO), and into a 28.5° transfer orbit for HERMES.

	h_p (km)	h_a (km)	i (deg)	ω (deg)
GTO	300	36000	10	180
SSO	800	800	98.6	-
HER	100	460	28.5	?

Table 4: Target orbit parameters for three different missions

2.4 Constraints for the ascent with L5 (automatic missions)

For the optimal ascent into GTO without the splash-down condition the empty H155 will fly in an elliptic orbit and it will be difficult to predict the splash down point. Therefore, the ascent trajectory must be modified to ensure that the empty H155 will return in the first orbit. This can be achieved by requiring that the perigee altitude of the elliptic orbit be sufficiently low, see f.i. [32]. An additional deorbit impulse might be necessary. In the same way as was done for the injection into GTO the state at burn-out of the first stage (at t_3) is transformed into an inertial coordinate system. The relations for velocity and path inclination are

$$V_{H155}^2 = V^2(t_3) + r(t_3)\omega_E \cos\delta(t_3) \left[2V(t_3)\cos\gamma(t_3)\sin\chi(t_3) + r(t_3)\omega_E \cos\delta(t_3) \right]$$

$$\sin\gamma_{H155} = V(t_3)\sin\gamma(t_3)/V_{H155}$$

where the subscript $H155$ designates variables of the empty H155 in the inertial coordinate system. These variables are related to the semi-major axis a_{H155} by

$$a_{H155} = r(t_3)\mu_e / (2\mu_e - r(t_3)V_{H155}^2)$$

Eccentricity e_{H155} and true anomaly f_{H155} are related to the state vector by

$$e_{H155} \sin f_{H155} (1 + e_{H155} \cos f_{H155})^{-1} = \tan\gamma_{H155}$$

$$a_{H155} (1 - e_{H155}^2) (1 + e_{H155} \cos f_{H155})^{-1} = r(t_3)$$

The splash-down constraint is imposed by requiring

$$h_{pH155} = r_{pH155} - R_E = a_{H155}(1 - e_{H155}) - R_E = 50 \text{ km, for instance with } h_p \text{ as perigee altitude.}$$

Alternatively, the splash-down constraint could be imposed by requiring an additional boundary condition on the state of the 5th optimization stage at $t=t_5$, for instance.

Further constraints observed during the ascent are the dynamic pressure constraint

$$q(h, V) = \frac{\rho(h)}{2} V^2 \leq q_{\max}, \text{ typically } q_{\max} = 40 \text{ kPa,} \quad (14)$$

and a constraint on heat flux after fairing jettisoning

$$q_h(h, V) = \frac{\rho(h)}{2} V^3 \leq q_{h \max}, \quad t_4 \leq t \leq t_f \quad (15)$$

with t_4 indicating the time of fairing jettisoning. $t_4 \leq t \leq t_f$. A typical value for $q_{h \max}$ is 50 kw/m^2 .

2.5 Constraints for ARIANE V with HERMES

The empty H155 is to splash down in the Atlantic. Mathematically this is handled in the same way as the splash down constraint for missions into GTO. In case the true anomaly f_{155} is negative at t_3 and the perigee altitude is sufficiently low the splash down will occur. It is not clear yet whether a deorbit impulse might be necessary to ensure splash down into the Atlantic well outside the African coastline.

In case of a malfunction of the H155 after jettisoning of the P230's a safe return of the HERMES space plane restricts the altitude-velocity domain in which flight with the burning H155 can occur, see Fig.4.

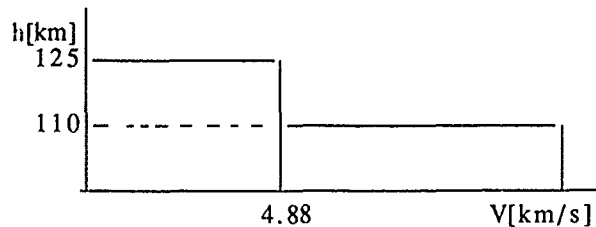


Fig. 4: Altitude-velocity constraint for ARIANE V/HERMES

2.6 Mission and vehicle data for descent

The HERMES space plane is to return from a circular orbit with an altitude of 460km and an inclination of 28.5° to Kourou or to Istres(France). It has a mass of approximately 16000kg. The reentry is initiated by a deorbit impulse which generates a new orbit with a sufficiently low perigee. The amount, the direction, and the timing of the applied velocity increment determines the initial conditions for reentry into the atmosphere. Although this portion of the descent can easily be included in the optimization it is usually treated separately since for a given deorbit impulse the trajectory from that point down to a certain altitude is basically fixed. Thus the reentry phase really begins at a particular altitude, velocity and path inclination. Similar considerations are applied to the last portion of the descent: The space plane becomes "airplane like" at about $M=2$ and about 25km altitude. From this point on, the trajectory can be determined by a quasisteady analysis. This point is defined as the beginning of the TAEM (terminal area energy management) phase, which serves to guide the space plane towards the runway with the proper velocity, altitude, path inclination and heading. There is not much to be optimized in the TAEM phase. Therefore, the purpose of entry optimization is to find trajectories from a given initial altitude, velocity, path inclination, and heading (as a result of the deorbit burn) to the TAEM initiation conditions, satisfying all vehicle- and mission constraints while extremizing a particular performance index. For this entry optimization the differential equations (1) are used with controls angle of attack - or lift coefficient - and velocity bank angle as given in (5). Lift- and drag coefficients as functions of angle of attack α and Mach number M are taken from [39].

2.7 Performance indices and boundary conditions for descent

One of the most important performance criteria for a lifting entry vehicle is the achievable crossrange from a given initial state

$$I(\alpha, \mu) = \Lambda(t_f) \equiv \max. \quad (16)$$

This performance index is used in [15],[16],[33] and many other studies. Alternatively, one can ask for reentry trajectories minimizing the accumulated heat at a particular point of the vehicle, usually taken to be the stagnation point, along the flight path

$$I(\alpha, \mu) = \int_{t_0}^{t_f} \dot{Q}(h, V, \alpha) dt, \text{ f.i. } \dot{Q} = \dot{Q}_{SP}(h, V, 0) \approx C_p \frac{1}{2} V^3 \quad (17)$$

for the stagnation point where C is a constant for a particular geometrical shape. Of course, one could also take other points on the vehicle such as points on the leading edge or at the lower surface of the wing. At angles of attack greater zero it is difficult to define analytical expressions for the heat flux \dot{Q} since it depends not only on the three variables given in (17) but in addition on the type of boundary layer, on the temperature of the wall and on other parameters. (17) is used as performance index in a study for designing a minimum weight heat shield for the US shuttle, see [34].

Another performance index used in [28] is to minimize accumulated heat per crossrange

$$I(\alpha, \mu) = \int_{t_0}^{t_f} \dot{Q} dt / \Lambda(t_f). \quad (18)$$

The initial conditions for a landing in Istres are given in Table 5.

V(km/s)	$\chi(^{\circ})$	$\gamma(^{\circ})$	$\Lambda(^{\circ})$	$\delta(^{\circ})$	h(km)
7.5	77	-1.65	-25.9	free	122

Table 5: Initial Condition for Reentry to Istres

As final conditions altitude, velocity, and path-inclination are prescribed as given in Table 6.

V(km/s)	$\chi(^{\circ})$	$\gamma(^{\circ})$	$\Lambda(^{\circ})$	$\delta(^{\circ})$	h(km)
0.76	free ≈ 25	free ≈ -5	43.52	4.92	30

Table 6: Initial Conditions for TAEM interface

2.8 Constraints for descent

Most importantly, the temperature at the skin of the heat shield must remain below a maximum value which depends on the material used and on the construction of the heatshield itself. This temperature constraint can be met by limiting the heat flux at critical points on the vehicle surface during the reentry. Usually, the stagnation point is used as the most critical point although flight results from the US shuttle have shown, that other points, f.i. at the engine pods, experience extremely high temperatures, too. Heat flux at the stagnation point is computed as given in (17). Other path constraints are due to maximum permissible hinge moments of the control surfaces – for HERMES less than 32kNm –, maximum permitted load factor $n=L/W \leq n_{\max}=2.5$, and maximum permitted dynamic pressure $q \leq q_{\max}=10\text{kPa}$. In addition, it is required that $\gamma \leq 0$ throughout the reentry. This constraint arises from guidance considerations. All of these constraints define the so called "entry corridor" which is shown in Fig.5 for the HERMES space plane. All data are taken from [28]. Any reentry trajectory must lie within the boundaries and a typical optimal reentry trajectory first encounters the temperature constraint, then the hinge-moment constraint, and at the end the dynamic pressure constraint. The max. load factor constraint usually does not become active.

3 OPTIMAL CONTROL PROBLEM

3.1 Piecewise Continuous OCP

The equations of motion for a multi-stage system can be written in the form

$$(P1) \quad \dot{x}(t) = f^j(x, u, p^d, t), \quad t_j \leq t \leq t_{j+1} \quad j = 1, \dots, m-1;$$

$$t_0 = t_1, \quad t_f = t_m, \quad t_0: \text{initial time}, \quad t_f: \text{final time}$$

with $m-1$ stages where f^j is continuous and continuously differentiable within each stage, p^d is a vector of design parameters of dimension n_p^d , the state vector x has dimension n , the control vector dimension l . The objective is to determine $u(t)$, the staging times t_j , and the design parameters p^d such that the functional

$$I = \phi(x(t_0), x(t_f), p^d, t_j)$$

is minimized. At each staging time, boundary conditions of the form

$$\Psi_i(x(t_j), p^d, t_j) = 0, \quad i = 1, \dots, n_b, \quad j \in \{1, \dots, m\}$$

must be satisfied. Within each stage inequality constraints

$$g(x, p^d, t) \leq 0 \quad \text{or} \quad g(x, u, p^d, t) \leq 0, \quad t_j \leq t \leq t_{j+1}$$

have to be satisfied where g is either a vector or a scalar. In addition, at staging, jump conditions (stage separation)

$$x_i(t_j^+) = h_k(x_i(t_j^-), t_j), \quad i \in \{1, \dots, n\}, \quad j \in \{2, \dots, m-1\}, \quad k = 1, \dots, n_h$$

might be imposed. The complete vector of parameters to be adjusted in the optimization is $p = (t_1, \dots, t_m, p^{dT})^T$. Constraints are dynamic pressure constraint, integrated heat flux, splash down constraints. Jump conditions are the jumps at booster jettisoning, and at stage separation, at payload fairing jettisoning.

3.2 Transformation into a Continuous OCP

By introducing a new independent variable in each stage

$$t_{\text{new}}^j = \frac{t - t_j}{t_{j+1} - t_j}, \quad j = 1, \dots, m-1$$

the differential equations are rewritten as

$$\frac{dx^j}{dt_{\text{new}}^j} = (t_{j+1} - t_j) f^j(x^j, u^j, t_{\text{new}}^j, t_{j+1}, t_j), \quad j = 1, \dots, m-1.$$

Next, a new notation is introduced:

$$x_{\text{new}} = (x^1 T, \dots, x^{(m-1) T})^T, \dim x_{\text{new}} = n_{\text{new}} = n(m-1),$$

$$u_{\text{new}} = (u^1 T, \dots, u^{(m-1) T})^T, \dim u_{\text{new}} = \ell_{\text{new}} = \ell(m-1),$$

$$f_{\text{new}} = \begin{bmatrix} (t_2 - t_1) f^1 \\ \vdots \\ (t_m - t_{m-1}) f^{m-1} \end{bmatrix}, \dim f_{\text{new}} = \dim x_{\text{new}}$$

$$g_{\text{new}} = g(x_{\text{new}}, p), \quad g_{\text{new}} \text{ either a scalar or a vector.}$$

The jump conditions become

$$x_i^j(0) = h_k(x_i^{j-1}(1), p), \quad j \in \{2, \dots, m-1\}, \quad i \in \{1, \dots, n\}, \quad k = 1, \dots, n_h.$$

In addition, continuity conditions

$$x_i^j(0) = h_k(x_i^{j-1}(1))$$

most hold for all components of i and j that are not present in the jump conditions. The h_k , $k = n_h + 1, \dots, n(m-2)$ are designating identities. There are altogether $n(m-2) - n_h$ conditions. Jump and continuity conditions can be added as boundary conditions to the ψ -vector obtaining

$$\psi_{\text{new}} = \begin{bmatrix} \psi_1 \\ \vdots \\ \psi_{n_b} \\ x_i^j(0) - h_1(x_i^{j-1}(1), p) \\ x_i^j(0) - h_{n_h} x_i^{j-1}(1), p \\ x_i^j(0) - h_{n_h+1}(x_i^{j-1}(1), p) \\ x_i^j(0) - h_{n_h+(m-2)}(x_i^{j-1}(1), p) \end{bmatrix}, \quad \dim \psi_{\text{new}} = n_{b\text{new}} = n_b + n(m-2)$$

In this way the piecewise continuous OCP may be transformed into a continuous one. Omitting the subscript new in the variables above one obtains

$$(P2) \quad \min I(u, p) = \phi(x(0), x(1), p)$$

subject to

$$\begin{aligned} \dot{x} &= f(x, u, p, t), \quad g(x, u, p, t) \leq 0, \quad 0 \leq t \leq 1 \\ \psi(x(0), x(1), p) &= 0, \\ \dim(u) &= 1, \dim(p) = n_p, \dim(x) = n, \dim(g) = 1 \text{ or } n_g, \dim(\psi) = n_b. \end{aligned}$$

3.3 Parameterized optimal control (PROMIS)

3.3.1 Parameter Vector and Constraints

The problem under consideration is

$$(P3) \quad \min I(u, p^d) = \phi(x(1), p^d) + \int_0^1 L(x(t), u(t), p^d, t) dt$$

subject to the same constraints as in (P2). The basic idea is to reduce the infinite dimensional problem to a finite dimensional one. Here, a version of an algorithm is described that uses multiple shooting in connection with parameterization of the control. To this end several grids are introduced:

a multiple shooting grid

$$0 = \begin{array}{|c|c|c|c|c|} \hline & \tau_1 & \tau_2 & \tau_j & \tau_{j+1} & \tau_{m-1} & \tau_m = 1 \\ \hline \end{array}$$

where at the gridpoint $\tau_j, \dots, \tau_{m-1}$ the state vector is estimated to be $x(\tau_j) = X_j$,

a control grid attached to each mesh of the multiple shooting grid

$$\begin{array}{c} \begin{array}{|c|c|c|c|c|} \hline & \tau_j & & & \tau_{j+1} \\ \hline \end{array} \\ \tau_j = \begin{array}{|c|c|c|c|c|} \hline \tau_1^u & \tau_2^u & \tau_i^u & \tau_{i+1}^u & \tau_{m_j^u}^u = \tau_{j+1} \\ \hline \end{array} \end{array}$$

where m_j^u is the number of gridpoints in the control grid,

a constraint grid attached to each mesh of the multiple shooting grid

$$\begin{array}{c} \begin{array}{|c|c|c|c|c|} \hline & \tau_j & & & \tau_{j+1} \\ \hline \end{array} \\ \tau_j = \begin{array}{|c|c|c|c|c|} \hline \tau_1^c & \tau_i^c & \tau_{i+1}^c & \tau_{m_j^c}^c = \tau_{j+1} \\ \hline \end{array} \end{array}$$

where m_j^c is the dimension of the constraint grid in the j -th multiple shooting grid.

The control vector u in (P3) is approximated over the control grid by piecewise constant, linear, or cubic spline functions. For a linear approximation one obtains in each subinterval of the control grid $\tau_i^u \leq t \leq \tau_{i+1}^u$

$$u(t) = U_{ji} + \frac{U_{j(i+1)} - U_{ji}}{\tau_{i+1}^u - \tau_i^u} (t - \tau_i^u) \quad (19)$$

where $U_{ji}, U_{j(i+1)}$ are estimates of the control vector at the control gridpoints, $\dim U_{ji} = \ell$, where i indicates the control grid index in the j -th multiple shooting subinterval. Altogether, the control vector in each multiple shooting mesh consists of

$$p_j^u = (U_{j1}^T, U_{j2}^T, \dots, U_{jm_j}^T u)^T, \dim p_j^u = \ell^* m_j^u, j=1, \dots, m-1. \quad (20)$$

For numerical reason, the design parameter p^d is copied $(m-1)$ times and is designated as p_j^d in each multiple shooting mesh. The total parameter vector thus consists of

$$p = (p_1^T, p_2^T, \dots, p_{m-1}^T)^T \quad (21)$$

with

$$\begin{aligned} p_1 &= (X_1^T, p_1^d, p_1^u)^T \\ p_2 &= (X_2^T, p_2^d, p_2^u)^T \\ &\vdots \\ p_{m-1} &= (X_{m-1}^T, p_{m-1}^d, p_{m-1}^u)^T. \end{aligned}$$

The boundary conditions are assumed to be separable, that is

$$\begin{aligned} \psi_1(X_1, p_1^d) &= 0, \psi_m(p_{m-1}) = 0 \\ \dim \psi_1 + \dim \psi_m &= n_b. \end{aligned} \quad (22)$$

The following continuity conditions must be satisfied at the multiple shooting gridpoints:

in the first subinterval

$$x_1(\tau_2, X_1, p_1^d, p_1^u) - X_2 = 0, \quad p_1^d - p_2^d = 0, \quad U_{1m_1}^u - U_{21} = 0$$

in the j -th subinterval

$$\begin{aligned} x_j(\tau_{j+1}, X_j, p_j^d, p_j^u) - X_{j+1} &= 0, \quad p_j^d - p_{j+1}^d = 0, \quad U_{jm_j}^u - U_{(j+1)1} = 0 \\ j &= 2, \dots, m-2. \end{aligned}$$

The state inequality constraints are to be satisfied at the gridpoints of the constraint grid as "point constraints". At the j -th multiple shooting grid one defines the constraint vector

$$\begin{aligned} \xi_{j1} &= g(X_j, p_j^d, U_{j1}) \\ \xi_{jk} &= g(x(\tau_k^c, X_j, p_j^d, p_j^u), p_j^d, u(\tau_k^c, p_j^u)) \\ k &= 2, \dots, m_j^c, j = 1, \dots, m-1. \end{aligned} \quad (23)$$

3.3.2 Parameter Optimization Problem

Introducing the above definitions into (P3) gives the nonlinear programming problem

$$(P4) \quad \text{minimize } F(p) = \phi(X_{m-1}, p_{m-1}^d) + \sum_{j=1}^{m-1} \int_{\tau_j}^{\tau_{j+1}} L(t, x(t, X_j, p_j^d, p_j^u)) dt$$

subject to the constraints

$$\begin{aligned} \dot{x}_j &= f(t, x_j(t, p_j)), \quad j = 1, \dots, m-1 \\ \psi_1(p) &= 0, \quad \psi_m(p) = 0 \\ x_j(\tau_{j+1}, p_j) - X_{j+1} &= 0, \quad j = 1, \dots, m-2 \\ g_j(p_j) &\geq 0, \quad j = 1, \dots, m-1 \end{aligned}$$

For the special case $m = 2$ (P4) becomes a parameterized OCP with single shooting as presented in [22],[23], and [25]. In this case the continuity conditions are not present. The NLP-solver needs gradients of F, ψ , and g with respect to the parameters. Table 7 contains the gradient of the equality constraints for the special case $m = 3$, Table 8 contains the gradient of the inequality constraints w.r.t. the parameter vector.

$$\begin{bmatrix} \frac{\partial \psi_1}{\partial X_1} & \frac{\partial \psi_1}{\partial p_1^d} & 0 & & & \\ \frac{\partial x_1(\tau_2)}{\partial X_1} & \frac{\partial x_1(\tau_2)}{\partial p_1^d} & \frac{\partial x_1}{\partial p_1^u} & -I & 0 & \\ 0 & I & 0 & 0 & -I & 0 \\ & 0 & I & 0 & 0 & -I \\ & & & 0 & \frac{\partial \psi_m}{\partial X_2} & \frac{\partial \psi_m}{\partial p_2^d} & \frac{\partial \psi_m}{\partial p_2^u} \end{bmatrix}$$

Table 7: Jacobian of equality constraints for PROMIS of dimension $(n_{b1} + n + n_p^d + n_p^u + n_{b2}) \times (n + n_p^d + n_p^u + n + n_p^d + n_p^u)$, $n_{b1} + n_{b2} = n_b$, $n_{p1}^u + n_{p2}^u = n_p^u$

$$\begin{bmatrix} \frac{\partial g_1}{\partial X_1} & \frac{\partial g_1}{\partial p_1^d} & \frac{\partial g_1}{\partial p_1^u} & 0 & \dots & \\ 0 & \dots & 0 & \frac{\partial g_{m-1}}{\partial X_{m-1}} & \frac{\partial g_{m-1}}{\partial p_{m-1}^d} & \frac{\partial g_{m-1}}{\partial p_{m-1}^u} \end{bmatrix}$$

Table 8: Jacobian of inequality constraints for PROMIS with dimension $(2 * n_g) \times (n + n_p^d + n_p^u + n + n_p^d + n_p^u)$

3.3.3. Algorithm

i) Find the numerical solution of the initial value problems

$$\begin{aligned} \dot{x}_j &= f(t, x_j(t), p_j), \quad \tau_j \leq t \leq \tau_{j+1} \\ x_j(\tau_j) &= X_j, \quad j = 1, \dots, m-1 \end{aligned}$$

Let $x_j(t, X_j, p_j^d, p_j^u)$ be the solution in the interval (τ_j, τ_{j+1}) .

- ii) Compute the constraints at τ_1, τ_m and compute the jumps at $\tau_j, j = 2, \dots, m-1$, compute the inequality constraints vectors g_j along the constraint grid τ_1^c .
- iii) Compute the gradients of the cost function and the constraints by numerical approximation, that is by solving initial value problems as in i) with perturbed parameters.
- iv) Use an NLP-solver such as SLSQP to compute a new estimate of the parameter p .
- v) Repeat steps i) – iii) in each iteration of the NLP-solver until the convergence criteria are satisfied.

3.4 Direct collocation method(TROPIC)

Currently, optimal control problems(OCP) of the type (P2) can be solved with TROPIC. In direct collocation the OCP is reduced to a nonlinear programming problem(NLP) by approximating the state $x(t)$ and the control $u(t)$ by piecewise polynomials. To this end the interval $[0,1]$ is partitioned into $m-1$ subintervals $0=\tau_1<\tau_2<\dots<\tau_m=1$, and in each subinterval the control $u(t)$ is approximated by a linear (19) or piecewise constant function and each component of the state $x(t)$ is approximated by a cubic Hermite polynomial

$$\begin{aligned} q_i(t) &= a_i + b_i(t-\tau_i) + c_i(t-\tau_i)^2 + d_i(t-\tau_i)^3, \tau_i \leq t \leq \tau_{i+1} \\ \dim q_i &= n \end{aligned} \quad (24)$$

with

$$\begin{aligned} q_i(\tau_i) &= x(\tau_i), \quad q_i(\tau_{i+1}) = x(\tau_{i+1}), \quad \dot{q}_i(\tau_i) = \dot{x}(\tau_i), \quad \dot{q}_i(\tau_{i+1}) = \dot{x}(\tau_{i+1}) \\ i &= 1, 2, \dots, m-1 \end{aligned} \quad (25)$$

and the time derivatives of the state evaluated at τ_i by

$$\dot{x}(\tau_i) = f(x(\tau_i), u(\tau_i), p, \tau_i).$$

From (24) and (25) one obtains the polynomial coefficients by solving the linear system of equations

$$\begin{bmatrix} 1 & 0 & 0 & 0 \\ 0 & 1 & 0 & 0 \\ 1 & h_i & h_i^2 & h_i^3 \\ 0 & 1 & 2h_i & 3h_i^2 \end{bmatrix} C_i = \begin{bmatrix} X_i \\ \dot{x}_i \\ X_{i+1} \\ \dot{x}_{i+1} \end{bmatrix}$$

where $h_i = \tau_{i+1} - \tau_i$, $C_i = (a_i, b_i, c_i, d_i)^T$, X_i, X_{i+1} are the estimates for the state, \dot{x}_i, \dot{x}_{i+1} are obtained from evaluating the differential equations with X_i, X_{i+1} . The subscripts i designate variables associated with the i -th node time τ_i . Inverting the above 4 by 4 matrix yields the coefficients

$$C_i = \begin{bmatrix} 1 & 0 & 0 & 0 \\ 0 & 1 & 0 & 0 \\ -3/h_i^2 & -2/h_i & 3/h_i^2 & -1/h_i \\ 2/h_i^3 & 1/h_i^2 & -2/h_i^3 & 1/h_i^2 \end{bmatrix} \begin{bmatrix} X_i \\ \dot{x}_i \\ X_{i+1} \\ \dot{x}_{i+1} \end{bmatrix}.$$

The resulting piecewise polynomials are C^1 throughout $[0,1]$ and satisfy the differential equations at all nodes τ_i . As collocation checkpoints the center of the intervals are used, that is

at $\tau_i^c = (\tau_{i+1} - \tau_i)/2$ the polynomials (24) are evaluated

$$x_i^c = x(\tau_i^c) = \frac{1}{2}(X_i + X_{i+1} + \frac{h_i}{4}(\dot{x}_i - \dot{x}_{i+1})), \quad (26)$$

and the derivatives of the polynomials are evaluated

$$\dot{x}_i^c = \dot{x}(\tau_i^c) = \frac{3}{2h_i}(X_i - X_{i+1}) - \frac{1}{4}(\dot{x}_i + \dot{x}_{i+1}). \quad (27)$$

As a measure how well the polynomial satisfies the differential equations the collocation error in each subinterval is defined as

$$K_i = \xi(X_i, U_i, X_{i+1}, U_{i+1}, p) = \dot{x}_i^c - f(x_i^c, u(\tau_i^c), \tau_i^c, p). \quad (28),$$

where U_i, U_{i+1} are the estimates for $u(\tau_i), u(\tau_{i+1})$. Assuming that the cubic polynomial can drive the collocation error to zero by systematically varying the values for X_i and U_i an approximation to the solution of P2 can be obtained. The constraints are enforced pointwise, that is at each collocation grid τ_i constraints of the form $g(X_i, U_i, X_{i+1}, U_{i+1}, p) \leq 0$ are added.

The NLP resulting from the direct collocation transformation can be stated as follows. Define the parameter vector P as

$$P = (X_1^T, U_1^T, X_2^T, U_2^T, \dots, X_m^T, U_m^T, p)^T,$$

collect all collocation- and boundary constraints,

$$C_e(P) = \begin{bmatrix} K_1(X_1, U_1, X_2, U_2, p) \\ K_2(X_2, U_2, X_3, U_3, p) \\ \vdots \\ K_{m-1}(X_{m-1}, U_{m-1}, X_m, U_m, p) \\ \psi(X_1, X_m, p) \end{bmatrix} = 0 \quad (29)$$

and all path constraints

$$C_i(P) = \left[g_i(X_i, U_i, X_{i+1}, U_{i+1}, p) \right] \leq 0. \quad (30)$$

In this way the OCP can be transformed into an NLP

$$(P5) \quad \min \bar{F}(\bar{P}) \text{ w.r.t. } \bar{P} \text{ subject to } C_e(\bar{P}) = 0 \text{ and } C_i(\bar{P}) \leq 0$$

where the number of parameters is $n_p = m(n+1) + \dim(p)$. The performance of the method of direct collocation depends crucially on the performance of the NLP code used for solving P5.

Several codes have been checked in [35],[36] for realistic trajectory problems and SLSQP [37] as well as NPSOL from the Stanford Optimization Laboratory show consistently better performance than others.

3.4.1 Implementation Considerations

Experience in developing the software has shown that two items strongly influence the numeric behaviour of the method. The first is concerned with scaling. It is expected in TROPIC that the user gives to the program a realistic range of critical parameters of his problem. TROPIC then scales all variables to $[-1,+1]$. The second item is concerned with noding. The location as well as the number of nodes are crucial in satisfying a given collocation error tolerance. A static stepsize control algorithm is added which determines the best location of nodes for given initial estimates (only once at the beginning). A dynamic noding, that is a node position change has been added recently, both features that previous versions, f.i.[30], of the collocation algorithm do not have.

The NLP solver needs values of the cost function and the constraints as well their gradients. In TROPIC an approximation to the Jacobian is computed numerically by using either forward or central differencing. This Jacobian has a special structure

$$\frac{\partial C}{\partial P} = \begin{bmatrix} G_{11} & G_{12} & 0 & \dots & \dots & 0 & G_{1,t} \\ 0 & G_{21} & G_{22} & 0 & \dots & \dots & 0 & G_{2,t} \\ 0 & \dots & \dots & G_{j1} & G_{j2} & 0 & 0 & G_{j,t} \\ 0 & 0 & \dots & \dots & 0 & G_{m-1,1} & G_{m-1,2} & G_{m-1,t} \\ G_1^e & G_2^e & \dots & \dots & \dots & G_{m-1}^e & G_m^e & G_t^i \\ G_1^i & G_2^i & \dots & \dots & \dots & G_{m-1}^i & G_m^i & G_t^i \end{bmatrix}$$

with

$$G_{j1} = \begin{bmatrix} \frac{\partial K_j}{\partial X_j} & \frac{\partial K_j}{\partial U_j} \end{bmatrix}, G_{j2} = \begin{bmatrix} \frac{\partial K_j}{\partial X_{j+1}} & \frac{\partial K_j}{\partial U_{j+1}} \end{bmatrix}, G_{jp} = \begin{bmatrix} \frac{\partial K_{jp}}{\partial p} \end{bmatrix} \quad (31)$$

$j=1, \dots, m-1.$

The last two blocks are the user prescribed equality- and inequality boundary and path constraints. Although the matrix is sparse, the sparsity depends very much on the particular problem, and therefore no structure assumptions are made. The expressions in (31) are obtained by evaluating the right hand sides, assuming linear interpolation for the control as given in (19)

$$\frac{\partial K_j}{\partial X_j} = \frac{-3}{2h_j} I - \frac{1}{4} \frac{\partial f(X_j, U_j, p, \tau_j)}{\partial X_j} - \frac{\partial f(x_j^c, u_j^c, p, \tau_j^c)}{\partial x_j^c} \frac{\partial x_j^c}{\partial X_j}$$

$$\text{with } \frac{\partial x_j^c}{\partial X_j} = \frac{1}{2} I + \frac{h_j}{8} \frac{\partial f(X_j, U_j, p, \tau_j)}{\partial X_j}$$

$$\frac{\partial K_j}{\partial U_j} = -\frac{1}{4} \frac{\partial f(X_j, U_j, p, \tau_j)}{\partial U_j} - \frac{\partial f(x_j^c, u_j^c, p, \tau_j^c)}{\partial u_j^c} \frac{\partial u_j^c}{\partial U_j}, \text{ with } \frac{\partial u_j^c}{\partial U_j} = \frac{1}{2} I.$$

In the same way one obtains

$$\begin{aligned} \frac{\partial K_j}{\partial X_{j+1}} &= \frac{3}{2h_j} I - \frac{1}{4} \frac{\partial f(X_{j+1}, U_{j+1}, p, \tau_{j+1})}{\partial X_{j+1}} - \frac{\partial f(x_j^c, u_j^c, p, \tau_j^c)}{\partial x_j^c} \frac{\partial x_j^c}{\partial X_{j+1}}, \\ \text{with } \frac{\partial x_j^c}{\partial X_{j+1}} &= \frac{1}{2} I - \frac{h_j}{8} \frac{\partial f(X_{j+1}, U_{j+1}, p, \tau_{j+1})}{\partial X_{j+1}}, \\ \frac{\partial K_j}{\partial U_{j+1}} &= -\frac{1}{4} \frac{\partial f(X_{j+1}, U_{j+1}, p, \tau_{j+1})}{\partial U_{j+1}} - \frac{\partial f(x_j^c, u_j^c, p, \tau_j^c)}{\partial u_j^c} \frac{\partial u_j^c}{\partial U_{j+1}}, \text{ with } \frac{\partial u_j^c}{\partial U_{j+1}} = \frac{1}{2} I. \end{aligned}$$

Therefore, only the partials of $f(x,u,p,t)$ with respect to x,u,p need to be computed numerically to determine the $G_{j,1}, G_{j,2}$ for $j=1,\dots,m-1$.

4. NUMERICAL RESULTS

Fig. 6 shows numerical results obtained with TROPIC for an ascent of the ARIANE V into a geostationary transfer orbit with elements as given in Table 4. The staging times t_2 and t_3 are fixed, there is no coasting arc, the only design parameter to be optimized is t_f . The objective function is the payload. The discontinuous OCP is transformed into a continuous one as described in section 3.2. In the normalized interval 8 collocation points are chosen which results in $8*(6 + 6 + 7 + 2 + 2 + 2) + 3 = 203$ parameters to be optimized in (P5). Initial estimates are selected by integrating the differential equations (1) forward from given initial conditions assuming a gravity turn ($\alpha=0, \beta=0$) for all launcher stages. The initial conditions for the second and third stage are selected by trial and error, such that a "crash" of the vehicle will not occur. From this estimate TROPIC needs about 3 iterations to produce a first optimal trajectory using SLSQP from [37] as the NLP solver. To obtain this first trajectory 3 function evaluations and 3 evaluations of the Jacobians of the constraints are needed. However, as is usually the case in optimization, the first solutions lacks accuracy and/or smoothness requirements, and therefore additional solutions have to be generated. The solution shown is obtained after 2 continuations steps. TROPIC needs about 47 CPU seconds per iteration on a APOLLO DN 10000 computer. Achievable relative accuracy in constraint satisfaction is about 10^{-4} .

Fig.7 shows an ascent of an ARIANE V/L5 vehicle into a sun-synchronous orbit with target elements as given in Table 4, Fig.8 shows an ascent trajectory of ARIANE V with HERMES into a target orbit as specified in Table 4. Neither the splash-down nor the altitude-Machnumber safety constraints are imposed yet. The unconstrained solution violates the safety constraint considerably for $M \geq 4.8$ (137 instead of 125km), slightly for $M \leq 4.8$ (112 instead of 110km).

Fig. 9 shows a solution of a HERMES descent from a 28.5° orbit to ISTRES minimizing the performance index (17) with initial and final conditions as given in Tables 6 and 7. This solution is obtained with PROMIS using a multiple shooting grid with $m = 7$ taking 0.1, 0.2, 0.4, 0.6, 0.8, 1.0 as gridpoints in the normalized interval. For the control grids $m_1^u = 2$ spaced at 0, 0.08, $m_2^u = 2$ spaced at 0.1, 0.15, $m_3^u = 3$ spaced at 0.2, 0.3, 0.32, $m_4^u = 4$ spaced at 0.4, 0.45, 0.5, 0.55, $m_5^u = 3$ spaced at 0.6, 0.68, 0.74, $m_6^u = 4$ spaced at 0.8, 0.86, 0.94, 1.0. Altogether there are $6*6 + 18*2 + 1 = 73$ parameters for (P4). Initial estimates for the states and the controls are obtained using forward integration of the differential equations (1) with initial conditions in each shooting interval from trial and error. A first

solution is obtained after 40 iterations, continuation steps need about 10 iterations each, CPU time on a APOLLO DN10000 is 10s per iteration. Achievable accuracy is higher than with Tropic since the integration accuracy can easily be controlled. In the solution presented constraints on dynamic pressure and hinge moments are not considered yet.

5. CONCLUSIONS

Some recent development in trajectory optimization of aerospace vehicles have been discussed in light of ascent and descent optimization of a conventional launcher and a future European spaceplane. Two new software packages under development generate solutions for the test problems with reasonable accuracies and relatively little CPU time. Both methods share the advantages of not relying on adjoint differential equations for gradient generation. This feature makes the methods flexible as far as changes in problem formulation are concerned. In addition, both methods have similar data structures and are being provided with an advanced user interface that will allow graphical input and graphical output assisting the user in changing initial estimates, in looking at intermediate results, in analyzing the results, and in displaying the results. Both methods share the disadvantage of not producing a feasible solution until convergence of the NLP solver has been obtained. PROMIS can be used as a single shooting technique if needed. Both methods need efficient NLP solvers such as SLSQP or NPSOL, other solvers have been tested and shown to be inferior in performance, especially in connection with trajectory optimization methods where accuracies in function and constraint values and their partial derivatives are low. Presently, there is a limit on the maximum number of parameters of about 400-500 these NLP codes can handle and still work efficiently. It is desirable to be able to increase this number by exploiting the structure of the Jacobians in TROPIC and PROMIS. Both methods are robust with respect to modeling weaknesses such as linear interpolation of multidimensional tables. The penalty for not using smooth data is an increase in CPU time by a factor of 2. At present there are no accurate mathematical models available for the launcher ARIANE V with or without HERMES, all results presented are with data collected from various sources. The same situation exists for the HERMES spaceplane. Therefore, the results presented should not be considered as trajectory design suggestions but rather as demonstrations of the capabilities of the new trajectory optimization software under development at DLR. Ascent trajectory optimization of future launch vehicles with airbreathing engines is of particular importance since engine performance and angle of attack time history are coupled, and engine design and operation depends on the selected trajectory. Here, the new methods offer an attractive tool for the analysis of these systems.

6. REFERENCES

- [1] Miele, A., Flight Mechanics, Vol.1, Theory of Flight Paths, Addison-Wesley Publishing Company, Inc., Reading, 1962.
- [2] Bryson A.E., Ho, Y.C., Applied Optimal Control, Blaisdell Publishing Company, Waltham, 1962.
- [3] Kelley, H.J., Method of Gradients, Optimization Techniques, edited by G. Leitmann, Academic Press, New York, New York, 1962.
- [4] Miele, A., Recent Advances in Gradient Algorithms for Optimal Control Problems, Survey Paper, dedicated to Prof.A.Busemann, Journal of Optimization Theory and Applications, Vol. 17, No.5/6, 1975.
- [5] Tolle, H., Optimierungsverfahren, Springer, 1971.
- [6] Speyer, J., Kelley, H.J, Levine, N, Denham, F., Accelerated Gradient Projection Technique with Application to Rocket Trajectory Optimization, 1971.
- [7] Bruschi, R.G., A Nonlinear Programming Approach to Space Shuttle Trajectory Optimization, Journal of Optimization Theory and Applications, Vol. 13, pp 94-118, Jan. 1974.

- [8] Johnson, I.L., Optimization of the Solid-Rocket Assisted Space Shuttle Ascent Trajectory Optimization, *Journal of Spacecraft and Rockets*, Vol. 12, pp.765-769, Dec. 1975.
- [9] Bruschi, R.G., Trajectory Optimization for the Atlas/Centaur Launch Vehicle, *Journ. of Spacecraft and Rockets*, 14(9), pp.550-555, 1977.
- [10] Edge, E.R., Powers, W.F., Function Space Quasi-Newton Algorithms for Optimal Control Problems with Bounded Controls and Singular Arcs, *Journal of Optimization Theory and Applications*, Vol. 20, pp.449-473, 1976a.
- [11] Edge, E.R., Powers, W.F., Shuttle Ascent Trajectory Optimization with Function Space Quasi-Newton Techniques, *AIAA Journal*, Vol.14, pp.1369-1376, 1976b.
- [12] Bulirsch, R., Die Mehrzielmethode zur numerischen Lösung von nichtlineare Randwertproblemen und Aufgaben der optimalen Steuerung, Report of the Carl-Cranz-Gesellschaft e.V., Oberpfaffenhofen, 1971.
- [13] Bock, H.G., Numerical Solution of Nonlinear Multipoint Boundary Value Problems with Application to Optimal Control, *Zeitschrift für Angewandte Mathematik und Mechanik*, Bd. 58, pp.407-409, 1978.
- [14] Duffek, W., Shau, G.C., Optimization of the Ascent Trajectory of a 4-Stage Vehicle for Missions, *ESA-TT-180*, 1975.
- [15] Dickmanns, E.D., Pesch, J., Influence of a Reradiative Heating Constraint on Lifting Entry Trajectories for Maximum Lateral Range, *Proceedings of the 11th International Symposium on Space Technology and Science*, Tokyo, 1975.
- [16] Pesch, J., Numerische Berechnung optimaler Steuerungen mit Hilfe der Mehrzielmethode dokumentiert am Problem der optimalen Rückführung eines Raumgleiters unter Berücksichtigung von Aufheizungsbeschränkungen, Diplomarbeit, Mathematisches Institut, Universität Köln, 1973.
- [17] Järmark, B., Some Aspects on Improvements of a First-Order Dynamic Optimization Algorithm, *Saab-Scania TN Ae 73*, 1973.
- [18] Dixon, L.C.W., Biggs, M.C., The Advantage of Adjoint-Control Transformations when Determining Optimal Trajectories by Pontryagin's Maximum Principle, *J. Royal Aeronautical Soc.*, pp.169-174, March 1972.
- [19] Bartholomew-Biggs, M.C., Recursive Quadratic Programming Based on Penalty Functions for Constrained Minimization, In *Nonlinear Optimization Theory and Applications*, edited by L.C.W.Dixon, G.P.Szeg and E.Spedicato, Birkhauser, 1980.
- [20] Dixon, L.C.W., Bartholomew-Biggs, M.C., Adjoint Control Transformations for Solving Practical Optimal Control Problems, In *Optimal Control Applications and Methods*, 2, pp.365-381, 1982.
- [21] Bartholomew-Biggs, M.C., Dixon, L.C.W., Hersom, S.E., Maany, Z.A., Flury, W., Hechler, M., From High Thrust to Low Thrust: Application of Advanced Optimization Methods to Mission Analysis, *ESA Journal*, Vol. 11, 1987.
- [22] Kraft, D., On Converting Optimal Control Problems into Nonlinear Programming Problems, in: K.Schittkowski (ed.): *Computational Mathematical Programming*, Springer, Berlin, 1985.
- [23] Horn, M.K., A FORTRAN Program for Solving State/Control-Constraint Optimal Control Problems with System Equations Having Expressions Involving Tabular Data, *DFVLR Internal Report 515-83/1*, 1983.

- [24] Bock, H.G., Plitt, K.J., A Multiple Shooting Algorithm for Direct Solution of Optimal Control Problems, Proc. of the 9th Worldcongress of the IFAC, Budapest, Hungary, July 2-6, 1984.
- [25] Horn, M.K., Solution of the Optimal Control Problem Using Software Package STOMP, Proc. of the 8th IFAC Workshop on Control Applications of Nonlinear Programming and Optimization, Paris, France, June 7-9, 1989.
- [26] Well, K.H., Tandon, S.R., Rocket Ascent Trajectory Optimization Via Recursive Quadratic Programming, Journal of the Astronautical Sciences, Vol.30, NO.2, pp.101-116, 1982.
- [27] Wolff, H., Optimierung von Aufstiegsbahnen für Trägerraketen, MBB Technical Note TN-ERR51-130/86, 1986.
- [28] Horn, M.K., Optimal Reentry Trajectories Phase B, MBB Technical Report TN-HERMES 15, March 1989
- [29] Well, K.H., ARIANE V Ascent Trajectory Optimization with a First-Stage Splash-Down Constraint, Proc. of the 8th IFAC Workshop on Control Applications of Nonlinear Programming and Optimization, Paris, France, June 7-9, 1989.
- [30] Hargraves, C.R., Paris, S.W., Direct Trajectory Optimization Using Nonlinear Programming and Collocation, Journal Guidance, Control & Dynamics, Vol. 10, No. 4, 1987.
- [31] Flury, W., Prieto-Llanos, T., ARIANE V performance in GTO with configuration 2P230/H155/L5, ESOC memorandum, 22.5.1987.
- [32] Landiech, Ph., Aumasson, C., Optimal Trajectory of Ariane V Type Launcher with First Stage Fallout Constraint, Preprint of the 37th Congress of the IAF, paper IAF-86-230, Innsbruck, Austria, Oct. 4-11, 1986.
- [33] Vinh, Optimal Trajectories in Atmospheric Flight, Elsevier, Amsterdam, 1981.
- [34] Garcia, F., Fowler, W.F., Thermal Protection System Weight Minimization for the Space Shuttle through Parameter Optimization, AIAA Journal of Spacecraft, Vol.11, No.4, pp.241-245, 1974.
- [35] Jänsch, C, Kraft, D., Well, K.H., Comparative Study of Nonlinear Programming Codes for Trajectory Optimization, Technical Note TN1, ESA/ESTEC Contract No. AO/1-2161/88/NL/MAC, 1989.
- [36] Jänsch, C., Kraft, D., Schnepfer, K., Well, K.H., Survey on Trajectory Optimization Methods, Technical Report TR1, ESA/ESTEC Contract No. AO/1-2161/88/NL/MAC, 1989.
- [37] Kraft, D., A Software Package for Sequential Quadratic Programming, DFVLR Research Report FB 88-28, 1988.
- [38] Hechler, M., On Atmospheric Re-entry Trajectory Control Calculations, ESOC Mission Analysis Paper No. 277, May 1988.
- [39] Serrano-Martinez, HERMES Aero data from AMD-BAG-H-NT-1-256 (DEA-8301).

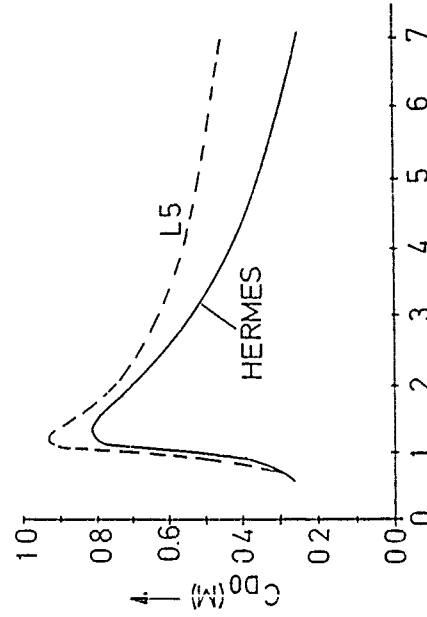
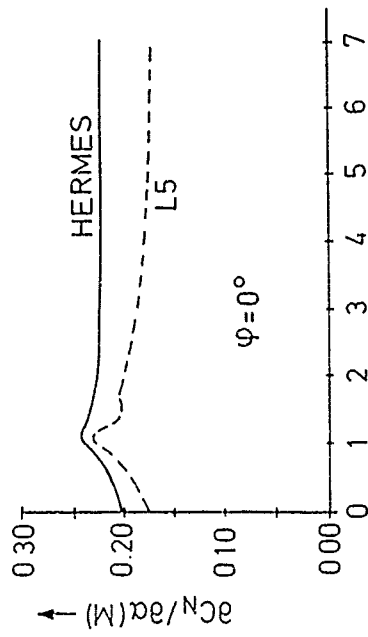


Fig. 1: Coordinate system of body axes and axial drag coefficient C_{D0} (M)

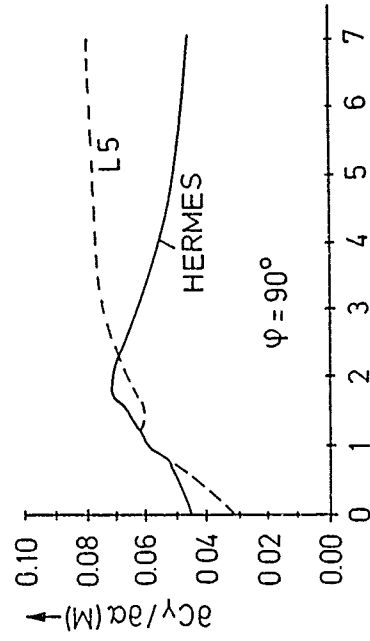
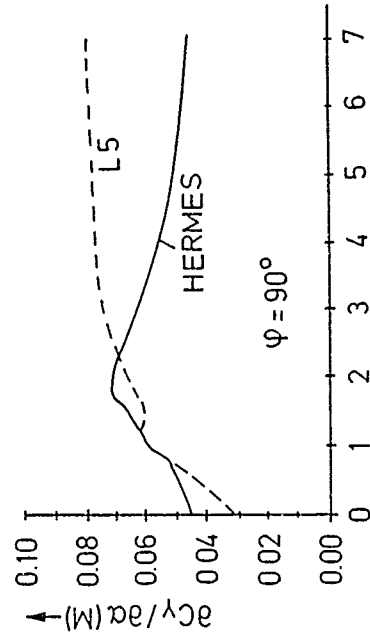
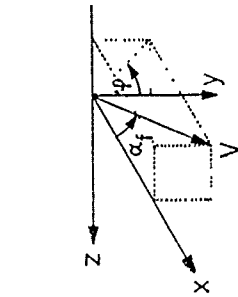


Fig. 2: $\frac{\partial C_N}{\partial \alpha}$ and $\frac{\partial C_Y}{\partial \alpha}$ (M)

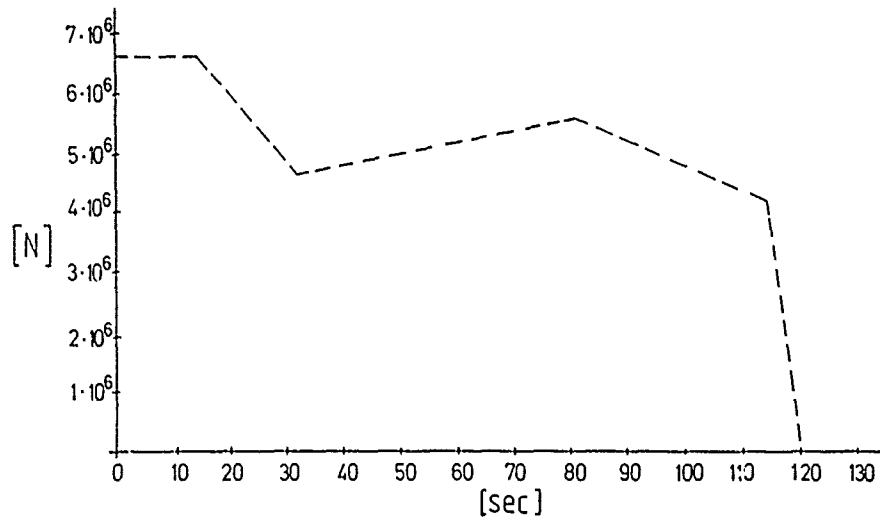


Fig. 3: Thrust time history for one booster P230, thrust in N

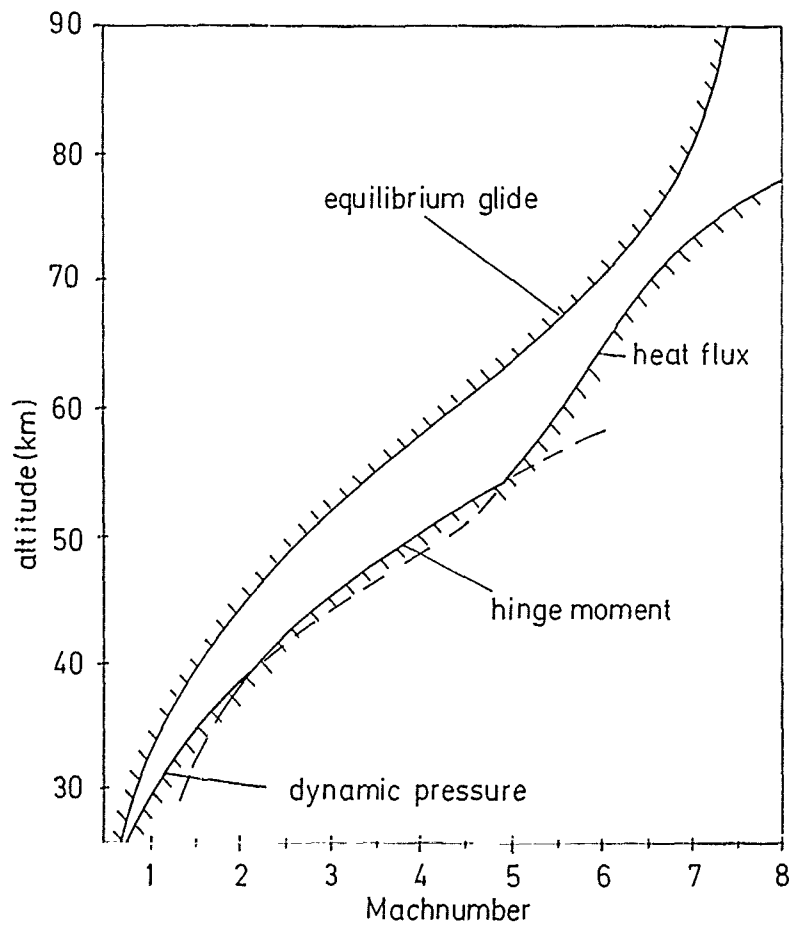


Fig. 5: Entry corridor for HERMES

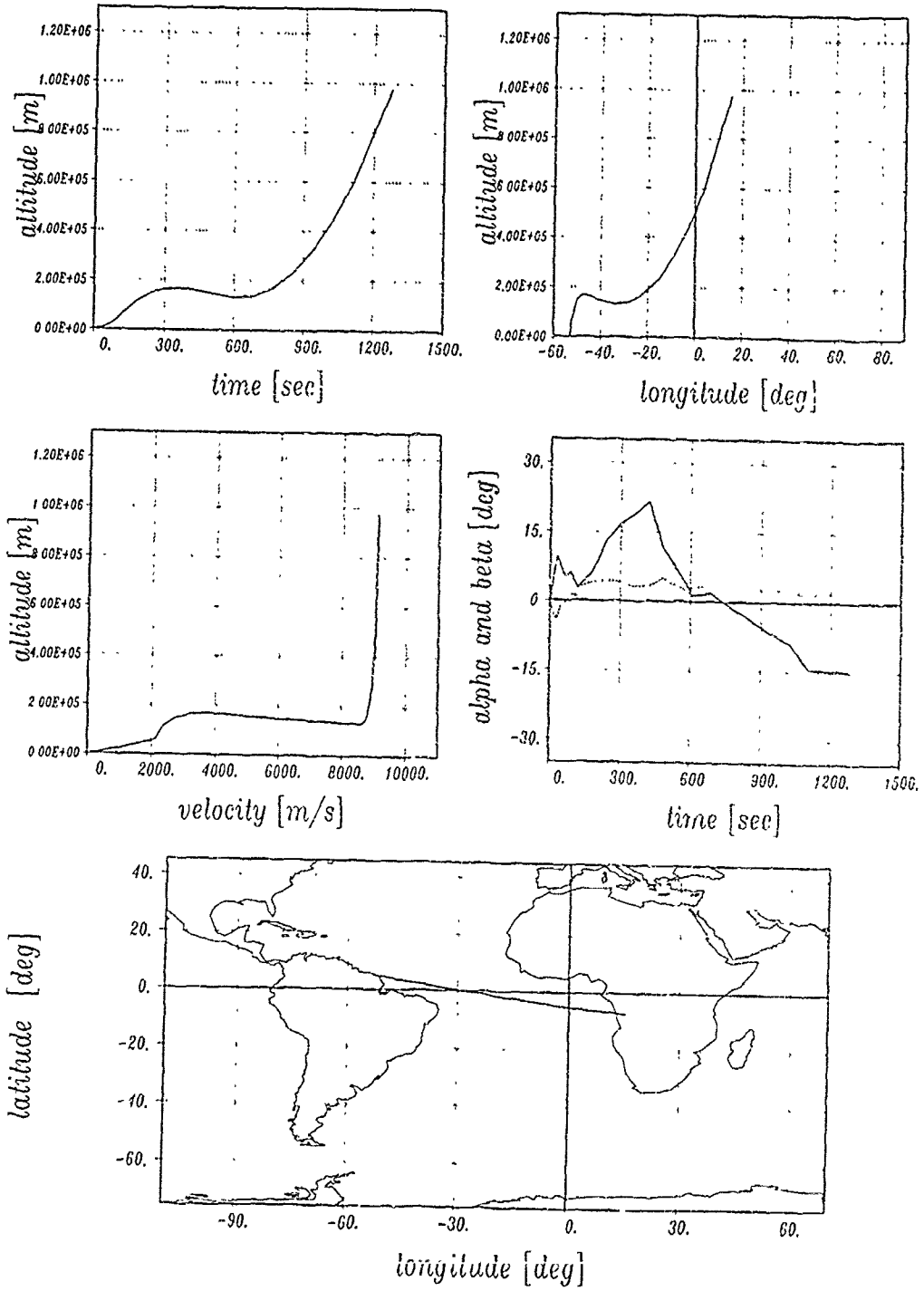


Fig. 6: Optimal ARIANE V/L5 ascent into GTO without splash-down constraint

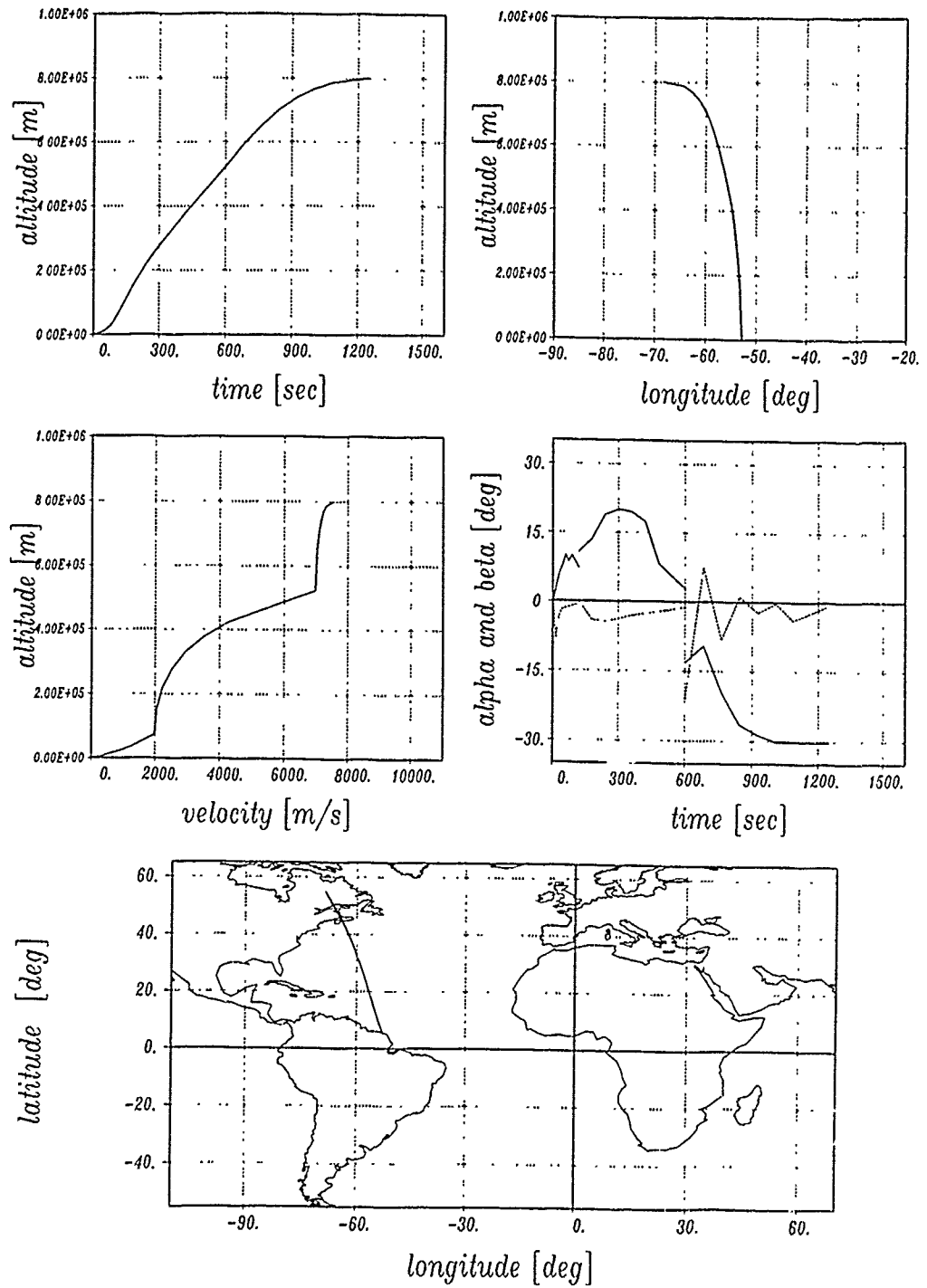


Fig. 7: Optimal ARIANE V/L5 ascent into a $800 \times 800 \text{ km} \times 98.6^\circ$ sun-synchronous orbit

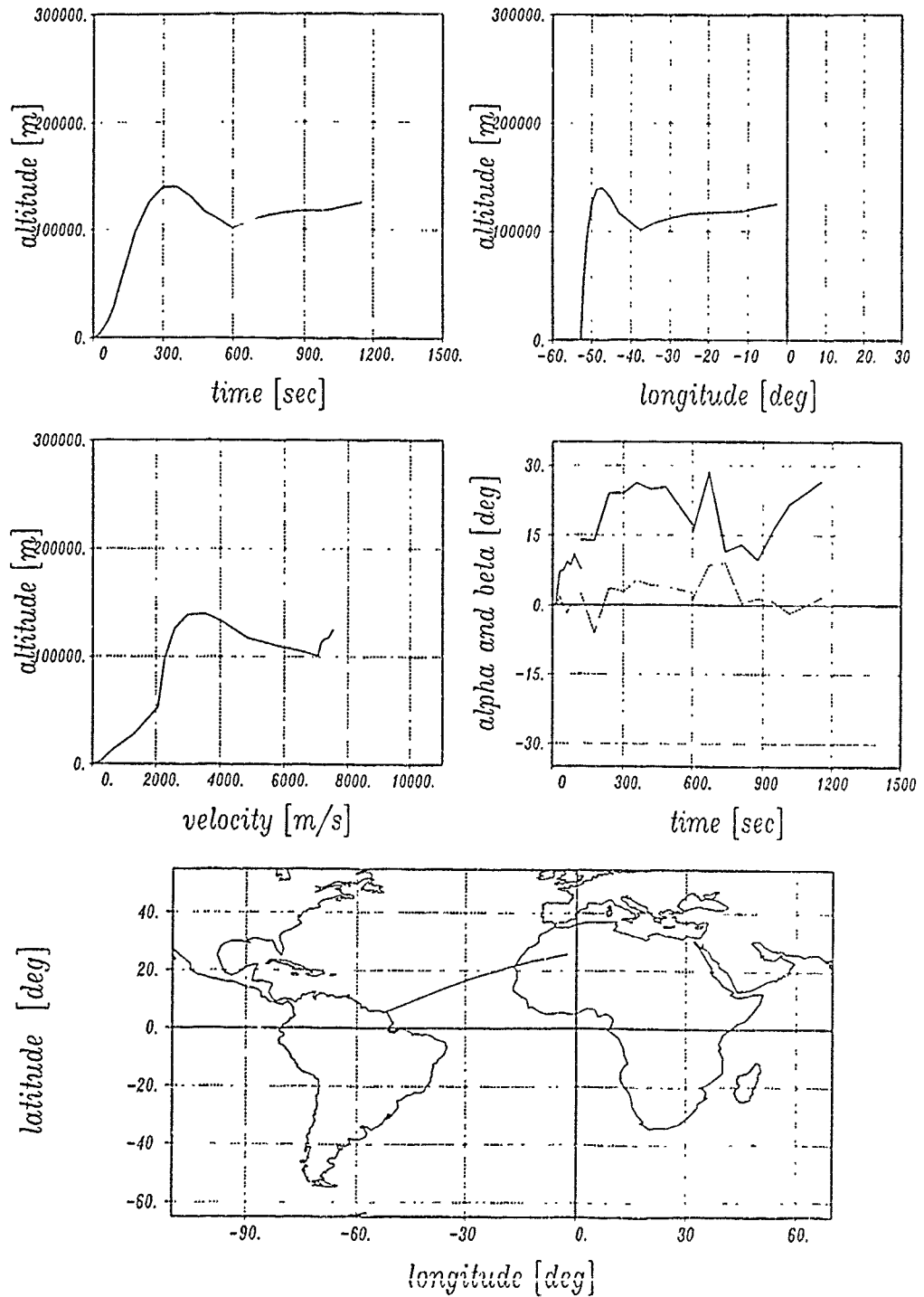


Fig. 8: Optimal ARIANE V/HERMES ascent into a $110 \times 460 \text{ km} \times 28.5^\circ$ transfer orbit without splash-down and altitude-Machnumber constraint

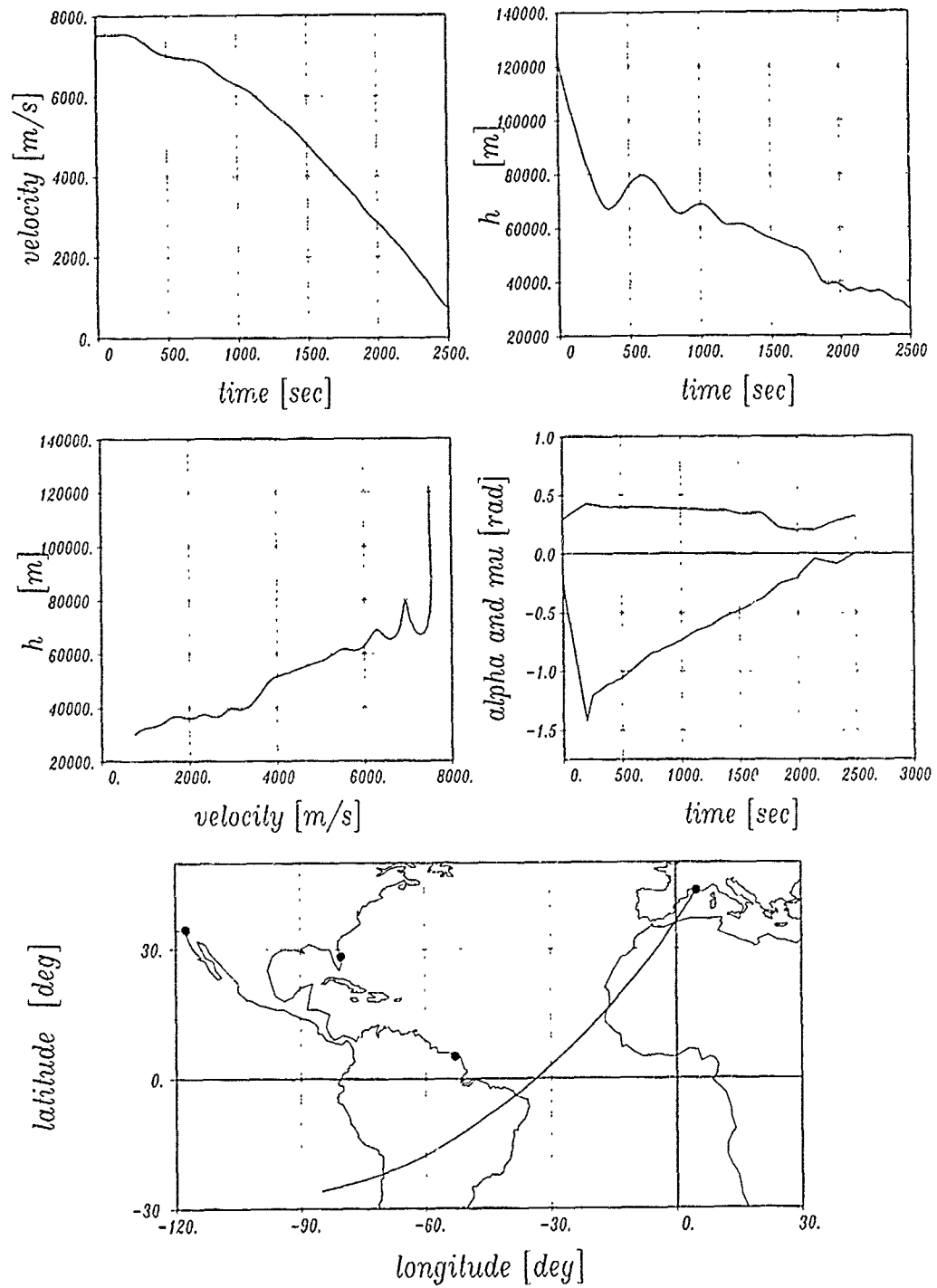


Fig. 9: Minimum heat reentry of HERMES to Istres from a $460 \times 460 \text{ km} \times 28.5^\circ$ orbit requiring maximum crossrange

ADVANCED LAUNCH VEHICLE CONFIGURATIONS AND PERFORMANCE TRADES

BY

PETER R. GORD, KEVIN J. LANGAN, and MICHAEL E. STRINGER
Wright Research and Development Center
Flight Dynamics Laboratory
WRDC/FIMG
Wright-Patterson Air Force Base OH 45433-6553

USA

SUMMARY

A concept for a near-term multi-stage space launch system has been proposed. The configuration incorporated full reusability, horizontal take-off and landing characteristics, and a payload goal of 50,000 lbs into a 100 n.mi. circular polar orbit. The first stage (booster) employed a multi-cycle high Mach number airbreathing propulsion system, augmented by conventional rocket propulsion as required. The second stage (orbiter) featured a high lift-to-drag ratio aerodynamic design with a dedicated high volume payload bay. Propulsion for the second stage was provided by a conventional rocket engine. The orbiter component was carried nestled within the booster mold lines and staged through a bottom drop mode. Sensitivity studies were performed on the synergisms between elements of the boost propulsion system; dynamic pressure effects on system performance; degraded ramjet thrust at high Mach numbers; and booster weight at staging. The configuration evolution and results from the sensitivity studies are described in detail.

INTRODUCTION

Studies conducted over the past several decades have clearly established that highly efficient, aerodynamically tailored vehicles boosted to orbital velocities and altitudes can perform a number of useful and unique missions, including synergetic plane changes and minor circle turns (Ref 1). In addition, high hypersonic lift-to-drag ratios (L/D) allow considerable flexibility in exercising re-entry options and abort modes, and in landing site selection. Although attractive from many perspectives, this class of vehicle has found little favor within the space transportation community. This is due in part to the resulting slender configurations which are not compatible with the large payload bay volumes required for efficient commercial/logistics applications. For maximum flexibility, however, it appears prudent to re-evaluate the potential of the high L/D orbiter in concert with the resurging interest in the application of airbreathing propulsion in the boost stage.

This paper addresses the concept formulation and performance sensitivities of a two-stage space launch system with a highly efficient orbiter design. The first stage (booster) incorporated a high speed airbreathing propulsion system, while the second (orbiter) stage relied on conventional rocket propulsion. Full consideration was given at the onset to the inclusion of a dedicated, high volume payload bay in the orbiter component.

The study was initiated by the Wright Research and Development Center's (WRDC) Flight Dynamics Laboratory (FDL), and has been ongoing since 1986. Originally involving only a small study team within the FDL, the program was expanded in 1987 to include contractual support from the Boeing Aerospace Company (Fig 1). The program to date has incorporated both analytical and experimental phases.

Underlying precepts were that the concept: (1) be a near-term staged system; (2) represent doable technology levels; (3) use existing systems (particularly propulsion) wherever possible; and (4) offer significant performance improvements over current operational types. Specific study requirements (Fig 2) included full reuseability of all stages, all azimuth launch capability, horizontal take-off for the mated system with horizontal landing capability for all components, and a performance capability to place a 50,000 lb payload into a 100 n.mi circular polar orbit. To facilitate ground handling and logistics operations, the orbiter was to be mated to the booster lower surface and staged through a bottom drop mode.

CONFIGURATION DEVELOPMENT

BOOST PROPULSION CYCLE

A key element in the design synthesis process was to identify a realistic boost propulsion cycle compatible with the horizontal take-off requirement for the mated two-stage configuration, while meeting the study guidelines of using existing or near-term propulsion components wherever possible. For purposes of discussion in this paper, the boost propulsion cycle is defined as the propulsion mode employed during the acceleration phase from take-off to orbiter staging. The original cycle proposed used the orbiter rocket engine for take-off and acceleration to the booster airbreather takeover speed ($M=2$ to 3). The orbiter rocket engine was then shut down,

with the booster accelerating the combined system to the staging point (Fig 3). This approach had the advantage of maximizing the use of the onboard propulsion components while minimizing their size, weight and overall complexity. One salient feature was, however, that the orbiter be mated to the booster in such a manner that its propulsion system was free to operate in the combined mode. During the period when the orbiter rocket engine was in operation, fuel would be cross-fed from tanks in the booster to ensure orbiter staging with a full fuel load.

Early in the study, JP fueled turbofans were added to the booster component to provide a measure of ferry capability and facilitate orbiter retrieval from remote landing sites. Logically, these turbofans could also assist the orbiter rocket engine during take-off and low Mach number acceleration. The boost propulsion cycle was upgraded to include this capability.

Ultimately, the synergisms between the boost propulsion components would become a major player in overall system performance, as will be discussed in more detail later in this paper.

STAGING MACH NUMBER SELECTION CRITERIA

The orbiter staging Mach number was selected based on several interrelated criteria, which included the theoretical velocity potential (ΔV) capable of being built into the orbiter, the requirement for realistic near-term airbreathing and rocket propulsion systems for the booster and orbiter components, respectively, and the thrust/weight ratio of the orbiter at staging.

The near-term rocket propulsion requirement virtually dictated that the orbiter be powered by an existing (or derivative) Space Shuttle Main Engine (SSME). Since it would be required to operate efficiently from sea level to orbital insertion, a dual bell nozzle derivative was selected. This unit offered sea level and vacuum Specific Impulses (ISP's) of 393 and 464 seconds, respectively, with a vacuum thrust rating of 516,000 lbs. To provide preliminary orbiter sizing and performance characteristics, a wing-body configuration (Fig 4) from a previous WRDC study was selected as a starting point. With known mass and volume characteristics, the configuration was scaled using established procedures to yield the curve of theoretical ΔV vs gross stage weight shown in Figure 5. Marked on the curve for reference are the orbiter velocity inputs required to reach a 100 n. mi. polar orbit for several launch Mach numbers. Clearly the orbiter weight increases disproportionately fast as the staging Mach number drops below M=6 to 8, suggesting that this Mach range should represent the minimum staging speed.

Figure 6 shows the typical operating envelopes for several candidate airbreathing engines for application to the booster stage. The near-term propulsion constraint precluded consideration of the supersonic combustion ramjet (SCRAMJET), as this represented an "as-yet-to-be-proven" technology level. Turbojet propulsion was, on the other hand, limited to maximum Mach numbers in the 3 to 4 range, which would have resulted in orbiter weights on the order of one million lbs (Fig 5). The subsonic combustion ramjet appeared to be the only remaining near-term option. Consultations with propulsion specialists indicated that, fueled with liquid hydrogen (LH_2), the subsonic combustion ramjet could operate with high levels of efficiency and confidence up to M=6, and in all probability could be extended out to M=8.

One final point to be considered was the thrust/weight (T/W) ratio of the orbiter at staging. For the M=8 case, preliminary assessments indicated an orbiter staging weight on the order of 550,000 lbs. This yields a T/w ratio (with a single SSME) sufficiently high that it does not degrade orbiter performance significantly. A M=6 launch would be too heavy for a single SSME, resulting in a more complicated orbiter propulsion system. (More discussion on the impact of orbiter T/W ratio at staging appears later in this paper).

Based on consideration of the above criteria, the final orbiter staging Mach number was fixed at M=8. Staging altitude varied throughout the study, usually between approximately 85,000 ft to 100,000 ft. In the final phases, however, it was fixed at 100,000 ft. This altitude allowed the orbiter to separate, rotate to an angle of attack near L/D max, and stabilize in a one "g" flight condition prior to committing to the orbital ascent phase.

ORBITER SELECTION

The wing-body orbiter was replaced early in the design cycle by the lifting-body configuration shown in Figure 7, and remained essentially fixed throughout the rest of the study. This configuration had a high degree of aerodynamic efficiency (Fig 8) with lift/drag ratios of nearly 3.5 at M=10, H=100,000 ft, and M=20, H=200,000 ft. The results shown here were calculated using the Supersonic Hypersonic Arbitrary Body program, and were based on fully turbulent flow assumptions at M=10, and fully laminar at M=20 (Ref 2). The lifting body design allowed room for considerably more internal fuel and featured a dedicated payload bay measuring 15 ft x 40 ft., the latter sized specifically to carry the two-stage Inertial Upper Stage (IUS) plus payload. The payload bay, with in excess of 7000 cubic ft of volume, could also accommodate additional fuel which could be used for synergistic plane changes, orbital maneuvers, etc. The dual bell SSME derivative used on the wing-body orbiter was retained. The

estimated weight of the orbiter at staging was 555,000 lbs, which included the 50,000 lb payload and approximately 418,000 lbs of fuel (Fig 9).

Further design iterations resulted in modifications to the upper body contours and payload bay door arrangement (Fig 10). A more indepth structural assessment resulted in a fully fueled staging weight of just over 603,000 lbs with the 50,000 lb payload (Fig 11). The heavier configuration fell short of meeting the reference payload mission from the M=8 staging point, but was maintained as the baseline configuration as it represented the practical upper limit of the orbiter size compatible with a single SSME propulsion system. Final capabilities included approximately 42,000 lbs to a 100 n. mi. polar orbit, and 64,000 lbs to a 100 n. mi., 28.5° Eastern orbit. Typical orbiter ascent trajectory parameters, as functions of time from staging, are presented in Figure 12 for insertion into a 100 n. mi. polar orbit. Trajectory parameters shown were calculated using the optimization procedures described in Ref 3 (More information on this subject will be presented later in this paper).

As mentioned earlier, the payload capability to orbit is sensitive to the orbiter T/W ratio at staging. Figure 13 presents the results from a study conducted on the final lifting-body orbiter design, showing the impact of T/W ratio on payload capability to a 100 n.mi. polar orbit. If the orbiter SSME thrust could be increased by an additional 25-30%, the reference 50,000 lb payload capability could be met.

BOOSTER EVOLUTION

The booster design synthesis followed a more protracted development phase. Of particular concern was the development and integration of the airbreathing propulsion system in concert with the bottom drop staging mode. The orbiter integration was further complicated by the requirement that its primary propulsion system be free for operation at various times during the boost acceleration phase. Several concepts were suggested for the orbiter integration, ranging from external to full internal carriage, as discussed in the following paragraphs. The booster designs studied are identified according to series, Series 4 representing the definitive design produced to date (Fig 14). A pictorial of the booster development is presented in Figure 15.

Series 1 - This was an early concept formulation phase to investigate possible mating arrangements compatible with the bottom drop staging mode. Two generalized classes of vehicles were looked at: a twin-pod arrangement with external orbiter carriage (Fig 16), and a slender single body with the orbiter partially submerged within the body (Fig 17). The former featured two conical bodies connected by a central wing structure. Ramjet inlets were mounted on the lee side to minimize interference and facilitate landing gear integration. Although simple and attractive from structural and mating considerations, a number of drawbacks were noted, including analysis of the multi-body flow field interference problem, engine out asymmetries, and large wetted area for the required volume. For the latter concept several engine integration schemes were considered, ranging from the central lee side shown in Figure 17 to various 2-D and 3-D wing installations. The wing installations were compromised by bow shock ingestion at some points during the boost phase, plus the potential problem of engine out asymmetries, and were subsequently discarded. The submerged orbiter carriage did eliminate most of the multi-body flow field problems, particularly for the lee side engine installation, and hence was viewed as the most promising concept with which to proceed. There were, however, a number of points to upgrade. Propulsion specialists preferred a more uniform inlet flow field with some degree of pre-compression, and the new lifting-body orbiter posed more complicated integration problems than did the wing-body design. This configuration concept thus became the subject for a new design to be developed in Series 2.

Series 2 - Developed to be compatible with the lifting-body orbiter, this design featured full internal carriage of the orbiter component. The booster retained the central lee side installation for the hypersonic airbreathing system, and incorporated turbofans to act as accelerators and provide booster ferry capability. The basic booster body was an 8° half angle, half cone/cylinder with a flat bottom (Fig 18). The accelerators were conventional 30,000 lb thrust class turbofans, mounted in two separate nacelles (4/nacelle) on the wing lower surface just outside the body mold lines. A number of wing planform parametric studies were completed. The design shown in Figure 18 represented a compromise between take-off and hypersonic flight performance. The complete integrated configuration (sans vertical fins) is presented in Figure 19. (Longitudinal control surfaces shown here were for sizing purposes only and do not reflect realistic installations). Specific booster details are presented in Figure 20.

Complete aerodynamic and propulsion data sets were prepared and performance analyses run. However, the large base area and poor transonic area distribution precluded closure with the available propulsion system. A number of options were suggested, but ultimately a second SSME was added, this one to the booster component. The boost propulsion cycle now included the operation of both SSME's and turbofans from take-off through M=2 (Fig 21). Above M=2 and to the staging point, total impulse was provided by the booster ramjet system. With both SSME's operating at 115% power (above ref. max for the SSME) and the 8 turbofans, sufficient thrust was available to achieve system closure for a take-off weight of just over 2.0×10^6 lbs. A flight time history showing altitude, velocity and thrust for a typical ascent trajectory is presented in Figure 22.

Although system closure had been demonstrated, considerable concern had arisen over a number of specific propulsion related integration details. These included off-design performance, the design of a practical variable geometry inlet system, and the ability to integrate the ramjet/turbofan cycles into a common unit. Since there were limited options available to rectify these potential problem areas, work on the Series 2 concept was terminated.

Series 3 - This was the first iteration for a new booster concept with a more credible hypersonic airbreathing propulsion system. A general arrangement drawing showing the preliminary layout is presented in Figure 23. The wing was similar to that developed for the Series 2 concept with an overall span of 180 ft. The fuselage featured rectangular cross sections and was designed to incorporate a large internal volume. The wing was mounted high at the rear of the fuselage with the ramjet engines integrated beneath the wing, attached to the fuselage sides. Overall fuselage length and width were 260 ft and 60 ft, respectively. The orbiter was carried fully internal with its rocket propulsion system extending beyond the base. The booster SSME installation introduced on Series 2 was retained.

Specific details on the airbreathing engine design are shown in Figure 24. The units are 2-dimensional ramjets with the inlets arranged in a horizontal fashion to provide positive compression with angle-of-attack. A three-ramp variable geometry inlet system maintained shock-on-lip conditions through $M=6$. The turbofan accelerators are integrated within the ramjet structure, and exhaust into the nozzle area to reduce nozzle base drag when the ramjets are not in use. Operational range for the ramjets was from $M=3$ to $M=8$.

The propulsion concept shown, though never fully completed by the FDL, was sufficiently promising to warrant further development work. The booster concept was, however, overly large with high drag levels. Considerable re-design would be required to minimize the booster size and weight, and fully qualify the new ramjet propulsion system. The re-designed configuration resulted in Series 4.

Series 4 - The final concept studied to date, this series was essentially a refinement of the Series 3 configuration and propulsion system. To improve the transonic drag levels, the fuselage cross-sectional area was reduced and the area distribution modified by moving the engine nacelles forward. The SSME on the booster was retained, as were the 2-D ramjets with integrated turbofan accelerators. The boost propulsion cycle included operation of both SSME's and turbofans through $M=3$ (Fig 25), with the ramjet operating alone from $M=3$ to 8. Figure 26 presents the general arrangement layout for the Series 4 concept as developed by the FDL. The booster had an overall body length of 240 ft, a wing span of 180 ft, and a theoretical wing area of 14,100 ft².

The concept was then subjected to a joint evaluation by the FDL and Boeing Aerospace Company to provide a more definitive analysis. The most challenging aspect was to fully qualify the booster airbreathing propulsion system, which had only been conceptually studied by the FDL. Additional configuration details in areas such as fuel disposition, control surface integration, landing gear designs, etc. were required, which could most easily be met by the expertise of a major airframe designer.

Figure 27 presents a sketch of the upgraded airbreathing propulsion system. The unit is a completely enclosed system with variable geometry inlet ramps and nozzles. Cold flow is maintained through the ramjet prior to ignition, which occurs at approximately $M=1$. Thrust developed at ignition is low, but this procedure is effective in reducing nozzle drag before full thrust is realized (i.e. $M=3$). The turbofans operate up to approximately $M=3$, after which they are shut down.

A drawing of the booster design showing the integration of the fully enclosed ramjet propulsion system is presented in Figure 28. The fuselage area distribution and cross section shape have been further refined to reduce drag. The contractor also established that the current operational envelope of the SSME does not include shut down/restart capability over the short period of time during boost cycle operation. Hence it was necessary to operate the orbiter SSME continuously from take-off to orbital insertion. Subject to this, the boost propulsion cycle (here-after referred to as the reference cycle) becomes as shown in Figure 29. The booster SSME operates at full thrust to $M=3$, then is shut down. The orbiter SSME operates at full thrust to $M=3$, then is throttled back to 65% (current minimum setting) for the remainder of the boost acceleration phase (after staging, the orbiter SSME returns to the maximum power setting). The turbofans operate up to $M=3$ and the ramjets from $M=1$ to $M=8$.

The final design weight statement is presented in Figure 30. The 2.11×10^6 lbs includes a fuel allotment of approximately 1.05×10^6 lbs for operation during the boost phase. The fuel allotment specified was for design purposes only, and was used primarily for fuel tank sizing, structural loads assessment, landing gear design, etc. It does not reflect the actual fuel required to reach the $M=8$ staging point. The weight specified in Figure 30 does, however, represent the maximum allowable within the current configuration design constraints.

A number of trade sensitivity studies were conducted on the Series 4 configuration to assess its performance characteristics during the boost acceleration phase. The Optimal Trajectory by Implicit Simulation computer program (OTIS) was used to compute all trajectory results. The program features a three-degree-of-freedom trajectory simulation model that employs non-linear programming optimization routines to provide an advanced trajectory optimization capability. This approach differs from traditional (explicit) numerical trajectory optimization techniques in that it treats the equations of motion as constraints, then iterates within the constraints and other boundary conditions to find an optimal solution. The program can simulate and optimize the trajectories for a large variety of flight vehicles ranging from subsonic aircraft to hypersonic vehicles and spacecraft. The program was particularly useful for application during this study since known end points could be specified, then optimal solutions for the initial conditions developed, subject to specified boundary conditions.

In all cases a target weight to be delivered to the orbiter staging point was selected, then the model worked backwards to establish the minimum lift-off weight. The reader is cautioned to note that the procedure was applied only to the lift-off point; no specific take-off analyses were run. Preliminary estimates suggested, however, that on the order of 80,000 lbs of rocket and JP fuel would be consumed during the take-off ground roll phase. The lift-off weights discussed in the following paragraphs do not reflect this weight addition. All analyses were based on a lift-off speed of $M=0.5$ (approximately 380 miles/hr). Unless otherwise specified, the target weight at staging was set at 1.1×10^6 lbs, and consisted of the fully fueled orbiter (600,000 lbs) and the empty booster plus residuals and return JP fuel (500,000 lbs). The analyses completed were limited to the powered boost acceleration phase only. No consideration was given in this paper to the performance of the booster after staging.

Figure 31 presents typical boost acceleration phase trajectory time history results for the Series 4 reference configuration. A peak thrust of 2.25×10^6 lbs was reached approximately 200 seconds after lift-off. Total time to reach the orbiter staging point, exclusive of the take-off ground roll, was just over 500 seconds. Maximum angle-of-attack at lift-off was 5.4° . A minimum angle-of-attack of approximately -2° was observed as the configuration descended to pick up the reference dynamic pressure (q) line (1500 lbs/ft^2 for this case).

The first sensitivity study completed was in response to the previously mentioned requirement that the orbiter SSME remain in operation during the ramjet acceleration phase (i.e. from $M=3$ to $M=8$). During the study, the orbiter SSME was run at full throttle up to $M=3$. Above $M=3$, separate runs were made with the orbiter SSME at selected throttle settings within its normal operational envelope. A reference run was also made with the orbiter rocket turned off at $M=3$. The dynamic pressure during the ramjet acceleration phase was stabilized at 1500 lbs/ft^2 up to $M=7.5$, then allowed to taper off to meet the staging conditions. The results, as presented in Figure 32, clearly show that operation of the orbiter SSME during the ramjet acceleration phase is highly counterproductive; the lift-off weight at the 65% reference throttle setting was some 265,000 lbs heavier than with the engine turned off at $M=3$. In keeping with the study guidelines of using near-term or existing systems wherever possible, the 65% throttle setting position was retained as the reference value since no system modification would be required. However, it must be emphasized that very significant overall weight savings could be realized by modifying the SSME operational cycle. Lift-off weight for the 65% throttle setting case was 1.85×10^6 lbs. Including the estimated 80,000 lbs fuel used for ground roll would result in a take-off weight of 1.93×10^6 lbs, well below the design maximum of 2.11×10^6 lbs.

Another area of interest was the sensitivity of the system to the dynamic pressure during the ramjet acceleration phase. With the orbiter SSME operating at the reference throttle setting of 65% above $M=3$, the trajectory was varied to produce dynamic pressures (q) ranging from 1000 lbs/ft^2 to 2500 lb/ft^2 over the Mach range from 3 to 7.5. Above $M=7.5$, the trajectory was again tailored to meet the $M=8$ staging conditions.

Figure 33 presents altitude vs velocity, and thrust and dynamic pressure vs time for the cases considered. For the high q run a peak thrust of more than 3.0×10^6 lbs was reached when all engines were operating. Acceleration time to the $M=8$ staging point was 400 seconds. For the low q run, acceleration times increased to over 600 seconds with peak thrust falling off to just under 2.0×10^6 lbs. The impact of dynamic pressure on the lift-off weight is presented in Figure 34. Although continuing to decline with increasing dynamic pressure, the lift-off weight is relatively insensitive to q for values greater than 1500 lbs/ft^2 . Increasing q from 1500 to 2500 lbs/ft^2 decreased lift-off weight less than 6%, while decreasing q from 1500 to 1000 lbs/ft^2 , increased lift-off weight by more than 6%. Considering the more critical thermal problems associated with high q flight, and the minimum reductions in lift-off weight realized, the 1500 lb/ft^2 value was retained for the reference mission.

A follow on study was conducted to determine the sensitivity of system lift-off weight to the booster SSME operational cycle. The booster SSME normally runs at maximum throttle setting from take-off to $M=3$, then is shut down. For this study, it was

systematically shut down earlier, until in the limiting case, it was not used at all. The results, as presented in Figure 35, show that the minimum lift-off weight was achieved by the reference cycle (i.e. running the booster SSME to M=3). Little change was observed when the booster SSME was shut down at M=2, since the ramjet thrust had already built to a significant value by then. For shut down Mach numbers below 2, however, increased overall lift-off weights were observed. For the limiting case of not using the booster SSME at all, an increase of approximately 160,000 lbs was observed compared to the reference case. Note here that adding the estimated 80,000 lbs of fuel expended during the ground roll phase would result in a take-off weight approaching the design maximum.

The performance of the ramjet units at higher Mach numbers was another area of concern, since the system was clearly operating on the outer envelope of the subsonic combustion ramjet. The problem was further complicated by a Series 4 design change which allowed bow shock ingestion at higher Mach numbers (to improve the transonic drag problem, the ramjet engines were moved forward). Although propulsion specialists were confident with the ramjet design, it seemed prudent to perform a sensitivity study to assess the impact of possible ramjet thrust degradation at high Mach numbers on overall system performance. For the study, the ramjet thrust at M=6 and above was reduced by 25% and 50%, and its impact on lift-off weight determined. Target weight at M=8 remained 1.1×10^6 lbs. The reader is reminded that the orbiter SSME is also in operation during this phase, and even at the reduced throttle setting, is producing in excess of 300,000 lbs thrust. The results from the thrust sensitivity study are presented in Figure 36, and show that a 50% reduction in ramjet thrust at M=6 and above, produced a 170,000 lb increase in lift-off-weight. Figure 37 shows the corresponding thrust schedules as functions of velocity.

The final study to be discussed here dealt with the booster weight at staging. During all of the preceding analyses, this had remained fixed at 500,000 lbs. For this study, it was varied in 10% increments from -10% to +30%, yielding booster staging weights ranging from 450,000 lbs to 650,000 lbs. The target weights were adjusted accordingly, from 1.05×10^6 lbs to 1.25×10^6 lbs. The results are presented in Figure 38, and show that a 200,000 lb variation in booster weight at staging produces a 360,000 lb change in lift-off weight.

CONCLUDING REMARKS

The results from the study verified the concept formulation and performance potential of a near-term two stage space launch system featuring a high L/D orbiter component. A payload capability of approximately 42,000 lbs into a 100 n. mi. polar orbit was demonstrated for a lift-off weight of approximately 1.85×10^6 lbs.

Significant performance improvements may be realized by further upgrading the SSME propulsion system used on the orbiter component. A 25% to 30% increase in baseline thrust will allow the 50,000 lb reference payload capability to be met. Modification to the basic operational cycle to allow shutdown/restart capability of the orbiter SSME would reduce lift-off weight by 265,000 lbs (14%) to 1.58×10^6 lbs.

The system lift-off weight was only moderately sensitive to dynamic pressure, once a value of 1500 lbs/ft² had been reached. Increasing dynamic pressure during the ramjet acceleration phase from 1500 lbs/ft² to 2500 lbs/ft² reduced lift-off weight by less than 6%.

Reducing ramjet thrust by 50% at M=6 and above increased lift-off weight by 170,000 lbs (9.3%).

Weight sensitivity studies established that a 1 lb increase in booster weight at staging produced a 1.8 lb increase in lift-off weight.

REFERENCES

1. Draper, Alfred C., and Buck, Melvin L., "Lifting Bodies - An Attractive Aerodynamic Configuration Choice for Hypervelocity Vehicles", AGARD-CP-428, Aerodynamics of Hypersonic Lifting Vehicles, 6-9 April 1987, Paper No 30.
2. Fisher, Carren M.E., "Experiences Using the Mark IV. Supersonic Hypersonic Arbitrary Body Program", AGARD-CP-428, Aerodynamics of Hypersonic Lifting Vehicles, 6-9 April 1987, Paper No 31.
3. Hargraves, C.R., and Paris, W.W., "Direct Trajectory Optimization Using Nonlinear Programming and Collocation", Journal of Guidance, Control, and Dynamics, Vol 10, No.4, July - August 1987, pp 338-342.

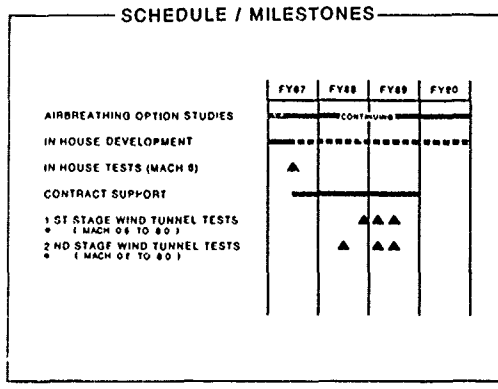


FIG. 1 PROGRAM SCHEDULE/MILESTONES

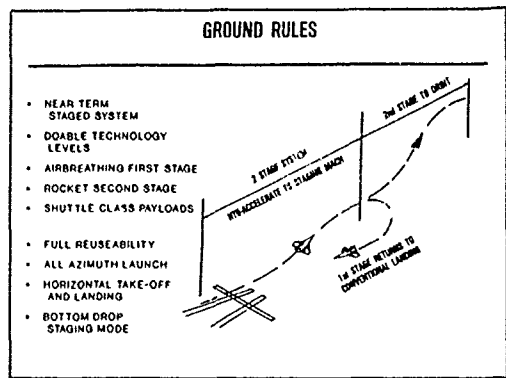


FIG. 2 STUDY GROUND RULES

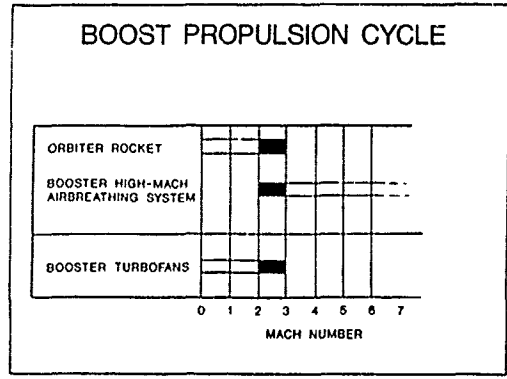


FIG. 3 BOOST PROPULSION CYCLE-ORIGINAL PROPOSAL

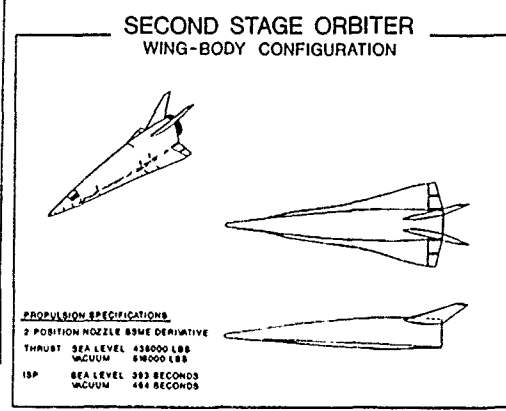


FIG. 4 PRELIMINARY WING-BODY ORBITER

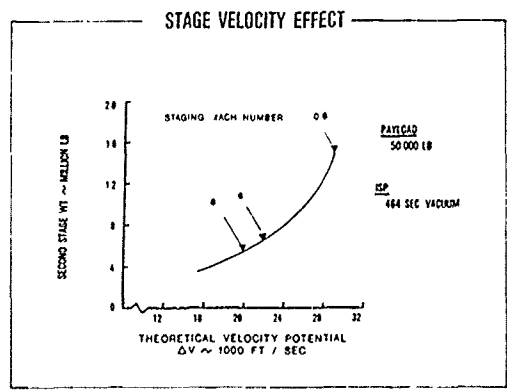


FIG. 5 VELOCITY REQUIREMENT EFFECT ON STAGE WEIGHT

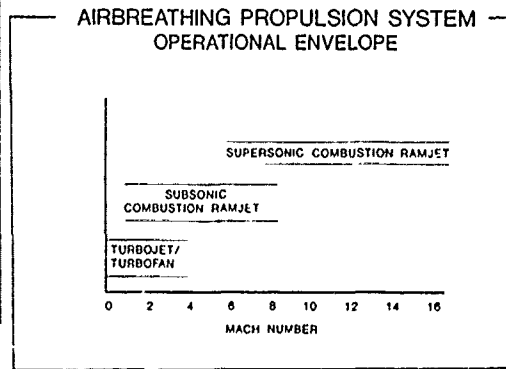


FIG. 6 CANDIDATE AIRBREATHING PROPULSION SYSTEMS

11-11-87 10:16 AM

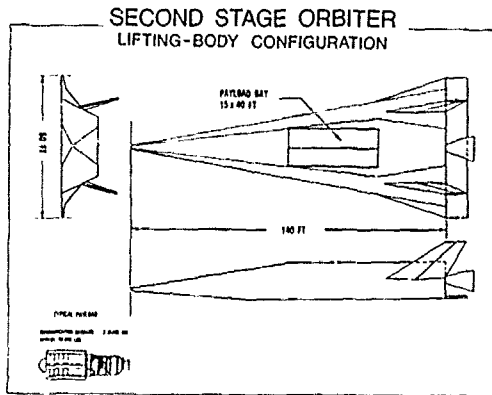


FIG. 7 LIFTING-BODY ORBITER (INITIAL)

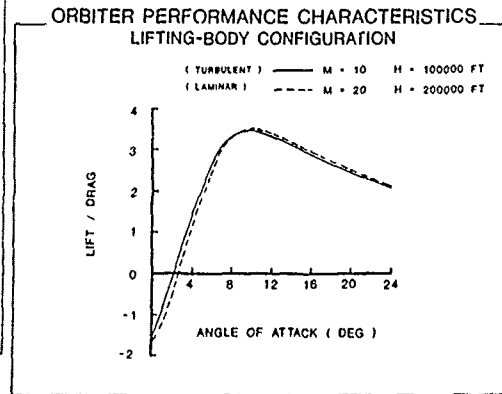


FIG. 8 ORBITER PERFORMANCE CHARACTERISTICS

INITIAL LIFTING-BODY ORBITER

WEIGHT STATEMENT

TOTAL STRUCTURE	58,402 LBS
SUBSYSTEMS	12,087 LBS
CREW / ACCOMMODATIONS	4,280 LBS
PROPULSION GROUP	8,400 LBS
LANDING GEAR	4,119 LBS
WEIGHT EMPTY	87,288 LBS <
PAYLOAD	50,000 LBS <
FUEL	417,732 LBS <
STAGING WEIGHT	555,020 LBS <

FIG. 9 ORBITER WEIGHT STATEMENT (INITIAL)

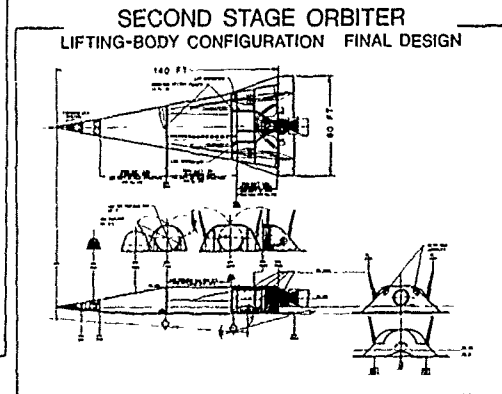


FIG. 10 LIFTING-BODY ORBITER (FINAL)

FINAL LIFTING-BODY ORBITER

WEIGHT STATEMENT

AERODYNAMIC SURFACES	6,884 LBS
BODY STRUCTURE	49,562 LBS
THERMAL PROTECTION SYSTEM	9,892 LBS
LAUNCH / RECOVERY / DOCKING	6,226 LBS
PROPULSION RELATED SYSTEMS	13,132 LBS
SUBSYSTEMS	11,753 LBS
CREW STATION / PROVISIONS	656 LBS
GROWTH FACTOR	1,945 LBS
EMPTY WEIGHT	99,850 LBS <
CREW	458 LBS
TOTAL NON ASCENT FUELS & LOSSES	7,833 LBS
TOTAL ASCENT FUEL	445,300 LBS <
PAYLOAD	50,000 LBS <
STAGING WEIGHT	603,453 LBS <

FIG. 11 ORBITER WEIGHT STATEMENT (FINAL)

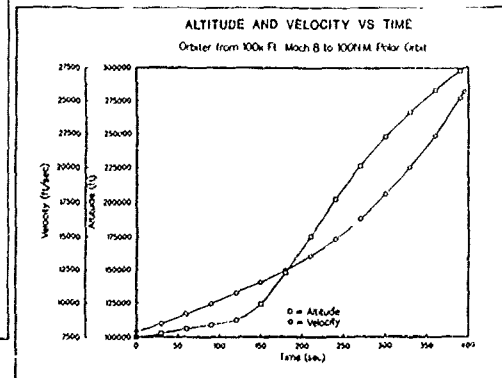


FIG. 12 ORBITER ASCENT TRAJECTORY (ALTITUDE/
VELOCITY VS TIME FROM STAGING)

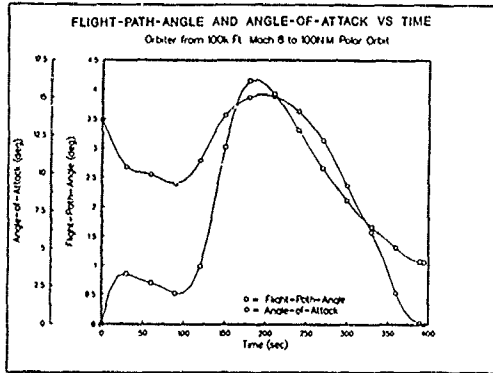


FIG. 12 CONCLUDED (FLIGHT-PATH-ANGLE/ANGLE-OF-ATTACK VS TIME FROM STAGING)

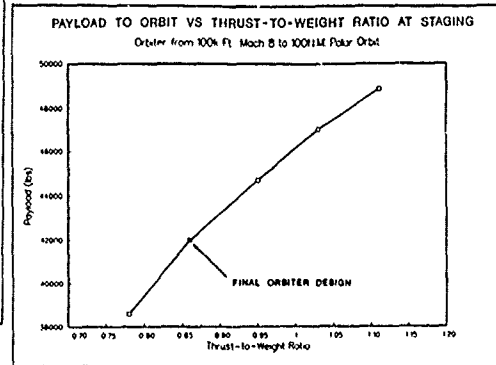


FIG. 13 IMPACT OF ORBITER THRUST-TO-WEIGHT RATIO AT STAGING ON PAYLOAD CAPABILITY

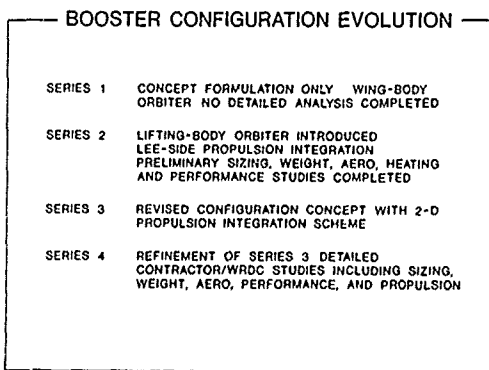


FIG. 14 BOOSTER CONFIGURATION EVOLUTION AND SERIES IDENTIFICATION

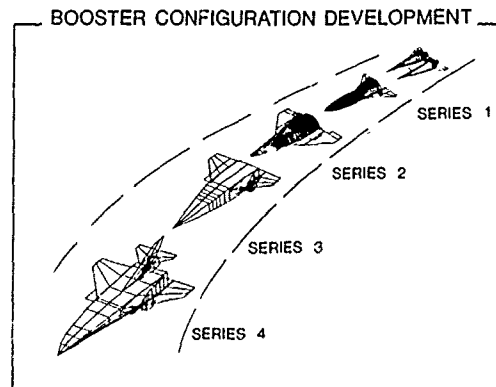


FIG. 15 SCHEMATIC OF BOOSTER CONFIGURATION DEVELOPMENT

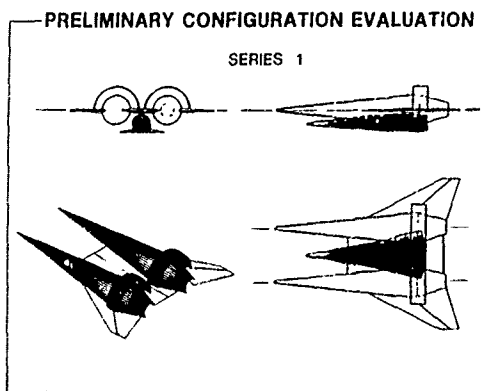


FIG. 16 SERIES 1-TWIN POD/EXTERNAL CARRIAGE CONCEPT

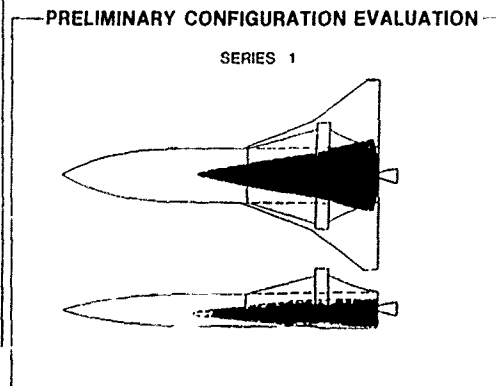


FIG. 17 SERIES 1-PRELIMINARY INTERNAL CARRIAGE CONCEPT

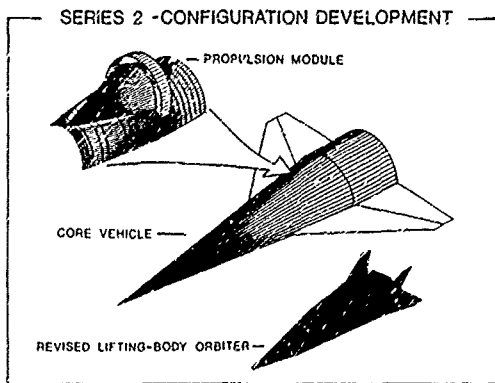


FIG. 18 SERIES 2-DEVELOPMENT MODEL

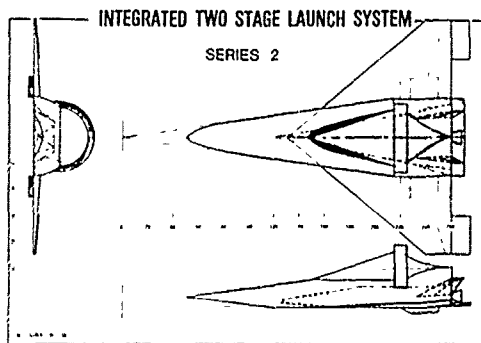


FIG. 19 SERIES 2-INTEGRATED TWO STAGE LAUNCH SYSTEM

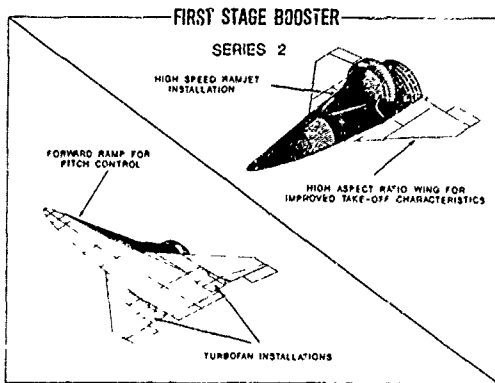


FIG. 20 SERIES 2-BOOSTER DETAILS

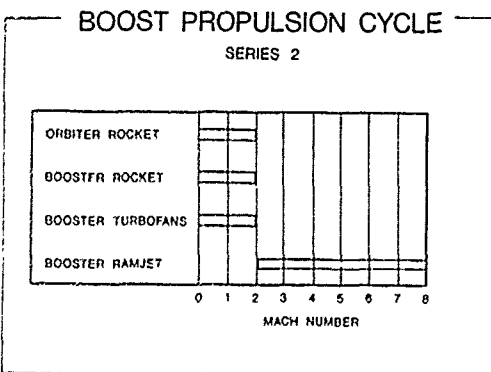


FIG. 21 SERIES 2-BOOST PROPULSION CYCLE

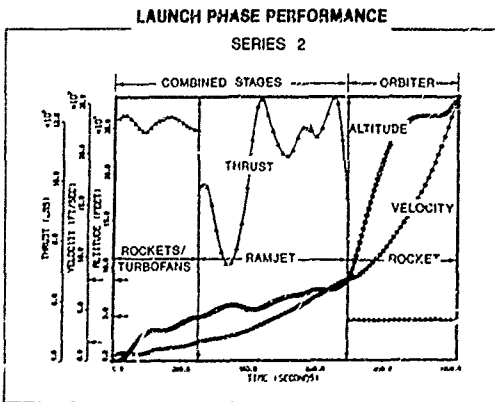


FIG. 22 SERIES 2-LAUNCH PHASE PERFORMANCE

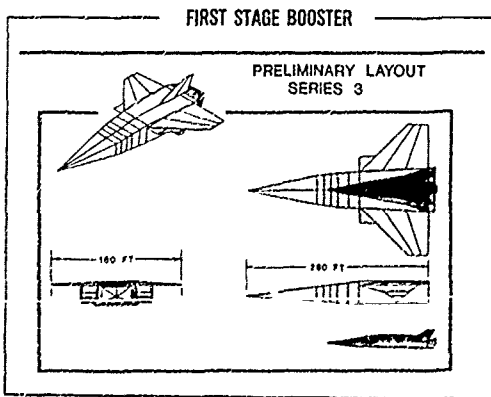


FIG. 23 SERIES 3-PRELIMINARY LAYOUT

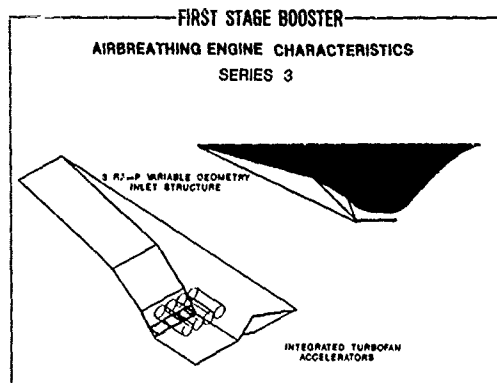


FIG. 24 SERIES 3 MULTI-CYCLE AIRBREATHING ENGINE DETAILS

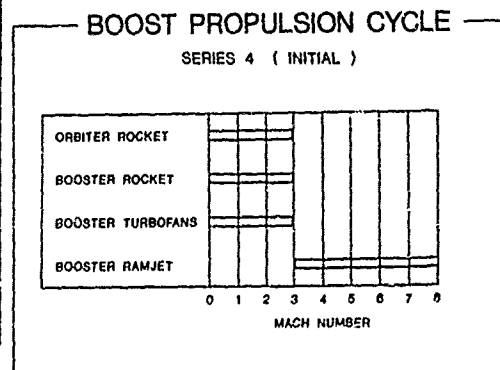


FIG. 25 SERIES 4-BOOST PROPULSION CYCLE (INITIAL)

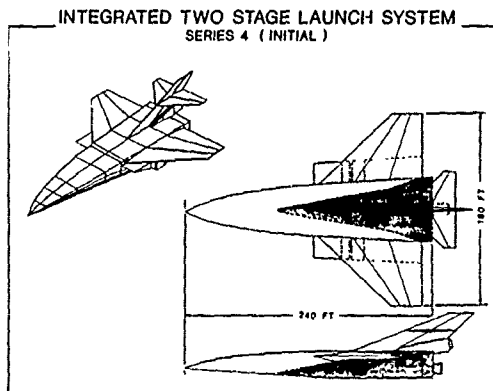


FIG. 26 SERIES 4-INTEGRATED TWO STAGE LAUNCH SYSTEM (INITIAL CONFIGURATION)

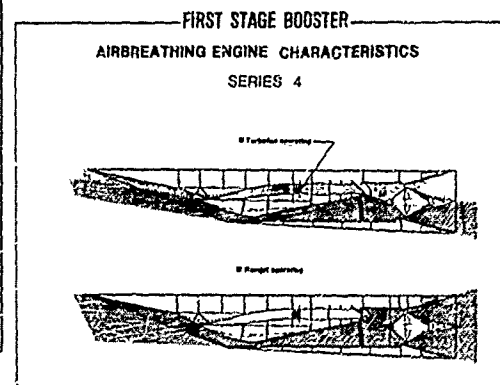


FIG. 27 SERIES 4 MULTI-CYCLE AIRBREATHING ENGINE DETAILS

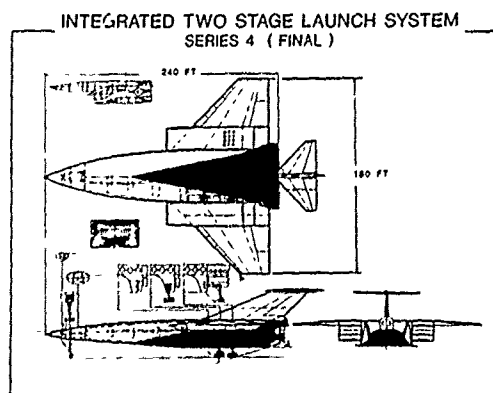


FIG. 28 SERIES 4-INTEGRATED TWO STAGE LAUNCH SYSTEM (FINAL CONFIGURATION)

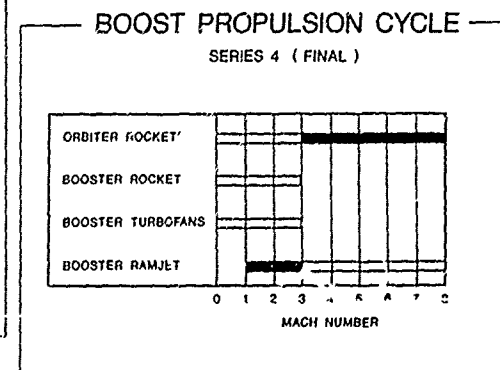


FIG. 29 SERIES 4-BOOST PROPULSION CYCLE (FINAL)

INTEGRATED TWO STAGE LAUNCH SYSTEM

WEIGHT STATEMENT

AEROTHERMO STRUCTURE	302,325 LBS
EQUIPMENT (SUBSYSTEMS)	14,568 LBS
PROPULSION SYSTEM	117,208 LBS
GROWTH MARGIN	8,583 LBS
EMPTY WEIGHT	442,684 LBS ◁
USEFUL LOAD (CREW / RESERVOIRS / PRESSURANTS)	10,575 LBS
NON ASCENT PROPELLANTS / LOSSES	7,854 LBS
ASCENT PROPELLANTS	
IP4	62,200 LBS
LH ₂	231,513 LBS
LO ₂	752,817 LBS
TOTAL BOOSTER	1,507,647 LBS ◁
ORBITER	603,453 LBS
SYSTEM GROSS LIFT OFF WEIGHT	2,111,100 LBS ◁

FIG. 30 SERIES 4-FINAL WEIGHT STATEMENT

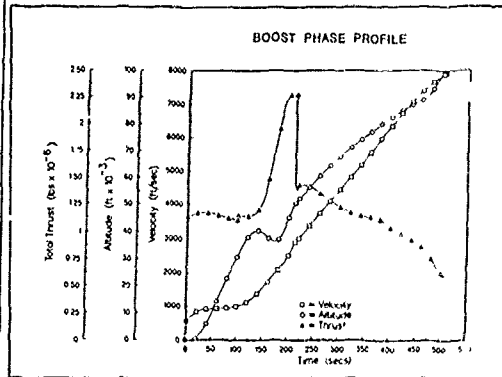


FIG. 31 SERIES 4 REFERENCE CONFIGURATION BOOST PHASE PARAMETERS (THRUST / ALTITUDE / VELOCITY VS TIME FROM LIFT-OFF)

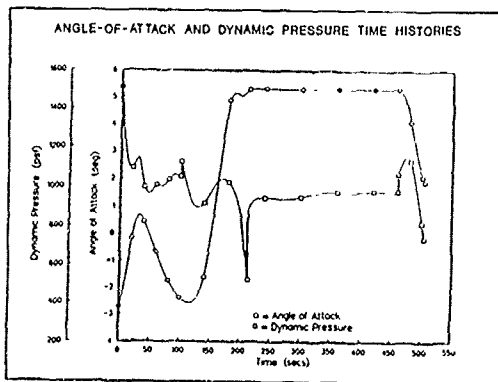


FIG. 31 CONCLUDED (DYNAMIC PRESSURE/ANGLE-OF-ATTACK VS TIME FROM LIFT-OFF)

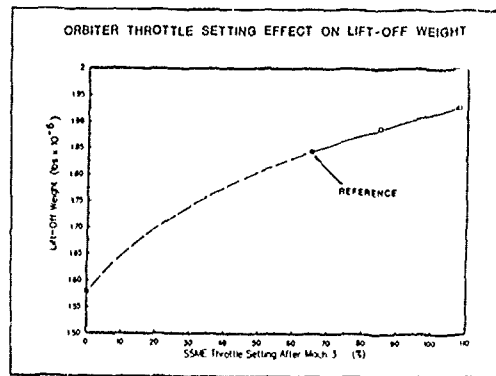


FIG. 32 ORBITER THROTTLE SETTING EFFECT ON LIFT-OFF WEIGHT

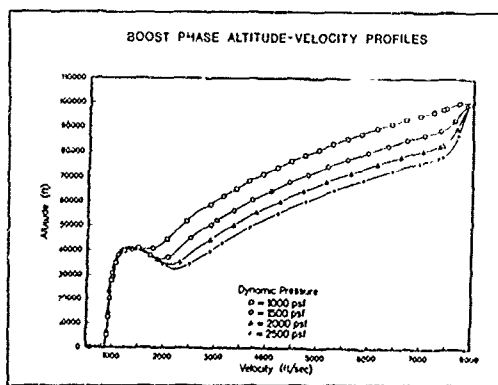


FIG. 33 DYNAMIC PRESSURE SENSITIVITY RESULTS (ALTITUDE VS VELOCITY)

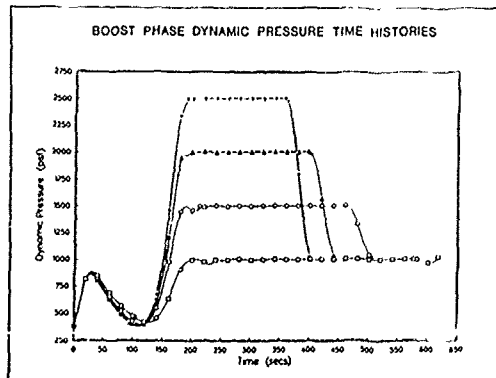


FIG. 33 CONTINUED (DYNAMIC PRESSURE VS TIME FROM LIFT-OFF)

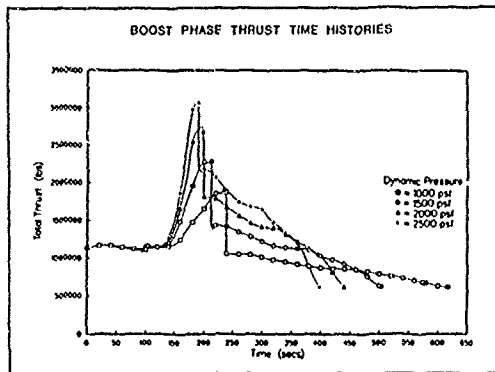


FIG. 33 CONCLUDED (TOTAL THRUST VS TIME FROM LIFT-OFF)

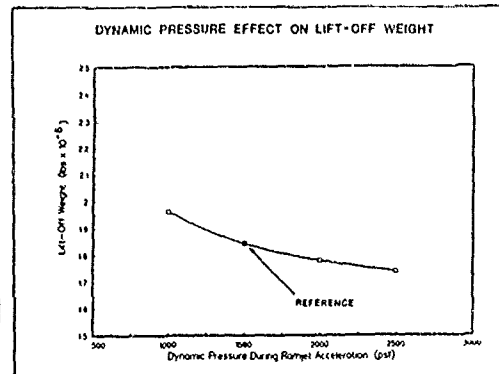


FIG. 34 DYNAMIC PRESSURE EFFECTS ON LIFT-OFF WEIGHT

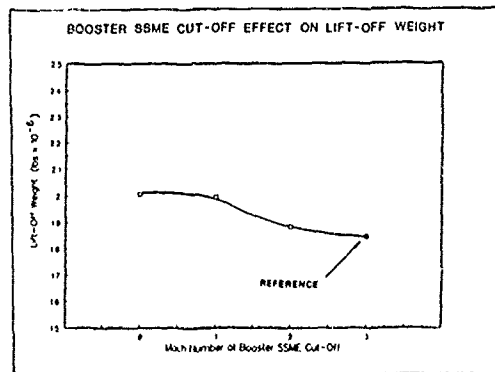


FIG. 35 EFFECT OF BOOSTER SBME OPERATION ON LIFT-OFF WEIGHT

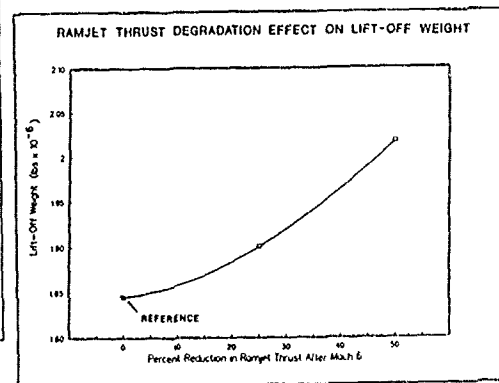


FIG. 36 SENSITIVITY OF LIFT-OFF WEIGHT TO REDUCTIONS IN RAMJET THRUST

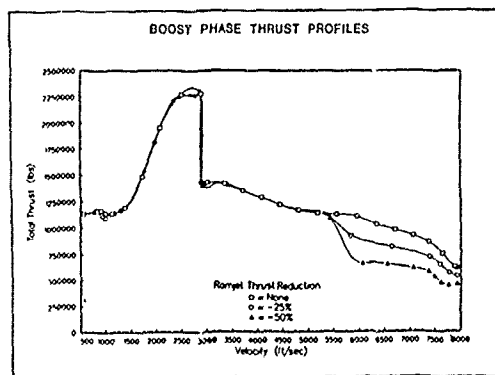


FIG. 37 THRUST TIME HISTORIES FROM RAMJET THRUST SENSITIVITY STUDY

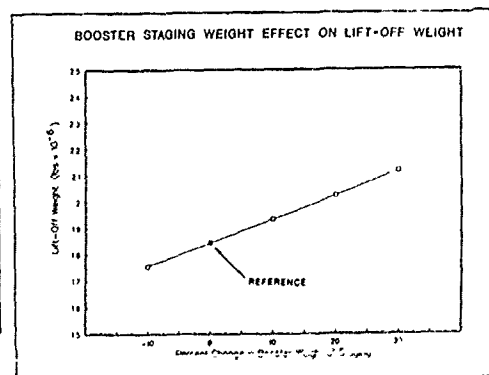


FIG. 38 IMPACT OF BOOSTER STAGING WEIGHT ON LIFT-OFF WEIGHT

POSSIBLE TRAJECTORY PROFILES TO ACHIEVE THE GEOSTATIONARY ORBIT WITHOUT ANY DRIFT PHASE

Giovanni Vulpetti

Telespazio SpA per Le Comunicazioni Spaziali
Via Tiburtina 965, 00156 Rome, Italy

ABSTRACT

In this paper we are concerned with two mission strategies for achieving a station longitude on the Geostationary Earth Orbit (GEO) starting from either a Low Earth Orbit (LEO) or from ground with no parking in LEO. Such trajectory profiles are somewhat different from the conventional ones used for targeting a longitude position in GEO for, typically, a telecommunication satellite. Neither of profile types here presented requires a drift orbit. The new strategy would fully exploit the liquid bi-propellant engines and additional capabilities of some of the current commercial launchers for inserting a satellite beyond GEO. The final goal of these strategies is to reach the desired station longitude in a time ranging from tens of hours to a few days, at most, with no additional propellant consumption with respect to the traditional trajectory profiles involving drifts. The new profiles may result in a significant increase of mission success probability together with less workload for the ground control centre.

1 INTRODUCTION

It is a well-accepted idea that telecommunication satellites can exploit the advantages of the liquid bi-propellant (monomethyl-hydrazine and nitrogen tetroxide) propulsion [1-4]. Confirmations come from recent and near-future large satellites such as the INTELSAT VI and VII series, OLYMPUS, ITALSAT, ARABSAT, DRS, SARIT to cite few projects. However, these satellites are planned or have achieved their operational orbits by means of the usual strategy of mission: a suitable Geostationary Transfer Orbit (GTO), where the satellite is left by the launcher or the perigee booster, is transformed into a Near-geoStationary Orbit (NSO) by means of one or more of so-called *apogee burnings*; after them, the satellite is generally found at a longitude somewhat different from its operational one. As a consequence, the semi-major axis of an NSO is made to be slightly higher or lower than the geostationary one (42164.3 Km) according to the sign (West or East, respectively) of the ensuing longitude increment the spacecraft has to run on in order to achieve its final longitude. In fact, in an NSO the satellite *drifts* with respect to the Earth surface. Because an NSO has both semi-major axis and inclination different from the GEO's, an additional transfer is required (usually an Hohmann-like profile) to match the desired conditions on GEO. All transfer requires up to 20-25 days of flight, most of it being due to the drift orbit. The workload at the control centre is rather heavy for the whole flight, also because an optimal profile calls for a *minimum* of four manoeuvres: two large orbital thrustings from GTO to NSO plus two small ones to finally put the satellite into its station. A so long time of a space centre involvement means a high cost, especially if the GTO/NSO control centre is different from the operational-orbit control centre (as it often takes place in Europe).

It may be interesting to remember that the above transfer strategy was born when the telecommunication satellites were equipped with solid engines (called the apogee kick motors) which fired only once at the prefixed apogee. Neither control upon the orbital vector radius nor engine restart were possible.

Another consideration regards the future utilisation of the GEO. It will host large multi-payload platforms and/or large satellites for global direct broadcasting and Earth sciences. In-orbit repairing payloads and/or retrieving satellites could become an advantageous policy which adds to the normal operations of geostationary satellite positioning by a fully-reusable high-energy propulsion LEO-GEO-LEO shuttle. It is plain that a rapid ascent-phase, namely, of the order of tens of hours instead of tens of days, would increase the operational goals success significantly, especially when a long payload inactivity entails strong off-services and drawbacks to, ultimately, final users.

Cutting the drift orbit phase would mean not only a cost saving (that is, reduced operations at the ground control centre), but also an increase of mission success because the "transition time toward the final equilibrium" is reduced. In fact, (1) the number of manoeuvres - together with all that implies in terms of ranging/angles acquisition, orbit determination and attitude control on-board - is halved at least, (2) if the longitude change from NSO to GEO is large, the full satellite visibility from ground may entail *additional* tracking/monitoring stations or using a data relay satellite. Finally, rescue missions to GEO may become a reality in a future.

The idea of studying optimal transfers which would avoid drift orbits for telecommunication satellites equipped with liquid bi-propellant engines can be traced back to the XXXV IAF Congress. In fact, in ref.-5 it has been proposed such strategy through an example showing one of the several capabilities of the Telespazio's Mission Analysis Interactive System (MAIS) [6]. The example regarded the Italian satellite ITALSAT, although too advanced in its development for the strategy being considered actually in the related project. Since that time no other potential no-drift applications occurred in Italy. However, other geostationary satellites powered by liquid bi-propellant thrusters are planned in Italy for the next decade. As a consequence, the importance of new trajectory profiles may be traded off with the classical ones.

After the Shuttle-Challenger disaster in February 1986, many expendable rockets have been upgraded to as commercial launchers in USA. Some of them have a high-energy performance together with both a sophisticated Guidance (that means an high-accuracy targeting) [7]. The possibility to achieve the GEO through an outer-geostationary transfer orbit, in order to decrease the fuel for the orbital change, has been studied by General Dynamics for its Atlas-G/Centaur launcher [7,8]. However, no *no-drift* profile capability has been included hitherto [9].

Advanced liquid bi-propellant engines allow a spacecraft to control: (a) the orbital vector velocity *and* the vector radius during a finite-burn manoeuvre, (b) (indirectly) the time of the coasting following an intermediate burning, (c) the orbital inclination change, if any. Finite-burn losses and number of manoeuvres can be kept very low because liquid bi-propellant propulsion exhibits thrust acceleration comparable or higher than the GEO altitude gravitational acceleration (0.023 g).

The *no-drift* LEO-GEO trajectory needs nothing more than the already-existing above-mentioned properties. From a dynamics viewpoint, what is substantially requested to a mission analyst is to perform the optimisation of a trajectory the final state of which (the GEO satellite) is *partially unspecified* in an Inertial Frame. In contrast, the analyst has to specify the station longitude and the "actual GEO inclination" ¹. The flight time can be prefixed or left open, according to the mission constraints. This is what we are going to do in the next sections.

2 STATEMENT OF THE PROBLEM

Let us consider the mean-equinox-and-equator-of-date (for instance, date= launching date) Earth-centred inertial-frame (IF) for our calculations. We denote the spacecraft state by the vector $S = [M, R, V]$ (M =instantaneous mass, R =vector radius, V =vector velocity), longitudes with respect to Greenwich by λ , propulsion parameters (thrust and exhaust jet) by T and U , respectively. The time-dependent thrust direction in IF is denoted by u . In addition, vector magnitudes are denoted by normal-face symbols; the subscripts 'o' and 'f' are used to specify epoch and final quantities, respectively; variables referred to *thrusting* or *coasting* are superscribed by a T or C, respectively.

Figure 1 displays the scheme for a GTO-GEO transfer. For simplicity of presentation, we have pictured an inner trajectory to a station longitude. By means of the formalism of the *state transition matrices* we can write:

$$(1) \quad \begin{aligned} S_{2j-1} &= A_j^C S_{2(j-1)} & j &= 1, \dots, N \\ S_{2j} &= A_j^T S_{2j-1} & j &= 1, \dots, N \end{aligned}$$

where j denotes the order number of the generic trajectory phase which is characterised by the transition matrix A_j . Equations 1 imply that $S_{2N} = S_f$. Thus, the satellite is required to pass through an even number of phases to achieve GEO. From Eqs.-1 one carries out:

$$(2) \quad S_j = \prod_{k=N}^1 (A_k^T A_k^C) S_0$$

¹ It may be suitable that the final longitude be reached with a residual inclination (instead of zero) for satellite station-keeping reasons. That, though, is independent of the particular transfer trajectory strategy

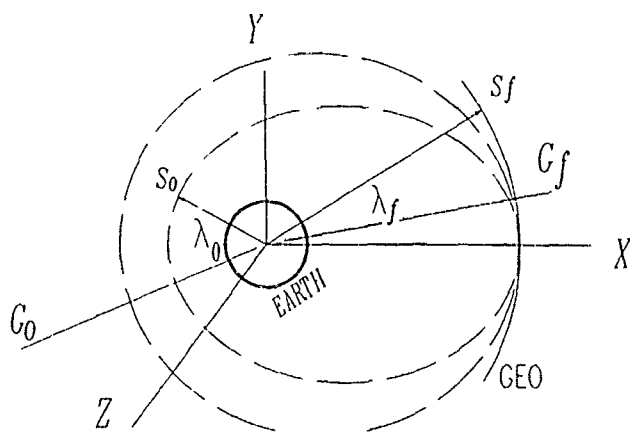


Fig.-1 Scheme of a No-Drift GEO Insertion. X-axis points vernal point. G denotes the Greenwich Sidereal Angle. S denotes the Spacecraft

Note the decreasing order of the matrix products. If we assume that the satellite matches (at the beginning of its operational life) a non-zero inclination GEO with the vector velocity parallel to the equator, then the final state can be expressed as follows:

$$(3) \quad S_f = \begin{pmatrix} + R_{GEO} \cos(i) \cos(\lambda_f + G_f) \\ + R_{GEO} \cos(i) \sin(\lambda_f + G_f) \\ + R_{GEO} \sin(i) \\ - V_{GEO} \sin(\lambda_f + G_f) \\ + V_{GEO} \cos(\lambda_f + G_f) \\ 0 \end{pmatrix}$$

where the orbit inclination is i and the final Greenwich Sidereal Angle (GSA) is given by:

$$(4) \quad G_f = G_0 + \omega (t_f - t_0)$$

ω being the Earth angular speed. The spacecraft initial state can be related to the following cases:

- A: a lower-than-GEO GTO onto which a launcher leaves its payload;
- B a generally-circular parking orbit where a booster is activated to transform it into a lower-than-GEO GTO;
- C. a higher-than-GEO GTO onto which a launcher leaves its payload;

It is important to determine the optimal no-drift profile by explicitly considering in the computation the vehicle boosting the proper satellite into a transfer trajectory (that the satellite engines will modify). That is essentially because the mission analyst has additional realistic degrees of freedom to optimise the flight profile in order to synchronise the satellite injection at the desired longitude.

There are a number of constraints and realistic conditions of flight which one should consider in order to prove the feasibility of the no-drift concept:

1. the thrust orientation should be somewhat simple, possibly constant, during a burning in the inertial frame. That ultimately aims at easy mechanising the vector steering. The thrust direction generally changes from burning to burning;
2. the liquid bi-propellant engine currently exhibits an intermediate level of thrust (490 N); that means long burning times in order to carry a heavy satellite into operation. The European Space Agency is supporting the development of liquid bi-propellant thrusters of 3 KN [1];
3. the number of thrustings is to be kept as low as possible; however, it is not advisable at all to try to perform *one* burning; the multi-burn policy entails not only a saving propellant, but also allows to correct the satellite trajectory dispersions by the last burning;²
4. although the total transfer time to station is short compared to the classical strategy, however both the satellite-Greenwich synchronisation and the spent propellant also depend on perturbations to the ideal keplerian field;
5. no limitation on the station longitude value is desired for the no-drift concept is applicable; however, it is well known that there are GEO zones particularly attractive (and crowded) so that a real analysis is less severe

A remark about points 2 and 3 is in order. When thousand-newton engines are available, one could obtain the insertion into GEO by one thrusting even for satellites as heavy as 6000 Kg. Nevertheless, point 3 could be particularly important for future GEO spacecrafts and a two-burn strategy may result in the optimal strategy. That would have the additional advantage to enlarge the launch window from the no-drift longitude achievement viewpoint.

3 COMPUTER CODE

The optimal constrained trajectory profiles have been computed through the special NO-DRIFT option of the program MAIS, a multi-burn minimum-propellant two-boundary trajectory optimisation code [6]. MAIS has been written in FORTRAN-77 and currently consists of about 25,000 lines, including comments. It runs in double precision on an IBM-3081 under the VM/CMS operating system and on a 25-MHz 32-bit COMPAQ/Weitek-1167 work-station under the MS-DOS 3.31 operating system. The current version of MAIS requires up to 4 MB of memory to run; in fact, MAIS can perform a flight design optimisation involving up to 9 thrusting and 9 coasting in any sequence³. MAIS allows to simultaneously optimise up to 99 control parameters (90 of them describe independent azimuth/right-ascension and elevation/declination components of the thrust direction) while up to 13 state/time equality constraints and up to 37 control/mass inequality constraints can be specified altogether. Launching-from-ground simulations (with in-atmosphere-working engine behaviour), variable-thrust (for chemical and ion propulsion) and computation of stochastic trajectory dispersions are allowed.

With regard to the current set of mission profiles, the special NO-DRIFT option allows a dynamical update of the unknown final state in order to synchronise the satellite orbit with Earth rotation to the desired station longitude at the end of the last burn. The transfer time is generally left open⁴, while best epoch depends on the selected station longitude. Booster dry mass or other mass jettisoning, if any, and J2 perturbation and high-atmosphere drag are taken into account. The high-atmosphere model consists of an exponential-like model with parameters coming from the NASA Standard Atmosphere-1977⁵; no truncation is made in the differential field equations; in particular, the correct J2 perturbation has been considered in all phases of flight. The minimisation algorithm consists of a modified version of the Levenberg-Marquardt method [10] which allows the analyst to use a rough guess of the control parameters as starting solution. Although MAIS is designed to offer a very wide spectrum of thrusting control law, however it has been used here for constant thrust solutions, though varying from burn to burn, in the light of what said in sect.-2 (point-1).

² This last option can be increased in performance if the orbit determination process were either implemented onboard or accomplished in the control centre by a filtering technique.

³ For instance, particularly complex flights could imply sequences such as OTTCCCTTTC, TTTCCCTCCCT and so on. Thrusting and coasting sectioning in MAIS takes place through arc-dependent parameters.

⁴ However, MAIS can be run in fixed-flight-time mode if a particular spacecraft requires to synchronise its final longitude at some specified time.

⁵ When a launching-from-ground is computed, the whole standard atmosphere model is considered

4 APPLICATIONS

We present results for the cases A-B and C separately. From a dynamics point of view the launcher's upper stage of case A is equivalent to the booster of case B; in fact, both can be fired in such a way to leave the satellite in that sub-stationary transfer orbit that minimises its fuel, while the orbit synchronisation with the Earth rotation to the desired operational longitude is performed by the satellite propulsion system. It is important to realise that, although the profile optimisation is accomplished simultaneously on all control parameters, is only the satellite propellant that is to be minimised in order to guarantee a long operational life. Thus, we discuss flights of type B only for the lower-than-GEO transfer.

4.1 LEO-GEO Transfer by Inner-Stationary Trajectory

Figures 2 through 4 show the impulsive delta-V from a classical GTO to GEO as function of the perigee distance and for GTO inclination angles ranging from 0 to 90 degrees. Such behaviours are useful to quantitatively evaluate how much excess propellant the no-drift best profile requires. Note that, since the perigee stage and the J2 perturbation are taken into account in the flight computation, the impulsive reference propellant consumption in cases A-B is determined by the *osculating* perigee and inclination just before the beginning of the first finite-thrust burn. Although the corresponding osculating apogee is generally lower than the GEO radius, however this difference is small so that Figs. 2-4 can be used; instead, it is correct to consider such discrepancy as a consequence of the finite-burn losses.

In order to prove the feasibility of the no-drift concept, we have chosen a difficult mission configuration. The purpose is to prove the concept in a case of both *limited* booster performance and *low* thrust on the satellite, which, in turn, is *more* massive than the current telecommunication satellites ⁶. As a consequence, the low-acceleration propulsion system of the satellite has to accomplish both a strong inclination change and longitude synchronisation. Practical satellites may be in more favourable conditions for achieving station longitudes without drifting in an NSO.

The considered GEO satellite weighs 2500 Kg and is powered by 500-N 310-s liquid bi-propellant restartable engines. The specific impulse value is to be meant the effective one. The solid booster weighs about 4.5 tonnes (its propellant mass depends on the particular optimised profile) and exhibits a mean thrust of 100 kN and a specific impulse of 290 s. The booster+satellite vehicle is left in a circular parking orbit 300 Km high and 30 degrees in inclination. The booster type is not of particular matter in the no-drift calculation; in contrast, its class determines to what extent the first GTO may be adjusted. The same function could be accomplished by the *integrated* propulsion system of future spacecrafts. With no loss of generality we simplify the reference frame of Fig.-1; in fact, the mean equatorial plane at epoch is considered as reference plane, whereas the X-axis coincides with the intersection between the (ideal) GEO and the parking orbit at epoch ⁷.

One should realise that a no-drift trajectory is independent of the particular launch day during a year (at least, if we limit ourselves to dynamical considerations, thus excluding, for instance, solar array and sensor problems which, on the other hand, there also exist in the NSO option). In contrast, during a day the spacecraft longitude at epoch affects the propellant consumption to a desired final longitude in GEO; in other words, a launch window is expected ⁸. The main purpose here is to show and discuss the launch window for the vehicle described above. Here, launch means the start of flight at some suitable point in the parking orbit (for instance, the instant of the vehicle separation from an orbiter); epoch is referred to such a point. Different initial points behave merely as a (small) scale shift for transfer time and initial longitude of the considered satellite.

Figures 5a-5c show the behaviours of excess delta-V, propellant, flight time, right ascension at insertion and burn distribution as function of the spacecraft longitude at epoch. The final longitude is required to be 340 degrees here. The impulsive solutions of reference in Fig.-5a are in the sense of what said at the beginning of this section. In contrast, the impulsive solution in Fig.-5c is the best one, taking J2 and drag into account, for this vehicle, namely, a limited booster plus a satellite of mass beyond the booster capability with respect to the full orbital change. Figures 5a-5c refer to as the minimum fuel flights lasting the shortest time. In fact, real satellites could require to add to the first transfer

⁶ The envisaged satellite is about 10 percent heavier than the INTELSAT VII series satellites (which are in progress)

⁷ Epoch is usually chosen in the half orbit preceding the perigee burn. This corresponds to the real arc where the booster+satellite complex is deployed by some low-altitude launcher. Thus, the relative nodes line at the perigee thrusting is very close to the defined X-axis

⁸ The desired station longitude represents a point with a fixed arc from the intersection between the ideal GEO and the Greenwich meridian plane. Thus, it may be pictured as a point-like weightless body that revolves the Earth with a certain own phase. Thus, a real satellite should perform a "rendezvous" with such a fictitious body.

Fig-3 GTO-GEO Impulsive Delta-V as function of GTO perigee and Inclination

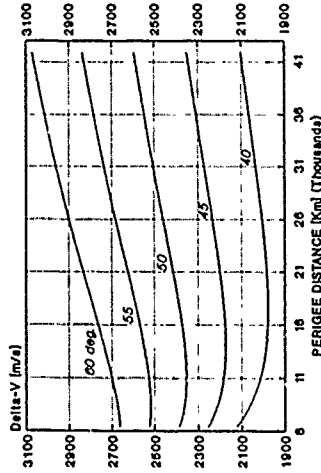


Fig-4 GTO-GEO Impulsive Delta-V as function of GTO perigee and Inclination

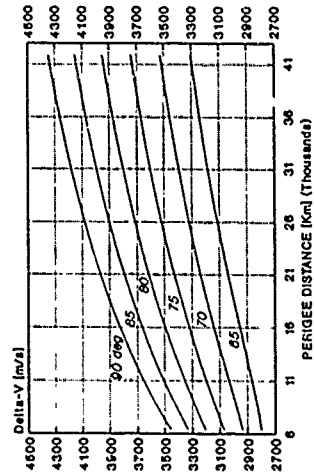


Fig-2 GTO-GEO Impulsive Delta-V as function of GTO perigee and inclination

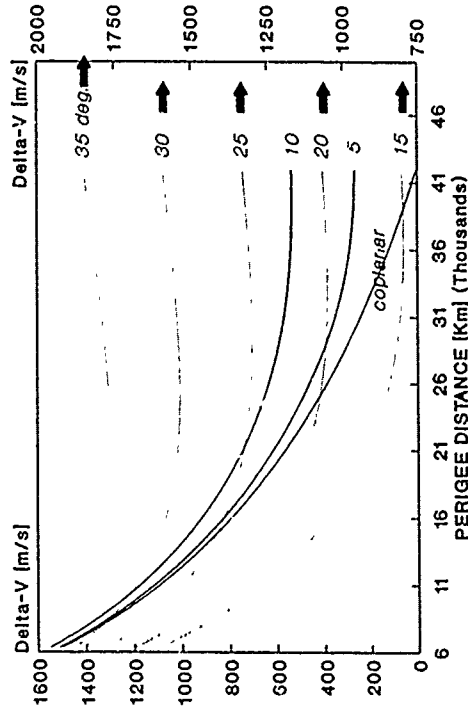


Fig-5a Launch window for minimum-fuel inner-stationary no-drift transfer

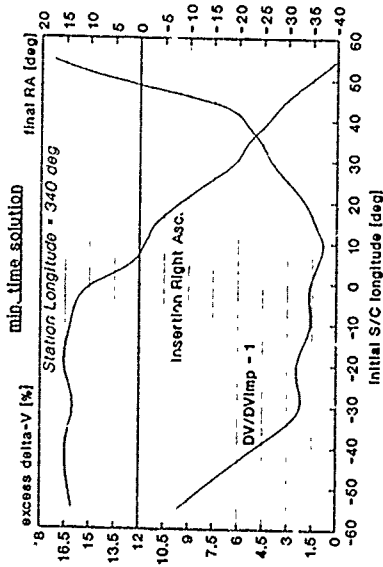


Fig-5c No-Drift Inner transfer Satellite Propellant (min. time)

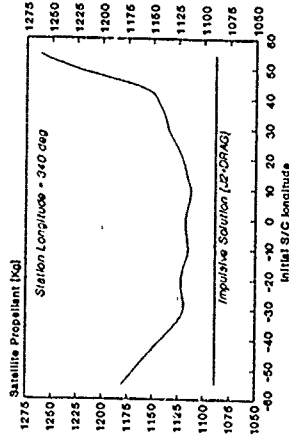
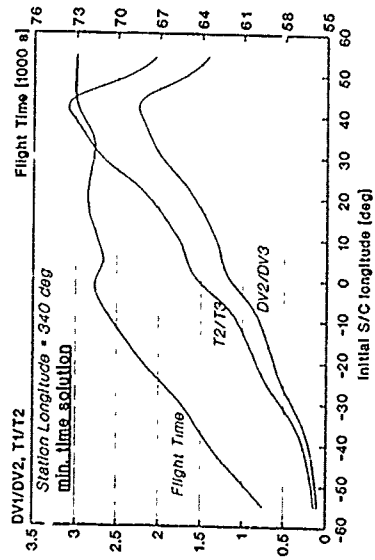


Fig-5b No-Drift Inner Transfer flight-time and S/C burn distribution



arc (about a semi-ellipse) a number of integral orbits because of some sub-system constraints. In these cases behaviours similar to those ones presented here (but corresponding to a different range of initial longitude) there exist. For this reason and the probable situation that future automated spacecrafts will perform flights to GEO in short times, we discuss about the minimum-fuel+minimum-time results. Another remark regards the final station longitude; the fact that we selected 20 degrees West (a zone rather crowded) for our discussion is of no matter for the no-drift concept.

The most important result from Figs.-5a/5c is perhaps the existence of a launch window of 4 hours to within which the spacecraft fuel penalty (with respect to the impulsive solution) ranges from 0.7 to 3.3 percent. Such values are less than the corresponding excess fuels spent by most of the large current telecommunication satellites which are delivered to their station longitudes by means of classical strategies. The amplitude of the above window is of the order of or greater than the usual telecommunication satellite windows. Beyond the 3 percent value, the no-drift penalty increases rapidly with the absolute value of the initial spacecraft longitude. In contrast, inside the window there exist a quasi-plateau zone and an optimum value of the initial longitude. The fine-structure of the launch window partially depends on the fact that thrust is to be kept constant in a burn for adding no further complexity to the satellite AOCs. That does not allow the thrust direction to be updated very smoothly as it happens in unconstrained-in-thrust-direction solution.

Figure 5b shows that the minimum time solutions entail flights lasting from 17 to 20 hours. In addition, the symmetric satellite burn solutions, either equal delta-V or equal burning time, are well within the above window and imply almost the same cost, namely, an excess of about 1.7 percent. Such feature may be attractive from a hardware viewpoint (for instance, the battery subsystem).

4.2 LEO-GEO Satellite Transfer by Outer-Stationary Trajectory

From the data of [7,9] we have arranged a simulation of a launcher upper stage (a little different from the actual Centaur) capable to deliver a heavy payload into an outer-stationary (or super-stationary) transfer trajectory. The payload is endowed with liquid bi-propellant to perform two manoeuvres. The first one takes place at high altitude to simultaneously raise perigee and accomplish most of the orbital change; in fact, although better in performance than the boosters generally used for inner-stationary transfers, the current launcher upper stages are not yet able to change all of a high inclination (28.5 deg. this case) for a massive satellite (2500 Kg). The second burn occurs close to the geostationary altitude to circularise, including a residual orbital change, and complete the synchronisation to the final longitude. Thus, the satellite has to use its own engines to transform a super-GEO trajectory into a GEO; the two long coasting times are to be controlled (by the previous burnings) in such a way the desired station longitude may be achieved at the end of the last thrusting. Such a thrusting is obviously a braking propulsion phase.

Figure 6a shows the launch window for the outer-stationary flight in terms of delta-V and distance of the upper burning. The horizontal line represents the delta-V of the reference impulsive transfer of Fig.-5c, namely, 1740 m/s or, equivalently, 1089.5 Kg for a 2500-Kg 310-s satellite. The apparent gain is plainly caused by the high-altitude orbital change. Thus, incidentally, the current result also emphasises a particularly interesting application of what proposed in Refs. 8,9 about a super-stationary profile. Figure 6a is truncated on the right at the launcher limit. A launch window of 10 hours, at least, exists for the current case of 20 West station longitude. Figure 6b shows that such transfers last from 29 to 38 hours, a situation better than the sub-stationary transfer times with respect to the time required by some satellite operation (e.g. attitude acquisition). The same Figure also shows that there is an interval of initial longitude entailing the final thrusting inside the geostationary orbit, this interval is followed by another one where the satellite approaches GEO externally. Note that the final right ascension is always greater than 180 degrees in the considered interval of initial longitudes. In contrast to the inner-stationary transfer, the first satellite burning last much more than the second burning. That is displayed in Fig.-6c. There is also shown the upper stage's propellant excursion, about 3 percent over the current window.

As a general remark, we point out that a super-stationary transfer is able to exhibit a large window simply because the transfer trajectory arcs are not constrained to evolve to within a limited zone such as the GEO circle. In addition, trajectory dispersions are more manageable; in fact, although the launcher upper stage errors are amplified at high altitude, however: (1) a long thrusting there could be adjusted to compensate for these errors, (2) the uncertainties caused by the apogee burning (are reduced at perigee and) could be corrected by the final short manoeuvre near GEO. The last long (from 12 to 18 hours) coasting could be easily observed from ground, the full trajectory state may be updated in real-time by means of a filtering technique, the braking manoeuvre may be rapidly computed and the related commands sent to the satellite in time. In addition, the pseudo-period of the first quasi-ellipse could be chosen (by selecting the

Fig-6a Launch Window for Minimum-Fuel Outer-Stationary No-Drift Transfer

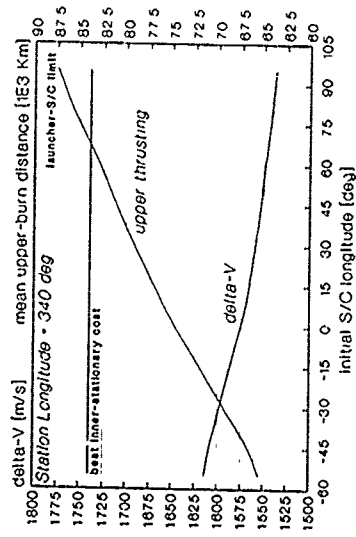


Fig-6c Outer-Stationary Transfer Burn Propellant vs Initial Longitude

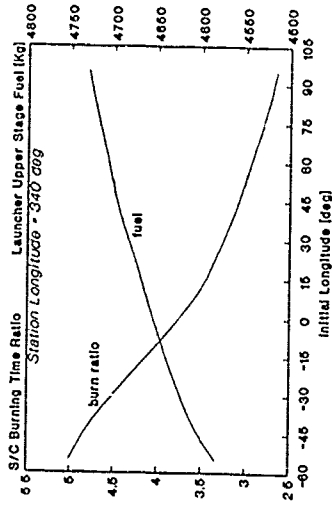
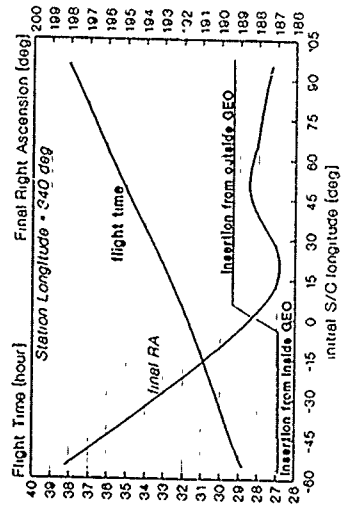


Fig-6b Outer-Stationary Transfer: flight-time and final insertion behavior



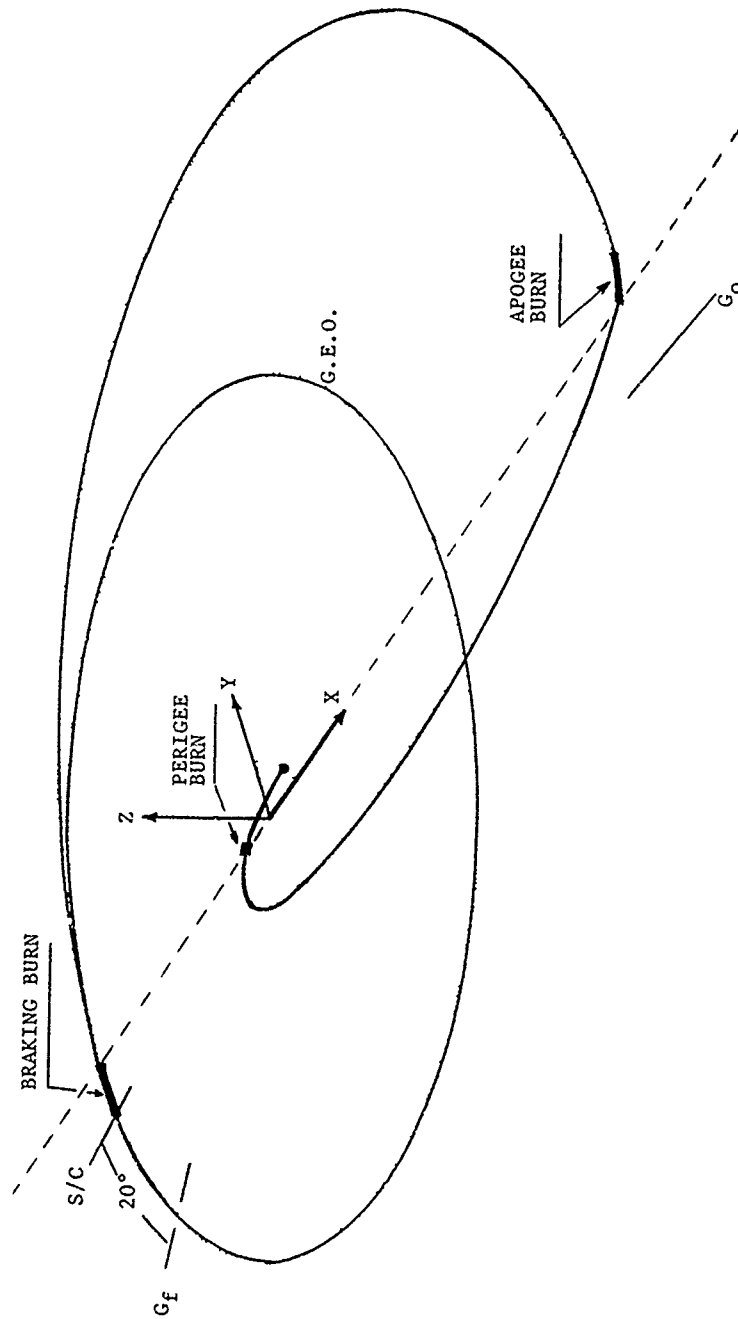


FIG.-7 EXAMPLE OF SUPER-STATIONARY TRANSFER TO GEO. THE FINAL LONGITUDE OF THE SATELLITE ON GEO HAS BEEN FIXED AT 20 DEGREES WEST. THE ORBITAL INCLINATION BEFORE THE PERIGEE BURNING IS 28.5 DEG.

appropriate initial longitude) close to 24 *sidereal* hours (about 86164 s), namely, the first transfer orbit could be a *synchronous* orbit. This would have the advantage to add a few periods for satellite and ground operations, without changing the "rendezvous conditions" to the station longitude and keeping the total transfer time less than three or four days. Figure 7 and Tab.-1 show an example of outer-stationary no drift, minimum-propellant transfer to insert a spacecraft into GEO at 20 deg. West in longitude.

TABLE 1. Parameters of the trajectory shown in Fig.-7.

Epoch (before the perigee thrusting): date = 1991 Dec. 31		
time = 17:00:00		
Initial Spacecraft Longitude = -264.62 deg		
Coasting + Launcher Upper Stage Burning Time = 1274.40 s		
First Transfer Coasting:		
Initial semi-major axis	47449.5	Km
eccentricity	0.36252	
inclination	23.817	deg
asc. node R.A.	181.200	deg
perigee argument	0.625	deg
eccentric anomaly	359.019	deg
longitude	-181.47	deg
Final semi-major axis	47096.5	Km
eccentricity	0.86143	
inclination	23.806	deg
asc. node R.A.	181.126	deg
perigee argument	0.76	deg
eccentric anomaly	172.262	deg
longitude	-195.73	deg
coasting time	46833.0	s
satellite mass	2500	Kg
Super-Stationary Burning:		
Final semi-major axis	64944.6	Km
eccentricity	0.35079	
inclination	1.155	deg
asc. node R.A.	183.952	deg
perigee argument	1.244	deg
eccentric anomaly	177.283	deg
mass	1779.3	Kg
longitude	-210.61	deg
burning time	4381.8	s
Thrust: magnitude	500	N
right ascension	91.39	deg
declination	16.07	deg
Second Transfer Coasting:		
Final semi-major axis	64946.8	Km
eccentricity	0.35083	
inclination	1.155	deg
asc. node R.A.	183.949	deg
perigee argument	1.250	deg
eccentric anomaly	356.270	deg
longitude	-20.40	deg
coasting time	82927.8	s
Braking/Insertion Burning:		
Final semi-major axis	42164.3	Km
eccentricity	0.00000	
inclination	0.00000	deg
right ascension	187.305	deg
declination	1.1E-10	deg
mass	1507.5	Kg
longitude	-20.000	deg
burning time	1652.3	s
Thrust: magnitude	500	N
right ascension	96.27	deg
declination	-8.22	deg

5 CONCLUSIONS

In this paper we have analysed the possibility for liquid bi-propellant propulsion telecommunication spacecrafts of achieving their station longitudes without using the drift-orbit strategy. Two configurations have been studied: (a) transfer trajectories whole inside the geostationary orbit, (b) transfer trajectories going beyond the geostationary altitude. Launch windows in terms of delta-V as function of the initial spacecraft longitude have been carefully computed for both mission configurations. The considerable advantages of a no-drift profile with respect to the traditional strategy have been emphasised. These are by no means definitive in selecting a strategy to put a satellite in a GEO station. The spirit of this work is to suggest, on a quantitative basis, to consider - in a real space project - a careful trade-off between classical transfers and new transfer profiles offered by both satellite unified propulsion systems and high-performance launcher upper stages. Such an analysis could and should start since the phase A and, in any case, should be completed during the phase B.

6 REFERENCES

1. "Mechanical Systems: Propulsion and Aerothermodynamics" in ESA ANNUAL REPORT, 1988
2. Chen Qizhi, Gao Hanru, "Theoretical Study and Testing of the Bi-Propellant Variable-Thrust Liquid Rocket Engine", IAF-89-284, Torremolinos (Malaga, Spain) 7-13 Oct. 1989
3. S. Ueda, H. Miyajima, "Bi-Propellant Performance of N₂O₄/MMH Mixed Fuel in a Regeneratively Cooled Engine", IAF-89-286, Torremolinos (Malaga, Spain) 7-13 Oct. 1989
4. R. P. Thomas, C. G. Balan, K.S. Nair, "Some Developmental Aspects of Injectors for Use in a High-Performance Upper-Stage Liquid-Engine with N₂O₄/MMH Propellant Combination", IAF-89-287, Torremolinos (Malaga, Spain) 7-13 Oct. 1989
5. G. Vulpetti, "A Non-Variational Approach to Multiple Finite-Burn Propellant Optimisation", Acta Astronautica, Vol. 12 No. 10, pp. 837-845 (1985)
6. G. Vulpetti, "MAIS (Mission Analysis Interactive System): Mathematical Theory and Implementation on Computer, Version B.2" Telespazio SpA, Mission Analysis div., July 1989
7. "ATLAS-G/CENTAUR Mission Planner's Guide", GENERAL DYNAMICS Space System Division, Dec. 1987
8. M. Steinman "Super-Synchronous Transfer Perigee Velocity Augmentation", GENERAL DYNAMICS, Space System Division, *private communication*, San Diego (California), Sept. 1987
9. B. A. Matsumori, G. Wong, "Continued Enhancements to the Commercial ATLAS Launch system", IAF-89-197, Torremolinos (Malaga, Spain) 7-13 Oct. 1989
10. J. J. Moré, "The Levenberg-Marquardt Algorithm: Implementation and Theory", *Numerical Analysis*, G. A. Watson (Ed.), *Lectures Notes in Mathematics*, Springer-Verlag, New-York (1978)

Reentry Trajectory Optimization and Control

P. Strohmaier, A. Kiefer, D. Burkhardt, K. Horn

Messerschmitt-Bölkow-Blohm, FE 126, 8012 Ottobrunn, FRG

Summary

There are several possible methods to increase the cross range capability of a winged reentry vehicle, for instance, skip trajectories, a powered cruise phase, or high lift/drag ratio flight. However, most of these alternative descent strategies have not yet been investigated sufficiently with respect to aero-thermodynamic effects and the design of the thermal protection system. This problem is treated by two different means. First, a nominal reentry trajectory is generated based on a phase concept, and then the same problem is again solved using a numerical optimization code to determine the control functions, i.e., the angle of attack (AOA) and the roll angle schedule.

The nominal reentry trajectory design presented first subdivides the total reentry trajectory into several segments with partially constant control/state parameters such as maximum heat flux and deceleration. The "optimal" conditions for a given segment can then be selected. In contrast, the parameterized optimization code selects the control functions "freely", i.e., local perturbations are judged with respect to the effect they have on the entire trajectory. Both approaches consider a mass point simulation which uses realistic model assumptions for atmosphere, earth, and gravity. Likewise, both approaches satisfy all flight regime limitations and boundary conditions such as thermal constraints throughout the flight path and specified speed and altitude at the final time. For the optimization of high cross range reentry trajectories the cross range per total absorbed heat represents an appropriate cost function. The optimization code delivers quite a different flight strategy than that usually generated by the nominal reentry design program, first flying longer along the temperature boundary at highest possible AOAs (utilizing higher average turn rates), and afterwards performing flare-dive segments to reduce heat flux and to increase range.

Finally, the report considers the aspect of guiding the nominal or optimized reentry trajectory during a cross range flight. The vertical guidance is performed with both angle of attack and roll angle control. The roll angle is primarily used for controlling sink speed, thus correcting the altitude/speed profile to the predetermined nominal profile. Range control can be affected by AOA modulation using predetermined gradients as a function of range-to-go.

1. Introduction

Since European space transportation concepts such as ARIANE V/HERMES and SAENGER/HORUS define new mission requirements with respect to the maximum cross ranges of the winged upper stages, the need for higher lift/drag-ratio vehicle design as well as optimal control of the reentry trajectory flight path and guidance becomes increasingly important.

Figure 1 compares the nominal cross range requirement of several existing and future concepts. Due to the different geographical locations of European landing sites, trajectories yielding large cross ranges are needed. Considering a reference orbit 300x300 km and 28.5° inclination, the Saenger-HORUS glider concept, for example, has a minimum mission requirement of about 2500 km cross range, in order to perform a landing maneuver on German territory. Even the

HERMES vehicle needs 1700 to 2000 km cross range to achieve specific mission requirements, e.g., a landing at Istre. In addition, the required angle of attack in the hypersonic regime differs greatly among the vehicle types. Compared to the successful SHUTTLE concept, the Saenger model shows a significant decrease from 40° down to around 25°, which also yields increasing aero-thermodynamic loads (heat flux and total absorbed heat). For the HERMES vehicle, the AOAs required in the hypersonic regime are on the order of 32° to 35°.

Four different flight strategies have been identified for the purpose of flying extended cross range trajectories:

- Nominal Trajectories (High L/D)
- Skipping Trajectories (See Ref. 1.)
- Reentry Trajectories with a Boost Phase (H = 50 Km) (See Ref. 2.)
- Optimal No-Skip Trajectory Control ($\gamma < 0$)

The basic effects on the design of a thermal protection system (TPS) and the corresponding heat load assessments are described in Ref. 2. The main design drivers for a TPS for high cross range mission requirement are identified in Ref. 2 as:

- Maximum heat flux level determines selection of TPS material
- Total accumulated heat dimensions the TPS overall weight
- Max. temperature gradients influence the mechanical strength of the TPS.

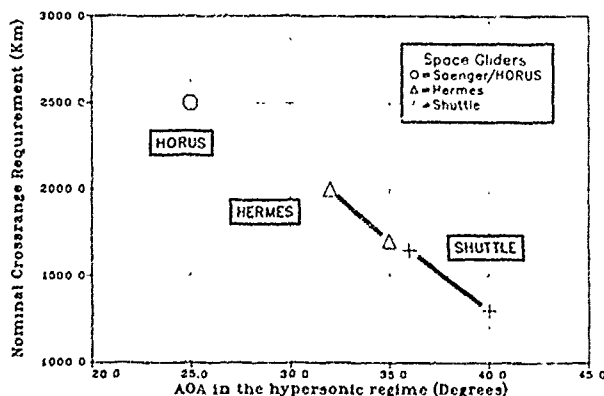


Fig. 1. Nominal cross range mission requirement for several space glider concepts.

This paper deals with the aspect of optimizing the control functions of a nominal trajectory in order to fly a certain cross-range at the lowest possible heat loads. The conventional method of achieving a high cross range is to fly at the highest lift/drag-ratio levels which can be utilized inside the flight regime limitations for as long as possible during a reentry mission. However, such a flight strategy, due to the extended flight time, leads to high values of total absorbed heat with the corresponding adverse effects on the thermal protection system design. Hence the optimization performed consists of minimizing the absorbed heat for a given cross range, without violating the max. reference heat flux level of the corresponding nominal trajectory too much.

2. Control Function Effectiveness

The control functions for the reentry trajectory are the angle of attack, α , and the roll angle, μ .

This section summarizes the influence of the control functions on the long period trajectory dynamics (mass point simulation). Whenever the trajectory lies above the equilibrium glide condition (balance of lift, centrifugal force, and weight), the actual vertical lift is less than needed to maintain a horizontal glide trajectory; for flight below this condition, the opposite is true. As a result the vehicle performs long period oscillations around the equilibrium glide trajectory. This trajectory motion possesses dynamic stability for speeds below circular speed.

In order to understand the following nominal reentry trajectory design, the typical control function effectiveness on the flight dynamics is discussed briefly. A change in the angle of attack, for example, results in a sudden change of the total lift/drag situation (fixed $dC_L/d\alpha$ characteristic), however, a change in the roll angle changes "only" the vertical lift component. This control characteristic of the total aerodynamic forces is used for the design of nominal reentry trajectories and the vertical guidance of a glider.

Figure 2 uses a simple block diagram to illustrate the relationship of both controls on the flight dynamics. (See Ref. 3.) The control of downrange by lift constitutes a fourth-order system, involving vertical velocity, altitude, horizontal velocity, and downrange. (This is the product of four integrations, $1/s$, where $1/s$ is the differential operator notation.) The lift force is acting essentially in the vertical direction and affects the rate of change of the vertical velocity. The integration ($1/s$) of the vertical velocity gives a variation in density altitude. This change in density altitude affects the drag force and consequently the rate of change in horizontal velocity. An integration of the horizontal velocity results in variations in the range along the path.

The change of vertical lift can be generated by both controls, but a direct change in the total drag can only be achieved by a change in AOA. Nevertheless, as a secondary control effect, total drag can also be modulated by flying at a different density altitude, which is also possible by changes of the vertical velocity, controlled by the roll angle. In principle, the roll angle control would be sufficient to fly a nominal reentry trajectory, which has a specified range requirement. Thus, for the design of a nominal reentry trajectory the roll angle primarily controls altitude inside the flight regime limitations, and the angle of attack level primarily determines the downrange. Additionally, there are flight segments, in which both controls need to be used, for example, in the final descent to the terminal area in which final speed and altitude requirements must be matched.

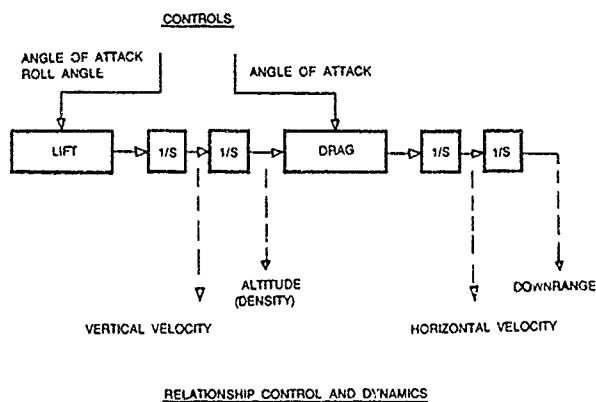


Fig. 2. Schematic diagram of control function effects on flight dynamics.

3. Operational Constraints

In addition to the requirement of having sufficient cross range to reach a certain landing site from a fixed orbit, the reentry trajectory has to satisfy several operational constraints. These constraints result from the limited load capacity of the structure and the thermal protection system, as well as from comfort considerations for the crew on board. (See Appendix 1.)

Figure 3, in an altitude versus speed plot, shows the relevant constraints and the nominal reentry corridor for a descent from a low earth circular orbit ($H = 460$ km) with 28.5° inclination. These constraints are a function of both Mach number and (with the exception of the dynamic pressure limit) angle of attack. For determining the limit lines, the AOAs along the speed/altitude profile of the nominal trajectory are used, i.e. for a given speed, the altitude limits are calculated. The shaded area between the highest and lowest nominal path is the nominal atmospheric entry corridor. Any actual guided trajectory is assumed to lie within this area which takes into account all types of nonstandard conditions, such as density deviations or errors in the predicted aerodynamic data. The two extreme trajectories are determined from the standard nominal trajectory by adding a deceleration margin of $\pm 20\%$. This corresponds, for example, to a deviation in density of $\pm 20\%$.

The temperature limit curve in Fig. 3 represents an envelope of the different temperature limits corresponding to critical points on the surface of the vehicle, for example, at the stagnation point of the fuselage or on the body flap. This envelope is also a function of the angle of attack and is difficult to compute. The reference heat flux limitation can be taken as a substitute for the temperature limits if they are not available. The reference heat flux is the heat flux at the stagnation point of a sphere with 1 meter radius and is (as a first approximation) proportional to the wall temperature at this point. The temperature constraint limits the reentry path at altitudes between 70 and 80 km, which is the portion of the trajectory at which the first flare occurs.

In addition to the absolute wall temperatures, the total accumulated heat during reentry is also of interest. This value

determines the heat buildup inside the structure and is a design parameter to be minimized. The absorbed heat is strongly influenced by the flight time. To find the best compromise between having sufficient cross range and minimizing the absorbed heat is an optimization problem. The absorbed heat in this report always means the integrated reference heat flux.

The dynamic pressure, the load factor, and the hinge moment represent the structural loads. In the example presented, the allowable hinge moment limits the reentry trajectory at medium velocities (roughly, $12 < \text{Mach} < 18$) while the dynamic pressure becomes critical towards the end of the trajectory ($\text{Mach} < 9$).

Skip-out and recovery ceiling are not considered here for the design of nominal trajectories at circular entry speeds.

4. Physical Modeling

The modeling of the vehicle is based on a realistic physical model including the equations of motion with all physical effects that influence the trajectory (See Appendix 2.). Since the use of analytic models having simplified assumptions for earth, gravity, and atmosphere can lead to sizeable discrepancies compared to results obtained with detailed modeling of these features (see, e.g., Ref. 4), the model considered incorporates the following:

- Earth form : GEM 10 (rotating ellipsoid)
- Gravity : radial and lateral components of gravity are taken into account
- Atmosphere : US Standard 1966 mid latitude spring/fall
- Reference heat flux : Detra/Kemp/Riddell cold wall (reference radius 1 m)

The three equations of motion (force equations) are given with respect to the earth fixed system using the spherical coordinates longitude, latitude, and altitude. The earth modeling includes the (1) oblateness of the earth which results in radial and lateral components of the gravity, and (2) the constant earth rotation which leads to additional terms in the differential equations. The gravity and the atmospheric data are functions of both the geometric altitude and the latitude (Ref. 5).

The temperature over altitude profile of the standard atmosphere consists of several linear segments with abrupt slope changes. Using such a model gives a simulation of a constant heat flux phase with unrealistic jumps in the roll angle profile occurring at these slope discontinuities in the temperature profile. To avoid these unrealistic edges, the temperature profile has been smoothed by inserting circular arcs in the regions of abrupt slope change. These modifications provide a smooth temperature profile and atmosphere. To investigate non-standard atmosphere profiles it is now possible to define a factor on the density as a function of the altitude and to define the sea-level conditions.

The reference heat flux is a characteristic design parameter for comparing two trajectories with respect to the thermal loads. In first approximation, the reference heat flux is proportional to the temperature occurring at the stagnation point of the fuselage. The model defines the heat flux as being that at the stagnation point of a sphere with one meter radius.

The aerodynamic data are given in the form of trimmed aerodynamic coefficients. These coefficients for lift, drag, and hinge moment are functions of the angle of attack and the Mach number. The discrete tabular data are interpolated linearly.

The control parameters for influencing the reentry path are the angle of attack, α , and the roll angle, μ . For the deorbit maneuver a constant thrust in the X-body axis direction is used. After this deorbit impulse (which determines the state parameters at the entry interface, 120 km altitude), no more thrust is available for the atmospheric reentry trajectory.

To compute the nominal reentry path, the control functions are selected so as to maintain a specified constant state parameter level, e.g., a heat flux of 375 kW/m^2 , and are input for the simulation module (See Appendix A2.) using the above physical model. (The optimization package, on the other hand, selects the controls using the strategy outlined in Section 6.) In either case, the trajectory is the result of a real point mass simulation with all dynamic effects.

The boundary conditions of the trajectory are:

- Initial condition : State parameters of the orbit at begin of deorbit maneuver.
- Final condition : Altitude $\approx 24.5 \text{ km}$, Mach ≈ 2 (Start of terminal area energy management phase)

5. Nominal Reentry Trajectory Design

Nominal trajectories are required to provide reference data for a flight control system. For the nominal design loop, only standard conditions without disturbances in the atmosphere or in aerodynamics data are considered. Such disturbances are then later incorporated for determining a complete flight path corridor.

A very simple and yet effective method for satisfying all constraints and boundary conditions during reentry consists of subdividing the path into segments, each of which is dominated by a specific critical parameter, e.g., by heat flux or deceleration. The magnitude of these parameters determines the altitude/speed profile of the path as well as the transition points between the various phases. (See Refs. 6 and 7.)

During each phase, a certain schedule of the control function is required to satisfy the fixed parameter level. The end of one phase is reached, when the parameter of the subsequent phase becomes a more critical parameter than the current one. Accordingly, by a variational study of these phase parameter magnitudes, a sub-optimal solution for the complete trajectory can be found.

Special effort has been made to obtain a smooth transition between these phases. A direct concatenation of the phases

would cause jumps in some state variables, especially in the path angle. To avoid these difficulties, several short transition phases have been inserted between the main phases.

All segments of the reentry trajectory (deorbit maneuver, Keplerian flight path, atmospheric flight phases) are calculated with the equations of motion (given in Appendix 2) and with the physical model described in the previous chapter. The program takes the initial state variables at the deorbit point (defined as time $t=0$) and calculates the path in fixed time steps. Thus, a real mass point simulation is performed, which incorporates all dynamic effects. Due to the iterative selection of one control function at each time interval (which is, in principle, a simple vertical guidance concept), disturbances in atmosphere and errors in the predetermined aerodynamic coefficients can be analyzed which still give trajectories lying within the flight path corridor.

The next chapters describe the different flight phases. Figures 3 and 4 show (1) the profiles of altitude and deceleration over velocity and (2) the controls as functions of time for the phases described. These results are also illustrated in Table 1.

5.1 Hypersonic Flare

The first phase after the deorbiting maneuver is the initial flare in the hypersonic Mach regime which begins at a defined entry interface of 120 km altitude. Although the atmosphere above this altitude has been taken into account during the computation of the deorbit maneuver, the density effects on the magnitude of the aerodynamic forces actually first become significant during the computation of the hypersonic flare, i.e., only in the regime below 120 km altitude.

During the hypersonic flare the angle of attack $\alpha = \alpha$ -entry remains constant and the roll angle is zero (giving maximum possible vertical lift).

The reentry path angle and the maximum available lift both have a strong effect on the maximum temperatures occurring during the first part of the reentry trajectory. For given aerodynamic characteristics and wing loading, Fig. 3 shows the relationship between (1) the angle of attack during the initial reentry phase, (2) the entry path angle, and (3) the maximum reference heat flux. Since α -entry has to be within certain boundaries which result from thermal requirements, the maximum allowable heat flux defines the entry window of the path angle. The thermal angle of attack corridor used in this report ranges between 32° and 40° and is active as long as the reference heat flux is above 175 kW/m^2 . γ -entry is determined by the selection of a defined deorbit impulse, i.e. the duration of the deorbit engine burn, with the requirement to achieve a specified heat flux at the end of the first flare in the hypersonic regime.

The end of the hypersonic flare (or the start of the heat flux phase) is defined as the point at which the heat flux begins to decrease again (path angle nearly zero).

5.2 Heat Flux Control Phase

The heat flux control phase is initiated by a roll angle build up, which is required in order to avoid an uncontrolled skipping of the vehicle into higher atmosphere. The objective is to obtain a flight path which has a continuous decrease in both speed and altitude and which also complies with the thermal limitations (max. wall temperature).

This requirement can be met by keeping the reference heat flux constant at the maximum value of the preceding flare phase. As already stated, this approximately corresponds to constant wall

ALTITUDE OVER VELOCITY

ORBIT: $460^\circ/460 \text{ KM}/28.5 \text{ DEG}$ $\alpha_E=35 \text{ DEG}$ $\gamma_E=-1.44 \text{ DEG}$
 $dq/dt_{\text{max}}=380 \text{ kW/m}^2$ $dv/dt_{\text{nominal}}=-7. \text{ m/s}^2$

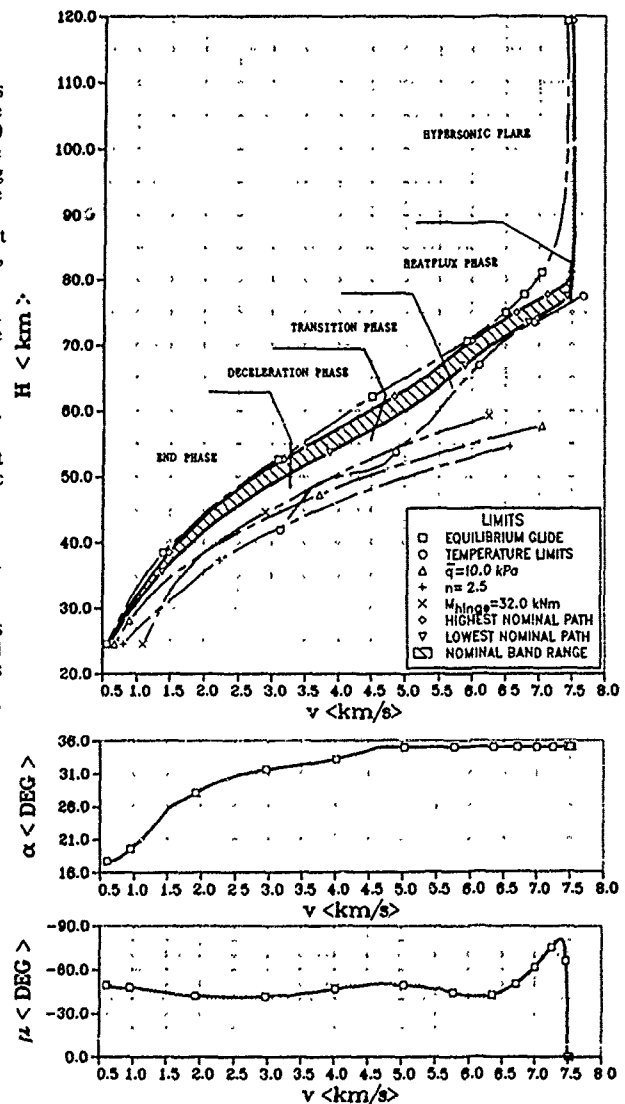


Fig. 3. Altitude vs Speed profile for nominal reentry corridor (showing phase concept partitioning, equilibrium glide condition, and active constraints) along with the control functions: α and μ as functions of speed.

temperature. Flight path control during this phase is performed by roll angle adjustment, while the angle of attack is held constant (at α -entry). Constant heat flux during this phase simultaneously corresponds to a continuous buildup of deceleration.

5.3 Transition Phase

The steadily increasing deceleration during the heat flux control phase is combined with increasing load factors. To limit the load factor to the maximum allowable value, it is necessary to limit the deceleration of the preceding phase. This can now be done by controlling the deceleration via the angle of attack. To obtain a constant deceleration level, decreasing angles of attack are required as the altitude decreases.

However, decreasing the AOA also implies higher thermal loads, which could lead to a violation of the thermal limits. Hence, prior to reaching the maximum deceleration limit, a reduction of the heat flux level is necessary to provide for a regime within which the AOA can be adjusted without violating the thermal angle of attack corridor. This is the purpose of the transition phase.

The reduction of the heat flux is achieved by limiting the increasing sink rate. In the transition phase, the roll angle controls the sink rate, while α is held constant at α -entry. The sink rate slowly stagnates to a constant value, and the deceleration continues to increase.

The transition phase ends when the maximum deceleration is reached. This maximum deceleration needs to be limited.

5.4 Deceleration Control Phase

In the deceleration control phase, the magnitude of maximum deceleration is used as a dimensioning phase parameter. Deceleration during this phase is held constant by a continuous reduction of the angle of attack ($\dot{v}_{\max} = \text{const}$). Its magnitude also determines the maximum load factor that occurs, and it also has a great effect on cross range and longitudinal range, yielding reduced distances for high values of deceleration.

Additionally, the sink rate is held constant in order to keep the dynamic pressure at a moderate level at the end of this phase. The sink rate at the end of the preceding transition phase can be sustained throughout the deceleration phase by continuously adjusting the roll angle. This limitation of the sink rate prevents the dynamic pressure constraint at the end of this phase from being exceeded. It also increases the flight time and, consequently, the cross range of the vehicle.

5.5 End Phase

The purpose of the final reentry phase is to ensure that the end conditions are in compliance with the starting conditions defined for the landing phase, generally referred to as the "Terminal Area Energy Management Phase" (TAEM). This is achieved by predetermined profiles for deceleration and sink rate. These profiles ($\dot{v}(H)$ and v_s) are determined such that, at the defined final altitude, a defined speed is also obtained.

The end phase starts at a fixed Mach number (e.g. Mach = 10), with the corresponding altitude, deceleration, and sink rate as obtained from the preceding deceleration phase. As in the deceleration phase, α is used to maintain a predetermined deceleration profile, and the roll angle is used to adjust the sink rate. Deceleration as well as the sink rate at the defined final altitude are free parameters. However, by assuming a linear change in the sink rate $v_s(H)$, and a parabolic change in the deceleration \dot{v} (with vertex at the phase starting point), one of the two free parameters becomes fixed, if the other one is assigned a specified value.

5.6 Main Design Parameters

The reentry path is mainly influenced by the hypersonic angle of attack α -entry and by the maximum deceleration during the deceleration control phase. These two parameters determine

DECELERATION OVER VELOCITY

ORBIT: 460*460 KM/28.5 DEG $\alpha_E=35$ DEG $\gamma_E=1.44$ DEG
 $dq/dt_{\max}=360 \text{ kW/m}^2$ $dv/dt_{\text{nominal}}=-7.0 \text{ m/s}^2$

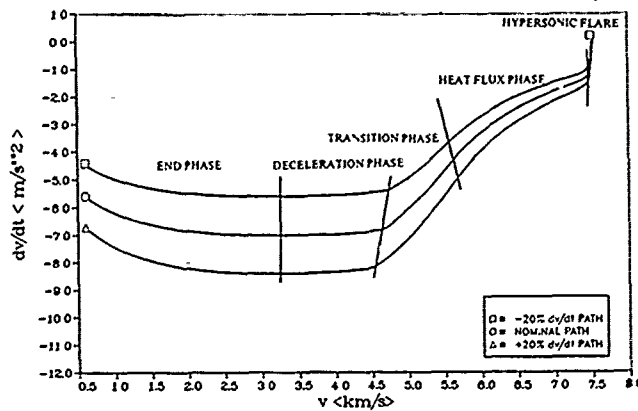


Fig. 4. Deceleration vs Speed profile for the entire reentry path corridor.

Phase	Angle of Attack	Roll Angle	End Condition	Altitude $\langle \text{km} \rangle$
Hypersonic Flare	Alfa_E	0	$\dot{q} = 0$	120...80
Heatflux Phase	Alfa_E	controls	$\dot{v} = \dot{v}_{tr}$ $\dot{q} = \dot{q}_{\max}$	80.. 65
Transition Phase	Alfa_E	controls	$\dot{v} = \dot{v}_{\text{nom}}$ $v_s = v_{str}$	65...60
Deceleration Phase	controls	controls	$\dot{v} = \dot{v}_{\max}$ $v_s = v_{str}$	60...50
End Phase	controls	controls	$\dot{v} = f_1(H)$ $v_s = f_2(H)$	Ma = 2 50...25

Table 1. Phase structure of nominal trajectory: critical parameters and switching conditions

the ranges and the absorbed heat and can be chosen freely within certain bounds. A third important parameter is the value of the maximum heat flux in the heat flux control phase. This value corresponds to the maximum wall temperature reached and also has a strong influence on ranges and absorbed heat. In this study the maximum heat flux is held fixed and is determined through the maximum allowable wall temperature for the nominal reentry path. The reference orbit for the following results is a 460 km circular orbit with 28.5° inclination.

In Fig. 5 the absorbed heat and the longitudinal range are presented as functions of cross range, showing the effect of a variation in α -entry. The main effect of a change in α -entry is a change in the hypersonic L/D ratio. The greater the value of α -entry, the worse the resulting L/D-entry. The fact that α -entry remains constant for a long time during reentry greatly influences the resulting trajectory. The longitudinal range, as well as the cross range, increases as α -entry decreases. The longer ranges require a longer flight time for the path, which results in a higher absorbed heat, meaning a larger loading on the thermal protection system.

If the orbit and the landing site are specified, the required cross range is fixed. The plots show, the maximum value of α -entry that one can have and still satisfy the cross range requirement. This maximum α -entry should be chosen, because lower values would increase the thermal load (absorbed heat). The specific thermal load (defined as the ratio of absorbed heat per cross range) becomes smaller for greater values of α -entry. α -entry is bounded through the thermal angle of attack corridor (in this example between 32° and 40°).

Figure 5 also shows the results of the variation of the maximum deceleration during the deceleration phase. An increase in the deceleration results mainly in a decrease in the flight time. For a larger deceleration, a larger α is necessary to increase the drag. A higher α causes more lift, so that a higher roll angle is necessary to maintain the same vertical lift force. The decreasing flight time shortens the ranges and also decreases the absorbed heat.

The specific thermal load becomes smaller with smaller decelerations. But this effect is reversed when a certain minimum deceleration is reached (in this example about -6 m/s²). With smaller decelerations, the roll angles, and thus the turnrates during reentry become very small. The smaller turnrates then decrease the cross range, thus increasing the specific thermal load.

6. Optimal Trajectories with STOMP

The reentry trajectory problem discussed in Section 5 has been investigated further using the parameterized optimization program, STOMP (Ref. 8). The STOMP package is an MBB improved/extended version of Trajectory Optimization by Mathematical Programming (Ref. 9). (The "S" stands for "spread" due to the features recently incorporated for reducing CPU time.) In this section, we discuss recent improvements made to STOMP at MBB, and how these improvements have been effective in determining optimal trajectories for high cross range reentry problems. The model used is the same as that in Section 5, with the control functions and the final time to be selected by the STOMP package rather than by the controls laws discussed earlier. No phase concept is incorporated. Rather the optimization package itself determines the optimal strategy.

6.1 Cost Function and Boundary Constraints

The STOMP program, used in conjunction with a parameterized optimization code, is required to minimize a user-supplied function while satisfying given constraints at the final time (and/or throughout the entire flight path). These con-

MAIN DESIGN PARAMETER

ORBIT: 460*460 KM / 28.5 DEG

Variation of α_E and $dv/dt_{nominal}$

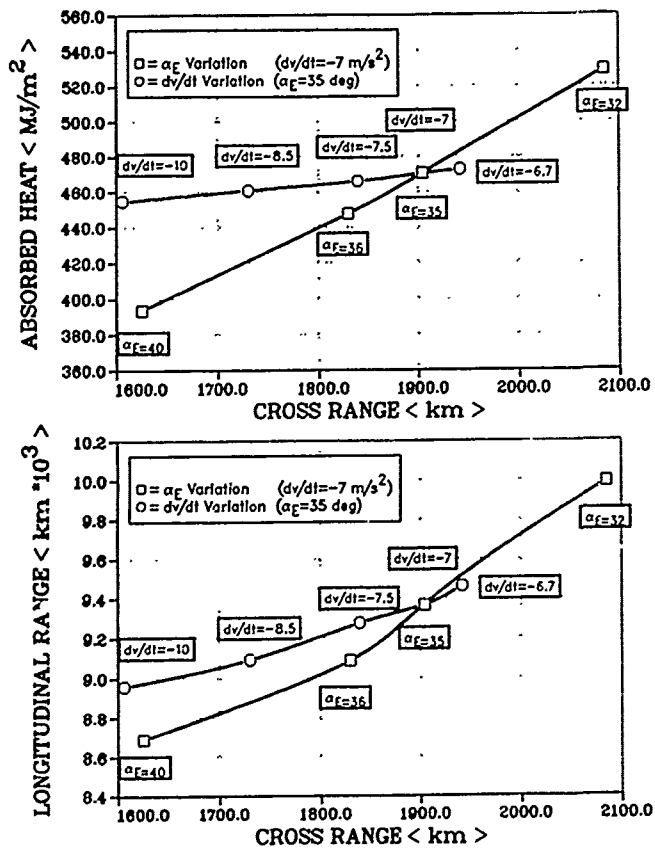


Fig. 5. Absorbed heat and longitudinal range as functions of cross range, showing effects of α -entry and deceleration bounds.

straints may be either equality or inequality constraints.

Applied to a Hermes or Horus, no-skip, reentry trajectory problem, a typical cost function would be

To minimize: Total absorbed heat per cross range

while satisfying the equality constraints at the final time:

Mach number = 2.0 Altitude = 24.5 km

Boundary constraints are imposed throughout the entire flight path: (1) the thermal and structural limits in Section 3, as well as (2) the no skip condition, $\gamma_{\max} < 0$. A function, f -violation is defined which measures any violation of these constraints, and the STOMP program drives this violation towards zero by imposing the inequality constraint: f -violation $< \epsilon$ at the final time.

6.2 Control Functions and Design Parameters

The STOMP package receives a set of "points" from the parameterized optimization code and constructs continuous control functions out of subsets of these points. In addition, STOMP labels a subset of the points as design parameters, e.g., final time. Control functions for the reentry trajectory are angle of attack, $\alpha(t)$, and roll angle, $\mu(t)$.

6.2.1 Definition of Control Functions

The control functions are defined as follows:

1. The user defines a set of grid points for each control function. (See Fig. 6.)

These grid points are: (1) distinct points in time, (2) they need not be evenly spaced, and (3) each control function may have different spacings. Most important, the user may designate any of the points to be "movable", and the positioning will be selected optimally during the solution of the problem, i.e., these points become elements in the optimization vector.

2. Subsets of the optimization parameter vector will then be used to define the control functions at the grid points.

These control function values at the grid points may be designated as "fixed" or "free". The fixed values are not changed during the solution; the free points are adjusted during the optimization process.

3. The controls are defined as a function of time by connecting the values defined at the grid points using: (1) linear segments, (2) cubic splines, or (3) spline and linear sub-segments.
4. The user may place upper and lower bounds on all movable control points and on all movable grid points.
5. The structure of each control function is independent of the other controls in type, grid spacing, bounds, etc.

6.2.2 Improvements in STOMP concerning Control Functions

The movable grid point feature is one of the most important new aspects in the STOMP program. Such points permit optimal positioning of sudden changes in the control functions, e.g., placement of roll reversals, and they allow for positioning of local maximum and minimum.

For example, the reentry problem requires a strong roll in the early part of the trajectory followed by a roll back toward zero to avoid violating thermal and structural constraints. STOMP can position both the onset of the roll and the time corresponding to the minimum value of the function for an optimal roll back point. (Naturally the magnitude of the roll is also optimized.)

"Fixed" and "free" points in the control function can be switched on and off easily (between optimization runs) so that the model can be adapted during development as the user detects "problem areas."

In general, linear control functions are used because the STOMP program has features which reduce the CPU time by about 30% over that required using the smoother cubic splines. A spline/line control is also available which has user-selected combinations of spline and linear segments. The spline/line feature has some CPU reduction potential and provides more smoothness than the linear functions.

6.2.3 Design Parameters

The STOMP program also supplies design parameters: scalar parameters which can be incorporated into the model. In

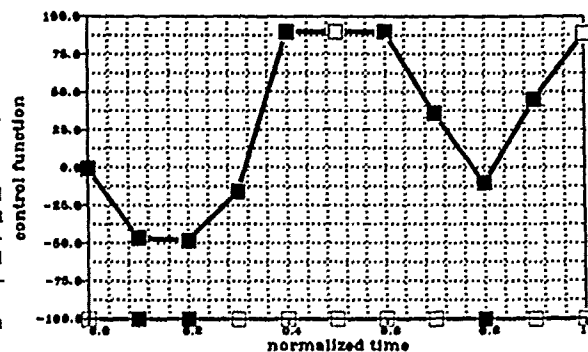


Fig. 6. Typical control function with both "fixed" (●) and "movable" (■) control points and grid points.

the reentry problem, the final time is used as a design parameter to be adjusted optimally. The most frequent use of design parameters is to supply switching times for which changes in the system occur, e.g., the time to eject the thrust system. However, the design parameters need not be time-related.

6.3 System Modeling and the Integration Package Root-solver

The STOMP program is linked with a Runge-Kutta-Fehlberg integration package which has been adapted to locate all zero points of a user-supplied vector of stopping conditions (Refs. 10 and 11.) The root-solver is an excellent tool for constructing differential equation systems in which branching occurs.

For example, the thermal angle of attack corridor in Hermes reentry problem is in effect until the heat flux is 175 kW/m^2 . By defining a stopping condition: $\text{PHI} = \dot{q} - 175$, a new branch of a control function could be activated at the time for which $\text{PHI} = 0$. Switching out of the thermal corridor optimally reduces computing time. The alternative is for the optimizer to isolate the switching time using penalty functions which requires more CPU time.

The user may also specify time-values as stopping conditions. These are located particularly efficiently and enable the user to define branching accurately.

7. Optimization Results

While the nominal reentry trajectories (generated by introducing partially constant control and/or state parameters during prescribed phases of the flight path) provide good cross range and acceptable total absorbed heat values, control schedules can be determined which generate flight paths having even more favorable conditions. The application of the STOMP program to the reentry problem has yielded (1) trajectories which have significantly lower absorbed heat with no sacrifice in cross range and (2) trajectories which have extended cross range for equivalent absorbed heat values. Savings in absorbed heat per cross range are as high as 22%.

The questions arise: (1) what strategy has the optimizer developed to reduce heat flux and/or to extend cross range, and (2) can such adaptations be incorporated into the strategy in Section 5?

7.1 Numerical Results

Figures 7, 8, 9, and 10 present the results for an optimized trajectory for a HORUS reentry from an orbit of $460 \times 460 \text{ km}$, 28.5° inclination. The comparison nominal trajectory has been computed using identical conditions. The physical model for both trajectories is that described in Section 4 and in Appendix 2.

The trajectory has been optimized from the deorbit point to the TAEM interface (24.5 km). The effects of the deorbit burn result in "initial conditions" at the atmospheric interface which can be expressed as a function of γ -entry. In the nominal trajectory, γ -entry is selected to control the maximum heat flux level. In the optimal trajectory, γ -entry is a design parameter for reducing the cost function (total absorbed heat per cross range). For the nominal trajectory, γ -entry = -1.4° , for the optimal trajectory, -1.2° .

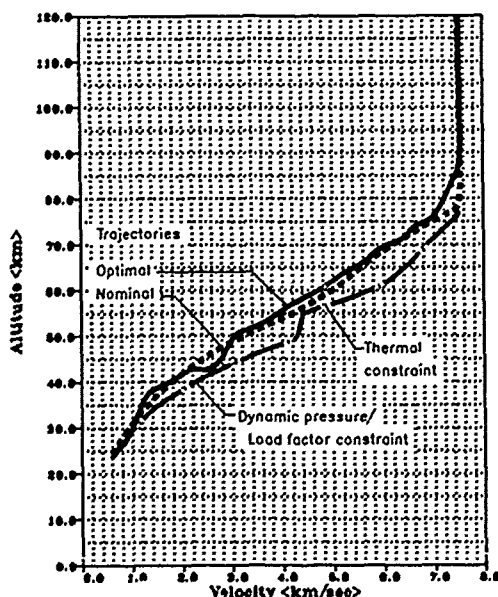


Fig. 7. Altitude-velocity diagram for optimal and nominal trajectories for a Horus reentry problem.

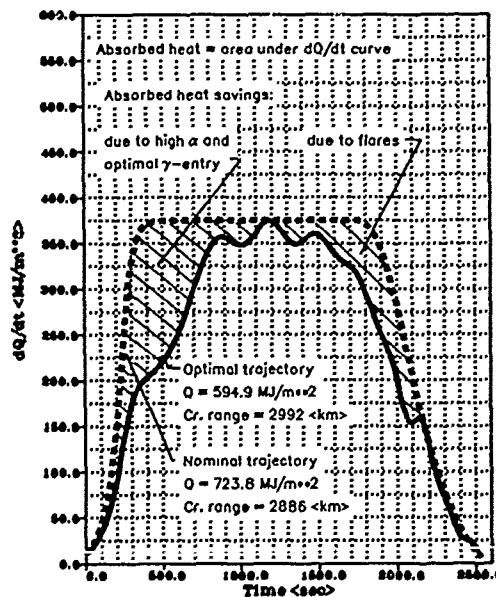


Fig. 8. Heat flux profile for optimal and nominal trajectories. (Absorbed heat equals the area under the respective curve.)

The H-v diagram (Fig. 7.) compares the nominal and optimal trajectories, showing the different structure of the two flight paths. The optimal trajectory has a higher initial flare and incorporates a sequence of flare-dive segments at the end.

The effect of the initial flare at higher AOA, coupled with the optimized value for γ -entry, is clearly evident in Fig. 8. The absorbed heat is equal to the area under the \dot{q} (heat flux) curve. There is clearly a large "pocket" of savings due to the position of the first flare. An equally substantial savings is evident due to the flare-dive sequence. The optimal solution is allowed to overshoot the \dot{q} max curve but does so only slightly.

Figures 9 and 10 compare the control functions for the optimal trajectory with those for the nominal trajectory. In the optimal flight path α is initially raised to 40° and then reduced to near the thermal- α corridor limit after the initial flare. For altitudes between 50 and 70 km, the optimal and nominal α -profiles are fairly similar. The optimal trajectory reduces α below the thermal- α limit as soon as the conditions allow, while the nominal trajectory delays this reduction. The final fluctuations in the optimal α -profile are needed to match the prescribed boundary conditions.

The initial roll and the time point corresponding to the global minimum of μ are nearly identical for both the nominal and optimal trajectories. Below 60 km altitude, the two profiles are somewhat different but they follow similar trends.

7.2 Optimal Strategy for High Cross Range at Low Total Absorbed Heat

7.2.1 Strategy in the Initial Flare

In the initial flare regime, the STOMP solution raises the angle of attack to the maximum permitted value. Such a strategy causes a reduction in cross range in the nominal trajectory approach. The optimal flight path, however, avoids this loss by achieving cross range through higher average turn rates (higher side force at $40^\circ \alpha$) and a flare-dive strategy in the latter portion of the trajectory.

The savings in absorbed heat, which is clearly evident in Fig. 8, is achieved because of the optimal γ -entry value and because the flare occurs at a higher altitude for $\alpha = 40^\circ$ than it does for the nominal trajectory value, $\alpha = 25^\circ$ (the two limiting values).

The movable grid point option has been used to locate three critical control function points in the initial part of the trajectory: (1) the positioning of the strong roll, (2) the time at which the roll back starts, and (3) the point at which the initially high alpha is reduced from 40° .

7.2.2 Flare-Dive Strategy

The trajectory has been restricted by the no-skip condition, $\gamma < 0$. As a substitute for skipping, the optimal flight path has developed a sequence of flare-dive segments--near skips followed by dives. These flares cause strong braking, reducing the velocity optimally, and they extend range--both desirable features. The movable grid point option has been used to locate the critical point in the development in the flare-dive sequences, namely, the location of the heat flux related "alpha-switching condition": $\dot{q} = 175 \text{ kW/m}^2$. Below this heat flux bound the vehicle may fly at an improved L/D for extending range.

7.3 Summary of Optimal Strategy

The optimal trajectories have three important segments in their structure

- high angles of attack in the initial phase of the trajectories, which are effective in reducing absorbed heat (and need not affect cross range),
- flight along the thermal- α bound, which gives rise to the peak heat flux values, and
- a flare-dive strategy, which is an excellent means both for reducing velocity (and hence heat flux) and for extending cross range.

Both (1) the high values of α in the hypersonic flare and (2) the later flare-dive sequences have favorable effects on the total absorbed heat and the range. However, the flight along the thermal- α bound is a critical portion of the trajectory

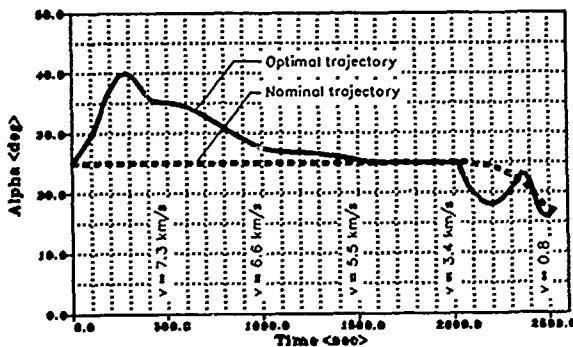


Fig. 9. Optimal trajectory control function, α as a function of time.

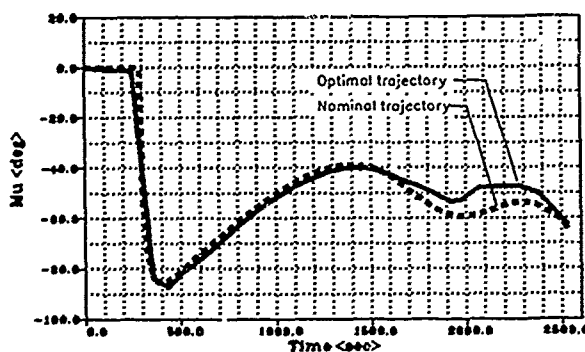


Fig. 10. Optimal trajectory control function, μ as a function of time.

because of the high heat flux values attained. Thus, the transition into and out of the flight along the thermal- α bound must be located optimally.

8. Range/ Terminal Speed Control Effectiveness

For the vertical guidance and control of a reentry trajectory, it is important to know how a change in the nominal control functions would effect the terminal speed and range of the vehicle. The nominal trajectories, derived from the control concept described in Section 5, are used originally to generate these gradients. Both control functions are changed (by a constant amount of 1 to 3 degrees), for example, as a function of range-to-go for the remainder of the trajectory. The resulting gradients deliver time dependent influence coefficients, which can easily be used in a guidance concept to predict the final range and speed at terminal area interface. The gradients also depend upon the basic nominal AOA in the hypersonic regime. In addition, they are useful "numbers", which show the control efficiency of both controls around the nominal trajectory design. Figures 11 and 12 show typical gradients dR/da , $dR/d\mu$, dV_e/da , and $dV_e/d\mu$ for a nominal reentry trajectory of HORUS. These gradients can be analytically described by linear segments and easily stored without a great storage requirement. As a result it can easily be seen, that the final range and especially the final speed at the terminal area interface can best be controlled by the angle of attack (per degree angular change). Also, speed corrections by change in α are still possible as the range to go becomes small.

9. Guidance Aspect

9.1 General

Winged space vehicles, during the initial phase of atmospheric reentry, are confined to a relatively narrow band of speed/altitude variations. Any significant deviations from the nominal or optimal profile of speed vs. altitude may result in excessive heat loads. Hence, the primary objective of flight path control must be to follow the correct profile as closely as possible. The most critical parameter during this phase is the angle of attack of the vehicle. On one hand, in order to obtain maximum flexibility for adjusting range -- as well as cross range, it would be favorable to utilize the entire regime between

maximum lift and optimal lift/drag ratio. However, for heat load considerations as well as trim requirements, the angle of attack is confined to a limited operational regime during the initial portion of the reentry flight path, e.g. 30°-40°. Accordingly, the second objective of flight path control must be to "make the best" of the available control regime.

Another control parameter is the roll angle which does not suffer from rigid limits and which provides for instantaneous normal-force variations. Accordingly, roll-angle control is best suited for achieving the specific sink rate schedule which results in the required altitude/speed profile.

Considering the guidance concept, it is important to note that a sink-rate control by means of roll-angle variations has practically no short time effect on deceleration compared to the deceleration of the nominal schedule. At the small flight path angles typical for reentry (below 1 degree), the gravity component in the direction of flight, which is a function of sink-rate, is negligible compared to the aerodynamic drag. The problem of achieving a predetermined altitude/speed profile can therefore be decoupled from the problem of controlling the range.

There is, however, a basic difference between these two control tasks: In order to maintain the altitude/speed profile, a continuous roll-angle modulation, as a function of instantaneous speed, sink-rate and altitude is required. Range control, on the other hand, can be regarded as a long term strategy, i.e., it is immaterial whether the vehicle is flying on a fixed nominal path as long as it can still reach its landing area with the correct speed and altitude. For this purpose it is appropriate to adjust a predetermined α schedule by a corresponding correction. Contrary to the altitude/speed control, there is no need for continuous α -modulation. Since the magnitude of the α correction is made according to pre-

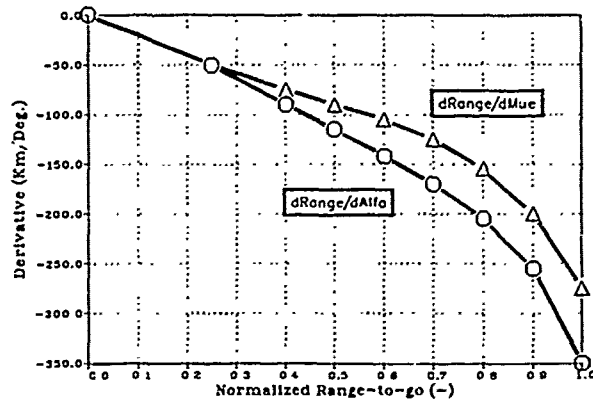


Fig. 11. Range control effectiveness: $dRange/da$ and $dRange/d\mu$ as a function of (normalized) range-to-go.

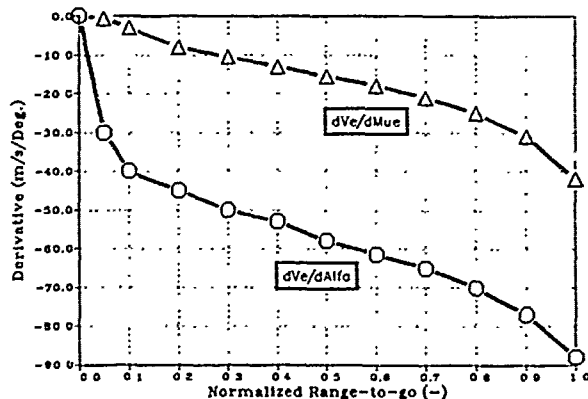


Fig. 12. Final speed control effectiveness: dV_e/da and $dV_e/d\mu$ as a function of (normalized) range-to-go.

determined derivatives $d\text{Range}/d\alpha$, it is considered fully sufficient to perform an update after a fixed time interval (e.g., one minute), during which $d\alpha$ is held constant. This update will produce a "correction of correction", e.g. the α -change relative to the nominal schedule will be relatively small. This, too, is an important feature, because any α -change perturbs the vertical balance of forces and has to be counteracted by a roll-angle change. Hence, any step-control input with respect to α should be as small as possible, which is a strong motivation for spreading a range correction over the major part of the reentry path rather than for forcing the vehicle back onto its nominal trajectory by introducing powerful control inputs. In the latter case, the decoupling of the speed/altitude-control and the range-control (resulting in a very simple overall control concept) would no longer be possible. This guidance and control concept has been investigated in more detail in Ref. 6.

9.2 Guidance Aspect of an Optimized Trajectory

The optimal trajectories derived in Sections 6 and 7 have quite different schedules for control functions and state parameters (such as deceleration and heat flux) than do the nominal trajectories described in Section 5. Due to the improvement in the total accumulated heat, a flight strategy change compared to the nominal higher L/D strategy would be desirable. Future work should therefore concentrate on designing a phase concept having, for instance, partially constant control and/or state parameters and simultaneously incorporating features of the optimal trajectory, e.g., the flare dive segments.

Such a phase concept could be designed, in principal, out of the following flight segments:

- Flare in the hypersonic regime ($\alpha = \text{constant}$)
- Thermal control phase at max. α (high turn rates)
- Transition phase to high L/D .
- Flare-dive phase below max. deceleration limit.
- Flare-dive phase below max. dynamic pressure limit.
- End phase matching final speed and altitude requirement.

Such a new phase concept would deliver improved (near optimal) nominal trajectories, which could be generated without a great amount of computing time. Those improved nominal trajectories could then be used as basis for improved guidance strategies combining the required coupling strategy of the α and μ profiles needed for flare-dives, and still giving smoother control profiles than those required by the optimized trajectories in Section 7.

10. Conclusions

A nominal trajectory strategy has been presented based on a phase concept. The flight path is subdivided into segments during which a specific state or control parameter plays a dominant role. The magnitudes of these parameters have been varied, with the selected values producing reasonable, sub-optimal flight paths. Such an approach has several advantages: (1) one obtains a good overview of the entire reentry problem, (2) such trajectories can be simulated using simple control laws, (3) model variations can be studied efficiently yielding an entire flight path corridor, (4) the results can be easily verified, and (5) the entire analysis requires a relatively small amount of CPU time.

The same problem has been studied using a numerical optimization program. It has been shown that for equally large cross range mission requirements, the accumulated heat is significantly less for an optimized reentry strategy than for a conventional nominal reentry design trajectory, although the final flight times are quite similar. During the first part of the optimal trajectory, two advantageous features have been exploited. On the one hand, max AOA provides for moderate heat flux levels at the temperature boundary (flying at a higher density altitude), and, on the other hand, higher average turnrates can be achieved afterwards which result in faster heading change at higher average deceleration levels. The nominal trajectory, in contrast, flies at higher L/D levels which results in a lower flare altitude and consequently higher heat flux values.

In the final part of the optimal trajectory, flare dive-segments, ($\gamma < 0$) are performed at reduced AOA values to take advantage of reduced heat flux levels as well as "skip-like" range flight characteristic. However, this sophisticated reentry cross range strategy can deliver somewhat fluctuating control functions. This might be a disadvantage for a guidance and control system, but could be managed by designing a similar trajectory shape as the theoretical one but utilizing partially constant control/state parameters. This new concept then, would deliver all relevant information, i.e., deceleration schedules and control functions, in order to satisfy the guidance and control requirements of a selected system. Finally, the resulting TPS weight could be reduced significantly, which would be favorable for the overall design of the reentry vehicle, especially for the payloads achieved.

References

1. Chern, J.S., C.Y. Yang, C. Shan, and N.X. Vinh, "Optimal Three-Dimensional Reentry Trajectories Subject to Deceleration and Heating Constraints", IAF-82-309, October, 1982.
2. Kuczera H., K. Keller, W. Mueller, K. Demleitner, P. Strohmaier, "High Crossrange Reentry Vehicle with Trajectory and Thermal Protection System Optimization", IAF-89-232, 1989.
3. Wingrove, R.C., "Survey of Atmosphere Re-Entry Guidance and Control Methods", AIAA Journal, September 1963.
4. Brüning, G. and E.D. Dickmanns, "Zur Genauigkeit analytischer, Näherungslösungen für Wiedereintrittsbahnen in der Erdatmosphäre". Z. Flugwiss. 14 (1966), Hef. 1.
5. Vinh, N.X., "Optimal Trajectories in Atmospheric Flight" Elsevier Scientific Publishing Company, 1981
6. Strohmaier, P., P. Bitterle, D. Burkhardt, T. Koegler, "Aerodynamic Reentry Trajectories", MBB Report TN-ESA 6718/85-3
7. Kiefer, A., "Hermes 94 Nominal Trajectories (Status report)", MBB-TN-HERMES-13, 17.01.89
8. Horn, M.K., "Solution of the Optimal Control Problem Using the Software Package STOMP", MBB-Pub-S-370, 6718/85-3 1989.
9. Kraft, D., "FORTRAN Computer Programs for Solving Optimal Control Problems", DFVLR Report 80-03, 1980
10. Shampine, L.F. and H.A. Watts, "Practical Solutions of Ordinary, Differential Equations by Runge-Kutta Methods." SAND 76-0585, 1976. Sandia Laboratories, Albuquerque, New Mexico, (Dec. 1976)
11. Horn, M.K., "RK45T - A Runge-Kutta 4/5 Software Package with, User-Supplied Stops Involving the Dependent Variables and First Derivatives," DFVLR-Oberpfaffenhofen Interne Bericht, 515-83/3.

Physical Limits /Appendix A1Dynamic Pressure

$$v = \sqrt{2 q_{\max} / \rho}$$

Hinge Moment Example

$$M_{h\max} = 8.557 \rho / 2 v^2 \sin^2 (0.7082 \alpha + 1.116 (\epsilon(\alpha, Ma) + 6^\circ))$$

Structural Load Factor (Body axis)

$$n_{\max} = (c_L(\alpha, Ma) \rho / 2 v^2 S \cos \alpha + c_D(\alpha, Ma) \rho / 2 v^2 S \sin \alpha) / (m g_0)$$

Temperature Envelope

$$v = f(H, \alpha) \quad (\text{Table})$$

Equilibrium Glide

$$\dot{\gamma}, \dot{\delta} = 0$$

$$0 = v/r + 2 \omega_E \sin \chi \cos \delta - g/v + r \omega_E^2 / v \cos^2 \delta + c_L(\alpha, Ma) \rho / 2 v^2 S \cos \mu / (m v)$$

Equations of the Model /Appendix A2Differential Equations of Motion

$$\begin{aligned} \dot{v} = & r \omega_E^2 (\cos^2 \delta \sin \gamma - \sin \delta \cos \delta \cos \gamma \cos \chi) - g_{\text{rad}} \sin \gamma - g_{\text{lat}} \cos \gamma \cos \chi + \\ & + (T \cos \alpha - D)/m \end{aligned}$$

$$\begin{aligned} \dot{\chi} = & v/r \cos \gamma \sin \chi \tan \delta + 2 \omega_E (\sin \delta - \cos \chi \cos \delta \tan \gamma) + \\ & + r \omega_E^2 / (v \cos \gamma) \sin \chi \sin \delta \cos \delta + g_{\text{lat}} / v \sin \chi \\ & + (L + T \sin \alpha) \sin \mu / (m v \cos \gamma) \end{aligned}$$

$$\begin{aligned} \dot{\gamma} = & v/r \cos \gamma + 2 \omega_E \sin \chi \cos \delta + r \omega_E^2 / v (\cos^2 \delta \cos \gamma + \sin \delta \cos \delta \sin \gamma \cos \chi) - \\ & - g_{\text{rad}} / v \cos \gamma + g_{\text{lat}} / v \sin \gamma \cos \chi + (L + T \sin \alpha) \cos \mu / (m v) + \end{aligned}$$

Kinematic Equations

$$\dot{r} = v \cos \gamma \sin \chi / (r \cos \delta)$$

$$\dot{\delta} = v \cos \gamma \cos \chi / r$$

$$\dot{\epsilon} = v \sin \gamma$$

List of Variables

Mass
Altitude
Radius
Mach number
True air speed
Structural load factor
Lift
Dynamic pressure
Hinge moment
Drag
Thrust
Reference area

m Latitude
 H Longitude
 r Angle of attack
Mach Roll angle
 v Glide path angle
 n Heading
 ρ Density
 q Lift coefficient
 H Drag coefficient
 D Gravity lateral
 T Gravity radial
 S Body flap/elevon angle

 τ δ α μ γ χ ρ c_L c_D g_{lat} g_{rad} ϵ Gravity

$$g_{\text{rad}} = k/r^2 (1 + 3/2 J_2 (R_e/r)^2 (1 - 3 \sin^2 \delta))$$

$$g_{\text{lat}} = 3k/r^2 J_2 (R_e/r)^2 \sin \delta \cos \delta$$

Earth Form

$$R_E = R_p (1 + 1/2 e^2 \cos^2 \delta + 1/3 e^4 \cos^4 \delta)$$

Reference Heatflux: Stagnation Point Fuselage

$$\dot{q} = c_q \sqrt{\rho} v^3 \quad ; (R=1m)$$

Constants

Polar radius of earth $R_p = 6356768 \text{ m}$
Equatorial radius of earth $R_e = 6378150 \text{ m}$
Eccentricity of earth $e = 0.0818198$
Turn rate of earth $\omega_E = 7.2921157 \cdot 10^{-5} \text{ rad/s}$
Gravity constant $k = 398600 \text{ km}^3/\text{m}^2$
Gravity oblatenes $J_2 = 0.001082627$
Detra/Keap/Riddell const. $c_q = 1.7 \cdot 10^{-7} \text{ s}^3 \text{ m}^{-7/2} \text{ kg}^{-1/2} \text{ kV}$

TRAJECTOIRES DE SAUVEGARDE AU LANCEMENT D'HERMES.
CONSEQUENCES SUR LA TRAJECTOIRE D'ARIANE 5.

par

Ph.Delattre, AMD-BA et A.Wagner, CNES
Aérospatiale
B.P. 96
78133 Les Muraux Cedex
France

SOMMAIRE

0. ABSTRACT
1. INTRODUCTION
2. TRAJECTOIRES DE RENTREE D'HERMES EN CAS DE
PANNE AU LANCEMENT
 - 2.1 Cas sans propulsion
 - 2.2 Cas avec propulsion
3. CONSEQUENCES SUR LA TRAJECTOIRE DE LANCEMENT
D'ARIANE 5
 - 3.1 Cas sans propulsion
 - 3.2 Cas avec propulsion
 - 3.3 Compromis entre la performance et les
contraintes HERMES
4. CONCLUSION
5. PLANCHES

**HERMES emergency reentry trajectories
consequences on the ARIANE 5 trajectories**

Ph. Delattre AMD-BA
A. Wagner CNES

France

0. ABSTRACT

HERMES emergency reentry trajectories occur in case of any failure during that part of the launch phase from jettisoning the burn-out solid propellant boosters till the ignition of the MPH. In that case the Crew Escape Module cannot be used because of high MACH numbers and very severe constraints that would result of its low lift coefficient.

The maximum constraints on the HERMES space plane are obtained in the atmospheric reentry phase of the emergency trajectories. Their important level is due to the deep flight path angle attained during the ballistic arc of the trajectory. Their values are depending on the instant of launch abort.

These maximum constraints are very depending on the launch trajectory. The maximum HERMES constraints have been represented in the altitude-velocity plane as a maximum altitude boundary for the ARIANE 5 launch trajectory.

Unfortunately a performance loss is the result of the requirement for a reduction of the culmination altitude. This has lead to a launch trajectory optimisation that will be detailed in this paper.

As an out-come of this study two important decisions have been made by CNES :

- choice of a L6 for the HERMES propulsion module.
- choice of the boundary that constraints the launch trajectory.

Important efforts have been made on HERMES in order to reduce the maximum constraints, in the field of aerodynamics (moment coefficient reduction, increase of the maximum angle of attack), centre of gravity location (in order to reduce control surfaces hinge-moments and temperatures) and elevon-body-flap differential deflection.

NOTATIONS

ATO	:	Abort To Orbit; injection en orbite dégradée
EAP	:	Etage Accélérateur à Poudre
EPC	:	Etage à Propulsion Cryogénique
LEO	:	Low Earth Orbit; orbite basse (ici 460 km)
MPH	:	Module Propulsif d'HERMES
MRH	:	Module de Ressource d'HERMES
P230	:	EAP d'ARIANE 5
H150	:	EPC d'ARIANE 5
L6	:	version du MPH utilisée dans cette étude, avec 6t d'ergols liquide et 60KN de poussée
RHF	:	Référence Horizontale Fuselage; c'est l'axe de référence avion
V	:	Vitesse sol
Z	:	Altitude
Va	:	Vitesse sol à l'apogée d'un arc balistique
Za	:	Altitude à l'apogée d'un arc balistique
γ	:	Pente
ρ	:	Masse volumique
μ	:	Constante gravitationnelle géocentrique
Tp	:	Instant de panne dans la chronologie de la trajectoire de lancement
FC	:	Facteur de charge
CDG	:	Centre De Gravité

1. INTRODUCTION

Ce papier a pour but de présenter les conséquences de la prise en compte d'un échec du lancement d'ARIANE 5 sur le dimensionnement du planeur hypersonique HERMES et sur le choix de la trajectoire de lancement.

Le scénario de lancement d'ARIANE 5 est présenté sur la figure 1.

Ce papier ne traite que des échecs survenant après le largage des Etages Accélérateurs à Poudre (EAP) jusqu'à l'allumage du Module Propulsif d'HERMES (MPH); dans cette phase la propulsion est assurée par le VULCAIN, moteur de l'Etage à Propulsion Cryogénique (EPC). En cas de panne juste avant l'extinction normale de l'EPC, HERMES est injectée par le MPH sur une orbite moins énergétique que prévu. Cette manoeuvre, envisagée pour l'GRBITER, est baptisée Abort To Orbit (ATO).

L'objectif en cas de panne est de tenter de ramener l'avion sur une piste d'atterrissage. Malheureusement, pour la plupart des instants de panne, HERMES ne peut atteindre aucune piste. L'amerrissage d'HERMES n'étant pas envisagé, la cabine est séparée de l'avion en fin de trajectoire de sauvegarde. Elle assure la limitation de la décélération lors de l'impact à un niveau supportable par l'équipage, ainsi que sa survie en mer. Dans ce cas l'avion est détruit.

Le niveau des contraintes structurales et thermiques subies par HERMES lors d'une rentrée en sauvegarde est très élevé. Ceci est dû à des conditions de rentrée sévères qui sont dépendantes de l'instant de panne et de la trajectoire de lancement.

La première partie de ce document présente les trajectoires de rentrée en sauvegarde d'HERMES et les contraintes associées, ceci pour une trajectoire de lancement donnée. Les lois de commande employées pour minimiser les charges subies pendant la rentrée y sont décrites.

Cependant les fortes contraintes rencontrées par HERMES en sauvegarde nécessitent une action sur la trajectoire de lancement. La seconde partie de ce document montre comment la limitation des contraintes de sauvegarde sur HERMES a été introduite dans la boucle de définition des trajectoires d'ARIANE 5. La prise en compte de ces limitations par ARIANE 5 se traduit par une réduction de la masse en orbite de transfert dont il faut minimiser l'effet sur la perte de charge utile d'HERMES.

Les résultats présentés ici ont été obtenus sur la base de l'avion HERMES 94 (5M2) et de la configuration H150-P230 du lanceur ARIANE 5. La mission considérée est la mission de base pour le dimensionnement d'HERMES: c'est une mission LEO (Low Earth Orbit) correspondant à une orbite d'inclinaison 28,5°. Le site de lancement est KOUROU.

2. TRAJECTOIRES DE RENTREE D'HERMES EN CAS DE PANNE AU

LANCEMENT

L'objet de cette partie est de décrire les trajectoires de sauvegarde d'HERMES avec les lois de commande qui permettent de minimiser les contraintes subies par l'avion.

La trajectoire de lancement d'HERMES par ARIANE 5 est supposée fixée et constitue une entrée de l'étude. Une trajectoire d'ARIANE 5 non contrainte par les problèmes de sauvegarde a été choisie comme exemple pour cette présentation. Les cas de panne considérés ici sont ceux qui nécessitent l'interruption du lancement, ce qui est rendu inévitable en cas de perte des capacités propulsives du moteur VULCAIN. Les instants de panne étudiés vont de 126s (largage des P230) à 585s (extinction du VULCAIN). La panne est supposée n'induire aucune perturbation sur la position et l'attitude nominales du composite HERMES+MPH à l'instant de panne. Les conditions initiales de la trajectoire de sauvegarde d'HERMES (V, Z, Y) sont donc identiques aux conditions nominales de vol à l'instant de panne.

Cette partie présente successivement les trajectoires d'HERMES sans propulsion, qui correspondent à la séparation d'HERMES seul sans MPH, puis les trajectoires de sauvegarde avec utilisation du MPH.

2.1 Cas sans propulsion

L'objectif est de minimiser, pour un instant de panne donné, les contraintes maximales rencontrées à la ressource. Ces contraintes sont de nature mécanique (pression dynamique, facteur de charge, moment de charnière des gouvernes) ou thermique.

Cet objectif conduit à pratiquer une rentrée à gîte nulle à l'incidence la plus forte possible pour maximiser la portance, ce qui permet d'élever au maximum le point de ressource et par là de réduire les contraintes liées à la masse volumique. Cette incidence maximale dépend du nombre de Mach et provient de diverses limitations, par exemple thermiques, de stabilité aérodynamique ou de braquage des gouvernes.

Cependant la minimisation des contraintes telles que le facteur de charge ou les moments de charnière qui dépendent directement de l'incidence conduit à modifier la loi de commande à incidence maximale. Dans ce cas, la phase à incidence maximale est suivie d'une phase dite d'écrêtage qui consiste à réduire l'incidence pendant la ressource. Cette manoeuvre est réalisée en choisissant à chaque instant la valeur de l'incidence qui permet de conserver une valeur constante pour la contrainte concernée. Cette valeur d'écrêtage est minimisée en profitant au mieux de la plage d'incidence autorisée. La limite basse de la plage d'incidence est due à des limitations thermiques (e.g. sur le pare-brise) ou de pilotage.

Après la ressource hypersonique, les contraintes vont décroître. L'objectif va être alors de rejoindre un profil de rentrée analogue à celui de la rentrée normale. Ceci peut être réalisé par un rebond contrôlé à incidence et gîte constantes.

La planche 2 montre un exemple de trajectoire de rentrée en sauvegarde d'HERMES pour un instant de panne de 250 s. Les courbes représentées sont l'incidence, la gîte, la pression et les contraintes de facteur de charge, de moment de charnière (levons et de température (ici sur les premières tuiles d'intrados) en fonction du temps. L'origine du temps correspond à l'instant de panne. Le profil de vol est également présenté dans le diagramme altitude-vitesse avec la trajectoire de lancement nominale.

Un échantillon de quelques trajectoires de rentrée en sauvegarde figure dans le domaine altitude-vitesse sur la planche 3. Un réseau d'iso-pression dynamique et d'iso-flux y est également présenté; il s'agit ici du flux de référence défini par $CQ \cdot \sqrt{V} \cdot V^3$, avec $CQ=1.7E-4SI$. Ce flux de référence correspond au flux atteint au point d'arrêt d'une sphère de rayon 1m et donne une indication sur le niveau des contraintes thermiques. En situant les points de ressource des trajectoires de sauvegarde dans ce réseau d'iso-pression dynamique et d'iso-flux, il apparaît que les contraintes structurales sont maximales pour des instants de panne de l'ordre de 250 s pour lesquels la vitesse initiale est proche de 3 km/s. Les contraintes thermiques sont maximales pour des pannes survenant dans la zone des 450 s, ce qui correspond à des vitesses de l'ordre de 5 à 6 km/s.

POINT HAUT

La loi de commande étant maintenant définie, les contraintes maximales rencontrées ne vont plus dépendre que des conditions initiales de la trajectoire de sauvegarde, soit (Z, V, γ) . La position initiale a été prise dans tous les cas à une latitude nulle et avec une route de 61.5° (inclinaison de l'orbite visée: 28.5°). En effet, pourvu que la relation latitude-route soit celle correspondant à l'orbite choisie, la position du point initial a une influence négligeable sur les trajectoires de sauvegarde.

Dans l'ensemble de tous les points initiaux (Z, V, γ) , il est possible de définir la relation d'équivalence suivante:

$$(Z_1, V_1, \gamma_1) \text{ EQ } (Z_2, V_2, \gamma_2)$$

si et seulement si

$$Z_{a1} = Z_{a2} \text{ et } V_{a1} = V_{a2}$$

avec : Z_a et V_a altitude et vitesse de l'apogée de la trajectoire balistique passant par (Z, V, γ) .

Une classe d'équivalence est donc l'ensemble des conditions (Z, V, γ) qui proviennent d'un même apogée qui sera appelé point haut. C'est aussi l'ensemble des conditions (Z, V, γ) d'un même arc orbital.

Par conséquent toutes les conditions initiales d'une classe d'équivalence, pourvu qu'elles soient en dehors de l'atmosphère (ou plus précisément dans une zone où les forces aérodynamiques sont négligeables vis à vis des forces d'inertie), vont conduire aux mêmes contraintes à la rentrée. Ces contraintes peuvent être associées au représentant de la classe d'équivalence qui est le point haut:

$$(Z_a, V_a) = \text{contraintes: } PC, \text{Moment, températures}$$

Il est alors possible de tracer dans le domaine Z_a, V_a des points hauts des iso-contraintes HERMES à la rentrée en sauvegarde.

Un réseau d'iso-contraintes est représenté sur la planche 4. Il s'agit d'iso-facteurs de charge, d'iso-moments de charnière gouverne et d'iso-températures dans la zone de l'intrados avant. Le décrochement observé sur les iso-températures d'intrados traduit la discontinuité des températures au passage de la transition laminaire-turbulent. La remontée rapide des iso-températures correspond à des points de ressource venant tangenter la limite de transition. Pour les vitesses les plus fortes, l'iso-contrainte est obtenue pour des altitudes Z_a très élevées car la ressource a lieu en écoulement laminaire. Le réseau présenté sur la planche 4 montre que le niveau des contraintes maximales croît rapidement avec l'altitude du point haut.

2.2 Cas avec propulsion

Il est intéressant d'utiliser le MPH d'HERMES pour réduire les contraintes subies à la rentrée en sauvegarde. Cette réduction des contraintes est obtenue en remontant l'altitude du point de ressource par une utilisation adéquate de la poussée disponible.

Les conditions d'utilisation du module propulsif sont cependant limitées par l'instabilité aérodynamique du composite. Cette instabilité rend nécessaire la séparation d'HERMES du MPH dès que la pression dynamique atteint un seuil critique qui a été pris égal à 20 hPa pour la configuration décrite dans ce document.

Le point haut est invariant sur une trajectoire balistique sans propulsion. L'introduction d'une poussée va modifier à chaque instant le vecteur vitesse et donc déplacer le point haut associé au point de vol considéré. Pendant toute la phase propulsée l'orientation de la poussée a été supposée libre de toute contrainte. Cette orientation (qui correspond à l'assiette d'HERMES) est déterminée de façon à déplacer, pour un point de vol donné, le point haut correspondant perpendiculairement aux iso-contraintes dans le domaine Z_a, V_a . L'assiette optimale de poussée, i , est alors définie par:

$$\text{tg}(i) = \frac{V_v \cdot \frac{R_a + d \cdot V_a}{d \cdot (V_a \cdot V_h - \mu \cdot R / R_a^2) - V_a \cdot R + R_a \cdot V_h}}{\quad} \quad (1)$$

avec (1,d) : direction de la tangente aux iso-contraintes au point (Z_a, V_a)
 Z_a, V_a : point haut associé au point de vol
 R_a : Z_a + rayon terrestre
 R : altitude + rayon terrestre
 V_h : composante horizontale de la vitesse
 V_v : composante verticale de la vitesse
 μ : constante gravitationnelle géocentrique

On peut vérifier par (1) que le signe de i est donné par V_v . La loi de commande obtenue consiste donc à pousser vers le bas tant que la pente est positive, et vers le haut dès que la pente est négative. Un exemple de trajectoire de sauvegarde avec MPH est présenté sur la planche 5. Le MPH considéré ici est un L6, étage utilisant deux moteurs de 30 kN et chargé à 6t d'ergols. Les contraintes maximales sont réduites par rapport au cas sans propulsion. Elles sont présentées en fonction de l'instant de panne sur la planche 6.

Elles sont cependant très supérieures aux contraintes en rentrée normale et aux limites acceptables pour la sauvegarde. La réduction des contraintes rencontrées en sauvegarde peut être obtenue par une modification de la trajectoire de lancement. Ceci fait l'objet de la seconde partie de cette présentation.

3. CONSEQUENCES SUR LA TRAJECTOIRE DE LANCEMENT D'ARIANE 5

Dans le processus de dimensionnement en sauvegarde d'HERMES, la trajectoire de lancement a une importance essentielle. Cependant la modification de la trajectoire d'ARIANE 5 pour réduire les contraintes atteintes en sauvegarde s'accompagne d'une désoptimisation de cette trajectoire, ce qui conduit à une réduction de la charge utile au lancement.

Il faut donc envisager une solution globale du problème de la sauvegarde d'HERMES qui nécessite de nombreuses itérations de calcul de trajectoires d'HERMES et d'ARIANE 5.

Dans le but de réduire le temps nécessaire à ce processus itératif, un interface entre les trajectoires d'HERMES et celles d'ARTANE 5 a été défini sous la forme de gabarits.

La description de ces gabarits dans les cas sans ou avec propulsion ainsi que l'optimisation de la charge utile globale font l'objet de cette seconde partie.

3.1 Cas sans propulsion

Les iso-contraintes présentées dans le domaine des points hauts (Z_a, V_a) associées à des limites sur les contraintes HERMES pour la sauvegarde, permettent de définir un domaine de points (Z_a, V_a) qui respecte ces contraintes limites. La limite haute de ce domaine est appelée gabarit.

Ce gabarit de contraintes HERMES est directement utilisable pour la détermination des trajectoires d'ARIANE 5. Il permet de vérifier immédiatement si une trajectoire de lancement satisfait ou non les contraintes maximales imposées à la rentrée en sauvegarde d'HERMES.

Pour cela il suffit d'associer à chaque point de la trajectoire d'ARIANE 5 le point haut correspondant et de situer le lieu des points hauts de la trajectoire de lancement dans le gabarit HERMES. Les contraintes seront respectées si les points hauts associés à la trajectoire de lancement sont en dessous du gabarit de sauvegarde. La trajectoire représentée sur la planche 7, qui dépasse le gabarit HERMES, conduit donc en sauvegarde sans MPH, à des niveaux de contraintes inacceptables pour HERMES.

3.2 Cas avec propulsion

Dans le cas où le MPH d'HERMES est utilisé pour les trajectoires de sauvegarde, la simplification employée dans le problème sans propulsion n'est plus applicable. En effet deux points de vol de la même classe d'équivalence (pour la relation d'équivalence définie au § 2.1) ne conduisent plus au même niveau de contraintes, ceci parce que la propulsion ne s'appliquera pas durant la même durée dans les deux cas et donc ne modifiera pas la trajectoire de la même façon.

Dans ce cas la notion de point haut n'est plus utilisable. Cependant des gabarits de contraintes HERMES peuvent encore être définis en se plaçant dans le domaine des conditions initiales (Z, V, δ).

L'utilisation de ce type de gabarit est la suivante : pour une trajectoire de lancement donnée, la limite d'altitude pour une vitesse V est fournie par le gabarit HERMES avec la pente de la trajectoire de lancement à cette vitesse.

La figure 8 présente le gabarit des contraintes pour HERMES avec un MPH L4 (le L4 est un étage utilisant 2 moteurs de 20 kN et chargé à 4 t d'ergols). Le fait de disposer d'un module propulsif permet à HERMES de réduire les charges subies à la rentrée en sauvegarde et donc de relâcher le gabarit des contraintes. Les courbes d'iso-flux de référence qui figurent sur ce gabarit donnent une indication sur les contraintes thermiques subies par le composite ARIANE 5-HERMES lors du lancement. La trajectoire d'ARIANE 5 devra se situer au dessus de l'iso-flux admis pour le lancement.

La figure 9 présente le gabarit des contraintes dans le cas d'un MPH L6. Ainsi que l'on pouvait s'y attendre, le gabarit de la configuration L6 est moins contraignant que celui de la configuration L4, et à plus forte raison que celui sans module propulsif.

En plus de cet effet favorable sur le gabarit de sauvegarde HERMES, le L6 permet, à iso-performance et à iso-contraintes lanceur (e.g. problème de retombée de l'étage EPC), et hors problème de sauvegarde d'HERMES, de faire descendre la trajectoire de lancement.

Ces considérations ont conduit à retenir le L6 pour la propulsion d'HERMES dans la configuration 5M2.

La planche 10 présente une trajectoire de lancement L6 qui respecte le gabarit HERMES. Les contraintes de sauvegarde associées à cette trajectoire figurent sur la planche 11 et respectent bien les limites acceptables pour la sauvegarde d'HERMES.

3.3 Compromis entre la performance et les contraintes HERMES

Nous avons jusqu'à présent raisonné à contraintes avion fixées. La trajectoire de lancement peut être modifiée de façon à respecter les contraintes acceptables pour la sauvegarde d'HERMES, mais ceci au prix d'une perte de performance.

Cependant le niveau des contraintes acceptables par HERMES en sauvegarde peut être augmenté tant que des butées de faisabilité ne sont pas rencontrées.

Il faut donc traiter un problème d'optimisation global de la charge utile. En effet si l'on relâche les contraintes sur la trajectoire de lancement dues à HERMES, la réoptimisation de la trajectoire va conduire à un gain de performance du lanceur, mais l'augmentation des charges sur HERMES va exiger un accroissement de la masse de l'avion.

Ce problème d'optimisation de masse sous contraintes peut être simplifié et paramétré par rapport au point de culmination de la trajectoire de lancement.

A titre d'illustration, la figure 12 donne l'évolution de la perte de performance du lanceur en fonction de cette altitude de culmination. Lorsque l'altitude de culmination croît, la masse de l'avion compatible des contraintes de sauvegarde et la performance du lanceur augmentent. L'écart entre ces deux grandeurs représente le gain de charge utile embarquée par HERMES, qui est maximisée pour une culmination proche de 125 km.

4. CONCLUSION

Ce papier présente la méthode originale qui a été employée pour optimiser globalement la configuration ARIANE 5-HERMES pour la trajectoire de lancement, ceci du point de vue de la maximisation de la charge utile et compte tenu des contraintes imposées par la sauvegarde d'HERMES.

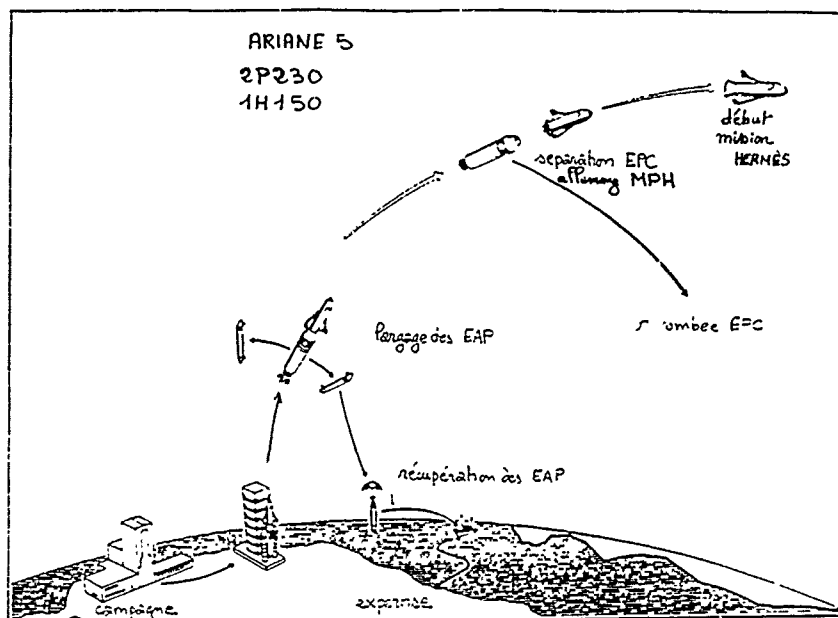
Ce processus a conduit à une trajectoire de lancement de référence pour la mission LEO HERMES. Cette étude a été réalisée sur la base de l'avion HERMES 94 (5M2) et est effectuée à nouveau sur la base de la configuration 00.

Plus généralement cette méthodologie est applicable à la définition de la trajectoire de lancement optimale de tout véhicule spatial habité posant le problème de la sauvegarde de l'équipage.

5. PLANCHES

LISTE DES PLANCHES

1. Scénario de lancement
2. Trajectoire de sauvegarde sans propulsion pour une panne à 250 s
3. Trajectoires de sauvegarde dans le domaine altitude-vitesse
4. Iso-contraintes HERMES dans le domaine des points hauts
5. Trajectoire de sauvegarde avec propulsion
6. Evolution des contraintes maximales en fonction de l'instant de panne
7. Exemple de trajectoire d'ARIANE 5 dans le gabarit HERMES sans propulsion
8. Gabarit L4
9. Gabarit LG
10. Gabarit associé à une trajectoire de lancement L6
11. Contraintes maximales fonction de l'instant de panne
12. Perte de performance en fonction de l'altitude de culmination



CHRONOLOGIE DU LANCEMENT

DATE (S)	ÉVÉNEMENT
0	Allumage du Volcano
3	Allumage des P230 et décollage
8	Début de basculement
18	Fin de basculement
126	Largage des P230 - Fin de la phase à incidence nulle
585.46	Largage du H150 et allumage des moteurs du H.P.E.
881.75	Injection sur l'orbite de transfert

PLANCHE 1 SCENARIO DE LANCEMENT D'ARIANE 5

HERMES 5M2 CAS SANS MPH instant de panne : 250 s

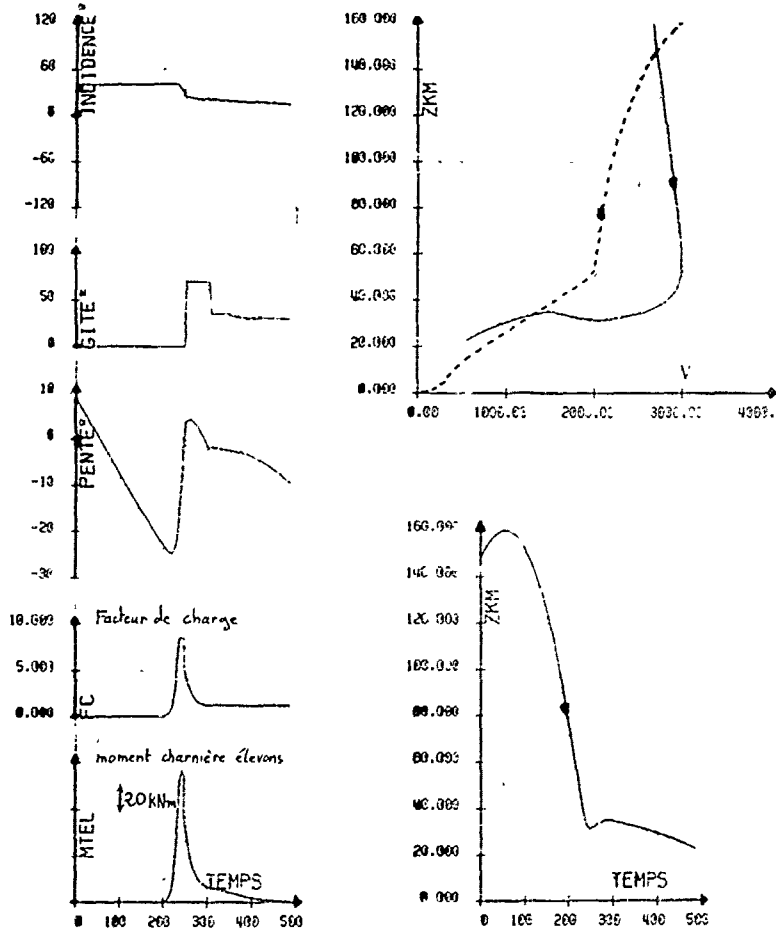


PLANCHE 2 EXEMPLE DE TRAJECTOIRE SANS PROPULSION

HERMES SM2 CAS SANS PROPULSION

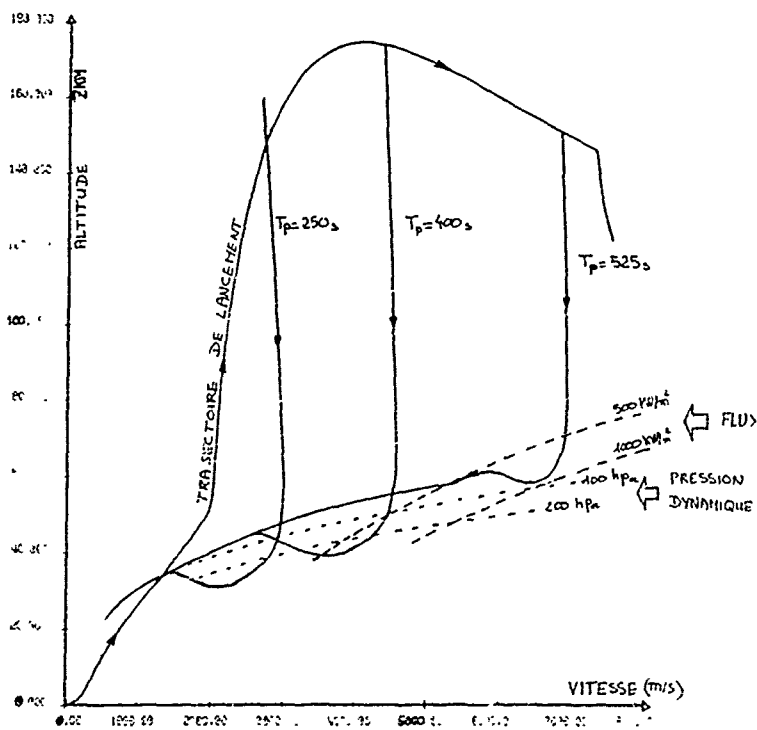


PLANCHE 3 TRAJECTOIRES DANS LE DOMAINE DE VOL Z-V

HERMES 5M2 RENTREE EN SAUVEGARDE CAS SANS PROPULSION

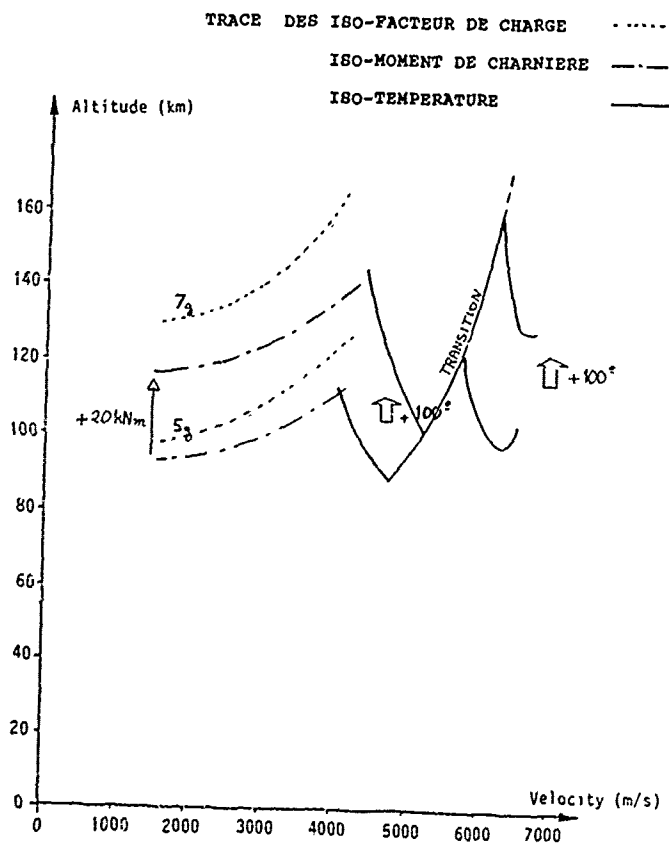


PLANCHE 4 ISO-CONTRAINTE DANS LE DOMAINE DES POINTS HAUTS

HERMES 5M2 CAS AVEC MPH instant de panne : 250 s

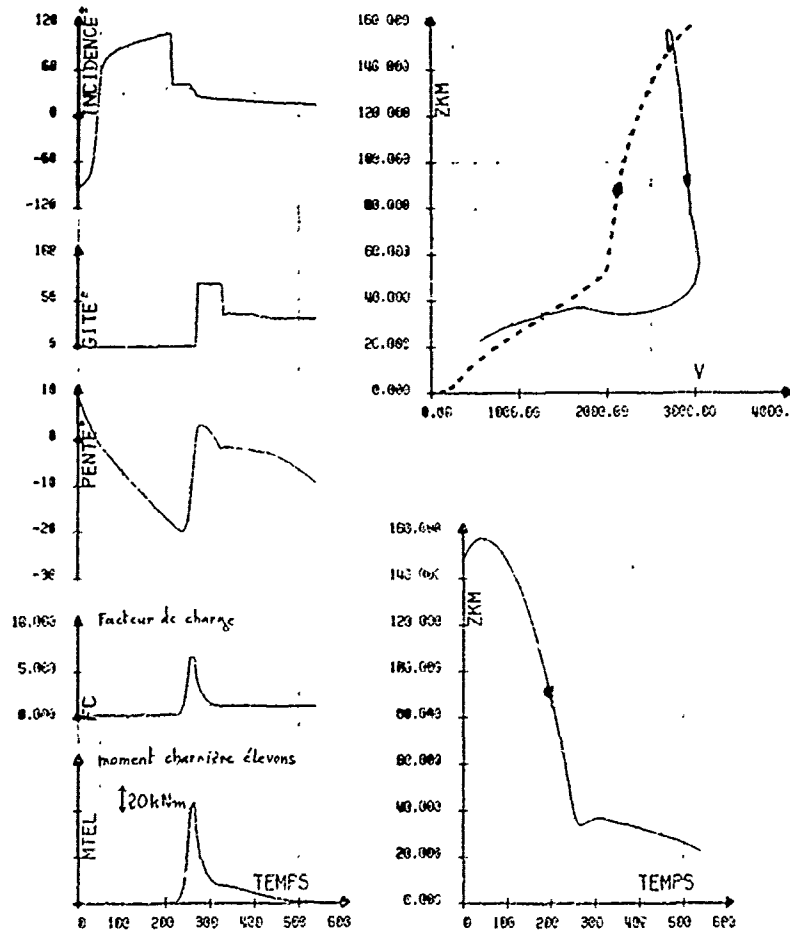
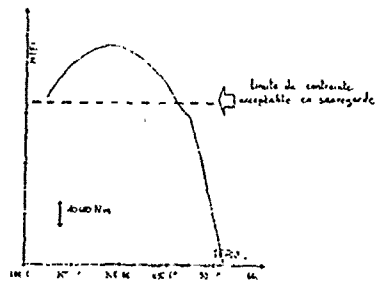


PLANCHE 5 EXEMPLE DE TRAJECTOIRE AVEC PROPULSION

HERMES 5M2 CAS AVEC PROPULSION

MOMENTS DE CHARNIERE ELEVONS



TEMPERATURE DES PREMIERES TOILES

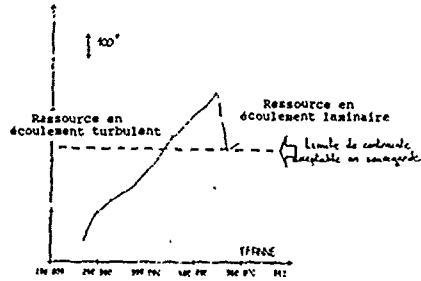


PLANCHE 6 CONTRAINTES MAXIMALES FONCTION DE L'INSTANT DE PANNE

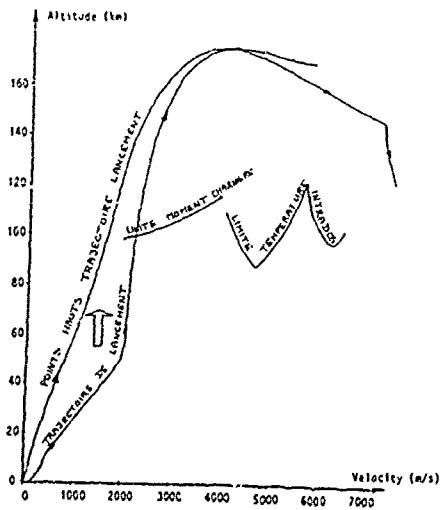


PLANCHE 7 TRAJECTOIRE ARIANE 5 DANS LE CABINET SANS PROPULSION

001-010-011-012-013-014-015-016-017-018-019-020-021-022-023-024-025-026-027-028-029-030-031-032-033-034-035-036-037-038-039-040-041-042-043-044-045-046-047-048-049-050-051-052-053-054-055-056-057-058-059-060-061-062-063-064-065-066-067-068-069-070-071-072-073-074-075-076-077-078-079-080-081-082-083-084-085-086-087-088-089-090-091-092-093-094-095-096-097-098-099-100-101-102-103-104-105-106-107-108-109-110-111-112-113-114-115-116-117-118-119-120-121-122-123-124-125-126-127-128-129-130-131-132-133-134-135-136-137-138-139-140-141-142-143-144-145-146-147-148-149-150-151-152-153-154-155-156-157-158-159-160-161-162-163-164-165-166-167-168-169-170-171-172-173-174-175-176-177-178-179-180-181-182-183-184-185-186-187-188-189-190-191-192-193-194-195-196-197-198-199-200-201-202-203-204-205-206-207-208-209-210-211-212-213-214-215-216-217-218-219-220-221-222-223-224-225-226-227-228-229-230-231-232-233-234-235-236-237-238-239-240-241-242-243-244-245-246-247-248-249-250-251-252-253-254-255-256-257-258-259-260-261-262-263-264-265-266-267-268-269-270-271-272-273-274-275-276-277-278-279-280-281-282-283-284-285-286-287-288-289-290-291-292-293-294-295-296-297-298-299-300-301-302-303-304-305-306-307-308-309-310-311-312-313-314-315-316-317-318-319-320-321-322-323-324-325-326-327-328-329-330-331-332-333-334-335-336-337-338-339-340-341-342-343-344-345-346-347-348-349-350-351-352-353-354-355-356-357-358-359-360-361-362-363-364-365-366-367-368-369-370-371-372-373-374-375-376-377-378-379-380-381-382-383-384-385-386-387-388-389-390-391-392-393-394-395-396-397-398-399-400-401-402-403-404-405-406-407-408-409-410-411-412-413-414-415-416-417-418-419-420-421-422-423-424-425-426-427-428-429-430-431-432-433-434-435-436-437-438-439-440-441-442-443-444-445-446-447-448-449-450-451-452-453-454-455-456-457-458-459-460-461-462-463-464-465-466-467-468-469-470-471-472-473-474-475-476-477-478-479-480-481-482-483-484-485-486-487-488-489-490-491-492-493-494-495-496-497-498-499-500-501-502-503-504-505-506-507-508-509-510-511-512-513-514-515-516-517-518-519-520-521-522-523-524-525-526-527-528-529-530-531-532-533-534-535-536-537-538-539-540-541-542-543-544-545-546-547-548-549-550-551-552-553-554-555-556-557-558-559-560-561-562-563-564-565-566-567-568-569-570-571-572-573-574-575-576-577-578-579-580-581-582-583-584-585-586-587-588-589-590-591-592-593-594-595-596-597-598-599-600-601-602-603-604-605-606-607-608-609-610-611-612-613-614-615-616-617-618-619-620-621-622-623-624-625-626-627-628-629-630-631-632-633-634-635-636-637-638-639-640-641-642-643-644-645-646-647-648-649-650-651-652-653-654-655-656-657-658-659-660-661-662-663-664-665-666-667-668-669-670-671-672-673-674-675-676-677-678-679-680-681-682-683-684-685-686-687-688-689-690-691-692-693-694-695-696-697-698-699-700-701-702-703-704-705-706-707-708-709-710-711-712-713-714-715-716-717-718-719-720-721-722-723-724-725-726-727-728-729-730-731-732-733-734-735-736-737-738-739-740-741-742-743-744-745-746-747-748-749-750-751-752-753-754-755-756-757-758-759-760-761-762-763-764-765-766-767-768-769-770-771-772-773-774-775-776-777-778-779-780-781-782-783-784-785-786-787-788-789-790-791-792-793-794-795-796-797-798-799-800-801-802-803-804-805-806-807-808-809-810-811-812-813-814-815-816-817-818-819-820-821-822-823-824-825-826-827-828-829-830-831-832-833-834-835-836-837-838-839-840-841-842-843-844-845-846-847-848-849-850-851-852-853-854-855-856-857-858-859-860-861-862-863-864-865-866-867-868-869-870-871-872-873-874-875-876-877-878-879-880-881-882-883-884-885-886-887-888-889-890-891-892-893-894-895-896-897-898-899-900-901-902-903-904-905-906-907-908-909-910-911-912-913-914-915-916-917-918-919-920-921-922-923-924-925-926-927-928-929-930-931-932-933-934-935-936-937-938-939-940-941-942-943-944-945-946-947-948-949-950-951-952-953-954-955-956-957-958-959-960-961-962-963-964-965-966-967-968-969-970-971-972-973-974-975-976-977-978-979-980-981-982-983-984-985-986-987-988-989-990-991-992-993-994-995-996-997-998-999-1000

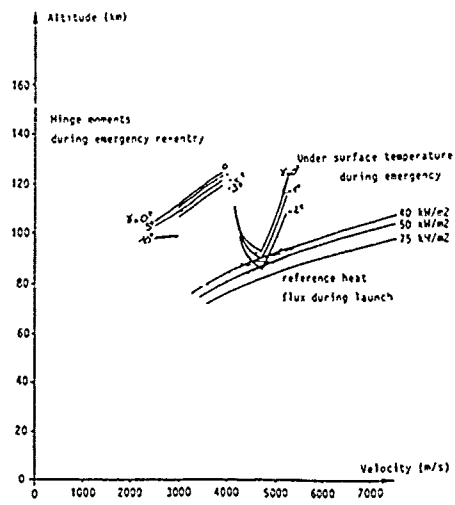


PLANCHE 8 GABARIT L4

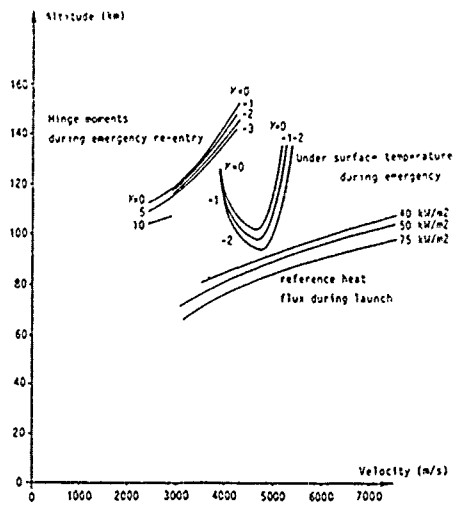


PLANCHE 9 GABARIT L6

HERMES SM2 TRAJECTOIRE DE LANCEMENT QUI RESPECTE LE GABARIT DES CONTRAINTES

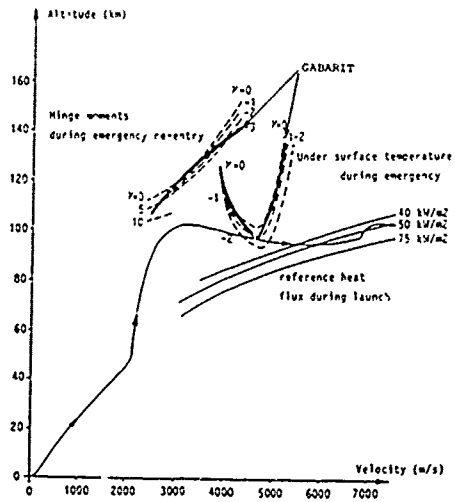


PLANCHE 10 GABARIT ASSOCIE A UNE TRAJECTOIRE DE LANCEMENT L6

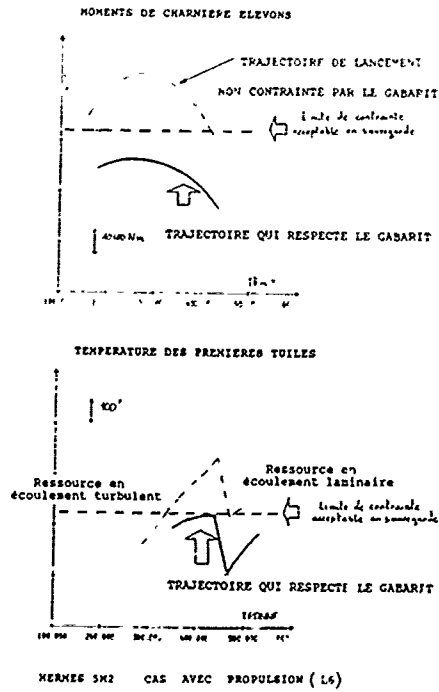


PLANCHE 11 CONTRAINTES MAXIMALES FONCTION DE L'INSTANT DE PANNE

PERTE DE PERFORMANCE DU LANCEUR ⇨ (A)
 ET AUGMENTATION DE LA MASSE D'HERMES FONCTION ⇨ (H)
 DE L'ALTITUDE DE CULMINATION

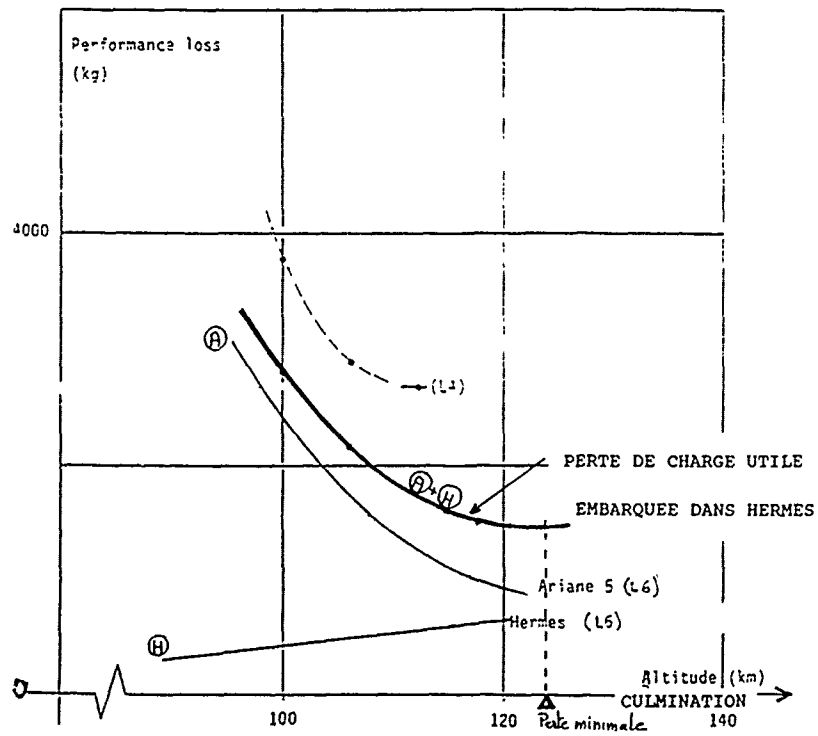


PLANCHE 12 PERTE DE PERFORMANCE EN FONCTION DE LA CULMINATION

**SPACE SHUTTLE DESCENT FLIGHT VERIFICATION BY SIMULATION:
A CHALLENGE IN IMPLEMENTING FLIGHT CONTROL SYSTEM
ROBUSTNESS**

Vict H. Nguyen, Supervisor, Entry Flight Control System
John T. Nishimi, member of technical staff
Thomas H. Payne, member of technical staff
Earl W. Woosley, retired
Rockwell International
Space Transportation Systems Division
12214 Lakewood Blvd.
Downey, California 90241, USA

SUMMARY

The Space Shuttle flight control system (FCS) is a digital fly-by-wire system that provides vehicle stability, response, and handling qualities necessary to return safely from orbit, ending with a pinpoint landing on a 300-by-15,000-foot (90-by-4,600-meter) runway. Furthermore, on its first flight, it had to fly successfully the entire envelope—manned. Thus, the FCS was subjected to one of the most extensive programs of certification by analysis and simulation ever conducted.

This paper starts with an overview of the entry and landing FCS along with the requirements and considerations used in the design process. The next section addresses the network of simulation programs used in the FCS design and verification. The final sections present the flight test results and the current issues related to landing and roll-out.

SYMBOLS

A/A	Accelerometer assembly
A/L	Approach/landing
ADTA	Air data transducer assembly
ALDF	Aircraft Landing Dynamics Facility (NASA Langley Research Center)
Alpha	Angle of attack
CCS	Control stick steering
DAP	Digital autopilot
DOF	Degree of freedom
FCS	Flight control system
FO/FS	Fail operational/fail safe
FSL	Flight Systems Laboratory
FSSR	Functional Subsystem Software Requirements
GPC	General-purpose computer
HAC	Heading alignment cone
JSC	Johnson Space Center
KSC	Kennedy Space Center
L/D	Lift-to-drag ratio
L/R	Landing/roll-out
LVAR	Lateral variation uncertainty
MDM	Multiplexer/demultiplexer (software/hardware interface)
MIL	Man in the loop
NWS	Nose wheel steering
OFT	Orbital flight test program
OI	Operational increment
PIO	Pilot-induced oscillation
PRL	Priority rate limiter
PTI	Programmed test input
RCS	Reaction control system
RGA	Rate gyro assembly
RM	Redundancy management
SAIL	Shuttle Avionics Integration Laboratory (NASA Johnson Space Center)
SES	Shuttle Engineering Simulator (NASA Johnson Space Center)
STS	Space Transportation System (Space Shuttle)
T.FS	Total In-Flight Simulator
VMS	Vertical Motion Simulator
WOW	Weight on wheels

INTRODUCTION

For the new generation of spaceplanes, such as the Space Shuttle, flight regimes extend beyond wind tunnel capabilities and flight testing is limited. Therefore, simulators offer a viable means to achieve robust designs while reducing risks.

Unique features of the Shuttle program demanded a robust, descent-phase FCS verified prior to flight test. First, the Shuttle orbiter is a hybrid spacecraft/aircraft, using pure reaction control effectors in exoatmospheric flight and conventional aircraft surfaces in subsonic approach/landing, with a blend of the two in hypersonic and supersonic flight. Second, the lack of an aerodynamic data base for much of this vast flight regime required heavy dependence on wind tunnel testing. The difficulties in

matching similitude parameters imposed large uncertainties on the resulting aerodynamic data base, particularly regarding the reaction control system (RCS) and aerodynamic interactions. Finally, the first flight had to cover the entire flight regime: the program denied the luxury of starting at benign flight phases with the customary gradual extension of flight envelope. Since the vehicle lacked sufficient static margin for unaugmented control, the FCS had to work properly the first time with sufficient robustness to handle large uncertainties.

DESIGN REQUIREMENTS

The basic guideline used during design and verification can be summarized as follows: maintain acceptable nominal stability, response, and handling qualities while providing maximum coverage for off-nominal aerodynamics, environmental conditions (atmosphere, mass properties, trajectory dispersions, winds), navigation errors, sensor/effector uncertainties, and uncertainties in structural characteristics (modal frequency, mode shape, damping).

Specifically, the flight control requirements are classified in three basic performance levels designated as Level 1, Level 2, and design assessment (Figure 1). Each is defined below:

- Level 1 performance
 - Stability
 - Gain margin = > 6 dB
 - Phase margin = > 30 degrees
 - Pilot rating (Cooper Harper): 3 or better
 - Step response within specified envelopes
- Level 2 performance
 - Stability
 - Gain margin = > 4 dB
 - Phase margin = > 20 degrees
 - Pilot rating: 6 or better
 - Large-signal operation stable
- Design assessment
 - Performance is such that there is no loss of vehicle control.

These requirements must be maintained under the following conditions:

- Winds
 - Steady state, up to 99-percentile directional (worst month)
 - Discrete gust
 - Turbulence
 - Wind shear
- Atmosphere (annual extremes)
 - Density
 - Temperature
- Aerodynamic uncertainties
 - Lift-to-drag ratio (L/D) plus pitching moment coefficient
 - Stability derivatives
 - Reaction control system/aerodynamic interaction
- Bent airframe/Ycg offsets
- Failures—fail operational/fail safe (FO/FS)
 - One failure: Level 1 performance except for loss of air data (Level 2)
 - Two failures: Level 2 performance except for the loss of two RCS jets (Level 1) or of two auxiliary power units (design assessment)

Similar requirements apply to the stability of the structural modes, as summarized in Figure 1.

OVERVIEW OF THE DIGITAL AUTOPILOT

Satisfying these requirements would produce a robust design. This goal was achieved through careful consideration of the subsystem off-nominal performances and the aerodynamic uncertainties.

Mission Profile

During entry, atmospheric drag is used to dissipate the orbiter's energy. An angle-of-attack (α) profile, scheduled as a function of earth-relative velocity, is flown and roll angle is used to control energy dissipation. The cross range is controlled by alternating the sign of the roll commands. Typical α , roll angle, and drag profiles are shown in Figure 2. The orbiter is steered to intercept either of the two heading alignment cones (HAC's) located tangent to and on either side of the runway centerline. The approach/landing (A/L) phase normally occurs at 10,000 feet (3 kilometers) in altitude and 290 knots (150 meters per second) equivalent airspeed (KEAS), when the orbiter acquires the 19-degree steep glide slope; the transition to a 1.5-degree

inner glide slope is made at 2,000 feet (610 meters) above ground. Nominal touchdown is at 2,500 feet (760 meters) past runway threshold at 195 KEAS (100 meters per second). After touchdown, directional control is achieved by a combination of rudder, nose wheel steering, and differential braking.

Flight Control

The digital autopilot (DAP) has both manual (with stability augmentation) and automatic flight control modes. All inner-loop flight-critical functions (e.g., rate damping and stability augmentation) are computed at the fast minor-cycle rate of 25 Hz. Other less critical computations, such as updating gain schedules, are done at slower rates.

The control effectors consist of aerodynamic surfaces and aft-mounted reaction control jets (Figure 3). The four elevons are moved symmetrically for elevator and antisymmetrically for aileron control. The rudder panels split open for speed brake functions. The primary aerosurfaces are driven by three independent hydraulic systems—one active and two standby. A software rate and authority limit function is used to maintain the commanded surface rates within the capability of the hydraulic system. The utilization of the control effectors during entry is illustrated in Figure 3.

Figure 4 shows an overview of the entry FCS. The quad-redundant system architecture ensures compliance with the FO/FS requirement. Four general-purpose computers (GPC's) operate in a parallel redundant set, and the fifth acts as a backup reserve in case of a generic software failure of the primary redundant set. The FCS sensors consist of four sets of rate gyro assemblies (RGA set = pitch, roll, yaw rates), four sets of accelerometer assemblies (AA set = lateral, normal accelerations), and two air data transducer assemblies (ADTA's) with two probes on each. The software redundancy management (RM) system has failure detection logic to identify and remove faulty signals, and a selection filter to send the "best" sensor estimate to the FCS. The effector systems have a similar level of redundancy (e.g., force-summing aerosurface secondary actuators, jet selection logic, and reaction-jet-driven assemblies).

Aerodynamic Uncertainties

Aerodynamic uncertainties played an important role in the design of the FCS. A set of seven "worst case" uncertainties, called lateral variations (LVAR's), was developed on the basis of wind-tunnel-to-flight-test differences from past aircraft programs and used to certify the FCS. They represented a reasonable estimate of the maximum possible errors in the preflight predictions (Figure 5):

- LVAR 2: poor bank-angle control
- LVAR 9: poor lateral/directional damping
- LVAR 11: worst case aileron control
- LVAR 12: best-on-best aileron control
- LVAR 19: maximum aileron control for Ycg trim
- LVAR 20: maximum RCS required for Ycg trim
- LVAR 23: maximum beta during heating region

The sensitivity of flight control performance to aerodynamic uncertainties is illustrated in Figure 6, in which the progressive destabilizing effect of LVAR 9 is evident. The system damping ratio of 0.82 with nominal aerodynamics is drastically reduced by the partials of CIA (rolling moment caused by aileron, Increments 5 to 6) and CIYJ (rolling moment caused by yaw jet, Increments 11 to 12), forcing a well-behaved system to be slightly unstable (damping ratio less than zero). The FCS sensitivity to off-nominal aerodynamics is further aggravated by the aerodynamic sensitivity to angle of attack, as shown in Figure 7, in which coalignment of the vectors is evident.

While RCS effectiveness in a vacuum was well defined, there were large uncertainties in the effect of the interaction between the flow from the jets and the normal airflow around the orbiter. These RCS uncertainties were combined with the LVAR's to further stress the FCS design. The general technique was to combine very effective jets with high-gain aerodynamic conditions and less effective jets with low effective aerodynamic surfaces.

The pitch-axis aerodynamic uncertainties received similar attention; but since they are more benign than those in the lateral axes, they are not discussed in this paper.

DESIGN AND VERIFICATION BY SIMULATION

The inability to conduct a normal progression of flight tests requires the FCS to be designed and verified extensively by analysis and simulation. Three basic approaches are used in the design process: (1) classical linear stability analysis with describing functions representing key nonlinear elements, (2) nonlinear time-domain analysis, and (3) man-in-the-loop (MIL) simulation. In addition, extensive integrated hardware/software MIL testing is performed to verify system readiness for flight.

The Use of Simulation

The simulation programs differ in complexity but complement each other. A design normally starts in the frequency domain: the subsystem dynamics are modeled as linear transfer functions, the airframe dynamics are linearized at a flight condition, and the system transport delays and sampling effects are properly included. The total system sensitivities to aerodynamic variations, subsystem off-nominal performances, vehicle dynamic uncertainties, and feedback variables are established in terms of stability margins. Then analyses using off-line time-domain simulation programs follow, employing a more accurate representation of the nonlinear characteristics of the elements of the system, such as aerosurface and RCS effectors. The FCS design is assessed along the trajectories flown while subjected to environment changes and even subsystem failures. These time-domain analyses offer limited evaluation of the system margins but provide excellent assessment of the system performance.

The MIL digital engineering simulators are the next facilities used to evaluate the design for man/machine/mission compatibility. The math models used are normally of the same fidelity as the off-line simulation programs, but here the challenge is to represent the system timing delays accurately while maintaining the correct system dynamics. The inherent delays in the real-time simulators that generate visual displays or produce the motion cues have to be compensated for; otherwise, the pilot ratings suffer. Delays caused by the effects of sampled-data system feedbacks also have to be adjusted for. Usually, a combination of special integration techniques to introduce phase lead into the system along with the reduction of known orbiter flight systems delays is employed to offset the simulator lags. The possible subsystem failures also must be modeled to assess the pilot's responses.

The design process is always an iterative one among the frequency domain, off-line time domain, and real-time MIL; confidence in the design is progressively built by evaluation from different viewpoints. However, to gain confidence for flight, an integrated MIL simulator is needed that brings together all the hardware/avionics subsystems, the flight software, and the astronauts. Here, the software and the interfaces can be thoroughly checked out. The redundancy management scheme is verified through the facility's ability to simulate any combination of subsystem failures and/or off-nominal performances. When it is impractical to include the actual hardware, a high-fidelity model is substituted and the verification efforts are supplemented with testing at the Kennedy Space Center (KSC) or the manufacturers' facilities. The crew checklist and procedures are also verified for nominal missions, aborts, or failure recoveries.

Common to all the simulation programs and facilities is the extensive aerodynamics data base. It ranges from Mach 0.25 to an altitude of 600,000 feet (183 kilometers), an alpha of -10 to 50 degrees, and sideslip of up to ± 10 degrees, providing more than adequate coverage of the flight envelopes and ensuring that drastic pilot maneuvers will not invalidate the results.

Key Simulation Programs and Facilities

Linear Stability Analysis Programs (CRAM, DIGIKON). CRAM and DIGIKON computer programs are linearized three-degree-of-freedom (DOF) point-stability tools used to assess rigid-body as well as flexible stability margins

CRAM solves simultaneous linear equations in the S-plane and derives transfer functions, root loci, frequency response, and step-response solutions. The system's transport lags and sampling effects are modeled with second-order Padé approximations. DIGIKON solves state-variable equations in the Z- and W-planes. It also derives transfer functions, frequency response, and step-response solutions, and accurately simulates multirate sampling and transport lags. Because the two programs produce matching results over the frequency range of interest, they serve as a good cross check of each other. DIGIKON is further used in the assessment of flex stability and the design of bending filters.

Non-Real-Time Simulation Programs (SDAP, SIMEX, SDAPFLEX, SIMFLEX). These nonlinear time-domain simulation programs vary in complexity—from a relatively simple point-response tool (SIMEX) to a complex six-degree-of-freedom trajectory program (SDAP) complete with emulations of flight software, sensors, nonlinear effectors, earth motion, gravitational and atmospheric environment. SDAPFLEX and SIMFLEX are used to analyze integrated orbiter/payload flexures and their potential effects on RCS consumption. All of these non-real-time programs are extremely useful for parametric and sensitivity studies well as anomaly resolution. They are validated not only against each other but also by comparison with stability predictions made by CRAM and DIGIKON.

MIL Engineering Simulators (SES, VMS, TIFS). MIL engineering simulators are absolutely necessary in the design process to ensure man/machine/mission compatibility and to assess flying and handling qualities. The fixed-base Shuttle Engineering Simulator (SES) at NASA JSC has a cockpit mockup with digitally generated visuals of the commander's forward view. This user-friendly and readily available tool can be operated by one person without compromising the quality of the results. Normally the first facility employed to obtain pilot comments on a new design, it plays an important part in many software changes affecting vehicle performance and safety.

The Vertical Motion Simulator (VMS) at NASA Ames Research Center is a motion-based, six-DOF facility (Figure 8). The simulator cabin is fitted to replicate the orbiter, with seats in the commander and pilot positions, hand controllers and pedals, critical instrument displays (including the head-up display), and switches. The cabin has forward and corner windows with high-resolution, computer-generated visual scenes. Motion limits are ± 30 feet (9.1 meters) vertically, ± 20 feet (6.1 meters) laterally, and ± 4 feet (1.2 meters) longitudinally. In addition, pitch, roll, and yaw actuators provide the three rotational degrees of freedom. Maximum simulated accelerations approach $2/3$ g vertically and $1/2$ g horizontally. The valuable motion cues produced by this simulator greatly influence the assessment of the approach, landing, and roll-out phases. The pilot's quicker reaction to the motion feedback sometimes leads to loss of vehicle control if the gain of the control effector is too high (e.g., the nose wheel steering), which might not be the case if the test is conducted in the SES.

The U.S. Air Force's Total In-Flight Simulator (TIFS) is a test simulator used solely (in the Shuttle program) to evaluate the approach/landing phase. It is a highly modified C-131 aircraft with an evaluation cockpit in addition to the normal C-131 cockpit manned by safety pilots. The simulation pilot's control commands are input to the model's computer, which calculates the orbiter response to be reproduced. These responses, along with TIFS motion sensor signals, are used to generate feed-forward and response-error signals that drive the six TIFS effectors (elevator, aileron, rudder, throttle, direct-lift flaps, and direct side-force surfaces). The result is a high-fidelity reproduction of the motion and visual cues at the pilot position. Figure 9 is an illustration of TIFS.

MIL Verification Simulators (FSL, SAIL). The Flight Systems Laboratory (FSL), located in Downey, California, was used to verify entry avionics/software integrated performance until 1984, when that function was transferred to NASA's Shuttle Avionics Integration Laboratory (SAIL) in Houston, Texas. The Downey facility was a multistation laboratory that permitted simultaneous studies from simple end-to-end checks of the flight software to mission verification tests using the full six DOF with MIL. The laboratory used a mockup of the orbiter cockpit and contained flight instruments and controls necessary for pilot evaluation of system performance. Actual avionics flight hardware included the GPC's, multiplexer/demultiplexers (MDM's), FCS sensors, display electronics, and pilot controls and flight instruments. A model board for visual scene projection was available at the commander's window for A/L tasks. Digital computers simulated vehicle dynamics and environment, and allowed test engineers to insert failures. Analog computers were used to model aerosurface actuators, hinge moments, and turbulence.

The FSL could also be connected with the full-scale model of the orbiter hydraulic system, located next door in the Flight Control Hydraulics Laboratory, to assess performance of the hydraulic actuators

SAIL, equipped with a full shipset of flight avionics hardware, is used to perform verification tests of all mission phases from ascent through entry. As in the FSL, digital computers simulate vehicle dynamics, the vehicle states acting as stimuli to drive hardware (or software-modeled) sensors and test sets. SAIL has no hardware actuators and limited capability to troubleshoot software within the GPC's. Figure 10 is a functional block diagram of the facility

Site Acceptance Tests

A process called site acceptance, or validation, ensures that all tools used in FCS design, analysis, and verification produce accurate and similar results. A series of static, dynamic, and integrated performance tests is conducted. The static tests (aerodynamic slices, effector step and frequency responses, sensors, etc.) verify that the unit models by themselves are correctly implemented. The dynamic tests (bare-airframe frequency and step responses, FCS open-loop frequency responses, closed-loop step responses, gain margins, navigation drift check) provide further detailed verification of the integrated system dynamics and the models' interfaces. The integrated performance tests, also called common facility tests, consist of six-DOF trajectories selected to demonstrate integrated system performance. The site acceptance signature data are obtained from other validated simulators.

Tool validation is a continuing process, conducted each time a major data base, control system, or model is updated. The availability of independent and validated simulators ensures the quality of the results and helps avoid setup problems.

Verification Process

The scope of the verification process is to validate FCS stability margins and in-flight performance against the previously stated design requirements. The verification process starts with the Functional Subsystem Software Requirements (FSSR) documents, which contain the requirements for the software to be coded by IBM. Point-stability analyses using CRAM/DIGIKON are performed for selected test conditions of the flight envelopes created by Monte Carlo runs with variations in winds, L/D uncertainties, and atmospheres. Analyses using non-real-time simulation programs supplement closed-loop performance verification at SAIL. The majority of SAIL testing falls into two categories: verification of OI (operational increment) software release and verification of mission-specific software for every flight. New OI software, released about every 6 months, incorporates changes resulting from safety concerns, performance improvement, system management, and software memory scrubs. For each set of OI software, a matrix of integrated performance tests is designed to validate correct implementation of the changes and their compatibility with existing software/hardware requirements. A generic test matrix used for each mission covers mission specific flight conditions (e.g., mass properties, atmospheric conditions, landing site) to demonstrate system readiness for flight. Testing also includes all the abort modes.

Supplementing system performance verification is the vehicle/subsystem interface checkout at Palmdale, California, and KSC in Florida. Astronaut training is done in the Shuttle Training Aircraft and the Shuttle Mission Simulator.

FLIGHT TEST DEVELOPMENT

The first four orbiter missions constituted the orbital flight test (OFT) program, and subsequent flights were considered operational flights. This definition was more programmatic than an actual reflection of testing status in that testing continued into the "operational era" and payloads were carried during OFT. To date, more than 30 successful missions have been flown. The success of these missions is made possible by the robustness of the design, the ability of the system to overcome multiple hardware failures, and the extensive verification efforts by simulation.

OFT Flights

The OFT flights performed nominally, as evidenced in the comparison plots of the roll reversals between STS-1 and FSL-predicted time response (Figure 11). Good agreements are seen during the initial response with auto engaged until the planned manual takeover occurs. A guidance phase change from equilibrium glide to constant drag occurred only 13 seconds earlier than predicted. From this first mission, only four anomalies were noted, two of which demonstrate the robustness of the FCS.

A low-frequency, high-amplitude lateral oscillation seen during the first roll maneuver was attributed to yaw jet aerodynamic interaction (Figure 12). In the low dynamic pressure region, the roll caused by yaw jet firing was found to be less than predicted, at about the variation level of uncertainty. This problem showed the wisdom of designing the FCS to handle large aerodynamic uncertainties. A software fix adding a filter on the sideslip-angle feedback was implemented on STS-5. Stability analyses predicted this low stability margin in the automatic but not in the manual control stick steering (CSS) mode, consequently, later flights were flown in CSS through the first roll maneuver with good response until the fix was implemented.

An undamped, low-amplitude 1/4-Hz oscillation in the Mach 2 to 1 region was seen on every flight (Figure 13). This anomaly resulted in restrictions of the allowable X-axis center of gravity for several years. Subsequent flight test data indicated lower-than-predicted aileron roll effectiveness (near the variation level) and higher rudder roll effectiveness with small surface deflections, which approached nominal effectiveness with larger surface motions. A software change was incorporated on STS-13 to increase the aileron forward-loop gain and reduce the lateral acceleration feedback gain in the rudder loop in this transonic region. Again, this anomaly illustrates the necessity to include uncertainties in FCS design.

Operational Flights

Flight testing continues in the operational era to support anomaly resolution and FCS enhancements, and to expand the center-of-gravity envelope. Beginning with the STS-5 mission, a programmed test input (PTI) logic was implemented in which

specific commands are preprogrammed to pulse the control effectors at a predesignated flight condition to garner aerodynamic data. The PTI logic significantly reduces the pilot's work load and facilitates the data reduction task of separating out the effectiveness of various control effectors.

The results of the operational flight tests have allowed quite a few FCS enhancements: e.g., pitch RCS usage was extended from $Q_{bar} = 20$ to 40 psf (957.6 to $1,915.2$ N/m²) to improve the pitch-axis low-frequency gain margin (STS-41B); the rudder activation point was moved up from Mach = 3.5 to Mach = 4.2 (STS-51F) and subsequently to Mach = 5 (STS-26) because it was found to be effective earlier than predicted, thus eliminating the lateral trim problem in this region; the CSS no-yaw-jet downmoding system was certified for emergency use (STS-26).

LANDING/ROLL-OUT (L/R) UPGRADES

Background and Issues

Many issues remain in the L/R phase. A combination of factors, including the lack of a taxi test program, the increase in vehicle gross weights, and the orbiter's high-speed landing, has shown the L/R subsystem design to be very marginal. The original design called for rudder and differential braking as the primary mode of control, the nose wheel steering (NWS) serving as backup. This decision resulted in reluctance to use the NWS at all because of uncertainties in the nonredundant system and the potentially disastrous effects of a hardover nose wheel. Other program concerns in the area of L/R include severe tire wear in KSC landings because of the "corduroy" runway surface, brake energy margins for high-cross-wind and/or short-field landings (abort runways), and orbiter controllability in the presence of cross wind and/or tire failure.

Simulations and Test Programs

Since 1983, the VMS has been used extensively as a substitute for a taxi test program in assessing L/R characteristics and potential improvements. Supporting this effort are testing programs at the NASA Langley Aircraft Landing Dynamics Facility (ALDF) and the Wright-Patterson Air Force Base dynamometer facility to garner landing gear, brake, tire, and tire failure frictional characteristics. The VMS features realistic motion and visual cues and the highest fidelity landing dynamic models. Topics studied include improvements in handling qualities and flying techniques, evaluation of DAP changes to enhance ground directional control, and feasibility of hardware modifications to reduce tire wear, lessen chance of tire failure, and increase braking capability. The simulator also serves as a realistic training ground for orbiter pilots to practice cross-wind landing and failure recovery.

As a result of the many simulations conducted, the following upgrades have either been implemented or approved for implementation (Figure 14):

NWS Improvements. In the STS-51D landing at KSC, the orbiter suffered a tire blowout near the end of roll-out. Overheating of the brakes because of the need for differential braking was identified as the major cause. This incident demonstrated the need for an operational NWS system, since the current mode of operation lacked sufficient authority to control a high-speed blowout. A two-phase approach was authorized in which the system would be made fail-safe (fail to castor) for immediate implementation and an FO/FS system would be developed for future use.

The original NWS had three selectable modes: manual direct (the pedal commands went directly to the steer box), castor, and GPC (the pedal commands went through the GPC's). The NWS was operated by a single power source and single hydraulic system. The steer box accepted commands from a single GPC, making it susceptible to hardover failure that could result in loss of control of the orbiter. In addition, both steering modes were too sensitive at high speed.

To achieve the Phase 1 objective, several changes were authorized. A software logic detects hardover failures in the GPC mode by using information from the new triplex position feedbacks: a fault is declared if the nose wheel is not moving in the correct direction or if it is moving too slowly and would trip the system to castor. To reduce steering sensitivity at high speed, the GPC mode was augmented with lateral acceleration feedback and the direct-mode command transducer was changed from linear to parabolic shaping.

The Phase 1 activities allowed an increase in cross-wind capability from 7 to 12 knots (3.6 to 6.2 meters per second), and eventually to 15 knots (7.7 meters per second). The system was flight-tested on STS-61A with very good results.

Phase 2, which is nearing completion, will provide redundancy in the command path, the power sources, and the hydraulic system. The unaugmented direct mode will be deleted because of its sensitivity at high speed and replaced by a second GPC mode similar to the first one.

KSC Runway. Because of unpredictable weather at the KSC landing site, the runway is grooved both laterally and longitudinally for good drainage. This surface has good frictional characteristics whether dry or wet. However, it also causes excessive tire wear, especially at spin-up, which could lead to tire blowout. Tests at Langley's ALDF and at Ames' VMS showed that grinding the first 3,500-foot (1,067-meter) touchdown zones at both ends of the runway can significantly reduce tire wear caused by spin-up while maintaining good frictional characteristics during roll-out. The grinding of the KSC runway was completed in April of 1988.

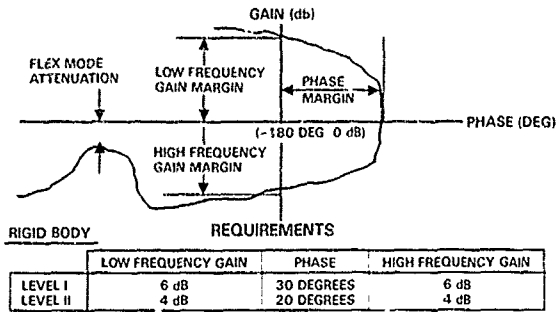
Drag Chute. It became apparent during numerous VMS simulations that the addition of a drag chute significantly improves margins, both in stopping distance and directional control, for the landing and deceleration subsystems. The drag chute allows the orbiter to stop safely on short abort runways, even with high gross vehicle weights. Furthermore, it stabilizes the vehicle directionally and drastically improves lateral control during recovery from a tire failure. Because of its attach point, the drag chute induces a pitch-up moment, forcing the elevator down for trim and, in the process, reducing the main gear loads (lessening the chance of tire failure) and increasing longitudinal control authority during derotation. Recognizing its many benefits, pro-

gram management approved the implementation of a drag chute system for all vehicles. The first test flight will occur in early 1991. VMS simulations dictated a baseline chute of 40 feet (12 meters) in diameter, reefed to 40 percent of its area for 3 seconds to reduce the transients caused by opening shock. It will be deployed after main gear touchdown.

Weight-on-Wheels (WOW) Redundancy. The current system of WOW recognition is simplex, based on one proximity switch per main gear and two on the nose gear. Early WOW moding because of failure while the FCS is still in the airborne mode would most certainly cause a loss of vehicle control from incorrect FCS. Therefore, the design of current software logic is extremely fail safe, issuing a WOW dilemma for any failure and keeping the FCS in the airborne configuration. This scenario would result in degraded slapdown handling qualities after touchdown, making the orbiter susceptible to pilot-induced oscillations (PIO's), as seen on STS-3, and possibly making NWS unavailable. Furthermore, in the automatic landing mode, a hard nose wheel slapdown would occur, since the orbiter would try to continue descent onto the runway. The system will be upgraded to triple redundancy for each gear, and wheel spin-up signals will be incorporated in the WOW decision logic in early 1992.

CONCLUSION

Simulation is an indispensable process. It provides a safe environment for the design of robust systems, maximizes flight safety, and can drastically reduce the cost of a flight test program. However, it cannot, and should not, be used as a substitute for a flight test program, since it has its limitations: the results can be only as good as the models used, and the fidelity of a simulator can be refined only with flight data. A well-planned simulation/flight test program ensures a robust design and a safe expansion of flight envelope, and reduces future design changes.



FLEX BODY

FREQUENCIES < 6 HZ

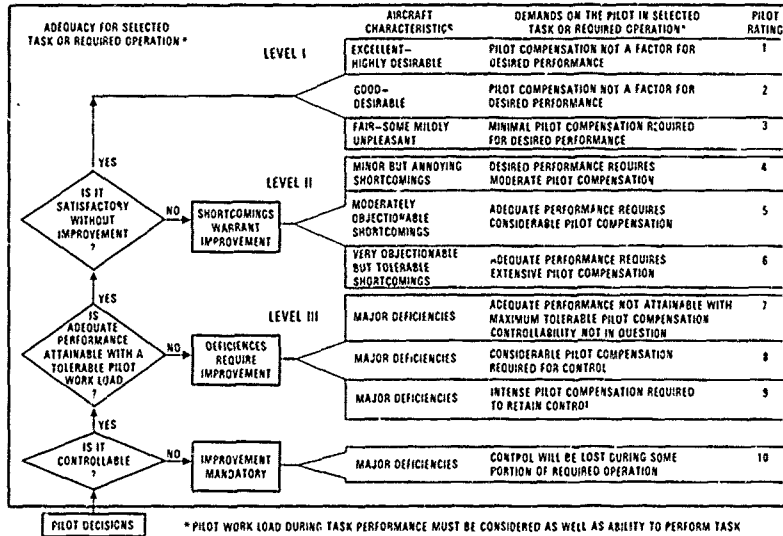
- NOMINAL SYSTEM 6 dB GAIN AND 30 DEGREE PHASE MARGINS
- OFF-NOMINAL * 4 dB GAIN AND 20 DEGREE PHASE MARGINS

FREQUENCIES > 6 HZ

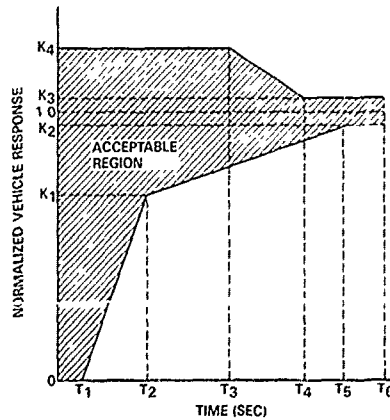
- NOMINAL SYSTEM 6 dB GAIN ATTENUATION
- OFF NOMINAL * 4 dB GAIN ATTENUATION

*THREE SIGMA ON ANY PARAMETER OR THREE SIGMA COMPOSITE (I.E. 1.5 SIGMA ON EACH PARAMETER IN WORST COMBINATION)

(a) Control Stability Margin Definitions



(b) Cooper-Harper Pilot Rating



(c) Normalized Step-Response Envelope

Figure 1. Entry FCS Design Requirements

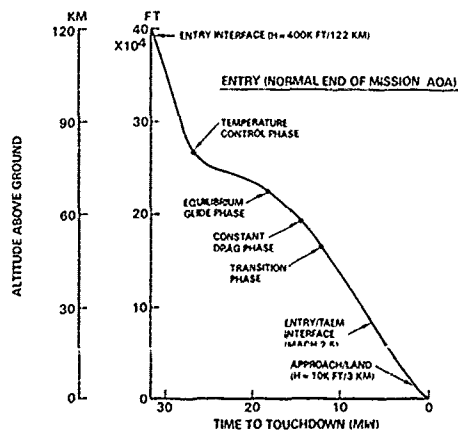
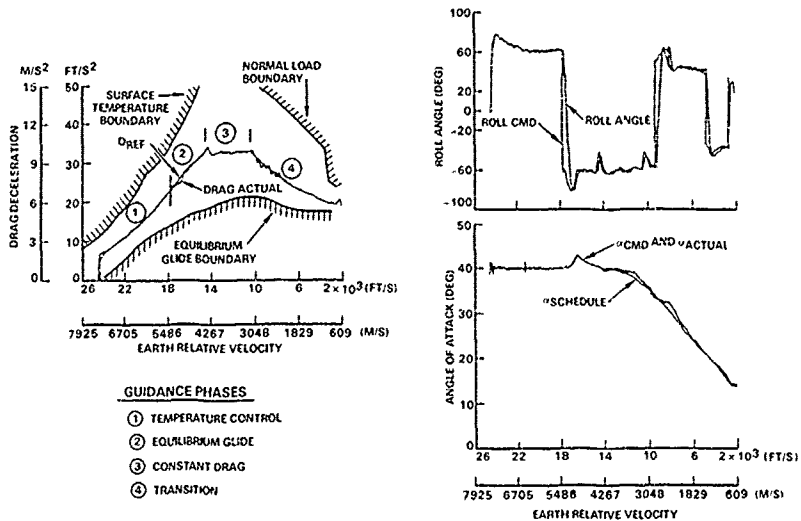
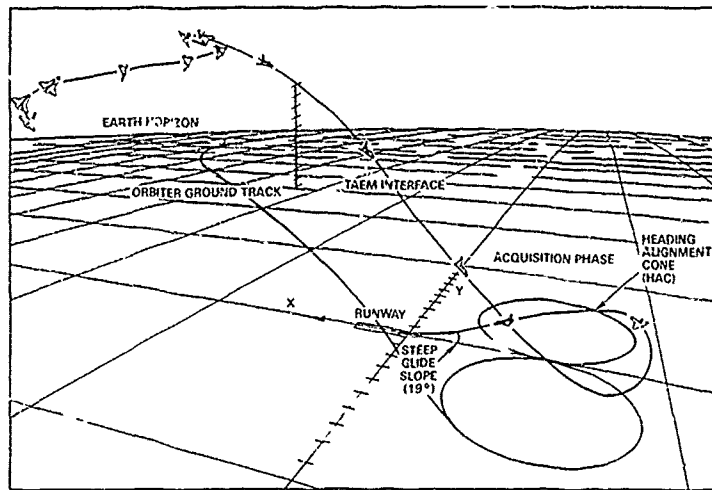
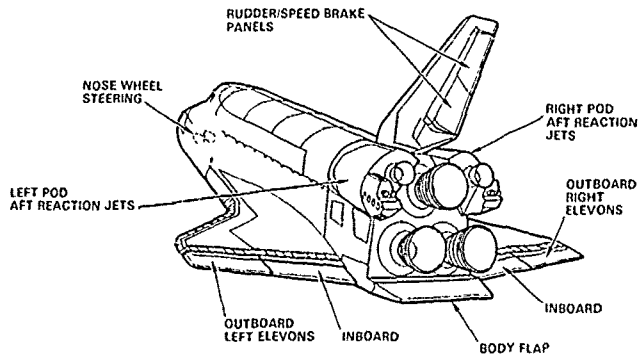
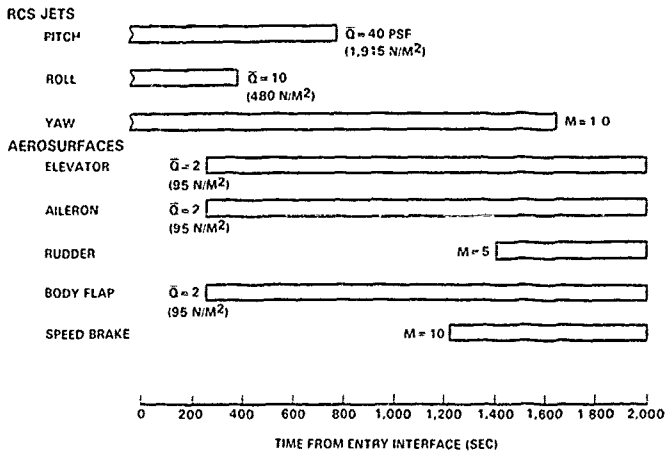


Figure 2. Typical Entry Flight Profile



(a) Flight Control Hardware Effector Elements



(b) Schedule for Use of Entry Flight Control Effectors

Figure 3. Entry Flight Control Effectors and Utilization Schedule

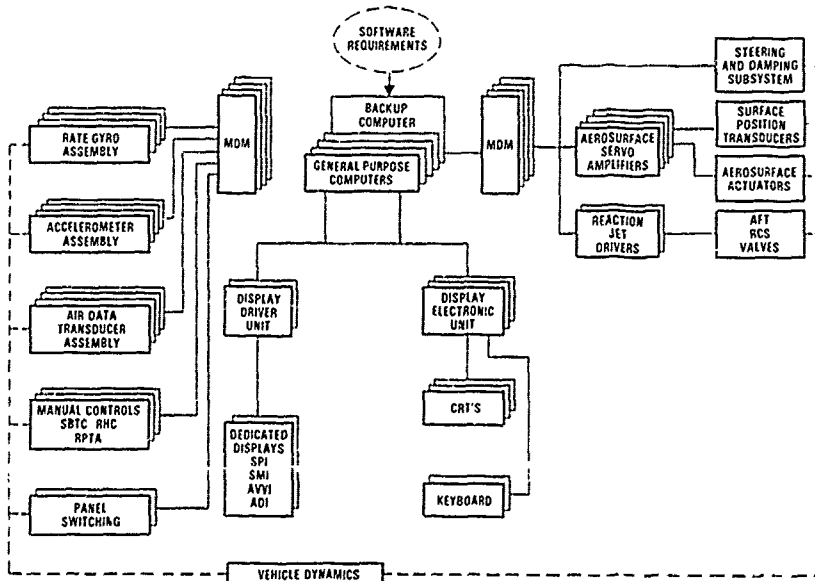


Figure 4. Entry Flight Control System

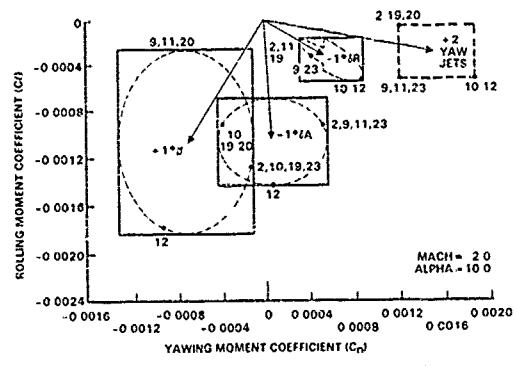


Figure 5. Lateral Aerodynamic Uncertainties

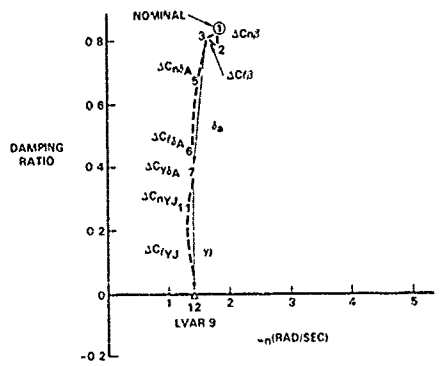
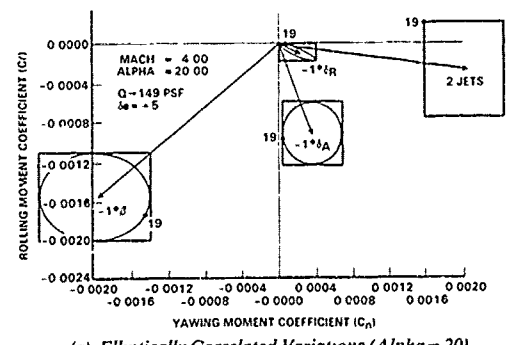
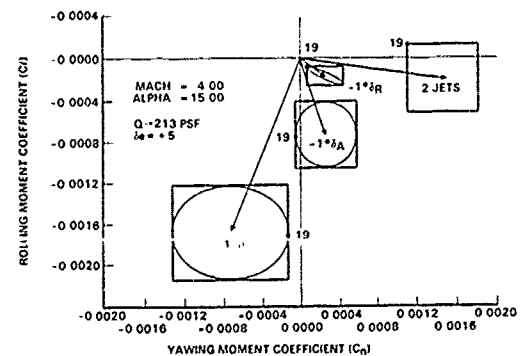


Figure 6. FCS Sensitivity to LVAR 9



(a) Elliptically Correlated Variations (Alpha = 20)



(b) Elliptically Correlated Variations (Alpha = 15)

Figure 7. Sensitivity of Aerodynamic Uncertainties to Alpha

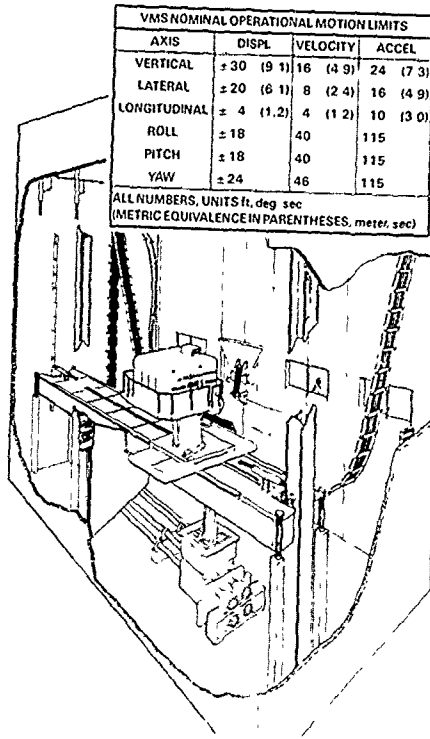


Figure 8. NASA Ames' Vertical Motion Simulator (VMS)

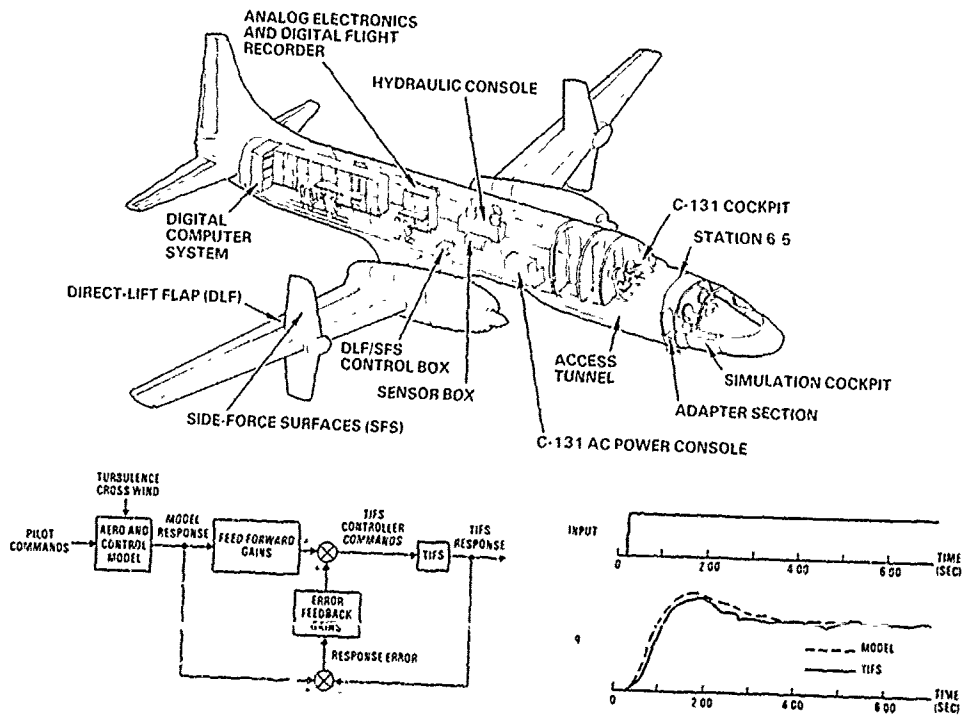


Figure 9. USAF's Total In-Flight Simulator (TIFS)

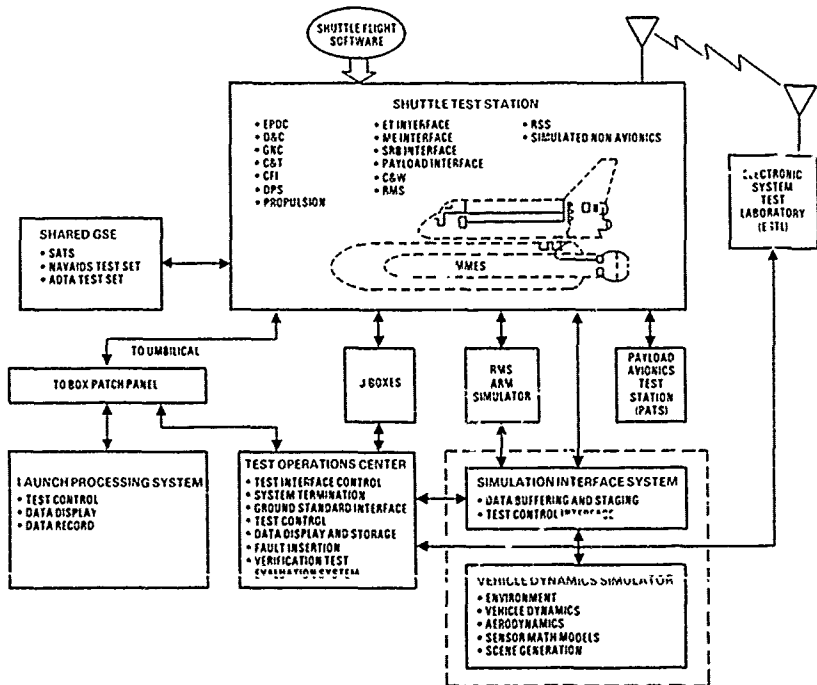
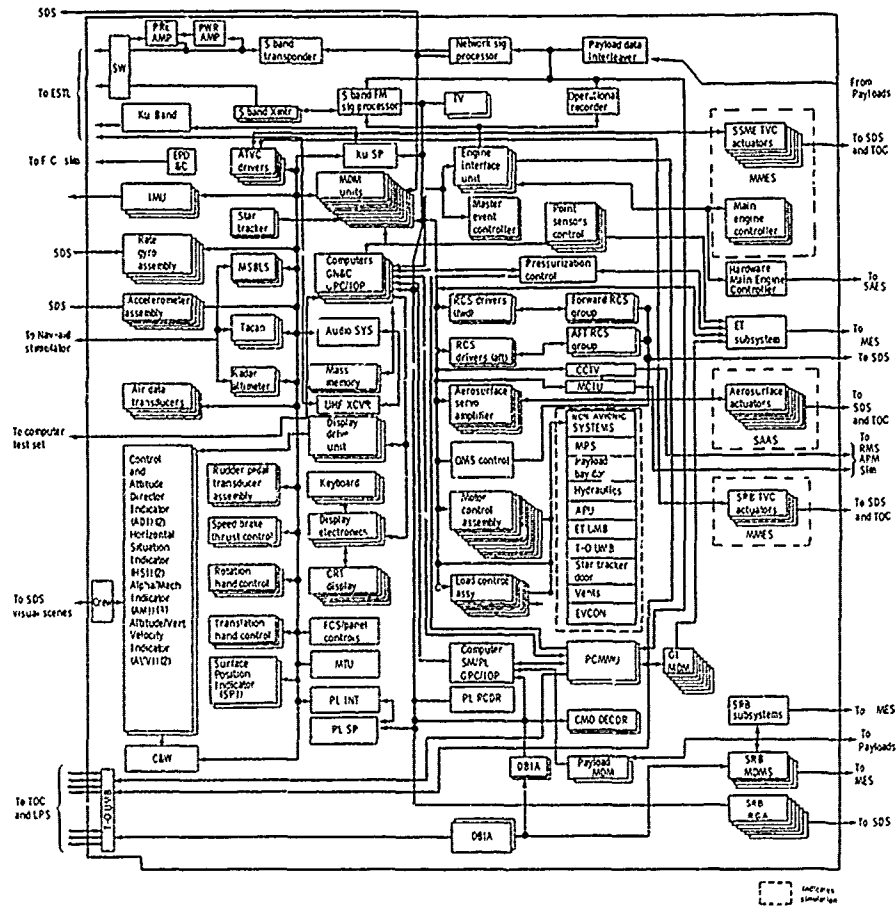
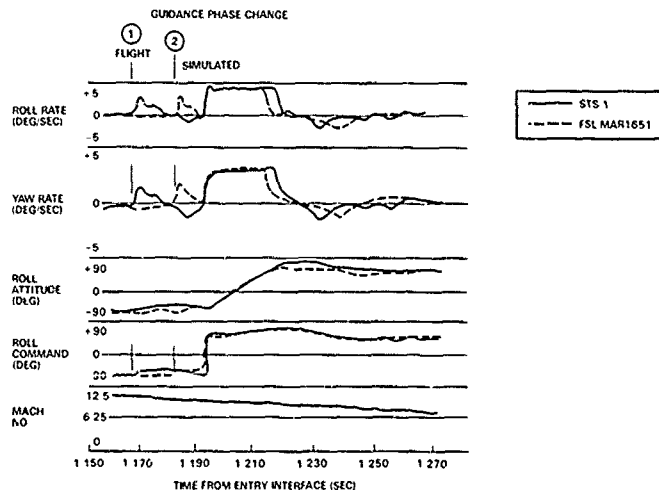
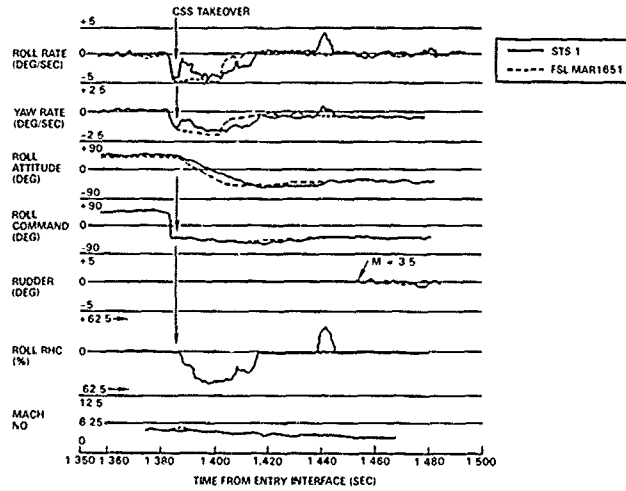


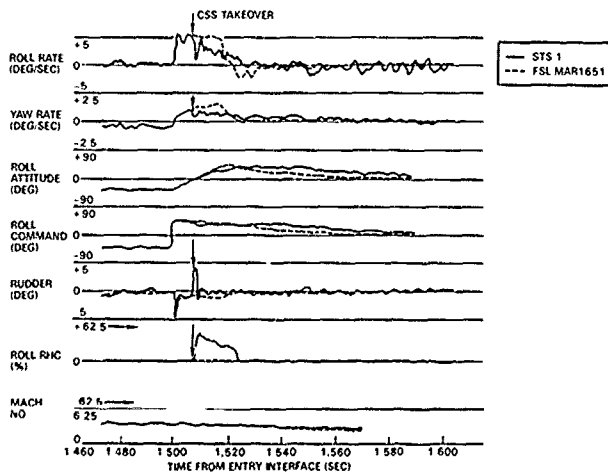
Figure 10. Overview of NASA's SAIL at JSC



(a) Second Roll Reversal



(b) Third Roll Reversal



(c) Fourth Roll Reversal

Figure 11. STS-1 Versus FSL Comparisons

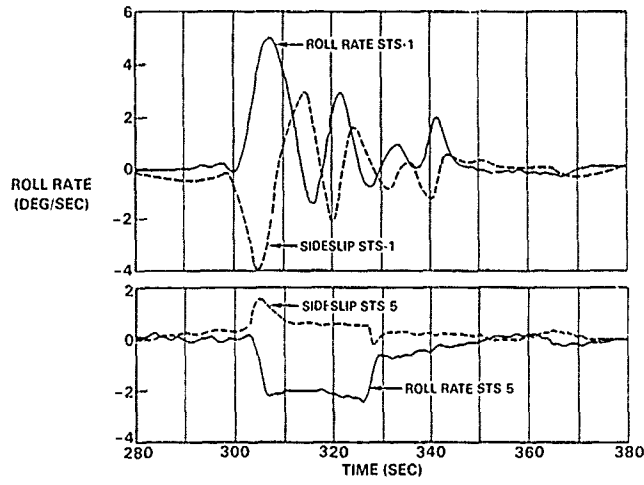


Figure 12. First Roll Maneuver. STS-1 Versus STS-5

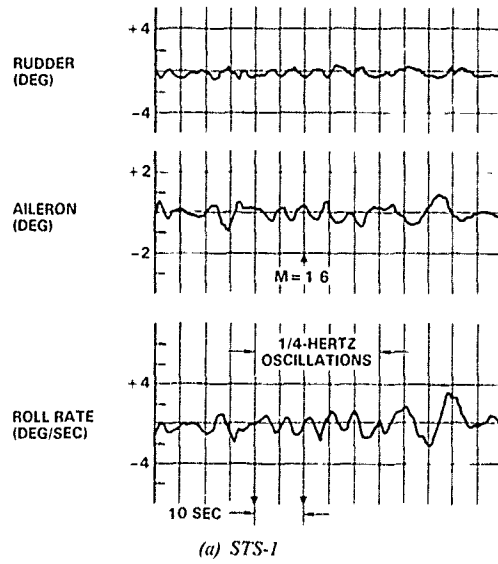
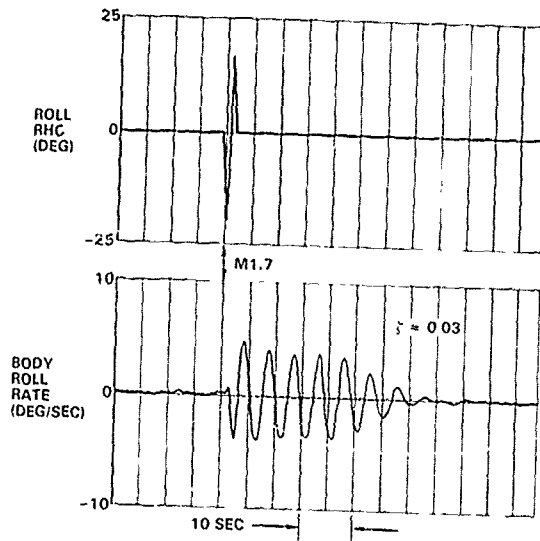
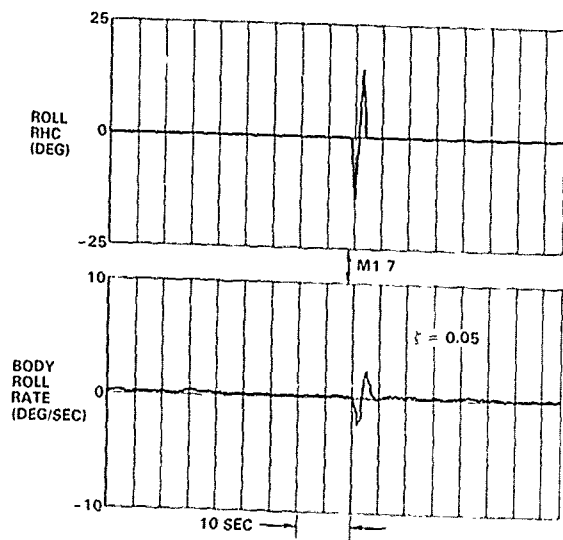


Figure 13. Quarter-Hertz Oscillations



(b) SES Simulation With Baseline FCS



(c) SES Simulation With Updated FCS

Figure 13 Quarter-Hull Oscillations (cont)

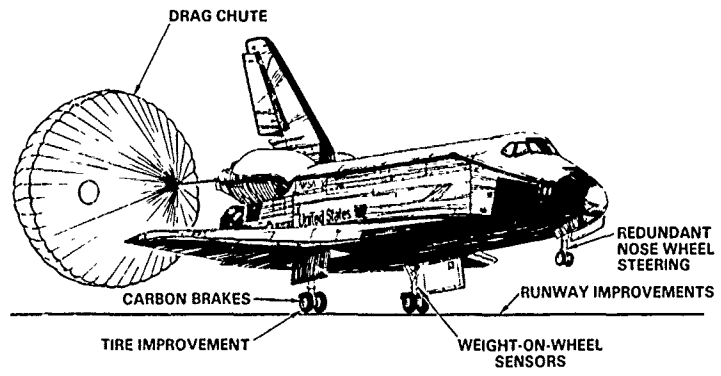


Figure 14. Landing/Roll-out Improvements

UNE INTRODUCTION AUX TRAJECTOIRES SPATIALES

par

J.-P. MAREC

Office National d'Etudes et de Recherches Aérospatiales (ONERA),
92320 Châtillon, France

RESUME

Cet exposé introductif à la Session sur les "Trajectoires" du Symposium "Space Vehicle Flight Mechanics" de l'AGARD/FMP (Luxembourg, 13-16 octobre 1989), est destiné à rappeler les notions de base de l'étude des trajectoires spatiales, naturelles et optimales, et à présenter les autres communications de la Session.

L'exposé est divisé en cinq parties.

Les trois premières parties rappellent les différents formalismes bien connus : newtonien, lagrangien et hamiltonien, et les appliquent, à titre comparatif, à la résolution d'un même problème, volontairement très simple mais essentiel, le problème des 2 corps.

Dans la première partie, le formalisme newtonien permet d'établir les formules de perturbations de Gauss, qui sont appliquées à l'étude des perturbations d'orbites dues au freinage atmosphérique.

Dans la deuxième partie, le formalisme lagrangien conduit aux formules de perturbations de Lagrange, qui sont utilisées pour étudier les perturbations d'orbites dues aux dissymétries du potentiel terrestre.

Dans la troisième partie, le formalisme hamiltonien permet d'obtenir les formules de perturbations anoniques et d'introduire la méthode de von Zeipel.

La quatrième partie souligne le lien entre la mécanique variationnelle et les méthodes modernes d'optimisation (Principe du Maximum de Contensou-Pontryagin).

Enfin, dans la cinquième partie, les méthodes d'optimisation sont appliquées à l'étude du problème des trajectoires spatiales optimales (transferts et rendez-vous optimaux, corrections optimales d'orbites, etc.).

INTRODUCTION

Lorsque la Commission de Mécanique du Vol de l'AGARD a envisagé d'organiser ce Symposium sur la "Mécanique du Vol des Véhicules Spatiaux", il est rapidement apparu qu'une des difficultés serait d'introduire convenablement le sujet auprès d'un auditoire dont au moins une partie risquait d'être peu familiarisée avec ce thème. En effet, l'intérêt de la communauté AGARD a été, dans le passé, plus orienté vers l'aéronautique et les missiles que vers l'espace.

Aussi a-t-il été décidé de faire précéder certaines sessions d'un exposé introductif, destiné à rappeler aussi simplement que possible les notions de base et à présenter les autres communications.

C'est le but du présent exposé, en ce qui concerne les trajectoires spatiales, naturelles et optimales.

Les théories de la Mécanique Céleste, des perturbations d'orbites des satellites artificiels, des transferts et rendez-vous optimaux, peuvent paraître assez éloignées des préoccupations d'un spécialiste de la mécanique du vol des avions et des missiles. Il découvrira cependant très vite, au cours de cet exposé, que les concepts utilisés lui sont plus familiers qu'il ne pouvait le croire et que l'extension de son domaine d'intérêt à l'espace est plus facile qu'il ne le pensait.

Il est alors possible d'espérer que ce symposium ne restera pas un cas isolé et que la Commission de Mécanique du Vol de l'AGARD pourra, après ce colloque à caractère général, envisager des symposiums plus spécialisés, sur des thèmes spatiaux, vraisemblablement en coopération avec d'autres Commissions comme celles de la Dynamique des Fluides, des Structures et Matériaux, de la Propulsion et Energétique, du Guidage et de la Commande etc.

D'après ce qui vient d'être dit, on comprendra que l'originalité de cette communication ne résidera pas dans les résultats présentés, qui sont très classiques pour les astrodynamiciens, mais peut-être, tout au plus, dans la manière d'introduire les différents concepts (Fig. 1). En particulier, l'accent sera mis sur le lien qui existe entre la Mécanique Analytique Variationnelle bien connue et les théories modernes d'optimisation comme le Principe du Maximum de Contensou-Pontryagin.

On évitera soigneusement d'aller trop loin dans l'abstraction et les développements mathématiques. Rappelons cependant que la Mécanique Analytique et la Mécanique Céleste viennent de bénéficier d'éclairages nouveaux apportés, en particulier, par les théories de la Géométrie Différentielle (variétés symplectiques, groupes de Lie), des Systèmes Dynamiques et des Développements Asymptotiques.

Il est demandé au lecteur spécialiste d'Astrodynamique de bien vouloir excuser un exposé aussi élémentaire, qui présente peut-être l'avantage de rassembler, de façon condensée, quelques résultats classiques importants. Pour plus de détails, voir, par exemple, les références [1] et [2].

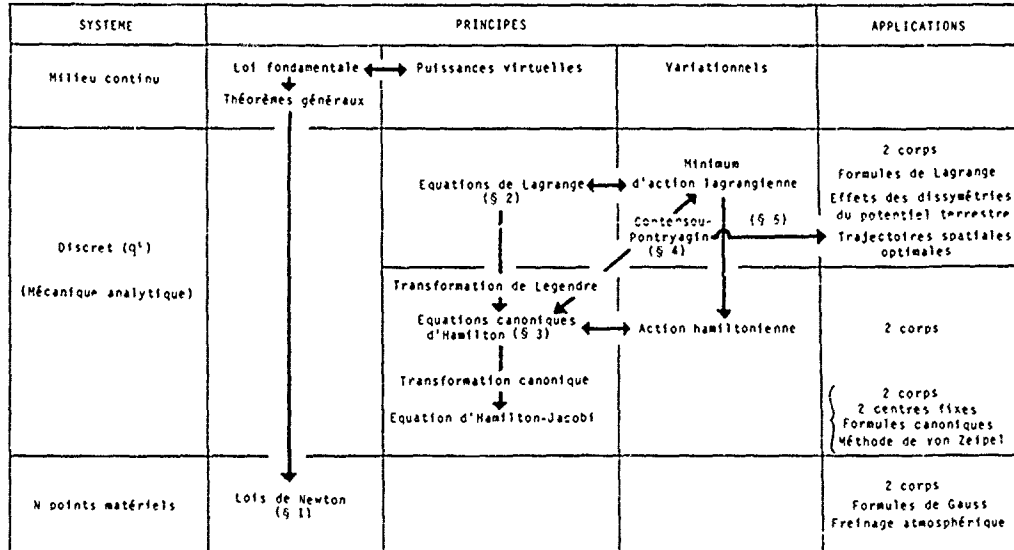


Figure 1

L'exposé est divisé en cinq parties (Fig. 1).

Les trois premières parties rappellent les différents formalismes bien connus : newtonien, lagrangien et hamiltonien, dans l'ordre d'abstraction croissante. Il a paru intéressant, à titre d'illustration comparative, d'appliquer ces différents formalismes à la résolution d'un même problème, volontairement très simple, mais cependant essentiel, le problème des 2 corps. Il apparaîtra que, dans ce cas trivial, le formalisme le plus abstrait n'est pas nécessairement le plus commode ! L'intérêt des méthodes les plus élaborées doit être recherché plutôt dans leur capacité de permettre la résolution des problèmes difficilement solubles - voire insolubles - autrement (par exemple : le problème des deux centres fixes), et de faciliter grandement l'étude des mouvements perturbés, en particulier de préciser la structure des solutions et le comportement à long terme.

Plus spécifiquement, la 1ère partie est consacrée au formalisme newtonien, appliqué à l'étude des systèmes de N points matériels. Ce formalisme permet de traiter de façon particulièrement simple le problème des deux corps, d'établir les formules de perturbations, dites de Gauss, et de les appliquer à l'étude des perturbations d'orbites dues au freinage atmosphérique.

Les deux parties suivantes traitent, plus généralement, des systèmes matériels discrets, tels que toute configuration à l'instant t puisse être définie par la donnée d'un nombre fini n de paramètres q^i .

La 2ème partie est ainsi consacrée au formalisme lagrangien, qui permet d'établir les formules de perturbations de Lagrange et de les appliquer à l'étude des perturbations d'orbites dues aux dissymétries du potentiel terrestre.

La 3ème partie introduit le formalisme hamiltonien, dont un des avantages majeurs est de faciliter les changements de variables par utilisation des transformations canoniques. Ces transformations permettent, d'une part, d'introduire une nouvelle méthode d'intégration, dite de Jacobi, appliquée à la résolution du problème des deux centres fixes et à l'écriture des formules de perturbations canoniques, et, d'autre part, de définir une méthode de résolution systématique, par approximations successives, des équations de perturbations : la méthode de von Zeipel.

La 4ème partie souligne le lien qui existe entre la Mécanique Variationnelle et les méthodes modernes d'Optimisation (Principe du Maximum de Contensou-Pontryagin).

Enfin, dans la 5ème partie, les méthodes d'optimisation sont appliquées à l'étude du problème des trajectoires spatiales optimales : définition d'un transfert optimal ; modélisation des systèmes de propulsion ; application de l'optimisation paramétrique aux transferts impulsions, en particulier dans le cas simple du transfert de Hohmann ; transferts optimaux dans un champ de gravitation général ; cas particuliers d'un champ de gravitation uniforme et d'un champ central. Des exemples sont donnés de corrections optimales d'orbites, de transferts de durée indifférente et de transferts à poussée faible.

1 - FORMALISME NEWTONIEN

1.1 - Mécanique newtonienne

La mécanique newtonienne a pour objet l'étude du mouvement des systèmes matériels discrets constitués d'un nombre fini N de points matériels M_p , de masses m_p ($p = 1, 2, \dots, N$).

La loi fondamentale de la dynamique (Fig. 1) se traduit par les lois de Newton, que nous n'expliciterons pas.

Dans le cas où les actions mutuelles entre M_p et M_q sont des attractions newtoniennes :

$$\vec{F}_{pq} = -\vec{F}_{qp} = -k \frac{m_p m_q}{\|M_p M_q\|^3} \overrightarrow{M_p M_q} \quad (1)$$

où k est la constante de la gravitation, on est conduit au problème des N corps de la Mécanique Céleste.

L'application des lois de Newton permettrait d'obtenir quelques résultats généraux concernant ce problème (intégrales premières, par exemple) ou, dans le cas $N=3$, de tirer déjà certaines conclusions intéressantes relatives au célèbre problème des 3 corps (figures d'équilibre relatif, courbes de Hill, par exemple), problème qui suscite actuellement un regain d'intérêt (théorie des Systèmes Dynamiques).

Mais il paraît plus intéressant de passer sans tarder à l'étude, triviale mais fondamentale, du problème des 2 corps, qui présente l'avantage d'être intégrable et qui servira de base à l'analyse des perturbations d'orbites des satellites artificiels. Cela nous permettra, au passage, de rappeler quelques notations utilisées en Mécanique Céleste et dont la connaissance est indispensable à la compréhension des exposés sur le sujet.

1.2 - Problème des 2 corps

L'étude du problème des 2 corps est très importante, car il est fréquent que la résolution d'un problème de N corps puisse être ramenée, en première approximation et avec une bonne précision, à la résolution d'un problème de 2 corps (cas du mouvement d'un satellite proche de la Terre), ou de plusieurs problèmes de 2 corps (cas du mouvement des planètes autour du Soleil), ou encore de la succession de problèmes de 2 corps (cas du mouvement héliocentrique et des mouvements planétocentriques d'une sonde interplanétaire).

De plus, comme nous l'avons dit, le problème des 2 corps étant complètement intégrable, sa solution sert de solution de base pour résoudre des problèmes plus compliqués (théorie des perturbations).

1.2.1 - Mouvements absolu et relatif de 2 corps

Les corps M_1 (de masse m_1) et M_2 (de masse m_2) sont supposés ponctuels (ou, du moins, à symétrie matérielle sphérique) et isolés dans l'espace (Fig. 2).

Le centre de masse G a un mouvement rectiligne et uniforme dans l'espace absolu et peut donc être choisi comme centre d'un système d'axes galiléens $Gx'y'z'$.

La loi fondamentale de la dynamique :

$$\vec{F} = m \vec{r} \quad (1)$$

appliquée successivement aux points matériels M_1 et M_2 , peut être écrite, dans ce système :

$$\frac{d^2 \vec{G} M_1}{dt^2} = k m_2 \frac{\overrightarrow{M_1 M_2}}{\|M_1 M_2\|^3}, \quad (2)$$

$$\frac{d^2 \vec{G} M_2}{dt^2} = -k m_1 \frac{\overrightarrow{M_2 M_1}}{\|M_2 M_1\|^3}. \quad (3)$$

G étant le centre de masse, on a :

$$m_1 \vec{G} M_1 + m_2 \vec{G} M_2 = \vec{0}, \quad (4)$$

d'où :

$$\overrightarrow{M_1 M_2} = \vec{G} M_2 - \vec{G} M_1 = -\frac{m_1 + m_2}{m_2} \vec{G} M_1 = \frac{m_1 + m_2}{m_1} \vec{G} M_2, \quad (5)$$

et finalement :

$$\frac{d^2 \vec{G} M_1}{dt^2} = -k \frac{m_2^3}{(m_1 + m_2)^2} \frac{\overrightarrow{G} M_1}{\|G M_1\|^3}, \quad (6)$$

$$\frac{d^2 \vec{G} M_2}{dt^2} = -k \frac{m_1^3}{(m_1 + m_2)^2} \frac{\overrightarrow{G} M_2}{\|G M_2\|^3}. \quad (7)$$

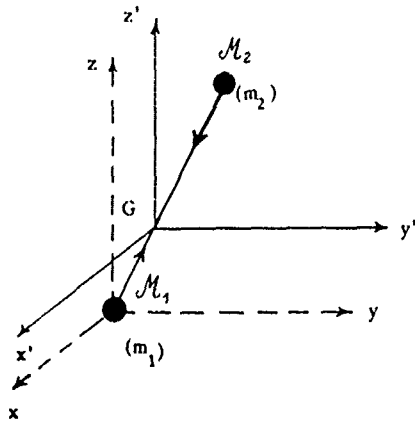


Figure 2

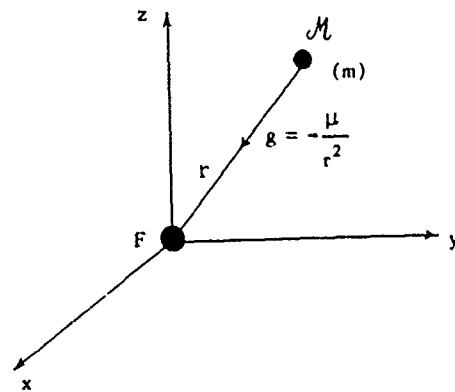


Figure 3

En pratique, les observations ne peuvent pas être faites depuis le centre de masse G des deux corps, mais plutôt depuis l'un des corps, M_1 par exemple. Il est donc souvent commode de rapporter le mouvement relatif de M_2 par rapport à M_1 à des axes non galiléens $x'y'z'$ (Fig. 2), centrés en M_1 et parallèles aux axes galiléens $x'y'z'$.

La différence (3) - (2) peut être écrite :

$$\frac{d^2 \overrightarrow{M_1 M_2}}{dt^2} = -k(m_1 + m_2) \frac{\overrightarrow{M_1 M_2}}{\| \overrightarrow{M_1 M_2} \|^3} \quad (8)$$

Les relations (6) et (7) montrent que, dans le mouvement absolu, tout se passe comme si chaque corps était attiré par le centre de masse G où serait concentrée la masse :

$$m' = \frac{\mu^3}{(m+M)^2} \quad (9)$$

où m est la masse du corps étudié et M celle de l'autre corps.

De même, la relation (8) montre que, dans le mouvement relatif, tout se passe comme si le corps étudié, de masse m , était attiré par une masse :

$$m'' = M + m \quad (10)$$

égale à la somme des masses M et m des deux corps.

Comme le montre (5), les mouvements absolu et relatif sont homothétiques. Il suffit donc d'étudier l'un des mouvements.

On pose :

$$\mu = \begin{cases} k m' = k M^3 / (m+M)^2 & \text{(mouvement absolu),} \\ k m'' = k (M+m) & \text{(mouvement relatif).} \end{cases} \quad (11)$$

Notons que si $m \ll M$ (c'est le cas pour le mouvement d'un satellite artificiel de la Terre), ces deux mouvements sont (pratiquement) identiques.

1.2.2 - Intégration élémentaire du problème des 2 corps - Trajectoires képlériennes

L'intégration du problème des 2 corps est triviale. Elle est rappelée ici essentiellement pour fixer les notations. Les appellations géocentriques seront utilisées, de préférence aux appellations héliocentriques, puisqu'on s'intéresse ici surtout au mouvement des mobiles circumterrestres.

Soit à étudier, dans les axes $Fxyz$ parallèles aux axes absolus (Fig. 3 ; F est mis pour "foyer", ce qui sera justifié par la suite), le mouvement du point M , de masse m , soumis à l'accélération de gravitation :

$$\ddot{\vec{r}} = -\mu \frac{\vec{r}}{r^3}, \quad (12)$$

où μ a la valeur (11).

Dans le cas du mouvement d'un mobile circumterrestre, Fxy est généralement le plan équatorial et Fz l'axe des pôles. Fz est orienté vers le point vernal γ .

La loi fondamentale de la dynamique s'écrit simplement :

$$\vec{r}'' = \vec{g} \quad (13)$$

et conduit au système différentiel d'ordre 6 :

$$\frac{d^2 \vec{r}}{dt^2} = -\mu \frac{\vec{r}}{r^3}, \quad (14)$$

dont la résolution nécessite 6 intégrations scalaires, qui introduisent 6 constantes d'intégrations scalaires appelées "éléments orbitaux".

L'intégration est facilitée par l'existence de trois intégrales premières (vectorielles ou scalaires ; au total : 5 intégrales premières scalaires), dont les deux premières sont très connues ; la troisième est peut-être moins bien connue, elle n'en est pas moins très utile.

* L'intégrale première vectorielle du moment cinétique (massique) :

$$\vec{r} \wedge \vec{V}' = \vec{h} = \text{vecteur constant} \quad (= \vec{r}_0 \wedge \vec{V}_0) \quad (15)$$

équivalent à 3 intégrales premières scalaires.

Le mouvement est donc soit rectiligne :

$$\vec{r} \wedge \vec{V}' = \vec{h} = \vec{0} \quad (16)$$

(cas étudié à part), soit plan, dans le plan perpendiculaire à \vec{h} (plan orbital, Fig. 4), repéré soit par le vecteur orientation, unitaire :

$$\vec{t} = \vec{h} / h \quad (h = \|\vec{h}\|), \quad (17)$$

soit par les deux angles :

$$i = (Fz, \vec{h}) \in [0^\circ, 180^\circ] \quad (\text{inclinaison}) \quad (18)$$

et

$$\Omega = (Fx, Fx_1) \in [0^\circ, 360^\circ] \quad (\text{ascension droite du noeud ascendant } N), \quad (19)$$

ce qui ne représente, dans les deux cas, que 2 constantes d'intégration scalaires.

Fx_1 est la ligne des noeuds, orientée vers le noeud ascendant N , c'est-à-dire de façon telle que le trièdre (Fz, \vec{h}, Fx_1) soit direct.

$\mathcal{M}XYZ$ sont les axes orbitaux tournants ($\mathcal{M}X$: radial ; $\mathcal{M}Y$: circonférentiel, dans le plan orbital ; $\mathcal{M}Z$: perpendiculaire au plan orbital, donc parallèle à \vec{h} et \vec{t}).

Dans le plan orbital,

$$r V \cos \gamma = r^2 \frac{d\theta}{dt} = 2 \frac{dA}{dt} = 2 \quad (\text{vitesse aréolaire}) = h = \text{constante} \quad (= r_0 v_0 \cos \gamma_0). \quad (20)$$

C'est l'intégrale première de la loi des aires, qui introduit la troisième constante d'intégration scalaire h . En des temps égaux, les aires A balayées par le rayon vecteur \vec{r} sont égales. Cette deuxième loi de Kepler a été historiquement énoncée pour les planètes, avec F = Soleil.

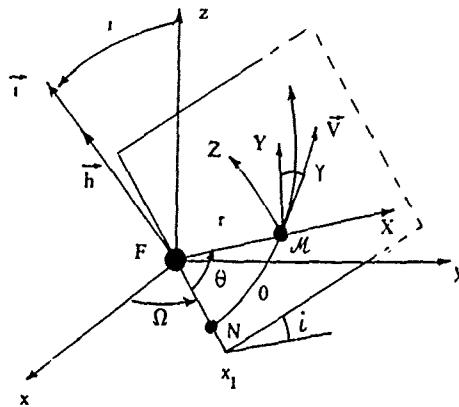


Figure 4

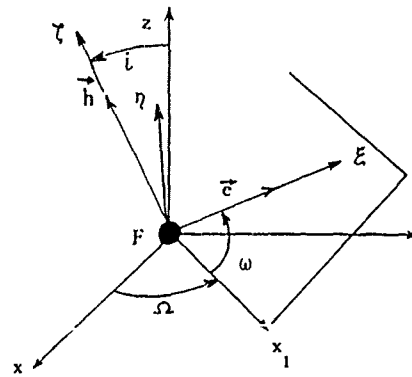


Figure 5

* L'intégrale première de l'énergie fait intervenir le potentiel newtonien massique :

$$V = -\mu/r \tag{21}$$

et s'écrit :

$$T + V = \frac{v^2}{2} - \frac{\mu}{r} = \text{constante} = \mathcal{E} \left(= \frac{v_0^2}{2} - \frac{\mu}{r_0} \right), \tag{22}$$

où T est l'énergie cinétique massique, ce qui introduit une quatrième constante d'intégration scalaire, l'énergie totale massique \mathcal{E} , indépendante de l'orientation de la vitesse initiale v_0 . Dans un mouvement donné (\mathcal{E} fixe), la grandeur V de la vitesse ne dépend que de la distance r au centre d'attraction.

* L'intégrale première vectorielle de Laplace :

$$\nabla \wedge \vec{h} - \mu \frac{\vec{r}}{r^3} = \text{vecteur constant} = \mu \vec{e} \left(= v_0 \wedge \vec{h} - \mu \frac{\vec{r}_0}{r_0^3} \right), \tag{23}$$

moins connue, équivaut à trois intégrales premières scalaires (e est mis pour "excentricité", ce qui sera justifié par la suite).

A la différence de l'intégrale première du moment cinétique \vec{h} (valable pour tout champ central) ou de celle de l'énergie \mathcal{E} (qui peut être étendue à tout champ central du type $1/r^2$), l'intégrale de Laplace \vec{e} n'est valable que pour un champ central en $1/r^2$.

Les 7 intégrales premières scalaires citées ne sont pas indépendantes : 5 seulement sont distinctes. En effet, on a les 2 relations scalaires suivantes, comme on le vérifie aisément :

$$\vec{h} \cdot \vec{e} = 0, \tag{24}$$

$$\vec{e}^2 = 1 + 2 \frac{\mathcal{E} h^2}{\mu^2}. \tag{25}$$

L'obtention de l'intégrale de Laplace ne nécessite donc, en fait, qu'une intégration supplémentaire (cinquième intégration) et n'introduit qu'une constante d'intégration supplémentaire (cinquième constante), l'argument du périhélie ω (Fig. 5), qui repère le vecteur \vec{e} (ou encore l'axe $F\xi$ dirigé suivant \vec{e}) dans le plan orbital.

Si $\vec{e} = \vec{0}$ (2 relations scalaires, car on sait déjà par (24) que $\mathcal{E} = 0$), ω est indéterminé. Ce cas (mouvement circulaire) est étudié à part.

Le mouvement est étudié maintenant dans les axes orbitaux $F\xi\eta\zeta$ orthogonaux, où $F\xi$ est perpendiculaire au plan orbital (Fig. 5).

Les angles Ω , i et ω apparaissent donc comme les angles d'Euler qui permettent de repérer le trièdre orbital $F\xi\eta\zeta$ par rapport au trièdre absolu $Fx_1y_1z_1$.

La trajectoire peut être obtenue, à l'aide de (23) et de (15), sans nouvelle intégration. Son équation polaire est :

$$r = \frac{p}{1 + e \cos v} \tag{26}$$

où $e = \|\vec{e}\|$, et où $v = (\vec{e}, \vec{r}) = (\vec{\xi}, \vec{r})$ est l'anomalie vraie (Fig. 6).

La trajectoire est donc une conique de foyer F (première loi de Képler, énoncée historiquement pour les planètes dans le cas $F = \text{Soleil}$), de grand axe $F\xi$ (\vec{e} est dirigé vers le périhélie P), d'excentricité e et de paramètre :

$$p = h^2 / \mu, \tag{27}$$

qui ne dépend que de la grandeur h du moment cinétique.

Le vecteur \vec{e} est appelé vecteur excentricité ou vecteur périhélie.

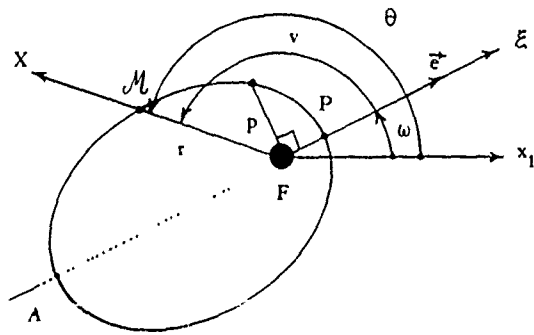


Figure 6

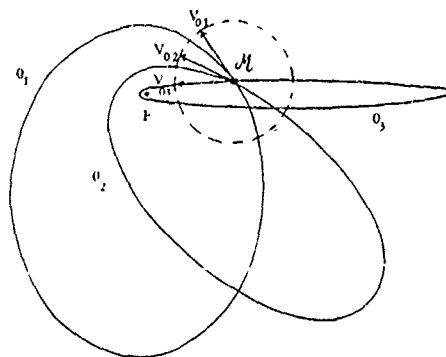


Figure 7

La relation (25) montre que la trajectoire est une ellipse ($e < 1$) ou une hyperbole ($e > 1$) selon que l'énergie \mathcal{E} est ≤ 0 . Le cas $e = 1$ correspond soit à une parabole, si $\mathcal{E} = 0$ (1 relation scalaire), soit à une conique plate (mouvement rectiligne déjà cité), si $\mathcal{K} = 0$ (2 relations scalaires seulement, à cause de (24)), c'est-à-dire une ellipse plate, si $\mathcal{E} < 0$, ou une hyperbole plate, si $\mathcal{E} > 0$.

Le demi-grand axe a de l'orbite est donné par :

$$a = \frac{P}{|1-e^2|} = \frac{\mu}{2|\mathcal{E}|} > 0. \quad (28)$$

Dans le cas elliptique, on a :

$$p = a(1-e^2), \quad (29)$$

$$a = -\mu / 2\mathcal{E}. \quad (30)$$

Le demi-grand axe ne dépend que de l'énergie de l'orbite. Il ne dépend donc pas de l'orientation de la vitesse initiale (Fig. 7).

Le demi-petit axe est :

$$b = a\sqrt{1-e^2}. \quad (31)$$

La détermination de la loi horaire $v(t)$ nécessite la sixième et dernière intégration scalaire et introduit la sixième et dernière constante d'intégration scalaire \mathcal{C} , instant de passage au périhélie. Elle est donnée, dans le cas elliptique, par les équations :

$$M = n(t - \mathcal{C}), \quad (32)$$

$$M = E - e \sin E, \quad (33)$$

$$\operatorname{tg} \frac{v}{2} = \sqrt{\frac{1+e}{1-e}} \operatorname{tg} \frac{E}{2}, \quad (34)$$

où M est l'anomalie moyenne, n est le moyen mouvement, tel que :

$$n^2 a^3 = \mu \quad (\text{donc } h = n a b), \quad (35)$$

et E est l'anomalie excentrique (voir Fig. 8).

La période orbitale est :

$$T = \frac{2\pi}{n} = 2\pi \sqrt{a^3/\mu}. \quad (36)$$

C'est la troisième loi de Képler*, énoncée historiquement pour les planètes dans le cas $F = \text{Soleil}$.

La quantité :

$$M_0 = -n\mathcal{C} \quad (37)$$

(anomalie moyenne pour $t = 0$) est appelée anomalie moyenne de l'époque.

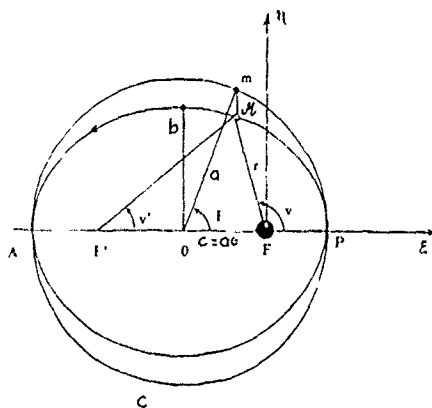


Figure 8

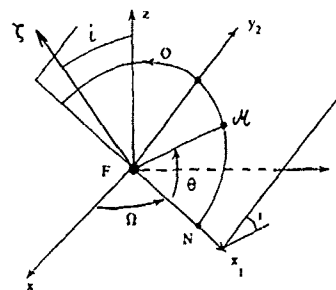


Figure 9

* Notons que la 3ème loi de Kepler "les carrés de périodes des mouvements des planètes sont proportionnels aux cubes des demi-grands axes de leurs orbites" n'est qu'approchée, car si M désigne la masse du Soleil et m la masse de la planète, le coefficient $\mu = k(M+m)$ varie quand on passe d'une planète à l'autre. Comme la valeur maximum du rapport m/M , obtenue par Jupiter, n'est que de l'ordre du millième, elle constitue néanmoins une bonne approximation.

Lorsque $T = 1$ jour sidéral, l'orbite est dite géosynchrone. Un exemple en est donné dans l'exposé [3]. Si, de plus, elle est circulaire et dans le plan équatorial, le satellite est géostationnaire.

Les relations (32) - (34) permettent de calculer aisément l'instant de passage à une position ν donnée. Le problème inverse (calcul de ν à t donné) est plus délicat, car il exige la résolution de l'équation (33), transcendante en E , ce qui se faisait jadis à l'aide de développements en séries ou de tables, et qui est maintenant grandement facilité par l'utilisation des calculateurs numériques.

Disons maintenant quelques mots des mouvements particuliers :

* Le mouvement circulaire ($e = 0$) (Fig. 9) est un cas particulier du mouvement elliptique, le périhélie P et les angles ν (et donc E et M) sont indéterminés, mais la somme $\theta = \omega + \nu$ (argument) est bien définie. Le mouvement est étudié dans les axes Fx_1y_2z . C'est un mouvement circulaire uniforme :

$$\theta = n(t - t_N), \quad (38)$$

où t_N est l'instant de passage au noeud ascendant. La vitesse orbitale circulaire C à la distance a est donnée par (22), où $\mu = \text{constante} = a$, et (30), d'où :

$$C(a) = \sqrt{\mu/a}. \quad (39)$$

Elle décroît comme l'inverse de la racine carrée du rayon de l'orbite circulaire.

Par exemple, dans le cas de satellites circumterrestres, on a le Tableau 1.

Tableau 1

Type de satellite	Altitude z	Rayon de l'orbite circulaire a	Période de révolution (en temps solaire moyen) T	Vitesse orbitale circulaire C
Satellite "rasant" (physiquement impossible à cause de l'atmosphère) (Terre sphérique)	0	6 371 km	84,5 mn	7,9 km/s
Satellite "bas" (Terre sphérique)	300 km	6 671 km	90 mn	7,75 km/s
Satellite équatorial "géostationnaire" (Terre aplatie)	35 786 km	42 164 km	23 h 56 mn 4,1 s (24 h sidérales)	3,075 km/s
Lune ☾ (pour mémoire, en supposant l'orbite circulaire)		384 400 km	27 ; 7 h 43 mn 11,5 s	1,017 km/s

* Pour le mouvement parabolique ($\mathcal{E} = 0 \Rightarrow e = 1$), on notera seulement que la vitesse L , dite parabolique ou de libération (Fig. 10), est donnée en tout point par (22), d'où :

$$L(r) = \sqrt{2\mu/r} = \sqrt{2} C(r). \quad (40)$$

Remarquons que la relation (22) peut être écrite, quelle que soit la nature du mouvement :

$$V^2 - L^2 = \text{constante} = 2E (= V_0^2 - L_0^2). \quad (41)$$

* Pour le mouvement hyperbolique ($\mathcal{E} > 0 \Leftrightarrow e > 1$), on notera seulement que la vitesse résiduelle V_∞ à l'infini du centre d'attraction (Fig. 11) peut être obtenue en faisant $r \rightarrow +\infty$, donc $L \rightarrow 0$, dans (41), d'où :

$$V_\infty = \sqrt{V_0^2 - L_0^2} (= \sqrt{V^2 - L^2}, \text{ en fonction du point courant}). \quad (42)$$

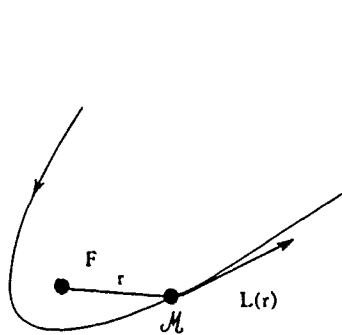


Figure 10

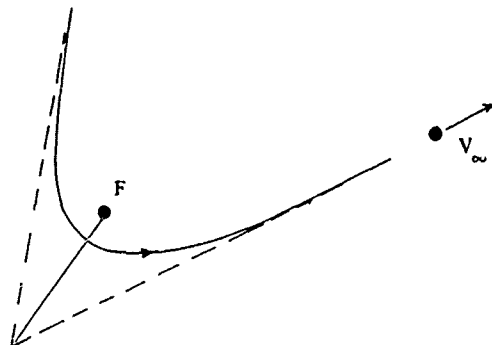


Figure 11

1.2.3 - Éléments orbitaux

Comme on l'a dit plus haut, on appelle éléments orbitaux les 6 constantes d'intégration q_j ($j = 1, 2, \dots, 6$) qui définissent un mouvement képlérien particulier. Ce nombre est réduit à 5 dans le cas parabolique (1 relation scalaire : $\mathcal{E} = 0$) et à 4 dans les cas circulaire (2 relations scalaires : $e_{x_1} = e_{y_2} = 0$; Fig.9) et rectiligne.

Dans le cas elliptique, il est possible de choisir pour éléments orbitaux $(a, e, i, \Omega, \omega, \tau)$ ou $(a, e, i, M_0, \omega, M_0)$. Le sixième élément est souvent remplacé par l'anomalie moyenne M , qui n'est pas une constante du mouvement képlérien, mais varie simplement (de façon affine) en fonction du temps et présente l'avantage de fixer directement la position du mobile sur l'orbite. On obtient alors les éléments orbitaux de Lagrange $(a, e, i, \Omega, \omega, M)$.

Les éléments orbitaux précédents ne sont pas bien adaptés au(x) cas des petites excentricités et/ou des petites inclinaisons.

En effet, lorsque $e \approx 0$, la position du périhélie P est mal définie, les angles ω, M et M_0 sont mal déterminés, et il est préférable de remplacer la donnée de e, ω et M (ou M_0) par celle de $e_{x_1} = e \cos \omega, e_{y_2} = e \sin \omega$ et $\omega + M$ (ou $\omega + M_0$) (argument moyen ou argument moyen de l'époque).

De même, lorsque $i \approx 0$, la position de la ligne des noeuds F_{x_1} est mal définie, les angles i, Ω et ω sont mal déterminés, et il est préférable de remplacer la donnée de i, Ω et ω , par celle de $i_x = \sin i \sin \Omega, i_y = -\sin i \cos \Omega$ et $\omega = \Omega + \omega$ (ascension droite orbitale du périhélie ; noter que l'on ajoute deux angles, Ω et ω , comptés dans deux plans différents, mais voisins).

Enfin, lorsqu'à la fois $e \approx 0$ et $i \approx 0$, il est préférable de remplacer la donnée de e, i, Ω, ω, M (ou M_0) par celle de $e \cos \omega, e \sin \omega, \sin i \sin \Omega, -\sin i \cos \Omega$ et $\omega + M$ (ou $\omega + M_0$) (ascension droite orbitale moyenne, ou ascension droite orbitale moyenne de l'époque, dans le cas géocentrique).

Il est parfois commode d'utiliser les éléments orbitaux vectoriels $(\vec{e}, \vec{h}, \vec{r}, M$ ou $M_0)$ (Fig. 12), qui ne dépendent pas du choix de l'orientation des axes $F \times q_2$, mais présentent l'inconvénient de ne pas être indépendants, mais d'avoir à satisfaire (24) et (25). Il est souvent préférable de faire alors appel aux composantes "utiles" de \vec{r} et \vec{e} en choisissant pour éléments $(e_x, e_y, a, \tau_x, \tau_y, M$ ou $M_0)$ (Fig. 13). Le remplacement de M (ou M_0) par $\omega + M$ (ou $\omega + M_0$), ou toute autre variable convenablement choisie, évite alors tous les inconvénients mentionnés pour $e \approx 0$ et/ou $i \approx 0$.

Nous noterons de façon générale q ou q_1 la matrice colonne 6 X 1 des éléments orbitaux q_j ou q_j ($j = 1, 2, \dots, 6$), en convenant que les q_j et les q_j^k ($k = 1, 2, \dots, 5$) sont constants et que q_1^6 varie simplement en fonction du temps. Par exemple :

$$\underline{q} = [a, e, i, \Omega, \omega, M_0]^T, \tag{43}$$

$$\underline{q}_1 = [a, e, i, \Omega, \omega, M]^T. \tag{44}$$

La donnée des éléments orbitaux \underline{q} ou \underline{q}_1 détermine le mouvement képlérien :

$$\underline{r} = \underline{r}(\underline{q}, t), \tag{45}$$

$$\underline{v} = \partial \underline{r}(\underline{q}, t) / \partial t = \underline{v}(\underline{q}, t), \tag{46}$$

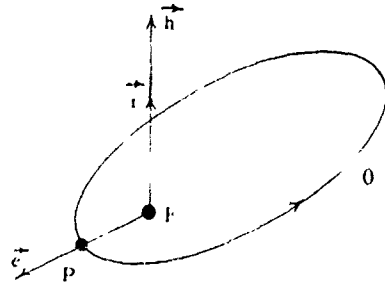


Figure 12

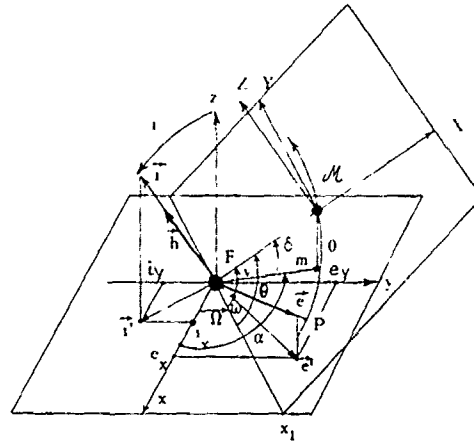


Figure 13

ou

$$\vec{r} = \vec{r}(q_1), \tag{47}$$

$$\vec{V} = \vec{V}(q_1). \tag{48}$$

Inversement, la donnée des éléments cinématique \vec{r} et \vec{V} , à l'instant t , détermine les éléments orbitaux :

$$\underline{q} = \underline{q}(\vec{r}, \vec{V}, t), \tag{49}$$

ou

$$q_1 = q_1(\vec{r}, \vec{V}) \tag{50}$$

Signalons, à la fin de ce paragraphe consacré aux orbites képlériennes, que le problème de la détermination d'une orbite à partir des observations (trajectographie) est évoqué dans l'exposé [4].

1.2.4 - Application : différence entre deux mouvements képlériens proches

Le calcul du vecteur différence $\delta\vec{r} = \vec{r}' - \vec{r}$ entre les rayons vecteurs \vec{r}' et \vec{r} de deux mouvements képlériens proches, sur des orbites $O' = O + \delta O$ et O voisines, est très important pour les applications pratiques en Astrodynamique (mouvement relatif des véhicules, dans le cas d'un rendez-vous ; cet aspect est évoqué dans l'exposé [5]. Notion de "satellite moyen", etc.).

1.2.4.1 - Calcul du vecteur différence $\delta\vec{r}$.

Il s'agit de calculer la différence $\delta\vec{r}$ correspondant à un petit écart δq sur les éléments orbitaux.

La linéarisation de (45) conduit à :

$$\delta\vec{r} = \frac{\partial \vec{r}(q, t)}{\partial q} \delta q. \tag{51}$$

Le calcul effectif est assez laborieux et conduit à l'expression suivante :

$$\delta\vec{r} = \frac{\vec{V}}{n} \delta\sigma - a \delta\vec{e}_{||} - \frac{r}{nb} (\vec{V} \cdot \delta\vec{e}) \vec{Y} - \vec{r} (\vec{r} \cdot \delta\vec{e}) + (2\vec{r} - 3t\vec{V}) \frac{\delta a}{2a}, \tag{52}$$

où

$$\delta\sigma = \delta M_0 + \frac{b}{a} \vec{\eta} \cdot \frac{\delta\vec{e}}{e}. \tag{53}$$

$\delta\vec{e}_{||}$ est la composante de $\delta\vec{e}$ dans le plan de l'orbite. \vec{Y} et $\vec{\eta}$ sont les vecteurs unitaires des axes $\mathcal{O}y$ et $F\eta$.

On remarque immédiatement que si $\delta a = 0$ (les deux orbites ont la même période), le terme en t disparaît et l'expression de $\delta\vec{r}$, donc le mouvement relatif, est périodique, de période T .

Dans le cas où l'orbite de référence O est circulaire ($e = 0$), l'expression (52) se simplifie et devient :

$$\delta\vec{r} = a \vec{Y} \delta\sigma - a \delta\vec{e}_{||} - a (\vec{Y} \cdot \delta\vec{e}) \vec{Y} - a (\vec{X} \cdot \delta\vec{e}) \vec{Z} + (\vec{X} - \frac{3}{2} nt \vec{Y}) \delta a, \tag{54}$$

où \vec{X} et \vec{Z} sont les vecteurs unitaires des axes $\mathcal{O}x$ et $\mathcal{O}z$.

Choisissons comme plan de référence Fxy le plan de O ($i = 0$, Fig. 13) et repérons le mobile M par l'ascension droite $\alpha = (F\alpha, FX)$. Les composantes de $\delta\vec{r}$ dans les axes orbitaux tournants $\mathcal{U}XYZ$ sont :

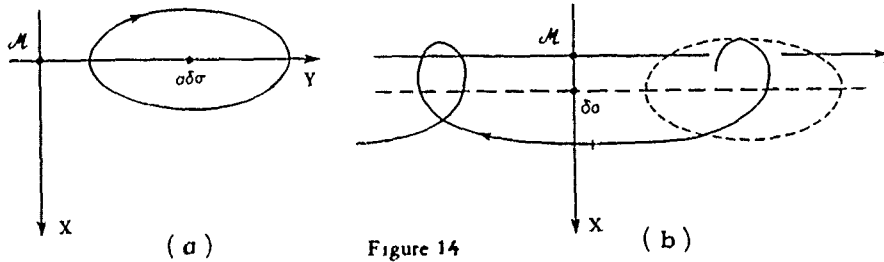
$$\delta X = \delta a - a\delta e_x \cos\alpha - a\delta e_y \sin\alpha, \quad (55)$$

$$\delta Y = a\delta\sigma - \frac{3}{2}nt\delta a + 2a\delta e_x \sin\alpha - 2a\delta e_y \cos\alpha, \quad (56)$$

$$\delta Z = -a(\vec{x} \cdot \vec{\delta v}) = -a\delta i_x \cos\alpha - a\delta i_y \sin\alpha. \quad (57)$$

Si $\delta a = 0$ (les deux orbites O et O' ont même période), M décrit une petite ellipse autour du point d'ordonnée $\delta Y = a\delta\sigma$ (voir sa projection sur le plan $\mathcal{U}XY$ sur la Fig. 14a), avec la période orbitale T .

Si $\delta a \neq 0$, l'ellipse est centrée en $(\delta a, a\delta\sigma)$ et le terme en $-(3/2)nt\delta a$ conduit à une translation parallèlement à l'axe $\mathcal{U}Y$ (et dans le sens des Y négatifs si $\delta a > 0$), et la projection du mouvement sur le plan $\mathcal{U}XY$ conduit aux festons représentés sur la Fig. 14b. Cette figure est essentielle, car elle se rencontre très souvent dans l'étude des rendez-vous en axes relatifs.



1.2.4.2 - Notion de "mobile moyen"

Considérons un mobile M' (Fig. 15) décrivant une orbite képlérienne O' quasi-circulaire ($e' \approx 0$), de faible inclinaison ($i' \approx 0$). Définissons un mobile M , voisin de M' , décrivant une orbite O circulaire ($e = 0$), d'inclinaison nulle ($i = 0$), de même période que O' (donc $\delta a = 0$), d'anomalie moyenne de l'époque M_0 telle que $\delta\sigma = 0$. Les expressions (55) - (57) se simplifient en :

$$\delta X = -a\delta e_x \cos\alpha - a\delta e_y \sin\alpha, \quad (58)$$

$$\delta Y = 2a\delta e_x \sin\alpha - 2a\delta e_y \cos\alpha, \quad (59)$$

$$\delta Z = -a\delta i_x \cos\alpha - a\delta i_y \sin\alpha. \quad (60)$$

Le mouvement du mobile M' peut donc être décomposé en :
 - mouvement circulaire d'un mobile "moyen" M , à la même période que M' ,
 - mouvement de M autour du mobile moyen M .
 Dans les axes orbitaux tournants de M , le mobile M' décrit une petite ellipse, centrée sur M , dont les dimensions sont de l'ordre de l'excentricité et de l'inclinaison de O' . Le mouvement de M représente une bonne approximation (circulaire) du mouvement de M' . Cette décomposition est utile pour l'étude de certains rendez-vous (rendez-vous "moyen").

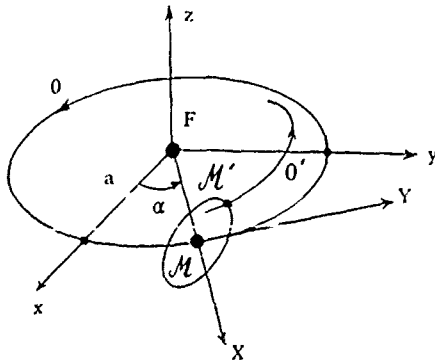


Figure 15

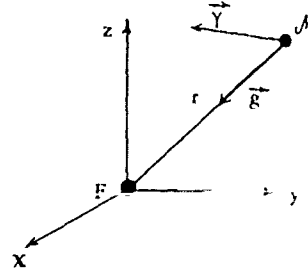


Figure 16

1.3 - Mouvement képlérien perturbé : formules de perturbation de Gauss

Comme il a déjà été dit plus haut, le problème des 2 corps correspond, en général, à une schématisation assez grossière. En réalité, dans le repère x, y, z déjà utilisé (Fig. 16), le point U est soumis non seulement à l'accélération de gravitation $\vec{q} = -\mu \vec{x} / r^3$, mais encore à une accélération perturbatrice $\vec{\gamma}$ qui peut avoir des origines très diverses (pour un satellite artificiel de la Terre : effet des dissymétries du potentiel terrestre, attraction des autres corps, freinage atmosphérique, pression de radiation, poussée des propulseurs, etc.). L'accélération perturbatrice $\vec{\gamma}$, qui sera précisée dans chaque exemple, est généralement fonction de la position \vec{x} et du temps t , parfois également de la vitesse $\vec{v} = \dot{\vec{x}}$. Les équations (13) et (14) sont donc remplacées maintenant par :

$$\vec{\Gamma} = \vec{q} + \vec{\gamma}, \quad (61)$$

et

$$\ddot{\vec{x}} = -\mu \frac{\vec{x}}{r^3} + \vec{\gamma}(\vec{x}, \dot{\vec{x}}, t). \quad (62)$$

Dans un premier temps, il ne sera fait aucune hypothèse sur les grandeurs comparées de \vec{q} et $\vec{\gamma}$. En effet, les formules de perturbation de la Mécanique Céleste peuvent être établies indépendamment d'une telle hypothèse.

Dans un deuxième temps, l'accélération perturbatrice $\vec{\gamma}$ sera supposée faible vis-à-vis de l'accélération de gravitation \vec{q} , ce qui est souvent le cas dans la pratique.

Cette hypothèse $\vec{\gamma} \ll \vec{q}$ ("hypothèse des petites perturbations", H.P.P.) facilite l'intégration des équations de perturbation. L'existence d'un "petit paramètre" γ/q permet en effet l'utilisation de la théorie des développements asymptotiques. On se bornera ici à une linéarisation des formules de perturbation, ce qui sera très utile, dans la 5ème partie, pour l'optimisation des corrections d'orbites. Enfin, à titre d'application des formules de perturbations de Gauss, l'effet du freinage atmosphérique sur les orbites des satellites artificiels sera étudié.

1.3.1 - Formules de perturbations de Gauss

Il s'agit donc de résoudre le système différentiel du 6ème ordre (62) (3 équations scalaires du 2ème ordre), qui peut être encore écrit sous forme d'un système de 6 équations scalaires du 1er ordre :

$$\dot{\vec{x}} - \vec{v} = \vec{0} \quad (63)$$

$$\dot{\vec{v}} + \mu \frac{\vec{x}}{r^3} = \vec{\gamma}(\vec{x}, \vec{v}, t), \quad (64)$$

aux fonctions inconnues $\vec{x}(t)$ et $\vec{v}(t)$.

1.3.1.1 - Méthode de la variation des constantes

Le point de départ de la théorie des perturbations est la remarque suivante : le système sans second membre de (63) - (64) :

$$\dot{\vec{x}} - \vec{v} = \vec{0}, \quad (65)$$

$$\dot{\vec{v}} + \mu \frac{\vec{x}}{r^3} = \vec{0}, \quad (66)$$

est équivalent au système (14) du problème des 2 corps. Il est donc intégrable et la solution obtenue est le mouvement képlérien (45) - (46), où q est la matrice des 6 constantes d'intégration, ou éléments orbitaux.

Dans la théorie des équations différentielles, et plus généralement des systèmes différentiels, une méthode classique de résolution du système avec second membre (63)-(64) est la méthode de variation des constantes. Cette méthode consiste à chercher la solution de (63) - (64) sous la forme (45) - (46), où q est considéré, cette fois, comme fonction inconnue du temps :

$$q = q(t). \quad (67)$$

La solution peut alors être écrite :

$$\vec{x} = \vec{x}(q(t), t), \quad (68)$$

$$\vec{v} = \vec{v}(q(t), t). \quad (69)$$

On ne restreint pas ainsi la généralité de la famille des solutions, compte tenu de l'équivalence qu'il y a entre la connaissance à tout instant des éléments cinématiques \vec{x}, \vec{v} et celle des éléments orbitaux correspondants q .

Avant d'aborder le problème de la détermination des fonctions $q^i(t)$, donnons immédiatement une interprétation géométrique de la méthode.

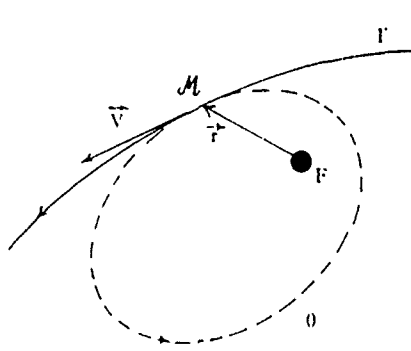


Figure 17

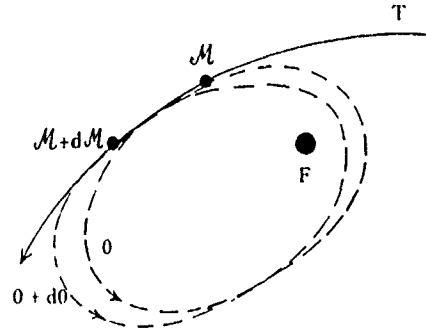


Figure 18

1.3.1.2 - Orbite osculatrice

Dans le mouvement perturbé, l'orbite képlérienne "osculatrice" à l'instant t est, par définition, l'orbite képlérienne O dont les éléments orbitaux q sont égaux à $q(t)$.

Il est évident, par (45) - (46) et (68) - (69), que, à l'instant t , les éléments cinématiques \vec{r}, \vec{v} sont les mêmes dans le mouvement perturbé sur la trajectoire réelle Γ (Fig. 17) et dans le mouvement képlérien fictif sur l'orbite osculatrice O . En particulier, Γ et O sont tangentes en M , mais, contrairement à ce qui laisserait supposer l'appellation de O , ces deux courbes ne sont pas (en général) osculatrices au sens géométrique. En effet, le plan osculateur à la trajectoire Γ est défini par \vec{v} et $\vec{r} = \vec{q} + \vec{\delta}$, alors que le plan osculateur à O est défini par \vec{v} et \vec{q} , c'est-à-dire par \vec{v} et \vec{r} . Pour cette raison, O est quelquefois appelée orbite tangente, ce qui ne rend néanmoins pas compte de l'égalité des grandeurs des vitesses dans les deux mouvements. Cette égalité fait que le mouvement képlérien "osculateur" représente une bonne approximation du mouvement réel sur un intervalle de temps suffisamment court. En effet, dans le mouvement réel sur la trajectoire Γ :

$$\vec{r}(t + \Delta t) = \vec{r}(t) + \vec{v}(t)\Delta t + \frac{1}{2}\vec{r}(t)\Delta t^2 + O(\Delta t^3), \quad (70)$$

et dans le mouvement képlérien fictif sur l'orbite osculatrice O à l'instant t :

$$\vec{r}_k(t + \Delta t) = \vec{r}(t) + \vec{v}(t)\Delta t + \frac{1}{2}\vec{q}(t)\Delta t^2 + O(\Delta t^3), \quad (71)$$

ce qui conduit à un écart :

$$\vec{r}(t + \Delta t) - \vec{r}_k(t + \Delta t) = \frac{1}{2}\vec{\delta}(t)\Delta t^2 + O(\Delta t^3), \quad (72)$$

d'ordre Δt^2 seulement. Il en serait cependant de même si l'on choisissait comme mouvement fictif le mouvement rectiligne uniforme :

$$\vec{r}_v(t + \Delta t) = \vec{r}(t) + \vec{v}\Delta t, \quad (73)$$

ce qui conduirait à un écart :

$$\vec{r}(t + \Delta t) - \vec{r}_v(t + \Delta t) = \frac{1}{2}\vec{r}(t)\Delta t^2 + O(\Delta t^3). \quad (74)$$

Toutefois, dans le cas d'une faible perturbation ($\delta \ll q$), le mouvement képlérien "osculateur" devient une très bonne approximation du mouvement réel, car l'écart (72) devient très faible. C'est très souvent le cas dans l'étude des mouvements naturels en Mécanique Céleste et c'est pour cette raison que l'orbite O a été appelée "osculatrice". Ce terme sera conservé également dans le cas général.

L'orbite osculatrice O à l'instant t est donc l'orbite qui décrirait M , si, à partir de l'instant t , cessait toute action perturbatrice. Dans la théorie des perturbations, le mobile M n'est plus considéré comme décrivant la trajectoire Γ , mais comme décrivant une orbite képlérienne O , qui se déforme progressivement (Fig. 18). L'avantage de la méthode est, sur le plan analytique, d'éliminer en quelque sorte la "partie intégrable" du mouvement perturbé.

Sur le plan géométrique, et dans le cas où la perturbation est faible ($\gamma \ll q$), la seconde interprétation permet en général de mieux se représenter le mouvement.

Sur le plan numérique, et toujours dans l'hypothèse $\gamma \ll q$, il est généralement plus intéressant, dans les calculs, d'utiliser les éléments orbitaux au lieu des coordonnées cartésiennes, car ils varient plus lentement. Cependant, la possibilité d'utiliser maintenant des calculateurs très puissants fait perdre aux éléments orbitaux une partie de leur intérêt ; il n'est pas rare que certains calculs d'orbites se fassent en coordonnées cartésiennes, si la durée (nombre de révolutions) n'est pas trop longue. L'exposé [4] insiste sur ce point.

1.3.1.3 - Formules de perturbations

Les formules de perturbations peuvent être obtenues par différentiation de l'expression (50) des éléments orbitaux q_1 de O en fonction des éléments cinématiques \vec{r}, \vec{v} :

$$dq_1 = \frac{\partial q_1}{\partial \vec{r}} d\vec{r} + \frac{\partial q_1}{\partial \vec{v}} d\vec{v} = \frac{\partial q_1}{\partial \vec{r}} \cdot \vec{v} dt + \frac{\partial q_1}{\partial \vec{v}} (\vec{g} + \delta) dt = \left(\frac{\partial q_1}{\partial \vec{r}} \cdot \vec{v} + \frac{\partial q_1}{\partial \vec{v}} \cdot \vec{g} \right) dt + \left(\frac{\partial q_1}{\partial \vec{v}} \cdot \delta \right) dt = dq_{1K} + (dq_1)_\delta \quad (75)$$

La variation dq_1 pendant l'intervalle de temps dt est donc égale à la somme de la variation "képlérienne" dq_{1K} (dont les 5 premières composantes sont nulles, puisque les éléments orbitaux correspondants q_1^k sont des constantes du mouvement képlérien), et de la variation $(dq_1)_\delta$, où la position \vec{r} est figée et où $d\vec{v}$ est remplacé δdt .

En divisant par dt , on obtient les formules de perturbation :

$$\dot{q}_1 = \dot{q}_{1K} + \frac{\partial q_1}{\partial \vec{v}} \cdot \delta \quad (76)$$

Ces formules peuvent être explicitées, d'abord pour les éléments orbitaux vectoriels, puis pour les éléments orbitaux scalaires.

Pour les éléments orbitaux vectoriels $(\vec{e}, \vec{h}, \vec{e}, M)$, les axes dans lesquels sont repérés les vecteurs \vec{h} et \vec{e} , ainsi que ceux dans lesquels est repéré δ ne sont pas spécifiés, ce qui conduit à des formules vectorielles, particulièrement condensées, qui permettent une certaine souplesse d'utilisation.

Pour les éléments scalaires de Lagrange $q_1 = [a, e, i, \Omega, \omega, M]^T$, δ est repéré soit dans les axes orbitaux tournants $\mathcal{O}XYZ$ (Fig. 19), la matrice colonne 3×1 représentative étant alors notée $\vec{y} = [\delta, \delta, \delta]^T$, soit plus rarement dans les axes intrinsèques classiques $\mathcal{O}t_n b$, la matrice étant alors notée $\vec{y} = [\delta_t, \delta_n, \delta_b]^T$. On passe aisément d'un système de composantes à l'autre grâce aux relations :

$$\cos \delta = V_0 / V = h / r V, \quad (77)$$

$$\sin \delta = V_2 / V = h \sin i / p V. \quad (78)$$

L'angle δ (notation normalisée) est la pente locale de la trajectoire, à ne pas confondre avec l'accélération perturbatrice !

L'explicitation des formules (76) est assez laborieuse, aussi ne ferons-nous le calcul que dans deux cas particuliers, à titre d'exemple, en établissant les formules de perturbation pour l'énergie \mathcal{E} et pour le moment cinétique \vec{h} . Nous donnerons ensuite l'ensemble des formules.

1.3.1.4 - Perturbation de l'énergie orbitale

La différentiation de \mathcal{E} donné en (22) conduit à :

$$d\mathcal{E} = d\mathcal{E}_K + d\mathcal{E}_P = d\mathcal{E}_T = \vec{v} \cdot d\vec{v} = \vec{v} \cdot \vec{\delta} dt = V \delta_t dt, \quad (79)$$

d'où :

$$\dot{\mathcal{E}} = \vec{v} \cdot \vec{\delta} = V \delta_t, \quad (80)$$

et, par dérivation logarithmique de (28), qui s'écrit encore :

$$a = - \frac{\mu}{2\mathcal{E}} \quad (81)$$

pour une ellipse (resp. une hyperbole), on obtient facilement :

$$\dot{a} = - \frac{a}{\mathcal{E}} \vec{v} \cdot \vec{\delta} = \pm \frac{a}{n^2 a} \vec{v} \cdot \vec{\delta} = \pm \frac{2V}{n^2 a} \delta_t, \quad (82)$$

Remarques

- 1) Seule la composante tangentielle δ_t de l'accélération perturbatrice perturbe l'énergie ou le demi-grand axe. L'énergie \mathcal{E} croît (resp. décroît) selon que la composante tangentielle δ_t est ≥ 0 , c'est-à-dire selon que $\vec{\delta}$ est appliquée dans le sens (resp. en sens contraire) du mouvement.

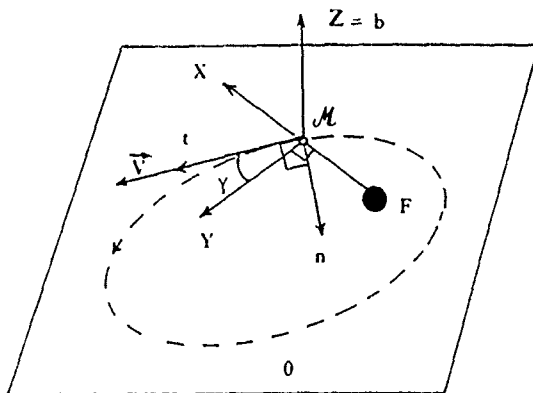


Figure 19

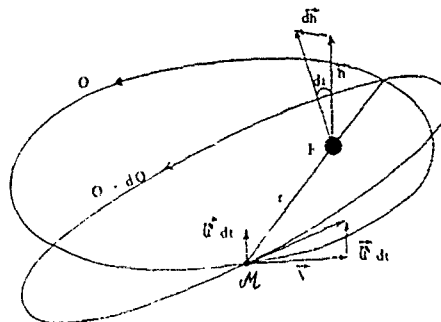


Figure 20

Une accélération perturbatrice $\vec{\gamma}$ dans le sens du mouvement ($\gamma_t > 0$) fait croître (resp. décroître) le demi-grand axe d'une ellipse (resp. hyperbole).
 Une accélération perturbatrice $\vec{\gamma}$ perpendiculaire à l'orbite ($\gamma_t = 0$) laisse l'énergie ou le demi-grand axe inchangés.

2) Une impulsion de vitesse élémentaire $\vec{\gamma} dt$, perturbatrice, tangentielle ($\gamma_t = \pm \gamma \geq 0$), est d'autant plus efficace pour perturber l'énergie ou le demi-grand axe que les variations spécifiques :

$$|\gamma_E| = \frac{|dE|}{\delta dt} = V, \tag{83}$$

et

$$|\gamma_a| = \frac{|da|}{\delta dt} = \frac{a}{|E|} V = \frac{2}{n^2 a} V, \tag{84}$$

proportionnelles à la vitesse V au point d'application, sont plus élevés, c'est-à-dire que la vitesse V est plus grande.

Elles sont donc maximales au périhélie et minimales à l'apogée (ellipse) ou à l'infini (hyperbole).

1.3.1.5 - Perturbation du moment cinétique

La différentiation de (15) conduit à :

$$d\vec{h} = d\vec{h}_k + d\vec{h}_r = d\vec{h}_r = \vec{r} \wedge d\vec{V} = \vec{r} \wedge \vec{\gamma} dt, \tag{85}$$

d'où :

$$\dot{\vec{h}} = \vec{r} \wedge \vec{\gamma}, \tag{86}$$

On en déduit aisément les formules pour \dot{h} , $\dot{\Omega}$ et \dot{i} .

Remarques :

1) Seule la composante \vec{W} de l'accélération perturbatrice $\vec{\gamma}$ qui est orthogonale au plan de l'orbite perturbe l'orientation de ce plan, qui tourne alors autour du rayon vecteur $\vec{r} = \vec{FM}$ du point d'application (Fig. 20) (et non pas autour d'une direction qui lui serait perpendiculaire !).

Une impulsion élémentaire $\vec{\gamma} dt$ orthogonale au plan de l'orbite ($\vec{W} = \vec{\gamma} dt$) produit la rotation :

$$di = \|\dot{\vec{h}}\| = \frac{r}{h} \gamma dt. \tag{87}$$

L'impulsion est d'autant plus efficace que la rotation spécifique :

$$\gamma_i = \frac{di}{\delta dt} = \frac{r}{h}, \tag{88}$$

proportionnelle à la distance r , est plus grande donc que la distance r est plus grande.

Dans le cas elliptique, pour une impulsion orthogonale au plan de l'orbite, de grandeur donnée, la rotation est maximale lorsque cette impulsion est appliquée à l'apogée. La rotation a alors lieu autour du grand axe.

1.3.1.6 - Formules de perturbation

Le calcul complet conduit aux formules suivantes :

Perturbation des éléments vectoriels :

$$\dot{\vec{e}} = \vec{\nabla} \cdot \vec{\gamma} \tag{89}$$

$$\dot{\vec{h}} = \vec{r} \wedge \vec{\gamma} \tag{90}$$

$$\mu \dot{\vec{e}} = \vec{\gamma} \wedge \vec{h} + \vec{\nabla} \wedge (\vec{r} \wedge \vec{\gamma}) = (2\gamma'_t + \mathcal{D}') \wedge \vec{h} - \frac{h}{r} \vec{\gamma} \tag{voir Fig. 21)} \tag{91}$$

$$\dot{M} = n - \frac{2}{na^2} \vec{r} \cdot \vec{\gamma} - \frac{b}{ae} \vec{y} \cdot \dot{\vec{e}}, \tag{92}$$

d'où :

$$\dot{M}_0 = \frac{1}{na^2} (-2\vec{r} + 3t\vec{v}) \cdot \vec{\gamma} - \frac{b}{ae} \vec{y} \cdot \dot{\vec{e}}. \tag{93}$$

Perturbation des éléments de Lagrange (cas elliptique) :

$$\dot{a} = \frac{2a}{nb} [e \sin v \mathcal{D} + (1 + e \cos v) \mathcal{C}] = \frac{2\mathcal{V}}{n^2 a} \gamma_t, \tag{94}$$

$$\dot{e} = \frac{b}{na^2} [\sin v \mathcal{D} + (\cos v + \cos E) \mathcal{C}] = \frac{1}{\sqrt{1 - e^2}} [2(e + \cos v) \gamma_t - \frac{2}{a} \sin v \gamma_n], \tag{95}$$

$$\dot{i} = \frac{2 \cos \theta}{r \sin i} W, \tag{96}$$

$$\dot{\Omega} = \frac{2 \sin \theta}{r \sin i} W, \tag{97}$$

$$\dot{\omega} = \frac{b}{na^2 e} [-\cos v \mathcal{D} + (\sin v + \frac{a}{b} \sin E) \mathcal{C}] - \frac{2 \sin \theta}{r \sin i} W = \frac{1}{e\mathcal{V}} [2 \sin v \gamma_t + (e + \frac{2}{a} \cos v) \gamma_n] - \frac{2 \sin \theta}{r \sin i} W, \tag{98}$$

$$\dot{M} = n + \frac{p}{na^2 e} [(\cos v - 2e \frac{r}{p}) \mathcal{D} - \sin v (1 + \frac{r}{p}) \mathcal{C}] = n - \frac{2}{e b \mathcal{V}} [2 \sin v (1 + e \cos v + e^2) \gamma_t + \frac{p}{a} \cos v \gamma_n]. \tag{99}$$

Insistons encore sur le fait que ces formules sont valables quelle que soit la grandeur de l'accélération perturbatrice $\vec{\gamma}$.

Les formules (94) - (99) peuvent être écrites sous la forme matricielle condensée :

$$\dot{\underline{q}}_1 = \underline{\dot{q}}_{1k} + \underline{K}_1 \underline{\gamma}, \tag{100}$$

où $\underline{\dot{q}}_{1k}$ est la matrice colonne 6 X 1 :

$$\underline{\dot{q}}_{1k} = [0, 0, 0, 0, 0, n]^T, \tag{101}$$

et où

$$\underline{K}_1 = \underline{K}_1(\underline{q}_1) \tag{102}$$

est la matrice 6 X 3 de perturbation. Le second membre de (100) n'est fonction que de l'accélération perturbatrice $\vec{\gamma}$ et des éléments orbitaux \underline{q}_1 .

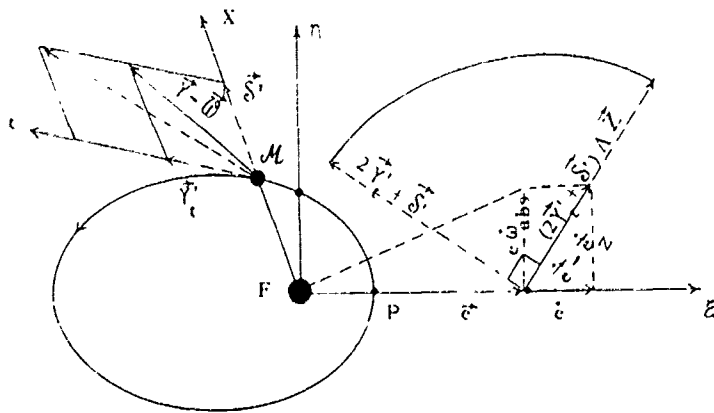


Figure 21

L'utilisation de l'anomalie moyenne de l'époque M_0 au lieu de l'anomalie moyenne M conduit à des formules du type :

$$\dot{q} = \underline{K} \underline{\gamma} \quad (103)$$

où cette fois

$$\underline{K} = \underline{K}(q, t) \quad (104)$$

dépend du temps t .

1.3.1.6 - Cas des petites excentricités et/ou des petites inclinaisons

Les difficultés rencontrées dans l'utilisation des éléments orbitaux de Lagrange dans le cas où $e \simeq 0$ et/ou $i \simeq 0$ ont déjà été évoquées au paragraphe 1.2.3. Elles sont évidentes sur les formules (94) - (99), où $\dot{\omega} \rightarrow \infty$ et $\dot{M} \rightarrow \infty$ lorsque $e \rightarrow 0$, et où $\dot{\Omega} \rightarrow \infty$ et $\dot{\omega} \rightarrow \infty$ lorsque $i \rightarrow 0$. Il faut alors faire appel à d'autres éléments orbitaux, tels que ceux proposés au paragraphe 1.2.3. Les formules de perturbation de ces nouveaux éléments peuvent être obtenues aisément à l'aide de (94) - (99). Il est à noter que ces nouvelles formules, qui ne seront pas développées ici, sont rigoureuses, et non pas seulement valables pour $e \simeq 0$ et/ou $i \simeq 0$; elles sont seulement mieux adaptées à l'étude de ces cas.

1.3.2 - Linéarisation des formules de perturbation

1.3.2.1 - Hypothèse des petites perturbations (H.P.P.)

Dans de nombreux problèmes d'Astrodynamique, l'accélération perturbatrice $\vec{\gamma}$ est faible ($\gamma \ll g$) (perturbations naturelles, propulsion à faible poussée) ou appliquée pendant de très courts instants (poussée éventuellement forte, mais impulsion totale de vitesse faible).

De façon plus précise, il sera supposé que :

$$\underline{I} = \int_{t_c}^{t_f} \gamma dt \ll V, \quad (105)$$

où $[t_c, t_f]$ est l'intervalle de temps pendant lequel on s'intéresse au mouvement, et V est la vitesse orbitale moyenne.

Il apparaît donc un "petit paramètre" $\varepsilon = I/V \ll 1$ dans le problème et l'intégration du système (103) de t_c à t_f montre que les variations Δq_i des éléments orbitaux sont telles que $\Delta q_i = O(\varepsilon)$ et, compte tenu de (93), $\Delta q_i = \Delta M_0 = O[\varepsilon(t_f - t_c)]$. L'orbite osculatrice O reste donc toujours proche de O_c ou O_f , l'écart étant d'ordre ε .

1.3.2.2 - Orbite nominale

Il est encore possible de dire que O reste toujours voisine d'une orbite nominale \bar{O} , fixe, proche de O_c et O_f , les écarts étant d'ordre ε . Compte tenu du rôle particulier joué par l'orbite nominale \bar{O} , il est commode de prendre son plan comme plan de référence Fxy (Fig. 22) et, dans le cas elliptique ($0 < \bar{e} < 1$), son grand axe, orienté vers le périhélie, comme axe de référence Fx , dans le cas circulaire ($\bar{e} = 0$), Fx est choisi arbitrairement dans le plan de \bar{O} . Notons qu'il est possible de prendre $\bar{x} = O$ lorsque e_c et e_f sont d'ordre ε .

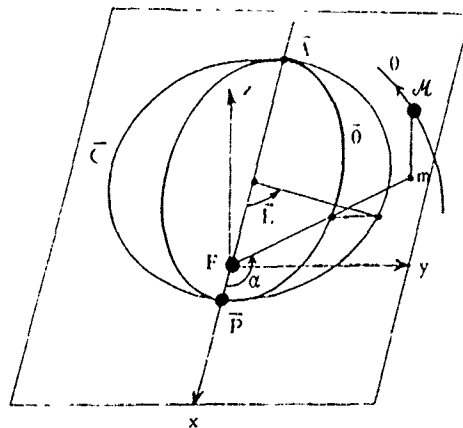


Figure 22

1.3.2.3 - Choix du sixième élément orbital

Pour aboutir à des formules de perturbation linéarisées générales, il est souhaitable de ne pas avoir à les modifier dans le cas où l'excentricité e est faible. Il est donc commode, puisque nous avons vu que l'inclinaison est également faible, d'utiliser les éléments i_x, i_y, e_x, e_y (Fig. 13) et de remplacer M_0 par $\bar{\omega} + M_0$, ou mieux, compte tenu de la forme particulière de l'équation (93) en M_0 , par :

$$\sigma = \frac{\bar{b}}{\bar{a}} \bar{\omega} + M_0, \quad (106)$$

puisque $\dot{\sigma}$ peut alors être écrit :

$$\dot{\sigma} = \frac{\bar{b}}{\bar{a}} \dot{\omega} + \dot{M}_0 = \frac{1}{na^2} (-2\bar{x} + 3t\bar{V}), \dot{\sigma} + \left(\frac{\bar{b}}{\bar{a}} \dot{\omega} - \frac{\bar{b}}{\bar{a}} \dot{y} \cdot \frac{\dot{e}}{e} \right), \quad (107)$$

et le dernier terme s'annule lorsque O coïncide avec \bar{O} , ce qui sera supposé à chaque instant, dans les seconds membres, lors de la linéarisation des équations.

Il est important de remarquer que, dans la dérivation de σ , le facteur \bar{b}/\bar{a} est considéré comme une constante.

1.3.2.4 - Choix de la variable de description

Il n'est pas recommandé de garder le temps comme variable de description. En effet :

1) A chaque instant, la position angulaire qui intervient dans les seconds membres des formules de perturbation doit être calculée sur l'orbite osculatrice O à partir de la donnée de t et σ . Dans la linéarisation, cette position devra être remplacée par la position nominale, calculée sur l'orbite nominale \bar{O} à partir de la donnée de t et de $\bar{\sigma}$. L'erreur angulaire, de l'ordre de $\varepsilon (t_f - t_0)$ au plus, peut devenir importante dans le cas d'une longue durée, disons de l'ordre de l'unité pour $t_f - t_0 = O(1/\varepsilon)$, ce qui conduirait à une erreur relative plus grande que $O(\varepsilon)$, et de ce fait inacceptable, sur les seconds membres des équations de perturbation, qui contiennent des fonctions trigonométriques de la position angulaire.

2) Le temps t n'est pas une variable d'intégration commode, car il intervient le plus souvent implicitement par l'intermédiaire de la position angulaire sur l'orbite osculatrice (anomalie vraie \mathcal{V} ou anomalie excentrique E), dont le calcul en fonction de t nécessite la résolution d'une équation transcendante. Une variable angulaire est préférable et il vient d'être vu qu'il est essentiel qu'elle exprime, avec une précision suffisante, dans les équations linéarisées, la position angulaire vraie du mobile.

Les considérations précédentes conduisent à choisir, comme nouvelle variable indépendante, la pseudo-ascension droite α du mobile \mathcal{M} (Fig. 22), ou mieux, dans le cas elliptique ($0 < \bar{e} < 1$), l'anomalie excentrique E correspondant à l'anomalie vraie α sur l'orbite nominale \bar{O} .

Le temps t est alors déduit du sixième élément orbital en utilisant $M = M_0 + nt$.

Dans cette approche, le mouvement est donc décrit explicitement en fonction de la position angulaire E (ou, dans le cas circulaire $\bar{e} = 0$, en fonction de l'ascension droite α), et seulement de façon implicite en fonction du temps t .

Il est important de remarquer que jusqu'à présent aucune approximation n'a été faite.

1.3.2.5 - Linéarisation

Seul le cas où l'accélération perturbatrice δ est faible est traité ici. Le cas où elle est forte, mais appliquée pendant des intervalles de temps très courts, se traiterai de même.

Comme $\delta = O[\varepsilon/(t_f - t_0)]$, les équations (103) peuvent être mises sous la forme :

$$\frac{dq}{dE} = \varepsilon f(q, E), \quad (106)$$

en faisant apparaître le "petit paramètre" ε du problème.

Compte tenu de la présence de ε en facteur dans les seconds membres, on obtient une approximation suffisamment bonne des variations dq/dE en remplaçant dans le second membre les éléments orbitaux par leur valeur nominale \bar{q} . La linéarisation des formules (106) consiste donc simplement à "figer" dans les seconds membres les éléments orbitaux à leur valeur nominale.

Compte tenu du choix des axes, on a évidemment :

$$\bar{i}_x = \bar{i}_y = 0 \quad (\text{c'est-à-dire, } \bar{i} = 0), \quad (107)$$

$$\bar{e}_x - \bar{e}, \bar{e}_y = 0 \quad (\text{c'est-à-dire, } \bar{e} = 0). \quad (108)$$

D'autre part, $\bar{\sigma}$ est constant, ou mieux, en prenant pour origine des temps l'instant où $\bar{E} = 0$ (ou $\alpha = 0$), et compte tenu de (108) :

$$\bar{\sigma} = 0. \quad (109)$$

* En effet, le plan de référence F_{xy} , qui est ici le plan de \bar{O} , ne coïncide pas en général avec le plan équatorial.

Compte tenu du rôle particulier joué par l'orbite nominale \bar{O} , il est commode, pour simplifier les calculs, de choisir les unités suivantes :

Unité de longueur : $\bar{a} = \text{demi-grand axe de } \bar{O}$.
Unité de temps : $T/2\pi = \sqrt{\bar{a}^3/\mu} = (\text{période sur } \bar{O})/2\pi$,

d'où :

Unité de vitesse : $C(\bar{a}) = \sqrt{\mu/\bar{a}} = \text{vitesse circulaire}$ |

Unité d'accélération : $g(\bar{a}) = \mu/\bar{a}^2 = \text{accélération de}$ | à la distance $\bar{a} = 1$.
gravitation |

On peut donc faire :

$$\bar{a} = 1, \quad (110)$$

$$\bar{n} = 1, \quad (111)$$

donc

$$\bar{n}^2 \bar{a}^3 = \mu = 1, \quad (112)$$

dans les équations, au risque de ne plus pouvoir vérifier les formules par des considérations d'homogénéité.

Compte tenu de toutes les hypothèses, la linéarisation des formules (106) conduit à l'expression suivante, où pour simplifier les expressions, le signe (-) a été omis sur les quantités nominales :

$$\frac{dq}{dE} = r K \delta, \quad (113)$$

où, la matrice de perturbation nominale K prend la forme simplifiée suivante :

$$K = \begin{bmatrix} 0 & 0 & K_{0z} \\ 0 & 0 & K_{0y} \\ K_{ax} & K_{ay} & 0 \\ K_{bx} & K_{by} & 0 \\ K_{cx} & K_{cy} & 0 \\ K_{dx} & K_{dy} & 0 \end{bmatrix} \quad (114)$$

Les éléments sont donnés dans le Tableau 2, en fonction de l'anomalie excentrique E dans le cas elliptique ($e \neq 0$), et de l'ascension droite α dans le cas circulaire ($e = 0$).

Sous forme développée, en fonction des composantes \mathcal{P} , \mathcal{C} , \mathcal{W} de l'accélération perturbatrice \mathcal{F} dans les axes orbitaux tournants nominaux, on a :

Cas elliptique ($e \neq 0$) :

$$\frac{dx_z}{dE} = r \sin E \mathcal{W}, \quad (115)$$

$$\frac{dy_z}{dE} = \frac{z}{b} (e - \cos E) \mathcal{W}, \quad (116)$$

$$\frac{dx_x}{dE} = 2e \sin E \mathcal{P} + 2b \mathcal{C}, \quad (117)$$

$$\frac{dx_y}{dE} = p \sin E \mathcal{P} + b (2 \cos E - e \cos^2 E - e) \mathcal{C}, \quad (118)$$

$$\frac{dy_x}{dE} = b (e - \cos E) \mathcal{P} + \sin E (2 - e \cos E - e^2) \mathcal{C}, \quad (119)$$

$$\frac{dz}{dE} = (3Me \sin E - 2a^2) \mathcal{P} + 3bM \mathcal{C}. \quad (120)$$

Cas circulaire ($e = 0$) :

$$\frac{dx_z}{dE} = \sin \alpha \mathcal{W}, \quad (121)$$

$$\frac{dy_z}{dE} = -\cos \alpha \mathcal{W}, \quad (122)$$

$$\frac{dx_x}{dE} = 2 \mathcal{C}, \quad (123)$$

$$\frac{dx_y}{dE} = \sin \alpha \mathcal{P} + 2 \cos \alpha \mathcal{C}, \quad (124)$$

$$\frac{dy_x}{dE} = -\cos \alpha \mathcal{P} + 2 \sin \alpha \mathcal{C}, \quad (125)$$

$$\frac{dz}{dE} = -2 \mathcal{P} + 3 \alpha \mathcal{C}. \quad (126)$$

Ces dernières formules sont particulièrement simples et très importantes, car elles permettent d'étudier les perturbations naturelles ou artificielles (poussée) au voisinage d'une orbite nominale circulaire, ce qui souvent le cas dans la pratique.

Tableau 2 : Elements de la matrice K

avec $a = 1$, $n = 1$, $b = \sqrt{1 - e^2}$, $p = 1 - e^2$, $r = 1 - e \cos E$, $M = E - e \sin E$.

	$e \neq 0$	$e = 0$
K_{1Z} x	$\sin E$	$\sin \alpha$
K_{1Z} y	$(e - \cos E) / b$	$-\cos \alpha$
K_{aX}	$(2e/r) \sin E$	0
K_{aY}	$2b/r$	2
K_{eX} x	$(p/r) \sin E$	$\sin \alpha$
K_{eX} y	$(b/r) (2 \cos E - e \cos^2 E - e)$	$2 \cos \alpha$
K_{eY} x	$(b/r) (e - \cos E)$	$-\cos \alpha$
K_{eY} y	$\sin E (2 - e \cos E - e^2) / r$	$2 \sin \alpha$
$K_{\sigma X}$	$-2r + (3Me \sin E / r)$	-2
$K_{\sigma Y}$	$3bMr$	3α

1.4 - Application : perturbation des orbites des satellites artificiels par le freinage atmosphérique

On se bornera ici à quelques remarques, essentiellement d'ordre qualitatif.

1.4.1 - Hypothèses

La résistance aérodynamique, bien que très faible dès que l'altitude est suffisante, a pour effet de limiter la durée de vie des satellites artificiels de la Terre. Cet effet sera estimé dans le cadre des hypothèses simplificatrices suivantes :

- (1) Terre sphérique.
 (2) Atmosphère non tournante, c'est-à-dire non entraînée par la rotation de la Terre sur elle-même.
 (3) Masse spécifique de l'air fonction parfaitement connue de l'altitude z ; par exemple, fonction exponentielle par morceaux, du type :

$$\rho = \rho_i e^{-(z-z_i)/H_i} \quad (127)$$

où les valeurs ρ_i et H_i (facteur d'échelle, appelé encore "pas" de l'atmosphère) sont variables dans la "tranche" d'altitude $[z_i, z_{i+1}]$.

En fait, une grande incertitude pèse sur la connaissance de la densité atmosphérique à haute altitude. Cette densité dépend essentiellement de l'activité solaire et de l'activité géomagnétique. On observe, de plus, des variations saisonnières, diurnes et géographiques (latitude et longitude). Des modèles empiriques ont été construits (NASA, CERGA, ...). Statistiquement, ils représentent la réalité à 25 % près sur 95 % de la durée de vie d'un satellite bas. Sur les 5 % restants, des orages magnétiques, dont la durée est de l'ordre de la journée, peuvent être responsables d'une erreur allant jusqu'à 100 %. Cette erreur est cependant relativement faible au minimum du cycle solaire, de période 11 ans environ. L'importance de ces orages peut être connue a posteriori, avec un délai de l'ordre de 15 jours. L'effet peut donc être pris en compte dans un traitement en temps différé.

- (4) Loi de "traînée aérodynamique" de la forme :

$$\vec{R}_x = -\frac{1}{2} \rho S C_x V \vec{V}, \quad (128)$$

où S est le maître couple et C_x le coefficient de traînée, compris entre 2 et 4, et supposé parfaitement connu. En fait, l'erreur sur le C_x peut être de l'ordre de 20 à 50 %. Mais la connaissance du C_x peut être améliorée à partir des mesures de poursuites de satellites.

1.4.2 - Perturbation de l'orbite

L'accélération perturbatrice $\vec{\gamma}$ est donc :

$$\vec{\gamma} = \frac{\vec{R}_x}{m} = -\frac{1}{2} \rho B V \vec{V}, \quad (129)$$

où $B = SC_x/m$ est le coefficient balistique du satellite.

Puisque l'accélération perturbatrice $\vec{\gamma}$ agit dans le plan de l'orbite osculatrice ($\vec{W} = \vec{0}$), les équations (96) et (97) montrent que :

$$\vec{L} = \text{constante}, \quad (130)$$

donc que le plan de l'orbite n'est pas modifié.

D'autre part, comme $\delta_t < 0$, (94) montre que $a < 0$, donc que le demi-grand axe décroît toujours.

Tant que le périhélie est suffisamment haut, l'accélération perturbatrice reste faible ($\gamma \ll g$) et il est possible, comme il a été vu au paragraphe 1.3.2 de calculer approximativement les variations Δq_i des éléments orbitaux sur une révolution en fixant l'orbite osculatrice O dans les seconds membres des formules de perturbations.

Si l'orbite initiale O_0 est elliptique, le freinage a lieu au début essentiellement au voisinage du périhélie P et la relation (91), qui s'écrit ici :

$$\mu \dot{\vec{e}} = -B \rho V \vec{V} \vec{h}, \quad (131)$$

ainsi que les Figs. 21 et 23, montrent que les contributions élémentaires $d\vec{e}_1$ et $d\vec{e}_2$ à $d\vec{e}$, pendant le temps dt , correspondant à deux points M_1 et M_2 symétriques par rapport au grand axe, sont elles-mêmes symétriques par rapport au grand axe. Donc $d\vec{e}_1$ et, par sommation, $d\vec{e}$ sont portés par le grand axe et dirigés en sens inverse de \vec{e} . Donc la direction du grand axe est invariante et l'excentricité décroît. Il est possible de vérifier qu'à l'issue de cette première phase l'excentricité s'annule.

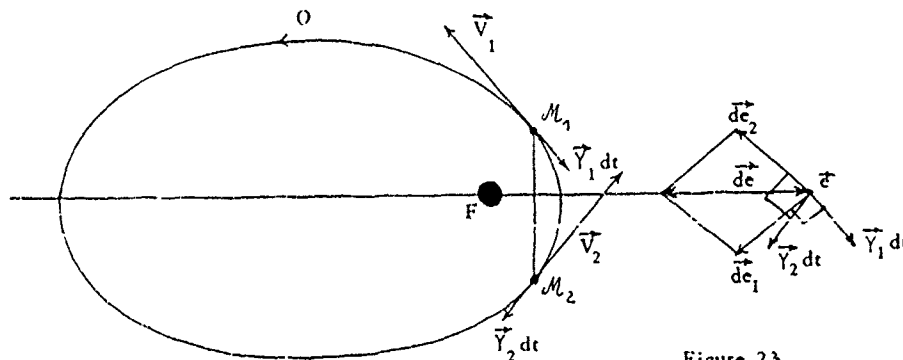


Figure 23

Un raisonnement analogue montrerait que la seconde phase est une spirale "circulaire" de rayon décroissant.

Enfin, lorsque le satellite arrive dans les couches denses de l'atmosphère, l'hypothèse $\gamma \ll q$ n'est plus valable et il faut reprendre le calcul à l'aide des formules de perturbation rigoureuses (89) - (92) ou (94) - (99), ou plutôt revenir aux équations cartésiennes (62), pour décrire la troisième phase de rentrée proprement dite.

En résumé, la déformation de l'orbite s'effectue en trois phases (Fig. 24) :

- (1) d'abord une "circularisation" progressive, où l'altitude de l'apogée décroît, à altitude de périhélie quasi-constante ;
- (2) puis, une "spirale" de rayon lentement décroissant ;
- (3) enfin, une "rentrée" relativement rapide dans les couches denses de l'atmosphère.

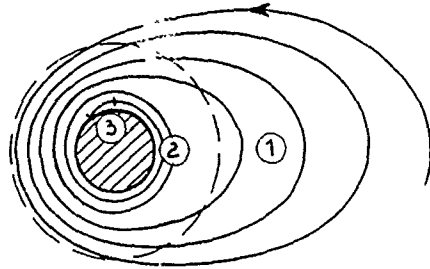


Figure 24

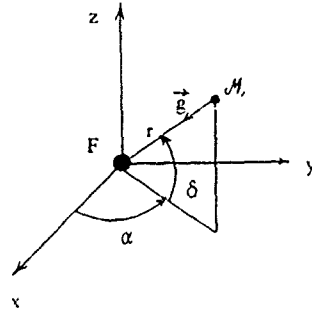


Figure 25

2 - FORMALISME LAGRANGIEN

2.1 - Mécanique lagrangienne

La mécanique lagrangienne a pour objet l'étude du mouvement des systèmes matériels discrets, tels que toute configuration à l'instant t puisse être définie par la donnée d'un nombre fini de paramètres q^i ($i = 1, 2, \dots, n$) (coordonnées généralisées) et éventuellement de t .

Le système de N points matériels de la première partie apparaît ainsi comme un cas particulier. Il est possible de prendre, par exemple, pour paramètres q^i les coordonnées x_p^s ($s = 1, 2, 3$) des \mathcal{M}_p ($p = 1, 2, \dots, N$). Dans ce cas $n = 3N$.

L'application du principe des puissances virtuelles, équivalent à la loi fondamentale de la dynamique (Fig. 1), conduit aux équations de Lagrange bien connues, qui, dans le cas particulier d'un système à Lagrangien, s'écrivent :

$$\frac{d}{dt} \left(\frac{\partial L}{\partial \dot{q}^i} \right) - \frac{\partial L}{\partial q^i} = 0. \quad (132)$$

2.2 - Problème des 2 corps

Le système des 2 points matériels étudié au paragraphe 1.2 est un système à Lagrangien. La symétrie sphérique du problème (Fig. 25) suggère l'utilisation des coordonnées sphériques (r, α, δ) (r : distance ; α : ascension droite ; δ : déclinaison), c'est-à-dire le paramétrage :

$$\underline{Q} = [Q^s] = [r, \alpha, \delta]^T \quad (s = 1, 2, 3). \quad (133)$$

L'énergie cinétique s'écrit :

$$T = \frac{1}{2} \vec{V}^2 = \frac{1}{2} (\dot{r}^2 + r^2 \dot{\delta}^2 + r^2 \cos^2 \delta \dot{\alpha}^2). \quad (134)$$

Le potentiel est :

$$V_K = - \frac{\mu}{r} \quad (135)$$

et le lagrangien :

$$L_K = T - V_K = \frac{1}{2} (\dot{r}^2 + r^2 \dot{\delta}^2 + r^2 \cos^2 \delta \dot{\alpha}^2) + \frac{\mu}{r}. \quad (136)$$

T , \mathcal{V}_K , et L_K sont des quantités massiques (par unité de masse). K est mis pour "képlérien".

Le mouvement peut être obtenu par intégration des équations de Lagrange :

$$\frac{d}{dt} \left(\frac{\partial L}{\partial \dot{\alpha}} \right) - \frac{\partial L}{\partial \alpha} = 0. \quad (137)$$

L'angle α est ignorable ($\frac{\partial L}{\partial \alpha} = 0$), d'où l'intégrale première :

$$\frac{\partial L}{\partial \dot{\alpha}} = r^2 \cos^2 \delta \dot{\alpha} = \text{constante} = \frac{\partial \mathcal{L}}{\partial \dot{\alpha}} \quad (\text{composante du moment cinétique sur } F_z). \quad (138)$$

Le système est conservatif ($\frac{\partial L}{\partial t} = 0$), d'où, puisqu'il n'y a pas de liaison, l'intégrale première de l'énergie :

$$T + \mathcal{V}_K = \frac{v^2}{2} - \frac{\mu}{r} = \frac{1}{2} \left(\dot{\delta}^2 + r^2 \dot{\alpha}^2 + 2ur^2 \dot{\alpha}^2 \right) - \frac{\mu}{r} = \text{constante} = \mathcal{E}, \quad (139)$$

qui sera utilisé à la place de l'équation de Lagrange pour r . L'équation de Lagrange restante, en δ , peut être écrite :

$$\frac{d}{dt} \left(\frac{\partial L}{\partial \dot{\delta}} \right) - \frac{\partial L}{\partial \delta} = \frac{d(r^2 \dot{\delta})}{dt} + r^2 \cos \delta \sin \delta \dot{\alpha}^2 = 0. \quad (140)$$

L'utilisation des équations (138) (139) et (140) permet d'intégrer le mouvement. Cette intégration est assez laborieuse, plus laborieuse qu'au paragraphe 1.2.2. En particulier le fait que le mouvement est plan ne s'obtient pas immédiatement comme dans le cas de l'utilisation de l'intégrale première du moment cinétique.

L'intégration conduit à :

$$\underline{Q} = \underline{Q}(q_1), \quad (141)$$

$$\underline{\dot{Q}} = \underline{\dot{Q}}(q_1), \quad (142)$$

où

$$q_1 = [q_1^j] = [a, e, i, \Omega, \omega, M]^T \quad (143)$$

sont les éléments orbitaux de Lagrange, introduits au paragraphe 1.2.3. Il y a bien 6 constantes d'intégration

$$q = [a, e, i, \Omega, \omega, \tau]^T. \quad (144)$$

Comme au paragraphe 1.2.3, la donnée des éléments orbitaux q_1^j est équivalente à celle des éléments Q^j, \dot{Q}^j .

2.3 - Formules de perturbations de Lagrange

Dans de nombreux problèmes de perturbation d'un mouvement képlérien (effet des dissymétries du potentiel terrestre ou effets luni-solaires sur l'orbite d'un satellite artificiel, perturbations planétaires, etc.), l'accélération perturbatrice $\vec{\gamma}$ dérive d'un potentiel perturbateur $R = R(\vec{x}, t)$, fonction de la position \vec{x} et, généralement, du temps t :

$$\vec{\gamma} = -\nabla R. \quad (145)$$

Les formules de perturbation des éléments orbitaux (94) - (99) peuvent alors être écrites sous une forme particulièrement commode, dite "de Lagrange", où les seconds membres sont exprimés en fonction des dérivées partielles $\frac{\partial R}{\partial q_j}$ du potentiel perturbateur par rapport aux éléments orbitaux q_j .

Cette forme pourrait être obtenue, par un calcul assez laborieux, en portant l'expression (145) de $\vec{\gamma}$ dans les formules de Gauss (94) - (99) "en $\mathcal{Q}, \dot{\mathcal{Q}}, \mathcal{W}$ ", en exprimant les composantes du gradient ∇R en fonction des dérivées partielles. Mais il est préférable, dans ce paragraphe consacré à la mécanique lagrangienne, d'utiliser l'approche élégante suivie par Lagrange pour résoudre le problème.

Le système "perturbé" est encore un système à lagrangien :

$$L = T - \mathcal{V}, \quad (146)$$

où, cette fois, le potentiel \mathcal{V} devient :

$$\mathcal{V} = \mathcal{V}_K + R = -\frac{\mu}{r} + R, \quad (147)$$

avec

$$R = R(Q, t) = R(r, \alpha, \delta, t). \quad (148)$$

Si l'on pose :

$$P_s = \frac{\partial L}{\partial \dot{Q}^s} = \frac{\partial T}{\partial \dot{Q}^s} \quad (\text{moments conjugués des } Q^s) \quad (149)$$

les équations de Lagrange s'écrivent :

$$\dot{P}_s = \frac{\partial L}{\partial Q^s} \quad (150)$$

La méthode d'intégration utilisée est encore une méthode de variation des constantes. Elle consiste à effectuer le changement de variables (141) (142) portant à la fois sur les Q^s et les \dot{Q}^s , où les q_i^j sont maintenant variables : ce sont les éléments orbitaux de l'orbite osculatrice O . D'où, également :

$$P_s = P_s(q_i^j) \quad (151)$$

Les équations de Lagrange (150) deviennent

$$\frac{\partial P_s}{\partial q_i^j} \dot{q}_i^j = \frac{\partial L}{\partial Q^s} \quad (152)$$

et la dérivation de (141) conduit à :

$$\frac{\partial Q^s}{\partial q_i^j} \dot{q}_i^j = \dot{Q}^s \quad (153)$$

Le but est d'éliminer les variables Q^s et \dot{Q}^s et d'obtenir des formules de perturbation en q_i^j . Cette élimination est possible. Elle met en jeu les crochets de Lagrange :

$$L_{ij} = [q_i^l, q_j^j] = \frac{\partial Q^s}{\partial q_i^l} \frac{\partial P_s}{\partial q_j^j} - \frac{\partial P_s}{\partial q_i^l} \frac{\partial Q^s}{\partial q_j^j} \quad (154)$$

qui peuvent être considérés comme des fonctions des q_i^j et qui sont en fait des constantes du mouvement képlérien, ce qui n'est pas évident a priori car $q_i^j = M$ varie en fonction du temps. Il est donc possible de les évaluer en un point particulier de l'orbite osculatrice O , le périhélie P par exemple, ce qui simplifie beaucoup les calculs. Tous calculs faits, on obtient finalement les formules de perturbation de Lagrange :

$$\dot{a} = -\frac{2}{na} \frac{\partial R}{\partial M} \quad (155)$$

$$\dot{e} = \frac{1}{na^2 e} \left[b \frac{\partial R}{\partial \omega} - p \frac{\partial R}{\partial M} \right] \quad (156)$$

$$\dot{i} = \frac{1}{nab \sin i} \frac{\partial R}{\partial \Omega} - \frac{1}{nab \cos i} \frac{\partial R}{\partial \omega} \quad (157)$$

$$\dot{\Omega} = -\frac{1}{nab \sin i} \frac{\partial R}{\partial i} \quad (158)$$

$$\dot{\omega} = \frac{1}{nab \cos i} \frac{\partial R}{\partial i} - \frac{b}{na^3 e} \frac{\partial R}{\partial e} \quad (159)$$

$$\dot{M} = n + \frac{p}{na} \frac{\partial R}{\partial a} + \frac{p}{na^3 e} \frac{\partial R}{\partial e} \quad (160)$$

où

$$R = R(q_i, t) = R(a, e, i, \Omega, \omega, M, t) \quad (161)$$

q_i^k ($k = 1, 2, \dots, 5$) sont constants, et $q_i^6 = M$ est fonction affine du temps.

2.4 - Application : perturbations des orbites des satellites artificiels dues aux dissymétries du potentiel terrestre

Il est bien connu que la Terre est sphérique en première approximation (1) (Fig. 26). Si elle est supposée, de plus, formée de couches sphériques homogènes, tout se passe comme si sa masse m_\oplus était concentrée en son centre, ce qui conduit à l'expression simplifiée du potentiel newtonien :

$$V = -\frac{k m_\oplus}{r} \quad (162)$$

utilisée en (21) et (135), et aux classiques orbites képlériennes.

En seconde approximation, la Terre peut être assimilée à un ellipsoïde de révolution aplati (2). Le renflement équatorial est responsable, en particulier, de perturbations dites "séculaires", qui, contrairement aux perturbations "périodiques", croissent linéairement en fonction du temps, et peuvent donc devenir très importantes au bout d'un temps suffisamment long. Ces perturbations, qui concernent les éléments Ω (ascension droite du noeud ascendant), ω (argument du périhélie) et M (anomalie moyenne) (Fig. 27), peuvent atteindre plusieurs degrés par jour comme nous le verrons plus loin.

L'influence des autres dissymétries sera également étudiée de façon très sommaire, qu'il s'agisse de dissymétries de révolution (par exemple, forme en "poire" de la Terre (3)), ou de dissymétries longitudinales (par exemple, ellipticité de l'équateur terrestre (4)).

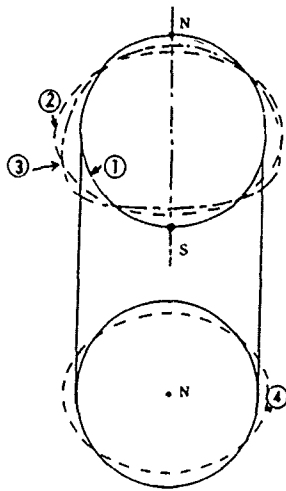


Figure 26 (Très schématique).

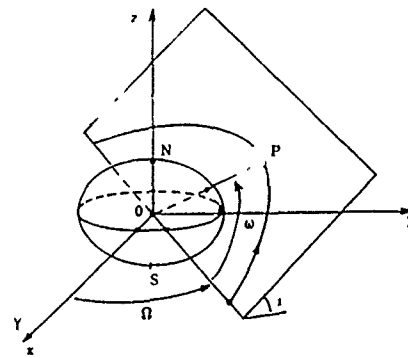


Figure 27

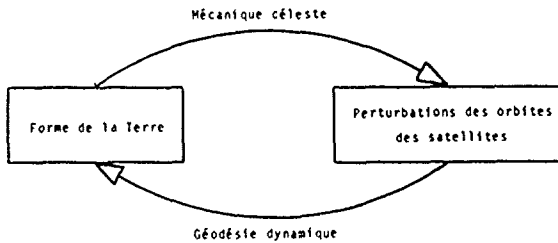


Figure 28

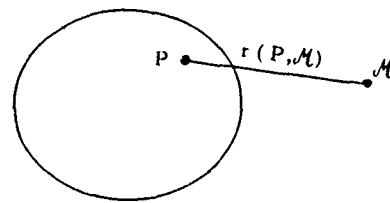


Figure 29

notons qu'inversement, l'observation des perturbations des orbites des satellites permet de se renseigner sur la forme de la Terre (géodésie dynamique) (Fig. 28) ; ce point sera souligné dans l'exposé [4].

Signalons enfin que, dans les études très précises, il faut tenir compte du fait que la forme de la Terre dépend du temps, à cause de l'élasticité et de la viscosité de ce corps (théorie de Love), soumis au champ de gravitation d'autres corps célestes (Lune et Soleil).

2.4.1 - Le potentiel terrestre

Dans le cas général (Fig. 29), il faut utiliser l'expression du potentiel :

$$V = -k \int \frac{\rho(P) dV}{r(P, M)} \quad (163)$$

où ρ est la masse volumique et $r(P, M) = \|\vec{PM}\|$

Il est bien connu que, à l'extérieur du corps, le potentiel newtonien est une fonction harmonique :

$$\Delta V = 0. \quad (164)$$

Il est donc logique de s'intéresser à la solution générale de (164), ou plutôt à une famille de solutions suffisamment générale pour qu'elle puisse servir de base pour repérer la fonction V définie en (163). Ce sont les harmoniques sphériques.

La forme quasi-sphérique de la Terre suggère le choix de coordonnées sphériques pour repérer la position du point courant M . Soit donc F le centre de masse de la Terre et $\vec{r} = x\vec{i} + y\vec{j} + z\vec{k}$ les axes géocentriques liés à la Terre (Fig. 30).

Il peut être montré que le potentiel terrestre V , défini en (163), admet un développement en harmoniques sphériques, que l'on écrit souvent :

$$V = -\frac{k}{r} \left[1 - \sum_{l=2}^{\infty} J_l \left(\frac{a_0}{r}\right)^l P_l(\sin \phi) + \sum_{l=2}^{\infty} \sum_{m=1}^l \left(\frac{a_0}{r}\right)^l P_{l,m}(\sin \phi) (C_{l,m} \cos m\lambda + S_{l,m} \sin m\lambda) \right], \quad (165)$$

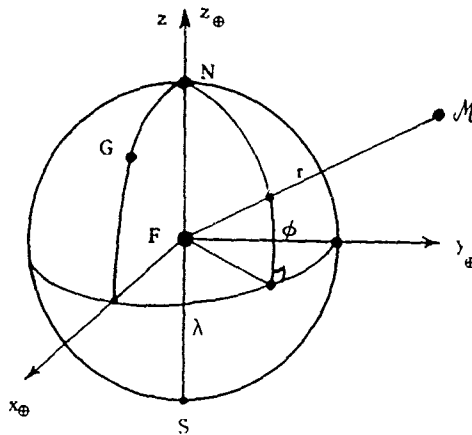


Figure 30

en séparant les harmoniques zonaux ($m = 0$) et tesseraux. Les termes en $l=1$ sont nuls car l'origine est prise au centre de masse de la Terre.

Dans ce développement, a_e est le rayon équatorial de la Terre ;

$$P_l(x) = \frac{1}{2^l l!} \frac{d^l}{dx^l} (x^2 - 1)^l, \tag{166}$$

est le polynôme de Legendre de degré l ;

$$P_{lm}(x) = (1 - x^2)^{m/2} \frac{d^m}{dx^m} P_l(x), \tag{167}$$

est la fonction de Legendre associée ; J_l, C_{lm}, S_{lm} sont des coefficients qui caractérisent le "corps" terrestre ; J_l est le coefficient de l'harmonique zonal de degré l ; C_{lm}, S_{lm} sont les coefficients des harmoniques tesseraux de degré l et d'ordre m .

On possède actuellement plusieurs modèles de potentiel élaborés à partir de mesures de poursuite de satellites et de mesures gravimétriques. Il s'agit de :

- GRIM 3, modèle européen ;
- GEMT₁, modèle du Goddard Space Flight Center ;
- WGS 84, modèle du DoD.

Ces modèles sont complets au moins jusqu'au degré et à l'ordre 36 pour les deux premiers, et 180 pour le dernier. Cependant le modèle WGS 84 est classifié et seuls les coefficients jusqu'à $l=m=18$ sont publiés. Il reste le modèle de référence utilisé pour la localisation des satellites NAVSTAR, situés à 20 000 km d'altitude.

Les modèles ne sont pas indépendants, puisque les mêmes satellites ont été utilisés pour les élaborer. Les coefficients les mieux connus sont ceux qui ont le plus d'influence aux altitudes des satellites observés.

Des matrices de covariances d'erreurs d'estimation existent, mais elles sont rarement publiées.

Il est important de remarquer que, le terme "d'aplatissement" J_2 est de l'ordre de 10^{-3} et que les autres coefficients J, C ou S sont de l'ordre de 10^{-6} au plus.

2.4.2 - Perturbations dues aux dissymétries du potentiel terrestre

2.4.2.1 - Potentiel perturbateur

Le potentiel terrestre V donné en (165) peut être écrit :

$$V = -\frac{\mu}{r} + R, \tag{168}$$

où R est le potentiel perturbateur :

$$R = \sum_{l=2}^{\infty} \sum_{m=0}^l R_{lm}, \tag{169}$$

avec

$$R_{lm} = \frac{\mu a_e^l}{2^l l!} P_{lm}(\sin \phi) (C_{lm} \cos m \lambda + S_{lm} \sin m \lambda), \tag{170}$$

Afin de pouvoir appliquer les formules de perturbations de Lagrange (155) - (160), il est nécessaire d'exprimer R non plus en fonction de la position "géographique" (α, λ, ϕ) du point M , mais en fonction des éléments orbitaux osculateurs $q = [\alpha, e, i, \Omega, \omega, M]$ et du temps t , comme indiqué en (161).

- Le temps t s'introduit évidemment par l'intermédiaire de l'angle

$$\Theta = (Fx, Fx_\oplus) = n_\oplus t, \quad (171)$$

de rotation des axes liés à la Terre $Fx_\oplus y_\oplus z_\oplus$, par rapport aux axes Fxy_z (Fig. 30).

n_\oplus est la vitesse de rotation de la Terre = 1 tour/jour sidéral, et t est alors l'heure sidérale de Greenwich.

Un calcul assez fastidieux, détaillé dans le livre de Kaula [6], conduit à l'expression :

$$R_{lm} = \frac{\mu a_0^2}{a^{l+1}} \sum_{p=c}^l F_{lmp}(i) \sum_{q=-\infty}^{+\infty} G_{2lpq}(e) S_{lmpq}(\omega, \Omega, M, \Theta), \quad (172)$$

où

$$S_{lmpq} = \begin{cases} C_{lm} \\ -S_{lm} \end{cases} \cos \alpha_{lmpq} + \begin{cases} S_{lm} \\ C_{lm} \end{cases} \sin \alpha_{lmpq}, \text{ selon } l-m \begin{cases} \text{pair} \\ \text{impair} \end{cases}, \quad (173)$$

avec :

$$\alpha_{lmpq} = (l-2p)\omega + (l-2p+q)M + m(\Omega - \Theta). \quad (174)$$

Comme il fallait s'y attendre, le temps t n'apparaît donc, par l'intermédiaire de l'angle Θ , que dans les termes tesseraux ($m \neq 0$).

Les fonctions $F_{lmp}(i)$ et $G_{2lpq}(e)$ ont des expressions générales assez compliquées.

Il est important de remarquer que, dans tous les cas, la partie principale de $G_{2lpq}(e)$ est en $e^{|q|}$, et que seuls les termes en $q=0$ sont non nuls pour $e=0$.

2.4.2.2 - Calcul des perturbations

Les formules de perturbation de Lagrange (155) - (160) peuvent être écrites sous la forme matricielle suivante

$$\dot{q}_1 = \dot{q}_{1k} + L(q_1) \left[\frac{\partial R(q_1, t)}{\partial q_1} \right]^T, \quad (175)$$

où \dot{q}_{1k} correspond aux variations des éléments orbitaux dans le mouvement képlérien osculateur :

$$\dot{q}_{1k} = [0, 0, 0, 0, 0, n]^T, \quad (176)$$

et où L est la matrice 6×6 de perturbation de Lagrange. Dans le potentiel perturbateur R , donné en (169), le terme prépondérant est le terme d'"aplatissement" :

$$R_{20} = \mu J_2 \frac{a_0^2}{a^3} \sum_{p,q} F_{20p}(i) G_{20pq}(e) \cos \alpha_{20pq}, \quad (177)$$

avec

$$\alpha_{20pq} = (2-2p)\omega + (2-2p+q)M, \quad (178)$$

car $J_2 = -C_{20}$ est de l'ordre de 10^{-3} alors que les autres coefficients C_{lm} et S_{lm} sont de l'ordre de 10^{-6} .

Il est alors commode de poser :

$$R = R_{20} + R_c, \quad (179)$$

où R_c est le potentiel perturbateur "complémentaire", correspondant aux autres termes zonaux ou tesseraux. Les formules de perturbation (175) deviennent alors :

$$\dot{q}_1 = \dot{q}_{1k} + L(q_1) \left[\frac{\partial R_{20}(q_1)}{\partial q_1} \right]^T + L(q_1) \left[\frac{\partial R_c(q_1, t)}{\partial q_1} \right]^T, \quad (180)$$

soit, en introduisant le "petit paramètre" $\varepsilon = J_2$:

$$\dot{q}_1 = f_{(0)}(q_1) + \varepsilon f_{(1)}(q_1) + \varepsilon^2 f_{(2)}(q_1, t). \quad (181)$$

La solution de (181) peut être alors cherchée sous la forme d'un développement asymptotique du type :

$$q_1 = q_{1(0)}(t) + \varepsilon q_{1(1)}(t) + \varepsilon^2 q_{1(2)}(t) + \dots \quad (182)$$

L'introduction de cette expression dans (181), le développement du second membre par la formule de Taylor et l'identification des termes de même puissance en ε permet, en principe, d'obtenir la solution pas-à-pas, par la résolution des systèmes différentiels correspondant aux différents ordres d'approximation.

a) Solution d'ordre zéro

La solution d'ordre zéro est donnée par :

$$\dot{q}_{1(0)} = f_{(0)}(q_{1(0)}), \quad (183)$$

et correspond au mouvement képlérien non perturbé.

b) Solution d'ordre 1

Le terme d'ordre 1 est donné par :

$$\dot{q}_{1(1)} = \frac{\partial f_{(0)}(q_{1(0)})}{\partial q_{1(0)}} q_{1(1)} + f_{(1)}(q_{1(0)}), \quad (184)$$

soit :

$$\dot{q}_{1(1)} = \frac{\partial f_{(0)}(q_{1(0)})}{\partial q_{1(0)}} q_{1(1)} + L(q_{1(0)}) \left[\frac{\partial R_{20}(q_{1(0)})/J_2}{\partial q_{1(0)}} \right]^T, \quad (185)$$

avec :

$$R_{20}(q_{1(0)}) = \mu J_2 \frac{a_0^2}{a_0^3} \sum_{p,q} F_{2cp}(i_0) G_{2pq}(e_0) \cos(\alpha_{20pq})_{(0)}, \quad (186)$$

où :

$$(\alpha_{20pq})_{(0)} = (2 - 2p + q) \omega_0 + (2 - 2p + q) M_{(0)}, \quad (187)$$

donc :

$$(\dot{\alpha}_{20pq})_{(0)} = (\dot{\alpha}_{20pq})_0 = (2 - 2p + q) n_0. \quad (188)$$

Dans le système différentiel (185), les $\dot{q}_{1(1)}^j$ sont des fonctions affines des $q_{1(0)}^j$. Il est donc possible de superposer les solutions. Or l'expression (188) montre qu'il faut distinguer dans R_{20} deux types de termes :

1) Perturbations séculaires ($2 - 2p + q = 0$):

Lorsque $2 - 2p + q = 0$, $(\alpha_{20pq})_{(0)}$ est constant par rapport au temps ; il en est donc de même de $R_{20pq}(0)$ et du deuxième terme du second membre de (185). On peut montrer que l'intégration de (185) conduit alors à des expressions des $\dot{q}_{1(1)}^j$, affines en fonction du temps. Ces perturbations sont appelées séculaires, car elles sont cumulatives et peuvent devenir très importantes au bout d'une durée suffisamment longue.

Tous les calculs faits on trouve les résultats suivants :

Les éléments a , e et i ne subissent pas de perturbations séculaires. M ne subit pas de perturbation séculaire induite par une perturbation séculaire sur a , puisque celle-ci est nulle.

Les éléments Ω , ω et M subissent les perturbations séculaires :

$$\dot{\Omega}_S = -\frac{3}{2} J_2 \left(\frac{ae}{a_0}\right)^2 n_0 \cos i_0, \quad (189)$$

$$\dot{\omega}_S = \frac{3}{4} J_2 \left(\frac{ae}{a_0}\right)^2 n_0 (5 \cos^2 i_0 - 1), \quad (190)$$

$$\dot{M}_S = \frac{3}{4} J_2 \left(\frac{ae}{a_0}\right)^2 (1 - e_0^2)^{-3/2} n_0 (3 \cos^2 i_0 - 1). \quad (191)$$

Ces perturbations dépendent de a_0 , e_0 et i_0 . Par exemple, pour une orbite circulaire ($e_0 = 0$), basse (altitude $Z_0 = 300$ km), on a $n_0 = 16$ révolutions/jour = $16 \times 360^\circ/j$, d'où :

$$\dot{\Omega}_S = -8,5 \cos i_0 \text{ } ^\circ/j, \quad (192)$$

$$\dot{\omega}_S = 4,2 (5 \cos^2 i_0 - 1) \text{ } ^\circ/j, \quad (193)$$

$$\dot{M}_S = 4,2 (3 \cos^2 i_0 - 1) \text{ } ^\circ/j. \quad (194)$$

Ces perturbations séculaires sont importantes.

Le noeud N se déplace dans le sens rétrograde ($\dot{\Omega}_S < 0$) pour une orbite directe ($0 < i_0 < 90^\circ$), d'autant moins rapidement que l'inclinaison est plus forte, il n'y a pas de perturbation séculaire de la ligne des noeuds dans le cas d'une orbite polaire ($i_0 = 90^\circ$).

Le plan de l'orbite garde la même orientation par rapport au Soleil lorsque $\dot{\Omega}_S \approx 1^\circ/j$, donc $\cos i_0 \approx 1/8,5$ et $i_0 \approx 96^\circ,75$ (orbite rétrograde). Cette orbite est dite "héliosynchrone".

La rotation du périégée P dans le plan de l'orbite se fait dans le sens du mouvement ($\dot{\omega}_S > 0$) pour une orbite d'inclinaison faible ($i_0 \approx 0$), et dans le sens opposé ($\dot{\omega}_S < 0$) pour une orbite de forte inclinaison ($i_0 \approx 90^\circ$). La perturbation séculaire est nulle pour $i_0 = i_c$ ou $180^\circ - i_c$, où i_c est l'inclinaison critique :

$$i_c = \text{Arc cos } \frac{1}{\sqrt{5}} = 63^\circ 26'. \quad (195)$$

2) Perturbations à courtes périodes dues à J_2 ($2 - 2p + q \neq 0$) :

Lorsque $2 - 2p + q \neq 0$, $(\alpha_{2pq})_{(0)}$ est une fonction affine du temps, $(R_{2pq})_{(0)}$ est une fonction sinusoïdale du temps, et il en est de même du deuxième terme du second membre de (185). L'intégration de (185) conduit alors à des expressions des $q_{2pq}^{(n)}$, périodiques à courte période (fréquence égale à $(2 - 2p + q)n_0$, donc période égale à un sous-multiple de la période orbitale T_0).

L'intégration introduit le facteur $(1/\alpha_0) \leq (1/n_0) \approx 10^3$. Mais comme, d'une part, n_0^2 est en facteur dans R_{20} , par l'intermédiaire de μ , et, d'autre part, n_0 figure en dénominateur dans les formules de perturbations, les dérivées $q_{2pq}^{(n)}$ sont bien de l'ordre de l'unité, et les perturbations sur les éléments orbitaux de l'ordre de $J_2 \approx 10^{-3}$. Ces perturbations ne seront pas détaillées.

c) Perturbations d'ordres supérieurs

Il est hors de question d'étudier ici en détail les perturbations d'ordre supérieur. On se contentera de quelques considérations qualitatives, pour mettre en évidence les perturbations les plus importantes.

L'étude précédente a montré qu'une bonne approximation de $\dot{\alpha}_{2mpq}$ était :

$$\dot{\alpha}_{2mpq} = (l - 2p) \dot{\alpha}_s + (l - 2p + q) \dot{M} + m(\dot{\Omega}_s - \dot{\Omega}) \quad (196)$$

avec :

$$\dot{M} = n_0 + \dot{M}_s \quad (197)$$

où $\dot{\Omega}_s, \dot{\alpha}_s$ et \dot{M}_s sont données en (189) - (191).

L'intégration des formules de perturbations introduit le facteur $1/\alpha$. Les perturbations les plus importantes sont obtenues lorsque α est petit. C'est le problème des "petits dénominateurs", classique en Mécanique Céleste. Cela conduit à distinguer, de façon générale :

1) Les effets séculaires, dus aux termes tels que $l - 2p = l - 2p + q = m = 0$. Alors $\dot{\alpha} = 0$ et l'intégration conduit, en fait, à un effet proportionnel au temps t . Ces effets séculaires sont dus aux termes zonaux ($m = 0$), pairs ($l = 2p$).

2) Les effets à longue période, liés au mouvement rotation du périhélie dans le plan de l'orbite. Ils apparaissent pour les termes tels que $l - 2p + q = m = 0$ et $l - 2p \neq 0$, donc $\dot{\alpha} = -q\dot{\omega}$ ($q \neq 0$). Comme $G_{2pq}(e) = 0$ ($e^{i\theta}$), l'effet, pour une orbite quasi circulaire ($e \approx 0$) est surtout important pour $q = +1$. Alors $|\dot{\alpha}| = |\dot{\omega}| \ll \dot{M}$. La période est alors celle de la rotation du périhélie dans le plan de l'orbite, soit 86 jours pour une orbite basse ($Z_c = 300$ km), polaire ($i_0 = 90^\circ$). Ces effets à longue période sont dus aux termes zonaux ($m = 0$), impairs ($l = 2p + 1$), dans le cas d'une faible excentricité.

3) Les effets résonnants, dus au couplage entre le mouvement d'orbitation du satellite et la rotation terrestre.

Dans l'expression :

$$\dot{\alpha} \approx (l - 2p + q)n - m \text{ révolutions/jour sidéral} \quad (198)$$

le moyen mouvement n dépend de l'altitude Z_c de l'orbite. Par exemple, pour 567 km $\leq Z_c \leq 894$ km, on a $15 \geq n \geq 14$.

Les effets résonnants ($\dot{\alpha} \approx 0$) les plus importants correspondent aux conditions $l - 2p + q = 1$, donc $m = 14$ ou 15 (à cause du facteur $(a_0/a)^2$, qui conduit à chercher des l petits) et $q = 0$ (pour avoir un effet direct important sur α , donc un effet indirect important sur M).

4) Les effets journaliers ou semi-journaliers, dus aux termes d'ordre faible ($m = 1$ ou 2). Lorsque $l - 2p + q = 0$, $\dot{\alpha} \approx -m\dot{\Omega}$ est petit pour m petit, par exemple $m = 1$, d'où $\dot{\alpha} \approx -1$ tour/jour, soit une période de 1 jour. Les effets les plus importants sont obtenus pour $q = 0$, donc $l = 2p$ (termes tesseraux pairs d'ordre faible).

3 FORMALISME HAMILTONIEN

Le formalisme hamiltonien est encore plus abstrait que le formalisme lagrangien. Les variables utilisées perdent de leur sens physique, mais la forme condensée des équations du mouvement (forme canonique) se prête bien à leur résolution et, en particulier, aux changements de variables (transformations canoniques). La recherche d'une telle transformation conduisant à des équations du mouvement particulièrement simples suggère une nouvelle méthode de résolution du problème mécanique : la méthode de Jacobi. Cette méthode très appropriée pour le traitement du problème des 2 centres fixes, est d'assez peu d'intérêt dans le cas du problème des 2 corps. Cependant, elle conduit à définir un jeu de variables canoniquement conjuguées, qui permet de traiter élégamment le problème du mouvement képlérien perturbé (formules canoniques de perturbations et méthode de von Zeipel).

3.1 - Equations canoniques3.1.1 - Hamiltonien

Soit un système à lagrangien, à n degrés de liberté, de lagrangien $L(q, \dot{q}, t)$.
Les équations de Lagrange (132), rappelées ici :

$$\frac{d}{dt} \left(\frac{\partial L}{\partial \dot{q}^i} \right) - \frac{\partial L}{\partial q^i} = 0 \quad (i = 1, 2, \dots, n), \quad (199)$$

constituent un système de n équations différentielles du second ordre pour les fonctions inconnues $q^i(t)$.

Ce système est équivalent au système :

$$\frac{dq^i}{dt} = \dot{q}^i, \quad (200)$$

$$\frac{d}{dt} \left(\frac{\partial L}{\partial \dot{q}^i} \right) - \frac{\partial L}{\partial q^i} = 0, \quad (201)$$

de $2n$ équations différentielles du premier ordre pour les $2n$ fonctions inconnues $q^i(t), \dot{q}^i(t)$.

L'inconvénient du système (200) (201) est qu'il n'est pas entièrement résolu par rapport aux dérivées premières dq^i/dt , $d\dot{q}^i/dt$ des fonctions inconnues q^i, \dot{q}^i .
Pour obtenir ce résultat, il est nécessaire de choisir $2n$ autres fonctions inconnues. La forme de (200) et (201) suggère le choix $q^i(t), p_i(t)$, avec :

$$p_i = \frac{\partial L}{\partial \dot{q}^i}. \quad (202)$$

p_i est appelé le moment conjugué de q^i .

3.1.2 - Système canonique

Lorsqu'on effectue, dans le système (200), (201) le changement de variables qui fait passer des variables de Lagrange q^i, \dot{q}^i aux variables de Poisson p_i, q^i on trouve que les nouvelles fonctions inconnues $p_i(t), q^i(t)$ doivent satisfaire le système de $2n$ équations différentielles du premier ordre, résolu par rapport aux dérivées premières, et de forme particulièrement simple et symétrique :

$$\dot{q}^i = \frac{\partial H}{\partial p_i}, \quad (203)$$

$$\dot{p}_i = - \frac{\partial H}{\partial q^i}, \quad (204)$$

où :

$$H = p_i \dot{q}^i - L = H(p_i, q^i, t) \quad (205)$$

est le hamiltonien (transformé de Legendre du Lagrangien par rapport aux variables \dot{q}^i).

Le système est appelé système canonique d'Hamilton.
De même que, dans le formalisme lagrangien, toute l'information concernant le mouvement étant contenue dans le lagrangien L , dans le formalisme hamiltonien, cette information est contenue dans l'hamiltonien H .

La variable q^i est dit ignorable ou cyclique si elle ne figure pas dans l'hamiltonien, c'est-à-dire si :

$$\frac{\partial H}{\partial q^i} = 0. \quad (206)$$

Lorsque q^i est ignorable, l'équation de Lagrange (204) correspondante peut être écrite :

$$\dot{p}_i = 0, \quad (207)$$

dont l'intégration conduit à l'intégrale première :

$$p_i = \text{constante} = a_i. \quad (208)$$

q^i peut alors être obtenu par une quadrature finale, après la résolution du système d'ordre $2n - 2$:

$$\dot{q}^j = \frac{\partial H}{\partial p_j}, \quad j \neq i, \quad (209)$$

$$\dot{p}_j = - \frac{\partial H}{\partial q^j}. \quad (210)$$

Le système est dit conservatif si la variable t ne figure pas explicitement dans l'expression de l'hamiltonien, c'est-à-dire si :

$$\frac{\partial H}{\partial t} = 0. \quad (211)$$

Or on a toujours :

$$\text{soit : } \frac{dH}{dt} = \frac{\partial H}{\partial p_i} \dot{p}_i + \frac{\partial H}{\partial q_i} \dot{q}_i + \frac{\partial H}{\partial t} = \frac{\partial H}{\partial p_i} \left(-\frac{\partial H}{\partial q_i} \right) + \frac{\partial H}{\partial q_i} \left(\frac{\partial H}{\partial p_i} \right) + \frac{\partial H}{\partial t} = \frac{\partial H}{\partial t}, \quad (212)$$

$$\frac{dH}{dt} = \frac{\partial H}{\partial t}. \quad (213)$$

Lorsque le système est conservatif, on a donc

$$\frac{dH}{dt} = 0, \quad (214)$$

dont l'intégration conduit à l'intégrale première de l'hamiltonien :

$$H = \text{constante}. \quad (215)$$

Cette intégrale réduit d'une unité d'ordre du système différentiel restant à résoudre. Il est possible de le réduire d'une unité supplémentaire par le choix d'une composante q^i , ou même d'une composante p_i , comme nouvelle variable indépendante, en considérant alors que le temps t comme une composante q^i supplémentaire (une variable ignorable puisque le système est conservatif).

Il est, bien sûr, impossible d'utiliser, comme nouvelle variable indépendante, le moment p_i conjugué d'une variable ignorable q^i , de même que la variable ignorable elle-même. Autrement, le bénéfice de la quadrature finale correspondante serait perdu.

De façon générale, l'analogie entre les équations (204) et (213) d'une part, et les intégrales (208) et (215) d'autre part, montre que le temps t joue un rôle relativement symétrique par rapport aux composantes q^i . Cette analogie peut être développée en posant $t = q^{n+1}$ et en choisissant une autre variable de description Z . Cela montre en particulier que le rôle de p_{n+1} est joué par $-H$, comme cela est visible sur (213), qui peut encore être écrit :

$$\frac{d(-H)}{dt} = -\frac{\partial H}{\partial t}. \quad (216)$$

3.1.3 - Application au problème des 2 corps

Il s'agit seulement de montrer comment se présente l'intégration du problème des 2 corps dans le formalisme hamiltonien, afin de comparer avec l'approche lagrangienne du paragraphe 2.2.

En coordonnées sphériques (Fig. 25), les variables P_S , conjuguées des Q^S , s'écrivent :

$$P_r = \frac{\partial L}{\partial \dot{r}} = \dot{r}, \quad (217)$$

$$P_\delta = \frac{\partial L}{\partial \dot{\delta}} = r^2 \dot{\delta}, \quad (218)$$

$$P_\alpha = \frac{\partial L}{\partial \dot{\alpha}} = r^2 \cos^2 \delta \dot{\alpha}, \quad (219)$$

ce qui conduit à l'hamiltonien :

$$H_K = T + \mathcal{V}_K = \left(P_r^2 + \frac{P_\delta^2}{r^2} + \frac{P_\alpha^2}{r^2 \cos^2 \delta} \right) - \frac{\mu}{r}. \quad (220)$$

L'angle α est ignorable, d'où l'intégrale première :

$$P_\alpha = \text{constante} = h_z. \quad (221)$$

L'angle α pourra être obtenu par une quadrature finale.

Le système est conservatif ($\partial H / \partial t = 0$), d'où l'intégrale première de l'hamiltonien :

$$H_K = T + \mathcal{V}_K = \frac{1}{2} \left(P_r^2 + \frac{P_\delta^2}{r^2} + \frac{P_\alpha^2}{r^2 \cos^2 \delta} \right) - \frac{\mu}{r} = \text{constante} = \mathcal{E}, \quad (222)$$

qui sera utilisée à la place de l'équation d'Hamilton en P_r . De plus, le temps t pourra être obtenu par une quadrature finale, à condition de changer de variable de description.

Les équations canoniques restantes peuvent être écrites :

$$\dot{r} = \frac{\partial H}{\partial P_r} = P_r, \quad (223)$$

$$\dot{\delta} = \frac{\partial H}{\partial P_\delta} = \frac{P_\delta}{r^2}, \quad (224)$$

$$\dot{\alpha} = \frac{\partial H}{\partial P_\alpha} = \frac{P_\alpha}{r^2 \cos^2 \delta}, \quad (225)$$

$$\dot{P}_\delta = -\frac{\partial H}{\partial \delta} = -\frac{P_\delta^2 \sin \delta}{r^2 \cos^3 \delta} = -\frac{h_z^2 \sin \delta}{r^2 \cos^3 \delta}, \quad (226)$$

Ce système peut être intégré comme au paragraphe 2.2. On retrouve les trajectoires képlériennes.

Dans cet exemple particulier, l'utilisation du formalisme hamiltonien ne présente pas un avantage marqué. Cependant la structure des équations canoniques d'hamilton est plus simple que celle des équations de Lagrange, et le formalisme hamiltonien s'avère particulièrement intéressant lorsqu'il s'agit, par exemple, d'effectuer des changements de variables.

3.2 - Transformations canoniques

L'intégration du système canonique d'Hamilton est évidemment d'autant plus simple qu'il y a un nombre plus important de variables ignorables. Or le nombre de ces variables dépend du choix du paramétrage. Ayant effectué un certain choix initial, il peut être désirable de changer de paramétrage en cours de calcul, tout en préservant la forme canonique des équations. On appelle transformation canonique un tel changement de variables.

Théorème :

Soit p_i, q^i , $2n$ variables canoniquement conjuguées, d'hamiltonien $H(p, q, t)$:

$$\dot{q}^i = \frac{\partial H}{\partial p_i}, \quad (i = 1, 2, \dots, n), \quad (227)$$

$$\dot{p}_i = - \frac{\partial H}{\partial q^i}. \quad (228)$$

On peut démontrer que la transformation :

$$p'_j = p'_j(p_i, q^i, t), \quad (j = 1, 2, \dots, n), \quad (229)$$

$$q'^i = q'^i(p_j, q^j, t), \quad (230)$$

est canonique, c'est-à-dire p'_i, q'^i sont $2n$ variables canoniquement conjuguées, d'hamiltonien $H'(p', q', t)$, soit

$$\dot{q}'^i = \frac{\partial H'}{\partial p'_i}, \quad (231)$$

$$\dot{p}'_i = - \frac{\partial H'}{\partial q'^i}, \quad (232)$$

si, et seulement si, la différence entre les formes différentielles :

$$\omega = p_i dq^i - H dt, \quad (233)$$

et

$$\omega' = p'_i dq'^i - H' dt, \quad (234)$$

est la différentielle d'une fonction $F_1(q, q', t)$, soit :

$$\omega - \omega' = p_i dq^i - H dt - (p'_i dq'^i - H' dt) = dF_1. \quad (235)$$

On déduit de (235)

$$p_i = \frac{\partial F_1}{\partial q^i}, \quad (236)$$

$$p'_i = - \frac{\partial F_1}{\partial q'^i}, \quad (237)$$

$$H' = H + \frac{\partial F_1}{\partial t}. \quad (238)$$

Il en résulte la méthode suivante pour obtenir une transformation canonique. On choisit arbitrairement la fonction $F_1(q, q', t)$, d'où les relations (236)-(238). Si les relations (236) sont solubles par rapport aux n variables q^i , elles définissent les équations de transformation (230). Les relations (237), où les q'^i ont été remplacées par les expressions obtenues, définissent les équations de transformation (229). Enfin (238) définit le nouvel hamiltonien.

On dit que F_1 est la fonction génératrice (de première espèce) de la transformation canonique.

3.3 - Méthode d'intégration de Jacobi

Soit à intégrer un système canonique engendré par l'hamiltonien H . Une méthode de résolution consiste à rechercher une transformation canonique conduisant à un nouvel hamiltonien H' particulièrement simple, nul par exemple.

$$H' = 0, \quad (239)$$

car alors, le système canonique (231) (232), qui devient :

$$\dot{q}'^i = 0, \quad (240)$$

$$\dot{p}'_i = 0, \quad (241)$$

peut être intégré immédiatement :

$$q'^i = \text{constante} = a^i, \quad (242)$$

$$p'_i = \text{constante} = -b_i. \quad (243)$$

Supposons connue la fonction génératrice $F_1(q, q', t)$ d'une telle transformation. Elle doit satisfaire la relation (238), qui compte tenu de (239), (236), (242) et en posant :

$$S(q, t; \underline{a}) = F_1(q, \underline{a}, t), \quad (244)$$

peut être écrite :

$$\frac{\partial S}{\partial t} + H\left(\frac{\partial S}{\partial q}, q, t\right) = 0. \quad (245)$$

Cette équation aux dérivées partielles du premier ordre est appelée équation d'Hamilton-Jacobi, à $n+1$ variables q, t . La fonction $S(q, t; \underline{a}) + a^{n+1}$, où a^{n+1} est une constante additive arbitraire, en constitue une intégrale complète (famille de solutions à $n+1$ paramètres \underline{a}, a^{n+1}), de laquelle il est possible de déduire sans intégration toutes les solutions de l'équation.

Inversement, supposons connue une solution $S(q, t; \underline{a})$ de l'équation (245) dépendant de n constantes arbitraires \underline{a} , non additives ($S + a^{n+1}$ est donc une intégrale complète). La fonction :

$$F_1(q, q', t) = S'(q, t; q') \quad (245)$$

est la fonction génératrice cherchée. En effet :

$$H' = H(p, q, t) + \frac{\partial F_1}{\partial t} = H\left(\frac{\partial F_1}{\partial q}, q, t\right) + \frac{\partial F_1}{\partial t} = H\left(\frac{\partial S}{\partial q}, q, t\right) + \frac{\partial S}{\partial t} = 0. \quad (247)$$

Les fonctions $q^i(t), p_i(t)$ sont obtenues sans intégration. Les premières sont telles que :

$$\frac{\partial S(q(t), t; \underline{a})}{\partial a^i} = b_i, \quad (248)$$

ce qui les définit implicitement en fonction du temps et des $2n$ constantes arbitraires $\underline{a}, \underline{b}$.

Ces fonctions étant connues, les moments conjugués sont obtenus à partir des relations :

$$p_i(t) = \frac{\partial S(q(t), t; \underline{a})}{\partial q^i}. \quad (249)$$

L'intégration des équations canoniques est donc ramenée à la recherche d'une intégrale complète de l'équation d'Hamilton-Jacobi.

Remarque : Séparation des variables

D'une façon générale, on peut montrer que l'intégration du système canonique et la recherche d'une intégrale complète de l'équation d'Hamilton-Jacobi sont des problèmes équivalents (les trajectoires dans l'espace des phases q, p sont les caractéristiques de l'équation d'Hamilton-Jacobi). Cependant dans de nombreux cas importants le second reçoit une solution simple par séparation de variables, et la méthode de Jacobi n'est utilisée pratiquement que dans cette hypothèse.

On dit que les variables q et t figurant dans l'équation (245) sont séparables s'il existe une solution de la forme :

$$S = S_1(q^1; a^1) + S_2(q^2; a^2) + \dots + S_n(q^n; a^n) + S_t(t; a^t). \quad (250)$$

3.3.3 - Première application : intégration du problème des 2 corps par la méthode de Jacobi

L'équation d'Hamilton-Jacobi correspondant à l'hamiltonien H , donné en (220), s'écrit :

$$\frac{\partial S}{\partial t} + \frac{1}{2} \left[\left(\frac{\partial S}{\partial r} \right)^2 + \frac{1}{r^2} \left(\frac{\partial S}{\partial \varphi} \right)^2 + \frac{1}{r^2 a^2 \sin^2 \delta} \left(\frac{\partial S}{\partial \alpha} \right)^2 \right] - \frac{\mu}{r} = 0, \quad (251)$$

dont l'intégration est possible, bien qu'assez laborieuse, par séparation de variables. On retrouve les trajectoires képlériennes.

Là encore, l'intégration du mouvement képlérien par la méthode de Jacobi est comparativement plus lourde que l'intégration par les théorèmes généraux. En particulier le fait que le mouvement est plan n'apparaît ici que très en aval dans la démonstration, alors que le résultat peut être immédiatement obtenu par application du théorème du moment cinétique. Cependant la méthode de Jacobi permet la détermination des constantes a^3, b_3 (constantes de Jacobi) :

$$\begin{aligned} a^t &= -\mathcal{E} , & a^r &= h , & a^\alpha &= h \cos i , \\ b_t &= \tau , & b_r &= \omega , & b_\alpha &= \Omega , \end{aligned} \quad (252)$$

dont la connaissance est essentielle pour l'étude des mouvements perturbés considérés plus loin.

3.3.4 - Deuxième application : intégration du problème des deux centres fixes par la méthode de Jacobi

Le mouvement d'un point matériel autour de deux points matériels fixes dans l'espace absolu, qui l'attirent selon la loi newtonienne (Fig. 31), peut être complètement intégré de façon particulièrement commode par la méthode de Jacobi, car les variables sont séparables en coordonnées sphériques. Ce résultat est particulièrement important en Astrodynamique, car, pour un choix convenable des paramètres, (masses m_1 et m_2 , distance $M_1 M_2$), le mouvement ainsi intégré constitue une excellente approximation du mouvement d'un satellite artificiel autour d'une Terre à symétrie massique non sphérique. On peut rendre compte du terme en J_2 (cas $m_1 = m_2$) et même en J_3 (cas $m_1 \neq m_2$). Ce mouvement peut servir de solution de base pour une étude de perturbations par les autres termes du potentiel terrestre (et les puissances de J_2 et, éventuellement de J_3). Par rapport à la méthode classique utilisant le mouvement képlérien comme solution de base, la précision est globalement améliorée dans un rapport 10^3 .

Ce calcul ne sera pas développé ici. Le lecteur est renvoyé à la référence [7].

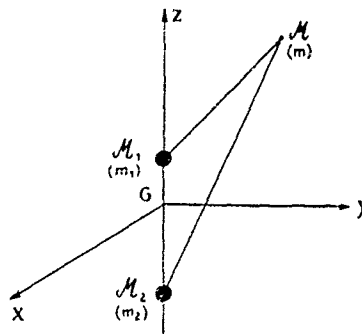


Figure 31

3.4 - Formules canoniques de perturbations

3.4.1 - Formules de perturbations

Dans le cas d'un mouvement képlérien perturbé par le potentiel perturbateur R , l'hamiltonien peut être écrit :

$$H = T + \mathcal{V} = T + \mathcal{V}_K + R = H_K + R , \quad (253)$$

où l'hamiltonien "képlérien" H_K est donné en (220).

Supposons (ce qui est le cas ici) que le mouvement képlérien, engendré par l'hamiltonien H_K , ait été intégré par la méthode de Jacobi, c'est-à-dire qu'il ait été possible de trouver une fonction génératrice $F_1(\alpha, \beta, \epsilon)$ qui engendre une transformation canonique $(P, Q) \rightarrow (P', Q')$ telle que le nouvel hamiltonien H'_K soit nul :

$$H'_K = H_K + \frac{\partial F_1}{\partial \epsilon} = 0. \quad (254)$$

Dans l'étude du mouvement perturbé engendré par l'hamiltonien H , donné en (253), il est possible d'éliminer le terme H_K , c'est-à-dire d'éliminer la partie "intégrable" du mouvement, en appliquant la même transformation canonique que précédemment. En effet, le nouvel hamiltonien :

$$H' = H + \frac{\partial F_1}{\partial \epsilon} = H_K + R + \frac{\partial F_1}{\partial \epsilon} = R \quad (255)$$

est égal à l'hamiltonien perturbateur R , qui doit être évidemment exprimé en fonction des nouvelles variables canoniquement conjuguées Q'_s, P'_s . Ces variables ne sont autres que les constantes d'intégration a_3, b_3 (éléments orbitaux) du mouvement képlérien. La méthode utilisée est donc, ici encore, une méthode de variation des constantes.

Dans le formalisme hamiltonien, les formules de perturbation peuvent être écrites immédiatement :

$$\dot{Q}'_s = \frac{\partial R}{\partial P'_s} \quad (256)$$

$$\dot{P}'_s = - \frac{\partial R}{\partial Q'_s}, \quad (257)$$

où :

$$R = R (P', Q', t). \quad (258)$$

De plus, ces formules sont sous la forme canonique, particulièrement commode pour les manipulations ultérieures.

Explicitons le système (256) (257) :

$$\begin{cases} \frac{d(\mathcal{E})}{dt} = \frac{\partial R}{\partial(\tau)} & , \quad \frac{dh}{dt} = \frac{\partial R}{\partial(\omega)} & , \quad \frac{d(h \cos i)}{dt} = \frac{\partial R}{\partial(\Omega)} & , \\ \frac{d(\tau)}{dt} = - \frac{\partial R}{\partial(\mathcal{E})} & , \quad \frac{d(\omega)}{dt} = - \frac{\partial R}{\partial h} & , \quad \frac{d(\Omega)}{dt} = - \frac{\partial R}{\partial(h \cos i)} & , \end{cases} \quad (259)$$

où R est supposé exprimé en fonction de $\mathcal{E}, h, h \cos i, \tau, \omega, \Omega$ et t .

3.4.2 - Passage aux variables de Delaunay

Il est évident sur (259) que les variables $-\mathcal{E}, h, h \cos i, \tau, \omega, \Omega$ (variables de Jacobi) sont également canoniquement conjuguées, l'hamiltonien correspondant étant R . Chaque instant, ces variables définissent les éléments orbitaux de l'orbite képlérienne osculatrice au mouvement.

Nous utiliserons de préférence, dans la suite, un autre système de variables canoniques, les variables Delaunay, qui a eu une grande importance dans le développement de la théorie de la Lune et qui reste un des systèmes les plus efficacement utilisés dans les problèmes de perturbations. Vérifions que les variables de Delaunay :

$$\begin{cases} L = \sqrt{\mu a} & , \quad G = h & , \quad H = h \cos i \quad (\text{ne pas confondre avec l'hamiltonien } H) \\ l = M = n(t - \tau) & , \quad g = \omega & , \quad h = \Omega & , \end{cases} \quad (260)$$

($M =$ anomalie moyenne ; $n =$ moyen mouvement, $n^2 a^3 = \mu$)

sont canoniquement conjuguées et calculons l'hamiltonien ϕ correspondant.

Une condition nécessaire et suffisante pour que la transformation :

$$(-\mathcal{E}, h, h \cos i, t; \tau, \omega, \Omega, -R) \mapsto (L, G, H, t; l, g, h, \phi)$$

soit canonique, est qu'il existe une fonction $F_1(\mathcal{E}, L, t)$ telle que :

$$-\tau d\mathcal{E} + R dt - (l dL - \phi dt) = dF_1(\mathcal{E}, L, t) \quad (\text{différentielle exacte}), \quad (261)$$

portant $\mathcal{E} = -\frac{\mu^2}{2L^2}$ et $\tau = t - \frac{l}{h} - t - \frac{L^3 l}{\mu^2}$ dans (154), la CNS s'écrit :

$$-\frac{\mu^2}{L^3} dL + (R + \phi) dt = dF_1(L, t) \quad (\text{différentielle exacte}). \quad (262)$$

Cette condition est vérifiée si et seulement si :

$$\frac{\partial(R + \phi)}{\partial L} = \frac{\partial}{\partial t} \left(-\frac{\mu^2}{L^3} \right) = -\frac{\mu^2}{L^3}, \quad (263)$$

d'où

$$R + \phi = \frac{\mu^2}{2L^2} + \text{constante}; \quad (264)$$

il suffit de prendre

$$\phi = \frac{\mu^2}{2L^2} - R. \quad (265)$$

L'hamiltonien ϕ doit être exprimé en fonction des variables de Delaunay.

* Ceci est à comparer avec les développements des § 1.3.1.3 et 2.3.

3.4.4 - Principe de la méthode de von Zeipel

La méthode consiste à résoudre le système canonique :

$$\begin{cases} \frac{dL}{dt} = \frac{\partial \phi}{\partial L} & , & \frac{dG}{dt} = \frac{\partial \phi}{\partial G} & , & \frac{dH}{dt} = \frac{\partial \phi}{\partial H} & , \\ \frac{dl}{dt} = -\frac{\partial \phi}{\partial l} & , & \frac{dg}{dt} = -\frac{\partial \phi}{\partial g} & , & \frac{dh}{dt} = -\frac{\partial \phi}{\partial h} & , \end{cases} \quad (266)$$

par une série de changements de variables canoniques indépendants du temps, réalisés à l'aide de fonctions génératrices du type $F_3^{(1)}$, que nous noterons $F(L', G', H'; l, g, h)$. Le changement de variable est :

$$\begin{cases} L = \frac{\partial F}{\partial L'} & , & G = \frac{\partial F}{\partial G'} & , & H = \frac{\partial F}{\partial H'} & , \\ l' = \frac{\partial F}{\partial l'} & , & g' = \frac{\partial F}{\partial g'} & , & h' = \frac{\partial F}{\partial h'} & , \end{cases} \quad (267)$$

et l'hamiltonien est conservé : $\phi' = \phi$. La fonction génératrice F , arbitraire, est choisie de façon que ϕ' ne dépende pas d'une des variables angulaires dont ϕ dépend. L'itération de la méthode permet d'éliminer toutes les variables angulaires et la dernière expression ϕ'' de l'hamiltonien n'est plus fonction que de L'' , G'' et H'' . Les trois premières équations finales :

$$\frac{dL''}{dt} = \frac{\partial \phi''}{\partial L''} = 0 & , & \frac{dG''}{dt} = \frac{\partial \phi''}{\partial G''} = 0 & , & \frac{dH''}{dt} = \frac{\partial \phi''}{\partial H''} = 0 & , \quad (268)$$

montrent que L'' , G'' , et H'' sont des constantes. Portant ces valeurs dans les trois dernières équations finales :

$$\frac{dl''}{dt} = -\frac{\partial \phi''}{\partial l''} = cte = n_l & , & \frac{dg''}{dt} = -\frac{\partial \phi''}{\partial g''} = cte = n_g & , & \frac{dh''}{dt} = -\frac{\partial \phi''}{\partial h''} = cte = n_h & , \quad (269)$$

on voit que l'' , g'' , et h'' sont fonctions affines du temps. On revient aux variables initiales L, G, H, l, g, h , à l'aide des diverses transformations (267).

L'application de cette méthode permet, en particulier, de retrouver simplement les perturbations séculaires (189) - (191).

4 - MECANIQUE VARIATIONNELLE - LIEN AVEC LES THEORIES D'OPTIMISATION

L'évolution des systèmes mécaniques considérés plus haut est régie par un principe variationnel global (minimum de l'"action"), dont le principe des puissances virtuelles n'est qu'une expression locale (dans le temps, c'est-à-dire "instantanée"). Il s'agit de rappeler ce principe et de montrer le lien entre cette mécanique variationnelle et les méthodes modernes d'optimisation, comme le Principe du Maximum de Contensou-Pontryagin (Fig. 1).

4.1 - Principe du Maximum de Contensou-Pontryagin [8, 9]

Le lecteur est certainement familiarisé avec la théorie classique du calcul des variations et l'utilisation des équations d'Euler. Cette théorie est suffisante pour traiter le problème de la mécanique variationnelle. Cependant, le Principe du Maximum de Contensou-Pontryagin, qui en est une généralisation, présente l'avantage de pouvoir être également utilisé dans l'étude des trajectoires spatiales optimales de la 5ème partie. C'est pourquoi nous l'introduisons dès à présent. Il sera appliqué, à titre d'exemple, à la mécanique variationnelle, puis largement utilisé dans la 5ème partie.

4.1.i - Problème de Pontryagin [9]

Soit un système évolutif quelconque, défini à chaque instant t par la donnée du vecteur état $\underline{x} = [x^i] \in \mathbb{R}^n$, vecteur colonne à n composantes x^i ($i = 1, 2, \dots, n$) (par exemple : coordonnées de position, composantes de la vitesse, masse, etc.).

L'évolution de ce système est gouvernée par les équations du mouvement :

$$\dot{\underline{x}} = \underline{f}(\underline{x}, \underline{u}, t), \quad (270)$$

où $\underline{u} = [u^j] \in \mathbb{R}^r$ est le vecteur commande à r composantes u^j ($j = 1, 2, \dots, r$), qui sont des fonctions arbitraires du temps (par exemple : position des gouvernes, orientation et grandeur de la poussée, etc.), soumises à des contraintes (par exemple : débattement maximum d'une gouverne, poussée maximale, etc.), telles que

$$\underline{u} \in U \subset \mathbb{R}^r, \quad (271)$$

(1) $F_3(p_i, q^i, t) = F_1(q^i, \dot{q}^i, t) - p_i \dot{q}^i$.

où \mathcal{U} est le domaine de commande. Les f^i sont des fonctions généralement non linéaires des arguments, que nous supposons suffisamment régulières [9] pour que les résultats qui suivent soient valables.

Le problème de Pontryagin (Fig. 32) consiste à chercher la loi de commande optimale qui fasse passer des conditions initiales fixées :

$$t_0 \text{ fixé}, \quad (272)$$

$$\underline{x}(t_0) = \underline{x}_0 \text{ fixé}, \quad (273)$$

aux conditions finales :

$$t_f \text{ fixé ou non}, \quad (274)$$

$$x^\alpha(t_f) = x_f^\alpha \text{ fixé } (\alpha = 1, 2, \dots, m), \quad (275)$$

telles que la fonction linéaire des composantes non fixées

$$\text{de l'état final : } S = C_\beta x^\beta(t_f) \quad (\beta = m+1, \dots, n), \quad (276)$$

soit maximum.

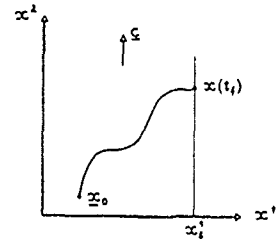


Fig 32

Cet énoncé paraît assez restrictif. En fait de nombreux problèmes d'optimisation peuvent être ramenés à un problème de Pontryagin. (Problèmes de Mayer, de Lagrange, de Bolza ; voir [2]). Un exemple de problème de Lagrange sera donné plus loin.

4.1.2 - Énoncé du principe du maximum de Pontryagin

Pour résoudre un problème de Pontryagin, il suffit :

- 1) d'introduire un vecteur adjoint $\underline{p} = [p_i]$, vecteur ligne à n composantes p_i ;
- 2) de former l'hamiltonien :

$$H = H(\underline{p}, \underline{x}, \underline{u}, t) = \underline{p} \underline{\dot{x}} = \underline{p} \underline{f}(\underline{x}, \underline{u}, t); \quad (277)$$

- 3) de déterminer, à chaque instant, la commande optimale \underline{u}^* qui maximise cet hamiltonien :

$$\underline{u}^* = \arg \max_{\underline{u} \in \mathcal{U}} H = \underline{u}^*(\underline{p}, \underline{x}, t); \quad (278)$$

- 4) de calculer l'hamiltonien maximal, en portant la commande optimale dans l'hamiltonien :

$$H^* = H^*(\underline{p}, \underline{x}, t) = H(\underline{p}, \underline{x}, \underline{u}^*(\underline{p}, \underline{x}, t), t) = \max_{\underline{u} \in \mathcal{U}} H; \quad (279)$$

- 5) enfin, de résoudre le système canonique engendré par H^* :

$$\dot{x}^i = \frac{\partial H^*}{\partial p_i}, \quad (280)$$

$$\dot{p}_i = - \frac{\partial H^*}{\partial x^i}, \quad (281)$$

par rapport aux $2n$ fonctions inconnues $x^i(t)$, $p_i(t)$, avec les conditions d'extrémités

$$x^i(t_0) = x_0^i \text{ fixé} \quad (n) \quad (282)$$

$$x^\alpha(t_f) = x_f^\alpha \text{ fixé} \quad (n) \quad (283)$$

$$p_\beta(t_f) = c_\beta \quad (n) \quad (284)$$

t_0 est fixé ; t_f est fixé ou, s'il est libre, il est calculé à partir de :

$$H^*(t_f) = 0. \quad (285)$$

La méthode est simple. La résolution est cependant, en général, difficile, même par voie numérique, car le problème se ramène à la résolution d'un système différentiel non linéaire avec conditions aux deux extrémités.

Il est important de souligner que le Principe Maximum n'est qu'une condition nécessaire d'optimalité : si une solution optimale existe, elle satisfait au Principe du Maximum. Mais elle n'est pas suffisante ; l'application du Principe du Maximum peut conduire à des solutions parasites qui ne correspondent pas à un maximum global, ni même éventuellement local, de l'indice de performance.

4.1.3 - Démonstration du Principe du Maximum dans un cas simple

La démonstration du Principe du Maximum peut être trouvée dans [9]. Nous en donnerons un aperçu dans un cas simple, qui peut être traité en faisant appel au calcul des variations classique. Les hypothèses simplificatrices sont :

- 1 - pas de contrainte sur la commande ($U = R^2$)
- 2 - on cherche seulement à rendre S stationnaire.
- 3 - t_f est fixé.

Pour rendre S stationnaire, il faut et il suffit d'annuler la variation première :

$$\delta S = c_p \delta x^\beta(t_f). \quad (286)$$

Dans cette expression, les variations $\delta x^\beta(t_f)$ ne sont pas indépendantes, à cause des contraintes non holonomes (270).

Une méthode classique d'élimination de la contrainte (270) consiste à introduire un multiplicateur de Lagrange (inconnue auxiliaire) $p(t)$, vecteur ligne à n composantes p_i , fonction du temps (puisque la contrainte (270) doit être écrite à chaque instant), et à rendre stationnaire l'indice de performance augmenté :

$$I = S - \int_{t_0}^{t_f} p (\dot{x} - f) dt = S - \int_{t_0}^{t_f} (p dx - H dt), \quad (287)$$

ou H est l'hamiltonien (277). Les n fonctions inconnues $p_i(t)$ sont déterminées a posteriori grâce aux n contraintes (270).

La variation de I s'écrit :

$$\delta I = c_p \delta x_f^\beta - \int_{t_0}^{t_f} \left\{ p \delta dx - \left[\frac{\partial H}{\partial x} \delta x + \frac{\partial H}{\partial u} \delta u \right] dt \right\}, \quad (288)$$

avec

$$\int_{t_0}^{t_f} p \delta dx = \int_{t_0}^{t_f} p d \delta x = \left[p \delta x \right]_{t_0}^{t_f} - \int_{t_0}^{t_f} \dot{p} \delta x dt, \quad (289)$$

Compte tenu des contraintes initiales (273) et finales (275), on a

$$\delta x_0 = 0, \quad (290)$$

$$\delta x_f^\beta = 0, \quad (291)$$

et (288) s'écrit :

$$\delta I = (c_p - p_{\beta f}) \delta x_f^\beta + \int_{t_0}^{t_f} \left[\left(\dot{p} + \frac{\partial H}{\partial x} \right) \delta x + \frac{\partial H}{\partial u} \delta u \right] dt, \quad (292)$$

où, grâce à l'introduction du multiplicateur de Lagrange $p(t)$, les vecteurs δx et δu peuvent être considérés comme indépendants. La condition

$$\delta I = 0, \quad \forall \delta x, \delta u, \quad (293)$$

conduit alors à (281), (284) et à :

$$\frac{\partial H}{\partial u} = 0, \quad (294)$$

qui est la forme "faible" de (279).

4.1.4 - Interprétation géométrique - Lien avec la théorie de Contensou

L'approche de Contensou [8], d'ailleurs antérieure à celle de Pontryagin, est plus géométrique. Contensou introduit les notions de domaine de manoeuvrabilité et de domaine accessible (Fig. 33).

Le domaine de manoeuvrabilité $D(x, t)$, dans l'état x , à l'instant t , est le domaine de l'espace hodographe (coordonnées \dot{x}^i), où peut être choisie instantanément la vitesse \dot{x} . C'est donc le transformé du domaine de commande U par les équations (270), à x et t constants.

Le domaine accessible $A(t_f)$, à l'instant t_f fixé, à partir du point x_0 à l'instant t_0 , est l'ensemble des points $x(t_f)$ de l'espace d'état (coordonnées x^i), accessibles en donnant à la commande $u(t)$ toutes les "valeurs" possibles. La connaissance de la frontière $\partial A(t_f)$ du domaine accessible permet de résoudre la plupart des problèmes d'optimisation intéressants dans la pratique. Par exemple, la résolution du problème de Pontryagin du paragraphe 4.1.1 dans le cas particulier où il n'y a aucune contrainte finale de type (275), revient à trouver la loi de commande optimale $u^*(t)$ conduisant au point $x^*(t_f)$ de la frontière $\partial A(t_f)$ le plus éloigné dans la direction du vecteur c de composantes c_β (où ici, $\beta = 1, 2, \dots, n$). Le balayage de la direction de c permettrait d'ailleurs de déterminer la frontière $\partial A(t_f)$.

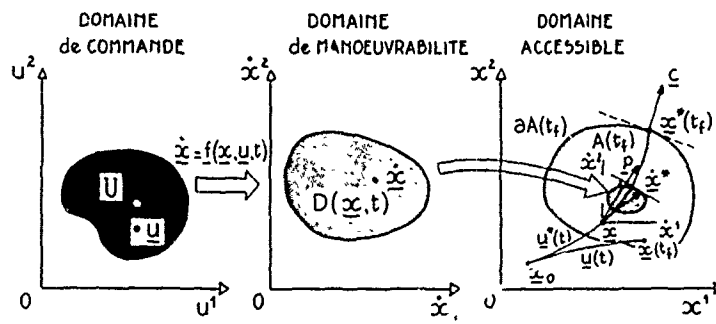


Fig 33 - Théorie de Contensou

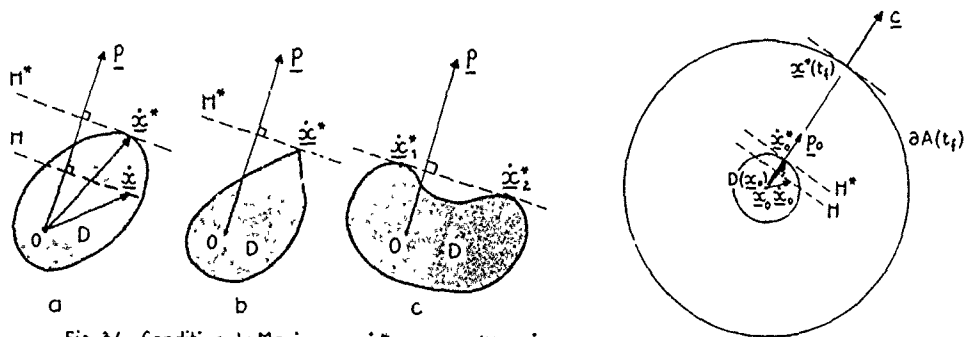


Fig 34 - Condition du Maximum : $\dot{x}^* = \arg \max_{\dot{x} \in D} (H = p \dot{x})$
 a. Point régulier
 b. Point "anguleux"
 c. Commutation ou arc singulier .

Fig 35

La condition du maximum (278) (279) indique que, localement, le point de fonctionnement \dot{x} (vitesse) doit être choisi dans le domaine de manoeuvrabilité $D(x, t)$, au point \dot{x}^* le plus éloigné de l'origine dans la direction du vecteur p , qui indique, en quelque sorte, la route à suivre (Figs. 33 et 34). Notons que si le domaine de manoeuvrabilité D ne dépend pas de l'état x , les équations adjointes (281) montrent que p est constant, donc

$$\underline{p} = \underline{p}_f = \underline{c} \quad (295)$$

Considérons, par exemple, le cas simple à deux dimensions (Fig. 35) où le domaine de manoeuvrabilité est, en tout point x , un disque D de rayon fixé, centré en x . La trajectoire est alors rectiligne, de x_0 à x^* , et la frontière $\partial A(t_f)$ du domaine accessible à l'instant t_f est un cercle centré en x_0 .

Si le domaine de manoeuvrabilité est un disque D de rayon fixé, mais excentré d'une quantité fixée Δ (Fig. 36), la trajectoire est toujours rectiligne, mais non colinéaire à $p = c$ et la frontière $\partial A(t_f)$ est un cercle excentré par rapport à x_0 .

Le vecteur p sert bien encore à indiquer la direction à suivre, mais la direction réellement suivie tient compte de la forme particulière du domaine de manoeuvrabilité. Elle n'en maximise pas moins l'indice de performance \mathcal{J} .

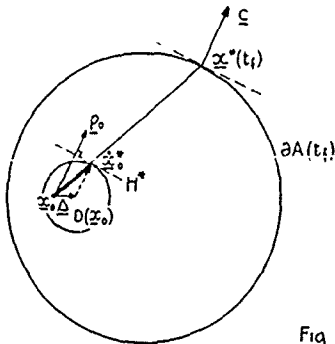


Fig 36

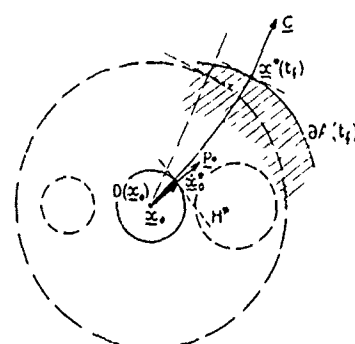


Fig 37

Considérons maintenant le cas où le domaine de manoeuvrabilité est un disque $D(x)$ centré en x , mais de rayon croissant avec x^1 (Fig. 37). Dans ce cas, H^* dépend de x et P n'est plus constant, à cause de (281). Il est évident que pour s'éloigner au maximum dans la direction de e , il y a intérêt à se déplacer d'abord vers les $x^1 > 0$. Le vecteur P sert bien encore à indiquer la direction à suivre, mais en tenant compte de la dépendance du domaine de manoeuvrabilité D par rapport à la position x .

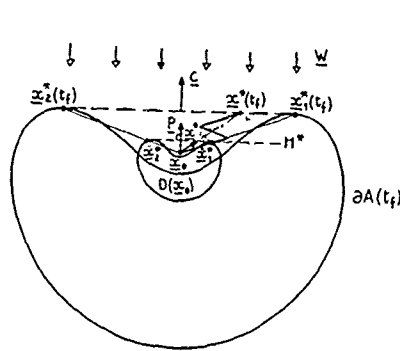


Fig 38

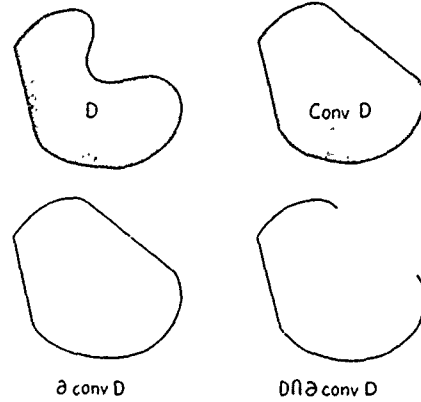


Fig 39

Considérons enfin le cas où le domaine de manoeuvrabilité est identique dans tout le plan et à la forme indiquée sur la Fig. 38. C'est le cas d'un voilier dans un vent uniforme W . Il est possible de "remonter le vent" en utilisant la vitesse x_1^* (resp. x_2^*), ce qui conduit au point $x_1^*(t_f)$ (resp. $x_2^*(t_f)$). Mais il est également possible d'atteindre tout point $x^*(t_f)$ du segment $(x_1^*(t_f), x_2^*(t_f))$ par une succession de virements de bord c'est-à-dire par des commutations successives (utilisation de x_1^* pendant Δt_1 , puis de x_2^* pendant Δt_2 , etc.). A la limite, pour des virements de bord "infiniment" rapides, la trajectoire est le segment (x_1^*, x_2^*) . Cela revient à utiliser la vitesse fictive x^* sur le segment (x_1^*, x_2^*) . Ainsi le domaine de manoeuvrabilité peut être convexifié. Contensou propose de construire le domaine convéxifié $conv D$ (Fig. 39) dès le début. Les points de fonctionnement optimaux sont sur sa frontière $\partial conv D$. Les points de D "réellement" utilisés sont ceux de l'intersection $D \cap \partial conv D$. L'utilisation d'un point tel que x^* d'une partie semi-affine artificielle de $\partial conv D$ équivaut à une réticence. Contensou poursuit alors l'étude par un parcours de $\partial conv D$ et se ramène à un problème de calcul de variation, qui est à rapprocher de celui étudié au paragraphe 4.1.3.

Le Principe du Maximum sera largement utilisé dans la 5ème partie, pour l'étude des trajectoires spatiales optimales. Mais donnons dès à présent un exemple simple d'application dans le cadre de la mécanique variationnelle.

4.2 - Application à la mécanique variationnelle

Le Principe du Maximum de Contensou-Pontryagin utilise un formalisme hamiltonien, qui n'est pas sans rappeler celui rencontré dans la 3ème partie consacrée à la mécanique hamiltonienne. Cette similitude n'est évidemment pas fortuite et peut être éclairée en faisant appel à la mécanique variationnelle. Il est bien connu en effet que l'évolution d'un système à lagrangien obéit à un principe variationnel de "moindre action", c i peut être déduit des équations de Lagrange ou de Hamilton.

Principe de moindre action :
Soit un système à lagrangien $L(q, \dot{q}, t)$. De tous les mouvements $q(t)$ faisant passer des conditions : $t_0, q(t_0) = q_0$ fixés, aux conditions : $t_f, q(t_f) = q_f$ fixés (Fig.40), le mouvement réel (régi par les équations de Lagrange ou de Hamilton) est l'un de ceux qui rendent minimum l'action lagrangienne :

$$A = \int_{t_0}^{t_f} L(q, \dot{q}, t) dt. \tag{296}$$

(On n'est pas assuré de l'unicité de la solution. En effet, les conditions imposées ne sont pas les conditions de Cauchy pour les équations de Lagrange).

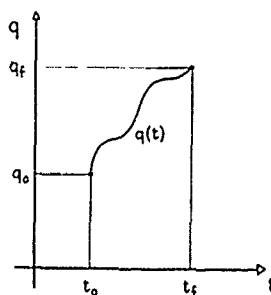


Fig. 40

Vérifions cet énoncé, en appliquant le Principe du Maximum de Pontryagin.

Définissons l'état à $n+1$ dimensions :

$$x = [x^l] = [q^i, q^{n+1}]^T \quad (l=1,2,\dots,n+1; i=1,2,\dots,n), \quad (297)$$

où

$$q^{n+1} = \int_{t_0}^t L(q^i, \dot{q}^i, t) dt. \quad (298)$$

Les équations du mouvement s'écrivent :

$$\dot{x}^l = f^l(x^i, u^i, t) \quad \left\{ \begin{array}{l} \dot{q}^i = u^i \\ \dot{q}^{n+1} = L(q^i, u^i, t) \end{array} \right. \quad (299)$$

Le problème d'optimisation se ramène à choisir les commandes $u^i(t)$ (vitesses), telles que

$$S = -q^{n+1}(t_f) = -A \quad (301)$$

soit maximum, avec les conditions d'extrémités, à t_0 et t_f fixés :

$$q^i(t_0) = q_0^i \text{ fixé}, \quad (302)$$

$$q^{n+1}(t_0) = 0, \quad (303)$$

$$q^i(t_f) = q_f^i \text{ fixé}. \quad (304)$$

C'est un problème de Pontryagin, qui peut être résolu en appliquant la méthode exposée au paragraphe 4.1.2.

1) On introduit l'adjoint

$$p = [p_l] = [p_i, p_{n+1}]. \quad (305)$$

2) On forme l'hamiltonien (augmenté) :

$$\bar{H} = \bar{H}(p_l, q^i, u^i, t) = p_l \dot{x}^l = p_i u^i + p_{n+1} L(q^i, u^i, t). \quad (306)$$

3) On le maximise par rapport à la commande u . Pour les systèmes mécaniques à lagrangien de la forme (146) $L = T - V$ que l'on considère ici, V ne dépend pas des \dot{q}^i . Le lagrangien L est alors, comme l'énergie cinétique T , une forme quadratique définie positive par rapport aux $\dot{q}^i = u^i$. En supposant que $p_{n+1} < 0$ (ce qui sera vérifié par la suite en (313)), cela revient à écrire :

$$\frac{\partial \bar{H}}{\partial u^i} = p_i + p_{n+1} \frac{\partial L}{\partial u^i} = 0. \quad (307)$$

La commande optimale est tirée de (307) en fonction de p_l, q^i et t :

$$u^{i*} = u^{i*}(p_l, q^i, t). \quad (308)$$

4) On porte cette expression dans \bar{H} , qui devient alors une fonction \bar{H}^* de p_l, q^i et t :

$$\bar{H}^* = \bar{H}^*(p_l, q^i, t) = \bar{H}(p_l, q^i, u^{i*}(p_l, q^i, t), t). \quad (309)$$

5) On résout le système différentiel canonique

$$\dot{x}^i = \frac{\partial \bar{H}^*}{\partial p_i}, \quad (310)$$

$$\dot{p}_i = - \frac{\partial \bar{H}^*}{\partial x^i}, \quad (311)$$

avec les conditions d'extrémités (302) - (304) et

$$p_{n+1}(t_f) = C_{n+1} = -1. \quad (312)$$

Comme q^{n+1} est ignorable ($\frac{\partial \bar{H}^*}{\partial q^{n+1}} = 0$), on a $\dot{p}_{n+1} = 0$,
donc :

$$p_{n+1} = \text{constante} = p_{n+1}(t_f) = -1 < 0. \quad (313)$$

Par (307) on a alors :

$$p_i = \frac{\partial L}{\partial u^i} = \frac{\partial L}{\partial \dot{q}^i}. \quad (314)$$

Les p_i sont donc les moments conjugués des q^i , définis en mécanique hamiltonienne.

On vérifie d'autre part aisément que

$$\bar{H}^*(p_i, -1, q^i, t) = H(p_i, q^i, t) \quad (315)$$

est l'hamiltonien de la mécanique.

Les équations canoniques (310) - (311) s'écrivent alors, pour q^i et p_i :

$$\dot{q}^i = \frac{\partial H}{\partial p_i}, \quad (316)$$

$$\dot{p}_i = - \frac{\partial H}{\partial q^i}. \quad (317)$$

Ce sont les équations canoniques d'Hamilton de la mécanique, qui régissent le mouvement réel.

5 - TRAJECTOIRES SPATIALES OPTIMALES

L'optimisation des trajectoires spatiales et, en particulier, des transferts et rendez-vous, est l'un des domaines privilégiés d'application du contrôle optimal.

Alors que l'étude des mouvements naturels des corps dans l'espace a été entreprise depuis fort longtemps et a conduit au développement bien connu de la Mécanique Céleste dont certains aspects ont été rappelés dans les Parties 1, 2, 3, l'étude des mouvements propulsés optimaux est évidemment beaucoup plus récente [10-26, 2-5], bien qu'abordée assez nettement avant l'ère de la conquête spatiale proprement dite. Seuls les aspects déterministes (c.à.d non stochastiques) seront considérés ici. Le texte qui suit est, à quelques détails près, le texte condensé figurant dans [25].

5.1 - Définition d'un transfert optimal

Les équations du mouvement d'un véhicule spatial \mathcal{M} , dans un système de référence galiléen (ou assimilé à un système galiléen) Ox_y_z , s'écrivent :

$$m \ddot{\vec{x}} = \vec{F} + m \vec{g}, \quad (318)$$

où m est la masse instantanée, \vec{x} la position, $\vec{g} = \vec{g}(\vec{x}, t)$ le champ de gravitation et $\vec{F} = \dot{m} \vec{w}$ la force de poussée due à une éjection de masse, avec le débit $-\dot{m} \geq 0$, à la vitesse d'éjection relative effective \vec{w} .

De façon générale, un "transfert" est un changement de position \vec{x} et de vitesse \vec{v} du véhicule, c'est-à-dire le passage des conditions cinématiques initiales $t_0, \vec{x}_0, \vec{v}_0$ aux conditions cinématiques finales $t_f, \vec{x}_f, \vec{v}_f$. Les mouvements naturels étudiés plus haut sont des transferts particuliers, de coût nul. Le transfert peut être complètement imposé (cas du "rendez-vous"), ou partiellement libre (par exemple, dans le cas d'une "interception", \vec{v}_f est libre).

Ce transfert doit être effectué de façon optimale. Parmi les nombreuses façons de définir cet optimum, seule la minimisation de la consommation de masse, c'est-à-dire la maximisation de la masse finale m_f sera considérée ici, car ce problème est souvent rencontré dans la pratique. Cependant les méthodes présentées sont très générales et pourraient être utilisées pour résoudre une grande variété d'autres problèmes (par exemple : transfert à temps minimum).

Il s'agit donc de choisir à chaque instant les meilleurs paramètres de commande : $\vec{D} = \vec{F}/F$ (direction de poussée), $q = -\dot{m}$ (débit) et F (grandeur de la poussée), compte tenu de contraintes éventuelles.

Il sera supposé ici que le système de contrôle d'attitude du véhicule permet la libre orientation de la poussée, mais des résultats concernant le cas où la direction de poussée est contrainte sont également disponibles.

Les contraintes sur q et F dépendent du système de propulsion considéré.

5.2 - Modélisation des systèmes de propulsion

Les systèmes de propulsion considérés le plus souvent sont des deux types suivants:

5.2.1 - Systèmes de propulsion à vitesse d'éjection constante (VEC)

Dans ces systèmes, les contraintes s'écrivent :

$$W = F/q = \text{constante} ,$$

et

$$0 \leq F \leq F_{\max} \quad (\text{système à poussée complètement modulable}), \quad (319)$$

ou :

$$F = 0 \quad \text{ou} \quad F_{\max} \quad (\text{possibilité d'extinction/réallumage}). \quad (320)$$

Si l'extinction/réallumage peut être "infiniment" rapide, (320) est théoriquement équivalent à (319).

Selon la grandeur de la poussée maximale F_{\max} , il est possible de distinguer :

- les systèmes à forte poussée (F_{\max} grand, W petit), c'est-à-dire la propulsion chimique classique. Parmi eux, les systèmes idéalisés à poussée infinie ($F_{\max} \rightarrow \infty$) ou systèmes impulsions sont capables de délivrer des impulsions, c'est-à-dire des changements instantanés de vitesse \dot{V} . Un exemple en est donné dans l'exposé [3].
- les systèmes à faible poussée (F_{\max} petit, W grand), c'est-à-dire la propulsion électrique.

Pour tous ces systèmes VEC, la masse instantanée m peut être avantageusement remplacée par la vitesse caractéristique :

$$C = \int_{t_0}^t \gamma dt = - \int_{m_0}^m (W/m) dm = W \text{Log}(m_0/m), \quad (321)$$

où $\gamma = F/m$ est l'accélération de poussée. L'indice de performance à maximiser est alors $-C_f$. Pour un système de propulsion impulsions, C_f est la somme arithmétique des impulsions :

$$C_f = \sum_i \Delta V_i .$$

5.2.2 - Systèmes de propulsion à puissance limitée idéalisés (PL)

Pour ces systèmes la seule contrainte concerne la puissance d'éjection :

$$0 \leq P = (1/2) q W^2 = F W / 2 = F^2 / 2 q \leq P_{\max} .$$

Ces systèmes sont des systèmes de propulsion électrique à faible poussée. Il est possible de montrer aisément que seule la borne supérieure F_{\max} doit être utilisée. La vitesse d'éjection W , et donc la poussée F , peuvent être modulées.

L'intégration de la quantité

$$- \dot{m} / m^2 = \gamma^2 / 2 P_{\max} ,$$

entre t_0 et t , conduit à

$$(1/m) - (1/m_0) = J / P_{\max} ,$$

où

$$J = (1/2) \int_{t_0}^t \gamma^2 dt \quad (322)$$

peut remplacer avantageusement m . L'indice de performance à maximiser est alors $-J_f$.

5.3 - Optimisation paramétrique : le transfert de Hohmann

L'étude des transferts optimaux a été, tout d'abord, limitée au cas d'un champ de gravitation central et de systèmes de propulsion impulsions. Si l'on admet, pour l'instant, que le transfert optimal est alors réellement impulsional, une méthode simple de résolution, très souvent utilisée dans la pratique, consiste à fixer a priori le nombre ν d'impulsions (le plus souvent $\nu = 2$) et de déterminer le point d'application, la direction et la grandeur de chacune de ces impulsions, pour que leur somme arithmétique soit minimale. Le problème est ainsi ramené à un problème classique d'optimisation paramétrique avec contraintes, qui peut être résolu numériquement (voir, par exemple, l'exposé [3]) ou même analytiquement dans les cas simples. L'utilisation de manoeuvres atmosphériques peut être envisagée, comme dans l'exposé [26].

Par exemple, il peut être montré aisément que le transfert optimal bi-impulsionnel, de durée indifférente, entre orbites circulaires, coplanaires, est le transfert de Hohmann bien connu (Fig. 41).

Cependant, pour être en mesure de déterminer le nombre optimal d'impulsions (par exemple, dans le problème exposé en [3]), trois impulsions sont nécessaires) et de pouvoir traiter le cas de systèmes de propulsion non impulsions, il est nécessaire de faire appel à une méthode d'optimisation plus élaborée, l'optimisation fonctionnelle, et plus précisément le Principe du Maximum de Contensou-Pontryagin qui a été présenté dans la 4^{ème} Partie.

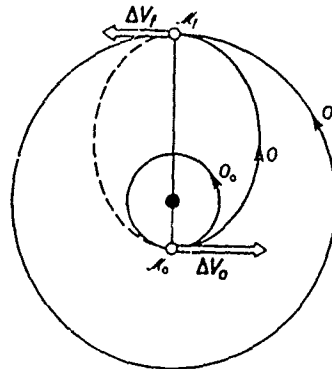


Fig. 41. - Le transfert de Hohmann.

5.4 - Transfert optimal dans un champ de gravitation général

L'état du véhicule à l'instant t peut être défini par \vec{r} , \vec{V} et J (PL) ou C (VEC). D'après (318), les équations d'état s'écrivent :

$$\dot{\vec{r}} = \vec{V}, \quad (323)$$

$$\dot{\vec{V}} = \vec{g}(\vec{r}, t) + \gamma \vec{D}, \quad (324)$$

et, d'après (321) et (322) :

$$\dot{J} = \gamma^2/2 \text{ (PL)} \quad (325a)$$

$$\dot{C} = \gamma \text{ (VEC)} \quad (325b)$$

Les commandes sont \vec{D} et γ , soumises, pour les systèmes de propulsion VEC, aux contraintes (319) :

$$0 \leq \gamma \leq \gamma_{\max} = F_{\max} / m(C), \quad (326)$$

ou (320).

Le problème consiste à passer de l'état $(\vec{r}_0, \vec{V}_0, J_0 = 0 \text{ ou } C_0 = 0)$ à l'instant t_0 , à l'état $(\vec{r}_f, \vec{V}_f, J_f \text{ ou } C_f)$ à l'instant t_f de façon que l'indice de performance $-J_f$ ou $-C_f$ soit maximal. Les conditions cinématiques initiales et/ou finales, $t_0, \vec{r}_0, \vec{V}_0$ et $t_f, \vec{r}_f, \vec{V}_f$ peuvent être partiellement libres. Ce problème est typiquement un problème de Pontryagin (du moins si $t_0, \vec{r}_0, \vec{V}_0$ sont fixés, seul cas hamiltonien s'écrit :

$$H = \vec{p}_r \cdot \dot{\vec{r}} + \vec{p}_v \cdot \dot{\vec{V}} + \left\{ \begin{array}{l} p_J \dot{J} \\ p_C \dot{C} \end{array} \right. = \vec{p}_r \cdot \vec{V} + \vec{p}_v \cdot [\gamma \vec{D} + \vec{g}(\vec{r}, t)] + \left\{ \begin{array}{l} p_J \gamma^2/2 \text{ (PL)} \\ p_C \gamma \text{ (VEC)} \end{array} \right.$$

où $\vec{p}_r, \vec{p}_v, p_J$ ou p_C sont adjoints aux éléments d'état \vec{r}, \vec{V}, J ou C .

→ La direction optimale de poussée \vec{D}^* , qui maximise H , est la direction de \vec{p}_v appelé le "primer vector" [12] :

$$\vec{D}^* = \vec{p}_v / p_v.$$

L'hamiltonien s'écrit alors :

$$\tilde{H} = p_v \gamma + \left\{ \begin{array}{l} p_J \gamma^2 / 2 \\ p_c \gamma \end{array} \right. + \text{termes indépendants de la commande.}$$

Pour les systèmes PL, H est maximum par rapport à γ pour :

$$\partial \tilde{H} / \partial \gamma = p_v + p_J \gamma = 0,$$

$$\partial^2 \tilde{H} / \partial \gamma^2 = p_J < 0 \quad (\text{condition qui sera vérifiée plus tard}),$$

d'où :

$$\gamma^* = - p_v / p_J. \quad (327)$$

La poussée optimale est modulée.

Pour les systèmes VEC, H est maximal par rapport à γ pour

$$\gamma^* = \gamma_{\max}(C) \mathcal{U}(p_v + p_c),$$

où $\mathcal{U}(x)$ est la fonction de Heaviside (échelon unité) :

$$\mathcal{U}(x) = (1 + \text{signe } x) / 2 = 1 \text{ ou } 0, \text{ selon que } x \geq 0.$$

La poussée optimale est un "tout-ou-rien" c'est-à-dire une alternance d'arcs à poussée maximale (AMAX) et d'arcs balistiques (AB), sauf dans le cas singulier où

$$\partial \tilde{H} / \partial \gamma = p_v + p_c = 0 \quad (328)$$

pendant un intervalle de temps non nul $[t_1, t_2]$. Dans ce cas la seule condition du Maximum ne fournit pas l'accélération optimale γ^* . On obtient un arc singulier AS, qui peut être soit un arc singulier à poussée intermédiaire (ASPI) ou un arc singulier réticent (ASR) (voir paragraphe 4.1.4) selon que (319) ou (320) est utilisé. L'hamiltonien maximal est

$$H^* = \vec{p}_2 \cdot \vec{V} + \vec{p}_v \cdot \vec{g}(\vec{r}, t) + \begin{cases} -p_v^2 / 2 p_J & (\text{PL}) \\ \gamma_{\max}(C) \mathcal{U}(p_v + p_c) & (\text{VEC}), \end{cases}$$

où $\vec{V}(\vec{r}, t) \times \mathcal{U}(x)$ est l'échelon unité de vitesse.

Le système adjoint s'écrit :

$$\dot{\vec{p}}_2 = - \partial H^* / \partial \vec{r} = - \vec{p}_v \cdot \vec{G}, \quad (329)$$

$$\dot{\vec{p}}_v = - \partial H^* / \partial \vec{V} = - \vec{p}_2, \quad (330)$$

$$\left\{ \begin{array}{l} \dot{p}_J = - \partial H^* / \partial J = 0, \\ \dot{p}_c = - \partial H^* / \partial C = -(\gamma^* / W)(p_v + p_c), \end{array} \right. \quad (\text{PL}) \quad (331a)$$

$$\left\{ \begin{array}{l} \dot{p}_J = - \partial H^* / \partial J = 0, \\ \dot{p}_c = - \partial H^* / \partial C = -(\gamma^* / W)(p_v + p_c), \end{array} \right. \quad (\text{VEC}) \quad (331b)$$

où $\vec{G} = \partial \vec{g} / \partial \vec{r}$ est le tenseur gradient de gravité.

Il faut noter que J est ignorable (c.a.d. ne figure pas dans H^*) mais non pas C car le domaine de commande pour γ , donnée par (326), dépend de C .

Pour un système PL, l'intégration de (331a) conduit à

$p_J = \text{constante} = p_{Jf} = -1 < 0$,
puisque c'est $-J_f$ qu'il s'agit de maximiser, d'où, par (327) :

$$\vec{\gamma}^* = \vec{p}_v.$$

Pour un système VEC, $\dot{p}_c \leq 0$, donc p_c est non croissant. Plus précisément $\dot{p}_c = 0$ et $p_c = \text{constante}$ lorsque $p_v + p_c \leq 0$, c'est-à-dire sur les AB et les AS. Par exemple, sur une trajectoire ne comportant que des AMAX et des AB, l'évolution de p_v , $-p_c$ et F peut avoir l'allure indiquée sur la Fig. 42a. Sur les AS, l'accélération optimale (ASPI) ou l'accélération moyenne (ASR) γ^* peut être obtenue par dérivation successive par rapport au temps t et sur l'AS de la condition de singularité (328), jusqu'à obtention d'un équation contenant γ . Cela se produit généralement pour la dérivée quatrième :

$$d^4(\partial \tilde{H} / \partial \gamma) / dt^4 = A \gamma + B = 0$$

par l'intermédiaire du terme \vec{G} , d'après le résultat général qui veut que la commande optimale apparaisse (de façon affine) dans une dérivée d'ordre pair (2 n).

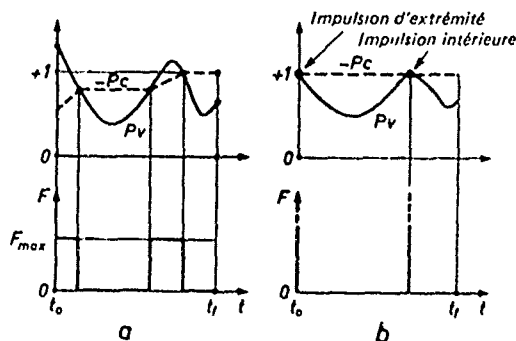


Fig. 42 - Évolution de p_v et $-p_c$ et loi de poussée optimale.
a) système VEC; b) système "impulsionnel".

L'accélération de poussée optimale est alors égale à

$$\gamma^* = -B/a,$$

et la condition nécessaire d'optimalité de Kelley-Contensou [18, 21] s'écrit :

$$(-1)^n \partial [d^{2n} (\partial \tilde{H} / \partial \gamma) / dt^{2n}] / \partial \gamma = (-1)^n a = \tilde{a} < 0, \quad (332)$$

puisque ici $n = 2$.

Pour les systèmes impulsionsnels, p_c = constante = -1, $p_v \leq 1$ (Fig. 42b), et les impulsions ne peuvent être appliquées que lorsque $p_v = 1$; pour les impulsions intérieures, on a $\dot{p}_v = 0$. Sur un AS, $p_v = 1$. Le raccordement d'un AB et d'un AS se fait généralement à l'aide d'une impulsion.

Dans le cas d'un champ de gravitation $\vec{g}(\vec{r})$ indépendant du temps, en plus des intégrales premières habituelles du système (323) - (325), (329) - (331), apparaît l'intégrale première de l'hamiltonien :

$$H^* = \text{constante},$$

car

$$\dot{H}^* = \partial H^* / \partial t = 0.$$

Les conditions d'extrémités, et en particulier les conditions de transversalité, dépendent du problème particulier à résoudre. La difficulté de résolution du problème différentiel non linéaire, à valeurs imposées aux deux extrémités, dépend de la complexité du champ de gravitation considéré.

5.5 - Transfert optimal dans un champ de gravitation uniforme

L'approximation $\vec{g} = \text{constante}$ peut être faite lorsque le transfert a lieu dans une région limitée de l'espace (par exemple, hypothèses : terre plate, $\vec{g} = \text{constante}$, dans le cas d'un missile balistique à courte portée). L'approximation $\vec{g} = 0$ peut être faite loin des masses attirantes (transferts interstellaires).

Le système adjoint cinématique (329) - (330) devient alors $\dot{\vec{p}}_r = 0$ et $\dot{\vec{p}}_v = -\vec{p}_r$, et peut être intégré selon : $\vec{p}_r = \text{constante}$ et

$$\vec{p}_v = -\vec{p}_r (t - t_f) + \vec{p}_{vf}.$$

La loi d'orientation de la poussée est affine ou homographique selon le choix des axes. Si la position finale \vec{r}_f est libre ($\vec{p}_r = 0$) ou si la vitesse finale \vec{v}_f est libre ($\vec{p}_{vf} = 0$), la direction de poussée est fixe. Dans les cas non singuliers, où $\vec{p}_r \neq 0$, le comportement hyperbolique de $p_v(t)$ montre qu'il y a au plus deux AMAX (ou à la limite deux impulsions) séparés par une AB.

5.6 - Transferts optimaux dans un champ de gravitation central

Ce problème est évidemment fondamental. L'approximation du champ central :

$$\vec{g} = -\mu \vec{r} / r^3 \quad (\mu = \text{constante}) \quad (\text{Fig. 43})$$

est généralement excellente pour l'étude d'un transfert géocentrique (plus généralement planétocentrique) ou de la phase héliocentrique d'un transfert interplanétaire.

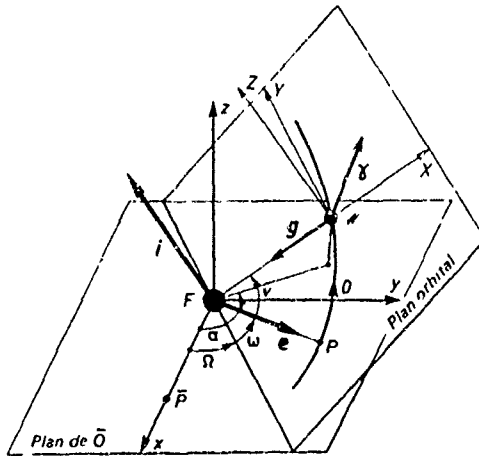


Fig. 43 - Champ central. Le centre est F, "Foyer" des orbites képlériennes osculatrices

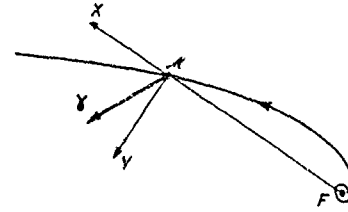


Fig. 44 - Spirale de Lawden.

Historiquement, le problème a d'abord été étudié en utilisant les coordonnées cartésiennes (ou plutôt sphériques) comme composantes d'état. Cette méthode reste encore intéressante pour l'étude de certaines questions comme les arcs singuliers ou les conditions de commutation [19, 22] dans le cas des transferts de durée indifférente. Il est généralement préférable d'utiliser les éléments orbitaux afin de pouvoir faire appel aux méthodes puissantes de la Mécanique Céleste et en particulier de la théorie des perturbations exposée dans les Parties 1, 2, 3. Le passage d'un système de coordonnées à l'autre peut être réalisé élégamment en utilisant des transformations canoniques [16] rappelées dans la 3ème Partie.

5.6.1 - Utilisation des coordonnées cartésiennes (ou sphériques)

L'équation adjointe (329) pour \vec{p}_v devient, sous forme matricielle :

$$\dot{\vec{p}}_v = -\underline{p}_v \underline{G} = -[S, T, W](\mu/r^3) \begin{bmatrix} 2 & 0 & 0 \\ 0 & -1 & 0 \\ 0 & 0 & 1 \end{bmatrix} = (\mu/r^3) [-2S, T, W], \quad (333)$$

où \vec{p}_v et \underline{G} ont été définis par leurs composantes dans les axes orbitaux tournants u, v, w (Fig. 43), en particulier $\underline{p}_v = [S, T, W]$.

L'hypothèse du champ central introduit de nouvelles intégrales premières :

$$\begin{aligned} \vec{r} \wedge \vec{p}_r + \vec{v} \wedge \vec{p}_v &= \text{vecteur constant} = \vec{A}, \\ \left\{ \begin{array}{l} 5J + 2\vec{r}_0 \cdot \vec{p}_r - \vec{v} \cdot \vec{p}_v - 3H^* t = \text{constante} = B \text{ (pour les systèmes PL),} \\ -p_c C + 2\vec{r}_0 \cdot \vec{p}_r - \vec{v} \cdot \vec{p}_v - 3H^* t = \text{constante} = B \text{ (pour les systèmes VEC)} \end{array} \right. \end{aligned}$$

sur les AB et les AS, et pour les impulsions.

L'élimination de \vec{p}_r entre (330) et (333) conduit à :

$$\vec{p}_v = (\mu/r^3) (3\vec{S} - \vec{p}_v).$$

Cette équation différentielle vectorielle linéaire du second ordre peut être intégrée sur un AB [12], ce qui conduit à :

$$\vec{p}_v \begin{cases} S = A \cos v + B \sin v + C I_1(v), \\ T = -A \sin v + B(1 + e \cos v) + [D - A \sin v](1 + e \cos v) + C I_2(v), \\ W = (E \cos v + F \sin v) / (1 + e \cos v), \end{cases} \quad (334)$$

où e est l'excentricité de l'arc képlérien, v est l'anomalie vraie (Fig. 43), A, B, C, D, E, F sont les six constantes d'intégration et $I_1(v), I_2(v)$ sont des fonctions connues de v , non explicitées ici. Le lieu (S) du point $\vec{p}_v(S, T, W)$ dans les axes u, v, w est appelé le "primer locus" [12].

Si on laisse de côté les questions d'origines, d'orientation et d'échelle, les arcs singuliers dépendent de trois paramètres. La condition nécessaire de Kelley-Cortensou (332) conduit à $S < 0$. En particulier la "spirale de Lawden" (Fig. 44) [12] n'est sûrement pas optimale. L'étude de l'optimalité véritable des arcs singuliers qui satisfont à la condition nécessaire conduit au résultat suivant : dans les transferts de durée indifférente ($H^* = 0$) entre ellipses extérieures à la planète attirante, les arcs singuliers ne sont jamais optimaux.

5.6.2 - Utilisation des éléments orbitaux

Comme il a été vu au paragraphe 1.2.3, la donnée à l'instant t des éléments cinématiques \vec{x}, \vec{v} du véhicule M est équivalente à la donnée des six éléments orbitaux q_i ($i = 1, 2, \dots, 6$), constantes du mouvement képlérien qui définissent l'orbite osculatrice O (Fig. 43) et la position de M sur cette orbite. Lorsqu'on utilise l'état orbital $q = [q^T]^T$, les équations d'état coïncident avec les formules de perturbation de Gauss (103) de la Mécanique Céleste :

$$dq/dt = K(q, t) \underline{\gamma}, \quad (335)$$

où K est la matrice de perturbation 6×3 et $\underline{\gamma} = [\gamma, \delta, \omega]^T$ est la matrice 3×1 des composantes de l'accélération "perturbatrice" $\underline{\gamma}$ dans les axes orbitaux tournants u, v, z .

- L'utilisation des éléments orbitaux présente de nombreux avantages :
- L'intégration sur les AB ($\gamma = 0$) est immédiate ; $q = \text{constante}$.
 - Pour les systèmes de propulsion à faible poussée, les éléments orbitaux varient moins rapidement que \vec{x}, \vec{v} .
 - Les conditions d'extrémités font souvent intervenir l'orbite osculatrice O elle-même.

Une théorie générale peut être développée à partir des équations d'état (335), mais c'est dans trois cas particuliers que l'étude analytique peut être poussée relativement loin.

5.6.2.1 - Théorie linéarisée : corrections optimales d'orbite elliptique

Lorsque la vitesse caractéristique C_f est petite vis-à-vis de la vitesse orbitale moyenne V , il apparaît un "petit paramètre" $\epsilon = C_f/V$ dans le problème, qui peut alors être linéarisé comme indiqué au paragraphe 1.3.2. L'intégration des équations de perturbation (335) montre que, pendant le transfert, l'orbite osculatrice O ne s'écarte jamais de plus de ϵ par rapport à l'orbite initiale O_i , ou encore par rapport à l'orbite finale O_f , ou enfin par rapport à une orbite nominale \bar{O} , choisie assez proche de O_i et O_f (écarts de l'ordre de ϵ). La linéarisation est effectuée "autour de \bar{O} ". Rappelons que la linéarisation des formules de perturbation (103) conduit à "figer" l'orbite osculatrice O dans sa position nominale \bar{O} dans le second membre de (335), qui devient :

$$dq/dE = \underline{r} K(e, E) \underline{\gamma}, \quad (336)$$

où K est grandement simplifiée : ses éléments non nuls sont des polynômes en $\sin E$, $\cos E$ et éventuellement E (Tableau 2).

L'équation de consommation (325) linéarisée s'écrit :

$$\begin{cases} dJ/dE = \underline{r} \gamma^2 / 2, & \text{(PL)} \\ dC/dE = \underline{r} \gamma, & \text{(VEC)} \end{cases} \quad (337a) \quad (337b)$$

où $\underline{r} = 1 - e \cos E$. Pour les systèmes VEC, la contrainte (326) linéarisée s'écrit :

$$0 \leq \gamma \leq \gamma_{\max} = F_{\max} / m_0.$$

La maximisation de l'hamiltonien :

$$\mathcal{H} = \underline{p} (dq/dE) + \begin{cases} P_J dJ/dE \\ P_C dC/dE \end{cases} = \underline{r} \underline{p} K \underline{\gamma} + \begin{cases} P_J \underline{r} \gamma^2 / 2 & \text{(PL)} \\ P_C \underline{r} \gamma & \text{(VEC)} \end{cases}$$

par rapport à la commande $\underline{\gamma}$ fournit l'accélération de poussée optimale :

$$\begin{cases} \underline{\gamma}^* = - \underline{P}_V^T / P_J, & \text{(PL)} \\ \underline{\gamma}^* = \gamma_{\max} \mathcal{U}(\underline{P}_V + P_C) \underline{P}_V^T / P_V, & \text{(VEC)} \end{cases}$$

où

$$\underline{P} = [P_{ix}, P_{iy}, P_a, P_{iz}, P_{e_z}, P_{\sigma}]$$

est l'adjoint orbital, et

$$\underline{P}_V = \underline{p} K(e, E)$$

est le "primer vector", dont il a été question plus haut et qui peut être écrit sous la forme vectorielle :

$$\underline{P}_V = 2 \underline{p}_a \underline{V} + \underline{r} \lambda \underline{P}_e + [\underline{P}_e \lambda \underline{V} + (\underline{P}_e / h)] \lambda \underline{x} + P_T (-\underline{e} + 3M \underline{V}), \quad (338)$$

où $\underline{r} = \underline{r} \lambda \underline{V}$ est le moment cinétique. La similitude entre les expressions (338) de \underline{P}_V et (52) de $\delta \underline{x}$ n'est pas fortuite (voir [2]).

Dans l'hamiltonien maximal

$$\mathcal{H}^* = \max_{\underline{\gamma}} \mathcal{H} = \begin{cases} -\mathcal{r} P_V^2 / 2 P_J, \\ \mathcal{r} \gamma_{\max} \mathcal{U}(P_V + P_C), \end{cases}$$

toutes les variables d'état sont ignorables. Donc l'adjoint $[P, P_J \text{ ou } P_C]$ est constant. En particulier $P_J = P_C = -1$ et

$$\begin{cases} \underline{Y}^* = P_V^T & \text{(PL)} & (339a) \\ \underline{\gamma}^* = \gamma_{\max} \mathcal{U}(P_V - 1) P_V^T / P_V & \text{(VEC)} & (339b) \end{cases}$$

L'expression (338) peut être considérée comme fournissant l'évolution de P_V sur l'arc "ballistique" $\bar{0}$. Les composantes correspondantes de P_V sur les axes orbitaux tournants $\mathcal{W} \times \mathcal{Y} \times \mathcal{Z}$ sont donc de la forme (334), où les constantes $\mathcal{C}, \mathcal{D}, \mathcal{E}, \mathcal{D}$, \mathcal{F}, \mathcal{F} sont liées aux composantes (constantes) de \underline{p} .

Pour un transfert sans rendez-vous, où $P_J = P_C = 0, P_V \rightarrow$ et donc \underline{Y}^* sont périodiques en E , de période 2π : la même loi de poussée est appliquée à chaque révolution.

Lorsque (339) est utilisé, les formules de perturbation (336) deviennent:

$$dq/dE = \mathcal{r} \underline{K} \underline{\gamma}^* = \mathcal{r} \underline{K} \gamma^* (P_V^T / P_V) = (\gamma^* / P_V) \mathcal{r} \underline{K} \underline{K}^T P^T = (\gamma^* / P_V) \underline{B} P^T,$$

où $\underline{B} = \mathcal{r} \underline{K} \underline{K}^T$ est une matrice symétrique 6 x 6. Donc, par intégration de E_0 à E_f , on obtient:

$$\Delta \underline{q} = \underline{q}_f - \underline{q}_0 = \underline{G} P^T, \tag{340}$$

où

$$\underline{G} = \int_{E_0}^{E_f} (\gamma^* / P_V) \underline{B} dE \tag{341}$$

est une matrice symétrique 6 x 6.

Le coût est obtenu par intégration de (337):

$$\left\{ \begin{aligned} \Delta J = J_f &= (1/2) \int_{E_0}^{E_f} \mathcal{r} P_V^2 dE = (1/2) \int_{E_0}^{E_f} \mathcal{r} \underline{p} \underline{K} \underline{K}^T P^T dE = (1/2) \int_{E_0}^{E_f} \underline{p} \underline{B} P^T dE = (1/2) \underline{p} \underline{G} P^T, & (342a) \\ \Delta C = C_f &= \int_{E_0}^{E_f} \gamma_{\max} \mathcal{U}(P_V - 1) dE. & (342b) \end{aligned} \right.$$

Pour les systèmes PL, (341) fournit aisément la matrice \underline{G} , car $\gamma^* = P_V$ et les éléments de \underline{B} sont des polynômes en $\sin E, \cos E$ et éventuellement E . Comme la matrice \underline{G} ne contient pas \underline{p} , le système (340) est linéaire par rapport aux inconnues (composantes non nulles de l'adjoint orbital et variations non imposées des éléments orbitaux). Par exemple, si toutes les variations des éléments orbitaux sont imposées, l'inversion de (340) conduit à:

$$\underline{p} = \Delta \underline{q}^T \underline{G}^{-1}$$

et (342a) donne

$$\Delta J = (1/2) \Delta \underline{q}^T \underline{G}^{-1} \Delta \underline{q}. \tag{343}$$

Le coût est une forme quadratique des variations des éléments orbitaux. Le problème est complètement soluble analytiquement (c'était un problème linéaire-quadratique). Pour un transfert sans rendez-vous ($P_J = 0$) en un nombre entier N de révolutions ($E_f - E_0 = 2N\pi$), (343) se simplifie en:

$$\Delta J = \left[\frac{1}{2} (E_f - E_0) \right] \left\{ 2 \Delta i_x^2 + [2(1-e^2)/(1+4e^2)] \Delta i_y^2 + (1/4) \Delta a^2 + [2/5(1-e^2)] \Delta e_x^2 + [2/5(1-e^2)] \Delta e_y^2 \right\}. \tag{344}$$

Pour les systèmes VEC, les points de commutation, où les extinctions ou réallumages se produisent, sont données par $P_V = 1$, ou encore $\mathcal{r} P_V^2 = \mathcal{r}$, soit:

$$\mathcal{r} P_V^2 = \mathcal{r} \underline{p} \underline{p}^T = \mathcal{r} \underline{p} \underline{K} \underline{K}^T P^T = \underline{p} \underline{B} P^T = 1 - e \cos E,$$

Pour un transfert ($P_J = 0$), il y a au plus six solutions en E , donc trois AMAX ou impulsions par révolution. L'intégration sous forme explicite de (341) sur les AMAX ($\gamma^* = \gamma_{\max}$) est généralement impossible à cause de la présence de P_V au dénominateur de l'intégrande. L'inversion de (340) est également difficile, car \underline{G} contient \underline{p} . Le problème ne peut être résolu analytiquement que dans un nombre limité de cas. Deux exemples sont donnés ci-dessous.

1 - Modification infinitésimale optimale du demi-grand axe

La seule composante de P qui ne soit pas nécessairement nulle est P_a . L'expression (338) montre alors que le "primer vector" $\vec{P}_V = 2 P_a \vec{V}$ est proportionnel à la vitesse \vec{V} . La loi de poussée optimale est très simple (Fig. 45'). Pour un système VEC, $\Delta a / N \gamma_{max}$ et $\Delta C / N \gamma_{max}$ peuvent être exprimées sous forme paramétrique en fonction de l'anomalie excentrique E_1 du point de commutation M_1 .

2 - Transferts optimaux, multi-impulsionnels, entre orbites quasi circulaires, proches

Pour un tel transfert, défini sur la Fig. 46a, il est possible de prendre $\bar{e} = 0$, et le "primer locus" (\mathcal{P}) est une ellipse (Fig. 46b). Si le transfert prend plus d'une révolution, cette ellipse doit se trouver à l'intérieur de la sphère \mathcal{M} de centre M_0 et de rayon 1. Les points de contact avec \mathcal{M} correspondent aux points d'impulsions sur l'orbite (Fig. 46c). Il y a quatre types de solutions : I, II, III et I' ; les types III et I' sont singuliers ($P_V = 1$). Le domaine accessible avec la vitesse caractéristique ΔC peut être représenté par ses sections $\Delta a = \text{constante}$ dans l'espace tridimensionnel $\Delta e_{\perp}, \Delta e_{\parallel}, \Delta j$ (Fig. 46d).

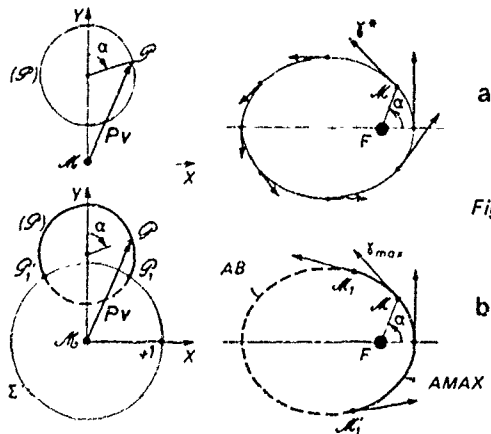


Fig. 45 - "Primer locus" et loi de poussée optimale. a) système PL ; b) système VEC

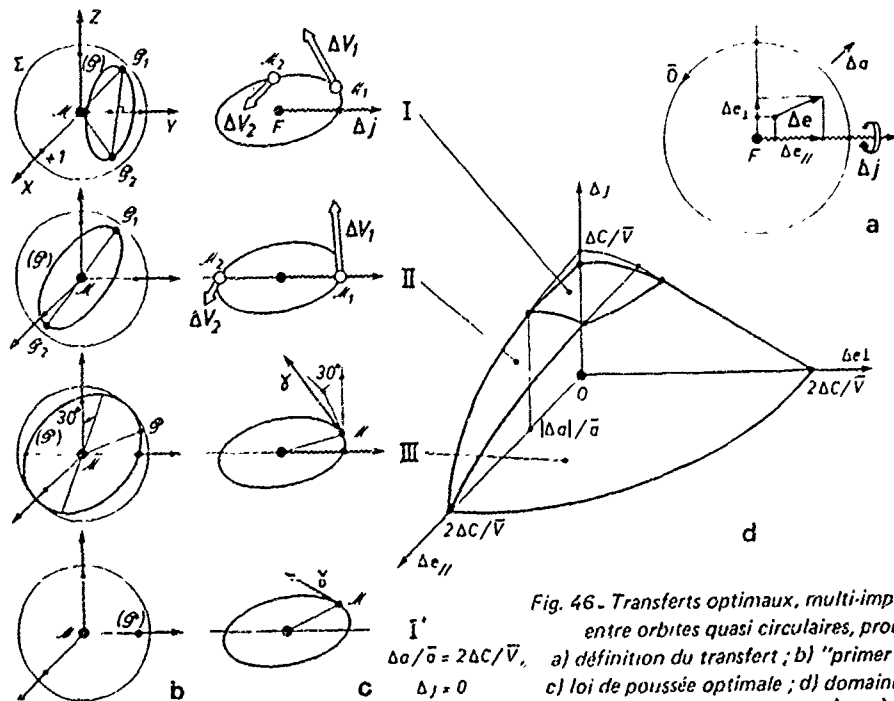


Fig. 46 - Transferts optimaux, multi-impulsionnels, entre orbites quasi circulaires, proches. a) définition du transfert ; b) "primer locus" ; c) loi de poussée optimale ; d) domaine accessible avec ΔC (limité à la région $\Delta e_{\perp} \geq 0$; $\Delta e_{\parallel} \geq 0$)

5.6.2.2 - Transferts de durée indifférente (systèmes VEC)

Dans ce cas les transferts entre paraboles sont théoriquement de coût nul, puisqu'ils peuvent être réalisés à l'aide d'impulsions infiniment petites, appliquées infiniment loin ; il est donc possible de séparer les phases elliptique et hyperbolique de tout transfert. Il reste donc trois problèmes :

- 1 - l'acquisition optimale du niveau parabolique (c.a.d. n'importe quelle parabole) à partir d'une ellipse ou d'une hyperbole (et inversement) ;
- 2 - les transferts ellipse-ellipse ;
- 3 - les transferts hyperbole-hyperbole.

Pour les transferts de type 2, toute poussée peut être décomposée en parties appliquées au cours des révolutions successives. Un rendez-vous éventuel ne coûterait pas plus que le transfert correspondant. En effet, il serait suffisant pour le réaliser, d'attendre, par exemple, assez longtemps sur une orbite intermédiaire très proche de l'orbite finale. Dans cette théorie, on peut se contenter d'utiliser l'état orbital réduit $\hat{q} = [q^k]$ ($k = 1, 2, \dots, 5$), en laissant de côté le sixième élément orbital, utile seulement pour les rendez-vous. Il est également commode de prendre la vitesse caractéristique C comme variable de description [11, 14].

Les formules de perturbation (335) deviennent :

$$d\hat{q}/dC = \hat{K}(\hat{q}, v) \underline{D},$$

où \hat{K} est la matrice de perturbation réduite 5 x 3.

Les commandes sont la direction de poussée $\underline{D} = \underline{\gamma}/\gamma$ (matrice 3 x 1) et l'anomalie vraie v [11, 14], car il est toujours possible d'attendre sur l'orbite osculatrice \mathcal{O} jusqu'à ce qu'une position convenable soit atteinte. L'hamiltonien est :

$$\hat{H} = \hat{p} (d\hat{q}/dC) = \hat{p} \hat{K} \underline{D} = p_v \underline{D},$$

où $p_v = \hat{p} \hat{K}$ est le "primer vector". \hat{H} est maximum pour $\underline{D}^* = p_v^*/p_v$ et alors pour la valeur v^* qui assure le maximum absolu de la fonction $p_v(v)$. Un changement brutal du point de fonctionnement v^* est une commutation. La réticence entre deux (ou plusieurs) points de fonctionnement v_1^*, v_2^* correspond aux arcs singuliers alternatifs (ASA) qui ne sont jamais optimaux (la condition nécessaire (332) de Kelley-Contensou n'est pas remplie).

Lorsque la dimension du problème le permet, cette maximisation de \hat{H} peut être effectuée en considérant le domaine de manoeuvrabilité $\mathcal{D}(\hat{q})$, c'est-à-dire le domaine de l'espace "hodo-graphe" ($dq^1/dC, dq^2/dC, \dots, dq^5/dC$) obtenu en donnant aux commandes \underline{D}, v toutes les valeurs possibles, pour une valeur fixée de \hat{q} (voir paragraphe 4.1.4). Par exemple, dans le cas d'un transfert entre orbites elliptiques coplanaires, d'orientation indifférente (Fig. 47), l'état orbital peut être défini par e et $b = a(1-e^2)^{1/2}$ (demi-petit axe) seulement, et le domaine de manoeuvrabilité \mathcal{D} est la région à quatre pointes représentée en grisé sur la Fig. 47b. Le point optimal de fonctionnement (ψ^*, v^*) est nécessairement choisi dans l'intersection $\mathcal{D} \cap \text{demi-cercle}$ de \mathcal{D} et de son contour convexe $\partial \text{uni} \mathcal{D}$ (rectangle $P^+ A^+ P^- A^-$), c'est-à-dire parmi les quatre pointes P^+, A^+, P^-, A^- , qui correspondent à $v = 0$ ou π et (indépendamment) $\psi = 0$ ou π .

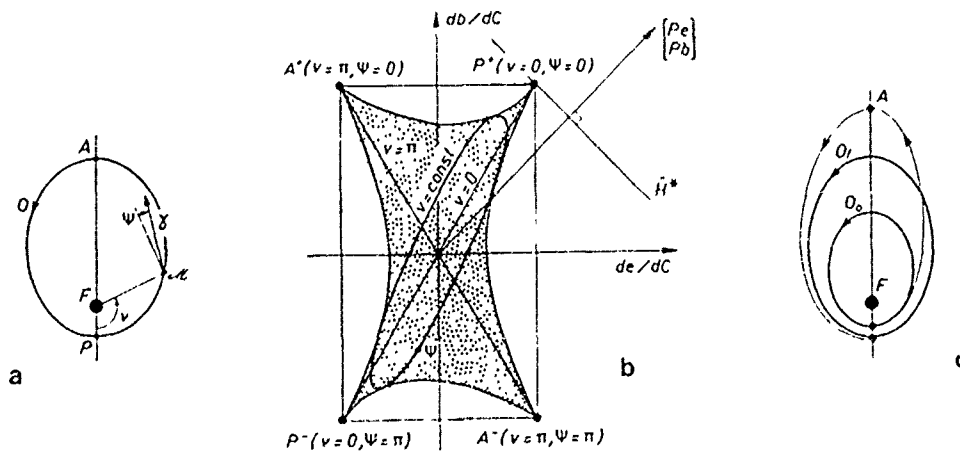


Fig. 47. Transfert entre orbites elliptiques, coplanaires, d'orientation indifférente.

a) notations ; b) domaine de manoeuvrabilité :

$$\begin{aligned} de/dC &= (b/na^2) [\sin \psi \sin \Psi + (\cos \psi + \cos E) \cos \Psi] \\ db/dC &= (1/n) \{ e \sin \psi \sin \Psi + [2 + e (\cos \psi - \cos E)] \cos \Psi \} \end{aligned}$$

c) transfert bi-elliptique

La poussée doit donc être appliquée seulement au péricentre ou à l'apocentre et tangentiellement vers l'avant ou vers l'arrière. Le choix de la "pointe" de fonctionnement dépend du signe de P_a et P_b . Les commutations peuvent être étudiées à l'aide du système adjoint. Il peut être montré que le transfert optimal appartient à la famille des transferts bi-elliptiques (Fig. 47c) et la comparaison directe des coûts de tels transferts (le coût dépend d'un paramètre, la distance de l'apocentre intermédiaire A) montre que le transfert optimal est soit de type Hohmann soit biparabolique (Fig. 48). Entre cercles, le rapport de rayons limite est $r_f/r_o = 11,94$.

Bien d'autres résultats analytiques sont disponibles dans le cas de la durée indifférente [19], en particulier pour les transferts entre ellipses coplanaires ou coaxiales et les transferts entre hyperboles.

Par contre, l'étude des transferts de durée fixée nécessite le plus souvent une approche numérique. Cependant, l'étude analytique peut être poussée assez loin dans le cas particulier ci-dessous.

5.6.2.3 - Transferts à temps fixé, à grand nombre de tours, entre orbites elliptiques (systèmes PL)

Le nombre N de révolutions du véhicule autour du centre attractif est supposé grand. Il est alors possible d'utiliser une méthode de "moyenne". On calcule tout d'abord le coût élémentaire dJ pour une révolution par la formule (344) (dans laquelle l'homogénéité a été préalablement restaurée). On choisit ensuite le trajet optimal $\vec{q}^*(t)$, dans l'espace d'état orbital réduit, de façon à minimiser le coût total :

$$J_f = \int_{t_0}^{t_f} dJ.$$

Les résultats principaux de cette approche sont :

- 1 - le coût J est une fonction linéaire du temps t ;
- 2 - l'énergie $\mathcal{E} = (v^2/2) - (\mu/r)$ de l'orbite osculatrice O est une fonction quadratique du temps ;
- 3 - pour un choix convenable des axes, le système différentiel des trajectoires optimales prend la forme simple suivante :

$$d\phi/d\theta = \pm [\cot^2 k - \cot^2 \phi \cos^2 i - \tan^2 \phi \sin^2 i \sin^2 \omega]^{1/2},$$

$$di/d\theta = \cos i \sin \omega \tan^2 \phi \sin i,$$

$$d\omega/d\theta = (\cot^2 \phi - \tan^2 \phi \sin^2 \omega) \cos i,$$

$$d\Omega/d\theta = (1/5) + \tan^2 \phi \sin^2 \omega,$$

où θ est un "pseudo-temps". $\phi = \text{Arcsin } e$ et k est une constante.

La Fig. 49 montre un exemple de trajectoire optimale en forme de spirale.

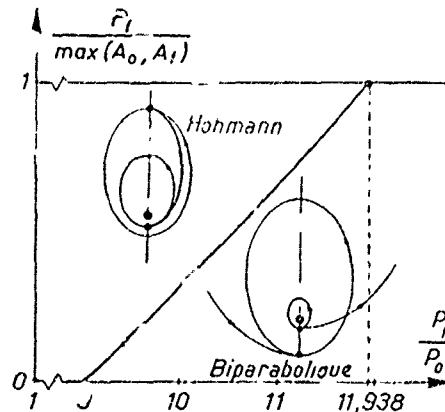


Fig. 48 - Discussion du type de transfert.

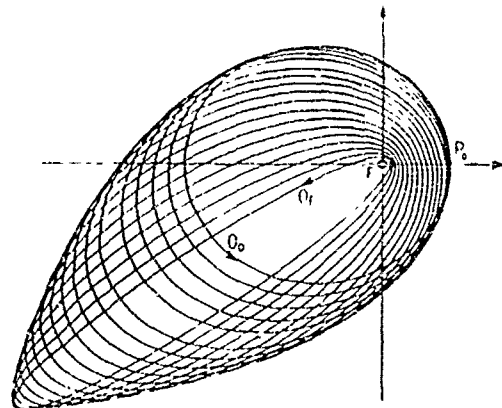


Fig. 49 - Projection de la trajectoire de transfert sur le plan de O_0 .

5.7 - Rendez-vous interplanétaires

Dans ce cas, le champ de gravitation $\vec{g}(\vec{r}, t)$ est très complexe. Il résulte de l'attraction du Soleil et des planètes du système solaire. Le problème d'optimisation est généralement simplifié en négligeant l'attraction des planètes pendant la phase héliocentrique du rendez-vous et l'attraction du Soleil et des autres planètes dans chaque phase planétocentrique, et en raccordant les différentes solutions "champ central" ainsi obtenues.

Le passage au voisinage d'une planète ou d'un satellite naturel peut donner lieu à un effet de "tremplin", qui peut être utilisé pour l'optimisation.

Pour les systèmes de propulsion "impulsionnels", le transfert de Hohmann (Fig. 41) est encore le transfert optimal bi-impulsionnel entre deux planètes massives sur des orbites circulaires et coplanaires. Chaque impulsion doit être appliquée aussi près de la surface de la planète que possible.

La propulsion électrique (Fig. 50) est particulièrement intéressante pour les voyages vers les planètes lointaines.

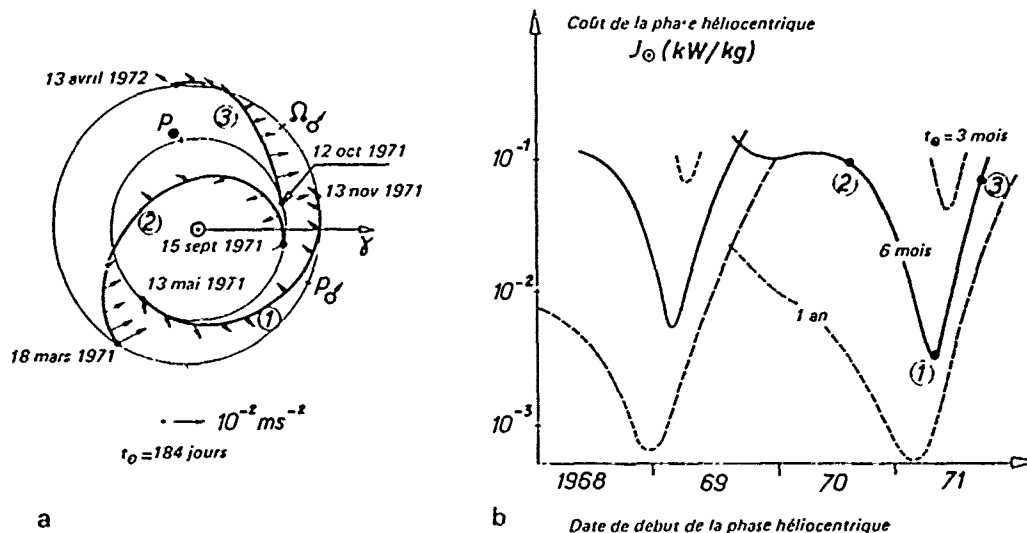


Fig.50 - Rendez-vous Terre - Mars. [13]

- a) trois exemples de rendez-vous correspondant à une durée héliocentrique $t_0 = 184$ jours ≈ 6 mois
 b) coût de la phase héliocentrique en fonction de la date du début de cette phase

CONCLUSION

Nous espérons que cet exposé introductif aura convaincu le lecteur spécialiste de mécanique du vol mais non nécessairement spécialiste d'Astrodynamique, que l'étude des trajectoires spatiales est plus simple qu'il n'y paraît. Le modèle de départ est simple : les forces d'attraction newtonienne sont bien connues, certainement mieux que ne le sont, en général, les efforts aérodynamiques qu'il doit également introduire dans ses calculs. Le problème se ramène finalement à la résolution du système différentiel non linéaire, alors que le mécanicien des fluides doit faire face à des systèmes d'équations aux dérivées partielles complexes. La théorie des perturbations repose sur une méthode classique de variation des constantes. Cela ne veut pas dire qu'il ne subsiste pas des difficultés, comme, par exemple, l'étude du comportement à long terme des solutions.

Cet exposé a été volontairement limité aux aspects les plus fondamentaux pour l'étude du mouvement, naturel ou contrôlé, des satellites artificiels. Des problèmes importants n'ont pas été abordés : problème des 3 corps, aspects relativistes, aspects stochastiques, navigation et trajectographie, guidage et pilotage. L'accent a été mis sur l'approche analytique, plus que sur l'approche numérique. D'autres exposés de ce Symposium - voire de Symposiums futurs - combleront cette lacune.

Cependant la portée des méthodes exposées dépasse largement le cadre de l'étude des trajectoires spatiales. Les formalismes newtonien, lagrangien et hamiltonien sont évidemment applicables à d'autres problèmes d'astrodynamique ou, plus généralement, de mécanique : par exemple, mouvement d'attitude (y compris dans le cas de satellites "flexibles", si une modélisation de type masses + ressorts + dashpots, ou une approche modale, est utilisée). Le Principe du Maximum de Pontryagin peut également servir à résoudre des problèmes de commande ou de contrôle d'attitude, ou d'optimisation de trajectoires de lanceurs ou de véhicules de rentrée.

Cette "introduction aux trajectoires spatiales" a présenté quelques outils et quelques exemples d'application. Elle ne se conçoit que par les prolongements qui pourront lui être donnés.

REFERENCES

- 1 - J.-P. Marec. Séminaires d'Option Astrodynamique, 1ère Partie, Mouvement des satellites artificiels, Cours de l'École Polytechnique, Paris (1983).
- 2 - J.-P. Marec. Optimal Space Trajectories, Elsevier, Amsterdam (1979).
- 3 - J. Bouchard et C. Aumasson. Optimization of the positioning of two satellites on geosynchronous, eccentric and inclined orbits, AGARD/FMP Symposium "Space Vehicle Flight Mechanics", Luxembourg (13 - 16 novembre 1989).
- 4 - P. Exertier, P. Sengenès et G. Tavernier. Orbit determination, AGARD/FMP Symposium "Space Vehicle Flight Mechanics", (Luxembourg 13 - 16 novembre 1989).
- 5 - M. Caldichoury et C. Champetier. Hermes rendezvous with the Space Station, AGARD/FMP Symposium "Space Vehicle Flight Mechanics", Luxembourg (13 - 16 novembre 1989).
- 6 - W.M. Kaula. Theory of Satellite Geodesy, Blaisdel, Waltham (1966).
- 7 - J.P. Vinti. New method of solution for unretarded satellite orbits, Journal of Research, BNS, Vol. 63 B, n° 2 (1959).
- 8 - P. Contensou. Note sur la cinématique du mobile dirigé, Bulletin ATMA n° 45 (1946).
- 9 - L.S. Pontryagin, V.G. Boltyanskii, R.V. Gamkrelidze et E.F. Mischenko. The Mathematical Theory of Optimal Processes, Interscience Publishers, Wiley, New York (1962).
- 10 - W. Hohmann. Die Erreichbarkeit der Himmelskörper, Oldenbourg, Munich (1925).
- 11 - P. Contensou. Etude théorique des trajectoires optimales dans un champ de gravitation. Application au cas d'un centre d'attraction unique, Astronautica Acta 8, 134-150 (1962).
- 12 - D.F. Lawden. Optimal Trajectories for Space Navigation, Butterworths, Londres (1963).
- 13 - W.J. Melbourne et C.G. Sauer. Optimum interplanetary rendez-vous with power-limited vehicles, AIAA J. 1, 54-60 (1963).
- 14 - J.V. Breakwell. Minimum-impulse transfer. Progress in Astronautics and Aeronautics (Ed : M. Summerfield et V.G. Szebehely), Vol. 14, Celestial Mechanics and Astrodynamics, p. 583, Academy Press, New York (1964).
- 15 - T.N. Edelbaum. Optimum power-limited orbit transfer in strong gravity fields. AIAA J. 3, 921-925 (1965).
- 16 - B. Fraeijs de Veubeke. Canonical transformation and the thrust-coast-thrust optimal transfer problem. Astronautica Acta 11, 271-282 (1965).
- 17 - G.L. Grodzovskii, H. Ivanov et V.V. Tokarev. Vol Cosmique à Poussée Faible (en russe). Nauka, Moscou (1966).
- 18 - H.J. Kelley, R.E. Kopp et H.G. Moyer. Singular extremals, in Topics in Optimization, ch. 3, p. 63, Academic Press (1967).
- 19 - C. Marchal. Synthèse des résultats analytiques sur les transferts optimaux entre orbites képlériennes (durée indifférente). Dans : Advanced Problems and Methods for Space Flight Optimization (Ed : B. Fraeijs de Veubeke), p. 91, Pergamon, Oxford (1969).
- 20 - F.W. Gobetz et J.R. Doll. A survey of impulsive trajectories ; AIAA J. 7, 801-834 (1969).
- 21 - P. Contensou. Conditions d'optimalité pour les domaines de manoeuvrabilité à frontière semi-affine, Colloquium on the Methods of Optimization, Lecture Notes in Mathematics n° 112, p. 139, Springer-Verlag (1970).
- 22 - N.W. Vinh et R.D. Culp. Optimal switching in coplanar orbit transfer. JOTA 7, 197-208 (1971).
- 23 - V.V. Ivashkin. Manoeuvres Spatiales Optimales avec Bornes sur la Distance à la Planète (en russe), Nauka, Moscou (1975).
- 24 - V.A. Ilin et G.E. Kouzma. Vol Optimal des Véhicules Cosmiques avec des Systèmes de Propulsion à Forte Poussée (en russe), Nauka, Moscou (1976).
- 25 - J.-P. Marec. Space-vehicle trajectories : optimization, in Systems and Control Encyclopedia (Ed. M. G. Singh), 4481 - 4490, Pergamon (1987).
- 26 - R.B. Norris et H.A. Karasopoulos. Synergetic plane change compared with impulsive maneuvers for future aeroassisted orbital transfer vehicles, AGARD/FMP Symposium "Space Vehicle Flight Mechanics", Luxembourg (13 - 16 novembre 1989).

CALCUL D'ORBITES

par

P. Exertier, P. Sengenès et G. Tavernier
 Centre National d'Études Spatiales (CNES)
 18 Avenue Edouard Belin
 31055 Toulouse Cedex
 France

RESUME

Depuis de nombreuses années, le CNES est impliqué dans les problèmes de calcul d'orbite. A l'origine ces études ont été menées dans un but expérimental. Puis elles ont été affinées pour des besoins opérationnels concernant les satellites en orbite basse, géostationnaires et les sondes interplanétaires. Plus récemment, le CNES a entrepris, en coopération avec la NASA, l'étude d'un satellite, TOPEX-POSEIDON, destiné à étudier la circulation océanique. L'emploi d'altimètres embarqués très précis (5 cm) impose une détermination d'orbite également très précise (de l'ordre de quelques centimètres sur l'altitude).

Cet article présente quelques aspects des techniques modernes de détermination d'orbite.

Le problème des satellites artificiels de la terre s'apparente, en première approximation, au problème à deux corps. En fait, le corps central principal (la Terre) ne peut être considéré comme une sphère homogène et rigide. La différence principale est son aplatissement, les plus faibles sont les inhomogénéités dans la distribution des masses à l'intérieur de la terre. De plus, ces irrégularités varient avec le temps à cause de l'élasticité et de la viscosité (hypothèse de Love) du corps central qui se trouve dans le champ gravitationnel d'autres corps célestes (Lune, Soleil).

La trajectoire du satellite est également perturbée par des forces d'origine non gravitationnelle. Les premières déterminations d'orbite effectuées à la division Mathématiques Spatiales du CNES ont pris en compte le freinage atmosphérique afin de prévoir l'évolution des trajectoires des satellites en orbite basse. De nos jours, d'autres effets non gravitationnels sont à prendre en compte dans une modélisation dynamique réaliste pour des applications requérant un calcul d'orbite de plus en plus précis (TOPEX-POSEIDON).

Un satellite artificiel de la terre peut être considéré comme un détecteur de forces dans l'environnement spatial. Ainsi le principe fondamental de la dynamique peut être appliqué. L'accélération résultante du satellite dans un référentiel inertiel est égale à la somme de toutes les forces (par unité de masse). L'extrapolation d'orbite consiste à résoudre cette équation différentielle du deuxième ordre à différentes époques, à partir d'une position et d'une vitesse initiales.

Historiquement, du fait de la faiblesse des moyens de calcul algébriques ou numériques, les "mécaniciens" ont essayé de développer des méthodes de résolution analytiques qui transforment les équations classiques de la dynamique en un nouveau système d'équations différentielles plus faciles à intégrer. Dans ce type de transformation de mécanique céleste, on applique la méthode générale des perturbations à la solution keplérienne triviale. Les calculs sont développés jusqu'à un certain degré de complexité qui donne le niveau de précision de la solution du mouvement orbital. Lorsque l'on recherche une solution de précision élevée, ces méthodes analytiques sont maintenant abandonnées au profit de méthodes d'intégration purement numériques des modèles de forces les plus réalistes.

La détermination d'orbite consiste à comparer les solutions numériques du système différentiel dynamique aux observations fournies par les systèmes de poursuite de satellite (mesures angulaires, de vitesse radiale, de distance ...). Cette comparaison permet d'améliorer la connaissance des conditions initiales de la trajectoire et de certains coefficients empiriques utilisés pour combler les petits écarts entre la réalité et la modélisation des forces. Cette amélioration est obtenue à l'aide d'algorithmes d'ajustement généralement basés sur la méthode des moindres carrés ; en fonction de l'application, on a recours au filtrage de Kalman ou à des méthodes globales de moindres carrés.

ABSTRACT

For many years, CNES has been involved in orbit computation. At the beginning these calculations have been made for experimental purposes. Then, they have been improved for operational projects such as low earth orbiting satellites, geostationary satellites and interplanetary probes. More recently, CNES has decided to work (in collaboration with USA) on TOPEX-POSEIDON project which is realized for oceanic circulation determination. The use of a very accurate (5 cm) on-board altimeter requires a very accurate orbit estimation (some centimeters on altitude).

This paper presents some aspects of modern technics of orbit determination.

Earth artificial satellites problem corresponds theoretically to the restrained two-body problem. In fact the main central body (the Earth) cannot be considered as an homogeneous rigid sphere. The main difference is the oblateness of the Earth and the least ones are the irregularities in mass distributions inside the Earth. Furthermore these irregularities are time dependant because of the elasticity and viscosity (Love hypothesis) of the central body which is in the gravitational field of other celestial bodies (Moon and Sun).

In the same way, the satellite is also perturbed by non gravitationnal effects. First orbit determination computed at CNES space mathematics division took into account atmospheric drag effects in order to predict the evolution of low altitude satellites trajectories. Nowadays, others non gravitational effects must be considered in a realistic forces model for applications requiring an even more accurate orbit determination (TOPEX-POSEIDON).

The Earth artificial satellite can be considered as a forces detector in spatial environment. Then the fundamental principle of the dynamics can be applied. The resulting acceleration of the satellite in an inertial reference frame is equal to the sum of all forces (per unit of mass). Orbit extrapolation consists in solving this second order differential equation at different epochs from initial position and velocity.

Historically, because of poor algebraic or numerical mean of calculation, mechanics tried to develop analytical resolution methods which roughly transform the classical equations of dynamics into a new differential equations system easier to integrate. In this kind of celestial mechanics transformations, we apply the general perturbations methods to the trivial keplerian solution. Calculations are developed up to a certain order of complexity which gives the level of precision of the orbital motion solution. For high precision solution, these analytical methods are today abandoned and replaced by purely numerical integration of the most realistic forces models.

Orbit determination consists in comparing the numerical solutions of the dynamic differential system to observations provided by satellite tracking systems (angular, radial velocity, range ... measurements). This comparison allows to improve the knowledge of initial conditions of the trajectory and some empirical coefficients used to fill up the small discrepancy between reality and forces modelisation. This improvement is achieved by fitting algorithms generally based on least squares methods ; depending on applications, Kalman filtering or global least squares methods are implemented.

INTRODUCTION

La localisation des satellites est rendue nécessaire par le besoin de :

- pointer sur eux des antennes de communication ou de localisation,
- prévoir l'évolution de la trajectoire sous l'action des accélérations perturbatrices,
- contrôler leur orbite (manoeuvres) afin de réaliser les objectifs de la mission.

La réalisation de ces tâches est possible avec une précision de l'ordre de quelques centaines de mètres, obtenue aisément grâce à une modélisation simplifiée des forces.

Pour certains satellites, la réussite de la mission nécessite une plus grande précision de localisation. On peut citer :

- Le positionnement de balises terrestres (GPS - DORIS). La précision de celui-ci est directement fonction de la précision de la localisation du satellite.
- La localisation de véhicules terrestres, aériens (GPS).
- L'altimétrie océanique ; l'altimètre est très utile pour l'étude de la circulation océanique (courants, tourbillons ...), à condition de connaître l'altitude du satellite avec une précision comparable à celle de l'instrument lui-même. On vise pour les années 90, un ordre de grandeur de 10 cm (TOPEX-POSEIDON).
- La cinématique terrestre. Il est possible, en suivant le mouvement d'un réseau de stations de poursuite terrestre par rapport à l'orbite inertielle d'un satellite, de mesurer les irrégularités de la rotation terrestre (STARLETTE, LAGEOS).

Comme nous venons de le voir, la précision requise par certaines missions est de l'ordre de quelques mètres, voir quelques centimètres. Il est alors nécessaire de modéliser beaucoup plus finement les forces agissant sur le satellite, et parfois d'élaborer des modèles adaptés à chaque type de mission (prise en compte de la géométrie et de l'attitude du satellite...).

Ce type de calcul d'orbite permet parfois, en retour, d'améliorer les modèles de forces (potentiel terrestre, densité atmosphérique...).

1. PRINCIPE DU CALCUL D'ORBITE

On dispose d'un modèle dynamique de l'évolution de la trajectoire du satellite, plus ou moins complexe en fonction des objectifs de la mission, mais toujours entaché d'erreur.

Il est donc nécessaire de recalculer la trajectoire prédite par rapport à des mesures de localisation (distance, angulaire, doppler, laser ...) à l'aide d'un algorithme de filtrage numérique de type moindres carrés ou Kalman.

L'évaluation de la précision de restitution de la trajectoire est délicate, faute de critère absolu.

On a donc recours, en phase d'analyse de mission, à des analyses de covariance ou à des simulations.

En phase opérationnelle, il existe plusieurs techniques souvent complémentaires comme :

- L'analyse des résidus (mesure observée - mesure calculée) par le calcul d'écart-types, le tracé d'histogrammes...
- L'étude des recouvrements : la valeur des écarts observés sur la période de recouvrement de deux éphémérides provenant de deux calculs d'orbite décalés dans le temps donne une estimation de la précision de ces calculs.
- Les comparaisons d'orbites calculées avec différents types de mesures ou différents logiciels.

2. QUELQUES EXEMPLES DE CALCUL D'ORBITE

Le CNES dispose d'un réseau 2 GHz de 4 stations, Aussaguel, Kiruna, Kourou et Hartebeesthoek permettant d'effectuer trois types de mesures, distance, avec une précision de l'ordre de 10 mètres, doppler, avec une précision de 0,3 Hz (correspondant à une précision de 2,5 cm/s sur la vitesse radiale) et angulaire (0,05'). Ce réseau sert à calibrer le matériel et les logiciels utilisés pour le calcul d'orbite de satellites géostationnaires comme TELECOM 1A, 1C ou TDF grâce à des campagnes de mesures spécifiques. La précision obtenue est de l'ordre de 20 à 40 m (max.). Il est également utilisé pour les satellites héliosynchrones d'observation de la terre, comme SPOT1. L'orbite opérationnelle est calculée avec une précision de 100 à 150 m (max.), des campagnes de calibration permettent de descendre à 15 m (max.).

La mise à poste de satellites géostationnaires est réalisée à l'aide du réseau CNES 2 GHz complété par les stations de Malindi (ESA), Goldstone et Canberra (DSN/NASA). Les objectifs de précision sont de 110 m sur le demi grand-axe, 9.10^{-5} sur l'excentricité, correspondant à 2,5 km le long de la trace, pour le premier apogée, et 40 m sur le 1/2 grand-axe et 1 km le long de la trace pour le quatrième apogée.

Le réseau TRANET comportant 3 stations CNES (une vingtaine de stations au total) permet d'effectuer des mesures de type Doppler avec une précision de l'ordre de 0,3 cm/s.

Lors de la campagne MERIT, les mesures recueillies par 20 stations ont été utilisées pour calculer l'orbite du satellite NOVA3. Les résidus en fin de traitement sont de 0,5 cm/s et la trajectoire est déterminée avec une précision de 2 à 5 m (max.). Plus récemment, les 3 stations TRANET du CNES ont donné, pour le satellite altimétrique GEOSAT des résidus de 0,6 à 1,3 cm/s et une précision de 15 à 20 m (max.) sur la trajectoire. Une des explications à la moins bonne qualité des résultats est la couverture moins complète de l'orbite avec seulement 3 stations.

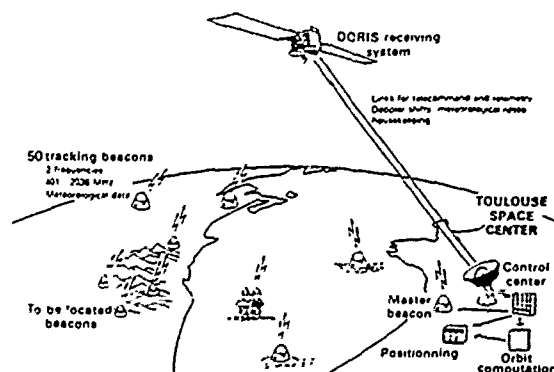


Figure 1 : Le système DORIS

Les mesures distances de type LASER sont parmi les plus précises à l'heure actuelle avec un bruit de mesure de 1 à 3 cm pour les stations les plus modernes. Des calculs d'orbite pour des arcs de 5 à 30 jours avec les satellites STARLETTE et LAGEOS conduisent à des résidus finaux de 15 à 30 cm (à 1 sigma) et une précision de 2 à 5 m (max.) sur la trajectoire.

Un nouveau type de mesures sera bientôt utilisé au CNES : les mesures DORIS, de type Doppler bifréquence (400 MHz - 2 GHz) dont la spécification de précision est de 0,3 mm/s. Le réseau comportera à terme 50 balises d'orbitographie (34 à ce jour) assurant une très bonne couverture géographique. La mise en oeuvre probatoire de ce système consiste à embarquer un instrument DORIS à bord du satellite d'observation de la terre SPOT2. L'emploi d'un nouveau modèle de potentiel (GEM-T2 ou GRIM4) et une meilleure modélisation des forces de surface doivent permettre d'atteindre l'objectif de précision de 5 m le long de la trace.

L'instrument DORIS sera ensuite embarqué sur le satellite altimétrique TOPEX-POSEIDON d'observation des océans. Ce satellite embarquera également deux altimètres de grande précision (10 cm). Plusieurs centres seront chargés du calcul de l'orbite précise avec un objectif de 10 cm en radial : le GODDARD SPACE FLIGHT CENTER (GSFC - NASA) avec le logiciel GEODYN, l'Université du Texas (UTEX) avec UTOPIA et le CNES avec ZOOM. Outre les mesures DORIS, des mesures LASER, GPS et TDRSS seront également utilisées pour les différents calculs d'orbite, précise et opérationnelle.

Un nouveau type de calcul d'orbite fait l'objet d'études : la navigation embarquée. Elle consiste à effectuer les traitements à bord du satellite. La puissance de calcul est donc limitée et impose de recourir à un modèle dynamique simplifié.

Un première étude concerne un navigateur DORIS embarqué, avec un objectif de précision de 500 m, qui pourrait servir par exemple au pointage du télescope PASTEL de communication optique.

Une autre étude est relative à l'emploi des mesures pseudorange et pseudorange-rate GPS à bord de la navette HERMES. Des simulations ont permis d'évaluer la précision à 25 m et 4 cm/s (3 sigmas), cette précision étant atteinte au bout d'une révolution.

3. LES PERTURBATIONS

Les orbites des satellites artificiels proches de la terre obéissent en première approximation aux lois de Kepler mais elles sont fortement perturbées et instables sous l'action des perturbations. Il est donc nécessaire de modéliser ces perturbations pour calculer des trajectoires de satellites de plus en plus précises, ceci afin de répondre à des besoins de localisation de plus en plus fins.

On distingue deux grandes familles de perturbations. Les perturbations d'origine gravitationnelle qui ne dépendent ni de la géométrie du satellite, ni de sa masse comme la non sphéricité du potentiel terrestre, les phénomènes de marées terrestres et océaniques et les forces d'attraction de la lune, du soleil et d'autres planètes du système solaire.

Les perturbations d'origine non gravitationnelle comme le freinage atmosphérique, les pressions de radiation solaire directe et indirecte et les manoeuvres de contrôle d'attitude et de maintien à poste.

On assimile également à une force perturbatrice une éventuelle accélération complémentaire d'entraînement due au choix d'un référentiel d'intégration non inertiel.

3.1. LE POTENTIEL DE GRAVITATION TERRESTRE

Les interactions de type Newtonien créent des accélérations gravitationnelles dérivant d'un potentiel de la forme :

$$U = \iiint \mathcal{G} \frac{dm}{r_{ps}}$$

avec r_{ps} = distance entre P, point élémentaire de masse dm et S, position du satellite

la somme étant étendue à toutes les masses.

$\frac{1}{r_{ps}}$ = $f(OP ; OS)$ peut être développé en polynômes de Legendre et le potentiel exprimé en coordonnées sphériques à condition de concentrer toutes les masses attractives dans une sphère où le satellite ne rentrerait jamais. Cela n'est possible qu'en séparant le potentiel gravitationnel en deux composantes, terrestre et luni-solaire.

La Terre n'étant ni sphérique, ni homogène, elle ne peut être considérée comme une masse ponctuelle à l'extérieur d'une sphère la contenant.

Le développement du potentiel terrestre en harmoniques sphériques conduit à l'expression :

$$U(r, \lambda, \varphi) = \frac{\gamma M_T}{r} \sum_{n=0}^{\infty} \sum_{k=0}^n \left(\frac{a_e}{r}\right)^n P_{nk}(\sin \varphi) (C_{nk} \cos k\lambda + S_{nk} \sin k\lambda)$$

avec P_n : polynômes de Legendre $P_n(x) = \frac{1}{2^n n!} \frac{d^n(x^2-1)^n}{dx^n}$

P_{nk} : fonctions de Legendre $P_{nk} = (1-x^2)^{k/2} \frac{d^k P_n(x)}{dx^k}$

M_T : masse de la Terre

a_e : rayon équatorial de la Terre

r, λ, φ : coordonnées sphériques du point S extérieur à la Terre (dans un repère terrestre).

3.1.1. PARTIE STATIQUE DU POTENTIEL TERRESTRE

Les coefficients C_{nk} et S_{nk} sont des fonctions du temps à cause de la non stationnarité de la répartition des masses terrestres qui est due :

- aux marées océaniques,
- à la réponse élastique de la Terre aux potentiels perturbateurs extérieurs (marée terrestre),
- à des phénomènes géophysiques internes.

Cette non stationnarité est cependant faible et les valeurs des coefficients de la décomposition $C_{nk}(t)$ et $S_{nk}(t)$ restent assez voisines des coefficients moyens :

$$\bar{C}_{nk} = \frac{1}{T} \int_0^T C_{nk}(t) dt$$

$$\bar{S}_{nk} = \frac{1}{T} \int_0^T S_{nk}(t) dt$$

Il est donc légitime de s'intéresser à la "partie statique du potentiel terrestre", c'est à dire au potentiel fictif dont la décomposition dans le repère terrestre aurait pour coefficient :

$$\bar{C}_{nk}, \bar{S}_{nk}$$

Les marées terrestres et océaniques seront prises en compte sous forme d'incrément's de coefficients du potentiel terrestre, variables dans le temps :

$$\Delta C_{nk}(t), \Delta S_{nk}(t)$$

Il est possible de définir des coefficients normalisés C_{1m}, S_{1m} avec :

$$C_{n0} = -\sqrt{2l+1} C_{10}$$

$$\begin{matrix} C_{nk} \\ S_{nk} \end{matrix} = \sqrt{\frac{(1-m)!(2l+1) \times 2}{(1+m)!}} \begin{pmatrix} C_{1m} \\ S_{1m} \end{pmatrix}$$

Le système d'axes du repère terrestre par rapport auquel sont définis les coefficients de potentiel est défini par :

- une origine en O, centre de gravité de la Terre d'où :

$$C_{10} = C_{11} = S_{11} = 0$$

- l'axe Oz est assimilé à l'axe principal d'inertie d'où :

$$C_{21} = S_{21} = 0$$

En fait le pôle d'inertie n'est pas fixe sur la croûte terrestre.

D'où introduction du pôle C10 ou d'un pôle moyen (fixe sur la Terre et assez voisin du pôle d'inertie) pour la décomposition du potentiel terrestre.

Un modèle de potentiel est donc défini par des constantes (γM_T), a_e et les coefficients C_{nk}, S_{nk} .

On peut citer les séries GRIM (GRGS - DFGI) et GEM (GSFC) : GRIM 3, GEM 10B et plus récemment GEM-T1 GEM-T2.

3.1.2. INTERPRETATION PHYSIQUE

Les termes C_{n0} , sont appelés harmoniques zonaux. Ils traduisent une symétrie de révolution par rapport à l'axe Oz ($k = 0$ donc ils ne dépendent pas de la longitude). Ils sont parfois notés J_n .

Le terme en J_2 traduit l'aplatissement des pôles (R équateur - R pôle = 20 km)

$$- J_2 P_{20} \sin^2 \varphi = - \frac{J_2}{2} (3 \sin^2 \varphi - 1)$$

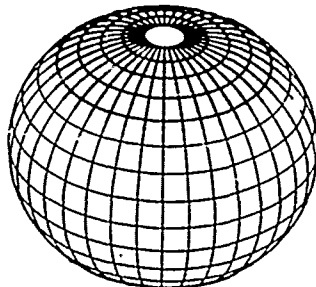


Figure 2 : Harmonique zonal (2,0)

Le terme en J_3 traduit la dissymétrie Nord/Sud de la Terre, celle-ci a une forme de poire

$$- J_3 P_{30} \sin^3 \varphi = - \frac{J_3}{2} (5 \sin^2 \varphi - 3 \sin \varphi)$$

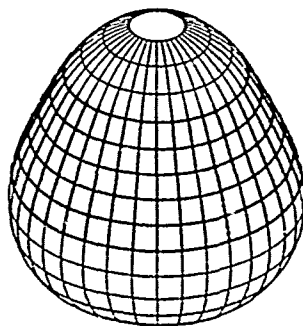


Figure 3 : Harmonique zonal (3,0)

Les termes C_{nk} , S_{nk} ($k \neq 0$) sont appelés harmoniques tesseraux. Les tesseraux correspondant à $n = k$ sont appelés sectoriels et traduisent une forme en "quartiers d'orange" de la Terre.

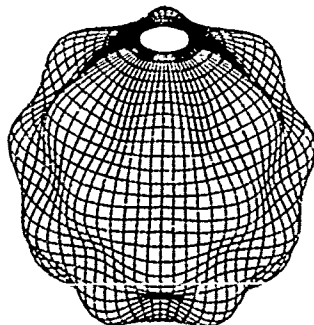


Figure 4 : Harmonique tesseral (9,6)

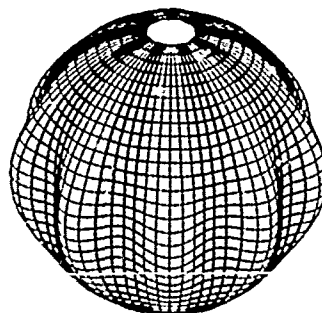


Figure 5 : Harmonique sectoriel (9,9)

Il faut noter que le terme principal est le terme central ou képlérien ($C_{00} = J_0 = 1$) tandis que le J_2 est de l'ordre de 10^{-3} et les autres termes de l'ordre de 10^{-6} ou plus petits.

3.1.3. EFFETS DES PERTURBATIONS LIEES AU MODELE DE POTENTIEL

Les coefficients zonaux et tesseraux du potentiel terrestre ont des effets séculaires et/ou périodiques sur les éléments orbitaux qui définissent l'orbite du satellite (figure 6)

- Paramètres d'orbite
- a : demi-grand axe de l'orbite (m)
 - e : excentricité
 - i : inclinaison (deg)
 - ω : argument du périégé (deg)
 - Ω : ascension droite du noeud ascendant (deg)
 - M : anomalie moyenne (deg)
 - t : date de l'événement

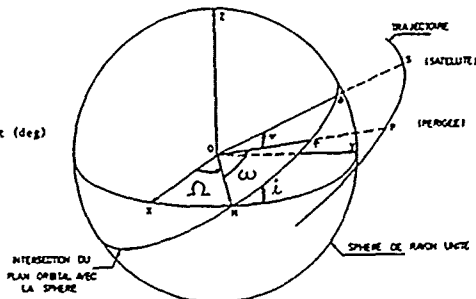


Figure 6 : Les éléments orbitaux

- Les zonaux pairs exercent des perturbations :

- . séculaires sur ω , Ω , et M
- . courtes ($\approx T/2$) et longues ($\approx T\omega/2$) périodes
- T = période du satellite
- $T\omega$ = période du périégé

- Les zonaux impairs exercent des perturbations :

- . longues périodes ($\approx T\omega$)
- . courtes périodes ($\approx T$)

- Les tesseraux exercent des perturbations :

- . moyennes périodes (1 jour ou une fraction de jour)
- . courtes périodes avec en particulier des phénomènes de résonance lorsque la période orbitale du satellite T est un sous-multiple de la période de rotation de la Terre sur elle-même (1 jour) : $T = T_{\text{Terre}}/n$. Les harmoniques tesseraux dont l'ordre est un multiple de n produisent des phénomènes de résonance comme par exemple C₂₂ S₂₂ pour les satellites géostationnaires ou les harmoniques d'ordre 13, 26, ... ou 14, 28, ... pour les satellites bas comme SPOT ou TOPEX. L'observation des résonances est très utile pour déterminer les harmoniques correspondants.

3.2. LE POTENTIEL LUNI-SOLAIRE

Intéressons nous maintenant à la deuxième partie du potentiel gravitationnel relative aux effets de la Lune et du Soleil.

En assimilant l'astre attracteur à une sphère homogène à l'extérieur de laquelle se trouve le satellite, la formulation de NEWTON s'écrit :

$$\ddot{\vec{r}}_s = \frac{GM_a}{|\vec{SA}|^3} \vec{SA} - \frac{GM_T}{|\vec{OA}|^3} \vec{OA}$$

- avec M_a : Masse de l'astre perturbateur
 S : Position du centre de gravité du satellite
 O : Centre de la Terre
 A : Centre de l'astre attracteur

Dans cette expression le terme en $\vec{SA}/|\vec{SA}|^3$ représente l'accélération effectivement subie par le satellite tandis que le terme en $\vec{OA}/|\vec{OA}|^3$ représente celle que subit la Terre.

$\ddot{\vec{r}}_s$ est donc bien l'accélération différentielle subie par le satellite dans un repère lié au centre de la Terre.

Cette accélération dérive d'un potentiel que l'on peut écrire :

$$W = \gamma M_a \left(\frac{1}{|SA|} - \frac{\vec{OS} \cdot \vec{OA}}{|\vec{OA}|^3} - \frac{1}{|\vec{OA}|} \right)$$

La constante d'intégration étant choisie telle que le potentiel s'annule à l'origine (si S est en O).

On peut alors la développer sous la forme :

$$W = \gamma M_a \sum_{n=2}^{\infty} \frac{r^n}{\rho^{n+1}} P_n(\cos \theta)$$

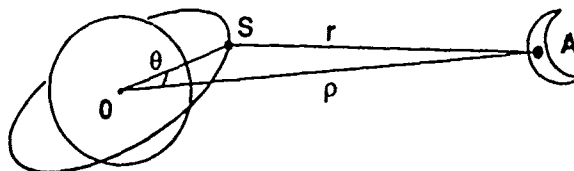


Figure 7 : Potentiel luni-solaire

Cette expression s'applique également aux autres planètes du système solaire si l'on veut prendre leur effet en compte.

Ce potentiel est appelé "potentiel des marées" car il crée des perturbations d'orbites terrestres mais également des déformations de la Terre élastique et de la surface des océans.

Le rapport r/ρ prend, lorsque A est le Soleil, des valeurs de $4 \cdot 10^{-5}$ à $2 \cdot 10^{-4}$ pour des orbites basses à géostationnaires.

Lorsque A est la Lune, il prend des valeurs de $1,6 \cdot 10^{-2}$ à 10^{-1} pour des orbites basses à géostationnaires.

Dans le cas des orbites basses ou de l'étude des marées on utilise l'expression de W jusqu'au degré 2 :

$$W = \gamma M_a \frac{r^2}{\rho^3} \frac{3 \cos^2 \theta - 1}{2}$$

Pour la prise en compte de la perturbation lunaire sur une orbite géostationnaire on utilise l'expression de W jusqu'au degré $n = 3$:

$$W = \gamma M_2 \frac{r^2}{\rho^3} \left[\frac{3 \cos^2 \theta - 1}{2} + \frac{r}{\rho} \frac{5 \cos^3 \theta - 3 \cos \theta}{2} \right]$$

Par les déformations de la Terre élastique et de la surface des océans qu'il provoque, le "potentiel des marées" crée une variation du potentiel terrestre. Ce phénomène est pris en compte sous forme d'un potentiel perturbateur du potentiel statique tel qu'il a été défini précédemment.

3.3. LE FROTTEMENT ATMOSPHERIQUE

Cette perturbation de type non gravitationnel résulte des chocs des molécules composant la haute atmosphère sur les parois du satellite. Malgré la faible valeur des densités atmosphériques rencontrées aux altitudes des satellites, ces derniers se déplacent à de telles vitesses (7000 à 10000 m/s) que le produit ρv^2 de la densité rencontrée par le carré de la vitesse (généralement proportionnel aux forces aérodynamiques) n'est pas négligeable.

Il en résulte une perturbation d'origine aérodynamique :

- prépondérante pour les orbites très basses (200 - 400 km)
- préoccupante jusqu'à 1000 km.

L'expression de cette accélération perturbatrice est, avec une hypothèse de portance nulle :

$$\dot{\vec{y}} = - \frac{i}{2} \rho C_D \frac{S}{m} |\vec{v}| \cdot \vec{v}$$

avec : ρ = densité atmosphérique
 C_D = coefficient aérodynamique (qui varie entre 2,2 et 2,8)
 S = surface de référence
 m = masse du satellite
 \vec{v} = vitesse relative du satellite par rapport à l'atmosphère

Les paramètres à prendre en compte dans la modélisation du frottement atmosphérique sont :

- l'état de l'atmosphère comme sa masse volumique, sa température et la masse moléculaire moyenne (calcul de la densité),
- les positions relatives du satellite et du soleil (densité),
- des paramètres physiques d'environnement comme le flux solaire, l'indice géomagnétique (densité), le taux de superrotation de l'atmosphère et les vents en altitude (calcul de la vitesse relative).

3.4. LA PRESSION DE RADIATION SOLAIRE DIRECTE

Cette perturbation présente de grandes analogies avec le frottement atmosphérique. Elle résulte des chocs entre un flux de photons et la surface du satellite. On distingue en général deux composantes :

- la pression de radiation solaire directe,
- la pression de radiation solaire rediffusée par la Terre.

L'expression de l'accélération perturbatrice résultant de la pression de radiation solaire directe est :

$$\vec{Y} = -k \frac{S}{m} \frac{L_0}{4\pi |\vec{SA}|^2} \cdot \frac{\vec{SA}}{|\vec{SA}|}$$

avec :

- k = coefficient lié aux qualités géométriques et réfléchives des parois du satellite
- S = section de choc dans la direction Soleil-satellite
- m = masse du satellite
- L_0 = flux lumineux émis par le Soleil par stéradian
- \vec{SA} = vecteur satellite-Soleil

L'accélération perturbatrice résultant de la pression de radiation solaire rediffusée est calculée à partir des éléments de la terre vus du satellite. Elle représente environ 25 % de la valeur de l'accélération due à la pression de radiation solaire directe. Ses effets sur l'orbite du satellite sont cumulatifs.

3.4.1. EFFETS DES PERTURBATIONS LIEES A LA PRESSION DE RADIATION SOLAIRE

La pression de radiation solaire n'entraîne pas de variation séculaire sur le demi-grand axe, mais des variations significatives sur l'excentricité et l'inclinaison.

On observe, pour un satellite sur orbite géostationnaire :

- un terme séculaire en inclinaison de 0,9°/an et un terme périodique avec une amplitude de 0,0035° à 13,66 jours et 0,023° à 182,65 jours,
- des termes séculaires sur la longitude moyenne, et des termes périodiques moyennes et longues périodes d'amplitude 0,019°,
- des termes courtes périodes sur le demi-grand axe d'amplitude 965 m,
- des termes courtes et moyennes périodes sur l'excentricité d'amplitude $5 \cdot 10^{-5}$.

On observe, pour un satellite sur orbite basse de type SPOT (altitude 832 km) :

- une résonance entre la rotation du plan de l'orbite et la rotation apparente du soleil,
- une dérive de l'inclinaison de $3,34 \cdot 10^{-2}$ degrés/an qui fait diminuer l'heure locale.

3.5. IMPORTANCES RELATIVES DES DIFFERENTES FORCES

Le terme central ou "Képlérien" du potentiel a une importance prépondérante. C'est lui qui donne une forme elliptique à la trajectoire d'un satellite terrestre. Tous les autres termes du potentiel ainsi que les autres forces ne font que déformer légèrement cette ellipse et faire tourner son plan.

Le second terme par ordre d'importance décroissante est le J_2 qui traduit l'aplatissement de la terre. Son ordre de grandeur est 10^{-3} par rapport au terme central. Tous les autres effets ont des ordres de grandeur inférieurs ou égaux à 10^{-3} par rapport au J_2 donc 10^{-6} par rapport au terme central.

Le frottement est très lié à l'altitude du satellite et à l'activité solaire.

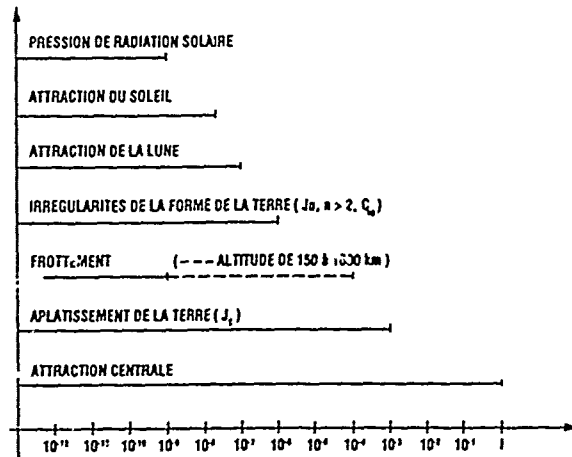


Figure 8 : Comparaison des forces

La figure 8 donne des ordres de grandeur mais son interprétation est délicate car le module de chaque force (en dehors du terme central) peut aller de 0 à la borne supérieure en fonction de la géométrie du satellite, de son altitude, de son attitude, et de sa position sur orbite.

4. LE TRAITEMENT DES PERTURBATIONS

Le calcul de la trajectoire d'un satellite se fait par intégration de l'équation fondamentale de la dynamique :

$$\left. \begin{aligned} \frac{d^2 x_i}{dt^2} &= f_i/m \quad (i = 1, 2, 3) \\ \text{à partir des conditions initiales :} \\ x_i(t=0) &= x_i^* \\ \dot{x}_i(t=0) &= \dot{x}_i^* \end{aligned} \right\} (1)$$

Dans le cas d'un satellite soumis uniquement à un champ newtonien de type $f_i/m = -\mu x_i/r^3$ avec $r^2 = \sum x_i^2$, la solution est une orbite képlérienne :

$$\begin{array}{ll} S_1 = a & S_4 = \omega \\ S_2 = e & S_5 = \Omega \\ S_3 = i & S_6 = M - nt : \text{anomalie moyenne initiale} \end{array}$$

le système (1) est alors équivalent au système :

$$\frac{dS_i}{dt} = 0 \quad i = 1, \dots, 6$$

Dans la réalité, le satellite est soumis à un champ newtonien perturbé ; la force principale agissant sur le satellite est celle due au terme newtonien mais il faut également prendre en compte des termes complémentaires, ce qui est réalisable de deux façons :

$$\frac{d^2 x_i}{dt^2} = -\mu \frac{x_i}{r^3} + Y_i \quad \text{avec} \quad Y_i \ll \mu \frac{x_i}{r^3} \quad (2)$$

ou :

$$\frac{dS_i}{dt} = P_i \quad \text{avec} \quad P_i \text{ petits} \quad (3)$$

La méthode des perturbations consiste à intégrer le système (3) de préférence au système (2).

Par contre, une intégration numérique du système (1) permet en général d'atteindre une meilleure précision.

4.1. L'INTEGRATION NUMERIQUE

Celle-ci consiste à approximer le système :

$$\left. \begin{array}{l} \dot{y} = f(y, t) \\ y(t_0) = Y_0 \end{array} \right\} \text{ où } f(y, t) \text{ est déterminée} \quad (4)$$

par :

$$\frac{Y_{n+1} - Y_n}{h} = f(Y_n, t_n) \text{ où } h \text{ est le pas d'intégration}$$

Le choix du pas d'intégration résulte d'un délicat compromis entre la nécessité d'une bonne approximation du système (4) et la maîtrise des problèmes numériques (erreurs de troncature et d'arrondis).

Les y sont alors calculés de proche en proche.

Les algorithmes utilisés sont de deux types :

- à pas séparés : le calcul du point $n + 1$ ne dépend que du point n (RUNGE-KUTTA par exemple)
- à pas liés : le recours à un processus itératif de prédiction correction permet un meilleur conditionnement numérique du système intégré, au prix d'un problème de constitution du tableau initial au démarrage du processus (COWELL par exemple).

L'intégration numérique des équations du mouvement est coûteuse en temps de calcul et les erreurs de troncature et d'arrondis ont un effet cumulatif. On peut remédier à ce dernier problème à l'aide de fonctions régularisantes qui réduisent artificiellement la rapidité de la variation des perturbations par convolution avec une fonction bien adaptée.

4.2. L'EXTRAPOLATION D'ORBITE

Celle-ci permet de connaître l'évolution des paramètres d'orbite au cours du temps, en fonction des perturbations qui agissent sur le satellite.

Il existe pour cela des méthodes analytiques qui permettent une représentation et une interprétation de chaque perturbation et une décomposition harmonique de celle-ci de la forme :

$$X = A_1 + B_1 t + \sum_i C_i \sin(\omega_i t + \varphi_i)$$

Il est alors possible d'identifier les différents paramètres.

La somme des décompositions harmoniques des perturbations agissant sur le satellite donne une décomposition du même type qui facilite l'envoi des paramètres (nombre limité de paramètres à transmettre pour permettre à un utilisateur d'effectuer sa propre extrapolation d'orbite).

Il est également possible de procéder à une intégration numérique. Comme nous l'avons déjà signalé précédemment, le point délicat de cette méthode est le choix du pas d'intégration. Pour un satellite bas comme SPOT, par exemple, on utilise un modèle de potentiel complet de degré et ordre n_{\max} .

La plus petite période des perturbations sera donc :

$$T_m = T/n_{\max} \text{ où } T \text{ est la période orbitale}$$

Le théorème de SHANNON impose une valeur maximale du pas d'intégration, si l'on veut que cette période soit observable par l'intégrateur :

$$h < \frac{T_m}{2} \text{ soit } h < \frac{T}{2 n_{\max}}$$

Pour SPOT ($T \approx 100$ min) on peut utiliser un modèle comme GRIM 3, pour lequel $n_{\max} = 36$, d'où une valeur maximale du pas de l'ordre de 80 s.

Dans la pratique on extrapole une orbite de type SPOT avec un pas $h = 1$ minute.

Une troisième méthode, mixte, consiste à éliminer analytiquement les variations à courtes périodes et à intégrer numériquement les effets à moyennes et longue période.

4.3. LE CHOIX D'UN REPERE POUR LE CALCUL D'ORBITE

Un choix classique en mécanique consiste à rechercher un repère inertiel ; en mécanique céleste on peut donc calculer une orbite dans le repère céleste moyen défini à une date t_0 (par exemple le J2000). L'intégration des équations du mouvement est alors immédiate mais l'expression des accélérations est délicate dans un tel repère inertiel. De plus il nécessite un passage des position-vitesse, en fin de traitement, du repère inertiel de calcul dans un repère terrestre ou céleste instantané. Ce choix complique également la prise en compte des mesures entre le satellite et les stations terrestres. Il nécessite un double changement de repère :

J 2000 → repère vrai de la date → repère terrestre de la date.

Le programme de calcul d'orbite précise GEODYN du GODDARD SPACE FLIGHT CENTER (NASA - Washington) fonctionne selon ce principe.

Une autre possibilité consiste à intégrer les équations du mouvement dans un repère "tournant" : le repère céleste vrai. La prise en compte des mesures est alors plus simple mais ce choix nécessite le calcul des accélérations d'entraînement et de CORIOLIS (dus à la précession et à la nutation de l'axe de rotation de la Terre). Ces accélérations peuvent être traitées comme des perturbations.

Le programme de calcul d'orbite précise ZOOM du CNES (Toulouse) fonctionne selon ce principe.

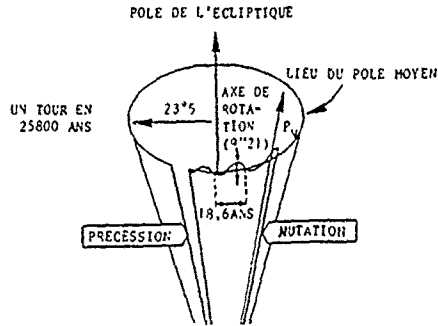


Figure 9 : Mouvement du moment cinétique terrestre

5. LES DIFFERENTS TYPES DE MESURES

5.1. LA MESURE DISTANCE

Son principe est la mesure d'un temps de propagation aller-retour.

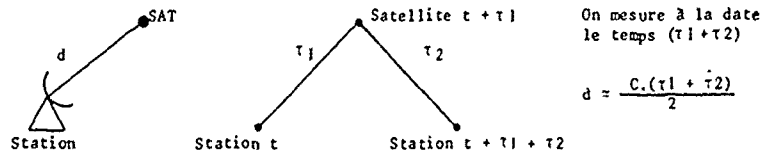


Figure 10 : Mesure distance : temps de propagation aller-retour

Il existe plusieurs techniques pour cela :

- le laser (paquets de photons)
- le radar (ondes centimétriques)
- les mesures par tons (signal défini à l'aide de sous-porteuses)

Ces dernières consistent à mesurer en station le déphasage entre l'onde émise et l'onde reçue.

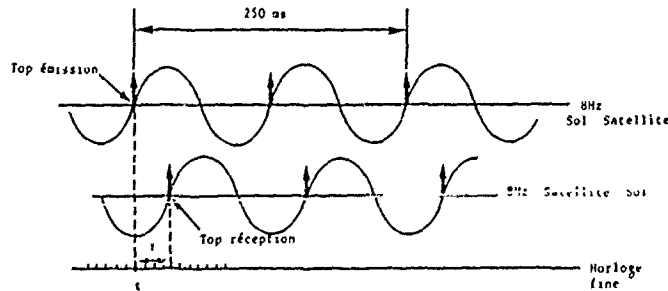


Figure 11 : Mesure distance par tons

La mesure est datée au top émission t précédant le top de réception qui arrête la valeur de la mesure .

La mesure du déphasage est effectuée avec une indétermination de $2\pi p$ (p entier). A cette indétermination, correspond une ambiguïté dans la mesure de la distance de :

$$\Delta d = \frac{c}{2f}$$

La précision de la mesure est liée à la résolution de la mesure de déphasage (fraction r de la période du ton) et à la fréquence du ton :

$$\sigma d = \frac{rc}{2f}$$

Il est nécessaire de trouver un compromis entre lever d'ambiguïté et précision. Il faut donc effectuer simultanément des mesures de distance à l'aide de plusieurs tons de fréquences différentes :

- le ton mineur permet de lever l'ambiguïté, par exemple pour 8 Hz :

$$\Delta d = \frac{c}{2f} = 18750 \text{ km}$$

- le ton majeur donne la précision du système de mesure, par exemple, pour 100 KHz $d = 1,5 \text{ km}$ (insuffisant sans le ton mineur) mais pour $r = 10^{-2}$ $\sigma d = \Delta d \cdot r = 15 \text{ m}$.

La précision de la mesure distance est affectée par son bruit :

- laser $< 1 \text{ m}$, 1 à 3 cm pour les stations de dernière génération
- radar $\approx 10 \text{ m}$
- réseau CNES 2 GHz $\approx 15 - 20 \text{ m}$

et par des biais liés au temps de transit en station (évalué régulièrement grâce à des mesures de calibration) et au temps de transit à bord (évalué grâce à des mesures de calibration avant le lancement, avec un problème de stabilité au cours de la vie du satellite).

5.2. LES MESURES ANGULAIRES

Les différentes techniques sont :

- optiques : photographie du satellite sur fond d'étoiles
- interférométriques : comparaison de phase
- relevé de la position de l'antenne, celle-ci pouvant avoir une monture azimutale ou à la cardan.

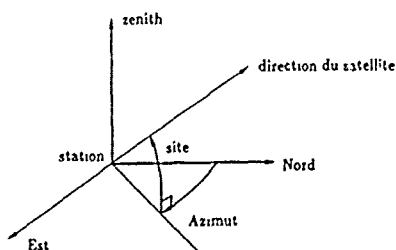


Figure 12 : Monture azimutale

Les bruits de mesures sont :

- optique : 1 seconde d'arc
- interférométrique : variable
- relevé de position d'antenne
 - . radar "Bretagne" $0.5 \text{ à } 1 \cdot 10^{-4} \text{ rad}$
 - . Antenne STL 4-6 GHz $2 \cdot 10^{-4} \text{ rad}$
 - . Antenne réseau CNES HBK 10^{-3} rad

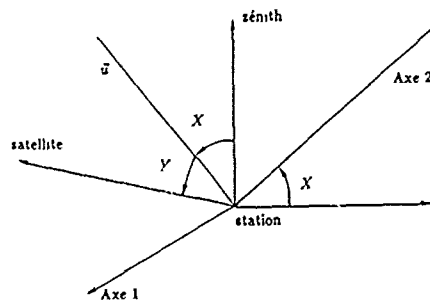


Figure 13 : Monture de cardan

Les biais sont dus au calage des axes mécaniques (évolutions périodiques et séculaires), aux écarts entre l'axe mécanique et l'axe radio-électrique et au trainage des asservissements.

5.3. LES MESURES DOPPLER

L'effet Doppler se traduit par la relation :

$$f_r = f_e \left(1 - \frac{v}{c}\right)$$

entre les fréquences émise et reçue

La méthode de mesure est la méthode "Quatant"

On compte à bord du récepteur qui peut être le satellite ou la station terrestre, un nombre N_0 de cycles reçus entre deux dates t_1 et t_2 .

Dans la pratique les fréquences f_e utilisées (et donc les fréquences f_r qui s'en déduisent) sont trop fortes pour qu'il soit possible de compter les cycles reçus directement. On fait donc battre la fréquence f_r avec une fréquence voisine f_s . On compte alors les battements du signal composé.

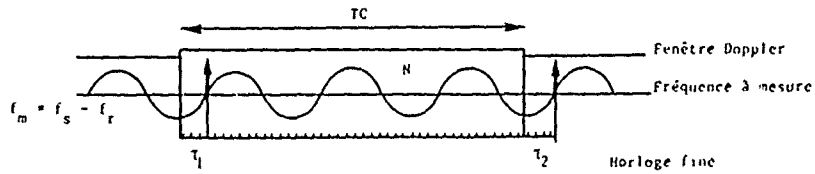
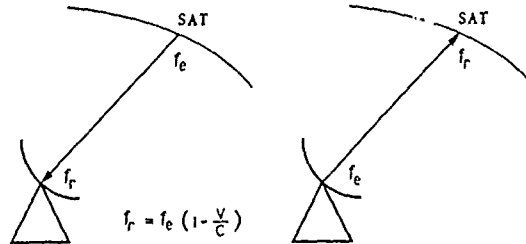


Figure 14 : Mesure doppler - comptage des cycles

La mesure est donc constituée des valeurs : t (date de la mesure), N (nombre de cycles comptés), T_C (temps de comptage), Z_1 (premier passage à zéro après l'ouverture de la fenêtre doppler), Z_2 (premier passage à zéro après la fermeture de la fenêtre doppler).

Les mesures doppler peuvent être de type :

- une voie (montante ou descendante)



Figures 15 - 16 : Mesure doppler une voie (descendante et montante)

- 2 ou 3 voies

fréquence f_e émise par une station 1, reçue par le satellite, $f_e (1 - v/c)$, réémise avec un facteur C_1 : $C_1 \cdot f_e (1 - v/c)$ et reçu par une station 2 :

$$f_r = C_1 \cdot f_e \left(1 - \frac{v}{c}\right)^2$$

$$\approx C_1 \cdot f_e \left(1 - \frac{2v}{c}\right)$$

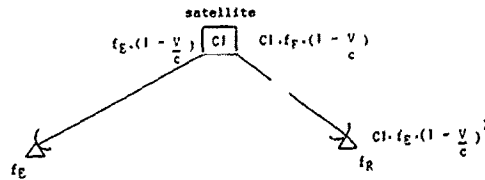


Figure 17 : Mesure doppler bi-voie

En bande S, $C_1 = \frac{240}{221}$

5.4. LA REFRACTION ATMOSPHERIQUE

La plupart des mesures sont affectées par ce phénomène qui a pour effet une courbure du trajet et l'allongement ou le raccourcissement de celui-ci.

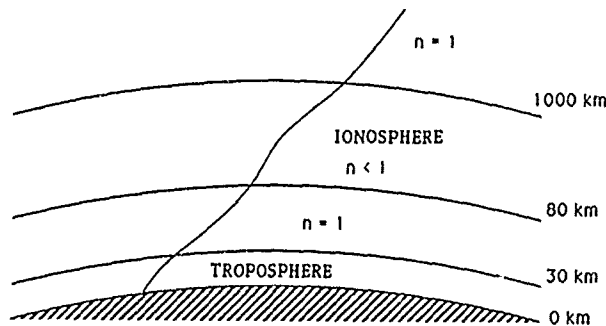


Figure 18 : La réfraction atmosphérique

5.4.1. LA CORRECTION TROPOSPHERIQUE

L'indice de réfraction de la troposphère est indépendant de la fréquence et fonction des conditions météorologiques (pression, température, humidité). Il existe des modèles de correction troposphérique d'une précision de l'ordre de 4%.

5.4.2. LA CORRECTION IONOSPHERIQUE

L'indice de réfraction de l'ionosphère est une fonction inverse du carré de la fréquence et du contenu électronique.

Ce dernier est très complexe à modéliser. Afin de limiter l'effet ionosphérique on augmente la fréquence de travail (2 GHz, 8 GHz, 30 GHz) et on utilise des méthodes de correction bi-fréquence (mesure à deux fréquences et élimination de l'effet ionosphérique au premier ordre, les erreurs sont résiduelles).

5.5. LA MODELISATION DES MESURES

Les différents types de mesures sont modélisés sous la forme :

$$O_C(t + \delta t) = f[X(t + \delta t), \dot{X}(t + \delta t), X_S, P] + b_t + b_s$$

avec :

- t ▪ date de la mesure
- δt ▪ erreur de synchronisation et/ou erreur d'estimation du temps de propagation
- (X, \dot{X}) ▪ position-vitesse du satellite dans le repère d'intégration
- X_S ▪ coordonnée de la station dans le même repère
- P ▪ paramètres technologiques
- b_t ▪ biais sur la mesure élémentaire (lié à l'instrument de mesure)
- b_s ▪ biais liés à la position du satellite sur son orbite (réfraction atmosphérique, attitude, correction de la monture, correction relativiste, ...)

La sensibilité de la mesure à différents paramètres est évaluée grâce aux dérivées partielles :

- état du satellite :

$$\frac{\partial O_C}{\partial X} = \frac{\partial f}{\partial X} \cdot \frac{\partial X}{\partial X_O}$$

$$\frac{\partial O_C}{\partial \dot{X}} = \frac{\partial f}{\partial \dot{X}} \cdot \frac{\partial \dot{X}}{\partial \dot{X}_O}$$

- station :

$$\frac{\partial O_C}{\partial X_S} = \frac{\partial f}{\partial X_S}$$

- datation et biais :

$$\frac{\partial O_C}{\partial t} = f \quad \frac{\partial O_C}{\partial t} = 1$$

$$- \text{paramètres du module de } b_s : \frac{\partial O_c}{\partial t} = \frac{\partial b_s(P_i)}{\partial P_i}$$

6. LA RESTITUTION D'ORBITE

Son objet est la connaissance au cours du temps des positions et vitesses du satellite.

La seule extrapolation d'orbite fournit une précision insuffisante du fait de la méconnaissance des modèles, d'un pilotage en attitude imparfait et des manoeuvres de maintien à poste (comportement des tuyères).

La restitution d'orbite consiste à élaborer des mesures théoriques entre le(s) satellite(s) et les stations sol à partir d'une orbite extrapolée (mesures de type distance, doppler ou angulaire).

Un algorithme d'estimation permet ensuite de réduire les écarts entre mesures observées et mesures théoriques par correction des paramètres orbitaux, dynamiques et de mesure à l'aide des dérivées partielles des mesures par rapport à ces paramètres (correction différentielle).

Le problème d'estimation se résoud en fonction des informations disponibles et des paramètres à estimer.

Les informations disponibles sont des informations à priori (dispersions, contraintes) et les mesures avec leurs erreurs.

Les paramètres à estimer peuvent être de différentes natures :

- paramètres d'orbite (bulletin initial) et de modèle dynamique (coefficient multiplicatif sur une force ...),
- paramètres de mesure (datation, écart de fréquence par passage ...),
- paramètres de géodésie dynamique et semi-dynamique (modèle de potentiel terrestre ...).

Ils peuvent être libérés (analyse de covariance : étude des corrélations entre paramètres) ou ajustés (restitution d'orbite proprement dite) en tenant compte de l'existence des contraintes.

Deux grands groupes d'algorithmes sont mis en oeuvre à cette fin :

- Les moindres carrés, adaptés à des traitements en temps différés, souvent implémentés sur de gros calculateurs et plutôt réservés à des applications de grande précision.
- Le filtrage numérique de KALMAN le plus souvent utilisé dans des applications de type temps réel ; ce type d'algorithme, pouvant être facilement mis en oeuvre sur les calculateurs qui équipent aujourd'hui les satellites, permet de doter ces derniers d'une capacité de navigation embarquée, ouvrant la voie à des véhicules spatiaux de plus en plus autonomes.

BIBLIOGRAPHIE

- | | |
|---------------|---|
| CARROU et al. | Le mouvement du satellite
Conférences et exercices de mécanique spatiale
CEPADUES Editions (1983). |
| CARROU et al. | Mathématiques spatiales pour la préparation et la réalisation
de l'exploitation des satellites
CEPADUES Editions (1984) |
| ZARROUATI O. | Trajectoires spatiales
CEPADUES Editions (1987) |

OPTIMISATION DE LA MISE A POSTE D'UN COUPLE DE SATELLITES
SUR DES ORBITES GEOSYNCHRONES EXCENTRIQUES ET INCLINEES

J. Bouchard et C. Aumasson

ONERA
BP 72
92322 Châtillon Cedex
FRANCE

RESUME

Un projet de système de télécommunication étudié par le CNES est basé sur l'utilisation de deux satellites évoluant sur des orbites géosynchrones 24h, excentriques et fortement inclinées, dont les noeuds ascendants sont décalés de 180°. Pour mettre à poste ces satellites, il est envisagé de les injecter dans un premier temps sur l'orbite de transfert géostationnaire standard (GTO) délivrée par un lanceur Ariane. Chacun d'eux est ensuite transféré individuellement de celle-ci sur son orbite finale. Les manoeuvres à deux ou trois impulsions permettant de réaliser cette seconde phase de la mise à poste pour une consommation d'ergols minimale ont été déterminées par une méthode d'optimisation paramétrique basée sur l'algorithme du gradient projeté généralisé mis au point à l'ONERA. Dans l'hypothèse où l'injection préliminaire des satellites sur orbite GTO est faite en deux lancements séparés, il est possible de réaliser les deux transferts ultérieurs par des manoeuvres identiques si la durée séparant les tirs est convenablement choisie. Si par contre on impose un lancement unique, les transferts sont a priori différents et conséquemment chacun une quantité d'ergols supérieure. Les manoeuvres optimales ont été déterminées dans les deux cas.

INTRODUCTION

La définition d'un système de télécommunication relayé par satellites impose le choix d'orbites bien adaptées à la zone géographique que l'on désire couvrir. En effet, tout point de cette zone doit être en visibilité permanente d'au moins un satellite relais sous le site le plus élevé possible pour assurer de bonnes conditions de communication, même en présence d'obstacles comme en zone urbaine ou montagneuse.

Si pour les régions équatoriales, l'utilisation d'un satellite géostationnaire permet de remplir aisément cette condition, il n'en est pas de même pour les latitudes plus élevées. Aussi le concept SYCOMORES du Centre National d'Etudes Spatiales (CNES) propose, pour couvrir la majeure partie de l'Europe, d'utiliser deux satellites placés sur des orbites géosynchrones 24h, excentriques et inclinées, dont les noeuds ascendants sont décalés de 180°. Les traces au sol de ces satellites seraient identiques, mais parcourues avec un décalage de temps de 12 heures de façon à assurer un service permanent sur l'Europe. Un site de visibilité toujours supérieur à 55° pour l'un au moins des deux satellites permettrait, dans le cas de communications entre véhicules terrestres, de doter ceux-ci de simples antennes non orientables pointées verticalement.

Pour mettre à poste les deux satellites, il est proposé de les injecter au moyen d'un lanceur Ariane 4 sur une orbite de transfert géostationnaire (GTO) standard. Un moteur à liquides ré-allumable permet alors de faire passer chaque satellite sur son orbite définitive en deux ou trois phases propulsives. Les deux satellites peuvent être injectés sur une même orbite GTO à la suite d'un lancement unique, auquel cas les transferts optimaux du point de vue de la masse d'ergols consommée ne seront pas effectués par les mêmes manoeuvres. La seconde solution consiste à injecter les satellites en deux lancements distincts (au cours desquels chacun d'eux pourrait éventuellement accompagner un géostationnaire). En choisissant convenablement l'intervalle de temps séparant les tirs, on peut toujours faire en sorte que la configuration géométrique de l'orbite finale par rapport à l'orbite GTO de départ soit la même pour les deux transferts. Par conséquent, les manoeuvres optimales permettant de les réaliser sont dans ces cas identiques pour les deux satellites.

Quelle que soit la procédure de lancement choisie (tirs séparés ou tir unique), la détermination des manoeuvres à deux ou trois impulsions permettant de transférer chaque satellite sur son orbite finale pour une consommation d'ergols minimale est un problème dont on ne connaît pas de solution analytique, étant donné que chaque transfert s'effectue ici entre des orbites qui ne sont ni coaxiales ni coplanaires [1]. Ce problème a donc été traité par une méthode d'optimisation numérique basée sur l'algorithme du gradient projeté généralisé de l'ONERA, qui présente l'intérêt de pouvoir prendre en compte facilement les contraintes opérationnelles du problème, sans avoir a priori une idée de la solution optimale. Les transferts optimaux à deux et trois impulsions ont ainsi été déterminés pour chaque procédure de lancement.

ORBITES SYCONORES [3]

SYCOMORES est un concept de télécommunication entre véhicules terrestres relayé par satellite. Il permettrait d'assurer en permanence un service de haute qualité sur la

plupart de l'Europe, ou sur toute zone de dimensions et de situation en latitude comparables. Il est prévu pour cela d'utiliser deux satellites remplissant à tour de rôle la fonction de relais par périodes de 12 heures. Les deux satellites seraient placés sur des orbites géosynchrones, excentriques et inclinées caractérisées par les paramètres suivants:

- demi grands axes:	$a_1 = a_2 = 42\ 164\ \text{km}$	(période 24 heures)
- excentricités:	$e_1 = e_2 = 0.35$	
- inclinaisons:	$i_1 = i_2 = 60^\circ$	
- arguments de périégée:	$\omega_1 = \omega_2 = 270^\circ$	

Pour que le système fonctionne convenablement, il faut que les deux satellites parcourent par rapport à la Terre une trajectoire unique, mais avec un décalage de 12 heures des temps de passage en un point donné. Cette condition est satisfaite grâce à deux équations liant les paramètres orbitaux restants:

- ascensions droites des noeuds ascendants:	$\Omega_2 - \Omega_1 = 180^\circ$	(1)
- anomalies moyennes:	$M_2 - M_1 = 180^\circ$	(2)

Le noeud ascendant de l'une des orbites coïncide donc avec le noeud descendant de l'autre, et l'un des satellites passe au périégée chaque fois que le second est à l'apogée.

La trajectoire décrite par rapport à la Terre, qui est la même pour les deux satellites et dont la trace au sol est représentée en figure 1, n'est pas entièrement définie par ce qui précède. Il faut spécifier en outre la longitude d'un de ses points, par exemple celle de l'apogée qui s'exprime par:

$$L_A = \Omega_1 + M_1 - \text{TSG} - \pi/2 \quad (3)$$

où TSG est l'angle repérant la position du méridien de Greenwich dans le repère absolu de référence, à l'instant pour lequel est donnée l'anomalie moyenne M_1 du satellite 1. La valeur de L_A actuellement retenue pour un service de télécommunication de couverture européenne est:

$$L_A = 8^\circ \quad (\text{Est})$$

Aucune condition supplémentaire n'étant requise pour le fonctionnement correct du système, il existe un degré de liberté dans la définition des orbites. Cela provient du fait qu'il n'est pas utile d'imposer de façon absolue la chronologie du mouvement des satellites: seul importe le décalage de 12 heures entre leurs temps de passages en un point donné de la trajectoire. En conséquence, on peut par exemple choisir librement la valeur de Ω_1 : Ω_2 est alors fixé par (1), et les valeurs de M_1 et M_2 à tout instant sont définies par (2) et (3).

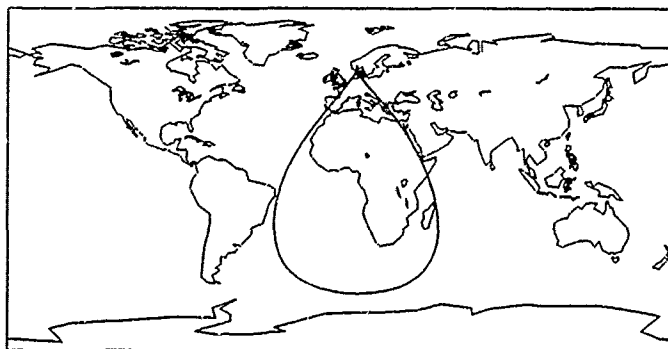


Fig. 1: Trace au sol des satellites SYCOMORES

Chaque satellite est utilisé comme relais de télécommunication pendant la période de 12 heures centrée sur l'instant de passage à l'apogée de son orbite. Les valeurs choisies pour les paramètres e , i et ω sont telles que le mouvement apparent du satellite par rapport à la Terre est alors de faible amplitude. En particulier, sa latitude et son altitude demeurent élevées durant les 12 heures de service. De ce fait, et grâce à l'utilisation de deux satellites, un des deux relais est vu en permanence en Europe sous un site nettement supérieur à celui sous lequel un géostationnaire peut être observé. Les communications sont donc moins sensibles aux obstacles, comme en zone

urbaine ou montagneuse. La figure 2 indique les limites de la région où le site de vue du satellite relais est à tout instant supérieur à 55° , ce qui est le critère choisi pour définir une utilisation satisfaisante du système.



Fig. 2: Zone de service permanent du système SYCOMORES (site $> 55^\circ$)

PROCEDURE DE MISE A POSTE

Pour mettre à poste les deux satellites relais du concept SYCOMORES, il est proposé de les injecter dans un premier temps sur l'orbite de transfert géostationnaire standard (GTO) délivrée par un lanceur Ariane 4. Il s'agit d'une orbite 200 km - 36 000 km inclinée à environ 10° sur l'Equateur. Son apogée, qui coïncide avec le noeud ascendant, appartient à l'orbite géostationnaire, si bien qu'une seule impulsion suffit en principe pour assurer la mise à poste d'un satellite sur ce type d'orbite. L'orbite GTO que nous avons considérée peut être caractérisée par les paramètres orbitaux suivants:

$$\begin{aligned} a_0 &= 24\,372 \text{ km} \\ e_0 &= 0.35 \\ i_0 &= 10^\circ \\ \omega_0 &= 180^\circ \end{aligned}$$

Quant à l'ascension droite du noeud ascendant Ω_0 , elle est fonction de l'instant de tir puisque la longitude (par rapport à la Terre) du premier passage à l'apogée est la même à l'issue de tous les lancements.

Il faut noter que ce choix de l'orbite GTO en tant qu'orbite de départ de la mise à poste résulte en premier lieu du souci d'utiliser une procédure de lancement éprouvée. Il autorise d'autre part l'injection simultanée d'un géostationnaire. Il aurait été cependant possible de définir, pour le lanceur retenu, une trajectoire de montée dédiée à la mise à poste des satellites SYCOMORES qui permette de faire de substantielles économies d'ergols: l'injection serait faite sur une orbite quasi coplanaire et sécante avec l'orbite visée, si bien que le transfert final serait fait en une seule impulsion [4].

Deux variantes sont en fait envisagées pour la mise à poste via l'orbite GTO. La première solution consiste à injecter les deux satellites en un seul lancement, de telle sorte qu'ils sont tous les deux placés sur la même orbite GTO. Chaque satellite est ensuite transféré sur sa propre orbite finale en deux ou trois arcs de poussée, au moyen d'un moteur à liquides ré-allumable. L'inconvénient d'une telle procédure est qu'elle requiert des manoeuvres a priori différentes pour les deux transferts, qui ne consomment donc pas forcément la même quantité d'ergol. En outre, la consommation totale est de toute façon supérieure à celle que nécessiterait la seconde technique de mise à poste proposée. Celle-ci consiste à réaliser l'injection préliminaire en deux lancements séparés, avec un intervalle de temps entre les tirs tel que les deux orbites GTO obtenues aient des noeuds ascendants diamétralement opposés par rapport au centre de la Terre. En effectuant les mêmes manoeuvres de transfert pour les deux satellites, on est donc assuré que leurs orbites finales présenteront elles aussi cette propriété, c'est-à-dire:

$$\Omega_2 - \Omega_1 = 180^\circ$$

ce qui est précisément ce que l'on recherche. Par conséquent, et contrairement à ce qui se produit dans le premier cas, le respect de cette contrainte n'influe en aucune manière sur la détermination des manoeuvres optimales, qui consomment la même quantité d'ergols pour les deux transferts. En contre partie, cette seconde procédure est un peu plus délicate d'un point de vue opérationnel, puisqu'il existe un seul instant de

lancement possible par jour pour le second satellite, une fois le premier satellite injecté. L'heure repérant cet instant avance de 4 minutes d'un jour à l'autre, soit la différence entre le jour solaire et la période de rotation terrestre.

Il s'agit en somme de quantifier le gain d'ergols que permet de réaliser la seconde procédure par rapport à la première, ce qui permettra de décider s'il justifie une procédure de mise à poste un peu plus contraignante.

TRAITEMENT DU PROBLEME

On souhaite déterminer les manoeuvres optimales permettant de transférer les deux satellites SYCOMORES sur leur orbite finale à partir d'une orbite GTO Ariane 4, dans les deux hypothèses d'injection (lancement individuel ou couplé). Le critère à maximiser est ici la masse utile des satellites, la masse initiale injectée sur orbite GTO étant fixée. Cela revient bien sûr à minimiser la masse d'ergol consommée par la mise à poste.

Nous avons choisi de ne pas limiter la durée des transferts. De même, nous ne nous sommes pas préoccupés de la position des satellites sur les orbites finales, ou de façon équivalente de la position de leurs traces à la surface de la Terre. On sait en effet que l'anomalie d'un satellite peut être corrigée au prix d'une consommation d'ergols minime, à condition de répartir cette correction sur une période suffisamment longue. D'autre part, aucune contrainte sur la direction et le module des impulsions, sur la visibilité des points de manoeuvres par des stations terrestres, ni sur les conditions d'éclairement solaire n'a été prise en compte.

Que la mise à poste soit couplée ou individuelle, nous avons cependant imposé à chaque transfert de respecter deux types de contraintes. D'abord, l'altitude de périégée des diverses orbites intermédiaires doit être supérieure à 200 km, afin d'éviter un freinage atmosphérique intense et pour assurer ainsi leur viabilité sur plusieurs révolutions. Ensuite, la distance de manoeuvre par rapport au centre de la Terre ne doit être ni trop petite, pour des raisons de visibilité par des stations terrestres, ni trop grande pour des raisons de bilan de liaison avec ces stations. Pour limite basse, nous avons adopté la plupart du temps la valeur 200 km (de sorte que cette contrainte est automatiquement satisfaite si la première l'est aussi). Pour limite haute, nous avons choisi la valeur arbitraire de 100 000 km, qui permet en outre de maintenir à faible niveau les éventuelles perturbations gravitationnelles de la Lune.

Pour cette première évaluation des coûts de mise à poste, le mouvement balistique des satellites a été considéré comme étant purement képlérien et les manoeuvres ont été modélisées par des impulsions, ce qui permet de définir chaque transfert par un nombre fini de paramètres. Le problème a donc pu être traité par un logiciel général d'optimisation paramétrique basé sur l'algorithme du gradient projeté. Cet algorithme permet, par opposition à ceux de type gradient conjugué, de prendre en compte directement des contraintes d'égalité ou d'inégalité, sans avoir à estimer des multiplicateurs de Lagrange ou des coefficients de pénalisation inconnus. La version que nous avons développée à l'ONERA bénéficie d'une amélioration de la technique de projection ("généralisée") qui permet de rattraper progressivement les erreurs de réalisation des contraintes. De la sorte, il devient possible d'initialiser le logiciel par un jeu de paramètres "non faisables", c'est à dire qui ne satisfont pas d'emblée toutes les contraintes [5].

L'algorithme utilisé est évidemment susceptible de converger non seulement vers l'optimum absolu, mais encore vers tout optimum local. C'est pourquoi nous avons systématiquement essayé un nombre assez important de jeux de paramètres initiaux, afin que la solution réellement optimale figure de façon quasi-certaine parmi les résultats obtenus. Cette technique a été grandement facilitée par la robustesse et la rapidité de traitement du logiciel.

Les deux procédures de mise à poste, individuelle et couplée ont été successivement étudiées, en considérant dans chacun des cas des transferts à deux et trois impulsions.

PARAMETRAGE D'UN TRANSFERT IMPULSIONNEL

Une façon naturelle de décrire un transfert entre deux orbites à N impulsions consiste à indiquer pour chacune d'elles:

- la position sur l'orbite courante du point où elle est effectuée, repérée par exemple par son anomalie vraie,
- les trois composantes de la variation de vitesse imprimée.

Si ce jeu de $4N$ paramètres définit entièrement le transfert, l'orbite finale obtenue à l'issue des N impulsions ainsi décrites n'a a priori aucune raison de coïncider avec l'orbite finale visée. Pour assurer l'égalité de ces deux orbites, il faut fixer autant de contraintes que de paramètres orbitaux imposés, c'est à dire au plus 5 dans le cas présent puisque l'on ne se préoccupe pas de la position des satellites sur les orbites finales. Dans le cas d'une orbite finale entièrement fixée (à l'anomalie près), il y a donc $4N-5$ degrés de liberté pour définir un transfert à N impulsions, soit 3 en bi-impulsionnel et 7 en tri-impulsionnel.

Plutôt que d'employer effectivement les paramètres intuitifs mentionnés ci-dessus, et d'imposer 5 contraintes d'égalité, il est préférable de choisir un jeu de 4N-5 paramètres qui les satisfasse d'emblée. Bien que le logiciel utilisé soit parfaitement capable de les prendre en compte, le traitement sera en effet d'autant plus rapide que les contraintes et les paramètres seront moins nombreux.

Que ce soit pour les transferts à deux ou trois impulsions, le jeu de paramètres effectivement choisi est basé sur le fait qu'il existe une seule orbite elliptique de paramètre donné $p=a(1-e^2)$ passant par deux points quelconques de l'espace, à condition toutefois que ceux-ci ne soient pas alignés avec le centre de la Terre.

Pour un transfert bi-impulsionnel, nous avons donc retenu comme paramètres:

- l'anomalie vraie v_0 de la première impulsion sur l'orbite initiale,
- l'anomalie vraie v_f de la seconde impulsion sur l'orbite finale,
- le paramètre p de l'orbite intermédiaire.

En réalité, ces 3 paramètres ne suffisent pas pour décrire entièrement le transfert. Si l'orbite intermédiaire est bien définie de façon unique, elle peut cependant être parcourue dans les deux sens. Il faut par conséquent ajouter en toute rigueur un quatrième paramètre discret M définissant le sens de parcours, par exemple:

- $M=1$ si l'ouverture de l'arc d'orbite est inférieure à 180° ,
- $M=-1$ sinon.

Quant au transfert tri-impulsionnel, il peut être caractérisé par les 7 paramètres continus suivants:

- l'anomalie vraie v_0 de la première impulsion sur l'orbite initiale,
- l'anomalie vraie v_f de la seconde impulsion sur l'orbite finale,
- les trois coordonnées sphériques de la seconde impulsion (distance d du centre de la Terre, ascension droite α , déclinaison δ),
- le paramètre p_1 de la première orbite de transfert,
- le paramètre p_2 de la seconde orbite de transfert,

auxquels il faut ajouter 2 paramètres discrets:

- M_1 et M_2 définissant respectivement le sens de parcours de la première et de la seconde orbite de transfert.

En définitive, il est possible de décrire un transfert bi ou tri-impulsionnel par des paramètres en nombre égal au nombre de degrés de liberté, si l'on fait abstraction des paramètres discrets définissant le sens de parcours des orbites intermédiaires. Aucune contrainte n'est alors nécessaire pour assurer la coïncidence entre l'orbite obtenue à l'issue des manoeuvres et l'orbite finale visée. Le paramétrage indiqué ci-dessus n'est cependant pas parfait dans la mesure où il n'est pas valide lorsque deux impulsions successives du transfert sont alignées avec le centre de la Terre. En ce qui concerne la mise à poste des satellites SYCOMORES, il semble toutefois que la solution optimale ne corresponde jamais à cette situation.

MISE A POSTE INDIVIDUELLE

On ne se préoccupe dans ce cas que de la mise à poste du premier satellite, puisque le transfert du second sera identique en manoeuvres et en coût si l'on choisit judicieusement l'instant du deuxième lancement. Rappelons qu'aucune contrainte n'est imposée à l'ascension droite Ω_1 du noeud ascendant de l'orbite finale du premier satellite, dont seulement 4 paramètres sont fixés. Avec le formalisme adopté ici, on considérera que l'angle $\Delta\varphi = \Omega_1 - \Omega_0$ entre les lignes des noeuds initiale et finale du transfert est un paramètre supplémentaire qu'il faut déterminer. Il y a donc au total 4 paramètres continus à optimiser en bi-impulsionnel, et 8 en tri-impulsionnel.

On souhaite maximiser la masse finale m_f du satellite après mise à poste, sa masse initiale m_0 étant fixée. Ces deux grandeurs sont liées par l'équation:

$$\frac{m_f}{m_0} = e^{-\Delta V/W}$$

où:

- W est la vitesse d'éjection des moteurs de mise à poste,
- ΔV est la "variation de vitesse caractéristique" associée au transfert (somme des normes des variations de vitesse du satellite produites par les impulsions).

Maximiser m_f est donc équivalent à minimiser ΔV , grandeur qui a le mérite d'être indépendante des performances du moteur, représentées ici par W . C'est donc la variation de vitesse caractéristique ΔV qui est classiquement choisie comme critère à minimiser.

La contrainte imposant à l'altitude de périhélie des diverses orbites intermédiaires du transfert d'être supérieure à 200 km est prise en compte pour les manoeuvres à deux comme à trois impulsions. Par contre, la limitation à 100 000 km de la distance entre le centre de la Terre et les points de manoeuvre n'a de raison d'être que dans le cas du transfert tri-impulsionnel. Elle est en effet nécessairement satisfaite en bi-impulsionnel, compte tenu de la nature des orbites initiale et finale du transfert.

En pratique, le transfert optimal a été déterminé de deux façons différentes. La première technique employée a consisté à ne pas traiter $\Delta\Omega$ comme un paramètre à optimiser mais comme une donnée: nous avons effectué toute une série d'optimisations pour des valeurs de $\Delta\Omega$ réparties entre -180° et 180° . La valeur optimale de $\Delta\Omega$ ainsi que celle du coût correspondant sont ensuite identifiées graphiquement. L'intérêt de cette méthode lourde et peu précise est qu'elle rend fort improbable la possibilité que la solution finalement obtenue ne soit pas l'optimum global du problème. Et surtout, les résultats de ce balayage permettront de résoudre aussi le problème de la mise à poste couplée. Par ailleurs nous avons également effectué une optimisation complète (à $\Delta\Omega$ libre) pour confirmer et affiner la solution fournie par la première méthode.

Transfert bi-impulsionnel

La technique de balayage permet de tracer l'évolution du coût du transfert optimal en fonction de $\Delta\Omega$ (figure 3). En réalité, quelque soit la valeur de ce paramètre, le logiciel d'optimisation converge toujours vers plusieurs solutions (généralement deux), selon l'initialisation qui lui a été fournie. Seul le coût de la plus économique d'entre elles a été représenté.

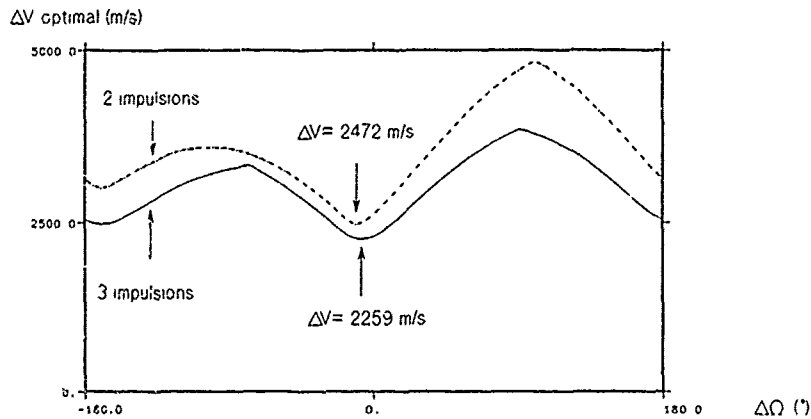


Fig. 3: Coût des transferts individuels optimaux

L'existence d'optima multiples explique la présence de deux points anguleux sur cette courbe. En effet, les diverses solutions obtenues pour une valeur donnée de $\Delta\Omega$ appartiennent à autant de familles d'optima locaux dont les paramètres et le coût sont des fonctions continues et dérivables de $\Delta\Omega$. Or suivant la valeur de ce paramètre, la solution optimale globale n'appartient pas toujours à la même famille de "candidats à l'optimalité". Les valeurs de $\Delta\Omega$ pour lesquelles se produisent les transitions correspondent à une discontinuité de pente de la courbe de coût, et à une discontinuité des paramètres optimaux.

D'autre part, on peut constater que, lorsque $\Delta\Omega$ varie, il existe deux minima nettement marqués pour les valeurs $\Delta\Omega \approx -9^\circ$ et $\Delta\Omega \approx -169^\circ$. La première conduit au coût le plus faible, soit $\Delta V \approx 2470$ m/s. Ces résultats sont entièrement confirmés par l'optimisation complète qui fournit la description précise du transfert, visualisé sur la figure 4:

$\Delta\Omega \approx -9.1^\circ$		
$v_0 = 170.4^\circ$	$\Delta V = 2472$ m/s	1 ^{ère} impulsion: 2330 m/s
$v_f = 237.7^\circ$		2 ^{ème} impulsion: 92 m/s
$p \approx 39150$ km		
$M = 1$		

La première impulsion représente 96% du ΔV total du transfert. Elle est réalisée au voisinage de l'apogée de l'orbite GTO ($v_0 = 170.4^\circ$), où la vitesse du satellite est la plus faible. Il est alors particulièrement facile de modifier son orientation et de faire passer le satellite sur une orbite intermédiaire presque coplanaire avec l'orbite finale visée. Au point d'intersection de ces deux orbites, la seconde impulsion effectue une correction minimale pour compléter la mise à poste.

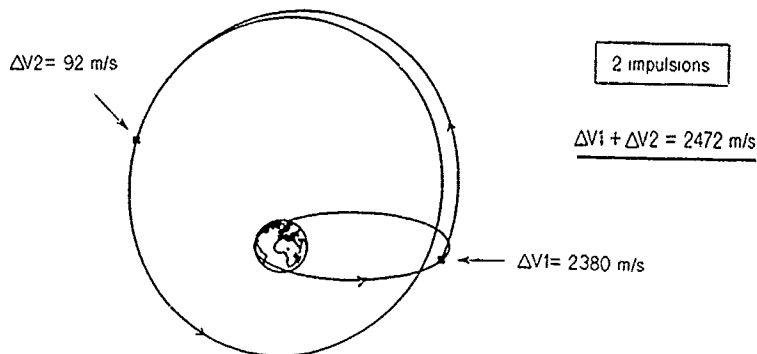


Fig. 4: Transfert bi-impulsionnel optimal (mise à poste individuelle)

Remarquons que la valeur $\Delta\Omega = -9.1^\circ$ permet d'amener l'apogée de l'orbite GTO à proximité du plan de l'orbite finale. C'est la configuration la plus favorable pour réaliser le changement de plan, qui est la partie la plus coûteuse du transfert. Cette configuration peut naturellement être obtenue pour deux valeurs de $\Delta\Omega$ distantes de 180° . Cela explique l'existence du second optimum pour $\Delta\Omega = -169^\circ$. Son coût est cependant plus élevé puisque l'inclinaison mutuelle des orbites est alors de 70° environ, au lieu de 50° dans le cas précédent.

Pour la solution optimale, l'altitude de périégée de l'orbite de transfert est d'approximativement 23 000 km. Il ne se pose donc aucun problème de perturbation par l'atmosphère. De plus, l'observation des points de manoeuvre par des stations terrestres est aisée. L'altitude de périégée est également supérieure à 200 km pour toutes les valeurs de $\Delta\Omega$ autres que -9.1° .

Transfert tri-impulsionnel

La courbe d'évolution du coût optimal en fonction de $\Delta\Omega$ est comparable à celle obtenue pour le transfert bi-impulsionnel (figure 3). Comme précédemment, il existe en fait plusieurs familles de solutions. L'optimum global appartient à l'une ou à l'autre selon la valeur de $\Delta\Omega$. Il existe en conséquence 2 points anguleux sur la courbe, correspondant à une discontinuité des paramètres. Il est intéressant de noter le transfert tri-impulsionnel consomme systématiquement moins d'ergol que le transfert bi-impulsionnel, quelque soit la valeur de $\Delta\Omega$. Le minimum du coût optimal lorsqu'on fait varier $\Delta\Omega$ est obtenu pour $\Delta\Omega \approx -7^\circ$. L'optimisation directe des 8 paramètres de la mise à poste confirme ce résultat et précise les caractéristiques du transfert optimal correspondant:

$\Delta\Omega = -6.9^\circ$		
$v_0 = 4.6^\circ$		
$v_f = 243.4^\circ$		
$\alpha = -6.1^\circ$		
$\delta = -1.1^\circ$		
$d = 100\ 000\ \text{km}$	$\Delta V = 2259\ \text{m/s}$	1ère impulsion: 442 m/s
$p_1 = 12\ 390\ \text{km}$		2ème impulsion: 1148 m/s
$p_2 = 56\ 230\ \text{km}$		3ème impulsion: 669 m/s
$M_1 = M_2 = 1$		

La première impulsion est effectuée à proximité du périégée de l'orbite GTO ($v_0 = 4.6^\circ$). Elle produit essentiellement une montée de l'apogée jusqu'à une distance voisine de la valeur maximale permise pour les manoeuvres (100 000 km), sans modifier les autres caractéristiques orbitales. En particulier, le plan de l'orbite reste inchangé. Les deux manoeuvres suivantes sont tout à fait comparables à celles du transfert bi-impulsionnel. La seconde impulsion, réalisée au voisinage de l'apogée de la première orbite de transfert, effectue le changement de plan; elle représente un peu plus de la moitié du coût total. La troisième impulsion assure la mise à poste finale au point d'intersection de la seconde orbite de transfert avec l'orbite visée (figure 5).

En éloignant l'apogée de l'orbite intermédiaire, la première manoeuvre permet de réduire nettement la vitesse du satellite en ce point, ce qui facilite grandement le basculement de plan réalisé par la seconde impulsion. Son coût a donc pu être réduit de moitié, de 2380 m/s à 1148 M/s. Malgré l'ajout d'une manoeuvre préliminaire et l'augmentation très nette du ΔV de la dernière impulsion, cette procédure reste avantageuse par rapport au bi-impulsionnel. Le gain global est de 213 m/s, soit l'équivalent de quatre années du maintien à poste d'un satellite SYCOMORES [3].

Quelque soit la valeur de $\Delta\Omega$, les orbites intermédiaires ont toujours une altitude de périégée supérieure à 200 km, comme dans le cas du transfert bi-impulsionnel. La première ne l'est cependant que de 3 km pour la solution optimale. La contrainte de distance maximale de manoeuvre est par contre systématiquement active. La suppression de cette contrainte s'accompagnerait donc de l'accroissement du paramètre d . Dans le cas du transfert optimal, un essai d'optimisation a été fait en portant à 1 000 000 km la valeur maximale imposée à ce paramètre: comme auparavant cette limite a été atteinte. Il semblerait donc que la solution optimale naturelle consiste à faire passer le satellite sur une orbite parabolique, à réaliser le changement de plan à l'infini pour un coût nul, et à revenir couper l'orbite finale visée sur un second arc de parabole. On retrouve là le transfert optimal "bi-parabolique" déjà connu pour des transferts plus simples [1].

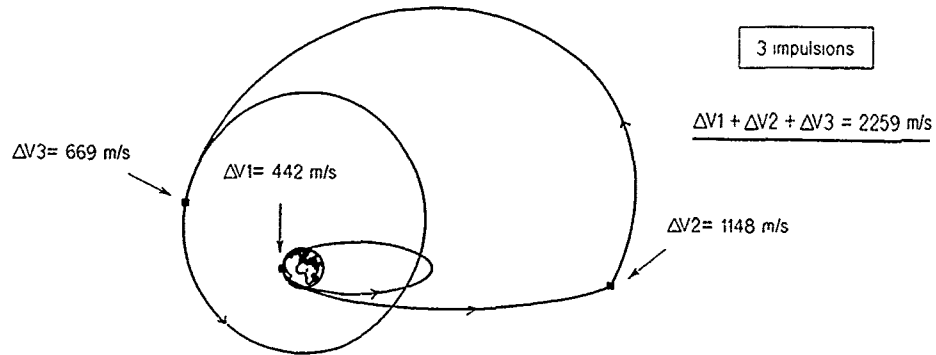


Fig. 5: Transfert tri-impulsionnel optimal (mise à poste individuelle)

Enfin, on peut remarquer que pour ce transfert tri-impulsionnel, une impulsion assez importante (la première) est délivrée au voisinage du périégée de l'orbite GTO, ce qui pourrait s'avérer gênant sur le plan opérationnel (difficulté d'établir une liaison directe avec des stations sol). C'est pourquoi nous avons refait un calcul d'optimisation en imposant une altitude minimale de manoeuvre de 2000 km. On constate que la perte de performance induite se limite à 53 m/s de vitesse caractéristique supplémentaire.

MISE A POSTE COUPLEE

Les deux satellites sont injectés simultanément sur une même orbite GTO, à partir de laquelle ils sont ensuite transférés individuellement vers leurs orbites finales respectives. Nous avons vu qu'il existe un degré de liberté dans le choix de leurs $2 \times 5 = 10$ paramètres orbitaux. La seule contrainte imposée aux ascensions droites Ω_1 et Ω_2 des noeuds ascendants de la première et de la seconde orbite est de vérifier:

$$\Omega_2 = \Omega_1 + 180^\circ$$

Comme auparavant, on considérera donc $\Delta\Omega = \Omega_1 - \Omega_0$ comme un paramètre supplémentaire du transfert à déterminer. Par contre, la configuration de la seconde orbite relativement à l'orbite GTO, définie par $\Delta\Omega' = \Omega_2 - \Omega_0$, sera alors imposée puisque:

$$\Delta\Omega' = \Delta\Omega + 180^\circ$$

Il s'agit donc d'optimiser $\Delta\Omega$ et le jeu de paramètres définissant chaque transfert, soit au total 7 paramètres continus en bi-impulsionnel et 15 en tri-impulsionnel. Le critère que l'on souhaite maximiser est toujours la masse finale m_f de chaque satellite après mise à poste, la masse totale $m_{01} + m_{02}$ placée sur orbite GTO étant fixée. Les satellites SYCOMORES remplissant une fonction identique, on impose naturellement que m_f soit la même pour les deux. Dans ces conditions:

$$\frac{m_f}{m_{01}} = e^{-\Delta V_1/W} \quad \text{et} \quad \frac{m_f}{m_{02}} = e^{-\Delta V_2/W}$$

où: - W est la vitesse d'éjection des moteurs de mise à poste,
- ΔV_1 et ΔV_2 sont les coûts en vitesse caractéristique des deux transferts.

$$\text{Par conséquent} \quad \frac{m_{01} + m_{02}}{m_f} = e^{\frac{\Delta V_1}{W}} + e^{\frac{\Delta V_2}{W}}$$

On peut définir une variation de vitesse caractéristique fictive ΔV correspondant à un transfert unique conduisant aux mêmes variations de masse:

$$\frac{m_{01} + m_{02}}{2 m_f} = e^{\frac{\Delta V}{W}} \quad \text{donc} \quad \Delta V = W \text{ Log} \frac{e^{\frac{\Delta V_1}{W}} + e^{\frac{\Delta V_2}{W}}}{2}$$

Maximiser m_f est équivalent à minimiser ΔV , qui est indépendant de la masse $m_{01}+m_{02}$ injectée sur GTO. C'est donc ΔV que nous avons choisi comme indice de coût. Il est intéressant de noter que la solution optimale dépend (un peu) de la vitesse d'éjection W , contrairement au cas du transfert individuel.

Avant d'effectuer l'optimisation complète des 7 ou 15 paramètres du transfert, nous avons traité le problème par simple exploitation des courbes donnant le coût optimal d'un transfert unique en fonction de $\Delta\Omega$, obtenues précédemment dans le cas de la mise à poste individuelle. En effet, pour une valeur donnée du paramètre $\Delta\Omega$, ces courbes donnent bien sûr le coût ΔV_1 du premier transfert, mais aussi le coût ΔV_2 du second, puisqu'il s'agit de la valeur correspondant à $\Delta\Omega+180^\circ$. Il est ainsi possible de calculer le coût global ΔV du transfert couplé pour toute valeur de $\Delta\Omega$. Nous avons donc représenté graphiquement l'évolution de ΔV en fonction de $\Delta\Omega$ dans le cas des manoeuvres bi et tri-impulsionnelles (figure 6). Le tracé aurait pu être fait pour des valeurs comprises entre -90° et $+90^\circ$ seulement, puisque la périodicité en $\Delta\Omega$ du problème de la mise à poste couplée est de 180° . La vitesse d'éjection a été fixée à 2800 m/s.

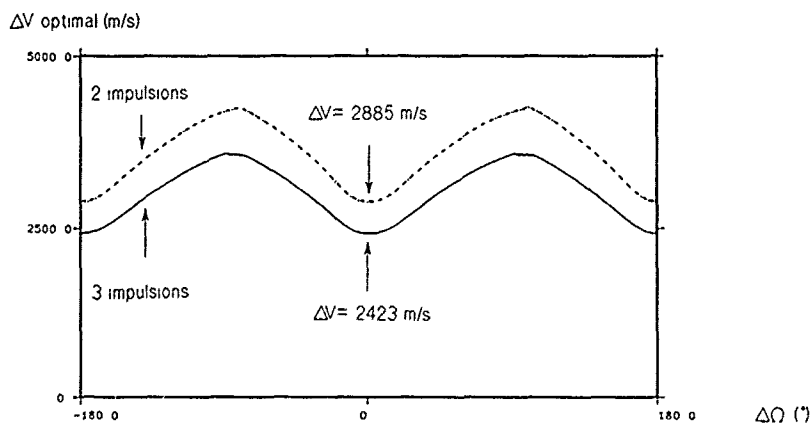


Fig. 6: Coût des transferts couplés optimaux

Les manoeuvres tri-impulsionnelles sont bien sûr plus économiques que celles à deux impulsions quelle que soit la valeur de $\Delta\Omega$, puisque c'était déjà le cas pour la mise à poste individuelle. Qu'il s'agisse des manoeuvres à deux ou trois impulsions, on constate l'existence d'un seul optimum pour une valeur de $\Delta\Omega$ voisine de 0° . L'optimisation directe de la mise à poste confirme les résultats obtenus et fournit les valeurs exactes des variations de vitesse caractéristique pour chaque transfert:

bi-impulsionnel:

$$\begin{aligned} \Delta\Omega &= 1.3^\circ \\ \Delta V &= 2885 \text{ m/s} \\ \Delta V_1 &= 2642 \text{ m/s} \\ \Delta V_2 &= 2885 \text{ m/s} \end{aligned}$$

tri-impulsionnel:

$$\begin{aligned} \Delta\Omega &= 0.6^\circ \\ \Delta V &= 2423 \text{ m/s} \\ \Delta V_1 &= 2306 \text{ m/s} \\ \Delta V_2 &= 2535 \text{ m/s} \end{aligned}$$

Comme prévu, les deux transferts de chaque mise à poste diffèrent par le coût (et donc aussi par les caractéristiques des impulsions). La différence de ΔV se chiffre à environ 230 m/s, en bi comme en tri-impulsionnel. Cela se traduit par un écart de 9% entre les masses initiales des satellites, juste après l'injection sur GTO. Il faut noter que dans l'hypothèse vraisemblable d'une structure identique pour les deux satellites, le réservoir d'ergols de l'un d'entre eux est par conséquent partiellement rempli au départ.

Le couplage des mises à poste conduit à une augmentation du coût global de 413 m/s pour le transfert bi-impulsionnel. Cette perte de performance très nette fait perdre dans ce cas tout intérêt à la procédure de lancement unique. L'augmentation du coût est plus raisonnable pour le transfert à trois impulsions: elle est de 164 m/s. Cela ne semble cependant pas suffisant pour faire de la mise à poste couplée une solution intéressante, en raison de la valeur déjà très élevée du coût nominal (2259 m/s).

CONCLUSION

Le problème de la détermination des manoeuvres bi et tri-impulsionnelles à consommation d'ergols minimale permettant de mettre à poste les deux satellites du concept SYCOMORES a été traité numériquement par une méthode d'optimisation paramétrique par gradient projeté généralisé mise au point à l'ONERA. Cet algorithme s'est montré d'un emploi très satisfaisant par son aptitude à converger rapidement vers une solution localement optimale quelles que soient les manoeuvres proposées pour l'initialiser. Grâce à cette robustesse, il a été possible d'essayer systématiquement un grand nombre d'initialisations, la meilleure solution ainsi obtenue étant vraisemblablement l'optimum global du problème. D'autre part, la faculté de la méthode de traiter efficacement des contraintes s'est avérée utile pour optimiser les transferts tri-impulsionnels, pour lesquels il est indispensable de limiter la distance maximale de l'impulsion intermédiaire.

Il est apparu que la procédure consistant à injecter simultanément les deux satellites sur une même orbite de transfert géostationnaire à la suite d'un lancement unique conduit à une consommation d'ergols différente pour les deux transferts ultérieurs. Elle est dans tous les cas supérieure à celle des manoeuvres qu'il est possible de réaliser en déployant les satellites en deux lancements distincts, faits à des instants séparés par une durée judicieusement choisie. La différence globale, qui se chiffre à 164 m/s de vitesse caractéristique dans le cas le plus favorable (tri-impulsionnel), semble trop importante pour faire de la mise à poste couplée une solution acceptable, en raison du niveau déjà très élevé de la consommation requise dans le cas de la technique des lancements séparés. La variation de vitesse caractéristique minimale, qui est alors la même pour les deux satellites, est en effet de 2472 m/s pour les manoeuvres à deux impulsions, et de 2259 m/s pour celles à trois impulsions. Cette dernière valeur dépend en fait de la distance maximale autorisée pour réaliser l'impulsion intermédiaire, la consommation étant bien sûr une fonction décroissante de ce paramètre.

Le choix des transferts tri-impulsionnels paraît justifié par l'économie d'ergols qu'ils offrent par rapport aux manoeuvres à deux impulsions. Cette économie, qui correspond à quatre années de maintien à poste des satellites, compense avantageusement les difficultés opérationnelles posées par la réalisation de la première des trois impulsions. Le problème provient de ce qu'elle est faite au voisinage du périée de l'orbite de transfert géostationnaire. L'altitude du satellite est alors proche de 200 km, et il est par conséquent délicat d'assurer à ce moment des communications avec une station de contrôle terrestre. La situation peut toutefois être améliorée en imposant une distance minimale de manoeuvre supérieure à 200 km. Si l'on porte cette limite inférieure à 2000 km, on ne désoptimise le transfert que de 53 m/s.

REFERENCES

- [1] C. Marchal
"Transferts optimaux entre orbites elliptiques (durée indifférente)",
Publication ONERA N° 120, 1967.
- [2] J.P. Marec
"Transferts optimaux entre orbites elliptiques proches",
Publication ONERA N° 121, 1967.
- [3] A.M. Mainquy, J.F. Dulck, V.N. Nguyen, J. Bouchard
"Sycomores constellations: positioning and station keeping",
IAF Paper 89-399, October 1989.
- [4] J. Bouchard, D. Flament, V.N. Nguyen
"Etudes de constellations de satellites pour la navigation",
Rapport technique ONERA 17/3605 SY, Février 1989.
- [5] C. Aumasson, P. Landiech
"Méthode itérative de type gradient projeté généralisé pour l'optimisation paramétrique et fonctionnelle de systèmes dynamiques soumis à des contraintes",
Note technique ONERA 1988-9, Février 1989.

NONCOPLANAR ORBIT TRANSFER OPTIMIZATION FOR AN AEROASSISTED SORTIE VEHICLE

H.A. Karasopoulos and R.B. Norris
Wright Research and Development Center, WRDC/FING
Wright-Patterson AFB, Ohio 45433-6553, USA

SUMMARY

Noncoplanar orbital plane change trajectories for an aeroassisted sortie vehicle (ASV) from a 220 nautical mile circular orbit at 28.5 degrees inclination to a 150 nautical mile circular polar orbit were optimized, subject to nose stagnation temperature constraints. Both synergetic and two-impulse-deorbit aeroassist trajectories were successfully optimized. The baseline aeroassisted sortie vehicle, a double-delta lifting body, had a maximum hypersonic L/D of 3.4. The ASV was powered by a liquid hydrogen/oxygen rocket engine. The optimized synergetic plane change trajectory resulted in the delivery of more pounds of payload to polar orbit than the two-impulse-deorbit aeroassist trajectory. The propulsive ΔV expended by the ASV during the baseline trajectory was less than half the propulsive ΔV required by a two-impulse, all-propulsive orbital transfer maneuver. By adding propellant drop tanks of approximately half of the gross weight of the ASV, the payload weight to polar orbit was almost tripled with an optimal two-impulse-deorbit aeroassist trajectory. This trajectory provided more payload to the final orbit for this ASV configuration than a synergetic maneuver preceded by an exoatmospheric propulsive plane change. To fully utilize an L/D capability greater than 3, the ASV must be able to sustain maximum nose stagnation temperatures up to 4500 degrees Fahrenheit.

1.0 INTRODUCTION

Since the early sixties, synergetic or aeroassisted orbital plane change maneuvers have been studied by a number of people and independent organizations, including the USAF Flight Dynamics Laboratory. Today, orbital changes from low earth orbit (LEO) to high earth orbits (HEO), particularly geosynchronous earth orbit (GEO) are accomplished by all-propulsive upper stages such as the Centaur and the Inertial Upper Stage (IUS), and rocket motors attached to the payload such as a propulsion assist module (PAM). All velocity changes and orbital inclination changes required to transfer to the required orbit are accomplished by a rocket engine burn. All of these upper stages are expendable.

Since the early 1970's, NASA has investigated reusable aeroconfigured upper stage concepts that use aerodynamic forces during a pass through the upper atmosphere to decrease the velocity and, depending upon the vehicle configuration (lifting shapes), perform small plane changes during transfer from a high earth orbit to low earth orbit. The maximum aerodynamic lift-to-drag ratio (L/D) of these concepts ranged from 0.25 for ballistic shapes to 1.5 for biconic shapes. These studies showed that by utilizing aerodynamic drag and lift to decrease velocity and change the orbital plane, significant reductions in propellant and tankage weight could be transferred into increased payload capability. This orbital transfer technique is called aerobraking. In 1980, two NASA studies [1,2] determined that ballistic aeroassisted orbital transfer vehicle (AOTV) concepts could realize a 40% to 50% increase in the payload delivered to geosynchronous earth orbit by employing aerobraking.

In 1983, the Air Force sponsored a study [3] to evaluate reusable orbital transfer vehicle concepts configured for maximum L/D ratios from 2 to 2.5. These lifting body concepts used rocket propulsion and aerodynamic lift and drag to perform orbital plane changes greater than 40 degrees. By using the synergetic plane change technique, these high L/D concepts could perform large plane changes with significant reductions in the propulsive energy (total velocity increment, ΔV) compared to all-propulsive orbital transfer vehicles (see Figure 1). Although these high L/D concepts could not carry as much payload to high earth orbits as the ballistic AOTVs, they could execute large plane changes and return to a base in low earth orbit.

2.0 CONFIGURATION

The aerodynamic configuration of the aeroassisted sortie vehicle (ASV) is designed to fly through the Mach 20 to 25 flight regime at a maximum lift-to-drag ratio (L/D) greater than 3, allowing the vehicle to perform aeroassisted orbital plane changes greater than 50 degrees. The ability to perform such a large orbital plane change gives the aeroassisted sortie vehicle great potential to perform a variety of atmospheric and exoatmospheric applications such as the deployment, recovery, or even servicing of LEO satellites with orbit inclination angles ranging from less than 28.5 degrees to more than 90 degrees. It should also provide the aeroassisted sortie vehicle with the ability to perform successive orbital overflights over a particular area of interest on the Earth's surface. Due to its high L/D, the ASV should also have a great downrange and crossrange potential upon atmospheric descent to a landing at a specific site on earth.

The vehicle configuration, shown in Figure 2, is a classical double-delta lifting body featuring small leading edges for low inviscid drag, small outboard strakes and a

full-span body flap for extra lift and longitudinal stability, and twin outboard vertical fins for directional stability. The body flap is divided into a center flap for extra trim control and right and left outboard flaps for integrated pitch and roll control. Each vertical fin has a trailing edge rudder for directional control.

Additional concept features shown in Figure 2 include an advanced liquid hydrogen and oxygen rocket engine and landing gear. The rocket engine has a vacuum thrust of 30,000 pounds and a corresponding vacuum Isp of 470 seconds. A passive thermal protection material is utilized to allow the ASV to sustain stagnation radiation equilibrium temperatures up to 4500 degrees Fahrenheit (F).

3.0 AERODYNAMICS

The longitudinal aerodynamic characteristics of the sortie vehicle configuration were estimated with the hypersonic aerodynamic methodologies in the Mark IV Supersonic-Hypersonic Arbitrary-Body Program [4]. Aerodynamic coefficients were computed at Mach numbers of 15, 20, 25, and 27, for altitudes of 150,000, 175,000, 200,000, 250,000, and 270,000 feet. At each flight condition, aerodynamics were computed at angles of attack from 0 to 40 degrees in increments of 5 degrees.

Figure 3 shows longitudinal stability and control surface effectiveness at Mach 20 for an altitude of 200,000 (200K) feet. The sortie vehicle is slightly unstable at low angles of attack, and is stable at the higher angles of attack where the vehicle will fly in the trimmed ($C_m = 0$) conditions. The stability and control characteristics are similar at all the other flight conditions.

The characteristics of trimmed lift-to-drag ratio at Mach 20 and 25 are shown in Figure 4. At Mach 20, the maximum L/D decreases from 3.4 at 200K feet to approximately 2.4 at 250K feet (Figure 4a), primarily due to the increase in laminar skin friction drag coefficient which is greater than 50% of the total drag coefficient at altitudes near 250K feet and above. At Mach 25 and 270K feet, the maximum L/D drops below 2 (Figure 4b).

4.0 NONCOPLANAR AEROASSISTED ORBIT TRANSFER

Several past studies [5,6] of aeroassisted noncoplanar orbital transfer have shown a variety of trajectories that are optimal for certain conditions. Figure 5, from Hanson [5], presents three major classes of aeroassist trajectories that can be the optimal minimum fuel mode depending on the characteristics of the flight vehicle, and on the final orbit sought.

The first of these modes is the one-impulse-deorbit aeroassist trajectory, which is named the aeroassist(1), for brevity. A flight vehicle initiates this trajectory with a single deorbit boost that may be applied out of the orbit plane. This causes the vehicle to enter the planet atmosphere where it maneuvers out of its orbital plane through execution of a banked glide. The vehicle then applies thrust to complete the plane change and to raise the apoapsis to the desired final orbital altitude. The trajectory ends with a circularizing thrust phase.

The second class of optimal aeroassisted orbital transfer trajectories is the two-impulse-deorbit aeroassist trajectory, or aeroassist(2). To initiate this trajectory, the vehicle performs a transfer boost to raise its apoapsis. A second boost is then performed at apoapsis to lower the periapsis, causing the vehicle to enter the planetary atmosphere. The remainder of the trajectory is similar to that of the aeroassist(1) trajectory.

The third mode of aeroassist transfer is the aeroparabolic trajectory. In theory, the vehicle boosts into a parabolic trajectory and travels nearly an infinite distance where it thrusts to change its orbit plane. The vehicle then returns to the atmosphere, utilizing aerodynamic drag to decelerate and to reach the desired final apoapsis. At this point, the vehicle performs a small thrust to circularize the orbit. Reducing the maximum altitude of the aeroparabolic trajectory to more realistic values will eventually drive the trajectory towards the aeroassist(2), where it becomes optimal to perform a portion of the plane change within the atmosphere. Practical limits on the duration of a manned orbit transfer for a vehicle like the ASV would forbid the use of an aeroparabolic trajectory. This aeroassist trajectory was therefore not further investigated in this study.

In his study of optimal aeroassisted orbit transfer, Hanson [5] compares the optimality of a number of trajectory classes for noncoplanar transfer between circular orbits. Some results of his work are presented in Figure 6. Hanson [5], and Vinh and Hanson [6] (in earlier work on optimal aeroassisted return from HEO with plane change) found that the optimal transfer mode depends on the maximum lift-to-drag ratio of the flight vehicle, the ratio of final orbital radius to the radius of the sensible atmosphere, the desired plane change angle, and the ratio of initial to final circular orbit radius (n). In Figure 6, $\Delta V/V_{2g}$ is the ratio of total velocity increment required by the vehicle to perform the plane change and the final circular orbit velocity.

For the baseline mission examined in this study, an orbital transfer with a 61.5 degree plane change, the value of n is 1.02. Maximum L/D for the sortie vehicle is 3.4. Figures 6a, 6b, and 6c present results for flight vehicles with maximum lift-to-drag

ratios of 1.0, 1.5, and 2.0, respectively, and for plane change angles ranging from 0 to 50 degrees. Although ΔV requirements for the ASV cannot be deduced from these plots without unreasonable extrapolation, a general trend can be observed. As L/D increases, the differences in optimality between three of the modes decreases. These three modes are the one and two-impulse-deorbit aeroassist maneuvers and the synergetic maneuver, where all the plane change is accomplished in the atmosphere. Liberal extrapolation of these curves to a plane change of 61.5 degrees and an L/D of 3.4 would make all three trajectory classes candidates for the optimal orbital transfer mode.

In Hanson's analysis, plane change can be accomplished during any of the thrust phases for both the aeroassist(1) and aeroassist(2) trajectories. It was also assumed that the next-to-last thrust phase applied in both the aeroassist(1) and aeroassist(2) trajectories occurred outside the atmosphere. The aeroassist(2) maneuver examined in the study that follows allows for plane change throughout the trajectory (with the exception of the small final recircularization boost) and the boost to final apoapsis which occurs within the atmosphere.

The synergetic orbital plane change trajectory is actually a special case of the aeroassist(1) trajectory, where all the plane change is accomplished within the atmosphere. Preliminary findings for the applications investigated in this report indicate that there was no significant advantage to performing the required plane change with the aeroassist(1) trajectory compared to the synergetic maneuver. Because the aeroassist(1) trajectory is exponentially more time consuming to numerically optimize than the synergetic maneuver (without promise of being more optimal for the baseline trajectory examined), the aeroassist(1) mode was not further examined in this effort.

In the literature, two restricted types of synergetic orbital plane change trajectories are often studied. These are the aerocruise and the aeroglide synergetic maneuvers. Plane change is performed in an aerocruise trajectory by a constant altitude banked turn with thrust throttled during the turn to equal drag. The aeroglide synergetic maneuver differs from the aerocruise in that propulsion is not applied until the entire plane change has been completed. The synergetic maneuver studied here neither employs the aerocruise restrictions of a constant altitude turn and a throttleable rocket engine, nor the aeroglide assumption that all plane change is exclusively performed aerodynamically.

A complete background of general aeroassisted orbit transfer can be found in two excellent survey papers. Walberg [7] provides an extensive review of past work on aeroassist maneuvers, missions, vehicles, and related technology. The second survey paper, Lichtenberg [8], presents a comprehensive review of the optimization of minimum fuel aerocruise orbital transfer between coplanar and noncoplanar orbits.

5.0 ANALYSIS

5.1 Numerical Trajectory Simulation and Optimization Methods

The Optimal Trajectories by Implicit Simulation (OTIS) computer program [9,10] was used to compute all trajectory results presented in this paper. OTIS is a three degree-of-freedom trajectory simulation computer program that employs nonlinear programming optimization routines to provide the code with an advanced trajectory optimization capability. OTIS can simulate and optimize the trajectories of a large variety of flight vehicles ranging from subsonic aircraft to hypersonic vehicles and spacecraft. OTIS contains options to incorporate a general spherical or oblate, rotating or non-rotating, planet model. A number of gravitational and atmospheric models are also available to the user.

This program differs from traditional (explicit) numerical trajectory optimization techniques in that it treats the equations of motion as constraints and basically iterates to find the optimal trajectory which satisfies these and other constraints, including boundary conditions. An implicit optimization procedure based on Hermite interpolation is used by OTIS to convert an optimal flight control problem to a nonlinear programming problem. OTIS then employs a nonlinear programming package called NPSOL to compute the optimal solution. NPSOL, developed by the Systems Optimization Laboratory at Stanford University, utilizes sequential quadratic programming methods. A thorough discussion of the formulation of the OTIS computer program and of the implicit optimization techniques utilized are presented in References 9 and 10.

Many past studies of the performance of the synergetic, or aeroassisted orbital plane change maneuver have assumed constant L/D, and in some cases, constant angle of attack and/or bank angle. The realistic variance of lift-to-drag ratio with altitude can be quite large as can be observed in Figure 4. In a recent study by Mease and others [11], it was found that constant angle of attack does not generally produce optimal results even for the restricted case of constant altitude, aerocruise, synergetic plane change. A number of studies [12, 13, 14, 15] of aerocruise, synergetic maneuver optimization have allowed angle of attack and bank angle to vary along the trajectory. However, some of these studies are based on restricted optimization of one or more prescribed functions for the control angles. Bursey and others [12] found optimal aerocruise and aeroglide synergetic trajectories based on angle of attack and bank angle polynomials of degree three or less for each major phase

of the trajectory. OTIS avoids these potential problems by utilizing quintic spline interpolations of the control angles at a large number of nodes within each phase of the trajectory. This feature effectively removes control angle restrictions inherent in many numerical optimization methods, allowing for complete freedom of the form of the optimized control schedules.

Due to limited computer resources, numerical optimization of the entire synergetic trajectory was not performed. To save computation time, an initial deorbit velocity increment of 316.6 feet per second was assumed, providing the ASV with an entry flight path angle of approximately -63 degrees and a relative velocity of approximately 24,683 feet per second at an altitude of 300K feet. From these initial conditions, the trajectory was simulated and optimized. Propulsion applied within the atmosphere was modeled with finite thrust times and atmospheric pressure losses. The final ΔV , applied to circularize the orbit of the aeroassisted sortie vehicle at an apogee of 150 nautical miles, was modeled as an impulsive burn and was determined by the optimization. The synergetic orbital plane change maneuver was therefore globally optimized from the initial condition prescribed at 300K feet to the final 150 nautical mile circular orbit (polar) conditions.

The entire trajectory of the two-impulse-deorbit aeroassist maneuver was globally optimized. Simulation commenced from the initial conditions of a 220 nautical mile circular orbit with a 28.5 degree inclination and ended at the final conditions of a 150 nautical mile circular polar orbit. The first three thrust phases were modeled with finite thrust times and optimized by the OTIS computer program. Thrust applied within the atmosphere was corrected for atmospheric pressure loss. The final velocity increment, applied to circularize the ASV at an apogee altitude of 150 nautical miles, was modeled as an impulsive thrust; its magnitude was determined by the optimization. To the best of the author's knowledge, no previous numerical, global optimization of the entire two-impulse-deorbit aeroassisted orbit transfer has previously been completed.

Initial and final conditions for both types of aeroassisted trajectories were specified in terms of flight path angle, inertial velocity, and altitude. Initial longitude was arbitrarily set to zero. Initial latitude and heading angle, however, were left free to be optimized for each trajectory. This ability to optimize the placement of the sortie vehicle within its orbit at the commencement of the maneuver proved to be valuable. The initial orbit for all of the trajectories studied was chosen to be a 220 nautical mile circular orbit with an inclination angle of 28.5 degrees. The final orbit was chosen to be a 150 nautical mile circular polar (90 degrees inclination) orbit.

Most analytical and numerical studies of aeroassisted orbital transfer have assumed a spherical, non-rotating Earth model. A 1986 study by Ikawa [16] of AOTV trajectories investigated possible trajectory simulation errors due to the non-rotating planet assumption. It was noted that numerical trajectory simulation using the non-rotating Earth model caused velocity errors which gave dynamic pressure (and hence, lift and drag) differences ranging up to 10% to 14%. Ikawa found that these differences may cause underprediction of the final altitude and overprediction of the attainable orbital inclination change in a non-rotating Earth analysis. Ikawa concluded that the rotating Earth effects must be included for realistic AOTV trajectory simulations.

In this study of noncoplanar orbit transfer optimization, a spherical, rotating Earth model with an inverse square gravitational field and a 1976 U.S. Standard Atmosphere were exclusively used. This analysis also assumed that the aeroassisted sortie vehicle maintained zero sideslip throughout all of its trajectory. Because of the high speeds involved in aeroassisted orbit transfer, heating constraints were incorporated in the trajectory optimization for realistic results. Hence, all trajectories examined in this study were optimized with radiation equilibrium temperature constraints.

5.2 Equations of Motion

The equations of motion used by the OTIS computer program for the ASV trajectory analyses are given below in flight path coordinates [6].

$$\begin{bmatrix} \dot{v} \\ v\dot{\psi}\cos\psi \\ -v\dot{\gamma} \end{bmatrix} = (\bar{F}_A + \bar{F}_P)/m + \bar{A}_G - \bar{V}_K \quad (1)$$

$$\begin{bmatrix} \dot{r} \\ \dot{\theta}r\cos\phi \\ r\dot{\phi} \end{bmatrix} = \begin{bmatrix} \sin\psi \\ \sin\psi \cos\psi \\ \cos\psi \cos\psi \end{bmatrix} \quad (2)$$

$$\dot{m} = \frac{dm}{dt} \quad (3)$$

where,

$$V_K = 2\omega_E V \begin{bmatrix} \text{Cos}\psi \text{Sin}\psi \text{Sin}\phi \\ \text{Cos}\phi \text{Sin}\psi - \text{Cos}\psi \text{Cos}\psi \text{Sin}\phi \\ \text{Cos}\phi \text{Cos}\psi \text{Sin}\psi \end{bmatrix} + r\omega_E^2 \text{Cos}\phi \begin{bmatrix} \text{Sin}\psi \\ 0 \\ \text{Cos}\phi \end{bmatrix} + \frac{V^2}{r} \text{cos}\psi \begin{bmatrix} \text{Sin}\psi \text{Cos}\psi + \text{Sin}^2\psi \text{Cos}\psi \text{Tan}\phi \\ \text{Sin}\psi (\text{Sin}\psi - \text{Cos}\psi \text{Cos}\psi \text{Tan}\phi) \\ \text{Cos}\psi \end{bmatrix} \quad (4)$$

and where,

\dot{m}	=	Vehicle mass flow rate
m	=	Vehicle mass
V	=	Earth relative velocity magnitude (speed)
ψ	=	Heading angle, clockwise from North
γ	=	Flight path angle, positive up
r	=	Radius from center of Earth
θ	=	Longitude, East from prime meridian
ϕ	=	Latitude
ω_E	=	Earth rotation rate
\bar{F}_A	=	Aerodynamic force
\bar{F}_P	=	Vectored propulsive force
\bar{A}_G	=	Gravitational acceleration

5.3 The All-Propulsive Plane Change

To show the benefits of high ω/D for an aeroassisted sortie vehicle to perform the baseline plane change to a 150 nautical mile polar orbit, the theoretical propulsive energy of the ASV can be compared to that required by an all-propulsive orbital transfer vehicle (OTV) to perform a two-impulse, exoatmospheric plane change. The required propulsive energy expended during the plane change maneuver is expressed as a theoretical impulsive velocity increment, ΔV , computed by the following equations.

$$\Delta V = I_{sp} g_o \ln \left[\frac{W_o}{W_f} \right] \quad (5)$$

where, W_o = Initial weight of the vehicle
 W_f = Final weight of the vehicle
 I_{sp} = Vacuum specific impulse of the rocket (470 seconds)
 g_o = Acceleration of gravity at a mean earth radius

The ΔV for the all-propulsive orbital transfer is computed by the following equation.

$$\Delta V = \sqrt{v_{1c}^2 + v_{2c}^2 - 2 v_{1c} v_{2c} \cos \Delta i} + [v_{2c} - v_{tp}] \quad (6)$$

where, Δi = Orbital plane change angle
 v_{1c} = Inertial circular orbital velocity (25,145.5 feet/second) at 220 nautical miles
 v_{ta} = Inertial apogee velocity (25,024. feet/second) for a Hohmann transfer orbit between the two circular orbits
 v_{2c} = Inertial circular orbital velocity (25,389.2 feet/second) at 150 nautical miles
 v_{tp} = Inertial perigee velocity (25,511.4 feet/second) for a Hohmann transfer orbit between the two circular orbits

The last two terms represent the additional ΔV required to circularize the orbit at an altitude of 150 nautical miles.

6.0 RESULTS

The aeroassisted sortie vehicle was sized to perform a synergetic orbital plane change from its space base in a circular orbit at an altitude of 220 nautical miles and 28.5 degrees inclination to a final 150 nautical mile circular polar orbit. Both the synergetic and two-impulse-deorbit aeroassist maneuvers were optimized for this trajectory. Because the synergetic maneuver trajectory proved to be optimal (provided more payload weight to the desired final orbit), it was adopted as the baseline ASV trajectory. Direct comparison between the equivalent synergetic and the two-impulse-deorbit aeroassist trajectories was not accomplished. When optimization of the two-impulse-deorbit maneuver was attempted for the baseline vehicle, the optimization routines caused the vehicle to initiate a synergetic trajectory.

Presented in a later section are results for a modified vehicle where the two-impulse-deorbit aeroassisted plane change is the optimal maneuver to attain the final circular polar orbit.

The following trajectory results represent optimized trajectories generated by the Optimal Trajectories by Implicit Simulation (OTIS) computer program.

6.1 Baseline Trajectory

The details of the baseline trajectory, a synergetic orbital plane change trajectory from an inclination of 28.5 degrees to 90 degrees, are shown in Figure 7. The vehicle entered the sensible atmosphere at an altitude of 300K feet, with a velocity of 24,683 feet per second, and a flight path angle of -6.3 degrees. For the baseline trajectory, the radiation equilibrium stagnation temperature at the vehicle nose was constrained to 4500 degrees Fahrenheit (F). The sortie vehicle flew an unpowered descent for 1421 seconds (Figure 7a). The rocket engine was then ignited and the vehicle climbed out of the atmosphere. The minimum altitude at 159,344 feet was reached at 1440 seconds, shortly after ignition of the rocket engine, shown as a sharp increase in axial acceleration in Figure 7b.

Optimal control of the synergetic plane change was effected by the modulation of angle of attack and bank angle (Figure 7c). During the initial descent, the angle of attack stayed near the value for maximum L/D (10 to 12 degrees), and the bank angle increased to -174 degrees to enable a quicker descent into the atmosphere for greater plane change. Angle of attack then increased to values between 18 degrees and 20 degrees and bank angle decreased to values between -80 degrees and -60 degrees, resulting in an increase in the rate of inclination angle change (Figure 7d). Throughout the trajectory, angle of attack and bank angle were optimally modulated to enable the vehicle to fly at a maximum nose stagnation temperature of 4500 degrees F (Figure 7e). For optimum inclination change subject to a heating constraint, the vehicle flew at angles of attack higher than that corresponding to maximum L/D, indicating a requirement for higher lift rather than maximum aerodynamic efficiency.

It can be seen from Figure 7d that more than half of the required inclination change was achieved before rocket ignition. The initial heading angle of 90 degrees, optimally determined by OTIS, indicated that the sortie vehicle began atmospheric entry at an apex (maximum latitude = -28.5 degrees) in the orbit. Total heading change was 90 degrees for this baseline trajectory.

As shown in Figure 7e, the wing leading edge stagnation temperature reached a maximum 3210 degrees F and the centerline static temperature reached a maximum 2909 degrees F. The centerline static temperature was computed at a point on the bottom surface of the aeroassisted sortie vehicle 5 feet aft of the nose.

The lift-to-drag ratio reached a maximum 3.04 during the unpowered descent phase and reached a maximum 3.09 during the powered ascent phase of the trajectory (Figure 7f). Prior to rocket engine ignition, the vehicle flew at an L/D near 2.5. For nearly the entire trajectory, the vehicle flew at angles of attack higher than that corresponding to the maximum L/D - on the "back side" of the L/D curve.

6.2 Effects of Varying Maximum Temperature Constraints

A series of optimized synergetic trajectories were run to determine the effect of varying the maximum nose stagnation temperature constraint on vehicle payload weight to polar orbit (Figure 8). For the baseline trajectory (maximum $T_{nose} = 4500$ degrees F), the sortie vehicle carried 2417 pounds of payload to polar orbit. For a maximum temperature of 4250 degrees F, the payload was only 440 pounds. For maximum nose temperatures of 5000 and 5400 degrees F, the payload weights delivered to a 150 nautical mile circular polar orbit were 4713 and 5392 pounds, respectively. Increasing the maximum temperature constraint allowed the vehicle to descend deeper into the atmosphere, utilizing the higher L/D, and thus resulting greater payload capability.

The sensitivity of payload weight to maximum temperature (with respect to the baseline trajectory values) is more acute at the lower maximum temperature constraints investigated. A 5.6% decrease in maximum allowable temperature for the baseline vehicle results in a 82% decrease in payload weight. An 11.1% increase in maximum allowable nose temperature for the baseline aeroassisted sortie vehicle increases the payload weight delivered to the final orbit by 95%.

6.3 Two-Impulse Aeroassist with Drop Tanks

Subjected to a maximum temperature constraint of 4500 degrees F, the baseline synergetic trajectory resulted in 2417 pounds of payload delivered to a 150 nautical mile circular polar orbit. To evaluate an increased payload capability, two external drop tanks were added to the aeroassisted sortie vehicle. This tankage was arbitrarily chosen to have a weight of 30,000 pounds, approximately half of the gross weight of the aeroassisted sortie vehicle. With an assumed mass fraction of .95, the drop tanks provided the sortie vehicle with an additional 28,500 pounds of propellants and an additional ΔV capability of 5513 feet per second. This simulation required the drop tanks to be emptied and discarded prior to atmospheric entry. For the case of the

two-impulse-deorbit aeroassist trajectory, the tanks were discarded after the second propulsive maneuver (See Figure 5).

The two-impulse-deorbit trajectory was programmed to allow global optimization of the complete trajectory. Initial optimization efforts quickly indicated that the aeroassist(2) orbital plane change maneuver was significantly more optimal than the synergetic maneuver for this configuration. Subjected to a maximum nose temperature of 4500 degrees F, the ASV with drop tanks delivered 7124 pounds of payload to polar orbit during the two-impulse-deorbit aeroassist trajectory. The equivalent synergetic maneuver, preceded by an all-propulsive plane change which emptied the drop tanks, delivered only 6167 pounds to polar orbit. Details of the atmospheric portion of the nominal two-impulse-deorbit aeroassist trajectory are presented in Figure 9.

For the nominal aeroassist(2) trajectory, the radiation equilibrium stagnation temperature at the vehicle nose was constrained at 4500 degrees F. The vehicle entered the sensible atmosphere at an altitude of approximately 300K feet with a velocity of approximately 27,200 feet per second and flight path angle of approximately -2.3 degrees. The minimum altitude of 174,581 feet, and minimum velocity of 19,935 feet per second were reached 8970 seconds into the trajectory (Figure 9a). At that time, the rocket engine ignited and the vehicle climbed out of the atmosphere, as indicated by the sharp rise in axial vehicle acceleration in Figure 9b.

Optimal control of the atmospheric portion of the trajectory, constrained by a maximum nose temperature of 4500 degrees F, was effected by the modulation of angle of attack and bank angle (Figure 9c). Comparison of angle of attack values between this trajectory and those of the baseline synergetic maneuver (Figure 7c) shows that much higher angles of attack are required during the unpowered portion of the aeroassist(2) trajectory to pull the vehicle out of the very fast and steep atmospheric entry. In both cases, the vehicle flew at angles of attack much higher than that corresponding to maximum L/D (10 to 12 degrees), indicating a requirement for higher lift.

As indicated in Figure 9d, approximately 50.4 degrees of inclination change was accomplished during the atmospheric portion of the trajectory. A considerable portion (over 14 degrees) of this inclination change was obtained above 200K feet during the descent due to the very high atmospheric entry velocity, characteristic of the two-impulse deorbit aeroassist maneuver.

The wing leading edge stagnation temperature reached a maximum 3692 degrees F and the centerline static temperature reached a maximum 3328 degrees F (Figure 9e). The centerline static temperature was computed at a point on the bottom surface of the aeroassisted sortie vehicle 5 feet aft of the nose.

The lift-to-drag ratio flown by the vehicle reached a maximum value of 2.88 for a few seconds during the powered ascent phase of the trajectory (Figure 9f). This value is approximately 85% of the maximum L/D potential for the vehicle. A time-averaged value of the L/D flown by the aeroassisted sortie vehicle below 200K feet altitude was approximately 2.4.

6.4 Effects of Varying Maximum Temperature Constraints on the Aeroassist(2) Orbital Plane Change

A series of optimized two-impulse-deorbit aeroassist trajectories were computed to determine the effect of varying the maximum nose stagnation temperature constraint on vehicle payload weight to polar orbit (Figure 10). For the baseline trajectory, the sortie vehicle carried 7124 pounds of payload to polar orbit. For a maximum temperature of 4100 degrees F, the payload was only 2207 pounds. The payload weights delivered to a 150 nautical mile circular polar orbit were 12,377 and 15,752 pounds for maximum nose temperatures of 5000 and 5500 degrees F, respectively. Increasing the maximum temperature constraint resulted in higher entry velocities, higher utilized L/D, and greater payload capability.

In comparison with the baseline synergetic trajectory, the 30,000 pound drop tanks increased the payload to polar orbit by 4704 pounds, approximately 190%. For the 5000 and 5500 degrees F nose temperature constrained trajectories, the aeroassist(2) maneuver with added drop tanks increased the payload capability by approximately 162% and 192%, respectively. The sensitivity of increased weight to increased maximum temperature was relatively high for the entire range of maximum temperature constrained aeroassist(2) trajectories investigated.

6.5 Max L/D Vehicle Trade Study

To evaluate the ability of different vehicle configuration classes to perform the baseline trajectory, optimal synergetic orbital transfer trajectories to a maximum final inclination angle were computed for the baseline high L/D vehicle (maximum L/D = 3.4), a medium (relative) L/D vehicle (maximum L/D = 3.0), and a low (relative) L/D vehicle (maximum L/D = 2.2). For each vehicle, optimized trajectories were computed with the maximum nose temperature constraint ranging from 3500 degrees F to 5000 degrees F. The payload was fixed at 1000 pounds for each trajectory.

To develop an approximate aerodynamic model for the medium L/D vehicle, the axial force coefficient of the baseline vehicle at zero angle of attack, Mach 20, and an

altitude of 200K feet was increased by 30%. This increment was then added to the axial force coefficient at each angle of attack for each Mach number and altitude condition. To develop an approximate aerodynamic model for the low L/D vehicle, the axial force coefficient of the baseline vehicle at zero angle of attack for the same conditions as above was increased by 100%. This increment was then added to the axial force coefficient at each flight condition. Also, the normal force coefficient at each condition for the low L/D vehicle was scaled by a factor of 0.9. The resultant values of L/D for all three vehicles at Mach 20 and an altitude of 200K feet are presented in Figure 11.

The synergetic plane change trajectory for the high L/D vehicle was essentially identical to the baseline trajectory presented in Figure 7. For brevity, this trajectory is not shown. The final orbital inclination attained by the high L/D vehicle was 94.9 degrees for the 1000 pound payload. The baseline trajectory resulted in 2417 pounds of payload delivered to polar orbit. As a result, increasing the final inclination angle by 4.9 degrees reduced the payload weight by 141 pounds.

The baseline synergetic plane change performance of the medium L/D vehicle is presented in Figure 12. Unlike the high L/D vehicle, the medium L/D vehicle flared near 230K feet and bounced out of the atmosphere to 345K feet. It then reentered the atmosphere and flew an altitude profile similar to the high L/D vehicle (Figure 12a). Rocket engine ignition occurred at 3100 seconds to boost the vehicle up to the polar orbit condition (Figure 12b). As the vehicle bounced out of the atmosphere after the initial flare, the angle of attack dropped to zero degrees twice before increasing to 20 degrees during the descent to the minimum altitude (Figure 12c). As the angle of attack dropped to zero, the L/D dropped to -0.25 (Figure 12d). For this trajectory, the medium L/D vehicle reached a final inclination of 91.9 degrees.

For the low L/D vehicle, the baseline synergetic plane change performance to polar orbit (Figure 13) showed trends similar to those of the medium L/D vehicle. Both vehicles skipped out of the atmosphere before reentering and performing the plane change, possibly indicating that the assumed initial deorbit ΔV was not optimal. These two dips into the atmosphere were approximately centered about two different nodes in the orbit, with the first dip providing only a couple of degrees of inclination change. The low L/D vehicle reached a final inclination of only 83.9 degrees.

The final inclination angle attained by each vehicle as a function of the maximum nose temperature constraint is presented in Figure 14. Between the 4000 degree F and 3500 degree F constraints, the high L/D vehicle and the medium L/D vehicle reached approximately the same final inclination, implying that the high L/D vehicle could not take full advantage of its aerodynamic performance capability. As the temperature constraint was increased above 4000 degrees F, the high L/D vehicle was able to attain increasingly larger values of the final inclination angle, compared to the medium and low L/D vehicles, respectively. The payoff of higher attainable final inclination angle for greater maximum temperatures decreased for all three vehicle classes as maximum temperature constraints increased.

To carry a 1000 pound payload from its base at an inclination of 28.5 degrees to polar orbit, a sortie vehicle with a nosecone material capable of sustaining radiation equilibrium stagnation temperatures up to 4500 degrees F need only have a maximum L/D of 3.0. This implies that nose and leading edge radii on the vehicle can be larger than those for a vehicle with a maximum L/D of 3.4, which will also result in reduced temperatures. To carry larger payloads to polar orbit, a vehicle with a larger maximum L/D is required.

6.6 Comparison with an All-Propulsive Plane Change

The theoretical impulsive ΔV capability and the ΔV required for all-propulsive orbit transfer are computed by equations 5 and 6, respectively. Without payload, the aeroassisted sortie vehicle alone has a ΔV capability of 12,817 feet per second. Depending on the maximum temperature constraint imposed on the sortie vehicle, this ΔV capability allows the ASV to place significant payload weight into polar orbit. For the synergetic baseline trajectory subjected to a maximum nose stagnation temperature of 4500 degrees F, the aeroassisted sortie vehicle can transport 2417 pounds of payload from a circular 220 nautical mile 28.5 degree inclined orbit to a 150 nautical mile circular polar orbit. This trajectory required a theoretical velocity impulse of 11,525 feet per second (equation 5). Placement of the same payload by a two-impulse, all-propulsive orbital plane change would require a theoretical velocity impulse of 25,774 feet per second (equation 6). Furthermore, an OTV having the same ΔV capability as the sortie vehicle could place a 1000 pound payload to a final inclination of only 58.4 degrees, instead of the 94.9 and 91.9 degrees achieved by the baseline high and medium L/D sortie vehicles constrained by a maximum nose temperature of 4500 degrees F.

Adding propellant drop tanks to the aeroassisted sortie vehicle increases its ΔV capability to 18,330 feet per second. This allows the placement of 7124 pounds of payload to polar orbit by the two-impulse-deorbit aeroassist maneuver constrained by a maximum temperature of 4500 degrees F. An OTV with this velocity increment capability can only reach a final inclination angle of 71.6 degrees with a two-impulse all-propulsive maneuver.

CONCLUSIONS

Noncoplanar orbital plane change trajectories for an aeroassisted sortie vehicle from 220 nautical mile circular orbit at 28.5 degrees inclination to a 150 nautical mile circular polar orbit were optimized, subject to nose stagnation temperature constraints. Both synergetic and two-impulse-deorbit aeroassisted trajectories were successfully optimized.

The synergetic maneuver, where all of the plane change occurred within the atmosphere, was found to be more optimal than the two-impulse-deorbit aeroassist maneuver for the baseline vehicle and trajectory. The optimized synergetic plane change trajectory resulted in the delivery of 2417 pounds of payload to polar orbit. The 11,525 feet per second of propulsive ΔV expended during this trajectory was less than half the propulsive ΔV (25,774 feet per second) required by a two-impulse, all-propulsive orbital transfer maneuver.

For the baseline trajectory, the two-impulse-deorbit aeroassist trajectory was the optimal plane change maneuver for the ASV with drop tanks. The entire two-impulse-deorbit aeroassisted orbital plane change trajectory was globally optimized. By adding 30,000 pound propellant drop tanks, approximately half of the gross weight of the ASV, the payload weight (7124 pounds) to polar orbit was almost tripled.

The effect of varying the maximum nose stagnation temperature constraint on vehicle payload weight delivery to polar orbit was investigated. Results showed a decrease in sensitivity at the higher maximum temperature constraints for both classes of aeroassist trajectories, with the decrease in payoff for the synergetic maneuver being more pronounced.

To evaluate the ability of different vehicle configuration classes to perform the baseline trajectory, optimal synergetic orbital transfer trajectories to a maximum final inclination angle with a fixed payload of 1000 pounds were computed for three different maximum L/D vehicles. To fully utilize an L/D capability greater than 3, the ASV must be able to sustain maximum nose stagnation temperatures greater than 4400 degrees F. For a vehicle with a maximum L/D of 2.2 to carry 1000 pounds payload to the baseline polar orbit, the maximum nose stagnation temperature must exceed 4900 degrees F.

Some general conclusions can be made concerning both the synergetic and two-impulse-deorbit aeroassist maneuvers. For either optimum inclination change for a fixed payload mass, or optimum payload weight for a fixed final inclination angle subject to a wide range of heating constraints, the sortie vehicle generally flew at angles of attack much higher than that corresponding to maximum L/D. This observation indicated a requirement for higher lift rather than maximum aerodynamic efficiency.

Increasing the maximum temperature constraint allowed the aeroassisted sortie vehicle to descend deeper into the atmosphere, utilizing increased atmospheric density to perform the plane change more quickly and efficiently. Increasing the maximum temperature constraint also allowed the sortie vehicle to fly at higher lift-to-drag ratios. There is a large performance payoff for increasing the maximum temperature constraint. However, the sensitivity of this payoff decreased with increasing maximum temperature, indicating the existence of a limit where increasing the thermal protection system of a flight vehicle would not be worth the added weight and/or the cost of increased technology for passive thermal protection systems.

It is anticipated that new passive thermal protection materials capable of sustaining temperatures up to 4500 degrees F (not a defined boundary) will be available by the late 1990's. To handle temperatures above 4500 degrees F, active cooling will be required, which will likely be less expensive than high-technology materials for passive cooling.

A planned insertion of a payload to polar orbit would be most efficiently accomplished by a ground launch directly into the desired low earth orbit. However, for fast response time requirements, to quickly service an ailing satellite, or for a variety of other applications, an aeroassisted sortie vehicle based in low earth orbit that has the potential to reach a large range of orbits (inclination ranging from at least 28.5 degrees to 90 degrees) could be a great asset. After accounting for the difference in additional structural and thermal protection system weight required by the sortie vehicle to fly in a high temperature environment, compared to the structural weight of the all-propulsive orbital transfer vehicle, the sortie vehicle will likely have significantly more payload capability to perform the baseline trajectory to polar orbit.

REFERENCES

1. Calouri, V.A. and Andrews, D.G., Boeing Aerospace Company, "Orbital Transfer Vehicle Concept Definition Study," 1980, Boeing Document D180-26090.
2. Heald, D.A., General Dynamics Convair Division, "Orbital Transfer Vehicle Concept Definition Study," 1981, GDC-ASP-80-012.
3. Andrews, D.G., Savage, R. T., and Paris, S.W., Boeing Aerospace Company, "Technology Identification for Aeroconfigured Orbital Transfer Vehicles," 1983, APWAL-TR-83-3090.
4. Gentry, A.E., Douglas Aircraft Company, "Mark IV Supersonic-Hypersonic Arbitrary-Body Program," 1973, AFFDL-TR-73-159.
5. Hanson, J.M., "Combining Space-Based Propulsive Maneuvers and Aerodynamic Maneuvers to Achieve Optimal Orbit Transfer," Paper No. 87-2567, AIAA Atmospheric Flight Mechanics Conference, Monterey, California, August 1987.
6. Vinh, N.X., and Hanson, J.M., "Optimal Aeroassisted Return from High Earth Orbit with Plane Change," ACTA ASTRONAUTICA, Vol. 12, No. 1, 1985, pp. 11-25.
7. Walberg, G.D., "A Review of Aeroassisted Orbit Transfer," AIAA Paper No. 82-1378, AIAA 9th Atmospheric Flight Mechanics Conference, San Diego, California, 1982.
8. Mease, K.D., "Optimization of Aeroassisted Orbital Transfer: Current Status," The Journal of Astronautical Sciences, Vol. 36, No. 1/2 1988, pp 7-33.
9. Hargraves, C.R. and Paris, S.W., "Direct Trajectory Optimization Using Nonlinear Programming and Collocation," Journal of Guidance, Control, and Dynamics, Vol. 10, No. 4, July/August 1987, pp. 338-342.
10. Paris, S.W. and Hargraves, C.R., Boeing Aerospace Company, "Optimal Trajectories by Implicit Simulation," 1988, APWAL-TR-99-3057, Vol. 1.
11. Mease, K.D., Vinh, N.X., and Kuo, S.U., "Optimal Plane change During Constant Altitude Hypersonic Flight," AIAA Paper No. 88-4341-CP, AIAA Atmospheric Flight Mechanics Conference, Minneapolis, Minnesota, 1988.
12. Bursey, C.H., Johnson, D.T., and Karasopoulos, H., Synergetic Plane Change Trades and an Application," AIAA Paper No. 85-1816-CP, AIAA 12th Atmospheric Flight Mechanics Conference, Snowmass, Colorado, 1985.
13. Joosten, B.L. and Pierson, E.L., "Minimum-Fuel Aerodynamic Plane Change Maneuvers," AIAA Paper No. 81-0167, AIAA 19th Aerospace Sciences Meeting, St. Louis, Missouri, 1981.
14. Ikawa, H. and Rudiger, T.F., "Synergetic Maneuvering of Winged Spacecraft for Orbital Plane Change," Journal of Spacecraft and Rockets, Vol. 19, No. 6, 1982, pp. 513-520.
15. Hull, D.G., and Speyer, J.L., "Optimal Reentry and Plane-Change Trajectories," The Journal of the Astronautical Sciences, Vol. XXX, No. 2, April-June 1982, pp. 117-130.
16. Ikawa, H., "Effect of Rotating Earth for AOTV Analysis," AIAA Paper No. 86-2133-CP, AIAA Atmospheric Flight Mechanics Conference, Williamsburg, Virginia, 1986.

ACKNOWLEDGEMENTS

The authors would like to thank David Kotker of Boeing Advanced Systems and Eric Wetzel and Jon Gailey of Boeing Aerospace and Electronics for the preliminary design of the Aeroassisted Sortie Vehicle. Gratitude is also owed to Steve Paris of Boeing Aerospace and Electronics for his assistance in trajectory optimization.

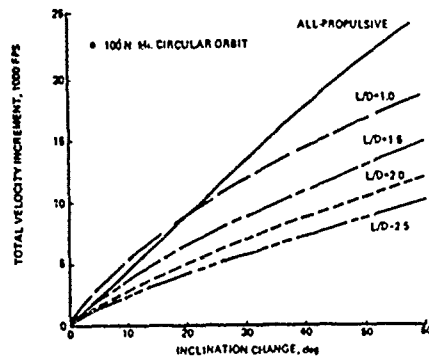


FIGURE 1. EFFECT OF L/D ON PLANE CHANGE CAPABILITY

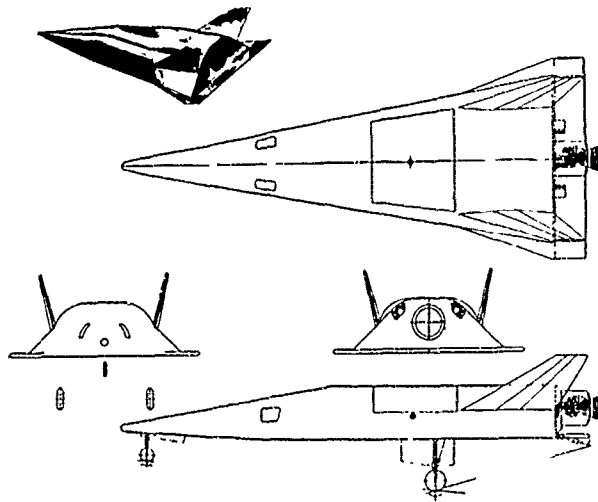


FIGURE 2. AEROASSISTED SORTIE VEHICLE CONFIGURATION

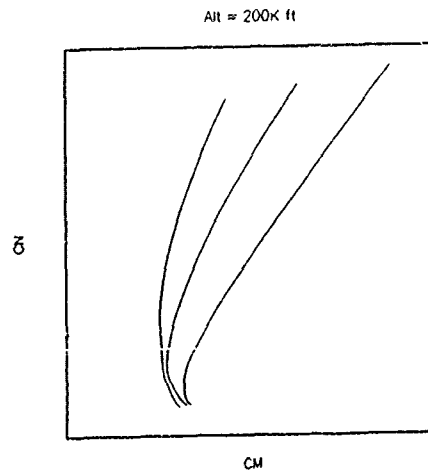


FIGURE 3. LONGITUDINAL STABILITY AND CONTROL; MACH 20

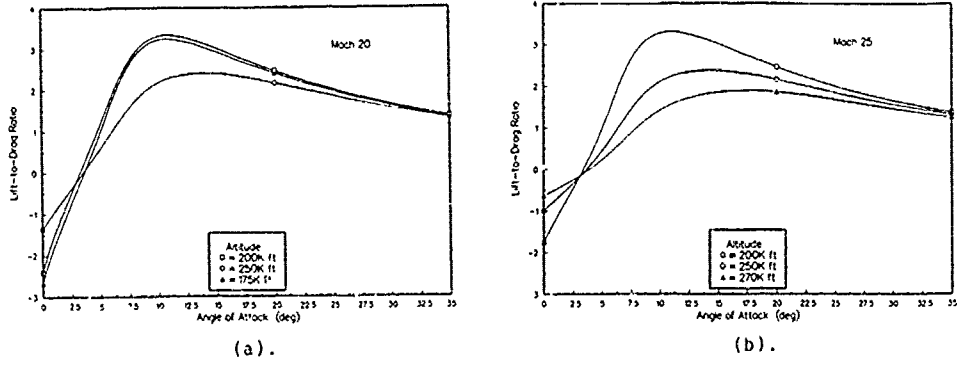


FIGURE 4. HYPERSONIC LIFT-TO-DRAG RATIO

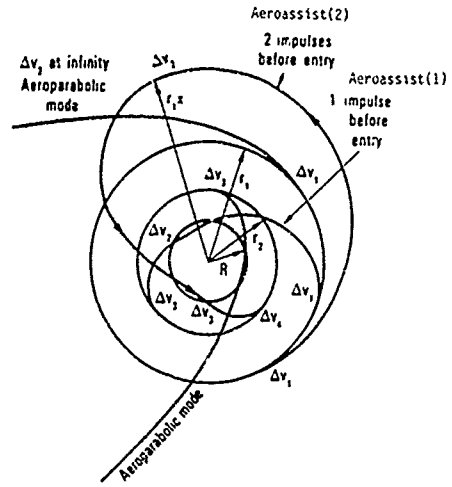


FIGURE 5. MODES OF OPTIMAL AEROASSISTED TRANSFER BETWEEN CIRCULAR ORBITS

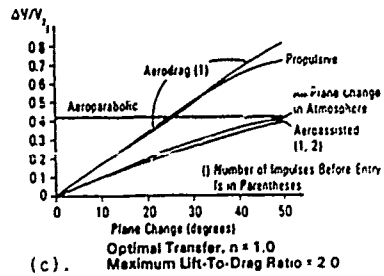
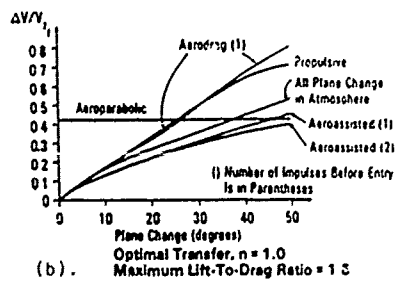
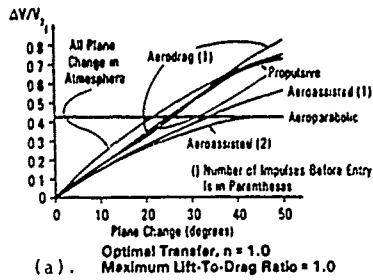
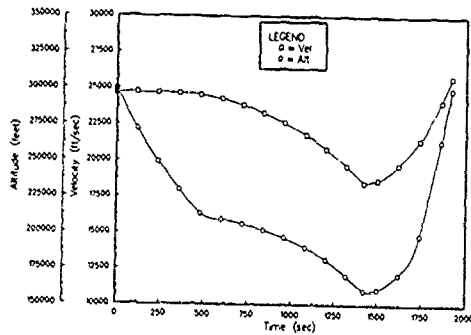
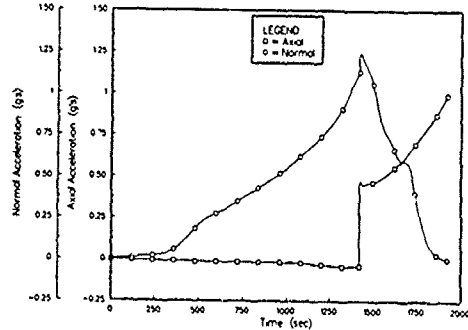


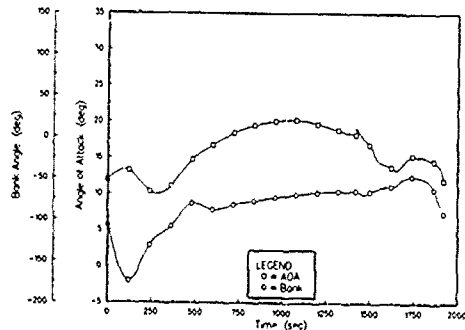
FIGURE 6. COMPARISON OF OPTIMAL ORBITAL TRANSFER MODES



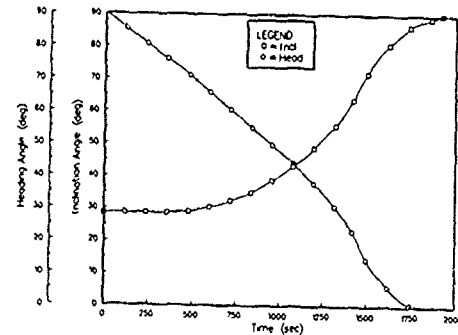
(a).



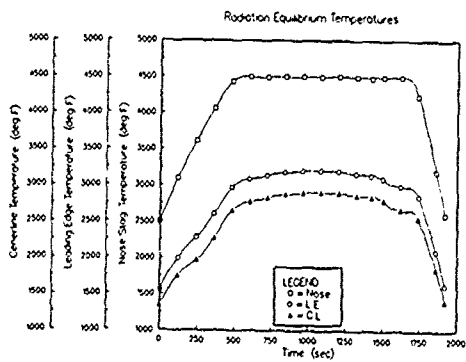
(b).



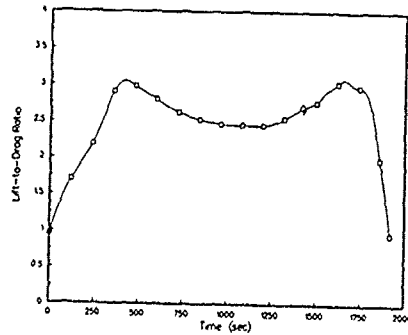
(c).



(d).



(e).



(f).

FIGURE 7. BASELINE SYNERGETIC TRAJECTORY PERFORMANCE

(1) 100% (2) 100% (3) 100% (4) 100% (5) 100% (6) 100% (7) 100% (8) 100% (9) 100% (10) 100% (11) 100% (12) 100% (13) 100% (14) 100% (15) 100% (16) 100% (17) 100% (18) 100% (19) 100% (20) 100% (21) 100% (22) 100% (23) 100% (24) 100% (25) 100% (26) 100% (27) 100% (28) 100% (29) 100% (30) 100% (31) 100% (32) 100% (33) 100% (34) 100% (35) 100% (36) 100% (37) 100% (38) 100% (39) 100% (40) 100% (41) 100% (42) 100% (43) 100% (44) 100% (45) 100% (46) 100% (47) 100% (48) 100% (49) 100% (50) 100% (51) 100% (52) 100% (53) 100% (54) 100% (55) 100% (56) 100% (57) 100% (58) 100% (59) 100% (60) 100% (61) 100% (62) 100% (63) 100% (64) 100% (65) 100% (66) 100% (67) 100% (68) 100% (69) 100% (70) 100% (71) 100% (72) 100% (73) 100% (74) 100% (75) 100% (76) 100% (77) 100% (78) 100% (79) 100% (80) 100% (81) 100% (82) 100% (83) 100% (84) 100% (85) 100% (86) 100% (87) 100% (88) 100% (89) 100% (90) 100% (91) 100% (92) 100% (93) 100% (94) 100% (95) 100% (96) 100% (97) 100% (98) 100% (99) 100% (100) 100%

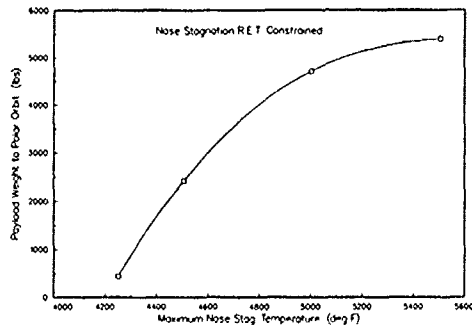
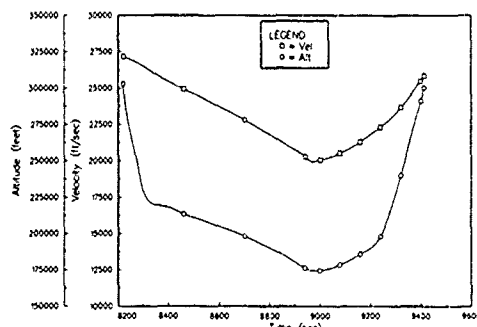
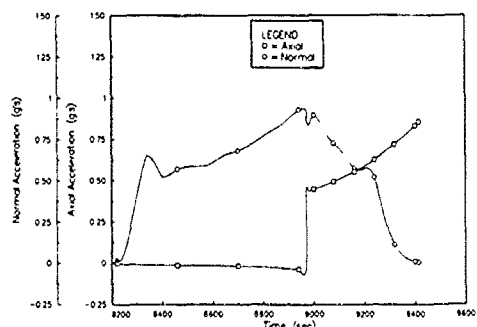


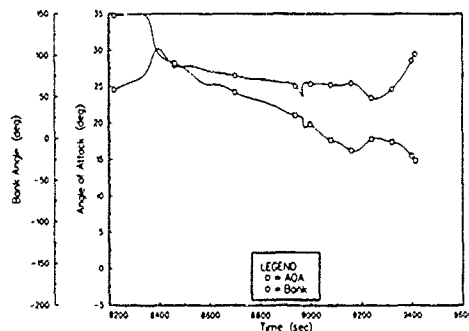
FIGURE 8. SYNERGETIC ORBITAL TRANSFER PAYLOAD SENSITIVITY



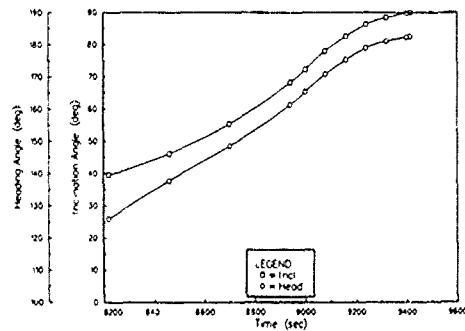
(a).



(b).



(c).



(d).

FIGURE 9. BASELINE AEROASSIST(2) TRAJECTORY PERFORMANCE

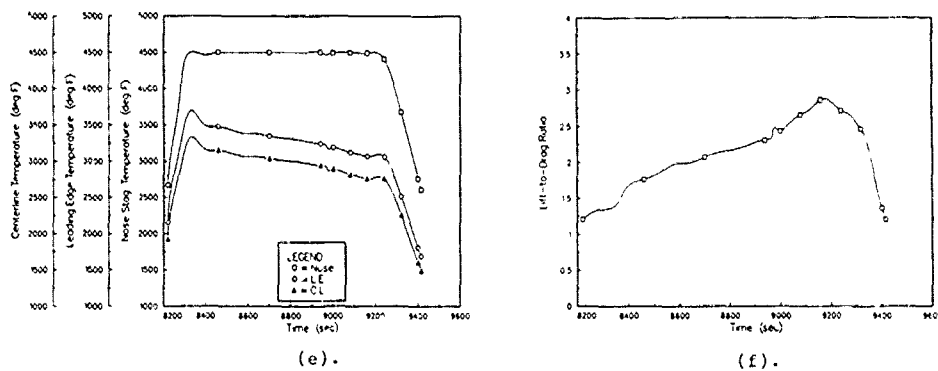


FIGURE 9. BASELINE AEROASSIST(2) TRAJECTORY PERFORMANCE (CONCLUDED)

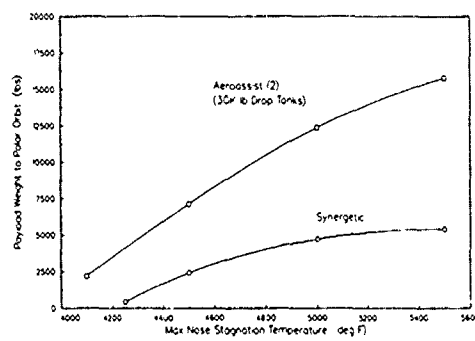


FIGURE 10. AEROASSIST(2) VS SYNERGETIC PAYLOAD COMPARISON

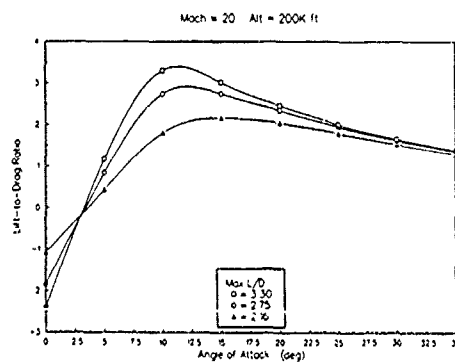


FIGURE 11. L/D FOR 3 CONFIGURATION CLASSES

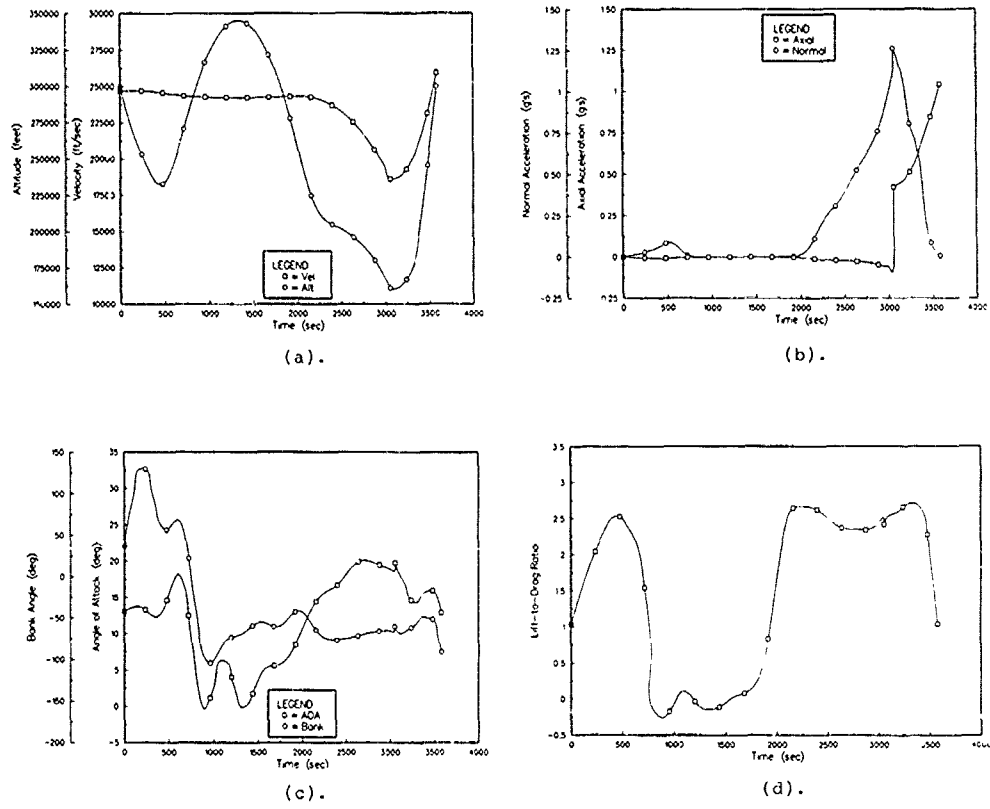


FIGURE 12. SYNERGETIC PERFORMANCE FOR L/D = 3.0 CONFIGURATION

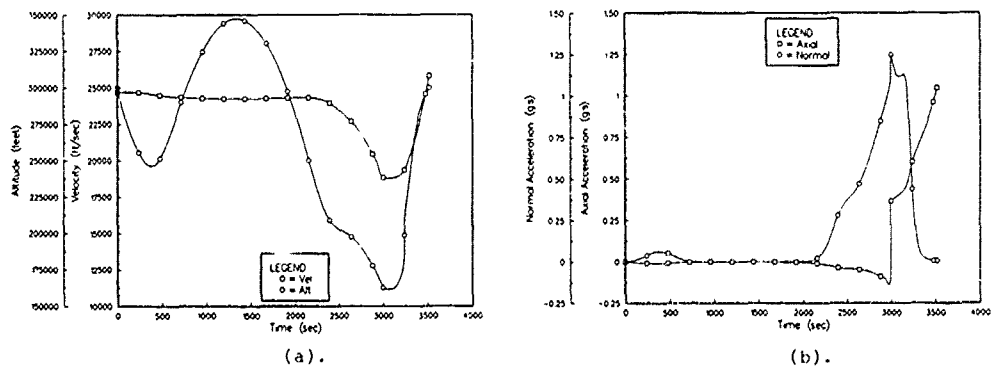


FIGURE 13. SYNERGETIC PERFORMANCE FOR L/D = 2.2 CONFIGURATION

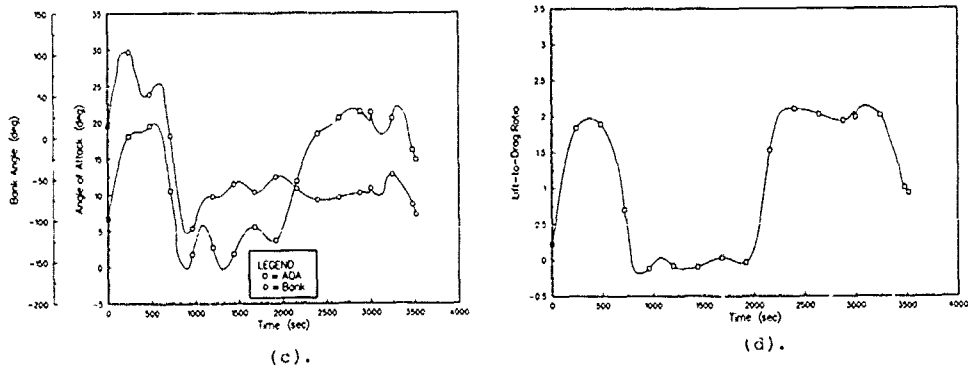


FIGURE 13. SYNERGETIC PERFORMANCE FOR L/D = 2.2 CONFIGURATION (CONCLUDED)

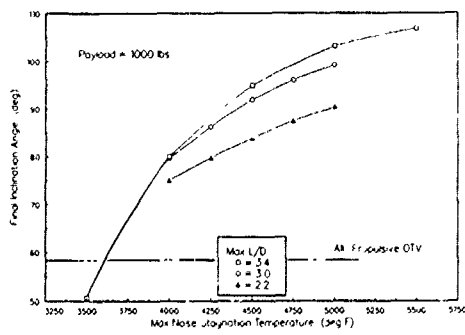


FIGURE 14. FINAL INCLINATION ANGLE FOR 3 VEHICLE L/D CLASSES

HERMES RENDEZ-VOUS WITH THE SPACE STATION

by

Michel CALDICHOURY, Calixte CHAMPETIER, Eric DESPLATS

Dynamics and Control Department

MATRA ESPACE

31 rue des Cosmonautes

31077 Toulouse

FRANCE

SUMMARY

This paper intends to present an overview of the requirements and concepts for the HERMES rendezvous system. A review of the mission requirements and constraints, mainly dictated by safety rules and man involvement, is first performed to highlight the impact of the vehicle configurations and environment on the definition of the GNC subsystem. The whole RV scenario from the end of the transfer phase up to the docking is described. A particular attention is devoted to the elaboration of guidance and control strategies for the homing and the final approach phases. The navigation system selected and designed for HERMES is presented, with some emphasis on the GPS navigation dedicated to the homing and closing phases and the optical navigation during the final approach. The redundant philosophy for the RV system and the crew involvement in the GNC and management process are also discussed.

LIST of ACRONYMS

CFF	Columbus Free Flyer
CG	Center of Gravity
CW	Clohesy-Wiltshire
DRS	Data Relay Satellite
FDJR	Failure Detection, Isolation and Recovery
FO/FS	Fail Operational / Fail Safe
GNC	Guidance, Navigation and Control
GPS	Global Positioning System
GPSS	GPS Satellite
HUD	Head Up Display
IMU	Inertial Measurement Unit
LOS	Line Of Sight
MMI	Man Machine Interface
RV	RendezVous
RVD	RendezVous and Docking
RVS	RendezVous Sensor
STS	STar Sensor
TDF	Target Docking Frame
TOF	Target Orbital Frame

1 - INTRODUCTION

Since several years in Europe, a great emphasis has been placed on the study and the development of new technologies which should enable to engage Europe on the path to manned space flight. The three cornerstones of the related preparatory program are ARIANE V for launching, COLOMBUS Free Flyer Laboratory (CFF) for orbital infrastructure and HERMES which performs the transportation of men and enables them to intervene on the CFF infrastructure. Among the various challenging stages arising in the HERMES-CFF mission, the Rendezvous and Docking operations are essential technologies which must be mastered. These operations require a complex Guidance, Navigation and Control (GNC) system to ensure, with safety aspects as majors drivers, the control, monitoring and supervision tasks.

This paper intends to present an overview of the requirements and concepts for the HERMES rendezvous system. A review of the mission requirements and constraints, mainly dictated by safety rules and man involvement, is first performed to highlight the impact of the vehicle configurations and environment on the definition of the GNC subsystem. The whole RV scenario from the end of the transfer phase up to the docking is described. A particular attention is devoted to the elaboration of guidance and control strategies for the homing and the final approach phases. The navigation system selected and designed for HERMES is presented, with some emphasis on the GPS navigation dedicated to the homing and closing phases and the optical navigation during the final approach. The crew involvement in the GNC and management process are also discussed. A large amount of the concepts described in this paper is not especially dedicated to the HERMES-CFF mission but may be applied to a generic rendezvous scenario. So, the reader should not be surprised if sometimes the generic terms "chaser" and "target" are used instead of "HERMES" and "CFF".

2 - MISSION DEFINITION AND REQUIREMENTS

2.1 - In-orbit Rendezvous and Docking (RVD) description

The in-orbit part of the RV mission between HERMES and the CFF space station can be divided into three main phases : transfer, homing/closing and final approach, with their symmetric counterparts : retreat, moving away, de-orbiting. The reference scenario can be described as follows. After the injection of HERMES by Ariane V in the orbital plane of the Space Station, a Hohmann boost is achieved to transfer the space plane on an orbit the apogee of which lies about 10 km below the circular target orbit, at the altitude of 450 km. When the apogee has drifted sufficiently close to the target, an other

Hohmann boost circularizes the chaser orbit. A coast phase then follows for navigation needs. The next phase consists in manoeuvring HERMES from its transfer orbit to a hold point located on the target orbit about 100 m behind. This phase can be divided in two subphases : the homing from the transfer orbit up to a stable point on the target orbit, 1 km behind, and the closing from this point to another point at 100 m from the target. Then, a slewing manoeuvre puts HERMES back to the target and the acquisition of the optical navigation means is performed. If the target is sun-pointed, or if the docking axis is not pointed along the target orbit, a fly-around is required. The CFF station, which is nominally sun-pointed, acquires an earth-pointed attitude during the RVD operation, so that the fly-around is avoided. The last RV phase is the final approach from 100 m to the docking. A hold point is planned at 20 m from the target in order to acquire the relative attitude of both vehicles. Figure 1 shows the reference RV profile drawn in the target orbital frame. The different subphases of the RV mission are summarized in Table 1.

Distance from the target	Subphase	Operations
80 km	S1	last transfer boost
	S1 - S2	coast phase - acquisition of the target GPS measurements
	S2 - S3	vertical homing phase
1 km	S3	hold point
	S3 - S4	closing phase ("hopping")
100 m	S4	hold point - slewing manoeuvre - RV sensor acquisition
	S4 - S5	final translation (earth-pointed target)
20 m	S4b	hold point - relative attitude acquisition
0 m	S5	docking operations

Table 1 . Reference operation sequencing

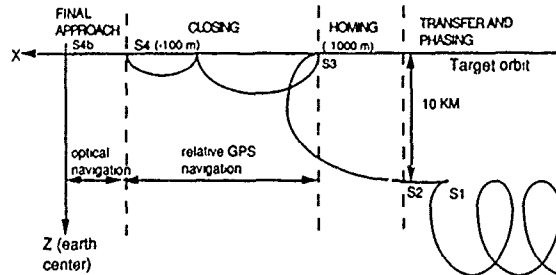


Figure 1 : Reference RV scenario

2.2 - Mission requirements and constraints

The RVD process is critical to both crew safety and mission success. Collision avoidance and safe separation are supreme requirements for crew safety, and the success of RV, docking and separation is a prerequisite for the achievement of the objectives of a servicing mission. The safety and mission assurance rests on a Fail Operational / Fail Safe (FO/FS) concept. In case of a single failure, the nominal operations continue by switching to redundant system functions. If the nominal operation cannot be continued, the mission must be achieved by repetition of nominal or contingency operations. If a double failure on the same function, or a combination of critical single failures on different functions occurs, the RVD mission is aborted. Separation and return to ground must be achieved safely.

Besides these safety constraints, some other specifications concerning the supervision by the crew and the operation timing have to be taken into account. Each subsequent phase in the approach scheme shall be released / initiated by the crew after verification of the achievement of the previous phase. The approach strategy must include time flexible elements to allow for success / system health verification and decision making. During the homing/closing phase and the final approach, the crew must have a direct or camera-assisted vision of the target. The last 50 meters and all the manoeuvres have to be performed during the orbital day. Time must also be foreseen at the end of the orbital day to undertake safing retreat in case of contingency. Furthermore, within these security constraints, the performances in terms of ergol consumption and manoeuvre precision must be optimized.

2.3 - Impact on the GNC subsystem requirements

The approach scheme has to be designed so that if a subsequent manoeuvre cannot be executed, the chaser will proceed on a collision-free trajectory. All possible natural trajectories resulting from forced trajectories or thrusting failing to operate must also be collision free. To be unable to perform some manoeuvre or to achieve some trajectory in the first attempt must not result in the loss of the mission. In particular, the guidance and control laws must be robust enough to permit the achievement of the mission despite failures such as temporary loss of the nominal navigation, thrusting failing on or thrusting failing to operate. Recovery by contingency operations must be possible. A direct consequence of these constraints

is that the homing/closing phase and the final approach must be closed-loop controlled phases. Homing/closing and final approach trajectories compatible with the safety rules as stated above and optimal in terms of consumption have to be designed.

It is clear that the specifications in terms of position and velocity dispersions become more and more stringent as far as the chaser approaches the target. Nevertheless, it is worth noting that as regards the operation management, homing/closing is a critical phase of the RV. Contrarily to the final approach, a delay in the progress of the operations which is not compatible with the robustness of the guidance and control strategies will cause severe consequences on the RV timing in terms of duration of the mission as well as consumption.

3 - GUIDANCE AND CONTROL CONCEPTS AND DESIGN

3.1 - Basic guidance trajectories

The mission requirements induced by the safety constraints as stated in the previous section must be taken into account for the design of guidance trajectories. The main constraints are the following

- the duration of the approach from 1km up to the docking is less than 2 orbital periods
- the last 50 meters are covered during the daylight
- up to the last 2.5 meters of the RV, the trajectories are collision-free in the case of thrusters failing to operate
- two hold points, at 100 m and 20 m behind the Space Station are mandatory
- the ergol consumption is to be minimized as far as possible

The guidance trajectories are calculated in the target orbital frame (TOF) as described on Figure 2. The equations describing the relative movement of the chaser in the TOF can be directly derived from the Kepler laws :

$$\frac{d^2 \vec{R}}{dt^2} = \frac{d^2 \vec{r}_c}{dt^2} - \frac{d^2 \vec{r}_t}{dt^2} = \mu \left(\frac{\vec{r}_t}{r_t^3} - \frac{\vec{r}_c}{r_c^3} \right) + \vec{\gamma}_c - \vec{\gamma}_t$$

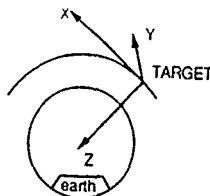
where the following notations are used

- \vec{r}_t earth center to target vector
- \vec{r}_c earth center to chaser vector
- \vec{R} relative position vector
- $\vec{\gamma}_c$ acceleration induced on the chaser by non gravitational forces
- $\vec{\gamma}_t$ acceleration induced on the chaser by non gravitational forces

When the target is on a circular orbit (period $T = 2\pi/\omega$), a first order expansion of the differential Keplerian acceleration leads to the following linearized equations, named as Clohessy-Wiltshire (CW) equations, expressed in the TOF

$$\begin{aligned} \ddot{x} - 2\omega \dot{z} &= \gamma_x + \gamma_x^{ext} \\ \ddot{y} + \omega^2 y &= \gamma_y + \gamma_y^{ext} \\ \ddot{z} + 2\omega \dot{z} - 3\omega^2 z &= \gamma_z + \gamma_z^{ext} \end{aligned}$$

where (x,y,z) are the coordinates of the chaser center of gravity (CG) in the TOF, $(\gamma_x, \gamma_y, \gamma_z)$ the thrust accelerations of the chaser, and $(\gamma_x^{ext}, \gamma_y^{ext}, \gamma_z^{ext})$ include all the other acceleration sources such as the differential air drag, the CW second-order neglected terms, the differential J2 term, ... The out-of-plane motion can be considered in a first approximation, as decoupled from the movement in the orbit plane and can be viewed as an harmonic oscillator movement which is quite easy to control. In the following, only the relative movement in the target orbit plane will be considered.



- X-axis : in the direction of the target velocity
- Y-axis : perpendicular to the target orbit plane
- Z-axis : in the target orbit plane, towards the earth

Figure 2 : Target Orbital Frame

Guidance trajectories for the homing phase

In the reference scenario, the first homing subphase consists in transferring HERMES from its drift orbit 10 km below the target orbit onto the target orbit, 1km behind the target. In order to minimize the consumption, the thrusts must be delivered

along the X-axis. The problem then becomes that of finding an acceleration profile which transfers the chaser from the initial conditions :

$$x_0 \text{ to be defined, } z_0 = 10 \text{ km, } \dot{x}_0 = \frac{3}{2} \omega z_0, \dot{z}_0 = 0$$

to the final desired conditions :

$$x_f = -1 \text{ km, } z_f = \dot{x}_f = \dot{z}_f = 0$$

The resulting trajectories will be called admissible. Theoretical admissible trajectories can be obtained by applying two Hohmann transfer boosts each of magnitude :

$$\Delta V_t = \frac{1}{4} \omega \Delta z, \quad (\Delta z = z_0 - z_f)$$

along the X-axis, separated by half an orbital period (see Figure 3). The first boost must be applied when :

$$\Delta x = x_f - x_0 = 3\pi/4 \Delta z$$

An other homing transfer (see Figure 3) can be performed with a constant level X-thrust of magnitude

$$\gamma_x = \frac{1}{4\pi} \omega^2 \Delta z$$

during one orbital period. This results in a forced path which starts when

$$\Delta x = \frac{3\pi}{2} \Delta z$$

The duration of the transfer itself is twice that of the Hohmann transfer, but the difference is only one quarter of period if time is compared from the same starting point. Both the resulting trajectories are safe w.r.t. the thrusting failing to operate (see Figure 4). It is worth noting that the above trajectories are both obtained with non realistic guidance acceleration profiles. In order to save ergol consumption for controlling the trajectory, the guidance laws must take into account the fact that the thrust is delivered without amplitude modulation.

Let γ_x be the achievable acceleration which can be applied to the chaser along the X-axis. The total impulse the target must receive :

$$\Delta V_x = \frac{1}{2} \omega \Delta z$$

corresponds to an overall thrust duration of

$$T_{thr} = \frac{\Delta V_x}{\gamma_x}$$

In the case of HERMES (see Table 2), $\Delta z = 10\text{km}$ yields $T_{thr} = 300 \text{ s}$ (compare with the orbital period $T = 5500\text{s}$).

The proposed approach consists in splitting the total impulse required for the whole transfer into N distinct boosts of duration :

$$\tau = \frac{1}{N} T_{thr} \quad (\text{see Figure 5}).$$

It can be shown that periodic boosts spaced by $\Delta T = 2\pi/N\omega$ yields admissible trajectories. The transfer duration becomes :

$$\frac{2\pi}{\omega} - (\Delta T - \tau).$$

$N = 2$ corresponds to a realistic Hohmann transfer while N large corresponds to a continuous-like steered transfer

Guidance trajectories for the closing phase

The problem now is to find admissible trajectories satisfying the following initial and final conditions :

$$\begin{array}{ll} x_0 = -1000\text{m} & x_f = -100\text{m} \\ z_0 = 0\text{m} & z_f = 0\text{m} \\ \dot{x}_0 = 0\text{m/s} & \dot{x}_f = 0\text{m/s} \\ \dot{z}_0 = 0\text{m/s} & \dot{z}_f = 0\text{m/s} \end{array}$$

The constraints on the trajectories are both timing constraints : transfer duration less than one orbital period, and safety constraints : collision-free trajectory after a thrusting failure. Furthermore, the crew must have the target in their field of view during all the transfer. So, the LOS must not be greater than 20° . Different concepts which may be applied for this transfer are summarized and compared in Table 3. A good compromise between the various requirements is fulfilled by the hopping trajectories for which the transfer boosts are performed along the Z-axis. The resulting free trajectories are ellipses centered on the target orbit. N-boosts realistic trajectories can be calculated as for the homing vertical transfer. As shown on Figure 6, the LOS requirement is not satisfied when a single hop is performed with $N=2$. In this case, two hops, which globally last one orbital period, have to be performed.

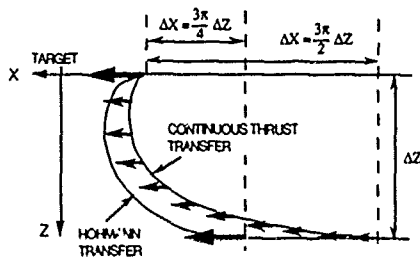


Figure 3 : Theoretical admissible trajectories

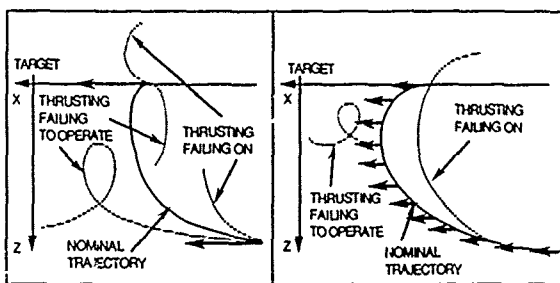
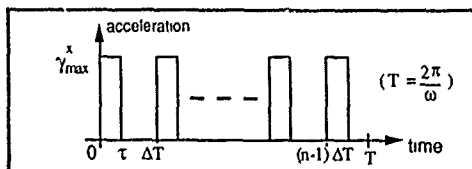


Figure 4 : Safe trajectories for the homing

AXIS	THRUST LEVEL		EFFICIENCY	SPECIFIC IMPULSE
	HOMING	CLOSING		
+ X	400 N	40 N	1	300 s
- X	40 N	40 N	1	300 s
± Y	20 N	20 N	0.7	300 s
± Z	20 N	20 N	0.7	300 s

mass = 23 t

Table 2 : HERMES Propulsion System



$$x_k - x_f = \frac{\gamma_x^{\max} \tau}{\omega} (-3 k \alpha_k + 4 u_k \sin \alpha_k)$$

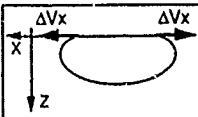
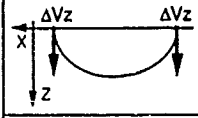
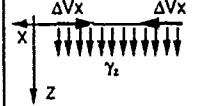
$$z_k = \frac{2 \gamma_x^{\max} \tau}{\omega} (k - u_k \cos \alpha_k)$$

$$\dot{x}_k = \gamma_x^{\max} \tau (3 k - 4 u_k \cos \alpha_k)$$

$$\dot{z}_k = -2 \gamma_x^{\max} \tau u_k \sin \alpha_k$$

$$u_k = \frac{\sin(k \pi / N)}{k \sin(\pi / N)}, \quad \alpha_k = (k - 1) \frac{\pi}{N} + \frac{\omega \tau}{2}$$

Figure 5 : Realistic admissible trajectory (acceleration profile and equations)

	DURATION	ΔV_x	ΔV_z	SAFETY
	1 ORBIT	0.11 m/s 0.86 kg	0	-
	1/2 ORBIT (2 boosts) 1 ORBIT (continuous thrust)	0	0.5 m/s 5.58 kg	+
	VARIABLE (Function of ΔV_x)	0.32 m/s 2.5 kg (duration 1 orbit)	2 m/s 22.3 kg	+

NOTA : ΔV AND CONSUMPTIONS FOR $\Delta X = 900$ M

Table 3 : Admissible guidance trajectories for the closing phase (1km - 100m)

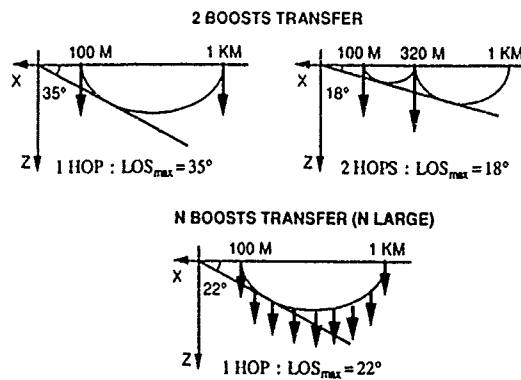


Figure 6 : LOS requirement analysis

Guidance trajectories for the final approach

Due to timing constraints, the final approach is based on forced paths along the X-axis from 100m to the docking. The analysis must be focussed on the safety requirement which becomes crucial during this phase. A safety domain around the target which the free-trajectories must not enter is first defined. A corner domain as shown on Figure 7 has been considered. Then the safety criterion can explicitly be expressed as constraints on the instantaneous axial velocity \dot{x} :

$$\dot{x} \leq \frac{\lambda}{2} \text{ for } x \leq z_s$$

$$\dot{x} \leq \frac{x^2 + z_s^2}{2 \lambda z_s} \text{ for } x \geq z_s$$

with $\lambda = \frac{1}{\omega} (\sqrt{7} - 3 \text{Arccos } \frac{3}{4}) = 426 \text{ s}$

which corresponds to the phase plane domain indicated on Figure 8. For the HERMES-CFF mission, we can take $z_s = 20\text{m}$. With $\lambda = 500\text{s}$ for providing a safety margin, the phase plane trajectory of Figure 9 can be performed. With this profile, the total duration of the last 100 meters is equal to 38 minutes without a stop at 20m, which is quite compatible with the timing constraints.

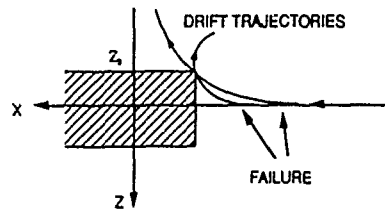


Figure 7 : Safety box around the target

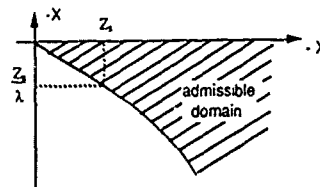


Figure 8 : Safety domain in the plane phase

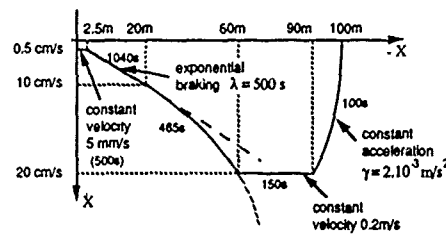


Figure 9 : Designed velocity profile for the last 100 m

3.2 - Guidance and control concepts for the homing/closing phase

For the homing/closing phase, two basic guidance schemes have been selected. In the first one, the chaser is kept on a reference trajectory by controlling both its position and its velocity. In the second one, control boosts are just performed so as to ensure the final kinematic conditions as desired (position at the desired location on the target orbit, velocity equal to zero) without requiring a control of the instantaneous position. Both schemes are now described and compared.

3.2.1 - Guidance on a reference trajectory

The guidance on a reference trajectory is based on the scheme shown on Figure 10. The guidance trajectories have been calculated from the CW equations. Their equations can be formulated as :

$$\dot{X}^* = A_{CW} X^* + B \Gamma^* \quad \text{with} \quad A_{CW} = \begin{bmatrix} 0 & 0 & 1 & 0 \\ 0 & 0 & 0 & 1 \\ 0 & 0 & 0 & 2\omega \\ 0 & 3\omega^2 & -2\omega & 0 \end{bmatrix}, \quad B = \begin{bmatrix} 0 & 0 \\ 0 & 0 \\ 1 & 0 \\ 0 & 1 \end{bmatrix}$$

where X^* is the desired kinematic state (position and velocity) of the chaser in the TOF and Γ^* the guidance boosts. For the control design, the relative position and velocity of the chaser are assumed to be perfectly measured. Let $\delta X = X - X^*$ be the difference between the desired state and the actual state. Its dynamic is described by :

$$\delta \dot{X} = A_{CW} \delta X + B \Gamma_c + \text{perturbations}$$

where Γ_c is the control acceleration. The time ΔT between two successive control boosts is assumed to be constant. In the case of N -boosts guidance trajectories with N large, the control boosts will be performed in addition to the guidance boosts. The

control boosts can be considered as discrete impulses. So, the continuous equations describing the error evolution along the reference trajectory may be replaced by the following discrete ones :

$$\delta X_{n+1} = A_d \delta X_n + B_d \Gamma_n$$

with

$$\delta X_n = \delta X(nDT), \Gamma_n = \Gamma_c(nDT), A_d = e^{A_c w DT}, B_d = e^{A_c w DT} B$$

An optimal state feedback $\Gamma_n = K_n \delta X_n$ can be calculated by minimizing a quadratic criterion of the form

$$J = \sum_{n=1}^N (\delta X_n^T Q \delta X_n + \Gamma_n^T R \Gamma_n)$$

The consumption is minimized by means of the weighting matrix R, while the performances are obtained via the weighting matrix Q. For N large, the steady-state feedback K obtained as N tends to infinity is quite sufficient for efficiently controlling the trajectory. This feedback can be expressed as :

$$K = (R + B_d^T P B_d) B_d^T P$$

where P is the positive solution of the discrete Riccati equation

$$P - A_d^T P A_d + A_d^T P B_d (R + B_d^T P B_d) A_d - Q = 0$$

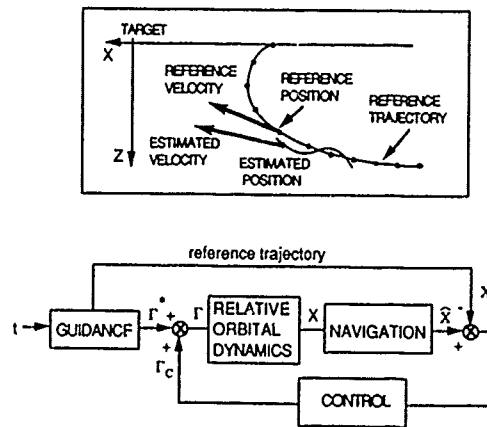


Figure 10 : Guidance on a reference trajectory

3.2.2 - Guidance to terminal point

In this guidance scheme, the reference trajectory is re-adjusted at each guidance step. An admissible trajectory going through the estimated position of the chaser and leading to the desired final kinematic conditions is calculated so that no position control is required. A velocity correction is just performed. The algorithm is efficient because through a given point goes one and only one admissible trajectory (see [5] for details). As the problem becomes singular near the end point, the guidance trajectory must be frozen a few steps before the arrival, and a position control is then required.

As regards the homing subphase, it is possible to release somewhat the specification on the end point abscissa. From a given admissible arrival interval on the target orbit $[x_f^{min}, x_f^{max}]$, one can enlarge the set of admissible trajectories to those which finish inside this interval. Now, through a given point (the estimated position of the chaser) go an infinity of admissible trajectories (see Figure 12). The set of all these trajectories is bounded by the trajectory arriving at x_f^{min} and that arriving at x_f^{max} . To the first one corresponds the smaller nominal vertical velocity, to the second one the larger. Furthermore, there exists a bi-univocal correspondence between the end point inside the arrival interval and the nominal vertical velocity. In order to minimize the consumption, the following procedure can be followed : from the estimated position of the chaser, the extremal admissible trajectories are calculated, together with the related vertical velocities. If the estimated vertical velocity of the chaser lies inside the admissible interval, only the horizontal velocity is corrected. Otherwise, the vertical velocity is also corrected taking into account as the reference velocity the closest bound of the admissible interval

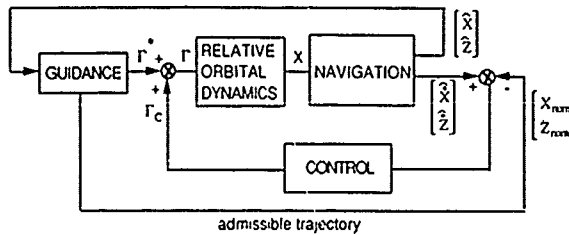
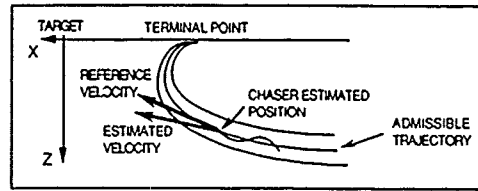


Figure 11 : Guidance to terminal point

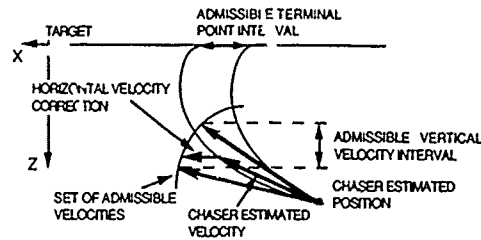


Figure 12 : Release on the end point abscissa specification

STRATEGY	PERFORMANCE (DISPERSION)	ROBUSTNESS	CONSUMPTION	ALGORITHMIC SIMPLICITY	BACK UP
N BOOSTS TRANSFER (N > 100) : CONTROL ON A REFERENCE TRAJECTORY	+	+	-	+	-
N BOOSTS TRANSFER (N > 100) : GUIDANCE TO TERMINAL POINT / VELOCITY CONTROL	+	++	+	-	++

HOMING (UP TO 1 KM)

STRATEGY	PERFORMANCE (DISPERSION)	ROBUSTNESS	CONSUMPTION	ALGORITHMIC SIMPLICITY	BACK UP
N BOOSTS TRANSFER (N > 100) : CONTROL ON A REFERENCE TRAJECTORY	+	+	+	+	-
N BOOSTS TRANSFER (N > 100) : GUIDANCE TO TERMINAL POINT / VELOCITY CONTROL	+	+	+	-	++

CLOSING (1 KM TO 100 M)

Table 4 : Comparison of guidance concepts for the homing and closing phases

3.2.3 - Performances and robustness evaluation

The performance of both strategies in terms of consumption and dispersion box at the terminal point as well as their robustness w.r.t. failures such as navigation failures, thrusting failing to operate, thrusting failing on have been evaluated

using adapted simulation tools (see Table 4). A typical number of one hundred guidance and control boosts is required in order to meet the specification in terms of final dispersion box, which are typically :

HOMING	CLOSING
$\delta X = 100 \text{ m}$	$\delta X = 10 \text{ m}$
$\delta Y = \delta Z = 10 \text{ m}$	$\delta Y = \delta Z = 5 \text{ m}$
$\delta \dot{X} = 2 \text{ cm/s}$	$\delta \dot{X} = \delta \dot{Y} = \delta \dot{Z} = 1 \text{ cm/s}$
$\delta \ddot{Y} = \delta \ddot{Z} = 2 \text{ cm/s}$	

From an algorithmic point of view, the guidance on a fixed trajectory is simpler. However, with such a strategy, the consumption is much increased when the chaser moves away from the reference trajectory. For the homing phase, considering a guidance to terminal point strategy, the release on the end point abscissa specification induces an important reduction of the propellant consumption. As regards the closing phase, the algorithmic singularity at the end point becomes important and the release on the final point constraints is not desired. So, for this subphase, the guidance on a fixed trajectory is recommended in the nominal mode. However, in a backup mode, a backup trajectory has to be defined w.r.t. the estimated chaser state, so that a guidance to terminal point algorithm should be available.

3.3 - Control scheme for the final approach

Only the dimensioning phase from a few meters from the target up to the docking is considered here. The basic difference with the previous phase is that the relative attitude of the target to the chaser must now be controlled. The attitude of the target is assumed to be unmeasured (no transmission of the target gyros information towards the chaser) but only estimated (see Section 4.3). During this phase, the desired relative axial velocity is typically 5 mm/s. The most stringent specifications on the kinematic conditions at docking are related to the relative attitude and angular rate and to the lateral position and velocity of the docking port center in the target docking frame (TDF) (see Table 5). To simplify the presentation, only the movements of the chaser in the target orbit plane are considered. The linearized equations of the motion can be set as :

$$\begin{aligned} \text{relative attitude} & \begin{cases} \dot{\theta}_r = \Omega_r \\ \dot{\Omega}_r = T_y / I_c - \dot{\Omega}_T + \text{pert} \end{cases} \\ \text{lateral motion} & \begin{cases} \dot{z} = \dot{z}_c + (X_c + L_T) \Omega_r + L_C \Omega_c \\ \dot{z}_c = F_z / M_C + \dot{X}_c \Omega_T + \text{pert.} \end{cases} \\ \text{axial motion} & \begin{cases} \dot{x} = \dot{x}_c \\ \ddot{x}_c = F_x / M_C \end{cases} \end{aligned}$$

where the following notations are used

(x, z)	deviation of the HERMES docking port center from its nominal trajectory expressed in the TDF
(\dot{x}, \dot{z})	axial and lateral deviation rates of the HERMES docking port center in the TDF
(\dot{x}_c, \dot{z}_c)	velocity of the HERMES CG in the TDF
Ω_c	chaser angular rate in the TOF
Ω_T	target angular rate in the TOF
Ω_r	relative angular rate
T_y	control torque on the chaser
(F_x, F_z)	control forces on the chaser
L_C	distance from CG to docking port of the chaser
L_T	distance from CG to docking port of the target
M_C	mass of the chaser
I_c	inertia of the chaser

As shown by these equations, the dynamics of the lateral deviation and the relative angular deviation of the docking ports are coupled. Taking into account this problem, the following guidance/control scheme has been proposed. The known perturbations due to Coriolis orbital accelerations are first compensated by the guidance forces. The axial and lateral deviations are then controlled using proportional-derivative feedbacks. The relative angular deviations are controlled so as to induce a rotational movement of the chaser around its docking port, keeping it fixed in the TDF. Such a coordinated movement requires a feedback of the relative attitude and angular rate on both the torque and the force command (see Figure 14). This guidance and control design has been validated by simulations (see Figure 15) taking into account the estimation of the required feedback variables from the available measurements : range, lines of sight and relative attitude angles (see the next section).

$$\begin{aligned}\Delta Z &\leq 40 \text{ mm} \\ \Delta \dot{Z} &\leq 2 \text{ mm/s} \\ \Delta \theta_r &\leq 1.5^\circ \\ \Delta \dot{\theta}_r &\leq 0.1 \text{ }^\circ/\text{s}\end{aligned}$$

Table 5 : Typical specifications on the kinematic conditions for docking

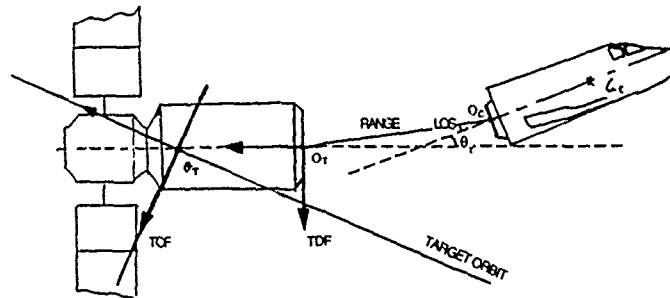


Figure 13 : Frames and measurements during the final approach

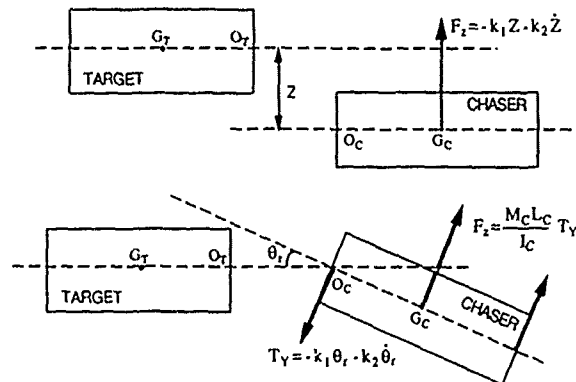


Figure 14 : Control strategies for the final approach

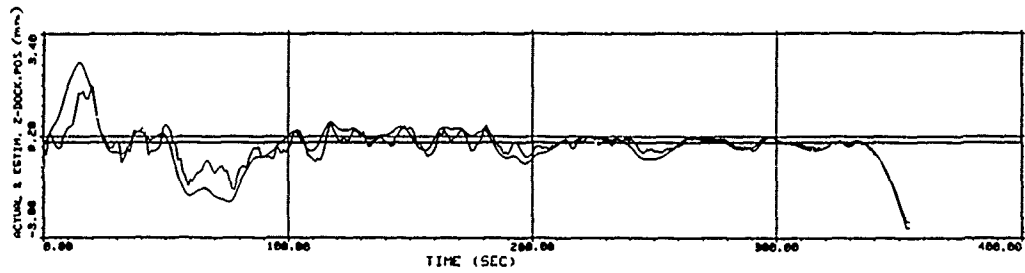
4 - HERMES ORBITAL NAVIGATION

4.1 - Navigation systems, architecture and equipments

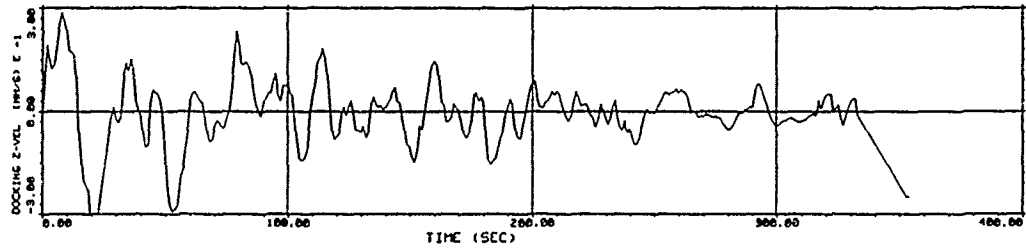
The long-range in-orbit navigation of HERMES is based on the NAVSTAR Global Positioning System (GPS) for the position and velocity estimation and on inertial measurements (IMU) updated by Star Sensor (STS) measurements for the attitude estimation. GPS navigation will be detailed in the next subsection. Design rules for the proposed attitude estimation can be found in [2]. As GPS is available only with the degraded C/A civil code, the achievable performances, admissible for the transfer, does no longer permits a precise and safe navigation near the target and would lead to an extra consumption. So, the baseline is to perform the homing/closing phase with a cooperative target which delivers its own GPS information to HERMES. The treatment of the GPS measurements from both HERMES and CFF generates a relative position/velocity estimation sufficiently precise to achieve a safe homing/closing.

During the RV proximity operations, from a typical relative distance of one hundred meters up to the docking, a dedicated navigation equipment is required for taking over the no more efficient relative GPS accuracy and for providing relative attitude measurements during the last meters. The current baseline for such a navigation system relies on optical RV sensors (RVS), the initial sensor acquisition being required before the final translation. Among the various candidate technologies, the proposed concepts are based on CCD camera (see Figure 16) which deliver two lines of sight (LOS) measurements, a relative range measurement and a relative attitude measurement during the last 20 meters.

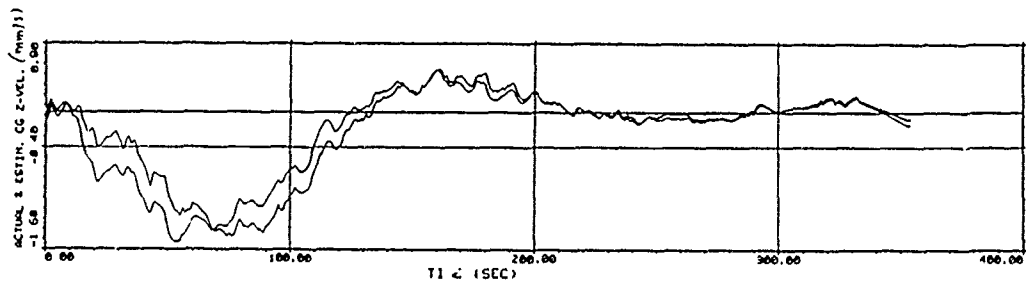
14-12



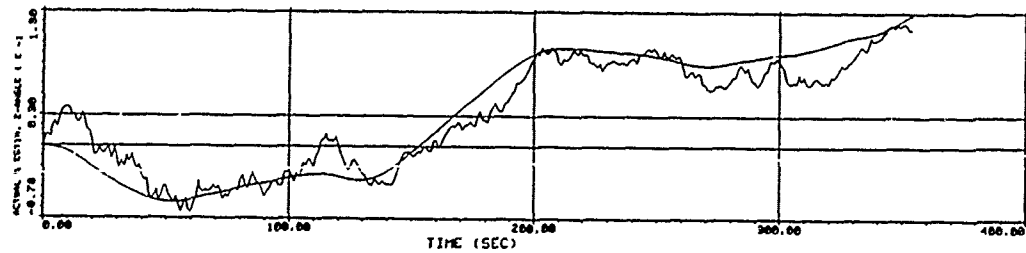
Actual and estimated lateral position of the chaser docking port in the TDF (mm)



Lateral velocity of the chaser docking port in the TDF (mm/s)



Actual and estimated lateral velocity of the chaser CG in the TDF (mm/s)



Actual and estimated relative attitude (degrees)

Figure 15 : Simulations for the last meters approach

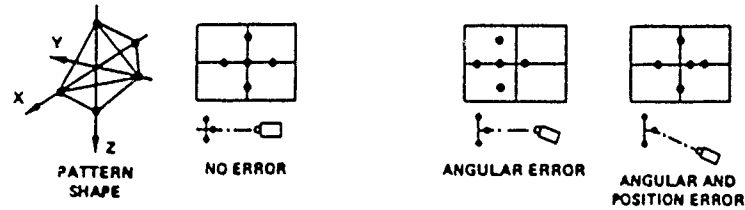


Figure 16 : RVS concept based on CCD cameras

The architecture of the navigation system must take into account the FO/FS and safety/reliability criteria as well as constraints on the mass and the complexity of the whole system. A compromise between these antagonist requirements leads to the following sensor configuration :

RVS	2
GPS	2
IMU	3
STS	2
HUD	1

In the case of a double failure requiring an emergency re-entry, a back-up mode compatible with re-entry constraints and using no additional hardware must be defined. To cover the contingency of a double GPS receiver or GPS unavailability, the selected back up mode is to use the DRS measurements processed on ground. This is the only case where the navigation function is not performed autonomously. The attitude estimation back-up mode uses the Head-Up Display (HUD) measurements before de-orbiting in order to bound the attitude estimation divergency and to enable orbital guidance, together with a specific deorbiting strategy coupled with GPS measurements for providing an improved initial attitude estimation to the re-entry navigation.

4.2 - Relative GPS navigation principle

An autonomous on-board orbit estimation is required and thus HERMES must be able to update an orbit model by its own measurement capabilities. The GPS system is the selected measurement mean for this orbit estimation. The good performances offered by GPS make it probably oversized for the only orbital drift phase, but first, its utilization can be optimized for power management and secondly, it offers the following mission oriented advantages :

- GPS can be used during reentry,
- Relative GPS navigation technique provides an accurate navigation during the rendezvous up to 100 m ,
- Differential GPS with respect to a ground beacon can be used during the landing.

The relative navigation principle using GPS will now be described.

4.2.1 - GPS measurements

The NAVSTAR GPS is based on a constellation of 18 satellites (minimum number) placed on circular orbits at the altitude of 20000 km. The information delivered by each GPS satellite (GPSS) consist in the current ephemeris of the satellite and the GPS date. Comparing the GPS date of the message with the HERMES time yields the so-called pseudo-range information :

$$\|\vec{r}_H - \vec{r}_i\| + c \delta t$$

where \vec{r}_H is the HERMES absolute position, \vec{r}_i the GPSS absolute position, δt the desynchronization between HERMES time and GPS time (the GPSS are all synchronized). A range rate measurement can also be performed using the Doppler effect on the GPS signal carrier. Proceeding by triangulation from three pseudo-range measurements would yield the desired absolute position if $\delta t = 0$. As the HERMES and GPSS clocks are not synchronized, a fourth pseudo-range measurement is required to recover a reliable position estimation. The triangulation accuracy crucially depends on the geometric distribution of the GPSS in visibility. If \vec{u}_i is the unitary vector defining the LOS HERMES-GPSS_i, and H the 4x4 matrix

of the selected

$$H = \begin{bmatrix} \vec{u}_1 & \vec{u}_2 & \vec{u}_3 & \vec{u}_4 \\ 1 & 1 & 1 & 1 \end{bmatrix}$$

LOS, then the positive number :

$$\text{tr}(H^T H)^{-1}$$

(named as the Global Dilution of Precision (GDOP)) characterizes the achievable positioning performances . the smaller it is, the better the localization. With more than four GPSS in visibility, a selection which minimizes the GDOP is recommended. Otherwise, in the frame of a pure GPS point navigation, the position is no longer observable due to the clock drift. The appearance frequency of such unobservability conditions highly depends on the receiver antenna aperture.

The main source of GPS measurement errors comes from the selective availability (SA) concept attached to NAVSTAR procedures : for civil applications, a low frequency coded degradation is superposed to the original signal. Other perturbations due to :

- the GPS receiver noise,
- the GPSS ephemeris errors,
- the ionosphere propagation,
- the clock divergence between HERMES and the GPSS.

are also to be considered. Table 6 gives the error allocation on the pseudo-distance measurements.

SOURCES	ERROR (1σ)
SA + GPSS ephemeris + satellite clock	30 m
user receiver	10 m
ionosphere	15 m
Total	33 m

Table 6 : Error allocation on pseudo-range measurements

4.2.2 - Relative GPS navigation filter

In the HERMES RV mission, the target is assumed to be equipped with GPS receivers and to transmit its own dated GPS pseudo-range to HERMES. An important improvement of the GPS absolute navigation can then be achieved by directly subtracting the pseudo-range measurements of both vehicules which leads to the relative pseudo-range "measurement" .

$$\vec{u}_i \cdot \vec{R} + c \delta t$$

where \vec{R} is the relative position of HERMES and CFF in the TOF and δt the clock desynchronization between both vehicules. In this operation, the slowly varying SA bias as well as the propagation disturbances and the GPSS ephemeris bias are nearly eliminated. Residual errors due to the non simultaneity of the chaser and target measurements are neglectable if a synchronisation better than 1 second is achieved. On the contrary, the GPS receivers noises are amplified by a factor $\sqrt{2}$. In order to prevent the bad GDOP configurations and to filter the measurement noise, an optimal filtering will be performed through a Kalman filter using an on-board prediction model of the chaser movement in the TOF (see Section 3.1) A two-order model of the clock drift is integrated to the prediction model. The global prediction model can be expressed as :

$$\dot{X} = A X + B \hat{U} + \hat{p}_x$$

and the measurement equation :

$$Y = C(t) X + p_y$$

where the following notations are used :

$$\begin{array}{ll}
 X = (x, y, z, \dot{x}, \dot{y}, \dot{z}, c \delta t, c \delta \dot{t}) & \text{relative state (position, velocity, clock drift)} \\
 \hat{U} = (\hat{\gamma}_x, \hat{\gamma}_y, \hat{\gamma}_z)^T & \text{estimated thrusting accelerations} \\
 \hat{p}_x & \text{estimated perturbations (differential air drag)} \\
 Y = (r_1, r_2, r_3, r_4)^T & \text{relative pseudo-range measurement (linearized)} \\
 \text{with } r_i(t) = \vec{u}_i \cdot \vec{R} + c \delta t \quad (\vec{R} = (x, y, z)^T) &
 \end{array}$$

$$A = \begin{bmatrix} A_{CW} & 0_{6,2} \\ 0_{2,6} & 0 \ 1 \\ & 0 \ 0 \end{bmatrix}, \quad B = \begin{bmatrix} 0_{3,3} \\ I_{3,3} \\ 0_{2,3} \end{bmatrix}$$

$$C = \begin{bmatrix} \vec{u}_1^T & & 1 \ 0 \\ \vdots & 0_{3,3} & \vdots \\ \vec{u}_4^T & & 1 \ 0 \end{bmatrix}$$

and the \vec{u}_i 's are the chaser-GPSS estimated LOS. The unmodeled perturbations which must be considered for designing the Kalman estimator are :

- the error on the thrust estimate (including attitude estimation error, thruster misalignment, thrust level error, ...),
- the neglected second-order terms in the CW dynamics,
- the residual term due to the target orbit eccentricity,
- the error on the differential air drag estimation,
- the differential effect of the J2 gravity term.

As seen above, the measurement errors essentially proceed from the GPS receiver noises. It is worth noting that the measurement model is non stationary since it varies w.r.t. the selected GPSS configuration. A discretized linear prediction model at a sample time T_p can be used :

$$X_{n+1} = F X_n + G \hat{U}_n + \hat{p}_n^X$$

$$Y_n = H_n X_n$$

with

$$F = \exp(AT_p), \quad G = \int_0^{T_p} \exp(A(T_p - \tau)) \cdot B \, dt$$

$$H_n = C(nT_p)$$

which leads to the Kalman estimation procedure described in Table 7 (R is the covariance matrix of the measurement noises)

	ESTIMATE	ERROR COVARIANCE	GAIN
PROPAGATION	$\hat{X}_{n+1} = F \hat{X}_n + G \hat{U}_n + \hat{p}_n^X$	$P_{n+1} = F P_n F^T + Q_n$	-
UPDATING	$\hat{X}_n^+ = \hat{X}_n + K_n (Y_n - H_n \hat{X}_n)$	$P_n^+ = (1 - K_n H_n) P_n (1 - K_n H_n)^T + K_n R K_n^T$	$K_n = P_n H_n^T (R + H_n P_n H_n^T)^{-1}$

Table 7 : Propagation of the state estimation

The optimal design results of a compromise between the rejection of the perturbing accelerations and the filtering of the measurement noise. As the perturbing accelerations are far from being ideal white noise, an artificial state perturbation matrix Q_n must be selected and tuned in order to achieve optimal performances. Due to the fact that the perturbation level greatly varies during the homing/closing, the matrix Q_n cannot be constant. At the interface between the transfer phase and the homing phase, the error covariance matrix is transmitted for the initialization of the filter.

4.2.3 - Navigation performance assessment

In order to assess the navigation filter performances, the mean and the covariance of the estimator error are propagated along the reference trajectory (see Section 3.1). Set :

$$\begin{aligned} e_n &= \hat{x}_n - x_n && \text{state estimation error} \\ \delta u_n &= \hat{u}_n - u_n && \text{thrust estimation error} \\ m_n &= E\{e_n\} && \text{mean value of the estimation error} \\ P_n &= E\{(e_n - m_n)(e_n - m_n)^T\} && \text{covariance of the centered estimation error} \\ Q_n^{nc} &&& \text{true covariance of the perturbations} \\ R_n &&& \text{covariance of the GPS relative measurements} \end{aligned}$$

Then, the error propagation is given in Table 8.

	ESTIMATION ERROR MEAN	ESTIMATION ERROR COVARIANCE
PROPAGATION	$m_{n+1} = F m_n + G \delta u_n + E\{p_n^X\}$	$P_{n+1} = F P_n F^T + Q_n^{nc}$
UPDATING	$m_n^+ = (1 - K_n H_n) m_n$	$P_n^+ = (1 - K_n H_n) P_n (1 - K_n H_n)^T + K_n R K_n^T$

Table 8 : Propagation of the estimation error mean and covariance

The global performance on the i^{th} position or velocity variable is obtained from the corresponding error mean m_i and the corresponding diagonal elements σ_i^2 of the error covariance matrix by the formula

$$\text{worst case performance / } i^{\text{th}} \text{ variable} = m_i \pm 3 \sigma_i$$

Navigation performance analysis during the homing and the closing phases have been carried out Figures 17 and 18 show typical propagations of the global performance for each subphases. The chaotic fluctuations are due to the GDOP variations of the selected GPSS which induces transient evolutions of the Kalman filter. This clearly illustrates the high degree of non stationarity of the estimation problem.

4.3 - Navigation during the final approach

The short range relative navigation of HERMES (from 100 m to the docking) is based on the use of RV sensors which provide one relative range measurement, two LOS measurements and three relative attitude measurements (the later during the last 20 meters). Typical performances of such sensors are shown on Figure 19. The proximity operation can be decomposed into two main subphases. From 100 m to 20 m, only the relative position and velocity of HERMES center of gravity (CG) are estimated via LOS and range measurements. The continuity with the previous phase is guaranteed since the estimated state and

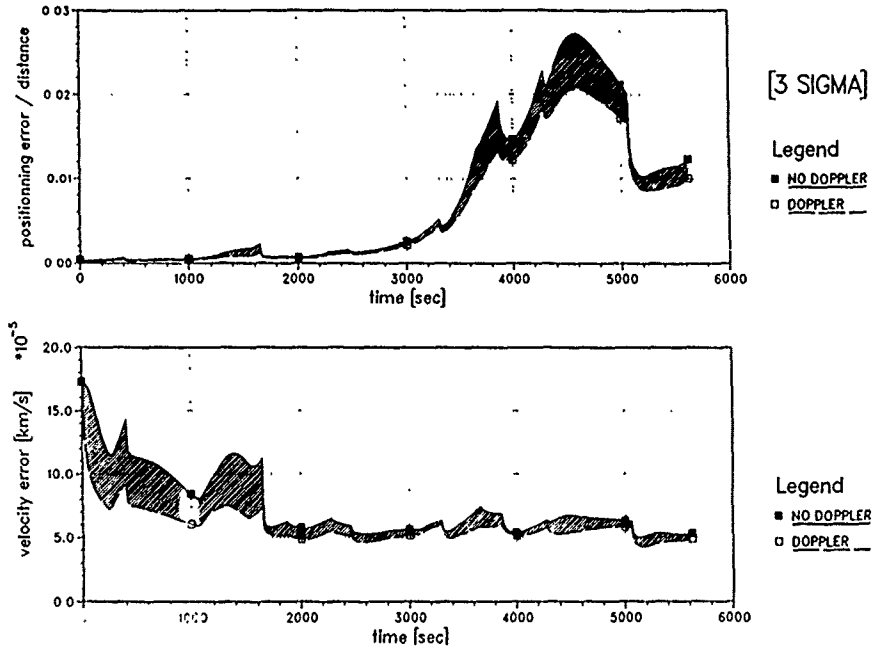


Figure 17 : Navigation performances during the homing (up to 1 km)

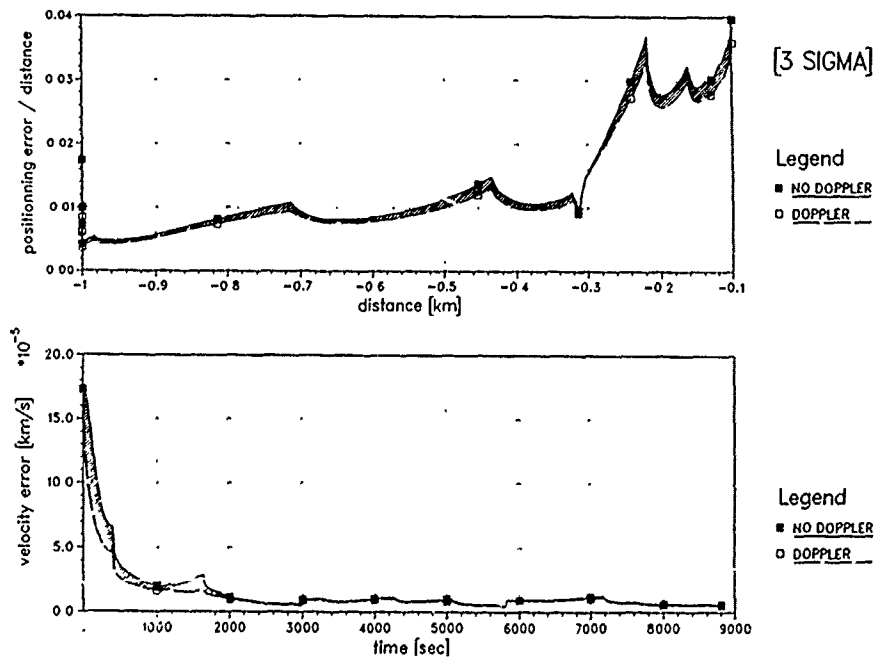


Figure 18 : Navigation performances during the closing (1 km to 100 m)

the prediction error model are the same. In the final path, from 20 m to the docking, the position and velocity of HERMES docking port center in the target docking frame (TDF) must be estimated and controlled. Then, the measurement of the relative attitude of HERMES w.r.t. the Space Station must be taken into account. During this phase, the HERMES gyro measurements are also used as well as an estimation of the absolute CFF attitude in its local orbital frame.

To simplify, the problem of estimation will be stated without considering the out-of-plane motion. Only the dimensioning phase 20m to 0m is considered. The notations correspond to those of Section 3.3. The function assigned to the navigation filter is to deliver an estimation of the following variables :

- 1) HERMES-target relative attitude θ , and target absolute angular rate,
- 2) axial position x and velocity \dot{x} of the HERMES docking port center in the estimated TDF,
- 3) lateral position z and relative velocity \dot{z} of the HERMES CG in the estimated TDF.

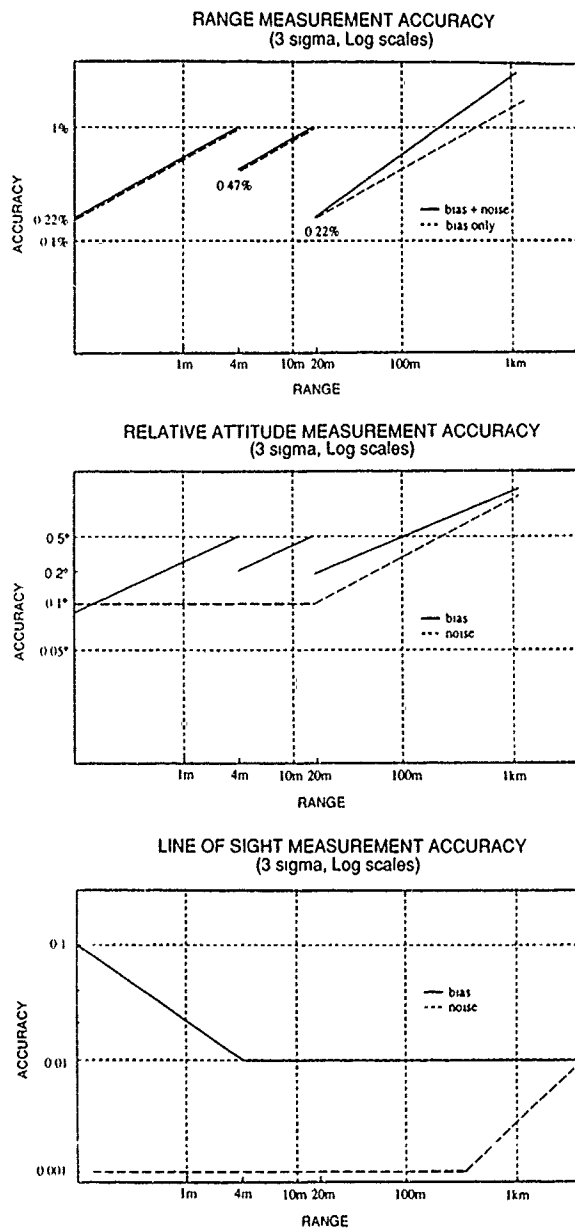
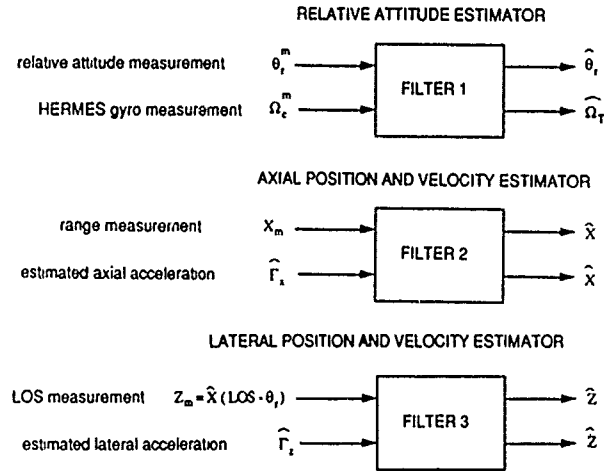


Figure 19 : RVS performances versus range

For a preliminar evaluation of the achievable navigation performances, an estimation filter has been designed as a triple of (α, β) -filters for each group of variables :



The predictor model is given by the dynamical equations described in Section 3.3. For convenience, the estimation of the relative lateral velocity is replaced by that of the relative velocity \dot{z} of HERMES CG in the estimated TDF. The (α, β) -filters equations then can be written as :

$$\begin{aligned}\dot{\hat{\theta}}_r &= \Omega_c^m - \hat{\Omega}_T + \alpha_1 (\theta_r^m - \hat{\theta}_r) \\ \dot{\hat{\Omega}}_T &= \beta_1 (\theta_r^m - \hat{\theta}_r) \\ \dot{\hat{x}} &= \dot{x} + \alpha_2 (x_m - \hat{x}) \\ \dot{\hat{x}} &= \beta_2 (x_m - \hat{x}) + \hat{\Gamma}_x \\ \dot{\hat{z}} &= \dot{z}_c + L_C \Omega_c^m + (\hat{x} + L_T) \hat{\Omega}_T + \alpha_3 (z_m - \hat{z}) \\ \dot{\hat{z}}_c &= \dot{x} + \hat{\Gamma}_z + \beta_3 (z_m - \hat{z})\end{aligned}$$

Owing to the coupling between the attitude and the lateral velocity chains, this design is not quite optimal but is expected to be representative of the actual on-board filter performances. The (α, β) -gains are to be optimized so as to obtain a good compromise between the filtering of RVS noise (low bandwidth required) and the attenuation of the perturbations due to the lack of knowledge on the target angular movement (large bandwidth required). The residual axial velocity required for the docking mechanisms fitting is a dimensioning parameter : the larger it is, the wider the desired bandwidth. An improvement of the navigation performances can be obtained in the case where the target gyro measurements are transmitted to HERMES. However, this possibility would be investigated only if necessary. A less constraining mean for reducing the required navigation bandwidth consists in switching off the attitude control system of the target during the last meters preceding the docking which makes easier the estimation tasks.

A covariance analysis of the navigation errors can be performed as described in the previous section. The main prediction errors which must be taken into account in this analysis come from :

- the guidance and control boosts misalignments and unaccuracies (calculated on a reference trajectory),
- the poor differential drag estimation,
- the target attitude behaviour,
- the plume impingement effects.

Preliminary simulation results are shown on Figure 20, which seem compatible with the specifications on the kinematic conditions for the docking.

	ΔZ	$\Delta \dot{Z}$	$\Delta \theta_z$	$\Delta \dot{\theta}_z$	$\Delta \dot{X}$
NAVIGATION PERFORMANCES BEFORE TARGET AOCS SWITCH (X = 50 cm)	3 mm	6 mm/s	0.28°	0.05°/s	0.4 mm/s
NAVIGATION PERFORMANCES AT TARGET AOCS SWITCH (X = 5 cm)	0.22 mm	1.6 mm/s	0.2°	0.01°/s	0.4 mm/s

Figure 20 : Navigation performances : final translation

5 - MAN INVOLVEMENT IN THE RVD TASKS

5.1 - Man Machine Interaction and Task Allocation

RVD with intensive intervention by man has been demonstrated many times in orbit with man acting as sensor, processor and actuator. However, the technology has also made it feasible to perform a completely automatic RVD. Although it is true that automatic systems perform better than man in tasks which require either fast processing of huge amounts of data, fast and accurate detection or actuation, continuous restless operation or operation in hostile environment, it must also be acknowledged that some human capabilities are still unchallenged by the most powerful automatic systems. This is due to the human ability to use judgement, to infer from fuzzy information, to react in case of unexpected or unanticipated events, to learn from experience, to formulate new strategies, ...

The allocation of tasks to man and machine cannot be an either/or process, i.e. either man is better and he is in charge, or the machine is better and man is excluded. This approach has been overtaken by technological progress and does not consider such important factors as the requirement for the man to be involved permanently in order to be ready to exercise his superior capabilities if necessary. Moreover, the either/or approach does not consider that the best performance of the automatic system can only be achieved if the real environment in which it has to operate actually corresponds to what was forecast during its design. This approach ignores the fact that man, although not as accurate and efficient in some automatic tasks, can intervene just to correct these unanticipated deviations by superimposing his correction to the action of the machine in order to achieve the desired performance.

Therefore, the allocation of tasks should rather be a result of an integrated design process. Man and automatic systems must then be considered from the beginning with their capabilities and limitations and proper criteria must be defined from which the allocation of tasks has to be performed. The ultimate goal is to obtain a symbiotic cooperation of man and machine, in which man and machine complement each other in order to obtain the safest possible system, and within such a system, to optimize the performance.

5.2 - Possibilities for man involvement in the GNC tasks

The possible levels of involvement of the pilot in the GNC process are shown in Figure 21. Their are related to :

- the manual update of the state estimation (point 1),
- the manual adaptation of guidance parameters (point 2),
- the manual guidance commands (point 3),
- the manual control commands (point 4),
- the manual command of individual thrusters (point 5)

Pilot involvement in GNC tasks may be planned for nominal modes which are not fully automatic, or for nominal modes which, although being fully automatic, could benefit from the intervention of man e.g. to correct unexpected biases, or for backup and emergency modes to replace a failed automatic system.

5.3 - GNC functions in nominal modes of RVD

On the basis of the results of past works on unmanned spacecraft RVD, and taking into account the requirements, capabilities and limitations of the automatic system and the pilot, a concept has been proposed for the HERMES GNC during RVD. The concept assumes that in nominal modes, GNC functions are performed by the automatic system. The pilot has the role of supervisory control which includes :

- involvement in the mission and in the vehicle configuration management tasks,
- monitoring of the operation of the GNC system, which requires complete observability, including visibility of the target at short distance,
- cooperation with the automatic GNC system to correct small deviations (vernier control).

The vernier control by the pilot is explained with reference to Figure 22. The automatic system estimates the relative chaser position and attitude. The pilot compares these estimations with the actual position and attitude as viewed via the video camera system and introduces an additional innovation to the state update block. This can be made by superposing a dynamic pattern generated by the automatic system from the state estimate with the actual pattern obtained by the video camera. Using the side stick, the pilot moves the artificial pattern and makes it coinciding with the real pattern. The motions of the artificial pattern are translated into innovation signals which are fed to the state update software of the automatic system. In this

concept, the resources of the automatic system are fully used and the pilot is called upon to supplement the system by correcting the unexpected errors.

The required observability is given to the pilot by means of :

- caution and warning function,
- synthetic data consistent with the current control mode,
- granting access to all system information on request,
- direct or camera-assisted view of the target during the final approach through the Crew Vision System (CVS).

The supervision by the crew passes through the Man Machine Interface devices, ergonomically arranged in the HERMES cockpit. The proposed cooperation between man and machine can be stated as follows. As regards to the mission management, highest authority for the selection of mission objectives and strategies belongs to the ground and the crew. The pilot sets strategy parameters and GNC system modes while the automatic system provides the pilot with the necessary aids to perform its role. Automatic operation sequencing and monitoring is performed, the pilot giving go ahead commands at key points. At any time, the pilot has the capability to override the automatic process. As concerns the vehicle management, the machine performs the vehicle configuration setting and keeping, including FDIR, and reports to the mission management level and to the pilot through the MMI. The pilot cooperates in FDIR tasks and may command vehicle configuration changes consistent with the selected operating mode.

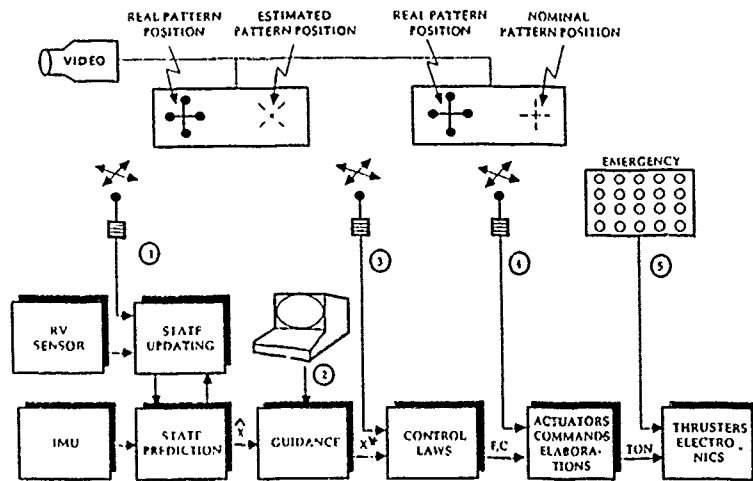


Figure 21 : GNC system operability by the pilot

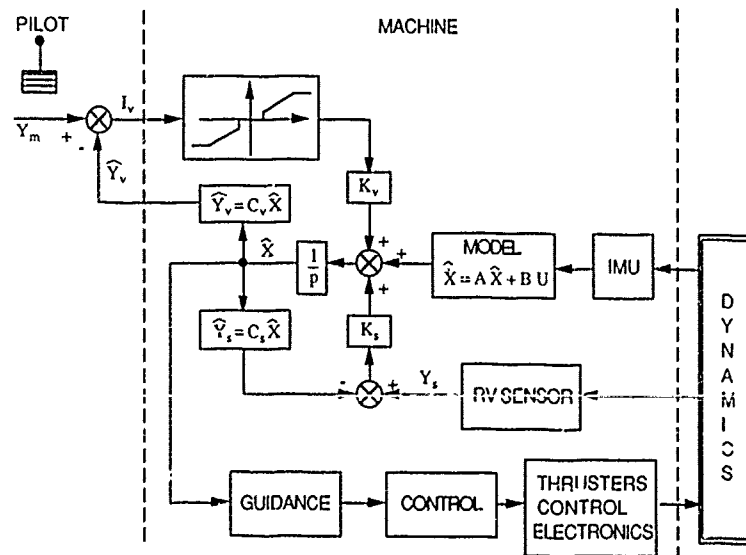


Figure 22 : Manual vernier control scheme

6 - CONCLUSION

In this paper, some concepts for the HERMES Rendezvous system have been examined. A particular attention has been devoted to the description of the mission requirements and constraints, mainly dictated by the safety rules attached to the HERMES-CFF mission. Strategies for the guidance and control design during the critical phases of the RV have been analysed and compared in terms of performances and robustness w.r.t. failure. The navigation system selected and designed for HERMES has been presented, with some emphasis on the GPS navigation dedicated to the homing phase and the optical navigation during the final approach. The crew involvement in the GNC and management process has been also discussed.

7 - REFERENCES

- [1] The role of pilot and automatic onboard systems in future rendezvous and docking operations,
W. Fehse, A. Tobias, A. Getzschmann, M. Caidichoury, P. Maute, M. Attanasio
39th Congress of the International Astronautical Federation, Oct. 1988, Bangalore, India
- [2] Multifunction spacecraft attitude estimation and navigation system,
J.C. Amieux, B. Claudinon
AGARD Conference, Septembre 1983, Florence, Italy
- [3] HERMES project : Etudes de navigation-guidage pour le rendez-vous - Phase B3
Technical Report - H-NT-1-001-MAT
F. Chaplais, V. Guillaud, P. Riant
Juillet 1988
- [4] HERMES Preliminary Navigation definition file
Technical Report H-DD-1-001-MAT
M. Frezet, M. Janvier, P. Riant, A. de Rosnay, L. Vandenhautte
June 1989
- [5] Rendez-vous en orbite : guidage, navigation et controle en phase de rapprochement
Final report, phase 2A, S375-RT-11.89
E. Desplats, C. Champetier
June 1989

SPACECRAFT ATTITUDE DYNAMICS: EVOLUTION AND CURRENT CHALLENGES

V.J. Modi

Department of Mechanical Engineering
The University of British Columbia
Vancouver, B.C., Canada, V6T 1W5

ABSTRACT

The paper briefly reviews complex interactions between flexibility, deployment, environmental forces and attitude dynamics during both steady state and transient phases. The available literature on the subject is cited through several review papers which would give fair understanding of its present state. Parametric studies suggest that critical combinations of system variables can drive the spacecraft unstable, however, suitable control strategies are available to restore equilibrium. Emphasis throughout is on methodology of approach to complex dynamical systems and analysis of results to gain better physical appreciation as to their response character. To that end mathematical details are purposely avoided. Evolution of the field and current challenges are illustrated through examples involving a variety of configurations of contemporary interest.

1. INTRODUCTION

Motion of a spacecraft presents two dynamical aspects of interest. The most obvious one is the trajectory traced by its center of mass which is governed by the classical Keplerian relations. However, spacecraft are not point masses as Kepler assumed in the analysis of planetary bodies. They have finite sizes and hence inertias. Thus a satellite while negotiating a trajectory may execute rotational motion about its center of mass commonly referred to as libration (Fig. 1). In this presentation we will be concerned with librational dynamics and stability of the Earth orbiting systems.

There are numerous situations of practical importance such as communications, scanning of cloud cover for weather forecasting, survey of earth resources, scientific and military observations, etc., where it is desirable to maintain a satellite in a fixed orientation with respect to the Earth. Unfortunately, even though a spacecraft may be precisely oriented at launch, it tends to deviate from this preferred orientation under the influence of environmental forces in the form of the solar radiation pressure, interactions with the Earth's gravitational and magnetic fields and, if the spacecraft happens to be close to the Earth, free molecular reaction forces (Fig. 2). Internal motion of payload, astronauts and sloshing propellant as well as coupling of the attitude dynamics with the orbital and flexural mechanics may add to the problem. This leads to undesirable librational motion which must be controlled for successful completion of a given mission.

Several methods of attitude control have been developed over the years. Broadly speaking they may be classified as active and passive techniques.

Active stabilization procedures involve large expenditure of energy usually in the form of microthruster units, momentum gyros and reaction wheels. Sometimes the whole satellite is turned into a gyroscope as with the spin-stabilized and dual-spin systems. But energy is a very expensive commodity aboard an instrument packed spacecraft. A satellite can carry only a limited amount of fuel (energy) for librational control. Once the energy supply is exhausted there is no attitude control left, the satellite succumbs to the disturbances, starts tumbling and the mission is disrupted. The spacecraft has to be discarded although its structural and electronic systems may be functional. This, of course, is quite extravagant. It is somewhat like discarding an expensive automobile just because it has run out of gas (petrol). Most early communications satellites used to have a life-span of 4-7 years which is now extended to 6-10 years thus requiring their periodic replacement at an enormous cost.

Stabilization techniques demanding very little or virtually no power consumption are termed passive. This is generally achieved by designing satellites with physical characteristics (such as booms; flaps like aileron, elevator and rudder of an airplane; magnetic dipoles, etc.) which interact with the environmental forces in a manner so as to maintain a specified orientation. Environmental forces such as the gravity gradient, solar radiation pressure, earth's magnetic field and, for near earth satellites, free molecular reaction forces are available for ever at no cost. Modi et al. have reviewed the relevant literature in two papers [1,2] citing 132 and 223 references, respectively. A subsequent paper by Markland, primarily aimed at the attitude control of communications satellites, complements the above two studies [3, 47 references].

The vast body of literature reflects logical evolution of the spacecraft design, the problems it posed and the analyses needed to explore their resolution. It can be classified in a number of ways depending on the objective, however, from dynamics and control considerations following areas of development appear distinct:

- (a) formulation methodologies particularly for multibody systems with open or closed topology;
- (b) dynamics and control of: (i) rigid systems; (ii) rigid systems in the presence of environmental forces; (iii) systems with flexible appendages; (iv) transient behaviour during deployment and retrieval, evolving structures such as integration of the proposed Space Station Freedom; (v) flexible systems in the presence of environmental forces.

Objective here is to briefly touch upon some salient features of dynamical performance through typical examples, each representing a large class of systems, with further details left to references.

2. RIGID SYSTEMS

To help appreciate physical aspects of the system dynamics, we will purposely consider a simple configuration of an axisymmetric, gravity oriented, nonspinning satellite in a circular orbit. Recognizing that the orbital perturbations due to librational motion are small [4,5], the classical Keplerian equations are still considered valid. This leads to the governing nonlinear, coupled equations of motion for inplane (α , pitch) and out-of-plane (γ , roll) degrees of freedom as [6]

$$\begin{aligned} \ddot{\alpha} - 2(\dot{\alpha} + \dot{\theta})\dot{\gamma} \tan \gamma + 3\dot{\theta}^2 K_i \cos^2 \gamma \sin \alpha \cos \alpha &= 0, \\ \ddot{\gamma} + [(\dot{\alpha} + \dot{\theta}) + 3\dot{\theta}^2 K_i \cos^2 \alpha] \sin \gamma \cos \gamma &= 0. \end{aligned} \quad (1)$$

Even without solving these equations one can get some appreciation as to the regions of possible motion and dynamical stability simply by studying the zero velocity plots,

$$C_H = (2H/I\dot{\theta}^2) - K_i = -\cos^2 \gamma (1 + 3K_i \cos^2 \alpha), \quad (2)$$

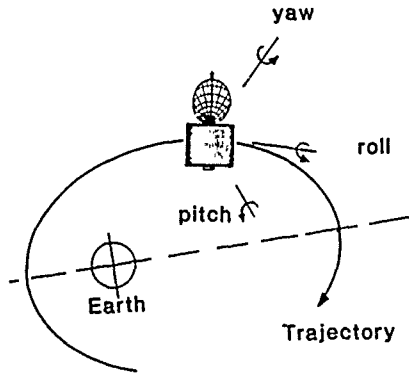


Figure 1 A satellite describing a trajectory and undergoing pitch, roll and yaw librations.

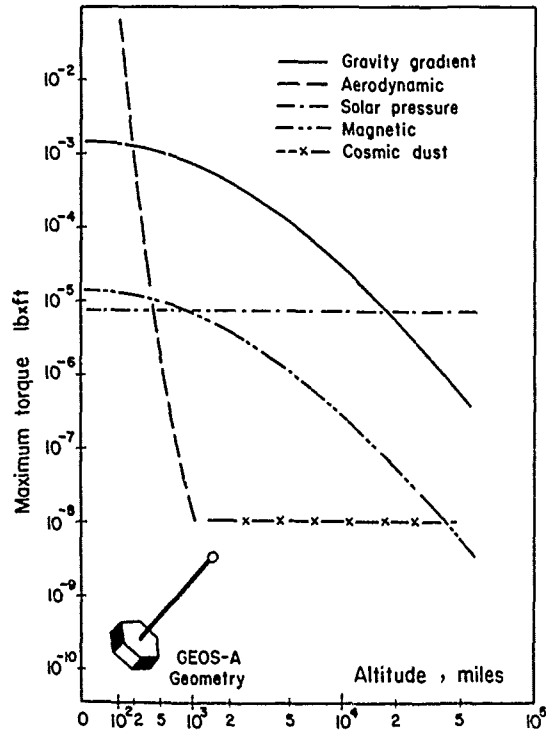


Figure 2 A chart showing the variation of environmental torques with altitude on GEOS-A satellite. Note, at the geostationary altitude of 22,300 miles (36,000 km) used by communications satellites, solar pressure and gravitational torques are of the same order of magnitude. Similarly for near earth satellites aerodynamic forces are dominant.

where, H , the Hamiltonian, is a constant of the motion as the Lagrangian function does not involve time explicitly. As the velocity becomes imaginary for a point outside a zero velocity curve, the librational motion can occur only when γ and α lie inside the domain bounded by the curve. Thus for: $C_H < -(1 + 3K_1)$, no motion is possible; $-(1 + 3K_1) \leq C_H \leq -1$, motion is bounded; $-1 \leq C_H \leq 0$, motion can be unstable only in α direction; $0 < C_H$, unbounded motion is possible in both coordinates. Typical zero velocity curves in α, γ -plane for $K_1 = 1$ are presented in Fig. 3.

Parametric analysis of a system, particularly with a large number of variables and a range of initial conditions of interest makes presentation of results in a concise form a challenging task. The concept of invariant surface or integral manifold, generated by what Hénon and Heiles [7] refer to as a 'numerical experiment', proves to be quite attractive to this end when the governing equations have periodic coefficient as in the present case. Modi et al. have described the process at length in a series of papers for gravity gradient [8-10] and spin-stabilized satellites [11,12] even in the presence of solar radiation pressure [13,14] and aerodynamic forces [15,16].

Consider, for example, an arbitrary satellite in an elliptic orbit of eccentricity 'e' undergoing planar librational motion governed by

$$(1 + e \cos \theta) \alpha'' - 2e(\alpha' + 1) \sin \theta + 3K_1 \sin \alpha \cos \alpha = 0, \tag{3}$$

where prime denotes differentiation with respect to θ , the true anomaly. An initial point $\alpha = \alpha_0, \alpha' = \alpha'_0, \theta = 0$ is chosen and equation (3) integrated over 2π . This produces a "consequent" point $\alpha = \alpha_1, \alpha' = \alpha'_1, \theta = 2\pi$ which may be considered as a new initial condition at $\theta = 0$. The process may be thought of as a transformation, defined by equation (3), of the initial point. The new starting point may itself be transformed, repeatedly, leading to a series of points in the α, α' -plane at $\theta = 0$. If any of the transformed points lies outside the region $-\pi/2 \leq \alpha \leq \pi/2$, all the points determined by the process lead to tumbling motion and may be plotted in the unstable region. Alternatively, the points may lie inside the region indicating stable operation and, when plotted, define a curve. This is an invariant curve of the transformation, i.e., the transformation of the curve lying in the $\theta = 0$ plane results in the same curve being generated at $\theta = 2\pi$. The two curves are connected by an infinity of trajectories defining a surface which may be called an "invariant surface".

Figure 4 represents such an invariant surface schematically. An initial condition interior to this surface results in the generation of a new surface which lies within the one shown. On the other hand, an exterior initial condition generates an external surface provided the motion continues to be stable. Hence the desired region of stability is represented by the interior of the largest invariant surface that can be constructed. Interior of the limiting invariant surface for $K_1 = 0.7$ and $e = 0.2$ is shown in Fig. 5.

The concept of a limiting surface represented in the phase space is very important. For a given eccentricity, it provides all possible combinations of initial angles and velocities to which a satellite may be subjected at any point in its orbit without causing it to tumble. Of equal significance is the fact that, at a critical combination of system parameters (e, K_1 , etc.), the stability region shrinks to a point; or in the phase-space representation the invariant surface degenerates to a single trajectory, showing the existence of a periodic solution.

One may explore a further possibility of condensation of information by taking an intercept of the manifold, say at $\theta = \alpha = 0$ as a measure of the system stability. Fig. 6 shows effect of eccentricity and inertia on the region of stability of a satellite undergoing planar librational motion. Note, for a dumbbell satellite ($K_1 = 1$), except for an isolated island, the system becomes unstable for $e > 0.33$ (Fig. 6a). For $K_1 = 0.1$ ($K_1 = 0$ is a sphere) the stability region has shrunk significantly, and stability beyond $e = 0.1$ does not exist. Of course, this is in absence of any active control. Thus the information can be used to advantage in designing an appropriate control depending on the system parameters and operating conditions.

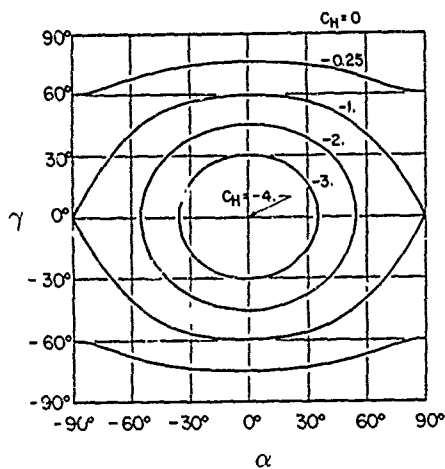
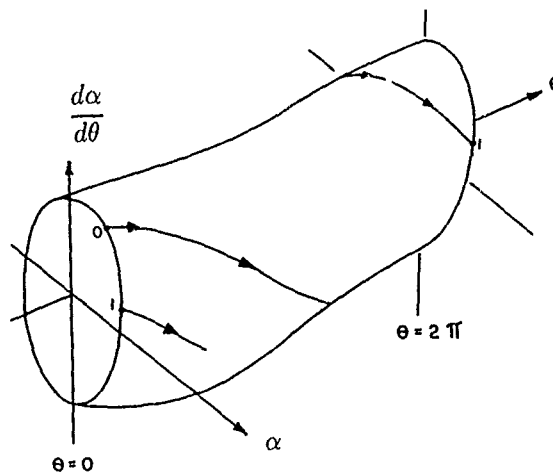
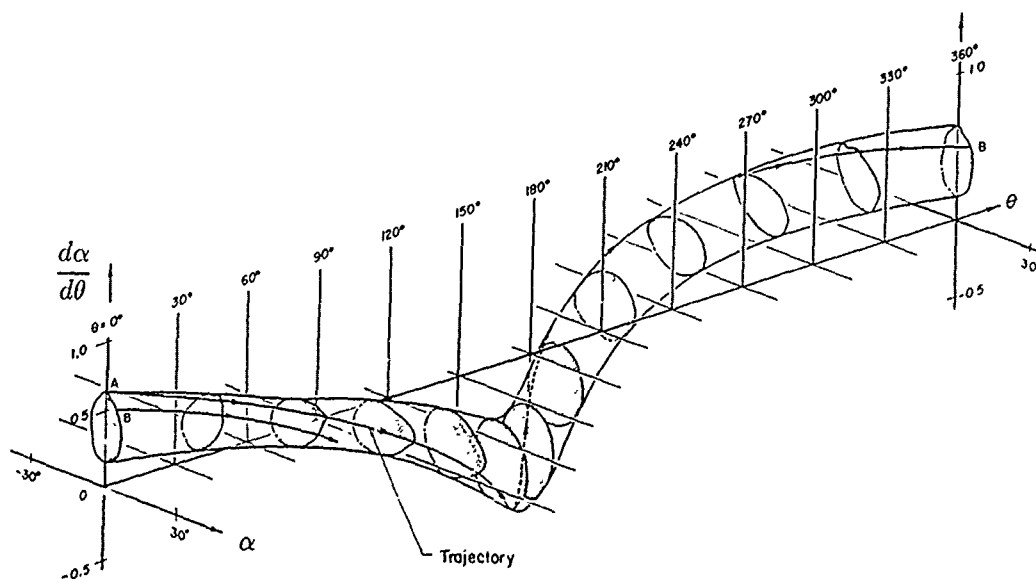
Figure 3 Zero velocity curves for $K_1 = 1$.

Figure 4 A schematic representation of an invariant surface.

As can be expected, environmental forces affect the margin of stability adversely [13,16]. A study of the spin stabilized satellites by Modi and Pande [17] brings home this point rather vividly. Significance of the inertia parameter $I(I_{yy}/I_{zz}$, ratio of the axial to transverse inertia, axisymmetric satellite), the spin-parameter σ (spin rate nondimensionalized with respect to the orbital rate) and the orbital eccentricity is quite apparent in Fig. 7. It shows variation of Φ , the angular deviation of the axis of symmetry from the orbit normal, as a function of θ . It is apparent that a judicious choice of parameter values is essential to avoid tumbling motion ($\Phi > \pi/2$). Of particular interest is a disturbing influence of the solar radiation pressure represented here by the parameter C . This dimensionless parameter depends on the satellite geometry and mass distribution, reflectivity and transmissibility of its surface, distance ϵ between the c.m. and the center of pressure, solar intensity and the perigee distance. Note that the value of C as small as 0.5, which would physically correspond to $\epsilon = 3$ cm for INTELSAT IV category of satellites causes the spacecraft to tumble over. Of course, in actual practice, a higher spin rate and/or active control system would counter this tendency. Nevertheless, the analysis clearly brings out the fact that the solar parameter C is of the same importance as I , σ and e in the design of the satellite attitude control system.

Figure 5 Limiting invariant surface showing the boundary of stability for $K_1 = 0.7$ and $e = 0.2$.

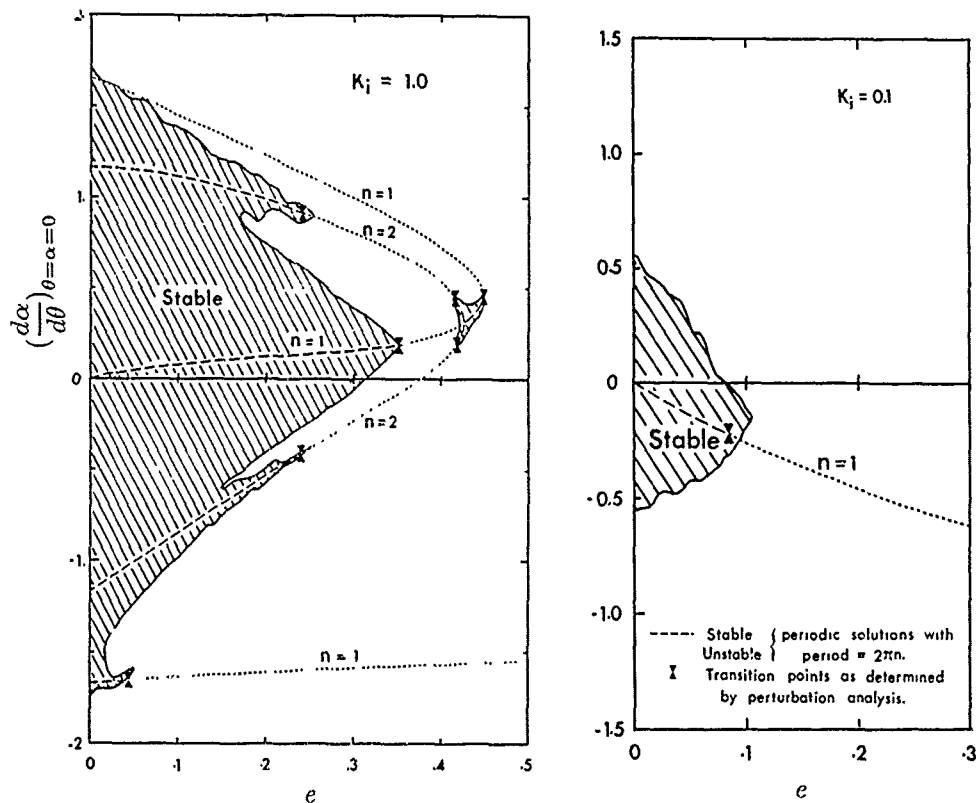


Figure 6 Stability in the presence of impulsive disturbances as affected by the orbital eccentricity: (a) $K_i = 1$; (b) $K_i = 0.1$.

2.1 Nonlinearity and Coupling

Nonlinearities and coupling between the degrees of freedom represent key factors governing response, stability and demand on the control system. To illustrate this point consider librational dynamics of the Orbiter. Fig 8 shows librational response of the Orbiter in a circular orbit when subjected to a relatively small disturbance of 0.05° in roll, yaw and pitch simultaneously. The response is evaluated using nonlinear as well as linearized approaches for the Orbiter in three different configurations. Note, except for local details, particularly at large angles of attack, the linearized approach seems to predict the trend towards instability accurately (Figs. 8a, 8b, 8c, 8d). During the small amplitude bounded motion (Fig. 8e), linear and nonlinear analyses yield virtually the same response as expected. The Lagrange configuration representing the minimum moment of inertia axis along the local vertical and the maximum moment of inertia axis aligned with the orbit normal is stable. Thus from control consideration, the Lagrange configuration will be less demanding in terms of fuel expenditure.

However, in the presence of a relatively large disturbance, the linear analysis would lead to misleading conclusions. This is clearly demonstrated through Fig. 9. The Lagrange configuration found to be stable under small disturbances is now subjected to a roll, yaw and pitch disturbance of 4° . Note, the linear analysis continues to predict bounded motion (Fig. 9a) while actually the system is unstable (Fig. 9c). It is of interest to recognize relatively large deviations from the equilibrium in the yaw degree of freedom (Fig. 9b), which becomes unstable within five orbits with a slightly larger disturbance (Fig. 9c).

To get better appreciation as to the system dynamics during transition to instability, the Lagrange configuration was subjected to pitch, yaw and roll disturbances separately (Fig. 10). With a pitch disturbance as large as 30° (Fig. 10a), the roll and yaw remain unexcited and the system is stable. The same is essentially true with a yaw disturbance (Fig. 10b). However, even with a relatively small roll disturbance (Fig. 10c), the diverging yaw oscillations set-in tending towards instability. Thus roll control seems to be a key to ensure stability of the Orbiter in the Lagrange configuration.

Figure 11 attempts to study the effect of roll control on the librational stability of the Orbiter in the Lagrange configuration. The spacecraft is in a circular orbit and is subjected to an initial disturbance in pitch as well as yaw of 4° . The roll is controlled using the primary and vernier reaction controls of the Orbiter with a typical time history over an orbit as reported by Budica and Tong [18]. Two different deadband limits are used, $\gamma_{max} = \pm 1^\circ$ (Figs. 11a, 11b) and $\pm 0.15^\circ$ (Figs. 11c, 11d), to have some appreciation as to the degree of control in roll needed to assure stability. The phase plane response in yaw is included to help judge the velocities involved. It is apparent that the roll control to the extent of $\pm 1^\circ$ is not adequate and the Orbiter becomes unstable in yaw within five orbits. However, with the deadband limits of $\pm 0.15^\circ$, the system returns to stability.

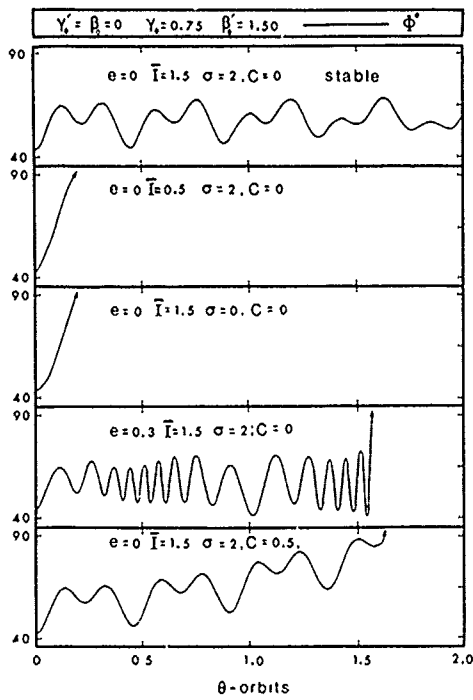


Figure 7 Response of a spinning satellite showing significance of various system parameters including the solar radiation pressure effect.

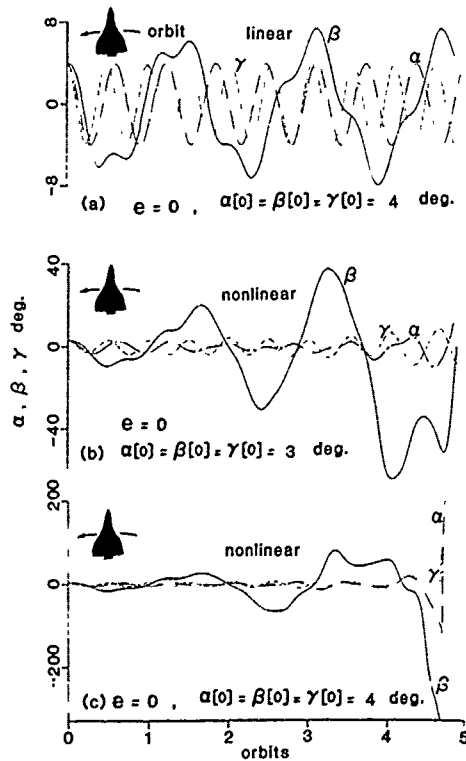


Figure 9 Plots showing inadequacy of the linear analysis to accurately predict instability of the Orbiter.

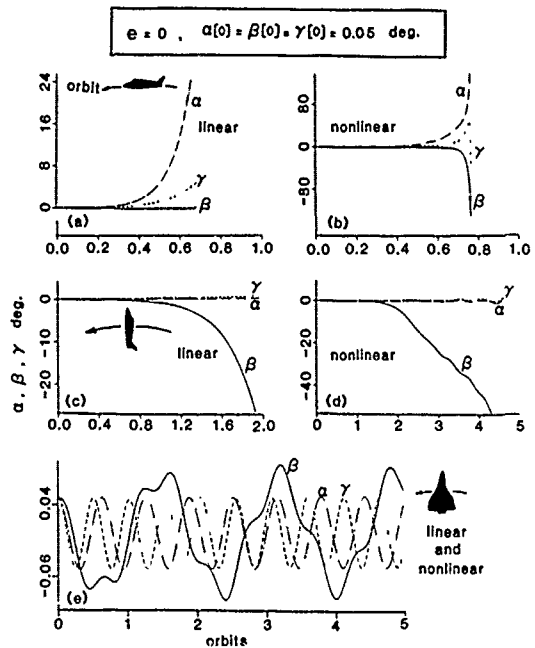


Figure 8 Comparison between linear and nonlinear responses to a small disturbance with the Orbiter in three different flight configurations.

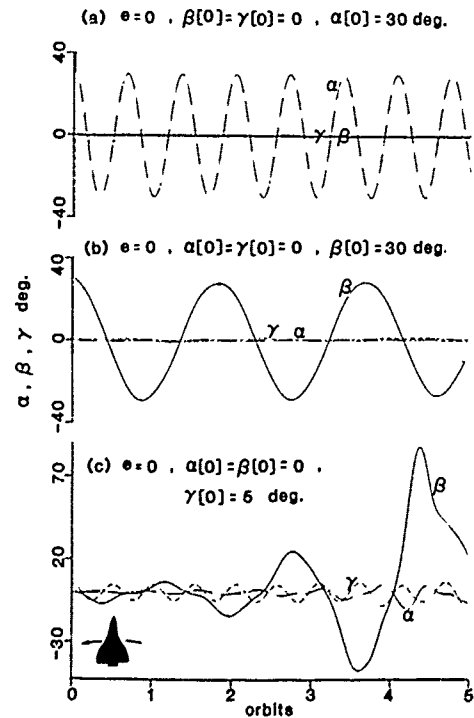


Figure 10 Librational response of the Orbiter to an independent excitation in pitch, yaw and roll. Note the pitch and yaw disturbances lead to essentially uncoupled stable motion. However, even with a relatively small disturbance in roll, the system appears to become unstable in yaw through its coupling with roll.

It was suspected that such a demanding control for stability may be due to sharp positive peaks in the roll time history caused by firing of the thrusters. Considerable extension in the deadband limits can be achieved through smoothing of the peaks. This is shown in Fig. 12, where the Orbiter's control strategy is improved to result in an approximately sinusoidal roll time history with the deadband limits of $\pm 6^\circ$. It also shows the effects of changing the roll control frequency. In Figs. 12a and 12b the roll control frequency is taken to be 2 cycles/orbit which approximately coincides with the natural frequency in roll of the uncontrolled Orbiter in the Lagrange configuration (Fig. 9). The system is unstable (Figs. 12a, 12b), however, with the frequency increased to 6 cycles/orbit the system regains stability (Figs. 12c, 12d). Thus an increase in the roll control frequency as well as reduction in the sharpness of the peaks in the roll time history appear to promote stability. This is a useful design information as at a frequency of around 13 cycles per orbit, normally used in the actual practice, the deadband limits can be further relaxed.

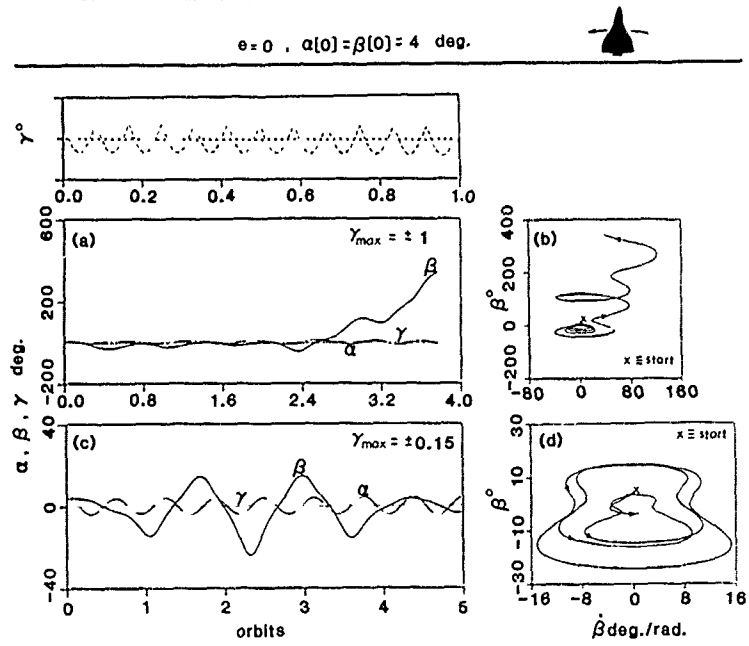


Figure 11 Librational response of the Orbiter in the Lagrange configuration with the time history of roll control actually used in practice.

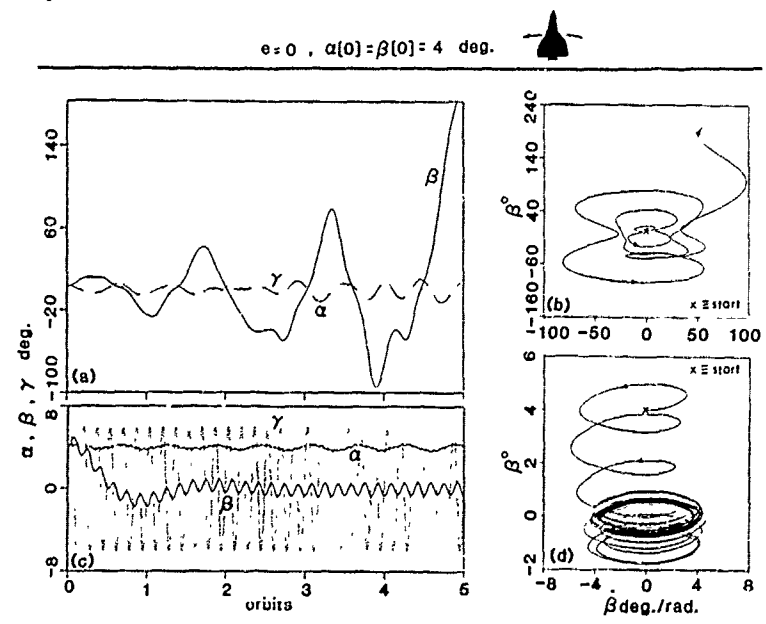


Figure 12 Effect of smoothing of the peaks and frequency of the roll control on the Orbiter's librational response.

NATIONAL AERONAUTICS AND SPACE ADMINISTRATION
 TECHNICAL REPORT NO. D-700

3. FLEXIBLE SPACECRAFT : PRELIMINARY REMARKS

In the early stages of space exploration, satellites tended to be relatively small, mechanically simple and essentially rigid. However, for a modern space vehicle carrying lightweight deployable members, which are inherently flexible, this is no longer true. Several typical examples stress this point:

- (i) Ever increasing demand on power for operation of the on board instrumentation, scientific experiments, communications systems, etc., has been reflected in the size of the solar panels. The Canada/USA Communications Technology Satellite (CTS, Hermes) launched in January 1976 carried two solar panels, 1.14 m x 7.32 m each, to generate around 1.2 kW of power.
- (ii) Use of large members may be essential in some missions. For example, Radio Astronomy Explorer (RAE) satellite used four 228.8 m antennae to detect low frequency signals.
- (iii) Preliminary configurations of the next generation of satellites such as the European Space Agency's L-SAT (Olympus), Canada/USA's proposed Mobile SATellite (M-SAT), and many others suggest a trend towards spacecraft with large flexible members extending to several scores of meters.
- (iv) The Space Shuttle being operational and having proved its versatility in undertaking diverse missions, several proposals for its utilization as a platform for conducting dynamics experiments have been presented. They range over stability and control of large flexible members, manufacturing of structural components for construction of the proposed Space Station 'Freedom', extension of solar panels for augmenting the Orbiter's power (Solar Array Flight Experiment-SAFE, Fig. 13), deployment of gigantic hoop-column type antennae for mobile communications systems, and several others. In fact, NASA has shown considerable interest in exploiting application of the Space Shuttle based tethered subsatellite system, extending to 100 km (Fig. 14); and an experiment involving 20 km long electrodynamic tether is scheduled for launch in early 1991.

We must recognize that flexibility is a design choice dictated in part by a dichotomy of extremes in the force environment: very high accelerations during delivery to orbit followed by very low accelerations in the operational life. Generally, configuration size and weight are often severely constrained as a result of the launch vehicle limitations or structural strength of the satellite components. As a solution, spacecraft are initially packaged as compact rigid bodies. Once in orbit, various elements deploy to establish the desired configuration. In case of the proposed space station when under construction, partially completed components will be continually added thus changing the mass, inertia, flexibility and structural damping characteristics. The presence of environmental forces will only add to the problem.

It should be emphasized that prediction of satellite attitude motion is by no means a simple proposition, even if the system is rigid. Flexible character of the appendages makes the problem enormously complex. It is, therefore, understandable why transient behaviour associated with the critical phase of deployment related maneuvers has received relatively little attention. On the other hand, although deployment effects are of a transient nature, they may be felt over a long period of time as a result of relatively small extension rates that are normally associated with long appendages. The Space Shuttle based tethered satellite system mentioned before may take 6-8 hours to deploy and much longer to retrieve. Construction of a space station may extend over several years.

One may wonder: why not conduct ground simulation studies before taking a structure or its subassemblies in space? Remember, we are dealing here with flexible structures in microgravity environment having time dependent geometry and structural properties. In this situation, ground based simulation studies of prototypes and scale models have proved to be of doubtful value. This has led to more reliance on analyses than in the past. Trend has been towards development of analytical and numerical procedures which can be used with an increased level of confidence. Even with scale models, accurate simulation of gravity and other environmental forces has proved to be elusive.

This being the case, flexibility effects on satellite attitude motion and its control have become topics of considerable importance. Over the years, a large body of literature pertaining to the various aspects of satellite system response, stability and control has evolved which has been reviewed quite effectively by Likins, Modi, Williams, Roberson, and others [19,25]. In fact, a relatively recent issue of the Journal of Guidance, Control, and Dynamics published by the AIAA (American Institute of Aeronautics and Astronautics) contains a series of articles reviewing the state of the art in the general area of large space structures [26].

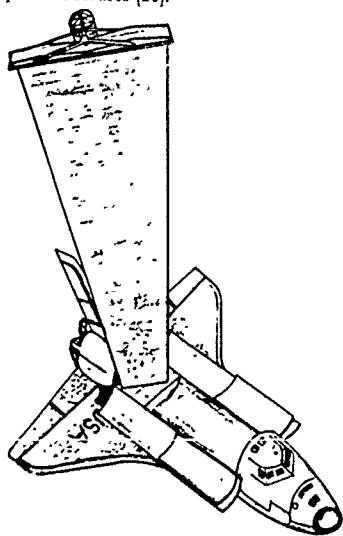


Figure 13 Orbiter based deployment of a 4x31 m solar array (Sept. 1984).

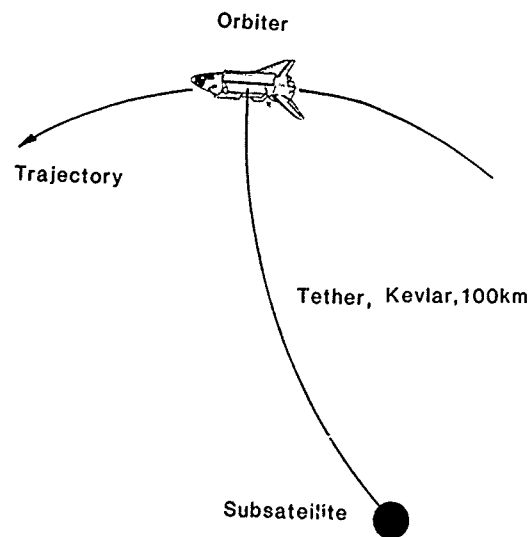


Figure 14 The Orbiter based tethered subsatellite system.

Attention is also directed towards planning of on-orbit experiments such as SCOLE (Spacecraft Control Laboratory Experiment) to check, calibrate and improve algorithms. It is generally concluded that on-orbit information acquired during the constructional phase of a space station is the only dependable procedure for its overall design. Obviously, this promises to open up an exciting area of in-flight measurements of structural dynamics, stability and control parameters necessary for design. With the U.S. commitment to an operational space station by late 1990's, the need for understanding structural response and control characteristics of such time varying, highly flexible systems is further emphasized.

4. MULTIBODY SYSTEM FORMULATIONS

Importance of flexibility, particularly with reference to large scale systems, having been recognized there have been considerable effort aimed at general formulation applicable to a wide class of systems. The models considered vary significantly, however, the ultimate aim is to have dynamic equations of motion for a system of arbitrarily connected flexible deployable members forming branched and closed loop topology. Formulation procedures aimed at dynamics of multibody flexible spacecraft have been developed by several researchers. These include the early contribution by Ho [27] using the direct path method to more recent ones by Singh et al. [28, Kane's approach], Meirovitch and Quinn [29, Perturbation technique], Vu-Quoc and Simo [30, rotationally fixed floating frame approach], Spanos and Tsuha [31, component modes method], Modi et al. [32, 33, Lagrangian approach], and others.

A comment concerning Lagrangian approach to the problem might be appropriate. It has not been popular in multibody dynamics because the kinetic energy expression can become extremely large and perhaps unmanageable (before the advent of high speed computers) as indicated by Hooker [34] and others. On the other hand, its effectiveness has been attested by a variety of problems in analytical dynamics for more than 200 years. More specifically, the approach automatically satisfies holonomic constraints. It provides expressions for useful functions such as Lagrangian, Hamiltonian, conjugate momenta, etc., and the form of the governing equations displays clear physical meaning in terms of contributing forces. Equally important is the fact that the equations are readily amenable to the stability study and well suited for the control design.

A key to the use of Lagrange's approach in multibody dynamics is the development of the kinetic energy expression in a concise matrix form, which can be differentiated as required. Obviously, the favored form for the kinetic energy is $(1/2)\dot{\mathbf{y}}^T \mathbf{M} \dot{\mathbf{y}}$ where $\dot{\mathbf{y}}$ and \mathbf{M} are the system velocity vector and mass matrix, respectively. Also the mass matrix should clearly display the system's dynamic character in a simple and meaningful form. Such a form for the kinetic energy is known for configurations such as a system of point masses, discretized vibrating structures, rigid bodies connected in a chain form [35], etc. To arrive at the form for a complex flexible multibody systems has been a challenge faced by dynamicists for a long time. The formulation procedures presented by Modi et al. resolves this problem quite elegantly [32,33]. Essential features of the general formulation may be summarized as follows:

- spacecraft of an arbitrary inertia distribution in a general orbit undergoing three-axis librations;
- arbitrary number and orientation of flexible appendages (tether, membrane, beam, plate, shell) deploying independently at an arbitrary velocity and acceleration;
- the appendage is permitted to have variable mass density, flexural rigidity and cross-sectional area along its length;
- governing equations account for gravitational effects, shifting center of mass, changing rigid body inertia, and appendage offset together with transverse oscillations;
- modified Eulerian rotations γ, β, α (roll, yaw, pitch, respectively) are so chosen as to make the governing equations applicable to both spin stabilized and gravity gradient orientations;
- the equations are programmed in nonlinear as well as linearized forms to permit the study of : (i) large angle maneuvers; (ii) nonlinear effects.

In what follows, this versatile formulation is applied to several systems of contemporary interest to illustrate current and future challenges in the general area of attitude dynamics and control. Details of the mathematical formulations and analyses being extremely lengthy are purposely omitted here, however, appropriate references are cited. Emphasis throughout is on the analysis of results and corresponding conclusions.

5. TRANSIENT DYNAMICS DURING DEPLOYMENT

The configuration selected for study corresponds to the Orbiter Mounted Large Platform Assembler Experiment once proposed by Grumman Aerospace Corporation (Fig. 15). Its objective is to establish capability of manufacturing beams in space which would serve as one of the fundamental structural elements in construction of the future space station. The assembler is fully collapsible and automatically deployed. It has some similarity to the experiment carried out by astronauts Jerry Ross and Sherwood Spring in November 1985.

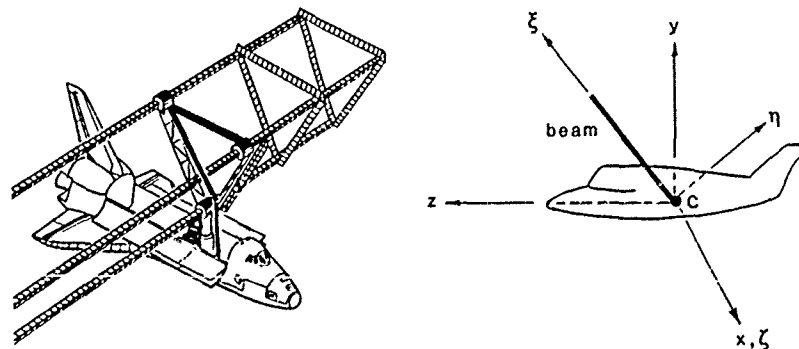


Figure 15 A schematic diagram showing the Orbiter based construction of beam-type structural members. The principal coordinates x, y, z having their origin at the instantaneous center of mass and beam coordinates ξ, η, ζ with the origin at the attachment point are also indicated. In general the two origins are not coincident.

For analysis, the flexibility and deployment rate parameters were taken to be of the same order of magnitude as used or likely to be employed in practice. In the diagrams e represents orbital eccentricity; EI is the beam flexural rigidity, assumed constant over the length in this particular example; and \dot{L} corresponds to the deployment rate. λ_{in} and λ_{out} denote beam inclinations to the local vertical in and normal to the orbital plane, respectively. The perigee was taken to be 331 km. The truss or beam vibrations were represented by a maximum of the first four modes, ψ_i , of a cantilever. P_i, Q_i represent generalized coordinates associated with the admissible functions used to represent beam-type appendage oscillations in the i th mode in ζ and η directions, respectively. \bar{P}_i and \bar{Q}_i represent transverse generalized coordinates normalized with respect to the total length.

Numerical values for some of the more important parameters used in the computation are given below:

Orbiter: Mass = 79,710 kg; $I_{xx} = 8,286,760 \text{ kg-m}^2$; $I_{yy} = 8,646,050 \text{ kg-m}^2$; $I_{zz} = 1,091,430 \text{ kg-m}^2$;
 $I_{xy} = 27,116 \text{ kg-m}^2$; $I_{yz} = 328,108 \text{ kg-m}^2$; $I_{zx} = -8,135 \text{ kg-m}^2$.

Beam: Mass (M_b) = 129 kg; Length (L) = 33 m; Flexural Rigidity (EI) = 436 kg-m^2 .

Here, x, y, z are the principal body coordinates of the Orbiter with the origin coinciding with the center of mass. In the nominal configuration x is along the orbit normal, y coincides with the local vertical and z is aligned with the local horizontal in the direction of motion. Only some typical results are presented here. More extensive discussion of the system behaviour has been presented in the references [25, 36-41].

Figure 16 shows tip response of the beam for two different orientations in the plane defined by the local vertical and the orbit normal, $\lambda_{out} = 20^\circ$ and 90° . Note, the two transverse motions ζ and η are coupled with the plane of vibration precessing, due to the Coriolis force, at a uniform speed which is governed by the beam inclination angle λ_{out} . For the case of $\lambda_{out} = 0$, the uncoupled motion showed no precession. On the other hand, the precessional velocity increased with an increase in λ_{out} and reached a maximum value at $\lambda_{out} = 90^\circ$. The plane of vibration of the beam precessed in one direction only (in this case clockwise for a given λ_{out}).

Effect of beam deployment on the tip dynamics is studied in Fig. 17. Initial tip deflection is the same as before. Two time histories with the same duration of deployment are considered. As can be expected, the frequency of oscillation in and out of the orbital plane gradually decreases with deployment finally attaining a steady state value upon its termination. It is of interest to recognize that they reach the same steady state amplitude, although it is much larger during deployment compared to the deployed case.

In practice the Orbiter's librations will be controlled to a specified tolerance limit. A typical time history [18] of the controlled Space Shuttle librations during an orbit is shown in Fig. 18. In the following results attention is focused on response of the deployed beam during such forced excitation of the Orbiter in the Lagrange configuration.

Figure 19 shows the forced tip response as well as the first two modes contributing to it for a beam deployed along the orbit normal with the Orbiter in the Lagrange configuration. At the outset it should be recognized that, for this out-of-plane configuration of the beam, the out-of-plane motion ζ and inplane response η are coupled as seen before (Fig. 16). Hence one would expect the Orbiter's yaw and roll to be reflected in both η (inplane) and ζ (out-of-plane) motions. The response shown in Fig. 19 precisely reveals these trends. However, the roll disturbance, being at a higher frequency and hence with a higher acceleration, appears to be dominant as apparent from the amplitude modulation of the response at the roll frequency (around 13 cycles per orbit).

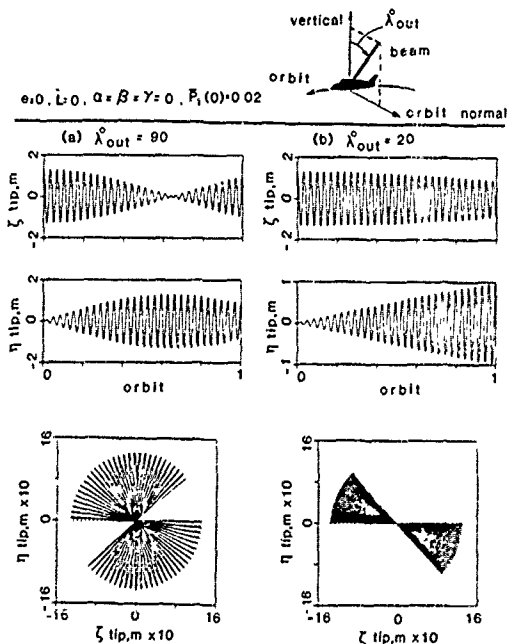


Figure 16 Response of the beam to a tip disturbance when located out of the orbital plane. Note, the transverse motions ζ and η are coupled and the vibration plane of the beam-tip precesses at a uniform rate.

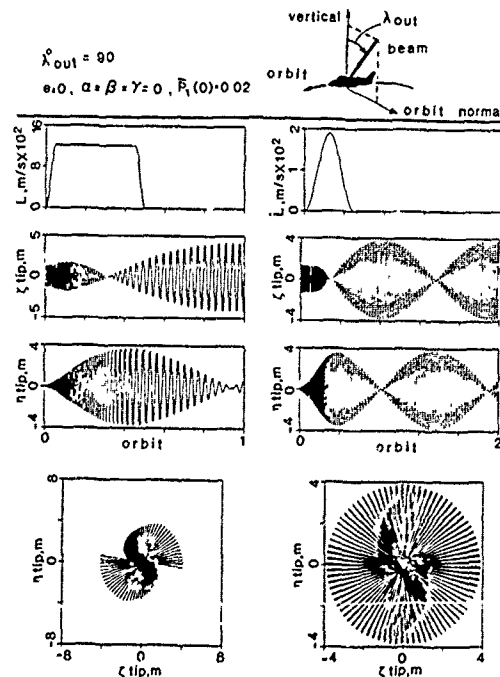


Figure 17 Effect of deployment strategies on tip response of a beam deploying normal to the orbital plane. Note a reduction in beam frequency during deployment.

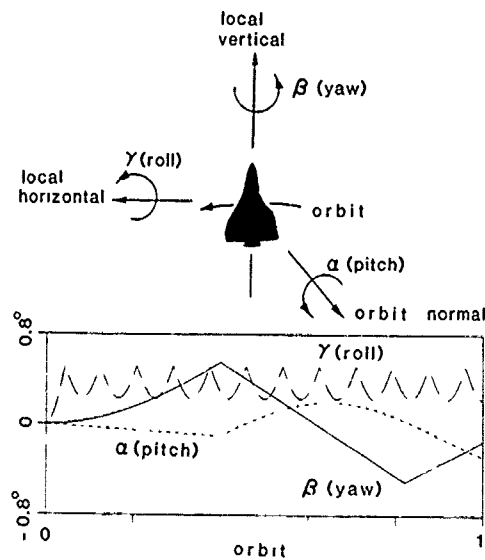


Figure 18 Representative controlled motion of the Orbiter during a typical orbit. The roll, yaw and pitch motions are with reference to the local horizontal, local vertical and orbit normal, respectively.

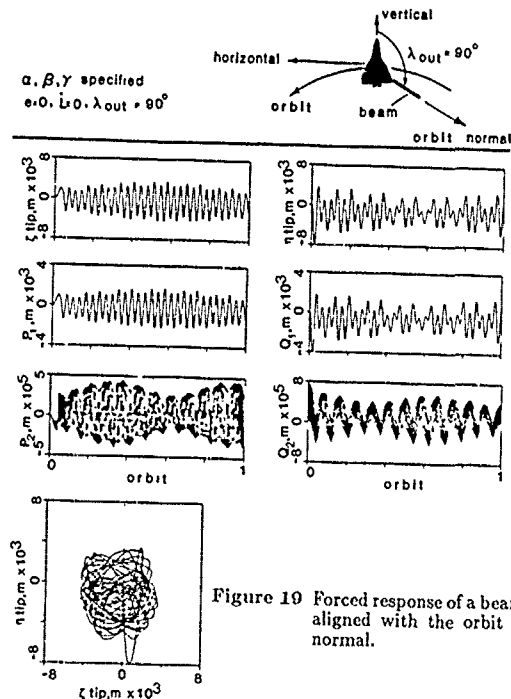


Figure 19 Forced response of a beam aligned with the orbit normal.

6. THE ORBITER BASED EXPERIMENT SCOPE

Obviously, the main objective of any attitude and vibrational dynamics study of a flexible spacecraft is to develop an appropriate control strategy so that the system response to disturbances remains within the specified limits. However, flexibility often results in low and closely spaced frequency spectrum, and a possibility of overlap with the control system bandwidth. This will demand evolution of high performance attitude control and vibration suppression procedures as well as observation algorithms with special emphasis on robustness to the parameter errors, spill over management, sensor/actuator locations, etc. Although a vast body of literature exists in this area, most of the proposed control strategies remain essentially numerical simulations and hence need to be validated. As pointed out before, it is generally recognized that gravitational, magnetic, plasma, solar radiation, and free molecular environments can not be modeled precisely with the ground based simulation facilities. Carefully planned on-orbit tests with flexible structures appear to be the only reliable approach for validation, refinement and calibration of the control algorithms.

Under the circumstances, NASA has proposed an experiment SCOPE [Fig. 20, Spacecraft Control Laboratory Experiment, 42]. It involves prescribed slewing maneuver of a reflector plate type antenna, attached to a flexible mast, supported by the Space Shuttle. A specified librational motion of the Shuttle provides the desired slow motion to the antenna, and the primary control task involves suppression of the resulting dynamics which may introduce error in the antenna's line-of-sight.

The general formulation is applied to assess dynamics of the SCOPE system through a parametric analysis. Such a study of complex interactions between flexibility, slewing maneuver (β_{31} , roll; β_{32} , pitch) and librational motion (ψ_1 , roll; ψ_2 , pitch; ψ_3 , yaw), revealed through coupling effects, is not only important during the preliminary structural design but is also useful in planning of the control strategy. The classical infinite time linear state feedback regulator, utilizing the Shuttle's primary and vernier thrusters, is designed to suppress the vibrations as well as control the Shuttle's attitude motion.

It should be noted from Fig. 20 that the SCOPE configuration involves the Orbiter based flexible truss structure (mast) asymmetrically supporting a rigid reflector antenna at its end. The mast, located at the c.m. (G_1) of the Shuttle, is permitted to execute a controlled slewing maneuver about the attachment point to the Shuttle. The truss, treated as an uniform Eulerian beam, is also free to undergo transverse (U_{31} , U_{32}) as well as torsional (θ_{33}) vibrations, represented by the first mode (torsion) or the first three modes (bending), involving the damping effects. The mast's fundamental bending frequencies, in pitch and roll directions, are 0.29 and 0.28 Hz, respectively, while that in torsion is 0.53 Hz. The effective modal damping ratio of each degree of freedom is taken to be 0.003. The Shuttle is considered to be in a 5303 s circular orbit corresponding to an altitude of 200 km. Other important properties are selected to represent a realistic situation of the SCOPE program :

Orbiter (Body 1): mass(m_1) = 92,986 kg; inertia matrix(I_1) = $\begin{bmatrix} 1228600 & 0 & 197243 \\ 0 & 9212160 & 0 \\ 197243 & 0 & 9615840 \end{bmatrix}$ kg-m²;

Mast (Body 3): mass(m_3) = 181 kg; length(l_3) = 39.62 m;

Reflector antenna (Body 5): mass(m_5) = 181 kg; diameter(d_5) = 22.86 m;

c.m. position with respect to Frame 5, (x_{51} , x_{52} , x_{53}) = (5.72, 9.91, 0) m.

Two types of maneuvers are considered here: (i) β_{32} - slewing maneuver, in the orbital plane of the mast through 20° from the nominal upright position at an average rate of $1^\circ/\text{s}$; (ii) β_{31} - slewing maneuver, out of the orbital plane, of the mast through 20° at the same rate as above. The nominal trajectory of the mast slewing motion is characterized by the acceleration to vary sinusoidally. It leads to both velocity and acceleration to be zero at the initial and terminal stages. This is desirable to minimize excitation of the flexible mast. Only a sample of representative results is presented here. Further details and response analysis data are recorded in earlier publications [43-45].

6.1 Uncontrolled Response

The first item of the interest is to have some appreciation as to the effect of the mast flexibility on the uncontrolled system response. Fig. 21 presents time histories of the librational response, mast tip acceleration and line-of-sight error corresponding to the desired direction for communication at 20° with respect to the local vertical. The flexible mast is undergoing the maneuver corresponding to case (i), with the Shuttle free to undergo three-axis attitude motion. The maneuver excites the uncontrolled librational motion that is unstable in roll leading to a secular variation of the out-of-plane line-of-sight error (ϵ_{31}). It is apparent that the effect of flexibility on the line-of-sight error and the mast tip acceleration, showing high frequency modulations, is indeed quite significant. Although the amplitude of modulations of the line of sight error is only 0.1° (ϵ_{32} , Fig. 21b), it is still undesirable as antenna pointing accuracy requires the error to be less than 0.02° in 20 s. On the other hand, the flexibility has virtually no effect on the attitude response because of their widely separated frequencies.

A closer look at Fig. 21 is necessary to better appreciate complex interactions between flexibility and coupling. Note, the line-of-sight error in pitch (ϵ_{32}) shows limit cycle oscillations about the equilibrium position of the flexible system which are absent for the rigid case. It should be noted that although the mast is slewed in the orbital plane, both inplane (μ_{31}) and out-of-plane (μ_{32}) oscillations are excited leading to inplane (α_{31}) and out-of-plane (α_{32}) mast tip accelerations. In fact, even the mast's torsional degree of freedom was found to be present (Fig. 21a) because of the asymmetrical mounting of the reflector. Thus the transverse and torsional degrees of freedom of the mast are strongly coupled. A difference in the transverse vibrational frequencies of the mast, caused by the asymmetric mounting of the antenna plate, results in a beat response with a period of around 36 s during the uncontrolled maneuver in pitch (Fig. 21b). Note, the mast tip accelerations are significant (10^{-2} g). It may be of interest to point out that an earlier study without the plate antenna showed the inplane and out-of-plane degrees of freedom (both librational and vibrational) to be uncoupled [43]. Thus asymmetric mounting of the antenna is a major cause of coupling.

6.2 Control Strategy: Infinite Time Optimal Linear Regulator

On linearizing about the zero equilibrium state, the original governing equations of motion reduce to the nonautonomous coupled set which can be represented in the standard form as:

$$\begin{aligned}\dot{\bar{x}} &= A\bar{x} + B\bar{u} \\ \bar{x} &= \{\bar{x}^T, \dot{\bar{x}}^T\}^T; \\ \bar{u} &= \bar{M} = \{M_{11}, M_{12}, M_{13}\}^T;\end{aligned}\quad (4)$$

where A, B are the system and control matrices, respectively, and \bar{u} is the control vector, consisting of the Shuttle's 3-axis control moments. Introducing a cost function to be minimized,

$$J = \frac{1}{2} \int_0^\infty [\bar{x}^T Q \bar{x} + \bar{u}^T R \bar{u}] dt, \quad (5)$$

the optimal control \bar{u} is given by,

$$\bar{u}(t) = R^{-1} B^T P \bar{x}(t). \quad (6)$$

The symmetric positive definite matrix P, based on the optimality principle, can be obtained by solving the algebraic Riccati equation,

$$A^T P + P A - P B R^{-1} B^T P + Q = 0, \quad (7)$$

where, R, Q are positive definite and semidefinite symmetric weighting matrices, respectively.

6.3 Controlled Response

The primary control task is to rapidly change the line-of-sight of the antenna mast, attached to the Shuttle, and to damp the induced structural vibrations for precise pointing of the antenna. Thus the objective is to minimize the time required to slew and settle, until the antenna line-of-sight remains within a specified tolerance limit [42].

The first logical step is to illustrate effectiveness of the full state feedback optimal linear regulator, which employs a set of Shuttle's thrusters to produce three-axis torques. A controller is designed so as to provide additional damping to the structural vibration through coupling while stabilizing the Shuttle attitude. Thus the line-of-sight error, which is quite susceptible to both the structural oscillations and attitude motion, can be reduced.

As against the earlier study, now the Shuttle is controlled to maintain the nominal position. Thus the desired line-of-sight is attained by slewing the mast in pitch (Fig. 22). The results demonstrate rather vividly effectiveness of the controller. The attitude motion originally unstable in roll leading to the secularly varying out-of-plane line of sight errors (Fig. 21a), regains stability. Undesirable mast vibrations are also significantly damped and the commanded antenna direction is acquired in less than 5 s after completion of the maneuver. Fig. 22c presents time histories of the Shuttle control moments. It may be pointed out that the maximum moments produced by the Shuttle thrusters were limited to 1.36×10^5 Nm as specified in the SCOLE design challenge [42].

Finally, an alternate way of attaining the line-of-sight by pitching the Shuttle is examined. Here the desired antenna pointing direction is acquired by pitching the Shuttle, not through slewing of the mast. Results show that the two maneuvers (slewing of the mast, Fig. 22; Shuttle pitch Fig. 23), though equivalent in terms of orienting the antenna, demand vastly different control moments. Note, in the present case of inplane maneuver, the control moment in pitch for the mast slew is about an order of magnitude smaller. This clearly suggests an enormous saving in control energy if the antenna is positioned in a desired orientation through mast maneuvers rather than maneuvering the Shuttle as suggested in the design challenge.

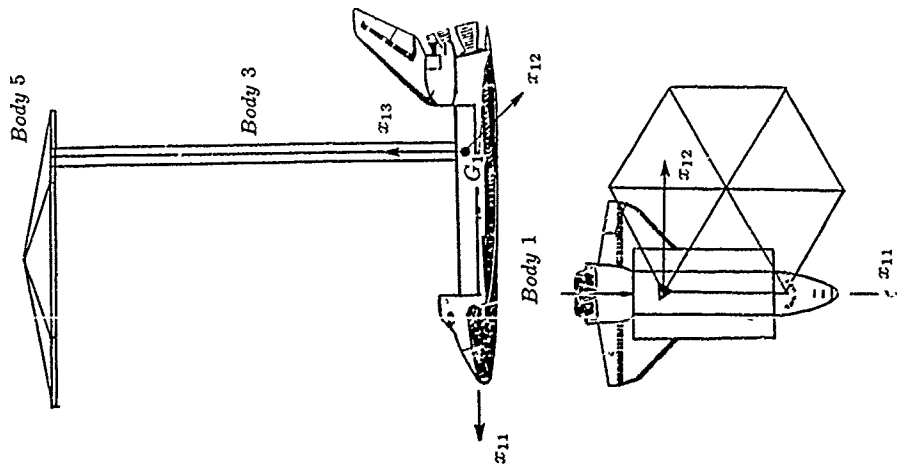


Figure 20 (SCO) configuration consisting of the rigid Space Shuttle based sieving flexible mast asymmetrically supporting a rigid reflector plate.

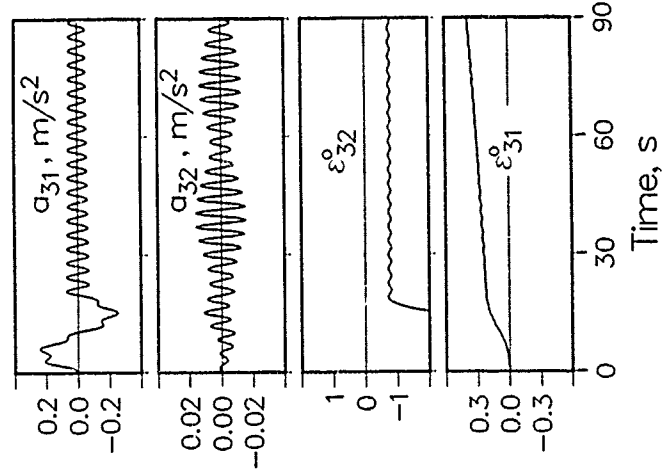
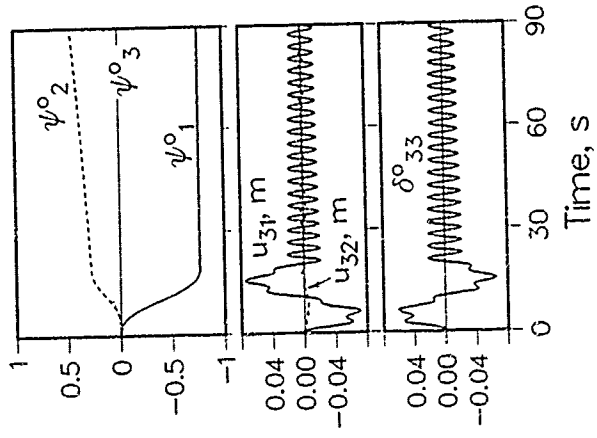
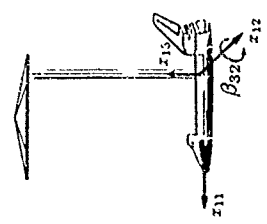


Figure 21 Uncontrolled response of the system to a pitch disturbance through slewing of the flexible mast: (a) time histories of the librational motion, mast tip deflection and rotation; (b) mast tip lateral acceleration and the antenna line-of-sight error.

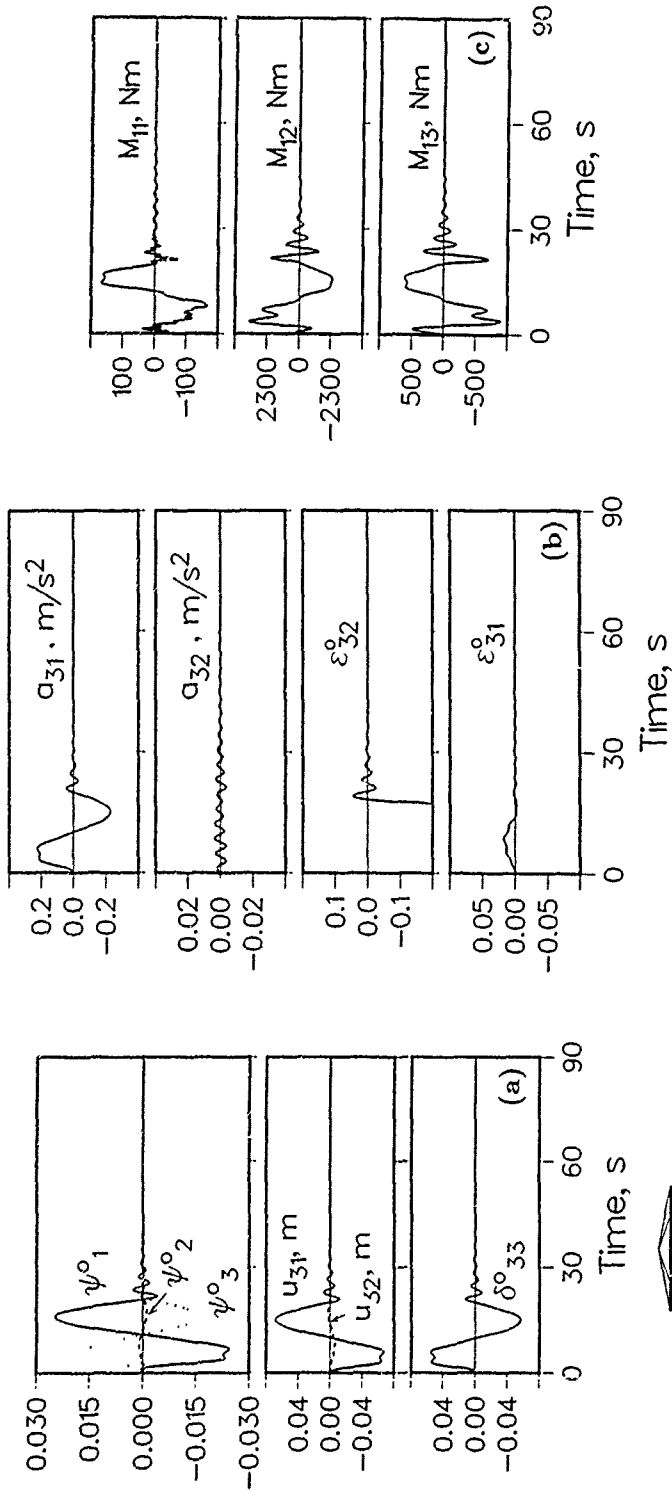
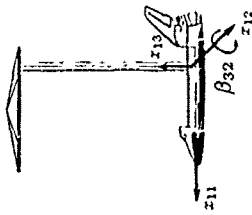


Figure 22 Controlled response of the system to a pitch disturbance through slewing of the flexible mast showing effectiveness of the LQR: (a) time histories of libration, mast tip deflection and rotation; (b) tip acceleration and line-of-sight error; (c) time variation of the control moment. The total control effort is 51,600 Nm-s.



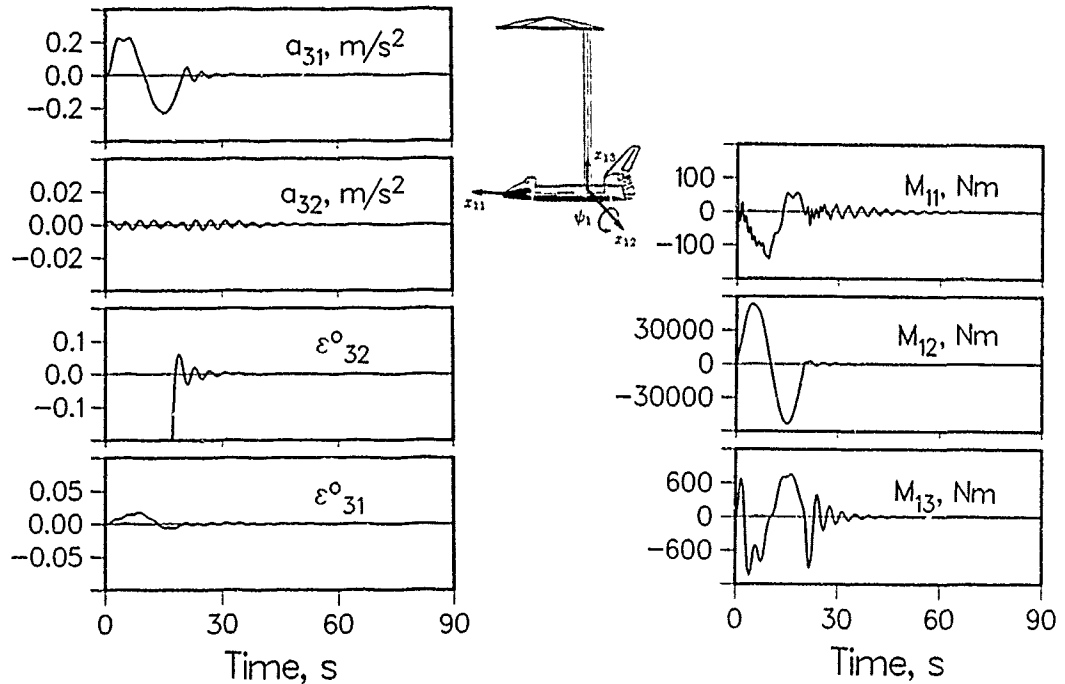


Figure 23 Plots showing the controlled response during the Shuttle pitch maneuver. Note the control moment in pitch is nearly an order of magnitude higher.

7. SPACE STATION: A LARGE SCALE SYSTEM

The United States led space station Freedom is progressively moving towards the design and development phases with its international partners (Canada, ESA and Japan) confirming the specific hardware elements they will provide. The primary design requirements is to develop a versatile, expandable, permanent, manned facility for undertaking significant advances in space science and technology. The Space Station will contain laboratories for research in such areas as communications, material processing and astrophysics. It will be used as a platform for satellite launch and repair as well as assembly of space structures which may be too large, in terms of size or weight, to transport in their entirety by the Space Shuttle.

The Space Station is planned to be assembled in orbit utilizing twenty Space Transportation System (STS) flights [46]. Fig. 24 presented earlier illustrates the Station configuration at the completion of the assembly sequence. The pressurized modules (habitation, laboratory and logistics) will be located near the geometric centre of the spacecraft while the servicing equipment will be placed along the power truss on either side of the clustered modules. Each end of the main truss will support photovoltaic arrays which will deliver 75 kW of power.

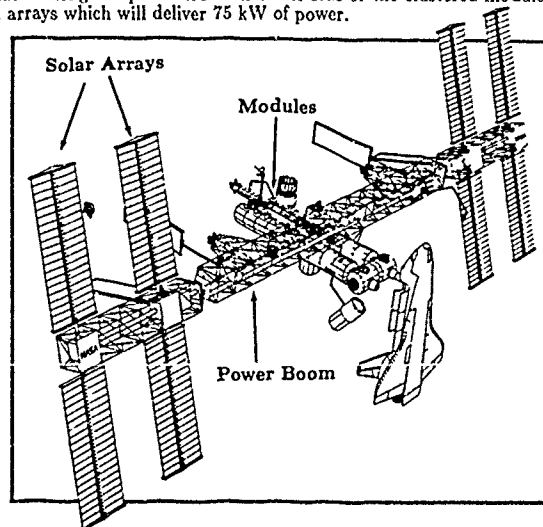


Figure 24 A schematic diagram of the proposed Space Station Freedom showing the baseline configuration as of August 1987.

The first Space Shuttle flight, referred in the acronym form as MB-1, will deliver four truss bays of the power boom, two of which are outboard of the articulating alpha joint (Fig. 25a), which allows the photovoltaic solar arrays to track the sun. Hardware delivered on this flight will also include a pair of solar arrays providing 18.85 kW of power, a panel radiator, 2 RCS modules, fuel storage tanks for flight control and reboost, and limited avionics and communication equipment. Once assembled, MB-1 will be a fully functional spacecraft awaiting the return of the second Shuttle flight to progress to the next stage of the assembly sequence.

The second flight (MB-2, Fig. 25b) will deploy six more bays inboard of the alpha joint, a station radiator, six Control Moment Gyros (CMG) for additional attitude control with a complete communications coverage provided by a TDRSS antenna. A telerobotic servicer will extend support to Extra Vehicular Activity (EVA) of a crewman during assembly and maintenance. Phase MB-3 (Fig. 25c) will add the aft port node, a pressurized docking adapter and a standard airlock. These elements will provide a base for deployment of the various modules for a permanently manned configuration (Fig. 25d), a simplified model of which is considered here for dynamical investigation.

The finite element procedure was applied to obtain the first forty system modes of the above mentioned four configurations. The First Element Launch consists of a 25 m long boom, a 11.5 m long array radiator (both modelled as beams) and a pair of solar panels ($33 \times 6 \times 0.25$ m) represented as plates. For the MB-2 model, the main truss is extended to 55 meters and an additional station radiator ($10 \times 5 \times 0.25$ m) is attached to it. The transition from the MB-2 to MB-3 configuration involves the incorporation of a lumped mass element at the lower end of the main truss representing the module support structure and the pressurized docking adapter (25,000 kg). Finally, the PMC configuration has a 105 meter main truss with a module cluster at its geometric centre (146,000 kg); a pair of array and station radiators located at 40 m and 21 m from the truss center, respectively; and solar arrays near each end of the truss. The frequency spectrums for the beginning MB-1 stage and the final PMC stage are presented in Fig. 26. It is of interest to point out that there are 31 modes (besides the rigid body modes) below 5 Hz for the MB-1 configuration! For example, the first elastic mode represents the arrays' fundamental bending (symmetric) at around 0.08 Hz. $f_{10} = 0.38$ Hz is predominantly the array second bending mode with the main truss in torsion. The main truss first bending mode occurs at $f_{40} = 3.79$ Hz. The MB-1 case is the only one where the main truss torsion frequencies (f_{10}, f_{19}) are below its fundamental bending frequency (f_{40}). For the PMC case both the length as well as the system weight have increased. This leads to more modes in a given frequency range. Now the lowest bending modes for the truss correspond to $f_{17} = 0.32$ Hz and $f_{20} = 0.35$ Hz.

Summarizing, it can be inferred that the appendages dominate the flexible dynamics and that modes involving their pure motion are not significantly affected by the evolutionary character of the Space Station. However, growth of the main truss and its interaction with the cluster of modules significantly affect the system modes as observed through the changes in the truss bending frequencies.

Modi, Suleman and Ng have studied length dynamics of the evolving space station using both system as well as component modes. Results were presented at the recently held workshop organized by ESA [47]. However, to have better appreciation of interactions between librational dynamics and flexibility let us focus attention on a relatively simple model of the Space Station as shown in Fig. 27. Modi and Suleman [48] have examined the system response using the first seven modes (Fig. 28) through a numerical analysis of the governing nonlinear equations as well as an approximate analytical approach leading to a closed form solution employing the variation of parameter method as proposed by Butanin [49].

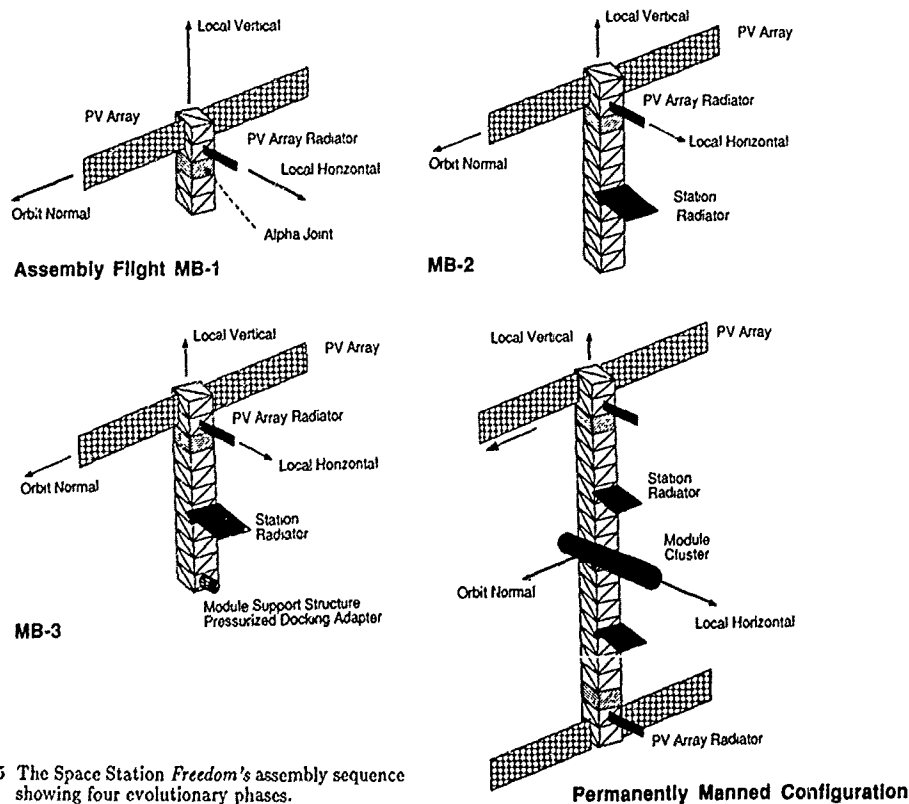
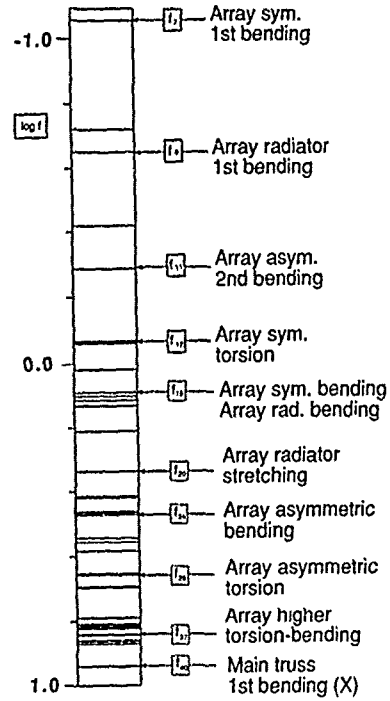
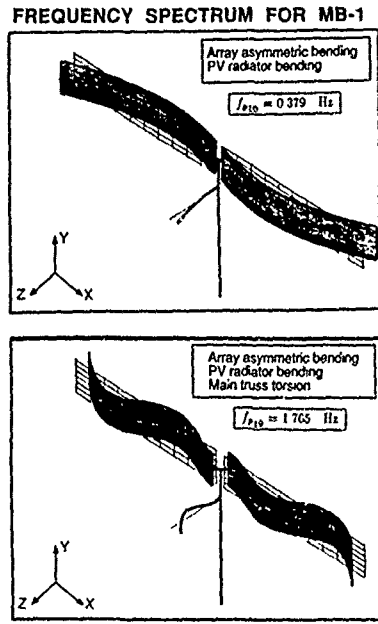


Figure 25 The Space Station Freedom's assembly sequence showing four evolutionary phases.

(a)



(b)

FREQUENCY SPECTRUM FOR PMC

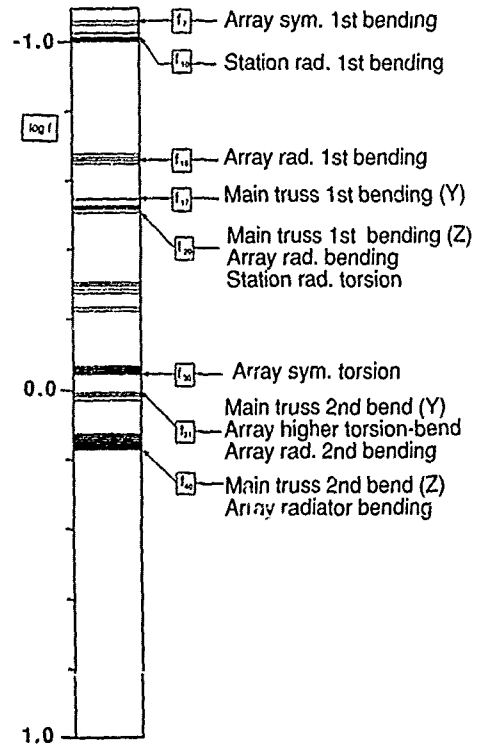
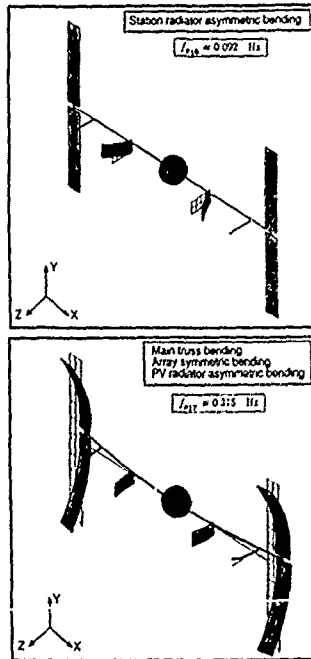


Figure 26 The frequency spectrum and three representative modes for: (a) MB-1; (b) PMC.

Downloaded by KTHN on September 10, 2015

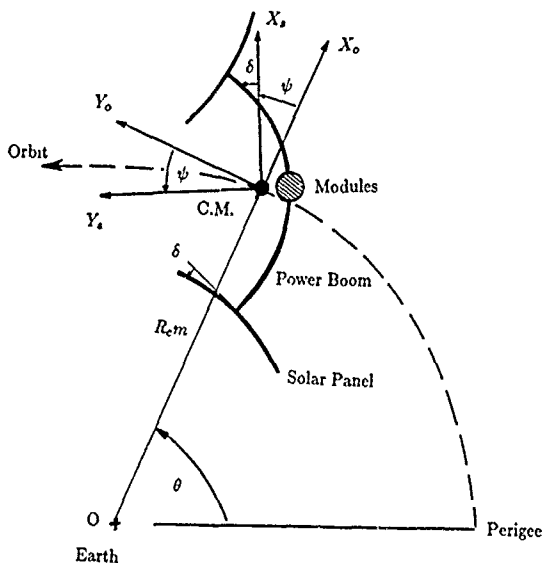


Figure 27 A simplified model of the Space Station undergoing planar librational and vibrational motions.

Figure 28 The first seven vibrational frequencies and associated system modes used in the analysis of the Space Station.

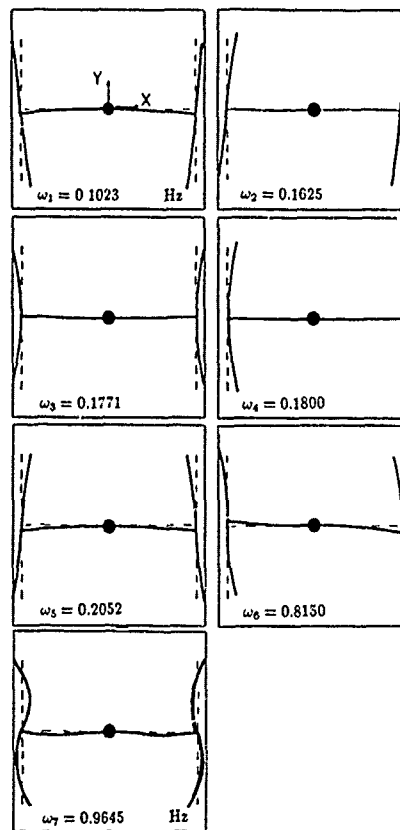


Figure 29 shows response of the system when subjected to a pitch disturbance of 5° . The ensuing librational, generalized coordinates associated with the vibrational response, as well as time histories of deflections at the upper tip of the power boom and free end of the top left solar panel are presented. Only the response of the generalized coordinates p_1 , p_2 , and p_5 (corresponding to the fundamental frequency f_1 , f_2 , and f_5 , respectively) is given as contribution of the remaining coordinates was found to be several orders of magnitude smaller. For the inertia values used, the theoretically predicted pitch frequency equals 1.44 per orbit, which agrees quite well with the period of the planar libration, ψ . The vibratory response is essentially a modulation of the above character at the system's fundamental frequency. The librational motion is able to excite p_5 primarily because of the proximity of f_5 to the fourth harmonic $4f_\psi$ (Fig. 30). Note, the solar panel tip deflection of $10^{-4}g$ which may not be acceptable for microgravity experiments.

Figure 31 shows the effect of vibratory disturbance on the system response. The Station is disturbed in its first two modes with the maximum deflection (in each mode) equal to 2.5% of the power boom length. Note, the coupling effect leads to a substantial pitch motion (0.5° amplitude) modulated at the Station's fundamental frequency. This, in turn, excites the vibratory response in p_5 due to its proximity to the fourth pitch harmonic as explained before. Furthermore, both the power boom and panel tip deflections are also significantly increased (panel tip amplitude 4.25 m, boom tip deflection 0.84 m). This level of vibrations may prove to be an important factor in the design of a control system.

As seen in Figs. 29 and 31, both the librational and vibrational disturbances failed to induce a significant response in p_3 , p_4 , p_6 , and p_7 generalized coordinates. Hence the system was purposely excited in these degrees of freedom to assess their effect on the Station response. The system is subjected to the panel tip deflection of 0.625% of the boom length in each of the third, fourth, sixth and seventh modes. Note, the total tip deflection at each panel is the same as before, however, the system is now excited in different modes. The results are shown in Fig. 32. It is of interest to recognize that now all the generalized coordinates are excited through coupling. A large amplitude pitch motion (1°) modulated at high frequency may prove to be of concern. Similar high frequency modulations are also observed in p_1 , p_2 , and p_5 . The beat-type response in the generalized coordinate p_6 may be due to the proximity of f_6 and the fifth harmonic of the librational frequency. The results seem to suggest that, depending upon the type of the disturbance, all the modes may be excited thus making the design of the control system all the more difficult.

Accuracy of the approximate, variation of parameter method based, closed-form solution was checked by comparing it with the numerical solution of the original nonlinear equations studied before. The comparison was carried out over a wide range of system parameters and initial conditions. The analytical solution predicted the response with a surprising degree of accuracy as indicated in the typical response plots presented in Figs. 33 and 34.

Figure 33 compares the analytical and numerical solutions when the system is subjected to a rather severe disturbance: librational displacement through 5° plus a vibratory disturbance in the first and second modes corresponding to the panel tip deflection of 5%. Note, there is virtually no difference between the two solutions. Even with the pitch disturbance as large as 20° (Fig. 34) the correlation continues to be quite good. Although small differences in amplitude and phase are noticeable, for all practical purposes, at least in the preliminary design stage, the results are indeed acceptable. The results also suggest that, in most situations, the contribution of higher modes is likely to be quite small. Thus, the solution promises to be a useful tool in conducting parametric studies of such a complex system with considerable saving (around 70%) in the computational cost.

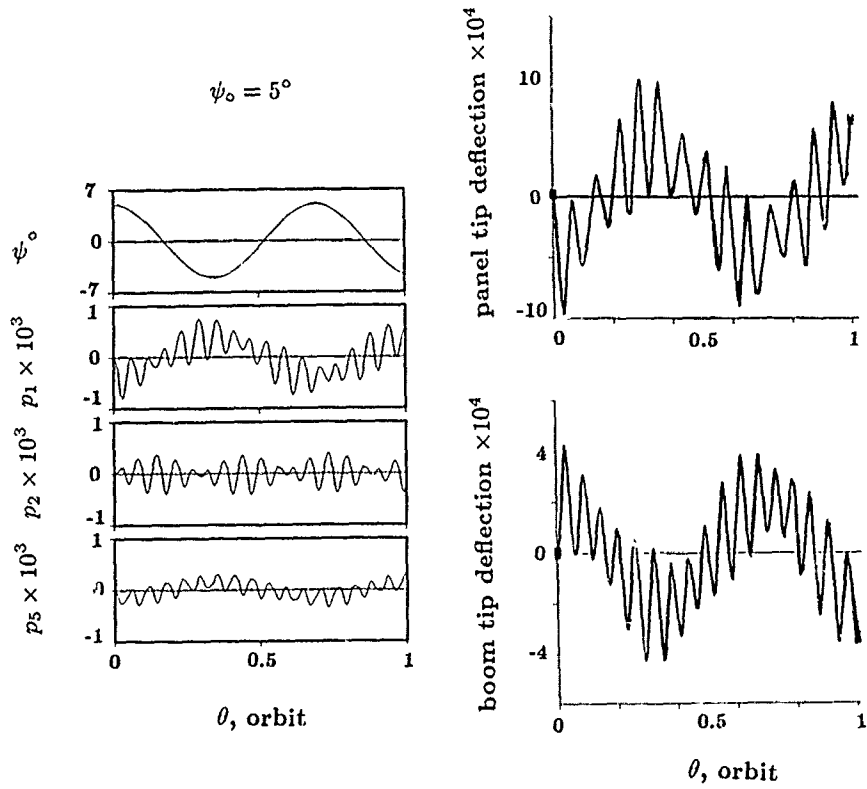


Figure 29 Response of the Space Station to a librational disturbance.

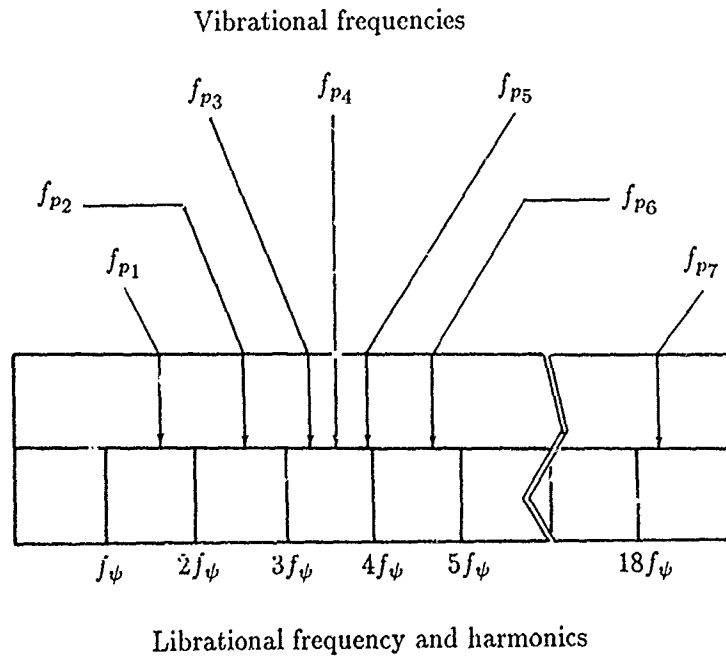


Figure 30 Librational and vibrational frequency spectra associated with a simplified model of the Space Station.

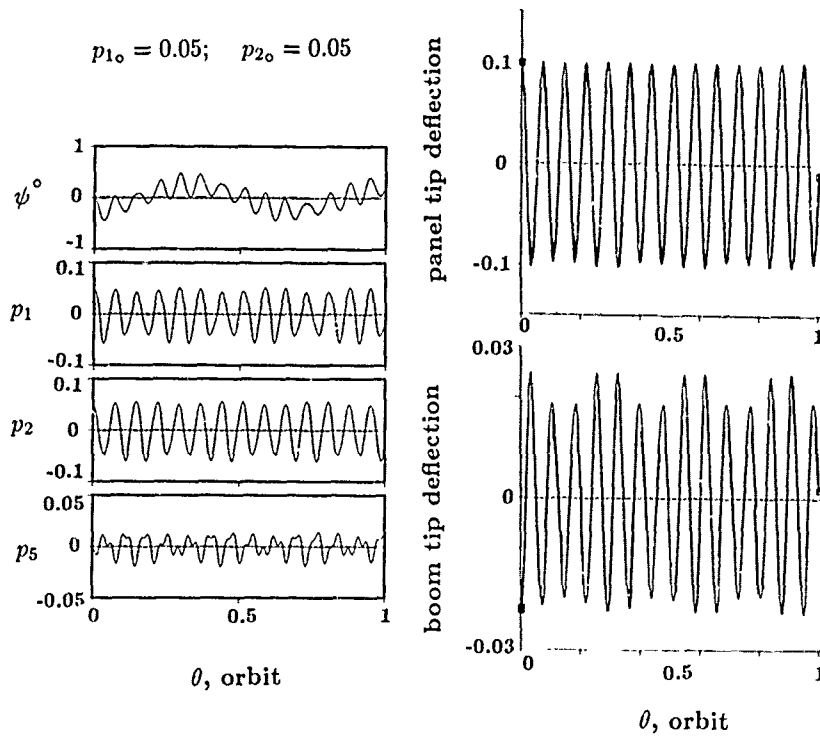


Figure 31 The Station response to a vibrational disturbance in the first and second system modes.

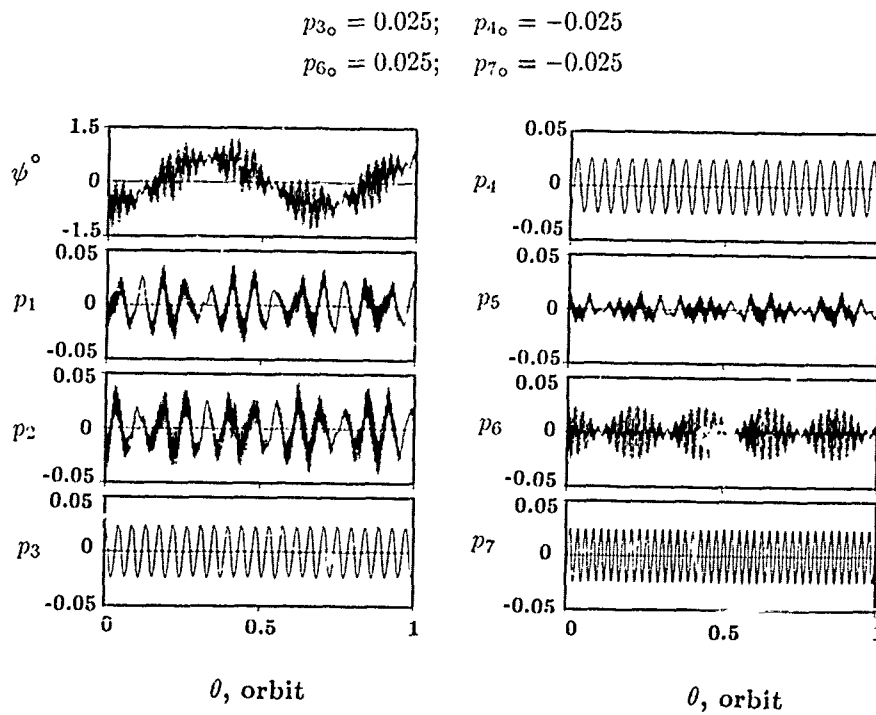


Figure 32 Response of the Station with a vibrational disturbance in the third, fourth, sixth and seventh modes.

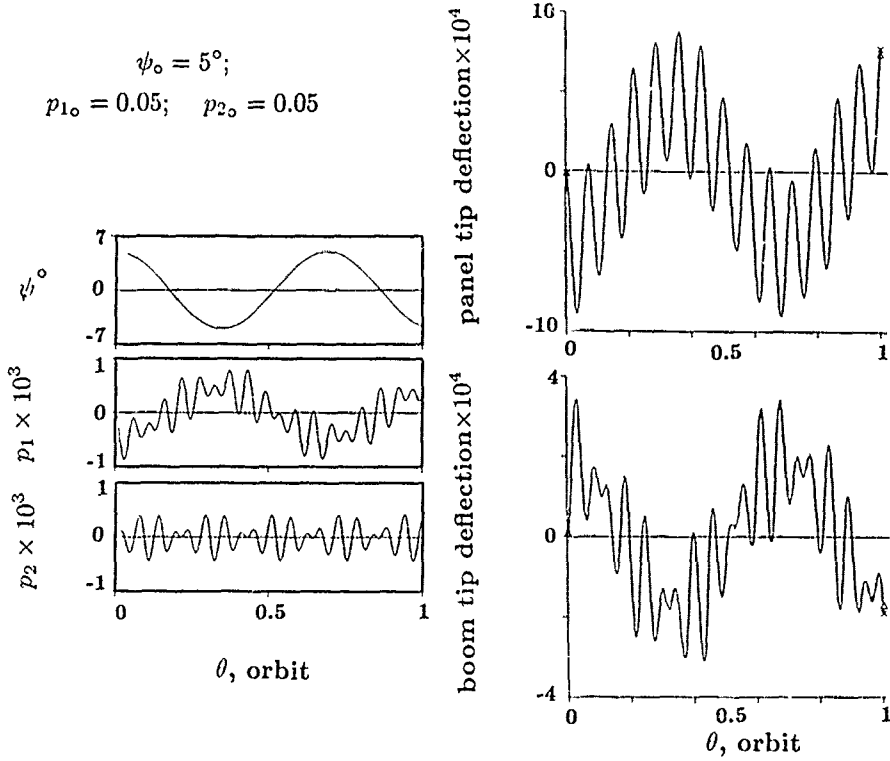


Figure 33 Comparison between the analytical and numerical solutions when the Space Station is subjected to a large pitch-vibratory disturbance. Note, the two solutions are almost identical.

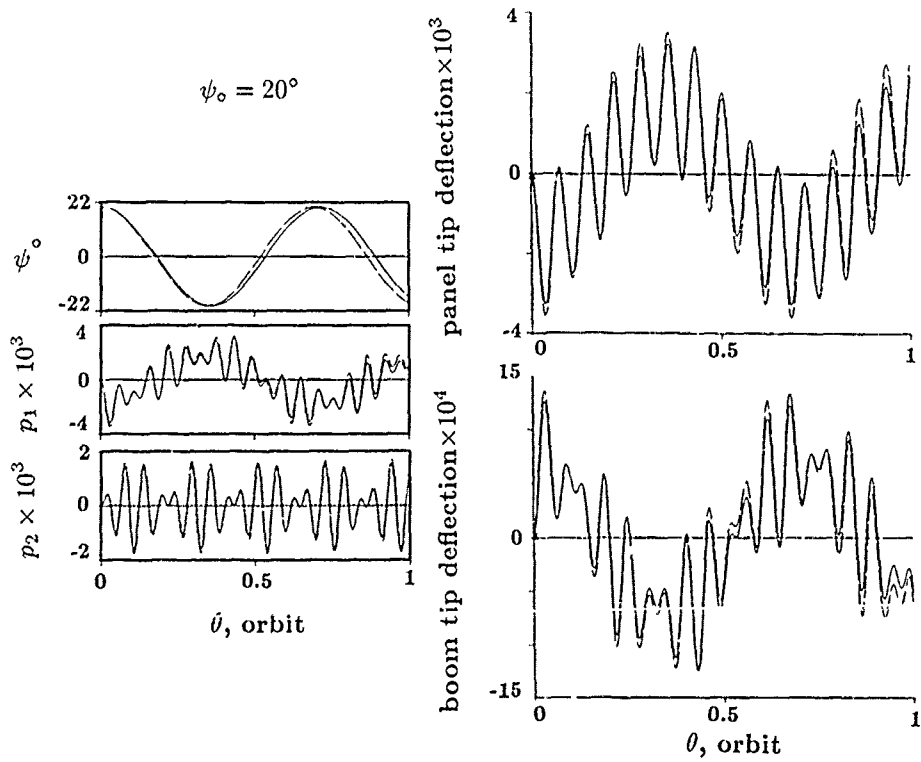


Figure 34 Effectiveness of the analytical solution with the system subjected to an extremely large pitch disturbance.

8. SPACE STATION BASED TETHERED PAYLOAD

As discussed before, advent of the Space Shuttle and the proposed Space Station have presented a wide range of possibilities for space exploration and exploitation. One approach to this end is the concept of Tethered Satellite System (TSS, Fig.35). Possible applications of the system cover a broad spectrum: (i) sophisticated scientific experiments aimed at gravity gradient, magnetic, ionospheric, aerothermodynamic and radio astronomy measurements; (ii) deployment of payloads into new orbits or retrieval of satellites for servicing; (iii) microgravity environment and manufacturing; (iv) generation of electricity (electrodynamic tether); (v) power and cargo transfer; and many others.

The vast potential of a tethered satellite system has led to many investigations concerning its dynamics during operational (i.e., stationkeeping), deployment and retrieval phases. In its utmost generality the problem is quite challenging as the system dynamics is governed by a set of ordinary and partial nonlinear, nonautonomous and coupled differential equations that account for:

- three dimensional rigid body dynamics (librational motion) of the station and subsatellite;
- swinging inplane and out-of-plane motions of the tether of finite mass;
- offset of the tether attachment point from the space station's centre of mass as well as controlled variations of it;
- transverse vibrations of the station;
- longitudinal and transverse vibrations of the tether;
- external forces due to aerodynamic drag and solar radiation effects.

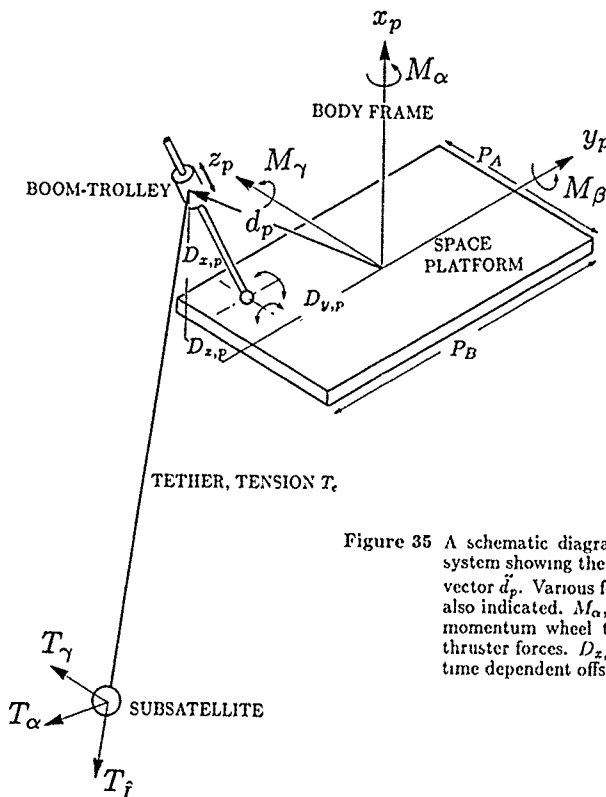


Figure 35 A schematic diagram of the platform based tethered satellite system showing the boom-trolley arrangement to vary the offset vector d_p . Various forces acting on the system due to control are also indicated. M_α , M_β , and M_γ represent nondimensionalized momentum wheel torques while T_α , T_γ , and T_f indicate the thruster forces. $D_{x,p}$, $D_{y,p}$, and $D_{z,p}$ are the three dimensional time dependent offset components.

Over the years, investigators have attempted to obtain some insight into the the complex dynamics of the system using a variety of models which have been summarized by Misra and Modi[50,51]. In general, the studies show that the dynamics of the system during deployment is stable, however, the retrieval dynamics is basically unstable. The system involves a n-gative damping approximately proportional to l'/l_{ref} , where l and l_{ref} are the unstretched and reference tether lengths, respectively, and prime denotes differentiation with respect to the true anomaly. This suggests a need for an active control strategy, particularly to limit inplane (α_t) and out-of-plane (γ_t) swing (librational) motions of the tether. The pioneering contribution that may help realize this objective is due to Rupp[52] who introduced a tension control law for the system. Librational motion in the orbital plane was analyzed and the growth of pitch oscillations during the retrieval phase noted. The system was further studied in detail by Baker and others[53] taking into consideration the three dimensional character of the dynamics and the aerodynamic drag in a rotating atmosphere. Several more sophisticated models have followed since[54], however, one of the major conclusions of all the analyses remains essentially the same. even when the various tension control schemes are used, large amplitude motion can result under certain conditions, particularly during retrieval, which may not be acceptable.

One of the major limitations of the tether tension control is its dependence on the gravity gradient which is governed by the tether length. Hence for a small flexible librating tether, the tension may be quite small or even negative, i.e., the tether may become slack. This can be avoided by introducing thrusters[55,56], however, their firing in the vicinity of the shuttle or the space station is considered undesirable due to plume impingement, safety and other considerations. The

problem is further complicated by the fact that any offset between the tether attachment point and the station's centre of mass imposes additional moments on the station. Thus, the dynamics of the station is intrinsically coupled to that of the tether.

A vast array of linear and nonlinear control strategies using tension and/or thrusters have also been reviewed by Misra and Modi [50,51; contain 67 and 97 references, respectively]. Modi et al. have introduced a new approach to the control through regulated motion of the tether attachment point, tested its performance using a realistic mathematical model [57-64], assessed its relative merit with reference to other control strategies [65] and substantiated the conceptual validity with a ground based experiment [66]. They have reviewed this literature at some length particularly with an emphasis on the offset control strategy [67; contains 23 references]. The offset control technique is similar to the act of balancing a rod on the palm of one's hand. As can be expected, for a given angular disturbance, the motion required at the point of attachment of the tether would grow proportional to the length of the tether. To assess the controller's performance, Modi et al. purposely considered demanding platform inertias, severe initial conditions and rapid retrieval rates. Table 1 compares relative performance of the three control strategies during deployment, stationkeeping and retrieval. As can be expected, the strength of the offset control lies at shorter tether lengths, where tension and thruster control approaches have limitations. Thus a hybrid control strategy, initially utilizing tension or thruster control with switch over to the offset control at an appropriate length, appears quite attractive as indicated in the Table.

9. CONCLUDING COMMENTS

Let me close with a few general remarks concerning desirable directions for future efforts:

- (i) It is apparent that there is a rich body of literature in the area of attitude dynamics and control. With the success of the Space Shuttle and the U.S. commitment to an operational Space Station by the end of this century, we may soon see spacecraft ranging from a few meters to several hundred meters in size. For such large scale flexible systems influence of the environmental forces will be necessarily significant, particularly with a trend towards higher pointing accuracy. Dynamics and control of flexible spacecraft in the presence of environmental forces remains a field that has received relatively little attention. Note, in general, flexibility interacts with the environmental forces as well as the control system while the latter two affect the flexible configuration. Thus the problem is inherently conjugate and should be treated as such.

The entire field is wide open to innovative contributions. Dynamics and control of such nonlinear, nonautonomous and coupled systems accounting for joint conditions, damping, external and internal nonconservative disturbances, etc., remain virtually untouched. Development of algorithms to predict the effect of mass, inertia, damping, environmental input, etc., on the dynamics and control parameters represents an exciting challenge for all, young as well as established researchers.

- (ii) With several relatively general formulations in hand and the programs operational, coordinated efforts should be made to develop a comprehensive data bank for spacecraft attitude dynamics and control. This should provide design charts over a wide range of system parameters and control strategies. Not only will it prove useful to design engineers involved in planning of future scientific, communications and other applied technology satellites but will also help in assessing dynamical, stability and control considerations associated with the time dependent evolving structures such as the Space Shuttle based construction of the proposed Space Station.
- (iii) As general approach to the problem gets well established, details should begin to receive more attention, e.g., quasi-steady, discrete or continuous representation of elastic appendages, modes to be used and their number from accuracy and computational considerations, robustness of control, step-size and numerical stability, etc.
- (iv) So far, complex character of the problem has limited most analyses to small deformations and librations. Studies aimed at dynamic response, stability and control in the large are, of course, formidable but promise to be equally exciting and rewarding.
- (v) There are two classes of problems which have already received some attention and their importance promises to increase in future:

Space Robotics: The Mobile Servicing System (MSS) or the space manipulator will be involved in all phases of the Space Station - construction, operation, maintenance, and future extension. However, as against the ground based robots, here we are faced with a problem of higher order of complexity. It involves dynamics and control of a flexible manipulator, supporting a flexible payload, freely traversing an orbiting flexible platform. Its operation in the presence of environmental forces would only accentuate the challenge. This represents an entirely new class of problems not encountered before. Although a promising beginning has been made [43-45,68,69], there is a long way to go.

Tethered Systems: With reference to the proposed Space Station Freedom, all the participating agencies have shown interest in the tethered supported facilities aimed at a variety of missions. Recognizing the highly flexible character of the Station, the problem of dynamics and control of the Space Station based tethered facility attains the challenge of a higher magnitude than that encountered or studied so far. Modi and Misra [50,51,56-64] have initiated investigations in that area, however, eventually one will have to make the models more sophisticated to account for station, tether and payload flexibility. Influence of free molecular reaction forces, solar radiation induced heating and electromagnetic forces for conducting tethers will have to be incorporated realistically. This class of problems has remained virtually untouched so far.

A new category of problems involving tether supported systems of three, four or more bodies is also receiving some attention lately. The objectives are quite varied ranging from simultaneous sounding of the environment at several altitudes to communication antenna, payload transfer and microgravity control. This represents a fertile field of considerable practical significance and promise.

- (vi) Finally, and perhaps most importantly, we urgently need carefully planned ground and space based experiments to validate and improve literally hundreds of algorithms aimed at flexible multibody attitude dynamics and control. Apparently, there are endless challenges, and so are the efforts needed to meet them. The ancient sages described knowledge as a tiny island surrounded by a vast ocean of ignorance. Like any process of inquiry, philosophical or scientific, no matter how far we advance, we will always be on the shores of an uncharted ocean. But then, a journey fulfills itself in every step. The end lies in the effort itself. Beyond that there are no permanent results.

ACKNOWLEDGEMENTS

The investigation reported here was supported by the Natural Sciences and Engineering Research Council of Canada, Grant No. STR-32682. Assistance of Mr. A. Ng. and Mr. A. Suleman, Postgraduate Fellows, in organization of the manuscript is gratefully acknowledged.

REFERENCES

- [1] Shrivastava, S.K., Tschann, C., and Modi, V.J., "Librational Dynamics of Earth Orbiting Satellites", Proceedings of the 14th Congress on Theoretical and Applied Mechanics, Kurukshetra, India, December 1969, ISTAM Publisher, pp. 284-306.
- [2] Modi, V.J., and Shrivastava, S.K., "Satellite Attitude Dynamics and Control in the presence Environmental Torques - A Brief Survey", Journal of Guidance, Control, and Dynamics, AIAA, Vol. 6, No. 6, Nov-Dec. 1983, pp. 461-471.
- [3] Markland, C.A., "A Review of Attitude Control of Communications Satellites," 32nd Congress of the International Astronautical Federation, Rome, Italy, September 1981, paper No. IAF-81-344.
- [4] Moran, J.P., "Effects of Plane Librations on the Orbital Motion of a Dumbell Satellite," ARS Journal, Vol. 31, No.8, August 1961, pp.1089-1096.
- [5] Yu, E.Y., "A Long-term Coupling Effects Between the Librational and Orbital Motions of a Satellite," AIAA Journal, Vol. 2, No. 3, March 1964, pp. 535-555.
- [6] Modi, V.J., and Brereton, R.C., "Stability of a Dumbell Satellite in a Circular Orbit During Coupled Librational Motions," Proceedings of the 18th Congress of the International Astronautical Federation, Vol. 1, Editor-in-Chief: M. Lunc, Pergamon Press, London, 1968, pp. 109-120.
- [7] Hénon, M., and Heiles, C., "The Applicability of the Third Integral of Motion: Some Numerical Experiments", Astronomical Journal, Vol. 69, No. 1, February 1964, pp. 73-79.
- [8] Modi, V.J., and Brereton, R.C., "Stability of the Planar Librational Motion of a Satellite in an Elliptic Orbit", Proceedings of the 17th International Astronautical Congress, Vol. 4, Gordon and Breach, Inc., New York, 1967, pp. 179-192.
- [9] Modi, V.J., and Brereton, R.C., "On the Periodic Solutions Associated with the Gravity Gradient Oriented System. Part I - Analytical and Numerical Determination", AIAA Journal, Vol. 7, No. 7, July 1969, pp. 1217-1225.
- [10] Modi, V.J., and Brereton, R.C., "On the Periodic Solutions Associated with the Gravity Gradient Oriented System: Part II - Stability Analysis", AIAA Journal, Vol. 7, No. 8, August 1969, pp. 1465-1468.
- [11] Modi, V.J., and Neilson, J.E., "Attitude Dynamics of Slowly Spinning Axisymmetric Satellites under the Influence of Gravity Torques", Proceedings of the 20th International Astronautical Federation Congress, Mar del Plate, Argentina, October 1969, Pergamon /Polish Scientific Publishers, 1971, pp. 563-596.
- [12] Modi, V.J., and Neilson, J.E., "On the Periodic Solutions of Slowly Spinning Gravity Gradient System", Celestial Mechanics - An International Journal of Space Dynamics, Vol. 5, No. 2, March 1972, pp. 126-143.
- [13] Modi, V.J., and Flanagan, R.C., "Attitude Dynamics of a Gravity Gradient Oriented Satellite Under the Influence of Solar Radiation Pressure", Aeronautical Journal, Vol. 5, No. 2, March 1972, pp. 126-143.
- [14] Modi, V.J., and Kumar, K., "Librational Dynamics of Gravity Oriented Satellites under the influence of Solar Radiation Pressure", Proceedings of the International Symposium on Computer-Aided Engineering, Editor: G.M.L. Gladwell, University of Waterloo Press, May 1971, pp. 359-377.
- [15] Shrivastava, S.K., and Modi, V.J., "Effect of Atmosphere on Attitude Dynamics of Axi-Symmetric Satellites", Proceedings of the 20th International Astronautical Federation Congress, Mar del Plate, Argentina, October 1969, Pergamon/Polish Scientific Publishers, 1971, pp. 563-596.
- [16] Modi, V.J., and Shrivastava, S.K., "On Coupled Librational Dynamics of Non-Autonomous Gravity Stabilized Systems in Presence of Atmosphere", AIAA 9th Aerospace Sciences Meeting, New York, January 1971, Paper No. 71-89; also as "Librations of Gravity-Oriented Satellites in Elliptic Orbits Through Atmosphere", AIAA Journal, Vol. 9, No. 11, November 1971, pp. 2208-2216.
- [17] Modi, V.J., and Pande, K.C., "Solar Pressure Induced Librations of Spinning axisymmetric Satellites", Journal of Spacecraft and Rockets, Vol. 11, No. 9, September 1973, pp. 615-617.
- [18] Budica, R.J., and Tong, K.L., "Shuttle On-orbit Attitude Dynamics Simulation", San Diego, AIAA/AAS Astrodynamics Conference, California, U.S.A., August 1982, Paper No. AIAA-82-1452.
- [19] Likins, P.W., "Dynamics and Control of Flexible Space Vehicles", NASA, TR-32-1329, January 1970.
- [20] Likins, P.W., and Bouvier, H.K., "Attitude Control of Nonrigid Spacecraft", Astronautics and Aeronautics, Vol. 9, May 1971, pp. 64-71.
- [21] Modi, V.J., "Attitude Dynamics of Satellites with Flexible Appendages - A Brief Review", Journal of Spacecraft and Rockets, Vol. 11, November 1974, pp. 743-751.
- [22] Williams, C.J.H., "Dynamics Modelling and Formulation Techniques for Non-Rigid Spacecraft", Proceedings of the ESA Symposium on Dynamics and Control of Non-Rigid Spacecraft, ESA SP 117. Frascati, Italy, May 1976, pp. 53-70.
- [23] Roberson, R.E., "Two Decades of Spacecraft Attitude Control", Journal of Guidance and Control, Vol. 2, January-February 1979, pp. 3-8.
- [24] Lips, K.W., "Dynamics of a Large Class of Satellites with Deploying Flexible Appendages", Ph.D. Dissertation, University of British Columbia, September 1980.

- [25] Lips, K.W., "Mathematical Modelling of Flexible Multibody Dynamics with Applications to Orbiting Systems", Ph.D. Dissertation, University of British Columbia, September 1980.
- [26] Special Section, "Large Space Structures Control: Early Experiments", Journal of Guidance, Control, and Dynamics, Vol. 7, No. 5, September - October 1984, pp. 513-562.
- [27] Ho, J.Y.L., "Direct Path Method for Flexible Multibody Spacecraft Dynamics", Journal of Spacecraft and Rockets, Vol. 14, No. 2, February 1977, pp. 102-110.
- [28] Singh, R.P., VanderVoort, R.J., and Likins, P.W., "Dynamics of Flexible Bodies in Tree Topology - A Computer-Oriented Approach", Journal of Guidance, Control, and Dynamics, Vol.10, No.5, September- October 1985, pp. 584-590.
- [29] Meirovitch, L., and Quinn, R.D., "Equations of Motion for Maneuvering Flexible Spacecraft", Journal of Guidance Control, and Dynamics, Vol. 10, No. 5, September-October 1987, pp. 453-465.
- [30] Vu-Quoc, L., and Simo, J.C., "Dynamics of Earth-Orbiting Flexible Satellites with Multibody Components", Journal of Guidance, Control, and Dynamics, Vol. 10, No. 6, November-December 1987, pp. 549-558.
- [31] Spanos, J.T., and Tsuha, W.S., "Selection of Component Modes for the Simulation of Flexible Multibody Spacecraft", AAS/AIAA Astrodynamics Specialist Conference, Stowe, Vermont, August 1989, Paper No. AAS 89-438.
- [32] Modi, V.J., and Ibrahim, A.M., "A General Formulation for Librational Dynamics of Spacecraft with Deploying Appendages", Journal of Guidance, Control, and Dynamics, Vol. 7, No. 5, September - October 1984, pp. 563-569.
- [33] Modi, V.J., and Ng, A.C., "Dynamics of Interconnected Flexible Members in the Presence of Environmental Forces: A Formulation with Applications", 39th Congress of the International Astronautical Federation, October 1988, Bangalore, India, Paper No. IAF-88-318; also Acta Astronautica, Vol. 19, NO. 6/7, 1989, pp. 561-571.
- [34] Hooker, W., "Equations of Motion for Interconnected Rigid and Elastic Bodies", Celestial Mechanics, Vol. 11, 1975, pp. 337-359.
- [35] Hughes, P.C., "Spacecraft Attitude Dynamics", John Wiley and Sons, New York, 1985, pp. 337-359.
- [36] Modi, V.J., and Ibrahim, A.M., "Dynamics of the Orbiter Based Construction of Structural Components for Space Platforms", Acta Astronautica, Vol. 12, No. 10, 1985, pp. 879-888.
- [37] Modi, V.J., and Ibrahim, A.M., "A General Formulation for Librational Dynamics of Spacecraft with Deploying Appendages", Journal of Guidance, Control, and Dynamics, Vol. 7, No. 5, September- October 1984, pp. 563-569.
- [38] Ibrahim, A.M., and Modi, V.J., "On the Orbiter Based Deployment of Flexible Members", 36th Congress of the International Astronautical Federation, Stockholm, Sweden, Paper No. IAF-85-230; also Acta Astronautica, Vol. 13, No. 10, 1986, pp. 319-331.
- [39] Ibrahim, A.M., and Modi, V.J., "A Formulation for Studying Steady State/Transient Dynamics of a Large Class of Spacecraft and its Applications", Proceedings of the 2nd International Symposium on Spacecraft Flight Dynamics, Darmstadt, W. Germany, October 20-23, 1986, Editors: T.D. Guyenne and J.J. Hunt, ESA Publications Division, The Netherlands, pp. 25-30.
- [40] Modi, V.J., and Ibrahim, A.M., "On the Orbiter Based Construction of the Space Station and Associated Dynamics", Progress in Astronautics and Aeronautics, Commercial Opportunities in Space, Editor-in-Chief: M. Summerfield, American Institute of Aeronautics and Astronautics, Vol. 110, pp. 96-113.
- [41] Modi, V.J., and Ibrahim, A.M., "On the Transient Dynamics of Flexible Orbiting Structures", Large Space Structures Dynamics and Control, Editors: S.N. Atluri and A.K. Amos, Springer-Verlag Publisher, New York, 1987, pp. 95-114.
- [42] Taylor Jr, L.W., and Balakrishnan, A.V., "A Mathematical Problem and a Spacecraft Control Laboratory Experiment (SCOLE) used to evaluate Control Laws for Flexible Spacecraft", NASA/IEEE Design Challenge, June 1984.
- [43] Mah, H.W., Modi, V.J., Morita, Y., and Yokota, H., "Dynamics and Control During Slewing Maneuvers", Acta Astronautica, Vol. 19, No. 2, 1989, pp. 125-143.
- [44] Modi, V.J., and Morita, Y., "Controlled Dynamics of a Shuttle Based Antenna System", Proceedings of the 28th Annual Conference of the Society of Instrument and Control Engineers, Matsuyama, Japan, July 1989, Editor: Y. Hashimoto, pp. 933-936.
- [45] Modi, V.J., and Morita, Y., "Dynamics and Control of the Shuttle Based SCOLE Type Large Antenna System", AAS/AIAA Astrodynamics Specialist Conference, Stowe, Vermont, U.S.A., August 1989, Paper No. NAS-89-436; also Advances in Astronautical Sciences, Vol. 67, Part 1, Editors: C.L. Thornton and J.E. Prussing, Univelt Inc., Publisher for the American Astronautical Society, in press; also Journal of the Astronautical Sciences, in press.
- [46] Basso, S.D., and Goldberg, G.D., "Modal Analysis of Selected Space Station Configurations", NASA, Report No. SSE-D-88-R8, June 1988.
- [47] Modi, V.J., Suleman, A., and Ng, A.C., "Modal Analysis and Dynamical Response of the Evolving Space Station", Proceedings of the ESA Workshop on Modal Representation of Flexible Structures by Continuum Methods, Noordwijk, The Netherlands, June 1989, Editor: D. Poelaert, in press.
- [48] Modi, V.J., Suleman, A., "A Dynamical Study of the Proposed Space Station Type Configuration", Acta Astronautica, Vol. 19, No. 5, 1989, pp. 377-391.
- [49] Butenin, N.V., Elements of Nonlinear Oscillations, Blaisdell, New York, N.Y., 1965, pp. 102-137.
- [50] Misra, A.K., and Modi, V.J., "Dynamics and Control of Tether Connected Two Body Systems - A Brief Review", Space 2000, AIAA, New York, 1983, pp. 473-514.

- [51] Misra, A.K., and Modi, V.J., "A Survey on the Dynamics and Control of Tethered Satellite Systems", NASA/AIAA/PSN International Conference on Tethers in Space, Arlington, Virginia, U.S.A., September 1986, Paper No. AAS-86-246; also Advances in Astronautical Sciences, Editors: P.M. Bainum et al., American Astronautical Society, Vol. 62, pp. 667-719.
- [52] Rupp, C.C., "A Tether Tension Control Law for Tethered Subsattellites Deployed Along Local Vertical", NASA TMX - 64963, September 1975.
- [53] Baker, W.P., Dunkin, J.A., Galaboff, Z.J., Johnston, K.D., Kissel, R.R., Rheirurth, R.R., and Siebel, M.P.L., "Tethered Subsattellite Study," NASA TMX-73314, 1976.
- [54] Ruying, F., and Bainum, P.M., "The Dynamics and Control of a Space Platform Connected to a Tethered Subsattellite," paper presented at the AIAA/NASA/PSN International Conference on Tethers in Space, Arlington, Virginia, U.S.A., September 1986.
- [55] Banerjee, A.K., and Kane, T.R., "Tethered Satellite Retrieval with Thruster Augmented Control," AIAA/AAS Astrodynamics Conference, San Diego, California, August 1982, Paper No. AIAA-82-1421.
- [56] Xu, D.M., Misra, A.K., and Modi, V.J., "Thruster Augmented Active Control of a Tethered Subsattellite System During its Retrieval," Journal of Guidance, Control, and Dynamics, Vol. 9, No. 6, Nov.-Dec. 1986, pp. 663-672.
- [57] Lakshmanan, P.K., Modi, V.J., and Misra, A.K., "Dynamics and Control of the Tethered Satellite System in the Presence of Offsets," Acta Astronautica, Vol. 15, No. 12, 1987, pp. 1053-1057.
- [58] Lakshmanan, P.K., Modi, V.J., and Misra, A.K., "Dynamics and Control of the Tethered Satellite System in the Presence of Offsets," Proceedings of the 11th Canadian Congress of Applied Mechanics Edmonton, Alberta, Canada, May-June 1987, pp. A-94 to A-95; also Fifth VPI & SU/AIAA Symposium on Dynamics and Control of Large Structures, Blacksburg, Virginia, U.S.A., June 1987, Editor: L. Meirovitch, pp. 563-578.
- [59] Lakshmanan, P.K., Modi, V.J., and Misra, A.K., "Dynamics and Control of the Space Station Based Tethered Payload," AAS/AIAA Astrodynamics Conference, Kalispell, Montana, August 1987, Paper No. AAS-87-434; also Advances in the Astronautical Sciences, Vol. 65, Part 1, Univelt Incorporated, Publisher for the American Astronautical Society, pp. 425-440.
- [60] Lakshmanan, P.K., Modi, V.J., and Misra, A.K., "Dynamics and Control of an Orbiting Platform Supported Tethered Satellite System", Proceedings of the IMACS/IFAC International Symposium on Modelling and Simulation of Distributed Parameter Systems, Hiroshima, Japan, October 1987, Editors: Y. Surahara, S.G. Tzafestas, and F. Tagami, Hiroshima Institute of Technology Publisher, pp. 367-374; also Mathematics and Computers in Simulation, Journal of the IMACS, in press.
- [61] Lakshmanan, P.K., Modi, V.J., and Misra, A.K., "Dynamics and Control of the Tethered Satellite System in the Presence of Offsets," 38th Congress of the International Astronautical Federation, Brighton, U.K., October 1987, Paper No. IAF-87-316; also as "Dynamics and Control of the Space Station Tethered Payload", Proceedings of the PSN/NASA/ESA 2nd International Conference on Tethers in Space, Venice, Italy, October 1987, Editors: L. Guerriero and I. Bekey, pp. 444-452; also Acta Astronautica, Vol. 19, No. 2, 1989, pp. 145-160.
- [62] Modi, V.J., Lakshmanan, P.K., and Misra, A.K., "Control of an Orbiting Platform Supported Tethered Satellite System", 11th IFAC Symposium on Automatic Control in Space, Tsukuba, Japan, July 1989, Editor: T. Tanabe, pp. 221-226.
- [63] Modi, V.J., Lakshmanan, P.K., and Misra, A.K., "Dynamics and Control of an Orbiting Tethered System", Proceedings of the 28th Annual Conference of the Society of Instrument and Control Engineers, Matsuyama, Japan, July 1989, Editor: Y. Hashimoto, pp. 941-944.
- [64] Modi, V.J., Lakshmanan, P.K., and Misra, A.K., "Offset Control Strategy for the Space Station Based Tethered Payload", AAS/AIAA Astrodynamics Specialist Conference, Snowe, Vermont, U.S.A., August 1989, Paper No. AAS-89-453; also Advances in the Astronautical Sciences, Vol. 67, Part 1, Editors: C.L. Thornton and J.E. Prussing, Univelt Inc., Publisher for the American Astronautical Society, in press.
- [65] Lakshmanan, P.K., Modi, V.J., and Misra, A.K., "Space Station Based Tethered Payload: Control Strategies and Their Relative Merit," Proceedings of the 3rd International Conference on Tethers in Space, AIAA/NASA/ASI/ESA, San Francisco, California, U.S.A., May 1989, pp. 166 - 177.
- [66] Modi, V.J., Lakshmanan, P.K., and Misra, A.K., "Offset Control of Tethered Satellite Systems: Analysis and Experimental Verification", 40th Congress of the International Astronautical Federation, Malaga, Spain, October 1989, Paper No. IAF-89-376; also Acta Astronautica, in press.
- [67] Modi, V.J., Lakshmanan, P.K., and Misra, A.K., "Dynamics and Control of Tethered Spacecraft During Deployment and Retrieval", Mechanics and Control of Space Structures, Progress in Astronautics and Aeronautics, Editor: J.L. Junkins, AIAA Publisher, in press.
- [68] Mah, H.W., Morita, Y., Modi, V.J., and Yokota, H., "A General Formulation for Studying Dynamics and Control of the Space Station Based Mobile Remote Manipulator System and its Application", AAS/AIAA Astrodynamics Conference, Kalispell, Montana, U.S.A., August 1987, Paper No. AAS-87-481; also Advances in Astronautical Sciences, Vol. 65, Part 2, Editors: A.K. Misra, R.E. Lindberg, et. al., Univelt Incorporated, Publisher for the American Astronautical Society, pp. 915-933; also Journal of the Astronautical Sciences, in press.
- [69] Mah, H.W., Modi, V.J., and Morita, Y., "A Relatively General Formulation for Studying Dynamics of the Space Station Based MRMS", AIAA 26th Aerospace Sciences Meeting, Reno, Nevada, U.S.A., January 1988, Paper No. AIAA-88-0674.

Table 1 Relative efforts during stationkeeping, deployment and retrieval for the three control strategies. Hybrid control demands are also included.

Case	Configuration	Tension	Thruster	Offset
Stationkeeping	Reference Case	169.3 Ns, 480.6 J	87.1 Ns, 503.2 J	22.9 Ns, 444.1 J
	$P_D/P_A = 2$	174.3 Ns, 502.7 J	97.2 Ns, 525.4 J	25.1 Ns, 467.4 J
	1000 m	190.2 Ns, 518.2 J	166.6 Ns, 556.1 J	42.3 Ns, 450.3 J
	$\rho_t = 1 \times 10^{-4}$ kg/m	181.4 Ns, 542.1 J	159.2 Ns, 560.7 J	56.9 Ns, 451.3 J
	$m_s = 500$ kg	190.1 Ns, 546.7 J	163.9 Ns, 569.6 J	57.1 Ns, 469.1 J
Deployment 10 m \rightarrow 1000 m	0.37 orbit	184.1 Ns, 513.5 J	159.7 Ns, 560.8 J	41.4 Ns, 450.1 J
Retrieval 100 m \rightarrow 10 m	1 orbit	1656.9 Ns, 546.5 J	1453.3 Ns, 573.9 J	385.0 Ns, 469.3 J
	0.68 orbit	1701.1 Ns, 555.8 J	1510.5 Ns, 594.7 J	495.7 Ns, 475.6 J
	0.37 orbit	1781.9 Ns, 581.4 J	1583.4 Ns, 609.8 J	585.3 Ns, 490.8 J
Retrieval 1000 m \rightarrow 10 m	0.37 orbit	6501.1 Ns, 641.1 J	6076.1 Ns, 649.2 J	10621.1 Ns, 509.3 J [*]
Hybrid Control Retrieval 1000 m \rightarrow 10 m	0.37 orbit tension/offset	3903.5 Ns, 312.9 J		503.7 Ns, 208.4 J
	0.37 orbit thruster/offset		2623.1 Ns, 280.6 J	525.5 Ns, 218.3 J

* Retrieval in one orbit with the initial tether disturbance reduced to $\alpha_t(0) = \gamma_t(0) = 1^\circ$.

P_A, P_D sides of the Space Station represented as a rectangular plate

ρ_t mass of the tether per unit length

m_s mass of the satellite

**A MODEL OF THE PERTURBED SPINNING
MOTION OF THE SAN MARCO 5th SPACECRAFT**

by

Prof. Carlo Arduini, Prof. Ord. "Sistemi Spaziali"
University Rome, La Sapienza, Italy

Ing. Giovanni La Neve
University/Telespazio, Italy

Ing. Daniele Mortari, "Progetto San Marco"
University Rome, La Sapienza, Italy

Lt.Colonel Eng. A.De Micco, Aeronautica Militare
Divisione Aerea Studi Ricerche e Sperimentazioni
Reparto Armamento, Pratica di Mare, Italy

SUMMARY

This paper describes models of the spin axis of a spacecraft moving in sub-equatorial orbit in a relatively dense atmosphere, and under non negligible gravity gradient and magnetic torque. These drift models have been used in the design of the San Marco 5th "Utafiti" aeronomy satellite for obtaining the most stable pointing condition and, also, for the refinement of the attitude measurements of the same spacecraft. The method of fitting is described and some results shown.

INTRODUCTION

SAN MARCO PROJECT (Co-operation University of Rome "La Sapienza" And Italian Air-Force)

The San Marco Project, which was formalized on May 31, 1962, is part of NASA's international cooperative program. The objective of this program is to pursue space research with the participatory country for the mutual benefit of both by entering into joint scientific programs wherein contributions of space research systems, including their cost and management responsibilities, are shared mutually. NASA's international activities are planned to provide opportunities for the participation of scientist and agencies of other countries in the task of increasing mankind's understanding and use of the spatial environment. The activities follow guidelines which establish a basis for sound programs of mutual value and contribute to the objectives of international cooperation.

A number of highly qualified University personnel belonging to the Italian Air-Force and to the National Council for Research are co-operating with the named San Marco Project in :

- a. spacecraft design, construction, integration and tests;
- b. range management, logistics, operation;
- c. rocket assembly, check-out and launch operations;
- d. ground station operation, mission control and data management.

The San Marco Project is based on the Scout vehicle system and on the Kenya Equatorial Range, located at Ngomeny bay, (2.9383 south latitude , 40.2125 east longitude) close to Malindi country. This site allows launches in a wide angular range from the equator to the pole and in particularly effective for low equatorial orbits. In the same site is located the San Marco Ground Station for Command and Telemetry in VHF, L, S, and X Bands.

SAN MARCO 5th SPACECRAFT

The San Marco 5th spacecraft (fig. 1) is an aeronomy satellite which was launched in a low nearly equatorial orbit (262 km perigee at B.O.L., 2.9 degrees inclination) and was operative down to altitudes lower than 150 km. During this lifetime period an attitude determination better than 0.2 degrees accuracy was needed. Due to the low altitude a relevant aerodynamic torque is acting on the spacecraft, together with an also non negligible gravity gradient torque (due to the presence of very long "cable booms" in the equatorial plane of the spacecraft). Under the action of these torques, the spin axis drift was nothing but negligible. It is not therefore possible improving the original quality of the attitude determination (based on horizon and sun sensors) by simple averaging or other statistical procedure, without a drift model of the spin axis under the combined action of the gravity gradient, magnetic and aerodynamic torques. The equations of the spin axis motion, linearized in the vicinity of the nominal pointing direction, have been solved in a closed form under the hypothesis of constant magnetic and gravity gradient torque and variable aerodynamic torque. The solution procedure has been based on appropriate changes of the reference system in such a way of having the " null torque " axis (or torque node) with the minimum variability with respect to the reference itself.

The torque node position has been also a major consideration in the design of the spacecraft, whose nominal pointing had to be the orbit anti-pole. The motion is basically a perturbed cone around the torque node. The approximated closed form solution, obtained in this way, has been used as an interpolation function for interpolating the experimental attitude points.

The paper will present the model and the results of its application to the attitude determination problem. From a theoretical point of view, the origin of the problems of the class described above can be traced back to the beginning of the space era and have been the object of many studies since then (Ref 3, 2, 8). The present application is characterized by the original closed form solution in the reference most suited to the interpolation requirements.

LINEAR DRIFT MODELS

Consider a gyroscopic spinning spacecraft with spin axis K ; the drift motion in the inertial reference under a torque M can always be described by; (Ref. 1)

$$(1) \quad \frac{dy}{dt} = \gamma \wedge H$$

where γ is the moment of momentum Unit Vector

$$\text{and } H = \frac{1}{\Gamma} (M \wedge \gamma) + z \gamma$$

Γ = Moment of momentum absolute value
 z = arbitrary constant

For particular torques M , the H vector is independent on γ . In this case the drift is "linear" and as a consequence the drift equation can be easily solved. This is for instance the case of the average magnetic torque (Ref. 1, 2, 3, 4) due to a constant intrinsic magnetic dipole. The gravity gradient torque, in general, is non linear (Ref. 1, 4) but for slightly variable attitudes it can be easily linearized. Also the aerodynamic torque can be linearized (see Appendix 1). So the eq. (1) can be used for the motion under the combined action of the three torques under the said hypotheses, which are, by the way, appropriate to the spacecraft under consideration. In addition the three considered torques, under the said hypotheses, are conservative, so the precession angle and the spin rate are bound to be constant (Ref. 1, 4).

So, if the motion is initially a pure spin, we have:

$$\gamma = K \quad (\text{spin axis unit vector}) \quad \text{and} \quad \Gamma = Cr = \text{const} \\ (\text{C} = \text{inertia moment around K, } r = \text{spin velocity})$$

the equation writes then:

$$(1') \quad \frac{dK}{dt} = K \wedge H$$

If the vector H is constant, the drift motion reduces to a cone around H , at a rate $|H|$. In the general case H is not constant in absolute value and in direction. For taking into account the modulus variations, we can easily refer to a modified variable:

$$\eta = \int^t |H| dt$$

and to the unit vector $h = H / |H|$, so we have:

$$(1'') \quad \frac{dK}{d\eta} = K \wedge h$$

If H is not constant in direction we may change the reference from the inertial to another, movable with respect to the inertial at rate ω

The (1') becomes, in the new reference:

$$\dot{K} + \omega \wedge K = K \wedge H \\ \text{that is} \\ (1''') \quad \dot{K} = K \wedge (H + \omega) = K \wedge H'$$

where \dot{K} is the derivative in the mobile reference. We see that the equation has the same form as the original one, the only difference is that H is replaced by:

$$H' = H + \omega$$

By an appropriate choice of the mobile reference (and therefore of ω) we can try to reduce the variability of the H direction. If, at the end, we succeed in having H' constant in direction, the drift is reduced to a coning around H' (in the mobile reference, of course). The change of reference can be applied in sequence as many times it is desired; most of the times it is not easy to arrive to $H' = \text{const.}$ in direction, but

it is always possible to obtain H' movable only over a coordinate plane. In this case it is possible to obtain a solution in iterative form in two important cases, namely: (Ref. 5)

- i) when the motion of the node is "slow" with respect to the coning period;
- ii) when the max angular displacement of the node is "small" with respect to the cone aperture.

For our spacecraft we have the situation of case (ii). The theory of (Ref. 5) has therefore been applied, as described in appendix 2.

THE INTERPOLATION OF THE ATTITUDE DATA

The theory of appendix 2 brings to the model:

$$\begin{cases} X_N = \Delta \cos(\bar{\omega} + \omega_n) + \gamma \cos \bar{\omega} - (\beta_* + \gamma \omega_n) \sin \bar{\omega} \\ Y_N = \Delta \sin(\bar{\omega} + \omega_n) + \gamma \sin \bar{\omega} + (\beta_* + \gamma \omega_n) \cos \bar{\omega} - \alpha \\ \bar{\omega} = \omega + \psi \end{cases}$$

The X_N , Y_N are the component of the spin axis unit vector in the "nodal reference" (X_N along the orbit ascending node, Z_N to the geographic North), ω is the argument of perigee, ψ is a small "asymmetry" angle, γ is a small parameter depending upon the perigee density variation with time, α is a small parameter depending upon the gravity gradient, and finally:

$$\omega_n = \dot{\omega}_n (t - t_0)$$

is an angle linearly varying with time. The rate $\dot{\omega}_n$ depends upon the perturbing torques, and mostly upon the gravity gradient and the magnetic torque. The Δ angle is related to the amplitude of the coning around the torque node, and depends upon the initial conditions. Among all these parameters only α can be evaluated "a priori" with fairly good accuracy, ω is in addition known from the orbital ephemerides. We will therefore consider α and ω known and we will try to evaluate the other parameters by fitting the experimental data. It is however convenient to fit the quantities:

$$\begin{cases} D_1 = X_N \cos \omega + (Y_N + \alpha) \sin \omega = \Delta \cos(\omega_n + \psi) + \gamma - (\beta_* + \gamma \omega_n) \psi \\ D_2 = -X_N \sin \omega + (Y_N + \alpha) \cos \omega = \Delta \sin(\omega_n + \psi) + (\beta_* + \gamma \omega_n) + \gamma \psi \end{cases}$$

in place of the original X_N , Y_N .

Since γ and ψ are "small quantities" and Δ and β_* finite quantities, D_1 is mostly a cosine curve, slightly perturbed by a small linear term, D_2 is a sinusoid with the origin shifted of the β_* value plus a small linear perturbing term. We may now consider two cases, namely:

- i) the interpolation is made over short period of times, such as to have a very small variation of ω_n with respect to its central value ω_c . In this case we have, by expanding the trigonometric functions in Taylor series:

$$\begin{cases} D_1 \approx a_1 + b_1(t - t_0) + c_1(t - t_0)^2 + \dots \\ D_2 \approx a_2 + b_2(t - t_0) + c_2(t - t_0)^2 + \dots \\ \begin{cases} a_1 = (\Delta \cos \omega_c + \gamma - \psi \beta_* - \gamma \psi \omega_c) \\ b_1 = -\Delta \dot{\omega}_n \sin \omega_c \\ c_1 = -(\Delta \dot{\omega}_n^2 \cos \omega_c)/2 \end{cases} \\ \begin{cases} a_2 = \Delta \sin \omega_c + \beta_* + \gamma \omega_c \\ b_2 = (\Delta \cos \omega_c + \gamma) \dot{\omega}_n \\ c_2 = -(\Delta \dot{\omega}_n^2 \sin \omega_c)/2 \end{cases} \end{cases}$$

By a parabolic fitting of the experimental data we can therefore obtain the six coefficients a_1 , b_1 , c_1 , a_2 , b_2 , c_2 .

- ii) The interpolation period is not as small as in the previous case, so that the full trigonometric formulas shall be retained. It is however still possible to consider constant the Δ , β_* , γ , ψ , $\dot{\omega}_n$ parameters.

In this case a least square fitting can be obtained by the following procedure:

- assume for $\dot{\omega}_n$ an initial guess;
- minimize the cost functional:

$$I = \int_{t_0}^{t_+} (|A+Bt+ C\cos\dot{\omega}_n t - D\sin\dot{\omega}_n t - D_1(t)|^2 + |A'+B't+ C\sin\dot{\omega}_n t + D\cos\dot{\omega}_n t - D_2(t)|^2) dt$$

where A, A', B, B', C, D are the unknown constants, related to the parameters of the physical model by the relationships:

$$A = \gamma - \Psi\beta_*$$

$$A' = \beta_* + \Psi\gamma$$

$$B = -\gamma\dot{\omega}_n\Psi$$

$$B' = \gamma\dot{\omega}_n$$

Notice that, since we have only three physical constants (β_* , γ , Ψ) against the four coefficients A, A', B, B' , the problem shall be intended as a "conditional minimum". The conventional method of the Lagrange multipliers brings in this case to non linear algebraic equations. This is the reason why an iterative procedure (based on the assumption $\Psi \ll 1$) has been preferred for the solution (Appendix 3);

- compute $I = I(\dot{\omega}_n)$, that is the the relative minimum of I for the given $\dot{\omega}_n$;
- search for the absolute minimum of " I " by varying the $\dot{\omega}_n$.

RESULTS AND DISCUSSION

Fig. (2, 3) show the experimental altitude points (days of the 1988 year from 114 to 163), in the vernal and in the "nodal reference". Fig. (4, 5, 6, 7) are the corresponding parabolic fittings of D_1, D_2 over the periods 114-139 and 139-163. Fig.(8, 9) are the fittings over the whole period by means of the trigonometric formulas. The mean square error is about 4 hundredths of degree for the two parabolic fittings, a little more (≈ 4.3 hundredths) for the trigonometric fitting. The max individual deviation of the experimental points of the set is about ± 0.2 degrees, Table I gives the coefficients of the fitting. It may be interesting to compare the parabolic and the trigonometric fittings: Fig. (10, 11).

Table I
TRIGONOMETRIC FITTING COEFFICIENTS, First period

A	APRIMO	B	BPRIMO	C	D
0.0024491	0.0404473	0.0000016	-0.0001380	-0.0265281	-0.0243701
BSTAR	GAMMA	PSI	OMD	DELTA	OMP
0.0404127	0.0029277	0.0118416	3.8886907	0.0361584	-2.70
Cost index I					
0.0000463					

We see certain discrepancies whose qualitative behaviour indicates variability of the parameters during the fitting period and could be described by a positive shift of the ω_n angle in the period 114 to 139, and a negative one in the remaining. Now, day 139 corresponds approximately to the min. of the diurnal density bulge located at the perigee, that is to a local asymmetry angle $\Psi = 0$.

We should have therefore negative in the first half of the period and positive in the second half, (instead of a constant and almost null value as given by the $\Psi = \text{const.}$ fitting). This evidences that the Ψ variations due to the density bulge have a detectable effect, and that an improvement of the fitting could be obtained by modeling this feature a variability of ω_n and $\dot{\omega}_n$ could however also depend upon induced magnetic dipole and/or non linear effects in aerodynamic torque). Table II, III, IV are giving the coefficients of the trigonometric fittings for different time periods. In each one of these periods the spacecraft is drifting freely (whilst, in between, correction maneuvers took place, with a consequent change in ω_n and Δ).

Table II
TRIGONOMETRIC FITTING COEFFICIENTS, 2^a period

A	APRIMO	B	BPRIMO	C	D
0.0077129	0.0373237	0.0000006	0.0000029	-0.0147464	-0.0325278
BSTAR	GAMMA	PSI	OMD	DELTA	OMP
0.0373066	-0.0000817	-0.2089327	4.2867541	0.0337144	-2.00
Cost index I					
0.0000299					

Table III
TRIGONOMETRIC FITTING COEFFICIENTS, 3_{rd} period

A	APRIMO	B	BPRIMO	C	D
0.0089488	0.0496719	-0.0000006	-0.0000033	-0.0445372	-0.0090789
BSTAR	GAMMA	PSI	OMD	DELTA	OMP
0.0496888	0.0000951	-0.1781835	-0.2010952	0.0454532	-2.00
Cost index I					
0.0000165					

Table IV
TRIGONOMETRIC FITTING COEFFICIENTS, 4_{th} period

A	APRIMO	B	BPRIMO	C	D
0.0192404	0.0821213	0.0000016	0.0000069	-0.0128541	-0.0798385
BSTAR	GAMMA	PSI	OMD	DELTA	OMP
0.0820851	-0.0001532	-0.2362612	4.5527580	0.0808666	-2.60
Cost index I					
0.0005424					

On the contrary continuity should be obtained in $\dot{\omega}_n$, $\beta = \beta_n + \dot{\gamma} \omega_n$. Fig. (12) shows the $\dot{\omega}_n$ and β behaviour. $\dot{\omega}_n$ is -2.7 degrees/day in the first period, 2.0 degrees/day in the second period and third, -2.6 degrees/day in the fourth period. Notice that $\dot{\omega}_n$ is the small difference of relatively large terms, and that $\dot{\gamma}$ is one of the contribution (which has been neglected) this can explain the relatively large $\dot{\omega}_n$ discontinuity. A discontinuity is observed also in the aerodynamic parameter β . An overall increasing trend can be noticed, and this is a little larger, but qualitatively in agreement with, for instance, the corresponding variation of the drag parameter of the orbit decay as given by the NORAD tracking elements (Fig. 13). Fig. 14 shows actual perigee force data during the first period, compared with the computed β . We see that the hypothesis of linear variation is actually far from reality and that we cannot expect improvements beyond the obtained accuracy without substantially improving the density model.

CONCLUSIONS

The fitting of the experimental data with the closed form model in the appropriate reference system made it possible to build smooth interpolated attitudes with r.m.s. and local deviations compatible with the experimenters requirements. It made also possible to understand the type of motion and its physical causes, although the detailed analysis of the parameters evidenced that some of the hypotheses, shall be revised if a better internal consistency is desired. In particular a density model incorporating at least the bulge effects should be used.

APPENDIX 1

THE MODELS OF THE ACTING TORQUES

The torques acting on the spacecraft can be modeled as it follows: (Ref. 1, 2, 3, 4)

Gravity gradient (orbital average)

$$A-1) \quad M_g = -Cr \dot{\omega}_p (k \wedge n)$$

k = spin axis unit vector; n = orbit normal unit vector;

$$\dot{\omega}_p^2 = (\dot{\omega}_p^2) \omega_p^2 \cdot \frac{C-A}{Cr} \cdot (k \cdot n); \quad \omega_p^2 = \frac{\mu(1-e^2)^{3/2}}{p^3};$$

μ = planetary constant; p = orbit parameter;
 C = max inertia moment of s/c ; A = min inertia moment of s/c ($B=A$);
 e = orbit eccentricity; r = spin velocity;
 $(k \cdot n) \approx -1$ for slightly variable K (linearization hypothesis) around the nominal position (the anti-pole of the orbit)

Magnetic torque (orbital and daily average)

$$A-2) \quad M_m \approx -Cr \dot{\omega}_m k \wedge [(\dot{\omega}_m^2) (\cos i) n - \dot{\omega}_m^2 N]$$

$$\dot{\omega}_m^2 = \frac{\mu_{pk} \mu_E (1-e^2)^{3/2}}{p^3 Cr} \cos I; \quad \mu_{pk} = \text{on board magn. dipole along spin axis};$$

μ_E = earth magnetic dipole; e = orbit eccentricity;
 i = orbit inclination; I = magnetic earth axis inclination;
 N = geographic north unit vector.

Aerodynamic torque

The geometry of the spacecraft is mostly axisymmetric, with only minor surfaces with polygonal symmetry (the four inertial booms, the four cable booms) or asymmetric. The spin around the axis of symmetry is, on the other hand, producing a complete axisymmetry for what is concerning the average drifting action. In these conditions the aerodynamic force passes necessarily through a point of the axis of symmetry (the center of pressure C.P.), where, on well balanced spacecraft, also the center of gravity (C.G.) is laying. In the hypothesis of Ref. 6, the force is also a pure drag, directed opposite to the spacecraft velocity relative to the atmosphere. This cannot be very different from the inertial velocity.

The instantaneous torque expression is then:

$$M = (\dot{\omega}_m^2) C_D \rho V^2 S d (k \wedge v)$$

where S is the surface normal to the wind, k the spin axis unit vector, v the velocity unit vector, ρ the local density, V the velocity and C_D a drag coefficient (generally close to the value $C_D = 2$). The "d" factor is the CP-CG measured along the symmetry axis.

S and d are generally variable with the incidence α ($\sin \alpha = k \cdot v$). For a sphere we have however $S = S_s = \text{const}$, $d = d_s = \text{const}$. For a body with "center" (Ref 9) (for instance a cylinder) we have $d_c = \text{const}$, $S = S(\alpha)$.

In the case of San Marco 5, the body is practically a sphere plus two small cylinders at the top and bottom, both equal and centered with respect to the sphere. The C.G. of the body is slightly down with respect to the center of the configuration above, so four winglets are attached to the bottom cylinder for lowering the overall C.P.

We have then:

$$S \cdot d = [S_s + S_1 \cos \alpha + S_b |\sin \alpha|] d_s + S_w \cos \alpha \cdot d_w$$

where S_s is the cross section of the sphere, S_1 the area of the two cylinders projected normal to the axis, S_b the base area of the cylinders, S_w the projected area of the winglets, d_w the distance of the winglets from the CG, d_s the eccentricity of the main body, α the "incidence": $\sin \alpha = k \cdot v$.
 in our case it is now

$$S_b / (S_s + S_1) = S_1 / S_s = (\sin \alpha) \leq 0,1,$$

so we may put:

$$S_s = (S_1 + S_b) d_s + S_w d_w = S_0 d_0 = \text{const}$$

within less than 1% of S_{ad} in the whole field of the possible incidences. The body can be therefore considered as an excentric sphere as far as the drift model is concerned. The corresponding torque is conservative and can be averaged as it follows (Ref. 5):

$$A-3) \quad M_a = -Cr \dot{\omega}_a (k \wedge \bar{Q})$$

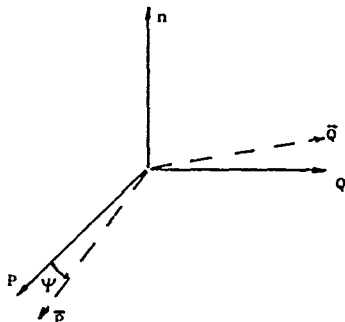


Fig. A-1

$$\begin{aligned} \bar{Q} &= n \wedge \bar{P}; \\ \bar{P} &= P \cos \Psi + \sin \Psi (n \wedge P) \approx P + \Psi (n \wedge P); \quad (\Psi \ll 1) \\ \bar{P} &= \text{"modified" perigee unit vector;} \\ P &= \text{perigee unit vector;} \\ \dot{\omega}_a &\approx \eta_p \rho_0 V_0^2 S d / Cr; \quad (C_D \approx 2) \\ \rho_0 &= \text{density at the perigee;} \\ V_0 &= \text{velocity at the perigee;} \\ S &= s/c \text{ surface normal to the wind;} \\ d &= CP/CG \text{ excentricity (computed along } k); \end{aligned}$$

$$\eta_p = \frac{(1-e^2)^{3/2}}{1+e} \exp(-\lambda) [I_1(\lambda) + e I_0(\lambda)];$$

$$I_1, I_0 \text{ Modified Bessel functions;} \\ e p$$

$$\lambda = \frac{(1+e)H_p}{(1+e)H_p};$$

$$H_p = \text{density scale height at perigee.}$$

The \bar{Q} unit vector refers to the resultant of the aerodynamic force in one orbit. For a keplerian orbit and for a density profile depending only upon the altitude, \bar{Q} should be coincident with Q , the normal to the perigee direction P . This is not however the case, mostly because of the diurnal density bulge, which is shifting \bar{P} with respect to P in the direction of the sun. This is taken into account by introducing an "asymmetry angle" Ψ , which reflects this bulge effect, together with other possible asymmetries (perigee precession, decay, etc.).

Solar torque

From the effected analysis, solar torque effects could not be detected.

Induced magnetic torque

No important ferromagnetic masses are present on board, so this torque shall be very minor, and its effects are in any case difficult to be separated from the intrinsic dipole torque. It has therefore been neglected in the present model.

APPENDIX 2

EQUATIONS OF MOTION AND DRIFT MODELS

1) Equations

In the inertial reference (or vernal reference γ, λ, N , $\gamma =$ vernal equinox, $N =$ North unit vector.)

$$A-4) \quad \frac{dk}{dt} = (M_a + M_g + M_m) / Cr$$

Let us consider a first rotating reference ν, μ, N (nodal reference):

$\nu =$ ascending node unit vector
 $N =$ geographic North unit vector

In this frame let us consider

$n^T \equiv (0, -\sin i, \cos i)$ orbit normal
 $i =$ orbit inclination measured clockwise from n to N

$\tau \equiv (0, \sin a, \cos a)$
 a measured clockwise from N to τ

This frame rotates with velocity $(\dot{\Omega}_N \cdot N)$ around N
($\dot{\Omega}_N =$ node advance rate (negative)).
The drift equation in this reference is

$$A-5) \quad \dot{k} = -k \wedge \{ (\dot{\omega}_g + (\pi/2) \cos i \dot{\omega}_m) n + (-\dot{\Omega}_N - (\pi/2) \dot{\omega}_m) N + \dot{\omega}_a 0 \}$$

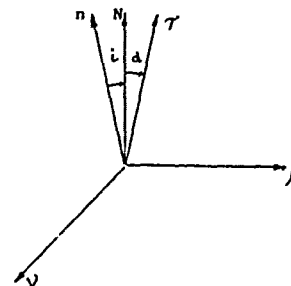


Fig. A-2

We put:

$$\begin{aligned}
 & (\dot{\omega}_o + (\pi/2) \cos i \dot{\omega}_n) n + (-\dot{\Omega}_N - (\pi/2) \dot{\omega}_n) N = \dot{\omega}_r \tau \\
 & \dot{\omega}_r = [-\dot{\Omega}_N - (\pi/2) \dot{\omega}_n + (\dot{\omega}_o + (\pi/2) \dot{\omega}_n \cos i) \cos i] * \\
 & * \left[1 + \frac{(\dot{\omega}_o + (\pi/2) \dot{\omega}_n \cos i)^2 \sin^2 i}{[-\dot{\Omega}_N - (\pi/2) \dot{\omega}_n + (\dot{\omega}_o + (\pi/2) \dot{\omega}_n \cos i) \cos i]^2} \right]^{1/2} \\
 \text{A-6)} \quad & \dot{\omega}_r \approx -\dot{\Omega}_N + \dot{\omega}_n + \dot{\omega}_o \quad \text{for } i \ll 1 \\
 & \sin \alpha = - \frac{(\dot{\omega}_o + (\pi/2) \dot{\omega}_n \cos i) \sin i}{\dot{\omega}_r} \\
 & \cos \alpha \approx 1 \\
 & \tau^T \approx (0, \sin \alpha, \cos \alpha)
 \end{aligned}$$

and we rewrite the equation:

$$\text{A-7)} \quad \dot{k} = -k \wedge [\dot{\omega}_r \tau + \dot{\omega}_a \bar{0}] \quad (\text{in the nodal reference } \gamma, \mu, N)$$

Let us now consider a second reference P', O', τ (modified orbital reference):

$$\text{A-8)} \quad \begin{cases} O' = (\tau \wedge \bar{P}) / |\tau \wedge \bar{P}| & \bar{P} = \text{modified perigee unit vector} \\ P' = O' \wedge \tau & (\text{see Appendix 1}) \end{cases}$$

This reference rotates at a speed which, at the first order in i , $(1+d)$ is $\dot{\omega}_n \approx \dot{\bar{\omega}}_r$, with: $\bar{\omega} = \dot{\omega} + \Psi$, $\dot{\omega}$ = rate of variation of the argument of perigee, $\dot{\Psi}$ = rate of variation of the "asymmetry" parameter.

The drift equation in this reference is therefore

$$\text{A-9)} \quad \dot{k} = -k \wedge [\dot{\omega}_r \tau - \dot{\omega}_a \bar{0} - \dot{\bar{\omega}} \tau] = -k \wedge ((\dot{\omega}_r - \dot{\bar{\omega}} + \xi \dot{\omega}_a) \tau + \dot{\omega}_a O')$$

where ξ is defined by

$$\text{A-10)} \quad \bar{0} = O' + \xi \tau$$

and it is

$$\text{A-11)} \quad \xi \approx (i+d) \cos \bar{\omega} \ll 1$$

We define now:

$$\text{A-12)} \quad \dot{\omega}_n = (\dot{\omega}_r - \dot{\bar{\omega}} + \xi \dot{\omega}_a) \left[1 + \frac{\dot{\omega}_a^2}{(\dot{\omega}_r - \dot{\bar{\omega}} + \xi \dot{\omega}_a)^2} \right]^{1/2}$$

If we consider $\dot{\omega}_a$ small of the first order with respect to $\dot{\omega}_r - \dot{\bar{\omega}}$, the corrective terms in $\dot{\omega}_n$ are of the 2nd order and therefore

$$\text{A-13)} \quad \dot{\omega}_n \approx -(\dot{\Omega}_N + \dot{\bar{\omega}}) + \dot{\omega}_n + \dot{\omega}_o.$$

We define in addition

$$\text{A-14)} \quad h^T = (0, -\sin \beta, \cos \beta) \quad \begin{cases} \sin \beta = - \frac{\dot{\omega}_a}{\dot{\omega}_n} & \cos \beta \approx 1 \\ \beta \ll 1 \end{cases}$$

and the equation becomes

$$\text{A-15)} \quad \dot{k} = -k \wedge \dot{\omega}_n h \quad \text{in the modified orbital reference } (P', O', \tau).$$

In scalar form

$$\text{A-16)} \quad \begin{cases} \dot{x} = -\dot{\omega}_n (y \cos \beta + z \sin \beta) \\ \dot{y} = +\dot{\omega}_n x \cos \beta \\ \dot{z} = +\dot{\omega}_n x \sin \beta \end{cases} \quad k^T \equiv (x, y, z)$$

β represents the effects of the aerodynamic drag.

2) The drift models.

We may build models corresponding to various hypothesis on the drag:

i) No drag $\beta = 0$. In this case the integration of 1) gives

$$A-17) \begin{cases} x = \sin \bar{\Delta} \cos \omega_n t & \omega_n = \omega_{n0} + \dot{\omega}_n(t-t_0) \\ y = \sin \bar{\Delta} \sin \omega_n t \\ z = \cos \bar{\Delta} = \text{const} \end{cases}$$

where x, y, z are the components of k in the P', O', τ reference. $\bar{\Delta}$ is an angle depending upon the initial conditions. The motion is a cone of constant aperture $\bar{\Delta}$, swept at constant angular rate ω_n .

ii) Constant drag $\beta = \text{const}$.

In this case Eq. A-16 integrates as:

$$A-18) \begin{cases} x = \sin \bar{\Delta} \cos \omega_n t \\ y = -\cos \bar{\Delta} \sin \beta t + \cos \beta \sin \bar{\Delta} \sin \omega_n t \\ z = \cos \bar{\Delta} \cos \beta t + \sin \beta \sin \bar{\Delta} \sin \omega_n t \end{cases}$$

when $\beta \ll 1$, $\sin \bar{\Delta} \ll 1$, $\cos \bar{\Delta} \approx -1$ (as in our case), we may refer to $\Delta = \pi - \bar{\Delta} \ll 1$ and use the linearised form:

$$A-19) \begin{cases} x \approx \Delta \cos \omega_n t \\ y \approx \Delta \sin \omega_n t + \beta \\ z \approx -1 + \beta \Delta \sin \omega_n t + (\beta^2 + \Delta^2)/2 \approx -1 \end{cases}$$

at the first order. The motion is again a cone of constant aperture $\bar{\Delta}$, but around

$$h^\tau = (0, -\beta, 1 - \beta^2/2) \approx (0, -\beta, 1)$$

iii) Variable drag.

In this case from Eq. 1 we obtain the solving equation in x :

$$A-21) \beta' (x'' + x) = \beta'' (x'' + x) - (\beta')^2 x$$

$$\text{where } (\cdot)' = \frac{d}{d\omega_n} = \frac{1}{\dot{\omega}_n} \cdot \frac{d}{dt}$$

We can solve exactly the case $\beta' = \text{const}$ and approximately the case of general variability of β at a very small rate.

3-1) Linearly variable β .

In this case we put $\beta' = \text{const} = \gamma$ and obtain:

$$A-22) \begin{cases} x'' + x(1 + \gamma^2) = \text{const} = b(1 + \gamma^2) \\ x = b + a \cos k \omega_n \\ y \cos \beta + z \sin \beta = ak \sin k \omega_n \\ x^2 + y^2 + z^2 = 1 \end{cases} \quad \begin{cases} k = (1 + \gamma^2)^{1/2} \\ \omega_n = \omega_{n0} + \dot{\omega}_n(t-t_0) \end{cases}$$

a and b are not independent. From the first two relationship we obtain in fact:

$$(x-b)^2 + \left[\frac{y \cos \beta + z \sin \beta}{k} \right]^2 = a^2 \quad \text{and, by derivation with respect to } \omega_n:$$

$$2(x-b)x' + 2 \left[\frac{y \cos \beta + z \sin \beta}{k} \right] \left[\frac{y' \cos \beta + z' \sin \beta}{k} - \dot{\omega}_n \frac{y \sin \beta - z \cos \beta}{k} \right] = 0$$

that is also, by recalling the original equations A-16):

$$A-23) \quad 2xx' - 2bx' - \frac{2x'}{k} \left[\frac{x}{k} - \gamma \frac{y \sin \beta - z \cos \beta}{k} \right] = 0 \quad \text{which give}$$

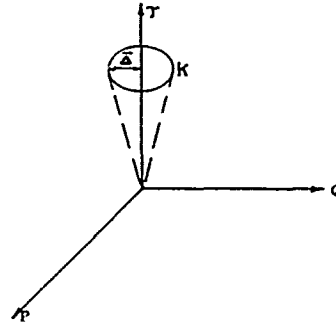


Fig. A-3

$y \sin \beta - z \cos \beta = -\gamma x + bk^2/\gamma$ by using this equation and the second of Eq. A-16 we get:

$$A-24) \begin{cases} y = -(\gamma x - bk^2/\gamma) \sin \beta - x' \cos \beta \\ z = (\gamma x - bk^2/\gamma) \cos \beta - x' \sin \beta \end{cases}$$

If we now apply the $x'^2 + y'^2 + z'^2 = 1$ we obtain the necessary condition:

$$x'^2 + x'^2 + (\gamma x - bk^2/\gamma)^2 = 1 \quad \text{With some algebra we obtain:}$$

$$A-25) \quad b = -\gamma \left[\frac{1}{k^2} - a^2 \right]^{1/2}$$

which is the necessary relationship between a and b. The constants a and ω_{n0} are then obtained from the initial conditions. In the practical case of very small $\beta' = \gamma \ll 1$ we have, at the first order $k^2 \gg 1$, and we may put also:

$$A-26) \begin{cases} a = \sin \bar{\Delta} \\ b \approx -\gamma \cos \bar{\Delta} \end{cases} \quad \text{and therefore}$$

$$A-27) \begin{cases} x \approx -\gamma \cos \bar{\Delta} + \sin \bar{\Delta} \cos \omega_n \\ y \approx \sin \bar{\Delta} (\sin \omega_n \cos \beta - \gamma \cos \omega_n \sin \beta) - \cos \bar{\Delta} \sin \beta \\ z \approx \cos \bar{\Delta} \cos \beta + \sin \bar{\Delta} (\sin \omega_n \sin \beta + \gamma \cos \omega_n \cos \beta) \end{cases} \quad \ll 1$$

When also $\sin \bar{\Delta} \ll 1$, $\cos \bar{\Delta} \approx -1$ (our specific case)
 $\sin \beta \ll 1$, $\cos \beta \approx 1$

We refer to $\Delta = \pi - \bar{\Delta}$ and we use the linearized form:

$$A-28) \begin{cases} x \approx \gamma + \Delta \cos \omega_n & \omega_n = \omega_{n0} + \dot{\omega}_n(t-t_0) \\ y \approx \beta + \Delta \sin \omega_n & \beta = \beta_0 + \dot{\beta} \omega_n \\ z \approx -1 + \Delta \beta \sin \omega_n + \Delta \cos \omega_n + \Delta^2 / z \approx \beta^2 / z \approx -1 \end{cases} \quad \begin{matrix} \gamma \ll 1 \\ \sin \bar{\Delta} \ll 1 \\ \sin \beta \ll 1 \end{matrix}$$

The instantaneous motion is still a cone of aperture Δ' around

$$A-29) \quad h'^T \approx \begin{bmatrix} -\gamma, -\beta, -1 + \frac{\beta^2}{2} + \frac{\gamma^2}{2} \end{bmatrix} \approx (-\gamma, -\beta, -1)$$

Since $\beta = \beta_0 + \dot{\beta} \omega_n = (\beta_0 + \dot{\beta} \omega_{n0}) + \dot{\beta} \dot{\omega}_n(t-t_0)$, the axis of the cone moves linearly parallel to the y axis.

iii-b) β arbitrarily variable, $\beta' \ll 1$. In this case from the solving equation A-21) we get:

$$A-30) \quad x'' + x = b_1 \beta' \quad \beta' \ll 1 \quad b_1 = \text{const} \quad \text{and we easily derive:}$$

$$A-31) \quad x = a_1 \cos \omega_n + b_1 \int_0^{\omega_n} \beta'(\lambda) \sin(\omega_n - \lambda) d\lambda$$

where a_1 and b_1 are constant and $\omega_n = \omega_{n0} + \dot{\omega}_n(t-t_0)$. (Iterations of the solution above are also feasible for larger values of β'). If $\beta' = \text{const}$ we have also:

$$A-32) \quad x = (a_1 - b_1 \beta') \cos \omega_n + b_1 \beta' = b + a \cos \omega_n$$

which therefore is coincident with the expression of the previous paragraph for $k^2 \rightarrow 1$ $\gamma \ll 1$, γ^2 negligible.

3) Our model for fitting the attitude data

In our physical case the drag is variable with time because of the lowering of the perigee, the orbit circularization and possibly other effects related to the dynamics of the atmosphere. In a first portion of the lifetime the drag variation can actually be thought as practically linear. The last portion of the lifetime is however characterised by a drag increasing much more than linearly in time. We will however limit the fitting to periods short enough for the drag to be considered linearly variable at least as average in the period, with $\gamma \ll 1$.

The drag velocity $\dot{\omega}_a$ will be always small enough, with respect to ω_n , to assume $\beta \ll 1$ and $\omega_n \approx \text{const}$ (on $\dot{\omega}_n$ actually there are playing also factors like $\dot{\omega}$, $\dot{\Omega}_n$, which are slightly variable, and $\dot{\omega}_a$, $\dot{\omega}_n$ which are variable too (for instance with the spin velocity). These variations are however minor, so that in every fitting period we accept $\omega_n = \text{const}$). Also the (small) Ψ parameter is actually variable (with a period of about 52 days, the perigee rotation period with respect to the sun). The effects of Ψ , although small, could be still detect. The present fitting is however based on $\Psi = \text{const}$, $\Psi = 0$, and the effects of this assumption will be discussed later on. The displacements of the spin axis from the torque node τ is always very small (most of the time $< 3^\circ$), so we have also $\Delta \ll 1$. In conclusion we are proposing the use of the A-28 model; we will study in particular the motion in the xy plane. In the modified orbital reference:

$$\begin{cases} x = \gamma + \Delta \cos \omega_n \\ y = \beta_0 + \gamma \omega_n + \Delta \sin \omega_n \\ h = \omega_{n0} + \dot{\omega}_n(t-t_0) \end{cases}$$

and try to fit the experimental data by the appropriate choice of the constants

$$\gamma, \Delta, \beta_0, \omega_{n0}, \dot{\omega}_n$$

Notice that the x and y coordinates are those in the (P', Q', τ) modified orbital reference system. The measurements are actually made in the vernal (γ, λ, N) reference. We have now from the geometry:

$$\begin{bmatrix} \gamma \\ \lambda \\ N \end{bmatrix} = \begin{bmatrix} \cos(\bar{\omega} + \Omega) & -\sin(\bar{\omega} + \Omega) & -a \sin \Omega \\ \sin(\bar{\omega} + \Omega) & \cos(\bar{\omega} + \Omega) & a \cos \Omega \\ -a \sin \omega & -a \cos \omega & 1 \end{bmatrix} \begin{bmatrix} P' \\ Q' \\ \tau \end{bmatrix}$$

$\bar{\omega} = \omega + \Psi$; ω = argument of perigee; Ψ = "asymmetry angle"; Ω = right ascension of the ascending node

The drift model in the nodal reference is therefore:

$$\begin{cases} X_N = \Delta \cos(\bar{\omega} + \omega_n) + [\gamma \cos \bar{\omega} - (\beta_0 + \gamma \omega_n) \sin \bar{\omega}] \\ Y_N = \Delta \sin(\bar{\omega} + \omega_n) + [\gamma \sin \bar{\omega} + (\beta_0 + \gamma \omega_n) \cos \bar{\omega}] - a \end{cases}$$

and in the vernal reference:

$$\begin{cases} X_\gamma = \Delta \cos(\bar{\omega} + \Omega + \omega_n) + [\gamma \cos(\bar{\omega} + \Omega) - (\beta_0 + \gamma \omega_n) \sin(\bar{\omega} + \Omega)] + a \sin \Omega \\ Y_\gamma = \Delta \sin(\bar{\omega} + \Omega + \omega_n) + [\gamma \sin(\bar{\omega} + \Omega) + (\beta_0 + \gamma \omega_n) \cos(\bar{\omega} + \Omega)] - a \cos \Omega \end{cases}$$

4) Orders of magnitude.

Orders of magnitude of the torques are:

Gravity gradient torque	$M_g \approx 1.10 \div 1.20 \cdot 10^{-4} \text{ Nm}$
Magnetic torque	$M_m \leq 1.5 \cdot 10^{-6} \text{ Nm}$
Aerodynamic torque (BDL)	$M_a \leq 2 \cdot 10^{-6} \text{ Nm}$
Aerodynamic torque (EOL)	$M_a \leq 5 \cdot 10^{-5} \text{ Nm}$
Solar torque	$M_s \leq 3 \cdot 10^{-8} \text{ Nm}$

APPENDIX 3

FITTING OF THE ATTITUDE DATA

As explained in the text, we apply a least square procedure based on minimizing the cost functional:

$$\begin{aligned} I &= \int_{t_0}^{t_f} ([A + Bt + C \cos \dot{\omega}_n t - D \sin \dot{\omega}_n t - D_1(t)]^2 + [A' + B't + C \sin \dot{\omega}_n t + D \cos \dot{\omega}_n t - D_2(t)]^2) dt = \\ &= K_1(A^2 + A'^2 + C^2 + D^2) + 2K_2(AB + A'B') + K_3(B^2 + B'^2) + 2K_4(CA + DA') + 2K_5(CA' - DA) + 2K_6(CD + DB') + \\ &\quad + 2K_7(CB' - DB) - 2AN_1 - 2A'N_2 - 2BN_3 - 2B'N_4 - 2CN_5 - 2DN_6 + N_7 \end{aligned}$$

where: $K_1 = (t_r - t_0)$; $K_2 = (t_r^2 - t_0^2)/2$; $K_3 = (t_r^3 - t_0^3)/3$;

$$K_4 = \frac{\sin(\dot{\omega}_n t_r) - \sin(\dot{\omega}_n t_0)}{\dot{\omega}_n}; \quad K_5 = \frac{\cos(\dot{\omega}_n t_0) - \cos(\dot{\omega}_n t_r)}{\dot{\omega}_n};$$

$$K_6 = \frac{t_r \sin(\dot{\omega}_n t_r) - t_0 \sin(\dot{\omega}_n t_0)}{\dot{\omega}_n} - \frac{K_5}{\dot{\omega}_n}; \quad K_7 = \frac{t_0 \cos(\dot{\omega}_n t_0) - t_r \cos(\dot{\omega}_n t_r)}{\dot{\omega}_n} + \frac{K_4}{\dot{\omega}_n}$$

$$N_1 = \int_{t_0}^{t_r} D_1 dt; \quad N_2 = \int_{t_0}^{t_r} D_2 dt; \quad N_3 = \int_{t_0}^{t_r} t D_1 dt; \quad N_4 = \int_{t_0}^{t_r} t D_2 dt;$$

$$N_5 = \int_{t_0}^{t_r} (D_1 \cos \dot{\omega}_n t + D_2 \sin \dot{\omega}_n t) dt; \quad N_6 = \int_{t_0}^{t_r} (D_2 \cos \dot{\omega}_n t - D_1 \sin \dot{\omega}_n t) dt;$$

$$N_7 = \int_{t_0}^{t_r} (D_1^2 + D_2^2) dt$$

The A, A', B, B' constants are not independent, but:

$$\begin{aligned} A &= \gamma - \Psi(\beta_0 + \gamma \omega_{n0}) & \Psi &= -B/B' \\ A' &= \beta_0 + \gamma \omega_{n0} + \Psi \gamma & \gamma &= \frac{1}{1+(B/B')^2} [A - (B/B')A'] = B'/\dot{\omega}_n \\ B &= -\gamma \dot{\omega}_n \Psi & \beta_0 &= \frac{1}{1+(B/B')^2} [(B/B')A + A'] - \gamma \omega_{n0} \\ B' &= \gamma \dot{\omega}_n \end{aligned}$$

So a condition does exist among these variables, namely $A - (B/B')A' = (B'/\dot{\omega}_n)[1 + (B/B')^2]$

This condition is not linear, and its treatment with the usual Lagrange multiplier method brings to a non linear algebraic equation. We prefer therefore the following iterative method:

i) the equations of the minimum are written as for all independent variables:

$$\begin{array}{cccccc|ccc} K_1 & 0 & K_2 & 0 & K_4 & -K_5 & A & & N_1 \\ 0 & K_1 & 0 & K_2 & K_6 & K_4 & A' & & N_2 \\ K_2 & 0 & K_3 & 0 & K_7 & -K_7 & B & & N_3 \\ 0 & K_2 & 0 & K_3 & K_7 & K_6 & B' & & N_4 \\ K_4 & K_5 & K_4 & K_7 & K_1 & 0 & C & & N_5 \\ -K_5 & K_4 & -K_7 & K_6 & 0 & K_1 & D & & N_6 \end{array} =$$

ii) the condition is expressed as $\beta = -\Psi B'$ and the β variable is eliminated from the equations accordingly:

$$\begin{array}{cccccc|ccc} K_1 & 0 & -\Psi K_2 & K_4 & -K_5 & & A & & N_1 \\ 0 & K_1 & K_2 & K_6 & K_4 & & A' & & N_2 \\ 0 & K_2 & K_3 & K_7 & K_6 & & B' & & N_3 \\ \Psi K_4 & K_5 & (K_7 - \Psi K_6) & K_1 & 0 & & C & & N_4 \\ -K_5 & K_4 & (K_6 + \Psi K_7) & 0 & K_1 & & D & & N_5 \end{array} =$$

The system is solved by assuming for Ψ a starting value (for instance $\Psi = 0$). We compute then:

$$\tan \omega_{n0} = D/C; \quad \text{sign}(\sin \omega_{n0}) = \text{sign}(D); \quad \Delta = D/\sin \omega_{n0}; \quad \gamma = B'/\dot{\omega}_n;$$

$$\beta_0 + \gamma \omega_{n0} = A' - [(\gamma - A)\gamma]/A'; \quad \Psi = (\gamma - A)/(\beta_0 + \gamma \omega_{n0})$$

iii) A new iteration is made with the computed Ψ value. When $|\Psi_{i+1} - \Psi_i| \leq \epsilon$ the process is terminated.

iv) The cost index $I = I(\dot{\omega}_n)$ is computed. The value of $\dot{\omega}_n$ is then varied for searching the $\dot{\omega}_n$ which corresponds to the absolute minimum of I .

REFERENCES

- 1) C. ARDUINI "Lezioni di Sistemi Spaziali (Space Systems)" course at Aerospace Engineering School of ROME (year 1988-1989).
- 2) M.L. RENARD "Attitude perturbations and magnetic Control of spin stabilized satellite" Part I and II (ESRO TR-1 and TR-2) january july 1966 .
- 3) G. COLOMBO "On the motion of Explorer XI around its center of mass" on: "Torque and attitude sensing in Earth satellites" S.F. Singer Editor-Academic Press 1964.
- 4) C. ARDUINI "Torque acting on the artificial satellites: a general model based on a class of vectors" L'Aerotecnica Missili e Spazio N° 3 -1978.
- 5) C. ARDUINI "Averaging processes in the analysis of the attitude perturbations of spinning satellites" Part I and II L'Aerotecnica Missili e Spazio N° 1,2 1978.
- 6) C. ARDUINI "Soluzioni analitiche per la correzione magnetica d'assetto nei satelliti stabilizzati a Spin" L'Aerotecnica Missili e Spazio N° 3-1979.
- 7) C. ARDUINI, G. LA NEVE, D. MORTARI "San Marco 5th Utafiti Attitude Data" C.R.A. Internal document N° 501 April 1989.
- 8) D.F.V.L.R "Applied Research Contract to improve mathematical model of the Spin axis drift motion of ESRO II and IV with special regard to aerodynamic drag and to compare the predictive capacity of model produced" ESRO CR(P) 461 june 1973.
- 9) C. ARDUINI "Coppie Aerodinamiche sui satelliti artificiali rotanti" Atti del C.R.A. N° 49 August 1977.

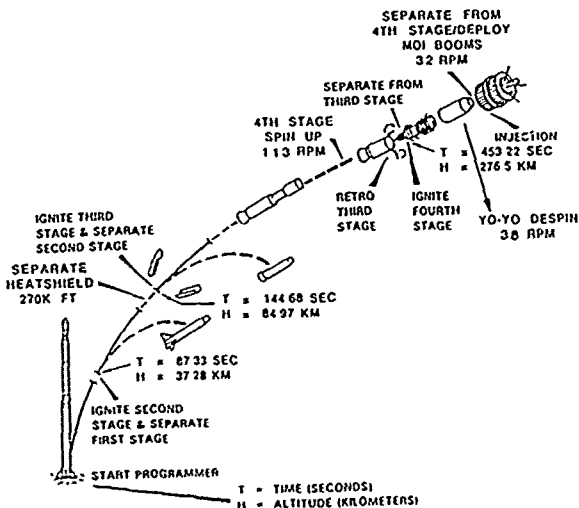


Figure Scout Mission Profile

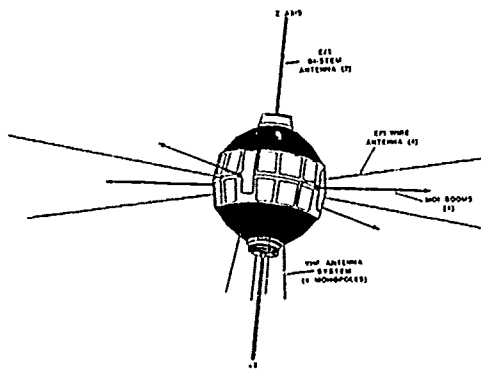


Fig. 1

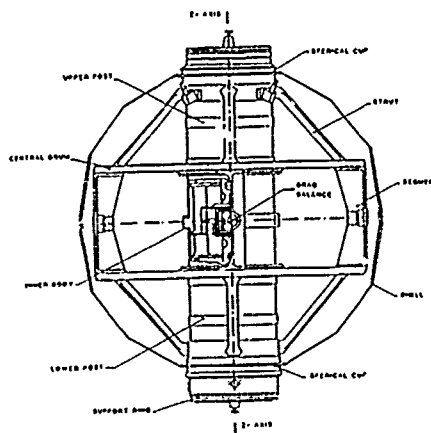


Figure San Marco D/L Configuration

Drift Vernal ref. from 04/23, doy 114.2903 to 06/11, doy 163.6632

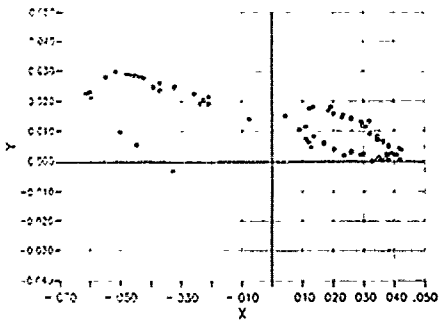


Fig. 2

Drift in Nodal ref. from 04/23, doy 114.2903 to 06/11, doy 163.6632

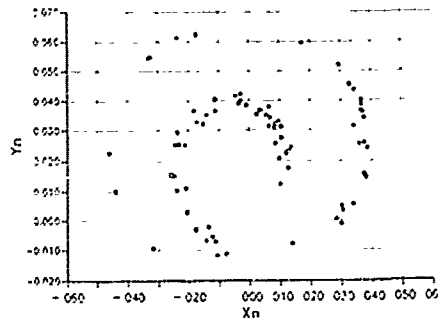


Fig. 3

D1 least square fitting

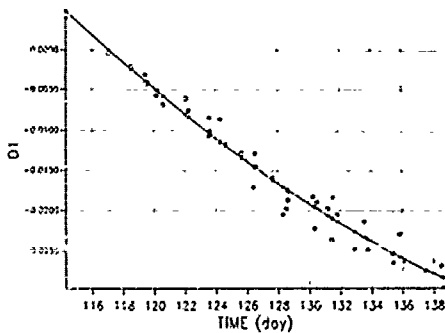


Fig. 4

D1 least square fitting

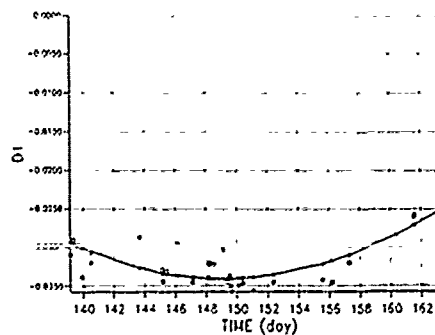


Fig. 5

D2 least square fitting

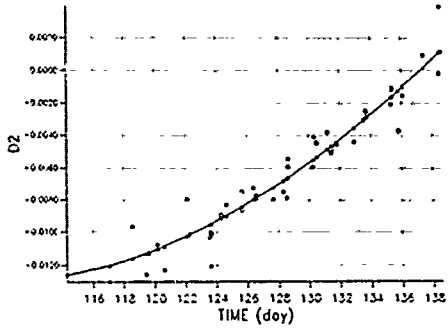


Fig. 6

D2 least square fitting

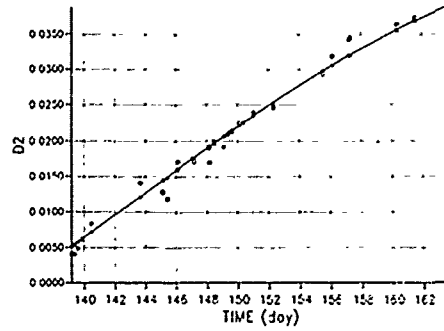


Fig. 7

Trigonometric fitting
first period (114.2903 - 163.6632)

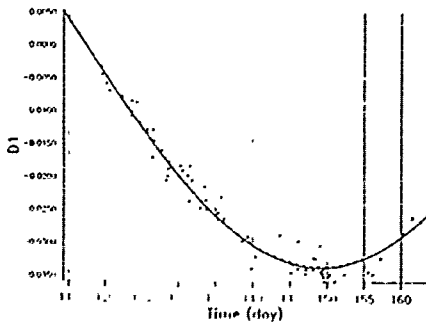


Fig. 8

Trigonometric fitting
first period (114.2903 - 163.6632)

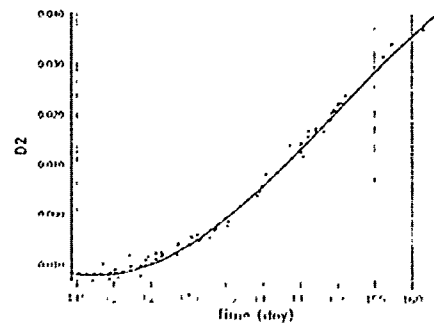


Fig. 9

Comparison (1 period)

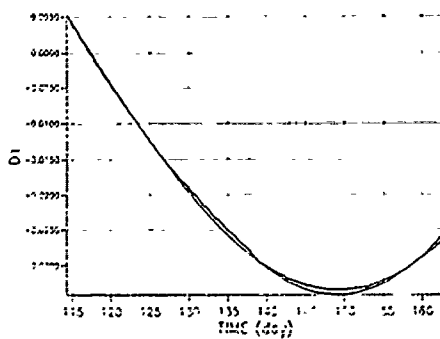


Fig. 10

Comparison

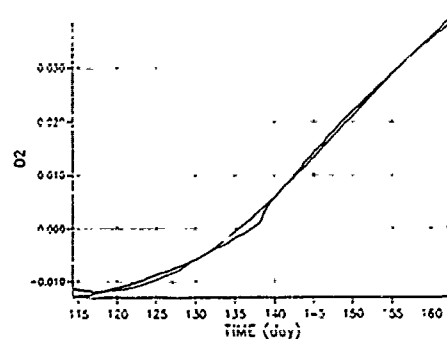


Fig. 11

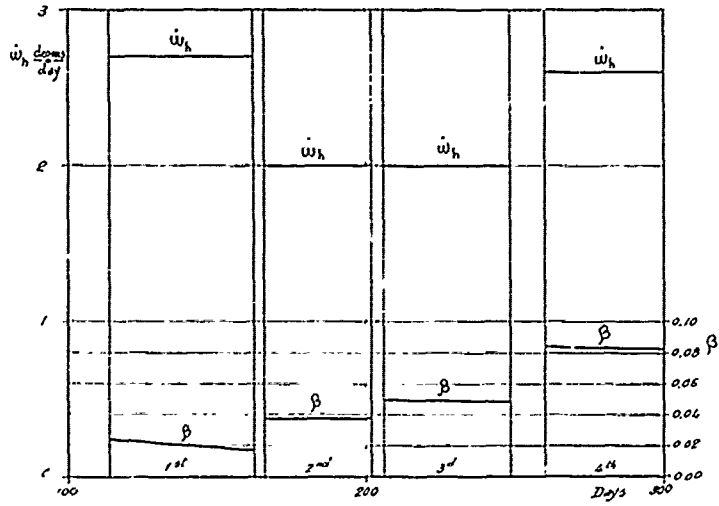


Fig. 12

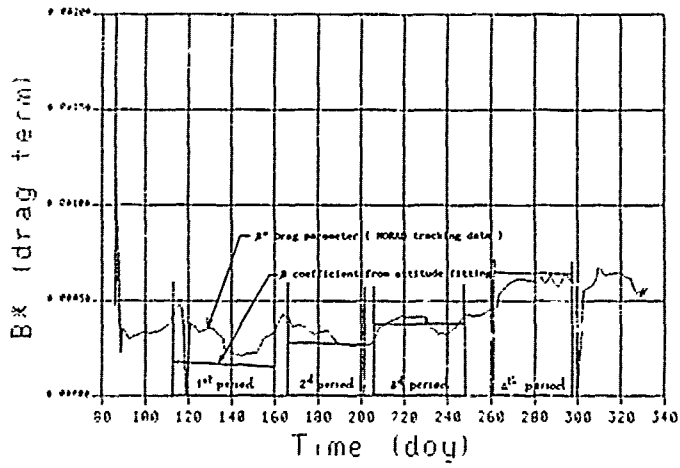


Fig. 13

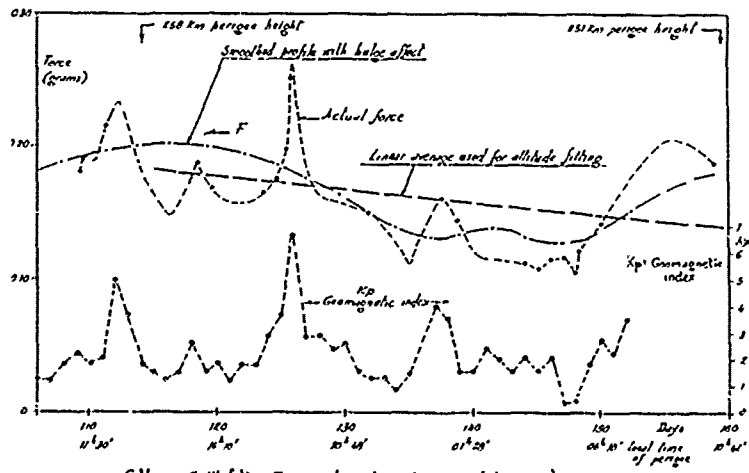


Fig. 14

S. Marco 5 Utafili - Forces at perigee (measured by DBI)

THE INSTRUMENT POINTING SYSTEM - PRECISION ATTITUDE CONTROL IN SPACE

Kalf Hartmann, Albrecht Woelker
Dornier GmbH, Transport & Orbital Systems Division,
7990 Friedrichshafen, West Germany

ABSTRACT

The Spacelab Instrument Pointing System (IPS) is a three axes gimbal system providing pointing and stabilization in the arcsec range to a variety of space experiments with a mass of up to 7000 kg. The IPS demonstrated its control performance during the maiden flight in July 1985, the Spacelab 2 mission on board the Space Shuttle Challenger.

The most challenging problem for attitude control in space is the disturbance compensation in the presence of structural flexibilities. Kalman filtering based on optical sensor and gyro measurements as well as flexible mode attenuation and feedforward control were indispensable to achieve high precision.

To further enhance the IPS pointing performance and versatility, a new, more autonomous computer and sensor concept has been conceived providing the capacity for a higher degree of automation as well as for improved pointing and closed loop tracking control.

The autonomy and control capacity of the enhanced IPS establish the basis to accommodate the IPS as long-term available tracking and pointing platform on the International Space Station Freedom (ISF).

1. IPS DESCRIPTION

Figure 1 depicts the Instrument Pointing System (IPS) as flown on the Spacelab 2 mission on-board Challenger. The scientific experiments mounted on the IPS were pointed towards the sun with an excellent precision and stability. Besides solar pointing, the IPS allows for various other applications such as stellar pointing and Earth observation.

To enhance the Shuttle capabilities with regard to experiment pointing, Dornier developed the IPS under contract of the European Space Agency (ESA). As a subsystem of Spacelab, two IPS flight units were delivered to NASA.

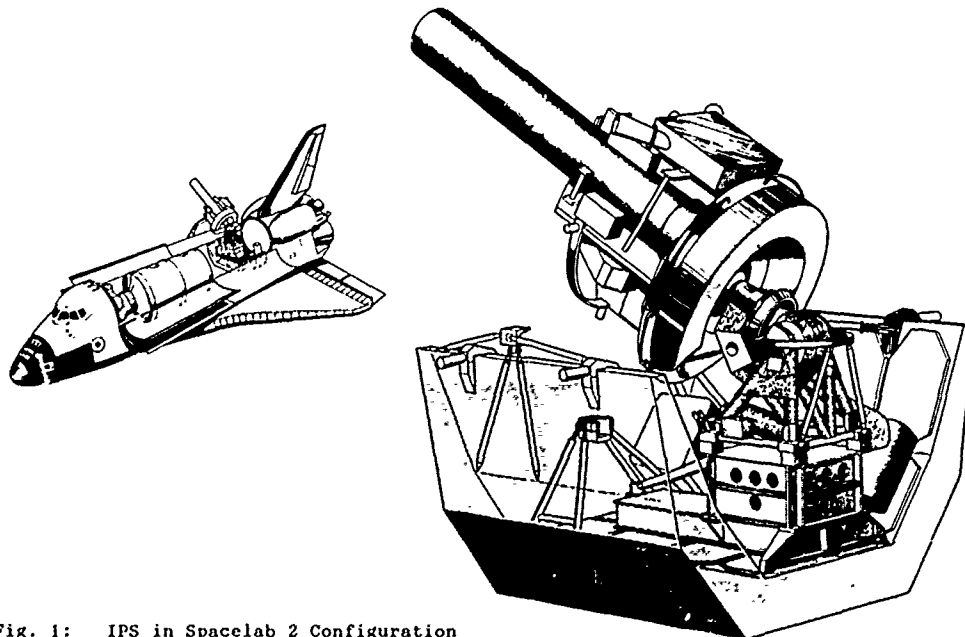


Fig. 1: IPS in Spacelab 2 Configuration

1.1 Mechanical Configuration

Figure 2 presents the IPS in an exploded view. The gimbal system is mounted via a support structure and four hardpoints at the aft end of a single suspended Spacelab pallet. A box type structure (Replaceable Column) supports the tubular framework and enables height adjustment of the gimbal center of rotation according to the payload dimensions.

The IPS gimbal system comprises three identical Drive Units (brushless DC torquers), each providing 30 Nm maximum torque. The Elevation Drive Unit (EDU) serves for IPS erection, the Cross-Elevation Drive Unit (XDU) enables side-looking out of the Shuttle cargo bay, finally the Roll Drive Unit (RDU) provides the payload rotation about the line-of-sight. The gimbal system yields a viewing range of 60° half cone angle, whereas the roll freedom is ±180°. For safety reasons, a spring loaded bumper device mounted at the rear end of the EDU hits a ring placed around the EDU in case a certain cone angle is exceeded.

The front end of the EDU is connected to the Equipment Platform (EPF) carrying electronic units and a mechanism which enables the separation and thus decoupling of the payload from the IPS during launch and landing.

The absence of gravity enables to mount the payload with its center of gravity far outside the gimbal center of rotation. Thus, a variety of payload masses and dimensions can easily be accommodated. The increased disturbance sensitivity was mainly reduced by feedforward control.

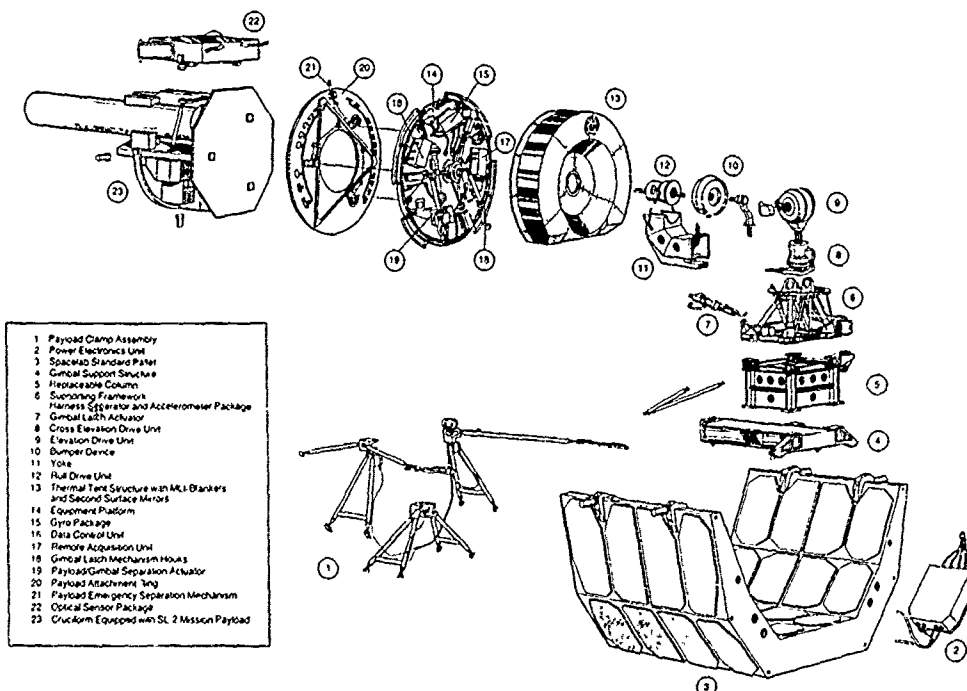


Fig. 2: IPS in Exploded View

1.2 Electrical Configuration

The actual IPS design assumes support by the Spacelab Command & Data Management System (CDMS) and Electrical Power Distribution System (EPDS). The IPS Power Electronics Unit (PEU), which is mounted on the Spacelab Pallet transforms the power from the EPDS to the necessary voltages and currents for the IPS electronics and electro-mechanical devices.

The IPS is operated by the astronauts via the CDMS and its keyboard and display located either in the Spacelab module or in the Orbiter aft flight deck. Whereas the CDMS is dedicated to operational procedures, the IPS Data Control Unit (DCU), mounted on the EPF executes the control algorithms for pointing and stabilization in fixed point arithmetics.

The absolute celestial reference for control is provided by the Optical Sensor Package (OSP) containing one boresighted and two skewed (image dissector tube type) fixed head star trackers (FHST). To minimize misalignments, the OSP is mounted on the payload. The boresighted tracker can also be configured for solar missions by using a sun beam splitter providing a negative star-like image. Three axes rate measurement is accomplished by three orthogonal and one (redundant) skewed gyro mounted on the EPF. Finally, a three axes accelerometer package on the lower framework enables feedforward disturbance compensation.

The payload is serviced with up to 1250 W (22 VDC) power and various control and data lines, including six high speed lines. The harnesses are coaxially routed across through entire gimbal system and are thus twisted with a certain resistance and friction during gimbal motions.

2. CONTROL SYSTEM

The envisaged pointing stability, the structural flexibility of the IPS with its payload in view of sharp disturbances of its mounting base and internal imperfections (noise, friction) imposed challenging requirements on the control system design.

The control system comprises a feedback loop with attenuation filters and PID control as well as feedforward compensation of external disturbances. Based on optical sensor and gyro measurements the attitude is determined via a special version of the Kalman filter.

The block diagram of the IPS control system is shown in Figure 3. The algorithms are executed by two computers: the fast control loop algorithms are implemented in the DCU, whereas the slow control loop tasks are allocated to the CDMS. The fast control loop feedback is established by the three axes IPS rate measurement of the gyro package. The rate is sampled with 100 Hz and transformed into the payload axes. The (prefiltered) rate is submitted to a quaternion integration to obtain the attitude and subsequently the attitude error. The quaternion representation of the attitude has been chosen to ease the computation load. The control law consists of a sequence of attenuation filters and a PID controller. The controller output must be transformed from the platform axes into the gimbal axes to exert the control torque via power amplifier and drive units.

The payload center of gravity is far outside the gimbal center of rotation to accommodate various types of payloads. However, this implies sensitivity to external disturbances, caused e.g. by Orbiter thruster firing or crew motion. Therefore, an accelerometer package (ACP) is essential to measure any linear acceleration at the IPS mounting base and thus to enable feedforward torque compensation.

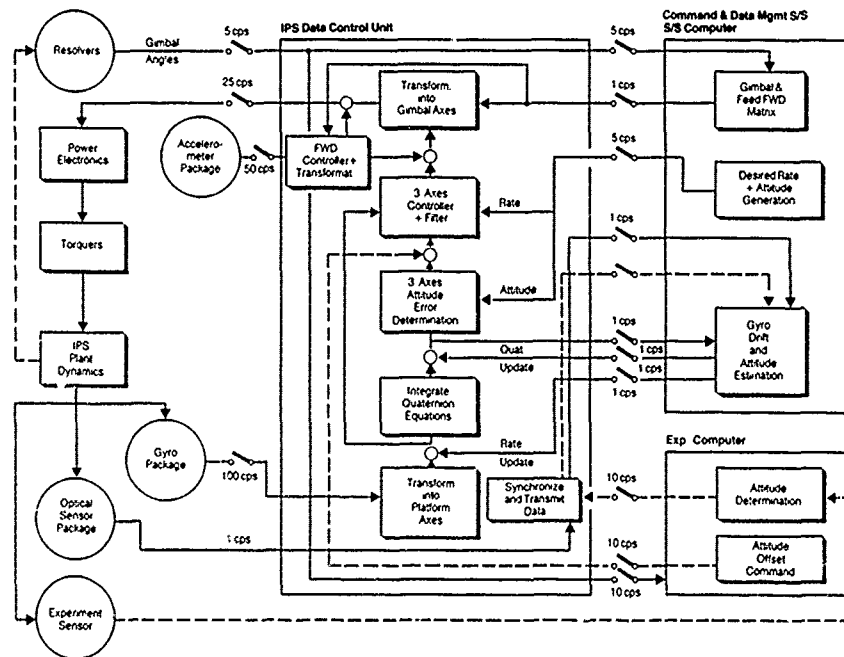


Fig. 3: IPS Control System Block Diagram

2.1 Attitude Determination

The absolute measurement reference is provided in three axes by means of the three Fixed Head Star Trackers (FHST) of the Optical Sensor Package (OSP). The optical sensor signals are sampled with 1 Hz for correction of the quaternions according to the actual attitude error with respect to the celestial target. To this end a dedicated Attitude Determination Filter (ADF in Figure 4) is applied. Referring to Figure 3 the loop comprising the quaternion integration block and the 'Gyro Drift and Attitude Estimation' block forms a modified version of the Kalman filter. This Kalman filter (or ADF) estimates the current quaternions, the gyro drift and the relative misalignment between the star trackers. The quaternion integration yields the current attitude with a sampling rate of 25 Hz. Considering the 1 Hz cycle, this signal represents the attitude estimate based on gyro information. Via the observation matrix this attitude is transformed into the optical sensor axes. This enables a comparison between the optical sensor measurements and the gyro based estimate. The resulting error signal is fed through the Kalman filter

gain matrix to obtain the corrections of the quaternions, the gyro drift and the tracker misalignments.

The signal correction and thus the main part of the Kalman filter is executed in the 1 Hz cycle. However, the quaternion integration running with 25 Hz frequency is part of the filter. This implies that the state transition matrix of the filter depends on the gyro rate signal during a 1 Hz cycle.

For the generation of the Kalman filter gain matrix the state transition and observation matrices are linearized to enable a precalculation of the Kalman filter gain matrix based on the following informations:

- o a time-invariant state and observation model. The model applies 10 states; 3 quaternions (one is redundant), 3 gyro drifts, and 4 misalignments (2 lateral misalignments of the two skewed w.r.t. the boresighted FHST),
- o the system noise due to gyro noise and numerical errors of the quaternions,
- o the measurement noise of the optical sensors.

These informations allow the generation of the time variant filter gains, which optimally combine redundant measurements according to the error sources to yield optimum attitude estimation. To ease computation load, these gains are approximated by hyperbola functions, which can be represented by a few coefficients only.

The attitude determination is the basis for achieving high pointing accuracy and stability in three axes by minimizing the effects due to gyro and optical sensor noise, gyro drift and sensor misalignments. After filter settling, lasting typically 100 sec from initial target acquisition, long term stabilization is provided to the experiments.

As an option, experiment sensors can substitute the OSP as absolute measurement reference. Also attitude offset commands from the experiments are accepted by the DCU.

2.2 Attitude Control

Figure 4 presents the IPS fast control loop which is for the most part implemented in the Data Control Unit (DCU). The three axes gyro loop applies a sequence of filters with different sampling frequencies. This is necessary because the DCU computer is not able to execute all filter algorithms within fastest (100 Hz) cycle. On the other hand the averaging of gyro data (100 Hz) and the prefilterers (50 Hz) require high sampling rates, in order to avoid aliasing of high frequency structural modes and gyro noise. The rate filters running with 25 Hz are designed to attenuate structural modes with minimum phase shift. Each filter consists of a transfer function with a second order nominator and denominator. Figure 4 also illustrates the ADF and PID control.

The second branch of the DCU consists in the three axes ACP loop. Although the ACP measurement is designed to form a feedforward, in fact it must be regarded as a feedback loop for stability analyses due to the coupling with the dynamics of the IPS. Hence in total six feedback loops establish the multivariable system. Consequently the ACP loop requires as well a sequence of filters, designed according to similar criteria as the rate filters.

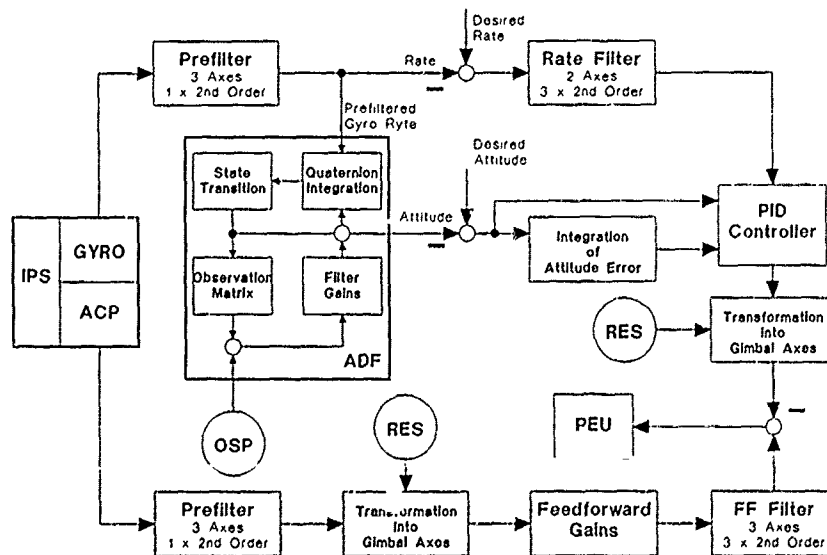


Fig. 4: Control Loop Block Diagram

2.3 IPS Performance Prediction and Flight Results

Table 2 summarizes the IPS performance in terms of the most relevant payload criteria, the quiescent stability and the disturbance response. All results are given for the worst of the two lateral axes.

The quiescent cases assume an undisturbed inertially fixed Orbiter, such, that any pointing error of the IPS is caused by its own internally generated effects as there are sensor noise, bearing friction, quantization misalignments etc. The lateral stability is kept below 0.7 arcsec in such quiescent periods, which are most valuable for experiments to obtain high quality images of their targets although these conditions are occasionally interrupted by external disturbances.

The disturbance response represents the variation of the attitude resulting from Orbiter thruster firing and crew wall push off. Except for free drift cases, the Orbiter performs limit cycling within +/-0.1 deg. by repeated 80 msec thruster firings. In this case the worst attitude variation was 5 arcsec. During the SL-2 flight also 1040 msec thruster firing occurred resulting in a disturbance response of up to 18 arcsec. Figure 5 demonstrates that upon such 1040 msec thruster firing, the IPS settles fairly quickly to provide high pointing stability to the experiments.

The man-motion disturbance results from two opposite wall push-offs by an astronaut in the Orbiter flight deck. Figure 6 presents the worst case in which the attitude variation was 17 arcsec.

Table 1 demonstrates a quite good coincidence between simulation and flight performance for the quiescent and thruster firing case whereas the man-motion impact is higher than predicted because the crew impulse unexpectedly caused a higher Orbiter acceleration and thus worse IPS response.

The IPS is designed to accommodate various types of payloads. For large payloads of up to 7000 kg and thus high inertias, the performance degradation is very low due to the effectiveness of the feedforward control and due to a merely slight reduction of the control system bandwidth from 0.7 Hz to 0.5 Hz. Therefore, it can be concluded that the disadvantage of the large center of gravity offset is minimized.

LOS Performance Characteristics	Unit	Simulation				Flight SL-2
		2 tons	7 tons	SL-2	SL-2	
<u>Quiescent Case</u>						
- pointing accuracy	arcsec	0.4	0.7	0.8	- *	
- rms stability	arcsec	0.7	0.8	0.7	0.7	
- rms stability rate	deg/hr	2.9	1.3	2.0	- *	
<u>Disturbance Cases</u>						
- man-motion	arcsec	5.1	8.9	8.5	17.0	
- 80 msec thruster firing	arcsec	6.7	7.1	5.6	5.0	
- 1040 msec thruster firing	arcsec	-	-	-	18.0	
Payload mass	kg	2 000	7 000	1 402	1 402	
Inertia about COR	kgm ²	15 740	132 200	5 980	5 980	

* could not be evaluated from flight data

Table 1: IPS Performance

3. IPS PERFORMANCE ENHANCEMENT

3.1 IPS Autonomy Concept

After the successful maiden flight further enhancement of the IPS has been investigated. The mechanical design is mature and does not limit the IPS capabilities. Considering the growth in computer and sensor technologies, significant improvements can be achieved by just replacing or adding electronic boxes but keeping the basic IPS design.

A major objective of the IPS improvement is to establish a highly autonomous system being independent of Spacelab and requiring only a minimum amount of external services. The Spacelab CDHS is replaced by a more powerful Operation and Control Computer (OCC) to provide enhanced IPS performance, operations and handling.

The driving demand of using the OCC autonomy concept is to provide the capacity to execute more complex control algorithms at higher sampling rates. This improves the pointing performance and to provides the capability for closed loop tracking of moving objects. Furthermore, autonomy implies the automatic execution of operational procedures by the OCC software which is important for fast and reliable object acquisition in tracking and pointing missions.

The automation and autonomy features of the improved IPS with the OCC form a basis to accommodate the IPS as a self-contained system on the International Space Station Freedom (ISF).

STS DATA BASE: SL2SF212
 LAST UPDATE: 12/12/86 17:36:06

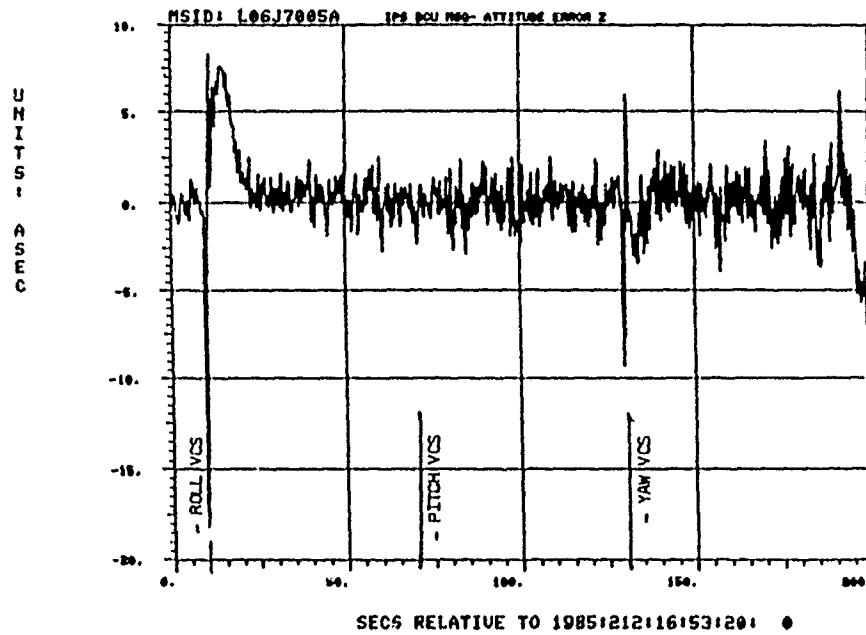


Fig. 5: Attitude Error Response to 1040 msec Thruster Firing (from ref. 1)

STS DATA BASE: SL2SF212
 LAST UPDATE: 12/12/86 17:36:17

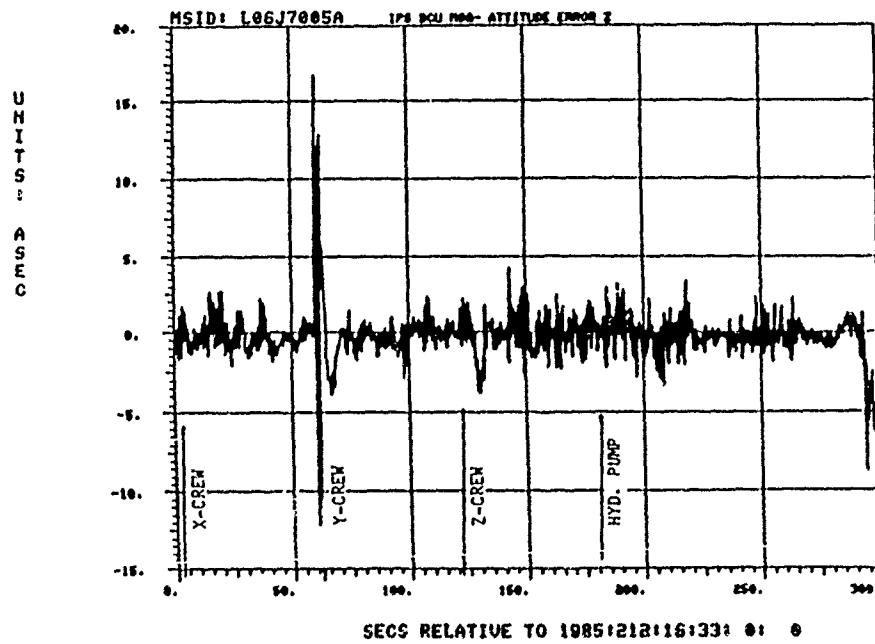


Fig. 6: Attitude Error Response to Crew Wall Push-off (from ref. 1)

3.2 Pointing Performance Improvement

For stellar and solar observation it is most important to provide a high stability with the IPS. The IPS demonstrated about 0.7 arcsec quiescent stability, however, there is still a demand for further improving the pointing performance. Table 2 shows the results of a sensitivity analysis for the quiescent performance.

Error Source	Relative Contribution to Quiescent Performance (%)
(1) DCU quantization	73
(2) Gyro noise	52
(3) Optical sensor noise	39
(4) Torque hysteresis	16
(5) Structural flexibility	10
(6) Torque roughness	8
RSS Sum	100

Table 2: Sensitivity analysis of internal generated disturbances

Consequently those error sources which are inherent to the basic IPS design, namely no. 4, 5, 6 have only a minor effect. The important error sources no. 1, 2, 3 can be reduced by exchanging or adding individual boxes.

The DCU quantization which is caused by its fixed point arithmetics can effectively be eliminated by use of the new OCC. Even without changing the control law the quiescent stability can be reduced to about 0.25 arcsec. A quiescent stability below 0.1 arcsec can be achieved by the following measures in addition to using the OCC:

- o Use of a new gyro with a noise of about 0.4'/hr and 25 Hz bandwidth. Alternatively, this can be achieved by an improvement of the IPS gyro electronic reducing the gyro noise by a factor of 5.
- o Use of an optical sensor with a noise of 0.2 arcsec at 1 Hz sampling which could be either IPS dedicated or user supplied. Alternatively, the optics of the IPS FHST can be improved to yield a factor of 4 of noise reduction.

In addition or as an alternative to the optical sensor and gyro improvement, the capacity of the OCC can be utilized to implement more efficient control algorithms. Using a filter sampling frequency of 100 Hz, aliasing effects arising from structural modes and gyro noise can be avoided. More flexibility in the design of the attenuation filters and control algorithms is gained by the higher storage and speed capabilities of the OCC. Furthermore, an enhanced Kalman Filter for attitude and rate determination applying on-line gain computation and avoiding delays of sensor measurements yields faster settling and higher stability.

With these measures, simulations have shown that IPS internally generated error source can be minimized to yield 0.1 arcsec for an inertially stabilized orbiter. If the orbiter is free drifting in a Earth pointing, the stability degradation is about 0.1 arcsec due to increased tearing and harness friction.

- The disturbance response upon man-motion and thruster firing can also be reduced by
- o relocation of the Accelerometer Package to a point, which is more sensitive to disturbances than to structural flexibilities,
 - o using 100 Hz sampling and filtering, optimization internal ACP filter presently necessary to avoid aliasing effects with low sampling rate,
 - o improved filters in the feedforward loop running at 100 Hz
 - o use of a rigid body disturbance observer.

3.3 Closed Loop Tracking

The IPS has been designed for high precision pointing towards inertial celestial objects. With the autonomy concept the IPS provides the capability for closed loop tracking of any objects moving at rates of up to 3 '/sec.

For tracking of object moving relative to the Shuttle the following scenario is assumed:

- o The IPS applies two (user supplied) sensors:
 - a coarse acquisition sensor with a field of view of about 5' x 5'
 - a fine tracking sensor with a field of view of about 0.5' x 0.5'.
- o The initial position of the object is known with an uncertainty less than the extension of the acquisition sensor field of view. This is the case for tracking of a fixed landmark or other cooperative spacecrafts.

Tracking is performed with the following automated sequence:

- (1) Tracking Preparation comprising
 - IPS supports calibration of the optical sensors and experiments
 - Gyro drift calibration and attitude initialization
 - Last uplink of object and mission parameters.

- (2) **Initial Positioning:**
The IPS is moved close to the end of the operational cone to a position which is located on a predefined trajectory derived from the knowledge on the initial object position. The Orbiter as well has to acquire the required position.
- (3) **Gyro Tracking:**
Automatic tracking is started before the object is visible in the acquisition sensor field of view (e.g. because the objective is behind the horizon). Hence, Gyro Tracking means closed loop control along a predefined trajectory (based on a imperfect a priori information), where the attitude error is the difference between the predefined trajectory and the actual attitude derived from gyro rate integration. Due to the relative object motion a high initial rate error effects a sharp acceleration of the IPS to the rate of the object (see initial torque profile in Figure 7). At about 30 secs, when object appears in the acquisition camera field, the rate error is small whereas the attitude error is about 1.4 deg. due to the imperfect a priori information on the object location.
- (4) **Object Acquisition:**
Once the acquisition sensor has acquired the object in its field of view, it generates an attitude error which causes a transient (second torque profile on Figure 7) into the field of view of the tracking sensor.
- (5) **Fine Tracking:**
Once the object is acquired by the tracking sensor and settling is performed, the IPS provides a fine tracking stability of 0.6 arcsec (3 μ rad) to a 2000 kg payload at a rate of up to 2.1°/sec, assuming an optical sensor noise of 2 arcsec (10 μ rad) and 30 Hz sampling. A maximum bias error of 23 arcsec (115 μ rad) after settling has been achieved with PID control. A second integrator or a trajectory predictor/estimator is found not suitable to further improve the accuracy. Due to the double integration of the plant, bias error results from the variation of the acceleration which can hardly be determined through a further integrator or observer.

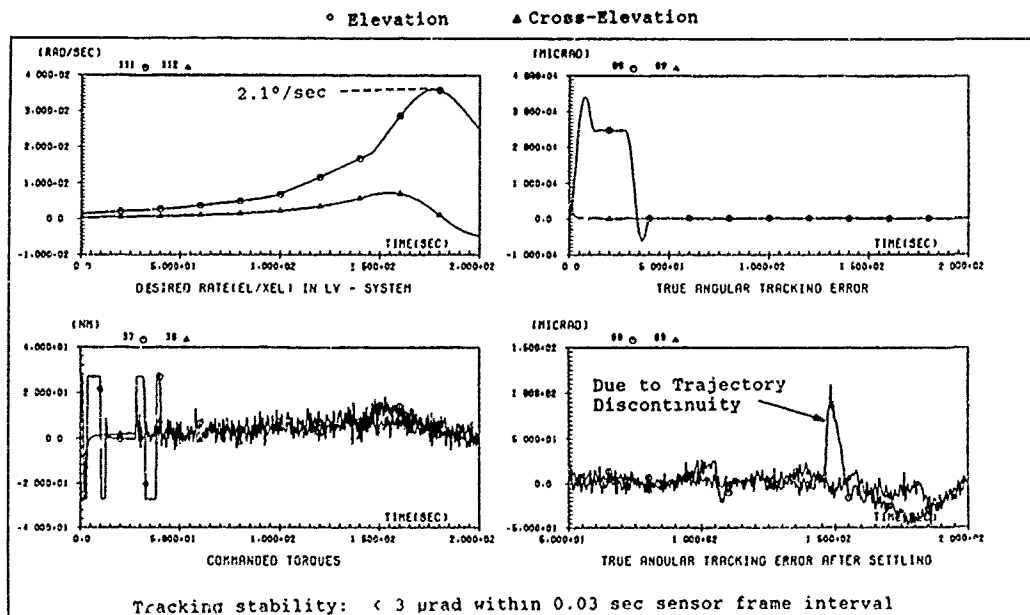


Fig. 7: IPS Tracking Stimulation

4. SPACE STATION ACCOMMODATION

There is only a limited number of satellites for astronomy and solar sciences, on the other hand the International Space Station Freedom (ISF) constitutes a large, long-term infrastructure for a variety of experiments. However the ISF is Earth pointed, has a limited maneuverability and is only coarsely stabilized and thus does not support tracking and pointing experiments. Consequently the IPS could expand the ISF versatility and range of utilization, because

- o the IPS supports a variety of payloads in terms of mass and accuracy,
- o the IPS is the only flight proven pointer presently available,
- o the IPS is designed for 50 Shuttle missions and 10 years lifetime and thus includes considerable design margins and a high robustness,
- o the IPS autonomy concept forms the basis for the accommodation of the IPS on the ISF
- o the basic IPS design can be retained, mainly add-on improvements like the OCC are required.
- o the openly exposed IPS Equipment Platform can be supplemented by an automatic Payload Berthing Adaptor which facilitates the experiment exchange with the Remote Manipulator Arm.

Figure 8 shows the IPS accommodated on the long ISF truss structure.

Compared to the Shuttle, the 155m long, lightweight ISF design imposes the IPS to cope with low frequency vibrations in the vicinity of the control system bandwidth. The control system structure is basically retained for first analyses, however the following adaptations are mandatory:

- o The processing capacity of the OCC is the basis to implement adapted attenuation filters running with 100 Hz cycle time.
- o The control system bandwidth has to be reduced from 0.64 Hz to 0.32 Hz to avoid interaction of the IPS with low frequency ISF vibrations and thus to ensure dynamic stability of the coupled dynamics system. The reduced feedback disturbance compensation is recovered by improving the feedforward loop as follows:
 - o Reduction of accelerometer internal filter time constant,
 - o Optimization of accelerometer location closer to the IPS center of rotation.
 - o Use of further accelerometers to observe the low frequency ISF vibration and direct feedforward compensation (not yet simulated).

Figure 9 depicts the IPS response upon crew wall push-off. The maximum attitude error is 25 arcsec. The wall pushoff effects an almost undamped vibration of the long Space Station truss, representing a continuing disturbance to the IPS which results in an oscillation error with an amplitude of 18 arcsec. For the present analysis it is assumed that the ISF does not stabilize its own disturbances.

Figure 10 demonstrates the effectiveness of the feedforward compensation with accelerometers: even though not yet optimized, the feedforward reduces the maximum error from 41 arcsec down to 10 arcsec in cross-elevation and even the ISF vibration response is decreased from 25 arcsec to 18 arcsec.

The attitude error upon ISF thruster firing is shown in Figure 11. The maximum error is 39 arcsec with feedforward control. Although the IPS is unfavorably located just above a thruster pod, that is at an antinode, the ISF vibration disturbance can be compensated by feedforward. After 20 sec the amplitude of the attitude error has been decreased to 6 arcsec.

Thus it is considered reasonable to further exploit the feedforward compensation. Since the IPS is disturbed by one (or two) dominant flexible ISF modes only, it seems to be well feasible to conceive a disturbance observer of limited order based on distributed accelerometers.

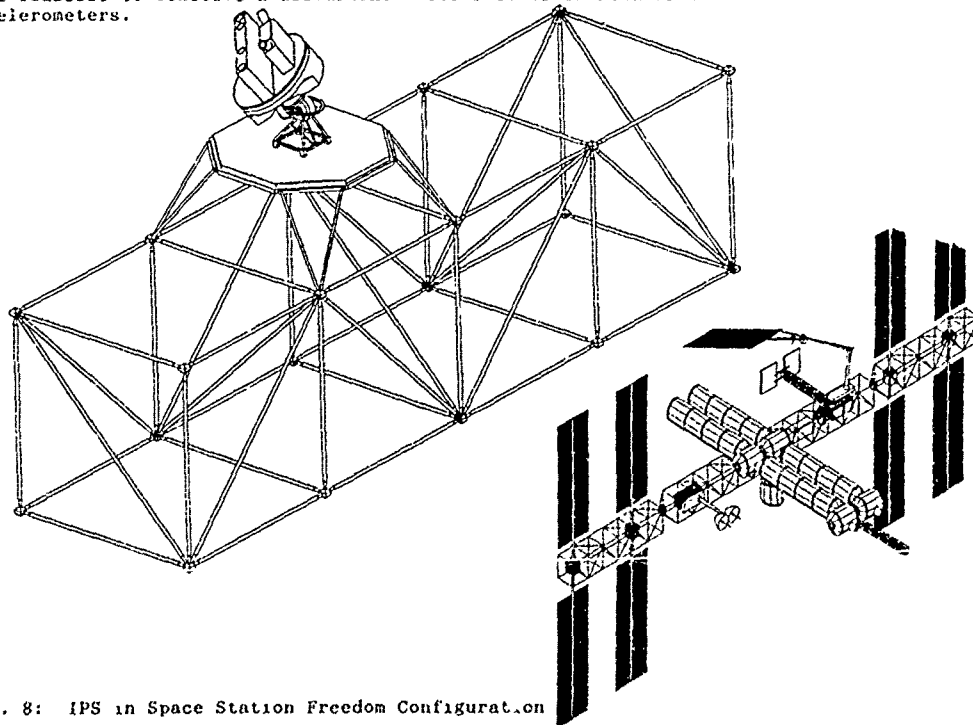


Fig. 8: IPS in Space Station Freedom Configuration

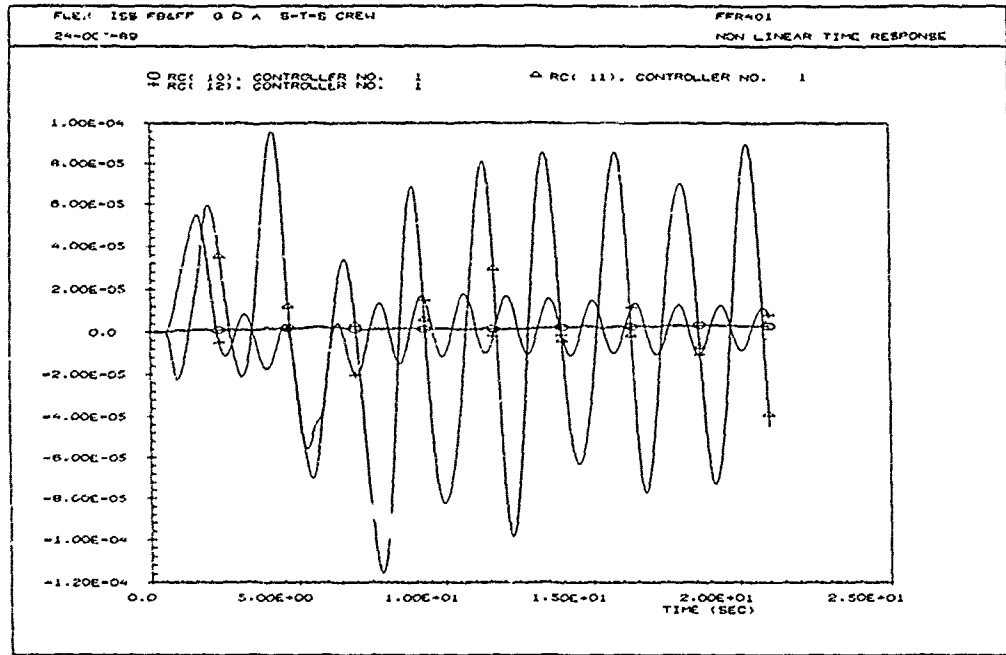


Fig. 9: IPS Man Motion Response on the ISF

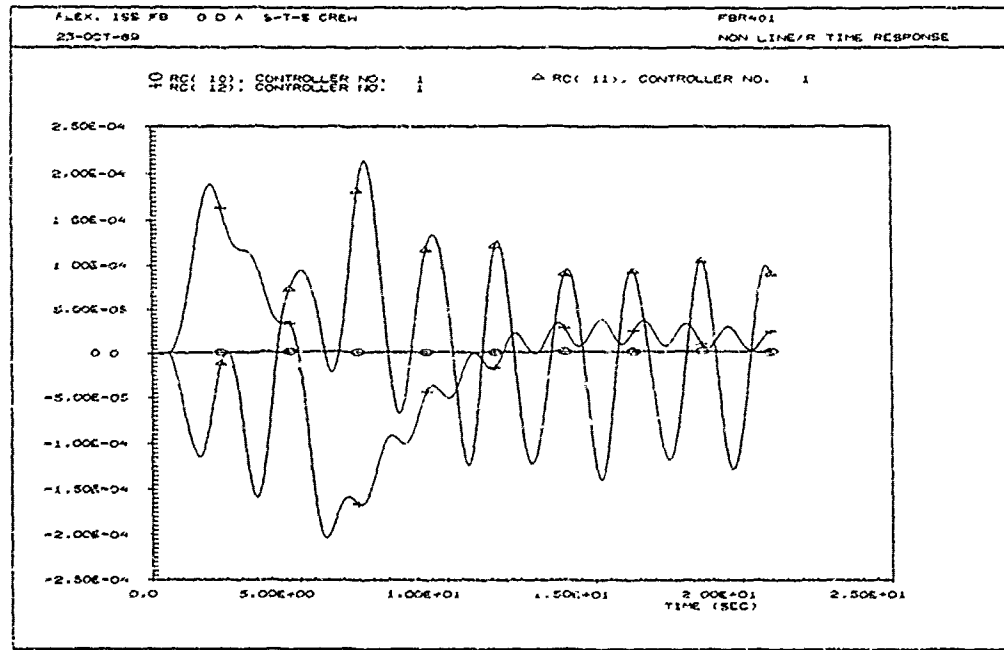


Fig.10: IPS Man Motion Response on the ISF (without feedforward)

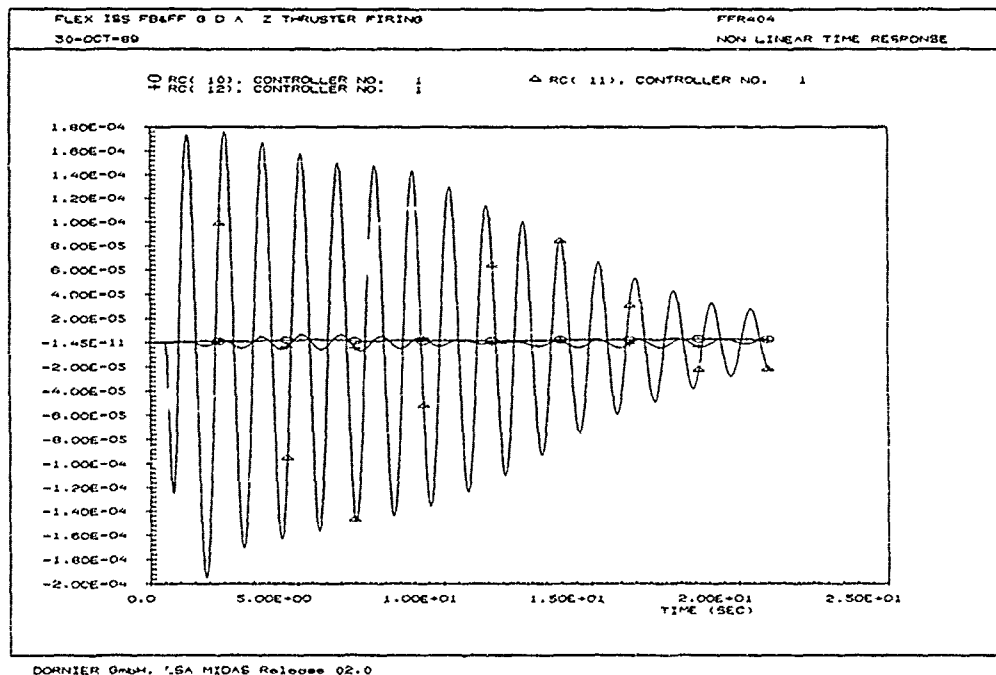


Fig. 11: IPS Thruster Firing Response on the ISF

5. CONCLUSION AND FUTURE OUTLOOK

The IPS performance during the Spacelab 2 mission rendered essential benefit for experiments. Attitude control with flexible mode attenuation and Kalman filtering based on optical sensor and gyro measurements enable precision pointing for the IPS as well as for satellites. The IPS specifically has to cope with step-like disturbances of its mounting base. Therefore further studies are ongoing to prove that the IPS can provide a pointing performance on the ISF being close to the Spacelab 2 results in order to enhance the IPS as long-term available platform for a variety of tracking and pointing experiments on the ISF.

6. REFERENCES

- [1] Spacelab Verification Flight Test (VFT) Program Report, MDC W5362A, Mc Donnell Douglas Astronautics Company, Sept. 1987.

FLEXIBLE STRUCTURE CONTROL AND RIGID BODY DYNAMICS

V. B. Venkayya
Wright Research and Development Center
Wright-Patterson Air Force Base, Ohio 45433-6553

ABSTRACT

The main interest of this paper is to promote the objectives of Control-Structure Interaction (CSI) in vibration suppression and attitude control of large space structures. Integration of multibody dynamics, flexible structures and control system design is considered extremely important in CSI research. The concepts of decentralized controls and optimization of lightly damped systems are the promising approaches for realistic applications.

1. INTRODUCTION

A number of future space systems are being planned at present for both military and civilian applications. Some of the common perceptions about these systems are: (a) they are large in size, (b) they are extremely flexible, and (c) they need both active and passive controls to assure adequate performance while subjected to a variety of disturbances. In addition, they are made of multiple bodies connected together in a tree fashion or in multiple closed loops. For example, the proposed NASA Space Station consists of solar panels, antennas, crew quarters, life support systems, etc., and each of these is a flexible body connected together by truss booms. The disturbances are a result of either large angle maneuvers or impact due to docking or crew and equipment movement. The vibrations induced by these disturbances need to be controlled for the proper operation of the spacecraft. Passive controls, though extremely important, alone are not expected to be adequate. Active controls are expected to play an important role in vibration suppression and shape control. The interaction of multibody dynamics and the extreme flexibility of the bodies can present significant problems in the design of control systems.

The integration of multibody dynamics, finite element models, and active and passive controls is going to be the major thrust of future research in large space structures design. Each of these disciplines presents numerous unsolved problems in their own right, and their integration appears to be an intractable problem at present. Early multibody dynamics research was primarily concerned with the formulation of the Equations of Motion (EOM). The controversy about the Newton-Euler formulation vs Lagrange's equations is largely resolved. The general consensus is that it is possible to obtain the same equations of motion by either route⁽¹⁾. However, the new formulation, known as Kane's formulation which reduces to the Lagrange's form of the D'Alembert's principle in special cases, is the preferred approach at present because of its generality⁽²⁾. The solution of the nonlinear equations of multibody dynamics is another major obstacle in the development of design methods. Most of these are approximate numerical methods, and their computational complexity, speed, and reliability of convergence are always in question.

The flexibility effects of large bodies in rapid maneuvers further confound the spacecraft design issues. Multiple bodies are built-up structures and their representation by continuum modeling is at best unsatisfactory. The popular finite element modeling, on the other hand, is fraught with the curse of dimensionality. Even though the finite element model is satisfactory to predict the dynamic behavior of a constrained flexible body, its inclusion in the multibody dynamics seriously alters the solution strategy. For example, in the numerical integration of the equations of motion the time step requirements of rigid body oscillations and flexible motions can be significantly different, and a balanced approach can be achieved only by extensive numerical simulation.

Model order reduction is one of the active research topics in the development of active control technology. The effects of unmodelled modes, truncated modes and model uncertainty are the issues that must be addressed seriously in the development of integrated design methods. The modern optimal control theory is entirely based on linear models. The nonlinear motions of multiple bodies and their flexibility require new approaches for design. The actuator/sensor dynamics further enhance the nonlinearities. A flexible structure subjected to rapid maneuvers can introduce instabilities.

Recent interest in multibody dynamics promoted development of a number of computer codes such as DISCOS⁽³⁾, CONTOPS⁽⁴⁾, ADAMS⁽⁵⁾, DADS⁽⁶⁾ etc. Most of these codes were originally intended for the simulation of rigid body dynamics. Since the size of the bodies is expected to be large in spacecraft applications, a realistic simulation cannot ignore the flexibility effects. The new enhancements of these codes are addressing the flexibility issue to a limited extent.

The dynamics of connected bodies is of interest in not only spacecraft design but in robotics as well. The major difference is that in the case of robots the analytical simulation can be verified reasonably well in experiments. However, in the case of a spacecraft the difficulties are far too numerous for such an experimental verification. The size of the spacecraft, zero gravity environment, absence of aerodynamic damping, and free-free motion are some of the impediments for experimental validation of an analytical simulation. The orbital motion of the spacecraft adds to the complexity. It is imperative that in the absence of such a validation, our understanding of the analytical models must be thorough and include as many elements as possible in the model.

The purpose of this paper is to identify the design issues arising from flexibility effects and active/passive control for vibration suppression of a multibody system.

2. EQUATIONS OF MOTION OF MULTIBODY SYSTEMS

The dynamics of a multibody system can be formulated in a number of ways. The Newton-Euler formulation, Lagrange's equations, D'Alembert's principle and Kane's formulation are some of the means for deriving the equations of motion. Generality, ease of formulation and solution are the key considerations in choosing the appropriate method^(1, 3, 7-9). An inertial reference frame and various body coordinate systems are the means for defining the configuration as well as the state space.

The basic equations of motion of a multibody system can be written by considering the dynamic equilibrium of the individual bodies.

$$m\ddot{V} = Q + F \quad (1)$$

where V is a set of generalized coordinates that describes the body configuration in the inertial frame. The generalized forces, Q , on the body include those induced by the environment of the orbiting spacecraft and inertia, elastic and damping forces of the deformable bodies. The environmental forces include gravity, gravity gradient, solar pressure, thermal gradient and aerodynamic drag in the case of a low earth orbit. They also include inertial forces due to centrifugal and Coriolis acceleration and the dynamic forces resulting from spin rate stabilization etc. F is a set of constraint forces transmitted from the interconnecting bodies. The left-hand side of equation 1 represents the inertia forces of the body. The essence of Eq 1 is that the environmental and constraint forces on the body are in dynamic equilibrium with the inertia forces of the body which is essentially the statement of D'Alembert's principle. It should be remembered that Eq. 1 covers both the forces and moments of the body, because the generalized coordinates V include both the translations and rotations. The constraint forces F are appended to the environmental forces Q through the Lagrangian multipliers, λ , which results in⁽²⁾

$$m\ddot{V} = Q + b^T \lambda \quad (2)$$

The constraint matrix, b , expresses the kinematic conditions of the interconnecting bodies in the form

$$\sum_i b_{ij} \dot{V}_j = \dot{\alpha} \quad (3)$$

The summation in Eq 3 is over the number of bodies. Equations 1 (or 2) represent n first order nonlinear ordinary differential equations, and Eq 3 represents m conditions of kinematic constraints. n represents the number of bodies and m represents the number of connections between the bodies. $\dot{\alpha}$ are the prescribed velocities across the bodies.

The most crucial element of multibody dynamic formulations is development of the mathematical equations for the generalized forces, Q . Research in mechanical systems (mechanisms) and space structures produced a wealth of information in the form of various formulations and prompted the development of the computer codes cited in the introduction. However, the difficulty is how to blend the complex interactions of an orbiting spacecraft and develop a coherent approach for the design of an effective control system for vibration suppression and attitude control.

3. ACTIVE AND PASSIVE CONTROLS

Vibration suppression and attitude control are the two major tasks of the control system for large space structures. Vibrations are the elastic motions of flexible structures which must be suppressed in a finite time to assure the desired performance. The spacecraft attitude, on the other hand, is primarily related to the rigid body motion. However, these two are generally coupled motions and must be controlled simultaneously.

Active and passive controls are the means of achieving the control objectives. In an active control system a set of actuators and sensors regulated by an onboard controller produce motions to counteract the vibrations induced by the external disturbances. If the disturbances are known a priori, an open loop control system can be designed to suppress the resulting vibration. Open loop control can be accomplished by actuator alone. When the disturbance is unknown, as in the case of random disturbance, a closed loop control system is necessary, and it would have both actuators and sensors.

The actuators are generally classified as mechanical, hydraulic and electromagnetic. Hydraulic actuators are generally not very suitable for space applications. Small rocket thrusters or reaction jets are particularly well suited for attitude control. They are being proposed for vibration suppression as well. Hydraulic cylinders, moment actuators, torque motors, proof-mass actuators, control moment gyros, reaction wheels, locks and brakes are some of the actuators⁽¹⁰⁾ being modeled in spacecraft control system design. More recently piezoelectric actuators are being investigated for space applications. Accelerometers, rate gyros, position sensors, tachometers, sun and star sensors etc. are the sensors being considered for space applications. Piezoelectric and fiber optic systems are the closest systems for distributed control. All others are considered as point actuators and sensors.

The elements of a passive control system are viscous dampers, friction dampers, viscoelastic systems, constraint layer damping and shock mounts. In addition, joints and other sources of sliding and/or slipping at the microscopic or macroscopic level contribute to structural damping inherent in the system. Structural damping is generally described by a concept called the complex modulus. Passive control is basically an open loop system. The mechanism of passive control in a vibrating system is through the dissipation energy counteracting the kinetic and potential energies. The damping forces are out of phase with the elastic and inertia forces of the dynamical system.

A combination of active controls and passive damping offers the best promise for vibration suppression and attitude control of future space systems. The total mass of the spacecraft, the energy available for control and the on-line computations are serious considerations in the design of a control system. Both passive damping and active controls significantly increase the total mass and energy requirements. It would be impractical to delegate the control function entirely to either active or passive controls alone. Instead, the best compromise appears to be a combined control system in which a lightly damped (passive) structure is designed a priori in an open loop mode, and then an active control law is implemented. The last section of this paper (Section 5) addresses the issue of designing a lightly damped system in the context of optimization with the structure, mass and damping parameters as variables.

4. ISSUES IN ACTIVE CONTROL

The problem statement of a Linear Quadratic Regulator (LQR) in the presence of continuous random disturbances can be written as⁽¹⁾ follows:

$$\dot{X} = AX + Bu + w \quad (4)$$

The optimization criterion for the stochastic regulator problem may be stated as

Minimize

$$J = E\left\{\int_{t_0}^{t_1} (X^T Q X + u^T R u) dt\right\} \quad (5)$$

where X is the random state variable, u is the control input, A and B are the plant and control matrices, and w represents a continuous stochastic disturbance. w is assumed to be white noise. In the quadratic performance criterion: Q and R are weighting matrices with the properties that Q is at least positive semidefinite and R is positive definite. It is assumed in the above formulation that the full state feedback is available at all times. In the case of output feedback with a finite number of sensors, the addition of a Kalman filter makes the problem LQG (Linear Quadratic Gaussian), and the necessary modification is as follows

$$\dot{X} = AX + Bu + w_1 \quad (6)$$

where the observed variable is given by

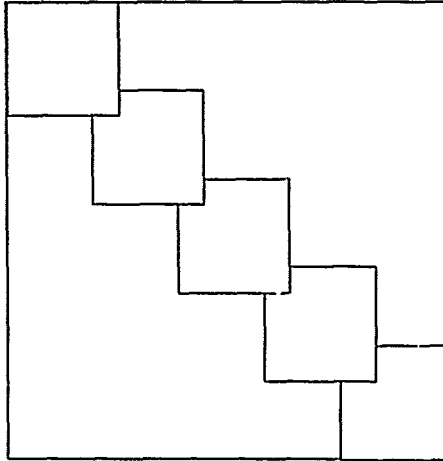
$$y = CX + w_2 \quad (7)$$

w_1 is the state excitation noise and w_2 is the measurement noise. The joint process of w_1 and w_2 is assumed to be white noise.

The mechanics of the control algorithm as described in Eqs. 4 to 7 are quite complex when applied to a spacecraft with interconnected flexible bodies. Multibody dynamics are in general nonlinear, and they are linearized at a particular state of interest in order to take advantage of the powerful analytical techniques developed for linear dynamic systems. The plant matrix A in Eq. 4 contains linearized multibody dynamics, flexibility, inertia, and the damping properties of the individual flexible bodies and the connecting appendages. In addition, it also contains a description of the actuator and sensor dynamics, the constraint forces between the bodies, the gravity gradient and other dynamic effects associated with the orbiting spacecraft. An analytical simulation and onboard implementation of a centralized control law for the entire spacecraft with multiple bodies is impractical for a number of reasons. The dimensionality of a multibody system can be very large, when all the flexible degrees of freedom of the bodies are added. Order reduction at such a large system level can be computationally demanding and can also introduce severe errors and uncertainties. In addition the diverse flexibilities of the interconnecting bodies and appendages require different input and output sampling rates, and a centralized control system would be hard pressed to respond. It is much more appealing to decentralize the control system at each body level for vibration suppression and design a separate control system for the attitude control. This process is akin to passive vibration isolation, even though it can be accomplished with a combination of active and passive controls.

The decentralized control system is based on the premise that the governing equations of the system can be decoupled at the individual body level. The decoupling extends to the state as well as the input and output of the system. A canonical transformation using the system's natural modes is the most direct approach for decoupling the system equations. However, such an approach is not practical, because identification of the appropriate natural modes of a large system with different bandwidth requirements of the bodies is not an easy task. Two approaches, which are used extensively in the solution of structural dynamics problems, are being considered for the decentralized control problem.

Analysis based on component mode synthesis is a well established method in the solution of structural dynamics problems. Similarly, dynamic reduction based on reduced basis vectors and static reduction (Guyan reduction) based on static condensation are available in many of the general purpose analysis codes such as NASTRAN. These methods are based on the physical and the related mathematical partitioning of the system and its equation. The solution is implemented in two or more levels. At the body or component level the dynamic properties of the flexible body and all the forces acting on it are transferred from the body internal degrees of freedom to the interfacing degrees of freedom with the other bodies. The system of equations can be written symbolically in block diagonal form as follows:



**MULTI-BODY SYSTEM
BLOCK DIAGONAL REPRESENTATION**

The overlapping degrees of freedom in the block diagram represent the interface between the bodies. Such a representation can include both open tree and closed tree topologies as well. In such a scheme there will be $n + 1$ sets of subsystem equations

$$m_j \ddot{v}_j = Q_j + F_j, \quad j = 1, 2, \dots, n \quad (8)$$

$$M \ddot{V} = Q \quad (9)$$

where n represents the number of flexible bodies, and M is the total mass of the system. Eq. 8 represents the dynamic equations of the j^{th} flexible body, while Eq. 9 represents the overall system, reduced to include only the interface degrees of freedom. Since the constraint forces are a system of self-equilibrating forces, they do not appear in the overall system equations.

A decentralized control system in such a scheme will have $n + 1$ controllers, one controller for each body and an overall controller for the total system. Control of the elastic motions will be the primary function of the individual body controllers, while the attitude control of the spacecraft will be relegated to the system controller.

In an LQG controller setting the body controller treats interaction from the other bodies as part of the stochastic disturbance. This concept of decentralization is very appealing. However, its implementation is fraught with many pitfalls. Most of the reduction schemes are approximate, and it is impossible to estimate their effect on the stability and performance of the controller without extensive numerical simulation⁽¹²⁾.

5. PASSIVE CONTROL

Passive control basically involves adjustment of mass, stiffness and damping of the flexible body in order to achieve some predetermined dynamic characteristics. The object is to design a lightly damped system to augment the active controls in vibration suppression. This damping issue can be addressed as an optimization problem at the individual body level. Optimization first involves formulation of an objective function and definition of constraints in the spirit of nonlinear programming. The mass of the body is an appropriate objective to minimize in spacecraft applications. The real and imaginary parts of the complex eigenvalues of the damped system are appropriate constraints. The structural (mass and stiffness) and damping parameters are the variables of the system. Optimal distribution of mass, stiffness and damping properties can be achieved by posing the optimization problem as follows⁽¹³⁻¹⁷⁾:

Minimize

$$F(x) = F(x_1, x_2, \dots, x_N) \quad (10)$$

Subject to inequality constraints

$$Z_i(x) \leq \hat{Z}_i \quad (11)$$

and equality constraints

$$Z_j(\mathbf{x}) = \bar{Z}_j \quad (12)$$

The constraints on the variables are defined as

$$\bar{x} \leq x \leq \bar{x} \quad (13)$$

In the context of a truss structure the mass minimization problem can be stated as⁽¹⁸⁾

$$F(\mathbf{x}) = \Sigma_i C_i x_i \quad (14)$$

subject to constraints on the real and imaginary parts of the complex eigenvalues. The constraint on the real part introduces a desired percentage of damping in the mode. The constraint on the imaginary part is to avoid resonance conditions. The variables, x_i , represent the mass, stiffness and damping properties of the structure. In this representation an increase in damping in an element can be tied to an increase in mass as well, so that there is penalty associated with the damping. The purpose of this optimization is to achieve an optimal distribution of damping, stiffness and mass properties with a minimal mass increase.

Once this problem is posed in a nonlinear programming setting, it is possible to take advantage of the many search algorithms readily available for optimization⁽¹³⁻¹⁷⁾. A lightly damped system augments the active control system and enhances the stability.

6. SUMMARY AND CONCLUSIONS

The interaction of multibody dynamics, the flexibility of the bodies and the control system is an important consideration in the design and dynamic response predictions of large flexible space structures. The concept of a decentralized control system for lightly damped structures is extremely appealing and needs further research in order to establish its validity. The approximations associated with order reduction and substructure representation need further assessment, before they can be accepted as viable design approaches. The design of lightly damped structures using nonlinear programming algorithms is a realistic approach for large order systems. However, these concepts need extensive numerical simulation in order to establish their validity for realistic applications.

REFERENCES

- 1 Likins, P.W., "Multibody Dynamics - An Historical Perspective," Proceedings of the Workshop on Multibody Simulations, Jet Propulsion Laboratory, California Institute of Technology, Editors Man, G. and Laskin, R., April 15, 1988.
- 2 Kane, T.R. and Levinson, D.A., "Formulation of Equations of Motion of Complex Spacecraft," Journal of Guidance and Control, Vol. 3, No. 2, 1980.
- 3 Bodley, C.S., Devers, A.D., Park, A.C. and Frisch, H.P., "A Digital Computer Program for the Dynamic Interaction Simulation of Controls and Structure (DISCOS)," Vols. 1 & 2, NASA Technical Paper 1219, May 1978.
- 4 Waites, H.B. and Singh, R., "Dynamics of Flexible Bodies: CONTOPS - A Computer Oriented Approach," Proceedings of the Workshop on Multibody Simulations, Jet Propulsion Laboratory, California Institute of Technology, Editors Man, G. and Laskin, R., April 15, 1988.
- 5 ADAMS 5.2 User's Manual, Mechanical Dynamics, Inc., April 1987.
- 6 DADS User's Manual, Computer Aided Design Software Incorporated, P.O. Box 203, Oakdale, Iowa.
- 7 Likins, P.W., "Analytical Dynamics and Non-Rigid Spacecraft Simulation," JPL Technical Report 32-1593, July 15, 1974.
- 8 Singh, R.P., VanderVoort, R.J. and Likins, P.W., "Dynamics of Flexible Bodies in Tree Topology - A Computer-oriented Approach," Journal of Guidance, Control and Dynamics, Vol. 8., No. 5, September-October 1985, pp 584-590.
- 9 Nikravesh, P.E., "Systematic Construction of the Equations of Motion for Multibody Systems Containing Closed Kinematic Loops," ASME paper no. 89-DAC-58, Montreal, Canada, September 17-20, 1989.
- 10 User's Manual for TREETOPS - "A Control System Simulation for Structures with a Tree Topology."
- 11 Kwakernaak, H. and Sivan, R., "Linear Optimal Control Systems," Wiley-Interscience, New York, 1972.
- 12 Young, K.D., "Hierarchical Controlled Component Synthesis of Large Space Structures," Lawrence Livermore National Laboratory draft report, UCRL 101639 - This is also a paper being prepared for submittal to the 11th International Federation of Automatic Control (IFAC) World Congress, August 1990.
- 13 Venkayya, V.B., "Aerospace Structures Design on Computers," WRDC-TR-89-3045, March 1989.

14. Venkayya, V.B., Tischler, V.A., Kolonay, R.M. and Canfield, R.A., "A Generalized Optimality Criteria for Mathematical Optimization," WRDC-TR-89-XXXX.
15. Vanderplaats, G.N., "A General-Purpose Optimization Program for Engineering Design," J. Computers and Structures, Vol. 24, No. 1, pp 13-21, 1986.
16. Haftka, R.T. and Kamat, M.P., "Elements of Structural Optimization," 2nd Edition, Martinus and Nijhoff in Press.
17. Morris, A.J., Editor, "Foundations of Structural Optimization: A Unified Approach," John Wiley & Sons, New York, 1982.
18. Khot, N.S., "Structures/Control Optimization to Improve the Dynamic Response of Space Structures," Journal of Computational Mechanics, Vol. 3, No. 3, 1988, pp 179-186.

DYNAMICS AND DYNAMICS EXPERIMENTS IN TSS-1*

by

Silvio Bergamaschi
Principal Investigator of Theoretical and Experimental Investigation on TSS-1 Dynamics
Department of Mechanical Engineering, University of Padua
Via Venezia 1, 35131 Padua, Italy

SUMMARY

TSS-1 (Tethered Satellite System-1) is the first retrievable space system to be tethered to the Shuttle in order to conduct scientific experiments.

The nominal profile of the mission will consist of:

- a deployment phase, where the tether is reeled out from the Shuttle until the satellite is 20 km above it
- stationkeeping, in which the tether length is almost constant and the scientific activity reaches its maximum
- retrieval, where the tether is reeled in, until the satellite is recovered in the cargo bay.

Two of the research proposals selected in 1984 by a joint U.S.-Italy commission are dedicated to the study of the dynamics of this novel system. Purpose of this paper is:

- to comment the mathematical models implemented so far to simulate TSS-1 dynamics
- to present the rationale of the investigation activity (being) carried out at the University of Padua and to survey its functional objectives.

INTRODUCTION

It is known that the origin of the concept of long tethers in space can be traced back to the end of the 19th century, when Tsiolkowskii [1]**] first proposed a tower anchored to the Earth and extending beyond the altitude of the geostationary orbit.

In the space era, the idea of tethering a satellite to the Space Shuttle, in order to conduct aeronomy, gravity gradiometry and electrodynamics experiments in LEO was first proposed in a SAO report [2]; investigations on the dynamics of such a system began in 1975, with two independent studies sponsored by NASA/MSFC [3] and ESA/ESTEC [4], the purpose of which was mainly to define the feasibility of deployment and retrieval manoeuvres.

In the second half of the seventies, a number of investigators developed models intended to take into account any aspect of the motion. However, the inclusion of tether elasticity caused most of them to require excessive computer time for the numerical integration of the resulting equations, so that they were abandoned and, in recent years, the trend has been to substitute "general purpose" models with a library of routines, each of them more limited in scope, but much more efficient from the point of view of computational flexibility [5].

In the meanwhile, at the beginning of the eighties, the TSS became a joint project between the U.S. and Italy, and funding was approved for the first mission, which was to be dedicated to:

- in flight verification of the concept of tethers in space
- dynamics experiments
- electrodynamics and plasma physics experiments

In april 1984, NASA and PSN (the National Space Plan of Italy, at present ASI) jointly requested proposals of experiments on TSS-1. The selection procedure was carried out in the summer of the same year and two proposals related to dynamics, by SAO (Smithsonian Astrophysical Observatory) and Padua University respectively, were approved.

At present, TSS-1 is manifested for flight in May 1991. The mission profile calls for the upward deployment of a 20 km conducting tether and an overall duration of some 36 hours. From fig. 1 (see page 2) is seen that the satellite remains in stationkeeping conditions for about 10 hours. A shorter time interval during which the tether length is nearly constant is also planned toward the end of retrieval.

(*) This research effort has been sponsored by ASI (Agenzia Spaziale Italiana)

(**) See References at end of paper

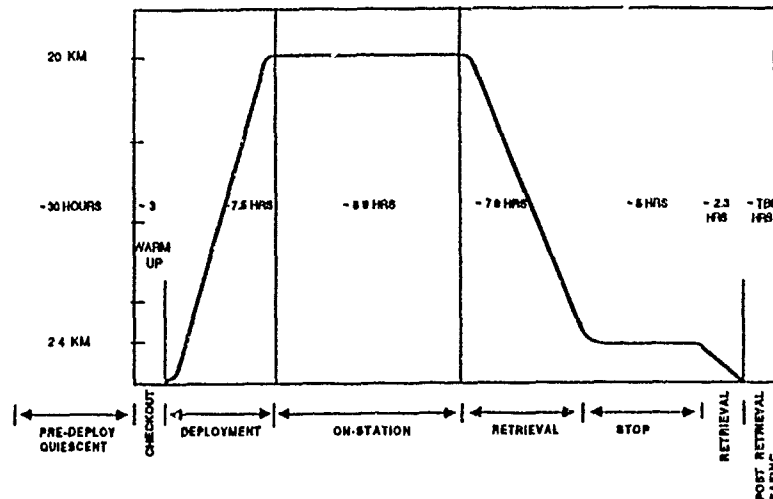


Fig. 1

In both such periods, part of the time will be dedicated to dynamics experiments. During the remaining part of the mission this kind of activity will be carried out on a non interference basis with other scientific experiments. The hardware to be used will primarily consist of a set of three linear accelerometers and three gyros with mutually orthogonal sensitive axes. While the accelerometers are part of the scientific core equipment, the gyros will also be used for attitude determination and control. The purpose and flight objectives of both the dynamics experiments are:

- Develop a number of mathematical models intended to simulate TSS-1 dynamics as close as possible
- Measure linear and angular accelerations at the satellite and compare experimental results with theoretical expectations.

HISTORY OF DYNAMICS SIMULATIONS

Rigid tether

The SAO report mentioned above did not include any simulation of the motion, although it was shown, by means of a quasi static model, that deployment manoeuvres are feasible. This is because, in a circular, unperturbed reference orbit, the system composed by the Shuttle, a tether and a subsatellite has four possible equilibrium configurations. Two of them, aligned with the local vertical, are statically stable, so that the tether can be deployed both upward and downward with respect to the reference orbit. Tether tension is provided by gravity gradient; if the mass of the tether is neglected, one can write:

$$\tau = 3mn^2l \quad (1)$$

where:

- τ is the tether tension
- m is the satellite mass
- n is the mean motion of the Shuttle orbit
- l is the tether length

The most important features of the dynamics of a TSS were studied shortly afterward, and the criticality of both deployment and (in particular) retrieval was readily apparent. Such features are reported here by commenting the equations of what can, perhaps, be considered as the simplest, but physically meaningful mathematical model used for the simulations. The assumptions are:

- The Space Shuttle is in a circular orbit, not perturbed by the satellite. This means that the c.o.m. of the overall system coincides with the c.o.m. of the Shuttle itself.

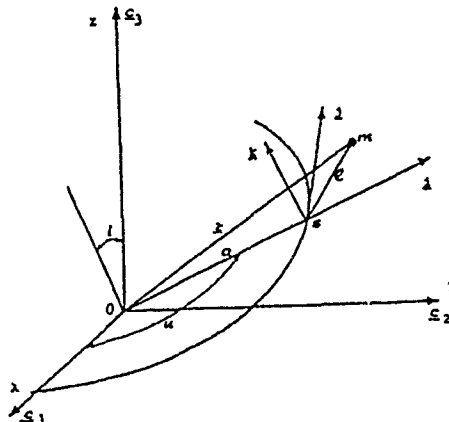


Fig. 2

- Both the Shuttle and the satellite are point masses. Tether inertia is neglected.
- The tether is rigid. As it will be apparent in the following, the assumption of neglecting tether elasticity has dramatic consequences.
- Control, or environmental forces, as thrust, air drag, J_2 effects, etc. are ignored. Only the gravitational attraction of the spherical Earth is taken into account.

If one further assumes that l is a control variable, the motion of m (see fig. 2) has two d.o.f.: the in plane (θ) and out of plane (ϕ) libration angles, measured starting at the local vertical. In writing the equations of motion, it is usually taken advantage from the fact that $l/a \ll 1$ (a is the semimajor axis of the Shuttle orbit), so that the gravitational potential at m is expanded in series and the terms with powers higher than the second of l/a are neglected. Finally, limiting the analysis to small angles, the dynamical equations are:

$$\ddot{\theta} + 2\frac{l}{a}\dot{\theta} + 3n^2\theta = -2n\frac{\dot{l}}{a} \quad (2a)$$

$$\ddot{\phi} + 2\frac{l}{a}\dot{\phi} + 4n^2\phi = 0 \quad (2b)$$

from which it is seen that small in plane and out of plane libration angles are uncoupled. First, let us consider the case with constant l (stationkeeping); in this situation, the motion is the composition of two harmonic oscillations with slightly different periods (see fig. 3, where the periods have been plotted vs. the orbital altitude), so that the system is dynamically stable.

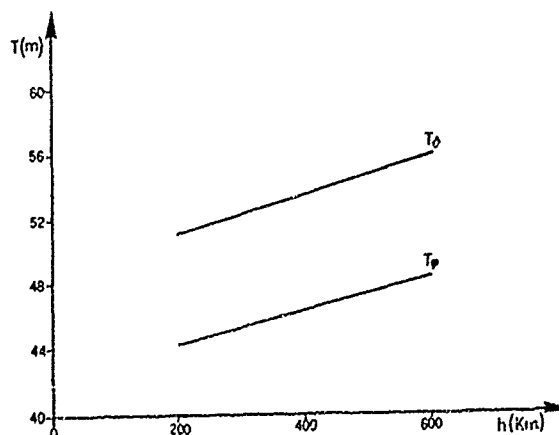


Fig. 3

Different is the case in which i is not zero. In the first place, the forcing term in eq. (2a), originated by the Coriolis acceleration, pulls the tether away from the local vertical. If the same control law is used during the manoeuvres, the destabilizing action is the same for deployment and retrieval. On the contrary, the angular velocities dependent terms cause, in both equations, the librations excited during deployment to be damped out as the tether is reeled out, while they originate self excited oscillations during retrieval. Thus, it can be concluded that, although the initial phase of deployment is also critical because tether tension is small (see eq. 1), the highest degree of dynamical instability occurs in the last phase of retrieval. For this reason, the simulations carried out at NASA/MSFC and ESA/ESTEC with different models and computational techniques, led to remarkably similar results, i.e., while 6-8 hours are sufficient to successfully complete a 100 km. deployment, depending on the control law being adopted, more than 1 day is needed to retrieve the satellite from the same distance.

Further dynamics studies were performed by MMC (Martin Marietta Corporation) at BASD (Ball Brothers Aerospace Division) during the phase B of the TSS-1 project, and shortly afterwards by Aeritalia in Italy. One of the main purposes was to shorten the excessive time interval required by retrieval. Two different approaches were proposed:

- to avoid excessive angular excursions from the local vertical by means of suitable manoeuvres of the Shuttle, in analogy with the well known fact that the dynamics of a pendulum can be controlled by the motion of its suspension point
- to consider an active satellite (with yaw control) with radial in plane and out of plane thrusters for libration damping.

Both alternatives showed promising results and allowed retrieval to be completed in 6-7 hours. Later on it was decided that the subsatellite should have been active and an additional set of thrusters, nominally parallel to the tetherline, was included in the final configuration, in order to ensure a minimum artificial tension of 2 N when gravity gradient is small.

The mathematical models used in this phase of the dynamics analysis were, of course, more general in scope than the one shown above. They were not limited to small angles, included tether inertia and took into account some environmental effects as air drag and J_2 perturbations; however, they shared the common feature to neglect tether elasticity. For this reason, they were relatively simple and numerical integrations were fast; on the other side, the simulation of tether longitudinal and lateral vibrations was ruled out.

Elastic tether

In the second half of the seventies, the novelty and intricacy of the problem of tether dynamics attracted a number of investigators who worked actively to relax the assumptions by which existing codes were constrained. The idea was to implement what was later called a "general purpose model", with the capability to simulate:

- tether elasticity effects
- environmental, thrust and control forces
- Shuttle and satellite attitude dynamics
- Shuttle elliptic orbit and orbital perturbations

The situation in those years is best summarized in [6]. In most models tether elasticity was simulated by means of discretization techniques (finite differences, or finite elements) and the resulting equations were integrated by means of numerical methods. Unfortunately, the frequencies of the elastic vibration modes are much higher than the mean orbital motion; on the other side, tether vibrations and rigid body librations are coupled in the equations of motion, so that very small integration steps have to be adopted to maintain the accuracy and computer time is likely to be excessive in many cases. To be more specific, let us consider the TSS-1 case where:

$$a = 6674 \text{ km} \qquad l = 20 \text{ km} \qquad m = 550 \text{ kg} \qquad (3)$$

while the tether density, Young modulus and diameter are respectively:

$$\rho = 1.5 \cdot 10^3 \text{ kg/m}^3 \qquad E = 7 \cdot 10^{10} \text{ N/m}^2 \qquad d = 2.5 \text{ mm} \qquad (4)$$

From fig. 3 it is seen that the frequency of the in plane libration is $2 \cdot 10^{-3}$ rad/sec, depending only on the orbit altitude. The frequencies of the two lower modes of the longitudinal vibrations of the tether are respectively:

$$\omega_1 = 1.77 \cdot 10^{-1} \text{ rad/sec} \qquad \omega_2 = 1.07 \text{ rad/sec}$$

Therefore, an integration step smaller than 1 sec is needed to simulate correctly this kind of vibrations up only to the second mode. If upper modes have to be included, the number of d.o.f. is increased and the step decreased correspondingly, so that it is not surprising that the time required for some numerical integrations can be as large as ten times the physical time.

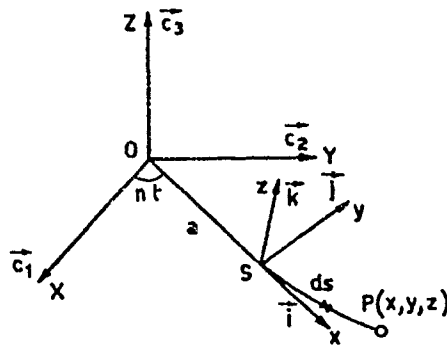


Fig. 4

As a consequence, in more recent years the trend has been toward the implementation of libraries of codes less general in scope, but more easy and less expensive to be used, each of them tailored to describe a few aspects of TSS-1 dynamics. The need for this kind of approach has been emphasized also by the fact that, in the meantime, several other applications of tethers in space, different from the TSS project, have been proposed. Such applications include attitude and c.o.m. location control of the Space Station Freedom, variable gravity tethered laboratories, creation of artificial gravity for the manned mission to Mars, etc., so that what could be considered a general purpose code for TSS-1 might be insufficient to describe some features of the motion, important in other applications. The conclusions above can be found in [5].

Going back to the specific problem of the simulation of tether elastic vibrations, in the eighties extensive use has been made of modal analysis. What follows is a summary, as short as possible, of one [7] of the so called analytical-numerical models, intended to reduce the computational burden.

Most of the assumptions valid in this case are the same made above, the fundamental difference being that now the tether is considered to be a perfectly elastic monodimensional continuum. No material damping is included in the model, because of lack of experimental information. Referring to fig. 4, let $(0, X, Y, Z)$ be an inertial reference system centered at the Earth c.o.m., the XY plane coincident with the equatorial plane and Z toward the north pole; let also (S, x, y, z) be a rotating frame with its origin at the Shuttle c.o.m., x along the ascending local vertical, y coincident with the direction of the Shuttle orbital velocity and z toward the orbit pole. Further, s is the space independent variable in the tether domain. The lagrangian density of this system can be written as:

$$L = \frac{1}{2} \mu \{ (\dot{x} - ny)^2 + [y + n(\alpha + x)]^2 + \dot{z}^2 \} - \frac{1}{2} EA \left[(x'^2 + y'^2 + z'^2)^{\frac{1}{2}} - 1 \right]^2 + \mu n^2 \alpha^2 \left(1 - \frac{x}{\alpha} + \frac{2x^2 - y^2 - z^2}{2\alpha^2} \right) \quad (5)$$

where μ is the tether mass per unit length, the dots mean time derivatives, while the primes denote differentiation with respect to s. With the assumptions made, the configurations with the tether along the local vertical are of stable equilibrium. In these conditions the tether is stressed because of the gravity gradient acting on it and on the satellite; therefore, considering the small amplitude oscillations around such configurations, the solutions have the form:

$$\begin{aligned} x(s, t) &= x_1(s) + \varepsilon x_2(s, t) \\ y(s, t) &= \varepsilon y_2(s, t) \\ z(s, t) &= \varepsilon z_2(s, t) \end{aligned} \quad (6)$$

where $x_1(s)$ is the solution in equilibrium conditions and ε a small ordering parameter. By substituting (6) in (5) and using standard methods, the strain in the equilibrium configuration can be obtained from the 0-th order lagrangian density.

In fig. 5 (see page 6) the elongations of the tether at the satellite have been plotted for lengths up to 100 km and three different diameters. Therefore, the elongation in the case of TSS-1 is expected to be less than 4 m, while in the second mission the tether would be lengthened by about 100 m.

The dynamical equations can be derived from the second order lagrangian density. They, together with the proper boundary conditions, are not reported here for sake of brevity; in any case, what turns out is that longitudinal and in plane lateral (taut string) vibrations are coupled, while lateral out of plane oscillations are uncoupled to them.

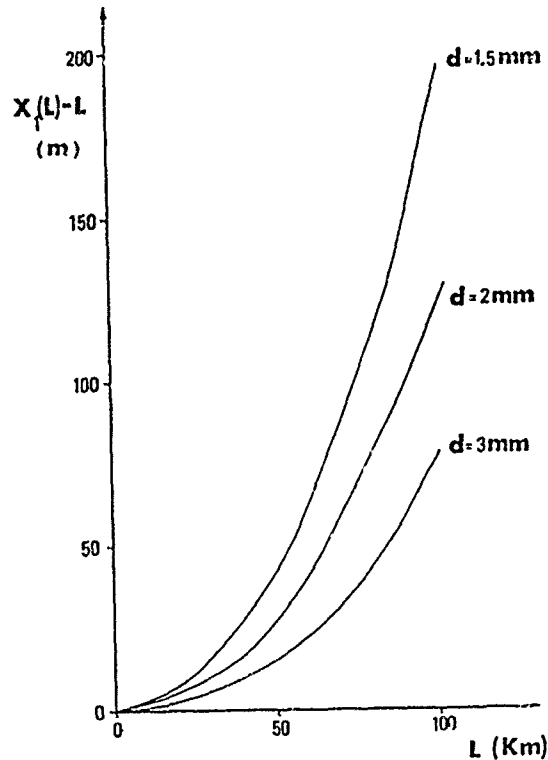


Fig. 5

Fig. 6 (see page 7) shows the frequencies of the out of plane oscillations (non dimensionalized with respect to n) as functions of the mode order, both for the TSS-1 and TSS-2 missions.

Fig. 7 (see page 7) shows the first three vibration modes for TSS-1. It is seen that the fundamental mode is a rigid libration with frequency equal to the one predicted by eq. (2b). It is noted that, in the higher modes, the vibration amplitude at the satellite, though small, is different from zero.

Similar results have been obtained for the longitudinal-in plane coupled vibrations.

FURTHER ASPECTS OF TSS-1 MOTION

From the assumptions made above, it is clear that different models are needed in order to simulate other important features of TSS dynamics and make the theoretical expectations closer to the real motion. In the following, an overview is made of other models used, or in the process of implementation, to describe the time evolution of degrees of freedom not included in the model just presented.

Orbit eccentricity. The residual eccentricity of the Shuttle orbit in nominal conditions is of the order of 10^{-3} , corresponding to a difference between apogee and perigee altitudes of about 14 km. From the theory of gravity gradient stabilisation of rigid satellites in low eccentric orbits [8] it is known that e forces the pitch motion to oscillate harmonically with frequency equal to the orbit mean motion. In the present case the amplitude, in radians, of the libration is equal to the eccentricity value.

Earth oblateness. The perturbation of the reference orbit originated by the Earth oblateness and the subsequent tether motion have been studied by several authors (see [9] for additional references). The related mathematics are somewhat involved, so that no formulas are reported here. It is sufficient to note that, since $J_2 = 0(10^{-3})$, the perturbations are of the same order of magnitude of the one caused by residual eccentricity. Computer simulations have shown that the acceleration level at the satellite is less than 10^{-8} g , not detectable by the accelerometers mounted on board TSS-1.

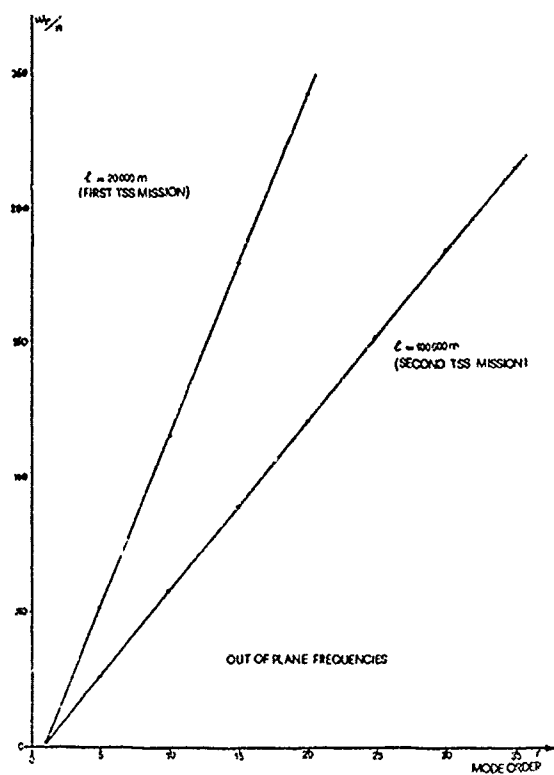


Fig. 6

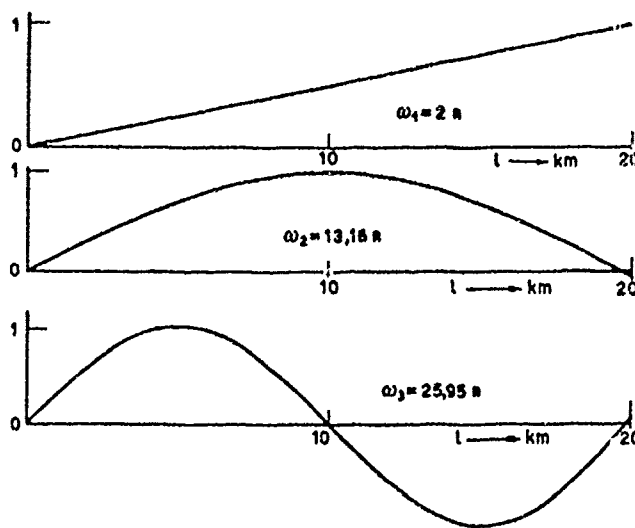


Fig. 7

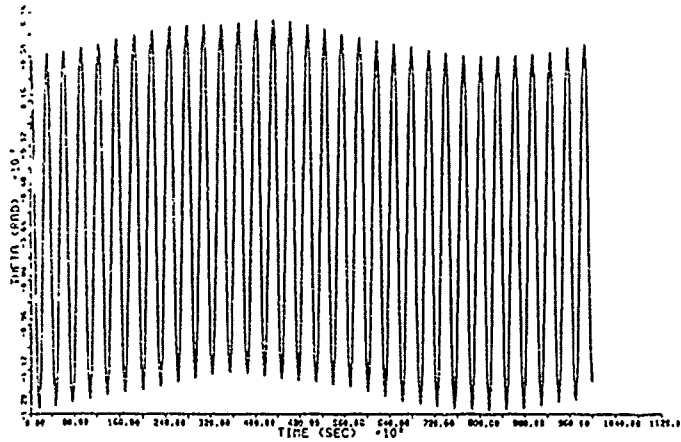


Fig. 8

Interaction of the conducting tether with the Earth magnetic field. Since the TSS-1 mission is dedicated also to electrodynamics and plasma physics experiments, the tether will be electrically conducting. As a consequence, the interaction of the conducting tether with the Earth magnetic field generates, according to Laplace laws, a perturbing force which pulls the satellite away from the local vertical. The force acting on an infinitesimal tether element of length ds is:

$$d\vec{F} = i_0 \vec{B} \times d\vec{s} \tag{7^*}$$

where:

- i_0 is the intensity of the current flowing in the tether
- \vec{B} is the induction of the Earth magnetic field at $d\vec{s}$

To assign a numerical value to i_0 is, in this case, a problem, because the intensity is precisely one of the quantities which will be measured in some of the electrodynamics experiments. From preliminary evaluations reported at the investigators Working Group meetings it turns out that i_0 will be in any case less than 1 A (more likely, a few 100 mA). Thus, dynamical equations have been written to describe the three dimensional motion of a rigid tethered system subjected to gravity gradient and force (7), where a tilted dipole model has been used to derive the expression of \vec{B} * [10]. The equations have been integrated numerically and some of the results for the time behaviour of the displacement angles θ and ϕ (already defined) in the case with $i_0 = 1A$ are shown in figs. 8 and 9.

It is seen that the maximum angular displacements in the orbit plane are about 0.7 deg., while ϕ_{max} is close to 0.3 deg. This means that the maximum linear acceleration at the satellite, when the tether is fully deployed, is about $5 \cdot 10^{-5}$ g. In conclusion, this kind of perturbation is at the limit of the detection capability of the accelerometers.

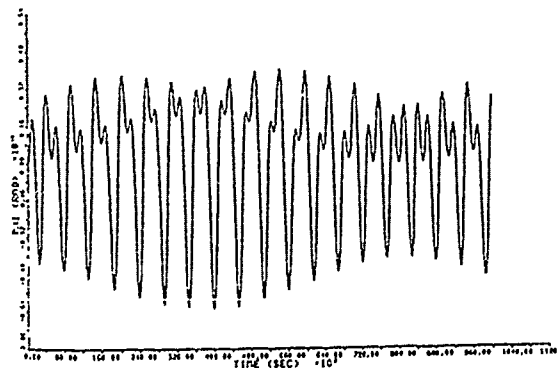


Fig. 9

(* The bar denotes vector

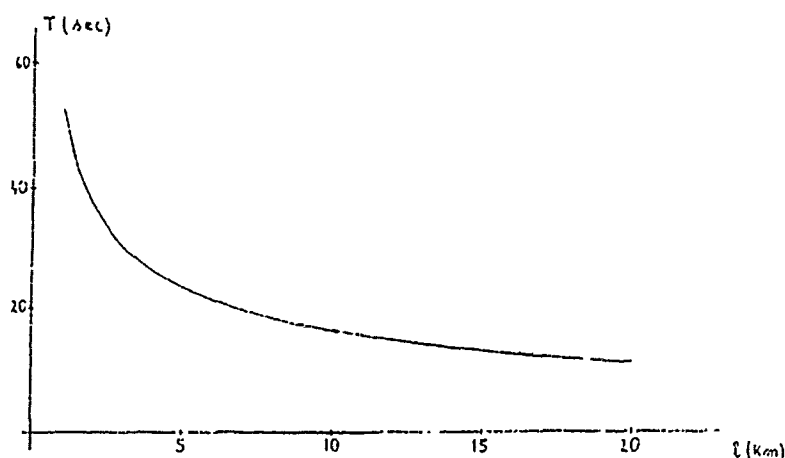


Fig. 10

Satellite attitude motion. So far, the satellite has been considered as a point mass, so that the d.o.f. relative to its attitude have been neglected. A more accurate model must simulate the satellite as a rigid body, but the problem arises that its oscillations around the tether attachment point are coupled to the librations and vibrations of the tether itself. Therefore, the simplification has sometimes been made to restrict the analysis to the case with the tether along the local vertical and to consider the tether action on the satellite as an external torque. At present, since the satellite will be spinning at 1 r.p.m. during part of the mission, a model based on Euler equations is under development to study the spin effect on the attitude.

However, preliminary information can be obtained from simpler models. For instance, fig. 10 shows the dependence of satellite pitch period on tether length. The period increase as l decreases is due to the weakening of the restoring gravity gradient torque. With $l = 100$ km, the period is about 5 sec.

Air drag. The effect of air drag on TSS-1 is expected to be small, both for the anticipated Shuttle altitude of 296 km and because of the upward deployment. Considering worst case conditions, it is found that the equilibrium configuration is displaced from the local vertical by about 0.1 deg. Therefore, the forcing acceleration at the satellite is not detectable by the instruments.

Completely different will be, of course, the case of TSS-2, where a downward deployment is planned and the final altitude is foreseen to be around 130 km.

Tether material damping and elastic properties. To the author's opinion, this is the most crucial problem of simulations. In fact, from a review of TSS dynamics models, it is easily seen that most frequently the tether has been simulated as rigid, or purely elastic, although several computer codes have the capability to take into account, at least in part, the damping action. This situation is due to a number of causes:

- The structure of the tether to be used for TSS-1 is far from simple. From fig. 11 (see page 10) it is seen that it is made up by 5 coaxial elements, while only one of them, made by braided kevlar, is needed to withstand mechanical stresses.
- Experimental work has been done in the past, but problems have been raised for data interpretation (i.e. viscous or structural damping ?) At present, it seems that the best available analysis is contained in [11]. Moreover, it is not trivial to extrapolate the results, obtained with 10-15 m long specimens, to a 20 km tether.
- Space conditions will be different from laboratory ones, so that it is questionable if the same damping mechanism apply (friction between elementary fibers ?). Further, outgassing might also alter the physical properties of the tether.

From these considerations, it appears that the problem of tether damping is quite open and that, possibly, the only viable method to gain insight in it will be to conduct in-flight experiments. As a consequence, some of the flight objectives of the dynamics experiments to be performed during the TSS-1 mission will be dedicated to the analysis of damping.

Also, it is important to note that other tether characteristics are known with limited accuracy. For example, it is usually assumed that its diameter is 2.5 mm and this value is used in the calculation of vibration frequencies, in the same way, the Young's modulus of kevlar is most frequently adopted. But how close are these assumptions to the characteristics of the real, composite tether ? Thus, it is seen that the quality of simulations can be reduced not only by simplifying assumptions on which, more or less, all the models are based, but also by limited knowledge of some of the parameters affecting the motion.

FIRST MISSION (TSS) CONDUCTING TETHER CONFIGURATION

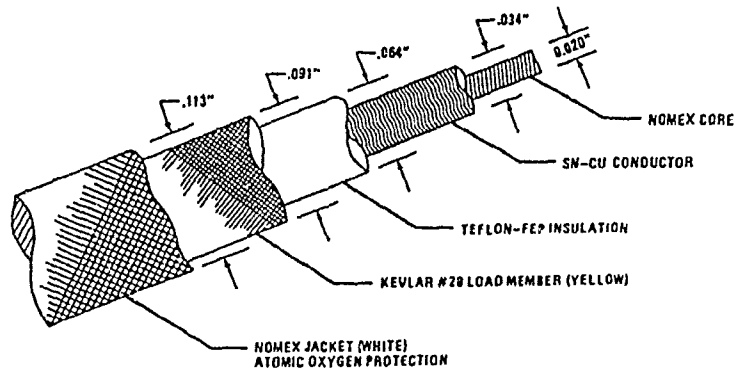


Fig. 11

Failure modes. In the course of several years, some investigators (among which is the author) have studied the dynamical behaviour of TSS-1 in the event that non nominal conditions occur during the flight. It is not the case here to go into the details of such special studies. However, models have been developed to study:

- tether slackness induced by jamming of the reel mechanism
- dynamics, after tether breakage, of both the part which remain in connection with the Shuttle [12] and the other one attached to the satellite
- instability induced by jettison of one of the deployable-retrievable booms to be used for RETE experiment
- decay time of satellite free orbit after tether breakage, in order to evaluate the rescue feasibility in a future Shuttle mission [13].

FUNCTIONAL OBJECTIVES

TEID (Theoretical and Experimental Investigation of TSS Dynamics) is the name given by the project to the Padua experiment. Its functional objectives (listed below) are the logical consequence of the present status of simulation models and of their limitations. It is noted that these F.O.-s are quite similar to the ones of the other dynamics experiment on TSS-1.

- F.O.1 Pre-deployment dynamics measurement.** It is desired to measure the dynamic noise on board the Shuttle, before the beginning of deployment. If possible, two sets of acceleration data will be generated: the first when the boom carrying the satellite is still stowed in the cargo bay, the second when it is fully extended with the satellite latched at the tip.
- F.O.2 Deployment profile.** Many interesting phenomena can be identified during deployment. In particular, since the frequencies of the motion of different d.o.f. depend on tether length, some of them are equal in some phase, thus affecting energy transfer between different components of the motion. For the purpose of this objective, no restrictions or inhibits are placed on other experiments.
- F.O.3 In line impulse response function.** This F.O. requires the application of a perturbation along the tether axis (e.g. applying reel brake) when the satellite is on station 1. From the analysis of the ensuing free longitudinal vibrations, information can be obtained on system damping and acceleration regime at the satellite.
- F.O.4 In line periodic perturbation on station 1.** The application of an in line perturbation (e.g. by means of the satellite in line thrusters) is required to study the forced oscillations regime and tether material damping.
- F.O.5 Transverse impulse on station 1.** It is required to apply a transverse impulse to the satellite, at the purpose of studying tether taut string vibrations, the so-called skip-rope motion and TSS attitude dynamics.

- F.O.6 Dynamic quiet measurements on station 1. The purpose of this F.O. is to measure the environmental forces acting on the system. During the corresponding time interval, internal perturbation sources as satellite thrusters acceleration, Shuttle attitude and orbit manoeuvres, etc. should be reduced to a minimum.
- F.O.7 Retrieval profile. The purpose is the same of the one of F.O.2.
- F.O.8 In line impulse response function on station 2. The same goals of F.O.3 apply. The vibration regime is different in this case, because of the much shorter tether.

The accelerometers to be used for the experiments are manufactured by Bell Aerospace. Their measurement ranges are:

- x,y axes (nominal local horizontals): from $1 \cdot 10^{-5}$ g to $1 \cdot 10^{-2}$ g
- z axis (nominal local vertical): from $1 \cdot 10^{-4}$ g to $0.8 \cdot 10^{-1}$ g

while their bandwidth is from DC to 1 Hz.

The three axis integrating gyro has two operating modes. In the fine mode angular velocities can be detected up to 0.8 deg/sec, while ω_{max} in the coarse mode is 2 deg/sec.

The constant drift in the two modes is 1 deg/hour and 2.5 deg/hour respectively and the short term random drift is less than 0.02 deg/hour in both modes.

It is also noted that many perturbations originated by the system itself are likely to be detected by the instruments. Knowledge of timing and features of such disturbances is of vital importance for the interpretation of data.

REFERENCES

- [1] G. Von Tiesenhausen - *Tethers in Space. Birth and Growth of a New Avenue to Space Utilization.* NASA TM-82571. MSFC. February 1984.
- [2] G. Colombo et al. - *Shuttle-borne Skyhook. A New Tool for Low-Orbital Altitude Research.* SAO Report. September 1974.
- [3] W.P. Baker et al. - *Tethered Subsatellite Study.* NASA TMX-73314. MSFC. March 1976.
- [4] P. Kulla - *Dynamics of Tethered Satellites.* Proceedings of the Symposium on Dynamics and Control of Non Rigid Spacecraft. Frascati. Italy. May 1976.
- [5] C.C. Rupp - *Summary of the September 16 Tether Dynamics Simulation Workshop.* AAS Paper n.86-247. In *Tethers in Space.* Vol. 62 of the Advances in the Astronautical Sciences. Univelt Inc. 1987. pp. 721-724.
- [6] A. Misra, V. Modi - *Deployment and Retrieval of a Subsatellite Connected by a Tether to the Space Shuttle.* AIAA/AAS Astrodynamics Conference. Paper n. 80-1693. August 1980.
- [7] S. Bergamaschi et al. - *A Continuous Model for Tether Elastic Vibrations in TSS.* AIAA paper n. 86-0087. AIAA 24-th Aerospace Sciences Meeting. Reno (Ne). January 1986.
- [8] M. Kaplan - *Modern Spacecraft Dynamics and Control.* John Wiley & Sons 1976 Ch. 5
- [9] S. Bergamaschi, C. Savaglio - *J₂ Perturbations on the Motion of Tethered Platforms.* AAS Paper n.86-239. In *Tethers in Space.* Vol. 62 of the Advances in the Astronautical Sciences. Univelt Inc. 1987. pp. 579-588.
- [10] S. Bergamaschi, B. Quadrelli - *Magnetically Induced Librations in Conducting Tethers.* AAS Paper n.87-435. In: *Astrodynamics 1987.* Vol. 65 (Part. 1) of the Advances in the Astronautical Sciences. Univelt Inc. 1988. pp. 441-453.
- [11] Xiaouha He, J.D. Powell - *Tether Damping in Space.* Proceedings of the Conference on Space Tethers for Science in the Space Station Era - Venice, Italy, October 1987 pp. 153-162.
- [12] S. Bergamaschi - *Tether Motion after Failure.* The Journal of the Astronautical Sciences, Vol. XXX, n. 1, January - March 1982 pp. 49-59.
- [13] S. Bergamaschi - *Orbit Evolution and Decay of Tether Launched Space Systems.* Proceedings of the Third International Conference of Tethers in Space - Toward Flight. San Francisco (Ca), May 1989 pp. 178-183.

NATIONAL AERO-SPACE PLANE—FLIGHT MECHANICS

Duncan E. McIver
Former Director, NASP Office
NASA Headquarters
Washington, D.C. 20546 U.S.A.

Frederick R. Morrell
NASA Langley Research Center
Hampton, VA 23665-5225 U.S.A.

ABSTRACT

The current status and plans of the U.S. National Aero-Space Plane (NASP) program are reviewed. The goal of the program is to develop technology for single stage, hypersonic vehicles which use airbreathing propulsion to fly directly to orbit. The program features an X-30 flight research vehicle to explore altitude-speed regimes not amenable to ground testing. The decision to build the X-30 is now scheduled for 1993, with the first flight in the late 1990's. The flight mechanics, controls, flight management, and flight test considerations for the X-30 are discussed.

1.0 INTRODUCTION

The National Aero-Space Plane (NASP) program is a joint DOD/NASA program to develop technology for a new class of aerospace vehicles that can takeoff from conventional runways and fly directly into Earth orbit or cruise at hypersonic speeds in the Earth's atmosphere (ref. 1). These vehicles will employ airbreathing propulsion systems, will be reusable, and are visualized as operating in an airline-like mode with significantly reduced operating costs relative to current conventional space vehicles. A key feature of the NASP program is a flight research vehicle, the X-30, shown in figure 1, for investigating flight conditions that cannot be simulated in ground facilities and to serve as a pathfinding vehicle for future hypersonic vehicles.

There are several hypersonic vehicle programs being pursued by other nations with goals similar to the NASP program. The United Kingdom has studied the Horizontal Takeoff and Landing (HOTOL), a single stage space vehicle that uses a combination of airbreathing and rocket propulsion. West Germany is investigating the Saenger vehicle which features airbreathing propulsion for the first stage and rocket propulsion for the second stage. The first stage is also proposed as a developmental vehicle for a future high-speed, Mach 5, civil transport. The Japanese have shown both single and two-stage conceptual hypersonic vehicles similar to the NASP and the Saenger. These programs were discussed at the recent AIAA First National Aero-Space Plane Conference in Dayton, Ohio, July 20-21, 1989.

The NASP program consists of three phases as shown in figure 2 and is currently in phase 2 or the technology development phase. Based on a recent review of the program by the U.S. National Space Council, the decision milestone for proceeding to Phase 3, the building and flight test of the X-30 flight research vehicle, is now scheduled for early 1993. If the decision is positive, flight tests will begin in the late 1990's.

The X-30 vehicle will be designed for atmospheric flight throughout an extremely large range of Mach numbers from 0 to 25. Flight control, propulsion control, structural cooling control, and structural active control functions will require integration to an unprecedented degree. Transitions between aerodynamic and reaction control will be frequent. For all these reasons, flight mechanics and control, as well as piloting responsibilities, levels of automation, and systems reliability are primary considerations. Simulation and handling qualities studies are also very important and are now underway.

The X-30 flight test program will be conducted by NASA and the Air Force at Edwards Air Force Base, California. As the test Mach numbers are increased, the flight test area will encompass virtually all of the continental U.S. Planning for the complex and extensive envelope expansion flight program has been initiated.

This paper will briefly summarize the status of the NASP program with emphasis on flight mechanics and flight systems, and flight test aspects of the X-30 flight research vehicle.

2.0 NASP PROGRAM PERSPECTIVE

The NASP program is in phase 2 developing technology for the X-30 flight research vehicle, which will be used to demonstrate the critical technologies for airbreathing hypersonic vehicles. The U.S. has a long history of involvement in hypersonics research, including the early X-series of research aircraft (ref. 2). The rocket powered X-15 set an altitude record of 354,200 feet and a speed record of Mach 6.72. The X-30 continues this heritage as shown in figure 3.

The significant characteristic of the X-30 is the use of airbreathing propulsion, ramjets and scramjets, for passage through the atmosphere at hypersonic speeds. As opposed to a pure rocket vehicle like the Shuttle, the NASP must linger in the atmosphere at high Mach numbers to extract its oxidizer and is, therefore, subject to severe aerodynamic forces and a high thermal environment. A comparison of trajectories of the Space Shuttle and the NASP or X-30 is shown in figure 4. In

addition, efficient propulsion requires a high degree of integration of the airframe and propulsion systems. It is clear that the flight mechanics and control of such a vehicle will be a major technical challenge.

The three major elements of the NASP program during phase 2 are the engine contracts, the airframe contracts, and the technology maturation effort. The two engine contractors, Pratt & Whitney and Rocketdyne, are involved in the design of the engine systems including ground tests of engine modules as shown in figure 5. The limit of ground test capability for reasonable sized engines, however, is about Mach 8. The X-30 is needed to explore the higher Mach numbers. The airframe contractors, General Dynamics, McDonnell Douglas, and Rockwell, are designing X-30 configurations, conducting wind tunnel tests, and fabricating sample vehicle sections as shown in figure 6. In the technology maturation area, government laboratories, NASA Research Centers (Langley, Lewis, and Ames), Air Force Wright Research Development Center, Johns Hopkins University, and others work closely with the contractors to improve critical technologies to reduce the risk in developing the X-30. Throughout the past year, important contributions have been made in the areas of propulsion, computational fluid dynamics, aerothermodynamics, advanced materials, and flight research planning.

In the propulsion area, industry and government researchers have provided improved understanding of the physical processes in the inlet, combustion chamber and nozzle of the scramjet engine, which is required for propelling the X-30 from Mach 5-6 to orbital speed. The application of the scramjet and other propulsion cycles in the airbreathing flight corridor is shown in figure 7. Tests have been completed on a large-scale inlet model and efforts continue on evaluating the potential of slush hydrogen as an X-30 fuel.

Advanced computational fluid dynamics (CFD) codes, which accurately predict aerodynamics and physical flow effects at hypersonic flight conditions, are being used by the contractors for evaluating their engine and airframe configurations. This information and other ongoing research is essential to achieving the desired aerodynamic and thermal performance of NASP and other hypersonic vehicles.

Excellent progress is being made in the critical area of advanced materials and structures needed for survival of the X-30 in the severe flight environment (ref. 3). One concept for a materials system including thermal control is shown in figure 8. This concept includes technologies such as: reusable, high temperature materials; long life composite fuel tank, nose cap transpiration cooling; leading edge heat pipe cooling; and ceramic/composite control surfaces. Centerpiece of the overall materials and structures effort is the unique consortium of the five NASP engine and airframe contractors, who are working closely to accelerate the development of the needed materials. A second consortium of this type is being established for the development of X-30 subsystems.

Wind tunnels, large computer systems, and other unique test facilities in industry and government are being used to support the NASP program. The engine contractors have conducted successful scale model tests of their engine concepts, and the airframe contractors have completed important wind tunnel tests of scale models of their X-30 vehicle configurations. These tests provide critical data for understanding the aerodynamic characteristics of this highly integrated engine/airframe configuration. These data also help to calibrate the CFD codes, which are needed for projection to flight conditions not available in ground facilities. These NASP design and analysis activities are made possible by the supercomputer capability now available in industry and government, and the excellent technical progress would not be possible without this capability.

Flight research and test planning is continuing to utilize simulations of NASP vehicles with predicted performance based on CFD results from wind tunnel tests. Approaches to the expansion of the X-30 flight envelope, cockpit displays, off-design operation of systems, and other facets of flight test are being evaluated on the simulations to establish a safe means to conduct the flight program and to determine the critical aerodynamic, propulsion, structures, and systems data needed from the flight program.

The NASP program is managed by a team of DOD and NASA personnel located in the Joint Program Office (JPO) at Wright Patterson Air Force Base and the NASP Inter-Agency Office (NIO) in the Pentagon, Washington, D.C. The U.S. Air Force leads this joint DOD/NASA team and reports to the NASP Steering Group which is chaired by the DOD Under Secretary for Acquisition, and the NASA Deputy Administrator is the Vice Chairman.

The next 3 years of the NASP program will feature extensive testing of engine modules and airframe structural components and acceleration of efforts in government and industry to reduce the risk in the critical technologies required to build the X-30. The overall national team numbers over 5000 people and involves some 200 companies in 40 states. The NASP program expects to continue to progress toward its key milestone, the decision to build and test the X-30 flight research vehicle, scheduled for 1993.

3.0 AIRBREATHING HYPERSONIC VEHICLE CHARACTERISTICS

For hypersonic vehicles such as the X-30, there are a number of factors which affect configuration design including vehicle flight mechanics, control, and flight management characteristics. The most basic factor is the requirement for satisfactory operation of several propulsion systems over the Mach range from 0 to 25. The vehicle must fly a high dynamic pressure (e.g. 1500 pounds per square foot) trajectory in the airbreathing corridor shown in figure 4 to insure that adequate air is supplied to the propulsion systems. This is critical for proper operation of the ramjet and scramjet above Mach 4. The upper bound of the airbreathing corridor is the limit for airbreathing propulsion and the lower bound is the structural limit.

The basic configuration requires a high level of engine-airframe integration as shown in figure 9, and has been referred to as an engine-frame or engines with attachments (ref. 4). The forebody, which needs to be long and wide to provide adequate air capture at high Mach numbers, is an integral part of the inlet. The design of this forebody must be carefully integrated with the combustor to insure efficient engine performance over the speed range, and this will probably require geometric

changes in the forebody to insure proper performance. The position of the shock wave and the boundary layer, for example, at the entrance of the combustor are critical for required thrust at high speeds. This same forebody-combustor must also operate efficiently at low and intermediate speeds. In a similar way, the aft body of the configuration becomes the nozzle and proper design is also critical for required performance.

In addition, the fuel must be hydrogen for speeds above Mach 5-6, and this will require a large, light weight tank structure. This suggests a large, relatively slender and flexible vehicle, which requires accurate trajectory and configuration control for proper engine performance. Other factors, such as low frequency structural and fuel slosh modes, could affect angle of attack and sideslip and reduce engine performance. Active controls may be required for structural integrity, and active thermal control required in such areas as the leading edges and the combustor entrance.

As these vehicles proceed through the atmosphere at higher Mach numbers, the aerodynamic forces become more complex with an expanding boundary layer transitioning from laminar to turbulent with attendant effects on propulsion efficiency and heating (refs. 5,6). Viscous effects become significant at hypersonic speeds and at very high Mach numbers and skin friction drag can account for 50 percent of the total drag. At Mach numbers above 10, real gas effects begin to appear and can affect the performance of aerodynamic control effectors. As the vehicles approach higher altitudes, they lose use of control effectors and must rely on rockets or reaction jets for stability and control. The propulsive-induced moments are significant and will have to be included in the control strategy.

4.0 FLIGHT MECHANICS AND FLIGHT SYSTEMS ISSUES

4.1 Stability and Controls, Trajectory Guidance, and Flying Qualities

For the single stage to orbit airbreathing hypersonic vehicles discussed above, the designers must consider vehicle characteristics such as stability and control over the entire trajectory, trajectory optimization and guidance, and flying qualities. The NASP contractors are addressing these characteristics in their respective X-30 designs.

Some typical hypersonic vehicle configurations are shown in figure 10. Although there are clear differences in projected performance, some of the flight mechanics and control issues can be discussed in a more generic fashion. All will have the airbreathing performance characteristics described in the previous section. NASA has done some analyses of the conical configuration, and the results are useful in understanding the dynamics of this class of vehicle (ref. 7). Stability and control analyses for this configuration have shown that at the higher Mach numbers, aerodynamic control effectiveness is sharply reduced. In addition, the aerodynamic center moved forward of the center of gravity creating a pitching moment, which when offset by the elevons, introduces significant trim drag. Hence, center of gravity management and thrust vectoring concepts will have to be considered.

Since there is a requirement for controlling the angle of attack accurately to insure proper propulsion performance, an analysis was run to evaluate the effects of gusts, wind shear, and turbulence aloft on control system effectiveness (ref. 8). The results, as shown in figure 11, indicate that a more advanced performance sensitive control system may have to be considered.

An optimal trajectory for the X-30 must be defined to reach the desired Mach number with minimum fuel consumption. The trajectory must also minimize thermal loads while meeting performance goals. Guidance along such optimal trajectories in the presence of changing atmospheric conditions will be a difficult but necessary task for the onboard guidance and control system.

Although the X-30 may be flown automatically over most of its trajectory, especially at high Mach numbers, flying qualities are a fundamental consideration for flight safety in takeoff and landing and in abort conditions. A flying qualities data base for hypersonic vehicles does not exist and is currently being developed in the NASP program. This data base is needed for design of the flight management system. Flying qualities criteria for high speed, low lift to drag landings, takeoffs, and hypersonic cruise are currently being studied. Fixed-base and motion-base X-30 simulations have been developed in preparation for in-flight simulation testing.

4.2 Control System

The control system for hypersonic vehicles like the X-30 will have to accommodate a wide range of functions and will be very complex because of the high level of system integration as shown in figure 12. The system will be responsible for flight controls, thermal controls, propulsion controls, and structural controls. The control laws will be complex, interactive, and be able to provide restructuring in case of subsystem failures.

The system will provide high levels of automation for all control functions and must be reliable. If this flight critical system fails, then the result would be the loss of the vehicle. In addition, since the control system plays such a critical role in vehicle operations, and since specific performance can be improved or enabled through the control system, it is vital that the control system be an integral part of the overall vehicle design.

4.3 Flight Instrumentation

Hypersonic vehicles will have a particular challenge providing sensor information to the onboard flight systems to maintain vehicle control and the desired path. Air data sensors will be required throughout the flight envelope for estimating velocity, angle of attack, and sideslip. Inertial sensors will have to be aligned accurately to assist in flight path control. Thermal load sensors will be integrated into the flight control system since trajectory adjustments based on thermal effects may have to

be considered. Since dynamic pressures will be high and wing thicknesses small, structural load sensors will be required to enable active control functions. In addition, accurate sensor information for scramjet propulsion at the inlet, combustor, and nozzle sections will be required.

4.4 Flight Management

The design challenges for a flight management system for an airbreathing hypersonic vehicle are shown in figure 13. This figure summarizes the control and pilot interactions discussed in the sections above. The crew-vehicle interface, in particular, will present difficult flight management challenges. The vehicle systems will be highly complex and highly automated, and provisions must be made to provide the crew with appropriate information during all phases of the flight. The vehicle must takeoff horizontally, accelerate to hypersonic speeds in the atmosphere, and eventually to orbit, reenter, and land horizontally. This represents an enormous set of data that must be presented to the crew in usable form.

Because the vehicle must maintain its carefully tailored aerodynamic configuration during all flight phases except for takeoff and landing, and maybe on-orbit, there will be restricted visibility at all times. For operations near the runway, pop-up vision systems may be possible. At other times, the view will be restricted and may have to be augmented with electronic vision systems. The conceptual cockpit, shown in figure 14, is being studied at NASA to address the flight management issues.

5.0 FLIGHT TEST CONSIDERATIONS

The flight test plan for the X-30 is currently being developed by the NASP Joint Program Office (ref. 9). Unlike the Space Shuttle, the X-30 will undergo a controlled envelope expansion as with other experimental aircraft, starting with short flights near the test site and eventually expanding to orbital flight. The test site will be Edwards Air Force Base in California, where NASA also has its Ames-Dryden Flight Test Center. The test plan has been implemented on a pilot-in-the-loop simulation of generic NASP vehicles, and various test scenarios have been evaluated. The plan includes several existing Air Force and NASA ground facilities for future flight tests

A preferred envelope expansion that has resulted from these studies is shown in figure 15. The early flights would be flown near Edwards, but as the vehicle speed increases, the flight path would extend beyond that boundary. The plan is for the X-30 to cruise at a low Mach number away from Edwards and at an altitude above air traffic. The vehicle would then turn back to the base and accelerate to the test Mach number and hold for a brief period of time. A real advantage is that the vehicle has to spend very little time at the test Mach number, which reduces the total heat load. Also, the vehicle is on the way back to the base as it completes the test. The vehicle would then return under power or dead stick back to the landing strip. This vehicle would then be inspected for any thermal or structural damage after landing.

Initial analyses show that there are sufficient tracking stations while the vehicle is over the U.S., to acquire the test data by telemetry, and the use of satellites looks promising. In addition, there appear to be satisfactory recovery bases if one is required. How long it takes to complete the envelope expansion is difficult to predict and will depend on many variables. It is vitally important to proceed carefully through the expansion process.

5.0 SUMMARY

In the face of emerging hypersonic vehicle interest in the world, the NASP program is the focus for the U.S. national effort. It is a very tough technical challenge, and the flight mechanics and flight systems elements are critical to vehicle performance and must be developed in parallel with other elements. A successful flight program of the X-30 will demonstrate the technology and permit us to exploit those advances in propulsion, materials and structures, computational sciences, controls, and flight mechanics technologies necessary for future aerospace vehicles.

- [1] Barthelemy, R. The National Aero-Space Plane Program. AIAA First National Aero-Space Plane Program, Dayton, Ohio, July 20-21, 1989.
- [2] Wierzbanski, Ted. The Challenge of X-30 Flight Test. AIAA First National Aero-Space Plane Conference, Dayton, Ohio, July 20-21, 1989.
- [3] Wright, Howard: National Aero-Space Plane Technology Development Overview. AIAA First National Aero-Space Plane Conference, Dayton, Ohio, July 20-21, 1989.
- [4] Hypersonic Technology for Military Application. National Academy Press, Washington, D.C., 1989.
- [5] McRuer, Duane T.; Ashkanas, I. L.; and Johnston, D. E. Flying Qualities and Control Issues and Features for Hypersonic Vehicles, Systems Technology Incorporated Technical Report TR 2361-1, May 1989.
- [6] Johnston, Patrick, Whitehead, Allea; and Chapman, Gary: Fitting Aerodynamics and Propulsion into the Puzzle. Aerospace America, September 1987, pp. 32-34.
- [7] Powell, Richard W.; Naftel, J. Christopher; and Cruz, Christopher L.: Flight Control Issues of the Next Generation Space Transportation Launch Vehicles. 75th Symposium of the AGARD Flight Mechanics Panel on Space Vehicle Flight Mechanics, Luxembourg, November 13-16, 1989.

[8] Shaughnessy, John and Raney, David: Response of a Hypersonic Vehicle to Atmospheric Disturbances During Ascent
NASP Technical Memorandum 1061, July 1989.

[9] See reference 2.

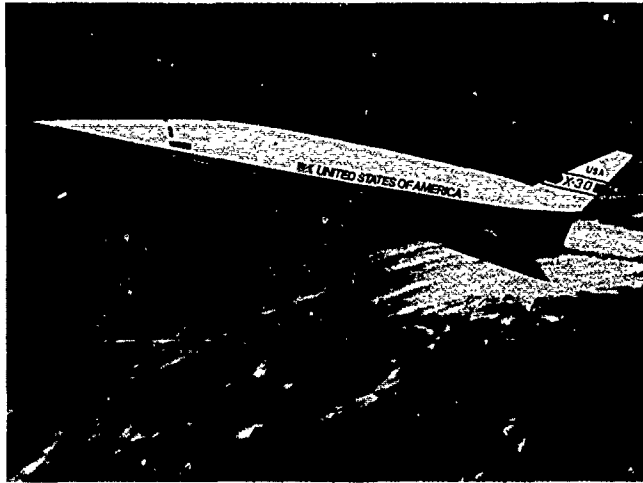


Figure 1.- The NASP X-30 flight research vehicle.

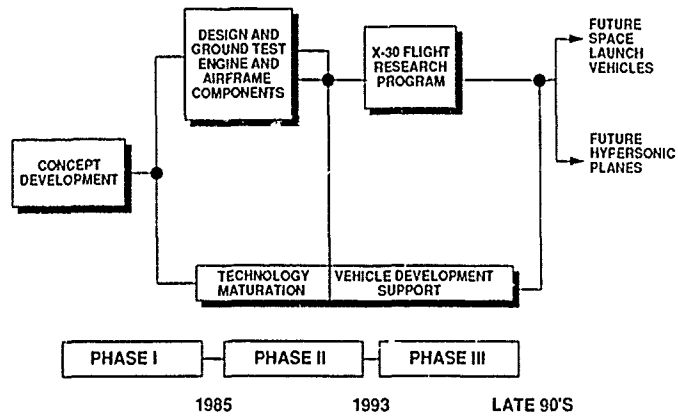


Figure 2.- The NASP program phases.

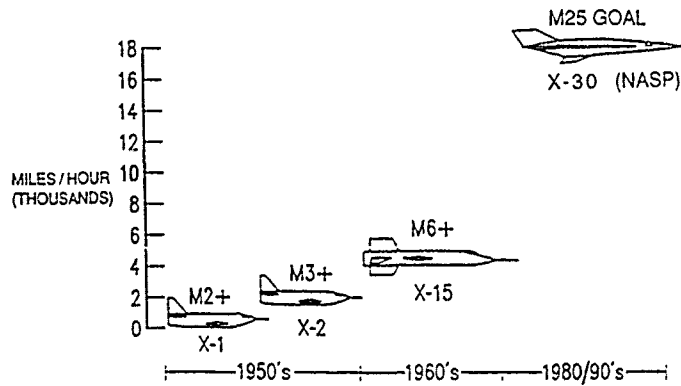


Figure 3.- Evolution of the X-Series research vehicles.

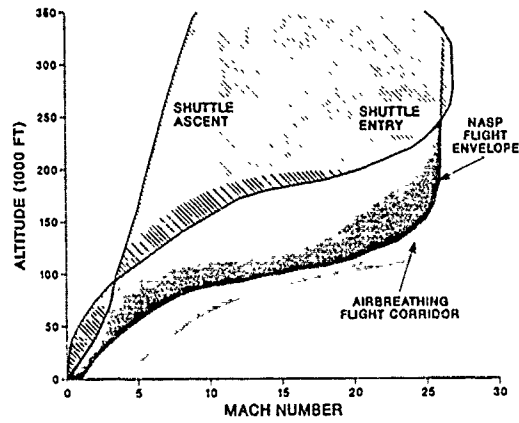


Figure 4.- Comparison of Shuttle and NASP trajectories.

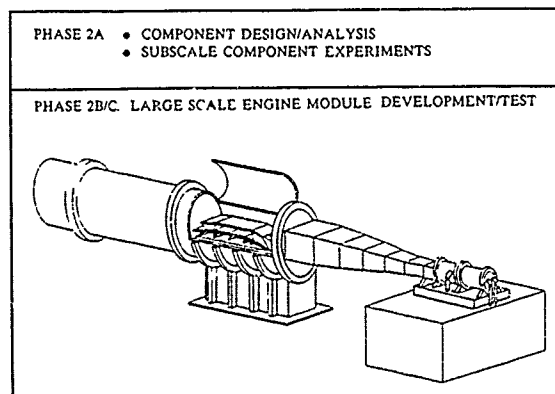


Figure 5.- NASP Phase 2 propulsion system module development.

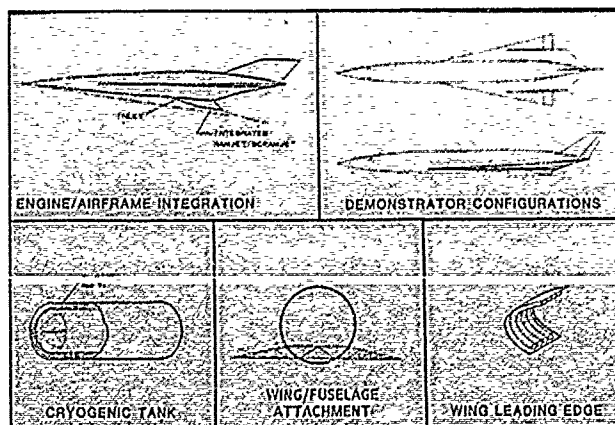


Figure 6.- NASP Phase 2 airframe/component development.

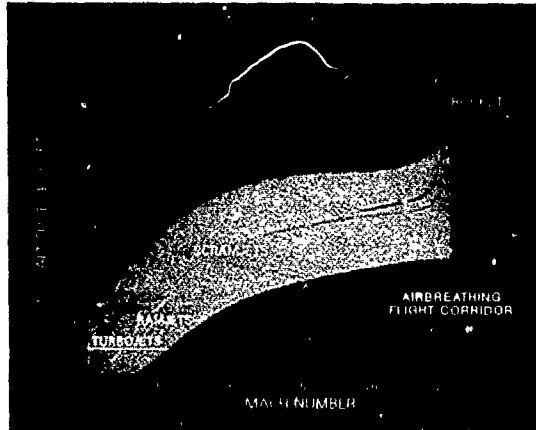


Figure 7.- Propulsion cycles in the airbreathing flight corridor.

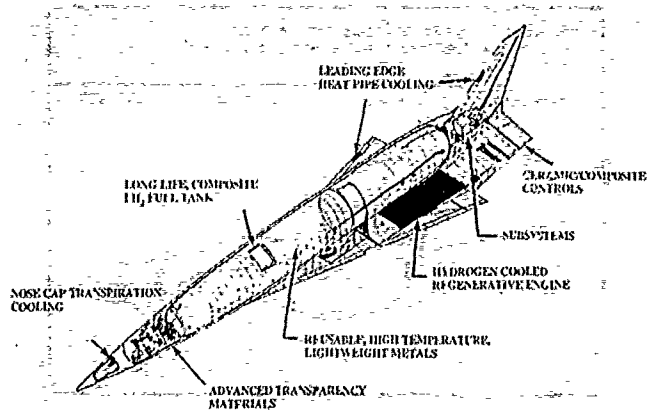


Figure 8.- Advanced materials and thermal control technologies.

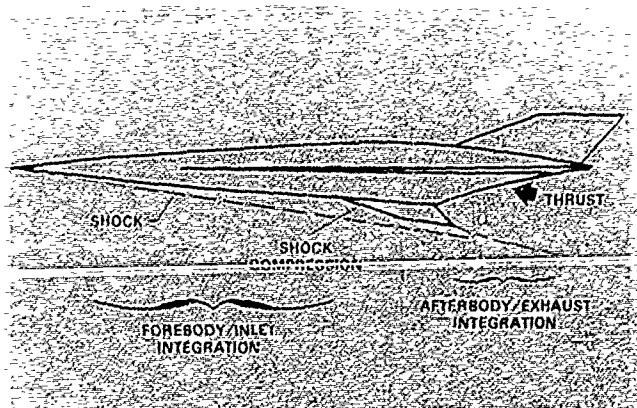


Figure 9.- Hypersonic vehicle engine-airframe integration.

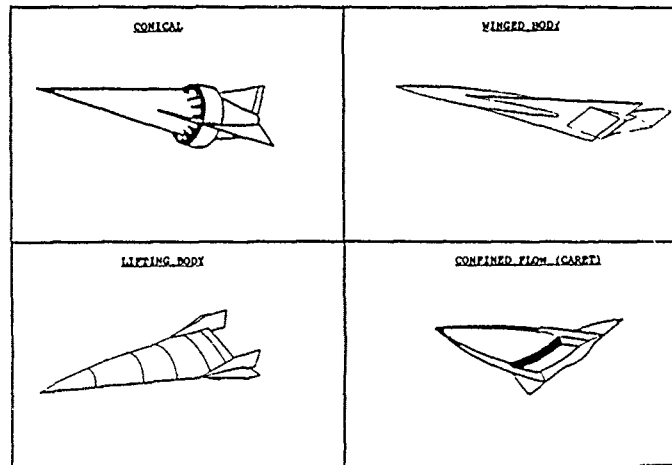


Figure 10.- Typical hypersonic vehicle configurations .

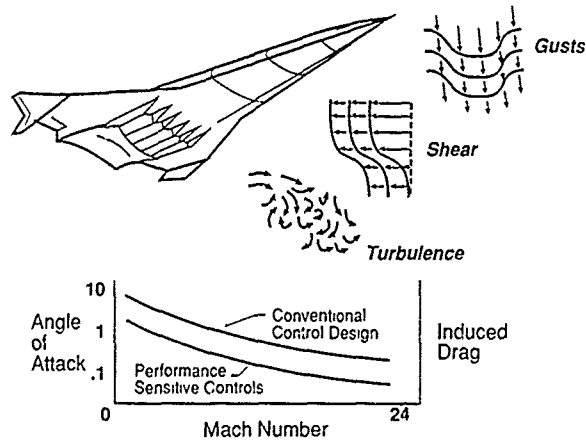


Figure 11.- Atmospheric effects on control system performance.

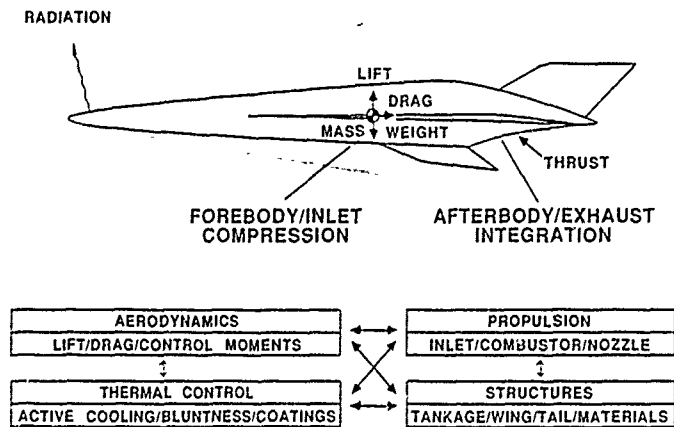


Figure 12.- Integrated control system .

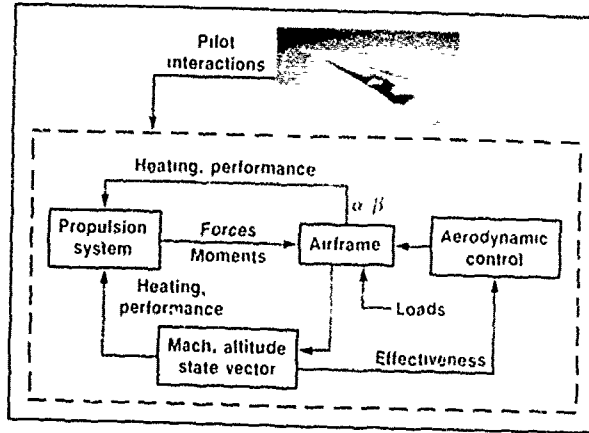


Figure 13.- Flight management system.



Figure 14.- Conceptual cockpit design.

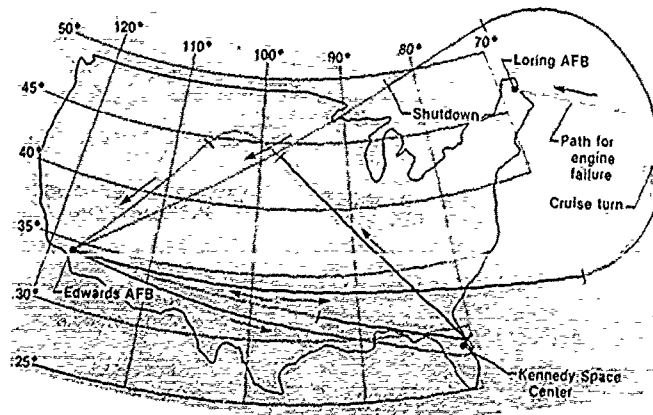


Figure 15.- Flight research envelope expansion.

OPTIMAL TRAJECTORIES FOR SÄNGER-TYPE VEHICLES

by

G.Sachs, R.Bayer and J.Drexler*
 Technische Universität München
 Arcisstraße 21, 8000 München
 Federal Republic of Germany

Abstract

The ascent performance of winged space transportation systems is considered. The system investigated consists of two stages the first stage of which is equipped with an airbreathing propulsion system. For the second stage, two rocket-powered vehicles are considered of which one is equipped with wings and the other is a fuselage type body.

It is shown which are key factors in regard to the ascent performance of the upper stage. This particularly concerns the performance enhancement due to its lifting capability. It is shown that an upper stage without wings also shows an ascent capability for small flight path angles at separation.

Furthermore, the separation flight maneuver is considered. It is shown that constraints (dynamic pressure and load factor limits) have a significant effect on the ascent performance achievable in regard to a most favorable separation condition for the upper stage. The effects of thrust increase due to a fuel-air ratio more than stoichiometric are considered. It is shown which improvements can be achieved for the separation flight condition.

Two optimization methods have been used. One is an indirect technique applying the minimum principle and the method of multiple shooting. The other represents a direct technique where the control vector function is parameterized.

1. Nomenclature

C_D	= drag coefficient	T	= thrust
C_L	= lift coefficient	t	= time
D	= drag	u	= control vector
g	= acceleration due to gravity	V	= speed (relative to rotating earth)
H	= Hamiltonian	x	= state vector
h	= altitude	α	= angle of attack
I_{sp}	= specific impulse	γ	= flight path angle
J	= performance criterion	δ	= throttle setting
K	= lift dependent drag factor	c_T	= thrust vector angle
L	= lift	λ	= lagrange multipliers
M	= Mach number	ρ	= atmospheric density
m	= mass	σ	= specific fuel consumption
q	= dynamic pressure, $q = (\rho/2)V^2$	φ	= bank angle
\dot{m}_{max}	= maximal fuel flow rate	ϕ	= latitude
r	= distance to earth center of gravity	ψ	= heading
r_e	= radius of earth	ω	= earth rotational rate
S	= reference area		

2. Introduction

The Sänger concept represents a new type of space transportation system proposed by MBB (Messerschmitt-Bölkow Blohm), Refs 1, 2. It has its origins in a concept of the rocket pioneer Eugen Sänger, Ref. 3. The Sänger system (Fig. 1) basically consists of two stages, the first of which is equipped with wings and airbreathing engines and is capable of performing a cruising flight. Two types of rocket-powered vehicles are considered for the upper stage. One is a vehicle equipped with wings and the other a fuselage-type body without wings.

The ascent of the Sänger transportation system is initially an airbreathing phase including a horizontal take-off and a cruise flight to a suitable latitude position where the separation of both stages takes place. After

* Prof. Dr.-Ing. Gottfried Sachs, Director of the Institute of Flight Mechanics and Flight Control.
 Dipl.-Ing. Robert Bayer, Research Assistant.
 Dipl.-Ing. Johannes Drexler, Research Assistant.

separation, the second stage performs an ascent to an orbit at about 450 km, while the first stage returns to its base.

This paper deals with the ascent optimization of two-stage vehicles similar to the Sanger system. The results presented are an outcome of a cooperation with MBB on the Sanger system. The investigation on trajectory optimization for new space transportation systems is part of a study sponsored by the Deutsche Bundesministerium fur Forschung und Technologie (German Ministry for Research and Technology).

In regard to ascent trajectory optimization, space vehicles with airbreathing engines and lifting capability have received greater interest not until recently (Refs. 4-18). Taking a Sanger type configuration as a reference, it is the purpose of this paper to show which are key factors for the ascent performance of winged two-stage vehicles with an airbreathing propulsion system. Particular emphasis is given to the optimization of the combination of the separation maneuver and of the ascent of the upper stage. This concerns the limited performance capabilities of airbreathing first stages as regards their capability of achieving significant flight path angles for optimal separating the upper stage at a hypersonic flight condition. Other topics addressed are related to the performance enhancement due to the lifting capability of the upper stage and the effects resulting from constraints such as maximum and minimum values admissible for load factor and dynamic pressure. In addition, the effect of thrust increase due to a fuel-air ratio more than stoichiometric is considered. It is shown which improvements can be achieved for the separation flight maneuver.

3. Modeling Considerations

The modeling of the vehicle is based on the equations of motion with reference to a spherical rotating earth (see also Fig. 2). They may be expressed as (Ref. 19)

$$\begin{aligned} \frac{dV}{dt} &= \frac{1}{m} [T \cos(\alpha + \epsilon_T) - D] - g \sin \gamma + \omega^2 r \cos \phi (\sin \gamma \cos \phi - \cos \gamma \sin \phi \sin \psi) \\ \frac{d\gamma}{dt} &= \frac{1}{mV} [T \sin(\alpha + \epsilon_T) + L] \cos \phi - \frac{g}{V} \cos \gamma + \frac{V}{r} \cos \gamma + 2\omega \cos \phi \cos \psi \\ &\quad + \frac{\omega^2 r}{V} \cos \phi (\cos \gamma \cos \phi + \sin \gamma \sin \phi \sin \psi) \\ \frac{d\psi}{dt} &= \frac{1}{mV} [T \sin(\alpha + \epsilon_T) + L] \frac{\sin \phi}{\cos \gamma} - \frac{V}{r} \cos \gamma \cos \psi \tan \phi \\ &\quad + 2\omega (\tan \gamma \cos \phi \sin \psi - \sin \phi) - \frac{\omega^2 r}{V \cos \gamma} \sin \phi \cos \phi \cos \psi \\ \frac{d\phi}{dt} &= \frac{V \cos \gamma \sin \psi}{r} \\ \frac{dh}{dt} &= V \sin \gamma \\ \frac{dm}{dt} &= - \frac{dm_{fuel}}{dt} \end{aligned} \tag{1}$$

where

$$g = g_0 \left(\frac{r_e}{r_e + h} \right)^2$$

The equations of motion are applied to the combined system consisting of both stages and separately to the second stage alone for its ascent. Accordingly, the symbols m , T , L etc. denote quantities valid for each case considered.

In regard to powerplant and aerodynamic characteristics, a realistic modeling is applied. For the combined system with its air breathing propulsion system (turbo-, ramjet combination), the thrust, lift and drag models

are

$$\begin{aligned} T &= \delta T_{max}(M, h, \alpha) \\ L &= C_L(\varrho/2)V^2S \\ D &= C_D(\varrho/2)V^2S \\ dm_{fuel}/dt &= \sigma(M, h)T \end{aligned} \quad (2)$$

where

$$\begin{aligned} C_L &= C_L(\alpha, M) \\ C_D &= C_{D_0}(M) + K(M)C_L^2 \end{aligned} \quad (3)$$

The thrust, lift and drag models of the rocket powered upper stages are (for simplicity, no subscripts are used for denoting the upper stages)

$$\begin{aligned} T &= \delta T_{max}(h) \\ L &= C_L(\varrho/2)V^2S \\ D &= C_D(\varrho/2)V^2S \\ dm_{fuel}/dt &= T/(g_0 I_{sp}) \end{aligned} \quad (4)$$

where

$$\begin{aligned} T_{max} &= \dot{m}_{max} g_0 I_{sp}(h) \\ C_L &= C_L(\alpha, M) \\ C_D &= C_{D_0}(M) + K(M)C_L^2 \end{aligned} \quad (5)$$

In general, the control variables are the lift coefficient C_L , throttle setting δ , thrust vector angle ϵ_T and bank angle φ which are subject to the following inequality constraints

$$\begin{aligned} C_{L_{min}} &\leq C_L \leq C_{L_{max}} \\ 0 &\leq \delta \leq 1 \\ \epsilon_{T_{min}} &\leq \epsilon_T \leq \epsilon_{T_{max}} \\ \varphi_{min} &\leq \varphi \leq \varphi_{max} \end{aligned} \quad (6)$$

The initial states of the lower stage for the separation flight maneuver are considered to be prescribed by a reference flight condition given by the end of the cruise flight

$$\begin{aligned} V(0) &= V_c & \gamma(0) &= 0 \\ h(0) &= h_c & m(0) &= m_c \end{aligned} \quad (7)$$

The separation conditions of the first stage flight are given by altitude and velocity

$$V(t_{sep}) = V_0 \quad h(t_{sep}) = h_0 \quad (8)$$

which represent initial conditions for the upper stage. Additional initial conditions for the upper stage are

$$\begin{aligned} \gamma(t_{sep}) &= \gamma_0 & m(t_{sep}) &= m_0 \\ \psi(t_{sep}) &= \psi_0 & \phi(t_{sep}) &= \phi_0 \end{aligned} \quad (9)$$

The final state of the upper stages is determined by the orbit that has to be approached. Thus

$$\gamma(t_f) = 0 \quad h(t_f) = h_f \quad (10)$$

The relations for $V(t_f)$ and $\psi(t_f)$ must account for orbit inclination and absolute speed. The final time t_f is considered to be free.

4. Optimization

4.1 Upper Stage

The optimization problem consists of determining ascent trajectories where the final mass of the upper stage in orbit is maximum, or its fuel consumed is minimum. This can be formulated by introducing the following performance criterion

$$J = m_{fuel}(t_f) \quad (11)$$

where $m_{fuel}(t_f)$ is the fuel consumed and t_f is the final time after approaching the orbit.

The optimization problem can now be stated as to find the control histories C_L, δ, ϵ_T and φ and the final time t_f which minimize the performance criterion $J = m_{fuel}(t_f)$ subject to the dynamic system described by Eq. (1), the boundary conditions given by Eq. (9) and (10) and the inequality constraints of Eq. (6).

Necessary conditions for optimality were used by applying the minimum principle. This is described in the following.

With the use of the vectors

$$\begin{aligned} x &= (V, \gamma, \psi, \phi, h, m)^T \\ u &= (C_L, \delta, \epsilon_T, \varphi)^T \end{aligned}$$

the dynamic system (Eq. (1)) may be expressed as

$$\dot{x} = f(x, u). \quad (12)$$

The Hamiltonian may be written as

$$H(x, \lambda, u) = \lambda^T f(x, u) \quad (13)$$

where the Lagrange multipliers

$$\lambda = (\lambda_V, \lambda_\gamma, \lambda_\psi, \lambda_\phi, \lambda_h, \lambda_m)^T$$

have been adjoined to the system Eq. (12). The Lagrange multipliers are determined by

$$\dot{\lambda} = -\frac{\partial H}{\partial x} \quad (14)$$

The controls are such that H is minimized. For this reason, they are determined by

$$\frac{\partial H}{\partial u} = 0 \quad (15)$$

or by the constraining bounds of Eq. (6).

The system described by Eq. (12) is autonomous so that H is constant. Since furthermore the final time t_f for approaching the orbit is considered free, the Hamiltonian is given by

$$H = 0 \quad (16)$$

With the use of the above relations, the optimization problem can be formulated as a two point boundary problem for integrating the state and costate equations, Eqs. (12) and (14). This problem was solved with the program BOUNDSCO (Ref. 20, 21).

4.2 First Stage

The cruise flight of the first stage and the separation flight maneuver for releasing the upper stage was investigated by applying a parameterization technique. The problem considered was to minimize fuel consumption for a flight to a prescribed separation flight condition. Particular emphasis was given to constraints of dynamic pressure and load factor, both for maximum and minimum values admissible. In the numerical investigation, the program TOMP (Ref. 22) was used.

5. Results

A typical optimal flight profile of a winged two-stage vehicle like the Sänger system is shown in Fig. 3. It may be decomposed into the following significant parts.

- cruise
- separation flight maneuver
- ascent of upper stage and return of first stage

The cruise type part of the flight profile corresponds to classical flight optimization. Accordingly, their characteristics which significantly depend on individual applications (short or long cruise distances) follow well-known lines, like a cruise-climb technique for example. Therefore, the present paper is mainly concerned with flight profile elements of a more recent type posing new problems in aircraft trajectory optimization. This particularly concerns the separation flight maneuver at a hypersonic Mach number and the ascent performance of an upper stage, including the performance enhancement due to its lifting capability.

The first part of this chapter deals with optimization of the ascent of the upper stage. Thus, it can be shown which are key factors for the ascent of an upper stage which has to start at a small flight path angle γ_0 and for which a lifting capability may be essential. This part of the investigation gives an indication of the performance requirements which the upper stage poses on the first stage with its airbreathing engines. Two types of upper stages are considered. One is equipped with wings. It is similar to the Horus vehicle of the Sänger system. The other which has no wings is similar to the Sänger upper stage called Cargus.

A Horus type upper stage the aerodynamic characteristics of which are illustrated in Fig. 4 is considered first. As an example, an optimal ascent beginning at a small flight path angle γ_0 at the separation point is presented in Figs. 5 and 6. They show a typical characteristic for trajectories starting with a small γ_0 since there is a significant utilization of the lifting capability which enables the vehicle to achieve an orbit even if it starts at a horizontal flight condition.

An evaluation of the effect of γ_0 on maximized final mass in orbit is shown in Fig. 7 for different thrust levels. As a main result, the final mass in orbit is significant even for small γ_0 values. This result is due to the lifting capability of the vehicle. It can be made evident by a comparison with a configuration without a lifting capability, as also shown in Fig. 7. A non-lifting configuration cannot perform an ascent below a γ_0 value quite large.

A factor which is of interest concerning the conditions for the begin of an ascent is the orbit inclination that has to be approached. Fig. 8 shows how the maximum final mass in orbit is affected for the range of γ_0 of practical interest ($0 \leq \gamma_0 \leq \gamma_{0opt}$). For the ascent trajectories computed, the latitude at the begin is considered to be equal to the inclination. The optimum heading at the separation point is practically zero (east) in all cases investigated.

Considering now a Cargus type upper stage, the following conclusion can be drawn from the results presented. An ascent would not be possible for such a configuration having no wings if it cannot produce a lifting force. This holds for γ_0 values of practical interest, i.e., for γ_0 values which can be achieved by an airbreathing first stage at a hypersonic flight condition. However, vehicles such as Cargus can have a lifting capability despite it is lacking a wing. This is due to the fact that fuselage type bodies can produce a lifting force not insignificant at hypersonic Mach numbers. An illustration is presented in Fig. 9 which shows aerodynamic characteristics of a vehicle similar to Cargus. This lifting capability can be utilized for a significant ascent performance enhancement.

In Figs. 10 and 11, an optimal ascent trajectory for a wingless upper stage similar to Cargus is shown. It may be seen, that an ascent is possible even for a horizontal flight condition at the separation point. As regards the controls and state variables history, basic similarities exist with the Horus type vehicle considered earlier.

An evaluation of the effect of γ_0 on the maximized final mass in orbit is shown in Fig. 12. Here again, similarities exist in regard to the results considered earlier. This concerns the significant amount of final mass in orbit even for small γ_0 values as well as the existence of an optimal γ_0 value and its magnitude (yielding the greatest amount of final mass in orbit). In addition, it may be seen that a non-lifting configuration would have an ascent capability for large γ_0 values only.

The results presented up to now describe the ascent capability as regards a flight condition at the separation point for a given altitude/Mach number combination. A further evaluation is presented in Fig. 13 which shows the effect of the separation flight condition on the maximized final mass in orbit, both for $\gamma_0 = 0$ and γ_{0opt} (where $\gamma_{0opt} = f(M_0, h_0)$). This Fig. makes evident the effect of altitude and Mach number. It may be of

interest to note that the variation of separation altitude has only a little effect, whereas the effect of separation velocity is of comparable significance as the effect of the initial flight path angle.

The second part of this chapter is concerned with the separation flight maneuver. In Figs. 14 and 15, an optimal maneuver for achieving maximum flight path angle at a prescribed Mach number/altitude condition is shown. According to the results presented, the separation flight maneuver may be decomposed into the following elements:

- transfer from cruise flight condition to flight at maximum dynamic pressure limit
- acceleration at maximum dynamic pressure limit
- pull up for reaching the flight condition at the separation point
- push down of first stage (for avoiding flight at dynamic pressure too low)

An evaluation of optimized separation flight maneuvers as described is presented in Fig. 16 which shows the maximum flight path angle achievable at the separation point as a function of speed and altitude (region indicated by A is excluded because of exceeding a prescribed upper fuel consumption limit of 25 tons). The results shown may be considered as the performance capability which the first stage with its airbreathing propulsion system can provide for the ascent of the upper stage.

A further evaluation concerning the performance capability at the separation point is shown in Fig. 17. In this Fig., the influence of constraints (n_{min}, q_{min}) effective in the flight phase after the separation point is considered. These constraints have a significant effect on the achievable amount of the flight path angle. It may be of interest to note that both the maximum flight path angle and the corresponding altitude at the separation point show comparatively small changes only. This is also an effect of the constraints n_{min} and q_{min} which become active after the separation point.

When combining the separation maneuver performance of the first stage (Fig. 17) and the ascent performance of the upper stage (Fig. 13), the maximum of the final mass which can be brought to orbit can be determined. This combination may be considered as the overall ascent performance capability of the whole system. The final mass in orbit is shown in Fig. 18. The results presented suggest a tendency towards a high speed at the separation point while an optimum value exists for altitude.

An evaluation concerning the fuel consumption of the first stage for the separation flight maneuver is presented in Fig. 19. From this Fig. it follows that the fuel consumption shows a pronounced increase above a certain speed level. The effect of altitude is comparatively small in the lower part of the speed range considered.

An improvement of the separation flight maneuver performance can be achieved by utilizing a fuel-air ratio more than stoichiometric for ramjet thrust increase. In Fig. 20, it is shown that thrust can be significantly increased by this technique. However, this is accompanied by a decrease of the specific impulse, Fig. 21.

The effect of the higher thrust capability resulting from a fuel-air ratio more than stoichiometric on the separation flight maneuver is shown in Fig. 22. Typically, this technique for thrust increase is utilized in the final part of the acceleration phase and for the pull-up maneuver. It may be of interest to note that the time at which a fuel-air ratio more than stoichiometric is applied is part of the optimization procedure.

An evaluation is presented in Fig. 23 which shows the speed and flight path angle achievable at the separation point. This Fig. makes evident that the optimal utilization of overfueled combustion provides a significant improvement which may be used in two ways. Either the maximum speed at the separation point can be increased when considering a prescribed amount of fuel consumption or the fuel consumption necessary for a given combination of speed and flight path angle may be reduced. It may be of interest to note that a reduction in fuel consumption can be achieved despite the fact that specific fuel consumption is increased.

6. Conclusions

For a winged two-stage vehicle similar to the Sanger space transportation system, optimum ascent performance is considered. In the first part, basic characteristics of optimal ascent trajectories of the upper stage are described. It is shown that the lifting capability of the upper stage is essential for achieving an ascent beginning at a small flight path angle at separation. This is confirmed by comparison with a non lifting case where an ascent is possible only at separation flight path angles quite significant. Furthermore, it is shown what amount of final mass can be brought into orbit for various initial conditions representing the end of the separation flight maneuver.

In the second part, the separation flight maneuver is investigated. It is shown, how an optimized maneuver compares with a simpler type of separation maneuver. Dynamic pressure and load factor constraints are

identified as having a significant effect. Furthermore, it is shown what combination of velocity, altitude and flight path angle at the end of the separation flight maneuver can be reached. Thus, it is possible to determine the best initial conditions for the upper stage such that the final mass in orbit is maximized.

Furthermore, the effect of thrust increase due to a fuel-air ratio more than stoichiometric is considered. It is shown that the separation flight maneuver performance can be improved by applying this technique.

7. References

- [1] Högenau, E., 1987, Raumtransporter, Zeitschrift für Flugwissenschaften und Weltraumforschung, Vol. 11, No.6, pp. 309-316.
- [2] Koelle, D. E., Kuczera, H., 1988, Sänger Space Transportation System, Status Report, Paper IAF-89-217.
- [3] Sänger, E., 1961-69, Vorläufige Vorschläge zur Entwicklung eines europäischen Raumfluggleiters, 40 Folgen, Hausberichte der Junkers Flugzeug- und Motoren-Werke.
- [4] Regenber, S., Tolle, H., Vogeler, K., 1966, Schubstufung als günstigstes Schubprogramm für den Aufstieg auf niedrige Kreisbahnen, WGLR-Jahrbuch 1966, pp. 232-239.
- [5] Shau, G.-C., 1973, Der Einfluß flugmechanischer Parameter auf die Aufstiegsbahn von horizontal startenden Raumtransportern bei gleichzeitiger Bahn-/Stufungsoptimierung, DLR-FB 73-86, Oberpfaffenhofen.
- [6] Dickmanns, E.D., Shau, G.-C., 1974, Optimale Stufung und Aufstiegsbahn für horizontalstartende zweistufige Raumtransporter, Zeitschrift für Flugwissenschaften und Weltraumforschung, Vol. 22, No.12, pp. 427-436.
- [7] Schöttle, U.M., 1982, Antriebs- und Flugoptimierung eines geflügelten Raumtransporters mit Raketen- und Staustrahlantrieb, DGLR-Jahrbuch 1982 III, pp. 76-1 - 76-28.
- [8] Schöttle, U.M., 1985, Steigerung der Transportleistungen luftatmender Raumtransporter durch optimale Steuerung des Staustrahl-Mischungsverhältnisses, DGLR-Jahrbuch 1985 I, pp. 102-1 - 102-22.
- [9] Schöttle, U.M., 1985, Performance Analysis of Rocket-Ramjet Propelled SSTO-Vehicles, XXXVIth International Astronautical Congress.
- [10] Tanatsugu, N., Lo, R.E., Manski, D., Schöttle, U.M., 1985, The Study on Two-Stage Launcher with Air-Breathing Propulsion, Joint AAS/ JRS Symposium.
- [11] Noton, M., Swinerd, G.G., 1987, Optimization of the Rocket-Powered Ascent of Hotol, IAF-87-329.
- [12] Nguyen, H.N., 1987, Trajectory Characteristics of Horizontal Takeoff Single Stage to Orbit Vehicle, AIAA-Paper 87-0448
- [13] Lantz, E., 1982, An Efficient System for Transportation to and from Earth Orbit, Acta Astronautica, Vol. 9, No.11, pp. 671-676.
- [14] Cunningham, M.J., Freemann, D.C., Jr., Wilhite, A. W., Powell, R.W., 1986, Thrust Vectoring for Single-Stage-to-Orbit, Horizontal Takeoff, Horizontal Landing, Space Vehicles, AIAA-Paper 86-1414.
- [15] Escher, W.J.D., Doughty, D.L., 1986, A Combined Cycle (Airbreathing/Rocket) Powered VTOVL Single Stage Orbital Transport, AIAA-Paper 86-1388.
- [16] Sachs, G., Drexler, J.: Optimal Ascent of a Horus/Sänger Type Vehicle, AIAA/AAS Astrodynamics Conference Proceedings, pp. 627-635, 1988.
- [17] Sachs, G., Wagner, O., Drexler, J.: Optimal Aufstiegsbahnen der Sänger-Oberstufe, DGLR-Jahrbuch, pp. 120-129, 1988.
- [18] Sachs, G., Bayer, R., Drexler, J.: Optimum Ascent Performance of Winged Two-Stage Vehicles, ESA SP-293, pp. 271-278, 1989.
- [19] Vinh, N. X., Buseman, A., Culp, R. D. 1981, Optimal Trajectories in Atmospheric Flight, Amsterdam-Oxford-New York, Elsevier Scientific Publishing Company, Chapter 2.
- [20] Bulirsch, R., 1971, Die Mehrzielmethode zur numerischen Lösung von nichtlinearen Randwertproblemen und Aufgaben der optimalen Steuerung, Bericht der Carl-Cranz-Gesellschaft, Oberpfaffenhofen.
- [21] Oberle, H.J., 1983, Numerische Berechnung optimaler Steuerungen von Heizung und Kühlung für ein realistisches Sonnenhausmodell, Institut für Mathematik der Technischen Universität München, TUM-M8310.
- [22] Kraft, D., 1980, FORTRAN-Programme zur numerischen Lösung optimaler Steuerungsprobleme. DFVLR-Mitteilung 80-03.
- [23] Data from MTU (Motoren- und Turbinen-Union GmbH), Munich, April 1989.

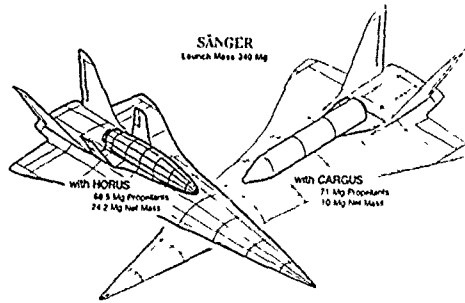


Fig. 1 SÄNGER space transportation system (from Ref. 2)

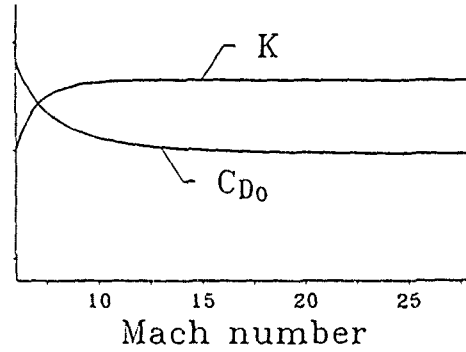


Fig. 4 Lift and drag characteristics of a winged upper stage similar to Horus

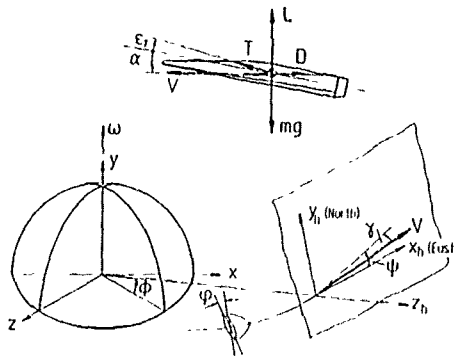


Fig. 2 Forces and coordinates

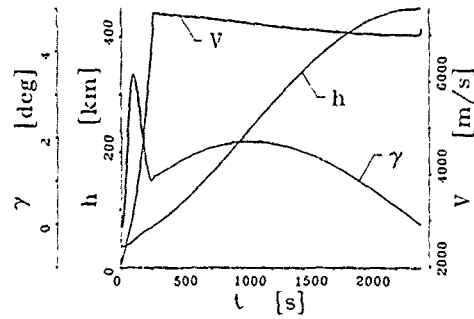


Fig. 5 Optimal ascent of a Horus type configuration ($\gamma_0 = 0^\circ, h_0 = 37 \text{ km}, V_0 = 2056 \text{ m/s}$), state variables

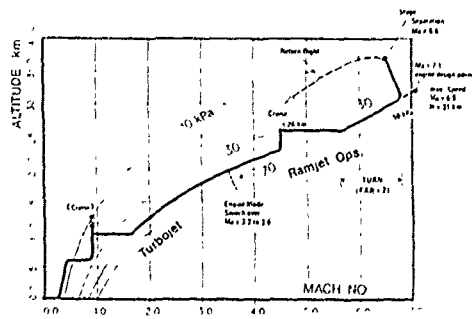


Fig. 3 Flight profile for cruise and ascent of the SÄNGER system (from Ref. 2)

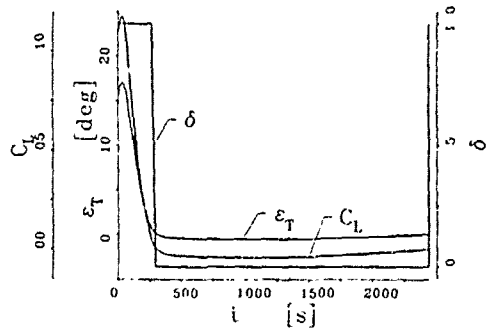


Fig. 6 Optimal ascent of a Horus type configuration ($\gamma_0 = 0^\circ, h_0 = 37 \text{ km}, V_0 = 2056 \text{ m/s}$), control variables

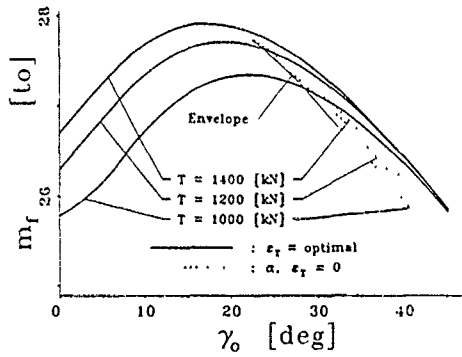


Fig 7 Maximized final mass in orbit for a Horus type configuration ($h_0 = 37 \text{ km}$, $V_0 = 2056 \text{ m/s}$)

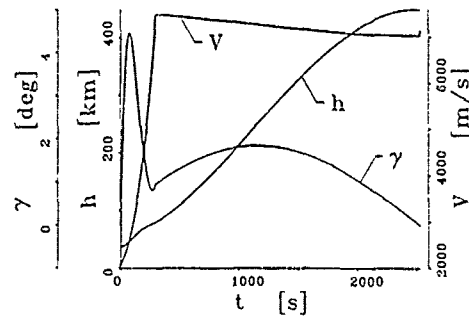


Fig 10 Optimal ascent of a Cargus type configuration ($\gamma_0 = 0^\circ$, $h_0 = 37 \text{ km}$, $V_0 = 2056 \text{ m/s}$), state variables

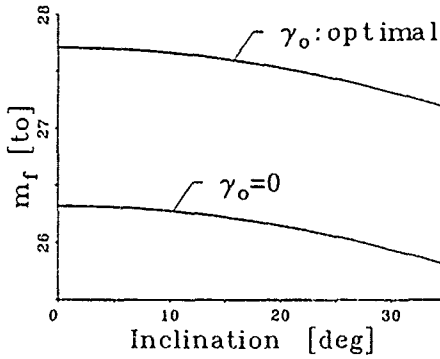


Fig 8 Effect of orbit inclination on maximized final mass in orbit for a Horus type configuration ($h_0 = 37 \text{ km}$, $V_0 = 2056 \text{ m/s}$, ϵ_T optimal)

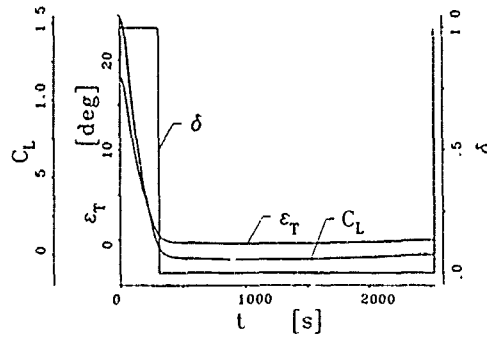


Fig 11 Optimal ascent of a Cargus type configuration ($\gamma_0 = 0^\circ$, $h_0 = 37 \text{ km}$, $V_0 = 2056 \text{ m/s}$, C_L based on cross section area), control variables

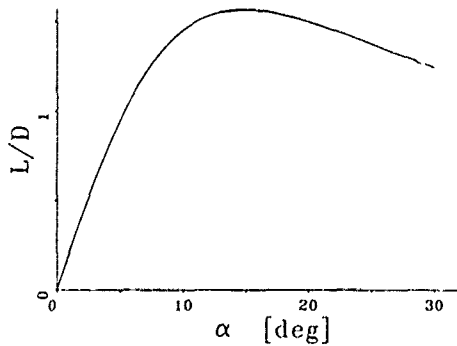


Fig 9 Lift/drag characteristics of a Cargus type configuration without wings

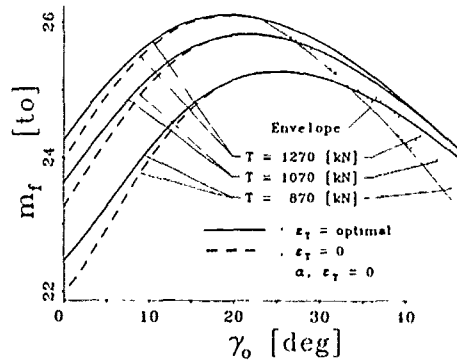


Fig 12 Maximized final mass in orbit for a Cargus type configuration ($h_0 = 37 \text{ km}$, $V_0 = 2056 \text{ m/s}$)

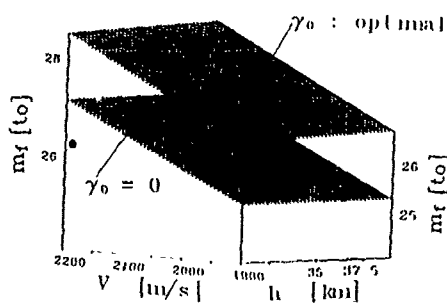


Fig. 13 Effect of separation conditions on final mass in orbit for $\gamma_0 = 0$ and γ_{0opt} for a Horus type configuration (e_T : optimal)

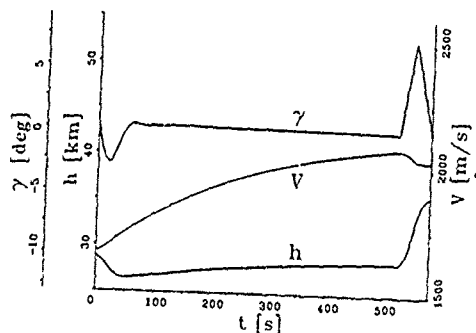


Fig. 14 Optimized separation flight maneuver with constraints ($n_{max} = 2$, $q_{max} = 50$ kPa), state variables

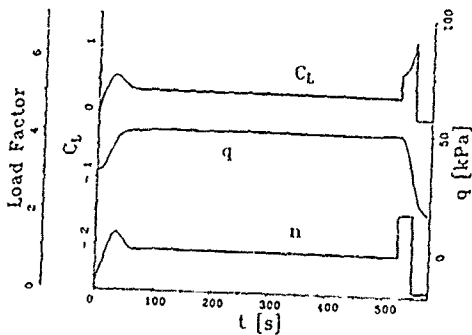


Fig. 15 Optimized separation flight maneuver with constraints ($n_{max} = 2$, $q_{max} = 50$ kPa), control variables and dynamic pressure

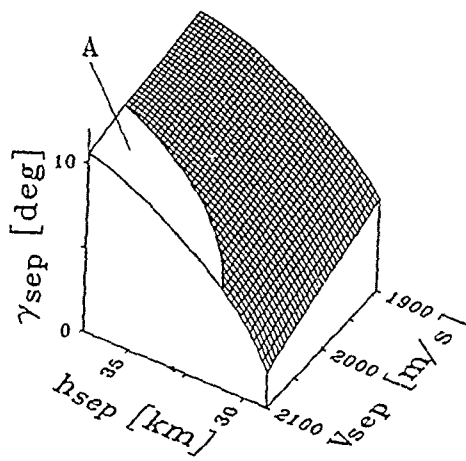


Fig. 16 Maximum separation flight path angle with constraints ($n_{max} = 2$, $q_{max} = 50$ kPa)

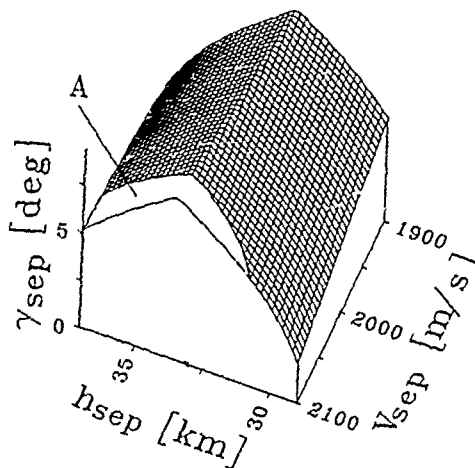


Fig. 17 Maximum separation flight path angle with constraints ($n_{max} = 2$, $q_{max} = 50$ kPa, $n_{min} = 0$, $q_{min} = 10$ kPa)

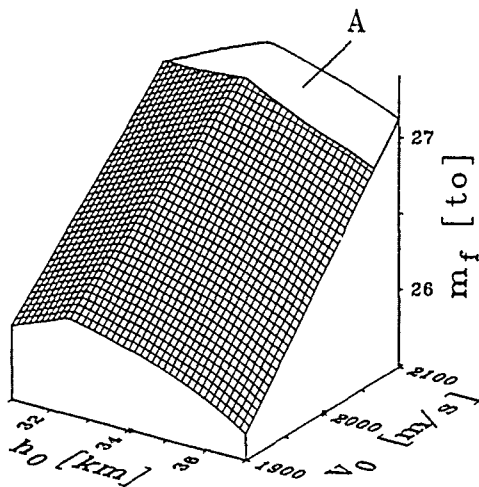


Fig. 18 Maximum final mass in orbit for constrained separation flight maneuver
 $(n_{max} = 2, q_{max} = 50 \text{ kPa}, n_{min} = 0, q_{min} = 10 \text{ kPa})$

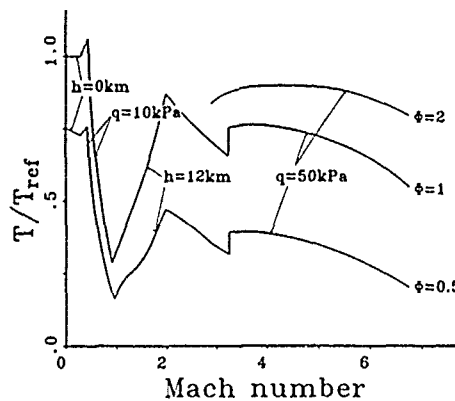


Fig. 20 Thrust characteristics for different fuel-air ratios (from Ref. 23)
 T_{ref} : reference value for $M = 0, h = 0, \phi = 1$ (stoichiometric combustion)

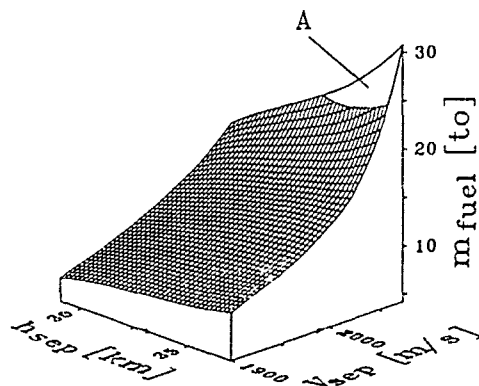


Fig. 19 Fuel consumption of lower stage for constrained separation flight maneuver
 $(n_{max} = 2, q_{max} = 50 \text{ kPa}, n_{min} = 0, q_{min} = 10 \text{ kPa})$

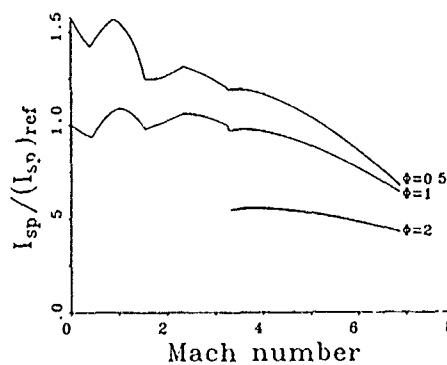


Fig. 21 Specific impulse characteristics for different fuel-air ratios (from Ref. 23)
 $(I_{sp})_{ref}$: reference value for $M = 0, h = 0, \phi = 1$ (stoichiometric combustion)

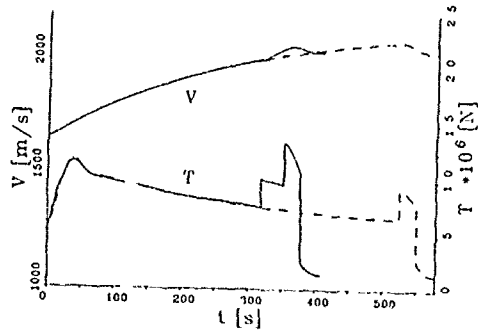


Fig. 22 Speed and thrust history for ramjet operation with fuel-air ratio more than stoichiometric (- - - - : $\phi = 1$)

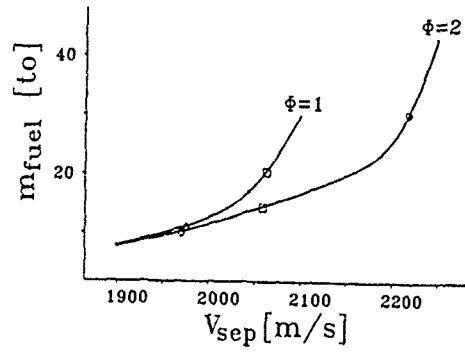


Fig. 23 Separation flight maneuver improvement due to ramjet operation with fuel-air ratio more than stoichiometric

Maximized final mass of Horus type upper stage:

- ◇ 26.5 to
- 27.0 to
- 28.0 to

ASCENT AND DESCENT OPTIMIZATIONS OF AN AIR-BREATHING LAUNCH VEHICLE

by

S. G. FURNISS
DEPUTY TECHNICAL MANAGER - HOTOL
BRITISH AEROSPACE (MILITARY AIRCRAFT) LTD,
WARTON AERODROME,
PRESTON, LANCs, PR4 1AX
ENGLAND

I. M. WALTERS
BRITISH AEROSPACE (SPACE SYSTEMS) LTD,
ARGYLE WAY,
STEVENAGE, HERTS, SG1 2AS
ENGLAND

SUMMARY

The design of an air-breathing winged launcher vehicle is a highly interactive process. The 'optimum' (minimum mass) vehicle is determined by a trade-off involving fuselage shape and its influence on drag and structural efficiency (mass/volume) together with the rocket and air-breathing propulsion mode of operation and system sizing. These effects must be coupled with the most efficient mission profile.

Contained in this paper are details of the ascent and descent optimization which must be conducted for a single-stage-to-orbit vehicle. Those parameters which have a significant influence on the selection of the air-breathing ascent, the rocket ascent, and the re-entry and autoland trajectories are described. The strong interactions between the various phases of flight, and their influence on the vehicle design and performance, are discussed. The launcher design mission is shown to have a significant impact on the ascent profile and the optimum configuration.

INTRODUCTION

Launch costs and reliability form a fundamental consideration for all space activity. Concepts for more dependable advanced launcher systems capable of greatly reducing launch costs have been studied for a number of years but, until recently, have not received great priority. The current upsurge in interest has been prompted by the realization that the launch capacity of the existing and currently planned launcher fleet will be inadequate to meet the predicted market beyond the late 1990s and, perhaps more importantly, high launch costs will stifle expansion of the market. The commercial exploitation of space is fundamentally dependent upon the ready availability of reliable, cost-effective and flexible launch systems.

These future launcher studies were given further impetus with the suspension of Space Shuttle flights after the 1986 *Challenger* disaster and the concurrent failures of three types of expendable launch vehicles.

To overcome the limitations of present launchers, the feasibility of a fully re-usable winged launcher powered by air-breathing propulsion for the initial ascent through the Earth's atmosphere is being studied in the United Kingdom, West Germany, France, USA, Japan and the USSR. Although the concepts are different in detail, they each share the common aim to operate like conventional aircraft. For a single-stage-to-orbit (SSTO) vehicle, the wing sizing is limited by the requirements of re-entry heating and cross-range performance, so it is entirely logical to use these wings to allow horizontal take-off with a much lower level of thrust and therefore engine weight than a vertical take-off vehicle. Horizontal take-off and landing, and aircraft-style ground handling and operation will allow these vehicles to be more flexible and less vulnerable to failures (particularly at take-off). The launch costs for these fully re-usable systems, operated with minimum support staff, will greatly reduce when compared to that of current launcher systems.

With new and anticipated technologies, the ultimate goal of an SSTO vehicle is now believed to be possible. The SSTO vehicle of course presents a greater design challenge but will have significant cost advantages over the two-stage-to-orbit (TSTO) vehicle.

With payload fractions of between 1.5% and 3.0% (depending on the mission) the performance of SSTO vehicles is extremely sensitive to the design assumptions. Consequently the design process is highly interactive. The 'optimum' (minimum mass) vehicle is determined by a trade-off involving fuselage shape and its influence on drag and structural efficiency (mass/volume) together with rocket and air-breathing propulsion mode of operation and system sizing. These effects must be coupled with the most efficient trajectory.

The performance of these vehicles can be greatly enhanced by a suitable choice of ascent and descent profiles. Although the performance of the TSTO vehicle can be significantly affected by the ascent and descent trajectories, it is the more sensitive SSTO vehicle where the impact on performance can be the most dramatic. Discussed in this paper is the SSTO ascent and descent trajectory optimization which must be conducted as part of the overall Total System Studies. Those parameters which have a significant impact on the choice of ascent and descent profile are described. The information presented here is based on four years' experience in the design evolution of HOTOL and a parallel study on winged launcher vehicles currently being conducted for the European Space Agency (ESA).

TOTAL SYSTEM MODEL

Before discussing the ascent and descent trajectories it is important to understand the process required to achieve the optimum Total System performance.

It is well known that the performance of an SSTO vehicle is extremely sensitive. It is because of this sensitivity that it is essential to have a detailed model of the Total System. The use of simple analytical representations is totally inadequate. The model must be capable of predicting the performance for a range of vehicle design schemes and configurations. The results must represent a consistent vehicle performance with, for example, a given engine performance, and vehicle drag, sufficient propellant capacity to complete the mission. At BAe (Military Aircraft)

Limited, Warton, design trade-off studies are performed using a Computer Aided Project Study Tool (CAPS). CAPS is a project study integrated design tool, developed progressively since the 1960s. A schematic of the use of the Total System Model is shown in Figure 1.

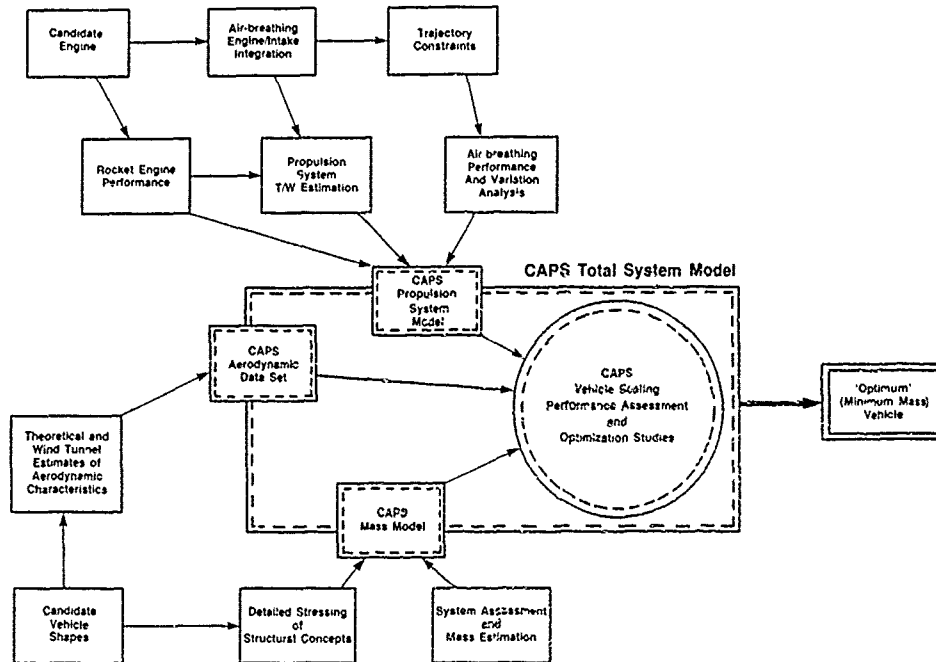


Fig.1 Schematic of Total System Model

The CAPS Total System Model is continually updated as the results from detailed engineering studies, reflecting new design concepts or requirements, become available. To assess the impact of the design changes on the performance, the vehicle must be re-optimized. The performance penalties for non-optimum design are very severe. At the early stages of vehicle design it is acceptable, and necessary, to re-optimize the vehicle. As the project progresses, a performance margin will be required to guarantee the completion of the mission. However, by completing a wide ranging Enabling Technology programme the uncertainties in design assumptions can be minimized, reducing the need for vehicle overdesign.

The ascent and descent trajectories, like the solution to any particular design problem, can not be considered in isolation. Considering the air-breathing ascent, the traditional methods of defining an optimum minimum fuel ascent, described by the locus of where specific excess power divided by fuel flow (SEP/Q_f - the product of thrust minus drag and velocity, divided by vehicle weight and fuel flow) is a maximum at each energy height (energy height is a measure of total energy = $h + V^2/2g$) are only applicable for a fixed vehicle and propulsion system. The optimum ascent trajectory can only be derived when its impact on propulsion system sizing and mass, vehicle control requirements (and hence actuation and power supply system mass), wing aerodynamics, wing design, and fuselage shape have all been addressed (Figure 2). It must combine minimum propulsion mass, optimum fuselage and wing shapes, with minimum ascent propellant.

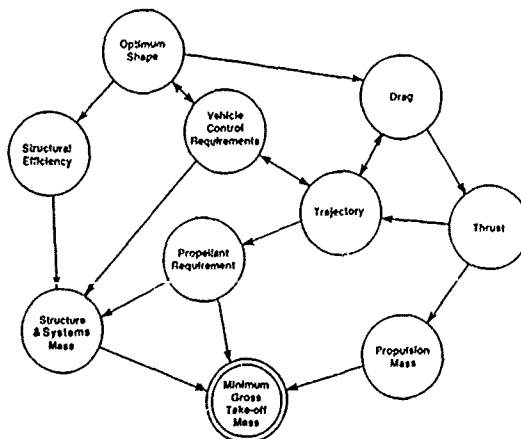


Fig.2 Configuration Optimum

ASCENT TRAJECTORY

The most efficient way to conduct these studies is to analyze the vehicle performance in two distinct, but coupled segments – the air-breathing ascent phase and the rocket ascent phase (Figure 3).

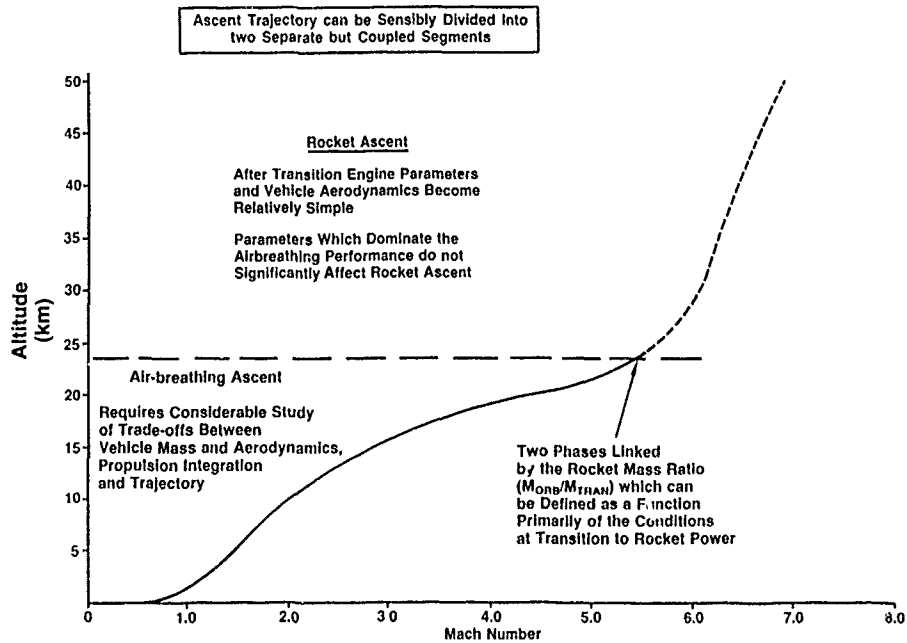


Fig.3 Ascent Trajectory

The parameters which dominate the air-breathing performance do not significantly affect the rocket ascent (except the conditions at the point of transition to rocket power). The difficult task of optimizing vehicle shape, propulsion integration and sizing, and the air-breathing ascent trajectory can be undertaken without computing the optimum rocket ascent each time, thus reducing computing time.

The air-breathing phase can be linked to the rocket ascent by the rocket mass ratio (mass on orbit divided by mass at transition – M_{ORB}/M_{TRAN}). The optimum rocket ascent is greatly influenced by the conditions at the point of transition to rocket power. The rocket mass ratios for various transition parameters – altitude, velocity, climb angle, rocket specific impulse, rocket thrust-to-weight, and vehicle hypersonic aerodynamic coefficient can be calculated as a set of analytical expressions using the rocket ascent optimization programme discussed later.

Air-breathing Ascent Trajectory

The optimization of the air-breathing ascent trajectory and the associated propulsion integration studies are particularly difficult because of the strong interactions. If conducted thoroughly, they can significantly enhance vehicle performance and greatly influence vehicle design.

The selection of the type of propulsion system to be used and the optimum air-breathing ascent profile will depend upon the vehicle design mission. If the aim is to provide cheap access into equatorial or near equatorial orbits, the vehicle will be launched from or near the equator. Such a vehicle is described as an 'accelerator'. Although it is obviously important to have both a high thrust-to-weight and specific impulse, for the accelerator vehicle which does not require a cruise phase the emphasis is to have a propulsion system with a high thrust-to-weight. If the vehicle is to be operated from a European launch site into equatorial or near equatorial orbits, then because of the possible need for a cruise capability a propulsion system with reasonable fuel economy is preferred. Because of the trade-off between accelerating and cruising phases of the ascent, and the requirement to manoeuvre the vehicle to a particular ground track to rendezvous with a specific orbit, the optimum ascent trajectory will be different from that of the 'accelerator' vehicle. It should be noted that the cost penalty for the privilege of a European launch is very large.

'Accelerator' Vehicle. The optimum ascent trajectory for an 'accelerator' vehicle can be divided into three main phases:

1. Accelerate from take-off to an airframe limited dynamic pressure and climb at this limit until the maximum engine operating design pressure is reached.
2. Climb at the maximum operating engine design pressure to the transition pull-up manoeuvre.

3. Conduct the pull-up manoeuvre prior to transition to rocket power for the final part of the ascent.

This is illustrated in Figure 4.

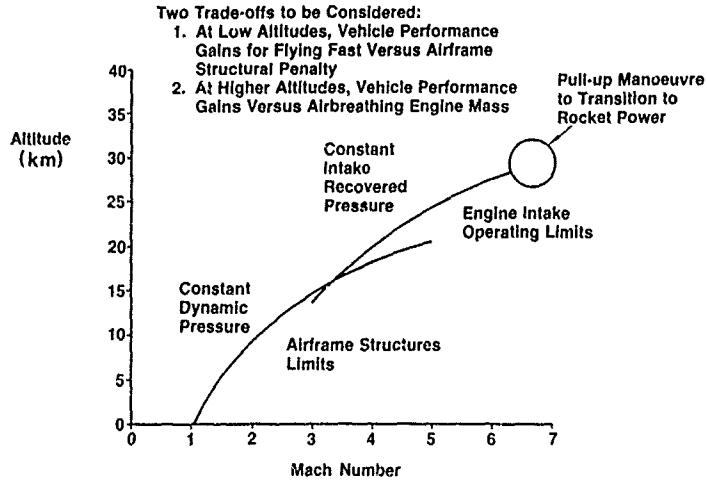


Fig.4 Air-breathing Ascent Trajectory

The initial part of the ascent represents a trade-off between engine performance and airframe structural considerations. Generally, air-breathing propulsion favours a 'fast and low' ascent profile. The higher specific excess power divided by fuel flow (SEP/Q_p) maximizes the ratio of energy gain to propellant usage and dominates the small structural penalty. This portion of the ascent would follow a constant equivalent air speed profile of between 600 and 700 knots equivalent air speed (KEAS).

The second phase of the ascent is limited by engine design considerations. The mass of the intake and air-breathing propulsion components is predominantly sensitive to the intake recovered pressure ($PT1$), which of course is dependent upon the ascent profile. A full air-breathing ascent trajectory optimization must involve the use of 'rubberized' models of the intake and propulsion units. The model must be capable of assessing varying engine/intake combinations stressed to different maximum operating design pressures.

The optimum maximum $PT1$ is derived from a trade-off between the increased propulsion efficiency at the high $PT1$ s, versus the increased mass of engine (and intake) these higher operating pressures will require. To illustrate this trade-off the results from a study of a vehicle powered by a rocket-ramjet propulsion system are presented in Figure 5.

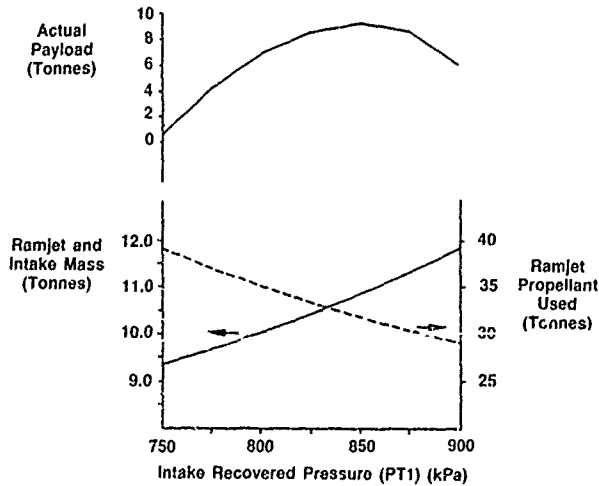


Fig.5 Trade-off Between Engine Mass and Propulsion Efficiency

If the high altitude ascent is made at a high PT1, then with the increased thrust, less fuel will be burnt in reaching the transition Mach number, or the air-breathing ascent could be extended to a higher transition Mach number. This must of course be paid for by a heavier ramjet engine.

For simplicity, in this example the engine size, the transition Mach number, the transition pull-up manoeuvre, and the initial ascent speed were not re-optimized for each of the maximum engine operating pressures. The thrust of the engine, as well as its mass, decreases with reducing engine maximum operating pressure. This will result in a lower optimum transition Mach number and possibly a pull-up manoeuvre which produces a less than optimum rocket ascent, and hence a poorer rocket mass ratio (M_{ORB}/M_{TRAN}). Obviously all these interactions need to be addressed when identifying the optimum ascent profile.

Engine Thrust Characteristics. The thrust of air-breathing propulsion systems shows a fairly rapid degradation at higher Mach numbers ($M > 3.5$) - Figure 6. This is because the exhaust velocity is limited by exhaust product dissociation, whereas ram drag continues to rise with velocity.

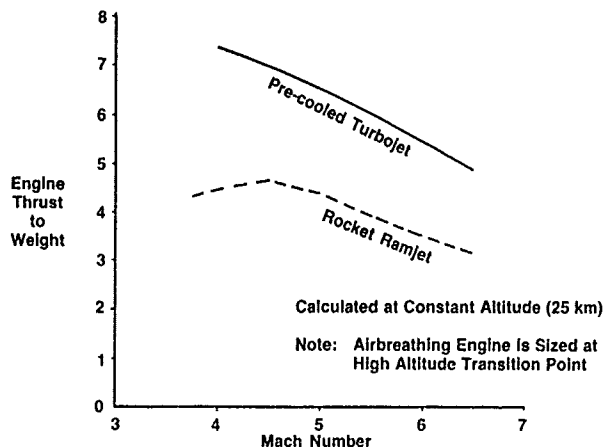


Fig.6 Engine Thrust Characteristics at High Mach Number

As the thrust minus drag at these high Mach numbers reduces, acceleration time increases and more and more hydrogen is consumed (Figure 7).

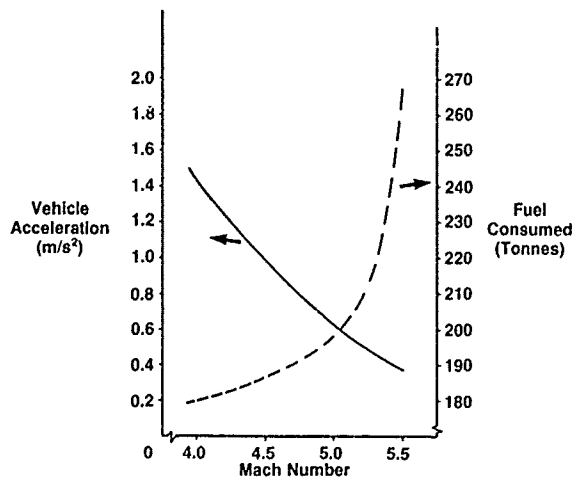


Fig.7 Vehicle Acceleration

The thrust margin will eventually become so poor that it is more efficient to switch to rocket power. The high Mach number performance could be improved and air-breathing operation extended to higher Mach numbers by installing a larger engine (or intake, depending on the type of propulsion system), but there comes a point where the additional mass of these items overrides the benefit of reduced fuel burn; identification of this point is part of the vehicle design optimization process.

Engine Overfueling. There are two critical areas in the ascent trajectory which can size the air-breathing engine. There must be sufficient thrust in the transonic regime, where drag is high, to allow reasonable acceleration and a low fuel burn. The transonic thrust margin is obviously strongly influenced by vehicle shape (drag). The second 'pinch' point is at the maximum operating Mach number. A thrust boost for these critical 'pinch' points can be obtained by overfueling the engine, but of course the engine specific fuel consumption will increase. The optimum engine size and the ascent trajectory, particularly the transition Mach number, could be significantly influenced by the effects of overfueling.

Rolls-Royce provided data for three levels of overfueling a ramjet engine. The vehicle was initially accelerated to effective ramjet operating speeds by a rocket system and so did not have transonic penetration difficulties. The influence of various levels of overfueling from the datum stoichiometric fuel air ratio (FAR) of 0.029, to a maximum FAR of 0.116, on the high Mach number portion of the ascent was assessed. The overfueling was progressively introduced during the ascent. The results from the studies, which are essentially a trade-off between extra fuel used against a possible reduction in ramjet engine scale and/or an increase in optimum transition Mach number, are shown in Figure 8.

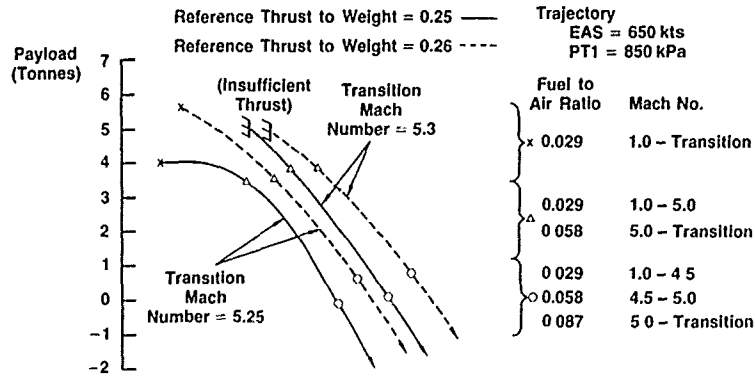


Fig.8 Payload Sensitivity to Ramjet Overfueling

The conclusion from this work is that overfueling does not improve the vehicle performance. However, although not considered here, there may be some benefit to be gained with very limited overfueling during the transition pull-up manoeuvre

Wing Design The air-breathing ascent trajectory can be significantly affected by the choice of wing design and sizing. The wing may be sized to give optimum ascent performance, but it must also provide satisfactory airfield performance, re-entry and cross-range performance, and adequate trim characteristics. Its size may be defined by the need to carry propellant in wing tanks. These various requirements are discussed in detail in Ref. 1.

If the wing size is selected to give optimum ascent performance, then the trade-off is between wing mass and aerodynamic and propulsion system performance. At high Mach numbers the induced drag makes up 50% of the total vehicle drag, thus a larger wing would significantly reduce the vehicle drag but at a mass penalty. In addition, if the vehicle with the larger wing was flown along the same ascent trajectory, then its incidence would reduce causing a loss of intake pre-compression and thus engine performance.

In a recent study, the wing size for optimum ascent performance was shown to be at a re-entry wing loading of 280 kg/m² (Figure 9)

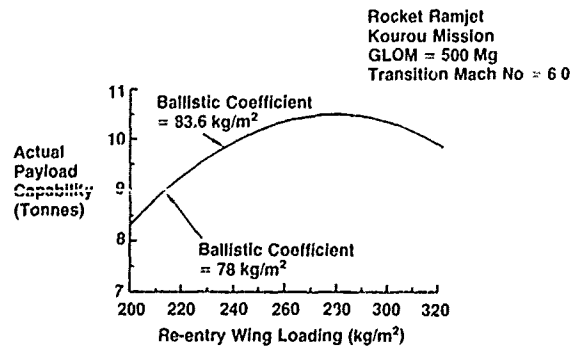


Fig.9 Wing Size Optimization

If it became necessary to increase the wing size to meet airfield or re-entry performance (heating, cross-range or pitch control) requirements, the optimum PT1 ascent and transition Mach number may change. In Figure 10, the optimum transition Mach numbers from air-breathing to rocket power for two wing loadings, one for optimum ascent performance (re-entry wing loading = 280 kg/m²), and one sized to meet particular re-entry heating and cross-range requirements (re-entry wing loading = 220 kg/m²), are illustrated.

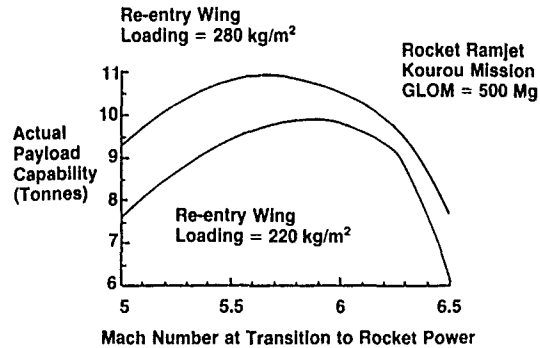


Fig.10 Optimum Transition Mach Number versus Wing Sizing

The optimum transition Mach number (in this study) for the wing sized for ascent performance was 5.7. If it became necessary to increase the wing size, thus reducing the induced drag component, then it would be beneficial to extend air-breathing operation to Mach 5.9. This re-optimization increased the payload for the vehicle with the larger wing by 500 kg. The fact that the optimum ascent trajectory can be significantly influenced by the re-entry requirements emphasizes the strong interaction of all the design assumptions for the SSTO vehicle.

Transition Pull-up Manoeuvre

The rocket performance is extremely sensitive to the vehicle climb angle at the point of transition (see later). For optimum rocket performance the initial climb angle should be approximately 20°. In reality, it is only possible while air-breathing to reach climb angles of between 7° and 8°. This is because as the vehicle performs the pull-up manoeuvre it climbs rapidly, losing thrust and decelerating (Figure 11)

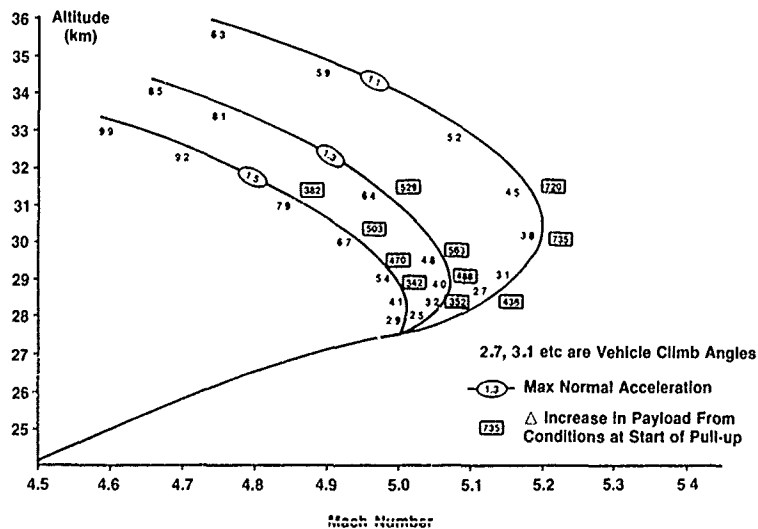


Fig.11 Pull-up Manoeuvre for Transition to Rocket Power

Shown in this figure is the variation in vehicle climb angle for constant normal acceleration pull-up manoeuvres. The predicted increase in payload is calculated assuming transition to rocket power at that particular instant. The optimum transition point is a trade-off between the change in rocket mass ratio, resulting from the changes in vehicle transition climb angle, velocity and altitude, and the additional air-breathing propellant required to perform the pull-up manoeuvre.

When optimizing the ascent trajectory it is essential to have a complete map of engine data (very large matrix) covering an appropriate range of altitude, Mach number and incidence (levels of intake pre-compression). The performance sensitivity of a ramjet engine to variations in vehicle incidence is shown in Figure 12.

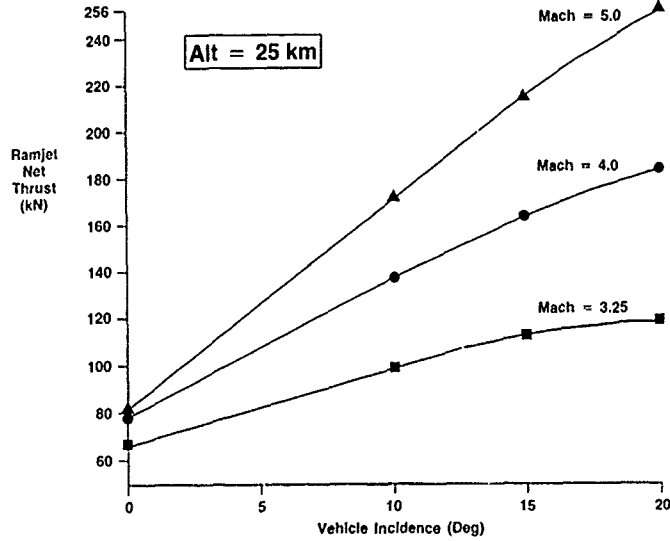


Fig.12 Ramjet Net Thrust Variation with Vehicle Incidence

The sensitivity to vehicle incidence, particularly at higher Mach numbers, can significantly affect the final part of the air-breathing ascent, particularly the pull-up manoeuvre (or high speed orbital track rendezvous manoeuvres, see European launch trajectory requirements discussed later). At $M = 3.25/25$ km an increase in pre-compression resulting from a 1° change in incidence gives a net thrust boost of 5%, whereas for the same increase at $M = 5.0/25$ km the thrust will increase by approximately 10% (in the incidence ranges of interest).

In early studies, to reduce the amount of engine data required, data was produced for an assumed incidence/Mach number profile. With such data only very limited trajectory and pull-up manoeuvre optimization could be undertaken. Meaningful optimization and propulsion integration studies can only be conducted if full incidence/Mach number dependent engine data are provided. Presented in Figure 13 is a comparison of an optimized ascent trajectory based on non-incidence dependent engine data (initially assumed incidence profile), with the new optimized trajectory using full incidence dependent performance data.

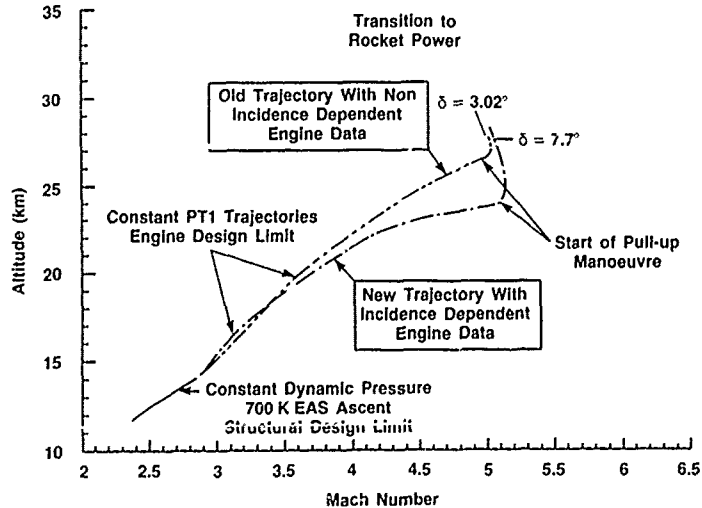


Fig.13 Transition to Rocket Power Pull-up Manoeuvre

The impact on the pull-up manoeuvre significantly changes the vehicle performance. An increase in vehicle climb angle of 4° at the point of transition to rocket power, would increase the payload by approximately 600 kg.

European Launch

The ascent trajectory optimization is complicated further if the vehicle is required to be launched from a European launch site. This may introduce the need for a cruise capability and, in addition, the vehicle will be required to manoeuvre to a particular ground track in order to rendezvous with a specific orbit (Figure 14)

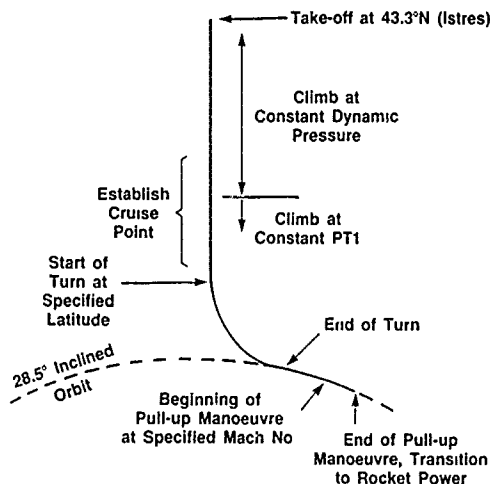


Fig.14 European Launch Trajectory

The optimum ascent is now defined by trade-offs between the accelerating phase and cruise requirements, and engine sizing (mass) and propulsion efficiency. Obviously if a large engine is installed then the vehicle will accelerate to the transition point more quickly, covering less range, and so to meet the specific orbit will require a longer cruise leg. (For optimum vehicle performance the vehicle must be in the required orbital plane prior to transition to rocket power.) In a similar way, if the vehicle climbs at a higher equivalent airspeed, or higher engine operating limit, then the vehicle will accelerate more quickly at the higher specific excess power and would then require a longer cruise leg. This trade-off between the cruise leg and the accelerating ascent will influence the selection of both initial and final ascent phases and of course the transition Mach number.

In a society becoming more concerned with environmental issues, the choice of altitude for the cruising phase, if required, may be restricted by the need to protect the ozone layer.

To optimize the turn required to manoeuvre the vehicle to a particular ground track to rendezvous with a specific orbit is a difficult task that will influence the whole ascent trajectory. It will influence the engine and wing sizing, and the selection of the transition Mach number as well as fuselage shaping (drag).

Presented in Figure 15 are the results of a study to investigate the effects of varying the latitude at the start of the positioning turn (and hence the normal load factor and turn radius) for a rocket ramjet powered vehicle. The vehicle was launched from Istres, France (latitude 43.3°N) into a 28.5° inclined orbit.

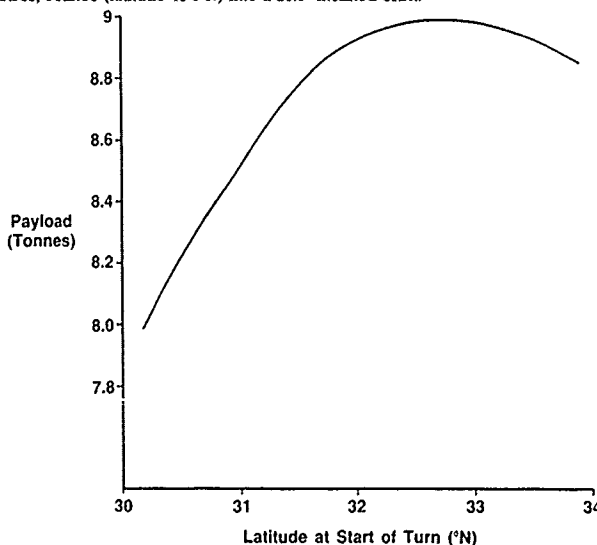


Fig.15 Payload Sensitivity to Latitude at Start of Positioning Turn

In this particular example the pull-up manoeuvre prior to transition to rocket power was performed immediately after the completion of the positioning turn. This will not necessarily produce the optimum transition point in each case. In this study the best performance was achieved by beginning a 1.07 'g' (nominal) turn at a latitude of 32.5°N.

The provision of a one hour launch window capability, at minimum performance penalty, imposes further constraints on the ascent trajectory. During this one hour period the launch site will move 15° of longitude eastward relative to the target orbit. By moving the launch point relative to the target orbit, a launch window study was conducted (Figure 16). It should be noted that the 0° reference launch longitude, is the launch point from which the vehicle would meet the target orbit at its most northerly point (see inset). All other launch points are relative to this datum.

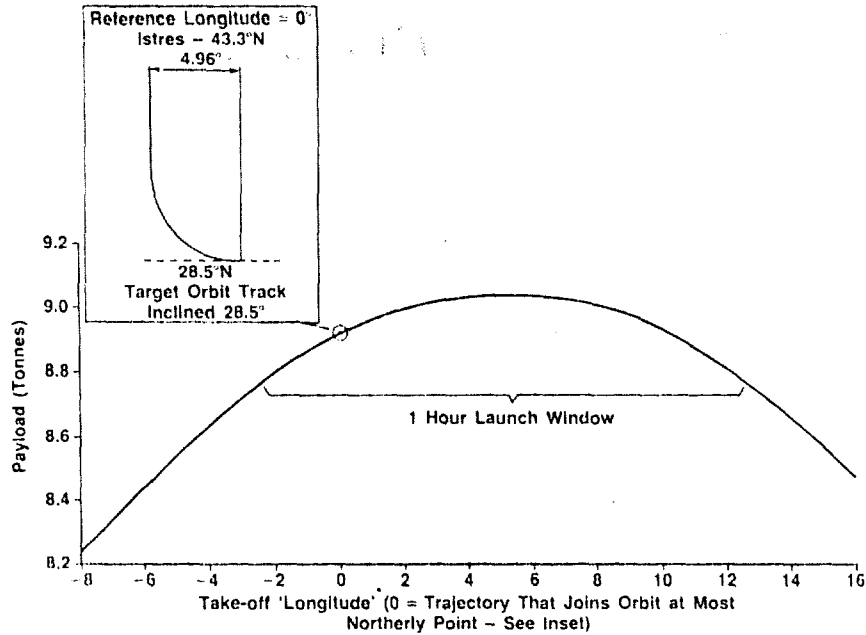


Fig.16 Provision of One Hour Launch Window

It can be seen from Figure 16 that the payload penalty for providing the one hour launch capability is only 240 kg. The optimum, the earliest and latest launch trajectories are shown in Figure 17.

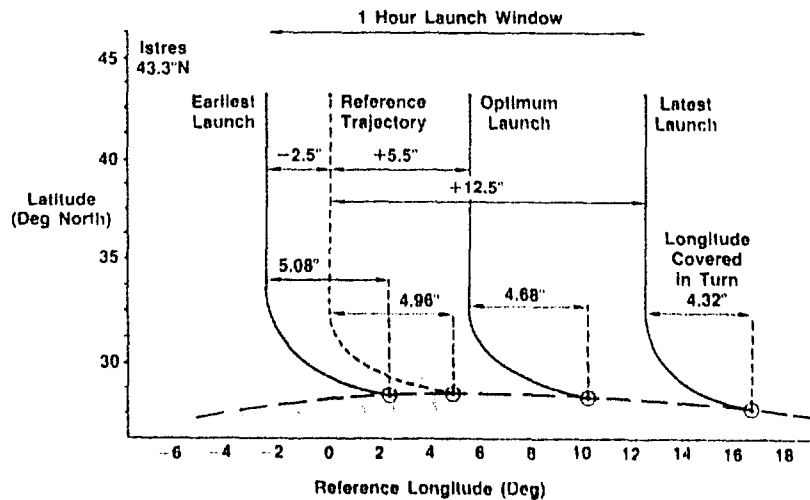


Fig.17 Launch Trajectories to Provide a One Hour Launch Window with Minimum Payload Penalty

Rocket Ascent Optimization

After transition, the engine parameters and aerodynamics become relatively simple, as the vehicle switches to rocket power and enters the hypersonic flight regime. This allows the trajectory from transition to Main Engine Cut-Off

(MECO) to be fully optimized. The equations of motion which govern the dynamics are a function of seven primary variables. These are:

The velocity at transition	V_t
The climb angle at transition	θ_t
The altitude at transition	h_t
The vehicle Thrust-to-Weight	T/W
The vehicle area to mass ratio	S/m
The vehicle zero incidence drag coefficient	C_{D0}
The engine specific impulse	I_{sp}

The trajectory can be optimized using vehicle incidence as the control variable, whilst meeting constraints on apogee and perigee altitude at MECO, and the ratio of mass at MECO to mass at transition (m_r^{MECO}) can be maximised (Ref.2).

Two methods of optimization have been applied. The first is generally referred to as the Indirect Method, which uses Pontryagin's Principle to define an optimum incidence profile indirectly as a function of a set of Lagrange Multipliers. This method has the advantage of being exact and reasonably fast computationally but is inflexible and may show poor convergence characteristics if the complexity of the problem is increased (by constraints for example)

The second method, known as the Direct Method, selects an incidence profile as a finite set of parameters and optimizes the ascent trajectory directly with respect to these parameters. This method has the advantage of relative simplicity but owing to the set of parameters being finite, is only an approximation to the true optimum profile. The larger the set of parameters the better the accuracy, but of course this must be paid for in computing time; a compromise must be sought.

Both methods have been applied at BAe and have given extremely close agreement in predicted propellant requirements. To achieve this accuracy the Direct Method required ten parameters.

The rocket mass ratio can be described by a function of the seven primary variables:

$$m_r^{MECO} = f(V_t, \theta_t, h_t, T/W, S/m, C_{D0}, I_{sp}) \quad (1)$$

This function is essentially non-analytic and must be evaluated point by point using the optimization procedure. For small deviations from a chosen nominal set of the seven variables, this function can be expanded as a Taylor Series to first order as follows:

$$m_r^{MECO} = m_r^{MECO(nom)} + \delta U \delta V_t (U_t - V_{t(nom)}) + \delta U \delta \theta_t (\theta_t - \theta_{t(nom)}) + \dots \quad (2)$$

Therefore the mass ratio for an arbitrary set of the seven variables can be found simply by knowledge of the seven sensitivity coefficients, $\delta U \delta x_i$, provided the deviations from the nominal condition remain small.

For a typical SSTO vehicle, the sensitivity coefficients are:

$$\begin{aligned} \delta U \delta V_t &= 6 \times 10^{-3} \text{ sec/m} & \delta U \delta C_{D0} &= -0.14 \\ \delta U \delta \theta_t &= 7 \times 10^{-4} / \text{deg} & \delta U \delta I_{sp} &= 7 \times 10^{-4} / \text{sec} \\ \delta U \delta h_t &= 2.5 \times 10^{-4} / \text{km} & \delta U \delta (T/W) &= 0.018 \\ & & \delta U \delta (S/m) &= -4 \times 10^{-4} \text{ m}^2/\text{kg} \end{aligned}$$

As can be seen from Figure 18, variations in m_r^{MECO} with T/W and transition altitude are not linear over a significant region, and care should be exercised to keep the variations small. When a new nominal configuration is adopted, the sensitivity coefficients should be re-evaluated, to keep the first order approximation valid.

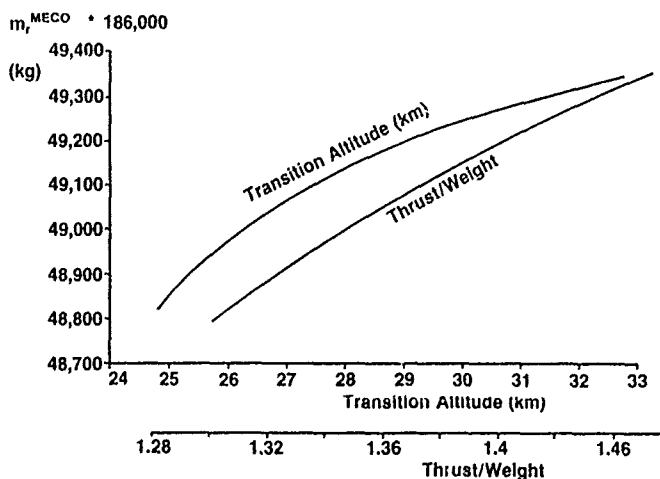


Fig.18 Variation in Mass at MECO With Transition Altitude and Rocket Thrust/Weight

The sensitivity coefficients lead to fairly obvious conclusions. The vehicle would prefer to be flying higher and faster and climbing steeper at transition, with less drag, more thrust and a higher specific impulse. Achieving these objectives however is a total system optimization problem, and the trade-off can only be performed by including the sensitivity coefficients in a global optimization program.

Compared to the air-breathing trajectory, the rocket powered ascent from transition onwards is relatively unconstrained. The dynamic pressure and wing loading decrease rapidly. The stagnation heating increases on the nose, foreplane, wing and intake leading edges but temperatures do not reach those experienced during re-entry.

The MECO point is selected such that the resulting transfer apogee meets the required target orbit. The perigee of this hypothetical transfer orbit, for minimum propellant usage, is at an altitude of approximately 60 km. However, other considerations may influence the choice of perigee. For example if the vehicle is required to re-enter successfully following a failure of the Orbital Manoeuvring System (so that circularization at apogee cannot be performed) and a landing at the launch site is desirable, then the transfer orbit perigee must be chosen carefully. Such a scenario is described as 'Abort-Once-Around' (AOA) and requires consideration of both ascent and descent phases. The transfer orbit perigee is very sensitive to the constraints imposed. To meet the AOA re-entry heating and cross-range requirements, for minimum performance loss, the perigee for a HOTOL-type launcher is approximately 20 km. Again, because of a requirement for AOA, the re-entry constraints have influenced the ascent trajectory.

DESCENT TRAJECTORY

Two aspects of the descent trajectory are considered; the re-entry and autoland.

Re-entry Trajectory Optimization

A vehicle of this type is assumed to be cooled by radiation; that is, the external aeroshell is allowed to reach a high temperature (in excess of 1200 K), so that the incoming heat generated in the boundary layer and convected to the surface is re-radiated back to the atmosphere according to Stefan's Law. This equation can be written in the following form:

$$\alpha \epsilon T_w^4 = S_1 \rho V (h - h_w) \times \frac{1}{2} S_1 \rho V^3 (1 - T_w/T_{rec}) \quad (3)$$

Where S_1 is the Stanton number, the functional form of which depends on the state of the boundary layer, h_w and T_w are the enthalpy and temperature at the surface and T_{rec} is the recovery temperature.

Assuming an ideal gas, it can be shown that on the attachment line of a cylindrical flow of radius r and incidence angle α (Ref.2):

$$S_1 = 1.03 \times 10^{-4} (\rho r)^{-1/2} \sin \alpha \quad \text{for laminar flow} \quad (4)$$

and

$$S_1 = 3.2 \times 10^{-3} (\rho r)^{-0.21} \sin \alpha \tan^{0.79} \alpha (1 + \tan^2 \alpha)^{-0.685} \quad \text{for turbulent flow} \quad (5)$$

A simple criterion for transition between laminar and turbulent flow is adopted. This assumes that if turbulent flow can occur, it will occur.

$$\rho r = 1.2 \times 10^{-4} \tan \alpha (1 + \tan^2 \alpha)^{-0.3} \quad (6)$$

At conditions of high enthalpy such as occur at re-entry speeds, dissociation and ionization of the air molecules will occur, which alter the properties of the boundary layer (in particular the density and specific heat capacity of the gas).

These properties can be explicitly calculated from a knowledge of the major chemical reaction rate equations, as a function of pressure and enthalpy, if it can be assumed that reaction equilibrium occurs between the various species. The result is merely to introduce a multiplying factor on the Stanton number which for turbulent flow can exceed 2.0, but for a laminar flow rarely exceeds 1.2. Laminar flow is thus seen as a desirable feature in high enthalpy flow.

From these equations it is possible to evaluate a good approximation to the radiation equilibrium temperature experienced on the surface of a re-entry vehicle in equilibrium real gas conditions. A re-entry profile can then be generated using this temperature as an inequality constraint.

The problem chosen is to minimize the mass of the Thermal Protection System (TPS) subject to inequality constraints on surface temperature, dynamic pressure and g-loads, and a final cross-range of 12° as an equality constraint. A solution to this problem was to control the bank angle so that the vehicle remained on an isotherm for the vehicle surface, and to vary the incidence profile to satisfy the remaining constraints. A three parameter incidence profile was chosen, similar in form to the profile adopted by the US Space Shuttle. This is depicted in Figure 19 with a typical bank angle profile.

was chosen, similar in form to the profile adopted by the US Space Shuttle. This is depicted in Figure 19 with a typical bank angle profile.

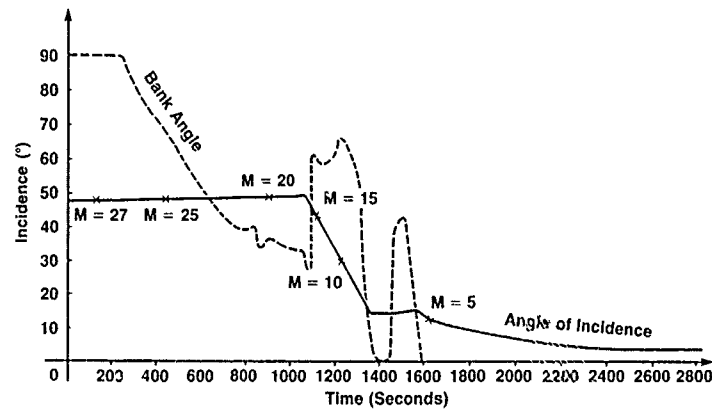


Fig.19 Typical Descent Incidence and Bank Angle Profile

The resulting temperature profile is shown in Figure 20. Note the jump in temperature as transition to turbulent flow occurs, this must be pre-empted by the control algorithm so that the constraint is not exceeded.

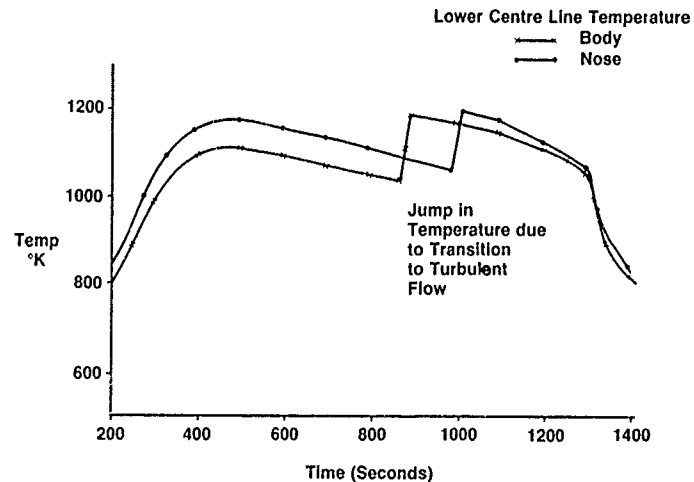


Fig.20 Re-entry Temperature Profile

The minimization is performed using a simple first order direct optimization method, whereby the incidence parameters are varied in turn in order to generate function and constraint gradients by numerical differences. This is similar to that used for the rocket ascent optimization but this time the problem is highly constrained. This method has proved to converge fairly rapidly and has the advantage that the number of incidence parameters (and hence the accuracy of the minimization) can be increased fairly simply.

The Indirect Method can be applied to this kind of problem and has been successful in a few simple cases (such as maximum cross-range descents) but it is BAe's experience that the method possesses intractable difficulties when applied to more representative re-entry optimization problems.

Once a re-entry trajectory has been defined, the sensitivity of this minimized TPS mass to the configuration parameters C_{D0} and ballistic coefficient can be found.

Figure 21 shows the result of this sensitivity analysis. It can be seen that a high area to mass ratio, and a low zero-incidence drag coefficient are beneficial in reducing the overall TPS mass, but the reduction is seen to be fairly small.

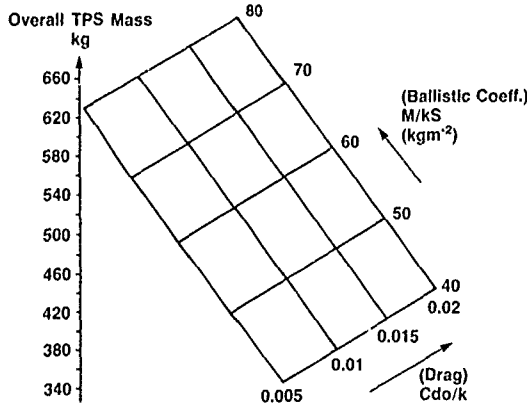


Fig.21 Thermal Protection Mass Sensitivity

Autoland

During re-entry and recovery, vehicle position, attitude and velocity information is obtained from Global Positioning Satellites, inertial, radar altimeter (in the final stages) and air data signals. These provide precise latitude, longitude, attitude and altitude information together with their associated rates. The Flight Control System uses these data to follow a pre-programmed trajectory to control heating rates and cross-range (as described previously) and to position the vehicle for the final Autoland manoeuvre.

Autoland for civil airliners is conventional, it has been in operation for the last 25 years. Autoland for an unmanned glider with a lift/drag ratio of 3.5 is a different matter. The strategy adopted is to fly a two-segment approach.

Initially the vehicle flies a steep glideslope (nominally 240 kt EAS along a 20° glideslope). This is significantly steeper than required for maximum lift/drag (L/D) ratio in order to cater for the effects of head- and tail-winds. Figure 22 shows the range of glideslope modulation that is available and the size of the still air Autoland window.

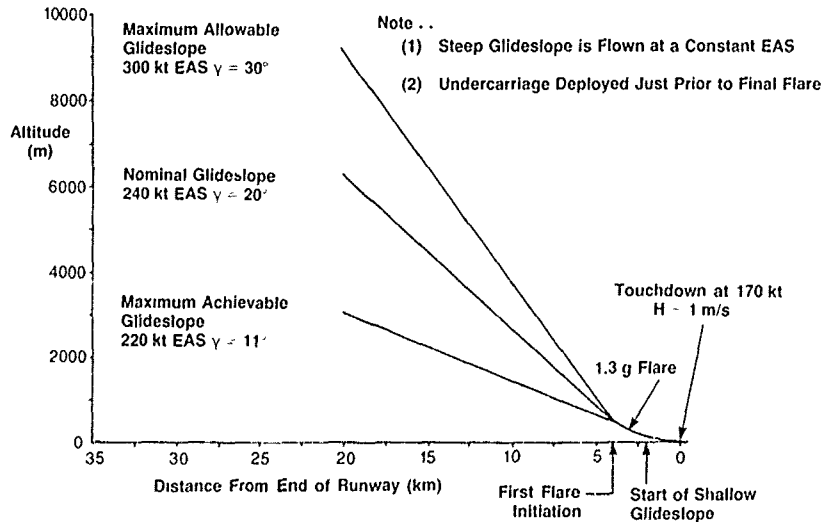


Fig.22 Autoland Glideslope Window

As the vehicle nears the ground a flare manoeuvre is required to check the descent rate. Trials in the USA have shown that it is possible to land successfully from glideslopes as steep as 30° using a single flare manoeuvre. It was found, however, that such a manoeuvre required very precise trajectory control in order to achieve the required speed and sink rate at touchdown.

A more conservative approach is to carry out an initial flare onto a shallow decelerating glideslope (3° was adopted for HOTOL, 15° is used by the Space Shuttle) which allows some scope for further adjustment. A final flare and touchdown then takes place. HOTOL lands at approximately 170 knots.

The Space Shuttle (which has a lower maximum L/D ratio than HOTOL subsonically) has demonstrated that such a strategy is feasible. To date, however, all landings have been under partial or complete manual control. Full Autoland has never been demonstrated. For HOTOL manual control is not a valid option.

A simulation was therefore set up at Warion which used wind tunnel derived aerodynamics and representative wind, turbulence and inertia models to develop a suitable control system. Figures 23 and 24 illustrate the final capture limits and touchdown scatter obtained with this system. Although some refinement is deemed necessary, notably to reduce dispersion of touchdown point and to reduce energy loss in turbulence, the results demonstrated the essential feasibility of successful repeatable Autoland for this class of vehicle.

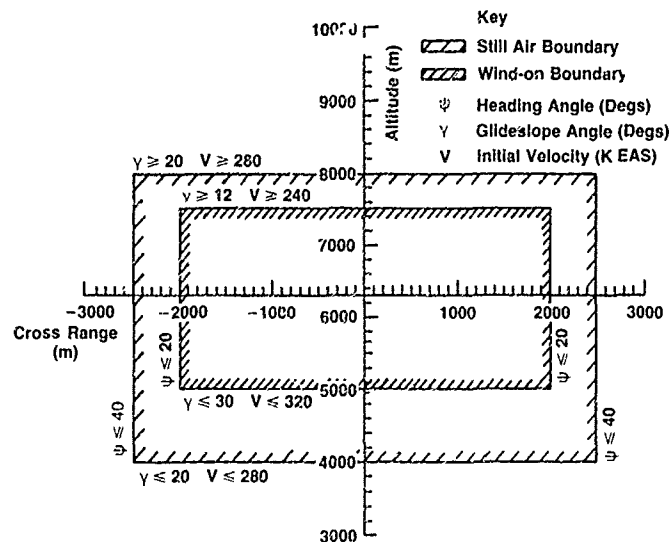


Fig.23 Autoland Window

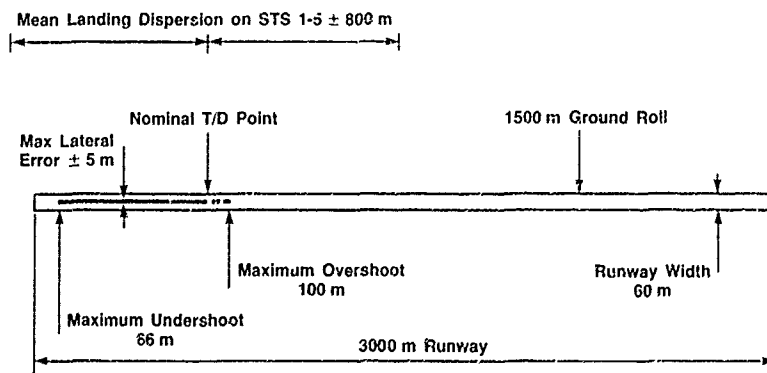


Fig.24 Summary of Touchdown Scatter

CONCLUSIONS

To meet the demand for a more reliable and cost-effective launch system, designers are again assessing the feasibility of fully re-usable winged launcher vehicles powered during the initial ascent by air-breathing propulsion systems. The performance of these vehicles is extremely sensitive, and because of this can be significantly enhanced by design optimization.

Part of the optimization process involves the identification of the most suitable ascent and descent trajectories. However for these vehicles, the selection of the optimum mission profile can not be considered in isolation. The traditional methods of defining optimum minimum fuel ascent are only valid for a final configuration. For air-breathing launcher vehicles the trajectory optimization must be part of a Total System Optimization. The correct selection of ascent and descent trajectories can only be made in conjunction with studies on fuselage design and shape, wing design and sizing, and propulsion integration, to name a few.

These studies are extremely complex but are essential. Although the performance of a TSTO vehicle can be affected by the selection of ascent and descent trajectories, it is the more sensitive SSTO vehicle where the impact on

performance can be the most dramatic. The penalty for a non-optimum design is very severe but the rewards for refinement of design and optimization of the trajectory can be very large

REFERENCES

1. Furuss S. G. 'SSTO Optimization' 40th Congress of the International Astronautical Federation, IAF-89-222
2. Noton M. and Swinerd G.G. 'Optimization of the Rocket-powered Ascent of HOTOL' 38th International Astronautical Federation Conference, Brighton 1987.

GLOBAL OPTIMIZATION OF AIR BREATHING LAUNCH VEHICLE TRAJECTORIES

by

F.Martel
 Aérospatiale/DSSS/Direction Etudes et Essais Systèmes
 Etablissement des Mureaux
 Route de Verneuil
 78130 Les Mureaux
 France

ABSTRACT

A trajectory global optimization method for single stage to orbit (SSTO) air breathing launch vehicle is presented. This method was involved in STS 2000 AEROSPATIALE studies to compare various air breathing candidate solutions, assess their performances and contribute to the definition of an optimized SSTO global design.

INTRODUCTION

The development of space applications at the beginning of the next century involves an increase in LEO payload delivery, lower costs of transportation and minimum turnaround time. Reusable air breathing launch vehicles are potential solutions to meet these requirements. Their characteristics will be an active use of aerodynamic lift in the atmospheric phase, propulsion means combining air breathing propulsion at low altitude and rocket propulsion at high altitude.

Many air breathing propulsion technologies are candidates for the concept of S.S.T.O. (Single Stage To Orbit). AEROSPATIALE associated with engine manufacturers has conducted for CNES, since 1986, parametric studies of S.S.T.O. (mainly) under the designation of STS 2000 study, comparing different aerodynamic shapes and propulsion solutions. As air breathing S.S.J propulsion design is characterized by strong interactions between the selection of thrust level, the ascent profile, the air intake sizing, the limits of use of each engine and the maximum payload, an optimization process can determine the best compromise between the design parameters to provide the maximum payload.

This paper presents the optimization methods involved in the STS 2000 studies through the use of the T.O.P.L.A. program. An example of optimized trajectory is discussed for a reference S.S.T.O. configuration with integrated turbo-rocket-ranjet-rocket engines.

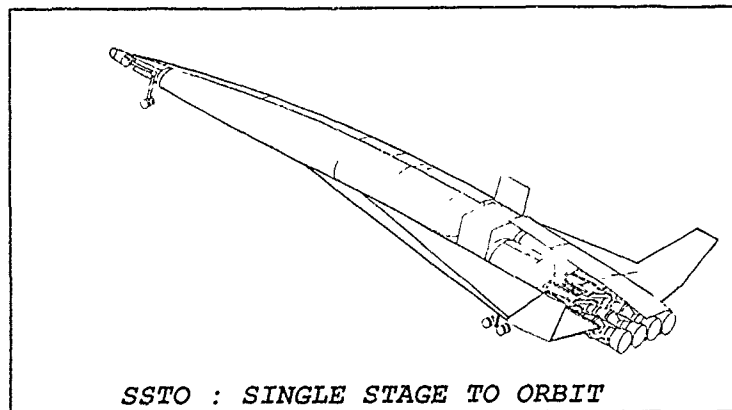


Figure 1.

GLOBAL DESIGN PROCESS

The global design process is illustrated in Figure 2.

Preliminary studies showed the high sensitivity of the maximum allowed payload to the aerodynamic drag coefficient and to the mass of structure and the strong influence of forebody interactions on propulsion performances. As a good evaluation of these parameters is necessary, the aerodynamic shape design was not included in the on-line optimization, but in an external highly interactive design loop with some main evolutions at certain steps of the study.

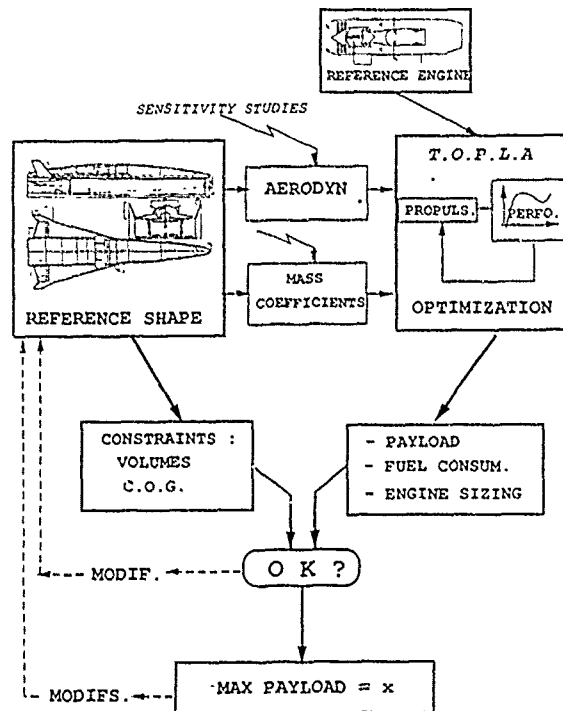


Figure 2. Design process

The basic design of the propulsion system is an input of the optimization process as well, although the sizing is unknown.

As some fixed assumptions are made on the takeoff mass and on the mission type, it results from the optimization an estimation of the maximum payload, the propellant consumption and the propulsion system mass (engines + air intake).

Some modifications may eventually occur if these parameters do not comply with the basic shape definition.

Mission assumptions

A reference scenario was assumed for the studies. After an assisted takeoff from Kourou and an ascent phase, the S.S.T.O. is injected on a 100/500 km/30 deg orbit. The orbit is then circularized at 500 km. The payload is maximized, the utmost objective being 7 tons of payload. After on-orbit operations, the S.S.T.O. is brought back on earth after an atmospheric re-entry phase.

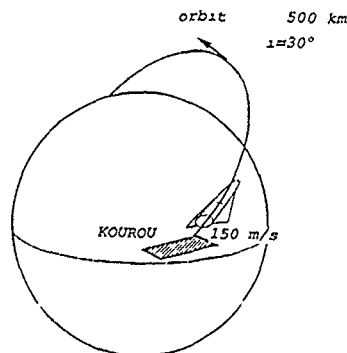


Figure 3. Mission scenario

Determination of the payload

The maximum payload that can be brought to orbit is the real optimization criterion. This payload results for each trajectory from the takeoff mass (fixed), the LO₂ and LH₂ consumption, the propulsion system mass (optimization variable) and the structure mass (Figure 4).

The structure mass results itself from a breakdown into:

- one part function of the takeoff mass (wings),
- one part function of the on-orbit mass (on-orbit operation and re-entry propellant, landing gear, thermal protections),
- one part for the propellant tank mass and one part for fixed mass.

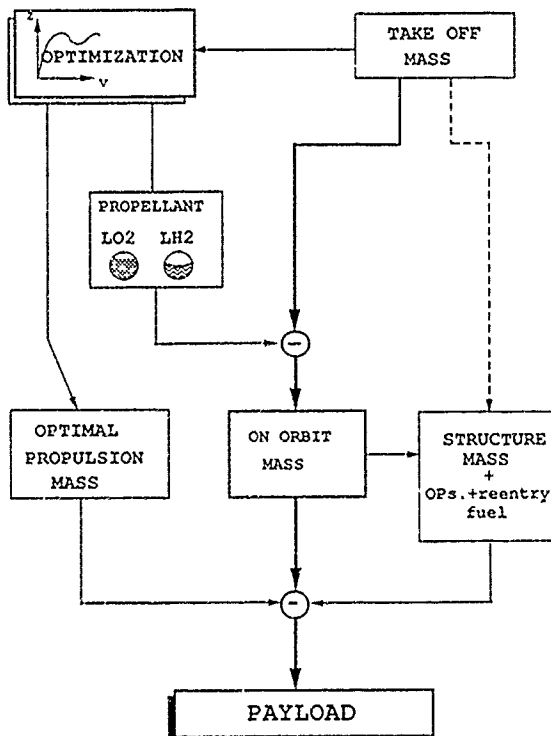


Figure 4. Payload determination

To determine the optimum propulsion, the engine mass and air intake mass are correlated with propulsion design drivers by relations of the form:

- air intake mass : $M_{int} = k (N \cdot A_c)^{\alpha_1} \cdot P_{si_{max}}^{\alpha_2} \cdot M_{max}^{\alpha_3}$
- air breathing engine mass : $M_{ae} = N \cdot M_{ae \text{ ref}}$
- rocket engine mass : $M_{re} = f(N, F_{max})$

with N : scale factor on the reference engine. It may be interpreted as a number of engines,

$P_{si_{max}}$: maximum air intake recovered pressure,

M_{max} : maximum operating Mach number of the air intake. Beyond this value, the air intake is closed.

F_{max} : maximum rocket thrust level,

A_c : air intake entry area

$k, \alpha_1, \alpha_2, \alpha_3$ are coefficients which depend on the air intake design.

CONSTRAINTS ON THE TRAJECTORY

The trajectory is subject to some physical constraints on state parameters and on control parameters.

Structural design and physiological constraints impose some limitations on dynamic pressure, transverse and longitudinal acceleration. The propulsion system design fixes some limits on the operating Mach numbers of the air breathing engines (turbojet, ramjet).

The angle of attack is constrained to be positive in ramjet mode. Practically, it is not necessary to consider upper limits on the angle of attack as the transverse acceleration limit is more stringent.

Aerodynamic and propulsive models

A complete modelization of aerodynamic and propulsive parameters as functions of the flight parameters Mach, altitude Z , angle of attack α , is included in the equation of motion. The above-defined N factor allows to derive propulsive coefficients from the basic coefficients of the reference engine:

- aerodynamic shape coefficients:

$$* C_Z = C_Z(\alpha, \text{Mach}),$$

$$* C_X = C_X(\alpha, \text{Mach}),$$

- additive aerodynamic forces: additive forces must be taken into account for subcritical air intake regime, i.e. when the engine airflow demand does not match the air intake available area.

$$* X_a = N \cdot X_{a_{ref}}(\text{Mach}, Z, \alpha),$$

$$* Z_a = N \cdot Z_{a_{ref}}(\text{Mach}, Z, \alpha),$$

$$* X_{culot} = N \cdot X_{culot_{ref}}(\text{Mach}, Z, \alpha),$$

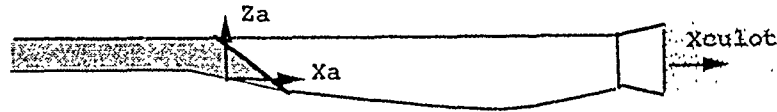


Figure 5.

- thrust

$$F = N \cdot F_{ref}(\text{Mach}, Z, \alpha)$$

- flow rates (air breathing phase):

$$* Q_{O_2} = N \cdot Q_{O_2_{ref}}(\text{Mach}, Z, \alpha)$$

$$* Q_H = N \cdot Q_{H_2_{ref}}(\text{Mach}, Z, \alpha)$$

The propulsive model for the rocket phase has an elementary form with constant coefficients.

Optimization

The optimization algorithm aims at maximizing the admissible payload with respect to the variables:

- air breathing and rocket phase ascent profile,
- initial azimuth,
- transition Mach between the engines: turbo jet, ramjet, rocket,
- "number of engines" N ,
- limit of air intake recovered pressure,
- thrust level in the rocket phase. Two levels (fixed) are optimized in this phase consistently with the limit on longitudinal acceleration (40 m/s^2). The transition between these two levels occurs when the acceleration reaches this limit.

This problem is solved by a parametric method. The air breathing ascent profile is split up into a finite number of segments in the altitude/velocity system of coordinates. The velocity or/and altitude components of each break-point of the profile can be optimized (figure n° 6).

A radial pursuit control law determines the angle of attack necessary to follow the profile (figure n° 7). The control is switched from one reference segment to the next one with some anticipation in order to track the profile smoothly. The trajectory is explicitly constrained by the limit on dynamic pressure and air intake recovered pressure as these limits may be defined according to velocity and altitude only. The air intake recovered pressure takes into account the air intake pressure recovery which depends also on altitude and velocity.

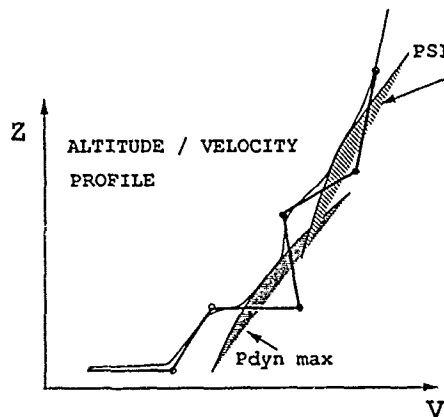


Figure 6. Air breathing ascent profile

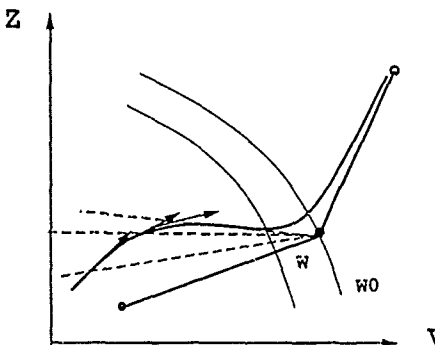


Figure 7. Ascent profile tracking

The bank angle during air breathing phase is maintained at zero as the initial azimuth is optimized. Some residual transverse corrections are made in the rocket phase in order to reach the prescribed orbit plane.

The rocket phase trajectory is directly optimized by means of an explicit guidance algorithm. A quasi-NEWTON method was also tested to optimize this phase, but it was less satisfactory with regard to computer time and robustness relatively to feasible initial trajectory.

The global optimization process consists in a cyclic monodimensional search on each parameter. This method, although conservative, does not require any weighting factor on the optimization parameters and has a robust behavior with respect to significant change in the various configurations of S.S.T.O. which had to be compared. Computer processing time was acceptable to implement this software on an ordinary work station.

Initialization of the optimization process

Trajectory optimization algorithms generally require a good initial guess of the optimization parameters. Classic methods of best ascent trajectory determination currently used for aircraft may be applied for that purpose. Such methods are detailed by RUTONSKI (reference [1]).

They rely on the minimization of the consumed fuel mass (Figure 8):

$$\Delta m = \int_{E/m}^{E/m^2} \frac{1}{d(E/m)/dm} d(E/m)$$

which is equivalent to maximizing at each energy level:

$$[(T-D) \cdot V / (m \cdot Q)]_{E/m} = \text{const.}$$

$$\text{with } E/m = gZ + v^2/2 \quad g \cdot Z + v^2/2$$

Z altitude,

V velocity,

T thrust,

D drag,

Q flow rate of fuel.

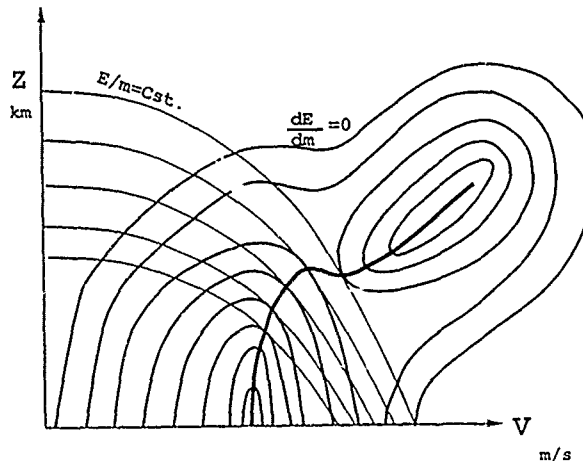


Figure 8. Ascent profile first guess

This method may be applied for a first guess of the air breathing ascent profile. It can take into account the dynamic pressure and air intake recovered pressure limit as these constraints may be expressed in the same (Z, V) plane. The first guess of air breathing engine thrust level is determined by trial and error.

Characteristic trajectories

The example of an optimized trajectory for a turborocket/ramjet/rocket engine (reference S.S.T.O.) is shown in Figures 9 to 12.

The aerodynamic shape was designed to provide a low drag in the transsonic phase and the turborocket engine was adapted for this phase. As shown in Figure 9, the air breathing ascent profile in (Z, V) plane begins by a segment at low altitude (no environmental or safety constraint was presently assumed), at Mach 0.7, after a pull-up maneuver, the vehicle climbs rapidly up to 3 000 m to pass the transsonic phase with a small positive flight path angle until the dynamic pressure constraint is reached. The profile follows then this constraint and the turborocket is switched over to ramjet propulsion at the optimized transition Mach 3.6. This Mach number was also the operating limit of this turborocket engine. After that transition, the air intake recovered pressure constraint becomes preponderant.

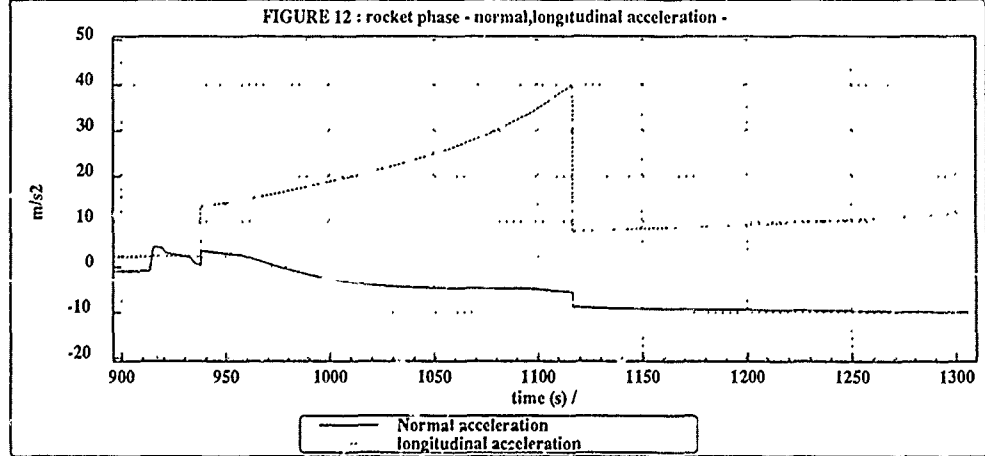
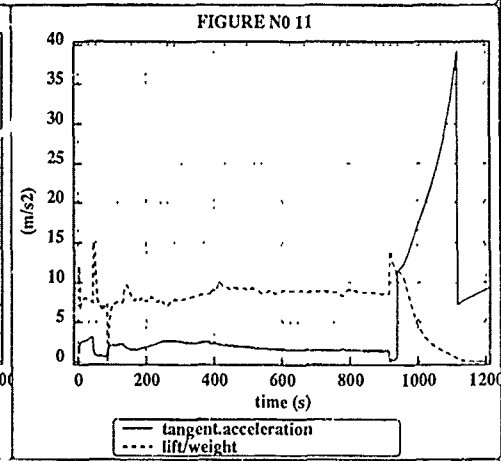
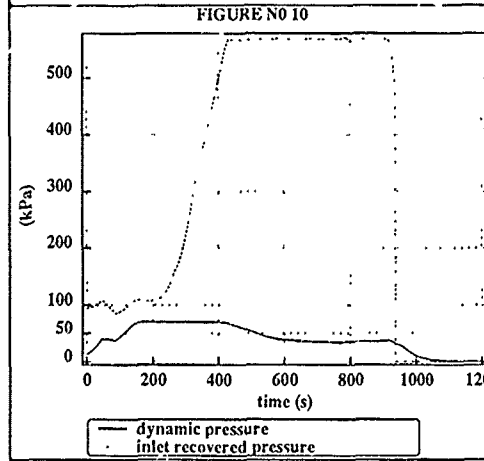
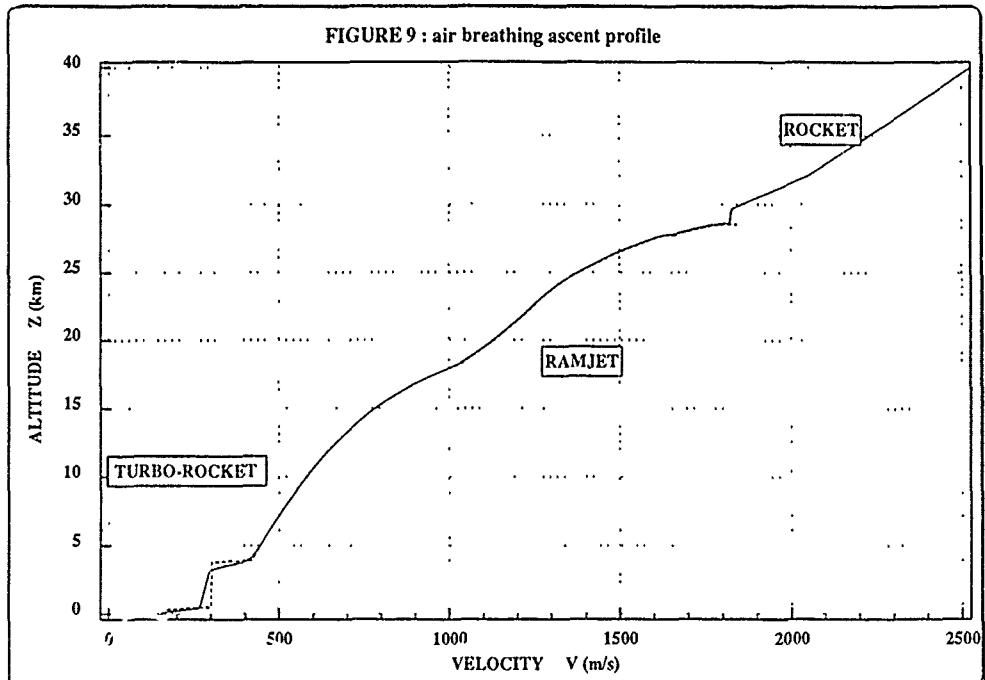
The ascent profile follows then the constraint up to the pull-up maneuver then increases the flight path angle before transition to the rocket phase. The optimized upper bound of Mach number during air breathing phase is Mach = 6. It was also the upper operating limit for that engine.

As shown in Figure 12, in the rocket phase, the longitudinal acceleration increases rapidly up to its limit of 40 m/s^2 . This condition triggers a second thrust level which is reduced to an optimized value. Earlier studies proved that the possibility to have two rocket thrust levels could bring an appreciable payload gain relatively to the solution with a single constant rocket thrust level.

For the previous S.S.T.O. configuration, the transsonic phase was passed at a relatively low altitude. Figure 13 shows the initial ascent trajectory of the same S.S.T.O. equipped with engines of better specific impulse but of lower thrust-to-mass ratio. The turbo engine is here adapted for takeoff instead of being adapted for the transsonic phase.

The transsonic phase occurs then at higher altitude and ends with some negative flight path angle. To compensate for this higher mass of engines, the optimum of air intake maximum Mach number is no more the operating limit of the ramjet engine. Therefore, the transition to rocket phase is done at Mach 4.5. The initial ascent profile of Figure 13 was composed of 7 optimized breakpoints. It is interesting to compare this profile with a reduced profile structure at 3 breakpoints. The trajectories (continuous lines) are comparable and the difference in payloads is practically negligible with respect to model uncertainties.

As a consequence, the choice of a parametric representation of the ascent profile in an altitude/velocity plane is well suited to the air breathing trajectory optimization.



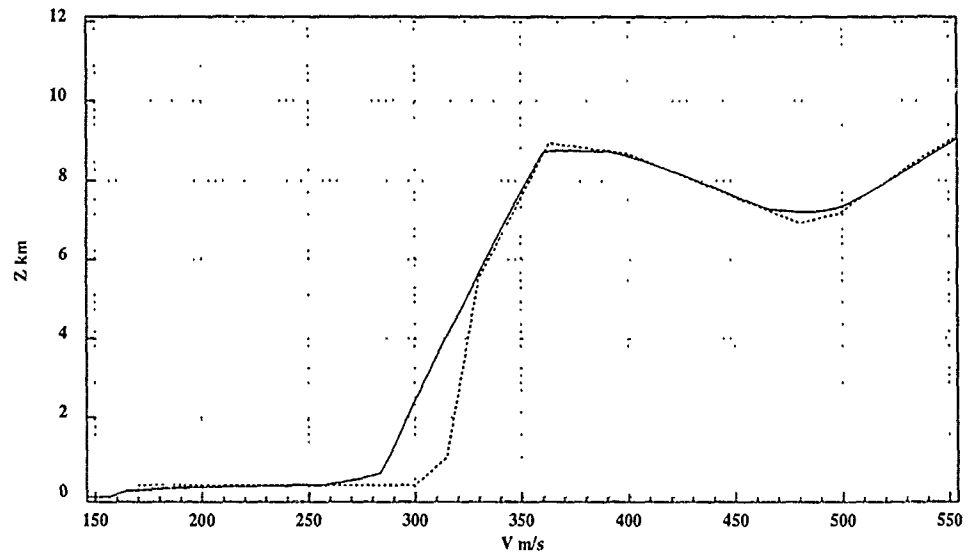


Figure 13. Transonic phase with low thrust-to-mass ratio

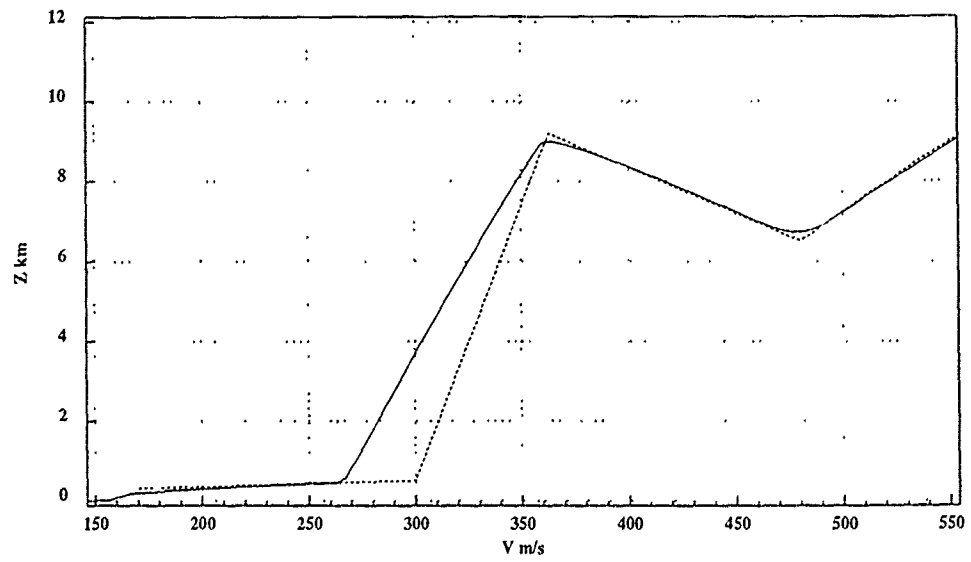


Figure 14. Trajectory with a reduced number of segments

CONCLUSIONS

The STS 2000 studies showed the relevance in optimizing the propulsion sizing parameters together with the trajectory. Parametric optimization methods with a representation of the air breathing ascent profile by broken lines in an altitude, velocity system of coordinates proved to be well suited to this task. It was then possible, by means of these methods, to efficiently compare numerous configurations of propulsion integration in order to select more rapidly the best solutions or give the orientation for future studies.

REFERENCES

- (1) E. RUTOWSKI
Energy Approach to the General Aircraft Performance Problem
Journal of the Aeronautical Sciences - March 1954
- (2) J.C. BOUILLOT, C. FAZI, S.M. ROUBERTIE - French approach in future launch systems - IAF-87-209, Brighton, Oct. 1987
- (3) J.C. BOUILLOT, C.FAZI, J.M. ROUBERTIE - Evolution of future launcher studies - IAF 88-183, Bangalore, Oct. 1988

THE CHALLENGE OF ASSEMBLING A SPACE STATION IN ORBIT

Vance D. Brand
 NASA Lyndon B. Johnson Space Center
 Houston, Texas 77058 USA

1. The Need for a Space Station

Seventeen years ago, America had a very capable space station in orbit. It was called Skylab. Skylab was a scientific space station which weighed approximately 90 metric tons and traveled in low Earth orbit with a crew of three.

The Space Station Freedom, an all-purpose scientific platform currently being developed by free world partner nations, will be a superior, much larger station with newer technology. It will weigh more than 225 metric tons and eventually will have a crew of eight. Freedom will be permanently manned and will be assembled in orbit in the late 1990's.

What are the unique attributes of any space station? Obviously, a space station is an excellent vantage point from which to view both the Earth and the universe. A space station is in an advantageous location to serve as a depot or transportation node for spacecraft destined to go further out into space, and it exists in an environment of weightlessness and near-perfect vacuum.

A space station is a scientific platform for observing both the universe and the surface of the Earth and, in addition, can be used to develop equipment that might be later transferred to unmanned satellites. A space station can serve as a transportation depot at which spacecraft may be refueled, repaired, or assembled. There is a strong possibility that a manned Mars probe may someday be assembled and fueled onboard a space station before starting its journey to Mars. A space station can be a laboratory for microgravity research where larger, purer crystals and other materials are processed. Life sciences research will be conducted there so that man's physiology may be better understood before long journeys into the solar system are initiated early in the next century. Space stations can have military as well as peaceful objectives. A space station must be part of the infrastructure of space capabilities of any nation or nations planning to extend the frontier of space exploration.

2. The Challenge of Space Construction

Although there are similarities between Earth construction and space construction, there are also some very important differences. The remoteness of the assembly site is a significant difference. Any space station in Earth orbit must be assembled at an altitude of at least 300 kilometers and at an approximate speed of 28 000 kilometers per hour. Obviously, if a space station is being built under those conditions, it is impossible to drive to a nearby hardware store to buy a wrench or any other tool that may have been forgotten or to replace building materials that might not be suitable. Thus, preplanning is a very important ingredient in space construction and even more important than in Earth-based construction projects. Another difference is the hostile environment of space. Orbiting above the Earth's atmosphere, the construction site is in a vacuum and is subject to radiation, micrometeoroid bombardment, and great thermal extremes. The workers on orbit must be protected from these hazards, and the space station must be designed to withstand the rigors of the environment. Although working in a space suit may appear to be fun, there are penalties associated with wearing such a garment. For example, today's space suits are massive and somewhat stiff in the joints and gloves. Thus, they are cumbersome, tiring, difficult to take into tight places, and reduce one's manual dexterity. These disadvantages are partially offset by extensive training in the suits.

Construction operations in the weightless environment offer both advantages and disadvantages. Advantages are that structures can be made lighter and that extravehicular crewmen can easily translate about the station. Disadvantages include the need for new techniques and tools and complete ground simulation of operations before flight. Unlike on Earth, in space there is no yard around the building site where materials may be stored. This means that components must be assembled as soon as they reach orbit, or secured in a temporary storage location.

3. Factors Which Influence Assembly Degree of Difficulty

Factors that determine the difficulty of construction on orbit include the configuration of the station, capabilities of the transportation system that will carry components to orbit, and the actual magnitude of the assembly work required by extravehicular (EV) crewmen or robots. The size and the complexity of the station are the primary configuration factors.

Capabilities of the transportation system that are of interest include the amount of mass and volume of materials that can be transported to orbit on each flight, man-hours of extravehicular activity (EVA) available on each flight, visibility to do the job, on-orbit stay time, and flight rate. Other factors include capabilities of the assembly work platform connected to the transportation system and of remote manipulators such as

the Space Shuttle remote manipulator system (RMS) that will be used for construction of the Space Station Freedom.

The magnitude of assembly work required by crewmen or robots pertains to the number of things that must be assembled on the station as opposed to those things that can be deployed automatically or can be operated as they arrive in orbit without any assembly or deployment. Generally, the on-orbit construction job is easier if devices such as solar panels, radiators, and antennas can be deployed automatically rather than assembled in orbit by human beings. Tradeoff studies must be made to determine whether hardware is best assembled or deployed. In either case, there is always the possibility that something will not work properly after it has been assembled or deployed which makes end-to-end ground checkout of hardware and software a must before flight. Design for reliability, quality control, and ground testing are paramount requirements.

4. The Optimum Choice

My opinion is that the best solution to the problem of constructing a large space station on orbit is to minimize assembly and, thereby, to maximize ground end-to-end checkout. For a large station, this method requires use of a large, wide-body launch vehicle. The use of such a transportation system allows a space station to be assembled on Earth, ground tested as a complete system, and placed in orbit in just one or two flights. Any assembly activities which follow are less time critical, reduced in scope, and staged from an already functional, orbiting base. Significant operational costs associated with many assembly flights and the risk inherent in extensive on-orbit assembly are avoided. Currently, the United States does not have an operational wide-body launch vehicle. The last one used in the United States was the Saturn V, which could lift more than 100 metric tons into low Earth orbit.

Obviously, without such a vehicle, a space station assembly sequence requires transporting many smaller loads into orbit, with extensive assembly on orbit by astronauts in space suits. The latter assembly method is actually a feasible, but more difficult, way of building a space station. On the positive side, assembly on orbit provides the space assembly knowledge and national capabilities for very large space projects in the future.

5. Description of the Space Station Freedom

The Space Station Freedom will consist of a long truss, several pressurized modules, and many items of equipment attached to the truss (Figure 1). The planned truss will eventually consist of 27 bays of composite truss construction and will be more than 145 meters long by 5 meters wide by 5 meters deep. Large photovoltaic panels, capable of producing an electric power output of 75 kilowatts, will be attached at the ends of the truss. The panels will gimbal so that the solar arrays are always facing the Sun.

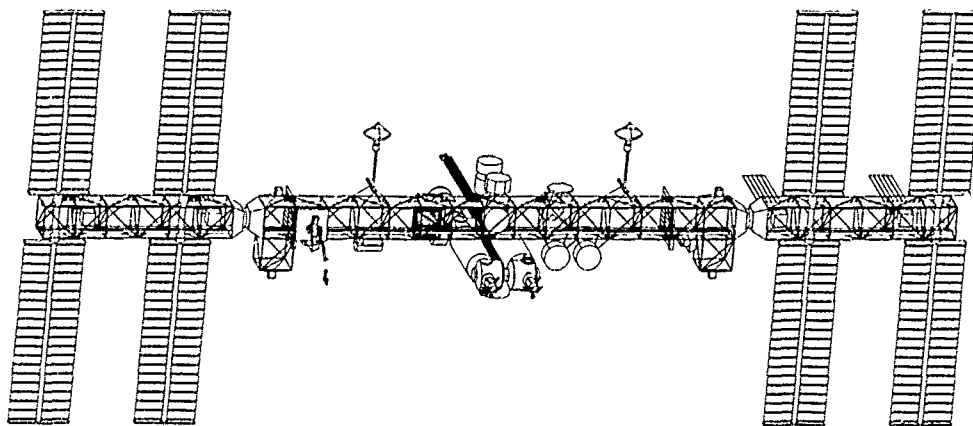


Figure 1.- Space Station Freedom (phase 1).

Eight pressurized modules will be attached to each other and to the center of the truss (Figure 2). The U.S. modules will be arranged in a racetrack (rectangular) arrangement. The core configuration will consist of a laboratory module, a habitation module, and four nodes attached at the corners of the rectangle. The nodes will serve as control centers, and will contain computer, stabilization, control, and other systems. The European Space Agency and Japan will each supply an additional pressurized laboratory to complete the module pattern. The Canadian mobile servicing center (MSC), a remote manipulator, will move along the long truss. The Space Shuttle docking systems will attach to docking systems on the forward nodes. At least 20 Space Shuttle assembly and provisioning flights will be needed to construct the Station. Currently, the Space

Shuttle has the capacity to carry approximately 18 000 kilograms to an orbital altitude of 400 kilometers.

6. Space Station Freedom Navigation and Control Systems

Magnetic passive dampers will be used for attitude control of the first stage of Freedom until arrival of the second assembly flight. The passive dampers are spherical devices having a mass of approximately 9 kilograms. They attach to the Station truss structure and damp attitude oscillations of the Station as it is flying in the gravity-gradient attitude. Each damper consists of a spherical shell inside a shell, with viscous damping fluid between the shells (Figure 3). The outer shell is attached to the spacecraft structure and the inner shell to a permanent magnet, which seeks alignment with the Earth's magnetic field. The result is that spacecraft oscillations about the gravity-gradient attitude are positively damped. With a sufficient number of dampers, a tumbling spacecraft can eventually be stabilized in the gravity-gradient attitude. As

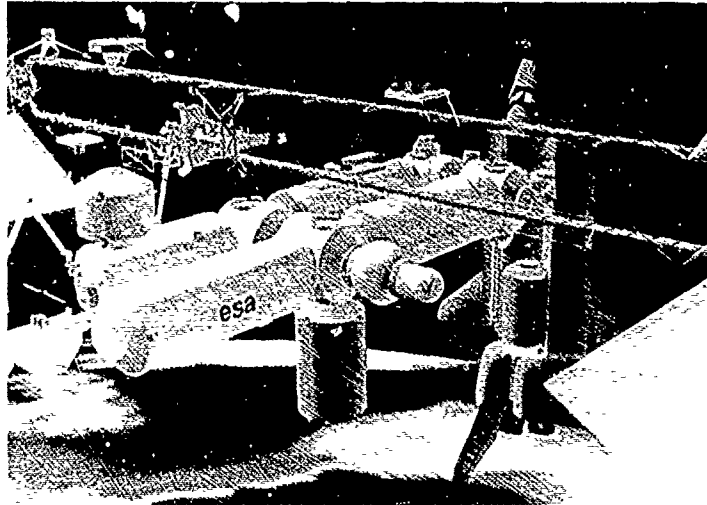
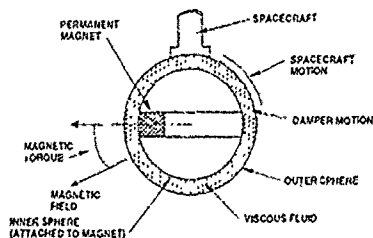


Figure 2.- Freedom's pressurized modules.

Concept of Magnetic Passive Damper



- ☑ Magnet attempts to align to magnetic field
- ☑ Spacecraft oscillates in gravity gradient mode
- ☑ Relative motion between spacecraft/magnet is damped
- ☑ Amplitudes of spacecraft oscillations diminish

Figure 3.- Concept of magnetic passive damper.

many as seven dampers may be required for the stage assembled on the first Space Shuttle flight. Passive dampers have been used on satellites in the past and are considered to be reliable. The NASA long duration exposure facility (LDEF), which currently is in orbit and will be returned to Earth late this year, is a 3-axis, passively stabilized

satellite successfully utilizing the magnetic passive damper. It has no active control; i.e., no reaction control system (RCS) or control moment gyros (CMG's).

A two-module RCS is installed on the second Space Shuttle assembly flight and will be enlarged to four modules on later flights. The completed RCS consists of four pods, each with several thrusters and hydrazine propellant. Two RCS pods are located near each end of the truss (Figure 4). In addition to reaction control jets, the completed Freedom has six CMG's to smoothly control attitude. The CMG's are mounted on a pallet attached to the truss and are desaturated by the RCS as required (Figure 5). The navigation and control system of the completed station receives inputs from star trackers and the global positioning system (GPS). Computers inside the pressurized modules maintain attitude and state-vector (position and velocity) knowledge by means of this system. In addition to maintaining attitude and desaturating CMG's, the reaction control jets also perform station altitude adjust maneuvers. Periodic posigrade maneuvers are required to offset drag by raising the orbital altitude of the Station.

7. Space Station Freedom Assembly Tools and Methods

The Space Station Freedom will be assembled on orbit, and there must be an optimum balance of construction resources to do the job. These resources consist of extravehicular crewmen, remote manipulators, robotic devices, and an assembly work platform. Two EV crewmen are sent out from the Space Shuttle for 6 hours at a time to assemble the Space Station Freedom. Because of resource limitations, each Space Shuttle flight has 24 man-hours of extravehicular crew time available, with a possible extension to 48 man-hours. Manipulators include the Space Shuttle RMS (sometimes called the "Canada Arm") and a larger, advanced version of the Canada Arm onboard Freedom called the mobile servicing center (MSC). Unlike the Space Shuttle RMS, the MSC is attached to the Space Station Freedom. The Station's arm moves about the truss on a device called the mobile transporter, and it serves a purpose similar to that of a crane at a building site here on Earth. Robots such as the U.S. flight telerobotic system and the Canadian special-purpose dexterous manipulator are attached to the ends of the manipulators and are capable of fine manipulations such as detailed construction and maintenance tasks. There is a work platform at the forward end of the Space Shuttle Orbiter payload bay. The work platform, called the assembly work platform, is a truss-building machine.

Two EV astronauts use the assembly work platform to build the Station's long, transverse truss described earlier (Figure 6). Astronauts attach composite struts to a fixture on the assembly work platform to build each 5-meter bay of truss. After each bay is completed, it is indexed straight out of the Orbiter payload bay. As the truss is being built and indexed out of the bay, utility runs are attached to the structure. After a section of truss is completed, avionics boxes and other components are maneuvered to the truss by the manipulators and latched into place by astronauts. Most items of equipment are assembled; the photovoltaic panels for the electric power generation system, which are deployed, constitute an exception.

8. The Early Assembly Flights

Each of the many assembly flights will have a distinctive cargo manifested in the Orbiter payload bay, and the assembly for each stage is performed differently. For

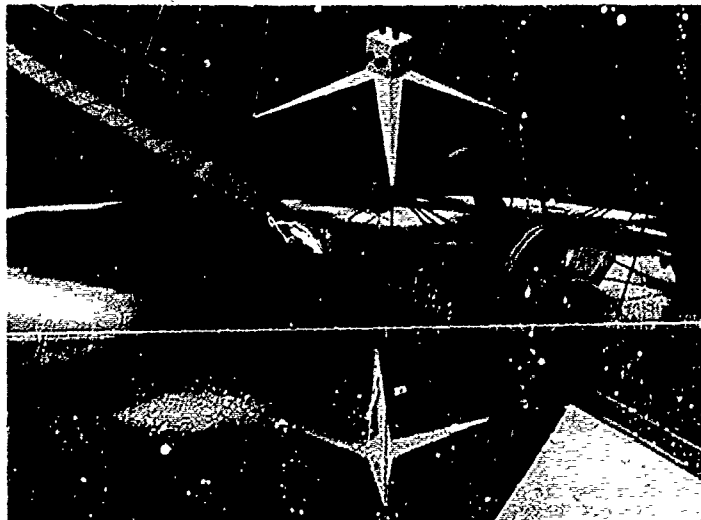


Figure 4.- RCS propulsion modules on truss.

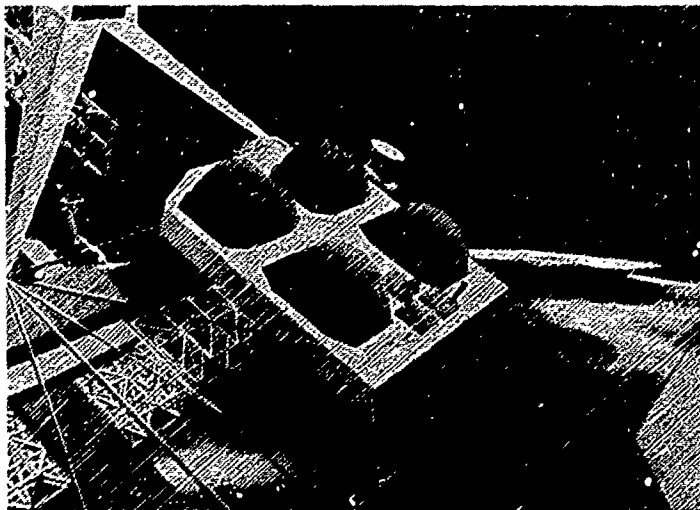


Figure 5.- Control moment gyro pallet.

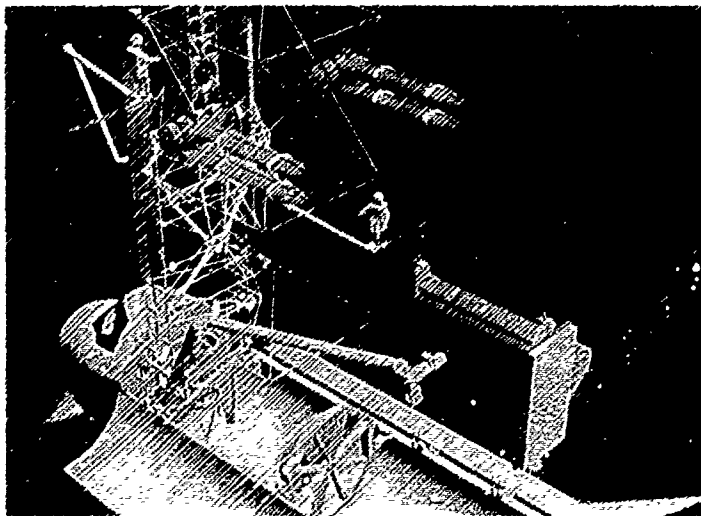


Figure 6.- Assembly work platform.

example, the first assembly flight requires two astronauts to assemble a few bays of truss and one quarter of the electrical power system. Other vital systems, such as navigation, control, propulsion, and environmental control, are not yet part of the assembly. After the Orbiter departs, the first stage remains in orbit passively stabilized by magnetic dampers in a gravity-gradient attitude until the Orbiter returns with a second load (Figure 7). The stage flies with its long axis pointed toward the center of the Earth.

Sufficient equipment arrives in orbit on the second flight to form a fully functional spacecraft, which is not yet the whole station - only a small piece of it. This fully functional spacecraft still flies in a gravity-gradient attitude on orbit but is stabilized by means of RCS propulsion. On a later flight, the first pressurized module, a node, is installed (Figure 8); then, the remaining half of the transverse truss is assembled (Figure 9). Each succeeding Space Shuttle flight results in assembly work which will increase the mass and complexity and systems capability of the Station. As previously described, the construction proceeds with crew-controlled remote manipulators moving items from the payload bay to the work site. Astronauts are involved in the assembly operations both as extravehicular assemblers and intravehicular manipulator operators.

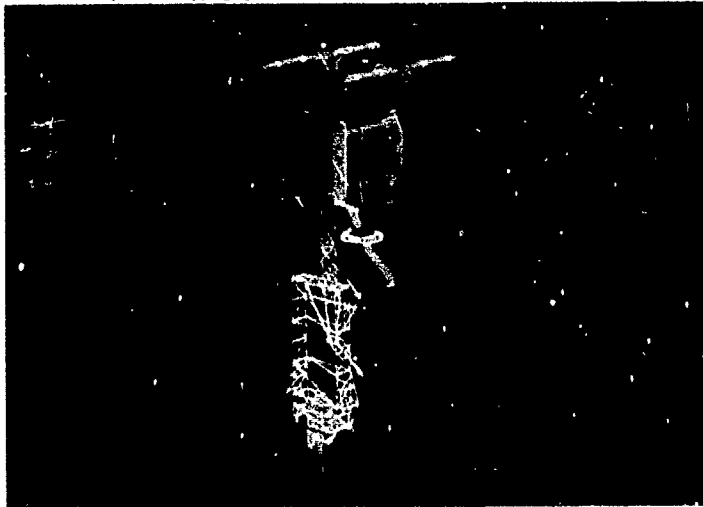


Figure 7.- Spacecraft passively stabilized after first assembly flight.

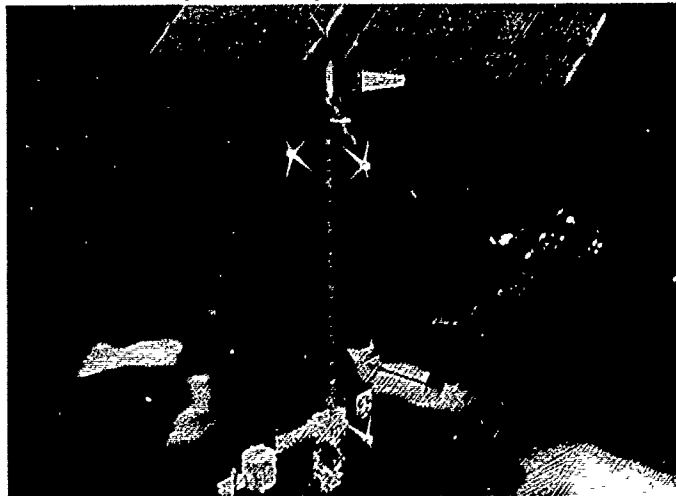


Figure 8.- Spacecraft after first pressurized node installed.

9. Challenges of Space Station Freedom

Although not necessarily in order of importance, the following are the significant challenges of the Space Station Freedom construction process. It is difficult to transport an adequate amount of functionality to orbit on the first assembly flight to achieve a self-sustaining spacecraft. Ideally, the first flight would have all of the necessary systems for flight control and survival until the Space Shuttle returns. It is a necessary compromise that the Space Station Freedom will be passively stabilized with magnetic dampers at the end of the first assembly flight and will not achieve the capability to control its own attitude until the second flight.

Another challenge is that of loading the 5- by 20-meter payload bay of the Space Shuttle in such a way that volume, center of gravity, and mass (lifting capacity) limits are not exceeded on each flight. Engineers must design compact launch packages which can be positioned in the payload bay to satisfy center of gravity limitations and later be easily unpacked and assembled on orbit.

An important objective and challenge is to minimize the number of assembly and outfitting flights so as to reduce operational costs during the construction phase. It may be possible to build and outfit a minimum station with less than 20 flights, then improve the Station with systems upgrades later in the program.



Figure 9.- Spacecraft after transverse truss completed.

Extravehicular activity time is a critical resource in the construction process. It is a challenge to stay within EVA man-hour limits, and the Station designer must honor that limitation.

Both the Space Shuttle and Space Station Freedom remote manipulators have constraints during use that cannot be ignored. For example, there are reach and articulation limitations. As with the human arm, the manipulator joints can reach only so far and are ineffective in certain positions. Assembly designers also must consider how well the manipulator operator can see the task being performed. Direct viewing through the Space Shuttle or Space Station Freedom windows is a design goal, but in most cases, direct viewing must be supplemented by displayed television views. Manipulator operations must be seen well to be conducted efficiently and safely.

Another challenge of Space Station Freedom assembly is the problem of unplanned interruptions to the assembly process. In the event of an unplanned departure resulting from a Space Shuttle or Space Station emergency, the Station must be capable of surviving, and the Space Shuttle must be capable of returning and docking to the Space Station to continue the assembly. This requirement places a burden on the assembly designer to think through each step of the assembly process from the standpoint of unplanned interruptions.

Each step of the assembly process must be verified on the ground before it is accomplished in flight. This means that assembly must be conducted on the ground in a simulation or other test before assembly on orbit occurs. Verifications are planned for the development contractor's facility. Many tests will occur at either the NASA Lyndon B. Johnson Space Center or the NASA John F. Kennedy Space Center. Ground simulations will include prototype hardware tests; underwater assembly demonstrations; and "man-in-the-loop" simulations to verify manipulator reach, operator visibility, timelines, and overall assembly feasibility. The ground simulation and verification process is vital since on-orbit operations will cease if a part does not fit, a tool is missing, a station stage is not controllable, or the assembly procedure is found to be impractical.

Development and integration of the Space Station Freedom from a management point of view is perhaps the greatest programmatic challenge for NASA in its 30-year history. Station components are being designed, developed, and tested by four NASA centers and four prime contractors, plus partners from Canada, the European Space Agency, Japan, and their contractors. The complicated management process is beneficial in that it pools monies and talent from several sources for a difficult task. However, the program complexity greatly increases the management challenge and results in increased management integration expense.

10. Incorporation of New Technologies

The NASA is conducting advanced development to bring new technologies on line for the Space Station Freedom. Some examples are an aluminum-coated composite truss structure with low sensitivity to thermal stress, a solar dynamics electric power generation system (Figure 10), and a flight telerobotics system. Other examples are utility conduits wound on large reels for transportation in the Space Shuttle and a unique assembly work platform to be used for truss building on orbit. Since some of the above advanced developments add programmatic risk and increase up-front costs, consideration is being given to use of more proven equipment in the early stages of assembly. After the Station

is permanently manned, more advanced equipment with improved performance may be retrofitted.

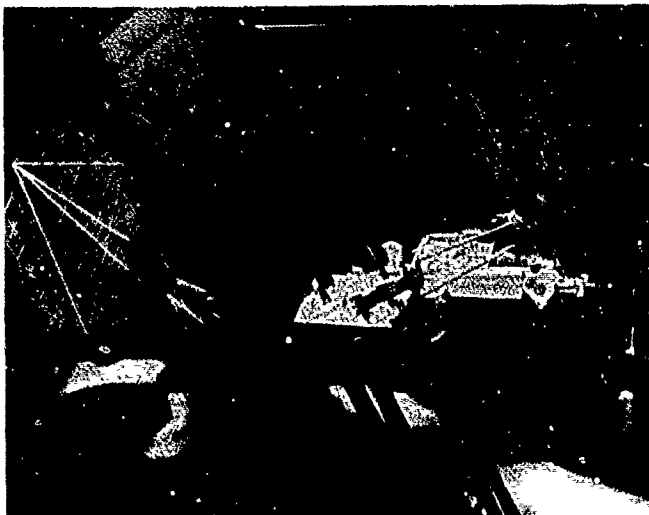


Figure 10.- Growth version of Freedom with solar dynamic power.

11. Summary and Conclusions

Assembly of a Space Station in orbit is a challenging and complicated task. If mankind is to exploit the knowledge already gained from space flight and continue to advance the frontiers of space exploration, then space stations in orbit must be part of the overall space infrastructure.

Space stations, like the Freedom, having relatively large mass which greatly exceeds the lifting capability of their transportation system, are candidates for on-orbit assembly. However, when a large wide-body booster is available, there are significant advantages to having a deployable space station assembled on Earth and transported into orbit intact or in a few large pieces. The United States will build the Space Station Freedom by the assembly method. Freedom's assembly is feasible, but a significant challenge, and it will absorb much of NASA's effort in the next 8 years.

The Space Station Freedom is an international program which will be the centerpiece of the free world's space activities in the late 1990's. Scientific information and products from the Space Station Freedom and its use as a transportation depot will advance technology and facilitate the anticipated manned space exploration surge to the Moon and Mars early in the 21st century.

IN-SPACE CONSTRUCTION AND DYNAMICS OF LARGE SPACE STRUCTURES

Martin M. Mikulas, Jr.
NASA Langley Research Center
Hampton, Virginia 23665-5225 USA

SUMMARY

In this paper, the types of equipment and structures that will be required to construct very large spacecraft in space are discussed. One of the basic issues that must be resolved is the appropriate mix of humans and machines in the construction process. While the use of robots offers the potential for reducing the number of Extra-Vehicular Activity (EVA) hours required for particular construction operations, the availability of humans greatly increases the reliability of complex construction tasks. A hybrid system is described which makes the best use of man and machine to provide a highly reliable and versatile construction approach. Such a system will provide an efficient method for constructing large spacecraft until fully automated, robotic devices can be perfected. Details are given on an extensive ground test program which was designed to evaluate and demonstrate large spacecraft construction. A discussion is presented on the use of the Space Station Freedom, or an appropriate derivative, as a construction facility. Finally, a construction scenario and assembly timelines are presented for constructing a 20-meter-diameter high precision reflector.

INTRODUCTION

Many new aggressive space missions are being considered which involve space components that are considerably larger than available launch vehicle payload volumes. Examples of these components are large support trusses for orbiting space stations, reflectors for deep space science studies, reflectors for earth environmental studies, large spacecraft for manned missions to Mars, and large, high-energy aerobrakes. The NASA Langley Research Center (LaRC) has conducted in-depth studies of the design and construction of such large space structures for the past 15 years (references 1-7). From these studies, the erectable structures concept emerged, whereby large truss structures such as platforms or curved reflectors are erected by astronauts or robots from individual struts and nodes. The compact stowage capability and high versatility of erectable structures is considered highly desirable however, they possess the disadvantage of requiring in-space assembly. Much of the research at LaRC over the past 15 years has been directed towards devising and demonstrating efficient methods for assembling hundreds, and perhaps thousands, of struts, nodes, and components into large spacecraft which would be impractical to achieve by other means. Studies have been conducted on techniques ranging from unaided EVA to fully automated assembly of large platforms (references 8, 9, and 10). Unassisted EVA was found to be inefficient for assembling large structures due primarily to the highly fatiguing translation required and the inability to hold a position at an assembly site due to the lack of foot restraints. Fully automated assembly, using dedicated assembly hardware, was found to be possible, however, this approach is still very much in the developmental stage.

A hybrid construction approach was developed, however, which eliminated the undesirable fatiguing aspects of unassisted EVA assembly. This provides mechanized foot restraints which rapidly and firmly position the astronaut at a workstation so that he can perform the detailed assembly tasks. It takes advantage of mechanization for the rapid and positive positioning functions required in construction, yet makes use of astronauts to conduct the actual joining operations which can be quite complex. The resulting construction approach has been demonstrated in numerous ground tests and in a flight test to be very efficient and reliable.

This paper will describe some of the major results of the research on erectable structures and how the construction approaches can be used to assemble large structures in space. NASA has chosen the erectable approach for assembling the Space Station Freedom and details will be given on the research that led to that decision. Current research is focused on extending the space station construction approach to the construction of large spacecraft required for a manned mission to Mars or to the Moon and on the construction of large, high precision reflectors which are needed for deep space science observations and earth environmental studies. An emphasis of this research is to

maintain a high degree of commonality in the spacecraft hardware and in the construction approaches to minimize expensive development programs.

UNAIDED ASTRONAUT CONSTRUCTION

The initial research in the construction of large space structures involved astronauts in an underwater neutral buoyancy simulator attempting to assemble elements of a large truss as shown in figure 1 (reference 9). In this test, the unaided astronauts were asked to assemble a simple tetrahedral segment of a large truss. The astronauts translated in a hand-over-hand fashion along the truss members and held themselves in position with one hand while constructing the truss with the other. The results of these tests indicated that unaided assembly operations, although achievable, were quite difficult and fatiguing.

MOBILE WORKSTATION

To circumvent the negative aspects of unaided construction, a mechanical device consisting of mobile foot restraints and a mechanized rail to translate the truss was conceived to assist the astronauts. The device is referred to as a mobile workstation in reference 11 and is shown being used in neutral buoyancy tests (simulated 0-g) in figure 2. The mobile workstation positioned the astronauts in foot restraints at a workstation which provided translation within a prescribed work envelope. Thus, the astronauts were relieved of fatiguing translation and were also provided with a mechanism to react forces and moments incurred during manipulation or assembly of the structural elements -- an extremely important feature. Working cooperatively, two astronauts were found to be very efficient building truss segments consisting of 6-meter-long struts. When completed, a segment of the truss was mechanically translated out of the work envelope to permit the addition of another segment or bay. This process was repeated until the desired structure was completed. Average unit assembly times of approximately 38 sec/strut were achieved from repeated tests.

SWING ARM BEAM ERECTOR (SABER)

Another version of a mobile workstation, presented in reference 12 and shown in figure 3, was configured to permit a single astronaut to assemble long booms using 2-meter-long struts. This device, referred to as a swing arm beam erector, moved a single astronaut around the beam and along its length a distance of one bay. After the astronaut assembled one bay of truss, the beam was mechanically translated to expose the next worksite. This procedure was repeated in an assembly line manner until the beam construction was completed. This construction approach permitted achieving unit truss assembly times of approximately 28 sec/strut.

ASSEMBLY CONCEPT FOR CONSTRUCTION OF SPACE STRUCTURES (ACCESS)

In November 1985, an erectable structures experiment was conducted on the Space Shuttle flight STS-25, described in reference 13. The beam assembled during this experiment is shown in figure 4. In this experiment, two astronauts were held in foot restraints while the beam was rotated and translated to present proper work positions. The complete 10 bay, 30-meter-long beam consisted of 96 individual struts and 30 joint clusters. The beam was assembled in 25 minutes, representing a construction rate of 16 sec/strut. This flight experiment, and the two previously discussed ground experiments, demonstrated that mechanically assisted astronaut operations can be a very efficient means for constructing large spacecraft trusses.

SPACE STATION

Truss Structure - Early in the design of the Space Station Freedom it became apparent that a truss structure would be required to separate the large solar arrays from the manned modules. The main reason for this requirement is to provide ample space for the space shuttle docking maneuvers and to minimize contamination of the arrays from the shuttle maneuvering thrusters. Various truss concepts were studied (see reference 14) and a trade study was conducted between deployable and erectable truss structures (see reference 15). The result of these studies was the selection of the 5-meter-deep erectable truss for the transverse boom of the Space Station Freedom shown in figure 5. The truss was designed with spherical nodes with multiple attachment points to permit complete, uninhibited three-dimensional growth in the future (see figure 6). The truss struts attach to the nodes with quick-attachment joints that are designed specifically for ease of assembly by astronauts (see figure 7). For example, the diameter of the joints was limited to 5 cm to permit effortless handling by the astronauts.

The 5-meter truss depth was a compromise between keeping the truss deep for stiffness and yet maintaining a size which was compatible with 4.2-meter-diameter space shuttle payloads. A major consideration in the design of the space station truss was maintaining high stiffness to minimize structural control interaction and to reduce structural response to random transient loadings. These dynamic considerations are discussed in detail in reference 16. An example of the benefit of high structural stiffness is shown in figure 8. This figure shows the results of an analysis that was conducted to investigate the effects of truss bending stiffness on the transient response of the space station. The dynamic model used in this study was a 100-meter-long transverse truss boom with 1500 Kg photovoltaic arrays at both ends and two manned modules in the center with a total mass of 40,000 Kg as shown in the upper left corner of figure 8. The truss was assumed to have 0.5 percent damping and was subjected to a transient load as shown in the upper right corner of figure 8. The two different truss depths (3-meter and 5-meter) which were studied covered the range of depths considered for a space station. The displacement results from this study are presented in a normalized form in the figure. These results indicate that the 5-meter-deep truss has about one-fourth as much displacement as the 3-meter-deep truss for the same force input. Also, as can be seen from the figure, the transient response damps out much quicker for the 5-meter truss for the same level of damping. This improved dynamic response for the deeper 5-meter truss was instrumental in its selection as the truss for the Space Station Freedom.

Space Station Construction - During the space station design process, the need was identified for a device that would support the astronauts performing EVA functions both for the initial station construction as well as for subsequent operations (references 15, 17, and 18). It was determined that this device, currently named the Mobile Transporter (MT), should possess mobility to transport men and materials (i.e., truss components, pressurized modules, payloads, etc.) around the space station as well as provide positioning foot restraints for the astronauts (see figures 9 and 10). The mobile transporter operates on mushroom-shaped guide pins which are provided on each truss node. The mobile transporter moves one bay at a time by sliding over the guide pins. It is propelled mechanically by a drawbar mechanism which pushes or pulls from an adjacent set of guide pins.

A primary function of the MT is to transport payloads and system components around the space station. Some of these components will be too large for astronauts to install without assistance. For example, during the space station construction process, large pressurized modules must be attached to the truss. A transposed shuttle remote manipulator system (RMS) or a similar space station RMS, as shown in figure 9, would be mounted on the mobile transporter base to assist in such operations.

Although the actual station construction process is still being developed, one construction approach considered is shown in figure 11. In this construction scenario, the truss structure is attached to the shuttle cargo bay and the MT moves out along the truss with the astronauts assembling the truss one bay at a time. A potential disadvantage to this approach is that the astronauts become positioned at some distance away from the warmth and safety of the shuttle cargo bay. An alternate approach being considered is one in which the MT is fixed to the cargo bay and the truss is mechanically sequenced out of the cargo bay as the construction of each truss bay is completed. In either case, the MT is a critical element in the station construction and provides a high degree of versatility and redundancy to the process.

MOBILE TRANSPORTER DEVELOPMENT AND TESTING

Langley Research Center (LaRC) has conducted considerable research into the development and testing of an MT concept as an aid for in-space construction of large spacecraft. The 5-meter erectable truss was selected as the space station baseline structure, on the basis of using a mobile transporter as part of an integrated construction and servicing system. The in-house LaRC research program in large space structures assembly over the past 4 years has been focused primarily toward the space station truss to demonstrate the utility of an MT and to provide a test device which could be used to examine structural assembly problems and provide realistic training to pressure-suited astronauts (see references 19 and 20). An MT laboratory test article, with limited capability, is shown in figure 12. This MT test article has an operable drawbar to index each bay of truss as it is completed and mobile foot restraints for each astronaut. The MT test article positions the astronauts with their heads toward the MT platform due to 1-g safety concerns. This is opposite to the preferred orbital orientation shown in the inset of figure 12. Relative motion between the MT and truss structure is accomplished by supporting the MT and moving the lower mass truss. A test program for this device is detailed in reference 19. This test program investigated use of the MT to erect several bays of space station truss structure, including installation of the utility trays.

Laboratory 1-g tests were initially conducted at LaRC to provide equipment operational checkout and establish assembly procedures. Although these tests did not simulate 0-g, they did provide valuable insight into proper assembly sequencing and expected timelines. The 1-g tests did not include installation of the utility trays, since they were quite heavy. The entire test apparatus was subsequently moved to Marshall Space Flight Center (MSFC) and installed in the Neutral Buoyancy Simulator (NBS) tank. A series of assembly tests were conducted, including installation of the utility trays. The underwater test setup with the trays in position attached to the truss is shown in figures 13a and 13b. Average assembly times of approximately 28 sec/strut were repeatedly obtained using well-trained engineers and astronauts to assemble three bays of truss. Installation of the deployable utility tray concept had a small influence on assembly time.

IN-SPACE CONSTRUCTION OF LARGE SPACECRAFT

Many of the proposed future space missions will require in-space construction of space spacecraft which are both large and massive. For example, a manned sprint mission to Mars would require two large vehicles; an unmanned cargo vehicle with a mass of several million kgm, and a manned sprint vehicle with a large amount of pressurized habitation volume. Similarly, establishing a manned lunar outpost will require large vehicles capable of ferrying cargo, people, and landers between Low Earth Orbit (LEO) and the moon. In addition to being large vehicles themselves, the components which make up the moon and Mars vehicles, such as aerobrakes, backbone trusses, landers, and pressurized habitation volumes will be large and massive. Unmanned missions, such as the Earth Observation Satellite (EOS) and Planetary Explorers, will require large precision structures (trusses, antennas, and telescopes), landers, sample return vehicles, and aerobrakes. The spacecraft required to accomplish many of these missions will be too large and massive to be placed in orbit by a single launch vehicle such as the space shuttle or even a heavy lift launch vehicle (see references 21 and 22). Successfully accomplishing these missions will require the capability to construct large structures in low earth orbit.

Affordable Missions Are Possible - A major impediment to pursuing bold new missions is the perceived ultra-high cost of constructing and operating large spacecraft in space. Due to their novel and one-of-a-kind nature, design and development costs dominate the total cost of current spacecraft. This is contrasted with civil engineering structures, where design and development represent less than 10 percent of the cost of large new structures. The major differences between these two approaches lies in the amount of off-of-the-shelf hardware used and the cost associated with construction. To make large spacecraft "affordable", two technological advances must be made. First, generic "off-of-the-shelf" building blocks, which can be used for many different large space structural systems, must be developed. As these basic building blocks are developed and matured through demonstrations, the verification costs of missions using these building block structures will decrease substantially. Second, an integrated in-space construction system, where the basic facility structural framework also serves as construction scaffolding, as well as a roadbed for construction aids, must also be developed. The integrated construction system must also provide an optimum balance of automated construction and EVA operations to maximize reliability.

Space Station as a Construction Facility - Space Station Freedom has been designed with all of the features necessary to be readily adapted into a completely integrated construction facility for large spacecraft. The 5-meter erectable space station backbone truss, in conjunction with the MT, was designed specifically to be used for such large-scale construction. The truss is not only expandable to meet all construction needs, but it can also serve as construction scaffolding and a vehicle hangar, as discussed in reference 21. By outfitting the MT with robotic end effectors, this combination would provide a complete capability for fully automated construction operations. Considerable experience for constructing large spacecraft will be gained when building the space station in the mid 1990's. By capitalizing on this experience and taking advantage of commonality with space station hardware, considerable cost savings could be realized in constructing future large spacecraft.

Dedicated Construction Facility - Although the space station would provide an excellent construction facility for other large spacecraft, the dynamic disturbances introduced during the construction process may not be tolerable. The space station will also be an experimental facility for a large number of continuous 0-g and observation experiments. If the disturbances are not acceptable for Space Station Freedom, a separate, special-purpose construction facility could be built using common space station hardware. Such a facility is shown in figure 14. This facility is built from the same 5-meter erectable truss hardware as Space

Station Freedom and would co-orbit with the space station to permit regular transfer of astronauts and equipment. The particular system shown in figure 14 was configured specifically for a large manned Mars vehicle. The truss shown in figure 14 is composed of 1800 individual struts and weighs about 20,000 pounds. Extra-vehicular activity (EVA) construction time for the truss alone would be on the order of 30 hours. The relatively short time required to construct the truss (disassembly time would be about the same) means that this facility could easily be reconfigured for other missions.

An important feature of this facility is the highly maneuverable space crane also shown in figure 14 (see reference 23). This space crane, which is 100 meters long, would be used to transfer and position spacecraft components and material from the shuttle cargo bay into the construction site for assembly into a large spacecraft (i.e., Mars vehicle). As with the construction facility truss, the space crane is constructed from the space station 5-meter struts. The rotary joint at the base is the same as the alpha rotary joint used on Space Station Freedom's transverse boom to track the sun. The MT is used to construct the crane in the same fashion that the space station truss was built. The MT is parked at the end of the crane and its 20-meter-long manipulator arm is used as an end effector. To minimize costs, commonality with space station hardware and procedures is maintained whenever possible. After use for a specific mission, the entire construction facility complex could be easily disassembled and restowed or reconfigured to meet the requirements of new missions.

HIGH PRECISION REFLECTORS

One future mission being studied which requires on-orbit spacecraft assembly due to its 20-meter-diameter size, is a submillimeter-astronomical laboratory shown conceptually in figure 15 and described in reference 24. This device incorporates a near optical quality reflector surface, made up of precise segment each of which is actively controlled to maintain overall accuracy. The active control system requires an accurate, stable and stiff foundation which is achievable through the use of a truss structure. A schematic of the geometry of such a reflector is shown in figure 16.

Reflector Assembly Method - The technique currently being examined for assembling the large, faceted truss reflector is shown in figure 17 and discussed in reference 20. A payload pallet, supporting a rotating spacecraft cradle, is shown in position at an appropriate location on the space station. The MT serves as a movable base, supporting and positioning astronauts to enable the assembly of struts, nodes and facets -- a supply of which is positioned nearby on the MT. As each "ring" of facets and supporting truss is added to the rotating assembly, the MT translates radially outward from the rotational center to permit the installation of the next ring. The cradle provides tilt, as well as rotation, to the reflector to maintain the construction site within reach of the MT and astronauts. The astronaut positioning capability of the MT is essential to efficiently assemble components of the reflector.

Reflector Assembly Time - The reflector structure shown in figure 16 contains 789 tubular struts, each approximately 2 meters in length; 198 nodes; and 90 precision hexagonal facets, approximately 2 meters in diameter. Based on past experience (references 12 and 13), the struts and nodes alone could be manually assembled in approximately 3.5 hours by two astronauts or in 6 hours by one astronaut. Installation of the 90 surface facets and an active control system wiring harness could add considerably to this time. Figure 18 shows estimated assembly times for the truss and facets as a function of the time required to install one facet and its associated wiring. The vertical estimation band (solid lines) for strut construction times is based on actual one-man and two-man test experience to date in either neutral buoyancy or on-orbit truss construction. It is noted that the orbital EVA assembly rate which was achieved during the ACCESS flight test using similar size struts (reference 13) was approximately the same as that achieved during neutral buoyancy tests. The horizontal estimation band (dashed lines) for panel installation time is the result of considering various EVA facet/wiring installation methods with or without RMS assistance, and estimating the installation time for each method. The overlapping bands bound the best estimate of EVA time required to assemble the reflector portion of this submillimeter astronomical laboratory.

As can be seen in figure 18, the fastest reflector assembly times are achieved with two astronauts without RMS facet installation assistance. It is also noted that EVA assembly of the truss, with a high part-count (789 struts and 198 nodes), requires only a fraction of the total assembly time (14 percent). The 90 reflector facets represent the smallest part-count, but due to their nature (size, complexity and fragility) require the majority of the estimated reflector assembly time (86 percent). Assembly times for other parts of the entire spacecraft will have to be added to the time

shown in figure 18 as designs and assembly techniques for these components are developed. These assembly times are estimates and need verification by neutral buoyancy tests.

CONCLUDING REMARKS

In this paper, the types of equipment and structures that will be required to construct very large spacecraft in space are discussed. Although considerable research has been conducted on developing various structures for space, very little effort has been applied to the development of on-orbit construction methods. One of the basic issues that must be resolved is the appropriate mix of humans and machines in the construction process. While the use of robots offers the potential for reducing the number of EVA hours required for particular construction operations, the availability of humans greatly increases the reliability of complex construction tasks. A hybrid system is described which makes the best use of man and machine to provide a highly reliable and versatile construction approach. Such a system will provide an efficient method for constructing large spacecraft until fully automated, robotic devices can be perfected. Details are given on an extensive ground test program which was designed to evaluate and demonstrate large spacecraft construction. The results of these tests have shown that large spacecraft can be rapidly and reliably constructed.

The Space Station Freedom has incorporated all of the basic design characteristics to permit its growth into an in-space construction facility for constructing very large spacecraft. However, since numerous 0-g and precision pointing experiments are onboard the station, a dedicated, co-orbiting construction facility may be required. Such a facility is described which could be built using truss hardware and systems previously developed for the Space Station Freedom program. The facility includes a 100-meter-long space crane which is used to position and assist in the construction of large spacecraft components.

An in-space construction scenario is presented for a 20-meter-diameter high precision faceted reflector. It is estimated that this reflector, which consists of 789 truss struts and 90 reflector facets, can be constructed in-space in about 30 EVA hours using the appropriate construction aids on the Space Station Freedom.

REFERENCES

1. Harold G. Bush and Martin M. Mikulas, Jr.: A Nestable Tapered Column Concept for Large Space Structures, NASA TM X-73927, 1986.
2. Martin M. Mikulas, Jr.; Harold G. Bush; and Michael F. Card: Structural Stiffness, Strength, and Dynamic Characteristics of Large Tetrahedral Space Truss Structures, NASA TM X-74001, 1987.
3. Harold G. Bush; Martin M. Mikulas, Jr.; and Walter L. Heard, Jr.: Some Design Considerations for Large Space Structures, AIAA Journal, Vol. 16, No. 4, April 1978, pp. 352-359.
4. Walter L. Heard, Jr.; Harold G. Bush; Joseph E. Walz; and John J. Rehder: Structural Sizing Considerations for Large Space Platforms, Journal of Spacecraft and Rockets, Vol. 18, No. 6, November - December 1981, pp. 556-564.
5. John M. Hedgepeth: Critical Requirements for the Design of Large Space Structures, NASA CR-3484, 1981.
6. Martin M. Mikulas, Jr. and John T. Dorsey: An Integrated In-Space Construction Facility for the 21st Century, NASA TM-101515, 1988.
7. Walter L. Heard, Jr.; Harold G. Bush; and Judith J. Watson: Space Truss Construction Studies, ASCE "Space 88 - Engineering, Construction, and Operations in Space" Conference, Albuquerque, NM, August 29-31, 1988.
8. G. G. Jacquemin; R. M. Bluck; G. H. Grolbeck; and R. R. Johnson: Development of Assembly and Joint Concepts for Erectable Space Structures, NASA CR-3131, 1980.
9. Lawrence J. Bement; Harold G. Bush; Walter L. Heard, Jr.; and Jack W. Stokes, Jr.: EVA Assembly of a Large Space Structure Element, NASA TP-1872, 1981.

10. Marvin D. Rhodes; Ralph W. Will; and Marion A. Wise: A Telerobotic System for Automated Assembly of Large Space Structures, NASA TM-101518, 1989.
11. Walter L. Heard, Jr.; Harold G. Bush; Richard E. Wallsom; and J. Kermit Jensen: A Mobile Work Station Concept for Mechanically Aided Astronaut Assembly of Large Space Trusses, NASA TP-2108, 1983.
12. Judith J. Watson; Walter L. Heard, Jr.; and J. Kermit Jensen: Swing-Arm Beam Erector (SABER) Concept for Single Astronaut Assembly of Space Structure, NASA TP-2379, 1985.
13. Walter L. Heard, Jr.; et al: Results of the ACCESS Space Construction Shuttle Flight Experiment, AIAA Space Systems Technology Conference, San Diego, June 9-12, 1986.
14. Martin M. Mikulas, Jr.; et. al.: Space Station Truss Structures and Construction Considerations, NASA TM-86338, July 1984.
15. Martin M. Mikulas, Jr.; et. al.: Deployable/Erectable Trade Study for Space Station Truss Structures, NASA TM-87573, July 1985.
16. Thomas R. Sutter; Paul A. Cooper; and John W. Young: Dynamics and Control Characteristics of a Reference Space Station Configuration, AIAA SDM Special Space Station Symposium, AIAA Paper No. 88-2485, Williamsburg, VA, April 21-22, 1988.
17. Martin M. Mikulas, Jr.; et. al.: A Manned-Machine Space Station Construction Concept, NASA TM-85762, 1984.
18. Harold G. Bush; Martin M. Mikulas, Jr.; Richard E. Wallsom; and J. Kermit Jensen: Conceptual Design of a Mobile Remote Manipulator System, NASA TM-86262, 1984.
19. Walter L. Heard, Jr.; et. al.: Results of EVA/Mobile Transporter Space Station Truss Assembly Tests, NASA TM 100661, November 1988.
20. Harold G. Bush; Mark S. Lake; Judith J. Watson; and Walter L. Heard, Jr.: The Versatility of a Truss Mounted Mobile Transporter for In-Space Construction, NASA TM-101514, November 1988.
21. Martin M. Mikulas, Jr. and John T. Dorsey: An Integrated In-Space Construction Facility for the 21st Century, NASA TM-101515, November 1988.
22. William M. Cirillo; Martin J. Kaszubowski; J. Kirk Ayers; Charles P. Llewellyn; Deene J. Weidman; and Barry D. Meredith: Manned Mars Mission Accommodation - Sprint Mission, NASA TM-100598, April 1988.
23. M. M. Mikulas, Jr.; R. C. Davis; and W. H. Greene: A Space Crane Concept: Preliminary Design and Static Analysis, NASA TM-101498, November 1988.
24. Timothy J. Collins and W. B. Fichter: Support Trusses for Large Precision Segmented Reflectors: Preliminary Design and Analysis, NASA TM-101560, March 1989.

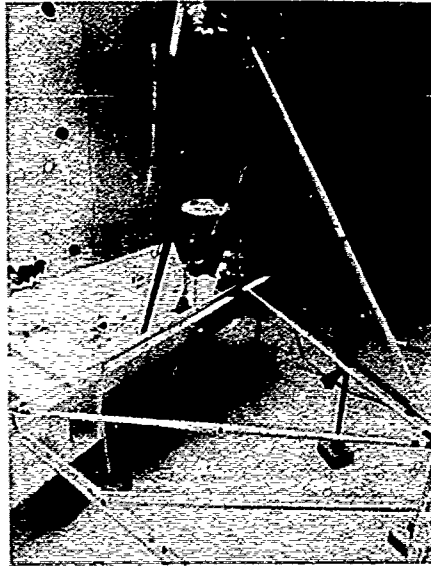


Figure 1. Unaided astronaut construction of a tetrahedral truss in a neutral buoyancy facility.

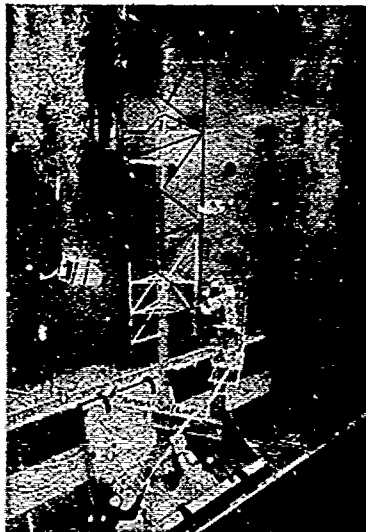


Figure 3. Machine assisted astronaut construction of a long truss beam in a neutral buoyancy facility.

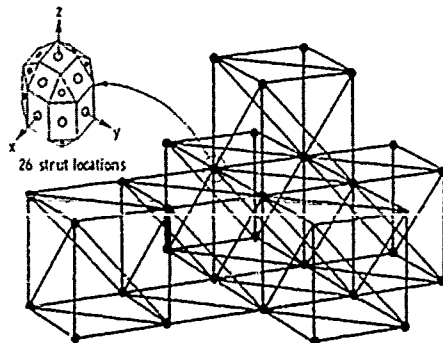


Figure 6. Schematic of space station truss and node showing 3-dimensional growth capability.

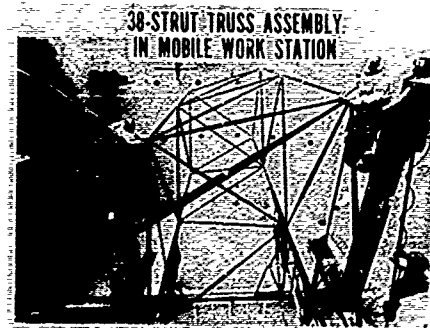


Figure 2. Machine assisted astronaut construction of a tetrahedral truss in a neutral buoyancy facility.

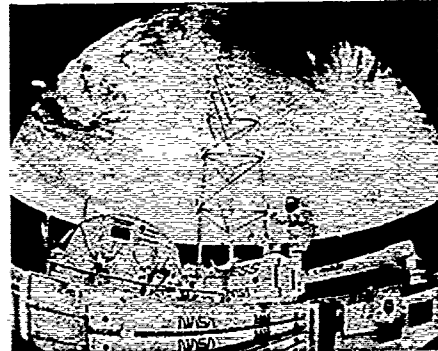


Figure 4. In-space flight experiment of astronaut construction of a long truss beam aboard STS-25.

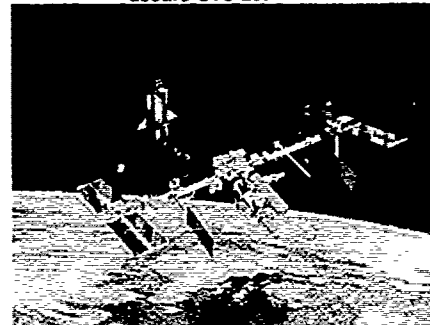


Figure 5. Artist rendering of the Space Station Freedom.

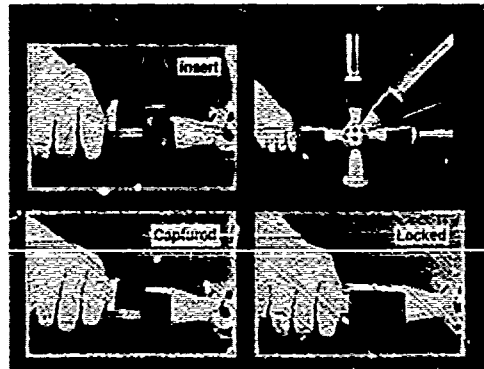


Figure 7. Quick attachment joint used for assembly of space station truss.

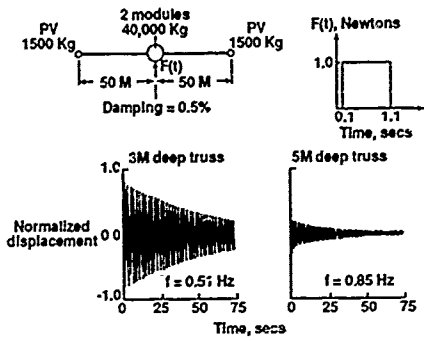


Figure 8. Effect of truss bay size on transient response of truss beam.

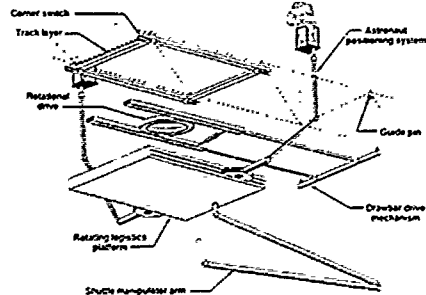


Figure 10. Mobile Transporter elements (exploded view).

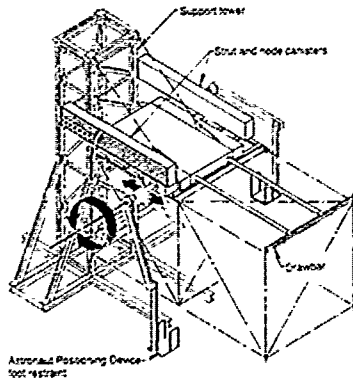
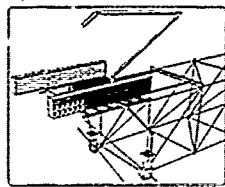


Figure 12. Schematic of Mobile Transporter 1-g mock-up.

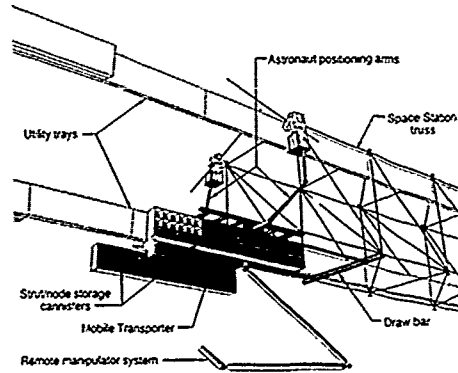


Figure 9. Mobile Transporter configured for space station truss construction.

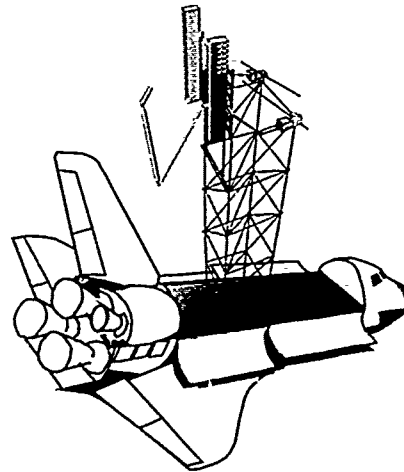


Figure 11. Initiation of space station construction out of shuttle cargo bay.



Figure 13a. First truss bay being constructed with Mobile Transporter in underwater neutral buoyancy simulation tests.

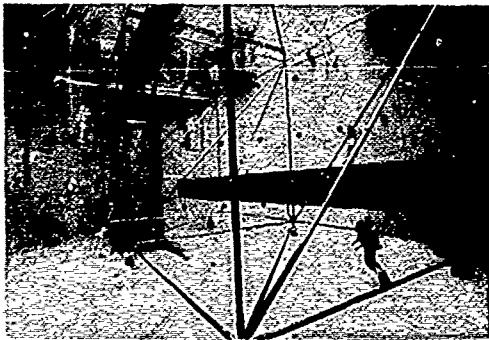


Figure 13b. Three truss bays completed in neutral buoyancy simulation tests.



Figure 15. 20-meter-diameter submillimeter astronomical observatory.

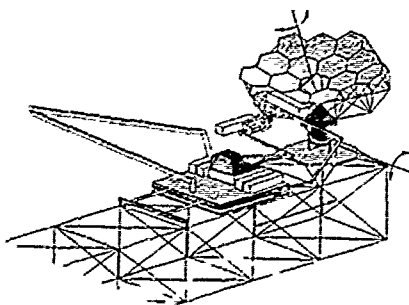


Figure 17. Construction of truss reflector from Mobile Transporter.

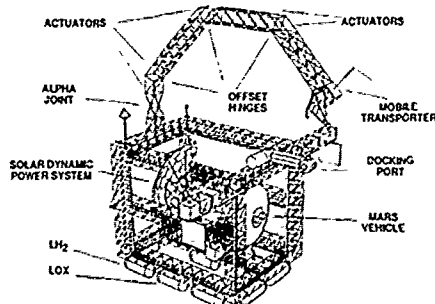


Figure 14. In-space construction facility with a space crane

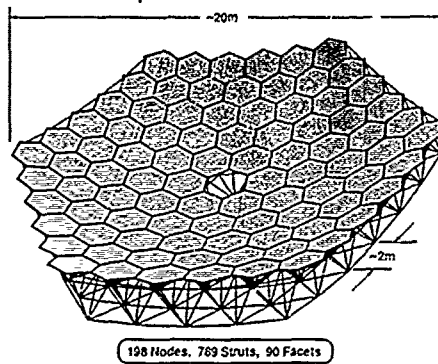


Figure 16. Geometry of precision segmented reflector for submillimeter astronomical laboratory.

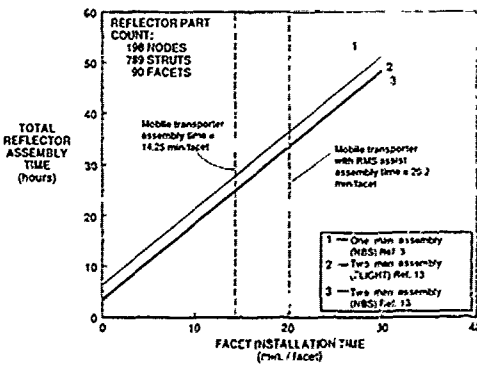


Figure 18. Estimated construction time for 20-meter-diameter reflector.

A NEW METHOD FOR A TETHERED SYSTEM AIDED SPACE STATION ASSEMBLY

by

Salvatore Ciardo* and Silvio Bergamaschi*
Aeritalia SAIPA, Space Systems Group
Corso Marche 41, 10146 Torino, Italy

ABSTRACT

During the Space Station Freedom building phase (i.e., from the 2nd to the 16th dedicated Shuttle flight) the major assembled item will be the main truss. A characteristic of such a physical body is that one of the principal moments of inertia is much smaller than the two others. Due to the gravity gradient torques, the stable equilibrium configuration is that with the minimum inertia aligned with the local vertical (yaw). Nevertheless, due to some user requirements, the planned building sequence imposes the same axis be pointed toward the pole of the orbit plane (pitch), in a configuration unstable at least in roll-yaw. Therefore, the Attitude Control System (ACS) has to be designed in such a way as to counteract the gravity gradient effects as well as the relatively small environment perturbing torques.

The study presented here (performed by Aeritalia under an ASI contract) was aimed at the investigation of the dynamic behavior of a system whose moments of inertia are substantially altered by means of the displacement of a certain amount of additional mass connected to the S.S. Freedom by means of one or two tethers. In this new configuration, the gravity gradient torques act on the whole system as restoring ones. This stabilization method has the fundamental advantage of being simple, low-cost and, at least in principle, passive, thus preventing the expense of the amount of energy required by an active control system.

The expected benefits and the potential disadvantages of the method will be discussed. The configuration selection (i.e., the two options, single or double tethered system) rationales will be analyzed, especially taking into account the operational aspects. A description of the relevant assumptions of the adopted dynamic model and an analytical deduction of the stability criteria shall be given. The results of an ad hoc developed computer program will be shown. The dynamic response of the system during non-nominal operative conditions (e.g., shuttle docking, tether imbalance, sudden tether cut) have been analyzed in order to provide a complete assessment. The additional disturbance to the station attitude both due to the presence of the tethered system and to the probability that the tether is severed by micrometeoroids or man-made debris will be computed. The analyses performed thus far, show that the method guarantees the stability around pitch and, properly sizing the involved physical-geometrical tethered parameters, the stability around roll-yaw.

In addition, during the building phase numerous substantial changes in the moments of inertia of the S.S. Freedom are planned. In these cases, the approach discussed in this paper permits a very versatile intervention strategy. In fact, it will be shown that a new stable configuration can be achieved by adjusting the tether length, the ballast mass or the length of the deployer boom. Since no critical areas have yet been identified, the approach can be judged highly feasible.

INTRODUCTION

The rationale for the current configuration of the S.S. Freedom is to provide an improved location for microgravity laboratories and for Earth and sky observation. Unfortunately, when using standard stability techniques for a rigid body the inertia ratios are such that the Freedom becomes unstable in roll-yaw due to the presence of the gravity gradient torque. This, in turn, penalizes the Attitude Control System (ACS) in terms of energy and fuel to balance the effect.

This aspect is even more critical during the assembly phase (i.e., between the 2nd and 17th dedicated Shuttle flight) when the major component of the structure, the main truss, has one of the principal moments of inertia (pitch) much smaller than the two others (roll and yaw), in a very unstable configuration.

Operational and fuel budget constraints suggest adoption of passive or, at least, semi-passive solutions which are simple, relatively low-cost and capable of minimizing the dynamic noise of the gyros on the microgravity experiments.

In principle, an appealing way to satisfy all these requirements would be a tethered system able to produce an additional stabilizing gravity gradient torque. The tethered system can be helpful even when the station has reached its definitive configuration. In fact, at that point it might be utilized to perform other activities, such as the active control of the center of gravity position in the microgravity laboratories.

(*) Now with Space Software Italia SpA (SSI)
(#) University of Padua

The purpose of this paper is the investigation of the performance of such a means of attitude control. The relevant literature shows that several configurations of the tethered system could be considered. However, only the simplest ones (i.e., those with one or two tethers) will be analyzed here.

A good solution in terms of simplicity, low cost and minimum interface with the Freedom appears to be the configuration with only one tether. In fact, the promise of this solution was demonstrated by showing that tethered ballast mass can stabilize the station, at least, in pitch, if a proper lever arm acting along the yaw axis is applied in order to improve the restoring gravity gradient torque value.

However, a serious limitation of the one-tether configuration is due to its inherent geometrical requirement: the tether attachment point to the Freedom must be located on the local vertical passing through its center of mass, thus avoiding static gravity gradient torque which disturbs the horizontal equilibrium. Unfortunately, the area around this point is the focus for a variety of operations, including Shuttle docking and EVA.

The second handicap is the displacement of the center of mass (c.o.m.) of the whole structure toward the ballast mass that deteriorates the static microgravity quality level in the laboratories. An obvious alternative configuration would be a double-tethered system with the following major features:

- a) equal tethered end-masses deployed one upward and one downward;
- b) equal tether lengths;
- c) attachment points located in an adequate symmetrical position with respect to the out-of-plane positions, far from the geometrical center of the station. Apart from any consideration about the stability problem which will be discussed later, such a configuration is of static equilibrium and nullifies both the resultant gravity gradient force and torque supplied by tethers.

In regard to the displacement of the attachment points discussed in point c) above, if one takes into account the horizontal attitude of the Freedom, the most logical solution appears to be the one with the offset chosen along the pitch axis. However, several other candidate solutions will be analyzed in depth.

THE MATHEMATICAL MODEL

The problem of modeling the proposed tethered system is quite complex for a variety of reasons. In fact, even ignoring aspects such as tether elasticity or the perturbations on the Freedom's orbit, a complete mathematical model simulating its rotational dynamics and the two tethered masses would be a system with 7 degrees of freedom. A step-by-step approach has been adopted in order to give an assessment of the relative merits of the solution and a judgement of feasibility. Even if at a conceptual level, the first step must employ an analytical approach in which the equations of motion are linearized based on the assumption that both angular displacements of the Freedom and the librations of the tether system/s are low enough.

As a second step, an ad hoc model has been developed. Thus, some reasonable simplifying hypotheses have been adopted, in order to gradually gain insight into several aspects of the problem:

- the S.S. Freedom is a rigid asymmetric body rotating on a circular unperturbed orbit;
- the S.S. Freedom is also equipped with control moment gyros; the only external torques taken into account are those originated by the gravity gradient;
- the actions of the tethered masses are simulated as external forces. This is actually quite restrictive because it means ignoring the librations of the tethers. On the other hand, just the coupling of the tether dynamics and the Freedom's stability substantially expands the dimensions of the simulation system.
- the tethers are rigid and massless
- the c.o.m. of the whole structure is coincident with the c.o.m. of the Freedom which is reasonably true in the case of the double-tethered system.

Referring to Fig. 1^(*), let $(0, \bar{e}_1, \bar{e}_2, \bar{e}_3)$ be the orbital reference frame with its origin at the Freedom's c.o.m., \bar{e}_1 parallel to ascending local vertical, \bar{e}_2 along the orbital velocity and \bar{e}_3 toward the pole of the orbit. Let $(0, \bar{a}_1, \bar{a}_2, \bar{a}_3)$ also be the principal inertia system of the Freedom with principal moment of inertia I_1, I_2, I_3 . The rotation sequence is shown in Fig. 1 where $\theta_1, \theta_2, \theta_3$ are the yaw, roll and pitch angle respectively.

To describe the attitude of the station the equations of motion used are those commonly employed for a simple gyrost consisting of a rigid body and an axisymmetric rotor whose axis and mass center are fixed in the rigid body frame.

A series of simplifying assumptions have been adopted for the scope of this preliminary assessment:

- because the axis of minimum inertia moment of the main truss is directed toward the orbit normal, it has been assumed that the rotor axis is directed along the same direction;
- the angular velocity of the rotor has been assumed constant, based on its being motor-driven (σ);
- the external torque is the sum of two parts, the gravity gradient torque and the control torque provided by the tethered systems. Therefore, in our case, the equations of motion are:

(*) See Figures and Tables at end of paper

$$\begin{aligned}
 I_1 \dot{\omega}_1 &= (I_2 - I_3) \omega_2 \omega_3 - J \sigma \omega_2 + M_{\sigma 1} + M_{t1} \\
 I_2 \dot{\omega}_2 &= (I_3 - I_1) \omega_1 \omega_3 + J \sigma \omega_1 + M_{\sigma 2} + M_{t2} \\
 I_3 \dot{\omega}_3 &= (I_1 - I_2) \omega_1 \omega_2 + M_{\sigma 3} + M_{t3}
 \end{aligned} \tag{1}$$

where ω is the angular velocity of the station and M_g and M_t are respectively the gravity gradient torque and the torque provided by the tethered system. The components of the gravity gradient torque are:

$$\begin{aligned}
 M_{\sigma 1} &= 3n^2(I_2 - I_3) \cos \theta_2 \sin \theta_3 \sin \theta_2 \\
 M_{\sigma 2} &= -3n^2(I_3 - I_1) \cos \theta_2 \cos \theta_3 \sin \theta_2 \\
 M_{\sigma 3} &= 3n^2(I_1 - I_2) \cos^2 \theta_2 \cos \theta_3 \sin \theta_3
 \end{aligned} \tag{2}$$

Considering that the tether attachment points are far from the c.o.m., both direction and magnitude of the gravity gradient forces acting on the displaced masses must be determined. Referring to Fig. 2, the component along the local vertical is:

$$F_{\sigma z} = 3n^2 z m \tag{3}$$

where z is the relative displacement. The component along the out-of-plane direction is:

$$F_{\sigma y} = -n^2 y m \tag{4}$$

y being the relative displacement. The component along the in-plane direction is zero. The equilibrium condition for the tethered mass is:

$$F_{\sigma x-l} + F_{\sigma y-l} = 0 \tag{5}$$

or:

$$3n^2(z+d) \sin \phi - n^2(b-l \sin \phi) \cos \phi \tag{6}$$

where l is the tether length, ϕ is the tilt angle, b the offset along the truss and d the lever arm length. It can be pointed out that the tilt angle ϕ is very small due to the ratio between b and l .

Summing up, the force acting on the station can be written as:

$$\bar{F}_g = mn^2[3(l\cos\phi + d)\bar{e}_1 - (b - l\sin\phi)\bar{e}_3] \quad (7)$$

The in-plane offset of the tether attachment point does not affect the gravity gradient torque.

In order to assess the correct expression of the torque applied to the station by the tethered masses, a distinction between single or double tethered systems is necessary.

As mentioned before, the one-tether solution imposes the requirement of having the attachment point on the same local vertical of the c.o.m. of the station. Moreover, a boom is essential to exploit the force produced by the gravity gradient as restoring torque. This torque is:

$$\bar{M}_t = -3mn^2 d(d+l)(\theta_2 \bar{a}_2 + \theta_3 \bar{a}_3) \quad (8)$$

The two-tether configuration offers more flexibility. The advantages are evident: the torque is zero in the configuration of equilibrium and no static acceleration is induced. The attachment points can be moved anywhere on the space station. Even if locations around the end of the main truss seem to be the best, at least in terms of simplicity, no particular a priori reason inhibits the moving of the attachment points along the roll axis.

In principle, the transversal dimension of the main truss could provide the required lever arm, but a previous assessment (2) shows that a longer external boom (about 10 m) allows the stability goal to be achieved with a relatively short tether and a sufficiently light ballast mass. If the two tethered systems are assumed to be located in proximity to the joint (at distance b from the c.o.m.) the expression for the applied torque is:

$$\bar{M}_t = 2mn^2 \{3/4b^2\theta_1 \bar{a}_1 + [3/4b^2 - 3d(d+l)]\theta_2 \bar{a}_2 - 3d(d+l)\theta_3 \bar{a}_3\} \quad (9)$$

(9) can be reduced to (8) if the conditions $b \rightarrow 0$ and $d \ll l$ are applied.

PRELIMINARY STABILITY ANALYSIS

Linearizing the equations (2) and introducing (9) in the (1) the equations of angular motion of the station, become:

$$\ddot{\theta}_1 + [-n(1+K_1) + J/I_1 \sigma] \dot{\theta}_1 + (-K_1 n^2 + J/I_1 \sigma n - 3/(2I_1) mn^2 b^2) \theta_1 = 0$$

$$\ddot{\theta}_2 + [n(1-K_2) - J/I_2 \sigma] \dot{\theta}_2 + \{4K_2 n^2 + J/I_2 \sigma n - 6mn^2 l_2 [b^2/4 - d(d+l)]\} \theta_2 = 0$$

$$\ddot{\theta}_3 + 3n^2 [-K_3 + 2/I_3 md(l+d)] \theta_3 = 0 \quad (10)$$

where:

$$K_1 = (I_2 - I_3)/I_1; K_2 = (I_3 - I_1)/I_2; K_3 = (I_1 - I_2)/I_3 \quad (11)$$

(10) can be considered of general application, due to the presence of both the control moment gyros and the double tethered configuration effects. For simplicity of notation, system (10) can be rewritten as:

$$\begin{aligned}
 \ddot{\theta}_1 + \alpha_{11} \theta_1 + \alpha_{12} \dot{\theta}_2 &= 0 \\
 \ddot{\theta}_2 + \alpha_{22} \theta_2 + \alpha_{21} \dot{\theta}_1 &= 0 \\
 \ddot{\theta}_3 + \alpha_{33} \theta_3 &= 0
 \end{aligned}
 \tag{12}$$

where the known features of the gravity gradient stabilization can be recognized. In fact, pitch is uncoupled with roll-yaw. The condition for stability in pitch is:

$$2md(l+d) > (I_1 - I_2) \tag{13}$$

If one keeps in mind the truss configuration where I_y is more or less equal to I_r , it is easy to satisfy this condition using a relatively short tether and/or small masses.

Roll-yaw stability requires that the roots of the characteristic equation:

$$s^4 + (\alpha_{11} + \alpha_{22} - \alpha_{12}\alpha_{21}) + s^2 + \alpha_{11}\alpha_{22} = 0 \tag{14}$$

where s is a complex number, have to be negative. In turn, the following inequalities must be satisfied:

$$\begin{aligned}
 \alpha_{11}\alpha_{22} &> 0 \\
 \alpha_{11}\alpha_{22} - \alpha_{12}\alpha_{21} &> 2(\alpha_{11}\alpha_{22})^{1/2}
 \end{aligned}
 \tag{15}$$

For an initial analytical approach, some simplifying assumptions are sufficient:

$$I_1 \approx I_2 \approx I, I_3 \ll I \rightarrow K_1 = 1, K_2 = -1 \tag{16}$$

$$b \ll l, d \ll l \rightarrow d(d+l) \approx dl$$

and then terms depending on b^2 are ignored.

If the control moment gyros are not active, the first of (15) gives:

$$mdl < 2I/3 \tag{17}$$

whereas the second gives the further condition:

$$mdl > I/2 \tag{18}$$

Thus, the final roll-yaw stability condition is:

$$I < 2mdl < 4/3I \tag{19}$$

An equivalent expression for the one-tether configuration can be found, simply using a double value of the product mdl .

Based on NASA data, a possible strategy for station assembly was hypothesized in order to have some figures for the major parameters needed to verify the stability of the station. Table 1 summarizes them for three different configurations after, respectively, the 2nd, the 6th and the 11th dedicated Shuttle flight. Based on this table, it is evident that condition (16) was a reasonable assumption. Quantitatively, assuming an average value for these two principal moments of inertia, the conditions of stability capable of satisfying (13) and (19) can be found. They are summarized in the last column of Table 1, where the range of the tether lengths which satisfy, in particular, (19) are shown. In fact (19) and (13) demonstrate that stability depends on the value of the product model not on its individual factors, thus increasing the system flexibility. In principle, once the boom length has been fixed, it is conceivable to change both m and l , but it seems more practical to increase l . Following this rationale, the values of the last column of Table 1 have been obtained assuming, respectively, for the three Shuttle flights:

$$\begin{aligned} \text{2nd : } I &= 3.1 \cdot 10^7 \text{ kg m} >> \\ \text{6th : } I &= 3.65 \cdot 10^7 \text{ kg m} >> \\ \text{11th : } I &= 9.8 \cdot 10^7 \text{ kg m} >> \end{aligned}$$

Moreover, the tethered mass value and the boom length have been assumed to be, respectively, 1000 kg and 10 m.

Looking at the results of the analytical approach it seems that the following conclusion can be stated: the same tether length can satisfy the stability condition for quite a long period.

Unfortunately, the results obtained with the computer program utilized change this scenario a little. In fact, with the same assumption, the tether length has been used parametrically in the range of stability, in accordance with (19). It has been assumed that the system was out of nominal condition due to an angular displacement in roll of 1 degree. The results obtained are shown in Fig.'s 3 and 4. When the tether length is around the lower bounds of the range (1500 m) a certain further angular displacement has to be reached before the tether systems begin to act as restoring components. On the contrary, when the tether length is around the upper limit the reaction is practically immediate and the phenomenon results bounded within the initial value of the disturbance. It is worthwhile to point out that no dumping effects have been taken into account, so the obtained results are, in this respect, conservative. In the same figures the behavior of the tethered system, in both the in-plane and out-of-plane components, are shown and their weak coupling with the station attitude is understandable.

On the other hand, a high level of accordance with the results of the analytical approach were found in terms of the identified stability range. Fig.'s 5 and 6 show that for length higher or lower than that previously shown in the table, the dynamic behavior of the system is unstable.

The assessment of the roll-yaw frequencies can be given too, by using an analytical approach. With the same above-adopted assumptions, (15) can be rewritten as:

$$\omega^4 - n^2(\beta - 1)\omega^2 - n^4(\beta - 4) = 0 \quad (20)$$

where:

$$\omega^2 = -s^2, \beta = 6mdl/l \quad (21)$$

The condition (19) now has the form:

$$3 < \beta < 4 \quad (22)$$

The roots of the equation (20) are coincident and equal to the mean motion n (in case $\beta = 3$) or one drops to zero while the other is equal to $\sqrt{3}n$ (in case of $\beta = 4$). In the intermediate cases, one of the frequencies is less than the mean motion, while the others range from n to $\sqrt{3}n$. As a quantitative example, if the value of β is $7/2$ the two characteristic periods are:

$$T_1 = 11900 \text{ sec and } T_2 = 3700 \text{ sec}$$

The numerical approach has completely confirmed these results. For a cost/benefit analysis, the amount of angular momentum that must be stored in the c.m.g.'s must be assessed. (20) is rewritten dropping the components due to the tethered system. In this case the coefficients of (15) are:

$$\begin{aligned}
 \alpha_{11} &= -n^2 + \alpha n^2 \\
 \alpha_{12} &= -2n + \alpha n \\
 \alpha_{21} &= -\alpha_{12} \\
 \alpha_{22} &= -4n^2 + \alpha n^2
 \end{aligned}
 \tag{23}$$

where:

$$\alpha = (J\sigma)/(In) \tag{24}$$

The characteristic equation is again (15) and both (16) must be satisfied. The first condition expressed by (16) is satisfied if:

$$\alpha < 1 \quad \text{or} \quad \alpha > 4 \tag{25}$$

while the second corresponds to:

$$\begin{aligned}
 \alpha_{11} + \alpha_{22} + \alpha_{12}^2 &> 0 \\
 (\alpha_{11} + \alpha_{22} + \alpha_{12}^2) &> 4\alpha_{11}\alpha_{22}
 \end{aligned}
 \tag{26}$$

The first of (26) gives:

$$\alpha > 1 + \sqrt{2} \quad \text{or} \quad \alpha < 1 - \sqrt{2} \tag{27}$$

while the second implies the solution of the fourth order algebraic equation:

$$P(\alpha) = \alpha^4 - 4\alpha^3 - 2\alpha^2 + 24\alpha - 15 > 0 \tag{28}$$

which is positive for

$$\alpha < -2.35 \quad \text{or} \quad \alpha > 0.72 \tag{29}$$

Thus, the stability conditions are:

$$\alpha < -7/3 \quad \alpha > 4 \tag{30}$$

or:

$$J_0 < -7/3 I_n \quad \text{or} \quad I_\sigma > I_n \tag{31}$$

In regard to the value of Table 1, this means that, after, for example, the 11th Shuttle mission the amount of the angular momentum that has to be stored in the c.m.g.'s must be larger than about $2.6 \cdot 10^5$ kg/sec.

ATMOSPHERIC DRAG TORQUE

The biggest continuous external disturbance exerted on the space station is the torque due to atmospheric drag. The drag force has the form:

$$\bar{F}_o = -1/2 C_D A \bar{v} |\bar{v}| = F_o \bar{e}_2 \quad (32)$$

where \bar{v} is the velocity along the flight direction. If $P(x,y,z)$ is the center of pressure in the principal system of inertia of the space station, the drag force is:

$$\bar{M}_o = \bar{F}_o \{ \bar{e}_2 \times [x \bar{\alpha}_1 + y \bar{\alpha}_2 + z \bar{\alpha}_3] - [(z + \theta_1 y) \bar{\alpha}_1 - (\theta_1 x + \theta_3 z) \bar{\alpha}_2 + (\theta_3 y - x) \bar{\alpha}_3] \} \quad (33)$$

and the new dynamic equations are similar to (10) plus the terms which come from (33). In the configuration of static equilibrium the angles are:

$$\begin{aligned} \theta_1 &= -F_o z / (-K_1 n^2 J + J \sigma n - F_o y) \\ \theta_2 &= -F_o (x \theta_1 + z \theta_3) / (4K_2 n^2 + J \sigma n + 6m n^2 d l) \\ \theta_3 &= -F_o x / (-3K_3 n^2 I_3 + 6m n^2 d l - F_o y) \end{aligned} \quad (34)$$

A preliminary assessment of the involved parameters is summarized in Table 2, where a double tether system has been analyzed with the above-used x,y,z parameter values obtained from a NASA source. The values of the angles were obtained without inclusion of inertial wheel effects. They appear well within the dead band of the Freedom's attitude control system.

The role played by the tethered masses can be seen as follows: θ_1 is not affected by the tethered system and the main restoring yaw torque is provided by the Freedom's gravity gradient. θ_2 is negligibly small and depends on the other two angles. θ_3 depends on the other two angles. θ_3 is small enough, as can be seen in Table 2, due to the tether effect. In fact, the first term of the denominator of the last of (34) is low due to the above discussed low value of the term:

$$K_3 I_3 = I_1 - I_2 \quad (35)$$

and thus θ_3 can be reduced to the desired value "timing" the terms due to the tethered masses gravity gradient.

Fig. 7 shows the behavior of the station in roll-yaw when the terms due to atmospheric drag are included.

A number of out-of-nominal conditions have been analyzed: Shuttle docking, tether imbalance and sudden configuration change due to tether cut. These conditions do not appear to be particularly critical for the system. Even when the tether is cut by micrometeoroids or debris (the probability of this occurrence can be reduced by properly sizing the tether diameter), the time available to intervene by means of a backup control system is quite long (see Fig. 8).

CONCLUSIONS

In the paper, attention has been focused on the attitude stability of the S.S. Freedom by means of tethered systems. The results of the analysis of the linearized equation system demonstrate that the concept deserves further attention. Proper values of the product m.d.l. can ensure the stability of the station attitude both in pitch and in roll-yaw. The basic model simulates a rigid station subject to a number of external torques, the actions of the tethers being one of them.

Preliminary analytical results are encouraging and a preliminary assessment, done by means of an ad hoc program, confirm the usefulness in continuing the investigation of the concept. The results can be summarized as follows:

- a) Tethered systems can stabilize the angular degrees of freedom of the space station if properly sized
- b) The impact on space station operations is acceptable if the configuration with two tethers is adopted.
- c) Tether breakage, which can cause extreme shifts in the station's attitude, impose the need for an active control system aboard as backup.
- d) Perturbing effects are well within the attitude requirements.

REFERENCES

- [1] Colombo G. - A New Tethered Platform Space Station Concept, *S.A.O. Final Report in fulfillment of Contract G 82678-3286*, October 1983.
- [2] Bergamaschi S., Lucchetti S., Bevilacqua F. - Some Evaluations of the Attitude Stability of a Class of Tethered Space Station, *Proceedings of the 25th Convegno Internazionale Sullo Spazio*, Rome, March 1985.
- [3] Kaplan M. - Modern Spacecraft Dynamics and Control, *John Wiley & Sons*, New York, July 1986.
- [4] Kane T., Likins P., Levinson D. - Spacecraft Dynamics *McGraw Hill*, New York 1983.

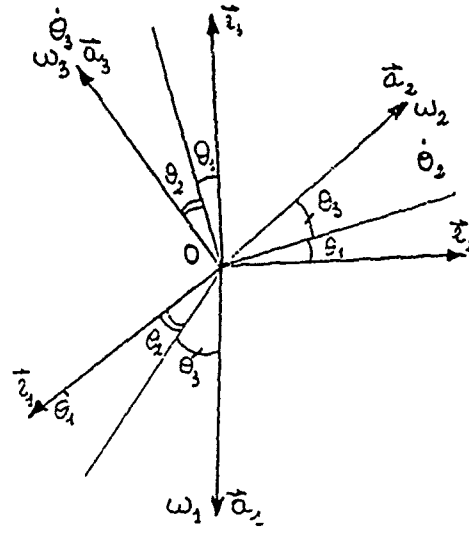


Fig. 1

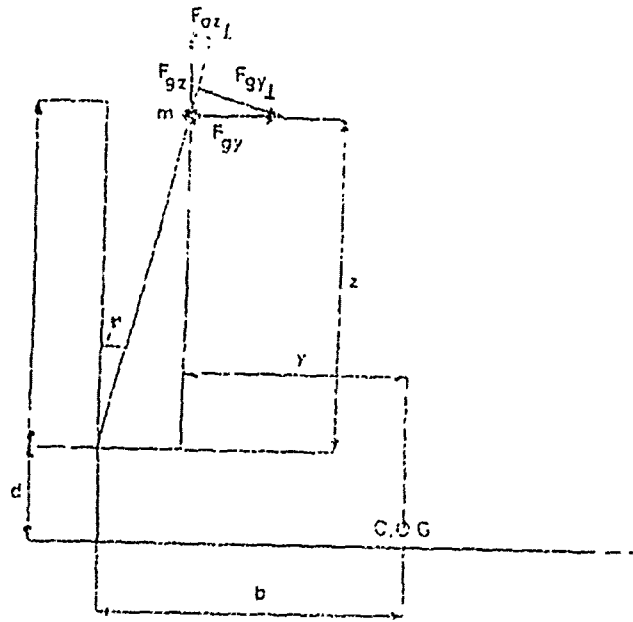


Fig. 2

1.0 DEG ROLL - L-1900 - 2ND FLIGHT - NO DRAG EFFECT

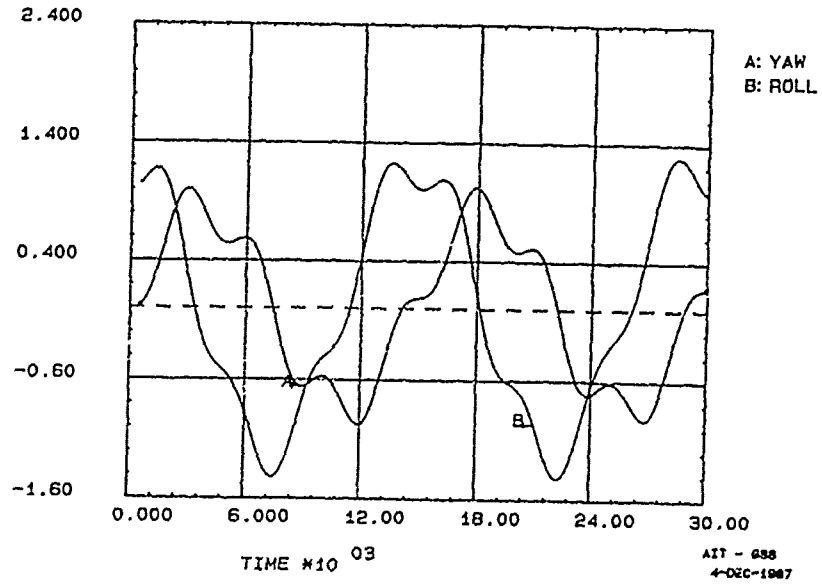


Fig. 3a

1.0 DEG ROLL - L-1900 - 2ND FLIGHT - NO DRAG EFFECT

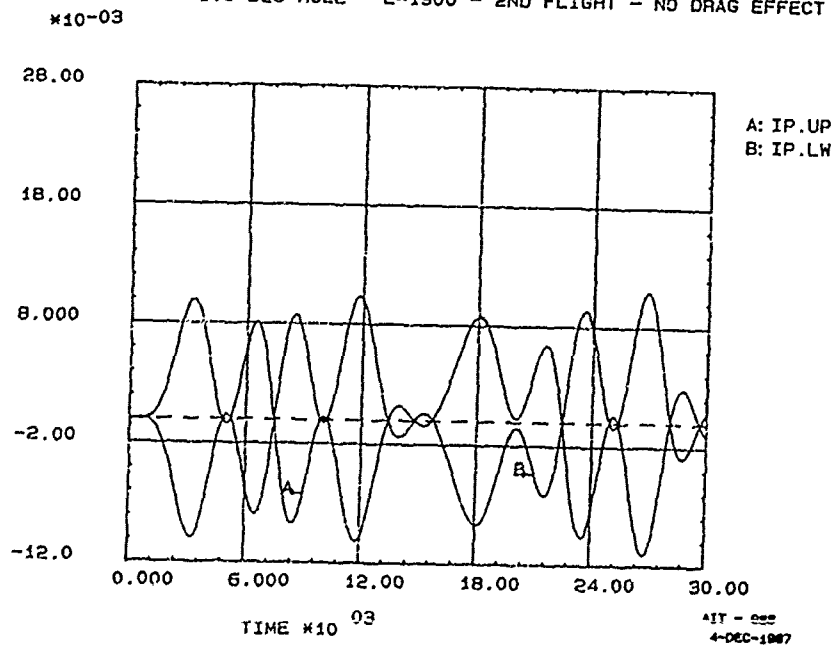


Fig. 3b

1.0 DEG ROLL - L-1900 - 2ND FLIGHT - NO DRAG EFFECT

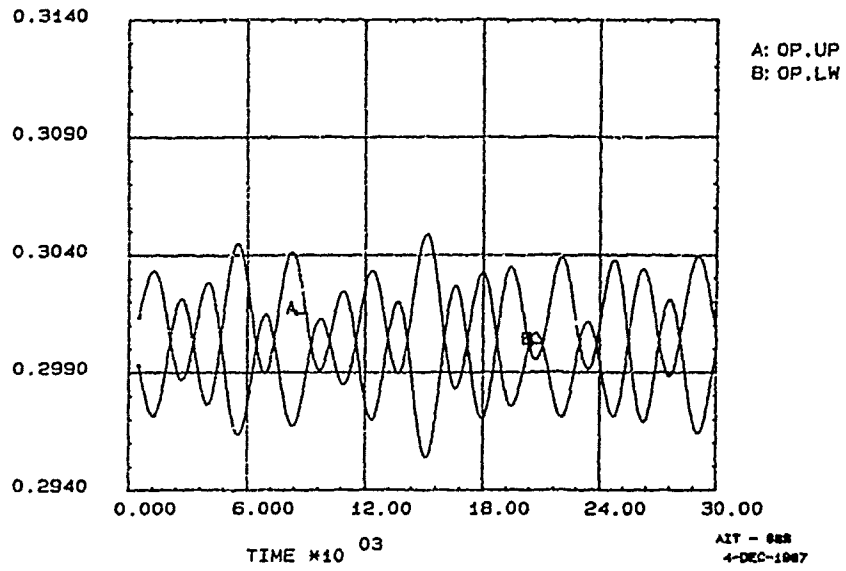


Fig. 3c

1.0 DEG ROLL - L-1500 - 2ND FLIGHT - NO DRAG EFFECT

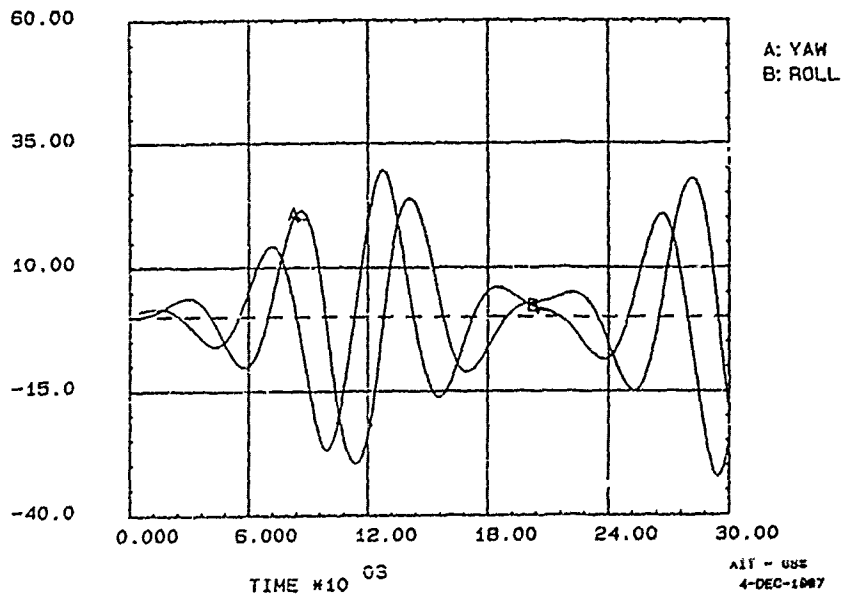


Fig. 4

1.0 DEG ROLL - I-1400 - 2ND FLIGHT - NO DRAG EFFECT

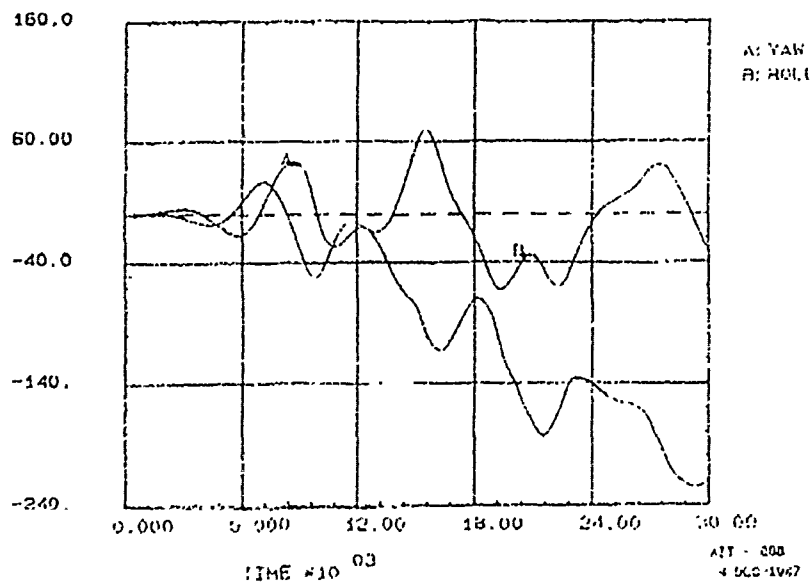


Fig. 5

1.0 DEG ROLL - I-2100 - 2ND FLIGHT - NO DRAG EFFECT

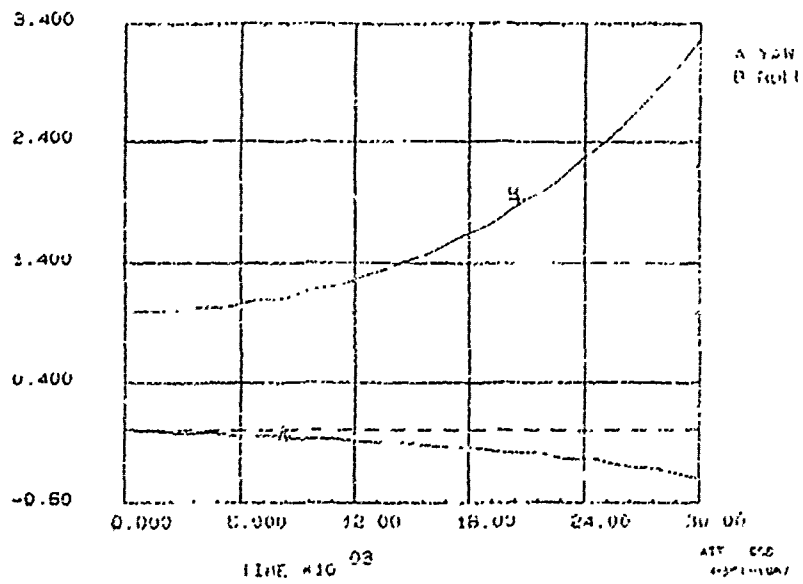


Fig. 6

STEADY - L=1700 - 2ND FLIGHT - TAKEN INTO ACCOUNT DRAG

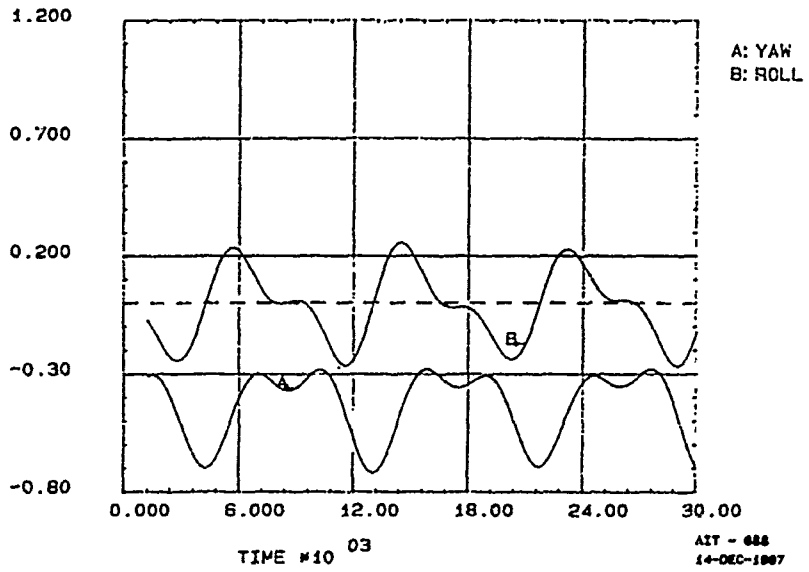


Fig. 7

FAILURE MODES - L=2000 - 2ND FLIGHT - DRAG

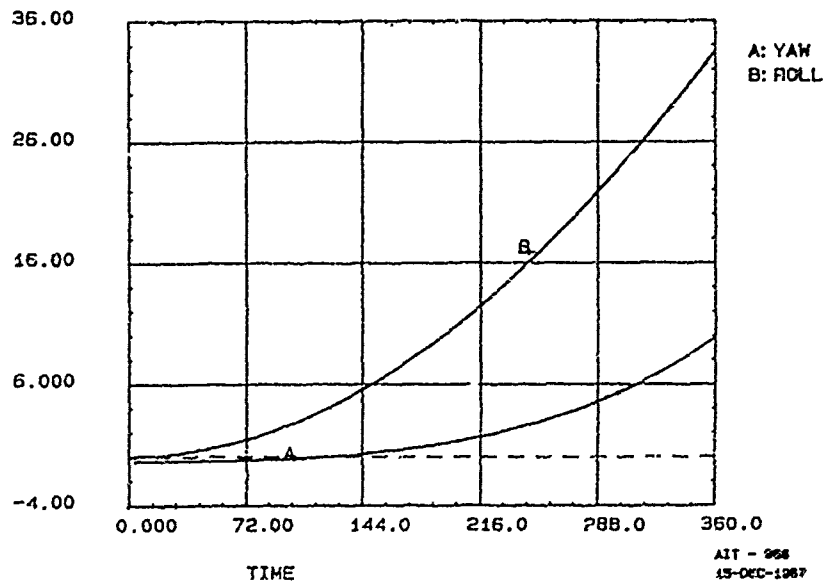


Fig. 8

Shuttle Flight	M kg * 10 ³	I _y kg · m ² * 10 ⁷	I _r kg · m ² * 10 ⁷	I _p kg · m ² * 10 ⁷	ΔI km
2	31.5	3.05	3.14	0.18	1.55 ÷ 2.07
6	99.5	3.65	3.65	0.41	1.82 ÷ 2.43
11	149.8	9.98	9.60	1.32	4.9 ÷ 6.53

Table 1

Flight	A ₄₅ (m ²)	x (m)	y (m)	z (n)	A _z (n)	θ ₁ (deg)	θ ₂ (deg)	θ ₃ (deg)
2	1287	2	3	1	20	-0.8	0	-0.4
6	1368	3.5	1.5	1	20	-0.8	0	-0.7

Table 2

DEPLOYMENT OF LARGE FLEXIBLE SPACE STRUCTURES

M. Gérardin * A. Cardona ** D. Granville ***
L.T.A.S. - Dynamique des Constructions Mécaniques
University of Liège
Rue Ernest Solvay, 21
B-4000 Liège, BELGIUM

Summary

The paper describes a fairly general methodology developed to simulate the deployment of large flexible space structures using the finite element concept. Three simulations of structural deployment are presented to demonstrate the effectiveness of the method: an elementary cell of astromast, an elementary cell of the ERA structure and a 3-D antenna.

1. Introduction

The difficulties associated with the simulation on earth of the deployment of large space structures has motivated the development of adequate numerical tools to complement the experimental set-ups that can be designed and tested.

Kinematics and dynamics of multibody systems is the engineering discipline which allows to perform computer simulation of such systems. It has evolved extensively during the last ten years, and computer codes now exist such as ADAMS and DADS [8], mainly based on the cartesian coordinate approach, which allow to simulate the motion of systems made of a relatively large number of interconnected rigid bodies. However, these codes do not address in its whole generality the problem raised by the large flexibility effects and possibly, the geometric nonlinearities which characterize the large structures to be deployed in space.

The present paper focuses on an alternative of the cartesian coordinate approach which relies upon the finite element concept and therefore, incorporates in the most natural way the elastic effects which may play an essential role in the deployment of large space structures. The finite element concept together with an appropriate description of finite rotation allows arriving at a methodology where rigid bodies and elastic members, mechanical joints, active and passive mechanical devices are just elements of a large library of mechanical components which may be assembled according to an arbitrary topology to represent a complex multibody system.

This methodology has been applied with much success to the analysis and simulation of many flexible articulated systems, including existing space structure projects.

The first example to be presented is the deployment of an elementary cell of astromast (K-beam design). It is an over constrained design whose deployment is rendered possible by the elastic deformation of the members. It will be shown how effectively the deployment of the experimental set-up may be simulated numerically using the proposed methodology.

The second example is the deployment of one cell of the ERA structure designed by Aérospatiale in the framework of the french participation to the MIR project. Emphasis is put on the difficulties raised by the simulation of the nonlinear springs providing the deployment energy to the system.

The third application is the deployment of a 3-D antenna, for which emphasis is put on the effectiveness of substructuring methods to incorporate properly the dynamics of large, flexible panels.

2. Finite rotation description

Numerous techniques exist to represent a finite rotation in space which have each their respective advantages and drawbacks. The main criteria to be considered for selecting an appropriate formalism are [1]

* Professor, University of Liège, Belgium

** Becario Externo y Miembro de la Carrera del Investigador del Consejo Nacional de Investigaciones Científicas y Técnicas de la República Argentina.

*** Research Assistant

- their physical meaning;
- the number of parameters involved (3 or 4);
- their algebraic properties;
- the treatment of singularities;
- the associated composition law for successive rotations.

According to these criteria, the system of parameters that we have selected is the set of 3 parameters formed by the cartesian components of the rotation vector

$$\tilde{\Psi} = n \Psi \quad (1)$$

where n represents the instantaneous rotation axis (figure 1), and Ψ is the rotation amplitude about it.

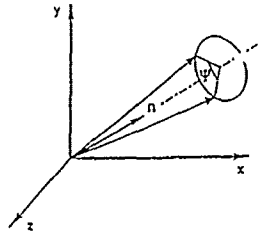


Figure 1: Rotational vector.

Let us recall that the exponential form

$$\mathbf{R} = \mathbf{1} + \tilde{\Psi} + \frac{1}{2!} \tilde{\Psi}^2 + \dots = \exp(\tilde{\Psi}) \quad (2)$$

allows constructing the rotation operator \mathbf{R} in terms of the vector (1), where $\tilde{\Psi}$ is the skew-symmetric matrix made of the components of Ψ ($\tilde{\Psi}_{ij} = -\epsilon_{ijk} \Psi_k$). If one denotes by $\tilde{\Theta}$ the material rotation increment, i.e. expressed in a referential frame attached to the moving and/or deforming body, the incremental rotation is then expressed by the matrix

$$\delta \mathbf{R} = \mathbf{R} \delta \tilde{\Theta} \quad (3)$$

and the material rotation increments are themselves related to the finite rotation parameters by a linear relationship of type

$$\delta \tilde{\Theta} = \mathbf{T}(\Psi) \delta \Psi \quad (4)$$

Equation (4), which forms the basis of the adopted formalism, allows computing the angular velocities with a similar relationship

$$\Omega = \mathbf{T}(\Psi) \dot{\Psi} \quad (5)$$

3. Beam representation of elastic members [2,3]

The appropriate description of flexible truss-like members during a development phase requires in many cases the use of a beam formalism which incorporates properly the geometric nonlinear effects such as geometric stiffening. It is therefore essential to rely upon a true nonlinear beam theory. The basic kinematic assumption adopted is summarized by the following equation

$$\mathbf{x} = \mathbf{x}_0 + X_I \mathbf{t}_I, \quad I = 2, 3 \quad (6)$$

where $\mathbf{x}_0(t)$ represents the position of the beam neutral axis in the global reference frame. The base vectors \mathbf{t}_i are attached to the beam cross section and therefore, give the instantaneous orientation of the material frame \mathbf{R} . Note that the shear deformation is implicitly allowed by eqn (6). The bending and twisting deformations are obtained by calculating the curvature tensor $\tilde{\mathbf{K}}$ in terms of the current parameter s along the beam neutral axis (observe the similarity with the angular velocity expression). The cartesian components (K_1, K_2, K_3) of the associated vector \mathbf{K} have then the meaning of twist and bending deformations. Similarly, the axial and shear strains are obtained by calculating the deformation of the centroidal line

$$\Gamma = \left(\mathbf{R}^T \frac{d\mathbf{x}_0}{ds} - \mathbf{E}_1 \right) \quad (7)$$

The variations of both expressions are given respectively by

$$\delta \mathbf{K} = \frac{d\delta \tilde{\Theta}}{ds} + \mathbf{K} \times \delta \tilde{\Theta} \quad (8)$$

and

$$\delta\Gamma = \mathbf{R}^T \frac{d(\delta\mathbf{x}_0)}{ds} + \left(\mathbf{R}^T \frac{d\mathbf{x}_0}{ds} \right) \times \delta\Theta \quad (9)$$

Both expressions are then used to construct the virtual work expression

$$\delta\pi_{int} = \int_{[0,L]} (\mathbf{N} \cdot \delta\Gamma + \mathbf{M} \cdot \delta\mathbf{K}) ds \quad (10)$$

where \mathbf{M} et \mathbf{N} are respectively the twisting and bending moments, the axial and shear stresses on the current cross section. Similarly, the kinetic energy contribution of the beam is

$$T = \frac{1}{2} \int_{[0,L]} (m(s)\dot{\mathbf{x}}_0 \cdot \dot{\mathbf{x}}_0 + \Omega \cdot \mathbf{II}(s)\Omega) ds \quad (11)$$

where $m(s)$ is the mass per unit length, and \mathbf{II} is the inertia tensor of the cross section. From (11) it is obvious that the main contribution to the inertia matrix of the system, which comes from the translational part, is expressed in terms of global coordinates and therefore, provides a time-independent contribution to the mass matrix of the assembled system. The finite element discretization of eqns (10,11) is then based on a linear interpolation of both displacements and rotation parameters

$$\begin{aligned} \mathbf{x}_0(s) &= N_I(s)\mathbf{x}_{0I} \\ \Psi(s) &= N_I(s)\Psi_I \end{aligned} \quad (12)$$

where \mathbf{x}_{0I} , Ψ_I are the nodal values of position and rotation parameters, $N_I(s)$ is the linear interpolation function corresponding to node I , and summation is extended to the two nodes of the element.

4. Kinematic constraints [4]

The formulation of kinematic constraints and their appropriate numerical treatment is one of the key issues for dynamic analysis of multibody systems.

In *classical dynamics*, it is usual to distinguish between two classes of constraints, namely holonomic and non-holonomic constraints.

Every constraint which can be expressed as an implicit function of the generalized degrees of freedom of the system, and possibly of time, is of holonomic type

$$\Phi(\mathbf{q}, t) = 0 \quad (13)$$

Most kinematic constraints which describe mechanical joints and transmissions fall into this category.

Among the non-holonomic constraints, further distinction between two subclasses has to be made:

- The bilateral constraints which involve further dependence with respect to velocities

$$\Psi(\dot{\mathbf{q}}, \mathbf{q}, t) = 0 \quad (14)$$

It can be shown that such constraints are behavior constraints, since they do not reduce the number of possible configurations of the system but merely restrain the possible ways to arrive to them. The rolling constraint is certainly the most popular constraint of this type.

- The unilateral constraints which are generated by mechanical contact:

$$\Phi(\mathbf{q}, t) \geq 0 \quad (15)$$

They are mainly characterized by the fact that the number of degrees of freedom of the system may vary during motion as it generally occurs in the deployment of space structures.

Holonomic constraints of type (13), which are the most frequent ones, may be included in the functional of the problem using the augmented lagrangian method. It consists of expressing the stationarity of the functional

$$\mathcal{F}^*(\mathbf{q}) = \mathcal{F}(\mathbf{q}) - \lambda \cdot \Phi + p/2 \|\Phi\|^2 \quad (16)$$

where $\mathcal{F}(\mathbf{q})$ is the functional describing the behavior of the unconstrained system, λ is a set of lagrangian multipliers and p is a penalty factor. The only role of the penalty term is to improve the numerical conditioning of the system.

In a Newton-Raphson context, both terms involving the constraint generate contributions to the out-of-balance forces and the tangent stiffness matrix of the system

$$\mathbf{G}_{int} = \begin{Bmatrix} \mathbf{B}(p\Phi - k\lambda) \\ k\Phi \end{Bmatrix} \quad \mathbf{S} = \begin{bmatrix} p\mathbf{B}\mathbf{B}^T & -k\mathbf{B} \\ -k\mathbf{B}^T & 0 \end{bmatrix} \quad (17)$$

where \mathbf{B} is the jacobian matrix of the constraints.

The bilateral nonholonomic constraints of type (14) may be treated in a somewhat similar manner.

As a consequence of the fact that they involve relations between velocities, they generate a pseudo-dissipation function in the system and therefore, contribute to the damping matrix.

The library developed so far in the MECANO software allows modeling kinematic constraints of various types:

- hinge, prismatic, screw, cylindrical, spherical and planar joints which are often classified as lower pairs according to their common property of generating surface contact between members.
- higher pairs such as the universal joint and a curvilinear slider.
- rolling contact.

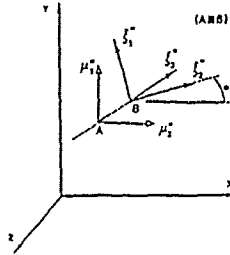


Figure 2: Hinge joint.

For example, the hinge joint (figure 2) is expressed by the following relationships

$$\begin{aligned}\Phi_{1,2,3} &= x_A - x_B = 0 \\ \Phi_4 &= \mu_1'' \cdot \xi_3'' = (R_A \mu_1) \cdot (R_B \xi_3) = 0 \\ \Phi_5 &= \mu_2'' \cdot \xi_3'' = (R_A \mu_2) \cdot (R_B \xi_3) = 0\end{aligned}\quad (18)$$

$\Phi_{1,2,3}$ express the fact that displacements on both members are the same at the point of contact. In a finite element context, they are handled in straightforward manner through finite element assembly. Φ_4 and Φ_5 express the orthogonality of two axes attached to the members at the point of contact. They have to be incorporated using the augmented lagrangian technique.

5. Dynamic substructuring for articulated flexible bodies [5]

Let us consider the case of a single flexible body for which the small displacement assumption holds in a dynamic (e.g. body attached) frame. Then, the complex geometry of the body can easily be handled through dynamic substructuring by making use of the modeling capabilities of any linear dynamic finite element package, and the resulting model integrated next in the model of the multibody system.

The underlying hypotheses are the following. Let us express the positions and rotations at any node of the model as the superposition of the arbitrary motion of a reference node on the body with a local, small deformation field:

$$\begin{Bmatrix} x_i \\ \Psi_i \end{Bmatrix} = \begin{Bmatrix} x_0 + R_0(X_i + u_i) \\ \Psi_0 \circ \psi_i \end{Bmatrix}\quad (19)$$

where x_0 is the position of the master node on the body; R_0, Ψ_0 is the rotation at the master node; X_i is the relative position of node i with respect to node 0; u_i is the displacement of node i in the local frame; ψ_i is the angular displacement of node i in the local frame. The symbol \circ expresses the composition of two successive rotations.

The deformation of the body is restrained next to a finite series of assumed modes which may be computed in various ways, giving rise to several possible methods for dynamic substructuring. In what follows one will assume without loss of generality that constrained vibration modes are used, just as proposed by Craig and Lampton [6] in their component mode method for linear systems.

$$\begin{Bmatrix} x_i \\ \Psi_i \end{Bmatrix} = \begin{Bmatrix} x_0 + R_0(X_i + \Phi_i y) \\ (\Psi_0 \text{ ref} \circ \Psi_0 \text{ inc}) \circ (\Phi_i y) \end{Bmatrix}\quad (20)$$

where Φ_i are the shape functions evaluated at node i ; y is the vector of generalized amplitudes.

The vector of generalized amplitudes is then partitioned into boundary and internal degrees of freedom

$$y = \begin{Bmatrix} u_B \\ \psi_B \\ y_I \end{Bmatrix}\quad (21)$$

The strain energy of the flexible body can be expressed in the form

$$\pi_{int} = \frac{1}{2} \mathbf{y} \cdot \bar{\mathbf{S}} \mathbf{y} \quad (22)$$

where the reduced stiffness matrix $\bar{\mathbf{S}}$ is obtained through projection of the original matrix on the modal basis adopted

$$\bar{\mathbf{S}} = \Phi^T \mathbf{S} \Phi = \begin{bmatrix} \bar{\mathbf{S}}_{BB} & \mathbf{0} \\ \mathbf{0} & \bar{\mathbf{S}}_{II} \end{bmatrix} \quad (23)$$

The variation of the flexible body parameters $\delta \mathbf{y}$ is calculated in terms of the superelement generalized displacements \mathbf{q} by

$$\delta \mathbf{y} = \mathbf{r} \delta \mathbf{q} \quad (24)$$

with $\mathbf{q}^T = \langle \mathbf{x}_0^T \quad \Psi_0^T \mathbf{i}_{in_0} \quad \mathbf{x}_B^T \quad \Psi_B^T \mathbf{i}_{in_0} \quad \mathbf{y}_I^T \rangle$.

The strain energy is derived next with respect to the \mathbf{q} to obtain the expressions of internal forces and stiffness matrix

$$\begin{aligned} \mathbf{G}_{int} &= \mathbf{r}^T \bar{\mathbf{S}} \mathbf{y} \\ \bar{\mathbf{S}}_{sup} &= \mathbf{r}^T \bar{\mathbf{S}} \mathbf{r} \end{aligned} \quad (25)$$

A very simple approximation to the inertia forces is constructed on the basis of a lumped mass assumption

$$\mathbf{G}_{iner} = \sum_{i=1}^N \mathbf{B}_i^T \mathbf{m}_i \ddot{\mathbf{x}}_i$$

where summation is performed on the N nodes of the body; the matrix \mathbf{B}_i is a function of the current configuration; \mathbf{m}_i represents the concentrated mass at node i ; $\ddot{\mathbf{x}}_i$ is the acceleration at node i , and is calculated by making the small displacement assumption in the local frame

$$\ddot{\mathbf{x}}_i = \ddot{\mathbf{x}}_0 + \mathbf{R}_0 (\ddot{\Omega}_0 + \ddot{\Lambda}_0) \mathbf{X}_i + 2 \mathbf{R}_0 \dot{\Omega}_0 \dot{\mathbf{u}}_i + \mathbf{R}_0 \ddot{\mathbf{u}}_i \quad (26)$$

where $\dot{\mathbf{u}}_i, \ddot{\mathbf{u}}_i$, the velocities and accelerations of node i in the local frame, are given by

$$\begin{aligned} \dot{\mathbf{u}}_i &= \Phi_i \dot{\mathbf{y}} \\ \ddot{\mathbf{u}}_i &= \Phi_i \ddot{\mathbf{y}} \end{aligned} \quad (27)$$

Finally, the mass matrix of the superelement may be expressed in the form

$$\bar{\mathbf{M}}_{sup} = \sum_{i=1}^N \mathbf{B}_i^T \mathbf{m}_i \mathbf{B}_i \quad (28)$$

6. Simulation examples

6.1 Quasi-static deployment phase of an astromast cell

The system considered is an elementary cell of astromast of triangular cross-section, and designed as an articulated flexible system. Each cell of the astromast (fig. 3-a) has three longerons and three diagonals; no successive cells are interconnected through a triangular batten. At each vertex of the batten is attached a rigid body to which the longerons and diagonals of two adjacent cells are interconnected. The members of the battens are rigidly connected to the corner bodies while the longerons and diagonals are hinged to them.

In order to permit folding, the diagonals are also hinged at their mid-length. The design is such that the folded and unfolded configurations are nearly stress-free, while the system structural hyperelasticity is such that significant axial twisting and bending stresses are observed during deployment. A slight initial prestressing is imposed to stiffen the deployed configuration by appropriate shortening of the diagonals.

A videotape exists which displays the deployment of a two-bay experimental setup. It will be used at the oral presentation to help at understanding the mechanical behavior of the system and compare it with the simulated one.

The system symmetry has been used to limit the simulation to one cell. The model numbers 72 finite elements (51 beam elements, 6 rigid bodies, 15 hinge joints) to model the physical components and 7 additional constraints to control the motion of the system. The model numbers a total of 391 DOF.

Figure 3-a displays the reference configuration (dashed line) and the prestressed initial configura-

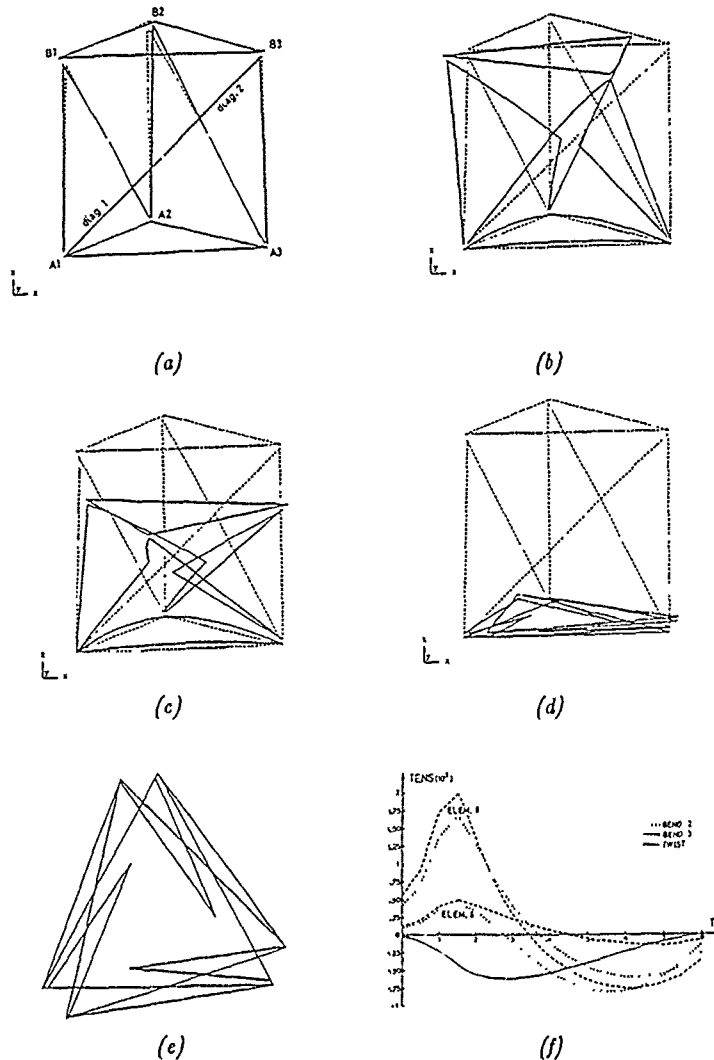


Figure 3. Kineto-elasto-static of a deployable astromast cell.
 (a) initial and reference configurations
 (b), (c) et (d) unlocking, intermediate and final configurations
 (e) top view of final configuration
 (f) bending and twisting moments in vertical longerons

tion obtained after mechanical assembly. The unfolding phase is then simulated in two displacement-controlled steps:

- a. In order to unlock the mechanism, the mid-diagonal nodes are moved inwards and normally to the lateral faces (fig. 3-b).
- b. The vertical displacement of the upper batten is controlled next up to complete folding (fig. 3-b, 3-c, 3-d). Figure 3-e displays a vertical projection of the final configuration. Figure 3-f shows an example of stress results. It displays the evolution of bending and twisting stresses in the longerons during folding.

This kineto-elasto-static simulation has been performed into 96 increments, with an average of 5.8 iterations per increment. It demonstrates the ability of the MECANO software to simulate the deployment of 3-D flexible multibody systems with complicated kinematics.

6.2 Dynamic analysis of the deployment of a large space structure

The system to be analyzed is one cell of a deployable space structure: the ERA platform designed by Aérospatiale deployed on the MIR space station. The cell has a triangular cross-section with three

longerons and six diagonals. Battens are articulated at the middle length to permit folding. The battens and diagonals are hinged to the corner bodies, while the longerons are rigidly attached to them. The total structure is composed by 24 modules like the one displayed in figure 4 disposed side by side forming an hexagon (figure 5).

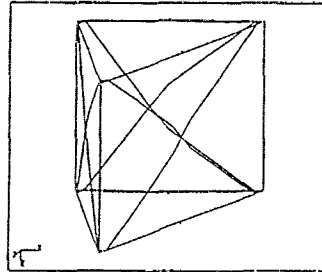


Figure 4: One cell model of the deployable structure (final configuration).

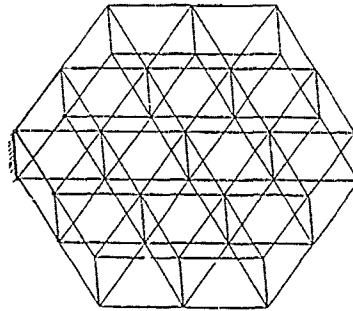


Figure 5: Global view of the ERA structure (scheme of deployed configuration).

The motorisation for deployment is provided by the elastic energy stored at rotation springs located at the hinges in the middle of the battens. They release energy through a nonlinear torque/angle law and provide a locking device which is activated at the final angle of deployment.

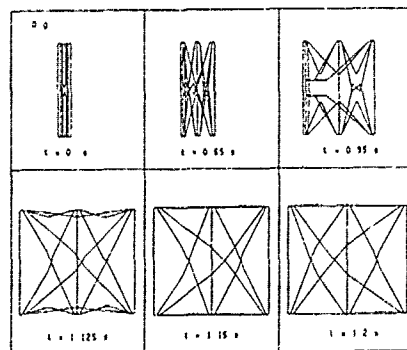


Figure 6: successive configurations from 0. to 1.2s.

The analysis was conducted supposing that the structure is acting in a 0-g field first, and next submitted to a small amount of gravity (0.01g) acting in the vertical direction. Figures 6 displays six successive configurations computed for the one cell model in 0-g environment, up to complete deployment and locking occurring at time $t = 1.2s$.

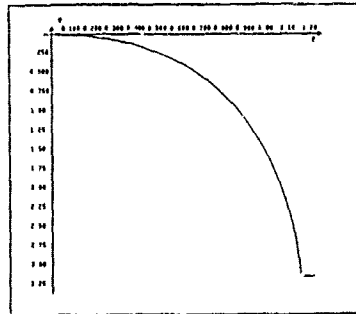


Figure 7: time evolution of a motored hinge angle

Figure 7 displays the time evolution of the rotation angle at one of the six motorized hinges of the system. The time of locking appears very clearly on this diagram.

This simplified model has 612 DOF and mean bandwidth of 79 ; 74 time steps are used to integrate in time the equations of motion. The CPU time consumption is 2 hours 20 minutes on an APOLLO DN-4000 workstation. Some experiences were done on a IBM 3090 ; the CPU time consumption for a similar simulation was 2.5 minutes without vectorization. Experiences with partial vectorization of the code evidenced a factor 2 of improvement on the CPU time.

The final mesh will have an order of 8000 DOF, with a mean bandwidth of 240. The estimated computational effort to time integrate the complete model is 150 times greater than the effort necessary to solve the one cell model.

We remark that the computational effort is largely influenced by the strategy adopted to solve impacts at the joints, since the time step is restricted by convergence at the shock instants. The approach currently adopted to solve shocks is based on the hypothesis of momentum conservation. This approach provides excellent computational efficiency since the discontinuity of velocities during impact is explicitly computed. Unlike a shock capturing algorithm in which the stop and locking device is represented as a high stiffness component, it allows to pursue the simulation beyond complete locking of the structure. In our example, one can see on figure 6 that the Oscillatory motion of the diagonals remaining after complete deployment is well represented. At the same time, this approach leaves the integration scheme unperturbed and therefore allows to increment the time step to reasonable values.

6.3 Dynamic analysis of the deployment of a 3-D satellite antenna

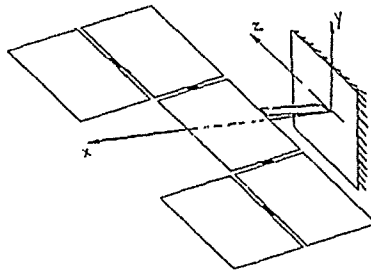


Figure 8: geometry of 3-D satellite antenna.

The 3-D antenna under consideration is made of five similar panels hinged together as shown by figure 8. In the numerical model (figure 9), each rectangular panel is visualized by the losange connecting the mid-edge points. The deployment is provided by the nonlinear springs acting at the hinges and providing the torque versus rotation angle law displayed by figure 10.

This curve exhibits hysteresis in the vicinity of the locking angle. The first peak corresponds to the locking value of the torque, while the second one is generated by the hysteresis effect occurring in a locking/unlocking phase.

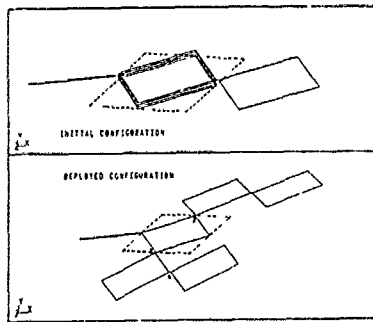


Figure 9: Simulation model of 3-D satellite antenna.

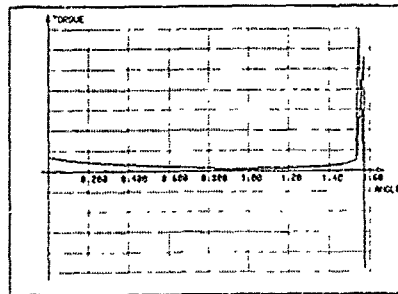


Figure 10: Torque/angle law at the hinges.

The effective stiffness properties of the panels have been taken into account using the substructuring technique described in section 5. Each panel of the real structure is a stiffened sandwich plate made of composite material. It has thus been modeled as a sandwich flat shell with orthotropic stiffness properties and local reinforcements. An idea of the finite element model is given by figure 11 which shows the decomposition of the structure into 4 zones with different elastic properties. A complete description of the model is given in [7]. Each substructure has 584 DOF initially and is reduced to the four connecting nodes and 4 internal modes, giving a total of 28 DOF per panel.

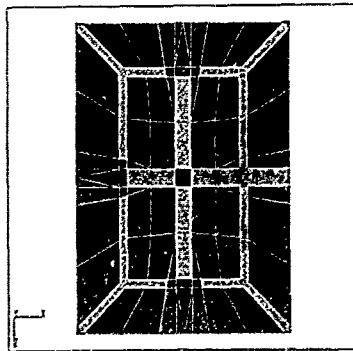


Figure 11: Finite element model and elastic properties of satellite antenna.

The resulting mechanism model used to predict the dynamics of the deployment has 230 DOF, with a mean bandwidth of 32. The time integration of the response has been performed on a time interval of 47s. As shown by figure 12, the structure is initially partially folded and complete deployment has occurred at time $T = 47s$. This time evolution has been obtained in 151 time steps and an average number of 5.1 equilibrium iterations per time step, giving a CPU consumption of 6 hours 15 minutes on an Apollo DN4000.

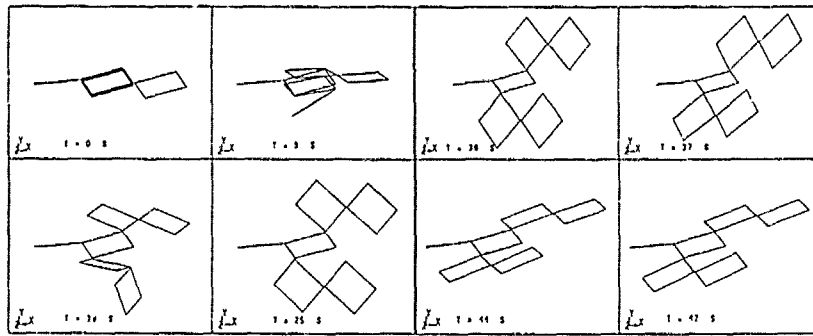


figure 12: successive configurations of antenna during deployment (0. to 47s.)

Figure 13 displays half the rotation angle versus time in the three active hinges. It increases regularly up to locking and then oscillates about the locking value. The corresponding torque in hinge 2 is displayed by figure 14. The hinge locks at time $T = 41$ s and never unlocks afterwards.

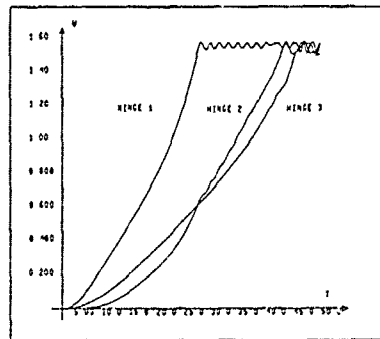


Figure 13: Rotation angles of active hinges.

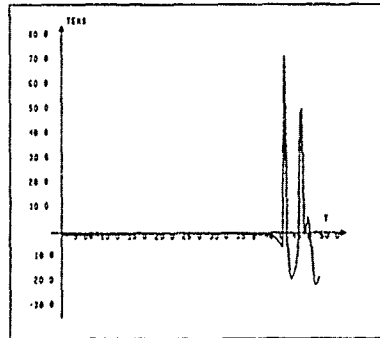


Figure 14: Torque versus time in hinge 2.

The elastic behavior of the panel can be predicted with much detail through appropriate postprocessing of the substructures.

For example, figure 15 shows at a given time ($t=47s$) the isovalues of bending deflection on one hand, and of upper skin equivalent stress on the other hand.

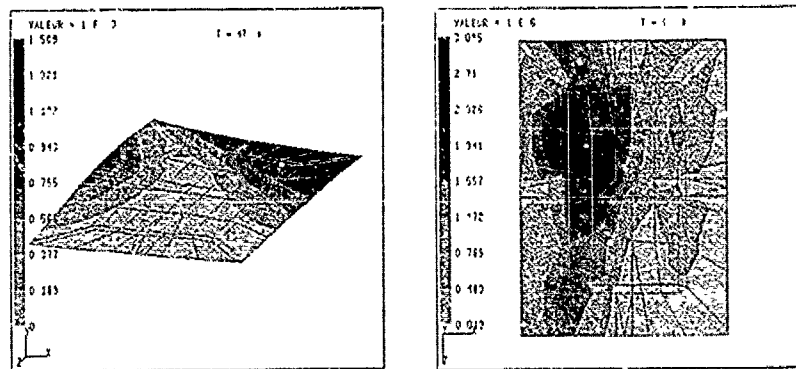


Figure 15: Isovalues of bending deflections and upper skin equivalent stresses in central panel.

References

1. GERADIN M., PARK K.C. and CARDONA A., "On the representation of finite rotations in spatial kinematics", LTAS report, University of Liège, Belgium (1988).
2. SIMO J.C. and VU-QUOC L., "A three-dimensional finite strain rod model. Part II: computational aspects", *Comp. Meth. Appl. Mech. Engng.*, Vol.58, pp.79-116 (1986).
3. CARDONA A. and GERADIN M., "A beam finite element non linear theory with finite rotations", *Int. J. Numer. Methods Eng.*, Vol.26, pp.2403-2438 (1988).
4. CARDONA A. and GERADIN M., *On the formulation of joints for mechanism analysis*, LTAS report, University of Liège, Belgium (1988).
5. CARDONA A. and GERADIN M., *A superelement formulation for mechanism analysis*, LTAS report, University of Liège, Belgium (1988).
6. CRAIG R.R. and BAMPTON C.C., "Coupling of substructures for dynamic analysis", *AIAA J.*, Vol.6, pp.1313-1319 (1968).
7. GRANVILLE D. and GERADIN M., *Calcul du deploiement d'une antenne tridimensionnelle par MECANO*, LTAS report, University of Liège, Belgium (1988).
8. E.J. HAUG, Editor *Computer Aided Analysis and Optimization of Mechanical Systems Dynamics*, NATO ASI series, series F: Computer and Systems Sciences, Vol. 9 (1984).

The Dynamics of Orbital Maneuvering: Design and Evaluation of a visual display aid for human controllers

Stephen R. Ellis¹ and Arthur J. Grunwald²
Aero-Space Human Factors Research Division
Ames Research Center Moffett Field, CA 94035,
USA

Summary

An interactive proximity operations planning system, which allows on-site planning of fuel-efficient, multi-burn maneuvers in a potential multi-spacecraft environment has been developed and tested. Though this display system most directly assists planning by providing visual feedback to aid visualization of the trajectories and constraints, its most significant features include 1) an "inverse dynamics" algorithm that removes control nonlinearities facing the operator and 2) a trajectory planning technique that reduces the order of control and creates, through a "geometric spread-sheet," the illusion of an inertially stable environment. This synthetic environment provides the user with control of relevant static and dynamic properties of way-points during small orbital changes allowing *independent* solutions to the normally coupled problems of orbital maneuvering. An experiment has been carried out in which experienced operators were required to plan a trajectory to retrieve an object accidentally separated from a dual-keel space station. The time required to plan these maneuvers was found to be predicted by the direction of the insertion thrust and did not depend on the point of separation from the space station.

Introduction

1.1 Control of the Hand

The insights of paleontology reveal the human hand to be a unique end product of millions of years of vertebrate and primate evolution. Indeed, it itself may have been an essential contributor to the development of the human capacity for abstract insight. The hand is a highly dextrous, general purpose manipulator capable of the fine touch needed to thread a pin and the more coarse control and force needed to lift an object heavier than the weight of its owner. However, like telerobotic effectors at the end of multilink robotic arms, control of the position and orientation of the hand in space can be computationally complex. The kinematics of the links that make up the arm complicate the relationship between the muscles which control each of them and the resulting position of the hand in space. Though cerebellar and other neuro-muscular diseases can reduce their victims to the necessity of conscious joint-angle control, in normal health our neurological control systems unburdened us of conscious control of the limb positions that determine our hand positions.

The unconscious ease of normal movement arises from the unique hierarchical control system that has evolved in association with the gross morphology of the hand. This system computationally separates lower order motor coordination functions from higher order commands concerning what to coordinate. One may think about some of the aspects of the lower order motor coordination as the inverse kinematics and dynamics that translate the higher order movement commands from egocentric coordinate space into a series of link movements in joint coordinate space [1]. This transformation greatly simplifies the planning task confronting the higher order motor centers. It also reinforces the functional and spatial separation of task planning from muscle coordination and provides us at a conscious level with position control over our hands. We command a position and orientation and our hand effortlessly assumes it.

1.2 Kinematic Complications of Control: Telerobotic Arms

In light of the characteristics of the neurological control of hand position, it is not surprising that for generalized telerobotic manipulation tasks some form of resolved control of teleoperators is found to be easier for operators to control than control of the joint angles and positions of the various links of the arm [3]. This resolved control is achieved computationally by inverting the transformation matrix describing the arm's forward kinematics. However, due to computational singularities and physical constraints on joint motion an inverse motion may not be unique, and indeed it may not be computable for some positions. Accordingly, implementation of resolved control over an arm requires the addition of information. This information may take the form of arbitrary limits on the movement parameters but more usefully may be in the form of kinematic or dynamic optimization criteria such as time optimality, minimum energy, or minimal path length [2] [4]. These criteria allow the resolution system to select one of the many possible patterns of joint movement that would result in the same movement or position.

1.3 Dynamic Complications of Control: Order of Control

In kinematically simple situations such as those that arise when a subject is engaged in a simple cross and square display tracking task using a two-dimensional joystick, factors other than kinematics determine the success of the tracking e.g. 1) the dynamic characteristics of the joystick itself, 2) the stimulus response compatibility of the control and display coordinate systems, 3) concurrent other tasks, and 4) the disturbance function and the dynamics of the controlled element. Large bodies of literature concerning the effects of these factors on tracking performance have been developed [5] [6]. Performance is generally best when the operator is provided with the lowest order of control possible subject to plant and disturbance characteristics.

¹Research Scientist at NASA Ames Research Center and Assistant Professor of Physiological Optics at U.C. Berkeley, USA

²Current address. Senior Lecturer, Department of Aeronautical Engineering, Technion Israel Institute of Technology, Haifa, Israel. The development of the proximity operations planning software described in this paper was part of Dr. Grunwald's NRC Fellowship project during his tenure at the Ames Research Center 1986-1988.

The difficulties subjects encounter in higher order control environments, e.g. 2nd order or acceleration control, arise from the difficulties they encounter in estimating velocity and acceleration from position and the additional control movements needed for changing final position. Thus, Poulton's [5, p360] recommendation for the design of a manual control system is to design an order of control as low as possible. This goal may be achieved within the control system itself, for example, by introducing an exponential lag that delays the full effect of the control input and reduces the likelihood that the operator of a higher order system will overshoot his target [5]. Higher order control situations also can be assisted by provision of displays using predictors that integrate the time derivatives of position and remove the need for the operator to perceive these rates directly [7] [8]. As will be discussed below, simple provision of a predictor is not, however, a sufficient display enhancement if control inputs interact in complex nonlinear ways.

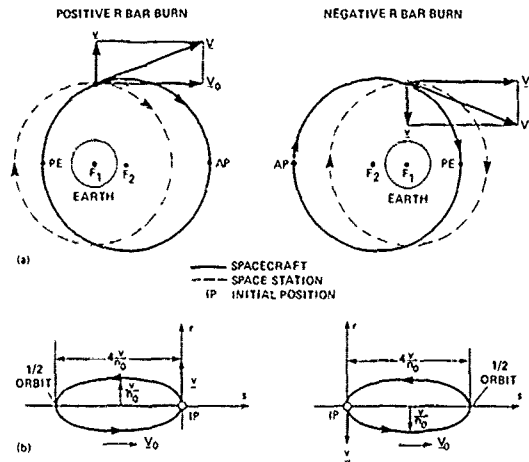


Figure 1. Orbital motion after R-bar burn. (a) Shape of orbit (b) Trajectory relative to the space station.

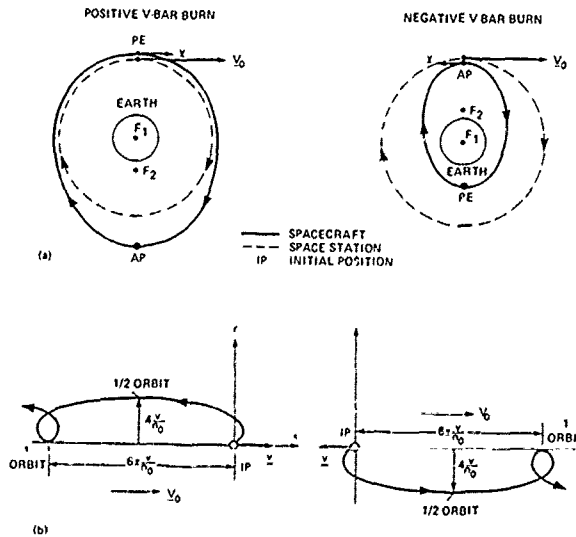


Figure 2. Orbital motion after V-bar burn. (a) Shape of orbit (b) Trajectory relative to the space station.

2. Proximity Operations Planning Display

2.1. The Orbital Environment

The proximate orbital environment of future spacecraft may include a variety of spacecraft co-orbiting in close vicinity. Most of these spacecraft will be "parked" in a stable location with respect to each other, i. e. they will be on the same circular orbit. However, some missions will require repositioning or transfers among them as in the case of the retrieval of an accidentally released object. In this case complex maneuvers are anticipated which involve a variety of spacecraft which are not necessarily located at stable locations and thus have relative motion between each other.

This multi-vehicle environment poses new requirements for control and display of their relative positions. Conventional scenarios involve proximity operations between two vehicles only. In these two-spacecraft missions, the maneuver may be optimized and precomputed in advance of the time of the actual mission. However, since the variety of possible scenarios in a multi-vehicle environment is large, a future spacecraft environment could require astronauts to execute maneuvers that may not have been precomputed. This demand will require an on-site planning tool which allows, fast, interactive, informal creation of fuel-efficient maneuvers meeting all constraints set by safety rules.

The difficulties encountered in planning and executing orbital maneuvers originate from several causes [9] [10] [11]. The first one is the counter-intuitive character of orbital motions as experienced in a relative reference frame. The orbital motions are expressed and tend to be perceived in a coordinate frame attached to a large proximate vehicle such as a space-station and, thus, represent relative rather than absolute motions. From experience in inertially fixed environments, it would be intuitively assumed that a thrust in the "forward" direction towards a target vehicle ahead but in the same orbit, i. e. in the direction of the orbital velocity vector, would result in a forward motion. However, after several minutes, orbital mechanics forces will dominate the motion pattern and move the chaser spacecraft "upwards", i. e. to a higher orbit. This will result in a backwards relative motion, since objects in a higher orbit have a slower orbital rate. Thus, a forward thrust ultimately has the opposite effect from that intended. The effect of this unexpected movement is compounded by the fact that a completed maneuver, which essentially is a timed orbital change, involves a potentially third order or higher order control process with both departing, maneuvering and braking thrusts. Even without the counter-intuitive dynamics such a process is difficult to control! [6]. Furthermore, corrective thrusts produce significant nonlinear effects on spacecraft positions complicating iterative, manual efforts to drive a spacecraft to a desired stable position.

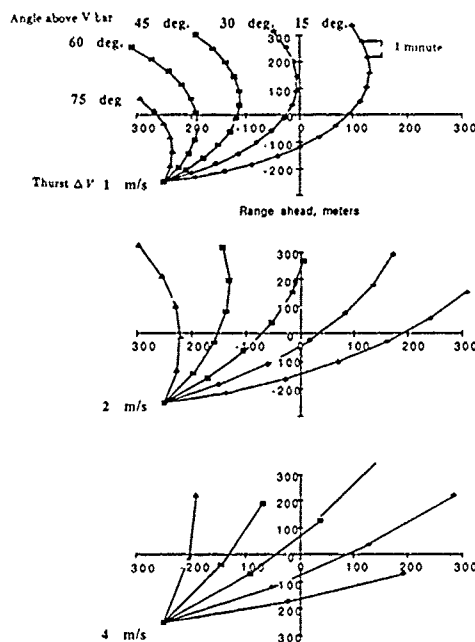


Figure 3. Relative orbital trajectories for different thrust magnitudes and angles for an insertion point below the space station's orbit and behind its center of mass. The space station is located with its center of mass at the origin. Note: that the effects of the orbital dynamics can be overpowered by increasing thrust.

A second cause of the difficulty is the different and unusual way in which orbital maneuvering control forces are applied. In atmospheric flight control forces are applied continuously in a way to correct for randomly appearing atmospheric disturbances, or to compensate for atmospheric drag. In contrast, space-flight in the absence of atmospheric disturbances, has a near deterministic character. Therefore, space-flight is mainly unpowered and undamped along a section of an orbit with certain characteristics. By applying impulse-type maneuvering forces at a given way-point, the characteristics of the orbit are altered. After application of the maneuvering force the spacecraft will coast along on the revised orbit until reaching the next intermediate way-point along its planned trajectory. Once it is positioned at a way point; however, it will not generally be at a stable relative position, but will tend to drift under the influence of orbital mechanics unless corrective thrusts are continually applied.

Third, multi-vehicle orbital missions are subject to safety constraints, such as clearance from existing structures, allowable approach velocities, angles of departure and arrival and maneuvering burn restrictions due to plume impingement or payload characteristics. Design of a fuel-efficient trajectory which satisfies these constraints is a non-trivial task.

It is clear that visualization of the relative trajectories and control forces in an easily interpretable graphical format, will greatly improve the feel for orbital motions and control forces and will provide direct feedback of the operators control actions. Furthermore, visualization of the constraints in a pictorial format will enable an interactive, graphical trajectory planning in which the design may be iteratively modified until all constraints are satisfied. Typical in-plane maneuvers are the V-bar burn, along the orbital velocity vector, and R-bar burn, along the orbital radius vector.

Consider a spacecraft located at the V-bar and thus at a stationary position relative to the space station. A small maneuvering burn in the direction of the R-bar will cause a small component Δv which will result in a small change in the direction of the orbital velocity vector. This will alter the parameters of the orbit. The orbit will become elliptical and after the burn the maneuvering spacecraft will be 90 deg. of orbital travel past the perigee of the new orbit. In Figure 1 the shape of the orbit and the corresponding relative motion trajectory is shown. The relative trajectory has a "closed" elliptical shape and after one orbit the spacecraft will return to its original location. The reason for this is that the radial burn did not significantly alter the magnitude of the velocity V_0 , and thus the total energy and mean motion did not change.

In contrast to the R-burn, a maneuvering burn along the V-bar, will alter the magnitude of the V_0 by the amount $|\Delta v|$ and will therefore alter the total energy. Figures 2ab show the shape of the orbit and the corresponding relative motion trajectory. For a burn in positive V-bar direction, the spacecraft will initially move forward but later on gain altitude and fall behind. The opposite is the case for a burn in negative V-bar direction. Here the spacecraft will initially move backwards but later on drop altitude and pull ahead. For a positive burn the spacecraft is initially at perigee and for a negative burn at apogee.

In general, a chasing vehicle's maneuvers in the orbital plane need not have solely V-bar or R-bar components but components of both. In addition it may also have out-of-plane components. Furthermore, its initial position may not be stable, i. e. offset with respect to its target's V-bar, and the desired flight time may be a fraction of an orbital period, i. e. 10 - 20 minutes. Under these circumstances the full effects of orbital dynamics are not given sufficient time to completely manifest themselves and are experienced as a kind of "variable orbital wind" blowing the controlled vehicle off a desired straight path. Figures 3 and 4 illustrate the kinds of deflections the "orbital wind" may produce for more generic maneuvers. In particular Figure 3 shows how the deflections caused by orbital dynamics can be partially overcome by using stronger thrusts, but this brute force technique can be very costly due to the fuel required both for departure and braking on arrival.

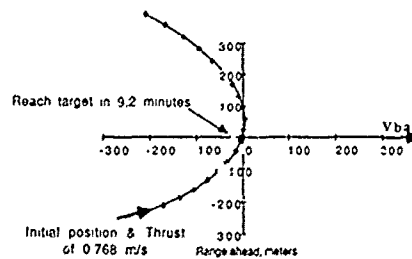


Figure 4. Rendezvous initiated by control of thrust and direction of a maneuvering burn, i.e. the forward method. Using a planning tool that provides a forward predictor of the effects of a planned maneuvering burn, a subject can find by trial and error a combination of thrust and insertion angle that will produce a trajectory to return to the space station from an offset position. Planning for a particular arrival time or selecting a fuel optimal maneuver is, however, manually very difficult with only a forward predictor to assist the operator.

2.2 Limitations of Present Techniques.

The present maneuvering techniques are well established and rely in most cases on visual contact and the use of a V-bar or R-bar reference in a Crewman Optical Alignment Sight (COAS), [9] [10] [12]. In a V-bar approach towards a target in positive V-bar direction, the initial burn is made in a direction slightly depressed downwards with respect to the V-bar. After a short while, the spacecraft will "ascend" and cross the V-bar. At the V-bar crossing a small downward R-burn is initiated which again "depresses" the spacecraft below the V-bar. This process is repeated several times. The spacecraft thus proceeds along the V-bar in small "hops" until the target is reached. However, this technique is highly restricted, is not fuel-optimal, and may not conveniently satisfy other operational constraints of a multi-vehicle environment.

But it is clear from the previous examples that orbital motion can be complex, highly counter intuitive, and involve tightly interacting parameters. A burn towards the target might have an unintended opposite result. Relative motion is, in particular, difficult to visualize for a combined R-bar V-bar burn at a non-stationary location. It is therefore very useful to graphically visualize the relative motion trajectories. Providing predictors on planning displays which foretell the final consequences of a maneuvering burn is, however, not sufficient symbolic enhancement to enable an operator to plan a timed maneuver. The nonlinear interaction between thrust magnitude and direction of thrust with time of arrival and final relative position preclude tractable manual control over the position and time of the predictor's endpoint.

2.3 Design of a Pictorial Orbital Maneuvers Planning System

The purpose of the interactive orbital planning system is to enable the operator to design an efficient complex multi-burn maneuver, subject to the stringent safety constraints of a future space-station traffic environment. The constraints include clearances from structures, relative velocities between spacecraft, angles of departure and arrival, approach velocity and plume impingement. The basic idea underlying the system is to present the maneuver as well as the relevant constraints in an easily interpretable pictorial format. This format does not just provide the operator with immediate visual feedback on the results of his design actions to enable him to meet the constraints on his flight path, but goes beyond conventional approaches by introducing geometric, symbolic, and dynamic enhancements that bring the intellectual demands of the design process within normal human capacity [8] [9] [13] [14] [15]. The specific methods for enabling interactive trajectory design and visualization of constraints have been discussed in detail elsewhere and will not be repeated here [16] [17]. Though the display also can handle planning out-of-plane maneuvers, the discussion will be limited to maneuvers in the orbital plane.

2.4 Example of a three-burn maneuver.

An illustrative example of a three-burn maneuver is shown schematically in Figure 5. The trajectory originates from relative position A at time $t = t_0$, and is composed of two way-points B and C which specify the location in space station coordinates at which the chaser spacecraft will pass at a given time. At a way-point the orbital maneuvering system or other reaction control system can be activated, creating a thrust vector of given magnitude for a given duration in a given direction in or out of the orbital plane. The duration of the burn is considered to be very short in comparison with the total duration of the mission. In the orbital dynamics computations this means that a maneuvering burn can be considered as a velocity impulse which alters the direction and magnitude of the instantaneous orbital velocity vector of the spacecraft, inserting it into a new orbit.

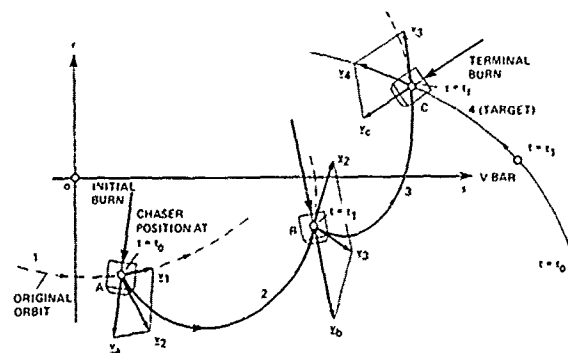


Figure 5. Example of a three burn maneuver.

Since the initial location A is not necessarily a stationary point, the magnitude and direction of the relative velocity of the chaser at point A is determined by the parameters of its orbit. If no maneuvering burn were initiated at $t = t_0$, the chaser would continue to follow the relative trajectory 1, subject to the parameters of its original orbit, see dotted line in Figure 5. However, a maneuvering burn at $t = t_0$ will alter the original orbit so that the chaser will follow the relative trajectory 2, subject to the parameters of this new orbit.

In Figure 5 v_1 and v_2 indicate the relative velocity vector of the chaser just before and after the maneuvering burn, respectively, where v_1 and v_2 are tangential to the relative trajectories 1 and 2, respectively. The vector difference between v_1 and v_2 , v_d , is the velocity change initiated by the burn, and corresponds with the direction

and magnitude or duration at which the orbital maneuvering system is activated. Likewise, at way-point B the burn v_b alters the orbit to orbit 3.

Location C is the terminal way-point and is in this case the location where the target will arrive at $t = t_f$. Since the target has an orbit of its own, orbit 4, it will have a terminal relative velocity of v_4 at $t = t_f$. The relative velocity between target and chaser is the vector difference between v_3 and v_4 , v_c . This vector determines the retro-burn that is needed at the target location, in order to bring the relative velocity between chaser and target to the minimum required for the docking operation.

2.5 Inverse method of solving orbital motion.

Interactive trajectory design demands that the operator be given free control over the positioning of way-points. However, the usual input variables of the equations of orbital motion are the magnitude and direction of the burn, rather than the time and relative position of way-points. Therefore an "inverse method" is required to compute the values of a burn necessary to arrive at a given way-point positioned by the operator. This method is outlined hereafter.

The equations of orbital motion can be computed from its momentary position and velocities, relative to a reference spacecraft with a known circular orbit [12] [16] [17] [18] [19]. Thus, for a given initial relative position A with $x(t_0)$ and an initial relative velocity $v(t_0)$, the relative position and velocities of a way-point at time $t = t_1$ can be computed. However, a maneuvering burn at $t = t_0$ will cause a change in the direction and magnitude of the relative velocity vector $v(t_0)$. As a result of this maneuvering burn, the position of the way-point at time t_1 , will change as well.

Consider v_a and α_a to be the magnitude and direction of the velocity change due to the maneuvering burn. Then the relative position and velocity at $t = t_1$, $x(t_1)$, will be a complex non-linear function of v_a and α_a . [16] [17] [17] (Grunwald and Ellis, 1988) Consider now that the operator is given direct control over v_a and α_a , by slaving these variables respectively to the x and y motions of a controller such as a mouse. A displacement of the mouse in either x or y direction will result in a complex non-linear motion pattern of $x(t_1)$. (See Appendix). Furthermore, this motion pattern will change with the initial conditions. This arrangement is highly undesirable in an interactive trajectory design process, in which the operator must have direct and unconstrained control over the positioning of way-points.

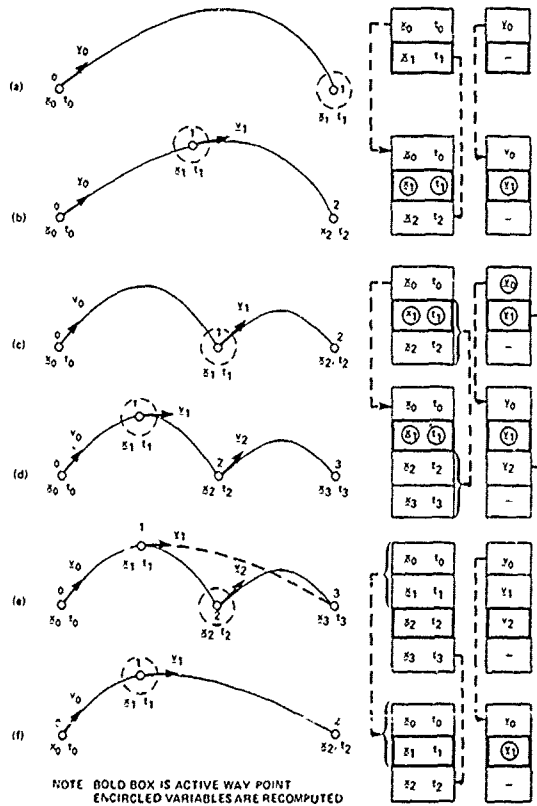


Figure 6. Editing of way-points.

It is therefore essential to give the operator direct control over the position and relative time of way-points rather than over the magnitude and direction of the burn. The inverse method by which this is accomplished computes the magnitude and direction of the burn required to bring the spacecraft from initial location $\underline{x}(t_0)$ to the way-point $\underline{x}(t_1)$ at $t = (t_1)$. This inverse technique contrasts with conventional display aids for proximity operations which are generally forward looking and provide a predictor [13] [14]. While forward looking displays are probably well suited as flying aids for real-time, out-the-window control, a planning system need not conform to this style of aiding.

2.6 The Active Way-point Concept

Although a trajectory may be composed of several way-points, only one way-point at a time, the active way-point, is controlled by the operator. While the position and time-of-arrival of the active way-point can be varied, the position and time-of-arrival of all other way-points remains unchanged. However, variations in the active way-point will cause changes in the trajectory sections and way-point maneuvering burns just preceding and just following the active way-point. The on-line solution of the inverse algorithm enables these changes to be visualized almost instantaneously and provides the operator with on-line feedback on his design actions.

2.7 Way-point editing.

The trajectory design process involves changes in existing way-points, addition of new points or deletion of existing undesired points. An illustrative example of this way-point editing process is shown in Figure 6. In the program the way-points are managed by a way-point stack, which includes an up-to-date sequential list of the position \underline{x} , the time-of-arrival t and the relative velocity \underline{v} just after initiating the burn, of all way-points.

Figure 6a shows two way-points, the initial point \underline{x}_0 and the terminal point \underline{x}_1 . The initial way-point is defined by the initial conditions of the situation and cannot be activated or changed by the operator. The terminal way-point \underline{x}_1 is thus the active way-point which can be changed and placed at a required location. The corresponding way-point stack is shown on the right. The active way-point box is drawn in bold. The relative velocity stack shows only the velocity \underline{v}_0 , which is the relative velocity just after the burn at way-point 0, computed by the inverse algorithm, and required to reach point \underline{x}_1 at time t_1 .

Figure 6b shows the addition of a new way-point. Though its time of occurrence may be manually adjusted later, the new way-point is added half-way in time on the trajectory section just preceding the active way-point. Thus its time-of-arrival is chosen to be $t = 0.5(t_1 + t_{i-1})$, where i is in this case 1 and relates to the stack before modification. The new position \underline{x}_1 and relative velocity \underline{v}_1 are computed by a conventional "forward" method, by computing the orbital position at the new time t , using the existing orbital parameters previously computed with \underline{x}_0 , \underline{v}_0 and t_0 . The newly computed way-point position, time and relative velocity are inserted between points 0 and 1 of the stack before modification and the new way-point is chosen to be the active one. The dotted lines in Figure 6 indicate variables which are transferred without modification and the encircled variables are the newly computed ones. It is important to note that since the relative velocities \underline{v}_0 and \underline{v}_1 are matched to the required way-points \underline{x}_1 and \underline{x}_2 , respectively, the inverse algorithm does not need to make any adjustments.

Figure 6c shows the results of changes in the newly created way-point on the way-point stack. Since \underline{x}_1 and t_1 are varied, the relative velocity at way-point 0, \underline{v}_0 will be readjusted by the inverse algorithm and likewise the relative velocity \underline{v}_1 .

Figure 6d shows the creation of an additional new way-point. Since the active way-point prior to the addition was point 1, the new point is added half-way between point 0 and 1 and its position and relative velocity are computed with the forward method. The new values are inserted between points 0 and 1 of the stack before modification and the new way-point is again set to be the active one.

In Figure 6e way-point 2 is activated. Apart from the shift in active way-point, the stack remains unchanged. The dotted line shows the direct-path section between point 1 and point 3 without the intermediate burn at point 2. Deletion of the way-point 2 will remove this point from the stack and after that close the gap, see Figure 7f. However \underline{v}_1 has to be readjusted to fit the new direct-path section. This adjustment is made on-line by the inverse algorithm.

The repetitive use of the inverse algorithm to calculate the trajectories linking each pair of way-points presents the planner with a kind of "geometric spread-sheet" that preserves certain relationships between point in space, namely that they are connected by fuel-minimum trajectories for their particular separation in time, while their other properties, namely their relative position in space, may be freely varied. To our knowledge this application of inverse dynamics to this kind of display problem is new and has some very helpful side-effects. The constant background computation to preserve the relative position and time of each way-point creates an illusion of an inertially stable space that assists planning of relative movements about a target spacecraft. Additionally, this technique assists planning by allowing separable solutions to the plume impingement, velocity limit, and traffic conflict problems. Once a way-point has been positioned to bring an aspect of a maneuver within prescribed limits, e.g. relative velocity, the adjustment can be isolated from the effects of earlier adjustment such those to satisfy a plume impingement constraint. This isolation of the solutions of the separate problems is an essential characteristic since without it, the solution to one maneuver problem would undo a solution to another.

2.8 Operational constraints

The multi-spacecraft environment will require strict safety rules regarding the clearance from existing structures. Thus, spatial "envelopes" can be defined, through which the spacecraft is not allowed to pass. These spatial constraints can be visualized as volumes on the display.

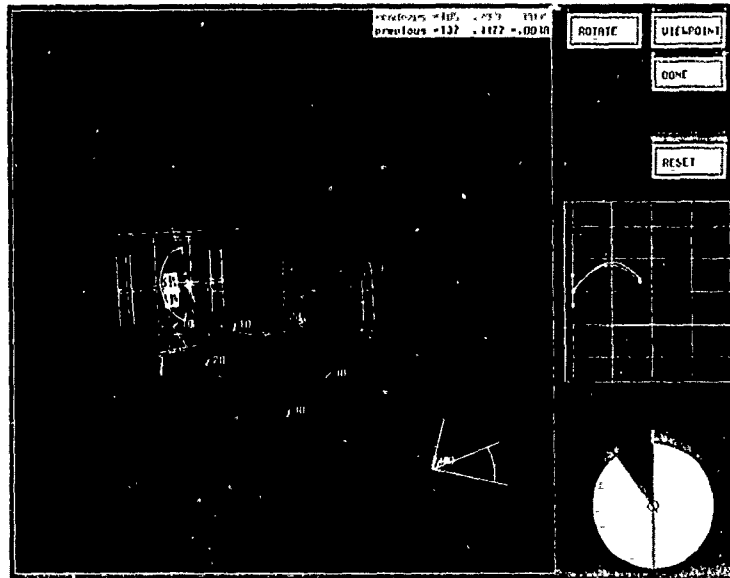


Figure 7. Screen image of the proximity operations planning tool. The upper right window shows the soft buttons for the viewpoint control mode. The out-of-plane display is shown in the middle right window. The lower right window shows the fuel display. The main viewport shows an incompletely planned mission for which three burns have been selected. The velocity vector or +V- bar is shown by the arrow pointing to the right on the central grid line. Note that the relative velocity vector on arrival, shown by the arrow in the lower right of the viewport, is outside of the entry arc indicating the acceptable range of relative velocity on arrival with the target craft.

Restrictions on angles of departure and arrival may originate from structural constraints at the departure gate or the orientation of the docking gate or grapple device at the target craft. Limits for the allowable angles of departure or arrival can be visualized as cones on the display. In addition the terminal approach velocity at the target might be limited by the target characteristics. Limits for the allowable start and end velocities can be visualized as limit arcs associated with the approach or departure cones (See Figure 7). The limit arc symbols on the display graphically show allowable ranges of magnitude and direction for thrusts and relative velocities.

Way-point maneuvering burns are subject to plume impingement constraints. Hot exhaust gasses of the orbital maneuvering systems may damage the reflecting surfaces of sensitive optical equipment such as telescopes or infra-red sensors. Even cold nitrogen jets might disturb the attitude of the target satellite. Maneuvering burns towards this equipment are restricted in direction and magnitude, where limits for the allowable direction and magnitude are a function of the distance to the equipment and plume characteristics. These limits can be visualized as limit arcs on the display.

Flight safety requires that the relative velocity between spacecraft is subject to approach velocity limits. In conventional docking procedures this limit was proportional to the range, [9] [10]. A commonly used rule-of-thumb is to limit the relative approach velocity to 0.1 percent of the range. This conventional rule is quite conservative and originates from visual procedures in which large safety margins are taken into account to correct for human or system errors. Although the future traffic environment will be more complex, and will therefore demand larger safety margins, more advanced and reliable measurement and control systems may somewhat relax these demands.

In this display the relative approach velocity is defined as the component of the relative approach velocity vector between the two spacecraft along their mutual line-of-sight. The limit on this relative approach velocity is a function of the range between the spacecraft. This function will depend on the environment, the task and the reliability of measurement and control equipment and can not be determined at this stage. For this display a simple proportional relation has been chosen. The approach velocity limit is visualized on the display as a circle drawn around the chaser indicating the minimum range between the two spacecraft allowed for the present approach velocity. If the target craft appears within this circle, the approach limit has been violated.

2.9 General Comments

The proposed interactive orbital planning system should be seen as a step in determining a display format which may be useful in a future dense spacecraft traffic environment. The examples shown here deal with the most general situation, which involves departures from or arrival at non-stationary locations. Such missions with spacecraft at non-stationary positions and substantial out-of-plane motion may represent worst-case situations but these are the ones most likely to require customized maneuvering.

It is hard to predict whether the constraints used here will be relevant and realistic in the future spacecraft environment. However, they encompass in a broad sense the general type of restrictions which are expected in the multi-vehicle environment, e.g. limitations on approach rates, plume impingement and clearance from structures.

A final restriction of the present display relates to the way the orbital maneuvering system is activated. Only pure impulse maneuvering burns are considered, in which the duration of the burn is negligible with respect to the duration of the mission and in which these burns cause major changes in the relative trajectories. Station keeping or fly-by missions however, require a more sustained type of activation, such as periodic small burns with several seconds intervals over a time-span of several minutes. A more "distributed" way of activating the orbital maneuvering system could be introduced in which the operator has control over the frequency and time-span of the activation.

A last comment relates to the way the spatial trajectory is visualized. The perspective main view shows the projection of the actual trajectory on the orbital plane, rather than the trajectory itself. The reason for this is twofold. The orbital trajectory, with its typical cycloidal shape, when shown without lines projecting onto the orbital reference plane, is ambiguous and might seem to come out of the orbital plane. This illusion may result from the viewers familiarity with common objects such as a coil spring and has been first reported earlier [16] [17] [20] (Ellis and Grunwald, 1987). Therefore, the trajectory can not be clearly shown without its projection on the orbital plane. However, since the symbolic enhancements and burn vectors relate to the in-plane motion and match with the trajectory projection on the orbital plane, both the trajectory and its projection should be visualized. However, for most views of a 3D display, both the trajectory and its projection on the orbital plane will show up as separate curves, a fact that may cause confusion. Therefore, a compromise has been sought, in which the projection is shown together with "pedestals" placed at the way-points orthogonal to the orbital plane, which mark the actual trajectory at the way-points. In spite of these restrictions the proposed display illustrates the usefulness of interactive graphical trajectory design.

3. Experimental Study

An experiment has been conducted with the above planning tool to determine the time required to plan a variety of rendezvous missions for which the target's orbital insertion parameters were systematically varied. In particular, we attempt to develop a regression predictive of the time required to plan a rendezvous with a vehicle simulating an inadvertently released object from a variety of positions along the main structures of a dual-keel space station configuration. The space station is modeled in a 480 km circular orbit inclined 28.5 deg. with respect to the equator. This corresponds to a V_0 orbital velocity of 7,623 m/sec or an orbital angular rate 0.0011 rad/sec. The chasing vehicle for the maneuver departed from a +V-bar location on the station and may be thought of as a craft attempting to recover an astronaut or small object such as a wrench accidentally released with either 0 or moderate (1.0 m/sec) Δv and which is drifting away under the influence of orbital mechanics. Out of plane components of the target were randomly selected to be ± 0.25 or ± 0.5 m/sec. The direction of the added Δv at insertion was systematically varied in 8 equal directions about the +V-bar. The 10 orbital insertion points for the targets were distributed along the port keel of the Space Station from 200 m above the center of mass to 150 m below it and randomly selected to produce 90 different recovery scenarios. The planned 1 way flight time was 20 minutes and the maneuver took place during orbital daylight. The scenarios simulate the rendezvous phase of a rendezvous and retrieval mission.

3.1 Task

The subject's task was to expeditiously plan a feasible in and out-of-plane trajectory from a Space Station +V-bar departure port to rendezvous with the target subject to plume impingement constraints on the station, avoidance of the station's structure, and alignment of the relative velocity vector on rendezvous to fit within the 30 deg. entrance cone. All subjects were told to complete their planning task quickly, much as they would wish to walk across a room without wasting time and not to worry about minimizing overall fuel use, though they were limited to 12 m/sec Δv of maneuvering fuel. Figure 9 illustrates a three burn partial solution to one of the experimental scenarios in which the relative velocity on rendezvous has not yet been adjusted to fit within the approach constraint shown by the approach cone.

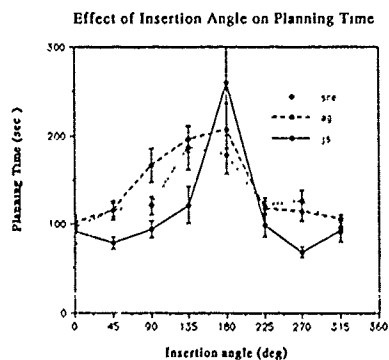


Figure 8. The mean planning time from each of three subjects shows a marked peak for target insertion angles around 200 degrees. The error bars are ± 1 standard error.

3.2 Subjects

Three highly practiced subjects very familiar with the operation of the planning tool planned rendezvous for the set of initial conditions which were generally novel to them.

3.3 Procedure and Design

Before beginning the experiment the subjects reviewed a training manual describing the display's controls and practiced their operation on a sample rendezvous. Thereafter, subjects were automatically presented through a UNIX C-shell script with the 90 rendezvous problems in four approximately equal groups of randomly ordered conditions. Data collection took about 6 hours and was generally spread across two days. Descriptive statistics were collected automatically by the IRIS computer to summarize planning time, fuel use, number of way-points used, and a large number of other detailed characteristics of the mission planning process.

3.4 Results

The planning time required for the selected missions was highly dependent upon the angle of the insertion delta v . (Figure 8) Analysis of variance on time ($F=7.968$ $df=7,14$ $p < .001$) showed that the effects of insertion angle were large, statistically reliable, and dominated effects due to the point of insertion. Planning time was not significantly affected by the selection of an insertion point. ($F= 0.584$ $df=9,18$ ns) and there was no statistical interaction between the insertion angle and the insertion point. ($F=0.870$ $df=63,126$ ns).

3.5 Discussion

In earlier experiments differences in planning time appeared mainly due to the misalignment of the approach cone axis with the relative velocity resulting from a two burn fuel-minimum intercept trajectory. These differences were reduced by practice, but maintained a rough proportionality [21] (Ellis and Grunwald, 1988). Thus, a rendezvous that took twice as long as another approximately maintained this proportion as practice reduced the times for both of them. Thus, the differences observed in the present experiment with highly practiced subjects probably reflect genuine differences in planning difficulty arising from the interaction of orbital dynamics and the mission constraints. For the particular conditions used, insertion angles near 135 degrees are particularly hard. Accordingly, potential chase vehicles should be positioned at several ports, V-bar and R-bar, to facilitate capture of inadvertently separated objects.

The results of the present and previous experiments make clear that experienced human operators can manually, quickly plan complex orbital maneuvers when their planning tool is adapted to their capabilities. It is, none the less, also clear that automatic systems could also plan these maneuvers. These results can help set performance criteria for these automatic systems since they should at least be capable of producing feasible plans in less than two minutes to beat a manually determined plan. Incorporation of all the mission constraints, however, can greatly complicate and lengthen an automatic search since these constraints may be arbitrary placed in space and in some cases may be discrete. The development of useable search algorithms is a current direction of research and certainly constrained random search strategies could be adopted if more efficient analytic methods do not work well [22] (Soller, Grunwald, and Ellis, 1989).

But it is also clear that however the maneuver is planned, any astronaut who would be flying the mission would want to foresee what the system has planned for him and be able to visualize his trajectory, if for no other reason to monitor its unfolding as it is flown. Automatically generated trajectories will only be as good as the designer's hindsight in selecting optimization criteria and mission constraints. Unique mission features or failures may arise that require the custom-tailoring of a trajectory. Significantly, the mission planning interface described in this paper also can serve as an interface to a mission "editor" that would allow an astronaut to visualize the planned trajectories and edit them if necessary to suit his special requirements.

4. References

- [1] Atkeson, Christopher G (1988) Learning arm kinematics and dynamics *Annual Review of Neuroscience*, 12, 157-183.
- [2] Pellionisz, András J. (1985) *Cerebellar functions*, Springer, Berlin. 201-229.
- [3] Pennington, Jack K. (1983) A rate-controlled teleoperator task with simulated transport delay. *NASA TM 85653*, September, 1983
- [4] Stark, Lawrence (1988) Biological redundancy. Proceedings of the NATO Workshop on Telerobotics (Abstract 303).
- [5] Poulton, E.C. (1974) *Tracking skill and manual control* Academic Press., New York.
- [6] Wickens, Christopher D. (1986) The effects of control dynamics on performance. in *Handbook of Perception and Human Performance* Boff, K. R., Kaufman, L., Thomas, J. P., Eds., Wiley, New York.
- [7] Palmer, Everett, Jago, Sharon, Baty, Daniel L., O'Connor, Sharon (1980) Perception of horizontal aircraft separation on a cockpit display of traffic information *Human Factors*, 22, 605-620
- [8] Palmer, Everett, (1983) Conflict resolution maneuvers during near miss encounters with cockpit displays of traffic information. *Proceedings of the Human Factors Society 27th Annual Meeting*, Human Factors Society, Santa Monica, CA. 757-761
- [9] NASA Lyndon B. Johnson Space Center, (1982) *Flight Procedures handbook*, JSC-10566, November 1982.
- [10] NASA Lyndon B. Johnson Space Center (1983) *Rendezvous/Proximity Operations Workbook RNDZ 2102*, 1983.
- [11] Allen, Joseph P. (1988) Physics at the edge of the earth in *Physics in a technological world*. A.P. French, Editor, American Institute of Physics, New York.
- [12] Kovalevsky, J. (1984) *Introduction to Celestial Mechanics* Translated by Express Translation Service, Springer-Verlag New York Inc., New York.
- [13] McCoy, W. K. Jr., and Frost G. G. (1966) Predictor Display Techniques for On-Board Trajectory Optimization of Rendezvous Maneuvers," Aerospace Medical Research Laboratories AMRL-TR-66-60, May, 1966.
- [14] Brody, A. R. (1988) A forward-looking interactive orbital trajectory plotting tool for use with proximity operations *NASA CR 177400*, June, 1988
- [15] Eyles, D. (1986) A Computer Graphics System for Visualizing Spacecraft in Orbit, In *Spatial Displays and Spatial Instruments*, Ellis, S.R. Kaiser, M., and Grunwald, A. Eds., *NASA-CP 10032*.
- [16] Grunwald, Arthur J. and Ellis, Stephen R. (1988a) Interactive orbital proximity operations planning system *Proceedings of the 1988 IEEE International Conference on Systems, Man, and Cybernetics*, Peking, China., IEEE CAT 88CH2556-9, 1305-13-12.
- [17] Grunwald, Arthur J. and Ellis, Stephen R. (1988b) Interactive orbital proximity operations planning system. *NASA TP 2839*
- [18] Taff, L. G. (1985) *Celestial Mechanics, A Computational Guide for the Practitioner* John Wiley & Sons, New York.
- [19] Thomson, W. T. (1986) *Introduction to Space Dynamics* Dover Publications, Inc., New York.
- [20] Ellis, S. R. and Grunwald, A. J. (1987) A New Illusion of Projected Three-Dimensional Space, *NASA TM 100006*, July 1987.
- [21] Ellis, Stephen R., Grunwald, Arthur (1988) A visualization tool for planning orbital maneuvers for proximity operations design philosophy and preliminary results. *Proceedings of the 23rd Annual Conference on Manual Control*, June 22-24, 1988, BBN Cambridge, Massachusetts
- [22] Soller, Jeffery, Grunwald, Arthur J., Ellis, Stephen R. (1989) Optimization of multiburn orbital maneuvers in proximity operations. *NASA TM in preparation*.

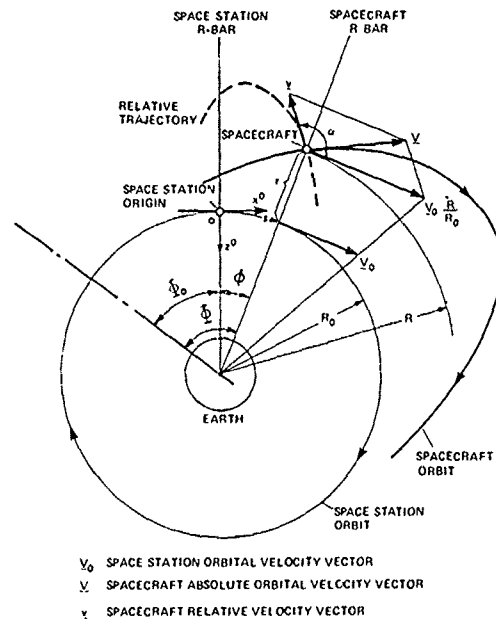


Figure 9. In-plane orbital situation showing the difference in phase angles Φ_0 and ϕ for the space station and another spacecraft. Note that the bold solid line represents the absolute spacecraft orbit and the dotted line represents its trajectory relative to the space station. The ratio of r to R_0 has been greatly exaggerated.

Appendix

Relative motion in space-station coordinates

The relative position and velocity of a co-orbiting spacecraft in space station coordinates are $x^0 \equiv \{x^0, y^0, z^0\}$ and $\dot{x}^0 \equiv \{\dot{x}^0, \dot{y}^0, \dot{z}^0\}$ and are obtained from space station based measurement equipment where $\dot{x}^0 = dx^0(t)/dt$ etc. denotes the time derivative.

Since the displacements and velocities in the out-of-orbital-plane direction y^0 are usually much smaller than the ones in the orbital plane, in x^0 and z^0 direction, and since out-of-plane maneuvering burn does not significantly alter the total orbital energy, the out-of-plane motion can be decoupled from the in-plane motion. Hence, the in-plane motion will be analyzed first.

At the initial time $t = t_0$ the radius of the space station orbit R_0 is given by: $R_0 = R_E + h$, where $R_E = 6,378,140$ m is the equatorial earth radius and $h = 480,000$ m is the altitude of the space-station orbit above the earth surface. The absolute orbital velocity of the space-station is then given by: $V_0 = (GM/R_0)^{1/2}$, where $GM = 3.986005 \times 10^{14}$ m³/sec² is the geocentric gravitational constant. For simplicity the curvature of the V-bar is assumed to be negligible, so that

$$\begin{aligned}
 s &\sim x^0 \\
 r &\sim z^0 \\
 v &\sim \sqrt{\dot{s}^2 + \dot{r}^2}
 \end{aligned}
 \tag{1abc}$$

$$\begin{aligned}
 \alpha &= \tan^{-1}(\dot{r}/\dot{s}) \quad \dot{s} \geq 0 \\
 \alpha &= \tan^{-1}(\dot{r}/\dot{s}) + 180^\circ \quad \dot{s} < 0
 \end{aligned}
 \tag{2ab}$$

where s is the distance measured along the V-bar between the space station and the spacecraft's R-bar, r the distance of the spacecraft above the V-bar, measured along the R-bar, v the magnitude of the relative velocity and α its direction, measured from the V-bar in upwards direction (positive rotation in the right-hand system). The relative velocity reflects the situation just after the activation of a maneuvering burn.

Although the general solution for orbital motion is fairly complex and non-linear, the relative motion between two co-orbiting spacecraft in close proximity, can be simplified by a first order approximation. This is known as the Euler-Hill solution which allows both the "forward" solution and the "inverse" solution. The forward solution computes at a given final time t_f and for a given relative initial position and initial velocity vector, the final relative position and velocity. On the other hand, the inverse solution computes for given t_f and given initial location, the required initial velocity vector to reach a given desired final location. The linearized Euler-Hill solution is derived as follows.

The in-orbital-plane motion of a spacecraft orbiting the earth is described by two degrees of freedom: the radius R and the orbital angle, Φ , with respect to an arbitrary fixed reference (see Fig. 9). Making use of Newton's first law and his law of gravity, the equations of motion of the spacecraft in the absence of external forces are given by:

$$\begin{aligned} \ddot{\Phi}(t) R(t) + 2\dot{\Phi}(t) \dot{R}(t) &= 0 \\ \ddot{R}(t) - \left\{ \dot{\Phi}(t) \right\}^2 R(t) + \frac{GM}{R(t)^2} &= 0 \end{aligned} \quad (3a,b)$$

The motion of the Space Station is described by $R_0(t)$ and $\Phi_0(t)$. $R(t)$ and $\Phi(t)$, can now be expressed as:

$$\begin{aligned} R(t) &= R_0 + r(t) \\ \Phi(t) &= \Phi_0 + \phi(t) \end{aligned} \quad (4a,b)$$

Since the spacecraft is in close proximity to the Space Station r and ϕ are relatively very small in comparison to R_0 and Φ_0 . Since the Space Station is in circular orbit, it follows that

$$\begin{aligned} R_0(t) &= R_0 = \text{constant and} \\ \dot{\Phi}_0(t) &= n_0 = \text{constant} \end{aligned} \quad (5a,b)$$

where n_0 is the mean motion or angular orbital rate of the Space Station in radians/sec.

Differentiating Eqs (4a,b) and using Eqs.(5a,b) yields:

$$\begin{aligned} \dot{R}(t) &= \dot{r}(t); \quad \ddot{R}(t) = \ddot{r}(t) \\ \dot{\Phi}(t) &= n_0 + \dot{\phi}; \quad \ddot{\Phi} = \ddot{\phi} \end{aligned} \quad (6a-d)$$

Substituting Eqs.(6a-d) in Eqs.(3a,b), neglecting products of r and ϕ and of their derivatives, using Kepler's third law:

$$n_0 = \sqrt{\frac{GM}{R_0^3}} \quad (7)$$

and using the definitions:

$$\dot{s}(t) = R_0 \dot{\phi}(t); \quad \ddot{s}(t) = R_0 \ddot{\phi}(t) \quad (8a,b)$$

yields the linearized equations for the relative motion of a spacecraft with respect to the Space Station (Euler-Hill equations).

$$\begin{aligned} \ddot{s}(t) + 2n_0 \dot{r}(t) &= 0 \\ \ddot{r}(t) - 3n_0^2 r(t) - 2n_0 \dot{s}(t) &= 0 \end{aligned} \quad (9a,b)$$

For given initial conditions $r_0, \dot{r}_0, s_0, \dot{s}_0$ where $r_0 \equiv r(t_0)$ etc., the solution for $r(t)$ and $s(t)$ written in matrix form is:

$$(10) \quad \begin{bmatrix} r(t) \\ s(t) \end{bmatrix} = \begin{bmatrix} a_{11} & a_{12} \\ a_{21} & a_{22} \end{bmatrix} \begin{bmatrix} \dot{r}_0 \\ \dot{s}_0 \end{bmatrix} + \begin{bmatrix} b_{11} & 0 \\ b_{21} & 1 \end{bmatrix} \begin{bmatrix} r_0 \\ s_0 \end{bmatrix}$$

where

$$(11a-f) \quad \begin{aligned} a_{11} &= \frac{1}{n_0} \sin(n_0 t) \\ a_{12} &= \frac{2}{n_0} [1 - \cos(n_0 t)] \\ a_{21} &= -a_{12} \\ a_{22} &= \frac{1}{n_0} [4 \sin(n_0 t) - 3 n_0 t] \\ b_{11} &= 4 - 3 \cos(n_0 t) \\ b_{21} &= 6 [\sin(n_0 t) - n_0 t] \end{aligned}$$

and the solution for the velocity vector components $\dot{r}(t)$ and $\dot{s}(t)$ is:

$$(12) \quad \begin{bmatrix} \dot{r}(t) \\ \dot{s}(t) \end{bmatrix} = \begin{bmatrix} d_{11} & d_{12} \\ d_{21} & d_{22} \end{bmatrix} \begin{bmatrix} \dot{r}_0 \\ \dot{s}_0 \end{bmatrix} + \begin{bmatrix} e_{11} & 0 \\ e_{21} & 0 \end{bmatrix} \begin{bmatrix} r_0 \\ s_0 \end{bmatrix}$$

where

$$(13a-f) \quad \begin{aligned} d_{11} &= \cos(n_0 t) \\ d_{12} &= 2 \sin(n_0 t) \\ d_{21} &= -d_{12} \\ d_{22} &= [4 \cos(n_0 t) - 3] \\ e_{11} &= 3 n_0 \sin(n_0 t) \\ e_{21} &= 6 n_0 [\cos(n_0 t) - 1] \end{aligned}$$

Eqs.(10-13) constitute the "forward" solution. For a given final time or time-of-arrival $t = t_f$ first the coefficients of Eqs.(11) and (13) are computed and after that with Eqs(10) and (12) the final position r_f, s_f and final velocity \dot{r}_f, \dot{s}_f are found, where $r_f \equiv r(t_f)$. With the "inverse" solution, the initial velocities \dot{r}_0 and \dot{s}_0 have to be computed for given time-of-arrival t_f and given initial position r_0, s_0 and final position r_f, s_f . These velocities are easily obtained from Eq.(10) according to:

$$(14) \quad \begin{bmatrix} \dot{r}_0 \\ \dot{s}_0 \end{bmatrix} = \begin{bmatrix} a_{11} & a_{12} \\ a_{21} & a_{22} \end{bmatrix}^{-1} \begin{bmatrix} r_f - b_{11} r_0 \\ s_f - b_{21} r_0 - s_0 \end{bmatrix}$$

where

$$(15) \quad \begin{bmatrix} a_{11} & a_{12} \\ a_{21} & a_{22} \end{bmatrix}^{-1} = \frac{1}{(a_{11} a_{22} - a_{12}^2)} \begin{bmatrix} a_{22} & -a_{12} \\ -a_{21} & a_{11} \end{bmatrix}$$

and then may be used to compute the angle and magnitude of relative velocity, α and v from Eq.(1) and Eq.(2).

EFFECTS OF LOW BOND NUMBER LIQUID
MOTIONS ON SPACECRAFT ATTITUDE

by
J.P.B. Vreeburg, R.F. van den Dam
National Aerospace Laboratory NLR
PB 90502. NL-1006 BM Amsterdam

SUMMARY

The introduction gives a short review of the effects that onboard liquid may have on the dynamics of the spacecraft. A distinction is made between arbitrarily moving craft and spin-stabilized vehicles. The modelling of rotating liquid behaviour is very complicated and generally allows only to make predictions on the stability behaviour of a spinning spacecraft.

A flight experiment with a model satellite, with liquid in an annular tank, during parabolic aircraft flight is described. From a filmed record of the unconstrained motion, the attitude of the satellite is reconstructed. Details of the image processing scheme are given.

The numerical simulation of the motion of the model satellite is explained. The liquid is inviscid and is assumed to move in the tank in two directions only, i.e. radial motion is neglected. Surface tension effects are important and are fully accounted for. The angular rates of the model following a short-duration torque, are presented. Plots of the liquid motion are included.

INTRODUCTION

Spacecraft attitude control is only one of the disciplines that are concerned with the dynamics of a solid body with a liquid reservoir. Terrestrial problem areas are represented by sloshing liquid in vehicles like trucks, ships or rockets but there are also dynamic problems governed by rotation of the tank such as spinning liquid-filled projectiles. In the sequel the tank will denote the solid part of the body with liquid. It is characterized by mass, moments of inertia, internal geometry and location and orientation of the void with respect to its center of mass. Although the elastic properties of the tank are important for some types of problems, these will be disregarded in the present paper, i.e. the tank is assumed to be rigid.

For spacecraft the effects of gravity on the liquid configuration in a partially-filled tank can be disregarded. This condition may also apply on earth; when the transient or centrifugal accelerations of the tank are much larger than g . However, in space the tank accelerations could be sufficiently low that the surface tension of the liquid has a considerable influence on its behaviour (Ref. 1). The order-of-magnitude relation between these two effects is expressed by the Bond number $Bo = \frac{aL^2}{\beta}$ where a = acceleration, β = kinematic surface tension and L is a characteristic dimension. Low Bond number conditions on earth can be achieved only by reduction of L , commonly to submillimeter dimensions (capillarity, porous media), or in a static configuration of two isopycnic immiscible liquids.

A further consequence of the space environment is the absence of supporting forces and thus, at least for some spacecraft, conservation of angular and linear momentum. This is of importance for the stability behaviour of spinning spacecraft; reference 2 illustrates how internal (viscous) dissipation destabilizes a top with constant angular momentum as compared to a top acted on by external friction. It is noted that this effect complicates the testing on earth of the attitude behaviour of spacecraft even with full tanks, i.e. without excursions of the center of mass (Ref. 3,4).

There have been meetings devoted to the dynamics of spacecraft with liquid (Ref. 5,6,7), although recent presentations were given at more universal conferences. A general opinion is that most real problems are intractable and can be solved only by numerical simulation. The behaviour of liquid as forced by surface tension in a tank with prescribed motion can be modelled satisfactorily (Ref. 8-11) but at a cost of long run times even on a supercomputer. The simulation of the coupled problem, where the rigid body moves under liquid forces, is less well developed (Ref. 12-14). The present paper applies and extends the method developed at NLR to a configuration that can be analysed by approximate methods.

Building blocks for a comprehensive body of knowledge exist. The basic theory is elaborated in the standard book of Moiseyev and Romyantsev (Ref. 15) and developed considerably since. The pure hydrodynamic aspects of capillary liquid motion, starting from a hydrostatic equilibrium configuration, are developed in reference 16. For spinning tanks a variety of stability criteria have been derived (Ref. 17,18) and detailed analyses for idealized liquid configurations are available (Ref. 19,20). Experiments with moving tanks in microgravity have been conducted and are reported in the literature (Ref. 21-26). The data generally consist of measurements of liquid response to a forced motion of the tank, as recorded by a dynamometer. Observations of coupled motions, reported in the sequel, are less common (Ref. 25; see also ONERA contribution in Ref. 7) but sometimes give data on actual spacecraft behaviour (Ref. 25,27). For early work the bibliography of reference 28 could be consulted.

The experiments and tests are, with exceptions, not performed on full-size spacecraft but on scale models. There are two types of objectives for such programs: 1) to test a crucial phase in the mission of the actual spacecraft (Ref. 24,25), or 2) to determine experimental values for parameters that figure in lumped parameter models of spacecraft behaviour (Ref. 29-32). The modelling laws are not very well known and so the scaled model experiments are not truly reliable. Progress in this area is most wanted.

BACKGROUND OF THE INVESTIGATION

At NLR, research on the effects of liquid on spacecraft motions started in connection with the IRAS satellite. This spacecraft was equipped with a large dewar with superfluid helium and had a manoeuvring capability in order to train a telescope at a desirable location on the celestial sphere. Over the years experiments on forced liquid behaviour in containers with simple geometric shapes have been conducted (Ref. 33,34). The present investigation has been conducted with a free-floating tank with annular cylindrical void. The article is denoted by Wet Satellite Model, or WSM. A sketch of its cross-section is given in figure 1.

The tank possesses inertial axisymmetry; its moment of inertia about the axis of symmetry is I_o , the (principal) moment normal to the axis is I_x . The liquid inside the tank cannot move swiftly in the radial direction, i.e. normal to the cylinder surfaces. This feature allows to model the liquid behaviour with only two velocity components, i.e. neglect the radial velocity. A further important simplification results if the liquid is assumed to be inviscid. In that case the liquid cannot exert a torque about the axis of symmetry since the forces from liquid pressure are either parallel to or intersect this axis. During a transient motion the forces at a stuck contact line could possibly result in such a torque but this remains to be investigated. First order corrections to the inviscid case with no radial flow can be obtained from solutions of the linear perturbation equations. Although the previous discussion has considered the wall pressures as the coupling between the liquid and the tank, it is more convenient to formulate the problem as if the liquid were solidified and correct for liquid motions by additional forces (Ref. 12,35,36).

The equations for the dynamics of the tank and the liquid are:

$$m\ddot{\underline{R}}_o + \underline{\dot{\omega}} \times m\underline{r} = -\underline{\omega} \times (\underline{\omega} \times m\underline{r}) - \int_{\text{liquid}} \rho \underline{a} dV - 2 \int_{\text{liquid}} \rho \underline{\omega} \times \underline{v} dV + \underline{K} \quad (1)$$

$$-\ddot{\underline{R}}_o \times m\underline{r} + I\dot{\underline{\omega}} = -\underline{\omega} \times I\underline{\omega} - \int_{\text{liquid}} \rho \underline{r} \times \underline{a} dV - 2 \int_{\text{liquid}} \rho \underline{r} \times (\underline{\omega} \times \underline{v}) dV + \underline{M} \quad (2)$$

$$\nabla \cdot \underline{v} = 0 \quad (3)$$

$$\underline{a} + \frac{1}{\rho} \nabla p - \nu \Delta \underline{v} = -\ddot{\underline{R}}_o - \underline{\omega} \times (\underline{\omega} \times \underline{r}) - \dot{\underline{\omega}} \times \underline{r} - 2 \underline{\omega} \times \underline{v} + \underline{F} \quad (4)$$

where a superposed dot indicates the rate of change in an inertial coordinate system. The body-fixed coordinate system Oxyz is at position \underline{R}_o in this inertial system and has angular velocity $\underline{\omega}$. The other variables are:

- m = total mass of tank with liquid
- \underline{r} = position of center of mass in Oxyz
- I = inertia tensor of frozen system about 0 } in general time-dependent for a partially filled tank
- \underline{r} = position of liquid element in Oxyz
- \underline{v} = liquid velocity with respect to Oxyz
- \underline{a} = liquid acceleration with respect to Oxyz
- \underline{K} = sum of all forces on the system
- \underline{M} = sum of all torques on the system
- \underline{F} = sum of body force accelerations on the liquid
- p = liquid pressure
- ρ = liquid density
- ν = kinematic viscosity

The solution of equation 4 requires boundary conditions (Ref. 15):

at the liquid-solid interface $\underline{v} = 0$

at the liquid-ullage interface $\frac{\partial f}{\partial t} + (\underline{v} \cdot \nabla) f = 0$

$$\sigma(\nabla \cdot \underline{n}_f) = p - p_{\text{ullage}}$$

at contact line $\underline{n}_f \cdot \underline{n}_{\text{wall}} = \cos \theta$ (moving contact line)

where $f = \text{const.}$ describes the free surface of the liquid

$$\underline{n}_f = \frac{\nabla f}{|\nabla f|} = \text{normal to the free surface}$$

- σ = surface tension
- θ = contact angle

Other conditions may be imposed at the contact line, depending on the physical properties of the material phases. Initial conditions complete the requirements for a solution of the equations. Equation 4 identifies at least three timescales, related to ω (spin), $\dot{\omega}$ (nutation) and $\ddot{\underline{R}}_o$ (slosh). For spinning liquids, additional time scale: result from inertial or Rossby waves (Ref. 37). Parametric resonances could occur when the timescales of different phenomena get in tune. The various frequencies are present

in the pressure field and thus also in the liquid force that acts on the tank. Identification of these frequencies is an important means of diagnosis of liquid behaviour. High frequency components are generally damped quickly in small geometries (by viscous friction) and so one may expect scale models for large spacecraft to represent fundamental modes behaviour only.

PARABOLIC FLIGHT EXPERIMENT

The experimental data have been collected during free-fall generated in an aircraft in parabolic flight (Ref. 38). The flight opportunity was provided by ESA during a campaign in August 1988 with NASA's KC-135 aircraft (Ref. 39).

Hardware

A sketch of the WSM is given in figure 1. The tank void has a height of 250 mm, between two cylindrical surfaces of radii $r_1 = 128$ mm and $r_2 = 144$ mm. The weight of the empty WSM is 4510 gr, its principal moments of inertia are $I_D = 0.0686$ kgm² about the axis of symmetry and $I_k = 0.0631$ kgm² normal to that axis. The moments have been determined by calculation and from experiment (torsional pendulum method).

Some stickers with characteristic shapes were glued to the WSM in order to establish its attitude on pictures. The contained liquid, water, was coloured with food colouring for better identification. A picture of the WSM in weightlessness is given in figure 2. The colouring did not affect the surface tension, as evidenced by measurement.

The momentum device and brake assembly (Fig. 1) consists of a gyroscope with 0.12 kgm²s⁻¹ of stored angular momentum and a mechanical brake. Upon release of the WSM, this brake is automatically applied and, within approx. 1 second, brings the rotor to a complete stop and so accomplishes the transfer of the angular momentum to the whole WSM. The performance of the brake has been measured. The results show that the transfer of momentum is reasonably constant, after a fast rise and before a steep decrease at the end of the braking period.

The momentum device can be affixed in two positions. The first option has the rotor axis aligned with the axis of symmetry of the WSM, the second has the rotor with an angle of $\pi/4$ with this axis at the center of the WSM.

Scenario

For the execution of an experiment, the operator holds the WSM steady at a central location in the aircraft. When the parabola is well-initiated, he releases the WSM. This action removes a power plug that provides the board electricity to the running gyro, and thereby also releases a spring that activates the mechanical brake on the gyro-rotor. The operator observes the WSM and recaptures it before it hits the wall or bottom of the cabin.

The behaviour of the WSM is recorded on 16 mm film, at 24 fps, by a cameraman who remains steady in the aircraft. From this filmed record the kinematics of the motion are to be reconstituted.

The dimensions of the WSM, for a given gyroscope, are selected such that surface tension effects can be expected to be important. In addition, the nutation frequency and the fundamental slosh frequency should be of comparable magnitude. This last requirement may be expected to produce a clearly different behaviour of the WSM as compared to a completely solid spacecraft.

The nutation frequency $\dot{\theta} = \frac{\epsilon}{\cos \alpha} \omega_s$ where ω_s is the rate of spin, $\epsilon = \frac{I_D}{I_k}$ and $\alpha =$ nutation angle. The value for ϵ as listed is for an empty, solid WSM. However ϵ is not expected to change much from liquid loading and will be about 1.1-1.2. Thus, for small nutation angles, $\dot{\theta} \sim \omega_s$.

The fundamental slosh frequency in the annulus can be related to the frequency in a cylinder as a function of Bond number (acceleration) (Ref. 40). If one assumes that a comparable relation holds for centrifugal fields, i.e. with a Weber number rather than a Bond number, the slosh frequency in the annulus can be related to the results for a rotating cylinder. Such data have been obtained during a D-1 experiment (Ref. 34). Substitution of the pertinent parameters produces a formula

$$\omega_A^2 = 25 \frac{\beta}{R^3} + 10 \omega_s^2$$

where ω_A is the fundamental slosh frequency in a spinning annulus, $\beta =$ kinematic surface tension and $R =$ outer radius of the annular void. The formula is expected to hold good only for high annulus ratios, i.e. $r_1/r_2 > 0.6$. Evidently $\omega_A > \omega_s$ and no interference between slosh and nutation frequencies may be expected for small nutation angles. Increase of ϵ could bring about such occurrence but this is undesirable since the consequent WSM motion would be very stable. If $\omega_s = 0$, $\omega_A = 0.72$ s⁻¹, possibly of importance during spin-up.

The initial spin-rate ω_0 of the WSM may be estimated from the transfer of angular momentum from the gyro-rotor to the empty WSM. Then

$$H = 0.12 \text{ kgm}^2 \text{ s}^{-1} = I_{\omega_0} = 0.0686 \omega_0$$

$$\text{or } \omega_0 = 1.75 \text{ s}^{-1} \sim 16 \text{ rpm}$$

This value will decrease corresponding to a transfer of angular momentum to the carried liquid. A reasonable order-of-magnitude value for $\omega = 1$ s⁻¹. Then the motion is characterized by a rotational Weber number We :

$$We = \frac{\text{centrifugal pressure}}{\text{surface tension}} = \frac{\omega^2 r^2 t}{\beta} = 4.0$$

where t is the width of the annulus and r the average radius. As a consequence one may conclude that capillary effects will have a strong influence on the motion. If a free-float time of 6 seconds is assumed (Ref. 24), only 1-2 full revolutions of the WSM will be accomplished, much too short for development of rotational flow.

Results

Although many test runs with the WSM were performed, only nine have been recorded for evaluation. Of these, two had the momentum device angled at the axis of symmetry and images of these runs have been analyzed.

It soon turned out that the manual release of a WSM of this size did not sufficiently guard against g-jitter disturbances on the contained liquid. As a consequence, the liquid was moving already prior to release and, moreover, was sometimes fairly arbitrary distributed over the tank. Therefore the comparison with the numerical simulation results, that start from well-defined initial conditions, can only be qualitative.

Image Processing

The flight film has been transcribed to 24 mm format in order to fit available image processing hardware. After some trials, a semi-automatic procedure was established for the extraction of WSM attitude data. Each film frame in sequence is digitized via a CCD camera and the image presented to the operator at an IRIS workstation. The operator controls a wire figure with the same outline as the WSM. Via a mouse the best coincidence of the wire frame with the WSM is generated. The attitude angles of the wire frame are taken as the WSM data.

Quantitative Data

Although the image translates with respect to the camera, the effect on the reconstitution of the attitude motion is slight, as confirmed by some tests. Rotational errors are much more influential; if the aircraft goes over the top of the parabola during the recording, a rotation of up to 90° in pitch could be superposed on the WSM. No corrections for this effect have been made and the camera is taken to fix an inertial coordinate frame.

The body-fixed coordinate system of the WSM is related to the inertial frame of the camera by three consecutive rotations. The relation between the two coordinate systems is given in figure 3. The unit vectors of the camera system have subscript 0, those of the WSM system 3. Then

$$\begin{bmatrix} \hat{i}_3 \\ \hat{j}_3 \\ \hat{k}_3 \end{bmatrix} = \begin{bmatrix} \cos\varphi_2 \cos\varphi_3 & \sin\varphi_1 \sin\varphi_2 \cos\varphi_3 + \cos\varphi_1 \sin\varphi_3 & \sin\varphi_1 \sin\varphi_3 - \cos\varphi_1 \sin\varphi_2 \cos\varphi_3 \\ -\cos\varphi_2 \sin\varphi_3 & \cos\varphi_1 \cos\varphi_3 - \sin\varphi_1 \sin\varphi_2 \sin\varphi_3 & \sin\varphi_1 \cos\varphi_3 + \cos\varphi_1 \sin\varphi_2 \sin\varphi_3 \\ \sin\varphi_2 & -\sin\varphi_1 \cos\varphi_2 & \cos\varphi_1 \cos\varphi_2 \end{bmatrix} \begin{bmatrix} \hat{i}_0 \\ \hat{j}_0 \\ \hat{k}_0 \end{bmatrix}$$

where φ_1 , φ_2 and φ_3 are the magnitudes of the successive rotations in figure 3. These quantities are sometimes referred to as Tait-Bryan angles. The WSM axis of symmetry is along \hat{k}_3 . The plane wherein the canted gyroscope axis is contained has to be determined a posteriori since no record was kept of the initial alignment of the WSM with the camera. The camera view direction is along $-\hat{k}_0$.

The recovered attitudes from 76 consecutive frames of film are plotted in figure 4. The ordinate (Row index) represents time steps of 1/24 seconds. The data could be smoothed in order to obtain angular rates in other coordinate systems, e.g.

$$\begin{aligned} \Omega_1 &= \dot{\varphi}_1 + \dot{\varphi}_3 \sin\varphi_2 \\ \Omega_2 &= \dot{\varphi}_2 \cos\varphi_1 - \dot{\varphi}_3 \sin\varphi_1 \cos\varphi_2 \\ \Omega_3 &= \dot{\varphi}_2 \sin\varphi_1 + \dot{\varphi}_3 \cos\varphi_1 \cos\varphi_2 \end{aligned}$$

represents the rates in the inertial system as a function of the Tait-Bryan angle rates.

NUMERICAL SIMULATION

Concept of the Mathematical Model

The theoretical investigation that complements the experiments is focused on the numerical simulation of the motion of the WSM. At NLR, a (Fortran-77) simulation environment has been developed that can efficiently be used to investigate numerous aspects of spacecraft motions. This simulation environment includes models for the liquid/solid-body dynamics, sensors, actuators, external disturbances, satellite trajectory generation and satellite control (see Fig. 5). Each model can be replaced by a substitute one that performs the same function. Thence, a simulation environment can be refined or coarsened where appropriate.

In this particular case study, only the models for the liquid/solid-body dynamics and the actuator are relevant. The gyro-and-brake assembly in the WSM has been modelled such that the total momentum of momentum is transferred, once the brake is applied, to the whole WSM within one second. In the simulation the gyro-axis and the tank-axis meet at an angle of 45°.

The model for the liquid/solid-body motion is based on the computer program ANVOF that has been developed at NLR to simulate narrow annular cylindrical tanks partially filled with liquid. In this model, two sets of equations may be distinguished: tank equations and liquid equations. In the tank

equations (1) and (2), the velocities $\dot{\mathbf{R}}$, $\underline{\omega}$ and the accelerations $\ddot{\mathbf{R}}$, $\dot{\underline{\omega}}$ are the unknown variables. In the liquid equations (3) and (4), however, the velocities and accelerations in the liquid are the unknown variables. The two sets of equations and their coupling is depicted in figure 6. The coupled equations are integrated explicitly. This means that, when a time step from time t to time $t+\Delta t$ is simulated, the two sets of equations are integrated in parallel (see figure 7). The tank model controls the time integration. At the new time level $t+\Delta t$, the two models exchange information which will be used in the integration of the next time step. The information transfer of the tank model to the liquid model consists of the parameters $\dot{\mathbf{R}}$, $\dot{\underline{\omega}}$, $\underline{\omega}$ and $\dot{\underline{\omega}}$, whereas the reverse information transfer consists of the contribution of the liquid to the position vector of the system center of mass, to the moment of inertia tensor and the integrals in the righthandside of (1) and (2).

Since the tank model needs information from the liquid model at time intervals Δt , the integration of the equations of motion of the liquid w.r.t. the tank may take several internal (smaller) time steps. This is the major advantage of the partitioning: time step restrictions in the liquid model have no effect on the time steps in the tank model. The numerical stability aspect of the method of partitioning is described in reference 12.

Numerical Results

In order to illustrate the influence of the liquid motion on the motion of the tank, first the tank without liquid is considered. The characteristic quantities of the tank are given in table 1. A torque \underline{M} about the center of mass and at an angle of 45° with the tank axis of symmetry is applied during one second. After the one second period, the simulation is concerned with a torque-free attitude motion only.

The results from the simulation program are shown in figure 8. As can be seen, the tank is given, almost instantaneously, a rotation along an axis in the x-z plane, with components of approximately .72 rad/sec and .84 rad/sec along the axis of symmetry and the x-axis, respectively. In the torque-free motion, the tank keeps its angular velocity of about .72 rad/sec around its axis of symmetry for the remaining part of the simulation.

The values of the angular velocity components along the body-fixed x-axis and y-axis, however, are changing as the simulation goes on. In fact, the value of ω_x varies harmonically between $[-.84 \text{ rad/sec}, +.84 \text{ rad/sec}]$, while the value of ω_y simultaneously changes such that $\omega_x^2 + \omega_y^2 = (.84)^2$. Thus, the angular velocity vector $\underline{\omega}$ keeps its constant value during the whole simulation: only the direction of its projection onto the x-y plane varies continuously as time progresses. The periodicity of this motion is approximately 47 seconds. Two cones can be used to describe the motion: a space cone that is attached to the angular momentum vector fixed in inertial space, and a body cone that is attached to the body-fixed coordinate system and aligned with the tank axis of symmetry. The motion can be visualized by the rolling of the body cone on the space cone, with $\underline{\omega}$ corresponding to the line of tangency (Fig. 9).

The second simulation has the tank partially filled with an inviscid liquid. The characteristic quantities of the system are given in table 2. Again a torque \underline{M} at an angle of 45° with the axis of symmetry is applied during one second. After the one second period, the system is allowed to move freely.

The time step in the liquid model is chosen to be .01 second. The time step in the tank model equals the time interval between consecutive information exchanges of the tank model and the liquid model: $\Delta t = .1$ second. In the initial configuration the liquid height is constant. The liquid mass is approximately 36% of the total mass. The calculations are performed for a surface tension of 70 mN/m and a contact angle of 70° .

In figure 10, the angular velocities around the body-fixed coordinate axes are shown. As in the first simulation, the tank is given, almost instantaneously, a rotation along an axis with components along the axis of symmetry and the x-axis. Again, the angular velocity around the first axis is practically constant during the whole simulation, only a moderate change of its value can be observed as time progresses. This could be due to the action of surface tension at the contact line.

The near equality of the principal moments of inertia of the tank makes the growth of the ω_x component very slow. It is apparent that the (inviscid) liquid is not very effective in coupling the rotation rate components. However, it is interesting to note that the values of ω_x and ω_y start with opposite sign, in distinction to the behaviour in figure 8.

In the figures 11 and 12, the tank has been cut lengthwise and subsequently unfolded. On the horizontal axis, the location at the tank periphery can be read. The liquid height is displayed vertically. In figure 11, it can be seen that, already in an early phase of the simulation (i.e. after 2.6 seconds), a particular column of liquid reaches the top of the tank. When the contact area of the liquid with the top of the tank, has increased to a certain extent, the liquid height at the "right" side of the contact area starts to decrease, while the contact area is expanding to the "left". The location of the contact area at different points of time is clearly displayed in figure 12.

The variation of the liquid height as function of the time is displayed in figure 13 for 4 different positions at the tank periphery. The positions are chosen such that they divide the tank cross-section in four equal parts. It may be noted that a more smoothly varying function will be obtained by using a finer spatial grid for solving the Navier-Stokes equations.

CONCLUSIONS

The presented results are preliminary. They constitute a first test of an experimental system and its numerical simulation. Various improvements and extensions of methods can be identified for additional work.

The experiments showed that microgee times of about 6 seconds are feasible for free-floating articles on an aircraft like the KC-135. Filmed records of 30-cm objects are sufficiently clear that they

can be reduced to numerical sequences of attitude angles via a non-dedicated image processing system. The aircraft environment does not allow to start with well-defined initial conditions in the tank unless special measures are introduced.

The numerical simulation of the combined liquid-tank motions has been accomplished for large, unconstrained amplitudes of these motions. Several difficulties have been surmounted, notably the modelling of the liquid behaviour upon contact of a confining wall.

After a closer comparison of experimental and numerical results, extension of the investigation is considered in the following areas:

- modify the WSM in order to start with known initial conditions of the liquid
- incorporate accelerometers on the WSM for direct recording of the motions ("ballistometry")
- introduce viscosity in the liquid model
- improve modelling of liquid behaviour, guided by the experimental data
- prepare for longer duration experiments.

ACKNOWLEDGEMENTS

Many colleagues of the Space and the Informatics Divisions of NLR have enthusiastically participated in the work that has been reported.

REFERENCES

1. Habip, L.M. On the Mechanics of Liquids in Subgravity. *Astron. Acta* 11(1965)6, 401-409.
2. Magnus, K. *Kreiselmehnik*. ZAMM 58(1978) T56-T58.
3. Hepner, D.J. et al. Pressure measurements in a liquid-filled cylinder using a three-degree-of-freedom flight simulator. ISA paper 87-0283.
4. Zedd, M.F., Dodge, F.T. Energy dissipation of liquids in nutating spherical tanks measured by a forced motion spin table. AIAA paper 84-1842.
5. Proc. Conf. Attitude control of space vehicles: technological and dynamical problems associated with the presence of liquids. ESA SP-219, Dec. 1977.
6. Intelsat/ESA Coll. Dynamic effects of liquids on spacecraft attitude control. Wash.D.C. 25-26 Apr. 1984.
7. CNES/ESA Meeting on Slosh Dynamics in Spacecraft. 5 May 1987.
8. Veldman, A.E.F., Vogels, M.E.S. Free-surface flow calculations on an Eulerian grid. NLR MP88060U, Oct. 1988.
9. Limarchenko, O.S. Behavior of a system of a cylindrical tank-fluid with a free surface under complex dynamic loading. *Sov. Appl. Mech.* 23(1987)3, 304-309.
10. Der, J.J., Stevens, C.L. Liquid propellant tank ullage bubble deformation and breakup in low gravity reorientation. AIAA paper 87-2021.
11. Utsumi, M. Liquid Sloshing in an Axisymmetric Container in Low-Gravity Environments. Proc. 16th ISTS, Sapporo, May 1988, 815-826.
12. Vogels, M.E.S. A numerical method for the simulation of liquid-solid body dynamics. NLR MP87030, Jul. 1987.
13. Aydelott, J.C. et al. Numerical Modeling of On-Orbit Propellant Motion Resulting From an Impulsive Acceleration. AIAA paper 87-1766.
14. Berry, R.L. An analytical tool for simulating large amplitude propellant slosh. AIAA paper 81-0500.
15. Moiseyev, N.N., Rumyantsev, V.V. *Dynamic Stability of Bodies Containing Fluid*. Springer, 1968.
16. Myshkis, A.D. et al. *Low-Gravity Fluid Mechanics*, Springer, 1987.
17. Agrawal, B.N. Stability of Spinning Spacecraft with Partially Liquid-Filled Tanks. *J. Guidance* 5(1982)4, 344-350.
18. Cochran Jr. J.E., Shu, P.H. Effects of Energy Addition and Dissipation on Dual-Spin Spacecraft Attitude Motion, *J. Guidance* 6(1983)5, 368-373.
19. Agrawal, B.N. The Dynamic Behaviour of Liquids in Spinning Spacecraft. Proc. 15th ISTS, Tokyo, 1986, 635-642.
20. Ebert, K. Modelling of liquid sloshing effects in multi body systems. ESA SP-289, 269-275, Jan. 1989.
21. Peterson, L.D., Crawley, E.F., Hansman, R.J. Experimental measurements of the non-linear coupled dynamics of fluids and spacecraft in low gravity. IAF paper 86-275.

22. Netter, G., Beig, H.C. Preliminary results from the EMTE fuel slosh flight experiment. ESA SP-265, 145-157.
23. Tegart, J.R. et al. Measurement of forces due to liquid motion in a propellant tank. AIAA paper 81-0566.
24. Reiter, G.S., Lee, D.A. Zero gravity stability testing of a liquid-filled space vehicle. *Aerosp. Chem. Eng.* 62(1966)61, 178-183.
25. Harrison, J.A., Garg, S.C., Furumoto, N. A free-fall technique to measure nutation divergence and applications. AAS paper 83-3.
26. Pocha, J.J. ed. Special Issue on Spacecraft Dynamics. *Space Comm. Broadc.* 5(1987)4.
27. Hubert, C., Goodzeit, N. The effects of propellant motion on a spinning satellite with vanned tanks. AIAA paper 83-2262.
28. Guibert, J.P. et al. Etude generale de l'influence des liquides contenus dans les satellites. ONERA RT 1/3307SY, Sep. 1978; also ESA CR(P)1166.
29. Mikishev, G.N. et al. Experimental investigation of the perturbed motion of a solid body containing cavities partially filled with liquids. *Cosmic Research*, 3(1965)2, 138-148.
30. Unruh, J.F. et al. Digital Data Analysis Techniques for Extraction of Slosh Model Parameters. *J. Spacecraft*, 23(1986)2, 171-177.
31. Kana, D.D. A model for nonlinear rotary slosh in propellant tanks. AIAA paper 86-0937.
32. Guibert, J.-P. Forced motion on spinning test for slosh-moment investigations. ESA SP-265, 109-117, Aug. 1986.
33. Vreeburg, J.P.B. Observations on behaviour of liquid in weightlessness. ESA SP-265, 129-136, Aug. 1986.
34. Vreeburg, J.P.B. Results of the forced liquid motion experiment FLIM. Proc. Symp. Sci. Res. DI, Norderney, Aug. 1986.
35. Gantmakher, F.R., Levin, L.M. The flight of uncontrolled rockets. Pergamon, 1964.
36. Meirovitch, L. *Methods of Analytical Dynamics*, McGraw-Hill, 1970.
37. Greenspan, H. *The theory of rotating fluids*, Cambridge UP, 1969.
38. Feuerherdt, G., Vits, P. Low-cost reusable systems for μ -g research. ZFW 10(1986)5, 312-327.
39. Microgravity experiments during parabolic flights of KC-135 aircraft. Sixth ESA Campaign, Aug. 1988. Summary Report. ESA-Estec WP1530, Jan. 1989.
40. Labus, T.L. Natural frequency of liquids in annular cylinders under low gravitational conditions. NASA TN-5412, Sep. 1969.

TABLE 1

TANK			
inner radius (cm)	12.8		
outer radius (cm)	14.4		
height (cm)	28		
mass (gr)	7247		
center of mass (cm)	0	0	0
inertia tensor (grcm ²)	996000	0	0
	0	996000	0
	0	0	1151000

TABLE 2

TANK			
inner radius (cm)	12.8		
outer radius (cm)	14.4		
height (cm)	28		
mass (gr)	4507		
center of mass (cm)	0	0	0
inertia tensor (grcm ²)	637000	0	0
	0	637000	0
	0	0	675000
LIQUID			
height (cm)	20		
mass (gr)	2740		
density (gr/cm ³)	1		
inertia tensor in (grcm ²)	359000	0	0
equilibrium position (grcm ²)	0	359000	0
	0	0	506000
NUMERICAL DATA			
number of points in liquid model	132		
time step in liquid model (sec)	.01		
time step in tank model (sec)	.1		
time between information exchanges(sec)	.1		

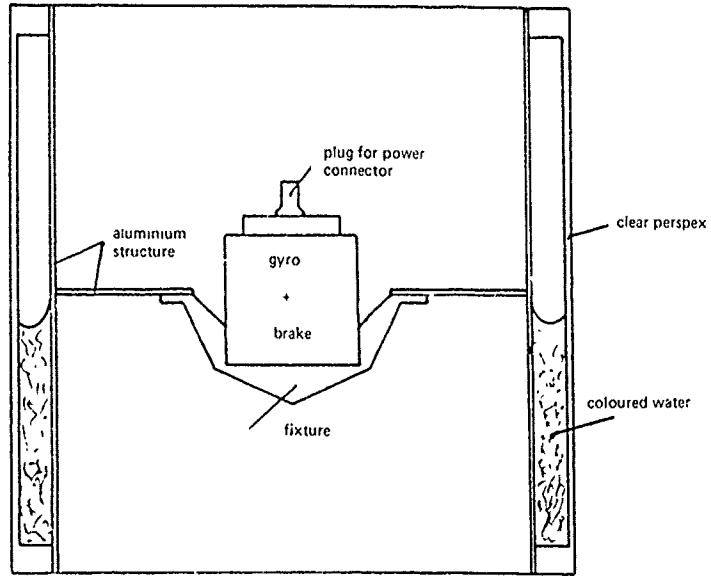


Figure 1 Cross-section of the WSM

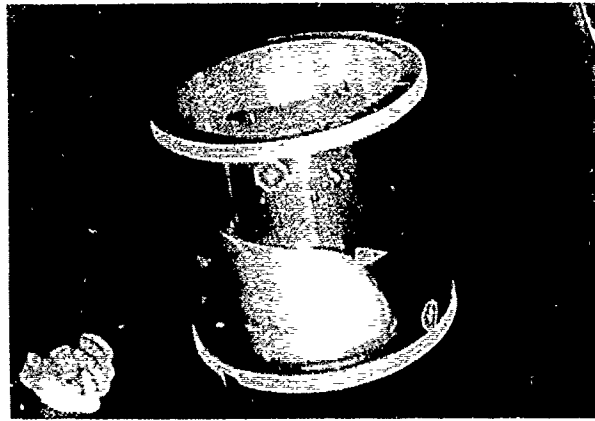


Figure 2 WSM during weightlessness in the KC-135 aircraft

$OX'Y'Z'$ is obtained from $OXYZ$ by 3 consecutive rotations

1. $R_1 = \underline{i}_0 \tan \frac{1}{2}\phi_1 + \underline{j}_1, \underline{j}_1, k_1$
2. $R_2 = \underline{j}_1 \tan \frac{1}{2}\phi_2 + \underline{i}_2, \underline{j}_2, k_2$
3. $R_3 = \underline{k}_2 \tan \frac{1}{2}\phi_3 + \underline{i}_3, \underline{j}_3, k_3$

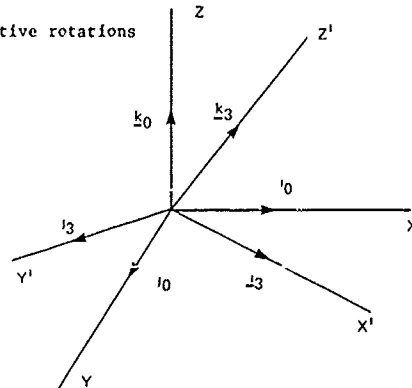


Figure 3 Relation between WSM and camera coordinate systems

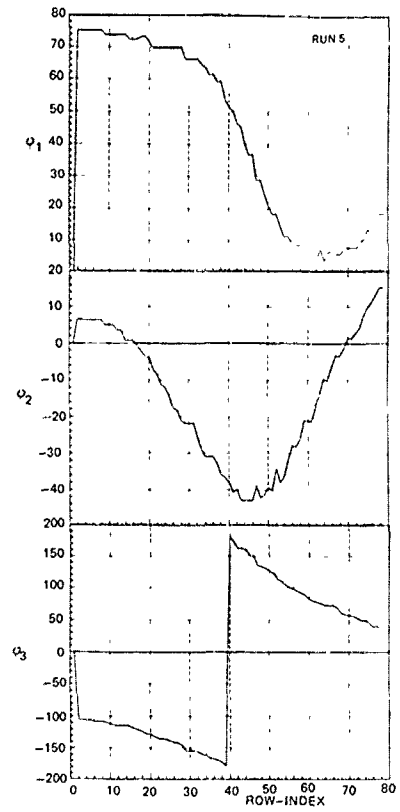


Figure 4 Reconstituted attitude angles of WSM

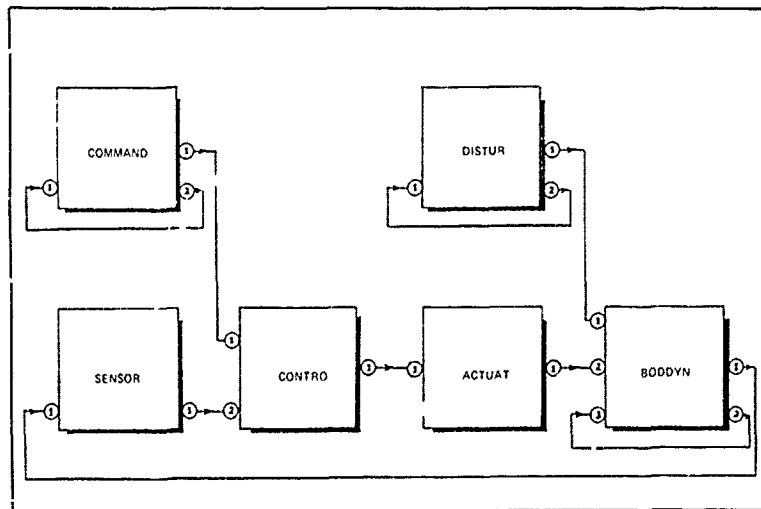


Figure 5 Simulation environment for spacecraft motions

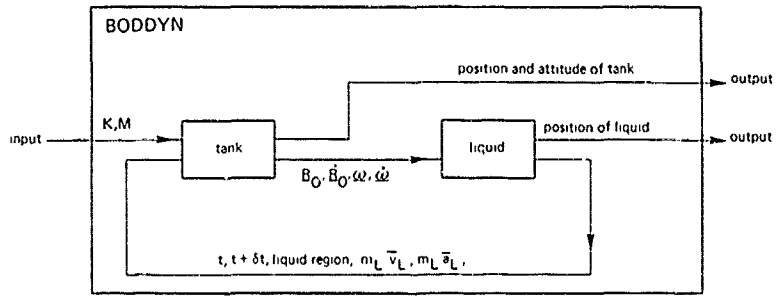


Figure 6 Technical concept of partitioning of the coupled liquid solid body system

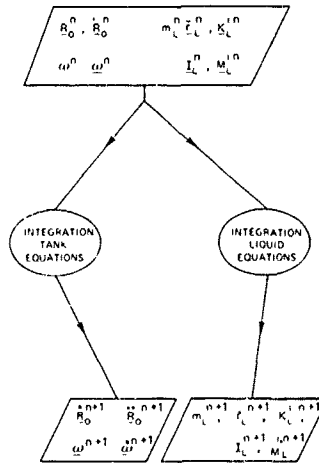


Figure 7 Numerical integration of the coupled equations of motions of the liquid-solid body system

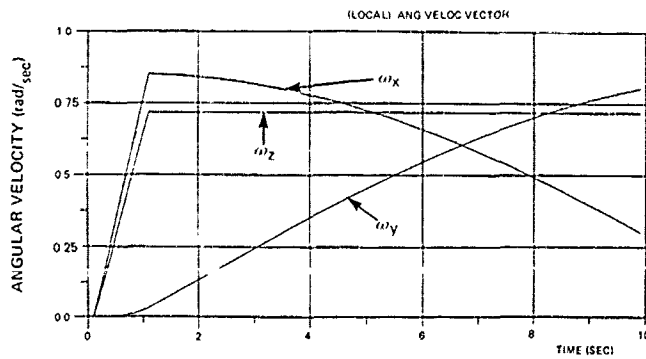


Figure 8 Angular velocities of the tank (without liquid) w.r.t. the body-fixed coordinate system

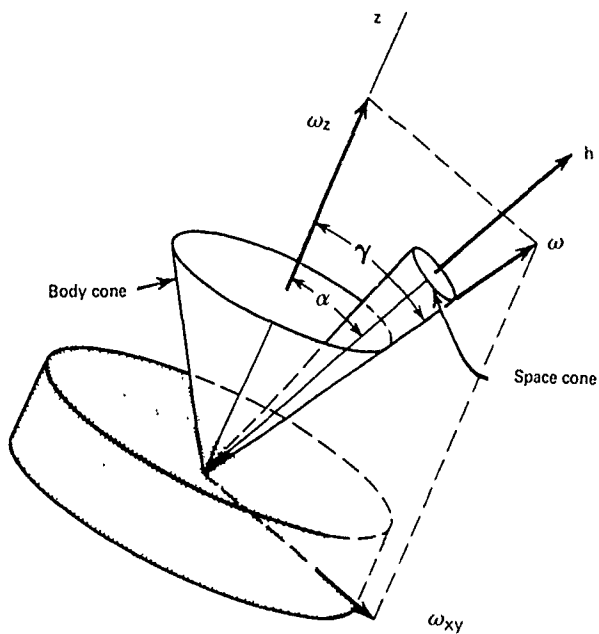


Figure 9 Body cone rolls on space cone

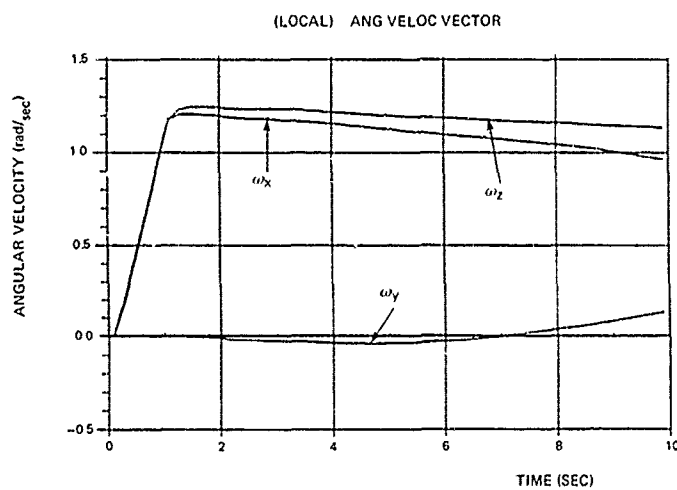


Figure 10 Angular velocity of the tank (with liquid) w.r.t. the body-fixed coordinate system

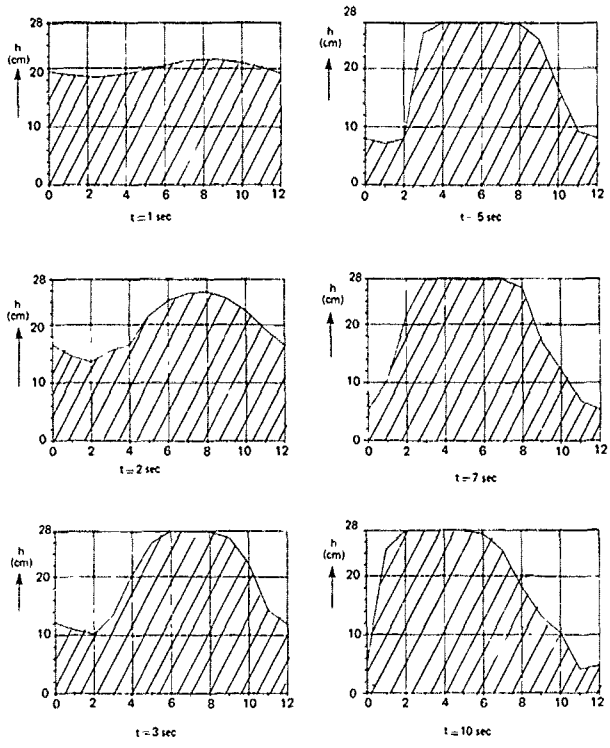


Figure 11 Liquid surfaces at different points of time

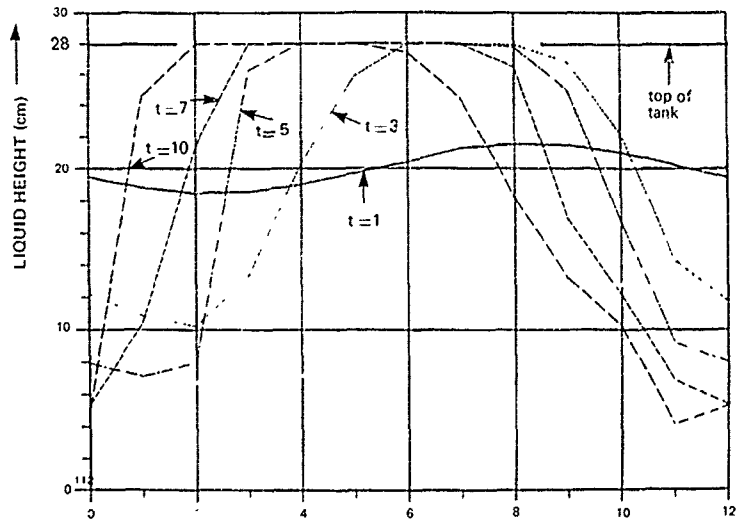


Figure 12 Liquid surfaces at different points of time

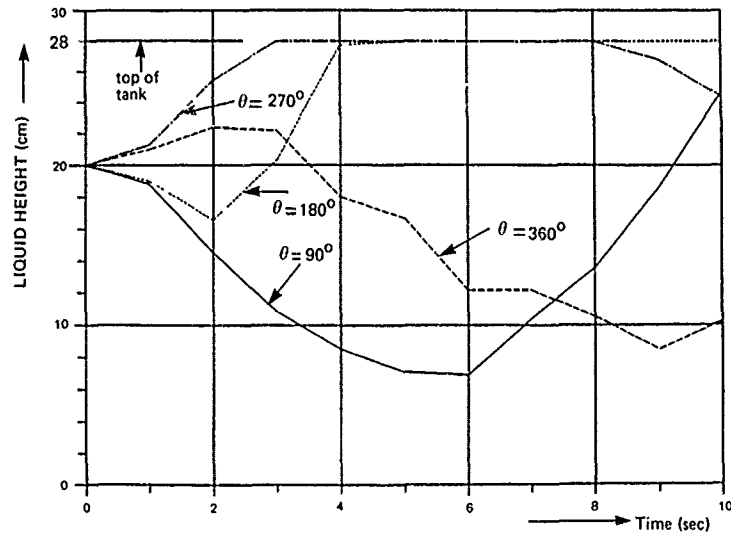


Figure 13 Liquid height as function of time at 4 positions at the tank periphery

**FLEXIBLE SPACE-BASED ROBOT
MODELLING AND REAL-TIME SIMULATION**

J.J.M. Prins, P. Dieleman and P.Th.L.M. van Woerkom
National Aerospace Laboratory (NLR)
P.O. Box 153,
8300 AD Emmeloord,
The Netherlands

SUMMARY

The Hermes manipulation system (HERA) is a sophisticated space manipulator system, which has to perform tasks ranging from berthing to tool operation in various operational modes from fully automatic to purely manual.

Development and qualification of such a space-based manipulator must be supported by computer simulation facilities.

The HERA system main contractor is Fokker Space & Systems B.V. (FSS). The National Aerospace Laboratory (NLR) in the Netherlands is responsible for the development of the so-called HERA Simulation Facilities (HSF).

The paper will focus on the HSF-P^{*}: a first 'pilot' real-time simulation facility. Design concept, simulation models and support tools are discussed in some detail.

1. INTRODUCTION

When the Hermes space plane has to perform external servicing of the Columbus Free Flying Laboratory, Europe's autonomous space station, a manipulator arm will be required. The Hermes manipulation system (HERA) is a sophisticated space manipulator system, which has to perform tasks ranging from berthing to tool operation in various operational modes from fully automatic to purely manual.

Development and qualification of such a space-based manipulator must be supported extensively by computer simulation facilities (Ref. 1). The HERA Simulation Facility Pilot (HSF-P) is the first ('pilot') facility in a series of simulators, both real-time and non-real-time, that is developed to support this in-orbit operations technology.

The simulation capability of the HSF-P offers:

- the basic operational environment required for research and development of the HERA manipulator system, allowing:
 - evaluation of operator-in-the-loop support software;
 - visualisation of manipulator operations;
 - analysis of operational aspects (e.g. time-lining);
 - feasibility experiments on manipulator operations;
 - development of hands-on experience with HERA-operations by HERA design engineers.
- a simulated environment with sufficient fidelity to allow experimental evaluation of real-world (shirt-sleeve) teleoperator station requirements.

This paper gives a concise description of the Hermes manipulation system to be simulated, the HERA simulation facilities involved and focuses on the pilot simulation facility HSF-P.

2. HERMES MANIPULATION SYSTEM

According to the present concept (Ref. 2) HERA is a manipulator with 6 degrees of freedom, i.e. during operational use the arm has six controllable joints. An additional degree of freedom is contained in the deployment mechanism which is fixed during normal operation and is used to move the arm to its initial operational position. Another additional degree of freedom is used to allow for relocation of the arm, e.g. move the arm from the Hermes space plane to the Columbus Free Flying Laboratory.

Operational functions to be carried out by HERA are at least:

- inspection;
- replacement and exchange of Orbit Replaceable Units;
- transfer of objects (spacecraft or tool);
- support of Extra Vehicular Activities (EVA);
- relocation of itself.

Tasks may also include (re-)berthing and capture of free flyers.

^{*} HSF-P is developed for European Space Agency ESA and Fokker Space & Systems FSS under contract 7222/87/NL by the National Aerospace Laboratory NLR (Amsterdam) and BSO/Buro voor Systemontwikkeling (Utrecht). The project has been sponsored by the Netherlands Agency for Aerospace Programs NIVR.

The manipulator, with a total length of approximately 10 m and a total weight of approximately 200 kg, will be capable of handling payloads of more than 20.000 kg. Appropriate control of the movements of the manipulator requires special attention for the following aspects related with system dynamics:

- effects due to flexibility of the long and slender beams;
- effects caused by elasticity of the gears used in the joints;
- effect due to the location of the manipulator at a moving base (e.g. Hermes) and effects caused by control interaction.

The arm will be provided with exteroceptive sensors to enable both man-in-the-loop and automatic control of the manipulations. These sensors are:

- camera's located on the elbow and on the end-effector, Hermes and the Free Flyer;
- torque/force sensor located in the end-effector to control operations in which interaction with the environment is involved (e.g. insertion and extraction operations).

The arm will be controlled from the Hermes co-pilot station by means of two handcontrollers, having three degrees of freedom each, a keyboard, a cursor positioning device, four video displays and an emergency switch board.

3. HERA SIMULATION FACILITIES

The HERA Simulation Facility (HSF) consists of three distinct facilities (Ref. 3):

- the HSF Pilot (HSF-P), a first 'pilot' real-time simulation facility;
- the Non-Real-Time HSF (HSF-NRT), the main HERA simulation tool for detailed design, analysis and verification. It will feature the highest model fidelity of all three facilities;
- the Real-Time HSF (HSF-RT), an extensive real-time facility to provide high fidelity real-time "hardware-in-the-loop" and "man-in-the-loop" simulation capabilities.

HSF-P was identified to be the first facility needed by the HERA system developer FSS. This facility has been developed and built by NLR and BSO during the last two years and passed its acceptance test in September 1989.

4. HSF-P DESIGN CONCEPT

HSF-P design has led to an architecture that contains as main components:

- the Flight Teleoperation Facility test bed, which is basically a mock-up of the Hermes cockpit (See figures 1 and 2) and comprises all hardware elements that form the astronaut's direct environment and allow the monitoring and control of the manipulator;
- Test Engineer Stations for preparation and evaluation of simulation runs;
- an Instructor Station for supervisory control and monitoring of a simulation run;
- the On-Board Software, being a (simulated) subset of the software used to control the manipulator, including the software used for interaction with the astronaut;
- the Dynamics Model Software for simulating the kinematic and dynamic behaviour of the electro-mechanical system, i.e. Hermes, HERA, payloads, tools, cameras, Free Flyer and the environment;
- the Image Generation Software, containing geometry models of Hermes, HERA, payloads, tools, Free Flyer and a star background, and software to generate two simultaneous simulated camera images;
- the Real-Time Simulation Tool Software which provides all supporting tools prior to, during and after a simulation run to allow for an appropriate and efficient use of the facility and building of new simulators.

Based on above architecture, the distribution of components has led to the following set of main HSF-P hardware elements (see figure 3):

- a (host) simulation computer for test control and real-time simulation of dynamics, kinematics and execution of on-board software (GOULD/SEL 32/6742 D, dual processor system);
- a graphics workstation for visualisation of the camera images in real-time (Silicon Graphics IRIS 4D/50GT);
- a Flight Teleoperation Facility test bed including two three degree of freedom handcontrollers, a keyboard, a tracker ball and a man-machine interface computer (SUN 3/50);
- an instructor station for simulator control, and
- two test-engineer stations for test preparation and processing of results.

The software as developed for HSF-P is split into model software and tool software. The HSF-P models are organised along a model tree. The HSF-P main-model consists of a number of sub-models (dynamics, on-board software), each built up of further sub-models. Each model can have several representations, having a different level of detail or a different method of implementation.

Model software includes:

- real-time dynamics models;
- On-board Software model in four levels;
- visualisation models.

Tool software allows the following functions:

- composition of models into simulators (model composition);
- preparation of simulations (pre-processing);
- execution of simulation runs (real-time executive, test control, image generation);
- preparation for result interpretation (post-processing, visualisation replay, video recording and collision detection).

The software has been fully documented according to the European Space Agency's (ESA) Software Engineering Standards (Ref. 4).

5. HSF-P MODELS

HSF-P model software includes real-time kinematics and dynamics models of the relevant flight elements, a model of the simulated on-board software and geometry models needed for visualisation and collision detection. Each of these will be elaborated in the subsections below.

5.1 Dynamics Models

The HSF-P dynamics simulation models include models of:

- the Hermes space plane;
- the Columbus Free Flying Laboratory, either free-flying or docked with Hermes;
- the HERA manipulator, located at Hermes;
- Payloads and tools, which may be attached to:
 - Hermes,
 - the Free-Flyer, or
 - the HERA End-Effector;
- camera pan and tilt kinematics.

A side view of the Hermes-HERA configuration as used for HSF-P is shown in figure 4. Note: this is not the current configuration.

The Hermes space plane is modelled dynamically as a 6 degrees of freedom rigid body and is equipped with an Attitude Control System.

The Columbus Free Flying Laboratory is modelled kinematically according to a prescribed trajectory. This mode is used to simulate capture operations. When docked the Free Flyer dynamics characteristics are combined with those of Hermes resulting in a single 6 degrees of freedom rigid body. When captured the Free Flyer dynamics characteristics are combined with those of the End-Effector.

The HERA manipulator is modelled as a dynamic multi-body system which consists of:

- 6 joints, 3 of which include gearbox flexibility.
- 6 links, including the End-Effector attached to the last link. The two long limbs are modelled as flexible containing two orthogonal bending modes and one (not yet implemented) torsion mode each.

Joint model

Each joint contains a motor model, gear flexibility, non-linear friction models (stiction, Coulomb friction and viscous friction, both on motor axis and joint output axis), a brake model and position encoder and tachometer models.

The joint model is illustrated in figure 5. Input is the commanded actuator motor current given by the joint control software; outputs are the actual motor axis and joint output axis angular position, angular velocity and torque.

During a simulation, one or more joints may temporarily be locked due to joint output axis stiction. When this occurs the system dynamics equations are reconfigured accordingly.

Link model

Limb flexibility is modelled through the introduction of fictitious joints, one for each of the clamped-free mode shapes of each of the flexible limbs. The elastic restoring torque and structural damping torque are represented by a fictitious linear spring and damper in that joint. A key advantage of this well-known modelling technique is that it allows re-use of existing rigid-manipulator software for the simulation of the dynamics of a flexible manipulator.

Although the fictitious joint technique allows qualitative representation of flexibility effects, its use introduces quantitative errors. These errors can in principle be suppressed through the introduction of additional fictitious torques and forces on the limb, according to a limb-based linear feedback law derived from the theory of Equivalent Flexibility Modelling (Ref. 5). This requires further modification of the rigid-manipulator simulation software. Work to validate the concept of Equivalent Flexibility Modelling (EFM) is currently under way.

The basic rigid-manipulator simulation software, then, uses an algorithm of the recursive type. It exploits the chain topology of the spacecraft-manipulator system. It constitutes a further development (Ref. 6) of the recursive algorithm proposed in Ref. 7 (method 3). Due to its recursive nature, the algorithm can be programmed easily, and execution times are comparatively short.

For HSF-P execution time is shortened further through the introduction of a multi-rate simulation scheme, in which the system inertia matrix and the Coriolis/centrifugal vector are evaluated at a low rate compared to the evaluation rate for the acceleration vector.

Tools and payloads of several types can be used. standard available payloads, modelled as rigid bodies, are:

- inspection tool;
- capture tool;
- Orbit Replaceable Units.

Once a payload is attached to the manipulator's End-Effector its dynamics characteristics are combined with those of the last link of the arm forming a new last link with the corresponding dynamic behaviour.

The resulting dynamics model of the Hermes-HERA system as currently modelled in HSF-P has a state vector of dimension 38. The model consists of a set of non-linear state-dependent differential equations (Ref. 6 and 8). The state-dependent coefficients of the equations are computed recursively, while the behaviour in time is computed by means of numerical integration. During the development of the dynamics models special attention was paid to numerical stability of the simulated model under the restrictions caused by the real-time demand for the given computer hardware. Stability is affected by the frequencies present in the system due to structural flexibility as well as by non-linearities in the manipulator and joint models. The model was implemented on a single processor of the target computer using:

- an update frequency of the state vector of 100 Hz;
- an update frequency of stiction statuses and mass matrix reduction and factorisation of 50 Hz;
- an update frequency of the mass matrix and Coriolis/centrifugal vector of 1 Hz;
- a Runge-Kutta scheme for numerical integration.

The reconfiguration process required in case of capture operations or grapple/release of payloads and tools is carried out automatically by the simulator in real-time, based on control commands generated by the human operator (e.g. grapple command). The required transition is performed by freezing the simulation process, followed by a re-initialisation of kinematics and dynamics variables and parameters and an automatic re-start of the simulation process. This re-initialisation is made transparent to the operator. Contact dynamics is not implemented. However, contact strain built up in the arm is part of the re-initialisation algorithms and becomes visible after payload/tool de-latch.

5.2 On-Board Software Models

The On-Board Software is a simulated subset of the software used to control the HERA manipulator and consists of four hierarchical layers:

- the Man-Machine Interface software,
- the Teleoperation Supervisory System software,
- the Teleoperation Executive Control software, and
- the Manipulator Arm Resident Software.

The relation between these On-board Software layers as implemented in HSF-P as well as the relation with the Hermes-HERA dynamics and kinematics elements is depicted in figure 6.

The Man-Machine Interface software provides:

- acceptance of keyboard and tracker ball inputs (control of: control reference frames, manipulator control modes, Attitude Control System, tools, camera selection, camera pan and tilt, brakes, etc.);
- acceptance of handcontroller inputs;
- display of numerical data on the Flight Teleoperation Facility test bed data display, in windows for e.g.:
 - Mission information;
 - Warnings and alarms;
 - Status information;
 - Functional information;

Main functions of the Teleoperation Supervisory System are to facilitate:

- payload data inspection and control;
 - relay of Hermes Attitude Control System signals;
 - relay and check of simulated switch board inputs;
 - camera control;
 - supervision of and interaction with lower level Onboard Software.
- and allow selection of inspection tool in/out state.

The Teleoperation Executive Control provides the following main functions:

- acceptance and scaling of rate commands in the selected reference frame in operator controlled mode;
- acceptance and scaling of rate commands in single joint mode;
- limitation and vectorial scaling of rates at several levels;
- interfacing with sensors;
- singularity avoidance;
- computation of manipulator inertia matrix (for On-board Software use);
- calculation of joint rate commands and joint controller gains;
- joint commanding during brake activation.

Teleoperation Executive Control is executed with 10 Hz.

Manipulator Arm Resident Software functions are:

- acceptance of rate commands from Teleoperation Executive Control and extrapolation to Manipulator Arm Resident Software control frequency;
- limitation of joint rate commands, positions and torques;
- acceptance and processing of sensor data (tachometer and position encoder);
- computation of feedback control;
- switching of joint brakes;
- relay of end effector and tool commanding;
- relay of end effector sensor data.

Manipulator Arm Resident Software is executed with 50 and 100 Hz.

5.3 Visualisation Models

For visualisation of the scene as seen via the camera's, and used by the human operator to monitor and control the system, the Image Generation System is used. A geometry model of the system was composed of the following main elements:

- the Hermes spacecraft;
- HERA with 6 links, 6 joints and the End-Effector;
- the Columbus Free Flying Laboratory, docked to Hermes or free-flying;
- capture Tool;
- inspection Tool (retracted or extended);
- payloads (Orbit Replaceable Units);
- environment consisting of star fields;
- grapple and capture fixtures and vision targets.

Based on these geometry models, the actual state of the system as computed by the dynamics models and the camera's selected by the human operator (2 out of 5), a simultaneous visualisation of two camera images is performed in real-time with an image refresh rate of at least 5 Hz. Each of the two displays, realised as windows on the IRIS display, has a resolution of 600x600 pixels. The image is generated using solid surface modelling, Gouraud and flat shading and hidden surface removal based on z-buffering.

Two examples of images as visualised by the Image Generation System are shown in figure 7. These images show the manipulator during a servicing operation, while Hermes and the Free Flyer are docked.

6. HSF-P TOOLS

The HSF-P simulation process is divided in a number of steps, that are supported by the HSF-P tool software (see figure 8):

- the composition of a simulator by integrating the model software in the simulator run-time system (simulator composition);
- preparation of a simulation (pre-processing);
- simulation execution (real-time execution, test-control, image generation);
- presentation of simulation results (post-processing, visualisation replay and collision detection).

During simulator composition a specific model is selected for each aspect of the system to be simulated. A simulator consists of a single representation of the real-world system to be modelled, and of tool software that controls the simulation process. All simulator parameters and variables are entered via the Simulation Data Document (see figure 8). This document includes a description, default value, minimum value, maximum value, unit, type and local name for each parameter and variable.

Specification of the simulation is supported by the pre-processing system. This system presents the contents of the simulator to the user, organised along the model tree. The pre-processing system translates the user-representation (model-tree) of the simulator to the internal representation and organisation of the simulator.

To prepare a simulator for simulation execution, the following information is to be specified:

- a list of deviations of parameters and variables from the default values given in the Simulation Data Document (simulation settings);
- a list of event definitions (scenario), either state driven, time driven, human operator action driven or instructor action driven;
- the sequence and frequency of activation of the simulator modules for generally n processors of the host computer (scheduling scheme), for HSF-P two processors are used;
- a selection of simulation variables that are to be stored during simulation execution in the simulation results file for post-run analysis and a selection of simulation variables for on-line data display.

The tool software that controls the simulation real-time execution performs the following functions:

- initialisation of the simulator state as specified during simulation preparation;
- activation of the simulator modules as specified in the scheduling scheme;
- visualisation;
- providing an interface to the instructor for simulator control (see figure 9) and on-line data presentation.

After simulation execution the simulation results are prepared for interpretation and analysis. The simulation results are presented by the post-processing system in plotted or printed form, or are converted to be processed by external engineering-database-management systems.

The Replay and Collision Detection System provides a post-run visualisation of a simulation run. During replay, the simulation can be run forth or back with various speeds, can be frozen, and the simulated system can be observed from different viewpoints (e.g. see figure 7). The visualisation results can be recorded on video tape. During replay any number of objects can be checked for collision with any other object. Such objects are selected prior to the replay run. When a collision is detected the replay halts and provides a collision report.

All HSF-P tool software has been developed for machine-independence as much as possible.

The tool software is also completely separated from the HSF-P model software. This ensures possible exchange of model software during HSF-P operational life, but also between different projects (e.g. real-time Rendez-Vous and Docking simulation) or different system configurations. Using the HSF-P tool software, the emphasis can be placed on the only real issue: modelling the physical reality of dynamic multi-body systems.

7. CONCLUSIONS

Acceptance tests and preliminary usage of the facility have shown that HSF-P can be regarded a very useful tool for HERA development.

Design and architecture of the facility, especially its flexibility in software structure (modularity) and software portability, facilitate the re-use of both software tools and model elements as present in the HSF-P. Re-use is already considered for the European Real-time Operations Simulator (EUROSIM) prototype development, the European Proximity Operations Simulation facility (EPOS) and the HERA Simulation Facilities (HSF-NRT and HSF-RT).

8. REFERENCES

1. Fehse, W and Bentall, R H. Motion Simulation For In-Orbit Operations, Proceedings First European In-Orbit Operations Technology Symposium, Darmstadt, 7-9 September 1987, ESA SP-272, 263 - 271.
2. Hamann, R J and Bentall, R H. The Hermes Robot Arm; System Description, Proceedings Second European In-Orbit Operations Technology Symposium, Toulouse, 12 - 14 September 1989, ESA SP (to be issued).
3. Prins, J J M, Dieleman, P and Hoogstraten, J A. The Hermes manipulation system (HERA), simulation facility development, Proceedings First European In-orbit Operations Technology Symposium, Darmstadt, 7-9 September 1987, ESA SP-272, 353 - 364.
4. ESA Board for Software Standardisation and Control. ESA Software Engineering Standards, ESA PSS-05-0 Issue 1, January 1987.
5. Woerkom, P Th L M van . Equivalent Flexibility Modelling : a novel approach towards recursive simulation of flexible spacecraft-manipulator dynamics, Proceedings Second European In-Orbit Operations Technology Symposium, Toulouse, 12 - 14 September 1989, ESA SP (to be issued).
6. Woerkom, P Th L M and Guelman, M. Dynamics Modelling, Simulation, and Control of a Spacecraft/Manipulator System, Proceedings First European In-orbit Operations Technology Symposium, Darmstadt, 7-9 September 1987, ESA SP-272, 439 - 448.
7. Walker, M W and Orin, D E. Efficient dynamic computer simulation of robotic mechanisms, Journal of Dynamic Systems, Measurement, and Control, Vol 104, No 3, Sept. 1982, 205 - 211.
8. Wang, L T and Ravani, B. Recursive Computations of Kinematic and Dynamic Equations for Mechanical Manipulators, IEEE Journal on Robotics and Automation, Vol RA-1(3), 1985, 124-131.

9. ACKNOWLEDGEMENT

The authors acknowledge with pleasure the dedication and contributions to this project, made by their colleagues in the HERA Simulation Facility Pilot team at the National Aerospace Laboratory NLR.

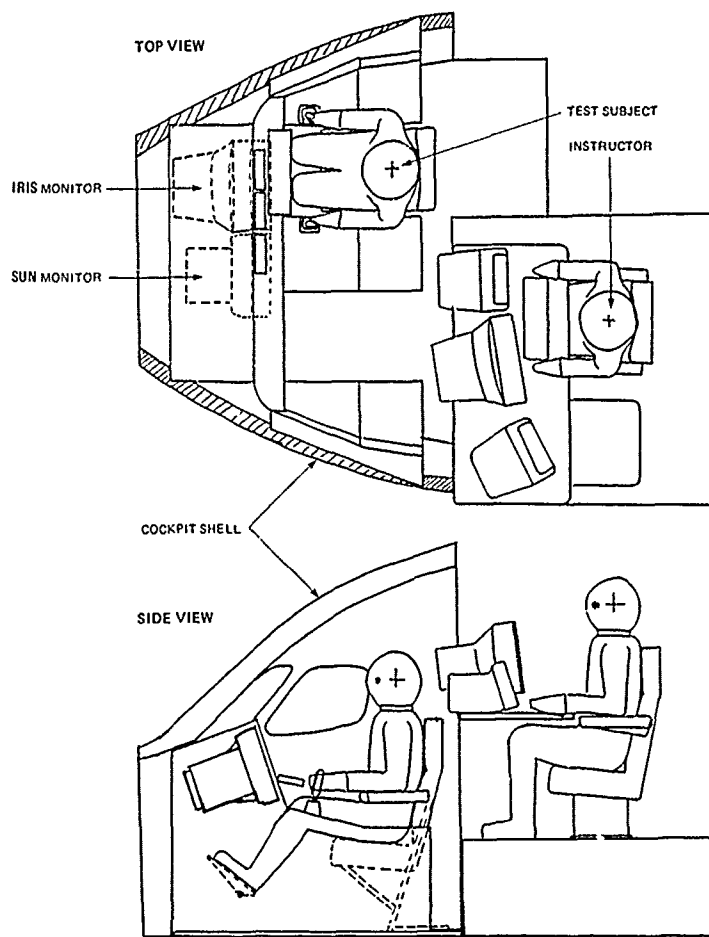


Fig. 1 HSP-P FTF test bed mockup, including cockpit shell and instructor station

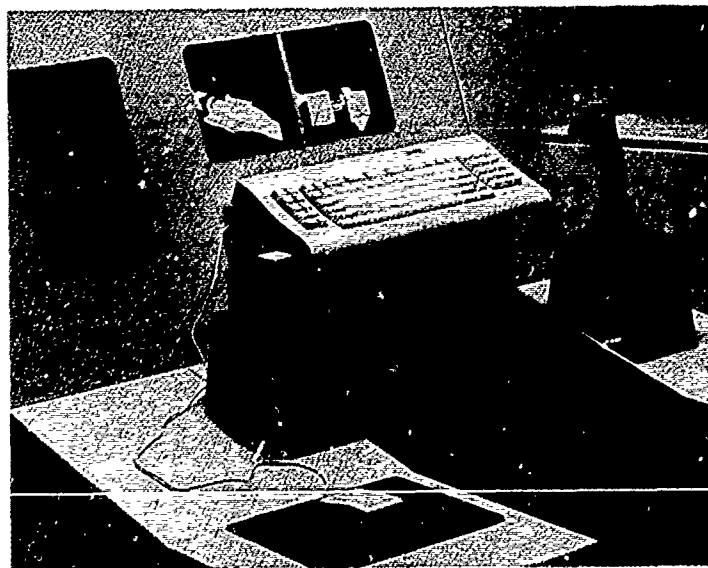


Fig. 2 Close-up of the Hermes co-pilot station as implemented for the HSP-P mockup

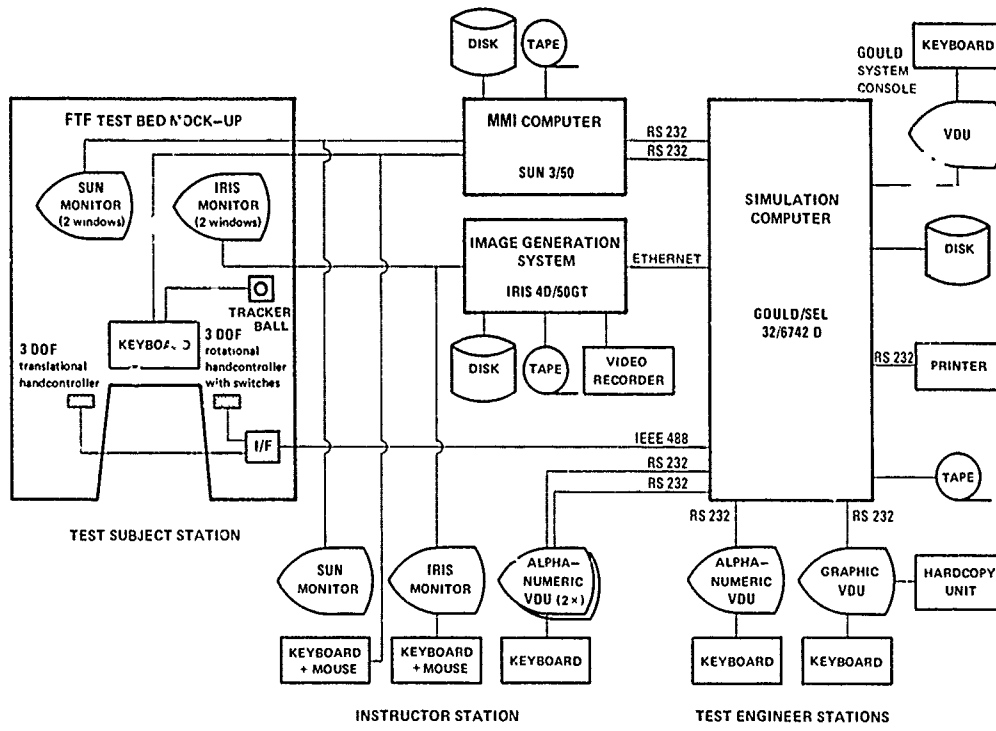


Fig. 3 HSF-P hardware setup

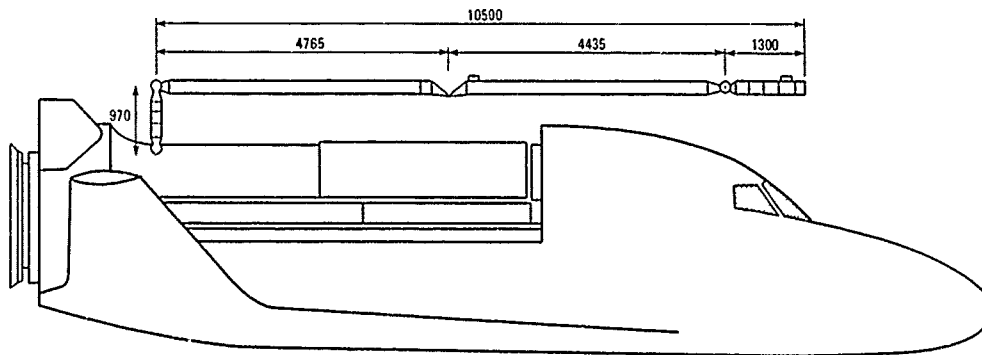


Fig. 4 Side view of the Hermes/HERA configuration as currently implemented on the HSF-P

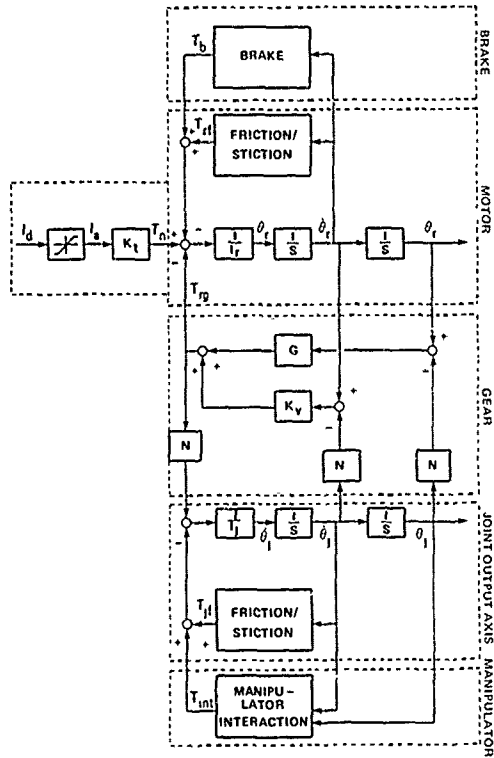


Fig. 5 HSF-P joint model including gearbox flexibility

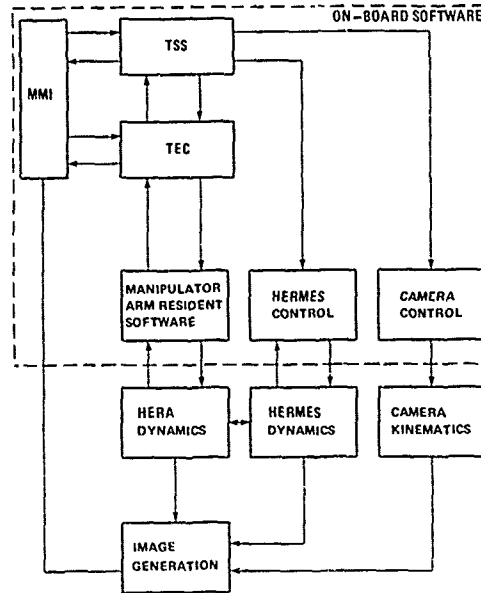


Fig. 6 HERA on-board control as implemented on the HSF-P

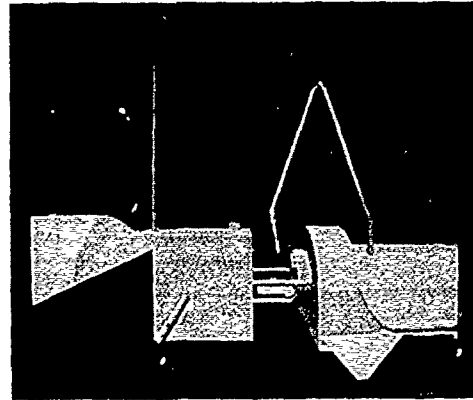
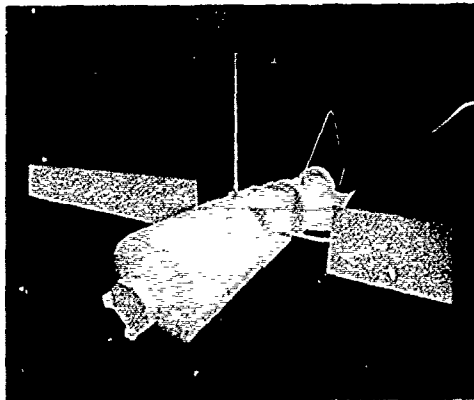


Fig. 7 Hermes/HERA/Free Flyer combination as visualised by HSF-P

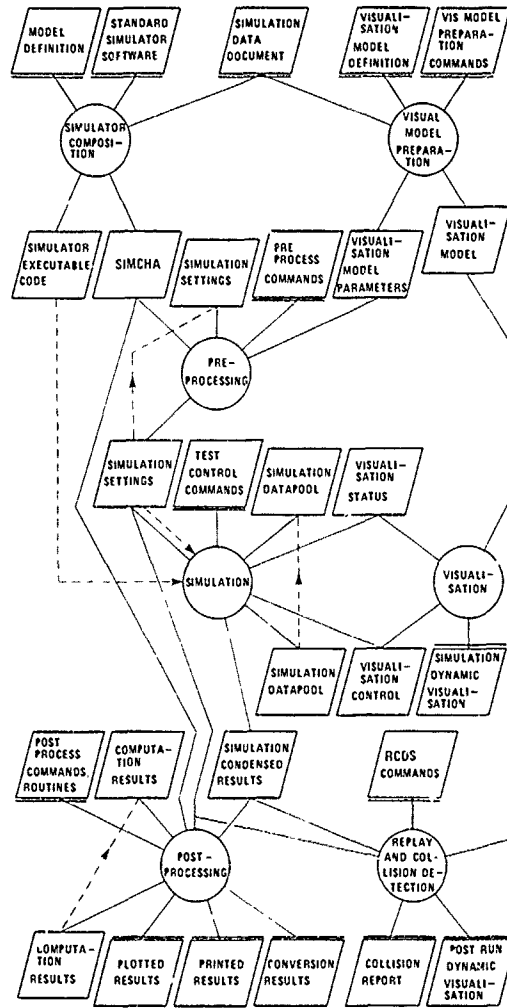


Fig. 8 Schematic overview of the HSF-P software

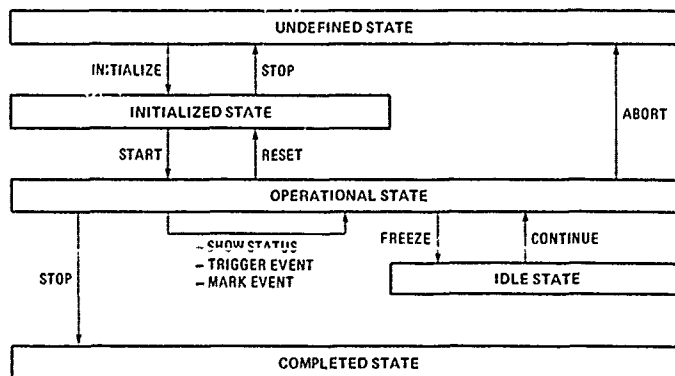


Fig. 9 Relation of test control commands and simulator states

**FLIGHT MECHANICS APPLICATIONS FOR TETHERS IN SPACE:
COOPERATIVE ITALIAN-US PROGRAMS**

by

Franco Bevilacqua and Pietro Merlina
Aeritalia SAIPA, Space Systems Group
Corso Marche 41, 10146 Torino, Italy

John L. Anderson
NASA Headquarters
Washington, D.C.
United States

ABSTRACT

Since the 1974 proposal by Giuseppe Colombo to fly a tethered subsatellite from the Shuttle Orbiter, the creative thinking of many scientists and engineers from Italy and U.S. has generated a broad range of potential tether applications in space. Many of these applications have promise for enabling innovative research and operational activities relating to flight mechanics in earth orbit and at suborbital altitudes.

- From a flight mechanics standpoint the most interesting of the currently proposed flight demonstrations are:
1. the second Tethered Satellite System experiment which offers both the potential for aerothermodynamics and hypersonics research and for atmospheric science research;
 2. the Tether Initiated Space Recovery System which would enable orbital deboost and recovery of a re-entry vehicle and waste removal from a space station; and
 3. the Tether Elevator/Crawler System which could provide a variable microgravity environment and space station centre of mass management.

This paper describes the outer atmospheric and orbital flight mechanics characteristics of these proposed tether flight demonstrations.

The second Tethered Satellite System mission will deploy the tethered satellite earthward and will bring it as low as 130 km from ground and thus into the transition region between the atmosphere (non-ionized) and the partially ionized ionosphere. The atmospheric flight mechanics of the tethered satellite is discussed and simulation results are presented.

The Tether Initiated Space Recovery System experiment will demonstrate the ability of a simple tether system to deboost and recover a reentry vehicle. The main feature of this demonstration is the utilization of a Small Expendable Deployer System (SEDS) and the low-tension deployment assumed to separate the reentry vehicle from the Shuttle. This low-tension deployment manoeuvre is discussed and its criticalities are outlined.

The Tether Elevator/Crawler System is a new space element able to move in a controlled way between the ends of a deployed tethered system. A Shuttle test of an Elevator model is planned in order to demonstrate the unique capability of this element as a microgravity facility and to test the transfer motion control. The basic dynamical features of the Elevator system are presented and a preliminary assessment of the Elevator-induced tether vibrations is discussed.

1. INTRODUCTION

Through the cooperative efforts of the National Aeronautics and Space Administration of the United States and the Piano Spaziale Nazionale (PSN) of Italy, and its successor the Agenzia Spaziale Italiana (ASI), the tether concept has moved beyond study and analysis to in-space demonstration programs for several applications. These cooperative programs of course are in addition to other non-tether cooperative space flight programs within the two countries.

Two joint agreements have permitted this progress. In particular, the "Memorandum of Understanding for Development of the Tethered Satellite System" became effective in March 1984. Its purpose was to enable joint planning and implementing of an initial TSS mission (TSS-1), a 20 km tether electrodynamics experiment from the Space Shuttle. This MOU also provides for the joint planning of two subsequent TSS missions. The TSS-2 mission to deploy a tethered research satellite 100 km downward from the shuttle into the outer atmosphere at about 130 km altitude is now in planning and could fly in mid-1995. Such an experiment could be the forerunner of a significant aerothermodynamics and hypersonic flight research capability at altitudes between 150 and 90 km.

A "Letter of Agreement for Conduct of Tether Applications in Space Studies" became effective in October 1984. Its purpose is to prepare NASA and ASI for undertaking future joint flight experiment and development programs. From studies under this LOA, technology demonstrations, special emphasis tasks, and potential system level development programs are being identified by both parties. The LOA also contains a provision for planning and developing specific joint flight demonstrations.

Three flight demonstrations have been planned and are currently funded:

- the Tethered Satellite System (first mission),
- the Small Expendable Deployer System, and
- the Plasma Motor Generator.

Four other possible demonstrations have had substantial definition and are capable of being flown in the next 4-7 years. From a flight mechanics standpoint the most interesting of the currently proposed flight demonstrations are:

1. the second Tethered Satellite System experiment (TSS-2)
2. the Tether Initiated Space Recovery System (TISRS)
3. the Tether Elevator/Crawler System (TECS)

2. SECOND TETHERED SATELLITE SYSTEM MISSION (TSS-2)

Scientific measurements of the upper atmosphere are needed to understand the causes of weather, atmospheric physics, chemistry, and dynamics, Sun-Earth interactions such as atmospheric diurnal bulges, ecosystem interactions, radio communications, and to comprehend in general the "upper atmosphere", between about 60 and 130 km, that is almost unexplored and unmeasured.

To properly design future space vehicles such as aeroassisted OTV, aerospace plane, re-entry vehicle, it is necessary to investigate within the upper atmosphere itself aerothermodynamic energy and momentum transfer by measuring free-stream and boundary-layer gas densities and composition, both at the shock layer and very near the vehicle surface.

A promising way of doing all this is to use the Tethered Satellite System (TSS) being proposed in a joint U.S.-Italian program to tow a craft at hypersonic velocities through the upper atmosphere at altitudes above about 120 km. Carried by the Shuttle, TSS has three major elements (see Figure 1): the Tethered Satellite, the Deployer and the Tether.

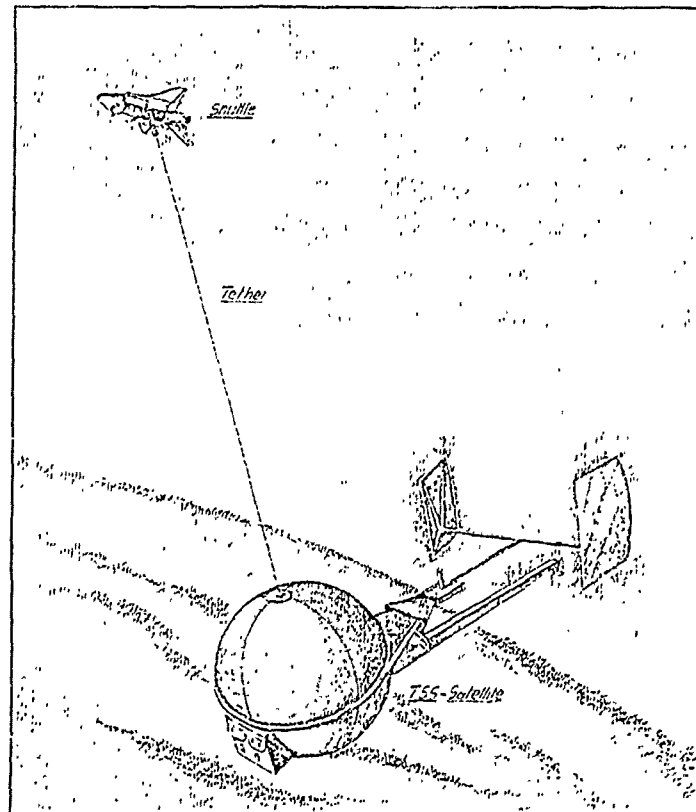


Fig. 1 - The TSS-2 Atmospheric Mission

The Satellite, a 1.6-m-diam. sphere, would carry scientific experiments to be performed up to 100 km from the Orbiter. The Deployer will deploy, operate, and retrieve the satellite and maintain it at selected orbital altitudes. The Tether, connecting satellite and deployer, must withstand high drag and temperature.

Operation of tethered systems subjected to high drag makes their control very important. Tether dynamics and control laws need to be defined and computer models formulated for simulation and definition of mission and tether requirements.

For the purpose of this work, we shall consider the Shuttle in a circular, 28.5° inclined orbit at 230 km altitude with a 100 km tether connecting the Shuttle with the 500 kg TSS satellite.

We first shall look at the equilibrium configuration of the system and then we shall examine the main features of the system dynamics in presence of drag forces due to the rotating atmosphere above 130 km.

We have to say that for TSS-2 mission an equilibrium configuration does not exist. In fact, for a non equatorial orbit, the combined effects of atmosphere rotation with Earth and density variations due to the oblate earth will cause, if the system is properly controlled, more stable librations than equilibrium of the system.

For the purpose of understanding the tether medium equilibrium shape during the atmospheric mission we shall consider a constant atmospheric density at given altitude, i.e., we shall consider a spherical Earth. In the first approximation, the elastic deformation of the tether is neglected and the Shuttle maintains the circular orbit.

The linearized equations of relative motion of the tether element with unit length can be written in a reference system centered on Shuttle center of mass with the Z axis along the vertical oriented toward Earth and the X axis in the velocity direction. The equations in the orbital plane, where the drag mainly acts, are:

$$\begin{aligned} \mu(s) \frac{\partial^2 z}{\partial t^2} + 2n\mu(s) \frac{\partial z}{\partial t} + \frac{\partial}{\partial s} \left(\tau \frac{\partial z}{\partial s} \right) + 3\mu(s) \frac{z}{a} g(a) &= 0 \\ \mu(s) \frac{\partial^2 x}{\partial t^2} + 2n\mu(s) \frac{\partial x}{\partial t} + \frac{\partial}{\partial s} \left(\tau \frac{\partial x}{\partial s} \right) - \frac{C_D}{2} \delta(z) A(s) v^2(z) \frac{\partial z}{\partial s} &= 0 \\ \left(\frac{\partial z}{\partial s} \right)^2 + \left(\frac{\partial x}{\partial s} \right)^2 &= 1 \end{aligned} \quad (1)$$

where:

s	=	tether length from origin to the center of the generic element ds of the tether
n	=	mean motion of Shuttle
v	=	absolute velocity of the tether element
a	=	Orbit radius
g(a)	=	Earth's gravitational acceleration
C _D	=	tether drag coefficient
A(s)	=	tether cross section per unit length
μ(s)	=	tether mass per unit length
τ(s)	=	tether tension
δ(z)	=	atmospheric density at Z distance from Shuttle

The boundary conditions have to be imposed and the equations of relative equilibrium can be easily found. The final equations have been numerically integrated and the result is shown in figure 2 (see pg. 4).

Two cases have been studied: one with atmospheric density (1000° K Exospheric Temperature) relative to the Equator crossing and representing the maximum drag experienced by the system during its orbit, and a second with the minimum drag experienced at 28.5° latitude.

From figure 2 we can evaluate the strong influence of air drag on the TSS-2 mission. The satellite displacement from local vertical is shown to vary from 3.5 to 4.8 km and the tether curvature, essentially present in the last 15 km near the satellite, is an evident sign of the tether drag area impact on the equilibrium configuration. In fact, the air drag force on the tether is an order of magnitude greater than the force on the satellite.

We have already said that for low altitude steady-state operation, the geometric effects of orbit shape on air drag produce libration perturbations. When the tether length is constant, the basic motion is composed of two librations with different periods. The periods are independent of tether length and their values are $2\pi / \sqrt{3} n$ for in-plane libration and π / n for out-of-plane motion.

Computer simulations have been performed to investigate the dynamics of the system in presence of drag perturbations due to orbit inclination, Earth rotation and Earth shape.

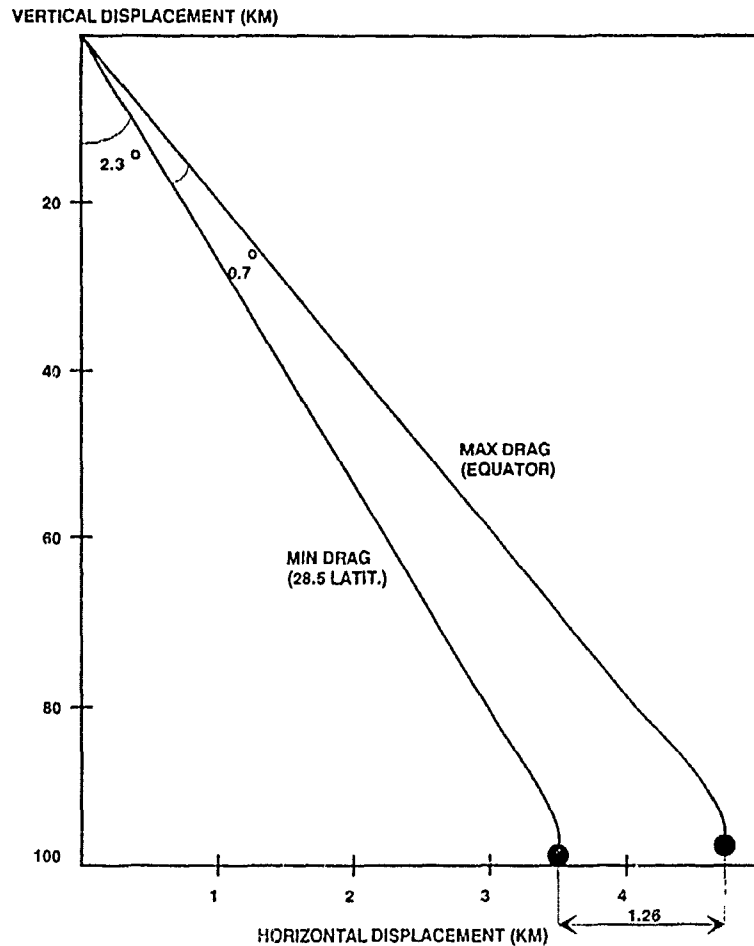


Fig. 2 - TSS-2 Atmospheric Displacement (130 km)
 CM Orbit ($H = 230$ km; $i = 28.5^\circ$)
 Tether (Diameter = 2.2 mm; Unit Mass = 5.2 kg/km)

A first simulation has been performed without any tether control maintaining the tether length constant. Figure 3a (see pg. 5) shows the in-plane librations of the satellite. They are characterized by the coupling between natural in-plane frequency ($\sqrt{3} n / 2\pi$) and drag perturbation frequency (n / π). Large in-plane libration is present (5° amplitude) and the motion is stable. Figure 3b (see pg. 5) shows the out-of-plane librations. They are characterized by the natural out-of-plane frequency (n / π) and drag out-of-plane orbital frequency ($n / 2\pi$). Stable librations are shown for a circular orbit, but in an inclined elliptical orbit, density variations can cause an unstable growth in the out-of-plane libration.

A second simulation has been performed utilizing a "yo-yo" damping control for the in-plane libration. Figure 4a (see pg. 5) shows the controlled in-plane libration that presents a twice orbit rate libration of reduced amplitude (1.4°) obtained by a same rate sinusoidal length variation and utilizing reasonable tether tension and rates. Figure 4b (see pg. 5) shows the in-plane trajectory of the satellite depicting the "yo-yo" control procedure.

The purpose here is just to show the main dynamics features of TSS 2 atmospheric mission. The described control concept must be improved to control the decay rate of the system (not considered) and the out-of-plane potential instability.

For the mission considered the main effects caused by the unusually large system drag have been described and as a general conclusion we can say that proper time-varying length control has to be used to dramatically improve the steady-state performances of the second Shuttle/Tethered Satellite System mission.

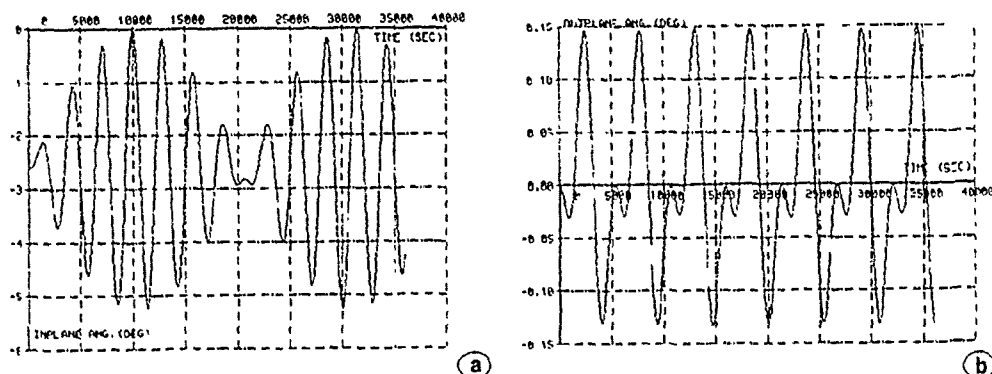


Fig. 3 - TSS-2 Steady Librations (Constant Tether Length)

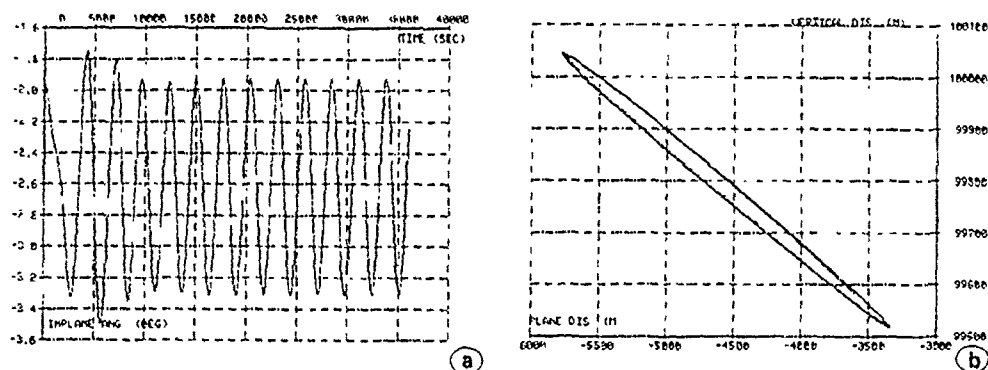


Fig. 4 - TSS-2 In-Plane Librations ("yo-yo" control)

3. TETHER INITIATED SPACE RECOVERY SYSTEM (TISRS)

The use of tethers for release of payloads to higher or lower orbits from the Space Station is a promising area of tether applications. In a system of two orbiting bodies connected by a tether, only a point close to the center of mass is in true gravitational equilibrium. All of the other points are subjected to a force tending to align the system along the local vertical since the outer mass moves at a velocity greater than the local circular velocity and the inner mass at a smaller velocity. Moreover, in the event that the end bodies have velocities relative to the rotating orbital system, there can be additional forces.

This additional effect can be achieved by effecting a low tension deployment which causes a large libration to the tether system. If the tether line is severed, both bodies are injected into elliptical orbits. The previous locations of the inner and outer masses become respectively apogee and perigee of the new orbits.

This mechanism can be exploited to transfer momentum from the downward deployed body to the upward deployed body. In the case of a deorbit maneuver, the momentum subtracted from the downward body must be such to put it in a re-entry trajectory.

The ASI/NASA Joint Task Group for Tether Flight Demonstration has given high priority to a demonstration which validates the concept of a tethered system used for a deorbit maneuver to re-enter/dispose of material from an orbiting infrastructure (e.g., the Space Station). This demonstration is called TISRS (Tether Initiated Space Recovery System). The idea is to use the existing hardware as much as possible to limit the cost and time to develop an Orbiter-based demonstration to be performed in 1992.

In order to perform the Orbiter-based TISRS demonstration, the following systems will be utilized:

- The Small Expendable Deployer System (SEDS) which is a simple, compact system that is entirely passive and uses an expendable tether;
- The re-entry vehicle (SRV) that will be used is an existing General Electric (G.E.) capsule. This is a simple ballistic capsule design which has flown several times and in which there is a high degree of confidence;
- A proper Instrumentation, Data and Communication System to measure and to monitor the mission performance that has to be developed by Acritalia and integrated into the G.E. capsule.

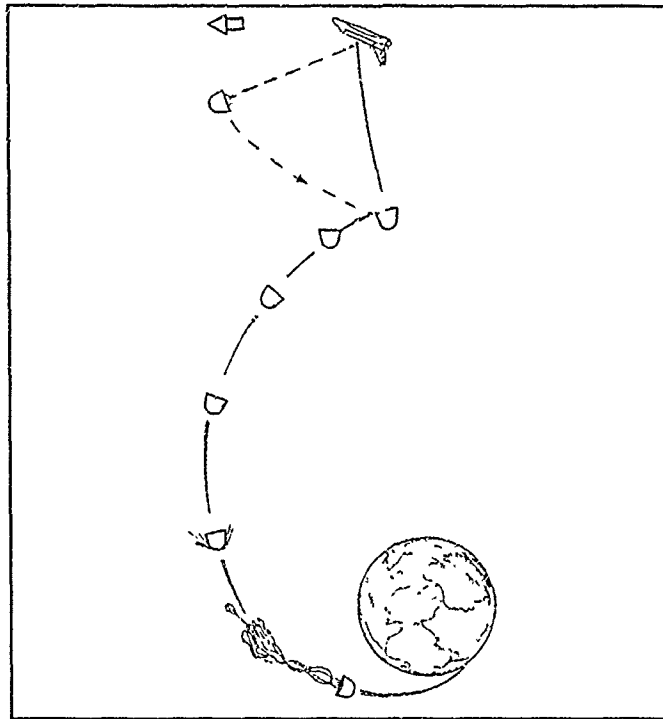


Fig. 5 - TISRS Deorbit Concept

Figure 5 shows the assumed deorbit concept. The re-entry mission starts when the capsule is removed from Payload bay accommodation by means of the RMS (Remote Manipulator System) and placed at some meters from the Orbiter. At this point a Shuttle orbit that moves it away from the capsule is set up by RCS (Reaction Control System) firing.

A slight tension is maintained on the tether and the capsule moves forward till the desired tether length is deployed. The tension is then gradually increased until the tether lengthening ceases. At this point the capsule starts swinging in pendulum fashion below the orbiter and is released into the re-entry trajectory when the system swings through the local vertical.

The objective of the TISRS flight is to demonstrate the capability of a tether system as a deorbit means. The demonstration is also intended to exploit the benefits offered by a dynamic release together with the use of a "passive" subsatellite. The word "passive" means in this context the lack of actuators onboard the subsatellite for controlling the tethered maneuver.

The dynamic or swinging release provides higher thrust capability than a static release but complicates the maneuver. While in the case of static release, the deployment can be effected earlier in order to have the tether aligned along the local vertical with a margin of time for an accurate timing of the release, in a swinging release, the timing of the maneuver and the momentum exchangeable are coupled.

The deorbit maneuver must guarantee:

- re-entry conditions compatible with the existing SRV which has been certified to fly in a certain range of re-entry velocities and angles;
- combination of deboost and instant of release which allows the reaching of the desired landing site.

The control of this maneuver (passive subsatellite for this demonstration) can be effected by:

- the tether tension;
- the Shuttle maneuvering;
- the instant of release.

The SEDS can only modulate the tension, therefore, the ejection velocity which initiates the deployment has to be provided otherwise. The current idea is to accomplish the ejection by firing the Shuttle. This deployment is then controlled by regulating the tension in the tether. The basic control of the SEDS is to sense the length unwound (deriving the length rate) and use it as input to a control algorithm which modulates the braking. The tension is opportunely modulated to obtain the swing effect when a desired length has been deployed. In order to have the highest deboost, the tether should be cut when the system swings through the local vertical.

At this point, it is necessary to consider the errors accumulated during the ejection/deployment phase. For a vehicle which doesn't make use of aerodynamic forces to steer its trajectory inside the atmosphere (as the ballistic SRV used for this demonstration) the range to be "flown" between the instant of release till the landing impact depends only on the conditions at the instant of release. Therefore, the errors due to position and velocity must be reduced during the tethered phase. (The use of a steering parachute makes it possible to recover a few miles; however, other dispersions resulting from atmospheric flight will occur.)

The target landing site can be reached with different deboosts imparted to the SRV but at different times provided that the following atmospheric heating is manageable by the SRV. The simplest way to control the landing site is by controlling the instant of release. Another way is by controlling deployment entirely using as feedback the relative position of the SRV. In any case, the relative position of SRV has to be known.

Another aspect is related to the release of the tether at both the Shuttle and SRV ends. The tether should be released from the SRV a finite time after it has been released from the SEDS in order to allow the free-floating tether to distance itself from the Orbiter and to avoid recoil and tangling on the Orbiter appendages as well as on the SRV. Moreover, as long as the tether remains attached to the SRV it affects the trajectory of the SRV because it is the compound system tether plus SRV which receives the deboost.

A low tether tension deployment (typically tension less than 0.1 N) is mainly characterized by the payload separation nearly horizontally with a braking at the end of the deployment that causes a large libration.

The deorbit momentum obtainable in this way (if the tether is severed near the vertical) is approximately 85% greater than if the same system is deployed nearly vertically. This means that to obtain the same deorbit effect a vertically deployed tether must be 85% longer than a swinging tether. This is a first advantage of this low-tension maneuver. A second advantage is that an horizontal deployment radically reduces the amount of braking required during the maneuver. A same deorbit performance vertical deployment requires approx. 50 times higher braking energy dissipation. The main drawback of low-tension deployment is that it requires a very accurate timing of the maneuver if precise re-entry is required.

Figure 6 shows the results of simulations performed to investigate this critical aspect. A nominal maneuver has been assumed with initial separation velocity of 0.76 m/s and minimum initial tether tension of 0.072 N. We have to

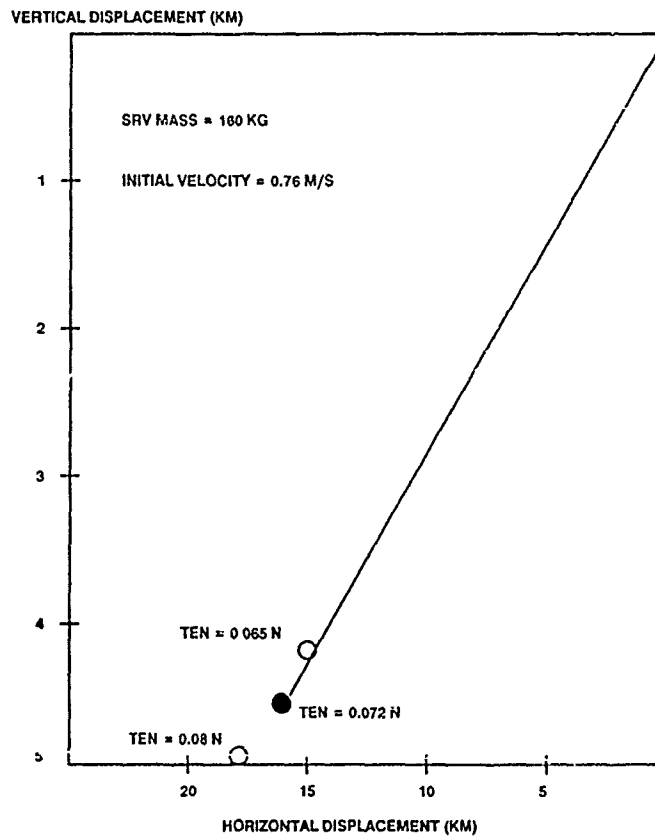


Fig. 6 - SRV Displacement vs Min Tether Tension

outline that a very low tension is required and tension control errors could be high. The nominal maneuver deploys after 5800 sec. 16982 m of tether. In the same time, 15655 m of tether are deployed if we consider a -10% error on nominal tension and 18228 m are deployed with a +10% error.

An interesting point is that increasing the tension accelerates the deployment and decreasing the tension retards it due to the tethered system dynamics.

The success of TISRS demonstration depends on the accuracy of the deorbit maneuver. System dynamics has to be well understood and proper control has to be devised in order to limit the strong impact of tension errors on the re-entry performances. The SRV motion during deployment has to be determined by a proper instrumentation system. Probably the relative SRV position must be known by the flight controller. This would allow the very accurate timing required. Moreover, the data could be used as a feedback in the control loop of the deployer (braking tension).

4. TETHER ELEVATOR/CRAWLER SYSTEM

A tethered microgravity facility seems to be a very promising concept. In fact, the microgravity scientists have considered this concept very intriguing because of the unique capabilities that it allows. In addition to cleanliness and high power, the requirements of microgravity applications call for a very stable dynamical environment with residual acceleration smaller than 10^{-5} , as well as the possibility of modulating the gravity level or of obtaining differential measurement at locations with different gravity levels. This has led to the consideration of a moving Elevator along a tether deployed to a fixed length.

The most promising feature offered by the Elevator is the unique capability to control with time the gravity acceleration level. In fact, since radial acceleration changes with position along the tether, the Elevator would be able to attain a continuous range and a desired profile vs-time of residual gravity level by the control of the Elevator motion.

Moreover, the utilization of the Space Elevator as a transportation facility, able to move along the tether providing easy access between the two tethered bodies, could be the tool for tethered systems evolution.

The demonstration of an Elevator model capability to provide the suitable microgravity environment and to control the transfer motion seems necessary due to the complexity of phenomena involved, essential to allow the development of new capabilities for microgravity applications and valuable to the assessment of the feasibility of this new concept.

Regarding the microgravity application, one is mainly concerned with perturbing accelerations propagating along the tether. The disturbances are originated mainly by the Space Station and by the Elevator motion.

Disturbances coming from these sources excite vibrations with a rate of damping increasing with frequency, but also a series of resonances with peaks not easily modelled because of the complexity of phenomena involved. Another unknown in the problem is the magnitude of the expected natural damping and what methods could be used for actively attenuating the disturbances.

Concerning the transportation application, the main problem is to control the transfer motion maintaining the dynamics disturbances within acceptable limits.

Controlled transfer motion is stable and tether deflection is bounded, but depending on the velocity profile perturbing oscillations can be excited. Tether lateral vibrations are induced by the Coriolis force acting on the Elevator as it moves along the tether. Longitudinal vibrations are induced by Elevator control forces to maintain the desired velocity profile.

The complexity of such phenomena advises an in-flight test of an Elevator model to evaluate the system dynamics response and to test the transfer control techniques.

The system proposed for a Shuttle flight test of the Elevator concept is made up of three major elements: a deployer system, a tethered satellite and the Elevator model (Fig. 7 see pg. 9).

As a general guideline it has to be considered that both cost and schedule constraints impose a necessity to reuse to the maximum possible extent the hardware under development. In particular, the capability to control and to measure the system dynamics is required for the objectives of this mission.

The Tethered Satellite System (TSS), constituted by the TSS-deployer and TSS-satellite, seems to be the unique existing system able to perform this demonstration without the need for any significant design change. The only new hardware development required would be the Elevator model.

The realization of a small Elevator model whose main feature is the ability to be hooked on the tether after TSS-satellite deployment, appears feasible from the analyses performed, although several technical problems need to be analyzed in further detail.

A theoretical analysis has been approached and, in particular, an attempt made to establish a control strategy for the Elevator motion and a preliminary assessment of the tether vibrations induced by the Elevator motion have been performed.

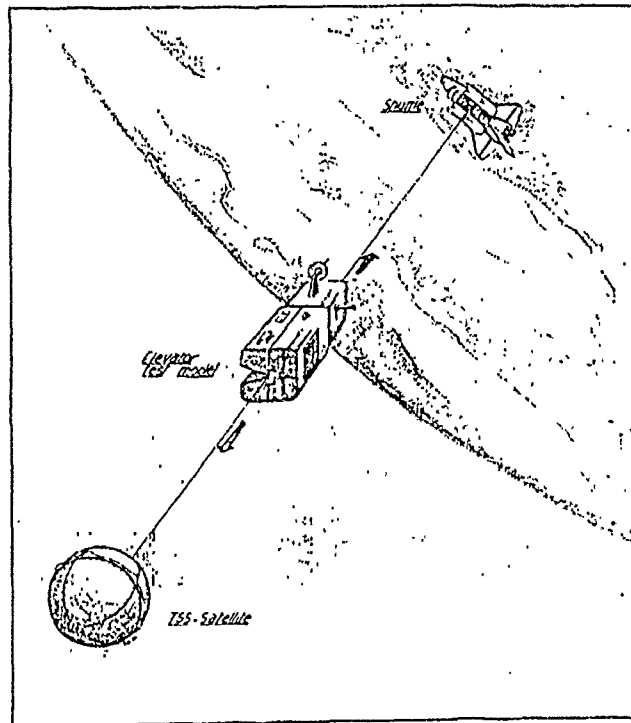


Fig. 7 - Tethered Elevator Test Flight

Here and in the following "the motion of the Elevator" has to be intended as the complete transfer from the Space Shuttle to the TSS Satellite, the utilization of the Elevator as transportation vehicle being the most severe situation from a dynamical point of view.

Because of the known weak coupling between tether elasticity and the general dynamics of the system, two different models have been developed.

The basic dynamics have been modelled by means of a 5 d.o.f. (degree of freedom) system composed (with reference to Fig. 8) of the TSS-satellite (m_2) and the Orbiter (m_0) connected by a rigid tether on which is moving the Elevator model (m_1).

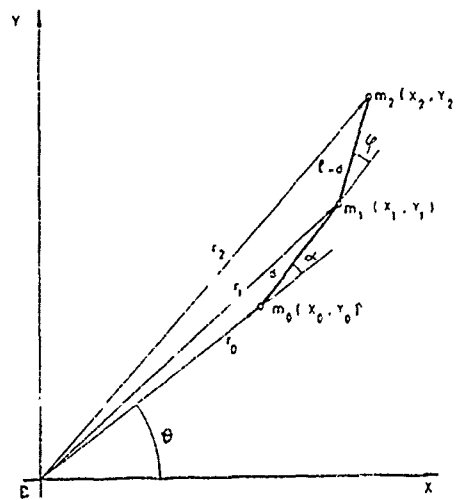


Fig. 8 - Reference System

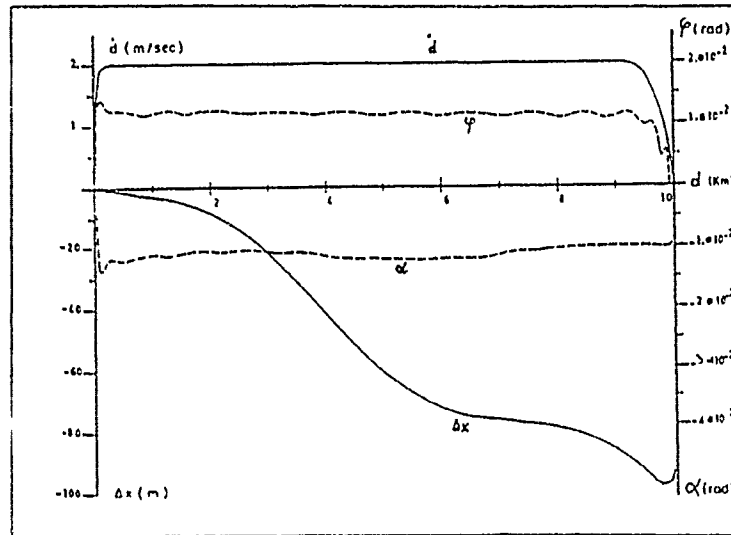


Fig. 9 - Elevator Controlled Motion - System variables behaviour as function of the travelled distance

The following notations are adopted:

α	=	angle between the local vertical and the first tether segment from m_0 to m_1 (deg)
δ	=	parameter of the decelerating phase of the control law (-)
d	=	travelled distance from STS to Elevator (m)
\dot{d}	=	instantaneous velocity of the Elevator (m/sec)
γ	=	parameter of the accelerating phase of the control law (-)
ϕ	=	angle between the first and the second tether segment, from m_1 to m_2 (deg)
l	=	total tether length (m)
v_0	=	steady state velocity (m/sec)

Due to the smallness of the physical dimensions of the space vehicles (few meters) with respect to the assumed tether length (10 km), all masses have been considered point masses. The effects deriving from the environment, i.e., residual atmosphere, Earth's oblateness etc. have been disregarded and only the components of the motion lying in the orbital plane have been taken into account.

As long as the positions of each system component and their derivatives can be utilized to write, as usual, the kinetic and potential energy expressions, the derivation of the Lagrangian is straightforward and the equations of motion can be found [6]. For brevity, these equations have not been reported and only the results of the numerical simulation are discussed in the following.

Some runs have been initially done to explore what happens when free motion of the Elevator is simulated. As a result, the excessively high value (about 75°) of the angle α (due to the Coriolis force) at the end of manoeuvre forces a need for a control strategy. In this view, the following aspects which influence the system behaviour must be accounted for:

- the Coriolis force depending on the magnitude of d (the system is as controllable as the velocity of the Elevator is small);
- the transients near both the ends of the tether have to be rigorously controlled in order to avoid dangerous induced librations of the short "equivalent pendulum".

So a three phase control has been identified (Fig. 9), a first one of acceleration, a second one at d constant and a third one of deceleration. Several control laws have been simulated, all using d as a control variable.

About the central phase a $d = 2$ m/sec has been identified as a reasonable maximum value in order to bound both α and ϕ (less than 1°). Good results have been obtained utilizing a simple law of the following form:

$$\dot{\alpha} = V_0 \operatorname{tg} h(\gamma \alpha) \quad (2)$$

for the initial phase, from $d = 1$ m to about the c.o.m.(center of mass) of the system, and

$$\dot{\alpha} = V_0 \operatorname{tg} h(\delta(1 - \alpha)) \quad (3)$$

for the final phase, from about $d = 9000$ m to the end.

The maneuver is performed in about one hour and a half, the displacement of the TSS Satellite (Δx) with respect to the local vertical is relatively small (< 100 m) and it is noted that this displacement causes a natural residual oscillation at the end of the maneuver, which has to be actively damped; the perturbation induced on the STS orbit by the displacement of the center of mass is of about 50 m. In view of these results, one could say that the system is potentially controllable.

An independent mathematical model has been developed to investigate the tethered taut string vibration induced by the motion of the Elevator.

The following simplifying assumptions have been adopted:

- tether equilibrium configuration is a straight line;
- Elevator velocity is anywhere constant and low enough to apply the linear theory at the tether induced vibrations;
- tension along the tether is assumed constant, disregarding the small contribution arising from the tether mass.
- Reference Notations:

E	=	elongation module (kg/m^2)
A	=	cross sectional area of the tether (m^2)
μ	=	linear mass density of the tether (kg/m)
T	=	tether tension (N)
y	=	transversal coordinate of the tether displacement (m)
x	=	longitudinal coordinate of the tether displacement (m)

The interaction between Elevator and tether has been simulated by means of external forces in the analysis of both the transversal and the longitudinal vibrations. The equation of motion used to model the transversal ones is:

$$\mu \frac{\partial^2 y}{\partial t^2} = T \frac{\partial^2 y}{\partial x^2} - 2m_1 V_0 n \delta(x - x_0) \quad (4)$$

where the forcing term has been written as a Coriolis force generated by a point mass (m_1) travelling at constant velocity (V_0) and distributed as a Dirac function centered on the Elevator instantaneous position (x_0).

Using essentially the same model the motion equation for the longitudinal vibration is:

$$\mu \frac{\partial^2 y}{\partial t^2} = E A \frac{\partial^2 y}{\partial x^2} + 3m_1 n^2 (x_0 - x_c) \delta(x - V_0 t) \quad (5)$$

where the forcing term is now modelling the force necessary to nullify the acceleration induced by the gravity gradient.

The transversal vibrations appear consistent quantitatively and qualitatively with the results of the basic dynamics, as it can be observed looking at Fig. 10 (see pg. 12).

The maximum lateral displacement of a specified point of the tether is reached just immediately after the Elevator has travelled on it. The short periods of longitudinal modes in comparison with the total time required for a complete transfer of the Elevator results in a very low disturbance in the axial directions: when the Elevator reaches the attachment point such a displacement is about 70 cm with respect to the unexcited situation.

In conclusion, although a more refined level of modelling is necessary, the preliminary results make us optimistic about the dynamical aspects of the Elevator motion.

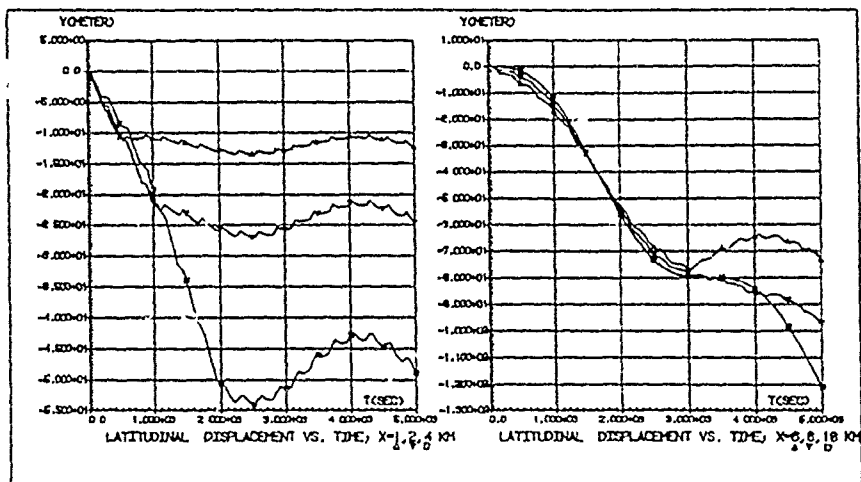


Fig. 10 - Tether lateral vibrations caused by the Elevator motion (vel. = 2 m/sec)

5. CONCLUSIONS

U.S. National Commission on Space has specifically suggested more attention be directed towards application of "Tethers" in space, particularly for Space Station missions.

Most of these applications give rise to very interesting and new problems of flight mechanics. Here the attention was focused on some intriguing topics characterizing three proposed tether flight demonstrations.

Continuing the cooperative effort of the U.S. and Italy on "Tethers" in space, the next step toward operational reality of tethered systems is already underway for the purpose of validating the dynamics and operating principles of this new space capability.

REFERENCES

- [1] Anderson J.L. - Outer Atmospheric Research - One Tether Capability, *2nd International Conference on Tethers in Space*, Venice, Italy, 1987
- [2] Anderson J.L., Wood W., Siemers P. - Research at the Earth's Edge, *Aerospace America*, Vol. 26, N. 4, pp. 30-32, April 1988
- [3] Anderson J.L. - Tethered Satellite System-2: A proposed Program, *3rd International Conference on Tethers in Space*, San Francisco, USA, 1989
- [4] Florence D. - Tethered Space Recovery Vehicle Deployment/Re-entry Demonstration, *2nd International Conference on Tethers in Space*, Venice, Italy, 1987
- [5] Merlina P., Burigo M. - Tether Initiated Space Recovery System (TISRS): Italian Activities Toward Flight Demonstration, *3rd International Conference on Tethers in Space*, San Francisco, USA, 1989
- [6] Bergamaschi S., Merlina P. - The Tethered Platform: A Tool for Space Science and Application, AIAA-86-0400, *AIAA 24th Aerospace Sciences Meeting*, Reno, USA, 1986
- [7] Merlina P., Bogo W., Ciardo S. - Tethered Elevator and Pointing Platform Demonstrations: A Shuttle Flight Test of Scaled Engineering Models, AAS 86-213, *1st International Conference on Tethers in Space*, Arlington, USA, 1986.

**TESTING DOD SPACE SYSTEMS:
THE CHALLENGE**

by

**W. Andrew Wisdom, Colonel USAF (Retired)
Institute for Defense Analyses
1801 N. Beauregard Street
Alexandria, Virginia 22311 USA**

and

**Lowell C. Keel, Colonel USAF
DDRE(T&E)/TFR
Washington, D.C. 20301 USA**

ABSTRACT

The advent of military space systems in the 1960's challenged the nation's test capabilities and demanded creation of new techniques and concepts to deal with the state-of-the-art complexities inherent in expensive, vital national assets. As the national dependence upon space systems increased over the past two decades, so too has the complexity of the hardware and software components needed to perform the assigned missions. This increasing complexity has required ever increasing sophistication and modernization of the Department of Defense test and evaluation capabilities, however, current concepts for new military space systems outstrip the present test capabilities. New test and evaluation techniques, concepts and capabilities are required to meet these new challenges. This paper reviews the challenges of testing military space systems and presents some of the new testing concepts and modernization initiatives being pursued.

TEST AND EVALUATION PROCESS

Test and evaluation (T&E) is an exacting process even for relatively simple designs and articles. The complexity and challenges involved with testing of a modern military system and the rapidly changing technical environment make the subject difficult to address effectively in a summary form. To help bound the discussion, the very term "test" deserves some discussion. The definition contained in The Glossary: Defense Acquisition Acronyms and Terms, Defense Systems Management College, July, 1987 is as follows:

A "test" is any program or procedure which is designed to obtain, verify, or provide data for the evaluation of: research and development (other than laboratory experiments); progress in accomplishing development objectives; or performance and operational capability of systems, subsystems, components, and equipment items.

Therefore testing in the context of this paper includes the full spectrum from early experimentation to validate system and design concepts through the establishment and qualification of specific designs and hardware. It includes prototype experiments which provide sufficient confidence to support major management decision milestones, extends from concept validation through operational evaluations to assess employment effectiveness and suitability, and ends with production quality verification to insure adequate consistency. Testing, however, is not an end unto itself. It is evaluation which transforms test results into useful information. Therefore, inherent in our use of the terms "test" and "testing" throughout this paper are the considerations imposed by the evaluation process.

THE CHALLENGES OF TESTING IN SPACE

Since the early 1950's, the testing of military designs and hardware has become very systematic for applications which have well established methodologies, mature instrumentation and a long history of success. As shown in Figure 1, the thought process for any system development follows a logical, traditional, flow from establishment of requirements for the system through the characteristics needed to satisfy the requirements, to the types of test methodology needed to prove the system and finally the testing and feedback

TEST AND EVALUATION HEIRARCHY

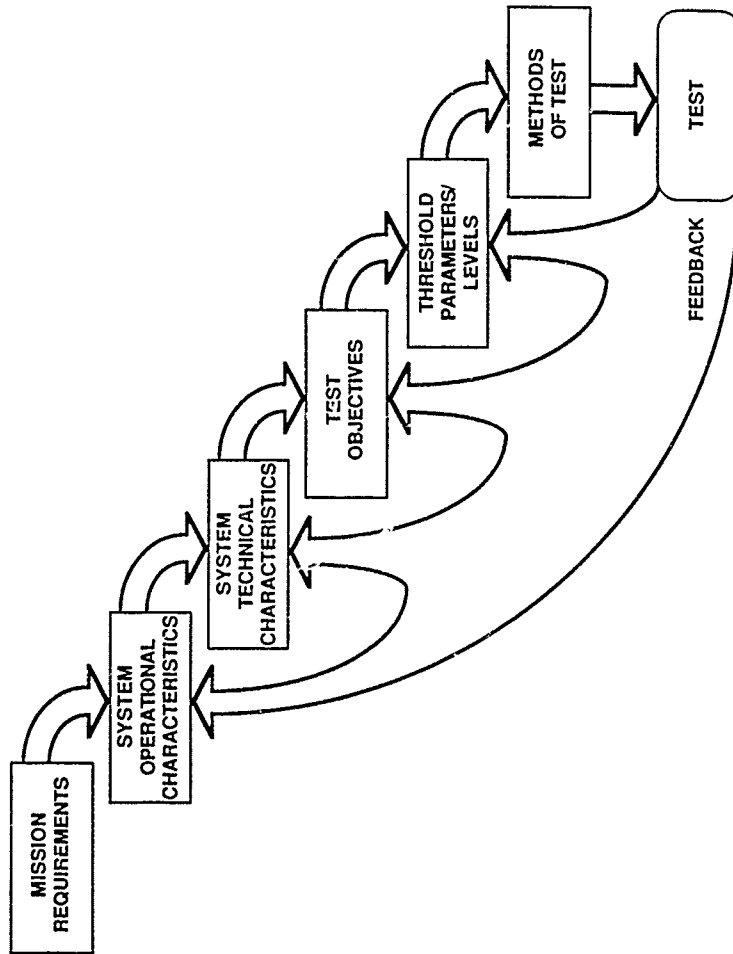


Figure 1

process. Testing of U.S. space systems, like their earth-environment counterparts, follow this thought process, but the implementation of test methodologies and the actual testing must accommodate special challenges.

Two basic facts circumscribe the difficulty of testing any system in space and are linked together in that the solutions to each are intrinsically intertwined - 1) space is basically a hostile environment and 2) space is inherently a distant place, very difficult to get to. The accommodation of these two facts provide the foundation stones of the challenges encompassing testing in space. The advantages of being able to use space as the high ground, however, more than offset the difficulties involved in producing and fielding space assets and the attendant testing problems.

The fact that space is basically a hostile environment impacts everything involved in the production of the test article - design, structure, materials, lubricants, command and control devices and techniques, navigation, power, communications, etc. Somewhat like autonomous, self-contained undersea test articles, everything needed to survive, operate and carry out the test mission must be taken on board and integrated into a single entity, but unlike the undersea test articles, space equipment is rarely recovered for after test evaluation.

The capability to survive and operate in space is considered as overhead to the tester, that is, the price that must be paid just to be able to test the article in the environment in which it is to operate. This overhead is not trivial. A space vehicle must be able to accommodate the difficult thermal environment, must contend with a variety of radiation effects, must deal with contamination, must be able to operate in vacuum (or near vacuum), must be able to exist for extended periods autonomously and must be able to reliably communicate with a control center. The solution to these first order problems requires complex electronics, exotic materials, and painstaking attention to detail in design, fabrication, integration and on-orbit operational concept development. These solutions also require a share of the limited on-orbit available electrical power, weight and command and control capability. For military systems these solutions require an even greater share of overhead because the systems must have a robustness to survive not only the natural environment, but projected hostile acts.

Since all test information must be retrieved via telemetry (excepting those rare occasions in which on-orbit test data is recorded on board and the test article is brought back to earth for analysis), the necessity to achieve the minimum fidelity and yet remain within the constraints of the telemetry system (band width, power, data point limitations, and baud rate) generally leads to a constrained design for the test capability. Any capability needed solely for on-orbit testing will claim additional shares of the on-orbit power, weight and control capabilities and further limits the amount of capability available for operations. Therefore it should come as no surprise that resources dedicated to on-orbit testing are most begrudgingly allocated.

The second stone in the foundation of challenges impacting space testing lies in the fact that space is remote, a distant place which is difficult to get to. Today, nearly twenty years after we achieved "routine accessibility to space", we face many of the same problems encountered by Columbus in his voyages of discovery to the New World - the mode of transportation is precarious, limited in its capacity and application, and very expensive in terms of expenditure of national treasury. Not only does the price per unit mass to low earth orbit approximate the price of a fine perfume, the environment imposed on the space test article during the launch phase forces severe design penalties on the space vehicle. High g-loading together with high vibrational, acoustical, aerodynamical, and thermal loads encountered during ascent impose shock and stress into the booster and payload which must be accommodated with still more "overhead" in order to survive the translation from 1-atmosphere and 1-g to near-vacuum and zero-g.

Practical difficulties are experienced in testing space articles simply by the fact that once in orbit they are not easily accessible for any of the common test activities such as reconnecting a connector, tightening screws, replacing a blown fuse, rerouting a cable or simply kicking the tires. Further the basic advantage of having a satellite in orbit, constantly changing its position relative to a point on earth, becomes a distinct disadvantage in the conduct of a test in that testing often must be limited to that time the test article is in view of a ground control station, which for a low earth orbit could be as little as 5 minutes every few days. Solutions to these practical difficulties increase the complexity of space testing enormously by requiring inclusion of additional circuitry and mechanical systems to provide capabilities for autonomous operations, to record on board performance and to monitor the health and status of the vehicle when not in direct ground control, to enable space/ground and space/space communication systems for worldwide

command and control and telemetry, etc., etc., etc. Eventually the point is reached where the testing, check out and operation of the supporting equipment and capabilities are as complex and expensive as the payload to be tested.

THE MILITARY CHALLENGE

The discussion to this point has been mostly generic, that is, it has been generally descriptive of problems facing any space system, military or civilian. What, then, are the added difficulties the military system demands in its test and evaluation?

Military space systems, because of their role and importance in national defense, have requirements for reliability and robustness which significantly increase the complexity of the resulting systems. As previously discussed, these complexities impact the entire design of the space asset requiring additional power, structural components, electronics and command, control, communications capabilities. The need to assess the performance of these attributes and the impact upon the entire system (ground and space) translates into increased performance and precision requirements for the supporting test capabilities.

In the early days of space systems, the test techniques employed were logical extensions of methodologies and technologies used in aircraft development, with the wind tunnel replaced by the vacuum chamber to simulate the environment in which the device would operate. As the understanding of the space environment grew, primarily pushed by high failure rates, new techniques were devised not only for the design of the systems, but for testing as well. The basic premise became over-design, over-build and over-test, as compared to traditional earth-environment systems. The only concern was that the machine work once it was in orbit, and under no circumstances could testing imperil the vehicle. Thus testing on-orbit, in the traditional sense, was limited, and usually constrained to determining the on-orbit performance characteristics of the particular vehicle such as the offset of the gyros, command link margins and antenna patterns, thermal balance, battery charging/discharging rates, etcetera. The payload was not tested per se. It was turned on and, hopefully, produced useful data. Whatever test data was actually produced was transported by the telemetry system and suffered from the fidelity and extent of the total data activity - the on-orbit measurement technique, conversion mechanism, data handling system, transmitter, ground-based receivers, relay links, data handling, and storage and processing systems. The cause of many on-orbit failures remained unresolved because of inadequate fidelity in the telemetry and data systems.

As can be inferred from Figure 2, it was (and still is) extremely important to develop a test and evaluation methodology which would detect problems at the earliest possible point in the development process since the cost to rectify a problem increases exponentially as the program maturity increases from circuit board to the system level. Because testing in space required a survivable, integrated platform and an extensive support system, development testing on space systems was primarily conducted on the ground. Testing began on qualification type components and subassemblies with the space environment simulated to the best extent possible in thermal/vacuum chambers, on vibration tables and in acoustical facilities. Electromagnetic interference could be injected into circuitry and the effects measured by monitoring output signals. Radiation effects were measured primarily on subsystems or components in various above ground radiation facilities and occasionally during underground nuclear tests. Unfortunately test facilities which effectively combine all of these test environments did not exist, therefore the results from many tests on many separate subsystems and components had to be combined through analysis and simulation techniques. Following rigorous subsystem testing, the entire space vehicle was assembled and usually underwent lengthy integrated systems testing in the thermal/vacuum environment and limited power-on testing in an acoustical facility.

Flight hardware generally was not (and still is not) tested to the qualification limits but rather to less stringent acceptance levels. Again driven by the premise that on-orbit failure must be avoided, acceptance levels were designed to stress the hardware beyond the normally expected on-orbit operational conditions, but well within the qualification points. Key in these test programs, particularly at the integrated system level, was the introduction of the technique of using precisely the same process inground testing for data sensing, data handling, transmission and ground processing as would be used when the hardware reached orbit. For in this manner the analysis and evaluation of on-orbit performance could be directly compared to the ground test results without the need of inducing additional error through conversion techniques or data translation.

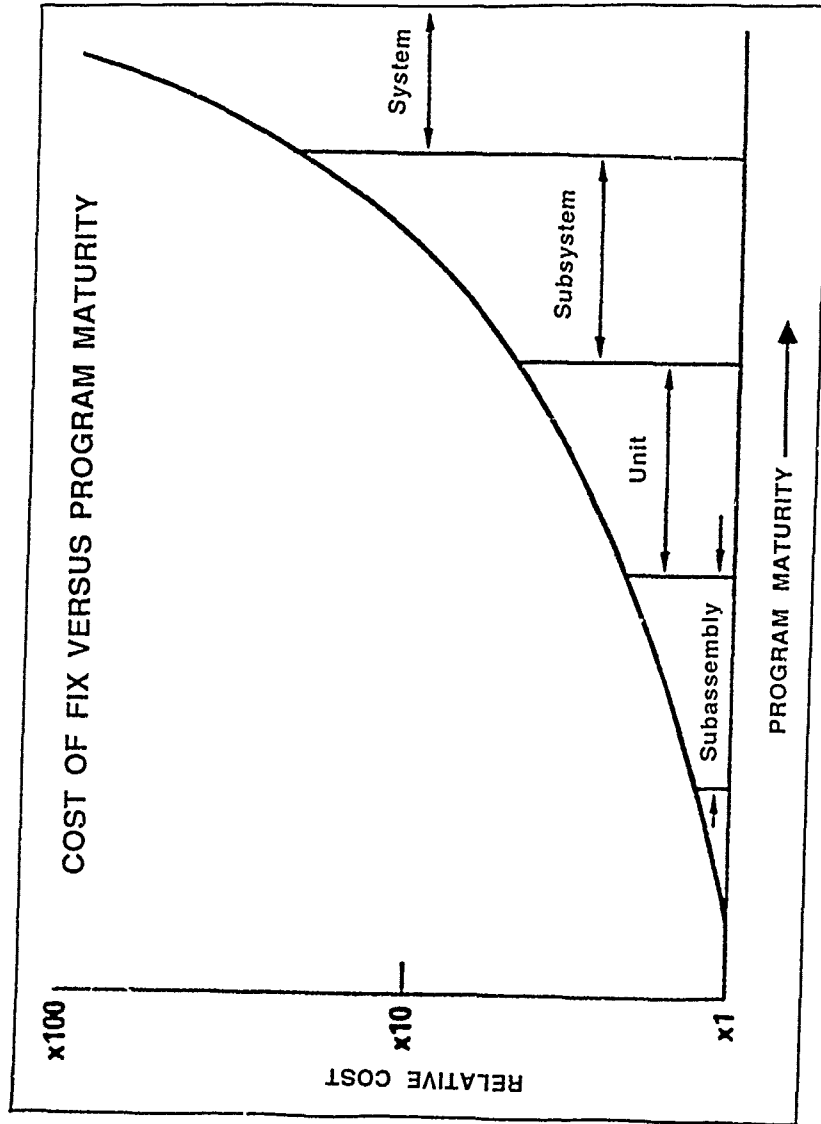


Figure 2

Today, given our tremendous advances in materials, electronics and computational capabilities, our test concepts are virtually the same! Ground testing is still the primary means of testing space assets and in a reasonable, disciplined test program, testing starts at the lowest component level and progresses in complexity to the integrated vehicle and its interface with the flight control and support elements. Given the large dependency on ground testing, it becomes obvious that one of the greatest challenges in testing military space assets has been to adequately model, replicate or simulate, on the ground, the environment in which the space vehicle must operate.

To briefly summarize, the challenges of testing in space dictate the necessity to have a complete, integrated system, both on the ground and in space, just to gain a useful orbit and operate in the space environment. That to arrive at a point of having a space ready system available for launch requires extensive and complex ground testing. Both the space test article and the supporting control systems are complex and extremely expensive in terms of national treasury. In short, the acquisition of a space asset and the supporting systems for on-orbit operation and testing have become so complex and expensive, and the nation's dependence upon them so great, that failure on-orbit cannot be accepted. This concept of insuring against the possibility of failure tends to force the inclusion of additional risk reducing elements, systems and circuits, which in turn further drive the complexity and cost of the total system.

With this background, the space system tester finds himself in an interesting dilemma. Space systems have become so complex that exhaustive testing is required for validation and proof, but because of the great expense and national dependence, rigorous testing to the point of over-stressing flight hardware or to the point of possible failure cannot be tolerated! The paradox is that because of the great complexity failure is unavoidable without rigorous, unambiguous testing! The result is that the distinction between testing and operations blur for space systems. This is particularly true when one thinks of testing in the traditional sense, meaning to gain data for use in assessing the ability of the test article to attain a specified performance and/or defining the extremes of the performance envelope. Often in the push to find the absolute performance edge failure results in the test article and test support equipment. In operational activities the extreme margins of performance are usually avoided to prevent the loss of the asset, except in an emergency situation. Thus we find with space systems, because of the limited number of assets and the tremendous cost involved in getting a system designed, fabricated and into orbit, there is extreme reluctance to press any part of the system to approach the point of failure, even if the test data is needed. This pressure not to induce a failure translates the tester into more of an operator and space testing more towards operational check out than true testing with respect to the earth-environment systems.

THE INCREASING CHALLENGE

Up until this point, we have limited our treatment of testing basically to space systems of limited or singular application. This is to say that space assets, while extremely complex, are generally treated as a single entity. For example, a single meteorological satellite, while it may be part of a constellation of satellites, can provide meteorological observations to ground controllers by itself without reliance on other similar satellites in the constellation. Thus testing the space asset, while still difficult and demanding, is limited to the stimulation and response of a single satellite and its interface with the ground control network. Additional space assets, e.g., more meteorological satellites, needed to make up the total on-orbit capacity are tested singularly and integrated into the constellation through the ground control network. When a satellite fails in orbit, the performance of the entire system is degraded, but the specific or individual performance of each of the other space assets is unaffected. This is not the case with the new, integrated, multi-platform, spaced based systems and concepts in which an individual space asset essentially has no independent mission, but must function as an integral part of the whole.

As the contributions from today's space systems are becoming increasing integrated into military operations at all levels, the interdependence among other assets and systems is increasingly evident. Using the currently envisioned space based US Strategic Defense Initiative architecture as an example (currently perhaps the most extreme example) of this interdependence in new, evolving military concepts, we find that the total system is built upon information and data flow between possibly hundreds of space and ground assets. Figure 3 attempts, in a limited sense, to illustrate some of this interdependence. Sensors in very high orbits detect enemy launches and provide early warning. Other sensors in lower orbits continue development of the attack corridors and establish the threat clouds. Still other functions determine the specific target points and assign engagement instructions, and

SYSTEM INTERDEPENDENCE

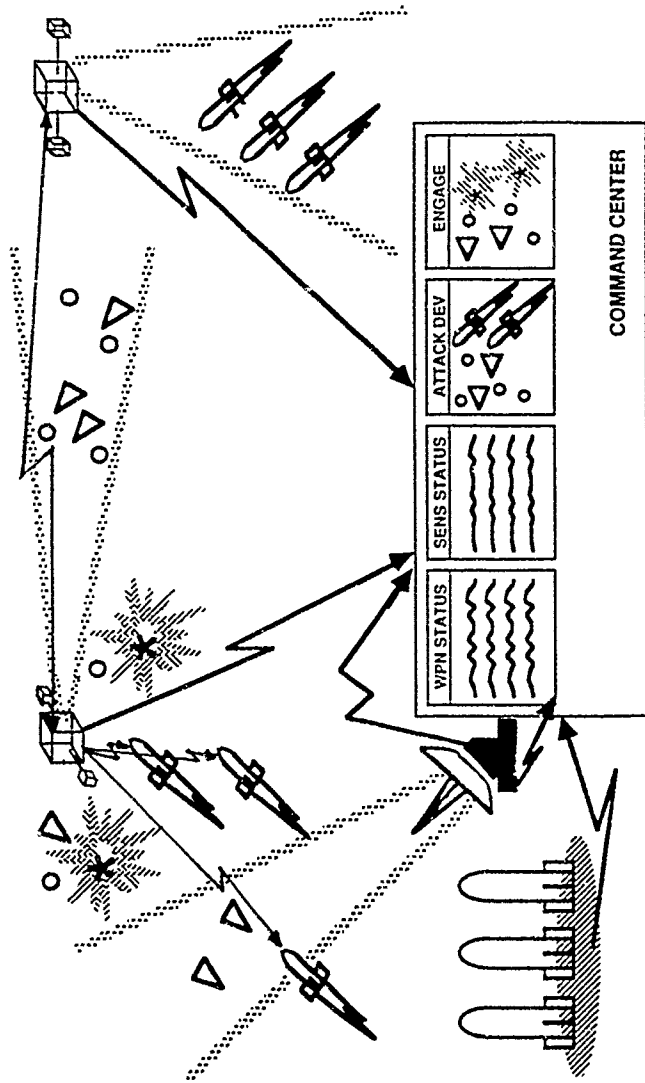


Figure 3

pass hand-off coordinates, state vectors and target object maps to specific, individual weapons. Assuming that not all of the enemy ICBMs would be launched at precisely the same instant, but staggered in order to effect the greatest offensive advantage, then many of the platforms which are in position at the initiation of the battle will soon be beyond the active battle space as they continue in their orbits. As more defensive assets orbit into the battle space, as more ICBMs are launched into the battle and as attrition eliminates both red and blue systems, more and more information must be exchanged between the defensive system components in order to continue with the defense. Each layer of the defense as well as each element is dependent upon the others, and each space asset cannot be thought of as an entity, but as a part of the whole.

From the tester's perspective, the earlier challenges and difficulties with testing military space systems pale in comparison with the challenges facing developing effective testing techniques for the multi-platform, highly interdependent system. The challenge becomes how to "test" a system which is comprised of many other systems.

MEETING THE CHALLENGE

Meeting the challenge of testing in space begins with the recognition that testing is not a separate entity or function which is added on like an appendage. Testing is an integral part of the development process and as such must be a carefully planned, disciplined process from the very beginning of a program. It begins on the drawing board with the design concept, is perfected on the ground during fabrication and buildup, and continues through to the orbital phase, with only that portion of the test and evaluation plan absolutely necessary executed in space. A key feature of any successful test program is the effective use of the feedback process (shown in Figure 1), for the critical use of all new information either builds confidence in previous assumptions or provides the basis to challenge and update these assumptions, follow on test tools, techniques and simulations. Test planning must describe the test methodologies and criteria at the top, or system level, then allocate requirements downward to the constituent element systems which will make up the aggregate system. The constituents within their development programs must define a test and evaluation process designed to bring that portion of the system on line in consonance with the top level system. In other words, a top level test philosophy must be established to bring proven elements into the system level and to test the ability of the aggregate system to perform to the top level specifications. This approach allows each element to be developed as much as a single entity as possible within the given allocations from the top level. Test data from the development testing of each of the constituent systems must be used to validate the top level system model prior to the delivery of the system components. This top down integration, bottom up validation technique provides flexibility in the development process to permit exploitation of technology advances during the development phase while at the same time providing some measurement of isolation to the aggregate system in the event of problems in a constituent level development. The use of models and simulations of the aggregate system allows top level development work on the overall concept as well as operational, both strategic and tactical, considerations in parallel with the development of the constituent elements.

Figure 4 illustrates the top down integration, bottom up validation interrelationship between the test flow of aggregate system and constituent levels for sensor systems needed to detect and track the boost phase, the mid course and the terminal portions of an ICBM trajectory. Similar relationships would be developed for all of the other system functions, e.g., discrimination, engagement, battle management, etc. The ability to conduct a test program with this philosophy is totally dependent upon the capability to conduct large simulations with provisions to connect hardware into the loop. If we continue to use the spaced based defensive system as our example, it becomes readily obvious that in order to make a system out of the multitude of space platforms needed to conduct a defense in space, some mechanism is required to orchestrate and integrate the parts into a whole. This mechanism is the battle management function with its attendant command, control and communication capabilities. Thus the key to successfully using large scale simulation as a testing technique becomes the ability to model the integrating management function (the battle management/C3 function in our example) together with the capability to connect battle scenarios and environment models and models and/or real hardware from the constituent elements into the aggregate system simulation.

The existence of a simulation capability of this magnitude permits the option to connect various portions of the system together for early (primitive) integrated testing long before the components of the system reach prototype maturity. This technique permits insight into aggregate system level problems early enough to impact the designs of the constituents or operational concepts, if necessary, thus saving cost and time in the overall development (per Figure 2). If the program must wait until each of the constituents has been developed

SYSTEM LEVEL - CONSTITUENT LEVEL T&E RELATIONSHIP

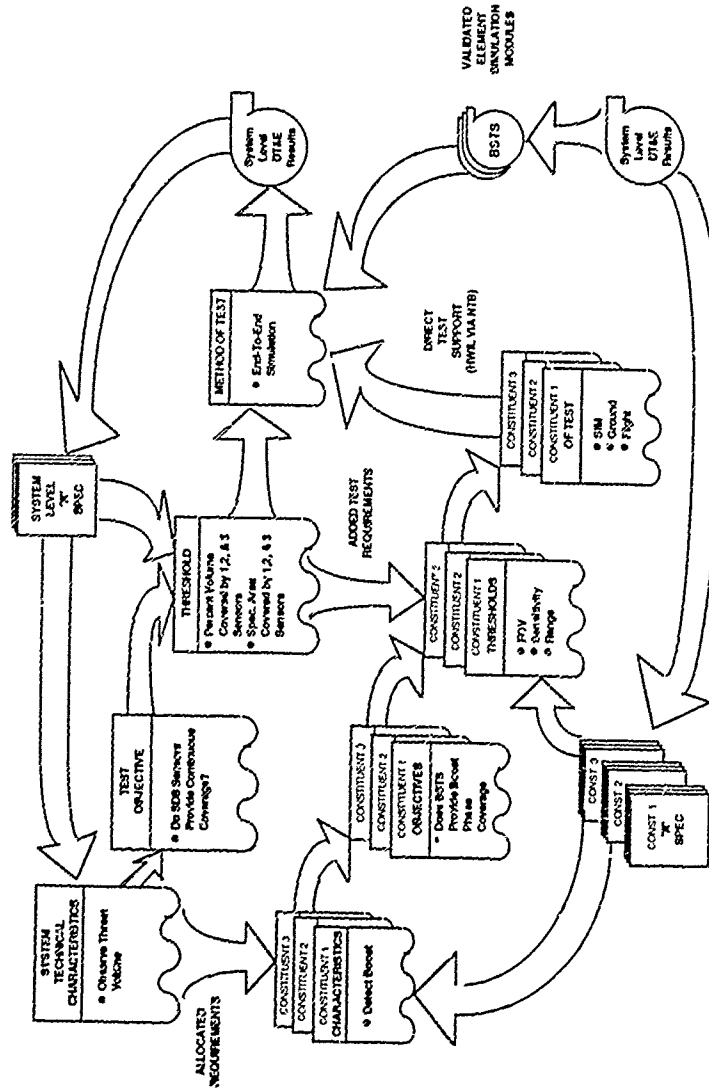


Figure 4

to the point of prototype or space flight before integrating the pieces into a system, tremendous expense will be incurred for problem resolution. This testing concept, in a sense the use of a highly capable test bed for early integration, is virtually mandatory for development of the new large, distributed software systems.

Figure 5 illustrates a simple early integrated test conducted between a sensor, battle management and a weapon early in their development. The figure shows a case in which the output of a sensor in a development test (being stimulated by a scene generator) is routed to a simulation center where the data is manipulated and operated upon by battle management algorithms and the output fed as an input to a development test of a weapon guidance and control unit. In this simple scenario, important gains are realized in normal development testing of various components as well as in the entire system without waiting for the completion of other than basically breadboard level hardware and early integrated software. Additionally, decision makers can be given system level insight far earlier than is usually the case.

Using the concept defined above requires that the test and evaluation program be developed and managed as vigorously and with as much discipline as the weapon development itself. Figure 6 shows that the integration test envelope can be expanded as the maturity of the hardware and software increases to the point that ground testing can accomplish no further gains in the overall test plan and the system must be taken to space, which returns us to the difficulties of testing in space!

ADDED CHALLENGES AND DIFFICULTIES

Unfortunately, or perhaps predictably, as our ability to build and successfully test military space systems has improved the requirements for new systems continues to outstrip test capabilities and techniques. Many of the new requirements physically cannot be tested in the earth-environment, while others require new testing concepts and techniques. For example:

- a. The requirement to acquire, track, discriminate and engage targets at unprecedented (intercontinental) ranges.
- b. The near instantaneous transition from long periods of dormancy or limited, standby modes to a war fighting status upon command.
- c. The inability to adequately approximate the zero-g structural dynamics of large space structures in an one-g environment.
- d. The inability to effectively determine and simulate the extent of the battle environment/threat, e.g., the nuclear enhanced environment, debris effects, direct energy weapon effects, etc.
- e. The growing interdependence between multi-participants.

The expansion of these examples provides excellent insight into the additional space testing problems which must be faced for military systems.

EXTENDED RANGE

The requirement for space based defensive systems to acquire, track, discriminate and potentially engage hostile targets at extreme ranges (greater than 3000 km) dictates pointing accuracies and platform stability specifications in the sub-micro radian class. Put in terms which most of us can begin to comprehend, some requirements will dictate not only the ability to look from New York and acquire a car's headlights in Los Angeles, but to be able to distinguish which headlight, the right or the left, has been acquired and is being tracked. The ability to conduct this type of test does not exist in the earth-environment, nor does a suitable reference system exist in space from which to measure the various deviations or errors in pointing angles or to truth or calibrate resulting test data. Related flight mechanics issues (platform attitude control, space, time position indications, pointing and tracking, structural modes, etc.) have been estimated to drive new instrumentation requirements in gyros and accelerometers 3-5 orders of magnitude beyond current state of the art. The testing requirements for this instrumentation of course imposes even more precision, perhaps exceeding the limits set by seismic stability of any ground testing facility.

Aside from difficulties in testing pointing and tracking, testing the engagement of a target by an interceptor presents a host of particularly difficult problems such as simultaneous, positive control of multiple platforms, measurement of miss-distance between interceptor and target, and debris containment. These problems increase exponentially when directed energy systems enter the equation. The traditional test safety methodologies which

SIMPLE EARLY INTEGRATED TEST

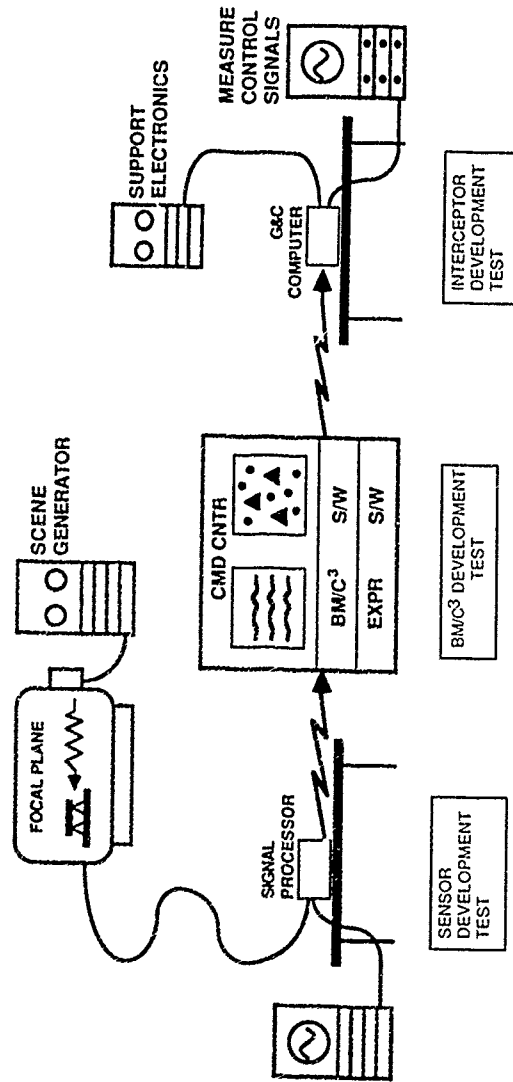


Figure 5

EXPANDING THE INTEGRATION TEST ENVELOPE

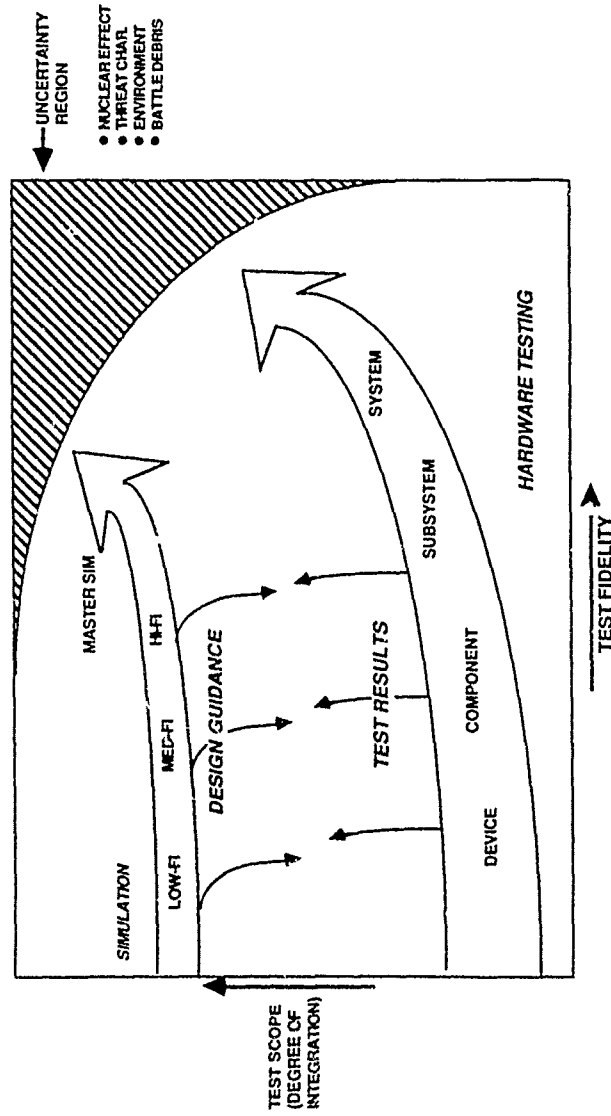


Figure 6

constrain earth-environment testing to specific well defined geographical areas now must expand to consider global extent and the resulting international considerations.

DORMANCY

A system which may undergo long periods of minimal activity or dormancy prior to near instantaneous full war fighting operation will require designs based upon an exacting knowledge of the aging effects of materials in the space environment. To date very little work has been done in long dormancy effects nor in the techniques for testing these effects. The changes brought on after long exposure to atomic oxygen, zero-g, solar radiation, x-rays, ionized particle impingement, etcetera, must be determined. Currently here on earth, there are not facilities which can impose the total space environment for the long periods needed to test the effects of aging in space nor are there known, valid techniques for accelerating the aging progress. Hopefully the Long Duration Exposure Facility experiment (LDEF) can be retrieved by the space shuttle before it catastrophically reenters the atmosphere in the very near future. This experiment, launched several years ago for a one year mission, has been stranded in orbit since 1986 waiting for the resumption of space shuttle operations. It has a wide variety of materials on board which should provide a wealth of insight to the space aging question if it can be retrieved. But in any case, much work appears to be required into the physics of material aging and test techniques and methodologies needed for evaluation of the aging process.

STRUCTURAL EFFECTS

The ability to adequately test large space structures does not exist in the one-g environment. Various techniques are used to reduce friction and the effects of gravity during ground testing of deployable components of a space vehicle such as solar arrays, antennas, gravity booms, air covers with varying degrees of effectiveness. Much analyses and guess work remains to translate the ground test results to expected performance once in orbit, and yet these components are almost trivial in comparison with the structures envisioned for large (30 meter class) directed energy mirrors or space station sized structures. Active and passive damping techniques as well as structural dynamics measurements demand in situ space testing capabilities.

SIMULATION

Military space systems cannot be tested in the hostile environment in which they may have to operate. Treaties and common sense prevent it. Hardening such systems against hostile interference or attack and providing the needed robustness is a critical concern. As we have discussed earlier, any measures added to enhance the survivability also add weight and require additional shares of the on-orbit available power and command and control capabilities. Therefore it becomes critical to understand the extent of the potential threat so that adequate countermeasures and protection can be built into the space system and still remain within the useful engineering margins for the on-orbit capabilities. The ability to minimally test the integrated survivability attributes of a system depend almost entirely upon the capabilities to model and simulate the potential hostile actions and environment. This modeling and simulation, to have credibility, is dependent upon data gained through phenomenology measurements of the space environment and blast/thermal/radiation testing of various systems and subsystems for validation. Currently, there are neither sufficient grand scale space environment phenomenological data nor facilities with the requisite blast/thermal/radiation spectra suitable for obtaining sufficient data which can be scaled to provide unquestioned credibility to large scale simulations and models. Further, improvement in computer systems are needed to provide the capacity and speed required for the increasingly complex simulations and the ability to provide verification and validation of the simulation as a creditable test tool.

MULTI-PARTICIPANTS

Evolving military systems are becoming increasingly complex and have a large interdependence between not only space assets, but also airborne, ground and sea components. The growing integration and interdependency is manifested in increasingly complex software and communication systems. Even with today's systems there are insufficient "flight hours" to fully test operational software in the operational environment, and the situation is becoming worse. Currently, using our best techniques on the fastest computers, some estimates indicate test times in terms of "years" of continuous testing will be needed to adequately, but not exhaustively, test some of the near term military applications. The introduction of extensive use of artificial intelligence techniques into the operational and test software systems will exacerbate the test problem by orders of magnitude.

INITIATIVES

In response to the increasing battle space, complexity and interdependence of virtually all classes of weapon systems, earth-environment as well as space, the Department of Defense has initiated a multi-billion dollar investment program to improve and modernize the U.S. national test capabilities base. This program is being implemented through a more encompassing coordination and validation process which will provide an enhanced, integrated approach to test capabilities investment through the individual service budgets. Additionally, Department funding has been earmarked for investment in joint or multi-service use facilities not normally contained within a single service or agency budget. Two of these initiatives bear directly upon improving the ability to test space systems and deserve discussion:

- a. A large, state-of-the-art computational and simulation facility known as the National Test Facility is being pursued under the Strategic Defense Initiative Organization to develop a capability to provide large scale simulations of the multi-platform space based defense concept. The facility will have the necessary computational power to conduct truly global scale simulations as well as the communications capabilities to tie many geographically separated test centers together in real time to conduct hardware-in-the-loop testing. In addition to weapons system testing, this test bed capability is essential in the development and testing of the "testing" concepts and techniques needed for testing future highly integrated and interdependent systems.
- b. The DoD Space Test Capability is a joint service initiative managed by the United States Air Force's new Consolidated Space Test Center to develop a space test range capability. This concept is structured much along the lines of a traditional test range, but will provide for the ability to schedule and internet existing space test assets, as required, into a long term global capability for those testing missions which require such an extended test envelop. Inherent in this initiative is the development of an ability to provide continuous command and control, data collection, tracking and test safety functions necessary for the space testing of advanced systems, including the application of the Global Positioning System to help solve time, space, position indication problems.

Several other initiatives, which have direct application to space testing, as well as earth-environment systems, are structured to improve specific instrumentation and test capability shortfalls such as multi-object tracking radar, hypervelocity test chambers, optical and infrared scene generation techniques, blast/thermal/radiation effects facilities, and potential new, effective testing techniques. However, as ambitious and expensive as these initiatives are, many shortfalls remain in areas such as large scale software integration and test capabilities, large space structure test capabilities, precise spaceborne instrumentation capable of sub-micro radian measurement, and missed distance measurement techniques and instrumentation. With the ever increasing dependence upon large software systems, perhaps the most near term, pressing issue is that of the ability to effectively test and validate massive software systems. Everything done in space today is dependant upon software, from the generation of a command on the ground to the uplink of that command, the receipt, processing and execution of the command, the measurement of the performance or reactions to that command, the processing of the response into a data stream, the transmission of the data to the ground, the reception, decryption and shredout of the data bit and the processing and display to the ground controller. At any point an error introduced by software can completely mask, or even generate false, failures or anomalous performance. This testing shortfall condition exists today, and is becoming exponentially worse as we begin to depend on multi-million lines of code simulations and on-board software systems. The development of effective test techniques to test and validate incorporation of artificial intelligence capabilities on a large scale will be a difficult and expensive process, a testing nightmare and one which has had relatively little exposure within the general test community.

SUMMARY

In summary, the national dependence and complexity of military systems have driven the costs to the point that failure caused by on-orbit testing is unacceptable. In most cases actual testing in space is more attuned to operational check out than testing in the traditional sense. As a result, the exhaustive testing required for a major space system is accomplished on the ground with only that portion of the test program absolutely necessary conducted in space. However, the ever increasing dependence upon the "high ground" of space and interdependence of multiple space and ground based components dictate improved test techniques and new capabilities both for the

ground testing and in the space environment. Large scale simulation with hardware-in-the-loop can be successfully used as the top level, critical method of test if the program is determined early in the concept development phase and is managed with as equal zeal as the weapon development activities. Increasing requirements for precision and ever enlarging envelopes of performance and battle space will force more of the test program to be conducted in the space environment.

Shortfalls in the ability to conduct the necessary space system testing are beginning to be addressed in a new, bold process within the U.S. Department of Defense which attacks the problem on two fronts - 1) a new investment policy for acquisition of specialized test capabilities and major modernization projects for existing activities and facilities, and 2) investigation of new test and evaluation concepts using large scale computer aided techniques.

While unfortunately advances in military space systems will continue to outpace the test and evaluation capabilities in the near term, the first major steps towards resolution have been taken by recognizing that shortfalls exist and their effects upon the decision process. This recognition will set free the creative process in the human mind from which solutions to the insolvable will flow.

REPORT DOCUMENTATION PAGE			
1. Recipient's Reference	2. Originator's Reference	3. Further Reference	4. Security Classification of Document
	AGARD-CP-489	ISBN 92-835-0567-0	UNCLASSIFIED
5. Originator	Advisory Group for Aerospace Research and Development North Atlantic Treaty Organization 7 rue Ancelle, 92200 Neuilly sur Seine, France		
6. Title	SPACE VEHICLE FLIGHT MECHANICS		
7. Presented at	the Flight Mechanics Panel Symposium held in Luxembourg from 13th to 16th November 1989.		
8. Author(s)/Editor(s)	Various		9. Date
			June 1990
10. Author's/Editor's Address	Various		11. Pages
			498
12. Distribution Statement	This document is distributed in accordance with AGARD policies and regulations, which are outlined on the Outside Back Covers of all AGARD publications.		
13. Keywords/Descriptors	<p>Flight characteristics Spacecraft Spacecraft launching</p> <p>Spacecraft recovery, Spacecraft simulation Flight tests. (60)</p>		
14. Abstract	<p>In the last thirty years we have seen a great increase in both manned and unmanned space flights for scientific studies, for communication and navigation, and for military purposes such as surveillance, reconnaissance and as a possible area of deployment for both offensive and defensive weaponry.</p> <p>The possible uses of flight at near-space conditions (i.e. above about 150,000ft.) are also under consideration and, at these heights, many of the technical problems have a common basis with those of space vehicles during the launch, recovery and transatmospheric phases.</p> <p>In all these areas, many problems remain only partly resolved and the relevant technologies are developing rapidly. It was considered that resolution of these problems and finding ways of using new technologies would benefit from the combined thought of the technology communities of the NATO nations. A symposium sponsored by the Flight Mechanics Panel of AGARD was seen as a timely forum for discussions on at least the flight mechanics aspects of this important topic.</p> <p>The symposium included the control and trajectory aspects of launch and recovery, in-orbit dynamics, trans-atmospheric flight and the dynamic aspects of assembly and operation in space and also covered simulation and flight test.</p> <p><i>keywords: Symposia,</i></p>		

<p>AGARD Conference Proceedings No.489 Advisory Group for Aerospace Research and Development, NATO SPACE VEHICLE FLIGHT MECHANICS Published June 1990 498 pages</p> <p>In the last thirty years we have seen a great increase in both manned and unmanned space flights for scientific studies, for communication and navigation, and for military purposes such as surveillance, reconnaissance and as a possible area of deployment for both offensive and defensive weaponry.</p> <p>The possible uses of flight at near-space conditions (i.e. above about 150,000ft.) are also under consideration and, P.T.O.</p>	<p>AGARD-CP-489</p> <p>Flight characteristics Spacecraft Spacecraft launching Spacecraft recovery Spacecraft simulation Flight tests</p>	<p>AGARD Conference Proceedings No.489 Advisory Group for Aerospace Research and Development, NATO SPACE VEHICLE FLIGHT MECHANICS Published June 1990 498 pages</p> <p>In the last thirty years we have seen a great increase in both manned and unmanned space flights for scientific studies, for communication and navigation, and for military purposes such as surveillance, reconnaissance and as a possible area of deployment for both offensive and defensive weaponry.</p> <p>The possible uses of flight at near-space conditions (i.e. above about 150,000ft.) are also under consideration and, P.T.O.</p>	<p>AGARD-CP-489</p> <p>Flight characteristics Spacecraft Spacecraft launching Spacecraft recovery Spacecraft simulation Flight tests</p>
<p>AGARD Conference Proceedings No.489 Advisory Group for Aerospace Research and Development, NATO SPACE VEHICLE FLIGHT MECHANICS Published June 1990 498 pages</p> <p>In the last thirty years we have seen a great increase in both manned and unmanned space flights for scientific studies, for communication and navigation, and for military purposes such as surveillance, reconnaissance and as a possible area of deployment for both offensive and defensive weaponry.</p> <p>The possible uses of flight at near-space conditions (i.e. above about 150,000ft.) are also under consideration and, P.T.O.</p>	<p>AGARD-CP-489</p> <p>Flight characteristics Spacecraft Spacecraft launching Spacecraft recovery Spacecraft simulation Flight tests</p>	<p>AGARD Conference Proceedings No.489 Advisory Group for Aerospace Research and Development, NATO SPACE VEHICLE FLIGHT MECHANICS Published June 1990 498 pages</p> <p>In the last thirty years we have seen a great increase in both manned and unmanned space flights for scientific studies, for communication and navigation, and for military purposes such as surveillance, reconnaissance and as a possible area of deployment for both offensive and defensive weaponry.</p> <p>The possible uses of flight at near-space conditions (i.e. above about 150,000ft.) are also under consideration and, P.T.O.</p>	<p>AGARD-CP-489</p> <p>Flight characteristics Spacecraft Spacecraft launching Spacecraft recovery Spacecraft simulation Flight tests</p>